Proceedings of:

The Seventeenth Annual Meeting

The American Society for Precision Engineering

October 20-25, 2002
Hyatt Regency St. Louis at Union Station
St. Louis, Missouri

The American Society for Precision Engineering (ASPE) is a multidisciplinary professional and technical society concerned with research and development, design, manufacture and measurement of high accuracy components and systems. ASPE activities encompass relevant aspects of mechanical, electronic, optical and production engineering, physics, chemistry, and computer and materials science. Membership is open to anyone interested in any aspect of precision engineering.

Founded in 1986, ASPE provides a new focus for a diverse but important community. Other professional organizations have covered aspects of precision engineering, always as a sideline to their principal goals. ASPE is based on the core of generic concepts necessary to achieve precision in any application; independent of discipline, ASPE intends to be the focus for precision technology — and to represent all facets from research to application.

ASPE — The American Society for Precision Engineering
301 Glenwood Avenue, Suite 205, Raleigh, NC 27603
P.O. Box 10826, Raleigh, NC 27605
Telephone: (919) 839-8444 Fax (919) 839-8039

Preface

This book comprises the proceedings of the 2002 Annual Meeting. The contributions reflect the authors' opinions and are published as presented to ASPE, without change. Their inclusion in this publication does not necessarily constitute endorsement by the ASPE, or its editorial staff.

Individual readers of this book and nonprofit libraries acting for them are permitted to make fair use of the material contained in this book to be used in teaching or research; provided they copy said paper in total, as written by the author. Permission is granted to quote excerpts from the scientific or technical works in this book with proper acknowledgment of the source to include: The author's name, the book name, and the ASPE tag line. Reproduction of figures and tables is likewise permitted from the contents of this book, provided that the same acknowledgment of the same source and content is permitted.

Any other type reproduction, systematic copying or multiple reproduction of any material in this book is expressly prohibited except with the written permission of the ASPE editorial staff, addressed to the Society's headquarters.

ISBN 1-887706-29-1

2002

American Society for Precision Engineering
301 Glenwood Avenue, Suite 205
Raleigh, NC 27603

Printed in the United States of America

Welcome Note

The American Society for Precision Engineering celebrates its Seventeenth Annual Meeting this year in St. Louis, Missouri. The remarkable growth and success of the Society is reflective of the increasing importance of precision engineering in a wide variety of fields of endeavor, from manufacturing to microelectronics to basic science. The Society serves as a focus for precision engineers across all of these fields. The Annual Meeting has evolved into a premier international forum for the exchange of ideas and presentation of research results relating to precision engineering, metrology, controls, and system integration. Precision engineers and scientists from private industry, government laboratories, and universities meet to learn about the latest developments and to exchange ideas about the future directions of these technologies.

This year's meeting continues the tradition of offering two full days of tutorials presented by some of the foremost precision engineers and scientists in the world. Many participants cite the tutorial program as one of the most valuable features of the meeting. The technical sessions and poster presentations offer the latest research results in the areas of ultraprecision machining, metrology, controls, precision grinding, micro-positioning, material processing, design, precision transducers, surface profilometry, machine tool metrology, and error compensation. The commercial exhibit will provide attendees with the opportunity to view and discuss the latest precision engineering equipment, products, and services that are commercially available. The open forum will give attendees the opportunity to express their opinions and pose questions for discussion by the group, enhancing the exchange of information.

The conference organizing committee is proud to present the program for the Seventeenth Annual Meeting of the ASPE. We welcome your participation.

Welcome to St. Louis.

2002 Organizing & Technical Program Committee

Jeffrey W. Carr, Chairman,
Lawrence Livermore National Laboratory

Vivek G. Badami, Corning Tropel Corporation
James F. Cuttino, University of North Carolina at Charlotte
Thomas A. Dow, North Carolina State University
Anthony E. Gee, Cranfield University
Bradley H. Jared, Corning Inc.
Bernhard Jokiel, Jr., Sandia National Laboratories
Patrice Kerevel, Corning Inc.
Don A. Lucca, Oklahoma State University
Stephen J. Ludwick, Aerotech, Inc.
Eric R. Marsh, The Pennsylvania State University
E. Ray McClure, Consultant
Michele H. Miller, Michigan Technological University
Alex Sohn, North Carolina State University
R. Ryan Vallance, University of Kentucky

2002 Scholarship Recipients

Anastasios John Hart, Massachusetts Institute of Technology
R.V. Jones Memorial Scholarship

Bala Muralikrishnan, University of North Carolina at Charlotte

2002 Annual Meeting
Contents

Preface ii

Welcome Note iii

Organizing Committee — 2002 Scholarship Recipients iv

Sponsor Members vi

Cooperating Sponsors—Technical Exhibitors vii

Program viii

Keynote Address ix

2002 Lifetime Achievement Awards x

Commercial Session/Open Forum 1

Technical Paper Index 2-10

Technical Papers 13-692

Authors Index 693-696

Sponsor Members of the ASPE

3M Company
St. Paul, MN 55144-1000
Contact: William J. Bryan
(651) 575-1465

ADCOLE Corporation
Marlborough, MA 01752
Contact: Addison D. Cole
(508) 485-9100

Agilent Technologies
Santa Rosa, CA 95403
Contact: Paul Lomeli
(707) 577-5514

Chardon Tool & Supply Company, Inc.
Chardon, OH 44024
Contact: Weldon Bennett
(440) 286-6440

Contour Fine Tooling, Inc.
Marlborough, NH 03455
Contact: Jeffrey Tomlin
(603) 876-4908

Corning Inc.
Corning, NY 14831
Contact: John Thomas
(607) 974-3842

Corning Tropel Corporation
60 O'Connor Road
Fairport, NY 14450
Contact: John H. Bruning
(585) 388-3400

Cranfield Precision, Div. of Landis Lund
A Western Atlas Corporation
Cranfield, Bedford MK43 OAL, England
Contact: Edric M. E. Brown
011-44-1234-754222

DAC International, Inc.
Carpinteria, CA 93013
Contact: James W. Drain
(805) 684-8307

Dover Instrument Corporation
Westboro, MA 01581
Contact: Michael Townsend
(508) 366-1456

Fabreeka International, Inc.
Stoughton, MA 02072
Contact: Robert P. Haley
(781) 341-3655

Fisba Optik, LLC
Rochester, NY 14623
Contact: John J. Nemechek
(716) 427-9155

ITW Polymer Castings
Chardon, OH 44024
Contact: Brian Eaton
(440) 286-9714

Lion Precision
St. Paul, MN 55126
Contact: Don L. Martin
(651) 484-6544

Mahr Federal, Inc.
Providence, R.I. 02940-9400
Contact: Robert A. Frick
(401) 784-3313

MicroE Systems, Inc.
Natick, MA 01760-1313
Contact: Donald K. Mitchell
(508) 903-5000

Mitutoyo America Corporation
Aurora, IL 60504-9102
Contact: Mark T. Izumi
(630) 820-9666

Moore Tool Company, Inc.
Bridgeport, CT 06607-0088
Contact: Kevin Uhlig
(203) 366-3224

Nano Corporation
Tokyo 146-0085, Japan
Contact: Akira Hayashi
011-81-3-3751-3311

New Way Machine Components
Aston, PA 19014
Contact: Andrew J. Devitt
(610) 494-6700

Philips CFT
Sunnyvale, CA 94085
Contact: Joe Spano
(408) 617-2445

Precitech, Inc.
Keene, NH 03431
Contact: David W. Davis
(603) 357-2511

Professional Instruments Company
Hopkins, MN 55343
Contact: James Arneson
(952) 933-1222

Reflexite-Precision Technology Center
West Henrietta, NY 14586
Contact: Steven M. Scott
(585) 272-0309

Seagate Technology
Scotts Valley, CA 95067
Contact: Bernd M. Seeger
(831) 439-3781

Veeco Instruments, Inc.
Tucson, AZ 85706
Contact: Chip Ragan
(520) 741-1044

Zygo Corporation
Middlefield, CT 06455-0448
Contact: Robert A. Smythe
(860) 704-8506

Cooperating Sponsors

Elsevier Science, Inc.

euspen – European Society for Precision Engineering and Nanotechnology

Japan Society for Precision Engineering

Technical Exhibitors

ADE Phase Shift

A.L.M.T. Corporation

Center for Precision Metrology—University of N.C. at Charlotte

Chardon Tool

Contour Fine Tooling, Inc.

CoorsTek, Inc.

Corning Tropel Corporation

Excel Precision Corporation

Fabreeka International, Inc.

Heidenhain Corporation

K & Y Diamond Ltd.

Kinetic Ceramics, Inc.

Kriterion

Lion Precision

Machine Dynamics Research Lab.—Penn State University

Mitutoyo America Corporation

Moore Nanotechnology Systems, LLC

New Way Machine Components, Inc.

Philips CFT

Polytec PI, Inc.

Precision Engineering Center—N.C. State University

Precitech, Inc.

Professional Instruments Company, Inc.

QED Technologies

Trechmetals, Inc.

Technodiamant, Inc.

Veeco Metrology Group

Program

2002 ASPE Annual Meeting

Time	Sun., Oct. 20	Mon., Oct. 21	Tues., Oct. 22	Wed., Oct. 23	Thurs., Oct. 24	Fri., Oct. 25
8:00						
9:00	Tutorials	Tutorials and Business Forum	Technical Session I	Technical Session III	Technical Session VI	Optional Tours
10:00			Break	Break	Break	
11:00			Technical Session II	Technical Session IV	Technical Session VII	
12:00			Lunch and Committee Meetings	Awards Lunch and Business Meeting	Lunch and Roundtable Discussions	
1:00						
2:00	Tutorials	Tutorials and Business Forum	Commercial Session	Poster Session II	Technical Session VIII	
3:00			Break	Break		
4:00			Poster Session I	Technical Session V		
5:00			Hospitality Hour	Hospitality Hour		
6:00						
7:00		Keynote Address	Dinner at the Arch			
8:00		Welcome Reception				
9:00						

Business Forum

Monday, October 21, 8:00 a.m. - 4:00 p.m.

Session Chairman: Dan E. Luttrell, Luttrell & Associates, LLC

The ASPE Executive Forum, which has been very popular in previous years, will be recast this year as the ASPE Business Forum. This forum is open to all attendees of the annual meeting and will be of particular benefit to those with interests in business or the management of technology. The program will combine business and technology issues pertinent to leaders in the precision engineering community. It will be held this year on Monday October 21, 2002, just prior to the start of the formal ASPE meeting and overlapping one day with the Tutorial Program. The session will be organized and chaired Dan E. Luttrell of Luttrell & Associates, LLC. The program will consist of a continental breakfast, morning and afternoon talks, a lunch break, and ample time to network with speakers and other attendees. The forum should conclude by mid-afternoon. As the talks are finalized they will be posted on the ASPE web site.

Keynote Address

Walter H. F. Smith

Monday, October 21, 6:30 p.m.

Session Chair: Jeffrey W. Carr, Lawrence Livermore National Laboratory

Dr. Walter Smith became interested in topography and mountain building processes while backpacking in the Sierra Nevada mountains as a teenager. He took his first geology course at Cuesta Community College in San Luis Obispo, and later earned the B.Sc. from the University of Southern California and the M.A., M.Phil. and Ph.D. from Columbia University. He worked in the Gravity Department of Columbia's Lamont-Doherty Geological Observatory, carrying out sea-going geophysical studies of seamounts on the ocean floor, and restructuring Lamont's data base software to permit global searching. Out of this grew the graphics software that he and Paul Wessel distribute freely over the Internet (http://gmt.soest.hawaii.edu). After the Ph.D., a Fellowship from the Cecil and Ida Green Foundation drew him to the Scripps Institution of Oceanography, where he began his collaboration with Prof. David Sandwell on the applications of satellite altimetry in ocean exploration. While at Scripps, Walter went on his fourth oceanographic cruise, unfortunately, during the wrong season: five typhoons disrupted his work. This, plus the increasing availability of new satellite data, encouraged his transition from sea-going scientist to desk-sitting, satellite-using modeler. Since 1992 he has been a Geophysicist in the Laboratory for Satellite Altimetry of the National Oceanic and Atmospheric Administration (NOAA) in Silver Spring, Maryland, where he applies real-time precision measurements of sea level from space to problems in ocean mapping and climate and hurricanes. His work on ocean floor mapping from space has been recognized with several awards and is the subject of this year's keynote address.

Mapping the Ocean Floor

The surfaces of the Moon, Mars, Venus, and Earth's land areas are much better mapped that the Earth's ocean floors. Orbiting vehicles can see dry planetary surfaces, but direct sensing of the ocean floor can only be done acoustically from vehicles on or in the water. Acoustic mapping is a slow process: a complete survey of the oceans would take hundreds of years of ship time at a cost of billions of dollars. Existing sounding data coverage leaves gaps; areas as large as Mid-western U.S. states (10^5 km^2) are devoid of even a single measurement. We have developed a means for mapping the ocean floors from space via an indirect technique using the Earth's gravity field. Ocean floor topography causes gravity anomalies that distort the ocean surface in ways that can be measured from space by a radar altimeter. Correlation between seafloor topography and sea surface shape is best in a band of (full-) wavelengths between 160 and 10 km, and ocean surface height changes, or slopes, must be measured in this band to reveal seafloor topography. Existing altimeter data resolve slopes to a precision of about 5 microradians (1 mm change in ocean surface height per 1 km of horizontal distance) and this is sufficient to reveal topography down to 30 km wavelengths. These data have confirmed the plate tectonic theory to first order but also revealed second order mysteries in how seafloor spreading works. As yet unmapped is the 10 km to 30 km wavelength band, a crucial control on ocean mixing rates required for modeling future sea level rise and climate change. A space-based measurement of sea surface slope to 1 microradian could obtain the necessary resolution using a proven technique - delay-Doppler altimetry - in a mission of 4 to 6 years duration, at a cost of about $60M. We have proposed such a mission and have also shown that the orbit of the International Space Station is ideal for this purpose. This talk will show some of the ocean science issues and also highlight the innovations and challenges in making the precise measurements the science requires.

2002 Lifetime Achievement Awards

Horst Kunzmann

Horst Kunzmann has made major contributions to the discipline of precision engineering both inside his own country and internationally. He joined the Physikalisch-Technische Bundesanstalt in 1966 in the "Line Scale Metrology" section and has never lost his love for ultra-precision measurement and the practical realization of the meter which is central to precision engineering.

While at PTB he earned his Dr.-Ing. Degree from the Technical University of Hanover in 1971. His promotions within this outstanding national laboratory were impressive. He became Head of Division in 1985 and created "Precision Engineering" at PTB leading three departments, Micrometrology, Dimensional Metrology, and Measuring Instruments Technology. In the early '90s he spearheaded the efforts to integrate the then "East German" precision engineering efforts into a national whole, an effort that was successful due to his personal and managerial skills. He is now a member of the Presidential Board of PTB and the head of PTB metrology activities for industry, the German Calibration Service and the Competence Center for Ultra-precise Surface Figure Measurement. As a leader and manager he is exemplary, but his contributions in the laboratory were also impressive. He led the international efforts to use lasers for metrology including straightness. Against serious opposition from those preferring the older light sources, he successfully developed and championed the use of frequency stabilized gas lasers as the practical length standard, an achievement which has dramatically altered metrology in our times. He also rebuilt the PTB program in Industrial Metrology bringing it into worldwide prominence introducing diamond turning and "factory floor" metrology.

He has more than 80 publications in our discipline in subjects ranging from laser applications to coordinate metrology. He also has 10 patents in the area of precision engineering. He is a great engineer with dedication, curiosity, kindness, insight, courage, and engineering know-how, an example to us all and an extremely deserving recipient of the ASPE Lifetime Achievement Award.

David J. Whitehouse

Dr. David Whitehouse has had a long and distinguished career as a designer of dimensional metrology instruments and the inventor of algorithms for processing data from these instruments. He holds 22 patents. He has written more than 200 technical papers and 5 books including the 1,000 page "Handbook of Surface Metrology" which is widely regarded as a classic in the field. His new book, "Handbook of Surface and Nanotechnology" (1100 pages) will be published in 2003.

Dave is often referred to as the "Father of Digital Metrology".

1) He was the first to rigorously define the mean line in the M-System of surface measurement and predict the output of a 2RC analog filter for any surface.

2) He was the first to implement a phase corrected filter.

3) He was the first to digitize and process surface metrology data to automatically evaluate the various surface parameters.

4) He was the first to digitize and process roundness metrology data to automatically determine the minimum radial zone (MRZ) center as well as the centers of partial arc measurements used in the ball bearing industry.

These algorithms are now provided as standard in all roundness and surface finish instruments produced throughout the world.

Dave's present interest is the rationalization of surface parameters in accordance with the systems approach using what he calls a "function map".

Dr. Whitehouse is a charter member of ASPE. He is an Active Member of CIRP, and a past President of the Committee for Surface Roughness. He is a Fellow Member of the U.K. Institute of Physics, the Institute of Measurement and Control, the Institution of Production Engineers, and the Institution of Electrical Engineers. He is an Honorary Member of The Japanese Institution of Precision Engineers and a Senior Member of the Chinese Society of Mechanical Engineers. He has received many honors throughout the world including the commemorative medallion of the Mendeleeve Institute of Metrology, Lenningrad, USSR.

Dr. Whitehouse is presently an Emeritus Professor of Engineering Science at the University of Warwick, a Guest Professor at the University of Tianjin in P.R. China, and Consultant Professor at the University of Harbin, P.R. China. He was previously a Professor and the Chief Scientist of the Dept. of Engineering at Warwick. He had a long career at Rank Taylor Hobson in Leicester. He started as a research engineer in 1961 as the protégé of Bill Reason, and completed his career in 1978 as Chief Research Engineer. He holds a Ph.D. as well as a D.Sc. from the University of Warwick.

Commercial Session / Open Forum

Tuesday, October 22, 1:30 - 3:00 p.m.

Session Chairman: William J. Bryan, 3M Company

The Commercial Session/Open Forum will take place early in the week on Tuesday afternoon. This is a special session where companies and participants are free to open discussions on a less-formal basis and to promote interaction on a variety of topics. In the first part of this session, company representatives are invited to make brief presentations (5 minutes) on new products associated with precision engineering. This provides participants with the opportunity to receive timely information on new technologies that have been commercialized into products and services, as well as information on advances that can be expected in the near future. In the second half, the floor is open to conference participants to discuss any topic of interest to the Society. So bring your overheads, problems, and experiences to this enlightening session of impromptu discussions! Sign up sheets will be available at the conference.

Technical and Poster Sessions Index

The technical program for the 2002 ASPE Annual Meeting contains over 144 papers on precision engineering advances. Papers that lent themselves to significant verbal interaction, concise but important discoveries, or strongly visual or tactile subjects have been selected for the poster session. Authors will be present to discuss their work on Tuesday, October 22, from 3:30 to 5:00 p.m., and again on Wednesday, October 23, from 1:30 to 3:00 p.m.

Session I
New Directions in Precision Engineering

Tuesday, October 22, 2002, 8:00 AM - 10:00 AM

Session Chair: Michele H. Miller (Michigan Technological University)

1. ***Requirements for Precision Engineering in the Development of Miniaturized Diagnostic Systems (Invited Paper)***
   Müller, U. R.; Patno, T.; Cork, W.; Marla, S.; Storhoff, J.; Garimella, V. (Nanosphere, Inc.); and Bao, P.; Yuen, P. K. (Corning Inc.) . . . . . page 13
2. ***Precision Requirements in Photonics Automation and Assembly (Invited Paper)****
   Formica, M. K. (Axsys Technologies, Inc.)
3. ***Innovative Dimensional Metrology of Meso-Scale Fusion Targets (Invited Paper)****
   Sebring, R. (Los Alamos National Laboratory)

Session II
Manufacturing at the Small Scale

Tuesday, October 22, 2002, 10:30 AM - 12:00 PM

Session Chair: Bernhard Jokiel, Jr. (Sandia National Laboratories)

1. ***Development of Micro Grinding Process Using Micro EDM Trued Diamond Tools (Invited Paper)***
   Wada, T.; Masaki, T. (Matsushita Electric Industrial Co., Ltd); and Davis, D. W. (Precitech, Inc.) . . . . . page 16
2. ***High Aspect Ratio SNOM Probe Fabricated Using Electron Beam Deposition and Focused Ion Beam***
   Tsuchiya, K.; Ooi, T.; Sakamaki, Y.; Nakao, M. (The University of Tokyo) . . . . . page 20
3. ***Smart Palm-size Injection Mold Using Zone-In-Cavity and Cycle-by-Cycle Process Controls to Precisely Replicate Miniature Products***
   Yoda, M.; Nakao, M. (The University of Tokyo) . . . . . page 24
4. ***Microscale Patterning of PZN-PT Single Crystals by Laser-induced Etching***
   Moon, K. S.; Levy, M.; Hong, Y. K.; Ghimire, S. (Michigan Technological University) . . . . . page 27

* *Abstract unavailable at press time*

Session III

Precision in Wafer Scale Processing

Wednesday, October 23, 2002, 8:15 AM - 10:00 AM

Session Chair: R. Ryan Vallance (University of Kentucky)

1. ***Advanced CMP Wafer Profile Control Using Multizone Carrier Technology (Invited Paper)****
   Ferra, M.; Schlueter, J.; Korovin, N.; Tushingham, R.; Epsheynk, Y. (SpeedFam-IPEC)
2. ***Investigation of Thermo-chemical Polishing and Laser Ablation of CVD Diamond Film***
   Chao, C. L. Liu, Y. H.; (Tam-Kang University); Ma, K. J. (Chung-Hwa University); Chen, T. T. (Chung-Cheng Institute of Technology); and Lin, H. Y.; Chang, Y. M. (Industrial Technology Research Institute) . . . . . page 32
3. ***Corrective Planarization Method Using Chemical Mechanical Polishing Assisted by Laser Particle Trapping***
   Kimura, K. (Sony EMCS Corporation); and Miyoshi, T.; Takaya, Y.; Takahashi, S. (Osaka University) . . . . . page 37
4. ***New Optical Measurement Technique for Si Wafer Surface Defects Using Annular Illumination with Crossed Nicols***
   Takahashi, S.; Miyoshi, T.; Takaya, Y. (Osaka University); and Abe, T. (Seiko Epson Corporation) . . . . . page 41

Session IV

Standards in Metrology

Wednesday, October 23, 2002, 10:30 AM - 12:00 PM

Session Chair: Vivek G. Badami (Corning Tropel Corporation)

1. ***A Tool for Determining Task-specific Measurement Uncertainties in GD&T Parameters Obtained from Coordinate Measuring Machines***
   Summerhays, K. D.; Henke, M. P.; Henke, R. P.; Baldwin, J. M. (MetroSage, LLC); and Brown, C. W. (Honeywell, Inc.) . . . . . page 47
2. ***White-light Interferometer with Internal Length Standard***
   Schmit, J.; Novak, E. L.; Olszak, A. G. (Veeco Metrology) . . . . . page 53
3. ***Film Thickness Standards on the Nanometer Scale***
   Hasche, K.; Ulm, G.; Herrmann, K.; Krumrey, M.; Ade, G.; Stümpel, J.; Busch, I.; Thomsen-Schmidt, P. (Physikalisch-Technische Bundesanstalt (PTB)); Schädlich, S. (Fraunhofer Institute for Material and Beam Technology (IWS)); Schindler, A.; Frank, W. (Institute for Surface Modification (IOM)); and Procop, M.; Beck, U. (Federal Institute for Material Research and Testing (BAM)) . . . . . page 57
4. ***Atomic Force Microscopy of Semiconductor Line Edge Roughness***
   Orji, N. G.; Raja, J. (University of North Carolina at Charlotte); and Vorburger, T. V. (National Institute of Standards and Technology) . . . . . page 63

Session V

Optical Metrology

Wednesday, October 23, 2002, 3:30 PM - 5:00 PM

Session Chair: Anthony E. Gee (University College - London)

1. ***Miniature Interferometers for Precise Distance Measurements (Invited Paper)***
   Schott, W. (SIOS Meßtechnik GmbH); and Jäger, G. (Technical University of Ilmenau) . . . . . page 67
2. ***Figure Metrology of a Free-Form Optical Surface***
   Sohn, A., Garrard, K. P. (North Carolina State University); and Ohl, R. G.; Mink, R.; Chambers, V. J. (NASA/Goddard Space Flight Center) . . . . . page 73

* *Abstract unavailable at press time*

3. **A Metrological Atomic Force Microscope**
Stein, A. J.; Trumper, D. L. (Massachusetts Institute of Technology); and Hocken, R. J. (University of North Carolina at Charlotte) . . . page 77
4. **Effects of Varying Incident Angle on the Contrast of the Fringe Metrology Using a Fresnel Zone Plate**
Joo, C.; Pati, G. S.; Chen, C. G.; Konkola, P. T.; Heilmann, R. K.; Schattenburg, M. L. (Massachusetts Institute of Technology); and Liddle, A.; Anderson, E. H. (Lawrence Livermore National Laboratory) . . . page 83

Session VI
Advances In Traditional Manufacturing
Thursday, October 24, 2002, 8:15 AM - 10:00 AM

Session Chair: James F. Cuttino (University of North Carolina at Charlotte)

1. **Machining of Monolithic Aerospace Components (Invited Paper)***
Smith, S. (University of North Carolina at Charlotte)
2. **Fast Optical Form Measurements of Rough Cylindrical and Conical Surfaces in Diesel Fuel Injection Components**
Dunn, T. J.; Michaels, R.; Lee, S.; Tronolone, M. J.; Kulawiec, A. W. (Corning Tropel Corporation) . . . page 89
3. **Piezoelectric Tool Actuator for Precision Machining on Conventional CNC Turning Centers**
Woronko, A.; Huang, J.; Altintas, Y. (The University of British Columbia) . . . page 94
4. **Evaluation of One- and Two-sided Geometric Fitting Algorithms in Industrial Software**
Shakarji, C. M. (National Institute of Standards and Technology) . . . page 100

Session VII
Precision Surfaces
Thursday, October 24, 2002, 10:30 AM - 12:00 PM

Session Chair: Bradley H. Jared (Corning Inc.)

1. **Influences on the Polishing Processes of Optical Glasses Using Synchrospeed-Kinematics**
Klocke, F.; Dambon, O. (Fraunhofer Institut für Produktionstechnologie) . . . page 105
2. **Burnishing of Hardened Steel Components – An Alternative Method of Finishing**
Luca, L.; Neagu-Ventzel, S.; Marinescu, I. D. (The University of Toledo) . . . page 110
3. **Elliptical Vibration Assisted Diamond Turning**
Dow, T. A.; Negishi, N.; Sohn, A. (North Carolina State University) . . . page 115
4. **High Precision Photomask Polishing with Magneto-Rheological Finishing (MRF)**
Tricard, M.; Golini, D. (QED Technologies) . . . page 120

Session VIII
Errors Sources in Precision Manufacturing
Thursday, October 24, 2002, 1:30 PM - 3:00 PM

Session Chair: Patrice G. Kerevel (Corning Inc.)

1. **Error Budget as a Design Tool for Ultra-Precision Diamond Turning Machines**
Walter, M. M.; Norlund, B.; Koning, R. J.; Roblee, J. W. (Precitech, Inc.) . . . page 126
2. **Prediction of Surface Location Error by Time Finite Element Analysis and Euler Integration**
Schmitz, T. L.; Soons, J. A.; Dutterer, B. (National Institute of Standards and Technology); and Bayly, P. V. (Washington University in St. Louis) . . . page 132
3. **Bonding Fixture Tolerances for High-Volume Metal Microlamination Based on Fin Buckling and Laminae Misalignment Behavior**
Wattanutchariya, W. (Chiangmai Univeristy); and Paul, B. K. (Oregon State University) . . . page 138
4. **Six Degree of Freedom Optical Sensor for Dynamic Measurement of Linear Axes**
Kroll, J. J.; Patterson, S. R. (University of North Carolina at Charlotte) . . . page 144

* *Abstract unavailable at press time*

Poster Session I

Tuesday, October 22, 2002, 3:30 PM - 5:00 PM

EQUIPMENT, MACHINES & INSTRUMENTS

Analysis & Modeling

1. ***Visual Based Motion Error Compensation for Precise Versatile Micro Robot***
   Fuchiwaki, O.; Aoyama, H. (University of Electro-Communications) . . . . . page 148
2. ***2 DOF Dynamic Accuracy Monitoring for Robot and Machine Tool Manipulators***
   Hanak, T.; Zirn, O.; Ruoff, W. (University of Applied Sciences (FHTE)) . . . . . page 152
3. ***Kinematic Coupling Interchangeability***
   Hart, A. J.; Slocum, A. H. (Massachusetts Institute of Technology) . . . . . page 158
4. ***Novel Linear Motor for High Precision Stage of Semiconductor Lithography System***
   Lee, M-G.; Kim, K.; Gweon, D-G. (Korea Advanced Institute of Science & Technology) . . . . . page 162
5. ***Construction and Alignment of a Kolsky Bar Apparatus***
   Rhorer, R. L.; Kennedy, M. D.; Dutterer, B. S.; Burns, T. J. (National Institute of Standards and Technology); and Davies, M. A. (University of North Carolina at Charlotte) . . . . . page 166
6. ***NanoSlider Modeling and Waveform Adaptation for Positioning Control***
   Shim, J. Y.; Kim, K.; Gweon, D-G. (Korea Advanced Institute of Science & Technology) . . . . . page 170

Controls

1. ***Track/Focus Control of Cantilever Type Near Field Optical Head for High Density and Fast Data Transfer Rate Data Storage Device***
   Lee, S-Q.; Song, K-B.; Kim, J-H.; Kim, E-K.; Park, K-H. (Electronics and Telecommunications Research Institute (ETRI)) . . . . . page 176

Design & Testing

1. ***An Instrument for Characterizing Stiffness of Protruding Optical Fibers***
   Carter II, J. A.; Shreve, S. M.; Vallance, R. R. (University of Kentucky); and Kiani, S.; Lehman, J. (Teradyne Connection Systems) . . . . . page 182
2. ***Precision Instrument for Characterizing Contraction and Extension of Nitinol Wire***
   Chikkamaranahalli, S. B.; Vallance, R. R.; Rawashdeh, O. A; Lumpp, J. E.; Walcott, B. L. (University of Kentucky) . . . . page 187
3. ***Segmented and Shielded Structures for Reduction of Thermal Expansion-Induced Tilt Errors***
   Hart, A. J.; Slocum, A. H. (Massachusetts Institute of Technology) . . . . . page 193
4. ***Design of a Dual Servo XYtheta Stage Using Double H Frame***
   Kim, K.; Lee, M-G.; Kim, D. M.; Gweon, D-G. (Korea Advanced Institute of Science & Technology) . . . . . page 199
5. ***System Design Methodology for Precision Layout Machines***
   Kim, M-S.; Chung, S-C. (Hanyang University) . . . . . page 204
6. ***A Study on Evaluation of Conceptual Designs of Machine Tools***
   Mishima, N. (National Institute of Advanced Industrial Science & Technology) . . . . . page 210
7. ***Spindle Motor Driven by Fluid Energy for Ultra-precision Machine Tool***
   Nakao, Y.; Mimura, M. (Kanagawa University) . . . . . page 215
8. ***New Die Design System for Injection Molding Using Multivariate Analysis***
   Nitoh, S.; Kobayashi, Y.; Shirai, K. (Nihon University) . . . . . page 219
9. ***Measurement and Calibration of High Accuracy Spherical Joints***
   Robertson, A. P.; Rzepniewski, A.; Slocum, A. H. (Massachusetts Institute of Technology) . . . . . page 223
10. ***Guidelines for Design Low Cost Micromechanics***
    Ruiz-Huerta, L.; Caballero-Ruiz, A.; Kussul, E. (Universidad Autónoma de México) . . . . . page 228

Mechatronics

1. ***Dynamic Displacement Measurement of PZN-PT Unimorph Microactuators Using Atomic Force Microscopy***
   Moon, K. S.; Levy, M.; Hong, Y. K.; Ghimire, S. (Michigan Technological University) . . . . . page 234

MEMS & Nanotech

1. **A 2D Optical Displacement Transducer to Measure Measure Nanometric Errors in Precision Machines**
   Albertazzi Jr., A.; Sousa, A. R.; Veiga, C. L.; Willemann, D. P. (Federal University of Santa Catarina) . . . . . page 238
2. **Precision Assembly and Metrology of X-ray Foil Optics**
   Forest, C. R.; Spenko, M. J.; Sun, Y.; McGuirk, M.; Slocum, A. H.; Schattenburg, M. L. (Massachusetts Institute of Technology) . . . . . page 244
3. **Development of Thin Film Actuator Using Electrostrictive Phenomena**
   Jung, Y.; Jeong, E.; Jeong, H. D.; Park, H.; Jo, N. (Pusan National University) . . . . . page 250
4. **Mesoscale Piezo-Motors: Scaling Issues and Performance Measurement**
   Leinvuo, J. T.; Wilson, S. A.; Whatmore, R. W.; Gee, A. E. (University College - London) . . . . . page 256
5. **Precision Microcomb Design and Fabrication for Constellation-X Spectroscopy X-ray Telescope Segmented Optic Assembly**
   Sun, Y.; Heilmann, R. K.; Chen, C. G.; Spenko, M. J.; Forest, C. R.; Schattenburg, M. L. (Massachusetts Institute of Technology) . . . . . page 261
6. **Thermal Energy Conversion Using a Microfabricated Shape Memory Alloy Structure**
   Zhang, Y.; Tran, H. D. (University of New Mexico) . . . . . page 267

Novel Systems

1. **Artificial Insemination System by Male and Female Micro Robots**
   Aoyama, H.; Takubo, H. (University of Electro-Communications) . . . . . page 271
2. **Precision Machining of Steel with Ultrasonically Driven Chilled Diamond Tools**
   Brinksmeier, E.; Gläbe, R. (Bremen University) . . . . . page 275
3. **Design of Accurate and Repeatable Kinematic Couplings**
   Culpepper, M. L.; Araque, C. A.; Rodriguez, M. E. (Massachusetts Institute of Technology) . . . . . page 279
4. **HexFlex: A Planar Mechanism for Six-axis Manipulation and Alignment**
   Culpepper, M. L.; Anderson, G. A.; Petri, P. A. (Massachusetts Institute of Technology) . . . . . page 285
5. **Kinematic and Stiffness Analysis of a Novel Ortho-guided Tripod Machine Tool**
   Hsu, W-Y.; Chen, J-S. (National Chung-Cheng University) . . . . . page 291
6. **Micro Turning System: A Super Small CNC Precision Lathe for Microfactories**
   Ito, S.; Iijima, D.; Hayashi, A.; (Nano Corporation); Aoyama, H. (University of Electro-Communications); and Yamanaka, M. (Tohoku University) . . . . . page 295
7. **Operation and Analysis of a Nanopositioning and Nanomeasuring Machine**
   Jäger, G.; Manske, E.; Hausotte, T. (Technical University of Ilmenau); and Schott, W. (SIOS Meßtechnik GmbH) . . . . . page 299
8. **Linear Motion Carriage Driven and Guided by Elastically Supported and Preloaded Lead Screw Nuts**
   Slocum, A. H.; Elmouelhi, A.; Lawrence, T.; How, P.; Cattell, J. (Massachusetts Institute of Technology) . . . . . page 305
9. **Development of a Micro Cutting and Deforming System for Glass Materials**
   Warisawa, S.; Karino, T.; Tangpornprasert, P.; Mitsuishi, M. (The University of Tokyo) . . . . . page 310

METROLOGY

Analysis & Modeling

1. **Design and Analysis of a Nano-stepping Device**
   Gao, Y.; Liu, X.; Yuen, K. (Hong Kong University of Science and Technology) . . . . . page 316
2. **Gross Measurement Error Identification Using the Grey System Theory**
   Wang, Z. (Henan University of Science and Technology); Gao, Y.; Tse, S. (Hong Kong University of Science and Technology); and Qin, P. (Xi'an Jiaotong University) . . . . . page 320
3. **Large Array Thermal Machine Monitor**
   Zhang, S.; Patterson, S. R. (University of North Carolina at Charlotte) . . . . . page 324

Form & Geometry

1. **Cutting Error Measurement of Harmonic Drive Gears Using Laser Probes**
   Furukawa, M.; Gao, W.; Kiyono, S. (Tohoku University); and Yamazaki, H. (Harmonic Drive Systems Inc.) . . . . . page 328
2. **In-process Measurement of Topography of Grinding Wheel by Using Hydrodynamic Pressure**
   Furutani, K. (Toyota Technological Institute); Ohguro, N. (Daikin Industries, Ltd.); and Nguyen, H. T.; Nakamura, T. (Nagoya Institute of Technology) . . . . . page 332

3. ***Precision Measurement of Aircraft Control Surface Axis Alignment Over 1-3m Scales****
Gee, A. E. (University College - London) . . . . . page 338

4. ***Development of Spherical Form Errors Measuring System — Design and Some Experimental Results***
Kawa, H.; Kanada, T.; Watanabe, T. (Kanto Gakuin University) . . . . . page 339

5. ***Development of Measuring Method for 3D Shapes and Dimensions of Micro-components***
Mitsui, K.; Shiramatsu, T.; Kawada, M. (Keio University) . . . . . page 343

6. ***Development of Micro Probe for Micro-CMM***
Ogura, I.; Okazaki, Y. (National Institute of Advanced Industrial Science & Technology) . . . . . page 349

7. ***Dimensional Stability of 17-7 Stainless Steel Springs***
Patterson, S. R.; Lawton, K. M.; Ren, D. (University of North Carolina at Charlotte) . . . . . page 353

8. ***Stylus Profilometry to Qualify Vee-Grooves for Optical Fiber Alignment***
Rachakonda, P. K.; Vallance, R. R. (University of Kentucky); and Kiani, S.; Hunsaker, B.; Lehman, J. (Teradyne Connection Systems) . . . . . page 357

9. ***A Self-calibration Method for Coordinate Measuring Machines***
Shimizu, H.; Kiyono, S.; Gao, W. (Tohoku University) . . . . . page 363

10. ***The Microprobe For Nano-positional Detection Using Optically Forced Vibration Method***
Takaya, Y.; Nishikawa, M.; Takahashi, S.; Miyoshi, T. (Osaka University) . . . . . page 367

Instrumentation, Design & Testing

1. ***Direct Measurement of Lattice Spacing on Crystalline Surface Using Scanning Tunneling Microscope and Laser Interferometry***
Aketagawa, M.; Rerkkumsup, P.; Takada, K.; Watanabe, T.; Sadakata, S. (Nagaoka University of Technology) . . . . . page 373

2. ***Micromachine Tool: Measurement and Control***
Caballero-Ruiz, A.; Ruiz-Huerta, L.; Kussul, E.; Baidyk, T.; Velasco-Herrera, G. (Universidad Autónoma de México) . . . . . page 377

3. ***Geometrically Compensated Measurement with a Laser Digitizer Equipped CMM***
Harris, J. O.; Spence, A. D. (McMaster University) . . . . . page 383

4. ***2-D Self-Calibration for Scale Based Metrology in Nanolithography***
Lu, X.; Tran, H. D. (University of New Mexico) . . . . . page 387

5. ***Kinematic Spindles for Portable Roundness Instruments***
Wolsing, E.; Hii, K-F.; Vallance, R. R. (University of Kentucky) . . . . . page 391

Machine Tool Metrology

1. ***Effective Measurement Method of Thermal Deformation of Machine Tools Caused by Linear Axis Motion***
Imai, N.; Shimizu, S. (Sophia University) . . . . . page 396

2. ***The Virtual-shape Approach for Modeling Volumetric Errors of Machine Tools***
Kim, K-D.; Chung, S-C. (Hanyang University) . . . . . page 402

3. ***Implementation of the Estler Face Motion Reversal Technique Using a Single Probe***
Salsbury, J. G. (Mitutoyo America Corporation) . . . . . page 407

Measurement Uncertainty

1. ***Phase-measuring Volumetric Interferometer for Three-dimensional Coordinate Metrology***
Kim, S-W.; Rhee, H-G.; Chu, J-Y. (Korea Advanced Institute of Science and Technology) . . . . . page 411

2. ***Finite Element and Experimental Validation of Stiffness Analysis of Precision Feedback Spring and Fexure Tube of Jet Pipe Electrohydraulic Servovalve***
Singaperumal, M.; Somashekhar, S. H.; Krishna Kumar, R. (Indian Institute of Technology Madras) . . . . . page 415

3. ***Evaluation of Task Specific Uncertainty for CMM Measurements***
Venkatachalam, S.; Raja, J. (University of North Carolina at Charlotte); and Uppliappan, B. (Caterpillar, Inc.) . . . . . page 421

4. ***A Study on a Novel Tool Temperature Measurement Method in High-Speed Machining of Titanium***
Zhang, X.; Yamazaki, K.; Yamaguchi, Y. (University of California, Davis) . . . . . page 425

5. ***Uncertainty Analysis in Integrated Measurement Processes***
Zhao, X.; Wilhelm, R. G. (University of North Carolina at Charlotte) . . . . . page 429

***Extended abstract unavailable at press time*

Surface & Subsurface

1. **A proposal for a Common Language for Sharing Surface Texture Data** page 434
   Muralikrishnan, B.; Raja, J. (University of North Carolina at Charlotte)
2. **A Fast and Accurate Non-contact Profiling Instrument for Assessing Areal Surface Texture and Flatness** page 438
   Saito, T.; Yanagi, K. (Nagaoka University of Technology); and Togawa, K. (Nagaoka National College of Technology)
3. **A Study of the Measurement Errors for Laser Beam Passing Through Flowing Parallel Layer for Surface Profile Measurement** page 442
   Tao, Z.; Gao, Y. (Hong Kong University of Science & Technology)
4. **A Method for Fast Gaussian Filtering for 3D Roughness Evaluation** page 446
   Zeng, W.; Xie, T. (Huazhong University of Science & Technology); and Gao, Y.; O, K.; (Hong Kong University of Science and Technology)

Poster Session II

Wednesday, October 23, 2002, 1:30 PM - 3:00 PM

OPTICS

Optical Fabrication

1. **Float Polishing of Calcium Fluoride Single Crystals for Deep Ultra Violet Applications** page 450
   Namba, Y.; Ohnishi, N.; Harada, K. (Chubu University); and Yoshida, K. (Osaka University of Technology)
2. **Comparison of Two Instrument Designs for Non-contact Measurement of Gossamer Mirrors** page 454
   Smith, P. T.; Vallance, R. R. (University of Kentucky)

Optics / Interferometry

1. **Displacement Sensor by a Common-path Interferometer** page 460
   Kamiya, K.; Nomura, T.; Hidaka, S. (Toyama Prefectural University); Tashiro, H. (Toyama University); Mino, M. (Tokushima Bunri University); and Okuda, S. (Computer Engineering & Consulting, Ltd.)
2. **Development of Shape Measuring System Using a Line Sensor in a Lateral Shearing Interferometer** page 465
   Nomura, T.; Kamiya, K.; Nagata, A. (Toyama Prefectural University); Tashiro, H. (Toyama University); and Okuda, S. (Computer Engineering & Consulting Ltd.)
3. **High Accuracy Measurement of Air Frefractive Index in Real-time** page 470
   Wang, Y.; Xie, G. (Excel Precision Corporation)
4. **Optical Mixing Errors in a Fiber-optic Coupled Heterodyne Interferometer** page 474
   Zhang, L.; Patterson, S. R. (University of North Carolina at Charlotte)

Optoelectronics

1. **Allocating Tolerances for Vee-Groove Fiber Alignment** page 478
   Barraja, M.; Vallance, R. R. (University of Kentucky); and Kiani, S.; Lehman, J.; Hunsaker, B. (Teradyne Connection Systems)

PROCESSES

Grinding

1. **The Application of an Empirical Tool Force Model on Vibration Assisted Cutting** page 484
   Fan, X.; Miller, M. H. (Michigan Technological University)
2. **Grinding of Microstructures in Hardened Steel with CBN Tools** page 490
   Hoffmeister, H.-W.; Hlavac, M. (Technical University of Braunschweig)
3. **Development of Chilled Air Cooling Technology for Precision Grinding: An Eco-Friendly Alternative** page 495
   Huang, H.; Ramesh, K.; Yin, L. (Singapore Institute of Manufacturing Technology); and Yui, A. (The National Defense Academy)
4. **A Basic Study on Processing Characteristics of OD-blade Saw Using Ultrasonic Vibration** page 501
   Ishikawa, K.; Suwabe, H.; Nokura, K.; Uneda, M. (Kanazawa Institute of Technology); and Take, Y. (Takesho Co.)
5. **Study on the Machining Accuracy of Round-off Truing Method — Experimental Analysis of Error Factors** page 505
   Kitajima, T.; Okuyama, S.; Wakatomo, T.; Yui, A. (The National Defense Academy); Suzuki, H. (Toyohashi University of Technology); and Hanasaki, S. (Osaka University)

6. ***A Study on the Micro Tool Fabrication Using Electrolytic In-process Dressing***
Lee, H. W.; Choi, J. Y.; Jeong, H. D. (Pusan National University); and Lee, S. W.; Choi, H-Z. (Korea Institute of Industrial Technology (KITECH)) . . . . . page 509

7. ***Force and Temperature Measurements in Vibration Assisted Grinding***
Mahaddalkar, P. M.; Miller, M. H. (Michigan Technological University) . . . . . page 515

8. ***Identification of the Static Stiffness of Grinding Wheels with Resin Bond***
Yamada, T.; Lee, H-S.; Shikauchi, T.; Matsushita, H. (Nihon University) . . . . . page 521

9. ***Relationship Between Stiffness of Grinding Systems and Depth of Affected Layers***
Yokoyama, S.; Lee, H-S.; Yamada, T. (Nihon University) . . . . . page 525

10. ***Grinding Wheel Condition Prediction and Improvement***
Zhang, P.; Miller, M. H. (Michigan Technological University) . . . . . page 529

11. ***3D Kinematical Analysis of Large Scale Substrate Surface Grinding***
Zhou, L.; Shimizu, J.; Shinohara, K.; Eda, H. (Ibaraki University) . . . . . page 534

Machining

1. ***Generation of Large-area Microstructured Surface by Diamond Turning with a Fast Tool Servo***
Araki, T.; Gao, W.; Kiyono, S.; Mito, M. (Tohoku University); and Sudoh, M. (Nissan Motor Co., Ltd.) . . . . . page 538

2. ***Generation of Freeform Surfaces by Diamond Machining***
Brinksmeier, E.; Grimme, D.; Preuss, W. R. (Bremen University) . . . . . page 542

3. ***A Framework of a Knowledge-based System for Predictive Characterization in Ultra-precision Diamond Turning***
Cheung, C-F.; Lee, W-B. (Hong Kong Polytechnic University) . . . . . page 546

4. ***Chipping Minimization During Dicing and Slicing***
Gatzen, H. H.; Karyazin, A. (Hanover University); and Jones, G. M. (Seagate Technology) . . . . . page 551

5. ***Dicing of Ultra-thin Silicon Wafers***
Gatzen, H. H.; Günzel, G. (Hanover University) . . . . . page 557

6. ***Mechanical Micromachining of High Aspect Ratio Micro-structures***
Gatzen, H. H.; Morsbach, C.; Karyazin, A. (Hanover University) . . . . . page 562

7. ***Cutting Conditions of an Engineered Tool with the Ultrasonic Excitation***
Hashimoto, H., Imai, K.; (Kanagawa Institute of Technology) . . . . . page 567

8. ***Lubrication at Tool-chip Interface by Oil Injection***
Kaneeda, T.; Matushita, S. (Okayama University of Science) . . . . . page 571

9. ***Evaluation of Machining Characteristics in the Micro Grooving Machine for the Mold of PDP Barrier Rib***
Kim, N. H.; Lee, D. W. (Pusan National University); and Lee, E. S. (Inha University) . . . . . page 575

10. ***Prediction and Simulation on the Machining Dynamics and Instability in Peripheral Milling***
Liu, X-W.; Cheng, K.; Webb, D. (Leeds Metropolitan University) . . . . . page 581

11. ***Machining Phenomena in EDM for Surface Modification with TiC Semi-sintered Electrode***
Moro, T.; Goto, A.; Saito, N. (Mitsubishi Electric Corporation); Mohri, N. (The University of Tokyo); Akamatsu, K.; Yamada, H. (MC Machinery Systems, Inc.); and Sata, T. (Toyota Technological Institute) . . . . . page 585

12. ***Surface Quality and Tool Wear in Interrupted Hard Turning of 1137 Steel Shafts***
Pavel, R.; Marinescu, I. D. (The University of Toledo); and Sinram, K.; Combs, D.; Deis, M. (Dana Corporation) . . . . . page 591

13. ***Ultra-Precision Cutting of Stainless Steel by Using Coated Carbide Bite***
Sakamoto, S.; Yasui, H.; Fujimori, A.; Kondo, S. (Kumamoto University) . . . . . page 597

14. ***Spectral Analysis of Acoustic Emission (AE) During the Ultraprecision Machining of Single Crystal InSb***
Silva, H. A. T.; Duduch, J.; Porto, A. J. V. (Universidade de São Paulo) . . . . . page 602

15. ***Observing Tool and Workpiece Interaction in Diamond Turning Using Graphical Analysis of Acoustic Emission and Force***
Valente, C. M. O.; Gomes de Oliveira, J. F. (Universidade de São Paulo); Echizenya, D.; Dornfeld, D. A. (University of California-Berkeley) . . . . . page 607

16. ***Microtools Shaped by Focused Ion Beam Milling and the Fabrication of Cylindrical Coils***
Vasile, M. J.; Adams, D. P. (Sandia National Laboratories); and Picard, Y. (University of Michigan) . . . . . page 613

Manufacturing

1. **Substrate Co-Molding of Micro and Meso Optics** page 618
   Gill, D. D.; Dow, T. A.; Sohn, A. (North Carolina State University)
2. **Closed Loop Control of Milling Tool Deflection** page 622
   Hood, D.; Clayton, S.; Buckner, G. D.; Dow, T. A.; Garrard, K. P. (North Carolina State University)

Manufacturing (precision mass production)

1. **Modeling of Residual Stress on Blasted Surface Using Indenting Method** page 626
   Saito, H.; Masuda, M. (Niigata University)

Non-conventional

1. **An Experimental Investigation of Heat Pipes at Low Power Inputs** page 630
   Borundia, A.; Tran, H. D. (University of New Mexico)
2. **Surface Texture Peer to Peer Data Sharing System** page 634
   Bui, S. H.; Raja, J. (University of North Carolina at Charlotte)
3. **Fabrication of Grinding Wheel with Dispersed Hard Powder by Electrical Discharge Machining** page 638
   Furutani, K.; Sunada, H. (Toyota Technological Institute)
4. **Nanoprobe Concepts for Field Emission Nanomachining** page 642
   Trinkle, C. A.; Vallance, R. R.; Mengüç, M. P. (University of Kentucky); Bah, A.; Javed, K. (Kentucky State University); Rao, A. M. (Clemson University); and Jin, S. (University of California-San Diego)
5. **Molecular Dynamics Simulation for EDM Die-sinking Erosion Process** page 647
   Zhao, Y.; Zhang, X.; Yamazaki, K. (University of California-Davis)

Polishing, Lapping & ECM

1. **Charging of Cast Iron with Abrasive During Lapping** page 652
   Barylski, A. W. (Technical University of Gdansk)
2. **Development of a Lapping Film Utilizing Agglomerative Fine Abrasives for Finishing of Optical Glass** page 657
   Enomoto, T. (University of Tokyo); and Zhang, J. (Ricoh Company, Ltd.)
3. **Applications of Fixed Abrasive Pad Using Hydrophilic Polymer in STI CMP** page 661
   Kim, H.; Park, B.; Jeong, H. (Pusan National University); Dornfeld, D. A. (University of California-Berkeley); and Lee, S. (Hynix Semiconductor)
4. **Generation of Quality Surface in Extrude Honing** page 667
   Narayanasamy, K.; Raju, H.P. (Indian Institute of Technology Madras)
5. **New Development of Combined Electrochemical Processes for Mirror-like Micro Grooves** page 671
   Park, J. W.; Moon, Y. H. (Pusan National University); and Lee, E. S. (Inha University)
6. **Material Removal Mechanisms in Abrasive Flow Machining** page 677
   Szulczynski, H.; Uhlmann, E. (Technical University Berlin)
7. **New Approach to Slicing and Lapping and Polishing in Precision Engineering** page 683
   Watanabe, T. (World Technology Instrument Co., Ltd.)
8. **High Removal Rate Ultra-Smoothness Polishing of NiP Plated Aluminum Magnetic Disk Substrate by Means of High Polishing Speed with High Polishing Pressure** page 689
   Yasui, H.; Fukamachi, T.; Sakamoto, S.; Takakura, S. (Kumamoto University)

Technical Papers

REQUIREMENTS FOR PRECISION ENGINEERING IN THE DEVELOPMENT OF MINIATURIZED DIAGNOSTIC SYSTEMS

Uwe Müller[§], Paul Bao[¶], Po Ki Yuen[¶], Tim Patno[§], William Cork[§], Sudhakar Marla[§], James Storhoff[§] and Viswanadham Garimella[§]
[§]Nanosphere, Inc., Northbrook, IL 60062
[¶]Corning, Inc., Corning, NY14831

Over the past decade the trend in *in vitro* diagnostics has been toward multiplexing and miniaturization. Combined with the requirement for ever increasing sensitivity even relatively simple biochemical assays have been turned into sophisticated assay systems, demanding precision engineering in all aspects of the system. Microarray technology applied to expression analysis serves as a case in point. The goal is to determine the relative amount of mRNA for a multiplicity of genes that are expressed in a sample tissue. This is done by comparing the RNA from a sample tissue (labeled with a green fluorophor) to that of a reference tissue (labeled with a red fluorophor) by hybridizing the RNA mixture (after converting to cDNA) to a DNA microarray as depicted in Fig.1.

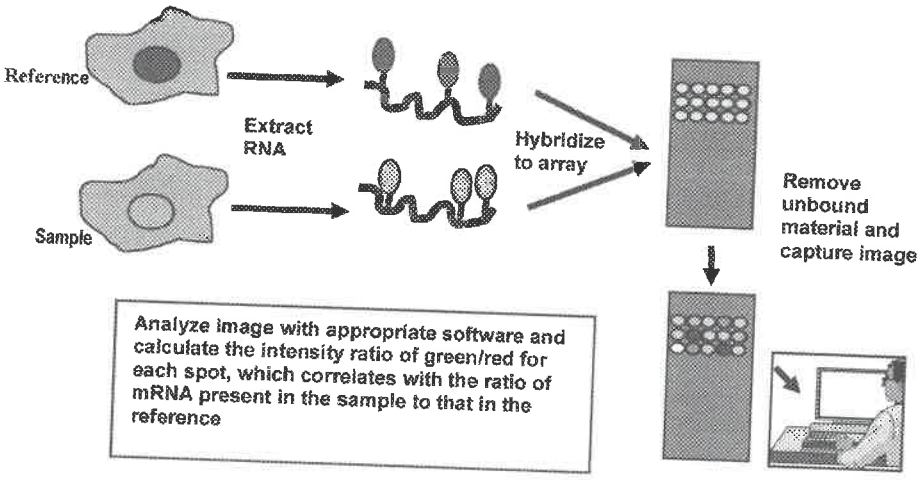
Reference
Sample
Extract RNA
Hybridize to array
Remove unbound material and capture image
Analyze image with appropriate software and calculate the intensity ratio of green/red for each spot, which correlates with the ratio of mRNA present in the sample to that in the reference

Fig.1: Outline of Microarray Based Expression Analysis

The need for analyzing thousands of different genes simultaneously, reproducibly, cost-effectively and conveniently with high sensitivity presents multiple challenges that require the integration of genetic, chemical, optical, mechanical and software engineering to provide a satisfactory solution.

The primary challenge is the development of manufacturing technologies that allows rapid printing of picoliter amounts of >10,000 different quality controlled DNA solutions into an area of less than 3x5 cm^2. Different approaches have been used successfully and two of them will be discussed with some detail.

With microarrays at hand the next step is to prepare sample by extraction of total RNA from both, a reference tissue as well as the sample tissue to be analyzed, and enzymatically converting the RNA molecules into cDNA, whereby fluorophors are introduced and covalently attached to the cDNA copies. The differentially labeled cDNA

preparations are then mixed and applied to the array under conditions that allows hybridization of the cDNA to complementary DNA sequences on the array. Since there are on the order of 20,000 different genes expressed in the typical cell, varying in concentration by 3-4 orders of magnitude, being able to capture the low expressors presents the challenge, especially in situations where only small amounts of starting material is available. In most conventional assay set-ups the hybridization reaction is diffusion limited, but recently microfluidic engineering solutions have become available that overcome diffusion and accelerate the hybridization kinetics, as shown in Fig.2.

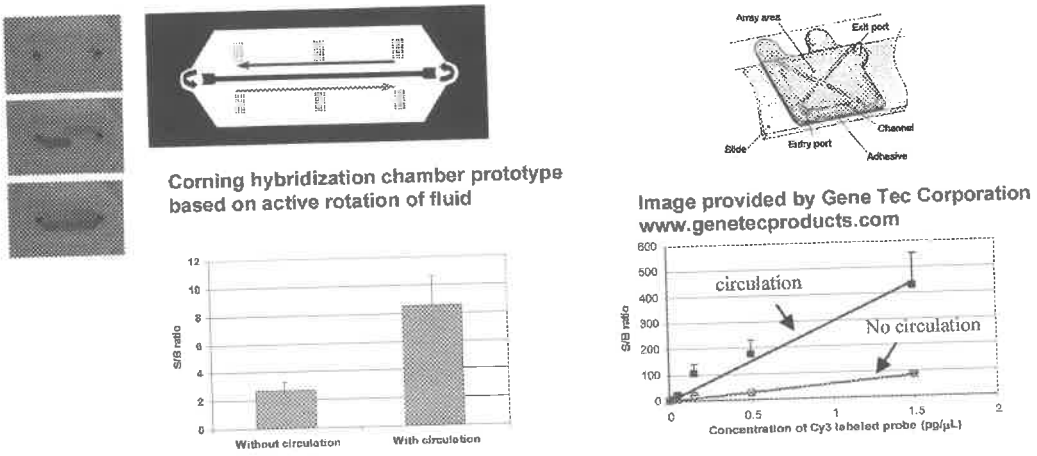

Fig.2: Acceleration of Hybridization Kinetics through Active Fluid Movement

After successful hybridization, unbound material is removed and the arrays are imaged to measure the light intensity for each target spot in each color.

Typical commercial imaging systems can detect on the order of 1-10 fluorophor molecules per μm^2, and sophisticated software is available to extract net signal intensities and determine relative amounts of mRNA present in the sample for each gene represented and detectable on the array.

Of course, in addition to appropriately designed imaging hardware and software the sensitivity of this system is to a large extent a function of the type of label used. Fluorescence (particularly the Cyanine dyes) is the most commonly used label technology, but newer more sensitive labels are on the horizon.

Metal based nanoparticles with diameters of 1-200 nm have recently been tested. When used as Raman labels multiple colors can be generated by using particles of different size or shape, and in principle these particles could be several orders of magnitude more sensitive, specifically if the Raman signal is amplified by covering the nanoparticles with a layer of silver (Surface Enhanced Raman Spectroscopy). In addition, this silver amplification allows simpler modes of detection, such as Rayleigh light scattering, with concomitant simplification of the imaging system. Especially for sensitive and high-throughput diagnostic systems this label and detection methodology provides a cost-effective solution. Fig.3 shows that 0.03 nanoparticles per μm^2 can be detected by scatter

analysis after silver amplification, 2-3 orders of magnitude better than Cy3 or Cy5 when compared on the same slide.

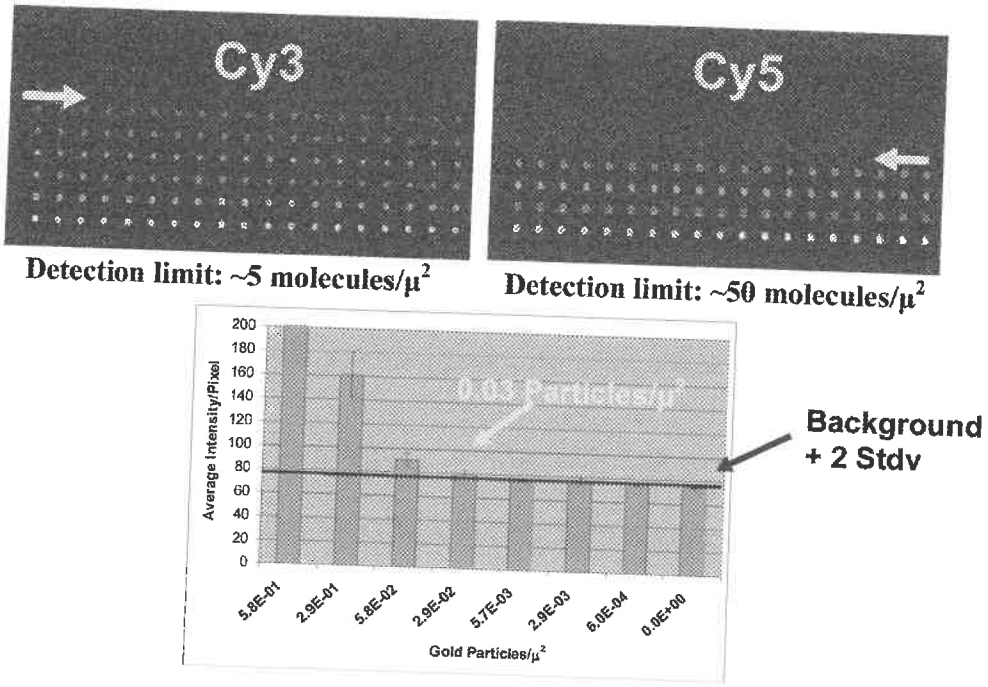

Fig.3: Detection of Silver Amplified 15 nm Gold Nanoparticles by Rayleigh Scatter.

Additional advantages of nanoparticle labeled probes includes a much sharper melting profile of oligo-hybridizations, as shown in Fig.4, and increased melting temperatures, which allows for improved sequence discriminations.

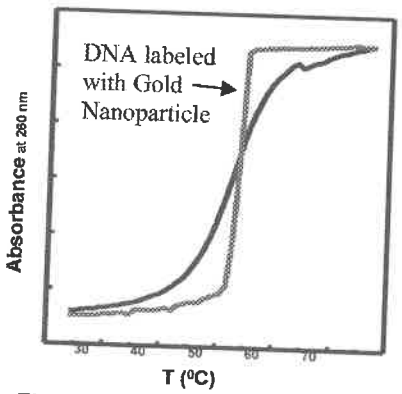

Fig.4: Comparison of melting transitions with unlabeled vs nanoparticle labeled DNA

Of course, this analysis only suggests that probes labeled with nanoparticles instead of fluorophors might provide for more sensitive and accurate assays, but that is subject to other parameters, such as diffusional drag, particles per probe, source of background, etc. We are currently investigating these issues and will discuss data that indeed show the advantages of nanoparticle labels over conventional fluorescence technology in specific diagnostic assays involving small arrays.

Development of Micro Grinding Process using Micro EDM trued Diamond Tools

Toshihiko WADA, Takeshi MASAKI and David W. Davis

Matsushita Electric Industrial Co., Ltd.[1]
Precitech, Inc[2]

Abstract

Micro mechanical and optical devices that have high precision and ultra-micro shapes are highly important to achieving Broadband digital-networks. These devices require sub micron-level accuracy, nanometer-order surface roughness and complex three-dimensional microstructure. There are many fabrication technologies such as etching, LIGA and micro EDM[1]. But, these technologies have limited material, shape and machining accuracy. This paper describes a micro grinding method using a Poly Crystalline Diamond (PCD) micro tool scanning on a high accuracy 3 axis machine platform. An accurate tool can be shaped using micro EDM. The EDM process can produce many tool shapes, therefore complex three dimensional microstructures can be realized. Experiments show that evaluation of EDM machining conditions results in a fine surface roughness, Ry=9nm.

Keywords: micro EDM, Poly Crystalline Diamond, micro grinding, micro optics

Introduction

With optical and electronic devices becoming ever smaller and more complex, the demand for higher precision micro machining has been growing. Sub micron-level accuracy of form and nanometer-order surface roughness are required in devices such as optical wave-guides, micro lens arrays, and fiber-optic connectors. There are many technologies for the fabrication of microstructure such as etching, LIGA, and micro EDM. But, the drawbacks to these technologies are limited material, shape and machining accuracy.

A new grinding method is developed using a polycrystalline diamond (PCD) tool which is trued by micro EDM. Micro-PCD tools of any shape can be easily fabricated using micro EDM, therefore processing high-precision complex microstructures, such as V-grooves can be realized. In this study, we investigated the potential application of micro grinding of Tungsten Carbide using a cylinder-shaped PCD tool. Machining conditions are evaluated to discover the optimal condition.

Experimental setup

A 3 axis machine platform (Precitech) was developed to process the micro grinding method. Figure 1 is a picture of the machine setup.

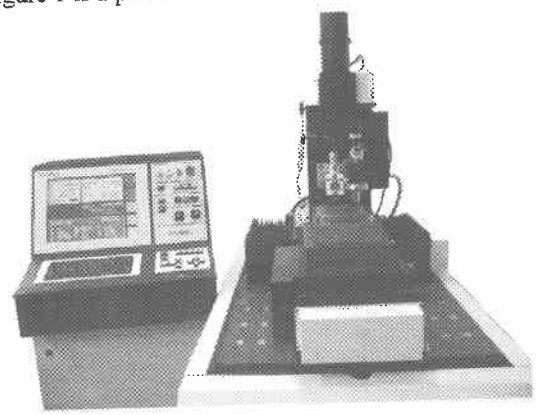

Fig 1: Precitech 3 axis machine platform

A PCD tool with a particle size of 0.5 μm (DA200, Sumitomo Electric Industries, Ltd.) is shaped using a micro electro discharge machine (MG-ED72, Matsushita Electric Industrial Co., Ltd.). The tool rotation accuracy is very important to achieve a high accuracy tool without run out. Therefore the same bearing system is used for the grinding machine and the micro EDM machine.

[1] 2-7 Matsuba-cho, Kadoma, Osaka 571-8502, Japan
[2] Keene, New Hampshire 03431 USA

The surface roughness of the tool can be varied by changing the electric discharge energy conditions for tool shaping. A grinding experiment was performed on the 3 axis machine platform. The tool was driven by a DC motor at 3000 rpm. Figure 2 is a diagram of the experimental setup.

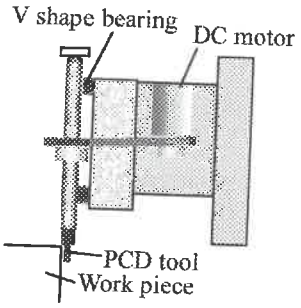

Figure 2: Experimental setup

Evaluation of Grinding Characteristics of the Micro PCD Tool

Effect of the tool's surface roughness on grinding efficiency

Using tools 100μm in diameter, we ground into Tungsten Carbide (FB20 micro-particle Tungsten Carbide, DIJET Industrial Co., Ltd.) using the tool's side while changing the feed rate of the tool, and measured the grinding depth to evaluate the grinding efficiency. Figure 3 is a diagram of the experimental method. Table 1 indicates the electro discharge conditions for shaping the tools used and the measurement results of their surface roughness (measured with an optical 3D profilometer, Keyence).

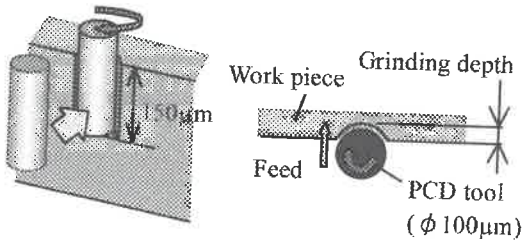

Figure 3:Experimental method

Table 1 Discharge conditions for tool shaping and measurement results of the tools' surface roughness

Tool No.		1	2
Discharge conditions	Capacitance of capacitor	10pF	3300pF
	Processing voltage	70V	110V
Tool's surface roughness (Ra)		0.20μm	0.78μm

The contact length of the tool's side and the work was 150 μm and the predetermined grinding depth of the work was 30 μm. Figure 4 shows the result of grinding depth. When the tool's feed rate is high, the desire grinding depth is not reached. And it is realized that grinding efficiency of Tool 2is higher than Tool 1.

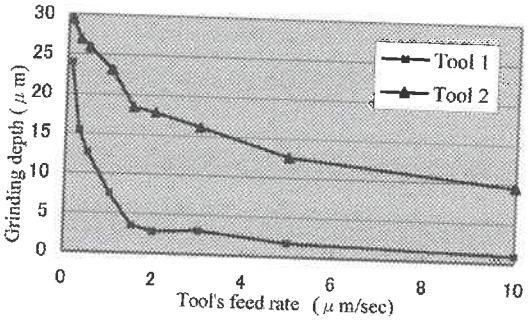

Figure 4: Result of grinding depth

Evaluation of Microground Surface Roughness

To measure the surface roughness of the surfaces ground with the micro-PCD tools, we performed surface grinding of Tungsten Carbide using the bottom surface of PCD tools 2 mm in diameter shaped with the electro discharge conditions indicated in Table 1. Figure 5 shows the experimental method. We then measured the surface roughness of the ground surface using a stylus-based surface roughness meter (Nanostep 2, Taylor Hobson). Figure 6 shows the measurement results, which indicate that the surface machined with Tool 1 is good with a Ry = 9 nm or less.

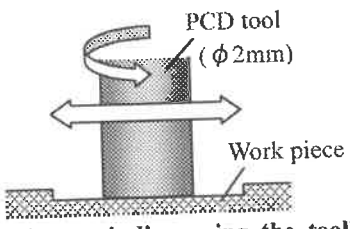

Figure 5: Plane grinding using the tool's bottom surface

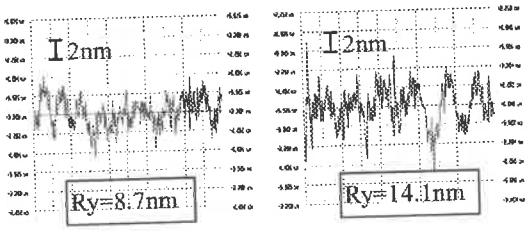

(a) Tool 1 (b) Tool 2

Figure 6: Measurement of surface roughness of the machined surfaces

Profiling in Tungsten Carbide

Figure 7 shows an example of Tungsten Carbide machined using a 95μm diameter PCD tool made under the same electro discharge conditions as Tool 1. The grooves have a pitch of 100 μm, a length of 90 μm, and a depth of 35 μm. For the machining, the work was first ground with the side of the tool which was moved horizontally at a rate of 0.1 μm/s. The tool was then raised vertically at 5 μm/s to prevent the tool's surface roughness from being transferred to the machined surface, thus making the surface smoother. It is clear that use of this method allows microstructures to be machined to a mirror finish with high shape accuracy.

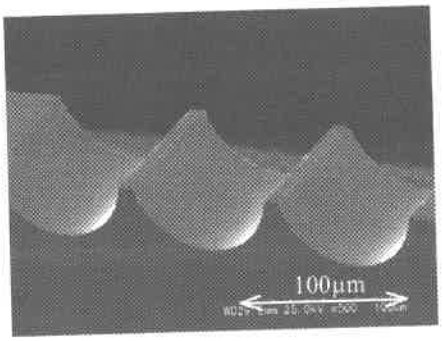

Fig 7: Examples of Micromachining

V-groove machining method and examination of machining mechanism

V-groove on Ni spherical surface

V-groove machining consists of using a cone-shaped PCD tool to carry out successive microgrinding by mechanically moving the rotating tool across a work piece at a fixed speed. By arbitrarily moving the tool on the work, you can obtain an arbitrary processing pattern. Figure 8 is an SEM image of the tool.

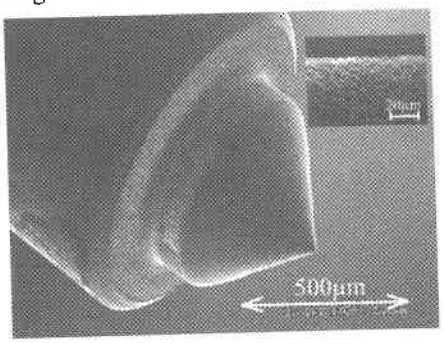

Fig 8:Tool sharpened by the micro EDM

Figure 9 shows the result of machining on spherically electroless plated Ni. In the center of the spherical surface of R = 10 mm, V-grooves with a groove width of 30 μm were cut to form a cross pattern. The tool was passed at a speed of 10 μm/s in the plane direction; and the work was processed in oil with a uniform cutting depth of 1 μm/s for the rough machining and 0.1 μm/s for the last 1μm finishing. It is clear that this machining enables the formation of smooth surfaces with very sharp edges.

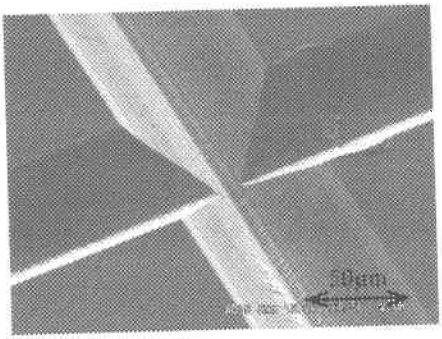

Fig 9: V-groove on Ni surface

Examination of processing mechanism

Figure 10 shows a conceptual diagram of the V-groove machining method and its mechanism. V-groove machining consists in using a cone-shaped PCD tip as the machining tool, cutting the work to the depth D with the tool revolving at the rotational speed R and mechanically removing the work area by moving the tool around at the feed rate F. By adjusting the vertex angle of the cone-shaped tip, V-grooves of any angle can be machined.

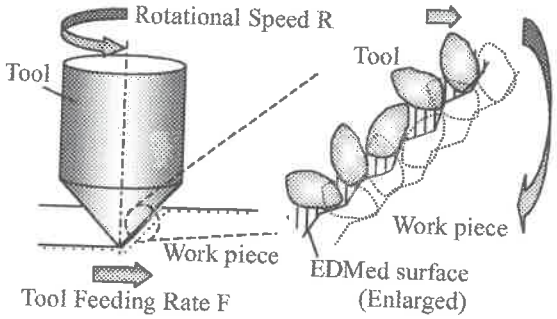

Figure 10: Conceptual diagram of V-groove machining mechanism

When performing ultra-accurate cutting of brittle materials, such as silicon, a common problem is the damage caused by ductile/brittle transition. It is reported, as a solution for this problem, that controlling the cutting depth with the cutting edge enables specular finishing in the ductile cutting mode. In this method, it is considered that the process develops through microscopic grinding caused by the surface roughness of diamond particles. The cone-shaped tool is an assembly of diamond-particle cutting edges, which perform numerous microscopic cuttings at the work surface as a result of the rotational motion of particles and feed movement of the tool itself. It is considered that, if the stress of the work surface during cutting exceeds a certain limit, the brittle fracture mode predominates, resulting in defects.

The volume V of work removed by each particle during one revolution of the tool is independent of the cutting depth of the tool but is given by the following equation using the tool feeding rate F and rotational speed R. It is considered that, if V exceeds a certain value, the cutting mode changes from the ductile cutting mode to the brittle cutting mode, which would cause defects in the work surface.

$$V = k*F/R \quad (k \text{ is a constant}) \qquad (1)$$

To verify the above equation, we performed a V-groove machining experiment with different feeding rates and rotational speeds of the tool and checked for occurrence of defects after machining. As the sample, we used single-crystal silicon wafers (Sumitomo Metal Industries, Ltd.). The worked surface was (1,0,0), and the sample was machined in stationary oil in the orientated flat and horizontal directions. We performed V-groove machining five times with cutting depth D=5 μm for a cutting length of 100 μm and determined the number of defects.

Figure 11 shows the relationship between the tool-feeding rate F and the number of defect occurrences at different rotational speeds R. It is realized that the greater the tool feeding rate F or the smaller the rotational speed R, the more often defects may occur: this agrees with the characteristics of the above equation.

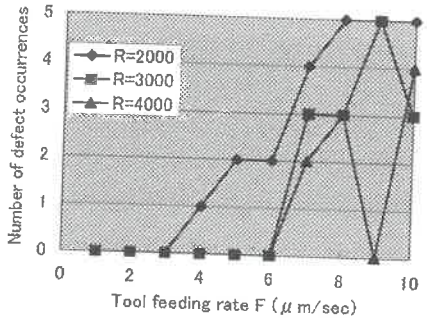

Figure 11:Tool feeding rate and number of defect occurrences

Conclusions

In consideration of the above described results, the micro grinding process using micro EDM trued diamond tools can be explained utilizing general grinding theory and is an acceptable method for fabricating micro optical devices.

Reference

[1]T. Masaki, K. Kawata and T. Masuzawa,"Micro Electro-Discharge Machining and Its Applications" *Proc.IEEE MEMS*, 1990,pp.21-26

High aspect ratio SNOM probe fabricated using Electron Beam Deposition and Focused Ion Beam

Kensuke Tsuchiya, Takeshi Ooi, Yuki Sakamaki and Masayuki Nakao
Graduate School of Engineering, The University of Tokyo
7-3-1 Hongo, Bunkyo-ku, 113-8656 Tokyo, JAPAN

1. Introduction

Fluorescence in situ hybridization (FISH) [1] is a primary method for visually mapping specific base arrangement on DNA fibers and chromosomes. This FISH method allows observing the target base arrangement that stands out as a fluorescent spot. The authors have developed a Scanning Near-field Optical Microscope (SNOM) for observing the detail of fluorescent spots high-lighted on chromosomes and DNA's. The wave length of the illumination light limits the resolution with optical microscopes due to optical refraction. Near-field light in the neighborhood of small apertures or scattering objects, in contrast, lacks this refraction property. SNOM takes advantage of such near-field light for its resolution that does not depend on the wave-length. A number of suggestions and tests have been reported about different types of SNOM [2]. The SNOM we used for our study was a type that scans a vibrating probe over the illuminated specimen surface and periodically disperses the near-field light that is then locked in for producing an image. For further enhancing the SNOM resolution, we produced a scattering probe with high aspect ratio and observed specimen with fluorescent surface.

2. Developing the scattering probe with high aspect ratio

The scattering type SNOM uses a cantilever (OMCL-HA100WS by OLYMPUS Optical Co., Ltd.) for the scattering probe, on the atomic force microscope (AFM), that scans the specimen surface. The low aspect ratio with the pyramid shaped conventional AFM cantilever causes such problems e.g., a blurred image that hinders observing small structures due to scattered rays from the probe other than its tip when the specimen has mixed size structures (Fig.1-(a)). Our study, to counter this problem, proposes a scattering probe with high aspect ratio, as Fig.1-(b) shows, produced using the electron beam deposition [3] inside an electron microscope. Electron beam deposition is a phenomenon that a small amount of residual gas, e.g., hydrocarbon, getting excited and decomposing within the electron microscope specimen chamber, and the decomposed material adhering and accumulating on the specimen surface. Fig.2 shows a SEM image of the scattering probe with high aspect ratio that we actually produced. The tip of the AFM cantilever has an approximately 1μm long needle, grown by electron beam deposition, with a tip diameter of about 20nm. The next chapter explains the detail of our method for producing the probe.

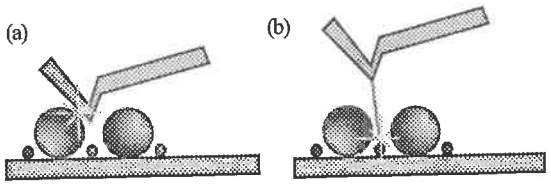

Fig. 1 Effect of probe aspect ratio: (a) scattering from area off the tip, (b) scattering only from the tip

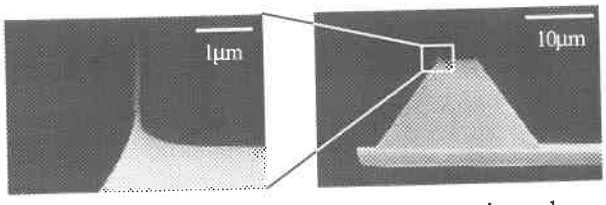

Fig. 2 SEM image of the high aspect ratio scattering probe

3. Evaluating the high aspect ratio scattering probe

For testing the performance of the high aspect ratio scattering probe, we made two different types of observations; one with a conventional AFM cantilever (low aspect ratio scattering probe), and the other with the high aspect ratio scattering probe. It is common to use an optical filter to block the illumination for fluorescent observation. The scattered light from a fluorescent source, however, is much weaker than the scattering from the illuminating light source, and thus we directly measured the scattering from the illumination without an using an optical filter. The specimen was a mixture of polystyrene beads with diameters of 20nm and 200nm. A semiconductor laser with a wave length of 670nm served as the illuminating source. The AFM cantilever made of silicon nitride passes all the illuminating semiconductor laser. This will illuminate undesired area on the specimen generating noise for the scattering light measurement. To suppress such noise, we produced the high aspect ratio scattering probe with the following procedure (Fig.3): First, we deposited Al (film thickness approximately 80nm) on the entire surface of the cantilever and about 10nm of Au to prevent oxidization. Next, with electron deposition machining, removed the Al film from the tip of the cantilever to make an opening with a diameter of about 2nm to illuminate only the target area on the specimen surface. Then electron beam deposition grew a high aspect ratio tip from this

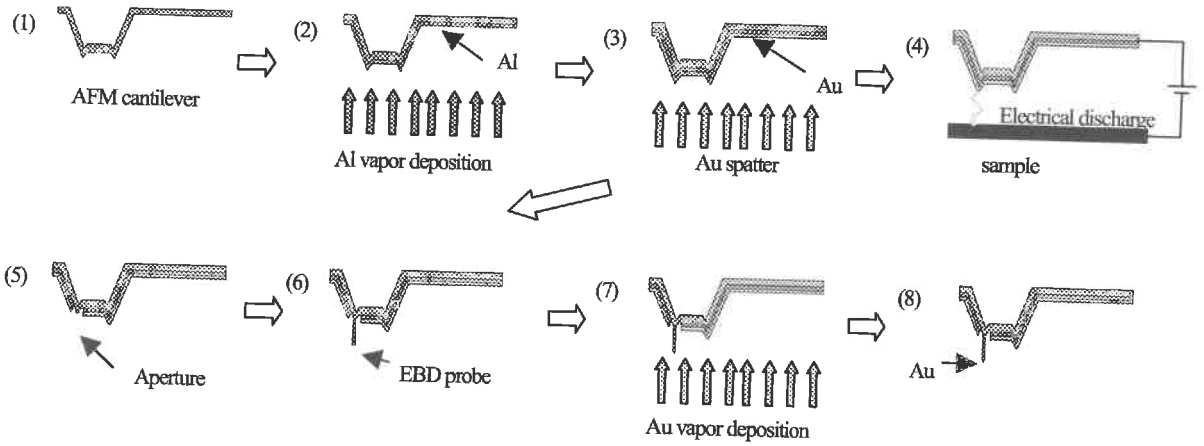

Fig. 3 Steps to produce high aspect ratio scattering probes for semiconductor laser

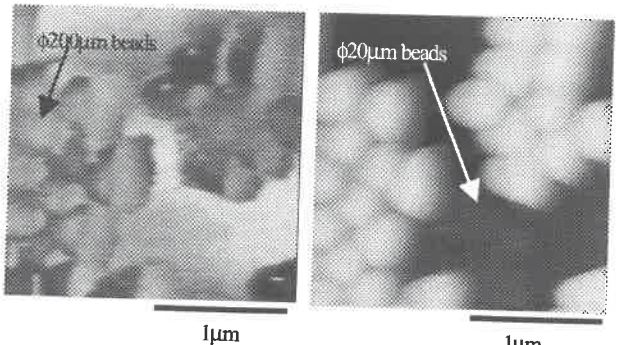

(a) SNOM image (b) AFM image

Fig. 4 Image of mixed ϕ20nm/ϕ200nm beads using a low aspect ratio probe

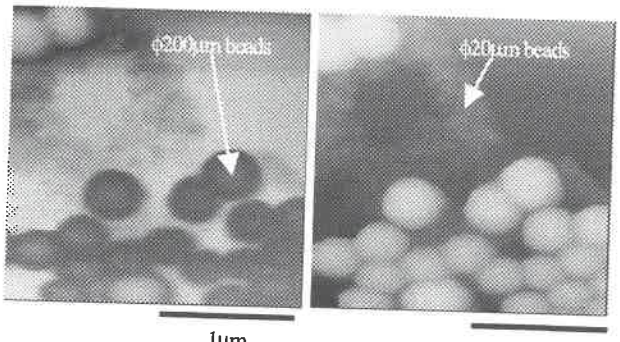

(a) SNOM image (b) AFM image

Fig. 5 Image of mixed ϕ20nm/ϕ200nm beads using a high aspect ratio probe

opening. We sputtered a small amount of Au on the tip to increase the scattering intensity. We controlled the height by varying the stage elevation to keep a constant AFM interatomic force. We simultaneously measured the signal image (optical image) of the scattering light intensity from the near-field light, and the regular AFM stage height signal image (shape image) for reference.

Fig.4 (a) and (b) are the images from observing with the low aspect ratio scattering probe. (a) is the optical image and (b) the shape image acquired together. The optical image (a) shows the ϕ200nm beads, however, not those of the ϕ20nm beads found on the shape image (b) in the lower center of the picture. This is due to scattering lights from the needle body other than its tip with the low aspect ratio scattering probe. Fig.5 shows (a) optical image, and (b) shape image made with the high aspect ratio scattering probe. The probe successfully produces images of both the ϕ20nm and ϕ200nm beads. Furthermore, the boundaries of the ϕ200nm beads are clearer in the optical image compared to that from the low aspect ratio scattering probe. These experiments verified that our high aspect ratio scattering probe is effective for high resolution observation.

4. Fluorescent observation with the high aspect ratio scattering probe

For verifying the feasibility of fluorescent observation with SNOM, we observed ϕ200nm beads with excitation/fluorescent wave lengths of 458/540nm. He-Cd laser with a wave length of 442nm illuminated the beads to excite fluorescent light from them. The He-Cd laser illumination does not pass through the cantilever material of silicon nitride. Thus, to illuminate the specimen surface, we applied the following steps to produce a high aspect ratio scattering probe with a small opening (Fig.6). First, we sputtered an Au film of about 10nm on the cantilever surface for Focused Ion Beam (FIB) observation, and formed an approximately 2μm square opening at the tip of the cantilever. Then we formed a high aspect ratio tip with electron beam deposition and finished by sputtering a small amount of Au on the very end. Fig.7 shows a SEM image of the probe we produced. An optical filter of wave length 540nm was installed on the photomultiplier tube to block the background light and allow measuring a signal image of the fluorescent light only (fluorescent image). At the same time, we measured the signal image at the regular AFM stage height (shape image) for reference.

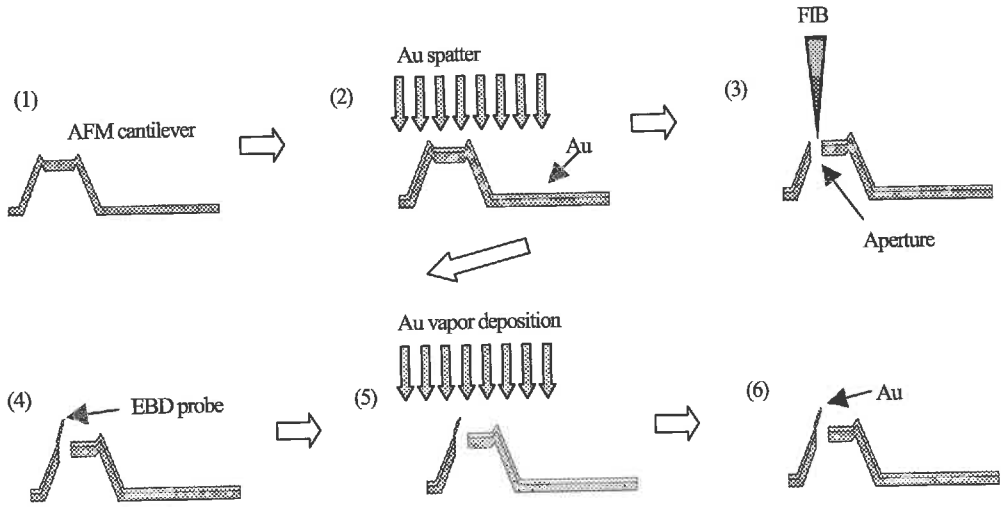

Fig. 6 Steps to produce high aspect ratio scattering probes for He-Cd laser

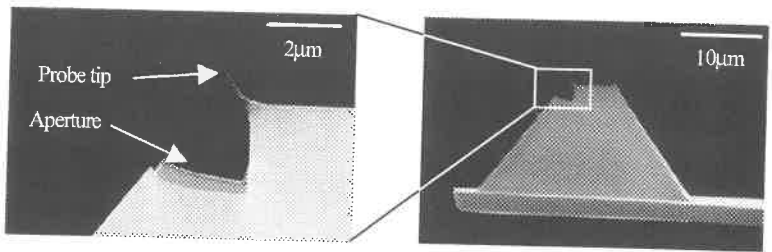

Fig. 7 SEM image of the probe tip produced with FIB

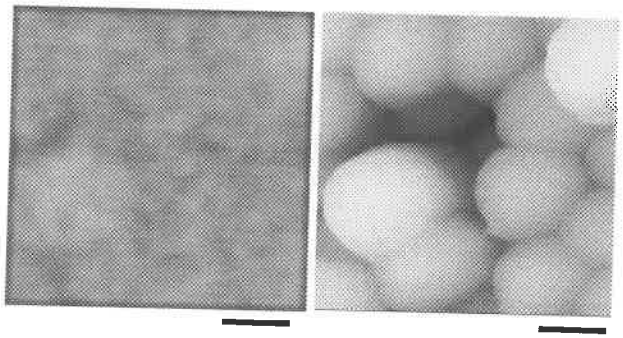

(a) SNOM image (b) AFM image

Fig. 8 Image of ϕ20nm fluorescent beads

Fig.8 (a) shows the fluorescent image and (b) the shape image. The fluorescent image (a) was processed through a 15th degree averaging filter. The shape image (b) shows fluorescent beads in the left center and upper right area of the picture, above the fluorescent beads concentration layer, and they are also identified in the fluorescent image (a). The fluorescent image (a), however, is unclear and does not show other fluorescent beads concentration. This was due to the weak fluorescent signal lost in the noise from the instrumentation and the background light. We further need to improve the S/N ratio to obtain clear fluorescent images to identify fluorescent beads concentrations using the FISH method. We believe that we can reduce the noise and improve the S/N ratio by acquiring tens to hundreds of data from 1 dot, instead of the current 1 datum from 1 dot, and averaging the data.

5. Conclusion

We developed a high aspect ratio scattering probe for near-field optical microscopes and tested its performance. The probe succeeded in obtaining an optical image of ϕ20nm beads, formerly unavailable with a cantilever on an interatomic force microscope, to demonstrate that high aspect ratio scattering probes are effective in high resolution observation. We also conducted an experiment of fluorescent observation and showed the feasibility of applying near-field optical microscopes for high resolution fluorescent observation.

References

[1] M. Ito, et al.: *J. Ame. Soc. Hort. Sci.*, **125**, pp. 59, 2000.

[2] W. Denk and D. W. Pohl: *J. Vacc. Sci.Tech. B*, **9**, pp. 510, 1990.

[3] M. Nakao, et al.: *Proc. of ASPE 1999 annual meeting*, **20**: pp. 41, 1999.

Smart Palm-size Injection Mold using Zone-In-Cavity and Cycle-by-Cycle Process Controls to Precisely Replicate Miniature Products

Makoto Yoda, Masayuki Nakao
The University of Tokyo, 7-3-1 Hongo, Bunkyo-ku, Tokyo 113-8656, JAPAN

1 Introduction

Injection molding technology can replicate precise μm-wide structures such as a 1μm-pitch grating pattern. It cannnot, however, obtain precise mm-wide forms such as a fine flatness of 0.1μm / 10$\times$10mm or a fine straightness of 1μm / 50mm because the mold cannot control physical phenomena of a plastic material in a cavity during processing cycle.

Generally, injection molds do not have enough sensors / actuators to measure / control the solidification process in each zone of the cavity. For example, plastic near an edge of the box replication solidifies quickly, causing a large bent at the center of the box. Moreover, the plastic is not uniform, creating a different characteristic during each cycle.

We introduce a "smart palm-size injection mold", which has micro-sensors for pressure / temperature / displacement in the cavity zones and has piezo elements and heaters for controlling these parameters for each cycle. The target replica products are small, for example, an optical f-θ lens, a plastic-bonded hard magnet, a micro multi-pins connector and so on.

2 Device for the Experiment

We used a compact hydraulic injection molding machine JUKEN JMW-015S-5t. This machine has a ϕ16mm vertical injection screw with a maximum injection pressure of 133MPa and a horizontal mold clamping unit whose available clamping force is 49kN. The mold temperature control is integrated in the machine using two band heaters and a thermo couple mounted to the surfaces of the movable part of the mold.

The schematic of prototype-I "the smart palm-size injection mold" is shown as fig. 1. There are three heat flux sensors 2.5$\times$2.5, 18mm long in the movable insert die for mesuring the heat flux and temperature at each zone of the cavity. Also, there is a force sensor behind two of four ejector pins for mesuring the cavity internal pressure and a displacement sensor on the parting plane for mesuring the cavity volume change. There are two micro ceramic heaters 20$\times$10$\times$2mm in the stationary insert die to control the heat flux in each zone of the cavity.

Fig. 2 shows the schamatic of the test part. A 30$\times$15mm plate with four 5mm-height-ribs. The thickness of the plate varies from 1 to 2mm to cause the ununiform tempatature distribution when it solidifies.

3 Results

3.1 Cycle-by-cycle temperature control experiment

As an example of cycle-by-cycle temperature control, we measured temperature variance at the center of the cavity across different cycles, and studied what control can improve the process and what effect it may have on the shape of the molded product. We measured the temperature at the center of the cavity for 20 shots without control and 20 shots with control. Fig.3 shows the data, respectively. Note that the graphs superimpose the 20 shots on top of each other.

When there was no control, as the graph shows, the temperature changed drastically three seconds after the start of injection. Fig.4 shows the temperature of each shot after 4.5 seconds. The figures clearly indicate that control reduces the temperature variance. Thick parts of the molding show shrinkage when the temperature declined and fluctuated. We found out that it is possible to eliminate the shrinkage of the molding by reducing the variance in temperature.

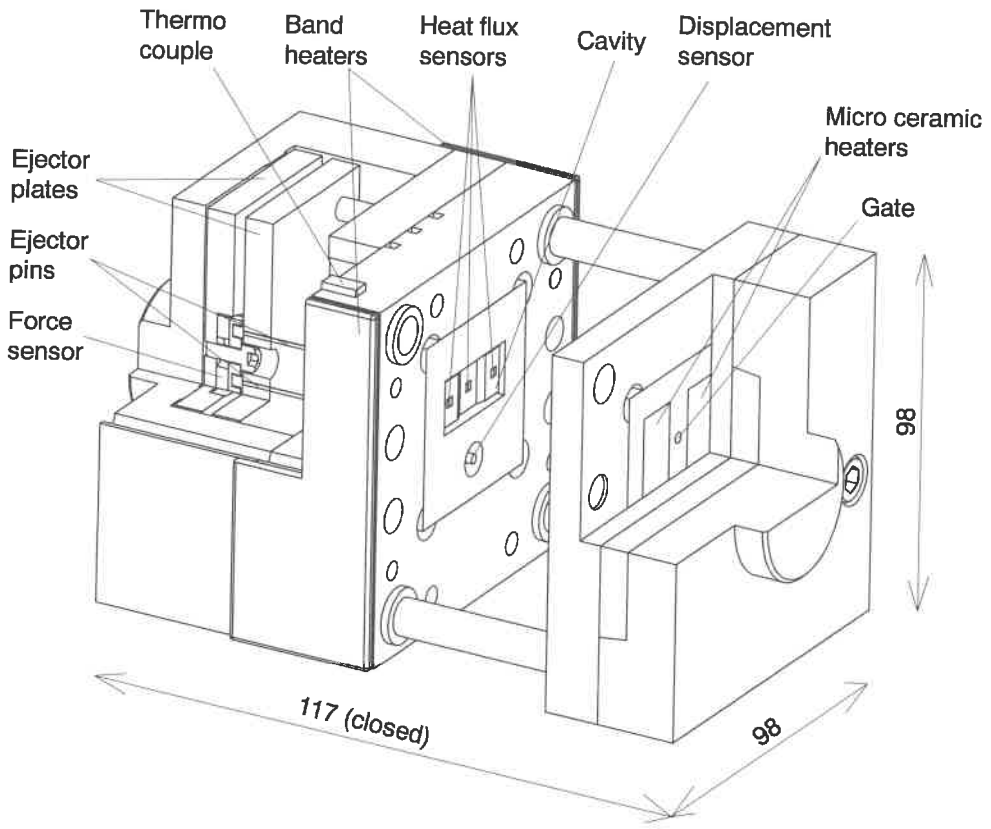

Fig.1 Schematic of "the smart palm-size injection mold"

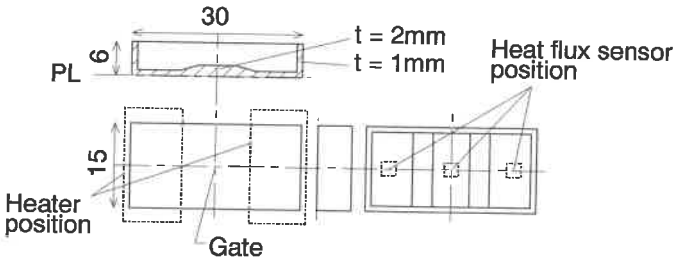

Fig.2 Schematic of the test part

The reading of the pressure sensors or the displacement sensors did not show wide variance or discontinuity. Therefore, we believe that the sudden decrease in temperature was caused as follows: Local minor shrinkage occurred to the plastic near the heat current sensor, which caused a gap to be formed between the hot resin and the sensor and furthermore prevented the actual temperature from reaching the sensor. Small heat current sensors may be more effective in detecting local shrinkage at the center of the molding than pressure sensors or displacement sensors.

3.2 Zone-In-Cavity temperature control experiment

We conducted two experiments of controlling zone-in-cavity temperature.

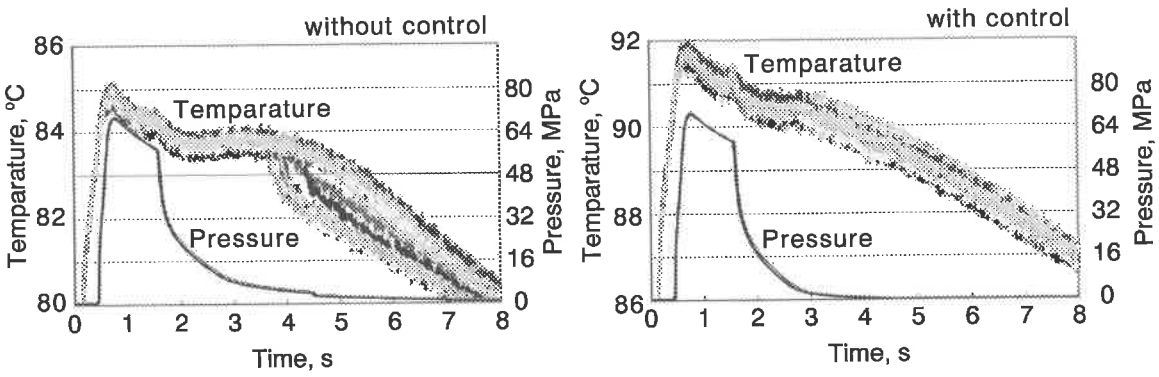

Fig.3 temperature at cavity center and cavity internal pressure

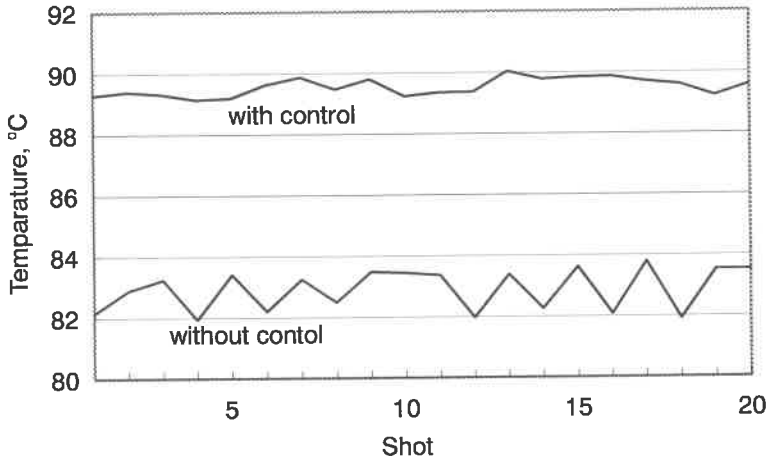

Fig.4 Variance in temperature

For Case A, we examined the shape of the product side as we varied the surface temperature of the heater. Fig. 5 shows the shape of the molding sides versus the heater temperature.

The figure indicates that higher heater temperature reduced the amount of deformation in the middle of the side walls. When the heater temperature was 175 degrees Celsius, the end points near the heater deformed by 3μm in the opposite direction. This indicates that local heating caused local deformation that affected the overall shape of the product. These facts suggest the possible application of fine temperature control for precise shape production with high degree of straightness or for precisely molded optical lenses.

For Case B, we attempted to eliminate the shrinkage at the top surface by uniformly cooling the center and the end points of the molded product using feedback heater control. Fig.6 shows the shape of the top surface with and without control provided.

The figures show that the control reduced the shrinkage which were present at the top end points and at the root of the ribs when there was no control. In other words, controlling local temperature allows better shape control of the external appearance of the molded product without changing the injection pressure or the metal model temperature. It is generally known that increasing pressure or temperature of the plastic improves shrinkage. In such cases, however, when increasing the pressure or temperature is not desired, local heating proves to be very effective for shape control.

Both cases A and B indicate that for further precision with injection molding, a much finer local

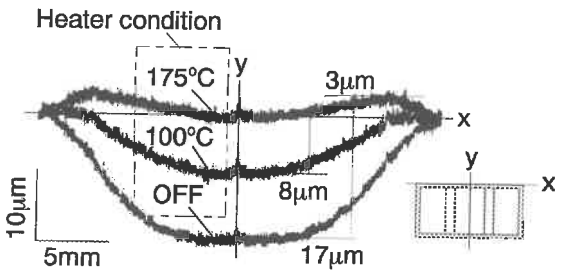

Fig.5 Case A: shape of molding sides

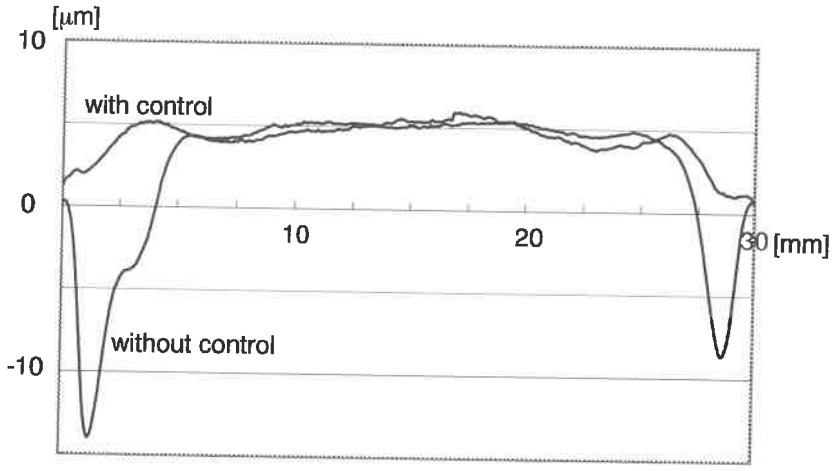

Fig.6 Case B: shape of top surface of molding

temperature control is necessary. The authors are currently investigating the second model, prototype-II 50×50×50mm, 1kg copper alloy mold with a ϕ2mm ceramic heater and a ϕ1mm fountain-type temperature controller. The model is currently in design.

4 Conclusion

(1) The authors developed a small metal mold that allows local temperature control for cycle-by-cycle and for zone-in-cavity temperature control.

(2) The authors confirmed that temperature control for each cycle managed the temperature variation of the plastic during cooling, improving the appearance of the final molding.

(3) The authors confirmed that controlling the shape of the molding by controlling local zone-in-cavity temperature, allows improving the external deformation without changing the plastic pressure or the metal mold temperature

References

Chin Yan, M.Nakao, T.Go, K.Matsumoto and Y.Hatamura: Injection molding for duplication of microstructures using mold-core extrusion mechanism and small sensors, 2001, J.JSPP Autumn, 139.

M.Yoda, M.Nakao, Chin Yan: Precise / Micro Mold Injection Using Miniature Smart Mold, 2002, J.JSPE Spring, 378.

MICROSCALE PATTERNING OF PZN-PT SINGLE CRYSTALS BY LASER-INDUCED ETCHING

Kee S. Moon*, Miguel Levy**, Yong K. Hong* and Shankar Ghimire**
*Dept. of Physics, Michigan Tech. University, Houghton, MI
**Dept. of ME-EM, Michigan Tech. University, Houghton, MI

Abstract

The development in recent years of ultra-efficient single crystal piezoelectric material lead zinc niobate-lead titanate (PZN-PT) has attracted considerable attention because of its potential use in a new generation of piezoelectric transducers, actuators and sensors. Laser induced etching is a versatile process that can be used to directly etch fine features in various materials. In this paper, it is shown that the PZN-PT single crystal films can be rapidly etched in an HCl solution with an argon-ion laser operating at 514 nm. We are able to obtain etched holes with a diameter of about 3μm and a typical depth of 1.5μm.

Introduction

In recent years, laser-induced etching processes have been investigated for a wide variety of applications in micro-fabrication. A number of studies have shown that laser-induced or laser-assisted chemical etching can be applied to a variety of materials such as metals, ceramics, semiconductors, and polymers. [1-3] The use of lasers to influence etch processes offers localized, non-contact micro-fabrication of a substrate through chemical processing of an illuminated region. These techniques also offer some advantages over conventional lithographic techniques in process simplicity, flexibility, and the ability for rapid prototyping.

The attractiveness of $Pb(Zn_{1/3}Nb_{2/3})O_3$-$PbTiO_3$ (PZN-PT) relaxor ferroelectrics lies in the fact that their piezoelectric coefficients and strain levels are significantly higher than $Pb(ZrTi)O_3$ (PZT), a material extensively used in commercial piezo-devices. In addition, they have lower hysteresis. [4, 5] Thus they can potentially be used to fabricate smaller and more cost-effective piezoelectric devices while attaining higher levels of performance and reproducibility than at present. Moreover, the development of micro-electromechanical systems (MEMS) has opened up a number of possibilities for the integration of single-crystal PZN-PT based components into useful micro-devices. Therefore, it is clear that the processing of PZN-PT is an important problem. The etching of the PZN-PT single crystal material is a process which has not, to date, been addressed by laser induced etching. In this paper, it is shown that PZN-PT single crystal samples can be rapidly etched in HCl solutions with an argon-ion laser operating at 514 nm.

Experimental setup

The laser induced etching system in our lab uses an argon-ion laser, a computer controlled XYZ stage and an integrated machine vision system to adjust the laser spot size on the sample surface (Fig. 1). The scanning apparatus is controlled by a computer with C-language based software to move the sample relative to the laser beam, thereby allowing the patterning of intricate features on PZN-PT samples. In this paper, we discuss a wet etching method that uses chemical reactions in liquid-solid surfaces. In our tests, a 500μm-thick PZN-PT substrate is mounted on a sample stage and immersed in a 34.8% hydrochloric acid (HCl) solution The wet etching method is illustrated in Fig. 2.

The energy source is an Argon-Ion laser with maximum available power of 4 W at a wavelength of 514 nm. The optical setup creates a focused spot of about 10 – 20μm diameter. A beam splitter passes 70% of the beam intensity through the objective lens (20x). The excitation spot, illuminated by the laser beam, etches faster than other areas of the sample surface. This difference in reaction rates between laser focused and un-exposed areas allows us to machine various features on the surface. The beam splitter also allows viewing of the patterned area of the sample through a CCD camera connected to a TV monitor and used both to focus the beam on the sample and to monitor the etching process.

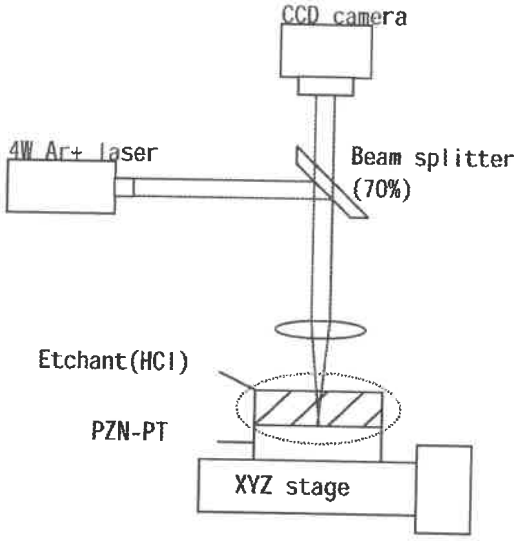

Figure 1: Experimental setup for a laser-induced etching.

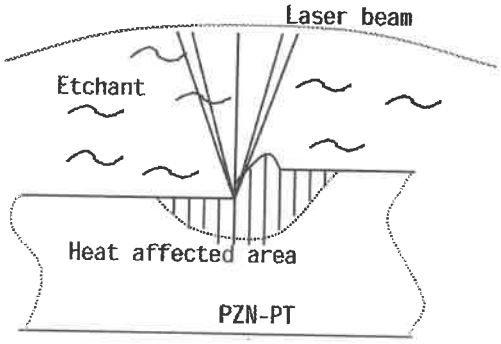

Figure 2: Wet etching method.

Experimental results

Two types of sample surfaces, prepared under different conditions, were tested. One was simply polished and the other was polished and helium-ion implanted (~4 MeV) normal to the surface to generate localized lattice damage in a sacrificial layer 7μm micron beneath the top surface. [6] After the laser induced etching process, the depth, width and surface of processed PZN-PT substrates were observed and measured by an optical interferometric metrology microscope (ADE PhaseShift).

Figure 3 shows the two surfaces obtained after the wet etching process. The effect of the etching is evident in the generated holes, which were obtained by varying the etching time. The measured diameter and the depth of the etched holes are given in Fig. 4. As shown in Figs. 3 and 4, the lateral etching rate is approximately 27.0 μm/min. for polished surfaces and 31.1 μm/min. for polished and ion implanted surfaces, respectively. The vertical etch rate is approximately 7.7 μm/min for polished surfaces and 9.5 μm/min. for polished and ion implanted surfaces,

respectively. It can be noted that the ion implantation results in a slightly enhanced etch rate. From the figures, it is clear that the diameter increases relatively more than depths with etch duration. This indicates that the chemical processes responsible for the etching act more effectively along the surface direction than in the vertical direction. We found that bubble irregularities, caused by chemical reaction, hinder the constant transfer of laser energy to the desired area.

Figure 5 shows a micro-rectangular structure (50 x 75μm^2) patterned at a scan speed of 2.5 μm/sec. The line width is 15 μm and the depth of the pattern is approximately 1.5μm, respectively. The scratches around the pattern were developed from fine surface defects created in the PZN-PT pre-treatment process of mechanical polishing.

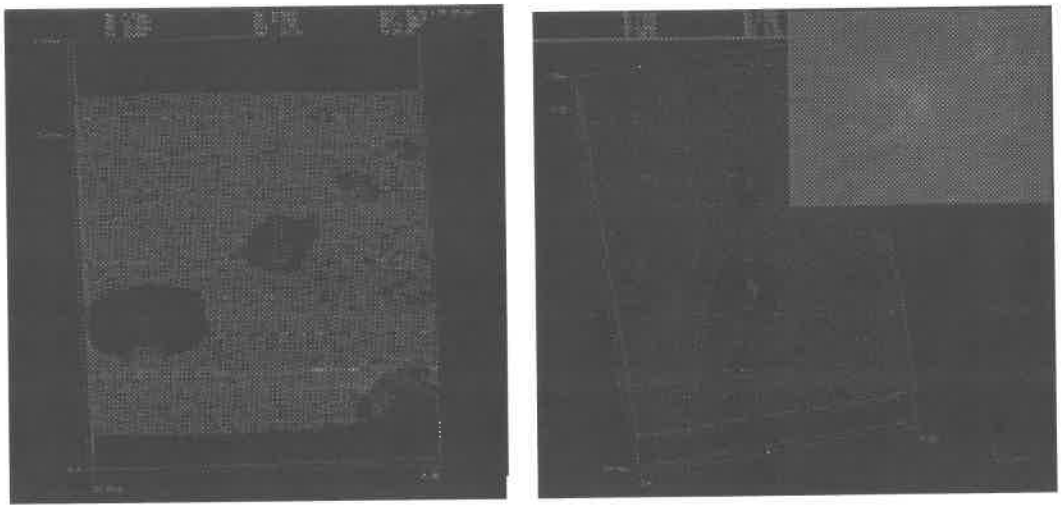

Figure 3: Holes produced on PZN-PT substrates before (left figure) and after Ion implantation (right figure).

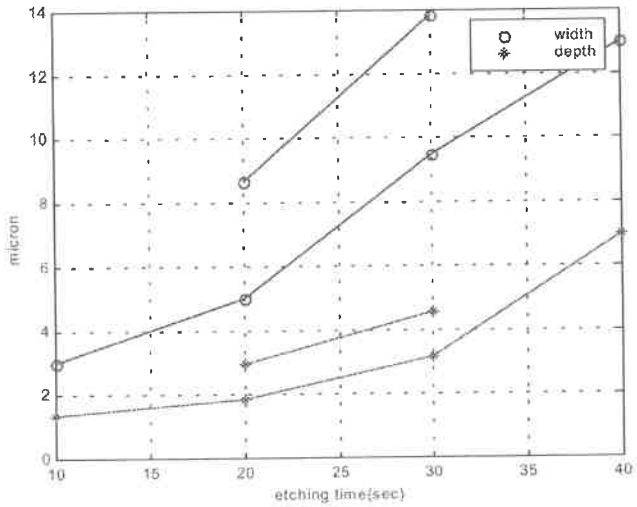

Figure 4: The measured diameter and the depth of the etched holes are given in Fig. 3.

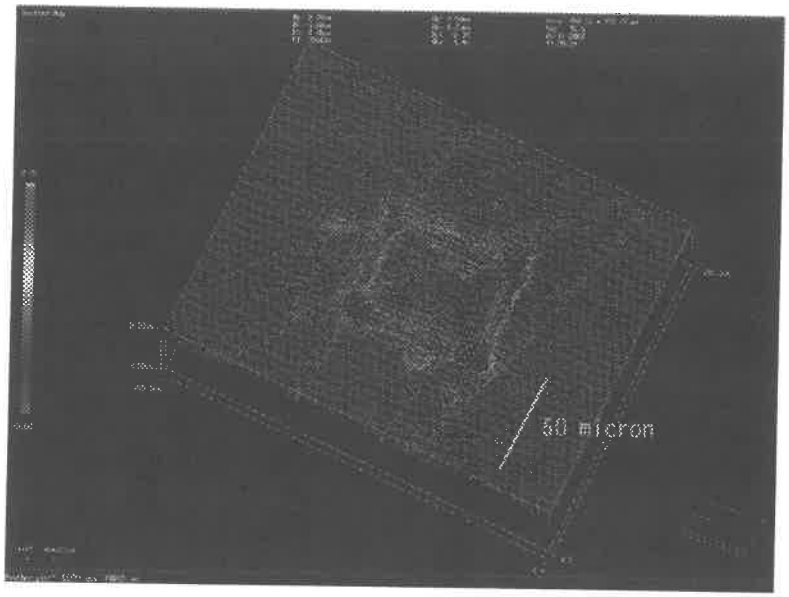

Figure 5: A micro rectangular structure (50 x 75 μm^2) was patterned at a scan speed of 2.5 μm /sec.

Conclusions

Due to its superior piezoelectric coefficients, PZN-PT ($Pb(Zn_{1/3}Nb_{2/3})O_3$-PbTiO) is considered a promising material for advanced piezo-devices. In this paper, it has been shown that a PZN-PT single crystal substrate can be patterned by direct laser writing in 34.8% dilution of HCl. . One of the advantages of the laser etching is that it permits localized processing on substrate surfaces. We are able to use the experimental arrangement to obtain etch rates as high as 30 μm per minute. At lower acid concentration, the etching speed was found to be impractically slow. The potential to realize more complicated pattern by using the method was also demonstrated. This research was partially supported by National Science Foundation under grant ECS-9980828.

References

1. Ritsko, J.J., F. Ho, and J. Hurst, "Laser-assisted chemical etching of copper," Appl. Phys. Lett., vol.53, no.1, 78-80, (1988)
2. Wysocki, G., S.T. Dai, T. Brandstetter, J. Heitz, and D. Bauerle, "Etching of crystalline Si in Cl_2 atmosphere by means of an optical fiber tip," Appl. Phys. Lett., vol.79, no.2, 159-161, (2001).
3. Holber, W., G. Reksten, and R.M. Osgood, Jr., "Laser-enhanced plasma etching of silicon," Appl. Phys. Lett., vol.46, no.2, 201-203, (1985).
4. Park, S.E. and T. R. Shrout, "Ultrahigh strain and piezoelectric behavior in relaxor based ferroelectric single crystals," J. Appl. Phys., vol.82, no.4, 1804-1811 (1997).
5. Fu, H. and R. E. Cohen, "Polarization rotation mechanism for ultrahigh electromechanical response in single-crystal piezoelectrics," Nature, vol.403, no.20, 281-283, (2000).
6. Levy, M., R. M. Osgood, Jr., A. S. Bhalla, R. Guo, L. E. Cross, A. Kumar, and H. Bakhru, "Stress tuning in crystal ion slicing to form single-crystal potassium tantalate films," Appl. Phys. Lett., vol.77, 2124 (2000).

INVESTIGATION OF THERMO-CHEMICAL POLISHING AND LASER ABLATION OF CVD DIAMOND FILM

C.L. Chao[1], K.J. Ma[2], Y.H. Liu[1], T.T. Chen[3], H.Y. Lin[4] , and Y.M. Chang[4]

[1] Department of Mechanical Engineering, E790, Tam-Kang University, No.151 Ying-Chuan Road, Tamsui, Taipei Hsien-251, Taiwan, R.O.C (Email: clchao@mail.tku.edu.tw)

[2]Dept. of Mechanical Engineering, Chung-Hwa University, Hsin-Chu, Taiwan, R.O.C.

[3]Department of Mechanical Engineering, Chung-Cheng Inst. of Technology, Taoyuan, Taiwan,R.O.C

[4]MEMS Division, MIRL, Industrial Technology Research Inst., Chu-Tung, Hsin-Chu, Taiwan, R.O.C.

EXTENDED ABSTRACT

Owing to the rapid development in the mobile telecommunication and optoelectronic area, SAW(Surface Acoustic Wave) devices such as SAW-Resonator、 SAW-Duplexer and SAW-Sensors are in great demand. Crystals such as $LiNbO_3$, $LiTaO_3$, and Quartz are frequently used as the substrate material for SAW devices. However, the surface acoustic wave velocity obtainable on these materials is relatively low. ZnO/Diamond structure has attracted a lot of attentions and heavy investment recently just because diamond has the capability of producing very high surface acoustic wave (around 10000m/s). In the present study, the microwave CVD method was employed to produce diamond films on silicon single crystal. Hot polishing together with laser ablation experiments were then conducted on the obtained diamond films. The underlying material removal mechanisms, microstructure of the machined surface and related machining conditions were also investigated.
Keywords: CVD diamond film, thermo-chemical polishing, laser ablation.

Introduction: Crystals such as $LiNbO_3$, $LiTaO_3$, and Quartz are frequently used as the substrate material for SAW devices (Senbo Takashi 2000; Nishizawa Toshio 2000). However, the surface acoustic wave velocity obtainable on these materials is relatively low (2500~4500m/s). The frequency of the device is governed by the equation $F = v / \lambda$, where F is the frequency, v is the velocity of the surface acoustic wave and λ is the wavelength which is determined by the line width of the IDT (Interdigital Transducer). This means that higher frequency can be obtained either by choosing a substrate material with a higher surface acoustic wave velocity or by reducing the line width of the IDT. Shown in table 1 are the line widths of various substrate materials when a 2.5GHz working frequency is required. It is clear that the required line width is much easier to achieve when diamond is used as substrate material.

Table 1

Substrate Materials	Velocity (m/s)	Freq.	IDT linewidth (μm) @2.5GHz
$LiTaO_3$	3300	800MHz	0.33
$LiNbO_3$	3500	900MHz	0.35
Quartz	3200	800MHz	0.32
ZnO/Glass	3200	800MHz	0.32
ZnO/Sapphire	5500	1.4GHz	0.55
ZnO/Diamond	10000	2.5GHz	1.0

ZnO/Diamond structure has attracted a lot of attentions and heavy investment recently just because diamond has the capability of producing very high surface acoustic wave (around 10000m/s). However, diamond has to be machined to the specified thickness and surface finish before it is to be used as substrate material of a SAW device (Higaki 1997; Kadota & Kitamura 1999). The trouble is that

diamond has the highest hardness number of the known materials and is extremely difficult to be machined.

Many researches have been conducted, in the past decades, on machining CVD-diamond film by mechanical grinding/lapping/ polishing (Tokura et al, 1991; Bhushan et al 1993; Spear & Dismukes 1993; Yoshikawa et al 1990, 1996; Jin et al 1992, 1995; Ramesham & Rose 1998, Nishimura et al 2000), by laser ablation (Tezuka & Yoshikawa 1990; Ravi & Zarifis 1993; Tokarev et al 1995; Chien et al 1995, Cappelli et al 1999), by laser-assisted etching(Ral'chenko et al 1995, Shafeev et al 1997), by ion-beam machining (Funamoto & Koseki 1991; Vivensang et al 1996) or by RIE (reactive ion etching) (Sandhu & Chu). Apart from material removal rate, the underlay physic/chemical phenomena involved in the wear of diamond and various machining techniques were also studied/reviewed in details by some researchers such as Paul et al(1996), Malshe et al (1999). Though some very promising results have been obtained, the problems related to the machining of CVD diamond film are still far from fully resolved. In the present study, the CVD diamond films were hot-lapped and laser polished to investigate its machinability.

Experimental Setup: Diamond wafers with thickness up to 100μm have been grown on silicon single crystal in this study by MWCVD process. The deposition is carried out in a plasma reactor (Axitron) having an ellipsoid cavity to generate intense, spatially extended plasmas from a CH_4/H_2 gas mixture. The microwave plasma reactor is powered with 6 kW microwave power, operating at 915 MHz. The substrate temperature is monitored by an optical pyrometer and is kept at 1200°C. To ensure the quality of the coated diamond film, the growth rate was kept relatively low at around 1~2μm/hr. Some of the important features of MWCVD diamond film include: (1) Optical broad band transparency from deep UV(~225nm) to far IR (sapphire: 0.25-4μm) (2) thermal conductivity at room temperature ~2000 W/mK (3) hardness ~90 Gpa.

Thermo-chemical polishing together with laser ablation experiments were then conducted on the obtained diamond films. Shown in Fig.1 is the schematic representation of the setup for hot polishing experiments. The iron/steel bar or plate was heated by either infrared irradiation or inductive heating devices to various skin temperature. In the case of turning experiments, the specimen was mounted on a flexure and was then brought to contact with the heated iron/steel bar. The contact force was monitored through the displacement of the flexure.

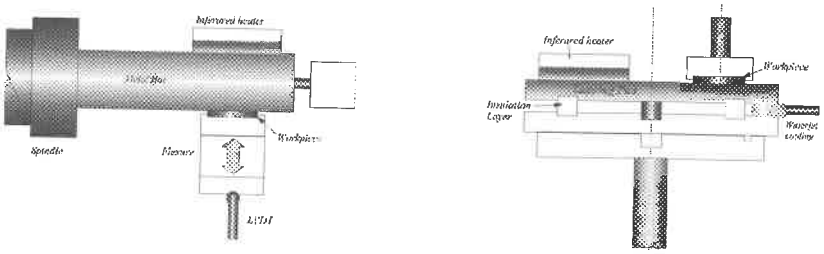

Fig.1 Schematic representation of the setup for thermo-chemical polishing experiments

The relative speeds of polishing, duration of polishing were also recorded. Some minimeters of the iron/steel bar or plate surface was taken off with a turning/dressing tool each time before starting a new set of experiment to ensure the surface conditions maintained as closely the same as possible.

The excimer lasers used in this study were the Lambda Physik LPX200 series (ArF 193nm) which had a maximum repetition rate of 100 Hz, maximum pulse energy of 400mJ and pulse duration of 20ns. A MicroLas made homogenizer and x10 condenser lens were used to homogenize the beam and increase the fluence respectively. The CVD diamond film, horizontally placed on an XY stage, was irradiated in air by excimer laser (ArF 193nm) at a 90° angle of incidence. The laser spot size was

approximately 1.4x1.4mm.

Results and Discussions: The micrograph of the surface of the as-grown CVD diamond film and it was irradiated by excimer laser (193nm, 385mJ /10Hz) for 500, 1000, 3000, 5000, 10000 shots were shown in Fig.2. The surface roughness (Ra) value was improved from 0.4μm of the as grown diamond film to Ra~0.1μm in 500shots. The peaks of the diamond grains were removed mainly by the photo thermal effects introduced by excimer laser. That is the high energy density and short pulse duration characters of excimer laser play important roles in raising the protruding diamond grains to an evaporating temperature. However, as the protruding peaks gradually removed from the surface the polishing rate decreases.

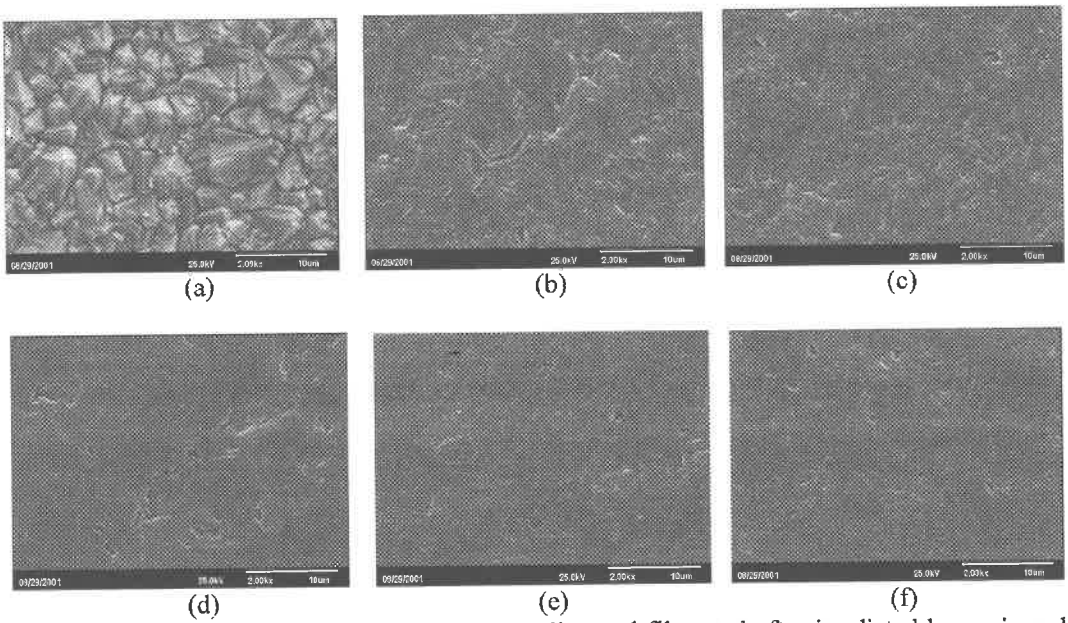

Fig.2 Surface morphology of the (a)as-grown CVD diamond film, and after irradiated by excimer laser (193nm, 385mJ /10Hz) for (b) 500 shots (c) 1000 shots (d) 3000 shots (e) 5000 shots (f) 10000 shots

The material removal mechanisms involved in the thermo-chemical polishing process are generally categorized into graphitization (metal catalyzed), diffusion (into metal), oxidation and formation of metal-carbon complex. Cast iron and steel with various carbon contents are used in this study as the catalytic materials to transform diamond into graphite which is subsequently removed by micro-chipping during the polishing process or diffusing into the iron/steel surface. The polishing temperatures, pressure and speeds used in the present study ranged from 50~650 °C , 0.5~4.5MPa and 2.0~5.7m/s respectively The iron/steel bar or plate were pre-heated to the designed temperature before the polishing experiments were carried out and the temperature was monitored during the polishing process by both infrared detector and thermal couple. Owing to the heat generated by the friction, the temperature at the contact zone should be higher than the pre-heated temperature. Shown in Fig.3 and Fig.4 were the SEM micrographs of the CVD diamond film which were hot polished for 30 minutes under various polishing speeds (2.1m/s and 4.27m/s) at a temperature around 450°C (skin temperature of the iron/steel just outside the polishing area). Based on the obtained results, some 1.5μm and 4.8μm deep of diamond film was successfully removed in 30 minutes in the case of polishing at a temperature around 450°C and at 2.1m/s and 5.7m/s respectively.

Shown in Fig.5 are the SEM images of the graphite and carbon-tube-like formations frequently

observed on the (iron/steel) debris outside the polishing area. According to the results of carbon-mapping, these fine features are mainly consisted of carbon. Further investigations by TEM are required to clarify their crystal structures and how they are formed.

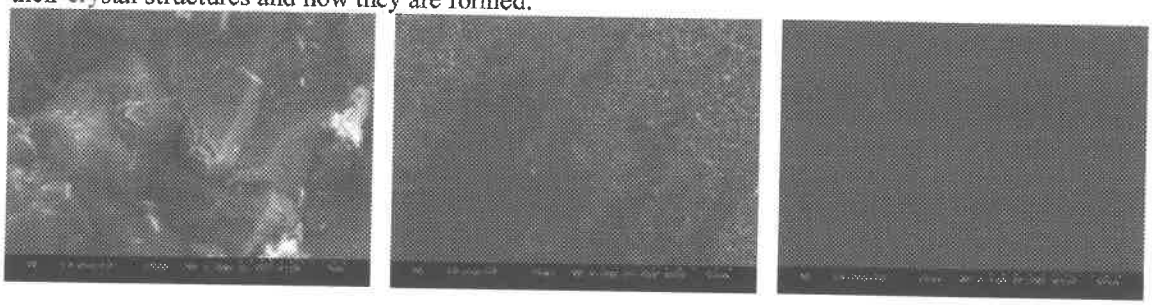

Fig.3, SEM micrographs of the thermo-chemical polished CVD diamond film (2.1m/s, 30min, 450°C, 3.8MPa)

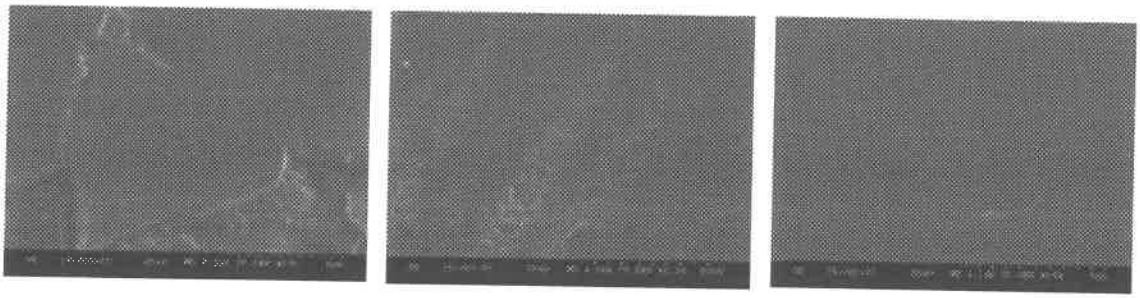

Fig.4, SEM micrographs of the thermo-chemical polished CVD diamond film (4.27m/s, 30min, 450°C, 4.2MPa)

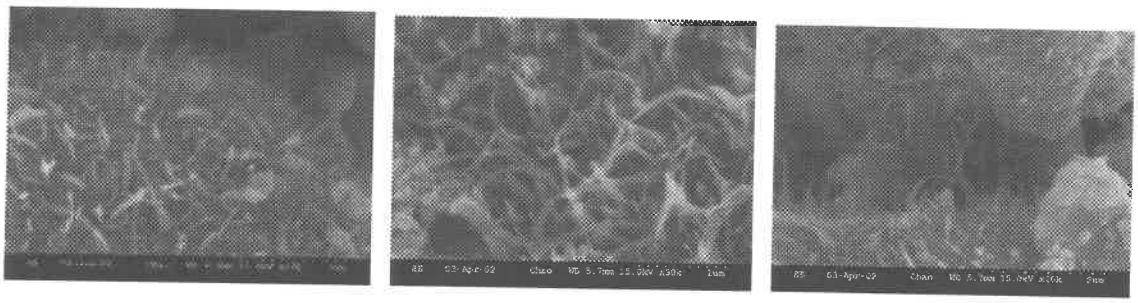

Fig.5, SEM micrographs of the graphite and carbon-tube-like formations observed on the debris outside the polishing area

Summary: Thermo-chemical polishing and laser ablation experiments were conducted on the CVD diamond films and results showed that 1. laser ablation could improve the surface roughness from above 0.4μm to around 0.1μm in a minute, however scanning would be required to cover a large area, 2. thermo-chemical polishing was proved to be able to remove the diamond film very effectively (4.8μm deep of diamond film was removed in 30 minutes when polishing at 450°C and 5.7m/s), 3. the removal rate increased with polishing speed and pressure.

References

Bhushan, B.; Subramaniam, V.V.; Malshe, A.; Gupta, B.K. and Ruan, J. 1993 J. of Appl. Phys., Vol.74, No.6, p.4174

Cappelli, E.; Mattei, G.; Orlando, S.; Pinzari, F. and Ascarelli, P. 1999 Diamond and Related Materials, No.8, p.257

Chien, T.; Cutshaw, C.; Tanger, C. and Tzeng, Y. 1995 Appl. Of Diamond Films and Related Mat. (Ed. Feldman, A. et al), NIST-SP-885, p.257

Funamoto, H and Koseki, O., 1991 Surface Coating Tech., Vol.47 p474

Higaki K.1997 "High Frequency Saw Filter on Diamond", IEEE MTT-S Digest, pp829-832, 1997.

Jin, S. and Graebner, T.H. et al 1992 Diamond and Related Materials Vol.1, p949

Jin, S. 1992 Appl. Phys.Lett. Vol.60(16), p.36

Jin, S.; Zhu, W. and Graebner, T.E. 1995 Appl. Of Diamond Films and Related Mat. (Ed. Feldman, A. et al), NIST-SP-885, p.209

Kadota, M.and Kitamura, T. 1999 "Influence of Leaky Surface Acoustic Wave Velocity of Glass Substrates on Frequency Variation of ZnO/Glass SAW Filters", IEEE Transaction on Ultrasonics, Ferroelectrics and Frequency Control, Vol. 46, pp817-822.

Malshe, A.P.; Park, B.S.; Brown, W.D. and Naseem, H.A. 1999 Diamond and Related Materials, No.8, p.1198

Nishimura, K.; Ohmori, H.; Lin W.; Makinouchi, A.; Ibuki, S.; Kono, T. and Takechi, O. 2000 J. of (Japan) Society of Grinding, Vol.44, No.8, p.383

Nishizawa, Toshio 2000 "Fujitsu Media Carves Out New Boundaries in SAW Filter Techniques", AEI July, pp.36-40

Paul, E.; Evans, C.J.; Mangamelli, A.; McGlauflin, M.L. and Polvani, R.S. 1996 Precision Engineering, Vol.18, p.4

Ral'chenko, V.G.; Korotushenko, K.G.; Smolin, A.A. and Loubnin, E.N. 1995 Diamond and Related Materials, No.4, p.893

Ramesham, R. and Rose, M.F. 1998 Thin Solid Film, Vol.320, p.223

Sandu, G.S. and Chu, W.K. 1989 Appl. Physics Letters, Vol.55, p.437

Senbo, Takashi 2000 "SAW Filter Improve To Keep Up With Small, Dual-System Mobil Phones", AEI May, pp.28-30, 2000

Shafeev, G.A.; Obraztsova, E.D. and Pimenov, S,M, 1997 Materials Science and Engineerig B, Vol.B46, p.129

Spear, K.E. & Dismukes, J.P. 1993, Synthetic Diamond-Emerging CVD Science and Tech., Wiley, NY

Tezuka, S. and Yoshikawa, M. 1990, New Diamond, Vol.17, p36

Tokarev, V.N.; Wilson, J.I.B.; Jubber, M.G.; John, P. and Milne, D.K. 1995 Diamond and Related Materials, No.4, p.169

Tokura, H. and Yoshikawa, M. 1991 Applications of Diamond Films and Related Materials, Elsevier, Amsterdam, p.227

Yaysuda, H.; Oguri, M.; and Horishima, T. 1995 "Miniature SAW Filters in GHz Range", 4th IEEE International Conference, pp.321-324, 1995.

Yoshikawa, M. 1990 Diamond Optics III, SPIE 1325, p.210

Yoshikawa, M. and Okuzumi, F. 1996, Surface & Coatings Technology, Vo.88, p.197

Vivensang, C.; Ferlazzo-Manin, L.; Ravet, M.F.; Turban, G.; Rousseaux, F. and Gicquel, A. 1996 Diamond Related Mater. No.5, p.840

Corrective Planarization Method Using Chemical Mechanical Polishing Assisted by Laser Particle Trapping

Keiichi KIMURA :
Sony EMCS Corporation, Tokyo, JAPAN

Takashi MIYOSHI, Yasuhiro TAKAYA, Satoru TAKAHASHI
Osaka University, Osaka, JAPAN

1. Introduction

The improvement in the integration of VLSI has resulted in the increment in the number of interconnect layers, and thus high planarity has been required. According to the 2001 ITRS Roadmap[1], the site flatness of 100 nm is required for the generation of DRAM 1/2 pitch at 100nm in the year of 2003, while the generation at 70nm in the year 2006 will demand the site flatness of 70nm. However, since it is difficult to achieve these goals with the current process of the CMP technology, developments in new planarization technologies are in need.

The requirements on CMP process in the VLSI's planarization process are as follows:

(1), To gain excellent images with exposure of patterns when creating interconnect layers by making planarization on interconnect layers, and reducing step height of silicon wafer surface smaller than the depth of focus of wafer stepper's projection lens;

(2) To build up the required structure of interconnect layers, by removing accumulated, unnecessary portions for metal interconnect layers such as Copper.

This research aims to realize the planarization with the chemical mechanical polishing where the aggregated marks of fine particles in slurry are created with the optical radiation pressure by irradiated laser beam, and to process selective material removal intentionally in small projected areas on the VLSI's circuit pattern.

In the previous report[2], the polishing property of material removal at the aggregated marks located on the surface of silicon wafer was investigated.

In this report, at first, the considerations to create the aggregated marks by laser beam irradiation onto the surface of silicon wafer were investigated. Furthermore, new planarization method, which fills up the dimples with laser aggregated marks and polish the area as one surface, was proposed and attempted to obtain high planarity on trench-shaped uneven surface which was processed by FIB(Focused Ion Beam) machining on the silicon wafer surface.

2. Conditions to Planarization

As the common idea of the planarization process, the planarity can be made by removing selected projections on uneven surfaces of silicon wafers. Generally, it is considered that material removals are achieved with the stress distribution, caused by the elastic contact between polishing pad and projections on silicon wafer surface. It is, however, not necessarily true that polishing pads contact with projected areas. Since polishing pads have large pores in size of 20 to 40μm and fluffy surfaces with fibers made by dressing, as shown in Fig.1, the polishing pads contact evenly with entire surface of silicon wafer in many occasions, though it is likely that they touch with projected areas. As a result, only material removals are progressed,

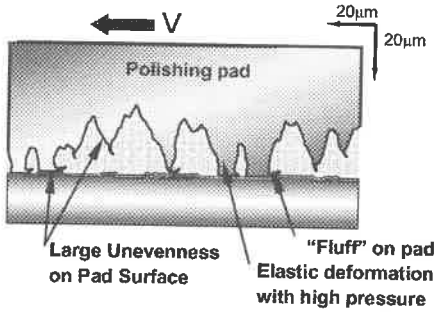

Fig. 1 Contact between polishing pad and surface of silicon wafer

while step height reductions do not show any changes despite a long-time polishing. This attributes to the fact that the whole surface of silicon wafer is evenly polished, although the step height reduction is slow.

This result shows us the necessity of "the Conditions to Planarization", which are listed as follows:

[A] ***Selective removal of projected areas on silicon wafer surfaces;***
[B] ***Simultaneous controls on removal of recessed areas.***

3. Laser Trapping by Optical Radiation Pressure

"Laser Trapping"[3] is a well-known phenomenon that captures dielectric particles with optical radiation pressures, which are larger in size than the wavelength of light. It is considered that changes in momentum of laser beam at reflection and refraction, provide the generation of forces, when the laser beam irradiates into particles.

On the other hand, with particles smaller than the wavelength, the scattering of light results in a different phenomenon than when considering light as rays. Therefore, it cannot be treated as the generation of optical radiation pressure by the change in momentum of rays, but it is possible to consider as Maxwell's stress is in effect.

Sugiura[4] attempted to calculate the fine particles' electric field with Mie's theory, and to obtain the force of optical radiation pressure with Maxwell's stress. It was clarified by the result that fine particles receive optical radiation pressure in a direction of light propagation, and the optical radiation pressure is amplified with the size of fine particles. Takaya, et al.[5] concluded, as shown in Fig. 2, that fine particles receive a thrust force to the focal point of laser beam, in parallel to the light propagation, and form aggregated marks on the focal point.

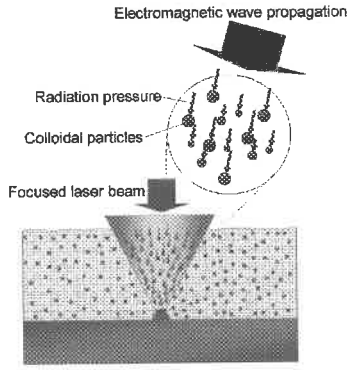

Fig. 2 Optical radiation pressure on fine particles

Generally, in colloidal solution, fine particles can keep stable state of dispersion with balanced forces between repelling forces caused by surface potential and van der Waals forces. At around the focal point, the forces by the optical radiation pressure are applied additionally. Fine particles are condensed and gathered on silicon wafer to form aggregated marks due to the effect of heat.

The experiment to form the aggregated marks was attempted with the experimental apparatus as illustrated in Fig.3. Laser beam is irradiated from the light source, Ar+ laser (λ=488m), and radiate into the test piece through objective lens (40x, NA=0.55). The test piece is diced silicon wafer (10x10mm) and was put on slide glass and filled with slurry. The piece was set on the piezo XYZ stage, and positioning, focusing, and laser beam scanning motion were carried out by the XYZ stage.

Fig.4 shows the aggregated marks which were created with the experimental apparatus. The width of aggregated marks is approx. 2-3μm, almost the same size as diameter of laser beam.

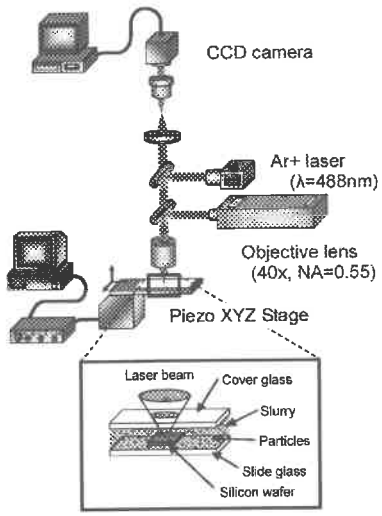

Fig. 3 The experimental apparatus for laser irradiation

4. Basic Concept of LAFP Method

In order to make planarization on irregular surface of silicon wafer, the removal of projected areas and the prevention to the removal of the bottom of the recessed parts are required simultaneously. Fig.5 shows the concept of the LAFP (Laser Aggregation, Filling-up & Polishing) method that enables to fulfill these conditions.

Firstly, dimples on uneven silicon wafer surfaces are irradiated by laser beams for the generation of aggregated marks, made of fine particles in slurry. In the next step, polishing is applied to that particular area. This series of processes makes dimples on uneven silicon wafer surfaces be filled by aggregated marks of fine particles. Then, the surface is polished.

As a result of these processes, the bottom of surfaces of recessed areas are masked with aggregated particles, and no material removal at recessed areas takes place during the polishing. Furthermore, the bottom of surfaces of recessed areas is polished only when polished surface of projection reaches down to the initial height of bottom of trenches. This result shows us a potential for polished surface with the higher level of planarity.

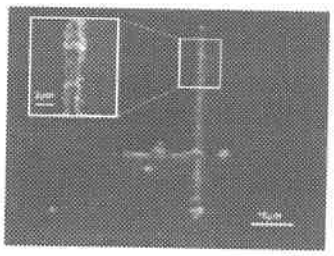

(a) SEM photograph

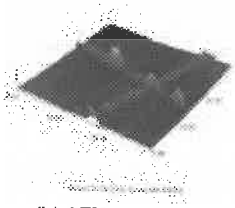

(b) AFM observation

Fig.4 Aggregated marks on silicon wafer

5. Polishing with LAFP method

Based on the LAFP concept, polishing experiments were implemented. Fig.6 illustrates polishing unit for the experiments. The polishing unit has ϕ20mm polishing pad and can control rotation speed and down force of polishing pad. Moreover, four trenches were shaped on the surface of test pieces of diced silicon wafer by FIB (Focused Ion Beam) machining. One test piece was for polishing experiment, and the other was polished after aggregated marks were formed at the bottom of two trenches.

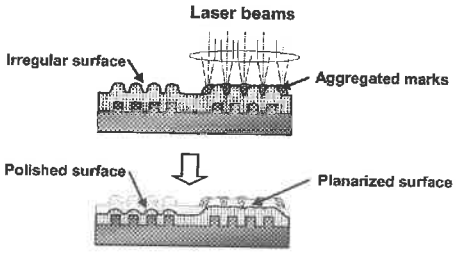

Fig. 5 Concept of LAFP method

Fig.7 shows the test piece with formed four trenches. The width of trenches is approx. 2μm, and the depth is approx. 57nm. Fig.8 shows the change in its cross-section during polishing. At T=9 min, the entire area of trenches was removed in concaved shape, and at T= 12min, the recessed geometry is remained after unevenness of trenches were disappeared.

Fig.9 shows the test piece which has two aggregated marks at two trenches of 120nm depth, and the height of the aggregated mark is approx. 520nm.

The cross-section of the trenches is illustrated in Fig.10. The aggregated areas are possible to control material removal as with masks, and whole area of aggregated marks created was slightly in convex shape at T= 12min. At T= 24min, surface where trenches were formed is planarized as a smooth plane with surface roughness. This result shows that the formation of aggregated marks with laser irradiation is useful for planarization on uneven surface of silicon wafer.

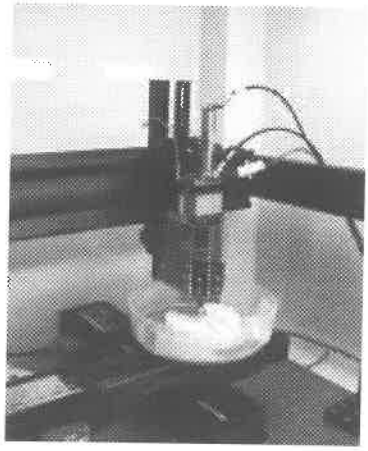

Fig. 6 Polishing unit for experiments

6. Conclusion

The new planarization method is proposed and attempted by experiments. This method indicates two unique points as follows:

(1) The aggregated marks are forms with laser irradiation on surface of silicon wafer. The aggregated marks are made of fine particles in slurry.

(2) After aggregated marks are formed and filled up at the recessed areas of surface of silicon wafer, polishing is carried out. This process is possible to realize high planarity on silicon wafer.

As a final result, the smooth surface with surface roughness is obtained with the LAFP (Laser Aggregation, Filling-up & Polishing) method, and the method has a high potential for planarization.

References

1) ITRS Roadmap, Front End Process 2001 Edition (2002)
2) K. Kimura et al.: Proc. of ASPE 2001 (2001) 537
3) A. Ashkin et al:Physical Review Letter, 24 (1970) 156
4) T. Sugiura : Osaka University Doctoral Thesis (1993)
5) Y. Takaya, K. Kimura et al : Proc. JUSFA (2002)

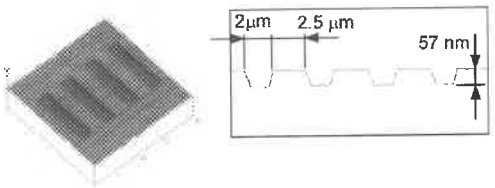

Fig. 7 Trenches formed on siliconw wafer by FIB machine.

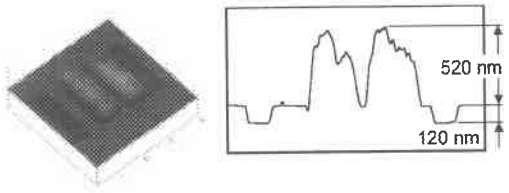

Fig. 9 Aggregated marks on the bottom of trenches

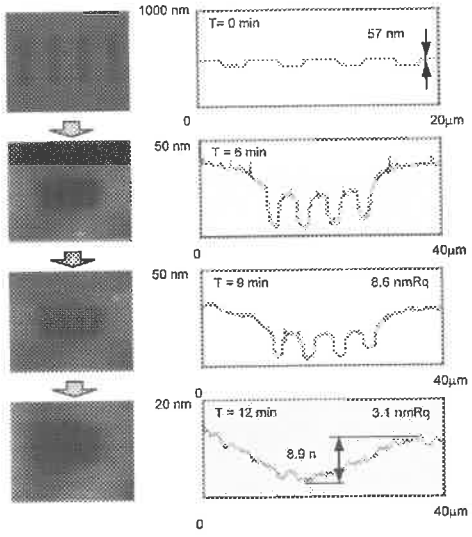

Fig. 8 Cross section of trenches during polishing

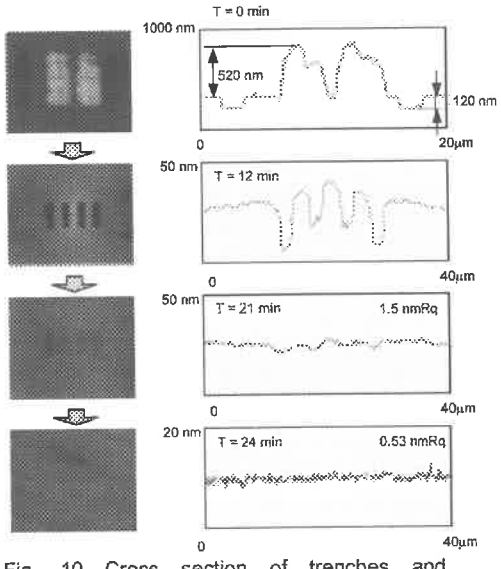

Fig. 10 Cross section of trenches and aggregated marks

NEW OPTICAL MEASUREMENT TECHNIQUE FOR SI WAFER SURFACE DEFECTS USING ANNULAR ILLUMINATION WITH CROSSED NICOLS

Satoru Takahashi[1], Takashi Miyoshi[1], Yasuhiro Takaya[1], and Takahiro Abe[2]
1 Department of Mechanical Engineering and Systems, Osaka University
2-1, Yamadaoka, Suita, Osaka 565-0871, Japan
2 Seiko Epson Corporation
3-3-5, Yamato, Suwa, Nagano 392-8502, Japan

Abstract: This paper presents new optical measurement method for evaluating the microdefects on a silicon wafer surface using annular illumination based on the Fourier transform optics with crossed nicols. In order to verify a feasibility of this new measurement technique, the basic experiments are carried out by measuring the various types of Si wafer surface defects such as microscratches, particulate contaminations, COP (Crystal Originated Particle) [1], etc. All defects employed in this experiment are identified by making the use of AFM (Atomic Force Microscope) and SEM (Scanning Electron Microscope). Then it is found that microscratches induced in the CMP (Chemical Mechanical Polishing) processes with the depth of only 10nm can be detected by this method independent of their directions. And another result is also presented that the proposed method enables to clearly discriminate the defect types by combining with the normal illumination.

Key words: laser applied measurement, surface inspection, silicon wafer, surface defects

1. INTRODUCTION

In modern semiconductor technology, the reduction of the density of Si wafer surface defects that may decrease device yield has become an important issue. In order to fabricate the semiconductor device with high reliability, it is necessary to measure directly them during processing and control the fabrication process. The light scattering methods[2-4] based on the total integrated scatter (TIS) using oblique illumination are very often used for the inspection of Si wafer surface texture. However these optical measurement methods have the following disadvantages:

(1) It is difficult to sensitively detect the oriented defects such as microscratches due to oblique illumination from one direction, because the oriented defects preferentially scatter perpendicular to their long dimension. The microscratches will be more important in CMP (Chemical Mechanical Polishing) processes and may be main yield-limiting in the next VLSI generation.

(2) It is hard to discriminate the different types of defects due to intensity detection of scattered light. Defect types for Si wafer surface are classified two types such as contaminant defects on the surface and pit defects at the surface. The contaminant defects mean particulate contaminants, film contaminants and so on, which are on the surface. And the pit defects do COP (Crystal Originated Particle) [1], microscratches, and so on, which are "surface-breaking" defects. And the wafer manufactures strongly need to classify into two types of contaminant defects and pit defects, because the strategy on management of yield is dependent on their defect types.

These disadvantages are great trouble to achieve the yield enhancement of VLSI in next generation. Therefore, the purpose of this study is to develop a new optical measurement technique resolving the above disadvantages, which can detect the microscratch with the depth of 10 nanometer scale and can discriminate the different types of Si wafer surface defects such as contaminant defects or

pit defects.

2. PRINCIPLE OF MEASUREMENT

The normal configuration of optical microdefect detection widely used as commercial instruments is illustrated in Fig. 1. The laser beam is obliquely illuminated to the work surface from one direction. The incident angle is usually near to 70 degree. The several detectors are placed at arbitrary angle except specular direction to pick up the scattered light of the defect surface. In this optical configuration, when there exists no defect on the silicon wafer surface, the detectors do not get any output about the scattered light because the scatter is confined to a small angle around the specular direction. On the contrary, if there exists any defect on the surface, the scatter results from the defect at wide angle and the detectors pick up some of the scattered light as shown at the top of Fig. 1. The sizes and the types of the microdefects are estimated from the detected intensity value of I_1, I_2 and I_3, namely the sum of the ratio of I_1, I_2 and I_3, the difference between I_1, I_2 and I_3, the ratio of I_1 or I_3 to I_2 and so on. This optical arrangement is equivalent to dark field optical system based on far field optics, however, it is difficult to sensitively detect the oriented microdefects such scratches due to oblique illumination from one direction as shown at the bottom of Fig. 1. In order to overcome this major disadvantage, we proposed a new optical measurement method, which can be applied to the oriented microdefects independent of their directions with high sensitivity.

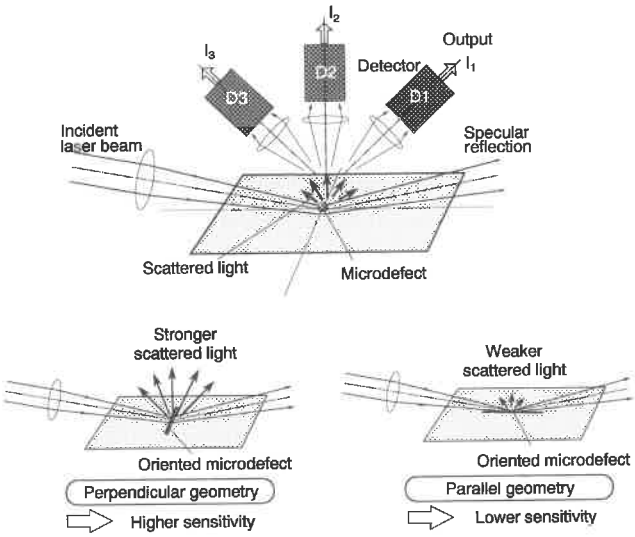

Fig. 1 Normal configuration of optical microdefect detection

Fig. 2 shows the principle of our proposed measurement technique, which is based on the annular illumination and the Fourier transform optical system with crossed nicols. And this measurement technique is expected to have the following characteristics.

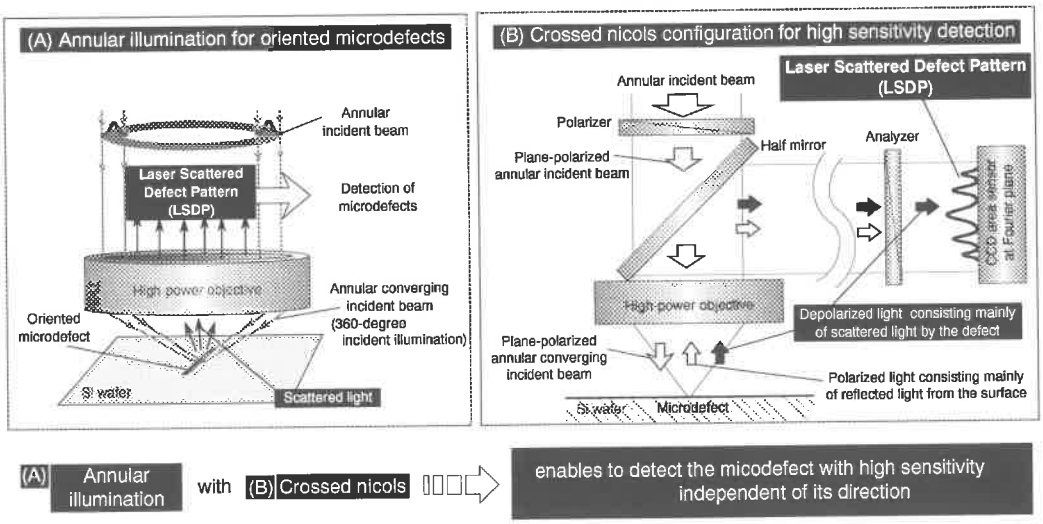
(A) Annular illumination for oriented microdefects
Annular incident beam
Laser Scattered Defect Pattern (LSDP)
Detection of microdefects
High power objective
Annular converging incident beam (360-degree incident illumination)
Oriented microdefect
Si wafer
Scattered light
(B) Crossed nicols configuration for high sensitivity detection
Annular incident beam
Laser Scattered Defect Pattern (LSDP)
Polarizer
Half mirror
Analyzer
Plane-polarized annular incident beam
CCD area sensor at Fourier plane
High power objective
Depolarized light consisting mainly of scattered light by the defect
Plane-polarized annular converging incident beam
Polarized light consisting mainly of reflected light from the surface
Si wafer
Microdefect
(A) Annular illumination
with
(B) Crossed nicols
enables to detect the micodefect with high sensitivity independent of its direction

Fig. 2 Principle of measurement based on annular illumination with crossed nicols

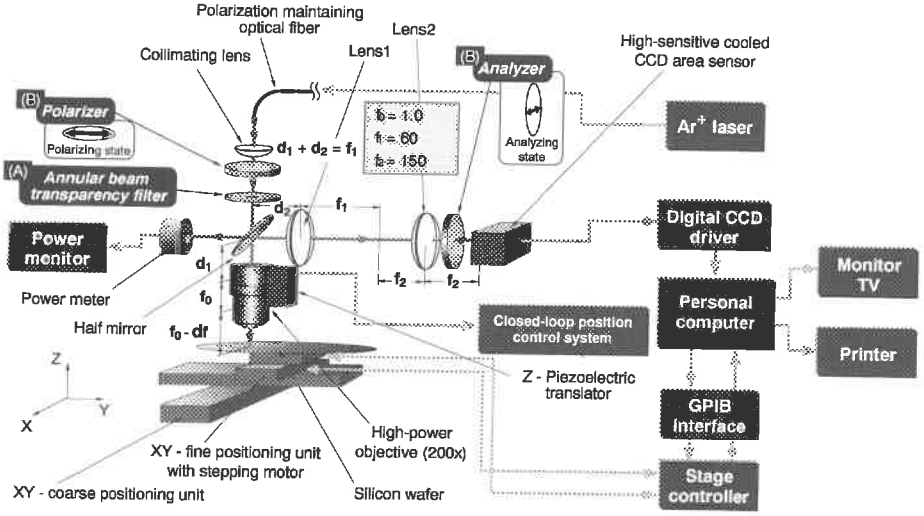

Fig. 3 Schematic diagram of silicon wafer surface defects measurement system

(1) The annular illumination generated by the high power objective, in which the Si wafer surface is obliquely illuminated from every direction, enables the oriented defects to be detected high sensitively independent of their directions(Fig. 2(A)). And the light polarizers arranged in the crossed nicols plays an extremely important role in enhancing sensitivity(Fig. 2(B)).

(2) As shown in Fig. 2(A)(B), since this optical measurement method detects scattering light intensity patterns of the defects (called "Laser Scattered Defect Pattern (LSDP)"[5,6]), which are generated based on the Fourier transform optics with crossed nicols, it is possible not only to detect the defects but also to discriminate the different types of ones such as contaminant defects or pit defects.

3. MEASUREMENT SYSTEM

Fig. 3 shows the schematic diagram of silicon wafer surface defects measurement system based on the measurement principle mentioned above. An Ar^+ laser of wavelength 488.0nm is used as the light source. After passing through the single-mode optical fiber (mode field diameter = 4.0μm), the beam is collimated and polarized. This polarized Gaussian beam is converted into annular incident beam by passing the transparency filter made of the glass plate with the inside Cr coat (the diameter of Cr coat is taken 1200μm). The annular light beam focused by the high-power objective (with the numerical aperture of 0.95) is illuminated on the silicon wafer surface with the beam spot of about 1μm. These configurations enable the annular oblique illumination with the average incident angle of 68 degree (from 63 degree to 72 degree).

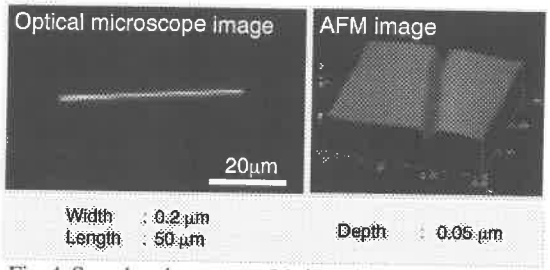

Fig. 4 Sample microgroove fabricated by FIB machining used in basic experiment

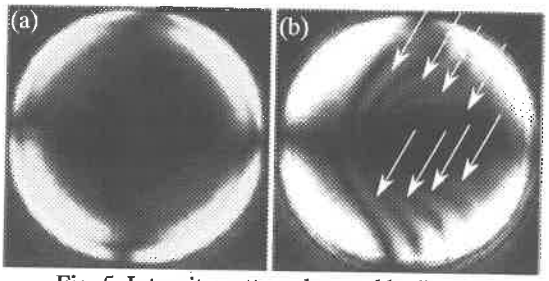

Fig. 5 Intensity pattern detected by Fourier transform optical system
(a) Reference pattern from smooth surface
(b) LSDP detecting the microgroove

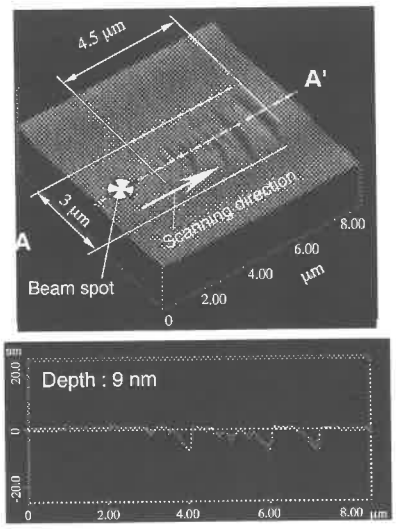

Fig. 6 AFM image of process inducing microscratch used in experiment

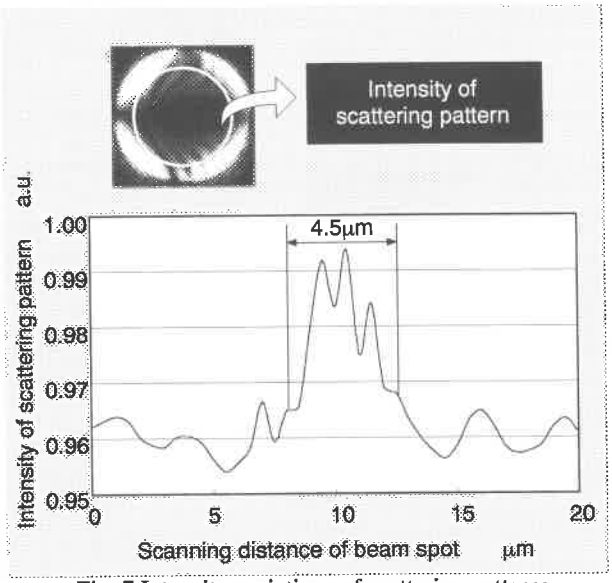

Fig. 7 Intensity variations of scattering patterns obtained from scanning experiments

The annular oblique beam spot is relatively scanned over the silicon wafer surface by the computer controlled xy-stage. The scattered light resulting from a microdefect within the annular oblique beam spot travels through the objective and the relay lens, and then forms LSDP corresponding to a Fourier transform image on the high sensitivity cooled CCD area sensor. The intensity distributions are converted to 12 bit digital image data and stored in the image memory.

4. EXPERIMENTAL RESULTS

4.1 Basic experiment for microgroove detection

In order to investigate the basic properties of this optical measurement method, primarily, experiments for detecting microgroove were carried out. Fig. 4 shows the optical and atomic force microscope image of the sample microgroove, whose size is 0.2μm wide, 50μm long and 0.05μm deep, which is fabricated as a typical oriented microdefect by FIB (Focused Ion Beam) machining. First, the intensity pattern of the smooth surface without any microdefects is detected as a reference one which is dark in the center part as seen in Fig. 5(a). Next, the defect pattern scattered from the microgroove is detected. Fig. 5(b) shows the defect pattern from the microgroove obtained as LSDP in Fourier transform optical system. As shown in LSDP of microgroove, a clear fringe image can be seen at the dark area in the intensity pattern. This fact means that a scattered light from the microdefect can be detect by this proposed optical system.

4.2 Scanning experiment for detection of microscratches induced in the CMP processes

Based on the basic experiment mentioned above, the scanning experiment for detecting the actual microscratches induced in the CMP (Chemical Mechanical Polishing) processes was performed by measuring the intensity variations of the scattering patterns. Fig. 6 shows the AFM image of the microscratches employed in this experiment, whose depth is only 9nm. Fig. 7 shows the intensity variations of the scattering pattern vs. the scanning distance of the annular oblique beam spot. In this experiment, the intensity of scattering pattern means the scattered light intensity monitored at the dark area of intensity pattern as shown at the top of this figure. This graph shows that the

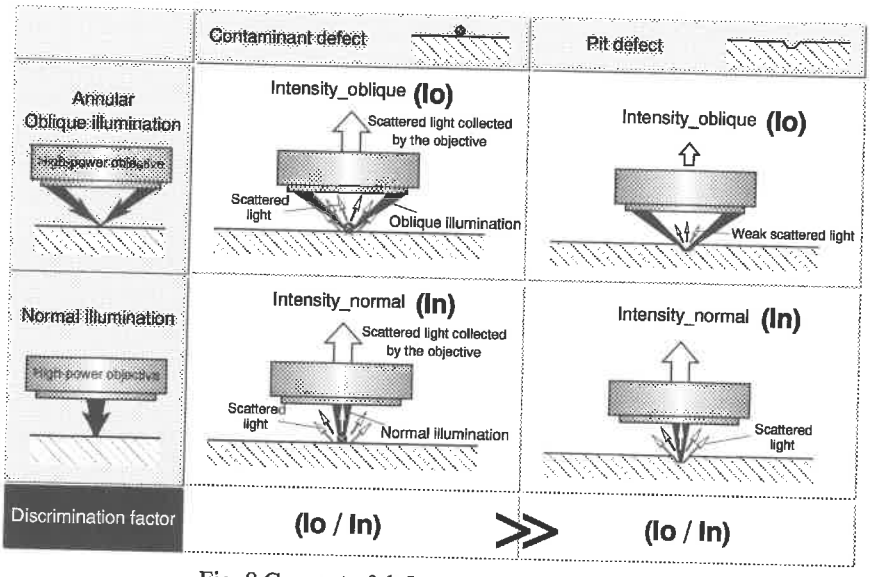

Fig. 8 Concept of defect type discrimination

intensity rapidly increases at the scanning distance of about 8μm and repeats up and down several times until about 12μm. The scanning range of about 4.5μm indicating the high intensity is equal to the horizontal size of microscratches area. This experimental results suggest that the proposed method can detect the oriented microdefects such as the microscratches induced in the CMP processes independent of their directions with the depth of 10 nanometer scale.

5. DISCUSSION OF DEFECT TYPE DISCRIMINATION IN COMBINATION WITH NORMAL ILLUMINATION

It is known that there is the difference between contaminant defects and pit defects coming from their responses to normal and oblique illumination. That is, in normal incidence, the scatter light from a pit defect is almost the same intensity as that from a contaminant defect, however, in oblique incidence, the scatter light from a pit defect becomes much smaller than that from a contaminant defect.Fig. 8 indicates the concept of defect type discrimination based on this characteristics using our proposed optical system. Here, in order to prevent the effect of absolute scattered intensity value dependent of defect sizes, normal illumination is combined with the annular oblique illumination mentioned before. And the ratio of scattered intensity at oblique illumination to one at normal illumination, Io/In, is employed as discrimination factor of the defect types

In order to verify a feasibility of this concept, the defect type discrimination experiments were

Table1 Microdefects employed in the defect type discrimination experiment

Type	Contaminant defects			Pit defects		
	Standard particle	Particulate conataminant	Film contaminant	FIB fabricating pit	COP defect	Microscratch
Microscope image	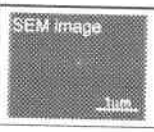			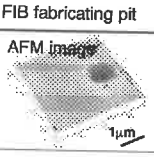	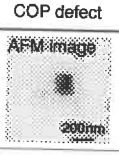	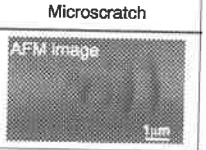
Horizontal size	0.21μm	0.28 x 0.31μm	0.66 x 0.90μm	0.8 x 1.0μm	0.15 x 0.20μm	4.5 x 3.0μm
Vertical size	0.21μm (Diameter)	91nm (Height)	110nm (Height)	65nm (Depth)	131nm (Depth)	5nm (Depth)

carried out by measuring the various kinds of Si wafer surface defects such as microscratches, particulate contaminants, film contaminants, COP, etc. All defects employed in this experiment are identified by making the use of AFM (Atomic Force Microscope) and SEM (Scanning Electron Microscope) as shown in Table 1. Fig. 9 shows the discrimination factor Io/In measured by each defect. The defect types, namely whether a contaminant defects or a pit defects, were clearly classified by the value Io/In in spite of various different kinds of defects.

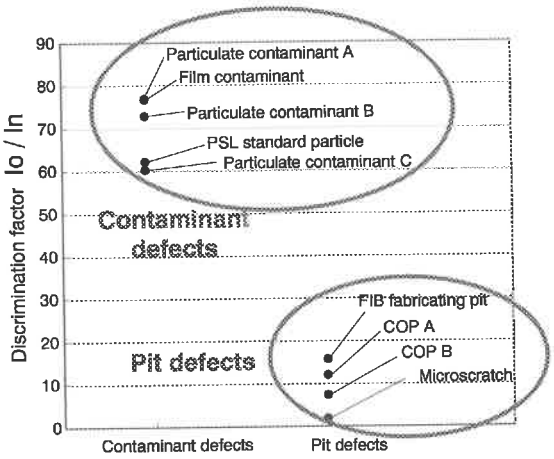

Fig. 9 Relationship between defect type and discrimination factor

6. CONCLUSIONS

In order to verify a feasibility of new optical Si surface defect measurement technique using annular illumination based on the Fourier transform optics with crossed nicols, the several basic experiments were carried. The results obtained in this paper are summarized as follows;

1. The microscratches induced in the CMP (Chemical Mechanical Polishing) process with the depth of only 10nm can be detected by the proposed method independent of their directions.
2. The proposed method enables to classify the various difference kinds of defects into two types of the contaminant defect and the pit defect by LSDP in combining with the normal illumination.

REFERENCES

[1] J. Ryuta, E. Morita, T. Tanaka, and Y. Shimanuki: Jpn. J. Appl. Phys., **29**/11(1990)1947.
[2] B. R. Locke and R. P. Donovan: J. Electronchem. Soc., **134**/7(1987)1763.
[3] Thomas A. Germer: Appl. Opt., **36**/33(1997)8798.
[4] Yu. Eremin and N. Orlov: Appl. Opt., **35**/33(1996)6599
[5] S. Takahashi, T. Miyoshi, Y. Takaya, and K. Saito: Annals of the CIRP, **47**/1(1998)459.
[6] T. Miyoshi, S. Takahashi, Y. Takaya, and S. Shimada: Annals of the CIRP, **50**/1(2001)389.

A Tool for Determining Task-Specific Measurement Uncertainties in GD&T Parameters Obtained from Coordinate Measuring Machines

Kim D. Summerhays[a], Michael P. Henke[a], Curtis W. Brown[b], Richard P. Henke,[a] Jon Baldwin[a]
[a]MetroSage, LLC and [b]Honeywell Inc., Federal Manufacturing and Technologies

Measurement uncertainty plays a vital role in establishing measurement traceability to national and international standards [1]. Likewise, it is a critical factor in the arbitration of issues pertaining to product conformance [2]. For dimensional metrology, it is necessary to associate with each GD&T parameter an estimate of its uncertainty at a specified level of confidence. As a result, for manufacturers to adhere to current standards, inspection reports must be supplemented with statements like, "The uncertainty of the diameter of this nominally ¼-inch diameter hole is 0.0008 inches, at 95% confidence." Obtaining uncertainty statements for measurements derived from a coordinate measuring machine (CMM) is not trivial. This stringent requirement is not satisfied by merely reporting the CMM manufacturer's estimate of the single point uncertainty, or by B89 test suite [3] results, or even by a full parametric characterization of the CMM. All potential sources of error must be considered and must be propagated in a statistically valid way to yield an uncertainty on each measurement result.

In recent years, various sources of CMM uncertainty have been studied. In addition a broadly applicable statistical method for treating uncertainty sources individually or in tandem has been developed by researchers at NIST [4]. In this paper we report on an implementation of this method for the concurrent treatment of uncertainty sources including the CMM itself, the probing system, environmental factors, sampling patterns, feature form errors, and geometric fitting algorithms.

While the intrinsic versatility of the CMM has led to its dramatic success in dimensional metrology, this same versatility makes task-specific measurement uncertainty estimation problematic. The wide range of measurands and of measurement methods and conditions argue strongly against use of estimation methods commonly employed for simpler devices used in a narrow range of applications. Thus direct comparisons with calibrated artifacts or even attempts at error budgeting have been recognized as generally impractical to meet the needs of CMM users in typical industrial circumstances. The need for alternative approaches has been addressed.

Among the legitimate approaches to CMM uncertainty estimation recognized by the International Standards Organization is that of modeling and simulation of the measurement process, including error sources [5]. Using this approach, we have developed a convenient tool, PUNDIT/CMM [6], for the estimation of CMM-based task-specific measurement uncertainties. (PUNDIT is actually an acronym for Predicts UNcertainty in Dimensional Inspection Techniques.) PUNDIT/CMM addresses all the influential error sources cited above and does so with a modular architecture that facilitates enhancements of the error models as the state of the art advances. It incorporates a full solid model of the part to be measured as well as data structures to support tolerancing and datum reference frames and it has as a key principle of operation the statistical methodology called Simulation by Constraints (SBC) developed by researchers at NIST [4]. SBC allows the treatment of data such as CMM or probe performance test results, which constitute a "bounding measurement set" while still not fully constraining the range of possible CMM (or probe) parametric errors. Thus users can estimate measurement uncertainties even when they have only quite limited data on their measurement systems. Only a brief review of SBC can be given here, as it applies to CMM errors. The reader is referred to [4] for further details.

Simulation by Constraints (SBC) for CMM Rigid Body Errors

In 1997, NIST researchers introduced SBC for treatment of CMM rigid body errors and their influence on measurement uncertainty [4]. One employs a standard methodology (e.g. the B89.4.1 tests [3]) to establish values for a CMM's "performance evaluation parameters." In the B89 case, these amount to estimations of linear accuracy for each axis and values for offset volumetric performance, volumetric performance and repeatability. But these parameters alone do not fully constrain the CMM in terms of its rigid body errors. There will generally be a significant population of CMMs (defined in terms of their rigid body errors) which, though differing from one another in important ways, are still all consistent with the performance evaluation results obtained. With no further data, it is impossible for the CMM user to know which of these may best represent his particular CMM. Of course full measurement of the rigid body errors can be undertaken. This can be a time-consuming process and is generally not undertaken frequently. Indeed even the B89 tests may not be made often at many facilities. The only information a CMM user may have about errors for his CMM may be the manufacturer's statements that it will be no worse than some particular set of published performance evaluation values. Leaving aside other factors for the moment then, we can see how SBC can be applied to a CMM's contributions to task-specific measurement uncertainty. The figure below shows the SBC approach to the problem: 1) establishing a set of hypothetical CMM error states found to be

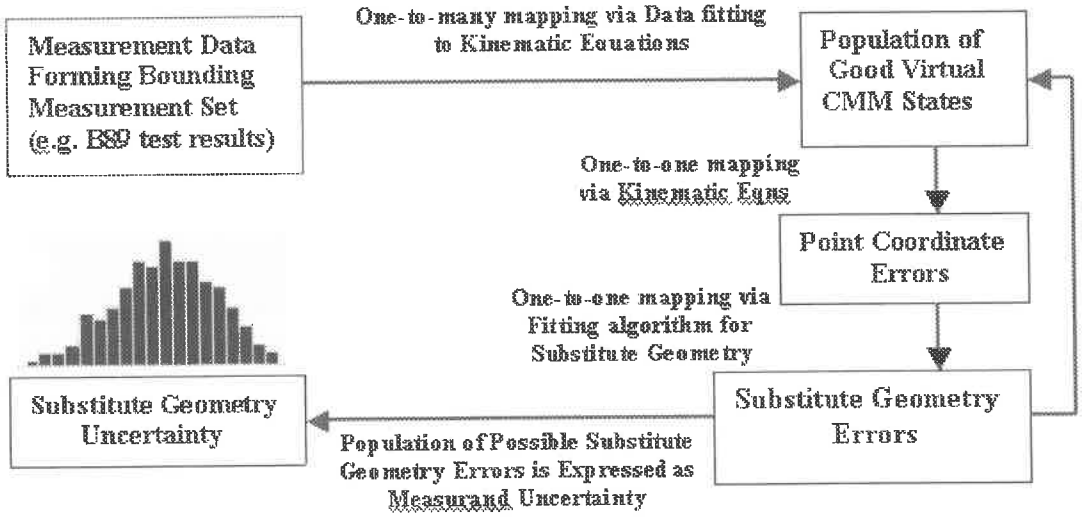
Measurement Data Forming Bounding Measurement Set (e.g. B89 test results)
One-to-many mapping via Data fitting to Kinematic Equations
Population of Good Virtual CMM States
One-to-one mapping via Kinematic Eqns
Point Coordinate Errors
One-to-one mapping via Fitting algorithm for Substitute Geometry
Substitute Geometry Errors
Substitute Geometry Uncertainty
Population of Possible Substitute Geometry Errors is Expressed as Measurand Uncertainty

consistent with the B89 values; 2) simulating inspection of the part using, in turn, each of the CMMs in this set; 3) noting the range of final measurement results obtained in the simulations.

PUNDIT/CMM

In PUNDIT/CMM we use the SBC method for CMMs and, by analogy, for many other factors that influence uncertainties in GD&T parameters obtained from CMM inspection procedures. We use performance evaluation data on probes, estimates of types and magnitudes of feature form errors, and environmental (thermal) conditions. Then, using chosen sampling strategies and analysis algorithms, we repeatedly simulate part inspection based on a randomized treatment of these states. The range of simulated inspection results for each measurand yields task-specific uncertainty. At its highest level, the PUNDIT/CMM user interface is a tabbed structure:

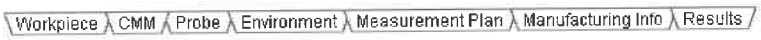

Workpiece and Tolerancing Definition

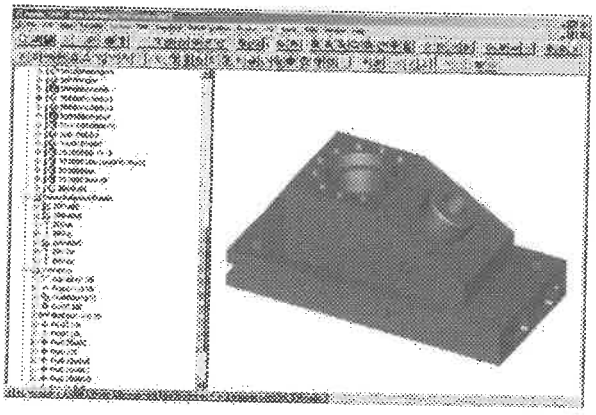

In the Workpiece Tab, the user creates or imports a solid model representation of the workpiece. PUNDIT/CMM recognizes tolerance features and allows definition of datums and datum reference frames and the establishment of specific tolerances for feature location, orientation, size and form. In addition PUNDIT/CMM can check the tolerancing to verify that it is complete, consistent and unambiguous. Problems encountered in this checking are clearly identified for easy correction.

Manufacturing Information for Feature Form Errors

Under the Manufacturing Info Tab, the user can assign specific types of systematic and/or random form errors to feature surfaces. These may be of classical analytic form or derived from dense measurement of representative features produced by particular methods of manufacture. Estimated amplitudes of these errors can also be specified. Shown in this example is a 3-lobe helical form often found in holes produced by drilling operations.

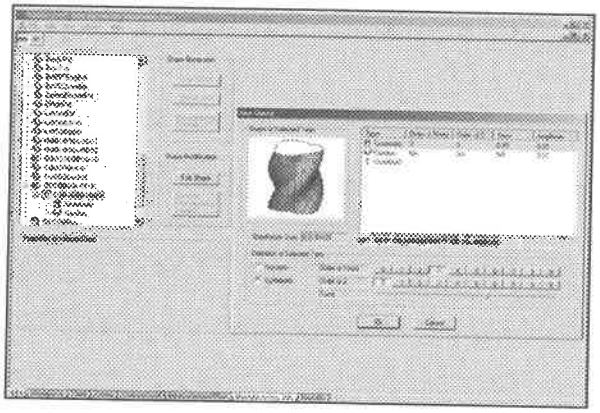

CMM Definition: Geometry, Working Volume and Error Model

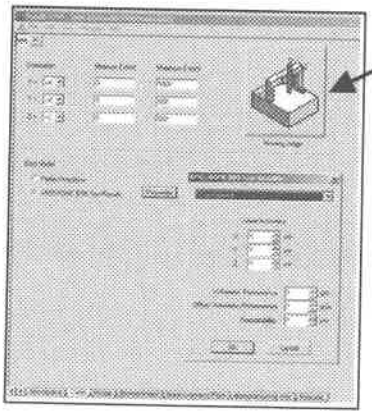

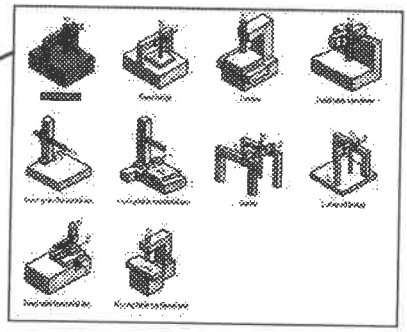

In the CMM Tab, the user identifies the CMM geometry type, the extent of the axes, and the desired error model. Perfect CMM is one option. Data from the B89.4.1 suite of performance evaluation tests can also be employed. Such data may be from tests on the user's own CMM or from the CMM manufacturer's data sheets. Each simulation of workpiece measurement employs a different "virtual CMM" (i.e. a different set of rigid body errors) that is consistent with the specified B89 data. These errors then propagate into individual measurement points in the inspection simulations and from there into the toleranced characteristics of the substitute geometry features.

Sensor Definition: Configuration, Error Model and Evaluation

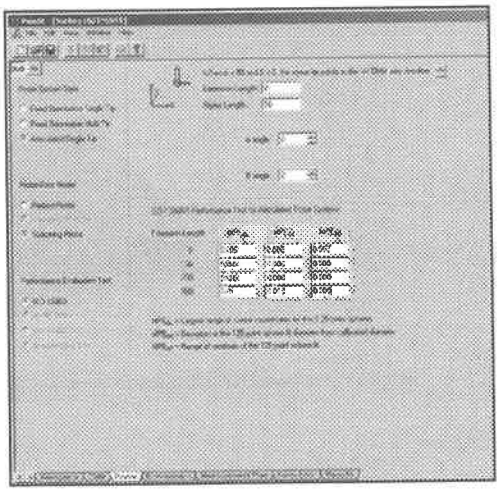

Sensors are defined under the PUNDIT/CMM Probe Tab. The user can select a single-tip fixed probe, a multi-tip fixed probe, or a single-tip articulated probe. Error models vary from perfect probe, to piezoelectric models, to switching probes. A variety of options are available for specification of performance evaluation. These include those mandated in ISO 10360-5, in B89.4.1, and in VDI/VDE 2617. In a way analogous to the treatment of CMMs, the measurement simulations are conducted with the introduction of probe errors on individual sample points. As with CMM errors, these too are propagated through fitting algorithms to yield errors in the final GD&T parameters of interest.

Environmental Effects

PUNDIT/CMM currently handles treatment of nonstandard temperatures for machine and for workpiece. The user can stipulate expansion coefficients, temperatures and their corresponding uncertainties (C_T, T, ΔC_T, and ΔT) for each of these entities as well as indicate whether the CMM software is set to make internal compensations for these nonstandard conditions. Even when that is the case, however, *uncertainties* in the values of the expansion coefficients (ΔC_T) and temperatures (ΔT) will give rise to contributions to overall measurement uncertainty.

Measurement Plan: Sampling Patterns, Sensor Usage, etc

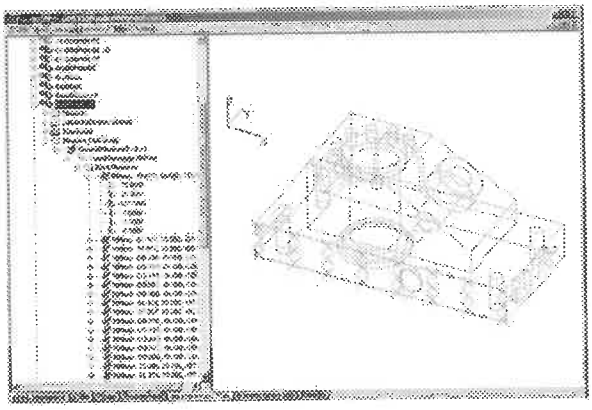

In the Measurement Plan Tab, the user stipulates the number and location of sampling points for features, the sensor(s) to be used in gathering that data, and the location and orientation of the workpiece in the CMM working volume. Convenient "wizards" are available to automate the sample point specification process. Regular rectangular (eclipsed) or staggered patterns of rows and columns can be selected, or point density methods may be used. Custom patterns may be created. The user can specify offsets from edges and any points falling into voids on feature surfaces are automatically discarded. Patterns can be easily edited and convenient three-dimensional displays show clearly where sample points are located.

Analysis and Results: Task-Specific Uncertainty Estimates

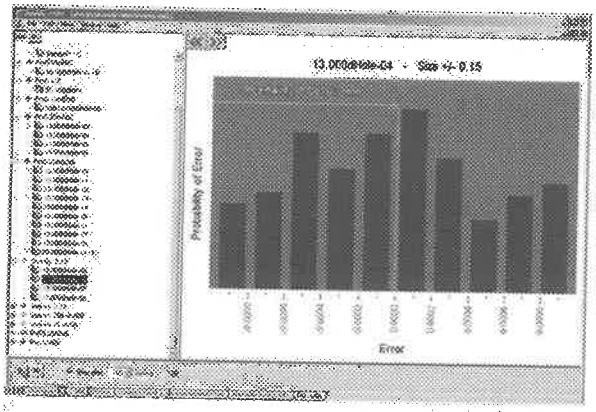

When all the influence parameters have been specified, the user can then move to the Results Tab, select the number of simulation cycles to run, and launch the simulation process. Every toleranced characteristic yields a histogram of results from which the measurement uncertainty can be inferred. Convergence generally occurs in one or a few hundred cycles, taking a matter of seconds to a few minutes on a Pentium class processor, depending on the complexity of the workpiece.

A Case Study: Cylinder Size, Position & Form Uncertainties

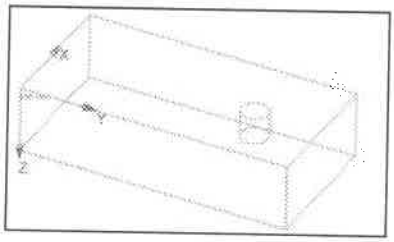

Here PUNDIT/CMM is applied to the study of a simple rectangular part with a blind cylindrical hole. The cylinder has a systematic 3-lobe form error of amplitude 0.0004 mm. We choose to sample the cylinder at seven equiangular positions on each of three levels over its length. Error contributions include the CMM, probe, and/or thermal factors in various combinations. The CMM model is based on B89 test results obtained for a machine at NIST: linear displacement accuracies for X,Y,Z axes were 3.0μm, 2.1μm and 2.5μm, respectively. Volumetric performance was 7.2μm; volumetric performance with an offset probe was 7.1 μm/m, and we took the repeatability to be 1 μm. For the probe, we used a random error model with $\sigma = 0.005$ mm. The CMM scales were treated as temperature insensitive and the part was treated as temperature compensated with an expansion coefficient of 22±2 ppm/°C (aluminum) and a part temperature of 25±3°C. Eight experiments were conducted, treating the three error factors (CMM, probe and thermal) as either present or absent in all possible combinations. In each case, uncertainties were obtained by carrying out 300 inspection simulations. We show results of uncertainty calculations for cylinder size, position and form (cylindricity). In the bar chart the factors included in each set of simulations are indicated by a shorthand binary notation where "1" indicates inclusion and "0" exclusion. The order is (CMM-probe-thermal). Thus a designation of 011 means that the CMM was taken as perfect while probe and thermal error models, as described above, were factored into the simulations. Thus the bar chart gives an indication of the relative importance of each of these factors to the uncertainties as calculated. While the inter-relationships among these factors are not treated explicitly, their relative independence from one another can be seen from the fact

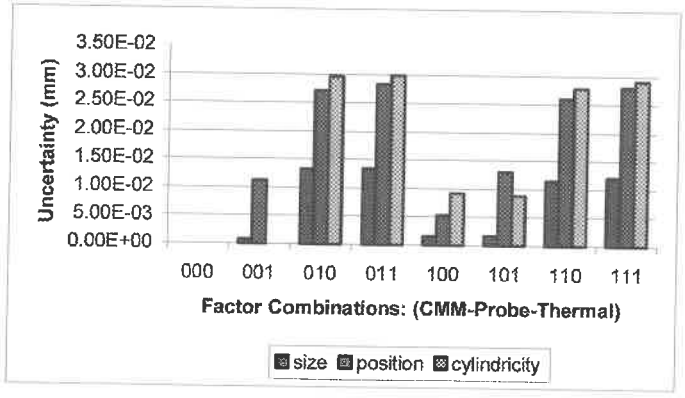

that the uncertainty values obtained from tandem treatment of multiple error factors do approximate what one would anticipate on the basis of root-sum-of-squares (RSS) calculations from the results generated for individual factors. Thus, for example the uncertainty in position for the (111) case was 0.0280 mm, while the RSS of the position uncertainties of (100), (010) and (001) exceeds that by only about six percent. Through studies of this sort, PUNDIT/CMM can aid the user in identifying factors that may dominate the estimated measurement uncertainty so that these may be addressed in an efficient manner to improve measurement practice.

Finally we consider how sampling patterns and feature form errors can interact in determining the uncertainty of GD&T parameters. We illustrate this for uncertainties in cylindricity of cylinders with either a pure 3-lobe systematic error of amplitude 0.0004 mm or both 3-lobe and random errors each with amplitudes of 0.0002 mm, the latter referred to as "mixed." 2-Level patterns of points, eclipsed or staggered radially, were employed and results are shown for various numbers of sample points. (For this study we treated the CMM and probe as perfect and introduced no thermal effects.) Note the oscillatory behavior when the number of points in each level is a multiple of 3. Staggering the levels helps to damp this effect, but it persists for small numbers of sample points even in the "mixed" case where random effects are as large as the lobing. With more points, uncertainty in the "mixed" case falls roughly linearly with the number of points.

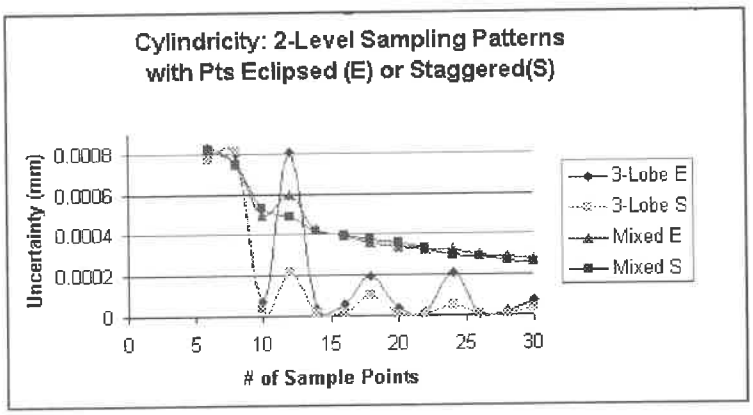

References

1. International Standard 17025 General requirements for the competence of testing and calibration laboratories, (1999).

2. International Standard 14025-1 Geometrical Product Specifications (GPS)—Inspection by measurement of workpieces and measuring instruments—Part 1: Decision rules for proving conformance or nonconformance with specification. (1998).

3. ASME B89.4.1-1997, Methods for Performance Evaluation of Coordinate Measuring Machines, New York: American Society of Mechanical Engineers, 1997.

4. Phillips, S.D.; Borchardt., B.R., Sawyer, D., Estler, W.T., Ward, D., Eberhardt, K., Levenson, M.S., McClain, M., Melvin, B., Hopp, T., Shen. Y., The Calculation of CMM Measurement Uncertainty via The Method of Simulation by Constraints, *Proceedings of the 12th Annual Meeting of the American Society for Precision Engineering*, October 1997, Norfolk, VA, 443-446.

5. International Standards Organization TC213/WG10 15530-4 Geometric Product Specifications (GPS) – Coordinate Measuring Machines (CMM) – Techniques for determining the uncertainty of measurement – Part 4: Use of computer simulation, 2002.

6. PUNDIT/CMM, © MetroSage, LLC, 2000-2002, http://www.metrosage.com.

White-light interferometer with internal length standard

Joanna Schmit and Erik Novak and Artur G. Olszak*

Veeco Metrology, 2650 E Elvira Road, Tucson, Arizona, USA

1. INTRODUCTION

White-light interferometric (WLI) techniques[1, 2] are often used in microscopy to measure the surface topography of objects such as height gauges, binary optics, machined parts, IC-packaging modules and micro-electro-mechanical systems (MEMS). These white-light interferometers, or optical profilers, have the advantage of delivering whole-field, non-contact, high-accuracy 3D topographic measurements of a number of different kinds of micro-objects. The principle of operation of these interferometers is based on the detection of the peak or phase of fringes that are narrowly localized around the surface at the best focus position. Narrow localization of fringes is obtained through the use of a low coherence light source, such as a halogen lamp that emits white light. The intensity signal is registered at each pixel of the CCD detector as the objective of the microscope is scanned along the optical axis through focus. Various algorithms are used to determine the best focus position at which the narrowly localized fringes achieve maximum contrast; these algorithms can also determine the phase of the fringes so as to enhance the resolution down to a sub-nanometer level. However, high sensitivity measurement does not automatically guarantee high accuracy; rather, high sensitivity depends on proper calibration of the scanner speed and the mean wavelength of the detected fringes. In this paper we describe these two major parameters that need careful calibration in a white-light interferometer. An addition of a laser-based interferometer into an optical profiler creates a primary length standard for calibration.

2. CALIBRATION OF WHITE-LIGHT INTERFEROMETER

A white-light interferometer achieves its high accuracy through the proper calibration of the system. It is important to understand all the parameters of the system that can alter calibration. Also, one must use a proper procedure and standard for system calibration in order to achieve the best accuracy of measurement. In a classical white-light interferometer the two parameters, the scanner speed and the mean wavelength of the detected fringes, are dependent on each other. Often the value of one is measured by assuming that the value of the other is well known and constant. However, these assumptions may not be correct and errors can be introduced into the measurement. Below, we first review current calibration procedures and different factors that influence the scanner speed and mean wavelength, then we present how these parameters can be measured independently. Our method allows us to measure these parameters at each moment of the scan, which then enables automatic, on-line calibration of the system during each measurement. This automatic calibration is achieved through the use of an internal length standard, namely the wavelength of the laser.

2.1. Scanner speed

The scanner speed can be calibrated to a calibration step height standard (SHS) with a certificate of traceability to NIST (National Institute of Standards and Technology)or other standards. The calibration takes place prior to measurement and the determined scanner speed is assumed to remain constant through a large number of scans. Any change in the scanner speed affects the measurement and reduces the system's repeatability and accuracy. If a scan is non-linear but has a repeatable and known behavior, this knowledge can be applied to the measurement algorithm which can account for scanner nonlinearity. In this case the absolute scanner position would need to be known to introduce proper corrections. In an alternate method, this information can be used for a hardware linearization of the scanner by monitoring the scanner position and using a hardware closed-loop system. These hardware solutions, which include capacitive sensors, linear variable differential transformers and linear encoders, are expensive or have rather limited resolution.

(*Artur Olszak is currently with Dmetrix, Tucson)

Typically, ideal or repeatable scanner behavior is not achievable, especially over a large scanning range on the order of millimeters. Interferometric techniques can utilize the measurement fringes to introduce some correction into the measurement, but they do so by assuming that the mean wavelength for fringes is well known and constant. The frequency of fringes as sampled along the scanning direction will vary with a change in the scanner speed; an average scanner speed can be determined from the sampled fringe frequency. Other techniques measure the phase rate of the fringes at each scanning step and apply this information to the algorithm, thereby reducing artifacts in the measurement and improving its repeatability. Two problems exist with this approach: first, the fringes may not be visible during each moment of scan and thus information about scanner speed may not be delivered during these blind times; second, these techniques rely on the mean wavelength of the measurement fringes which can be affected by many factors. In the next section we describe factors that affect the mean wavelength.

2.2. Mean wavelength

Knowledge of the precise value of the wavelength corresponding to the registered fringes is critical for accurate interferometric measurements. For laser-based interferometers the wavelength of the source is determined with great precision by the energy difference between transition states of the lasing media. For interferometers based on broad-band sources, such as a white-light halogen lamp, the mean wavelength needs to be determined. Sometimes band-pass filters with a determined mean wavelength are used to select a part of the spectrum from the white-light source. However, the mean wavelength of the source may slightly differ from the mean wavelength corresponding to the period of detected fringes for different reasons and this fact needs to be accounted for. Knowledge of the detected mean wavelength is important because some algorithms for fringe analysis are designed for a specific fringe sampling frequency and a departure from the nominal value introduces errors into the measurements. Hence, it is important to accurately know the period of the fringes. The wavelength is also the scaling factor between the phase of the fringes and physical quantities such as distance or height.

The conventional approach to determining the mean wavelength is pre-calibration. The mean wavelength of the detected fringes is calibrated prior to measurement by a proper procedure (such as measuring a step height standard) and then one assumes that the period of fringes does not change more than the tolerance required by the algorithms used. The mean wavelength corresponding to the detected fringes may differ from that of the source for several reasons. First, the spectral characteristics of the source as detected are altered by the spectral characteristics of the detector and optics. Second, high numerical aperture objectives alter the mean wavelength of the detected fringes. For these reasons wavelength calibration is needed. Assuming that the measured mean wavelength is constant is overly optimistic, for factors such as aging of the light bulb, change in its working point, the optical properties and shape of the analyzed object all affect the mean wavelength of the fringes. One might think that additional wavelength changes can be measured if the scanner speed is constant and well known, but it is impractical to assume this. Thus, in a conventional system scanner speed and the detected mean wavelength (period of the fringes along the optical axis) are mutually dependent.

All of the above system calibration procedures are sufficient for most required measurement tolerances, but with the trend toward producing more precise parts an instrument that provides time-stable measurement becomes a necessity. Our optical profiler enables measurement to tighter tolerances, as we implement an internal length standard based on a laser interferometer with a highly stable wavelength independent of numerical aperture, sensitivity of the detector, spectral characteristics of the filter or sample, and spectral characteristics of the light bulb. In our system the mean wavelength of the measured signal and the scanner speed are determined separately, thereby achieving the highest measurement precision at each moment of the whole range of the scan.

3. WHITE-LIGHT INTERFEROMETER WITH REFERENCE SIGNAL

In this section we describe our white light interferometer with an embedded Michelson interferometer[3] (see Figure 1) that, because it shares the same focusing mechanism, is capable of monitoring the progress of the scanner. This reference signal interferometer uses a separate narrow-band light source with a well-controlled mean wavelength. The signal in the reference interferometer is acquired by detectors, such as photodiodes,

and is sent to the computer for processing. Data acquisition is rapid compared to the CCD camera and more detailed scanner motion data is provided. During a measurement both the reference signal and sample signal are acquired simultaneously as the scanning rate is the same for both interferometers. The CCD camera used to capture intensity frames is governed by an internal clock with a typical accuracy better than 30ppm. The reference signal is acquired using a general purpose, data acquisition board with a programmable scan rate. The comparison and synchronization of both signals is based on the time stamp associated with each acquired data sample.

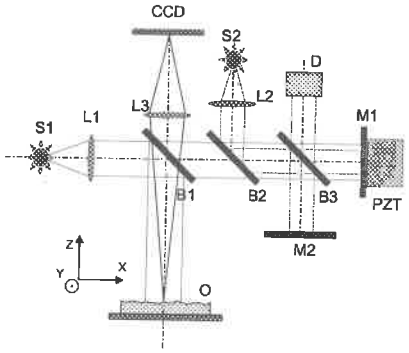

Figure 1. Basic arrangement of a optical profiler with internal length standard created by reference signal. S1 is low-coherence light source; S2 is the reference signal light source; L1 and L2 are collimators; B1, B2 and B3 are beam splitters; L3 is imaging lens; M1 is the scanner mirror; M2 is reference signal reference mirror; D is reference signal detector; PZT is the scanner transducer; O is object; CCD is camera detector.

In order to fully characterize the instrument we have built a prototype using a modified Wyko NT3300 Optical Profiler (Veeco Instruments Inc.) with a 20x Mirau objective and a 60 fps camera. As a light source we have used a regular tungsten light bulb. The reference signal interferometer was built using a He-Ne laser operating at its fundamental wavelength of 632.8 nm. The scanner used in the experiments was based on generic mechanical components and was driven by an electric motor without any feed-back loop. We have used the reference signal to characterize the scanner error position (speed) and applied it to WLI measurement of flats and steps. This software closed-loop solution increases measurement accuracy through the use of a reference signal that tracks the actual scanner position during the data acquisition process. Our setup does not correct the scanner motion; rather, we monitor the scanner motion and feed this information into the algorithm to achieve error-free surface measurements.

4. SELF-CALIBRATION OF WHITE-LIGHT INTERFEROMETER WITH REFERENCE SIGNAL

The reference signal allows us to measure the scanner position over the entire scan.[4] This obtained position information is based on the primary length standard - the wavelength of its light source, e.g., a He-Ne laser, and therefore, provides accurate position information during each scan. The influence of scanner errors is reduced or eliminated, and final result of the measurement yields a lower noise floor and more accurate height profiles. This position information can also be used to calibrate the period of the fringes during each measurement run and provide information about the mean effective wavelength registered by the camera. By direct referencing to a primary length standard, the uncertainties of step height standard can be avoided and significant increases in measurement accuracy can be achieved. No longer are step-height standards necessary for system pre-calibration since the relative stability of a He-Ne laser wavelength is at least an order of magnitude better than the step height standards used for pre-calibration. Obviating the need for system pre-calibration also reduces maintenance of the instrument.

The constant calibration of each system to the wavelength-based internal length standard during each measurement is much more reliable and accurate than current pre-calibration methods, thus allowing for better

system-to-system correlation. In essence the calibration process is reduced to setting the scanning speed to a nominal value that is within the tolerance of the algorithms. Any deviations from the ideal scanning speed or any change in the mean wavelength are corrected based on the information from the primary length standard delivered by reference signal. Thus the system is truly self-calibrating.

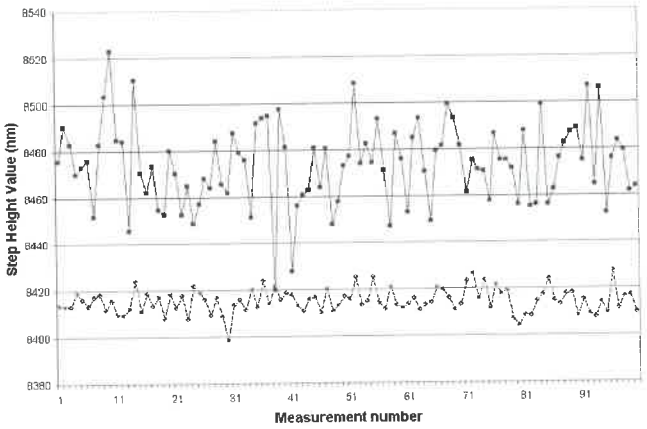

Figure 2. Step height standard numerous measurements with and without internal length standard

The reference signal interferometer yields highly accurate and repeatable results over a long scanning range, up to 8 mm, without resorting to using expensive capacitive sensors with often limited scan range. Even temperature and other environmental changes that influence system behavior are compensated for in this system. Figure 2 demonstrates the significant improvements in long-term repeatability of the reference signal interferometer. The measurement was performed using a WLI method with a reference signal using an inexpensive scanner without scan correction. The 60 nanometer offset was introduced between results for greater picture clarity. The correction of scanner errors improves system repeatability and helps maintain stable measurements over long time contributing to improved accuracy.

5. CONCLUSIONS

A practical self-calibration technique utilizes a reference signal interferometer, as an internal length standard, that directly measures the scanner motion during each scan and instantaneously applies information about scanner position to the algorithm. Thus, the measurement is traceable to the primary length standard - the wavelength of the laser and no step height standards are required for system pre-calibration. The system is insensitive to source wavelength drift, temperature and other environmental changes. Measurement linearity is guaranteed and resolution versus range dependencies is eliminated. The self-calibration routine reduces system maintenance and assures system-to-system correlation.

REFERENCES

1. M. Fleischer, R. Windecker, and H. J. Tiziani, "Theoretical limits of scanning white-light interferometry signal evaluation algorithms," *Appl. Opt.* **40**, pp. 2815–2820, 2000.
2. P. J. Caber, "Interferometric profiler for rough surfaces," *Appl. Opt.* **32**, pp. 3438–3441, 1993.
3. A. Olszak and J. Schmit, "High-stability white-light interferometry with reference signal for real-time correction of scanning errors." to be published in Opt. Eng.
4. C. Farrell, *New Algorithms for High Accuracy Phase Shifting Algorithms.* PhD thesis, University of Aberdeen, November 1993.

FILM THICKNESS STANDARDS ON THE NANOMETER SCALE

K. Hasche, G. Ulm, K. Herrmann, M. Krumrey, G. Ade, J. Stümpel, I. Busch,
P. Thomsen-Schmidt, S. Schädlich[1], A. Schindler[2], W. Frank[2], M. Procop[3], U. Beck[3]

Physikalisch-Technische Bundesanstalt Braunschweig and Berlin, Germany (PTB),
[1] Fraunhofer Institute for Material and Beam Technology, Dresden, Germany (IWS),
[2] Institute for Surface Modification, Leipzig, Germany (IOM),
[3] Federal Institute for Material Research and Testing, Berlin, Germany (BAM)

Abstract

Reference standards for film thickness and calibration techniques for two different kinds of measuring instruments being widely applied in semiconductor technology and other fields where film thickness in the nanometer range plays a significant role are developed, evaluated and tested. One is for typical X-ray methods, like X-ray reflectometry (XRR)under grazing incidence, X-ray fluorescence analysis (XRF) and electron probe microanalysis (EPMA). Calibration of thickness and evaluation of further parameters qualifying the artifacts as reference standards base primarily on XRR. The second type is created for ellipsometry and has a small topographic structure which allows determination of the film thickness by scanning force microscopy (SFM) in combination with additional evaluations by transmission electron microscopy (TEM). A short overview on manufacturing and some results of characterization for both types of reference standards are presented here.

1. Introduction

The scope of this paper is the development, manufacture and calibration of artifacts being applicable as reference standards for the thickness of films. The reference standards refer to two different application fields – on the one hand calibration of measuring instruments basing on the typical X-ray and the widely applied electron beam microanalysis methods (XRR, XRF, EMPA), and on the other hand ellipsometric measuring systems (SE) [1, 2].

The reference standards shall serve as elementary metrological standards giving the measuring instrument user preferably a simple indication of the correct metrological function of the appliance. The material combinations film/substrate and the film thicknesses have been chosen accordingly.

Depending on material combination and also on coating technology a more or less pronounced interdiffusion range must be expected between film and substrate which, with regard to the film thickness definition, may no longer be neglected in cases of film thicknesses of approx. 20 nm or smaller. In this paper the interdiffusion range is being estimated by incorporating measurement results from TEM investigations. In a not yet finalized discussion on calibration uncertainties of these reference standards the interdiffusion range will be taken into consideration. Thus measurement results will remain consistent even though the measuring instruments calibrated with these reference standards are subject to different physical interactions between detection system and film system.

2. Reference standards for XRR, XRF and EPMA

2.1 General remarks and comments on the manufacture of the artifacts

The artifacts consist of fused silica substrate (dimensions: length 60 mm, width 20 mm, height 10 mm). One large surface to be coated has to be smoothed by ion beam polishing to an RMS-value of roughness smaller than 0.3 nm [3]. The reason being the significant influence of roughness and deviation from flatness on the accuracy of the thickness determination by XRR.

As coating, a platinum film or a film system of carbon-nickel-carbon with a nominal metal thickness of 10 nm and 50 nm respectively are chosen. The carbon films serve as protection against oxidation of the Ni-film and to reduce interdiffusion of film and substrate.

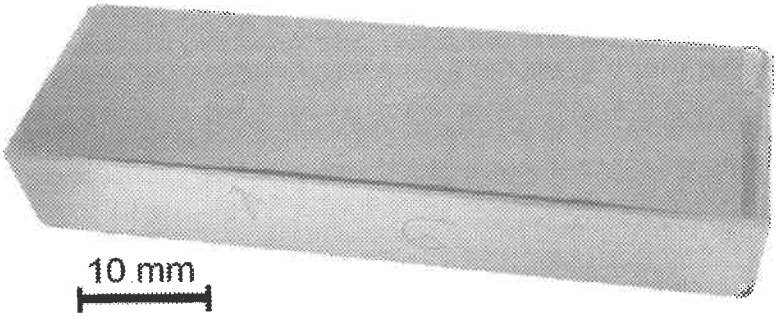

figure 1: 10 nm Pt-film on a fused silica substrate as thickness standard for X-ray facilities

Films are deposited by physical vapor deposition (PVD) technique being well approved in the field of X-ray mirror production [4] and adapted for this task. Fig. 1 shows a thickness standard.

2.2 Metrological characterization of reference standards for XRR, XRF and EPMA

Calibration of film thickness and determination of other parameters (e.g. variation of film thickness over the whole surface) characterising the artifact as reference standard base primarily on XRR. Results found on different facilities during independent investigations show satisfying consistence.

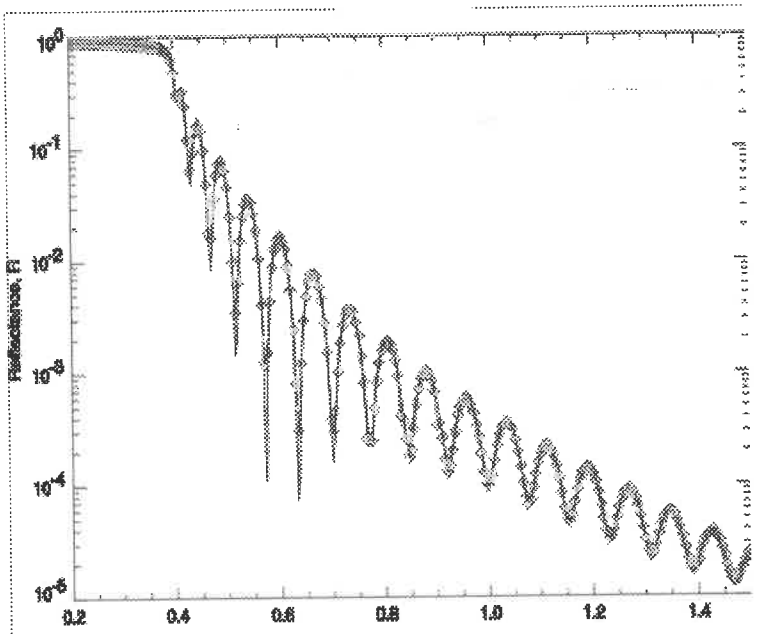

figure 2: Measured reflectance R as a function of the grazing incidence angle (E = 8.048 keV)

Fig. 2 shows the reflectance as function of the grazing incidence angle at a photon energy of 8.048 keV for a C-Ni-C film system with a nominal film thickness of 50 nm Ni as typical XRR measurement data.

sample	nominal film system	thickness value in nm	density of metal film in g/cm^3
POG 2	C – 10 nm Ni - C	9.84 ± 0.15	8.1
POG 8	C – 10 nm Ni - C	10.29 ± 0.15	8.1
POG 9	C – 50 nm Ni - C	53.5 ± 0.3	8.9
POG 10	10 nm Pt	15.62 ± 0.18	19
POG 4	50 nm Pt	28.8 ± 0.2	21.4

figure 3: Results of film thickness calibration by XRR

Fig. 3 contains the calibration values of the metal films (Ni resp. Pt) of 5 artifacts determined from the XRR measurement data incl. the measurement uncertainties established in the measurement process. The thickness of the C-films, not mentioned in this table, is about 2 nm. In the right hand column the densities of the metal films determinable from the measurement data are listed. The results give an impression of the outstandingly low uncertainty of this method applied at PTB's beamline at BESSY II [5] and by various facilities of other involved partners.

For nanometer films the metrological quality of the surface and interface between film material and substrate are essential and were therefore examined by SFM and TEM. Results arrived at by TEM are reported here. As a test a thin platinum film with a nominal thickness of 10 nm was deposited on an SiO_2-wafer (not comparable with smoothed surface) and analysed. The wafer has a thickness of 400 µm and is chosen as substrate to minimise the influence of preparation for the TEM cross section observations. The result of this investigation is documented in fig. 4. The surface of the SiO_2-wafer is shown on the left; its roughness is estimated at a value of 0.5 nm. On the right the surface is covered by a Pt-film with a thickness of 12.7 nm ± 0.8 nm. The interface between Pt-film and substrate material is blurred over a width of approx. 0.9 nm. The substrate surface seems to be roughened by the coating process.

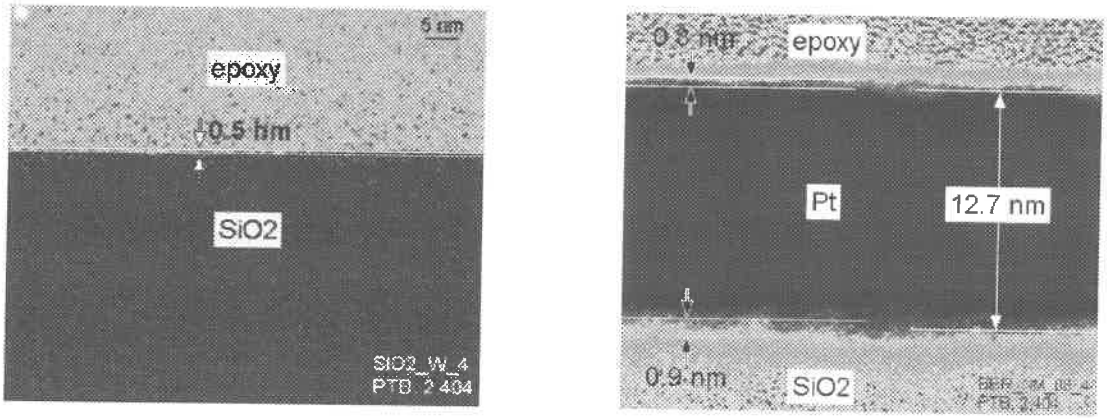

figure 4: TEM-investigation of the surface of an SIO2-wafer without a top layer (left) and with a Pt-film (right)

The film thickness variations over the whole surface pose another important question which is investigated by XRR and XRF. Fig. 5 shows a map of thickness values over a whole sample measured by XRF at BAM's beamline at BESSY II.

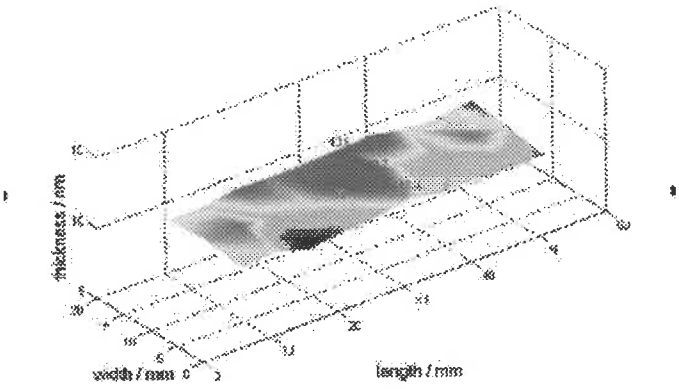

figure 5: Film thickness variations over the whole surface examined by XRF

The homogeneity of a film is examined by XRR in a two step procedure. To start with the reflectivity is measured as a function of the angle, and thereafter in a second step the angular value of a minimum in reflectivity is selected and the artifact is moved laterally along one axis. Reflectivity changes during such a scan indicate an inhomogeneous thickness and a second XRR measurement can be done at another position on the scanned line to verify this. As a result of such scanning on several artifacts thickness variations within ± 0.2 nm along the short axis of the artifacts are found. This value agrees with the value of uncertainty of a single XRR measurement at the center of the sample.

3. Reference standards for ellipsometry

3.1 General remarks and comments on the manufacture of the artifacts

On Si-wafers with a diameter of 150 mm and (100) surface orientation a film of thermal oxide is grown and subsequently structured by direct electron beam writing. By dry etching with plasma the thickness of the oxide film is reduced to a value of roughly around 100 nm. Wet etching in buffered hydrofluoric acid further reduces the residual oxide. After that the mask is removed and a protective film is deposited for separating the wafer into chips by sawing. Twenty identical chips (resp. artifacts) are located on a wafer. A number on each chip marks their location on the wafer. The chip size is 20 mm x 30 mm; the layout is shown in fig. 6. A frame around the main field with four marks serves as search structure.

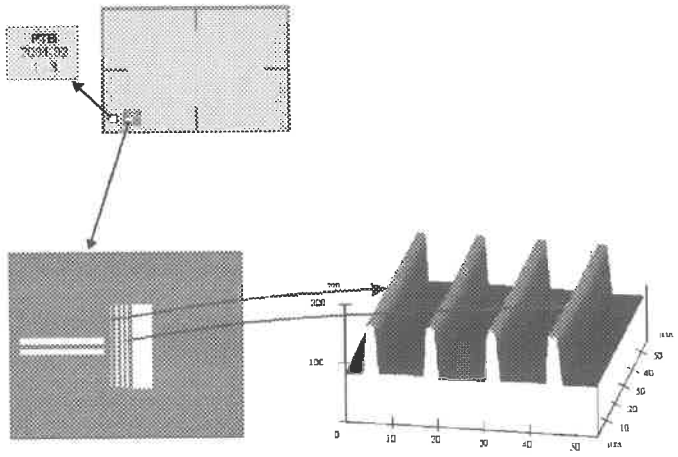

figure 6: Design of ellipsometry standards with a topographic structure for calibration by SFM (on the top the chip layout as a whole, bottom left the topographic structure and micro spot field, bottom right the topographic structure)

The main field on the chip can be used for thickness measurement by methods working with a probe beam like ellipsometry (or XRR). Two small frames are placed near the bottom left hand corner on the chip (see fig. 6, top). Within the left frame the chip's position on the wafer during the manufacturing process is defined by a number, the second frame serves the calibration process of the chip – it contains a search structure and 4 topographic structures, being further illustrated in fig. 6 by the SFM area scan at the bottom right, and a 200 µm wide field for micro spot investigations.

Chips are manufactured with nominal thickness values of 1 µm, 400 nm, 160 nm, 70 nm and 6 nm.

3.2 Metrological characterization of reference standards for ellipsometry

As mentioned above each calibration standard can be used for different measurement methods and is not limited to one type of instrument. Par example the scale on the z-axis of an SFM can be referred to XRR measurement results by these standards for the case of the two smallest values of film thickness. Therefore the homogeneity of the thickness over a chip has to be characterized carefully. As a first test a chip from the center and another from the perimeter of a wafer are investigated by TEM. The nominal thickness of the SiO_2 film is 6 nm. The chip from the center of a wafer has a measured thickness of about 5.9 nm ± 0.3 nm. The thickness of the film on a chip from the perimeter of the wafer is about 5.9 nm ± 0.5 nm.

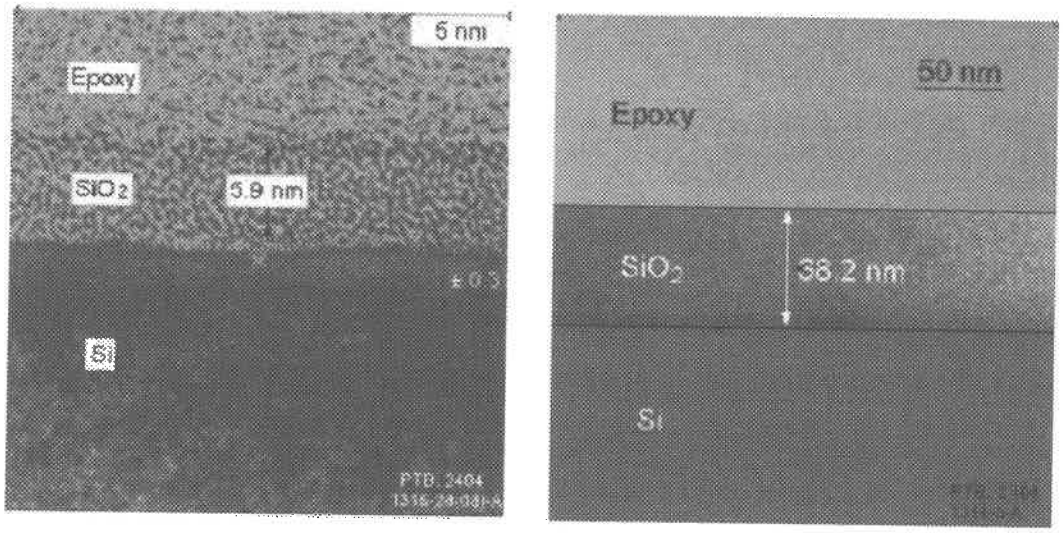

figure 7: Film thickness evaluation and interface inspection by TEM (the measured thickness values are 5.9 nm ± 0.3 nm and 68.2 nm ±0.9 nm)

Fig. 7 shows the image from a TEM evaluation in respect of to the chip with the nominal thickness of 7 nm.

Another example refers to an evaluation by TEM on a 70 nm artifact. A thickness of 68.4 nm was found in the center of the chip, and thicknesses of 68.2 nm and 68.5 nm near the bottom left hand corner. The estimated uncertainty was ± 0.4 nm.

An adequate homogeneity in film thickness over one wafer is also verified by XRR measurement. For a nominally 70 nm film thickness values of 69.2 nm and 68.9 nm are measured on two chips located at the center of a wafer, and 69.0 nm at the perimeter of the wafer. All these values are measured with an uncertainty of 0.2 nm.

Spectral ellipsometry (SE) shows variations of thickness values of 2 % over the whole wafer for the nominal 6 nm artifacts, and less than 0.5 % for the others.

sample	nom. thickness in nm	thickness value by SFM in nm	thickness value by SE in nm
1	6	5.8	7.5
2	70	70.2	68.1
3	160	164	163.6
4	400	388	387.5
5	1000	999	1009.7

figure 8: Results of SFM and SE measurements

Results of SE (spectroscopic ellipsometer with rotating analyser) and SFM measurements on similar artifacts are stated in fig.8.

The relative uncertainty of the SFM results is estimated to be smaller than 1 %, for the 6 nm artifact it is about 1 nm.

For a conclusive statement on this measurement uncertainty we have to take into consideration that SFM measurements are insensitive to interdiffusion phenomena. Therefore the force microscopic method must be seen in the context of complementary methods. Furthermore, we try to find comparable measurement results also for methods such as XRR, SE and TEM which are widely used for film thickness measurements in the nm-range. This is the background of current investigations aimed at consistent results based on the application of different methods. The model is still being adapted to achieve consistence with SFM results.

The results of the SE measurement depend on the model. The estimated uncertainty is 1 nm + 0.01 x d, d = film thickness.

4. Conclusions

Two different kinds of film thickness standards are fabricated and characterized by several techniques of film thickness measurement.
Calibration results for the X-ray methods' standards are consistent on an expanded uncertainty level below one nanometer.
The standards for film thickness determination by ellipsometry have been fabricated and some results are reported. These results show that consistence should be reachable on a relative standard uncertainty level below 1 % if the smallest film is excluded.
The involvement of complementary evaluation methods like XRR, XRF, SE, TEM and SFM seems to be a promising way in case of films in the nanometer range.
The full characterization of both types of standards has not yet been finalized.

5. Acknowledgement

This work is financially supported by BMBF via project no. 13N 7704 "Calibrated reference standards of coating thickness in the nanometre range".
Particular thanks to Mr. D. Hirsch, IOM, Mrs. M. Männ, BAM, and Dr. Min Xu, PTB, for valuable evaluations.

6. References

[1] K. Hasche, K. Herrmann, M. Krumrey, G. Ulm, S. Schädlich, W. Frank, M. Procop
Proc. euspen International Conference 2001, Turin, Italy, 2001, pp. 396-399
[2] K. Hasche, K. Herrmann, M. Krumrey, G. Ulm, G. Ade, P. Thomsen-Schmidt, S. Schädlich, W. Frank, M. Procop, U. Beck: PTB-Report F-44; Proc. 5th Seminar on Quantitative Microscopy, Bergisch-Gladbach, Germany, 2001, pp. 13-21
[3] R. Fechner, A. Schindler, T. Hänsel, F. Bigl, Proc. 9th ICPE, Osaka, 1999, pp. 249-254
[4] R. Dietsch, T. Holz, T. Mai, C.-F. Meyer, R. Scholz, B. Wehner: Applied Surface Science 127-129 (1998) pp. 451-456
[5] M. Krumrey and G. Ulm, Nucl. Istzr. Meth. A 467-468 (2001) pp. 1175-1178

Atomic Force Microscopy of Semiconductor Line Edge Roughness

Ndubuisi G. Orji, Theodore V. Vorburger†, Jay Raja
The University of North Carolina at Charlotte, Charlotte, NC 28223
†National Institute of Standards and Technology, Gaithersburg, MD 20899

1. Introduction

Over the last two decades the width of patterned lines on semiconductor devices has continuously decreased. Based on technology trends predicted by the International Technology Roadmap for Semiconductors (ITRS) [1], the linewidth of isolated gate lines on microprocessors will be reduced to less than 50 nm by 2012. This trend towards smaller feature sizes poses a great challenge to the tools, analysis methods, and calibration techniques used in linewidth measurements. State-of-the-art linewidth measurement involves the use of scanning electron microscopes (SEM), but as the feature sizes decrease, SEM techniques may become inadequate for such measurements.

Part of the difficulty of imaging patterned lines with the SEM lies with the uncertainties associated with determining the edges of lines; this can be attributed partly to the deviation of the line edge from the mean line, otherwise known as line edge roughness (LER). Another important part of the problem lies in the fact that the decrease in LER is not proportional to feature size as the industry move toward smaller features because the fundamental causes of LER are material and process dependent rather than size dependent [2]. Errors in the range of ~25 nm which were acceptable for linewidths of 500 nm or more will consume over half the lithography error budget for 100 nm linewidths and below [3].

Recent studies have correlated LER with increased current leakage [4,5] for linewidths below 100 nm, and thus highlight the need for an in-depth characterization of this parameter. This work explores the use of atomic force microscopes (AFM) for characterizing LER. The challenges involved with AFM characterization of LER are highlighted, and various scanning strategies and analysis techniques are presented. The objective of this work is to present some of the measurement and analysis techniques needed to extract valuable LER information using the atomic force microscope.

2. Imaging Technique

The atomic force microscope since its introduction [6] has gained wide usage in surface topography measurements at the very small scale. The ability of the AFM to produce three-dimensional maps at the nanometer scale has greatly increased its popularity as an imaging tool. The application of precision engineering principles in the construction and characterization of the AFM have also increased its usefulness as a metrology tool [7,8]. In addition to a variety of uses, it is increasingly being used as a process control tool, especially in the semiconductor industry, where it has become a major enabling tool in the measurement of very small features. In spite of the high resolution of the AFM and its increasing use in research and industry, the scanning electron microscope is still the imaging tool of choice in the semiconductor manufacturing industry. The depth-of-focus, high precision (< 0.7nm 3σ), and throughput of the SEM, make it especially attractive as a process control tool. However, as feature sizes get smaller, the SEM may no longer have the required resolution needed to measure certain parameters. One such parameter is LER, which the ITRS has set a long term target of reducing to 0.9 nm by the year 2013 [1]. The ITRS

defines LER in terms of linewidth variation over a range of four technology nodes, using all frequency components. This target is ambitious, and the ITRS indicates that at present there is no known method of achieving or verifying this target. One of the few tools with the resolution needed to characterize the LER down to the levels indicated on the roadmap (a short term target of 2.7 nm by 2006) is the atomic force microscope. Under optimum conditions the AFM can measure surfaces and features with sub-nanometer resolution. The use of the AFM as a process control tool of choice is perhaps a few years away, but this tool can be used in conjunction with other techniques and tools to perform an in-depth study of LER with the aim of understanding the origins, characterization methods, important spatial wavelengths, and correlation with performance. As much promise as the AFM holds for characterizing LER, there are some challenges. These include the inaccessibility of the tip to the sidewall, tip dilation (tip broadening), and errors due to non-conventional scanning strategies. A word on terminology, there is an ongoing debate on what term best describes line edge roughness. In some cases it is used interchangeably with linewidth uniformity, and sidewall roughness. We assume LER to be a general term. We use the term linewidth uniformity to represent deviations in linewidth as shown later in figure 3, and sidewall roughness to represent similar deviations, but for a single side. The techniques described are for measuring both parameters.

Here we present a combination of AFM measurement methods, and analysis techniques we are researching to acquire accurate images of the line edge and sidewall of semiconductor features. Conventional AFM imaging involves scanning the tip across the surface as shown in figure 1. The problem with this configuration when it comes to measuring sidewall roughness is that little or no sidewall information is obtained, in addition, tip dilation makes it almost impossible to image the line edge without errors. Slightly tilting the sample allows easier access to the sidewall. Most conventional AFM tips have an asymmetric cone angle (for example with front and back angles of 25° and 10° respectively, and 17° on each side), so depending on the sample tilt angle the image can be limited by the sidewall of the tip. A judicious selection of the scanning direction is required when using such a tip. To alleviate this problem we are using very sharp tips that have a more uniform conical shape. To gain increased access to the sidewall, one can also tilt the cantilever. Tilting the cantilever may not be as easy as tilting the sample, since this may require tilting the whole cantilever holder. Figure 1 shows some possible configurations.

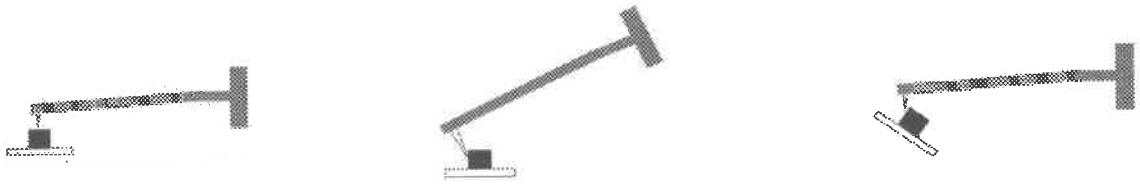

Figure 1 show possible AFM probe configurations (a) in conventional AFM imaging configuration, (b) cantilever slightly tilted and (c)with the sample holder tilted.

The methods outlined above will allow imaging of both the sidewall and the line edge, though only one side of the feature is being imaged.

If one is interested in only the sidewall, and one's system allows it, rotating the sample 90° is an option. This configuration is destructive because the sample must be cleaved to allow the tip unrestricted access to the sidewall. Figure 2 shows a schematic of such a configuration. In addition to sharp tips, we intend to take images using special cantilevers where the tips are at an angle.

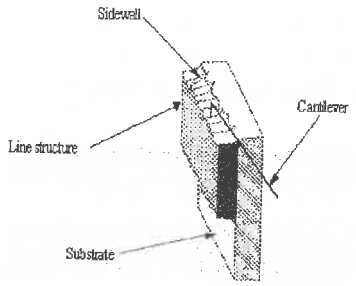

Figure 2 A schematic of a line structure rotated 90° for easy access to the sidewall.

3. Analysis Technique

In analyzing LER, analysis methods emphasizing different spatial frequency ranges maybe needed for the different types of linewidth uniformity and sidewall roughness. Also of great interest is the question of whether linewidth uniformity and sidewall roughness are correlated, and if so how. Since the SEM is the imaging tool of choice in the semiconductor industry, some of the most useful analysis techniques for AFM LER data will be those that can easily be correlated with the data taken with the SEM. Perhaps the most used technique is the rms roughness shown in equation 1 where δ is the deviation from the average line edge. In this case it is calculated as three standard deviations (3σ) of the values.

$$\mathrm{LER} = 3\sigma = 3\sqrt{\frac{N\sum\delta^2 - \left(\sum\delta\right)^2}{N(n-1)}} \qquad (1)$$

This can easily be applied to the data acquired using the techniques outlined above. Another technique [9] is to calculate the non-uniformity of the whole line structure. This method uses both sides of the line structure, so it cannot be used on data acquired by some of the techniques outlined above, but where possible gives a good indication of the uniformity of the line structure, and yields results that can easily be compared to information obtained from the SEM.

In order to obtain the type of data sketched in Figure 3, one has to determine where the line edge is, since the line profiles are likely to have rounded corners due to tip dilation. We will apply a geometric filter [10,11] to remove the influence of the tip. In this case the linewidth uniformity of the line will be calculated at a specified vertical threshold, a method employed in [12], we will also evaluate the influence of various threshold levels

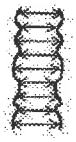

Figure 3 A top down image of a line structure. Showing Linewidth uniformity

on the results. The results obtained will only give linewidth uniformity and not sidewall roughness, but will give a very good indication of uniformity and quality of the line structure. This is also the definition used by the ITRS [1], which proposes the use of all frequency components and both edges, and evaluated over four semiconductor technology nodes.

4. Planned experimental work

We are currently taking measurements using a commercial AFM. We are measuring patterned lines of approximately 250 nm linewidth so we can first verify the utility of some of our techniques before using smaller, more expensive samples. A high-aspect-ratio conically shaped tip is being used. We intend to examine the influence of various tilt angles on the data, and what tilt angles give the "best" results. We also intend to obtain specially made samples with roughness of known values, and spatial frequencies.

Acknowledgements
This work is supported in part by the Office of Microelectronics Programs (OMP) at NIST. The authors are grateful to A. Vladar and J. Martinez for their careful reading of the manuscript.

References

1. The International Technology Roadmap for Semiconductors (ITRS) 2001, Semiconductor Industry Association, San Jose (2001)
2. G. P. Patsis, A. Tserepi, I. Raptis, N. Glezos, and E. Gogolides and E. S. Valamontes. Surface and line-edge roughness in solution and plasma developed negative tone resists: Experiment and simulation, J. Vac. Sci. Technol. B 18 (6), Nov/Dec 2000
3. A. E. Braun, CD-SEM: Precision or Accuracy, Semiconductor International, Feb 1999.
4. C.H. Díaz, H-J Tao, Y-C Ku, A. Yen, and K. Young, An Experimentally Validated Analytical Model For Gate Line-Edge Roughness (LER) Effects on Technology Scaling, IEEE Electron Device Letters, Vol. 22, No. 6, June 2001
5. K. Patterson, J. L. Sturtevant et al, Experimental determination of the impact of polysilicon LER on sub-100-nm transistor performance. Proc. SPIE Vol. 4344, 809-814 (2001).
6. G. B. Binnig, C. F. Quate, and Ch. Gerber, Atomic force microscope. Phys. Rev. Lett., (12)
7. J. E Griffith, D. A. Grigg, Dimensional metrology with scanning probe microscopes J. Appl Phys. 74 (9) R83 (1993)
7. R. Dixson, R. Koning, V. W. Tsai, J. Fu, T. V. Vorburger ; Dimensional metrology with the NIST calibrated atomic force microscope. Proc. SPIE Vol 3677, 21-2 (1999)
8. Winkelmeier S, Sarstedt M, Ereken M, et al., Metrology method for the correlation of line edge roughness for different resists before and after etch., Microelectron Eng 57-8: 665-672 (2001)
9. V. Srinivasan, Discrete morphological filters for metrology. Proc. 6th IMEKO ISMQC symposium on metrology for quality control and production, TU Wien, Austria, 1998
10. Villarrubia, J.S., Algorithms for scanned probe microscope image simulation, surface reconstruction, and tip estimation. J. Res. NIST, 102(4), 425-454, (1997)
11. C. Palmateer SC, Forte AR, et al, Comparison of metrology methods for quantifying the line edge roughness of patterned features, J Vac Sci Technol B 17: (6) 2488-2498 (1999)

Miniature Interferometers for Precise Distance Measurements

Walter Schott
SIOS Meßtechnik GmbH, Ilmenau, Germany
Gerd Jäger
Ilmenau Technical University, Ilmenau, Germany

1. INTRODUCTION

Not all tasks encountered in the field of laser interferometric distance measurement technology in industry and research can be solved using conventional laser interferometers. In many cases, they are too unhandy, too bulky and also too expensive. Therefore, small sensor systems are necessary whose measuring range, resolution, precision and measuring speed can be adapted because of their modular structure.

This paper presents a miniature laser-interferometric measuring system designed for making precision measurements in the field of microtechnology, nanotechnology, and macrotechnology. Resolutions of 1 nm and an accuracy of a few nanometers may be achieved over dynamic ranges as large as 5 m. The particular advantages offered by these fiberoptic-coupled miniature laser interferometers will be discussed, based on selected practical applications.

These miniature interferometer systems for precision distance measurements have the following major features:

- modular design,
- easy adaptation to a variety of tasks,
- compactly designed interferometer modules,
- complete coupling via optical fibres,
- nanometer resolution and accuracy for measuring ranges of 5 m, and
- comparatively low costs.

2. METROLOGICAL ANALYSIS

The following metrological analysis is intended to elucidate the capabilities and limitations of laser interferometry. The Michelson interferometer (cf. Fig. 1), which serves as the basis for all other types of interferometers, is thus the ideal basis for such analyses [1]. It will be assumed that the laser light source employed emits plane waves that are split into two coherent partial waves that interfere when superimposed on one another. The intensity distribution in the interferometer's image plane will then be given by Eq. 1:

$$I = I_1 + I_2 + 2\sqrt{I_1 I_2}\cos\left(\gamma + \frac{2\pi}{\lambda_0} n \cdot i \cdot s\right), \qquad (1)$$

where

γ is the phase angle of the incident beam,
λ_0 is its vacuum wavelength,
n is the refractive index of the ambient medium (air),
I is the interferometer factor, and
s is the path length to be measured.

From Eq. 1, if follows that:

$$s = \frac{\delta \cdot \lambda_0}{i \cdot n}, \qquad (2)$$

where δ is the order of interference.

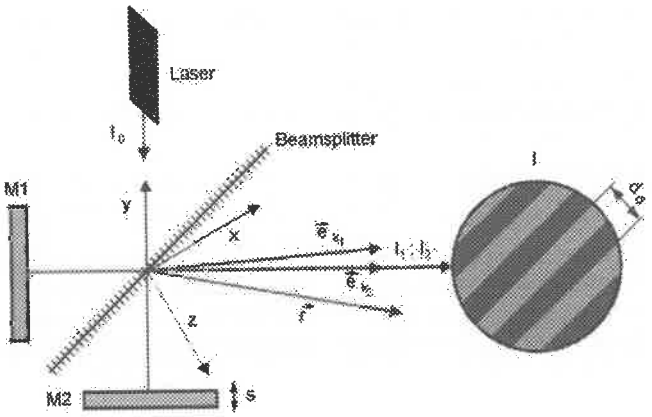

Fig. 1: A schematized Michelson interferometer.

Resolution

The smallest resolvable path-length increment, s_q, may be computed using Eq. 3:

$$s_q = \frac{\lambda_0}{e \cdot i \cdot n}, \qquad (3)$$

where e is an electronic interpolation factor.

Eq. 3 shows that extraordinarily fine resolutions are attainable. The current state of the art in electronic signal-analysis equipment allows resolutions of << 1 nm. Such high resolutions, which are achieved using precision interferometers, are also attainable over large path lengths, s, which allows reaching relative resolutions much better than those attainable using any other metrological method (e.g., for s = 10 m and s_q = 1 nm, the relative resolution will be 10^{-10}).

Precision

Various factors that limit the precision of laser-interferometric length measurements must be taken into account in determining the precision and accuracy of the method. Eq. 2 may be used to compute the effects of such factors on the results of length measurements, s.

The refractive index, n, of air is a function of the ambient temperature, barometric pressure, and absolute humidity. The extent to which these factors affect the results of length measurements may be seen from Table 1. Corrections may be made if these parameters are measured.

The stability of the wavelength, λ_0, of the laser light source employed is a second major factor affecting metrological precision. Table 2 lists the relative wavelength stabilities of various laser light sources. In order to determine the absolute modal wavelength of a frequency-stabilized He-Ne-laser, it must be slaved to an iodine-vapor-stabilized He-Ne-laser that is linked to the cesium atomic clock of a national standards institute. The number of increments (counter pulses) is the product of the order of interference, δ, involved and the electronic interpolation factor, e. The electronic interpolation factor, e, thus specifies the number of pulses into which a signal period is subdivided. The resultant interpolation errors should also be taken into account.

$\frac{\Delta n}{n} = -0.929 \cdot 10^{-6} K^{-1} \cdot \Delta\delta$,	where $\Delta\delta$ is the change in ambient temperature,
$\frac{\Delta n}{n} = +2.682 \cdot 10^{-9} Pa^{-1} \cdot \Delta p$,	where Δp is the change in barometric pressure,
$\frac{\Delta n}{n} = -3.84 \cdot 10^{-10} Pa^{-1} \cdot \Delta p_F$,	where Δp_F is the change in water-vapor partial pressure.

Table 1: The effects of ambient temperature, barometric pressure, and humidity on the refractive index of air, n.

Laser light source	$\pm \Delta\lambda_0/\lambda_0$
Unstabilized single-frequency He-Ne-lasers	$\approx 10^{-6}$
Unstabilized dual-frequency He-Ne-lasers	$\approx 3 \times 10^{-7}$ (for max. path-length differences < their resonator length)
Stabilized He-Ne-lasers (for the case of equal mode intensities)	$\approx 10^{-8}$
Iodine-vapor-stabilized He-Ne-lasers	$\approx 10^{-12}$
Diode lasers	$\approx 10^{-5}$ 10^{-6} short-term stability

Table 2: The relative wavelength stabilities of various types of laser light sources.

The fact that the aperture of the interferometer's illumination system also affects the accuracy of the results of length measurements is frequently overlooked. The following correction for that aperture should be applied:

$$\Delta s_A = -\frac{r^2}{4f^2} \cdot s, \qquad (4)$$

where

Δs_A is the correction to measured lengths be applied,
r is the radius of the aperture stop or of the core of the fiberoptic lightguide employed,
f is the focal length of the collimator employed, and
s is the measured path length.

If the laser beam is not normally incident on the moving mirror, M2 (cf. Fig. 1), then yet another systematic measurement error will have to be taken into account:

$$\Delta s_\alpha = -s \cdot (1 - \cos\alpha), \qquad (5)$$

where α is the angle between the incident beam and the normal to the reflective surface of M2.

Systematic measurement errors will also occur if the axis along which the moving mirror, M2, is translated is not parallel to the normal to its reflective surface:

$$\Delta s_\beta = -s \cdot (1 - \cos\beta), \qquad (6)$$

where β is the angle between its translation axis and the normal to its reflective surface.

3. LASER-INTERFEROMETRIC GAUGING PROBES

Fig. 2 depicts a laser-interferometric gauging probe that utilizes a fiberoptic-coupled miniature interferometer equipped with a retroreflector as its internal metrological system. This gauging probe has a motor-drive on its spindle that exerts an adjustable, constant, force on objects being measured over its full dynamic range. The technical data for this laser-interferometric gauging probe are as follows:

- Dynamic range: 20 or 50 mm
- Resolution: 1 nm
- Relative metric precision: $\leq 10^{-6}$
- Applied force: adjustable over the range 0.5 N to 1.5 N
- Fiberoptic-coupling of the gauging probe to the interferometer

Application areas of this laser-interferometric gauging probe include:

- thickness measurements on optical or mechanical components,
- measuring the thicknesses of foils,
- calibrating gauge blocks, and
- calibrating dimensional reference standards, precision metrological instruments, and sensors.

Working in collaboration with the Physikalisch-Technische Bundesanstalt (PTB), Brunswick, Germany, and Ilmenau Technical University, Ilmenau, Germany, we have developed a new type of gauge-block calibration system based on a laser-interferometric gauging probe that allows reducing the total number of gauge blocks required to around one-tenth of that normally necessary, while maintaining ultrahigh metric precisions.

Employing the laser-interferometric gauging probe as the upper gauging probe increased the dynamic range from the former few micrometers for the case of an inductive sensor to 20 mm, while maintaining the same, or better, metric precision, which allowed making more efficient gauge-block calibrations and cutting gauge-block recalibration costs. Fig. 3, below, depicts the metrological setup employed.

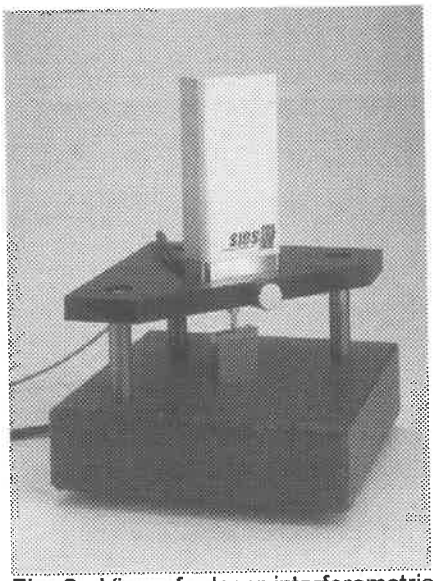

Fig. 2: View of a laser-interferometric gauging probe.

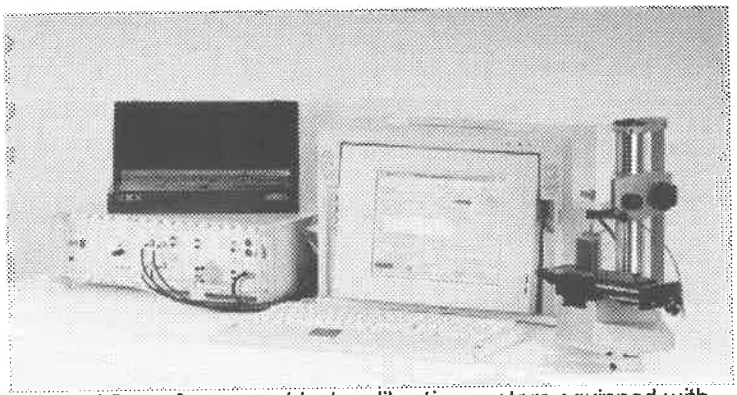

Fig. 3: View of a gauge-block calibration system equipped with a laser-interferometric gauging probe.

4. EMPLOYING MINIATURE INTERFEROMETERS AS MODULAR COMPONENTS OF METROLOGICAL SYSTEMS

Miniature interferometers are manufactured in versions equipped with retroreflectors and plane-mirror reflectors. Although both types of system have common metrological characteristics, their applications differ.

Their major technical data may be summarized as follows:

Parameter	Miniature interferometer equipped with a retroreflector (cf. Fig. 4)	Miniature interferometer equipped with a plane-mirror reflector (cf. Fig. 5)
Dynamic range	≤ 5 m	≤ 2 m
Resolution	1.24 nm	1.24 nm
Relative metric precision	≤ 1×10^{-6}	≤ 1×10^{-6}
Moving-mirror translation rate	≤ 600 mm/s	≤ 600 mm/s
Max. tilt of moving mirror relative to measuring beam	± 3°	≤ 2' for distances from the sensor head of 0.5 m or less

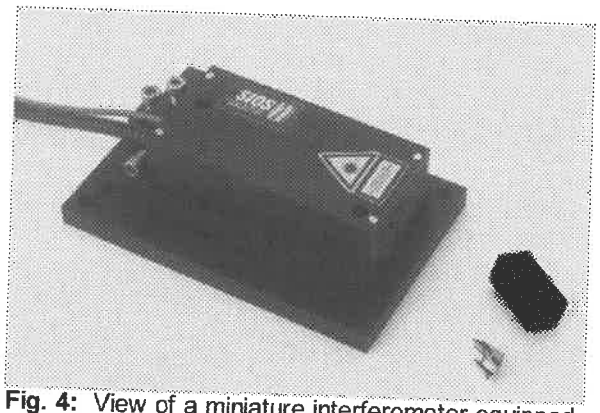

Fig. 4: View of a miniature interferometer equipped with a retroreflector.

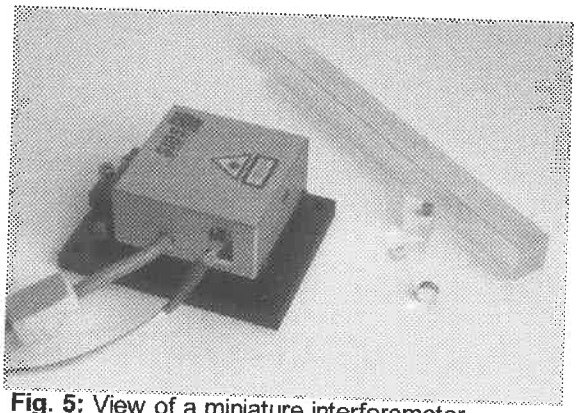

Fig. 5: View of a miniature interferometer equipped with a plane-mirror reflector.

Miniature interferometers are used as modular components of

- machine tools,
- metrological systems and measuring microscopes,
- coordinate-measuring machines,
- hardness testers, and
- materials-testing equipment,

as well as equipment for calibrating other types of length-measurement instrumentation and as precision length-measurement systems for use in research and development work.

5. MICROINTERFEROMETERS

Microinterferometers (cf. Fig. 6) operate on the same principle as miniature interferometers equipped with retroreflectors and are noted for their compact designs, fiberoptic coupling, and simple alignment. Among other applications, they are used on position controllers, hardness testers, materials-testing equipment, multi-axis translation stages, and calibration systems.

Their employment of fiberoptic coupling and discrete micro-optical components and their layout and interconnection hardware allow achieving extremely compact sensor-head dimensions of 28 mm x 25 mm x 15.5 mm and a sensor-head weight of just 35 g. Their employment of the wavelength of a frequency-stabilized He-Ne-Lasers as their dimensional reference standard and their inclusion of corrections for the refractive index of air as standard equipment, guarantee excellent metrological characteristics. A dynamic range of 5 m and resolution of 1.24 nm are also standard equipment. The maximum translation rate of their moving mirror is 0.6 m/s.

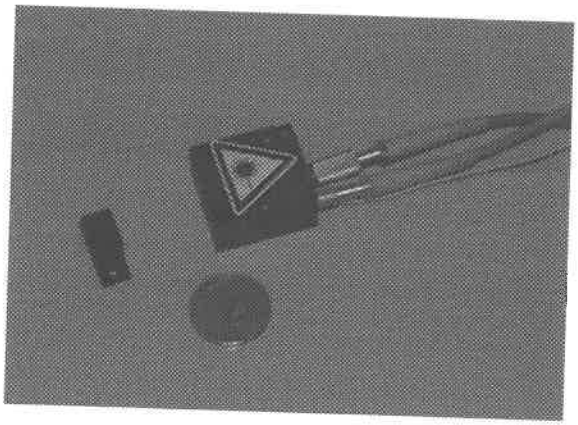

Fig. 6: A view of the interior of the microinterferometer's sensor head, showing the latter's moving retroreflector.

6. VIBROMETERS

Vibrometers equipped with miniature plane-mirror interferometers are employed in vibrational analysis. Their measuring beam is focused on the object whose vibrations are to be measured. Measurements are totally noncontacting. The surface finish of the object whose vibrations are to be measured is arbitrary, as long as it yields a reflectance of 5×10^{-4}, or better. The minimum resolvable vibrational amplitude is 0.3 nm. Fig. 7, below, presents plots of vibrational-amplitude resolution versus vibrational frequency for two vibrometer models (SM 01 and SM 02).

Analyzing the resultant vibrometer data using FFT-software allows performing vibrational measurements, including spectral analyses, at frequencies up to 500 kHz. Fig. 8 depicts the vibrometer units involved.

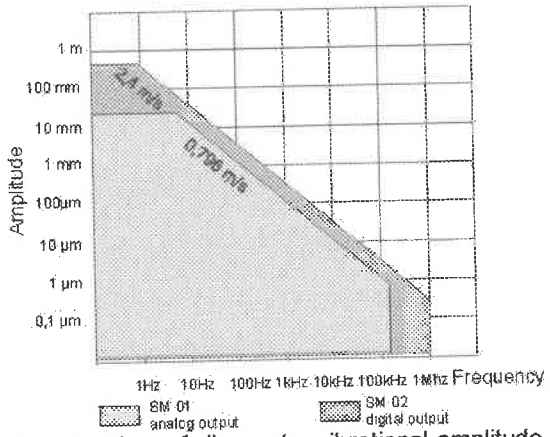

Fig. 7: Plots of vibrometer vibrational-amplitude resolution as a function of vibrational frequency.

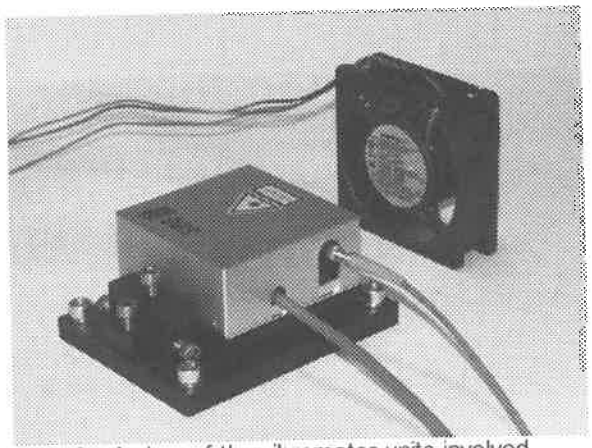

Fig. 8: A view of the vibrometer units involved.

7. ACKNOWLEDGMENTS

The developments described were supported by the German Federal Ministry of Education and Research and the Thuringian Ministry of Science, Research and Arts. The authors wish to thank all those colleagues who have contributed to the developments.

8. LITERATURE

[1] Jäger, G.: Precision distance measurement by means of miniaturized interferometers, Proceedings of the XIII. IMEKO World Congress; Volume 3; S. 1712-1716; Torino Sept. 1994

[6] Jäger, G.: Laserinterferometrische Messverfahren- Möglichkeiten, Grenzen und Anwendungen; Vortrag zur 3. ITGI GMA-Fachtagung Sensoren und Messsysteme; Bad Nauheim; 1998.

[7] Jäger, G.: Lasernanomesstechnik- Möglichkeiten, Grenzen und Anwendungen in der modernen Gerätetechnik; Vortrag zum 44. IWK; Ilmenau; 1999.

[8] Lemke, K.; Plagwitz, K.-U.; Henke, S.: Dynamische Messungen mit einem polarisationsoptischen Laserinterferometer; tm 67 (2000) 1; S. 20-26.

[9] Jäger, G.; Grünwald, R.: Mikrooptische Systeme für die Präzisionstechnik (MOSEP); Infobörse VDI/VDE-TZ IT GmbH Teltow; 2002.

[10] Schott, W.; Pöschel, W.; Jäger, G.; Grünwald, R.; Manske, E.; Wurzbacher, H.: Fibre-Coupled Microinterferometer; OPTO 2002 Conference; Erfurt; Mai 2002.

[11] Jäger, G.; Schott, W.; Manske, E.; Hausotte, T.; Büchner, H.; Grünwald, R.: Nanomeasuring Technology – Nanomeasuring Machine; ASPE 2001 Annual Meeting; Washington D.C.; Nov. 2001.

[12] Schott, W.; Anwendung von Mikrointerferometern; Technische Akademie Esslingen, June 2002

[13] Jäger, G.; International Symposium on Laser Metrology, Florianopolis, Brazil, 1999

Figure Metrology of a Free-Form Optical Surface

Alexander Sohn, Kenneth P. Garrard
North Carolina State University Precision Engineering Center
Campus Box 7918, Raleigh, North Carolina, USA
http://www.pec.ncsu.edu

Raymond G. Ohl, Ronald Mink, V. John Chambers
NASA/Goddard Space Flight Center, Code 551, Greenbelt, Maryland, USA
http://www.gsfc.nasa.gov

The Infrared Multi-Object Spectrograph (IRMOS) is a facility instrument for the Kitt Peak National Observatory's 3.8 m Mayall Telescope and an engineering prototype for a possible design of the Next Generation Space Telescope/Multi-Object Spectrograph. IRMOS requires a toroidal, off-axis, biconic camera mirror ("M4") on an aluminum substrate for near-IR imaging and spectroscopy. This mirror (shown in Figure 1) presents significant fabrication difficulties due to its non-rotationally symmetric (NRS) form and tight tolerances [1]. Combining the capabilities of a long range fast tool servo (FTS) with a 400 μm maximum excursion and a diamond turning machine (DTM) with a 600 mm diameter part capacity has made it possible to fabricate large, free-form optics for demanding scientific applications.

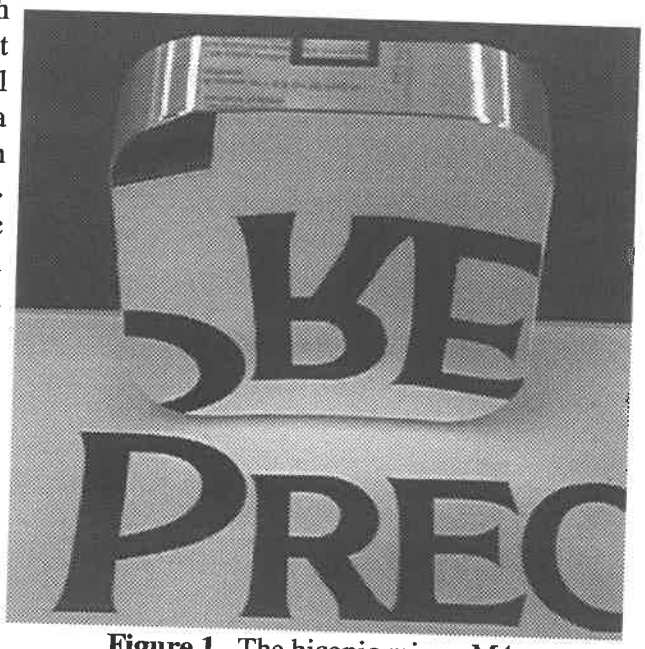

Figure 1. The biconic mirror M4.

Novel surfaces like M4 pose unique challenges for measuring figure error (i.e., surface error at spatial periods of 2 mm). Several methods are applied and evaluated for their merits and drawbacks. The use of computer-generated holographic (CGH) null elements in interferometry allow high-resolution measurements; however, alignment of the test setup can be time-consuming since the alignment tolerances are tight. We address this issue with a set of custom alignment fiducials built-in to the CGH and the M4 mirror. Additionally, CGH masks normally cannot be directly verified with a known standard. Stylus profilometry, on the other hand, is traceable since the instrument can be calibrated using known standards. Even with minimal probing forces the contact process can be destructive if local contact stresses leave witness marks on the surface. Depending on the system, profilometry data may also be time consuming and difficult to assemble and interpret.

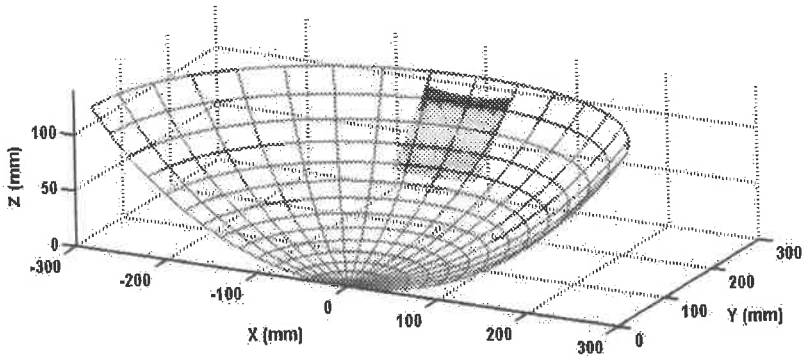

Figure 2. Aperture of M4 in its parent coordinate system.

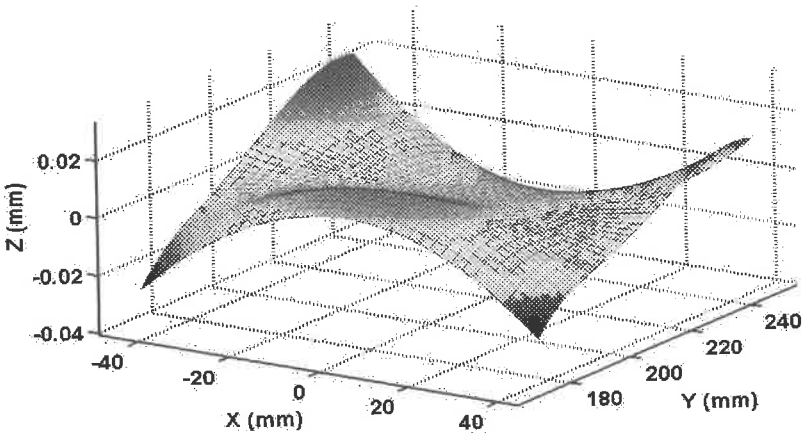

Figure 3. NRS component of M4 surface.

M4 Biconic

M4 defies conventional fabrication and metrology methods by virtue of the fact that it has no rotational axis of symmetry. As shown in Figure 2, M4 is an off-axis, 94 mm by 76 mm aperture of a concave, oblate ellipsoid. It is decentered by -2.01 mm and 227.41 mm in x and y, and has shape parameters,

$kx = 0.0778$,
$ky = 0.1265$,
$Rx = 377.3939$ mm
and $Ry = 406.8829$ mm.

The surface of M4 was separated into a rotationally symmetric 4th order asphere that can be machined on a DTM and an NRS component (Figure 3) to be machined simultaneously with an FTS. Machining was performed off-axis, although not in the parent orientation [1]. Accurate metrology of the mirror surface is an essential aspect of mirror fabrication since it allows troubleshooting of this complex machining process.

CGH Interferometry

While the idea of using a tailored diffractive element to measure non-standard surface shapes in an interferometer is certainly not new [2], the degree of sophistication for CGH metrology has dramatically improved with in the last few years. Now commercially available, the CGH masks are equipped with alignment fiducials essential in setting up a measurement [3]. This aids in both aligning the mask to the interferometer as well as aligning the sample to the mask. Since traditional methods of finding fringes often do not apply for free-form surfaces, such tools are indispensable for CGH metrology. Unfortunately, this also means that fiducials must be applied to the sample and other alignment tools such as theodolites are required. In the case of M4, a diamond flycut back surface was used to align tip and tilt and several crosshairs were used to align translation. The fiducials do, however, serve another function in that they will later be used to align the mirror in a complex optical system.

CGH Results

Initial alignment of the CGH and mirror using fiducials immediately showed fringes and allowed data collection. However, translation of the sample was required to minimize the error. This known translation was later correlated with a phase shift present in the FTS system. The residual error on the optimally aligned sample, shown in Figure 4, revealed a trefoil pattern identical to that of the servo excursion shown in Figure 3. While the amplitude of the measured error was about 8% of the servo excursion, the shape correlation led to the discovery of a scaling error in the FTS output that had to be corrected. A numerically generated reference surface confirmed these CGH results. A distorted (i.e., phase shifted and scaled) NRS component was added to the least squares aspheric component and compared with the interferometer data. These results show clearly that through the use of a CGH and proper alignment fiducials, one can troubleshoot a machining system in much the same way it would be done with a spherical or flat surface.

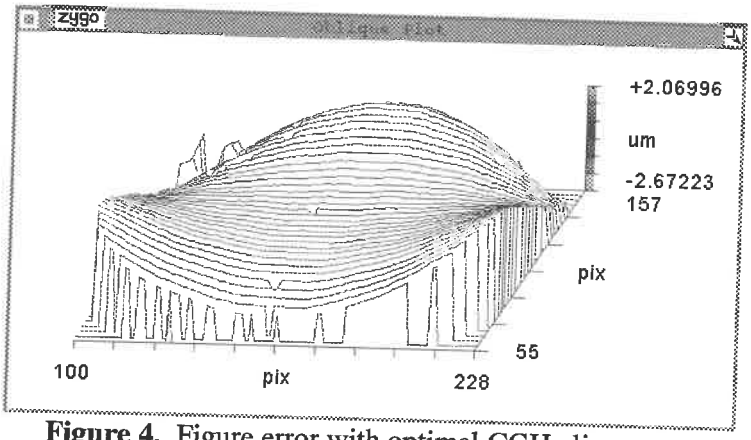

Figure 4. Figure error with optimal CGH alignment.

Profilometry

Since the CGH cannot be directly tested against a known standard, it is generally prudent to perform additional measurements with a method that can. While ultraprecision CMM's or multiaxis profilometers would be expertly suited to this task, they are not commonly available. Three-dimensional surface data can, however, be acquired by assembling multiple linear traces from a standard profilometer. One method, called the *Union Jack* [4], allows this assembly to be performed without the use of multiple axes. Fiducials placed on the surface of the part are used to relate the positions of the traces to each other. All of the intersections of the traces are then joined to assemble the data, as shown in Figure 5. Since each trace has multiple intersections, the redundant intersections can be used to test for alignment and measurement errors.

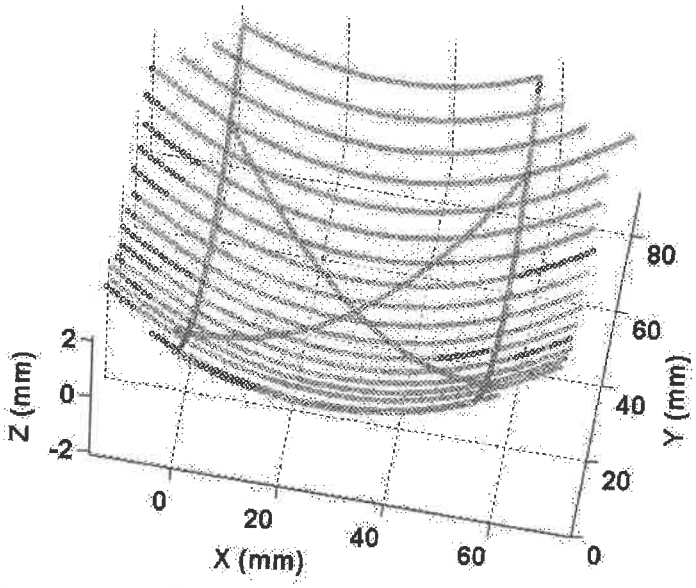

Figure 5. Profilometry measurements assembled into a 3-D surface using the *Union Jack* method.

Data Manipulation and Surface Fitting

Matlab™ software for automating 3D surface evaluation is being developed. Two data sets are input for comparison. One is a measurement, presumably either a profilometer or interferometer data set and the other is a reference datum. The reference may be an analytic function (e.g., a biconic equation) or an $[x,y,z]$ point cloud. The Levenberg-Marquardt unconstrained nonlinear optimization algorithm is used to align the two surfaces. The optimization merit function is the residual sum of squares error in either the parent z direction or the normal direction of the measurement. Parameters are the elements of a homogeneous transformation matrix (HTM) that is used to locate the measurement data set with 6 degrees of freedom. The measurement is translated in the reference coordinate system and rotated about a coordinate system whose origin is the geometric moment of the data set and whose z axis is normal to the surface. This was done to enhance the sensitivity of rotations for far off-axis data sets such as M4; otherwise small angle rotations are difficult to distinguish from translations. To speed up the alignment process and reduce the probability of convergence to a local minimum, a preliminary coarse alignment is done. The measurement is translated so that its center is coincident with the center of the reference and then rotated about that center point so that it has the same normal vector as the reference. Throughout the process, the reference surface remains at its original location in the parent coordinate system.

If an analytic function is not available as a reference datum, then the residual must be formed by interpolation. Either the reference surface can be triangulated onto the $[x,y]$ grid of the measured data or vice versus or both data sets can be interpolated onto a common grid. This must be done on each evaluation of the merit function since parameter adjustments necessarily misalign the data. For widely spaced, irregular data such as that from a *Union Jack* process, a closely spaced reference grid is triangulated onto the measurement grid to minimize interpolation errors. The results of this process are, 1) a residual error surface and the accompanying metrology statistics and 2) the composite HTM that aligns the measurement data.

Conclusions

The expanded use of free-form surfaces in optical systems is inevitable. As demonstrated in the case of the biconic mirror M4, figure metrology of these surfaces presents some unique challenges. While tools are available for measuring these surfaces, the techniques for doing so expediently and economically are not yet mature. CGH reference masks may take weeks to design and fabricate and 3-D profilometer measurements require an arduous process of data manipulation before meaningful results are available. Nevertheless, once results are obtained, they can be used in much the same way as standard ones for quality control, troubleshooting and performance assessment.

References

[1] Garrard, K.P., A. Sohn, R.G. Ohl, R. Mink, and V.J. Chambers. *Off-Axis Biconic Mirror Fabrication.* Proceedings of the Third International Meeting of EUSPEN, (2002).

[2] MacGovern, A.J., and J.C. Wyant, *Computer Generated Holograms for Testing Optical Elements.* Applied Optics, 10, pp 691, (1971).

[3] Diffraction International. Minnetonka, Minnesota, http://www.diffraction.com.

[4] Hume, K.J. Engineering Metrology, 3rd ed., Macdonald & Co. Ltd, London (1970).

A Metrological Atomic Force Microscope

Andrew J. Stein,[a] David L. Trumper,[a] Robert J. Hocken[b]

[a]Mechanical Engineering Department, Massachusetts Institute of Technology, Cambridge, MA, USA
[b]Center for Precision Metrology, University of North Carolina, Charlotte, NC, USA

Abstract

We have developed a metrological atomic force microscope (AFM), as part of the Sub-Atomic Measuring Machine (SAMM) project. This microscope uses a piezoelectric tube scanner with a quartz tuning fork proximity sensor to image three-dimensional sample topographies. The AFM utilizes a set of capacitance sensors, aligned so as to minimize Abbe offset error, for direct measurement of probe tip displacements. Using this system, we have successfully imaged a diffraction grating with RMS noise in the vertical measurement of roughly 5 nm.

1 Introduction

In previous work [1, 2], we have presented a high-accuracy precision positioning stage known as the Sub-Atomic Measuring Machine (SAMM). This stage uses a set of four linear motors to actuate a platen submersed in an oil bath, while three laser interferometers and three capacitance gauges provide its metrology. This system has demonstrated sub-nanometer resolution, 1 nm repeatability, and on the order of 30 nm accuracy, over a range of 25 mm x 25 mm x 0.1 mm. The Angstrom Stage [3] — an earlier six degree-of-freedom precision positioning stage, with a smaller range of motion — provided much of the groundwork for the SAMM project. Altogether, the Angstrom Stage and SAMM projects are aimed at advancing the state-of-the-art in precision motion control to the extent that macroscopic objects may be measured on the subatomic scale, a goal of particular consequence to the semiconductor field.

The SAMM provides an extremely stable and accurate scanning stage, which naturally lends itself to use in scanned probe microscopy. We have designed a metrological atomic force microscope (AFM) as a prototype for a similar microscope that will later interface directly with the SAMM. Our motivation for developing an AFM — as opposed to a scanning tunneling microscope (STM), in particular — largely stems from the relatively wide variety of surface types with which it is compatible.

We have designed our AFM with built-in metrology to directly measure the motion of the probe tip. Many commercial AFMs do not incorporate such means for direct position sensing. Instead, they approximate the shape of the scanned sample by relating the voltage commanded to the AFM's scanning element to the displacement of the probe tip. However, this method introduces nonlinear image artifacts when the scanning element is made from a piezoelectric material, as is most often the case. Various scanning and image processing techniques have been developed to account for the piezoelectric scanner's inherent nonlinearities. Nonetheless, these methods do not directly address the source of these errors and are therefore limited in their effect. We follow the general strategy previously exploited by Griffith [4] and Holman [5], among others, who have already demonstrated the gains in imaging accuracy obtained by integrating metrology with a scanned probe microscope head. However, our metrology configuration is novel.

2 Design of the Metrological AFM

Figure 1 shows a three-dimensional model of our metrological AFM, with the housing transparent to reveal the inner components. A piezoelectric tube scanner extends downward from the top of the housing. This tube provides three degree-of-freedom motion of the probe tip, with a range of roughly 10 μm x 10 μm x 1 μm at the tip. Six capacitance sensors are clamped to the housing and measure the displacement of a cone-shaped target, which is mounted to the end of the tube scanner.

Employing a technique developed by Karrai and Grober [6], and taught to us by Dr. Pat Moyer — who has experience with this approach from his work in near-field scanning optical microscopy [7] — we use the signal from a piezoelectric tuning fork taken from a watch crystal to determine the relative proximity of the probe tip to the sample surface. The fork vibrates a short length of optical fiber, which has been heated-and-pulled to a sharp tip. We operate the tuning fork sensor in 'shear mode,' wherein the tip oscillates laterally

while positioned a fixed distance of tens of nanometers above the sample surface. When the tip-sample separation falls within this range, the tuning fork's dynamics become sensitive to small changes in the gap size. We use a lock-in amplifier to measure the current flow through the tuning fork circuit, as the fork is driven slightly below its resonant frequency.[1] Through closed-loop control of the probe height, we maintain a constant current magnitude through the fork, which translates to a constant tip-sample separation. Then, as we scan the probe over an area of the sample, the tip traces the sample's topography.

The design of our probe metrology draws inspiration from the work of Ruijl [8], and Schellekens [9], in the design of small, high-precision coordinate measuring machines. We have aligned the microscope's capacitance sensors such that their measurement axes intersect at a single point below the cone-shaped target. By locating the probe tip at this point, we effectively eliminate Abbe offset error from measurements of tip displacement.

Figure 2 shows the assembled microscope head mounted on its base plate, which is bolted to a small vibration isolation table. The housing and scanner endpiece assemblies are both made of aluminum, a choice primarily motivated by cost and ease of machining, though at the consequence of a high coefficient of thermal expansion. We use a set of micrometers to provide coarse height adjustment of the probe. Three extension springs preload a kinematic coupling formed between balls on the ends of the micrometers and grooves in the base plate. During coarse approach, we visually monitor the proximity of the tip to the sample using a 30x magnification 'pocket microscope' mounted off the side of the head.

3 Results

Using a PC-based digital control system, we close the loop on both the lateral scanning and axial height regulation actions of the probe assembly. Figure 3 shows the block diagram for the lateral scanning loop. Here, we have implemented an integral controller, with a pole added beyond cross-over to further attenuate the 1 kHz resonance of the tube scanner's bending mode. We have measured a -3dB bandwidth of 189 Hz for this closed-loop system.

The axial height regulation system — which controls axial motion of the tube scanner on the basis of proximity sensing from the tuning fork assembly — provides an additional set of challenges. Since we are approaching this microscope as a prototype for the upcoming SAMM AFM, we have not yet undertaken the additional steps necessary to place the probe in a temperature and humidity-controlled clean-room environment. As a result, we have observed significant variability in the tuning fork sensor's behavior on a day-to-day basis, perhaps due to water films or other surface contamination. Nonetheless, we have had some success in closing the axial following loop, measuring a -3dB closed-loop bandwidth of up to 184 Hz using a lead-lag compensator. However, after running scans with a similar controller in which the loop occasionally went unstable — crashing the tip into the surface in the process — we decided to remove the lag element from the control scheme.[2] Figure 4 shows the block diagram for the controller we eventually settled on, which uses simple proportional control to attain a -3dB closed-loop bandwidth of roughly 130 Hz.

With this system, we have performed linescans of a squarewave diffraction grating with 105 nm step height and 3000 nm pitch (Figure 5). As seen in the figure, we have had success in detecting these features, though we still observe some image errors, particularly at the falling edges[3] and in the base portions of the squarewave pattern. Also, while the measured grating features are close to the stated sizes, we have measured consistently wider-than-expected pitches and taller-than-expected steps. This may be explained by the fact that our capacitance probes were not calibrated in situ on the conical target. We later plan to use the SAMM stage metrology to provide calibration to the AFM head metrology.

We have also taken some three-dimensional scans of the grating surface with our AFM. The image shown in Figure 6 represents the cleanest demonstration, to date, of the metrological AFM's imaging capabilities.[4]

[1] The manufacturer's quoted resonant frequency for our tuning forks is 32.768 kHz. For our application, the resonance occurs several hundred Hertz below this value, as a result of the additional mass of the optical fiber.

[2] Without the lag's free integrator, we avoid the potentially destabilizing effects of integrator windup.

[3] The probe was scanned from left to right.

[4] We used the aforementioned lead-lag compensator in obtaining this grating image.

4 Conclusion

We have successfully used our metrological AFM to image a sample with 100 nm-scale features, with an RMS vertical measurement noise of roughly 5 nm. We believe the novel configuration of the microscope's capacitance sensors provides a sound approach for optimizing imaging accuracy. As mentioned earlier, we presently operate the AFM in a poorly-controlled laboratory environment. By addressing this issue, and with additional advances in the production of probe tips, we should be able to greatly improve the performance of this system. We will continue to refine our design, with plans to install an improved version in the SAMM in the future.

Acknowledgments

The authors wish to thank Dr. Pat Moyer for his help in learning about the tuning fork proximity sensors. We also received assistance from Dr. Chunhai Wang, who worked extensively on the SAMM stage and provided our pulled fiber tips, and Professor Martin Culpepper, who offered insight into the design and fabrication of the AFM head's kinematic coupling. This work was funded by the United States National Science Foundation under DM11-9820126.

References

[1] Holmes ML, Hocken RJ, Trumper DL. The long-range scanning stage: a novel platform for scanned-probe microscopy. Precision Eng 2000;24(3):191-209.

[2] Hocken RJ, Trumper DL, Wang C. Dynamics and control of the UNCC/MIT sub-atomic measuring machine. CIRP Ann 2001;50(1):373-6.

[3] Holmes ML, Trumper DL. Magnetic/fluid-bearing stage for atomic-scale motion control (the angstrom stage). Precision Eng 1996;18(1):38-49.

[4] Griffith JE, Miller GL, Green CA, Grigg DA, Russell PE. A scanning tunneling microscope with a capacitance-based position monitor. J Vac Sci Technol B 1990;8(6):2023-7.

[5] Holman AE, Laman CD, Scholte PMLO, Heerens W Chr, Tuinstra F. A calibrated scanning tunneling microscope equipped with capacitive sensors. Rev of Sci Instrum 1996;67(6):2274-80.

[6] Karrai K, Grober RD. Piezoelectric tip-sample distance control for near field optical microscopes. Appl Phys Lett 1995;66(14):1842-4.

[7] Paesler MA, Moyer PJ. Near-field optics: theory, instrumentation, and applications. New York: Wiley-Interscience, 1996.

[8] Ruijl TAM. Ultra precision coordinate measuring machine. Ph.D. Thesis. Delft University of Technology, Delft, the Netherlands, 2001.

[9] Jansen A, Rosielle N, Schellekens P. A fully elastically guided 3-D CMM with a measuring volume of 1 cm^3. In: Proceedings of ASPE Conference, vol. 20, 1999, p. 452-5.

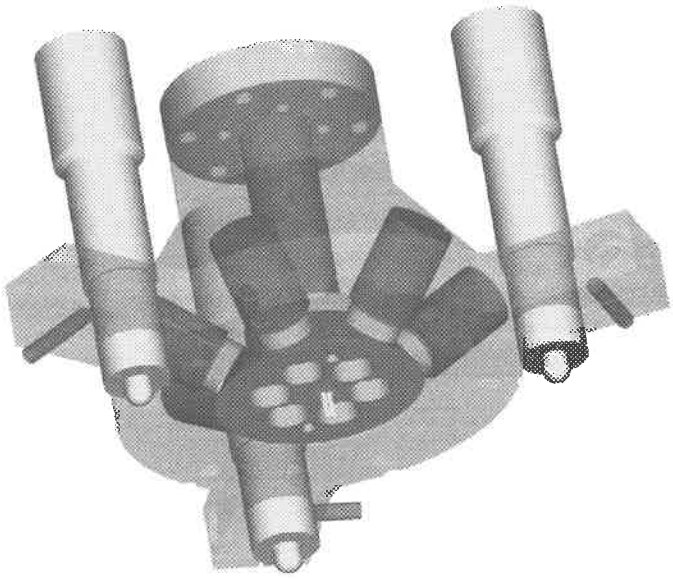

Figure 1: Three-dimensional model of the metrological AFM head. The housing is transparent, to allow a view of the inner components. A piezoelectric tube scanner extends downward from the top of the housing. Six cylindrical capacitance sensors arrayed around the base of the head measure the displacement of the cone-shaped target on the tube scanner's free end. The sensors' measurement axes intersect at the tip of a tapered optical fiber, which is mounted to the tuning fork seen protruding from the bottom of the cone.

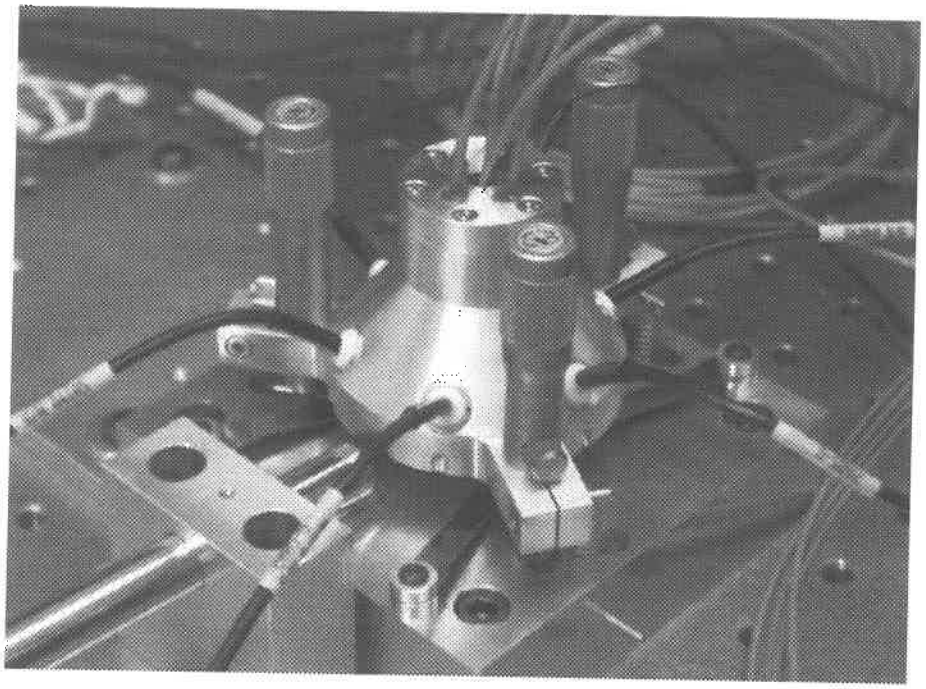

Figure 2: The metrological AFM head mounted on its base plate. Extension springs preload a kinematic coupling between balls at the ends of the coarse-approach micrometers and grooves in the plate. We use the pocket microscope shown in the lower-left corner of the picture to assist in positioning the probe over the sample.

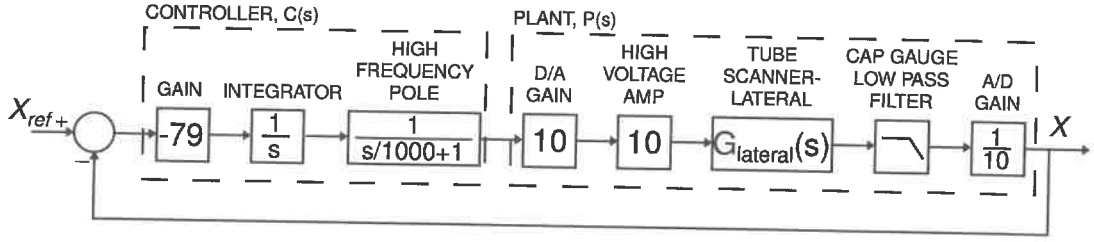

Figure 3: Block diagram for closed-loop lateral scanning.

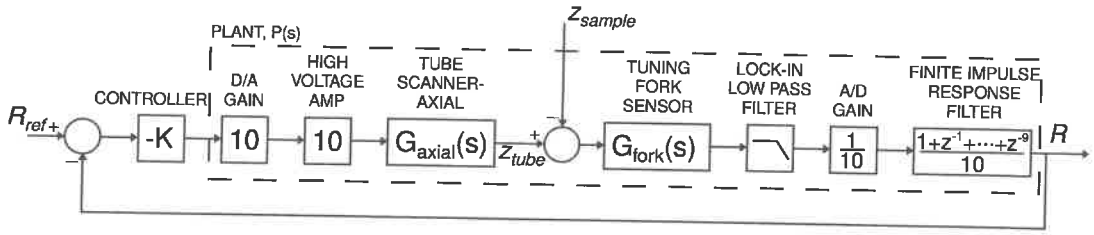

Figure 4: Block diagram for closed-loop axial height regulation.

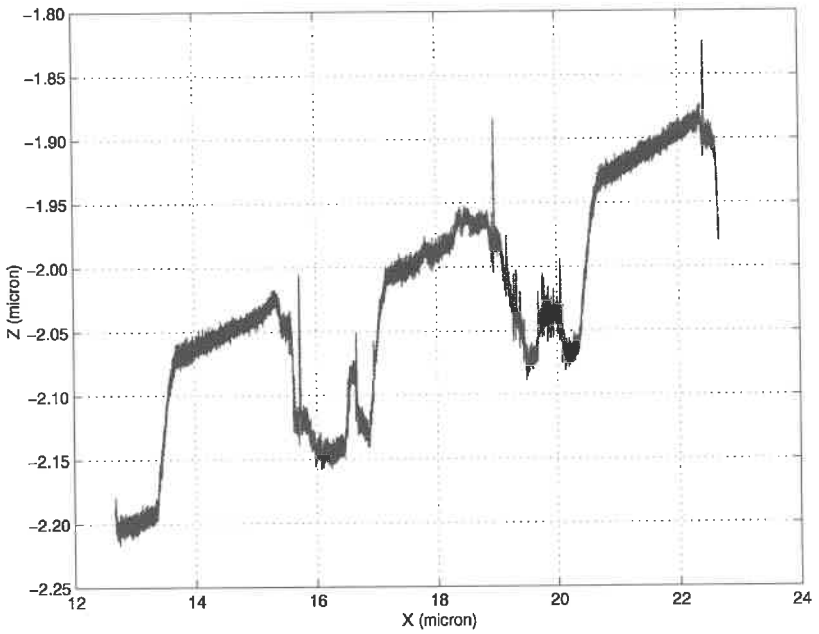

Figure 5: Linescan taken of squarewave grating with 105 nm peak-to-peak amplitude and 3000 nm pitch. Scan data errors are visible in the base portions of the scan. The cause of these errors is not yet determined.

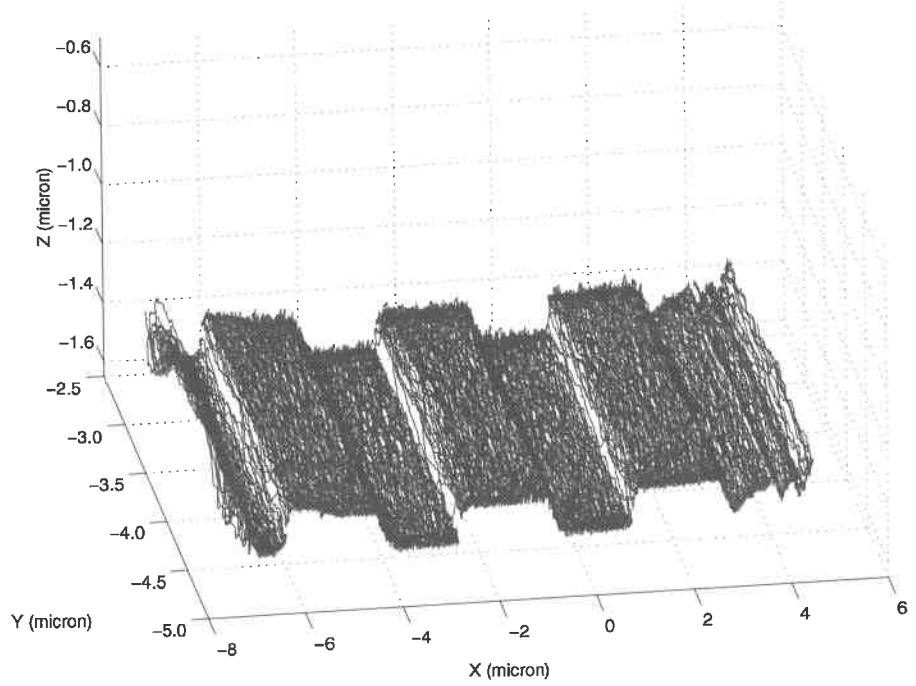

Figure 6: Three-dimensional image of grating surface taken with our metrological AFM head. Grating supplied with a calibrated step height of 105 nm and a pitch of 3000 nm.

EFFECTS OF VARYING INCIDENT ANGLE ON THE CONTRAST OF THE FRINGE METROLOGY USING A FRESNEL ZONE PLATE

Chulmin Joo[1], G. S. Pati, Carl G. Chen, Paul T. Konkola, Ralf K. Heilmann, and Mark L. Schattenburg
Massachusetts Institute of Technology, Cambridge, MA 02139

Alexander Liddle and Erik H. Anderson
Center for X-ray Optics, Lawrence Berkeley National Laboratory, Berkeley, CA 94720

INTRODUCTION

Variable period scanning beam interference lithography (VP-SBIL) [1], [2] is under development in our laboratory. It is a generalized concept of phase-locked scanning beam interference lithography [3], [4], [5] for patterning continuously varying (chirped or quasi-periodic) gratings. The detailed description of the design and operation of the VP-SBIL can be found in Ref. [2].

For sub-nanometer phase distortions across the substrate, the VP-SBIL calls for nanometer-accurate fringe metrology immune to variations in the beam angle and orientation since it enables the precise stitching of adjacent scans [5]. Previously, a novel interference fringe metrology has been proposed, which exploits two unique properties of Fresnel zone plates: (1) they contain a wide range of spatial frequencies, and (2) all spatial frequencies are phase symmetric with respect to the optical axis [6]. For the system, it is highly important to investigate the signal contrast variations with changing incident angles since the accurate measurement of fringe characteristics is critically dependent on the determination of signal properties, i.e., peaks and valleys.

In this paper, we report the theoretical study and simulation results on the contrast variations with changing incident angles.

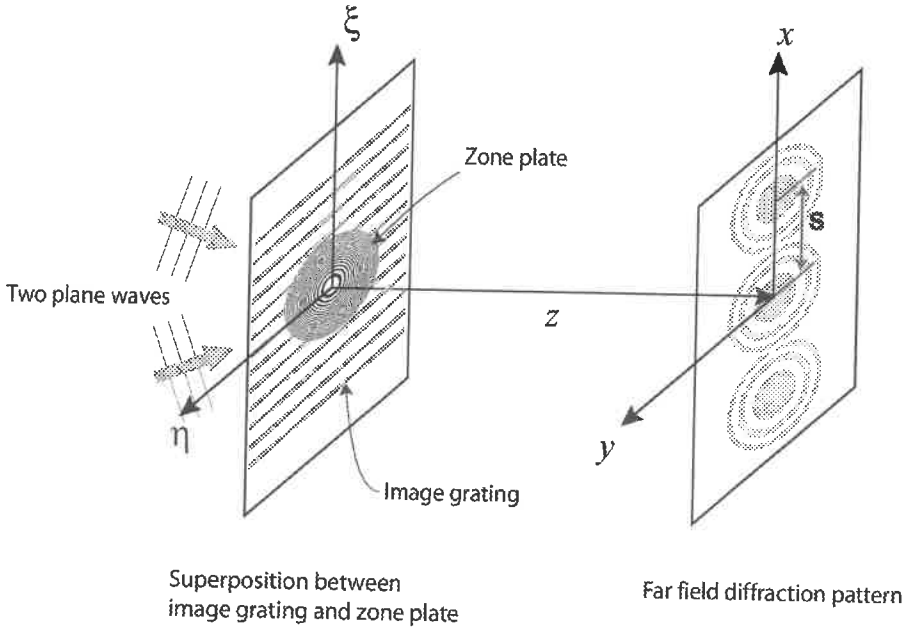

Figure 1: Diffraction geometry of a Fresnel zone plate and two plane waves.

[1]email: cmjoo@mit.edu.

THEORETICAL MODEL AND SIMULATION RESULTS

Consider two plane waves incident upon a Fresnel zone plate (Figure 1). The irradiance distribution in the far-field plane (x, y), which is at a distance z from the Fresnel zone plate, is given by

$$I(x,y) = g_1(x,y)^2 + g_2(x,y)^2 + 2g_1(x,y)g_2(x,y)\cos\phi \tag{1}$$

where $g_1(x,y)$ and $g_2(x,y)$ are the far-field diffraction patterns of the Fresnel zone plate corresponding to each plane wave (FFZP's), and ϕ is the phase difference between the two plane waves. Here, $2g_1(x,y)g_2(x,y)$ represents the far-field Moiré zone plates (FMZP) described in Ref. [6]. If two plane waves are assumed to have the same amplitude and incident angle θ, $g_1(x,y)$ and $g_2(x,y)$ have the same amplitude functions except that they are mirror symmetric about the z axis. Then, (1) can be re-written as,

$$I(x,y) = g(x+s,y)^2 + g(x-s,y)^2 + 2g(x+s,y)g(x-s,y)\cos\phi \tag{2}$$

where s, given by $s = z\sin\theta$, is the distance between the origin and the center of the FFZP, and $g(x,y)$ is a circularly symmetric chirped function.

If the irradiance (2) is integrated over the innermost zone of the first FMZP centered at the origin, the power is obtained as

$$\begin{aligned} P(s) &= \int\int_A \left\{g(x+s,y)^2 + g(x-s,y)^2\right\} dA + 2\int\int_A g(x+s,y)g(x-s,y)dA\ \cos\phi \\ &= D_A(s) + N_A(s)\ \cos\phi, \end{aligned} \tag{3}$$

and a contrast function can then be defined as,

$$C_A(s) = \left| \frac{\int\int_A 2\ g(x-s,y)g(x+s,y)\ dA}{\int\int_A \left\{g(x-s,y)^2 + g(x+s,y)^2\right\} dA} \right| = \left| \frac{N_A(s)}{D_A(s)} \right|. \tag{4}$$

The contrast would be unity, if $g(x-s,y) = \pm g(x+s,y)$ over the innermost zone of the first FMZP. However, since $g(x,y)$ is a quadratic chirped function, $g(x-s,y)$ cannot be equal to $\pm g(x+s,y)$ over the region for $s \neq 0$, meaning that the contrast cannot be unity.

To find the values of s where the contrast takes on maximum or minimum values, let us assume that the distance s between the origin and the center of FFZP is large enough that the FMZP can be produced. If s is not large enough, the FMZPs would no longer be formed, instead linear fringes will appear [7].

The defined integral region covers many outer zones of the FFZP. It is intuitive that $D_A(s)$ is not much affected by the change of s. The in-and-out movements of fine outer zones in the integral region do not greatly affect the values of $D_A(s)$ over the range of s considered, so that

$$\frac{dD_A(s)/ds}{D_A(s)} \ll 1. \tag{5}$$

For the values of s at which the contrast has extrema, it must be true that

$$\frac{dC_A(s)}{ds} = \left| \frac{\frac{dN_A(s)}{ds} D_A(s) - N_A(s)\frac{dD_A(s)}{ds}}{D_A(s)^2} \right| = 0. \tag{6}$$

Noting that the second term of the numerator in Equation (6) is negligible, and $D_A(s)$ cannot be zero in the innermost zone of the first FMZP, $dN_A(s)/ds = 0$ is obtained. If we assume that there is no phase difference between the two plane waves ($\phi = 0$), the derivative of power is expressed as,

$$\frac{dP(s)}{ds} = \frac{dN_A(s)}{ds} + \frac{dD_A(s)}{ds} = 0$$

Hence, the power has its extrema at the values of s where the contrast has its extrema. Furthermore, the maxima in contrast are observed when the power has extreme values over the integral region. The power reaches the peak or valley values when $N_A(s)$ has the maximum values in magnitude, but the opposite signs

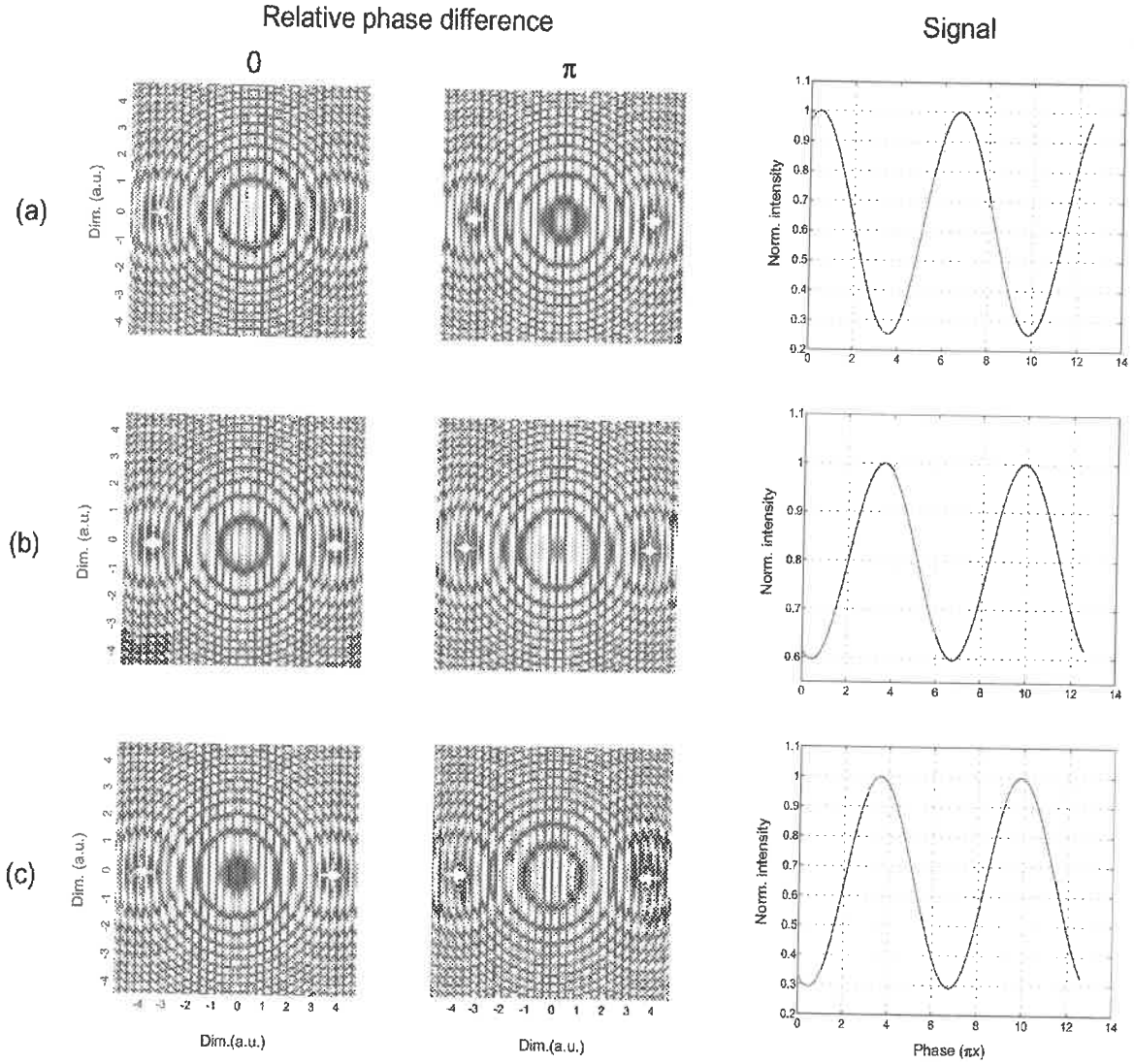

Figure 2: Simulated contrast variations at different incident angles. An amplitude Fresnel zone plate with an innermost zone radius of 265 μm is used. (a) incident angle = 17.19^o, contrast = 0.59, (b) incident angle = 17.58^o, contrast = 0.25,(a) incident angle = 18.06^o, contrast = 0.54.

in each case. Figure 2 demonstrates the contrast values and the signals produced by the phase difference at different incident angles. Note that the maxima in contrast are obtained when the power over the innermost zone of the first FMZP reaches its extrema as mentioned before.

Now let us assume the amplitude function $g(x,y)$ as shown below,

$$g(x,y) = \sum_{n=-\infty}^{\infty} A_n \exp[ik_n(x^2+y^2)] \tag{7}$$

where $A_n = A^*_{-n}$ since $g(x,y)$ is real. Then,

$$\begin{aligned} g(x+s,y)g(x-s,y) &= \sum_{m=-\infty}^{\infty} A_m \exp[ik_m((x+s)^2+y^2)] \sum_{n=-\infty}^{\infty} A_n \exp[ik_n((x-s)^2+y^2)] \\ &= \sum_{m=-\infty}^{\infty}\sum_{n=-\infty}^{\infty} A_m A_n \exp[ik_m((x+s)^2+y^2)] \exp[ik_n((x-s)^2+y^2)] \\ &= \sum_{m=-\infty}^{\infty}\sum_{n=-\infty}^{\infty} A_m A_n \exp[i(k_m+k_n)(x^2+2s\frac{k_m-k_n}{k_m+k_n}x+y^2+s^2)]. \end{aligned} \tag{8}$$

Since the first FMZP centered at the origin is being considered, $m = n$ [7]. Therefore,

$$g(x+s,y)g(x-s,y) = \sum_{n=-\infty}^{\infty} A_n^2 \exp[i2k_n(x^2+y^2+s^2)], \tag{9}$$

and

$$\begin{aligned} N(s) &= \int\int_A 2g(x+s,y)g(x-s,y)dA \\ &= \int\int_A 2\sum_{n=-\infty}^{\infty} A_n^2 \exp[i2k_n(x^2+y^2+s^2)]dA \\ &= \sum_{n=-\infty}^{\infty} 2A_n^2 \int\int_A \exp[i2k_n(x^2+y^2+s^2)]dA \\ &= \sum_{n=-\infty}^{\infty} 2A_n^2 \exp(i2k_n s^2) \int\int_A \exp[i2k_n(x^2+y^2)]dA \\ &= \sum_{n=-\infty}^{\infty} 2A_n^2 B_n \exp(i2k_n s^2), \end{aligned} \tag{10}$$

where $B_n = \int\int_A \exp[i2k_n(x^2+y^2)]dA$. The contrast function has zeros at the values of s where $N_A(s)$ satisfies

$$N(s) = \sum_{n=-\infty}^{\infty} 2A_n^2 B_n \exp(i2k_n s^2) = 0. \tag{11}$$

The contrast also has maximum values if

$$\begin{aligned} \frac{dN_A(s)}{ds} &= \frac{d\left[\sum_{n=-\infty}^{\infty} 2A_n^2 B_n \exp(i2k_n s^2)\right]}{ds} \\ &= 8si\sum_{n=-\infty}^{\infty} C_n \exp(i2k_n s^2) = 0 \end{aligned} \tag{12}$$

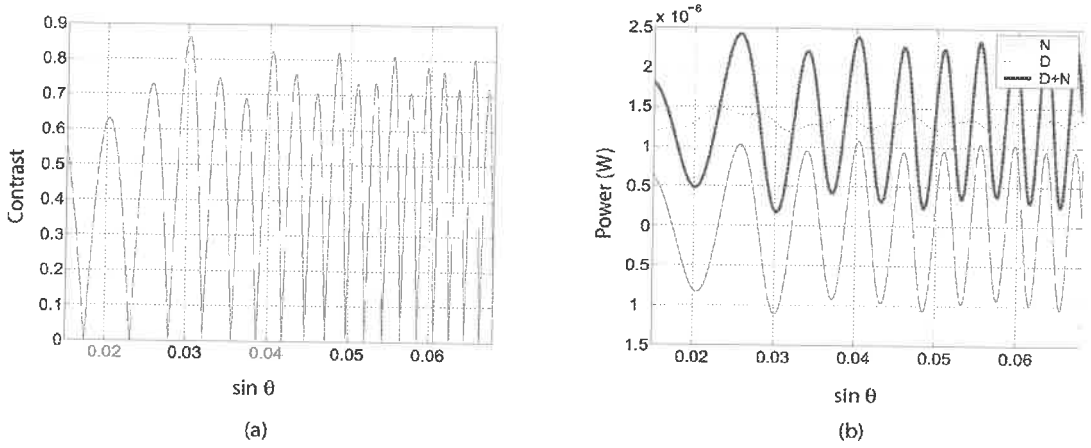

Figure 3: Simulated the contrast variations with varying incident angles. An amplitude Fresnel zone plate with an innermost zone radius of 16 μm is used. (a) Contrast variations with incident angles, (b) Power variations with incident angles.

where $C_n = k_n A_n^2 B_n$. Therefore, the contrast has the maxima at the values of s which satisfy the following equation

$$\sum_{n=-\infty}^{\infty} C_n \exp(i2k_n s^2) = 0, \tag{13}$$

for $s \neq 0$. Equation (11) and (13) are chirped functions in s which have the same as the $g(x, y)$ except for the coefficient and the fundamental spatial frequency. Hence, a lot of fluctuations are predicted for large s, or large incident angles, and small fluctuations over small incident angles. Figure 3 shows the contrast calculated over a range of incident angles using an amplitude Fresnel zone plate with an innermost zone radius of $\sim 16\mu m$. The power is also shown in Figure 3(b). Note the correspondence of the locations at which extrema of the power and peaks of contrast are observed. Also, high fluctuations for large incident angles and small fluctuations for small incident angles are shown. The small variations shown in the contrast maxima are due to the small variations in the D.

CONCLUSION AND FUTURE WORK

The contrast variations with changing incident angle were investigated for the interference fringe metrology using a Fresnel zone plate. It was shown that the contrast varies rapidly for large incident angles and slowly for small incident angles. Also, the incident angles where the peak and valley contrasts are observed can be predicted. It is desirable to have relatively high and uniform contrast in a wide range of incident angles, especially for the use of the VP-SBIL. The design of novel diffractive structures which have a uniform contrast variation are underway.

ACKNOWLEDGMENTS

The authors gratefully acknowledge the outstanding technical assistance of Robert Fleming and Edward Murphy. Student, staff, and facility support from the Space Nanotechnology Laboratory are also appreciated. This work was supported by DARPA under Grant No. DAAG55-98-1-0130 and NASA under Grant No. NAG5-5271.

REFERENCES

1. M.L. Schattenburg, C.G. Chen, R.K. Heilmann, P.T. Konkola and G.S. Pati, "Progress towards a general grating patterning technology using phase-locked scanning beams," *Proc. SPIE* **4485**, *Optical Spectroscopic Techniques and Instrumentation for Atmospheric and Space Research IV*, eds. A.M. Larar and M.G. Mlynczak, 378-384 (2002).

2. G. S. Pati, R. K. Heilmann, P. T. Konkola, C. Joo, C. G. Chen, E. Murphy, and M. L. Schattenburg, "A generalized scanning beam interference lithography system for patterning gratings with variable period progressions," submitted to J. Vac. Sci. Technol. B (2002).

3. M. L. Schattenburg, C. G. Chen, P. N. Everett, J. Ferrera, P. T. Konkola, and H. I. Smith, "Sub-100 nm metrology using interferometrically produced fiducials," J. Vac. Sci. Technol. B **17**, 2692-2697 (1999).

4. P.T. Konkola, C.G. Chen, R.K. Heilmann, G. Pati and M.L. Schattenburg, "Scanning Beam Interference Lithography," *Proceedings of the Sixteenth Annual Meeting of the American Society for Precision Engineering* (American Society for Precision Engineering, Raleigh, NC), 15-18 (2001)

5. C. G. Chen, P. T. Konkola, R. K. Heilmann, G. S. Pati, and M. L. Schattenburg, "Image metrology and system controls for scanning beam interference lithography," to be published in J. Vac. Sci. Technol. B **19**, 2335-2341(2001).

6. Chulmin Joo *et al.*, "Nanometer-accurate fringe metrology using a Fresnel zone plate," submitted to J. Vac. Sci. Technol. B (2002).

7. G. Harburn, T. R. Welberry, R. P. Williams, Selected Papers on Zone Plates, edited by Jorge Ojeda-Castaneda and Carlos Gomez-Reino (SPIE Milestone Series, 1996), p. 242.

Fast Optical Form Measurements of Rough Cylindrical and Conical Surfaces in Diesel Fuel Injection Components

Thomas J. Dunn, Robert Michaels, Simon Lee, Mark Tronolone, and Andrew Kulawiec;
Corning Tropel Corporation, Fairport, NY

1.0 Introduction

The requirements for a more efficient diesel engine with lower emissions have driven the form tolerances for fuel injectors beyond the limits of the automotive industry's current metrology capabilities. In order to generate the required pressure levels for fuel injection, the manufacturing tolerances for the cylindrical and conical surfaces of fuel injector components need to be monitored with sub micron resolution and accuracy. This is particularly difficult when the surfaces to be measured are buried deep within a blind hole where access is limited. An optical metrology system is preferred to allow rapid measurement suitable for a production environment; however, the surface roughness of the components exceeds the optical wavelengths used in most conventional instruments.

We present a new instrument in which form and geometry measurements of rough cylindrical and conical surfaces are made using a dual-wavelength interferometer system. The system uses two solid-state lasers at different wavelengths to extend the dynamic range of measurement to accommodate the surface roughness of the cylindrical and conical forms to be measured. The two laser beams are combined and sent through a unique probe that can deliver the beams to the desired measurement surface at the bottom of a 3.5 mm diameter by 45 mm deep blind hole. In this paper, we provide a description of the system's design, and present some measurement results that manifest its unique capabilities.

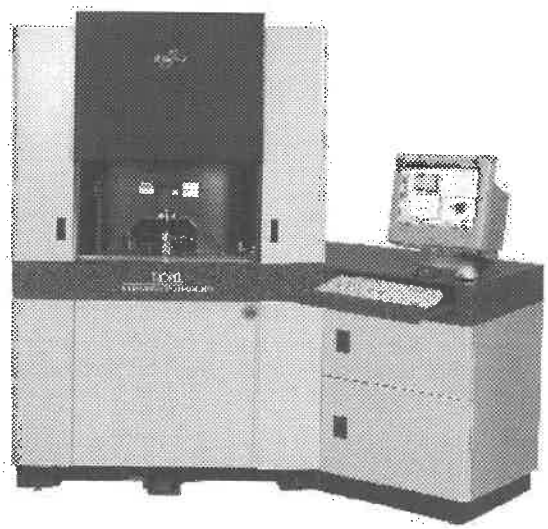

Figure 1. The new machine can measure rough cylindrical and conical surfaces inside of blind holes.

2.0 System Design

The heart of the new instrument is the dual wavelength interferometer system. One interferometer operates at 1310 nm and the second operates at 1550 nm. When the interferometric patterns at the two different fundamental wavelengths are analyzed together, a combined pattern with a synthetic wavelength of 8.46 μm is generated. Both interferometers are independently capable of measuring smooth parts and when the two wavelengths are used in conjunction, it is possible to measure ground parts with an R_z of 2 μm. Each interferometer uses a distributed feedback (DFB) solid-state laser as its source. The laser beam is split into a reference and measurement arm. The measurement arm is directed to the probe and focused onto the part to be measured. Light reflected from the part surface is imaged back through the probe and recombined with the reference arm in the sensor head (Fig. 2). The combined arms are imaged onto four

different detectors with an induced incremental 90-degree phase shift among them. A surface height map is generated from instantaneous phase measurements taken at individual points on the part as the focused beam is scanned over the part surface.

The machine employs a unique probe design that allows the test arms of both interferometers to be delivered to the bottom of a 3.5 mm diameter by 45 mm deep blind hole (Fig. 3). The probe includes miniature optics that split the test arms into two different beams. Each beam leaves the probe at a different angle for measuring two different surfaces: it may be a cone, a cylinder, or a flat. Both beams contain both wavelengths, but only one beam can be used for measurements at a time. Since each probe is capable of measuring at two different angles, relational measurements can be performed among different regions of the part such as runout, co-axiality, or perpendicularity. There are two different types of probes that have already been used with this machine: a cylinder-cone probe that is capable of measuring cylinders and cones with a 60 degree cone angle; and a cylinder-flat probe capable of measuring cylinders and flats. We are currently working on development for smaller diameter probes as well as for probes with different cone angles.

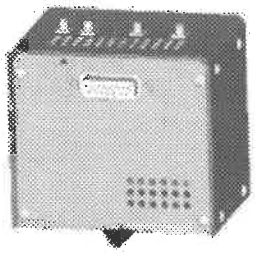

Figure 2. The sensor head contains the DFB laser, optics, detectors, and electronics.

Figure 3. The probe has miniaturized optics at the bottom of the probe stem.

Figure 4 shows the sensors and the two-angle probe mounted onto a rigid baseplate that rides on an X-Z stage system. Mirrors are used to combine the beams from the two sensors and direct them into the probe. The probe is mounted in a kinematic bracket with a magnetic preload that allows the probe to be removed and re-inserted so that it still maintains alignment. The bracket also incorporates a mechanical shutter to block the laser beam and detection electronics to prevent stage motion in case of improper probe loading.

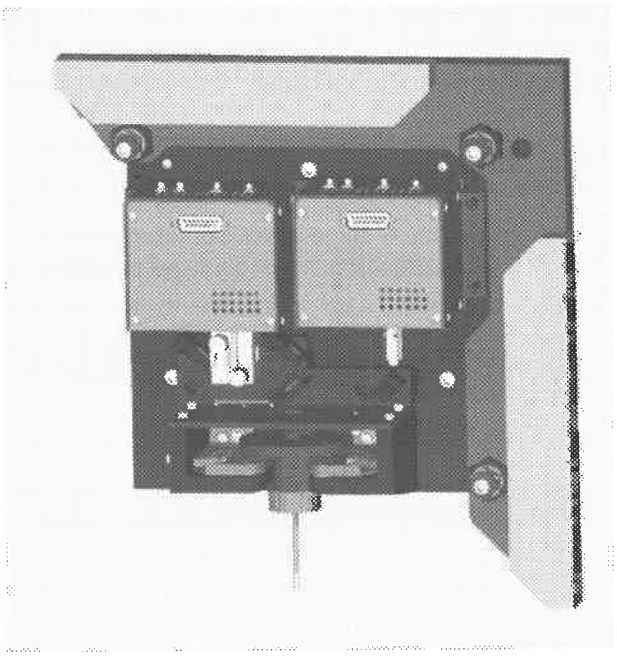

Figure 4. The sensors, probe, and stick mirrors are mounted on a rigid base plate which is carried by the X-Z stage system to move the focused laser beam along the surface of the part.

The depth of focus of the optical probe is about 40 μm. Motion profiles are optimized for each region on the part and for each type of part. The stages are mechanical crossed roller bearing stages with 2 mm pitch roller screws. The Z-stage has 180 mm of travel while the X-stage has 80 mm of travel. The stages are driven by brushless, slotless DC motors with integral encoders. The stages move the probe along the desired motion profile determined by the software in the computer. Since the stage motion is neither perfectly smooth nor straight, a three-axis displacement measuring interferometer is used to monitor the stage motion. There are two Zerodur "stick" mirrors mounted to the X-Z stage. A frequency-stabilized helium-neon laser beam is reflected from the Zerodur mirrors to

measure the straightness, yaw, and displacement errors of the stage motion. This data is recorded along with the phase data to remove errors caused by the stage motion.

The components to be measured are manually mounted to the air-bearing spindle by a hydraulic expansion chuck. The action of the chuck is very repeatable eliminating active alignment of the part to the spindle. The residual tilt and decenter of the part (typically less than several microns) is removed after the measurement during the software analysis. The air-bearing spindle rotates at 600 RPM and is powered by a direct-drive, brushless, DC motor with an integral high-resolution encoder. The quadrature signals from the spindle encoder are used to clock the data acquisition during the measurement. The data is simultaneously acquired from 8 channels from the two IR sensors and 3 channels from the HeNe displacement measuring interferometer.

For maximum measurement accuracy and repeatability, the entire measurement system is mounted on a granite base and riser block as shown in Fig. 5. The X-Z stage assembly is mounted on the riser block and the spindle is mounted in a hole through the base section. The granite structure is integrated into a cradle supported by a pneumatic isolation frame for increased immunity from external vibrational sources.

The external enclosure shown in Fig. 1 has two separate sections. The computer and control electronics are mounted within a cabinet that is rigidly attached to the enclosure and yet isolated from the temperature controlled environment. The operator accesses the chuck through a pneumatically controlled door operated by a foot switch. Space is also provided so that numerous parts, probes, fixtures, and calibration artifacts can all be stored in drawers, which are maintained at the same temperature as the measurement area. The enclosure serves as an environmental chamber to keep the entire measurement area at a constant temperature to within +/- 0.25 degrees Celsius. The environmental control system consists of a solid-state thermoelectric cooler and heater, a blower assembly, and control and monitoring electronics positioned at various locations throughout the enclosure.

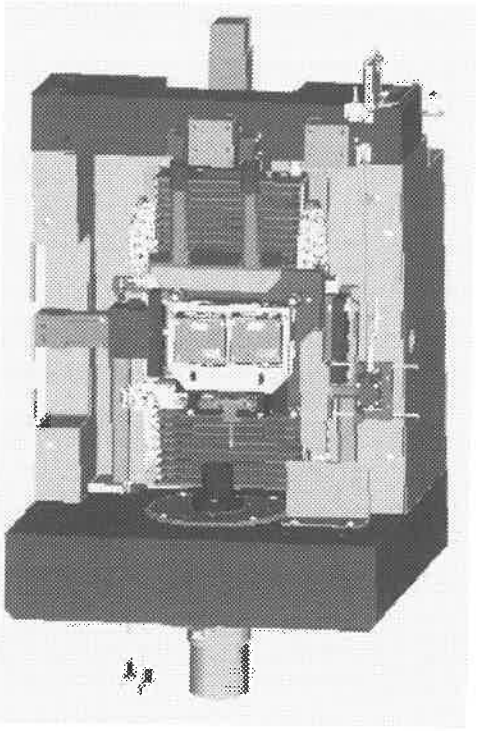

Figure 5. The stacked X-Z stage system is mounted to the vertical granite riser, and the spindle is mounted to the granite base.

3.0 Measurement Results

Figure 6 shows the two measurement regions of interest as well as the aspect ratio for the inside of the fuel injector nozzle. The conical section is about 1.5 mm high while the cylindrical section is 10 mm high. We show in Fig. 7 the measurement results from the inside cone of a fuel injector nozzle. This region lies at the bottom of the 40 mm blind hole and we are able to see the spray holes of the nozzle through which the fuel is injected. Fig. 7a shows the raw interferometric data including the tilt and decenter that results from the manual loading of the part into the collet. The part was spun at 600 RPM and the stage speed was chosen so that the spiral step size was 4 μm. This gives an array of 358 X 1024 points to cover this conic section. Fig. 7b shows the 3-D and 2-D plots of the same data set after the tilt and decenter was removed. Since the probe tip is scanned along a line parallel to the surface of the cone, an ideal part would be displayed in our software as a cylinder. The conical shape shown in Fig. 7b is a result of the angular error in the manufacturing of this part. The raw cone data was analyzed with a 50% Gaussian filter using 50 UPR in the radial direction and 0.08 mm in the axial direction. For the cylinder

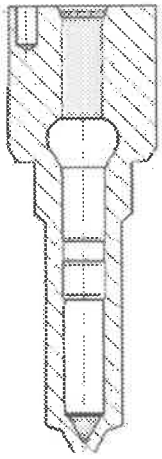

Figure 6. The measured regions of the fuel injector are highlighted.

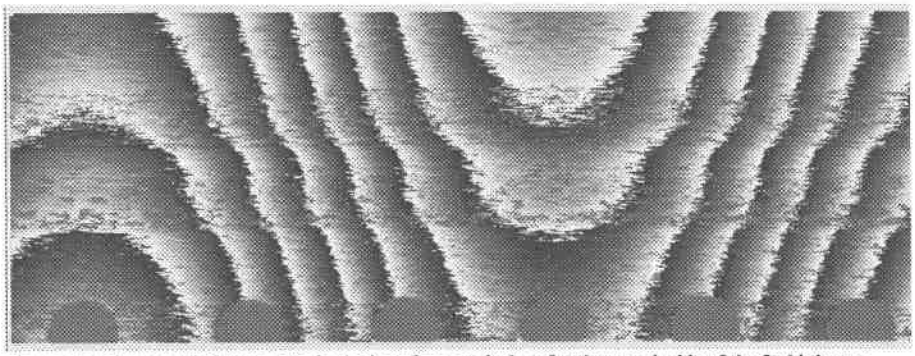

Figure 7a. The spray holes are seen in the interferometric data for the cone inside of the fuel injector

section the probe was scanned so that there was 50 μm between adjacent spiral scans resulting in a 225 X 1024 array after 0.2 mm edge exclusion. In this case the cylindrical data set was analyzed with a Gaussian filter using 50 UPR and 0.8 mm. Using the data from the cylindrical section of the part, we are able to establish a datum to determine the average radial runout over the entire cone. For this part the runout came to 2.6 μm.

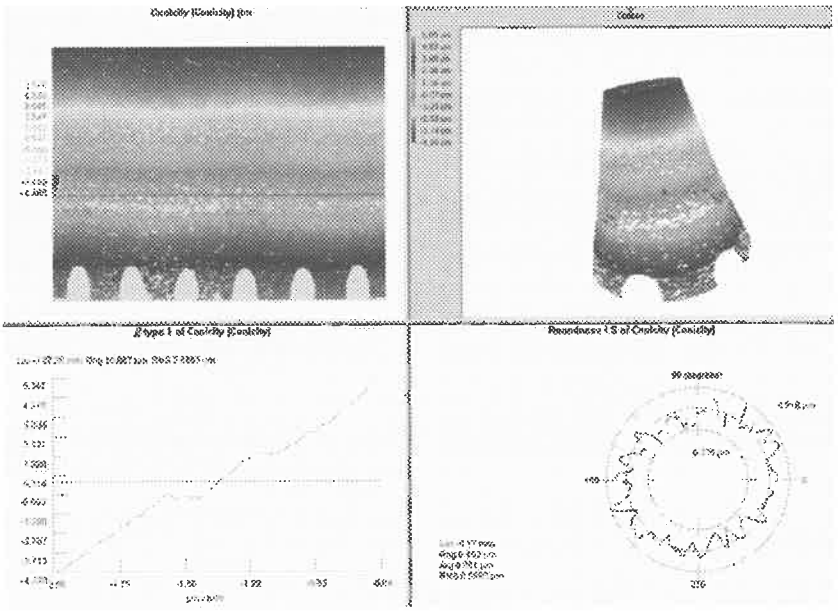

Figure 7b. Contour, 3-D, and 2-D plots are shown for the conical section inside of the fuel injector

The repeatability from this measurement technique is very high. We can typically achieve a standard deviation of 10 – 30 nm depending on the parameter being measured. We show in Fig. 8 the roundness results of the inside cone for 25 different parts measured 20 times over a period of 5 days. For this set of data the average standard deviation was 11 nm.

The accuracy of the measurements is verified through the use of artifacts certified at both NIST and PTB. We manufactured artifacts for each of the measured parameters: roundness, straightness, parallelism, angle, diameter, and runout. We performed gauge studies comparing the measured values to the certified values and achieved an accuracy of 40 nm or better for each of these parameters. A gauge study would typically consist of 25 measurements of the artifact in which the artifact was removed and reloaded before each measurement. We show in Fig. 9 a 3-D plot of the measurement of the roundness artifact. The PTB certified value for this artifact was 2.87 μm as measured by a Talyrond 73, and we measured 2.90 μm with a standard deviation of 11 nm. Similar results were achieved with the other artifacts.

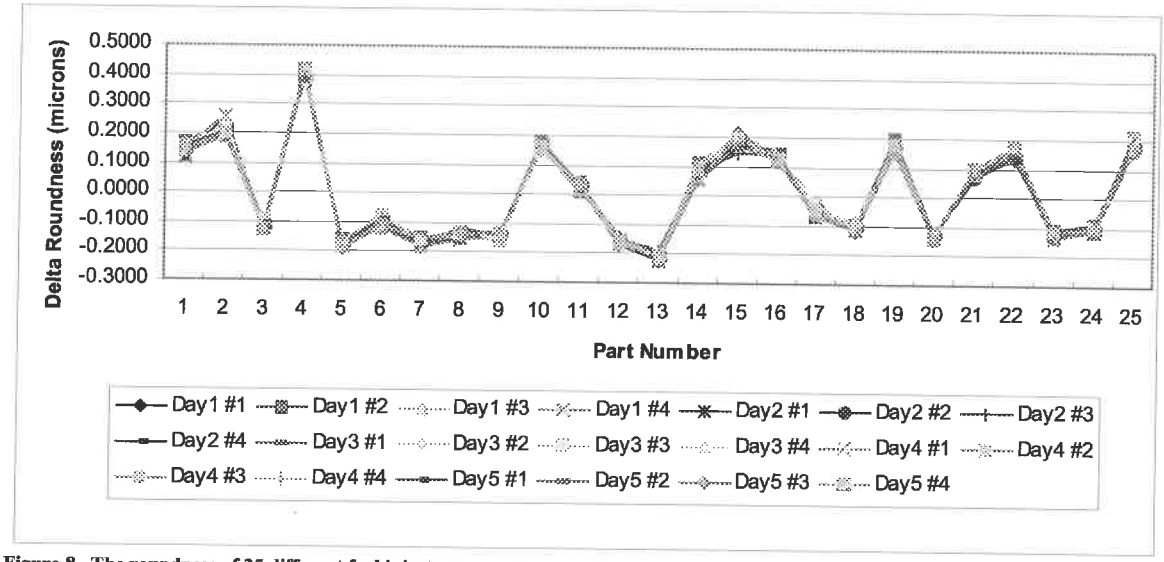

Figure 8. The roundness of 25 different fuel injector cones was measured 20 times over a period of 5 days. The average standard deviation over all of the measurements was 11 nm. Delta Roundness is the deviation of the measurement from the average roundness over all 25 parts.

Future efforts will be focused on the development of new types of probes that allow us to measure different cone angles and blind holes that have smaller diameters than the ones measured to date. In addition to automotive applications, we anticipate that this technology will address metrology needs for many other industries as well.

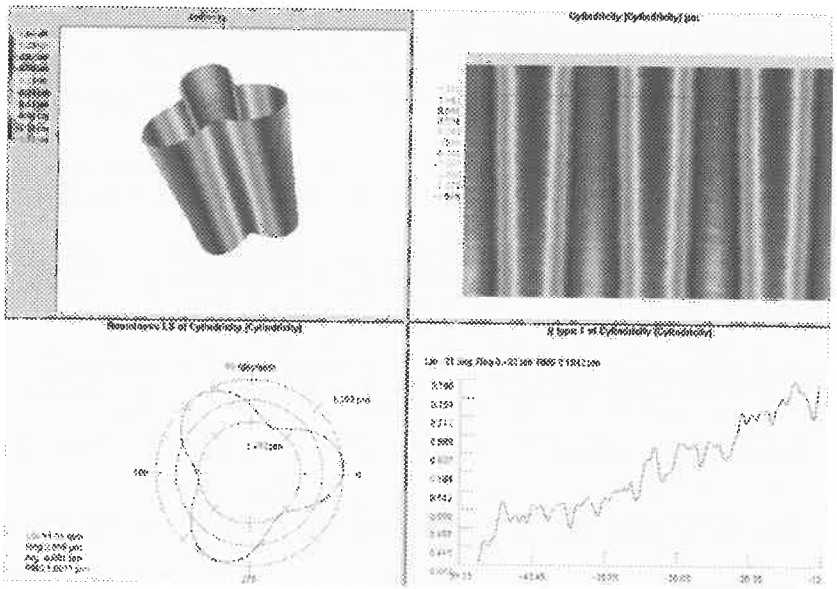

Figure 9. The roundness artifact was manufactured with three lobes. The difference between the certified and measured roundness is 30 nm.

Piezoelectric Tool Actuator for Precision Machining on Conventional CNC Turning Centers

Andrew Woronko, Jin Huang, Yusuf Altintas

Manufacturing Automation Laboratory, Department of Mechanical Engineering,

University of British Columbia, Vancouver, Canada, V6T 1Z4

Key words: Piezoelectric actuator; Precision turning; Sliding mode control

A typical precision shaft machining operation may involve both turning and grinding operations; the latter required to meet part tolerances on form and surface quality. The positioning error of conventional turning centers, hindered by friction and backlash, may be as high as 10 microns depending on the design and wear of the machine. Clearly components requiring dimensional tolerances in the micron range will require subsequent finishing operations. Although high precision lathes are available to meet precision turning requirements, the need for thermal and vibration isolation and high capital cost may not be justifiable for some applications. For components requiring high dimensional tolerance only in local areas (e.g. bearing surfaces) it may be more cost effective to deliver precise positioning via a tool actuator mounted to a conventional machine. Although there has been extensive research in tool actuator design and control for ultra-precision diamond turning [1]~[5], few researchers have addressed the use of piezo based fast tool servos for precision shaft machining on conventional CNC turning machines. This paper presents a piezo based fast tool servo for precision shaft machining on conventional CNC turning machines. The mechanical design, structural properties, and controller design for high performance tracking and precision positioning of piezo actuator driven tool are presented with experimental results for shaft machining.

An exploded solid model view of the actuator is presented in Fig. 1. A high voltage piezoelectric stack actuator is housed under preload within the monolithic guiding unit. Displacement in the radial (x) direction of the piezo stack is transmitted to the tool assembly via the use of four solid flexures, each with two circular hinges. The symmetric arrangement of the flexures is such that displacement is linear without parasitic error in the transverse direction. The tool adapter contains a Komet ABSN25 clamping system allowing for standard exchangeable tooling. Cutting force sensors are mounted at the fastener locations between the tool adapter and guiding unit. An alignment washer locates the piezo stack to the center of the assembly. The top and bottom plates support the guiding unit. A capacitive position sensor with 50 micron range and 10 nm resolution measures the relative displacement of the tool relative to the guiding unit mounted to the lathe turret. The sensor consists of a stationary probe fastened to the top plate, and the moving target mounted to the moving section of the guiding unit. Two clamping units, each containing a piezo stack and flexure assembly, serve to rigidly clamp the guiding unit if necessary for increased dynamic stiffness during roughing operations. The bottom plate provides a shank interface for standard lathe turrets. The overall envelope of the actuator body is 95.5 × 143 × 85 mm, with a tool stick out of 67 mm in the radial direction and 20 mm in the feed direction. The main structural components are machined from a titanium alloy (Ti-Al6-V4) using wire EDM to reduce contour errors and residual stresses. The overall stroke is 36μm, and the natural frequency in the radial direction is 3200 Hz with a stiffness of 370 N/μm, which can be increased to 620 N/μm by activating the clamping units.

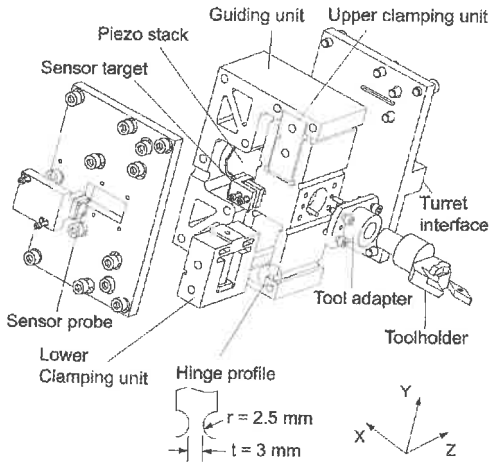

Fig.1: Exploded view of the actuator assembly

A sliding mode control design is implemented to reject cutting force disturbances and to compensate nonlinearities of a piezoelectric tool actuator, which is based on the algorithms developed at UBC MAL[10]. The piezo amplifier (G_a) and piezo stack (G_p) are modeled as constant gains, and the actuator body and flexures are modeled as a single degree of freedom mechanical system with mass (m), equivalent flexure spring constant (k) and damping (c) elements. The disturbance force (F_d) consists of not only the cutting forces in the radial direction of cut but the influence of nonlinear piezo stack hysteresis which deviates from the constant gain (G_p). The differential equation of the open loop system which includes the amplifier, piezo stack, the disturbance force and flexure structure are given by:

$$m\ddot{x} + c\dot{x} + kx = G_a G_p u - F_d \tag{1}$$

Equation (1) can be expressed alternatively by considering the influence of the force disturbance at the input:

$$A\ddot{x} + B\dot{x} + Cx = u - u_d \tag{2}$$

where

$$A = \frac{m}{G_a G_p}; \quad B = \frac{c}{G_a G_p};$$
$$C = \frac{k}{G_a G_p}; \quad u_d = \frac{1}{G_a G_p} F_d$$

A sliding surface S is designed to minimize both position and tracking errors of the piezo actuator as:

$$S = \lambda(x_d - x) + (\dot{x}_d - \dot{x}) \tag{3}$$

where the gain λ [1/s] specifies the bandwidth of the response; x_d and x are the desired and actual tool tip positions, respectively. As the sliding surface approaches to zero ($S \to 0$), the tool tip position converges to the desired position command ($x \to x_d$) with zero velocity error ($\dot{x} \to \dot{x}_d$). The following positive definite Lyapunov function, which is continuously differentiable, is selected for the control law design:

$$V[S,(u_d-\hat{u}_d)]=\frac{1}{2}\left[\hat{A}S^2+\frac{(u_d-\hat{u}_d)^2}{\rho}\right] \tag{4}$$

where $\hat{u}_d$ represents estimated disturbance and ρ is a disturbance observer gain. The observer estimates the sum of all the disturbances in the system, including cutting forces, errors in parameter estimates, and system nonlinearity caused by the piezo stack hysteresis. The derivative of the disturbance ($\dot{\hat{u}}_d$) is defined by:

$$\dot{\hat{u}}_d=\rho S\kappa, \text{ where } \kappa=\begin{cases}0 & \text{if } \hat{u}_d\le d^- \text{ and } S\le 0\\ 0 & \text{if } \hat{u}_d\ge d^+ \text{ and } S\ge 0\\ 1 & \text{otherwise}\end{cases} \tag{5}$$

where the disturbance estimate is bounded by upper and lower values, $\hat{u}_d\in[d^-,d^+]$, and selected based on the estimation of the cutting forces from the cutting mechanics and experience. According to Layapunov stability theorem, the system is asymptotically stable if the derivative of the stability function is negative, i.e. $\dot{V}<0$. For a constant disturbance, the derivative of the Lyapunov function is given by:

$$\dot{V}=\frac{\partial V}{\partial S}\frac{\partial S}{\partial t}+\frac{\partial V}{\partial(u_d-\hat{u}_d)}\frac{\partial(u_d-\hat{u}_d)}{\partial t}=\hat{A}S\dot{S}-\frac{(u_d-\hat{u}_d)}{\rho}\dot{\hat{u}}_d \tag{6}$$

$$\dot{V}=S(\hat{B}-\hat{A}\lambda)\dot{x}+\hat{C}Sx-Su+\hat{A}S(\lambda\dot{x}_d+\ddot{x}_d)+S\hat{u}_d+S(u_d-\hat{u}_d)(1-\kappa) \tag{7}$$

Since $S(u_d-\hat{u}_d)(1-\kappa)\le 0$ from Equation (5), the derivative of the Lyapunov function is guaranteed to be negative by the following expression:

$$S(\hat{B}-\hat{A}\lambda)\dot{x}+\hat{C}Sx-Su+\hat{A}S(\lambda\dot{x}_d+\ddot{x}_d)+S\hat{u}_d=-K_sS^2 \tag{8}$$

where $K_s>0$ is the selected positive feedback design gain of the control system. Equation (8) leads directly to the control law:

$$u=(\hat{B}-\hat{A}\lambda)\dot{x}+\hat{C}x+\hat{A}(\lambda\dot{x}_d+\ddot{x}_d)+\rho\kappa\int S dt+K_sS \tag{9}$$

where $K_s, \lambda,$ and ρ are the parameters of the sliding mode controller which are to be tuned. A block diagram of the controller is given in Fig. 2. The control law given in Equation (9) is in continuous time domain, and is transformed into discrete time domain with control sampling interval T_s. The derivative of the displacement and integral of the sliding surface can be evaluated at discrete time intervals as follows, where low pass filter parameter α is set to 0.5 to avoid noise in the digital integration:

$$\left.\begin{aligned}\dot{x}(k)&=\alpha\dot{x}(k-1)+\frac{1-\alpha}{T_s}[x(k)-x(k-1)]\\ \int S\,dt(k)&=\int S\,dt(k-1)+S(k)T_s\end{aligned}\right\} \tag{10}$$

The controller is implemented in digital form in an in house developed Fast Cyclic Executive operating system running on a Digital Signal Processing board (TMS320C32) with a PC host. The output control

signal (0~10V) is sent to a high voltage piezo amplifier (100 W power, 100 mA average current, 500 mA peak current), which outputs a signal of 0 to +1000 volts to the piezo stack. The feedback signal from the capacitive sensor is processed by the sensor electronics card, which outputs a voltage signal to the DSP board. The sensor was calibrated with a laser interferometer, and has 0.2 volt/micron sensitivity, and 3 KHz bandwidth. The identified plant parameters are $A = 0.08\times10^{-8}$ V/μm/s^2, $B = 190\times10^{-8}$ V/μm/s, and $C = 0.353$V/μm. The control sampling frequency was 7.5 KHz. The control parameters, tuned to achieve a step response rise time of 0.010 s with less than 1% overshoot, are $K_s = 2.3\times10^{-5}$ V/μm/s, λ =700 1/s, and $\rho = 0.6$ V/μm. The upper and lower bounds of the disturbance estimate are set to $\hat{d} \in [-\infty,+\infty]$ such that no limits are imposed on the control signal.

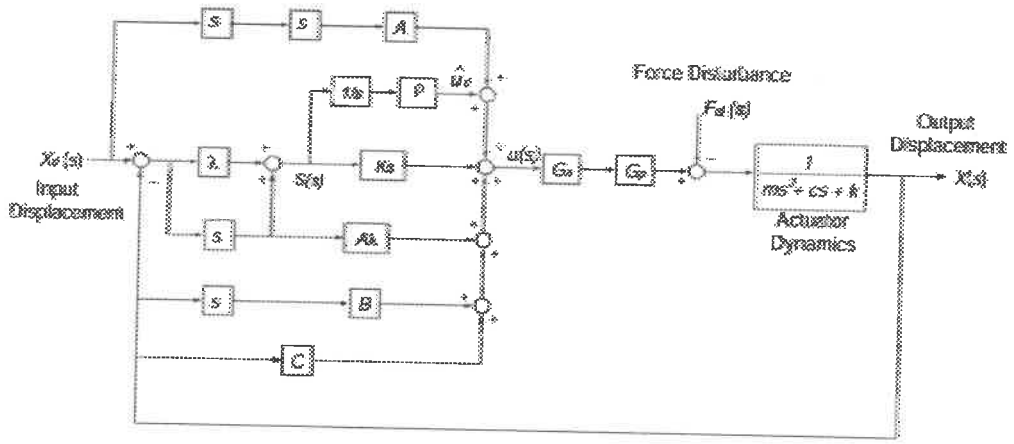

Fig. 2: Block diagram of the sliding mode controller

Hard turning trials were performed for two workpiece materials; AISI 4340 steel with 35-40 HRC hardness, and AISI 4320 steel with hardness 58-62 HRC. The inserts used were 35 degree V-type with 0.4 mm nose radius. For AISI 4340 steel, a PVD coated carbide tool was used, and for the high hardness steel a CBN tool with 0.1mm x 25° chamfer was used. The tool holder (MVJNL16) had –9° back rake, -5° side rake, and 3° approach angle. The tool position for the semi-finish pass was set by the x-axis feed drive of the CNC with the actuator controlled to a reference position. At the end of the semi-finish cut the CNC radial (x) position remains fixed, the actuator is retracted 10 microns to clear the workpiece, and the CNC z-axis drive returns the tool to the start of the cut. For the finishing pass the depth of cut is set solely by the actuator. For precision shaft machining of local areas such as bearing surfaces the finishing depth of cut is determined by comparing the part diameter after the semi-finish pass to the design value.

The tool position and the radial cutting forces during machining of the 4340 steel is presented in Fig.3 for both the open loop and controlled cases. The cutting speed was 125 m/min, the feed rate was 0.05 mm/rev, and the depth of cut was 5 microns over a length of cut of 10 mm. Clearly the static deflection due to an average cutting force of 6 N as well as the piezo stack nonlinearities are compensated for when the controller is active. Positioning resolution of 20 nm has been achieved during machining with feedback sensor uncertainty of 10 nm. The average and maximum roughness values were obtained from the filtered roughness profile (Gaussian filter with 50 percent amplitude transmittance at a cutoff value of 0.8 mm) over a sampling length of 8 mm. The maximum and average roughness for the 4340 steel is less than 2.0 microns and 0.3 microns, respectively. For the hardened 4320 steel the maximum and average roughness values are decreased to less than 0.85 and 0.15 microns, respectively. The frequency response function for position tracking as well as a sensitivity function of the actuator system is given in Fig.4. The experimentally obtained bandwidth is 200 Hz for position tracking.

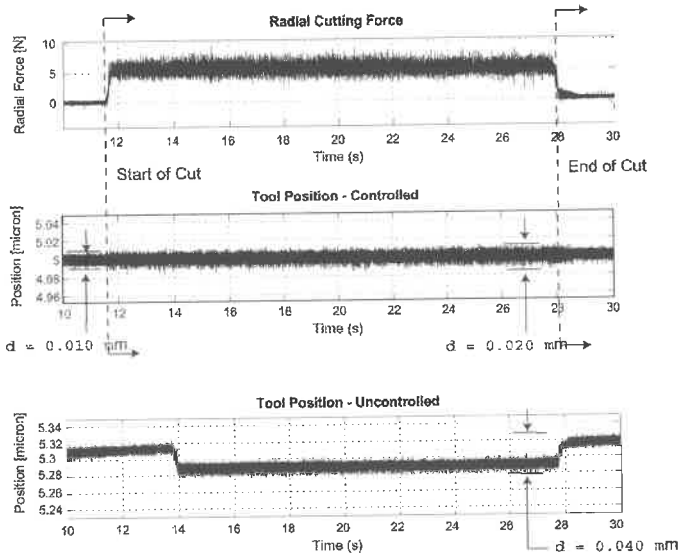

Fig.3. Tool position during finish machining at 5 micron depth of cut

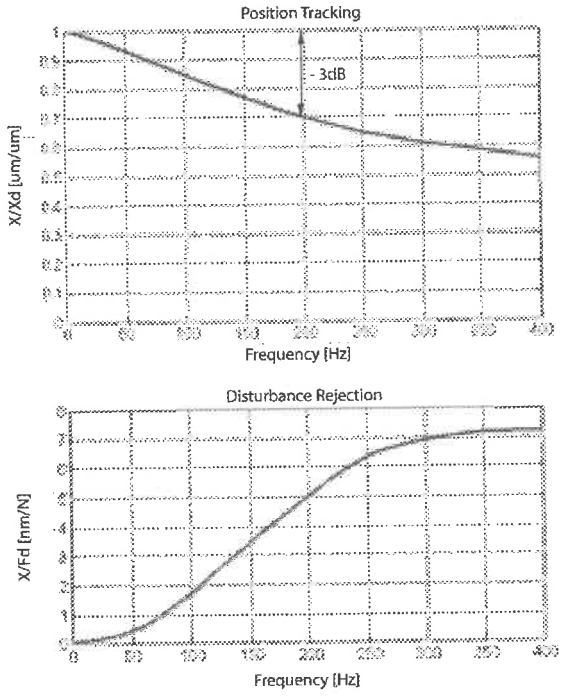

Fig.4: System frequency response function and sensitivity function

References

[1] Patterson, S. R., Magrab, E. B., Design and Testing of a Fast Tool Servo for Diamond Turning, Precision Engineering, 1985, Vol.7, No.3, pp.123-128.

[2] Okazaki, Y., A micro-positioning tool post using a piezoelectric actuator for diamond turning machines, Precision Engineering, 1990, Vol.12, No.3, pp.151-156.

[3] Shamoto, E, Moriwaki, T., Development of a "walking drive" ultraprecision positioner, Precision Engineering, 1997, Vol.20, No.2, pp.85-92.

[4] Shamoto, E., Moriwaki, T, Ultraprecision diamond cutting of hardened steel by applying elliptical vibration cutting, Annals of the CIRP, 1999,Vol.48, No.1, pp.441-444.

[5] Ludwick, S. J., Chargin, D. A., Calzaretta, J. A., Trumper, D. L., Design of a rotary fast tool servo for ophthalmic lens fabrication, Precision Engineering, 1999, Vol.23, pp.253-259.

[6] Schellekens, P., Rosielle, N., Vermeulen, J., Vermeulen, M., Wetzels, S., Pril, W., Design for precision: current status and trends, Annals of the CIRP, 1998, Vol.47, No.2, pp.557-586.

[7] Paros, J.M., Weisbord, L., How to design a flexure hinge, Machine Design, 1965, Vol.37, pp.151-157.

[8] Yang, R., Jouaneh, M., Design and analysis of a low profile micro-positioning stage, Precision Machining: Technology and Machine Development and Improvement, ASME PED, 1992, Vol.58, pp.131-142.

[9] Xu, G., Qu, L., Some analytical problems of high performance flexure hinge and micro-motion stage design, Proceedings of the IEEE International Conference on Industrial Technology, 1996.

[10] Zhu, W.-H., Jun, M.B., Altintas, Y., A fast tool servo design for precision turning of shafts on conventional CNC lathes, International J. of Machine Tools and Manufacture, 2001, Vol.41, pp.953-965.

[11] Kim, J.-D., Kim, D.-S., Waviness compensation of precision machining by piezo-electric micro cutting device, International J. of Machine Tools and Manufacture, 1998, Vol.38, pp.1305-1322.

[12] Kim, J.-D., Nam, S.-R., Development of a micro-depth control system for an ultra-precision lathe using a piezoelectric actuator , Int. J. of Machine Tools and Manufacture, 1997, Vo.37, No.4, pp.495-509.

EVALUATION OF ONE- AND TWO-SIDED GEOMETRIC FITTING ALGORITHMS IN INDUSTRIAL SOFTWARE

Dr. Craig Shakarji
National Institute of Standards and Technology
Gaithersburg, MD 20899-8260

Recent work in testing and comparing maximum-inscribed, minimum-circumscribed, and minimum-zone (Chebyshev) fitting algorithms indicates that serious problems can exist in present commercial software packages.

1. Introduction

The historical motivation for this work came as a result of the 1988 GIDEP alert [1] which warned of possible significant measurement uncertainty arising from least-squares fitting software embedded in coordinate measuring machines (CMMs). The National Institute of Standards and Technology (NIST) responded with the Algorithm Testing and Evaluation Program for Coordinate Measuring Systems (ATEP-CMS). This NIST special test service helps quantify the uncertainty of measurement due to least-squares fitting software for lines, planes, circles, spheres, cylinders, cones, and tori. The ATEP-CMS relies on internal least-squares reference fitting algorithms developed for all these geometries [2]. The test service proved successful, as it has revealed weak points in several least-squares fitting packages, which have been subsequently revised.

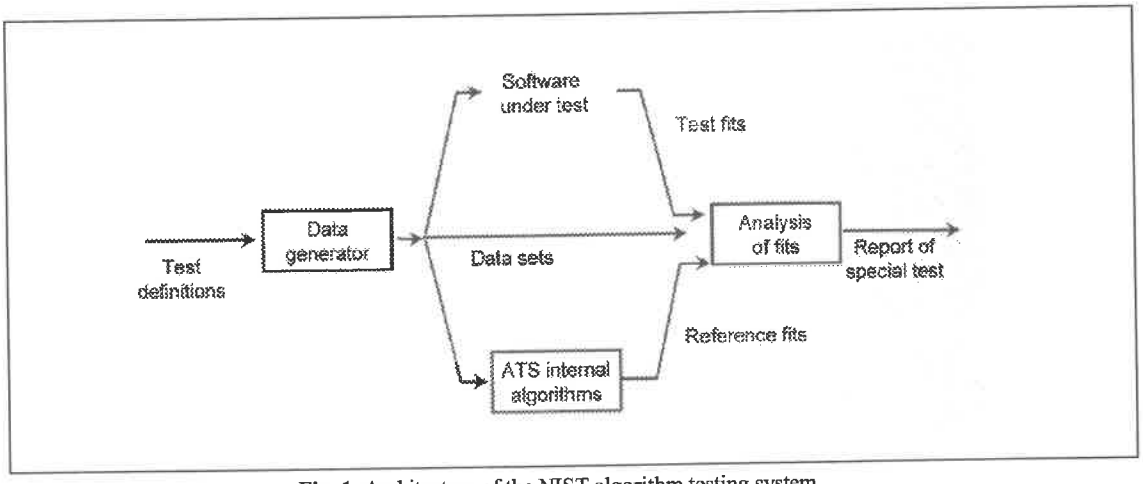

Fig. 1. Architecture of the NIST algorithm testing system.

As helpful as that work has been, the scope of the alert and the initial ATEP-CMS response was limited to least-squares fitting algorithms. Efforts have now been made to address software that performs feature fitting according to objectives that more closely mirror some of the language of geometric dimensioning and tolerancing —namely, fitting using a minimum-zone or (when applicable) a maximum-inscribed or minimum-circumscribed criterion.

2. New Reference Algorithms

NIST recently developed reference algorithms for these cases (Fig. 2). The reference algorithms were developed with emphasis on the criterion of generating a correct result; matters of speed, for example, were considered secondary. When results were compared with all these features and with some industrial vendor software, the results for the industrial non-least-squares cases were alarming. In several cases the reported fits erred to an unacceptably large degree. In some cases the reported maximum-inscribed fit was not even close to being an inscribed feature.

The choice of an optimization algorithm for a fitting problem depends on the nature of the problem. For instance, while the Levenburg-Marquardt method (or other "downhill only" approaches) was found to be suitable for a least-squares objective [2], it would be unacceptable for these new fits. This is primarily because these new objective functions often have their absolute minima hidden among several nearby local minima, causing a downhill-only approach to generally miss finding the true solution. For this reason the use of a seemingly straightforward minimization algorithm would be a naïve and unsatisfactory solution. Additionally, the minimization algorithm must be able to work with non-differentiable objective functions, which is often the case with these fits.

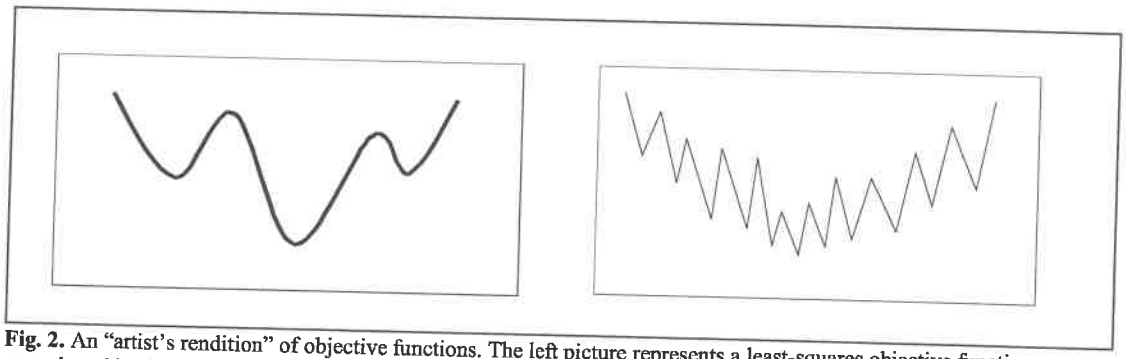

Fig. 2. An "artist's rendition" of objective functions. The left picture represents a least-squares objective function—smooth and having its global minimum away from other local minima. The picture on the right represents the objective function for fits in this paper where the function is non-differentiable and has its global minimum hidden among several nearby local minima. The actual objective functions are in several dimensions.

The minimization algorithm chosen is based on simulated annealing—a method known for finding a global minimum in the presence of local minima. We implemented a version of the algorithm that requires only function values and not any derivative information. The implementation was put through a battery of tests giving us confidence that it works extremely well. Additionally, in our comparisons with industrial software, when there are discrepancies the better fit can be easily determined based on a simple comparison of objective functions. For instance, if the problem is finding the maximum-inscribed circle, differing solutions can be compared by first ensuring the reported solutions are both inscribed circles and if they are, then the better solution is the one of larger radius.

	Lines	Planes	Circles	Spheres	Cylinders	Cones
Minimum-zone	x	x	x	x	x	x
Minimum-circumscribed			x	x	x	
Maximum-inscribed			x	x	x	

Fig. 3. New reference algorithms. An "x" indicates NIST has developed a reference algorithm for the indicated fit objective. Least-squares reference algorithms for ATEP-CMS already exist for all these geometries.

3. Industrial Intercomparison and Results

Our comparison with industrial software involves only two packages. It is acknowledged that a greater number of packages, say five, would be preferable. However, although resources of time limited the number, it is evident that even these are of substantial importance. As the results show, there are alarming problems in both packages. If five comparisons were performed and the additional three all agreed completely, there would still be sufficient cause for concern regarding industrial software. Hence, even this limited endeavor is enough to warrant a concern in these areas of fitting algorithms.

Each test data set was constructed using less than 200 points and simulated measurement and form errors were introduced totaling between 0.1% and 1.0% of the size of its nominal feature. Ten test data sets were used for each geometry in most cases.

Categories for the results are broken down as "acceptable" when the reported solution deviates from the reference by less than 10% of the size of the errors introduced into the part, "bad" when the deviation is between 10% and 50%, and "failure" (marked with an 'x') when deviation was greater than 50% or when the algorithm did not produce a result.

Maximum-Inscribed Fit Results

		Industrial Software A	Industrial Software B
Circles	Good	●●●●●●●●●●	●●●●●●●●●
	Poor		●
	Failure		
Spheres	Good	●●●●●●	
	Poor		
	Failure	x	xxxxxxxx
Cylinders	Good	●●●	●●●●●●●●●
	Poor	●	●
	Failure	xxxxx	

Table 1. Summary of fit results for the maximum-inscribed case

Minimum-Circumscribed Fit Results

		Industrial Software A	Industrial Software B
Circles	Good	●●●●●●●●●●	●●●●●●●●●●
	Poor		
	Failure		
Spheres	Good	●●●●●●	●
	Poor		
	Failure	x	xxxxxxxxx
Cylinders	Good	●●●	●●●●●●●●●●
	Poor	●	
	Failure	xxxxx	

Table 2. Summary of fit results for the minimum-circumscribed case

Minimum-Zone Fit Results

		Industrial Software A	Industrial Software B
Lines	Good	●●●●●●●	●●●●●
	Poor	●	
	Failure	xx	xxxxx
Planes	Good	●●●●●●●●●●	●●●●●●●●●
	Poor		
	Failure		x
Circles	Good	●●●●●●●●●●	●●●●●●●●●●
	Poor		
	Failure		
Spheres	Good	●●●●●●●●●	●●●●●●●●●
	Poor		
	Failure		
Cylinders	Good	●●●●●●●●●	(data not available)
	Poor	●	
	Failure		
Cones	Good		
	Poor	●●	
	Failure	xxxxxxxx	

Table 3. Summary of fit results for the minimum-zone case

4. Conclusions

The tables show alarming results. It is the opinion of the author that there is no reason why every block should show only good results. As a result of these findings, the ATEP-CMS service at NIST has planned a priority item to create a collection of reference pairs for industry—reference pairs being test data sets along with their correct fits according to the fit objectives studied here. These will be available for download from the Internet for industrial use.

5. References

[1] Walker, R., *CMM Form Tolerance Algorithm Testing*, GIDEP Alert X1-A-88-01, Government-Industry Data Exchange Program, DOD, Washington, D.C., 1988.

[2] C. M. Shakarji, *Least-Squares Fitting Algorithms of the NIST Algorithm Testing System*, J. Res. Natl. Inst. Stand. Technol. **103** (6), 633-641 (1998).

Influences on the Polishing Process of Optical Glasses Using Synchrospeed-Kinematics

Fritz Klocke, Olaf Dambon
Fraunhofer-Institute for Production Technology, Aachen, Germany

Background

The polishing of optical components results in a complex system consisting of the polishing pad, the suspension and the work piece material. Minor changes to one of these components can cause major irregularities in the polishing results. This complexity, meaning the interaction between the system components, has still not been fully understood to the present day. A comprehensive quantitative model describing the abrasion mechanisms does not exist.

In the past numerous efforts have been made to increase the transparency and thereby the predictability of the polishing process. The **hypothesis of abrasion** is based on purely mechanical processing which generates abrasion by inducing fine cracks. This hypothesis can at best be significant in the first phase of polishing when the peaks of surface roughness left by pre-machining operations are removed. The **flow hypothesis** finds the basic mechanism in a ductile displacement of material made possible by local softening of the surface due to frictional heat. The **chemical hypothesis** is based on the theory, that within the subsurface of the glass a gel layer is developed. This film created by an incorporation of water is thereupon removed. The **friction-wear hypothesis** finds its motivation in the mechanical stressing of the polishing grains, which uncovers faults in the crystal structure. The faults' reactivity cause a joining of the glass material and the polishing grain.

All of these hypotheses have something in common which is that they do not offer a quantifiable model of abrasion and also that the influence of the glass type is not taken into consideration. There are though combined hypotheses which have been developed in recent years, which focus particularly on the effects on the surfaces between glass and the polishing grain. Izumitani [IZU79] chose 18 different borate- and silicate glasses and put them into a 0.01 molar solution of HNO_3. Afterwards these controlled corroded glasses showed a correlation between the polishing rate and the Vickers hardness determined after the corrosion (Fig. 1). This hypothesis can therefore be seen as a combination between the abrasion- and the chemical hypothesis.

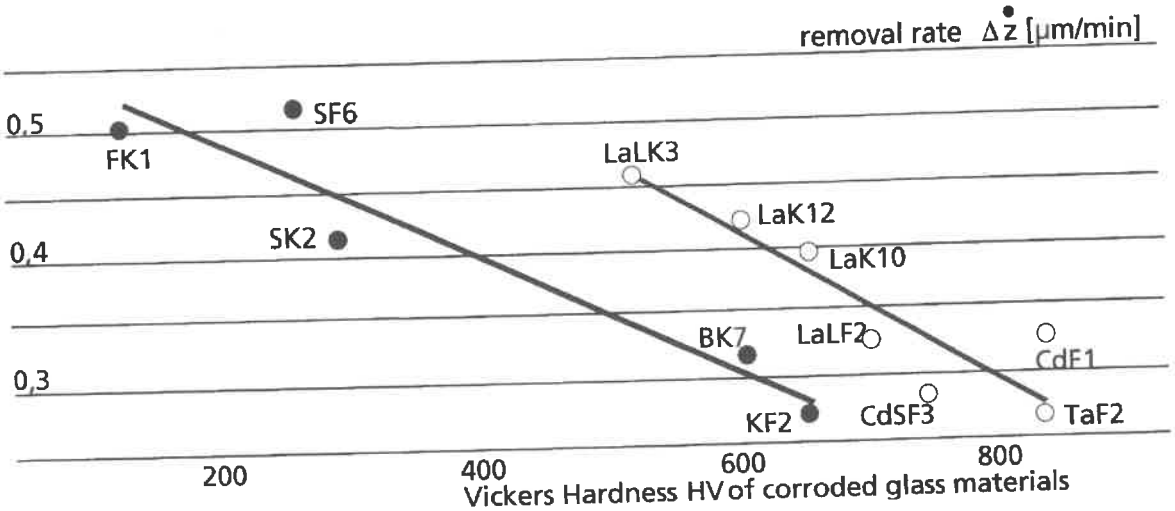

Fig. 1: Influence of corroded samples [IZU79]

However this hypothesis considers neither the polishing suspension nor the influence of the polishing pad. In addition, it should be mentioned that the theories presented here are based on experiments conducted with pitch as a carrier of the polishing agent. This particular polishing pad results in an abrasion one order of magnitude smaller than what would be expected with a common polyurethane foam. There has been to date no success in achieving the development of a comprehensive approach for the description of the complex tribochemical process occurring within the polishing gap.

The Polishing Characteristics of Different Glass Types

The experiments on polishing characteristics of different optical glasses have been carried out on a polishing machine called SPS 120 by LOH OPTIKMASCHINEN AG. This type of polishing machine is suitable for the polishing of spherical lenses in a diameter range from 20 to 120 mm. The concept is based on the synchrospeed theory. Using this method of polishing, it is almost possible to reach a constant relative velocity between tool and workpiece on spherical lenses with small aperture angles; which according to the Preston-hypothesis leads to constant rate of abrasion [PRE27]. As polishing pads, polyurethane foams are used because their mechanical stability allows higher pressures and rotation speeds compared to pitch.

During the experiments different glass types were observed. Cerium oxide with deionized water (DI-water) was used as polishing agent. In advance of each series, a new suspension was mixed. The polishing time was varied, single workpieces were polished for 2, 3, 5, 10 and 20 minutes. Afterwards, the series was repeated with new suspension (Fig. 2).

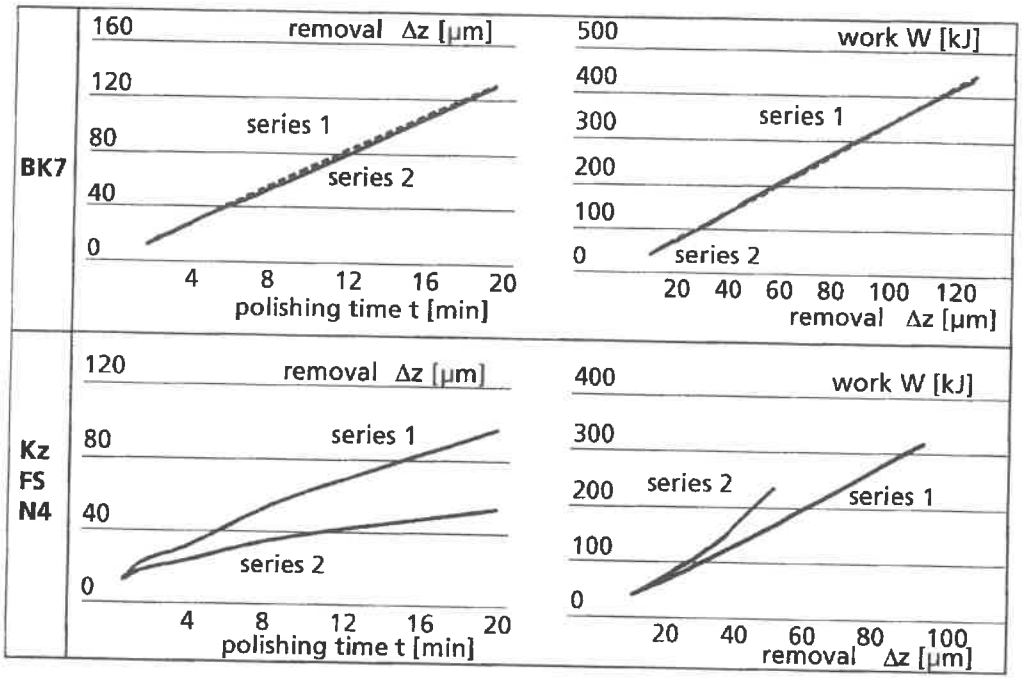

Fig. 2: Polishing characteristics of different glass types

What draws attention is, that while polishing certain glasses, e.g. BK7, there is a linear relation between the polishing time and material removal, even after the second series. However, when polishing KzFSN4 the removal rate evidently decreases during the second series. Obviously, a reaction between the glass surface and the polishing medium occurs. However when the polishing pad is dressed once again, this results in roughening the surface of the pad and the pores are thereby opened, the condition of series 1 is reached after a third series.

While performing the polishing series, it is noticeable that there is a correlation between the energy input and the material removal. However if wear to the polishing pad occurs, as observed when polishing KzFSN4, the amount of energy put in is reduced. Since the curve characteristic is a measure of how much energy is needed to generate material removal (»activation energy«), one can conclude that the activation energy rises with an increasing wear of the polishing pad.

This wear of the polishing pad is obviously related to the type of glass. The interesting question therefore is, which characteristics of the glass leads to the different polishing characteristics.

Pad Wear

The ideal situation is that during the polishing a stable liquid film builds up between the polishing pad and the workpiece. Pad and glass are therefore either divided by the fluid or by polishing grains. These conditions prevent abrasive wear to the pad. However if the film is torn open the soft pad gets in contact with the hard glass material and pad wear occurs. The wear to the polishing pad is thus directly related to the interaction between the polishing fluid and the glass material.

The polishing fluid is DI-water. Water is bound to the surface by physisorption. Consequently, the power of the adhesion between water and the surface is characterized by the polar fraction of surface of the individual glasses. This means that also the wear of the pad is influenced by the polar fraction of surface of the individual glasses when polishing optical glasses.

During the experiments it was identified that the interaction between glass and polishing fluid increases with a rising fraction of polar surface energy. This immediately leads to a stabilization of the liquid film and thus to a reduction of wear.

The resulting question is therefore which measures have to be taken in order to optimize the polishing of »critical« glasses such as KzFSN4? For that purpose the previously mentioned model for the description of the wear of the pad is used.

The wear can only occur once the pad gets in contact with the glass. Polishing grains between pad and glass prevent this contact. An increase of the concentration of the polishing agent therefore reduces the tendency of the pad to wear out (Fig. 3).

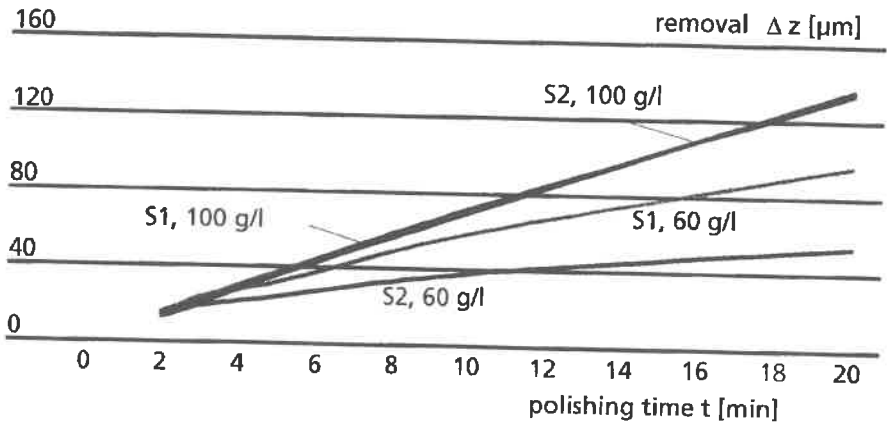

Fig. 3: Technological means to reduce wear (glass type: KzFSN4)

In this example, the concentration was increased from 60 g/l to 100 g/l during the polishing of KzFSN4. Throughout the following polishing, the same characteristics as in the first series could be observed. Wear to the pad does obviously not occur [HAB01].

Literature

[IZU79] Izumitani, T.: Treatise on Material Science and Technology. Academic Press. New York, 1979, pp. 115

[PRE27] Preston, F. W.: The Theory and Design of Plate Glass Polishing Machines. Journal of the Soc. of Glass Technology, Vol. 11, (1927)

[HAB01] Hambücker, S.: Technologie der Politur sphärischer Optiken mit Hilfe der Synchrospeed-Kinematik. Dissert. an der RWTH Aachen (2001)

BURNISHING OF HARDENED STEEL COMPONENTS - AN ALTERNATIVE METHOD OF FINISHING

Liviu Luca, Sorin Neagu-Ventzel, Ioan Marinescu
The University of Toledo
2801 W. Bancroft, MIME Dept., Nietschke Hall, Toledo, OH 43606

1. INTRODUCTION

The principle of the burnishing process, shown in Figure 1, is based on the rolling movement of a tool (a ball or a roller) against the workpiece's surface, a normal force being applied at the tool. As soon as the yield point of the workpiece's material is exceeded, plastic flow of the original asperities takes place. This phenomenon leads to a smoother surface. At the same time, compressive stresses are induced in the surface layer, followed by strain hardening and a series of beneficial effect on mechanical properties. Burnishing can improve both the surface strength and roughness. The increase of surface strength mainly serves to improve fatigue resistance under dynamic loads.

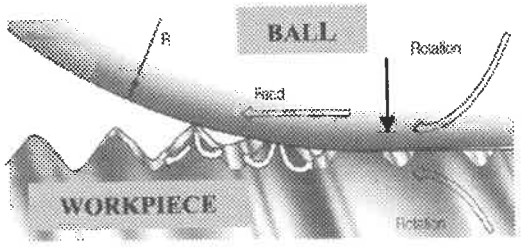

Fig. 1. Principle of burnishing [5]

Burnishing of hardened steel is applied to materials over 45 HRC, and is usually employed as a subsequent operation after hard turning. Surface roughness commonly ensured in burnishing is in the range from 0.2 to 0.8 μm. Economic studies prove that burnishing obtains surface quality corresponding to grinding, for costs corresponding to turning [2,3].

2. TOOL

The experimental equipment includes: CNC lathe, hydrostatic burnishing tool, hydraulic pressure unit, other accessories. The principle of the hydrostatic tool is shown in Figure 2. The basic piece of it is a 6-mm ceramic ball, behind which a hydrostatic pressure is applied, generating the normal force. The hydrostatic principle of this tool ensures the a series of significant advantages: the hard ceramic ball can burnish hardened steel, the normal force is constant and easily controllable through the pressure, the fluid in the system is the coolant itself, free rotation of the ball in any direction, low coolant consumption. The tool can be clamped on the CNC turret, so that burnishing is carried out in the same clamping of the part with hard turning. Minor adaptations at the machine were done. The maximum pressure delivered is 40 MPa.

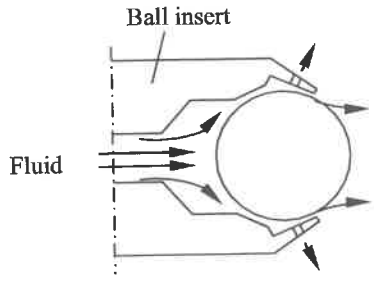

Fig. 2. Hydrostatic ball burnishing head

3. EXPERIMENTS

Parts to be involved in experiments were cylindrical shaped, 33-mm diameter, made of steel, carburized and case hardened at 610-64 HRC. In order to ensure the dimensional accuracy, they were previously hard turned.

For estimating the significant factors of influence and their trends in the process, a screening experiment was planned. The output parameter taken into consideration was the mean roughness *Ra*. Hydraulic pressure *p*, burnishing feed *fb* and speed *s* were the burnishing parameters. Since original asperities are known to play an important role in burnishing result, hard turning parameters, like feed *ft* and nose radius *R* were also chosen. In conclusion, the experiment was factorial 2^5, with one replica, due to limited number of components available.

The standardized effect for the aforementioned factors is shown in Figure 3. It is obvious that speed and its interactions have insignificant influence. At the same time, the parameters influencing initial roughness (*ft* and *R*) show the highest significance. The level of confidence for this analysis was 95%.

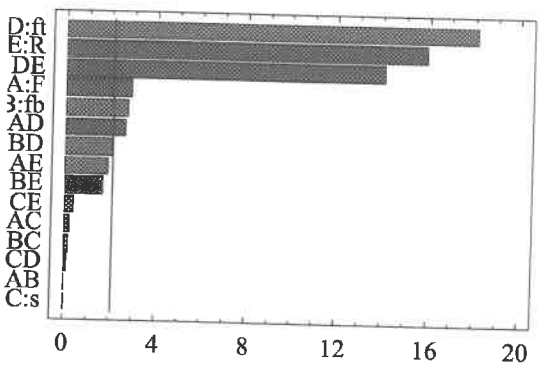

Fig. 3. Significance of parameters

Observations from this experiment led to the following premises for the next experiments: burnishing speed will be excluded from the next tests; hydraulic pressure will be kept constant at its maximum level (40 MPa). Finally, practically, only the hard turning feed *ft* and burnishing feed *ft* will be involved.

Next, factorial 3^2 experiments were designed, considering three nose radii for hard turning: 0.2, 0.4 and 0.8 mm. The regression equations for the three cases have the forms:

- For R=0.2: $Ra=1.220+19.480 \cdot ft+1.332 \cdot fb$ (1)
- For R=0.4: $Ra=0.337-.381 \cdot ft+13.148 \cdot ft^2+0.8 \cdot fb+2.272 \cdot ft \cdot fb$ (2)
- For R=0.8: $ln\ Ra=-1.892+8.733 \cdot ft-3.960 \cdot ft^2+1.091 \cdot fb-3.477 \cdot ft \cdot fb$ (3)

Figures 4, 5 and 6 show the surfaces for the aforementioned equations.

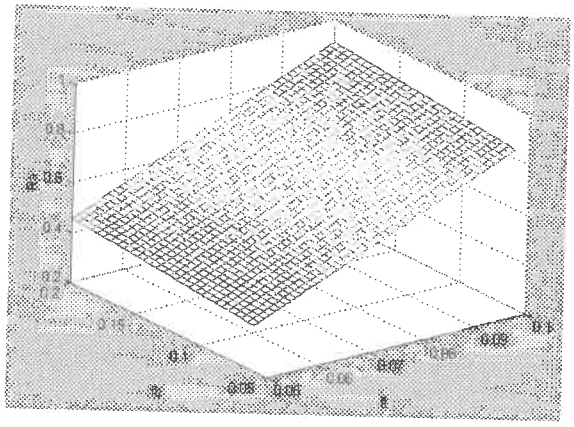
Fig. 4. Response surface for R=0.2

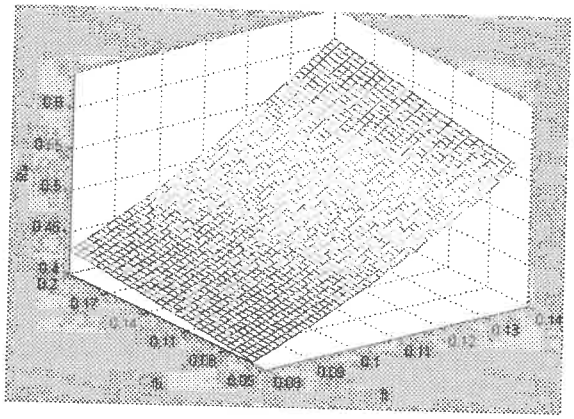
Fig. 5. Response surface for R=0.4

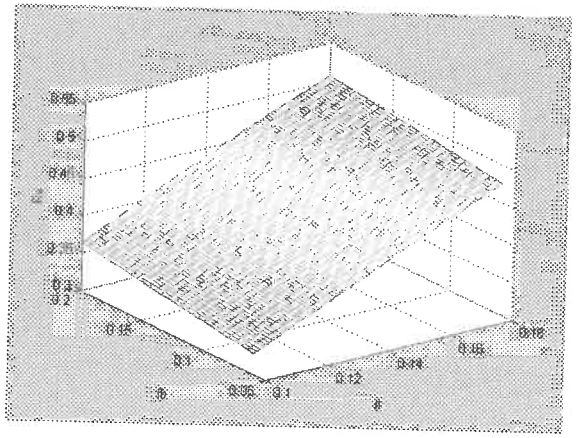
Fig.6. Response surface for R=0.8

It can be noticed that the best finish is obtained for combinations involving the lowest hard turning feed. Figure 7 shows the influence of *fb* on roughness *Ra*, for different original roughnesses (determined by *ft*), and different nose radii. The trend is an increase of roughness with feed for all nose radii employed.

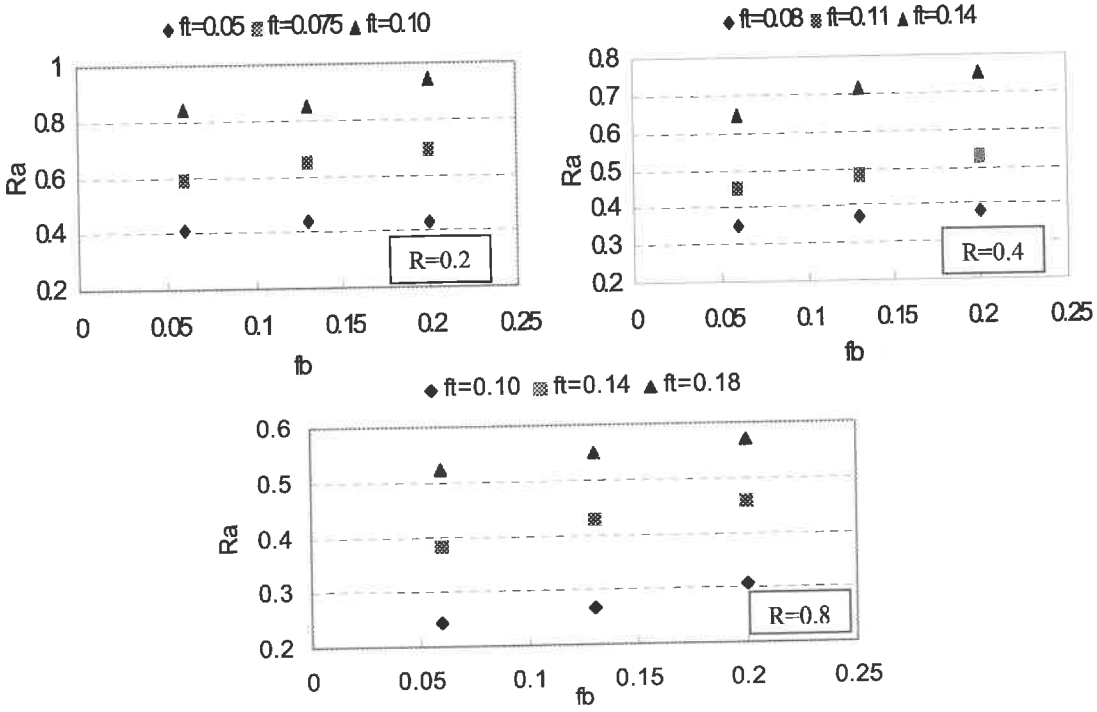

Fig. 7. Roughness vs. burnishing feed for different nose radii

Variation of the bearing length ratio (t_p)is shown in Figure 8. To note the faster evolution of bearing ratio length to 100% for burnished surfaces than for hard turned. Fig. 9 shows the typical profile aspect before and after burnishing. To note the change of the peak-type profile after hard turning into a more balanced one, with rounded asperities. Reduction of roughness is very clear.

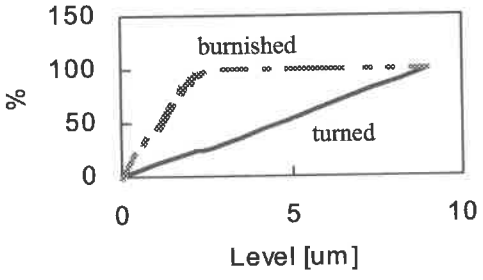

Fig. 8. Bearing length ratio evolution

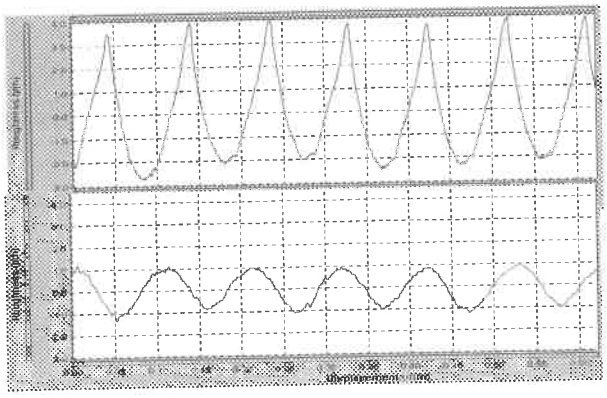

Fig. 9. Change of profile

4. 3D SIMULATION

The goal of the simulation was to create a consistent model of ball-burnishing with initial asperities. The ball was modeled as a rigid surface. Although the ceramic ball has a Young's modulus considerably larger than steel, it will deform. This deformation will introduce errors in the results of the simulation. Therefore, modification of the ball's radius becomes necessary [1]. The simulation will have two phases:

1. Determination of the radius of the deformed ball for the nominal normal force, plus indentation of the workpiece and comparison between the simulation and the real experiment.
2. Burnishing of three grooves. The distance between the grooves was equal to the feed, and the surface geometry was modeled with initial asperities from the previous operation (hard turning, nose radius 0.2 mm). A comparison between residual stresses at peak and valley areas was performed. The computed radius R_i was 5.139 mm, according to Fischer-Cripps formulae [1]. The next stages will employ this new radius. Initial conditions were taken from a real burnishing experiment.

The deviation between the new model and the experimental indentation (see Figure 10) isd characterized by two parameters: the depth of the indented hole (+6.6% for the new model), and the half-width of the indented hole (-11.11% for the new model).

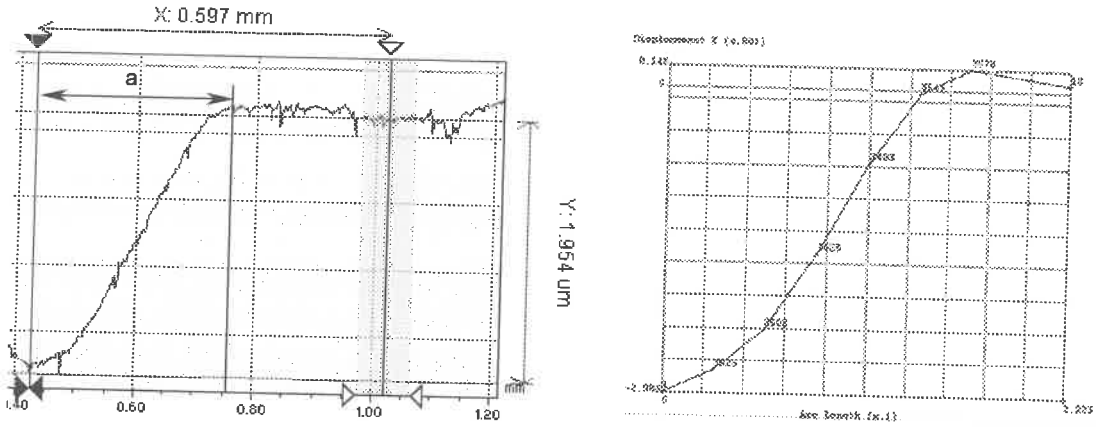

Fig. 10. Real indentation vs. modeled indentation

For the 3-path simulation, tetrahedral-type elements were preferred, because of a better adaptation of the meshing. Symmetry boundary conditions were applied only on one face of the part. Since computational requirements for the simulation of a 3-path burnishing are significantly higher, only a small portion of the workpiece was considered. In this case, a half-ball geometry was modeled, as a rigid surface with the new radius, computed in the previous stage. Two initial asperities were foreseen in the geometry of the workpiece. These asperities correspond to a previous hard turning operation with a feed of 0.2 mm/rev.

The simulation cycle consists of the following stages: pressing the ball against the workpiece until the nominal normal force is reached, rolling of the ball onto the workpiece with a certain angle, releasing, retiring in the initial position of the two bodies, moving the ball in the direction of the feed with a burnishing feed distance. This cycle is repeated two times. The final displacement map is presented in Figure 11. It can be seen that the displacements follow the rule stated in the literature: peaks are pressed down and valleys rise up to a certain level. The residual stresses in a middle cross section of the rolled path, after the third pass, are presented in Figures 12. High values of the residual compressive stresses, around 800 Mpa, were obtained. These stresses move together with the rolled path. On the old path, stresses decrease to about 100-200 MPa.

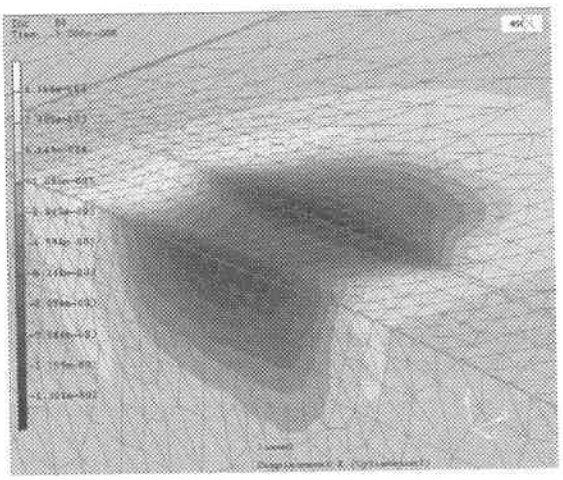

Fig. 11. Displacement map for 3-path simulation

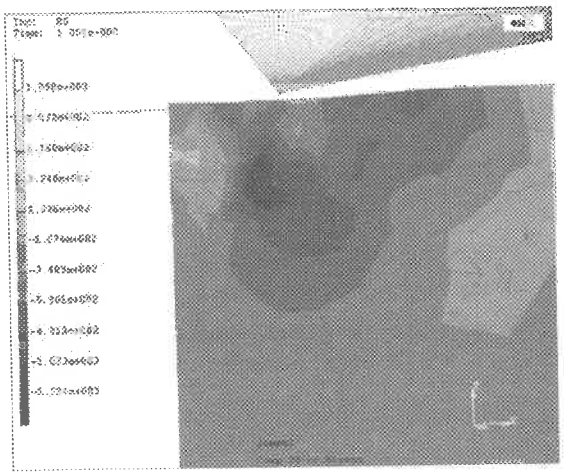

Fig. 12. Stress map for 3-path simulation

5. CONCLUSIONS

1. The possibility of burnishing steel components with high hardness, around 64 HRC, was proven.
2. The hydrostatic principle of the ball-burnishing tool employed offers a series advantages to the process: pure rolling contact, constant controllable normal force, low coolant consumption, use of the same machine as previous hard turning
3. The initial roughness from previous hard turning showed the most important influence on the burnishing final roughness.
4. When the burnishing feed increases, the roughness increases.
5. The bearing length ratio improves for burnished surfaces.
6. The unbalanced profile after hard turning changes into a rounded balanced profile after burnishing.
7. Roughness comparable to grinding could be obtained through burnishing.
8. Simulation tools offers the possibility to study displacements and residual stress formation in the surface layer.

REFERENCES

[1] Fischer-Cripps, A. "*Introduction to contact Mechanics*", Springer-Verlag Publishers, New York, 2000.

[2] Loh, N.H., Tam, S.C. *"Effects of ball burnishing parameters on surface finish – A literature survey and discussion"*, Precision Engineering 88, Vol. 10, No. 4, pp. 215-220.

[3] Murthy, R.L., Kotiveerachari, B. Burnishing of metallic surfaces – a review, Precision Engineering, Vol. 3, No. 3, 1981, 172-179

[4] Neagu-Ventzel, S. *"A Theoretical and Experimental Study of Single Roll Burnishing Process as Applied to Yokes"*, Ph.D. Thesis Dissertation, 2001, University of Toledo.

*** "*MARC/MENTAT Training Guide*", 1998.

[5] *** *"Tools for roller burnishing, deep rolling, forming"*, Prospectus, Ecoroll A.G. Werkzeugtechnik, 2000.

ELLIPTICAL VIBRATION ASSISTED DIAMOND TURNING

Thomas A. Dow, Nobuhiko Negishi and Alex Sohn
Precision Engineering Center, North Carolina State University, Raleigh, NC

1 INTRODUCTION

Diamond turning has become a mainstay of optical fabrication. However, it is limited to certain workpiece materials [1] due to tool wear. To address this issue, a new class of machining was born. This technique involved independent, cyclic displacement of the cutting tool with respect to the workpiece and was referred to as vibration cutting. In early experiments, the tool was moved in a straight line along the cutting path at ultrasonic frequencies. It took nearly two decades of research before the technology began to show practical value. In the early 90's, research into vibration cutting at both low and high frequency produced results sufficient for industrial applications [2]. This mature class of machining is called Vibration Assisted Machining (VAM). Moriwaki has shown that when the tool was moved in an elliptical path rather than a straight line, lower cutting forces and longer tool life were achieved [3,4]. However the evidence presented was anecdotal. There were no specific measurements of force during ultrasonic operation or tool wear details. The PEC has been working on this technology for several years and reported tool force and wear details using a low speed system in 2001 [5]. This paper describes a new design of the Ultramill with details of the tool path, chip shape, forces and surface finish.

2 APPARATUS

Mechanical Structure A photograph of the two Ultramill designs developed at the PEC are shown in Figure 1: the new high speed version is in the foreground at left and the original low-speed version [5] is shown in the background at right. The basis for each design is a pair of piezoelectric actuators that support the tool and allow it to move with small displacements at high speed. The original version uses a pair of long, thin cylindrical actuators whereas the new design uses a pair of larger cross-section triangular actuators (base 30mm, height 13 mm, depth 22 mm) shown in cutaway. This shape was optimized for stiffness using a finite element model. The original tool head was fabricated from steel and aluminum with a standard diamond tool attached with a screw. The new design uses a hollow alumina head and a diamond tool attached with high-temperature epoxy. The shape of the head was optimized to keep the center-of-gravity near the center line of the stacks and to minimize the mass moment of inertia. The first natural frequency of the new design is 5000 Hz as compared to 500 Hz for the original design. Unfortunately the constraints on the shape and material of the head made it difficult to fabricate and therefore expensive.

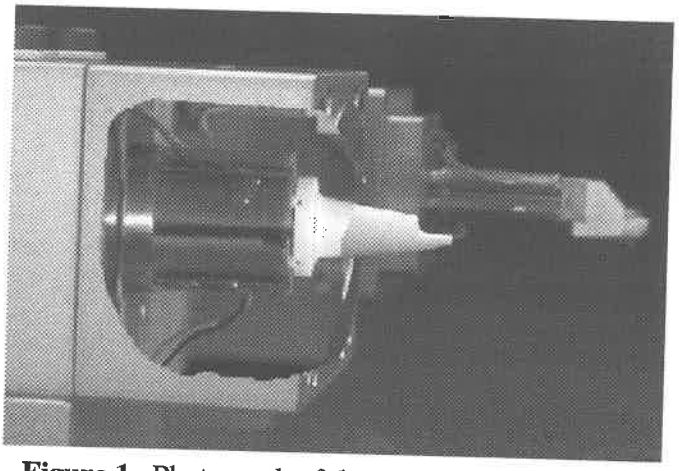

Figure 1. Photograph of the new high-speed design (left) and the original design (right)

The head rests on a pair of ceramic half-cylinders that allow the head to displace and pivot as required for the desired motion. A thin titanium flexure pushes the head onto the actuators and seals the actuator cavity for cooling. High-voltage signals (up to 1000 V_{p-p} at 10 KHz) in the shape of a sine wave and cosine wave drive the two actuators. This excitation produces an elliptical motion of the diamond tool with the minor axis (up to 7 μm) and the major axis (up to 33 μm) determined by the stroke and phase of the actuators and the geometry of the head.

Cooling System The large piezoelectric actuators used to drive the tool at high frequencies generate a significant amount of heat and an active cooling system is required for sustained operation. The system, shown in Figure 2, consists of a thermoelectric cooler and pump to circulate a dielectric fluid (3M Flourinert 3283) over the stacks at a flow rate of about 1 liter/min. The system uses the chiller to modulate the temperature of the inlet to the actuator cavity such that the outlet temperature (as measured by the resistance thermometer – RTD - in the return line) is kept constant. The chiller has a capacity to remove 400 watts, sufficient to operate the system constantly at full voltage.

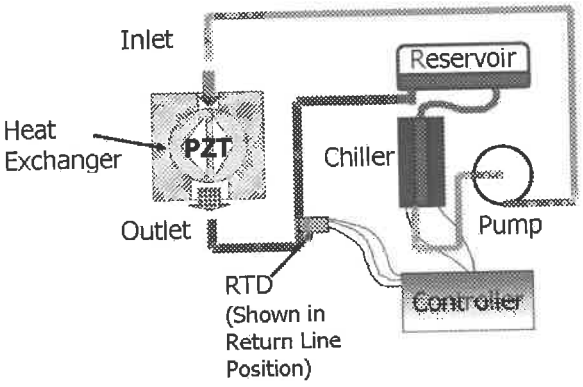

Figure 2. Active cooling system design for sustained high-speed operation of the actuator

3 TOOL MOTION

The desired tool motion for the Ultramill is generated in a different manner than other vibration assisted designs. In this case, the goal is to operate the system below its first natural frequency so that the motion can be changed in a controllable manner to study the details of the machining process. For elliptical cutting, the motion of the end of the tool is a combination of the elliptical motion from the actuator and the linear motion from the workpiece. Figure 3 shows the motion of the tool (exaggerated in the vertical direction for clarity) and defines the important parameters. Only two cycles of the tool are shown and the emphasis is on the second revolution (dotted line) which is the steady-state motion that removes material from the workpiece.

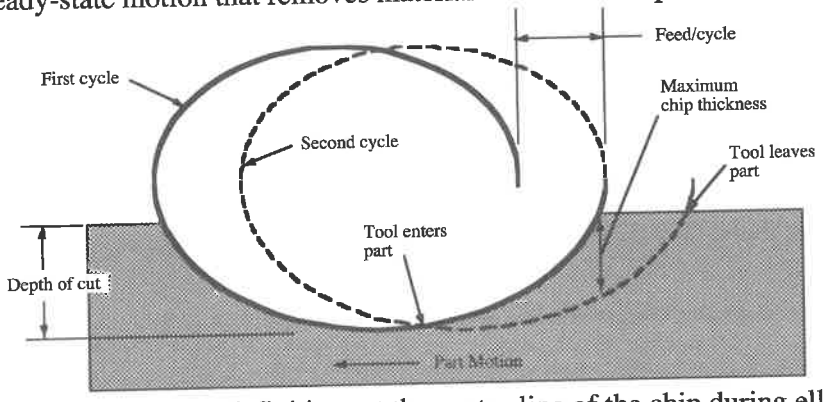

Figure 3. Tool motion and chip definitions at the center-line of the chip during elliptical cutting.

Chip Geometry Figure 3 also shows the chip geometry at the center of the cut as the tool moves through its elliptical path. The thickness of the chip is reduced as the tool frequency is increased or the part speed or depth of cut are reduced. SEM micrographs of non-overlapping groove cutting experiments in aluminum illustrate that chip geometry is directly related to cutting conditions. If the depth of cut is smaller than the minor axis of the tool motion, the chips are discontinuous (Figure 4), and if larger they are connected at the center (Figure 5). The discontinuous chips have a thickness related to the feed/cycle and are as wide as the cut. The continuous chips are longer because of the increased depth of cut but are discontinuous at each edge where the round nose tool leaves the flat workpiece. Notice that the chips appear transparent in the 1000x image of Figure 5, indicating a thickness less than 10 μm.

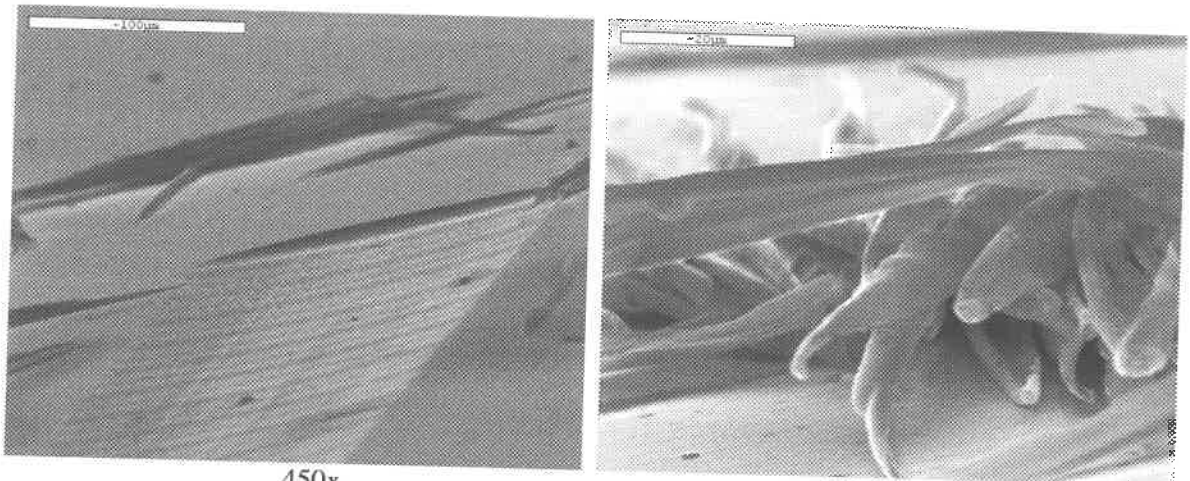

450x 1800x

Figure 4. SEM micrographs of discontinuous chip where depth of cut is 32% of the minor axis (depth = 1.4 μm and upfeed/cycle = 3.3, minor axis of elliptical motion =4.3 μm)

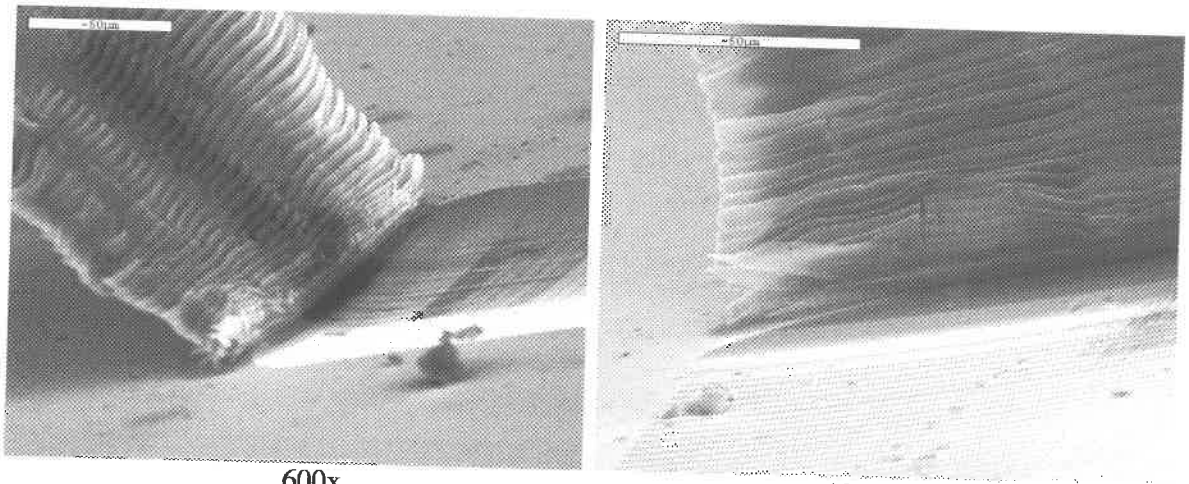

600x 1000x

Figure 5. SEM micrographs of continuous chip where the depth of cut is twice the minor axis (depth of cut = 8.9 μm and upfeed/cycle = 6.7 μm, minor axis of elliptical motion =4.3 μm)

4 TOOL FORCES

To measure the forces, a specimen was attached to a three-axis load cell mounted on the diamond turning machine. The oscillating tool was fed across the surface at a constant speed and depth of cut. The measured forces were acquired using a high-speed data acquisition system.

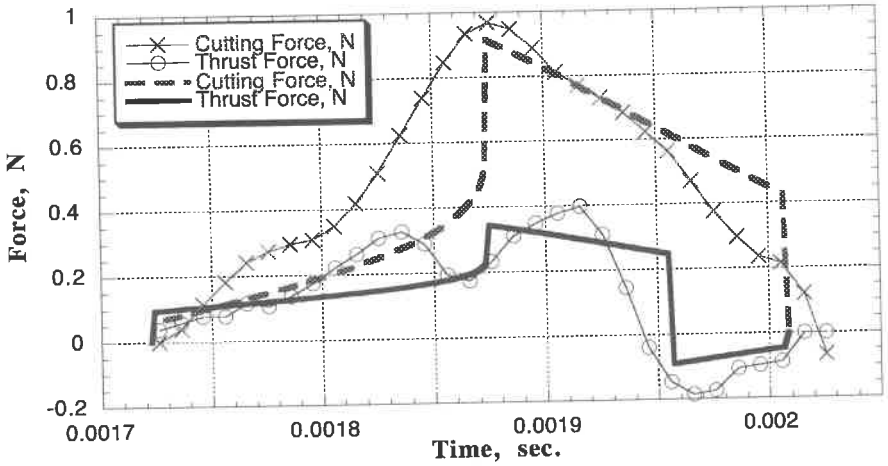

Figure 6. Theoretical and measured cutting and thrust forces during tool contact (material = 6061-T6 aluminum under same conditions as Figure 5)

The measured forces in the cutting and thrust directions as a function time are shown in Figure 6. The measurements are shown as a series of points connected by a line and the predicted forces are the solid and dotted lines. The workpiece was 6061 aluminum, the vibration frequency 1000 Hz, the depth of cut 8.9 μm and the upfeed/cycle 6.6 μm. Based on the geometry shown in Figure 3, the maximum chip thickness for this condition is 7.7 μm. For these cutting conditions, the maximum force in Figure 6 is about 1 N and the tool is in contact for 0.3 ms out of a cycle time of 1 ms (at 1000 Hz operation) or a duty cycle of 30%. The predicted values were in agreement within 0.1 N of the magnitude of the measurements. However, secondary vibrations due to the load cell dynamics are apparent, especially in the thrust direction with a 12 kHz frequency (the natural frequency of the load cell with specimen).

5 SURFACE FINISH

One of the advantages for vibration cutting is a reduction in the wear of diamond cutting tools as shown in [5]. However, the surface finish created must be of high quality for the technique to be accepted. To study the surface finish created using the Ultramill, PMMA test samples were cut at varying vibrational frequencies and amplitudes to thoroughly test the operation of the device. The example shown in Figure 7 illustrates the difference in the finish with and without the elliptical motion. Figure 7(a) shows the grooves created by the 1 mm nose radius tool with a feed rate of 12 μm/rev. The rms surface finish is 17 nm compared to the theoretical finish of 5 nm. When the 1 kHz elliptical vibration is added to the tool motion, the surface changes to Figure 7(b) where the cusps created by the Ultramill in the feed direction (left to right) are clearly visible and the rms finish increased by 40% to 24 nm as expected. There is, however, an additional vibration with a substantially lower frequency (60 Hz) that was evident on all of the samples. The DTM's slide vibration normal to the workpiece has a natural frequency of 60 Hz

and this frequency at an amplitude of 40-60 nm was recorded when the Ultramill and cooler were in operation. This vibration component is a significant contributor to the surface finish and will be addressed.

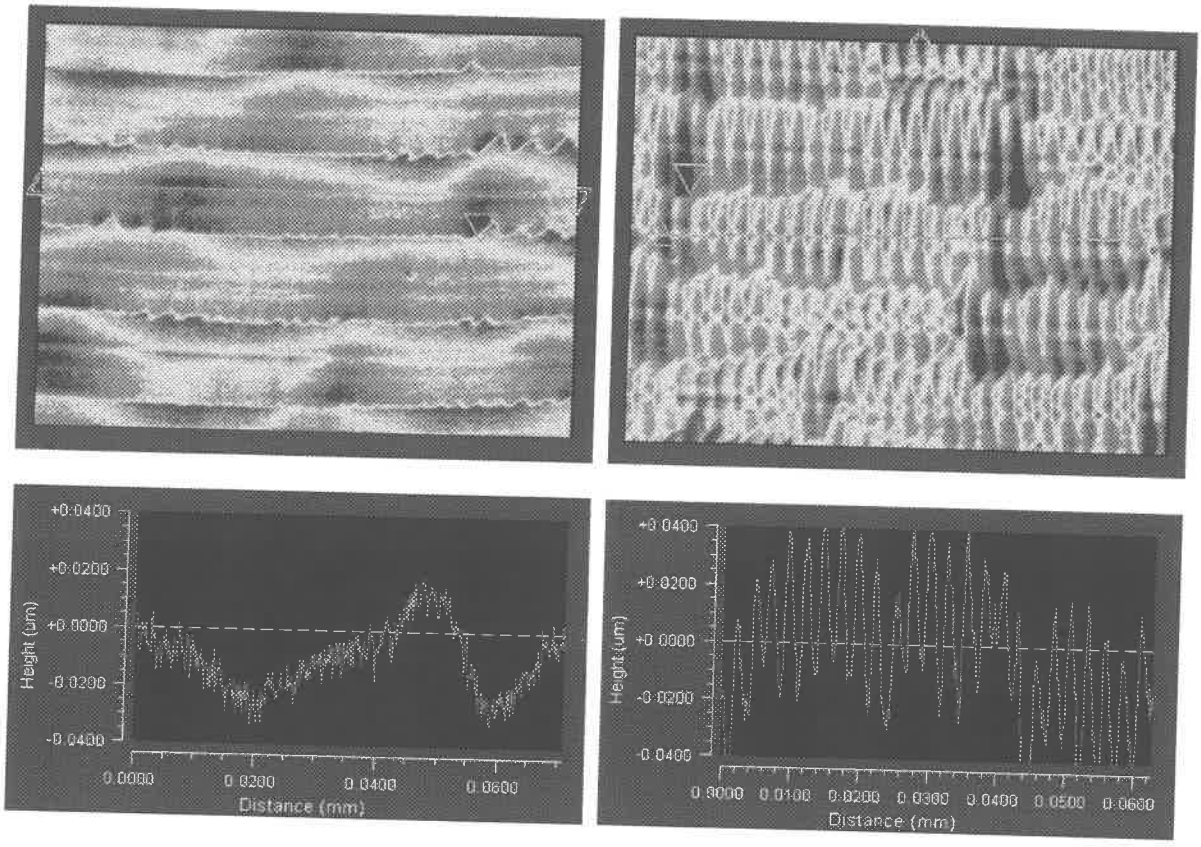

a) No elliptical excitation

b) Elliptical excitation at 1 KHz (feed/cycle = 2.6 μm)

Figure 7. Surface topography of PMMA surface cut with Ultramill (depth of cut = 6 μm, cross feed = 12 μm/rev, spindle speed = 20 rpm)

6 REFERENCES

1. Evans, C., Paul, E., Mangameli, A., McGlaufin, M., "Chemical Aspects of Tool Wear in Single Point Diamond Turning", Precision Engineering, Vol 18, 1996, pg 4-19.
2. Moriwaki, T., "Machinability of CBN Tools in Precision Engineering of Stainless Steel", Proc. 5th International Conf. on Mfg. Engineering, Wollongong, pg. 129-133, 1990.
3. Moriwaki, T. and Shamoto, E., "Ultra-precision Diamond Turnign of Stainless Steel by applying Ultrasonic Vibration", Annals of the CIRP, Vol. 40, Pg. 559-562, 1991.
4. Moriwaki, T and Shamoto, E., "Ultra-precision Diamond Cutting of hardened Steel by applying Elliptical Vibration Cutting", Annals of the CIRP, Vol. 48, Pg. 441-444, 1999.
5. Dow, Cerniway, Sohn and Negishi, "Vibration assisted diamond turning using elliptical tool motion", Proceedings 2001 ASPE Annual Meeting, Vol 25, 2001, pg 92-97.

High Precision Photomask Polishing with Magneto-Rheological Finishing (MRF)

Marc Tricard[1] and Don Golini
QED Technologies, Rochester, NY

Abstract

The December 2001 edition of the International Technology Roadmap for Semiconductors (ITRS) makes it abundantly clear that achieving the flatness requirements for "optical" lithography photomasks is becoming an increasing challenge. For Extreme Ultra-Violet Lithography (EUV-L), even the first generation of masks calls for a 50nm flatness requirement, which is recognized as an insurmountable "brick wall", beyond the capabilities of traditional lapping and polishing techniques. This paper will describe how Magneto-Rheological Finishing (MRF) technology is uniquely suited to achieving these flatness requirements economically.

1. Photomask requirements

a. Introduction

Photomasks are plates of glass covered on one side with a thin layer of chrome on which a magnified version (4 or 5x) of an Integrated Circuit is etched. As reported by Photronics more than 800,000 masks were made each year for all segments of the semiconductor world, representing a total market exceeding $2.7 billions[2]. Once etched with the appropriate pattern – say one of the many layers composing a microprocessor – these masks are inserted in a lithography tool ("stepper" or increasingly "scanner") during exposure of a silicon wafer. As the wavelength of these lithography tools gradually decreases (from 248nm to 193nm, then 157nm) to reach ever shrinking line-widths on the wafers, the flatness of the masks themselves becomes an increasing part of the total depth of focus budget allocated to the overall process. Inoue et al (ref 1) have for instance established the flatness requirements for optical lithography, and even shown that in some cases, a freestanding flat mask might not be the ideal form from a lithography depth of focus standpoint. The masks are indeed used chucked in a reticle holder, making the "as-chucked" flatness (instead of the "free-standing" mask flatness) the key figure of merit during exposure. Freestanding reticle geometries are therefore defined mathematically to become flat after mounting. Even though this is beyond the scope of this paper, these types of geometries could also be obtained with MRF.

b. ITRS projections

As presented in Table 59a and 59b (partially reproduced below) of the 2001 Edition of the International Technology Roadmap for Semiconductor[3] (ITRS 2001), standard 6" x 6" x 0.25" masks are anticipated to become:

- Increasingly difficult to manufacture: for "optical" mask, i.e. fused silica or fluorined doped fused silica masks, as the flatness requirements decreases from 250nm to 130nm.
- Impossible to manufacture with existing technology for EUV-L lithography, i.e. Low Thermal Expansion Material (LTEM) masks, as their flatness requirements starts at 80nm (in 2006) to decrease to 30nm (in 2016).

[1] Corresponding author. Tel: (585) 256-6540x120, E-mail: tricard@qedmrf.com.
[2] See http://www.photronics.com.
[3] See http://public.itrs.net/

Table 59a *Optical Mask Requirements*

Year of Production	*2001 130nm*	*2002 115nm*	*2003 100nm*	*2004 90nm*	*2005 80nm*	*2006 70nm*	*2007 65nm*
Substrate from factor	**152 x 152 x 6.35 mm**						
Blank Flatness (nm)	**250**	**250**	**200**	**180**	**280**	**160**	**250**	**140**	**220**	**130**	**200**

Table 59b *EUVL Mask Requirements*

Year of Production	*2006 70nm*	*2007 65nm*	*2010 45nm*	*2013 32nm*	*2016 22nm*
Mask substrate flatness (nm peak-to-valley) [O]	50	75	50	45	30
Substrate from factor	**152 x 152 x 6.35 mm**				

White-Manufacturable Solutions Exist, and Are Being Optimized, Yellow- Manufacturable Solutions are Known, and ■-Manufacturable Solutions are NOT Known.

c. Limits of conventional lapping & polishing technology

Photomasks are indeed typically manufactured today using a combination of grinding, lapping and "conventional" polishing process. In these later steps, large rotating platens are used to gradually thin down and smooth masks, typically using a simultaneous double side process. Unfortunately these types of "conventional" approaches tend to reach their limit for flatness below 0.5 micron (if not before) in light of the large normal forces applied on these thin plates (aspect ratio 24:1) during lapping and/or polishing. Flatness as low a 0.250 micron have sometimes been reported, but typically imply significant yield ("cherry picking" masks) and/or throughput reduction ("low pressure" polishing). It is therefore expected that for the semiconductor industry to successfully achieve tighter tolerances, new manufacturing processes will need to be implemented. An example of such state-of-the-art process – originally developed for the optics industry – is the Magneto-Rheological Finishing (MRF) technology described here.

d. Current state-of-the-art in mask flatness using "conventional" polishing techniques

As reported by Blaedel et al (Ref 2) "the lowest level of freestanding flatness of LTEM mask substrates is about 0.3um PV. As recently as July 2002, during which the latest EUV Mask task Force meeting[4] was held, Dr. Scott Hector from Motorola presented similar numbers. The results from 117 masks measurements, from 4 different suppliers (in red italicized) performed for the EUV-LLC were reported versus the Semi P37-1101 standard[5], with "best in class" flatness of 250 and 500nm for the front and back side flatness respectively, i.e. far lower than the 50nm Peak to Valley (PV) specification.

[4] Organized by Semiconductor Equipment and Materials International (SEMI). See their web site at www.semi.org for details.

[5] See http://www.semi.org/PUBS/SEMIPUBS.NSF/home/downloadable

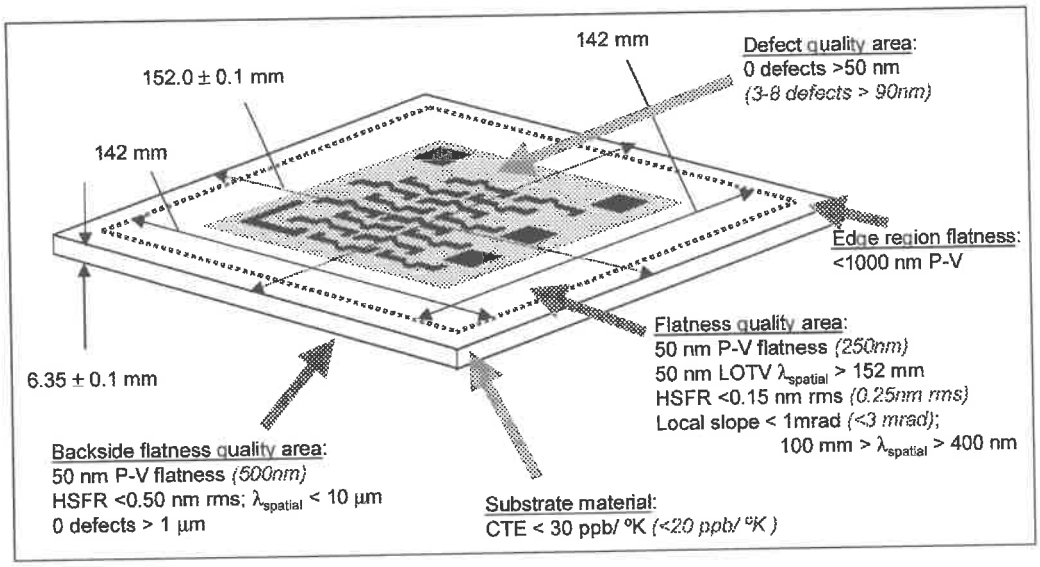

2. **MRF Technology:**

a. Overview

MRF is a polishing technique that utilizes the state of hydrodynamic flow of a magnetorheological abrasive suspension transported through a converging gap formed by a workpiece and a moving wall. The shear flow of the MR suspension is controlled by a magnetic field and results in the development of substantial stresses in the interface zone, as well as predictable material removal over a portion of the workpiece surface. Deterministic finishing is accomplished by moving the workpiece through the polishing zone with a CNC machine. A computer program generates both a dwell time schedule for the machine and an accurate prediction of finished surface shape, using a description of the material removal function and initial surface condition information as input.

MRF uses a magnetorheological polishing fluid to preferentially polish based on dwell time, with a typical removal function area of $1cm^2$. The process methodology characterizes the surface errors in the workpiece, and deconvolves the removal function with the surface error function, to create dwell time instructions for the process. The removal rate correlates with the fluid viscosity, which is continuously monitored and controlled to +/- 1%. The result is an extremely stable removal function. The MRF fluid forms a subaperture polishing tool that is perfectly conformal, and capable of polishing high precision surfaces.

The first generation of MRF equipment enabled the polishing of round, rotationally symmetric spheres, flats, and aspheres. A more recent generation of MRF equipment enables the possibility of polishing square or rectangular mirrors and windows by using a raster tool path (see

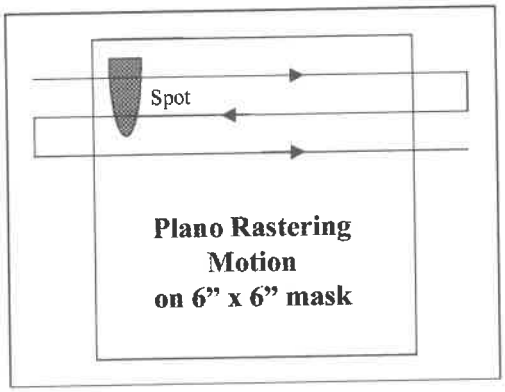

sketch). Working the edges of non-round components using conventional polishing techniques presents a significant challenge because the polishing tool performance near the edges and corners of the optic is unpredictable and often, severely degrades flatness. By raster scanning the work-piece, instead if spinning, a high-convergence MRF tool has been developed that lends itself perfectly to the polishing of fused silica or low CTE material photomasks.

b. MRF finishing process

As described in the following diagram two pieces of information are required for a successful MRF run: a good 3D metrology measurement of the part to be measured and a good "spot", i.e. a precise measurement of the material removal function. As much as taking spots (on LTEM materials such as ULE®, Zerodur® or ClearCeram® materials[6]) is an easy task – merely requiring having access to samples of these materials – 3D metrology of photomask, on the other hand, is a difficult problem.

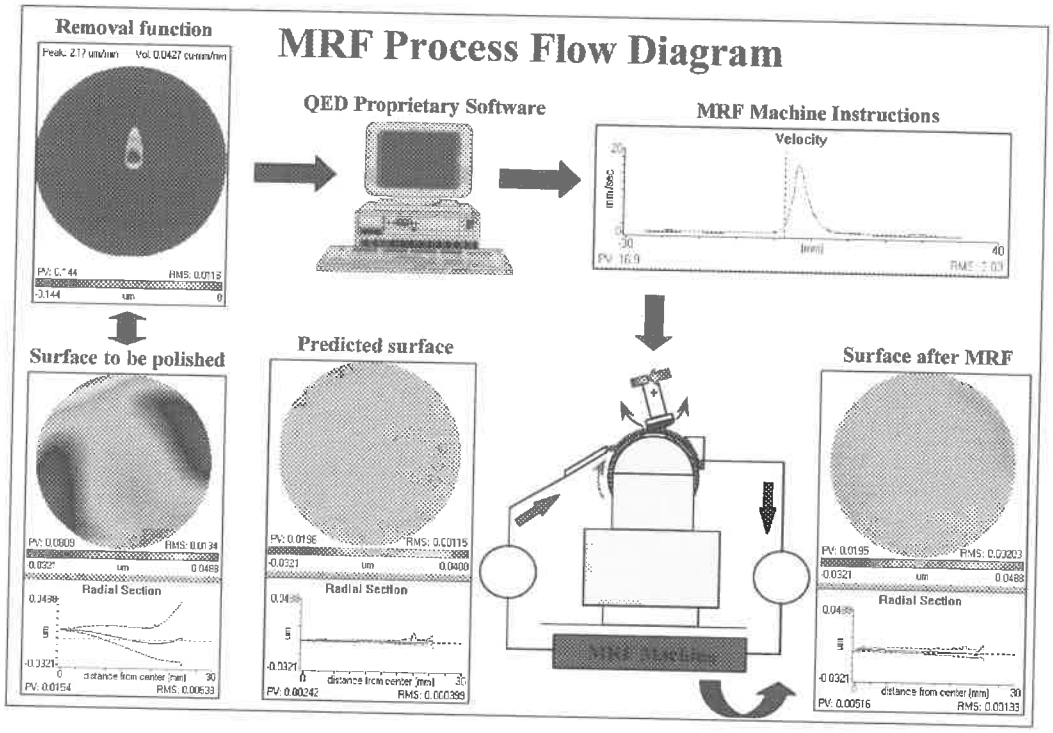

Conventional interferometric measurements of photomasks presents two main challenges:

- First a size issue: as noted typical optical or EUV masks are 6" x 6" x ¼", while most standard interferometers commercially available today have either a 4" or a 6" round aperture.
- A second issue is associated with the so-called "back-side reflection" problem present when ones attempt to measure thin, parallel pieces of glass: both the front and back side of the mask create interference fringes, thereby complicating an accurate measurement with most standard Fizeau interferometers.

As described in detail by Evans et al (ref 3) several techniques exist to alleviate these two problems. In the experiments described here we decided to use a larger interferometer (12"

[6] ULE®, Zerodur® or ClearCeram® are trademarks of Corning, Schott Glass and Ohara respectively.

aperture) and a petroleum gel ("Vaseline") to eliminate the backside reflection. Care was also taken to ensure repeatable mounting, with minimal gravity induced deflection during measurements through the use of a simple 3-point fixture.

3. **MRF ability to polish photomasks:**

a. MRF "insensitivity" to Z-axis errors & its pertinence to the polishing of high aspect ratio components

One – subtle –advantage of the MRF process is its insensitivity to position error in the ribbon of fluid. The part to be polished is immersed – let'ssay 0.5mm – into an MR fluid ribbon that is 2mm tall (all these parameters being variables that are easily changed during process set-up). As the following graphs attest, the material removal rate (in mm^3/mn on the bottom left chart) is quite insensitive to the exact position depth into the fluid. Or as illustrated in the top right chart, a 5% error in Z-axis positioning only translates into a 7-8% error in volumetric removal rate and a mere 2% error in peak removal rate, which would result in an outstanding process convergence of over 90%.

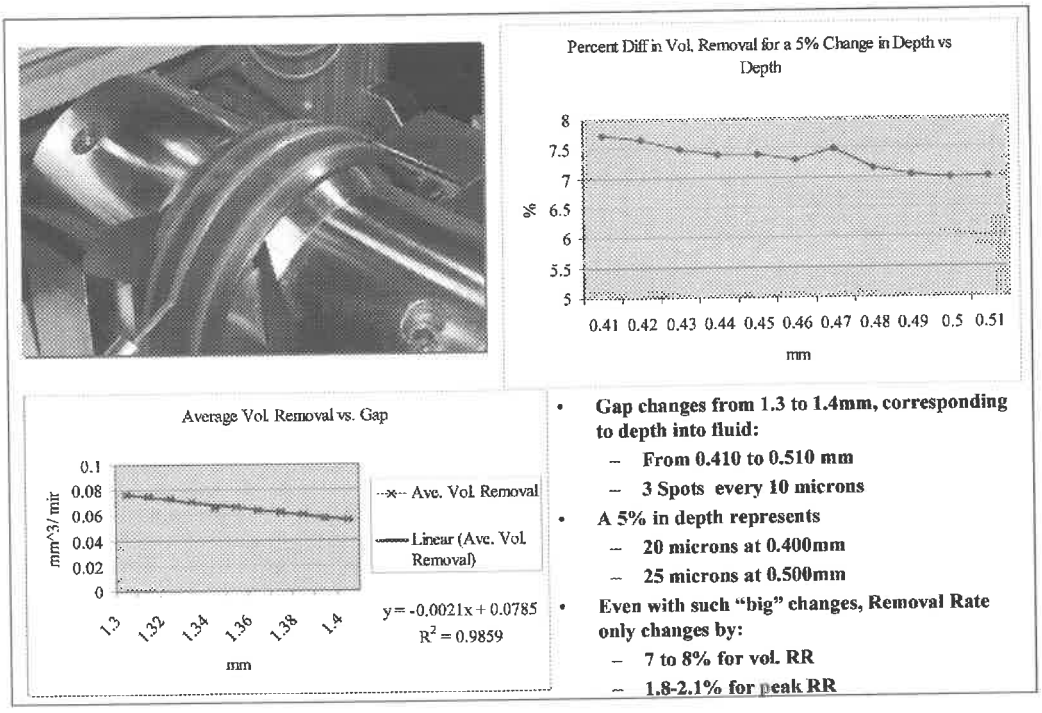

This has major consequences for polishing parts with high aspect ratios, such as photomasks (Aspect ratio of 24:1) or even silicon wafers (A.R. >200:1):

- Ability to polish parts which sag under their own weight
- Ability to polish parts which thermally distort (i.e. the environment around the MRF machine does NOT need to be temperature controlled).
- Same argument for vibration controlled environment.
- No need for high accuracy neither for mounting nor positioning of the part. "Standard" vacuum chucks, wax mounting, mechanical clamping, etc are appropriate.

b. Examples of photomasks polishing

Several series of photomasks were polished as part of these experiments:

- Different materials: Fused silica, ULE® and Zerodur®
- Different incoming quality, with pre-polished surfaces ranging in flatness from approx. 0.5 to 5.0um.

All samples were measured for both flatness (12" interferometer) and roughness (Zygo NewView white light interferometer) before and after polishing. As demonstrated in the previous section, MRF's insensitivity to Z-axis error motion also meant that only a simple custom-made vacuum chuck (with discrete vacuum lines in a 6" x 6" aluminum base) was required for part mounting during polishing.

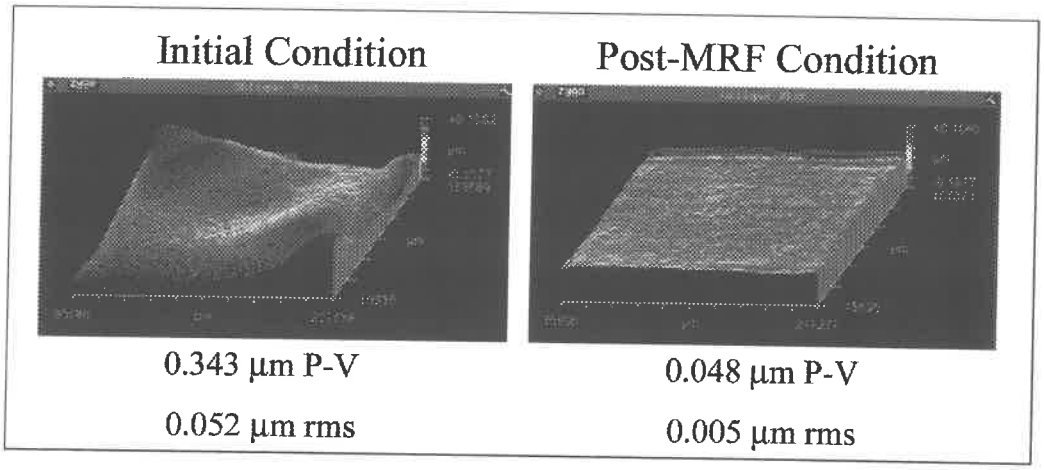

MRF was able to significantly improve PV flatness – regardless of material – with the number of iterations dependant on the incoming flatness. As illustrated above, PV flatness of less than 50nm could be demonstrated on the 142 x 142mm clear aperture required in the Semi P37-1101 standard.

4. Conclusions

MRF polishing of photomask substrates, either fused silica for optical lithography or LTEM for EUV lithography were successfully polished to flatness better than 50nm PV. Provided that metrology (especially back side reflection) does not become a limitation, it is also anticipated that MRF can further improved flatness to meet the requirements of the ITRS roadmap for many years to come.

Bibliography

(1) Inoue, Soichi ; Itoh, Masamitsu; Asano, Masafumi; Okumura, Katsuya; Hagiwara, Tsuneyuki, and Moriya, Jiro "Desirable reticle flatness from focus deviation standpoint in optical lithography", Proc. of Emerging Lithographic Technologies - SPIE Proceedings Vol. 4688, SPIE; 2002.

(2) Blaedel, K.L.; Taylor J.S.; Hector, S.D.; Yan, P.Y.; Ramamoorthy, A., and Brooker, P.D., "Vendor capability for low thermal expansion mask substrates for EUV Lithography', Proc. of the Emerging Lithographic Technologies VI - SPIE Vol. 4688, pp. 767-777, 2002.

(3) Evans, Chris J.; Parks, Robert E.; Shao, Lian-Zhen.; Schmitz, Tony., and Davies, Angela, "Interferometric Testing of Photomask Substrate Flatness", Proc. of the Metrology, Inspection, and Process Control for Microlithography XV – SPIE Vol. 4344, pp. 844-851, 2001.

Error Budget as a Design Tool For Ultra-Precision Diamond Turning Machines

Form Errors

Mark Walter, Bruce Norlund, Robert Koning, Jeff Roblee, Precitech, Inc. Keene, NH 03431 USA

Abstract

This paper describes how an error budget can be used as a design tool to enhance the performance of an ultra precision diamond turning lathe. By understanding error sources and their effects on the form of a work piece, it is possible to distinguish specific areas for machine improvement.
Keywords: Error Budget, Diamond Turning, Uncertainty Analysis

Introduction

Two axis diamond turning machines have been utilized for producing high quality, cost effective, axis symmetric, optical and mechanical surfaces. Current trends in diamond turning demand higher accuracy and truth of motion from the machine tool. As a builder of ultra precision machine tools, Precitech is constantly developing improvements that will allow our machines to produce higher quality parts. The following error budget is an analysis of the current state of the art Nanoform® 350 diamond turning lathe. This ultra precision machine tool utilizes a water cooled air bearing spindle and oil hydrostatic slide ways of 250 and 350 mm travel. The Nanoform® 350 has a maximum swing capacity of 350 mm diameter, and is capable of turning 75 mm diameter components to better than 0.1 micron form error. The error budget is used to expose the effectiveness of a proposed design change and it's correlation to the total machine accuracy. Future efforts will study spindle errors as well as surface finish effects in more detail.

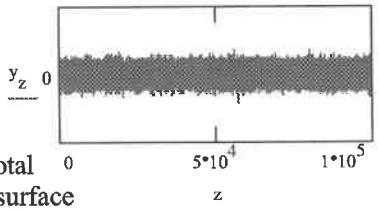

Figure 1 - Gaussian Data

Review types of Error Data

A Gaussian (bell curve) distribution is shown to the right, with data in Figure 1, and a histogram of the data in Figure 2. For this Gaussian type of error, sigma (standard deviation) represents the width of the data, where ±1 sigma about the center point encloses 68 percent of the data, ±2 sigma encloses 95 percent, and ±3 sigma encloses 99.7 percent of the data. Errors with Gaussian distribution include repeatability, reversal, some vibration data, and some thermal errors.

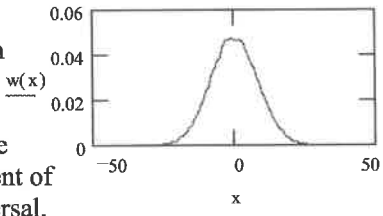

Figure 2 - Gaussian Histogram

Graphs of uniformly distributed data are shown to the right, with the data in Figure 3 and the histogram of the data shown in Figure 4 on the next page. The data is uniformly spread between well defined limits, and a data point has equal probability of falling anywhere within these limits. Uniform data is typical of alignment errors such as squareness, or spindle alignment to the axes.

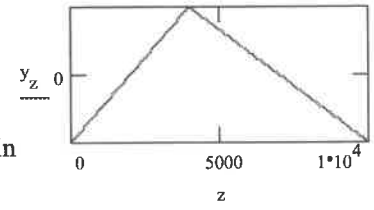

Figure 3 - Uniform Data

In order to add a uniform error with a Gaussian error, some common ground, unit-wise, must be reached. We have chosen to do this by calculating sigma for non Gaussian data sets. This is done by taking the boundary limits (P-V) and multiplying by a conversion factor. In the case of uniform distribution data, the factor is 0.289, which is also $1/\sqrt{12}$. This method allows various types of PV errors to be converted to sigma errors so that they can be added by RSS (root-sum of squares) calculations. [1] [2]

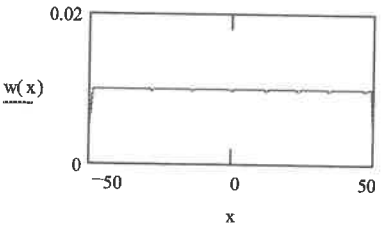

Figure 4 - Uniform Histogram

Another error source exists where the error amplitude changes sinusoidally. Examples of this type of error are scale interpolation error, spindle unbalance, spindle synchronous errors, etc. The sinusoidal form is shown to the right, with the data in Figure 5 and the histogram of the data in Figure 6. As you can see, there are more data points at the edge of the spectrum than in the center. This shifts the conversion factor for this error type to be a larger percentage of the Peak to Valley, namely 0.354 or $1 / \left(2 \cdot \sqrt{2}\right)$ times PV equals sigma.

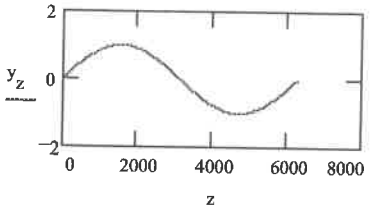

Figure 5 - Sinusoidal Data

We also calculated sigma for a banana curve shaped data set. In this case the histogram is not symmetric about the mean, and both sides of data must be considered to calculate a sigma. In this case sigma is 0.342 times PV. This is nearly the same as the sinusoidal factor. These factors are used in combining the errors from various sources at the end of this paper.

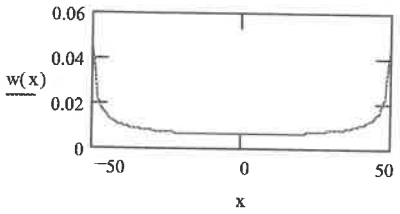

Figure 6 - Sinusoidal Histogram

Errors in a two axis lathe [3]

Form errors in a lathed part come from either the tool or workpiece not following an ideal prescribed contour in space and time. We have chosen to group the error sources into four categories: Stability errors, Length based errors; Time based errors, and Other errors. While stiffness (machine compliance) is not an error source by itself, cutting force deflects the machine, and variations in cutting force introduce additional part form errors. Some of the following data is preliminary and subject to change.

Nanoform 350 Stability Errors

Source	Specification	Actual X	Actual Z	Units	Type
Home Repeatability	0.25 PV	0.180	0.100	PV microns	Gaussian
Slide positioning repeatability, reversal		0.012	0.012	sigma microns	Gaussian
Feedback Scale Interpolation Error	0.10 PV	0.002	0.002	PV microns	Sinusoidal
Tool setter repeatability		0.200	N/A	PV microns	Gaussian
Tool setter reaction to temp fluctuations		0.2 / C	N/A	PV microns	Gaussian
Machine reaction to air temp fluctuations		0.2 / C	1.0 / C	PV microns	Sinusoidal
Machine reaction to spindle coolant variations		0.2 / C	1.0 / C	PV microns	Sinusoidal
Round off error		0.004	0.004	PV microns	Uniform

• The home position repeatability is the ability of the slide to 'home' to the same position of the slide travel. These errors are zero if the machine is not re-homed during a production cycle. These values are the PV (Peak to Valley) errors that are allowed and measured. • The slide positioning repeatability is the

deviation of position of the slide when repeatedly positioned to one location from both directions. Sigma errors represent one standard deviation of the Gaussian curve, or 1/6 of the equivalent PV errors.

• Scale Interpolation error: The position feedback devices are glass scales with holographic gratings. These scales have a grating pitch spacing of 0.55 microns but a resolution of .0086 microns. The fine resolution is obtained by interpolation (mathematical subdivision) of the sinusoidal output of the read head into divisions that are finer than the original grating pitch. This process depends upon the sinusoidal shape being true. If the sinusoid is imperfect, then the interpolation process will result in a slide position error that repeats every 0.55 microns. This error is present regardless of the interpolation level, i.e. changing the interpolation from 50X to 400X makes it look like there are 8 times more counts for the same distance; however the sinusoid imperfection is the same for both cases.

• The tool setter repeatability is the variation in offset values from the tool set routine, including removing and reseating the tool setter and examining the same tool repeatedly.

• The room temperature surrounding the machine can have a disturbing influence on the machine stability. • Similarly, if water cooling is used to maintain temperature of the machine components, temperature variations of this cooling source can be a disturbing influence on the machine.

• Round Off: The slide position is measured in counts from the encoder, each count representing 0.0086 microns. The desired machine position may be different from a multiple of the encoder count spacing by up to 0.0043 microns. The motion control board used in the Precitech Ultrapath machine tool controller sub divides the resolutions into finer increments, minimizing this type of error.

Nanoform 350 Length Based Errors

Source	Specification	Actual X	Actual Z	Units	Type
Slide scale length based error 0.4*L/100	1.4, 1.0	0.41	0.14	microns	Sinusoidal
Slide scale length error temp not 20C	-0.70	-0.70	-0.70	PPM / C	Uniform
Axis straightness horizontal	0.30, 0.20	0.23	0.13	microns	Sinusoidal
Axis straightness vertical	0.70, 0.50	0.53	0.48	microns	Sinusoidal
X slide Abbe error calculated and measured	9.55	5.50		microns	Uniform
Z slide Abbe error calculated and measured	2.72		4.50	microns	Uniform
Vertical straightness bimetallic change with temp				microns	Uniform
Spindle to Z parallelism (horizontal)	0.50	0.24		arc sec	Uniform
Spindle to Z parallelism (vertical)	10.00	3.00		arc sec	Uniform
Spindle to X perpendicularity (horizontal)	0.50		0.30	arc sec	Uniform
Spindle coning error	0.28		0.08	arc sec	Uniform
Spindle droop under load (vertical)	0.03	0.03		arc sec / in-lb	Uniform

Length based errors are those that will change value depending upon the dimensions of the part that is to be machined. It is easy to see that a smaller part will be made more accurately than a larger part in some respects. • The scale length based error is the error between the moved distance (measured at the scale) and the scale reading. • There is also a length based thermal error due to running the machine at a temperature different from 20C, where the scale is calibrated. • The straightness is measured using an electronic indicator at the tool height, and as a result, roll errors of the slide do not need to be measured. Vertical error sources are not critical to the performance of the machine and are left out of further analyses.

• Abbe errors are the difference between the slide travel at the scale and at the tool tip or workpiece. These are calculated using pitch and yaw motions of the slide coupled with the distance between the scale feedback device and the tool or part. The measured values were done using a laser distance measurement interferometer.

• When the machine temperature changes, a bimetallic effect can be seen between components with different coefficients of thermal expansion. For example, this causes a change in the vertical straightness in the X and Z axes since the slides are metal and the base is granite. Since vertical straightness has a second order effect on the accuracy of the work piece, the contribution of this error is small. This will affect the pitch angle error for the slide, and the axis compensation (if used).

Nanoform 350 Time Based Errors

Source	Time Constant	Steady State X Amplitude	Steady State Z Amplitude	Units	Type
Hydro system, scale electronics, work light	TBD	TBD	TBD	microns	Exponential
Linear motor servo active	TBD	TBD	TBD	microns	Exponential
Spindle	TBD	TBD	TBD	microns	Exponential
Spraymist	TBD	TBD	TBD	microns	Exponential

Time based errors are due to the thermal effects during the warm up period for the machine. In this case, the drift of the machine due to temperature gradients is determined from the time period required for the finish pass machining and input as a uniform distribution error. Each component of the machine that is powered or driven heats the machine, with an associated thermal time constant and resultant change of machine shape. Understanding this reaction helps the operator to estimate the error if the machine is not fully warmed up.

Nanoform 350 Other Errors

Source	Specification	Actual X	Actual Z	Units	Type
Spindle axial synchronous error	0.05		0.025	PV microns	Sinusoidal
Spindle radial synchronous error	0.05	0.017		PV microns	Sinusoidal

Other errors contain the error sources that do not fall easily into the previous categories. In this case, there is an error which is always the same, non-varying value. This could be a zonal defect in the tool edge. This zone will create an error of the same amplitude in the part, regardless of part size, feed rate, or dwell time. The spindle axial synchronous error shows up as a pattern at the center of the part. This may be a step or once per rev, or could have a pattern of spokes radiating from the center.

Typical diamond turning tool forces range from nearly zero up to perhaps 1 Newton. The machine stiffness in the Z direction is 40 Newtons per micron, so the deflection under these forces is less than 0.025 microns and typical finish pass deflections are less than 2 nanometers, making the deflection insignificant to this error budget.

Error Sources during Machine Operation

All of the following errors are dependent upon the operator to minimize where possible.

Tool out of roundness or worn zones
Tool placement / offset values in X and Z
Tool radius scallop height surface finish effect
Straight line motion error to desired curve (poor interpolation in programming)
Work piece centering, and balance / unbalance
Part distortion when mounted, part resonance or chatter, and distortion when at RPM
Thermal disturbance due to cutting coolant or operator involvement

Error Budget Summary

The stability PV errors are multiplied by a factor as outlined earlier depending upon the type of error distribution in order to create a sigma, or standard deviation for the error (see chart below). These are then RSSed together in order to provide a sigma for the spread of all of this type of error. In a similar fashion, the length based errors are combined using equal units of microns per mm of angle, to create a total error for each direction of travel. Typical time based errors are shown for a machine that has been fully warmed up. Because the final cut duration is often much shorter than the dominant thermal time constants, these errors can be treated as having a uniform distribution.

Stability	PV	Factor	X Sigma	Z Sigma	Type
Slide positioning repeatability, reversal			0.0120	0.0120	Gaussian
Feedback Scale Interpolation Error	0.005	0.354	0.0018	0.0018	Sinusoidal
Machine reaction to 1C air stability	0.100	0.289	0.0058	0.0289	Uniform
Machine reaction to 0.1 C coolant stability	0.050	0.289	0.0029	0.0145	Uniform
Round off error	0.004	0.289	0.0012	0.0012	Uniform
RSS of Stability Errors			0.0138	0.0345	um RMS

Length Based	PV	Length	X Sigma	Z Sigma	Type
	microns	mm	um/mm	um/mm	
X slide scale length based error	0.41	350	0.000415		XX Sinusoidal
X slide scale length error temp 29C	2.31	350	0.001907		XX Uniform
X axis straightness horizontal	0.23	350		0.000233	ZX Sinusoidal
Z slide scale length based error	0.14	250		0.000198	ZZ Sinusoidal
Z slide scale length error temp 29C	1.65	250		0.001907	ZZ Uniform
Z axis straightness horizontal	0.13	250	0.000184		XZ Sinusoidal
X slide Abbe error	5.50	350	0.004541		XX Uniform
Z slide Abbe error	4.50	250		0.005202	ZZ Uniform
Spindle to Z paralellism (horizontal)	0.24	arc sec	0.000336		XZ Uniform
Spindle to X perpendicularity (horizontal)	0.30	arc sec		0.000420	ZX Uniform
Spindle coning error	0.08	arc sec		0.000112	ZX Uniform
RSS of X direction errors with X movement			0.0049		um RMS/mm
RSS of Z direction errors with Z movement				0.0055	um RMS/mm
RSS of X direction errors with Z movement			0.0004		um RMS/mm
RSS of Z direction errors with X movement				0.0005	um RMS/mm

Time Based	PV	Factor	X Sigma	Z Sigma	Type
Hydro System, scale electronics, work light	0.02	0.289	0.0012	0.0058	Uniform
Linear Motor Servo Active	0.02	0.289	0.0012	0.0058	Uniform
Spindle	0.1	0.289	0.0058	0.0289	Uniform
Spraymist	0.02	0.289	0.0012	0.0058	Uniform
RSS of Time Based Errors			0.0061	0.0306	um RMS

Other					
Spindle Axial Synchronous error (affects Z)	0.025	0.354		0.0089	Sinusoidal
Spindle Radial Synchronous error (affects X)	0.017	0.354	0.0060		Sinusoidal

Example	X	Z	
Travel required to machine part	50	5	mm
Stability	0.014	0.035	um RMS
Length, 50 * 0.0049 (for X)	0.247	0.025	um RMS
Length, 5 * 0.0004 (for X)	0.002	0.028	um RMS
Time	0.006	0.031	um RMS
Other	0.006	0.009	um RMS
Total RSS	0.248	0.060	um RMS

If the length of travel needed to machine a part is known, a predicted error can be calculated. The above example uses 50 mm of X travel and 5 mm of Z travel. This shows the expected RMS error band for the machine in making this part. In this case, the X error is 0.248 microns RMS, and the Z error is 0.060 microns RMS.

The work piece error is measured normal to the surface, so for a flat part, the X error is not significant, regardless of amplitude. In reality, the X and Z values must be mapped against the surface normal to the part in order to determine the impact of the machine errors on the work piece. [1]

Also, the length based errors are repeatable, and thus can be reduced using error correction routines, such as the Ultracomp accessory for on-machine measurement and error correction of the work piece. These procedures can also correct for tool waviness, tool placement error, and the repeatable part of spindle growth errors. Removing the length based errors leaves a residual error of 0.047 microns RMS in the Z direction, but the accuracy limitations of the correction procedure must also be included in the error estimate. In the case of Ultracomp, a typical accuracy is 0.025 microns RMS, which gives a resulting part accuracy of 0.053 microns RMS.

Examine where to concentrate efforts to improve accuracy

It is now possible to compare the errors associated with each source. This indicates that positioning accuracy compensation of the axes would be the most productive place to improve machine accuracy. This method is limited in that it is only valid for one tool location and one workpiece length. It also assumes that pitch errors are repeatable, and the machine can change pitch with temperature as noted above. Accuracy can also be improved by entering the scale compensation value for the temperature of the machine in use instead of the calibrated values at 20C. Thermal stability effects are expected to also be a significant contribution to total error. Since thermal effects are more difficult to compensate, this may be the most important area to focus on in improving machine accuracy.

Conclusions

This paper summarizes the error budget process for a cost effective, state-of-the-art, ultra-precision diamond turning lathe. Furthermore, typical error values along with a method for combining errors has been displayed. This error budget has been found to be consistent with actual machine cutting results. Finally, advancements in ultra precision machining are occurring as a result of a fundamental understanding of machine tool error sources and their consequences.

References

[1] Donaldson, R. R., 1980, Error Budgets in Technology of Machine Tools, Volume 5, Machine Tool Accuracy

[2] Arenberg, J., On the Origins of the Law of Error Propagation and its Uses, ASPE 2002 Summer Topical Proceedings

[3] ASME B5.57-1998, Methods for Performance Evaluation of Computer Numerically Controlled Lathes and Turning Centers

PREDICTION OF SURFACE LOCATION ERROR BY TIME FINITE ELEMENT ANALYSIS AND EULER INTEGRATION

Tony L. Schmitz[a], Philip V. Bayly[b], Johannes A. Soons[a], and Brian Dutterer[a]
[a]National Institute of Standards and Technology, Gaithersburg, MD
[b]Washington University in St. Louis, St. Louis, MO

1.0 Introduction

Surface location error (SLE), which occurs when the machined surface does not lie in the commanded location due to the cutting process dynamics, is not traditionally considered when diagnosing part errors, even though the error magnitude can be as large or larger than those caused by the geometric or thermal errors of the machine tool. SLE can be visualized by considering a square that is produced by peripheral milling. Ideally, the tool will remove material to produce a square of the desired dimensions. However, due to the relative phasing between the cutter vibrations and the time at which the cutter produces the final surface (e.g., as the tool exits the cut in down milling), either more material may be removed than commanded (overcutting, which gives a smaller square) or less than commanded (undercutting, which produces a larger square). This relative phasing is defined by the system frequency response function and selected forcing frequency, i.e., spindle speed [1-2]. The expertise that has been gained in modeling cutter motions for chatter avoidance [e.g., 3-5] can be drawn upon to predict and compensate SLE and, more importantly, allow the pre-process selection of spindle speeds with significantly reduced errors. Surface location error is especially important in high-speed machining applications for three reasons: 1) due to the low damping in most systems, the surface location error changes dramatically for a small variation in spindle speed near the intentionally selected speeds; 2) the error magnitude grows near the system resonance which typically occurs at the high tooth passing frequencies preferred in high-speed machining; and 3) high-speed machining is often used to produce monolithic parts with thin-walled sections and the mechanical integrity of such features depends strongly on correct wall thickness.

In this study, time domain simulation tools are applied to predict SLE in milling and comparisons are made with high-speed machined part dimensions. The simulations include the time finite element analysis (TFEA) method [6] and the well-known time marching Euler integration scheme [1]. The cutting tests included slot machining, low radial immersion (5 %) cuts, and thin rib production. These tests were carried out over a number of spindle speeds, the control parameter in this case, using two 12.7 mm diameter tools.

2.0 Simulations descriptions

For both simulation methods in this study, a rigid workpiece is assumed. In the TFEA method, an exact solution for the X-Y displacement vector of the cutter is found using the system state transition matrix when the cutter is not in contact with the workpiece. When in contact, the time in the cut is broken up into multiple elements and the vector displacement during a single element is approximated as a linear combination of polynomial trial functions. The position and velocity at the beginning of the current time element are matched to the position and velocity at the end of the previous element. Using this formulation, a discrete version of the system (i.e., a linear map) is obtained that relates coefficients of the solution to coefficients one tooth passage earlier, which is required for the surface regeneration found in milling. The eigenvalues of the linear map determine its stability. The fixed points of the map represent the steady state solution, from which the displacement of the tool as it leaves the cut for down milling or enters the cut in up milling can be extracted. This displacement approximates the SLE of the finished surface. A complete description of the TFEA method can be found in reference [6].

The numerical time domain simulations used in this study are based on Tlusty's Euler integration scheme [1]. In this method, the cutter angle is sequentially incremented in a time-based manner and, if the current tooth is within the angle bounded by the prescribed radial immersion, the thrust and radial forces, F_t and F_r, respectively, are calculated using Eq. 1 (the same force model was used for the TFEA simulations) [7]. If multiple teeth are engaged in the cut, the force is summed over all active teeth. The cutter deflection is then calculated using this force and the cutter velocity and deflection values from the previous time step. If the deflection is large enough so that the tool leaves the cut, a nonlinearity occurs. It is accounted for by setting the forces equal to zero in this situation. In Eq. 1, b is the commanded axial depth of cut and h is the instantaneous chip thickness that depends on the selected chip load or feed per tooth, the current tool deflection, and the previously cut surface. This dependence of the actual chip thickness, and therefore the cutting force, on previous cutter deflections is referred to as *regeneration of waviness*

and provides the feedback that can lead to self-excited vibrations, or chatter. The specific cutting force coefficients that relate the cutting forces to the product of the chip thickness and axial depth of cut, k_{tc} and k_{rc}, and edge effect coefficients that relate force to axial depth, k_{te} and k_{re}, were 700 N/mm^2 and 210 N/mm^2 and 7 N/mm and 6 N/mm, respectively. These values were obtained empirically in reference [8] and were assumed to reasonably approximate the tool/material combinations selected for testing here, although the edge effect coefficients may vary from tool to tool. Two versions of the Euler simulation were implemented. In the first, straight cutter teeth and a circular tool path were assumed. In the second, the effects of helix angle, actual trochoidal tooth motion, and flute runout were modeled, and the machined surface was reconstructed using Boolean subtraction of the cut chip volume.

$$F_t = k_{tc} h b + k_{te} b$$
$$F_r = k_{rc} h b + k_{re} b \qquad (1)$$

3.0 Experiment description

The three types of cutting tests (slots, low radial immersion, and thin ribs) were performed in 6061-T651 aluminum using two 12.7 mm diameter carbide end mills: 1) 106.2 mm overhang, 2 flutes, 45° helix; and 2) 106.2 mm overhang, 3 flutes, 45° helix. The cutting conditions for the tests are summarized in Table 1. Modal parameters for the two tools were obtained by impact testing using an instrumented hammer (PCB 086C04) to excite the tools and a low mass accelerometer (PCB 353B17) to record the responses [9]. Table 2 lists the natural frequency, f_n, stiffness, k, and damping ratio, ζ, for the dominant mode in the cutting (X-Y) plane for each tool, where a modal mass correction of 4.2 g has been applied to both data sets to match observed frequencies for Tool 1.

The workpiece geometry for the slotting tests is shown in Fig. 1, where the left and right slots were machined at the lowest spindle speed to establish a baseline and the middle slots cut at each of the 11 spindle speeds (spindle speed increment was 100 rev/min). This part geometry was selected to minimize the influence of factors other than SLE on the results. In Fig. 1, the SLE slots are shown in gray. The two vertical slots, pre-machined prior to the cutting tests, served as spindle speed change locations. In all cases, 30 consecutive passes were completed to reach a full slot depth of 3.0 mm. The 0.1 mm axial depth per pass was selected to avoid chatter based on the stability behavior of the tool/material combinations.

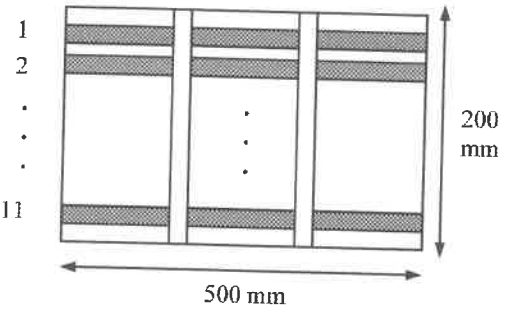

Figure 1: Geometry for slotting tests

Test	Tool	Cut direction	Spindle speed (rev/min)	Chip load (mm/tooth)	Axial depth of cut (mm)
Slotting	1	N/A	14000-15000	0.102	0.1
Slotting	2	N/A	18500-19500	0.102	0.1
5 % immersion	1	Down milling	13100-15200	0.102	0.813
5 % immersion	1	Up milling	13100-15200	0.102	0.813
Thin ribs (50.8 mm wide)	1	Down milling	14000-15000	0.102	0.813
Thin ribs (101.6 mm wide)	1	Down milling	14000-15000	0.102	0.813

Table 1: Summary of cutting conditions

Tool	X direction			Y direction		
	f_n (Hz)	k (N/m)	ζ	f_n (Hz)	k (N/m)	ζ
1	960.5	1.33×10^6	0.031	953.8	1.47×10^6	0.009
2	926.5	1.74×10^6	0.019	934.4	1.66×10^6	0.010

Table 2: Modal parameters for cutting tools

The workpiece geometry for the 5 % radial immersion (0.635 mm radial depth) tests is shown in Fig. 2. For these tests, existing slots (shown in gray) were widened using the 5 % radial immersion cutting parameters. Again, the pre-machined vertical slots were used as locations for spindle speed changes, the left and right sections were milled using the first spindle speed, and the middle sections were cut at ascending spindle speeds to see the effect on SLE. Two identical plates were machined for a total of 22 data points (spindle speed increment was again 100 rev/min).

The 0.635 mm thick by 31.75 mm high ribs were down milled at 5 % radial immersion. Two plates with 13 ribs each were machined. The spindle speeds for both plates were 14000 rev/min to 15000 rev/min in 100 rev/min increments with repetitions at the first and last spindle speeds to verify process repeatability. On the first plate, the rib width was 50.8 mm. On the second, the rib width was 101.6 mm. In both cases, the cutting paths were selected to avoid the effects of the machine tool reversal errors on rib thickness.

4.0 Experimental results

4.1 Slotting tests

As noted, slotting tests were performed with both two and three flute end mills. The fundamental difference is that both slot surfaces are produced simultaneously at a single tool deflection (assuming perfectly spaced teeth) for the two flute cutter, while the surfaces are produced at different instants in time, and therefore at different vibration states for the three flute cutter. The anticipated results are a stronger dependence of slot width on spindle speed for the three flute tool and a larger variation in actual slot location for the two flute tool.

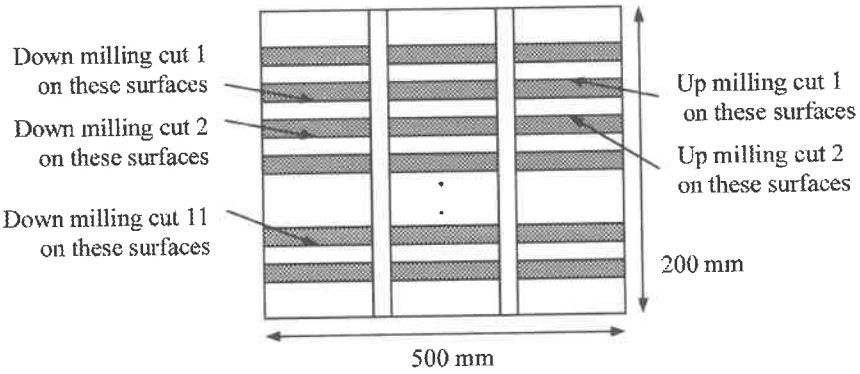
Down milling cut 1 on these surfaces
Down milling cut 2 on these surfaces
Down milling cut 11 on these surfaces
Up milling cut 1 on these surfaces
Up milling cut 2 on these surfaces
200 mm
500 mm
Figure 2: Geometry of 5 % radial immersion cutting tests

The experimental and simulated errors in slot width and slot location for the two and three flute end mills are shown in Figures 3-6, where a positive error in slot location corresponds to movement of the slot centerline toward the top of Fig 1. In all plots, the experimental data (open circles) are relative to the observed errors at the lowest, or reference, spindle speed and have been shifted so that the value at the lower spindle speed is numerically equal to the absolute error predicted by the Euler simulation at the same speed. Furthermore, the experimental data are the differences between measurements of the center slots and the mean of measurements of the left and right slots. Surface locations were recorded using a touch trigger probe coordinate measuring machine, or CMM, at various positions and elevations along the tool path and the results averaged. The values for multiple measurement cycles are shown in each figure to demonstrate the CMM repeatability. It is seen in Fig. 3 that the TFEA and Euler simulations show no slot width change for the two flute case, while the experimental results exhibit a 12 μm peak-to-peak variation with spindle speed. This discrepancy could be due to imperfectly spaced teeth or a dependence of spindle asynchronous error motions on rotational speed, for example. Similarly, in Fig. 4 the simulations predict near zero variation in slot location for the three flute cutter, while a 3 μm change is seen experimentally. In both figures, the trends in the unexplained experimental results are similar to the modeled trends in the other figures.

Figure 5 shows the slot location variation for the two flute case. The expected dependence on spindle speed is seen, as well as good agreement between the two simulation algorithms. Figure 6 demonstrates the large dependence of slot width on spindle speed for the three flute tool – a change of nearly 50 μm for a 1000 rev/min change in spindle speed is seen experimentally. Although the simulated results overestimate the error magnitude, the appropriate decreasing trend with increasing spindle speed is shown. Also, the same peak may occur in the experimental data slightly to the left of the recorded range.

4.2 Low radial immersion tests

The experimental and simulated surface location errors for down and up milling at 5 % radial immersion are shown in Figures 7 and 8, respectively, where a positive error corresponds to an undercut surface. The experimental data are again relative to the lowest spindle speed, have been shifted to be equal to the simulated value at the lowest spindle speed, and are calculated from the average of CMM points measured at various locations and elevations. There was an unexplained slope along the cutting tool axis in the down milled surface that varied with spindle speed; however, this effect was much reduced in the up milling case and did not appear at all in the slotting tests. For both down milling and up milling, the experimental SLE varies significantly as a function of spindle speed, with peak-to-valley amplitudes equal to 63 μm and 112 μm, respectively, over the selected 2100 rev/min spindle speed ranges. It is important to note that: 1) the observed error magnitudes are as large or larger than the more generally

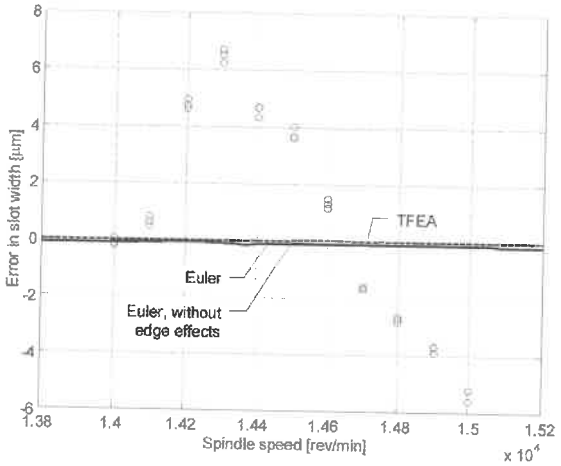

Figure 3: Slot width error (two flutes)

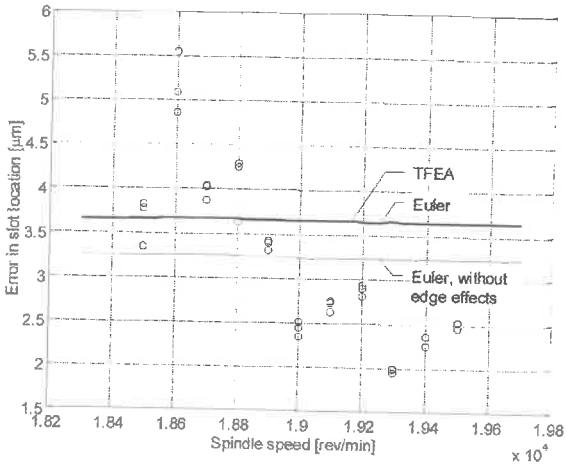

Figure 4: Slot location error (three flutes)

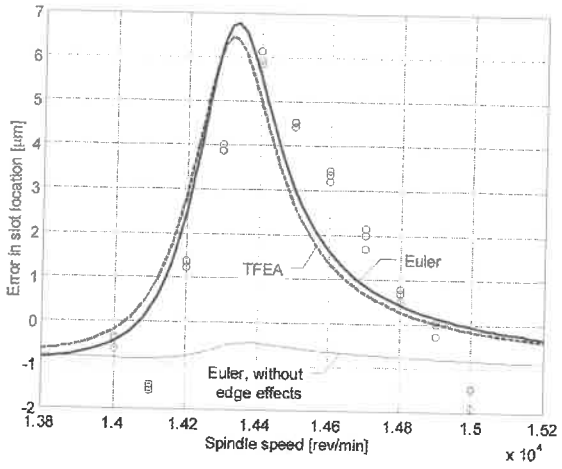

Figure 5: Slot location error (two flutes)

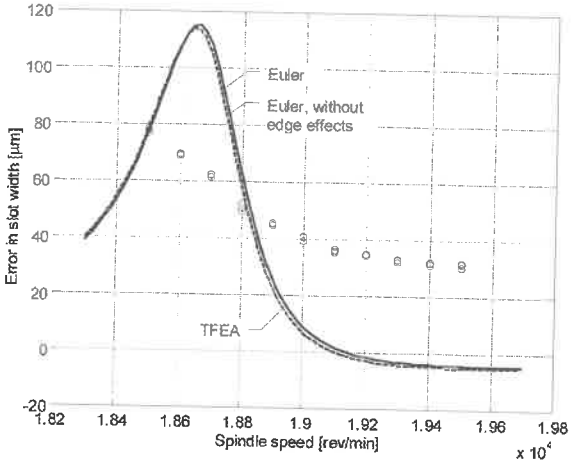

Figure 6: Slot width error (three flutes)

modeled/compensated geometric and thermal errors of machine tools; 2) if ignored, surface location errors could lead to unacceptable part quality; 3) the only process parameter changed during these cutting tests was spindle speed; 4) these errors were recorded for a very small radial immersion (5 % or 635 µm), such as might be seen in traditional finishing passes; and 5) the errors change significantly within a small spindle speed range making their compensation within this range difficult, even though spindle speeds yielding near zero SLE are available.

It should be noted that neither the TFEA nor Euler simulation takes into account a possible interaction of the current cutter deflection with the surface machined at the previous axial depth. For example, a tool pass can modify the 'finished' surfaces associated with all the axial segments above the axial segment being machined. Practically, this can be avoided by relieving the cutter flutes above the commanded axial depth, but that was not the case for these cutting tests.

In Fig. 7, although the TFEA and Euler simulation results agree using the full force model of Eq. 1, except at high spindle speeds where the Euler results roll off (similar to the experimental data) due to the Boolean subtraction surface regeneration, they overestimate the SLE. However, it is possible that the true peak in the experimental data was missed due to the rather coarse 100 rev/min spindle speed increments. On the other hand, the up milling simulation results in Fig. 8, which again agree, underestimate the experimental SLE. Although the appropriate trends are seen in each case, additional research will be required to improve the predictive capabilities.

Figure 9 shows simulation results for up milling taking into account the tool helix angle. Absolute surface location errors are plotted as a function of spindle speed for different heights along the tool axis bounded by the 0.813 mm commanded axial depth of cut. It can be seen that both the error difference between the top and bottom of the selected axial depth and zero crossings are dependent on spindle speed. The reader may note that the results for the TFEA method, which assumes straight cutter teeth, are bounded by the upper and lower Euler values.

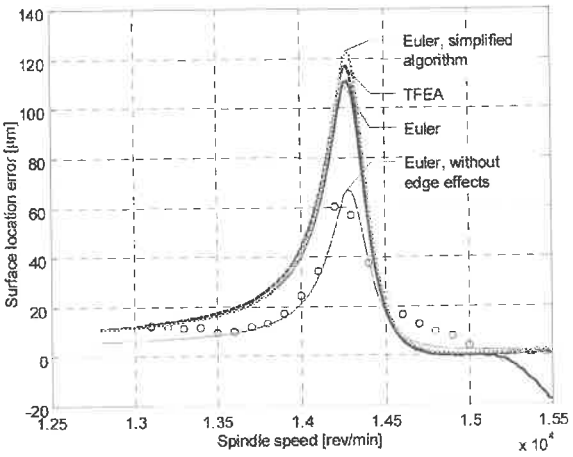

Figure 7: Down milling SLE

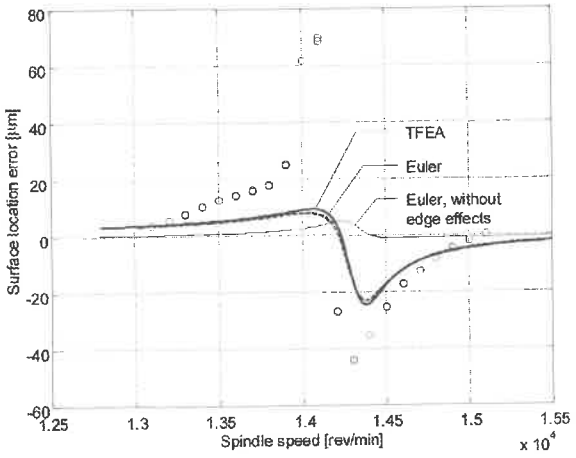

Figure 8: Up milling SLE

4.3 Thin rib tests

An example measurement of a 50.8 mm wide rib machined at 14000 rev/min is shown in Fig. 10. This data was obtained using a CMM with sample distances of 3.1 mm in X, along the rib width, and 1 mm in Z, along the rib height, from 1 mm below the rib top to 25 mm below. This result shows that the rib flexibility clearly influences the final wall thickness. It is seen that the rib is thicker by nearly 90 µm at the top center where the unsupported material is pushed away from the cutter during machining. Near the bottom of the rib, where it is supported by material both to the sides and from above, the thickness is nearly uniform. However, this intuitive static flexibility is not the only consideration. Figure 11 shows that there is also a dependence of rib thickness on spindle speed. This figure displays the difference between the rib thickness at the top center and bottom center locations, both calculated from an average of three different CMM measurement points, as a function of spindle speed. The open circles represent the 50.8 mm rib results, while the solid circles show the 101.6 mm rib results. The two data points at both 14000 rev/min and 15000 rev/min for each of the two data sets show that the process repeatability is substantially smaller than the recorded changes in rib thickness. It is also seen that the mean thickness difference is larger for the 101.6 mm wide ribs due to the increased rib flexibility, but the variation in rib thickness with spindle speed shows the same trend. For comparison purposes, the recorded thickness variation for a 101.6 mm wide machined at the same spindle speed as Fig. 10 is shown in Fig. 12.

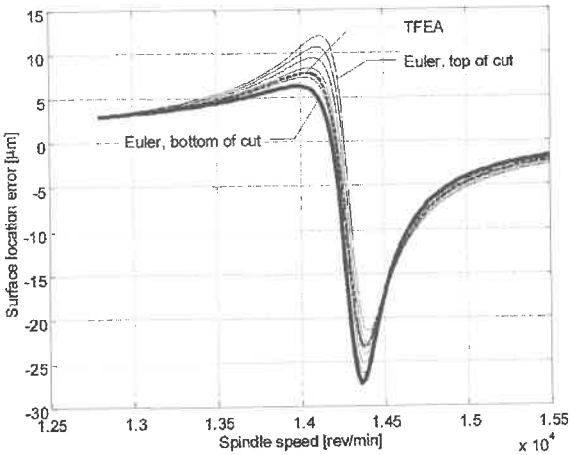

Figure 9: Variation in SLE along tool helix

5.0 Conclusions

This paper presents experimental and simulated results for surface location errors in milling. These errors occur due to the inherent flexibility in the workpiece/tool/spindle/machine system and are determined by the instantaneous tool deflection as it leaves the machined surface, i.e., entering the cut in up milling or exiting the cut in down milling, which is determined by the relationship between the system natural frequency and forcing frequency, or spindle

speed. Two different simulation algorithms were implemented including Bayly's TFEA method and a modification of Tlusty's Euler integration scheme. Good agreement between the two methods was recorded. Cutting tests were completed for 1) slot machining using both two and three flute end mills to show the stronger influence of spindle speed on slot width for three flute tools and slot location for two flute tools; 2) low radial immersion machining in both up and down milling cutting directions to demonstrate the large changes in part dimensions as a function of spindle speed; and 3) thin rib production to show a practical example of the importance of surface location errors. Experimental results showed surface location error amplitudes as large or larger than the more generally modeled/compensated geometric and thermal machine tool errors, even during low radial immersion cutting conditions such as might be used for traditional finishing passes.

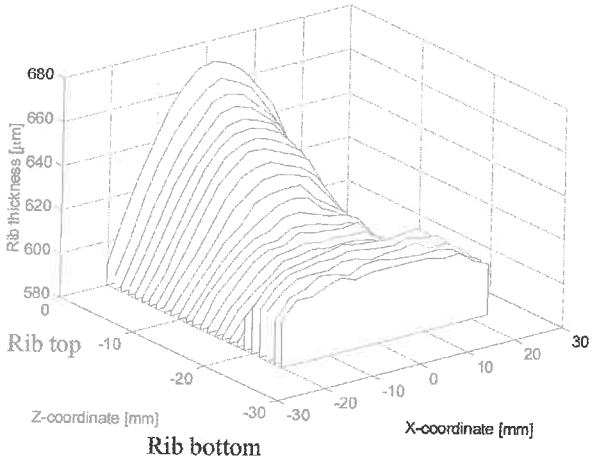

Figure 10: Thickness of the 50.8 mm wide rib machined at 14000 rev/min

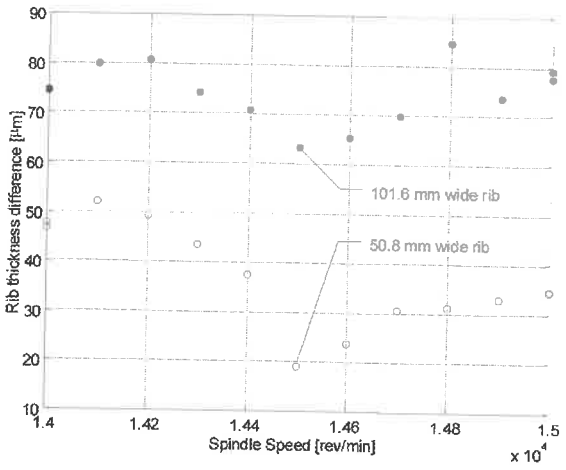

Figure 11: Thickness difference between top and bottom at rib center

References

1. Tlusty, G., 2000, Manufacturing Processes and Equipment, Prentice-Hall, Upper Saddle River, NJ, p. 380.
2. Schmitz, T. and Ziegert, J., 1999, Examination of Surface Location Error Due to Phasing of Cutter Vibrations, *Precision Engineering*, **23**/1: 51-62.
3. Tlusty, J., 1985, Dynamics of High-Speed Milling, in Handbook of High-Speed Machining Technology, R. I. King, ed., Chapman and Hall, New York, pp. 48-153.
4. Smith, S., and Tlusty, J., 1991, An Overview of Modeling and Simulation of the Milling Process, *Journal of Engineering for Industry*, Transactions of the ASME, **113**: 169-175.
5. Altintas, Y. and Lee, P., 1996, A General Mechanics and Dynamics Model for Helical End Mills, *Annals of the CIRP*, **45**/1: 59-64.
6. Bayly, P. V., Halley, J.E., Mann, B. P., and Davies, M. A., 2001, Stability of Interrupted Cutting by Temporal Finite Element Analysis, *Proceedings of the 18th Biennial Conference on Mechanical Vibration and Noise*, DETC2001/VIB-21581, ASME Design Engineering Technical Conferences, September 9-13, Pittsburgh, PA.
7. Altintas, Y., 2000, Manufacturing Automation – Metal Cutting, Mechanics, Machine Tool Vibrations, and CNC Design, Cambridge University Press.
8. Halley, J. E., 1999, Stability of low radial immersion milling, M.S. Thesis, Washington University, St. Louis, MO.
9. Commercial equipment is identified for completeness. Identification does not imply recommendation or endorsement by the National Institute of Standards and Technology, nor does it imply that the equipment is the best available for the purpose.

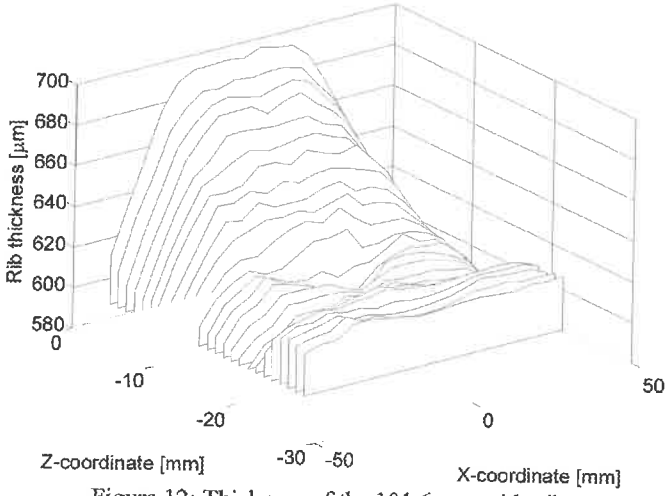

Figure 12: Thickness of the 101.6 mm wide rib machined at 14000 rev/min

Bonding Fixture Tolerances for High-Volume Metal Microlamination Based on Fin Buckling and Laminae Misalignment Behavior

Wassanai Wattanutchariya
Department of Industrial Engineering, Faculty of Engineering, Chiangmai University, Chiangmai 50200, Thailand
(011-6653) 944125, wattanwa@yahoo.com
Brian K. Paul
Department of Industrial and Manufacturing Engineering, Oregon State University, 118 Covell Hall, Corvallis, OR 97330 USA, 541-737-7320, fax: 541-737-5241, brian.paul@orst.edu

Abstract

Microlamination involves the patterning, registration and bonding of thin layers of material, called laminae, to produce monolithic devices with embedded micro-scale features. In energy, chemical and biological systems miniaturization, microlamination can be used to produce bulk microfluidic devices for mobile, compact or point-of-use applications. Thermally-Enhanced Edge Registration (TEER) is a registration technique used in metallic microlamination to precisely align laminae during high-temperature bonding cycles. Shape variation, such as channel misalignment or fin buckling, incurred during the TEER registration step can lead to lower system performance or even functional failure. This paper investigates the allowable tolerance limits in TEER fixtures in order to minimize fin buckling while attaining precise alignment. A high-temperature buckling model is developed to predict the onset of fin buckling within a TEER fixture. The results of the model are validated empirically. Results indicate that within the tolerance limits, μm-scale channel-to-channel alignment can be achieved free of fin buckling. In addition, the general relationship between the critical point of buckling and the device configuration is discussed for broader application.

Keywords: Microlamination; Bulk microfluidic devices; High temperature; Registration; Buckling theory; Fixture tolerances

Microtechnology-based Energy and Chemical Systems (MECS) are devices which process bulk fluids within highly-paralleled arrays of microchannels. These miniaturized energy and chemical systems enable large quantities of fluid to be processed without requisite pressure drop penalties. The use of microchannels results in shorter diffusional distances which permit shorter residence times in channels, shorter channel lengths and, ultimately, no increase in pressure drop. MECS devices have the potential to revolutionize the processing of mass and energy where a premium is placed on mobility, compactness, or point-of-use production. The miniaturization of bulk chemical and energy unit operations through the application of MECS devices is called process intensification (PI).

By and large, PI devices are produced through microlamination techniques involving the patterning, registration and bonding of thin material sheets or laminae. Microlamination techniques have been used to prototype a variety of PI devices for application in advanced climate control[1], solvent separation[2], microcombustion[3], fuel processing[4], high-temperature catalysis[5] and fluidic control[6] among others. Bulk microfluidic devices have been constructed in a wide array of materials with features as small as several μm. In addition to being used for PI, microlamination methods have been used in the past in applications ranging from pneumatic control systems to rocket engine fuel injection assemblies.[7,8,9,10,11] Even so, the major commercial impact of these methods has been limited mainly to non-bulk fluid processing applications including inkjet printing and more recently lab-on-a-chip for the life sciences.[12,13] Figure 1 shows the lamination scheme for fabricating a counterflow microchannel array, which could be used as a recuperative heat exchanger in PI applications.

Several previous investigations have found that the registration step is critical in microlamination. Paul, et al.[14] found that poor registration in intermetallic microchannel devices resulted in an

amplification in the fin warpage found within the device. Ashley[15] found that layer-to-layer bearing gaps on the order of 10 μm were necessary in order to operate the micro-scale turbine generator developed at MIT. In each of these applications, precision alignment of laminae was necessary in order to produce a functional device. Several registration techniques have been employed in microlamination methods including pin, edge, and self-alignment. The technique used depends on the bonding process chosen. The registration technique investigated in this study is called Thermally-Enhanced Edge Registration (TEER).[16] This technique can be used to register laminae during the high temperature diffusion bonding of polycrystalline metals. The TEER technique employs the difference in CTE between the bonding fixture and the laminated material to produce a registration force on the laminae at the bonding temperature. By making the bonding fixture from a material that has a lower CTE than the laminae, a clearance will exist between the fixture and the laminae at room temperature, making the loading of laminae simple compared with other mechanical alignment methods. At the same time, TEER is able to achieve a layer-to-layer registration accuracy as small as 5 μm.

During diffusion bonding, the metal laminae and the bonding fixture are heated up to a specific temperature, normally in the range of about 60% to 75% of the melting temperature of the base material. For metallic structures, this temperature can be 1000 °C or higher. Within a TEER procedure, the fixture and laminae will expand differently as the temperature is raised resulting in a registration force on the laminae at the bonding temperature. However, if this registration force is higher than the critical buckling load of the microchannel fin, buckling of the fin will occur. This is illustrated in Figure 2. When buckling develops, flow channels that are separated by the buckled fin are no longer uniform resulting in flow maldistribution and a drop in effectiveness of the microchannel array.

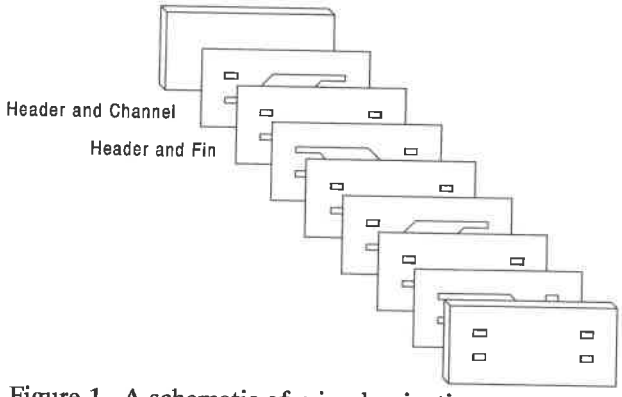

Figure 1. A schematic of microlamination procedure for producing a two-fluid counter-flow microchannel array

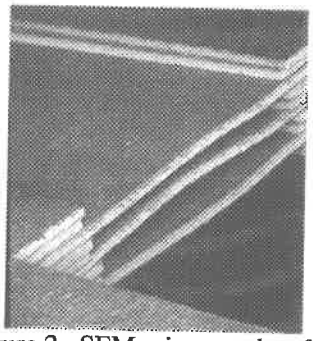

Figure 2. SEM micrographs of a microchannel heat exchanger with nonuniform flow channels after fin buckling

Figure 3 illustrates the result from a previous investigation conducted on TEER technique for stainless steel microlamination.[17] The graph shows the relationship between the allowance of the bonding fixture and laminae versus the amount of misalignment. This picture suggests that there is an interval of allowance between the laminae and the bonding fixture, where the misalignment is somewhat constant. From this graph, it is observed that once interference is established the accuracy of registration is not improved further. On the other hand, if this interference extends beyond a certain point, the fin will buckle. This indicates that interference should remain within a particular range. This range should constrain the allowable tolerance of the fixture, governed by the desired registration accuracy and the buckling of the laminae. The goal for this study is to predict the tolerance limits of TEER fixtures based on buckling theory and registration behavior.

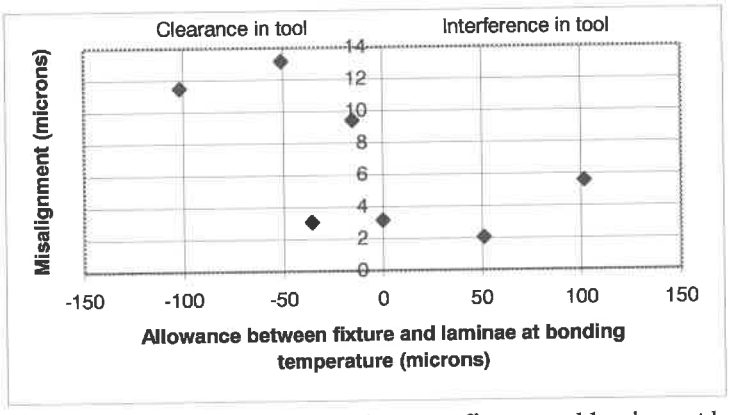

Figure 3. Graph of misalignment versus allowance between fixture and laminae at bonding temperature

To determine if a fin will buckle, the mode of failure needs to be confirmed by calculating several loads. For the fixed-ended boundary condition, the critical buckling load (P_c) can be calculated from:

$$P_c = \frac{4 * \pi^2 * E * I}{L_s^2} \quad (1)$$

where L_s is the fixture slot width at room temperature, E is Young's Modulus and I is the moment of inertia of the specimen. The second load to be considered is the yield load (P_y) defined as the load necessary to yield the fin in compression which is the product of the yield strength and the cross sectional area of the fin:

$$P_y = \sigma_p \cdot A_f \quad (2)$$

The final load to be considered is called the registration load (P_r) due to thermal expansion which occurs beyond the temperature at which the dimension of the fixture and laminae are equal to each other (called the registration temperature). The registration load can be calculated from:

$$P_r = A_f * E * (\alpha_{ss} - \alpha_g) * \Delta T_{eff} \quad (3)$$

where, in this investigation, α_{ss} is the CTE of stainless steel and α_g is the CTE of graphite and ΔT_{eff} is the temperature increase beyond the registration temperature at which the onset of inelastic buckling occurs (i.e. the bonding temperature must be above the registration temperature in order to produce a load).

If the yield load is greater than the critical load for fin buckling, the fin may buckle elastically if the registration force is less than the yield force. However, in the case where the critical load for fin buckling is greater than the yield load, the fin may yield in compression without buckling if the registration load is larger than the yield load but below the critical load for fin buckling[17]. In either case, if the registration load exceeds both the critical load for fin buckling and the yield load, the fin will permanently buckle.

The test specimen used in this experiment consisted of two-channel layers and a fin layer. All layers were made from a 304 stainless steel shim. A Nd:YAG laser operating at the fourth harmonic was used to pattern the shims of three different thicknesses (0.0508 mm, 0.0762 mm and 0.1016 mm). After patterning, all laminae were polished and cleaned with an ultrasonic cleaner to remove slag resulted from the laser machining process. Then, the fin lamina was measured by a Dektak3 surface profiler to record the initial flatness characteristics. Before bonding, all laminae were rinsed with Acetone, Ethanol, and De-ionized water (AED) to remove grease or any other residues on the surfaces so that a sound diffusion-bonded joint could be formed.

The fixture assembly was then put in a vacuum hot press chamber, and the bonding cycle began. The first step in the bonding process involved pumping down the chamber to achieve a satisfactory vacuum (approximately 10^{-4} mbar). The system was then heated up to the appropriate bonding temperature. Once the bonding temperature was reached, clamping pressure was applied to the fixture to

induce the diffusion bond. At the end of the bonding phase, the clamping pressure was removed so that the laminate could contract uniformly without inducing residual stress. The bonding conditions for this experiment were set up at 750 °C with 5 MPa applied pressure and a one hour dwell period. After the system cooled down, the laminate was taken out to check for possible characteristics of fin deflection using the surface profiler. Similar to the initial flatness measurements, warpage measurements were also taken to record the post-bonding characterization. The average deflection and standard deviation of each sample were calculated and were used for theoretical comparisons.

The allowance between fin width and the fixture slot was varied in order to evaluate the relationship between the fixture allowance and both types of shape variation. Fins with thicknesses ranging from 0.0508 mm to 0.1016 mm were used in this study. In general, the critical point of buckling is proportional to the thickness of the fin layer. The thicker the material, the greater the strength and the greater amount of interference needed before the fin starts buckling. However, this critical buckling load also needs to exceed the proportional limit of yield strength (or elastic property) to cause the fin to be permanently deformed after bonding. For laminae with thicknesses below 0.1016 mm, the load at the proportional limit is found greater than the critical point of buckling; therefore, all specimens in this experiment should have the same buckling behavior. *

The first experimental set up was designed to evaluate the effect of fin thickness on the buckling behavior of the fin. Since the buckling behavior of all fins in this experiment was supposed to be the same, each thickness was only tried at each 2 allowances. The significance of the thickness was checked using an analysis of variance (ANOVA). An additional test was performed to evaluate the difference between the theoretical and the experimental results. A paired t-test was used to verify this comparison based on the null hypothesis that the mean of the difference in theoretical data and experimental results is zero with alpha equal to 0.05. If both theoretical and experimental results are equal, a 95% confidence interval for the mean difference must include zero.

The measurement of channel-to-channel misalignment was performed at 200X on a LEICA DML optical microscope with a video measurement system. This microscopy technique has provided reliable results which are statistically comparable to using a scanning electron microscope. Reproducibility of the measurements was also evaluated by comparing the measurement results from two different inspectors and using an ANOVA to analyze the significance of the factor. For misalignment analysis, a test was designed so to evaluate main effects such as fin thickness and allowance on the amount of misalignment. This evaluation was analyzed by a multifactor ANOVA (Type III Sums of Squares) under the condition that the p-value for a significant factor must be smaller than 0.05.

Before any experiments were run, a number of preliminary tests were conducted to calibrate the high temperature dimensions of the test fixture. The most important feature of the test fixture to be determined was the slot width at elevated temperature. A variety of test coupons with different width span were tested on the bonding fixture to identify where interference started relative to the expansion of both stainless steel and the graphite fixture.

Upon variation of fixture allowance, the laminae and fixture are either over-constrained or under-constrained. Buckling was found when the laminae were over-constrained. In this case, the width of laminae was longer than the slot size at the diffusion temperature. The mechanism of this fin buckling occurs when the force, due to the difference in CTE between the stainless steel laminae and the graphite fixture, exceeds the critical point of buckling and elastic limit. The magnitude of fin buckling at different amounts of interference can be calculated based on buckling theory. On the other hand, when the device was under-constrained, the width of laminae was shorter than the slot size at the bonding temperature, resulting in channel misalignment. The maximum misalignment was evaluated by looking at the actual clearance between fin width and slot size at the bonding temperature.

---

* Additional buckling calculation such as critical point vs. stiffness relation and the magnitude of fin buckling can be found in the full version of this article.

Figure 4 illustrates the magnitude of maximum deflection of warpage due to fin buckling with respect to the fixture allowance at the diffusion temperature from both theoretical prediction and experimental data. As can be seen from the graph, buckling begins for all three fin thickness at 10 μm of interference. The magnitude of warpage also increases as the interference increases. According to the ANOVA, it was concluded that there is no statistical evidence that the magnitude of warpage depends on the thickness of the shim under the scope of this experiment (p-value = 0.50). Furthermore, there was conclusive evidence that the mean warpage from the experimental data and the theoretical result were equal (t-stat = 1.42, df = 8). Its 95% confidence interval ranged from -0.01 to 0.05, which includes zero.

The error bars shown in Figure 4 are 95% confidence interval of the measured warpage. Each side of the interval is equal to $2*S_m$, where S_m is the standard error calculated from the variation of the warpage measurement. As can be seen from the graph, there are some variations of experimental results from the theory. Sources of error for this experiment might include the deviation of fin width from the patterning step either due to variation of beam diameter or the residual ejecta. Furthermore, the materials that were used in this experiment are thin shims, which might contain residual stress from a cold work processing that could play a key role in this variation.

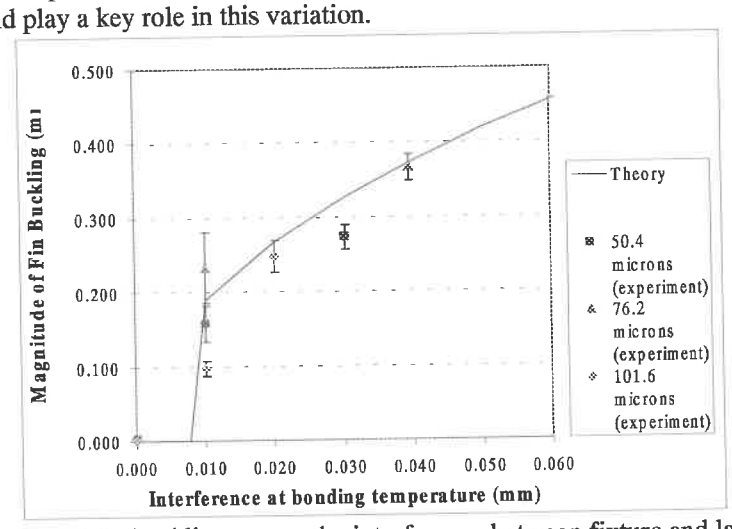

Figure 4. Magnitude of fin buckling versus the interference between fixture and laminae at bonding temperature with 95% confidence interval of standard deviation

Figure 5 displays the results for the misalignment analysis. Similar to Figure 4, this figure also presents the error bar based on the 95% confidence interval of the misalignment readings at 4 locations on the specimen. The test included the alignment analysis for both the under-constrained and over-constrained cases. With respect to this figure, precision alignment is achieved only in the area close to the exact constraint. As can be seen, the average and standard deviation for misalignment increases with clearance, and it also increases as the fin begins to buckle. Therefore, tight tolerance is required in order to attain a well-aligned channel. With respect to the ANOVA, the inspector factor was found to be not significant on misalignment (p-value = 0.9180) indicating a reproducible measurement technique. On the other hand, there is statistical evidence that misalignment depends on the allowance and measurement location (p-value < 0.05).

In conclusion, microlamination of metal structures for PI devices requires high temperature bonding. The TEER technique has been developed for precise alignment and bonding in the microlamination process. This research has been conducted to investigate the tolerance limits in a TEER bonding fixture for the purpose of minimizing the shape variation due to misregistration and fin buckling caused by excessive registration force during microlamination. Both analytical and experimental results are in good agreement within 95% confidence interval. Furthermore, it is evident that there are some

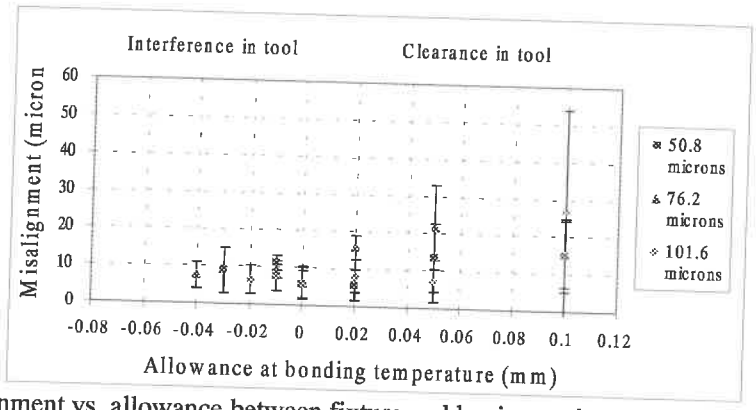

Figure 5. Misalignment vs. allowance between fixture and laminae at bonding temperature with 95%CI

tolerance limits in the TEER fixture that allows high-temperature microlamination to generate the multilayer structure with the minimal amount of shape variation. With respect to the nominal dimension specified in this study, the tolerance limit of 10 μm (interference) is where the fin starts to buckle, while the limit in misalignment is proportional to the clearance at the bonding temperature. The average channel-to-channel misalignment within this tolerance limit was about 6 μm. Finally, it was shown that the fixture tolerance has a finite fixed lower limit based on the elastic limit of the material. Therefore, as the thickness of laminae continues to decrease, the fixture tolerances will not need to continue to decrease below this lower limit.

[1] Martin, P. M., W. D. Bennett, and J. W. Johnson, "Microchannel Heat Exchnagers for Advanced Climate Control," Proc. SPIE (v2639, 1996), pp82-88.

[2] Matson, D. W., P. M. Martin, W. D. Bennett, D. C. Stewart, and J. W. Johnson, "Laser Micromachined Microchaneel Solvent Seperator," Proc. SPIE, (v3223, 1997), pp253-259.

[3] Matson, D. W., P. M. Martin, A. Y. Tonkovich and G. L. Roberts, "Fabrication of a Stainless Steel Microchannel Microcombustor Using a Lamination Process," Proc. SPIE (v3514, 1998), pp386-392.

[4] Tonkovich, A.Y.; Zilka, J.L.; LaMont, M.J.; Wang, Y. and Wegeng, R.S. 1999. "Microchannel reactors for fuel processing applications," Chemical Engineering Science, 54(13): 2947-2951.

[5] Paul, B. K., T. Dewey, D. Alman and R.D. Wilson, "Intermetallic Microlamination for High- Temperature Reactors," 4th Int. Conf. Microreaction Tech., Atlanta, GA, March 5-9, 2000, pp236-243.

[6] Paul, B.K. and T. Terhaar, "Comparison of two passive microvalve designs for microlamination architectures," J Micromech. Microengr., (v10, 2000), pp15-20.

[7] Esposito, A. 1988. Fluid Power with Applications. Prentice-Hall,380-381.

[8] NASA. 1988. National Space Transportation System Shuttle Reference Manual.

[9] Haas, R.W., (1995), "Further Development of MMW and SMMW Platelet Feed Horn Arrays," ASP Conf. Ser., Vol. 75, pp. 99-105.

[10] Haas, R.W., D. Brest, H. Mueggenburg, L. Lang, and D. Heimlich, (1993), Fabrication and Performance of MMW and SMMW Platelet Horn Arrays," Intl. J. Infrared and Millimeter Waves, 14(11), pp. 2289-2293.

[11] Young, M., (1997), "Platelet-Cooled Plasma Arc Torch," DOE Contract No. DE-AR21-93MC30361, Technology Development Data Sheet, (Morgantown, WV: Federal Energy Technology Center, 1997), 5-6.

[12] Anderson, J.J., 1989, U.S. Patent 4,875,619, Brazing of Ink Jet Print Head Components Using Thin Layers of Braze Material.

[13] Unger, M.A., H. Chou, T. Thorsen, A. Scherer and S. Quake. 2000. Science, 288: pp 113-116.

[14] Paul, B. K., Dewey, T., Alman, D., and Wilson, R. D., "Intermetallic Microlamination for High-Temperature Reactors," presented at 4th International Conference on Microreaction Technology, Atlanta, GA, 2000.

[15] Ashley, S., "Turbines on a dime," *Mechanical engineering*, vol. 119, pp. 78-81, 1997.

[16] Thomas, J. and B.K. Paul, "Thermally-Enhanced Edge Registration (TEER) for Aligning Metallic Microlaminated Devices," *Transactions of NAMRC XXX*, West Lafayette, IN, May 21-24, 2002, pp. 663-670.

[17] Gere, J. M. and Timoshenko, S. P., *Mechanics of materials*. Boston: PWS-KENT Pub. Co., 1997.

Six Degree of Freedom Optical Sensor for Dynamic Measurement of Linear Axes

Jeremy J. Kroll, Steven R. Patterson
Center for Precision Metrology
University of North Carolina at Charlotte, Charlotte, NC, USA

keywords: optical, sensor, dynamic, linear, metrology

Introduction

Up to 70% of the errors in CNC machine tools can be attributed to the quasistatic errors.[1] To correct these errors, measurements are made and a compensation scheme is implemented. Typically, linear and straightness measurements are done using interferometric techniques. Angular errors are usually acquired using either differential path or electronic levels. These measurements are usually performed separately, which commonly requires at least 21 measurements to fully characterize a machine.

To reduce the time required for error characterization, many systems have been developed to combine multiple error measurements in one setup.[2,3,4] The drawback of these systems has been that they require either an active or large moving element. Another drawback of current systems is the low bandwidth of at least some of the measurements. Feng et al. [5] has shown that dynamic errors can be significantly different from quasistatic errors.

This paper describes an optical system that will acquire motion data in six degrees of freedom from a linear axis in a single setup. With a 5 kHz sample rate it is able to characterize dynamic, as well as quasistatic, errors.

A key feature of the system is a single compact, passive (i.e., purely optical and not containing any electronics or requiring connection to the base unit) moving element. This element scales with beam size and can easily be reduced in size to a 25 mm cube that weighs approximately 50 grams. Since the sensor has a small mass, it can be used in high acceleration environments where the quality of measurement benefits from its low inertia.

Optical Design

The key requirements for the optical design are compact size and high geometric sensitivity. The system comprises three elements: a stabilized heterodyne laser source, a fixed measurement system and a small moving target. Heterodyne interferometry is used to measure linear displacement accuracy. Straightness is measured using a position sensitive photodiode. A position sensitive photodiode at the focus of a lens is used for pitch and yaw. Roll is measured optically using a heterodyne technique described by Patterson and Schmidt[6]. All six degrees of freedom are measured using a single optical layout.

Figure 1 shows the paths of the S and P polarizations of the heterodyne laser source through the system. First, the beam passes through a fixed optical measurement assembly consisting of two beamsplitters, a polarizing beam splitter, a retroreflector and a lens. The laser source enters the first beam splitter and the reflected portion enters the polarizing beam splitter. The polarizing beam splitter and retroreflector create the reference beam for the heterodyne linear displacement signal.

The portion of the beam that passes through the first beam splitter continues to the passive moving target consisting of a polarizing beam splitter, retroreflector and plane reflector. The beam reflects off the

mirror and returns to the fixed measuring assembly to provide measurement of pitch and yaw in the manner of an autocollimator. The beam transmitted by the target polarizer passes through a retroreflector and returns to the beam splitter in the fixed measurement assembly. This beam contains both the phase to determine the linear displacement and the intensity information to determine roll of the moving element. The position of this beam centerline also provides information to determine lateral motion of the target.

The beam reflected from the mirror on the moving target is passed through a lens upon reflection from the initial beam splitter then is incident on a position sensitive photodiode to yield pitch and yaw data. The retroreflected beam from the target is split at the initial beam splitter. The transmitted portion is used for the roll measurement. The portion reflected at the initial beamsplitter is split again by a second beam splitter. One split beam portion is recombined with the reference signal and used for heterodyne displacement measurement, while the other portion is incident on a position sensitive device which determines lateral motion of the target (straightness).

The system contains a total of four detectors. Two position sensitive devices and two high bandwidth

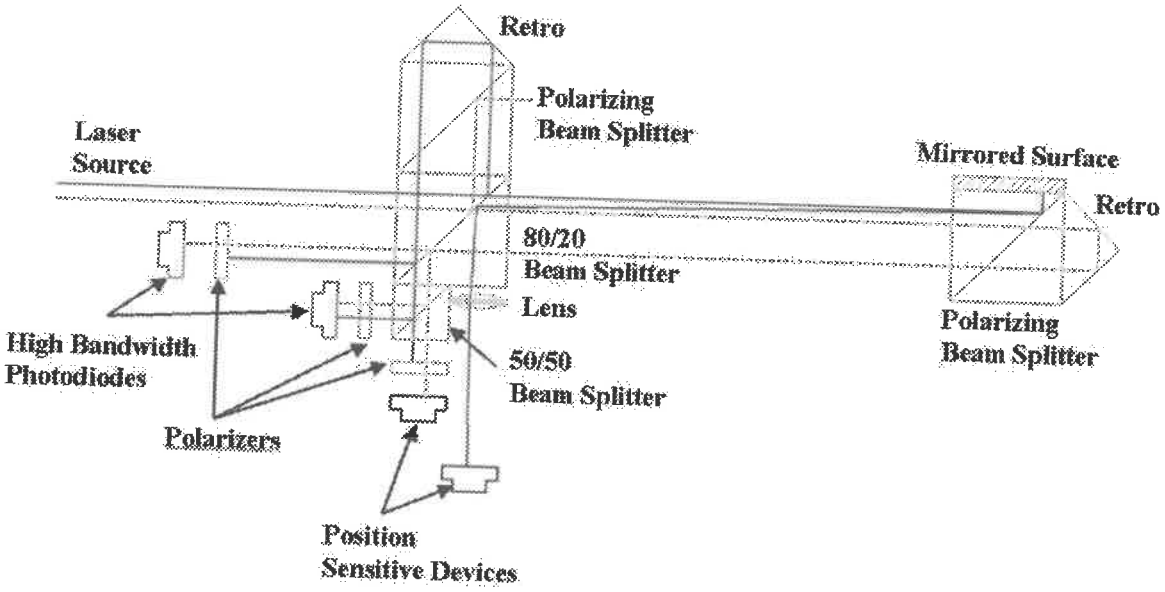

Figure 1 Schematic diagram of the optical design.

sensors capable of detecting the split frequency of the heterodyne source.

The initial 80/20 beam splitter, as shown in Figure 1, is used to maximize the signal to the roll detector. Of the individual measurements, the roll measurement signal to noise ratio is most limited by beam power the other measurements can achieve the required resolution at lower beam powers.

Position Sensitive Device

The sensors for the linear displacement and the roll measurement are high-speed photodiodes of the type common to heterodyne interferometers. This device also employs two-dimensional lateral-effect photodiodes for the straightness and angular error measurements. Driving factors in the design of the position sensitive devices are sensitivity and bandwidth. Most large area two-dimensional photodiode electronics are designed for sample rates less than 10 Hertz. Sensor signal conditioning electronics used

here are designed to obtain the required sensitivity and bandwidth for the straightness and angular lateral effect photodiodes. The duo-lateral photodiode was chosen not only for its linearity over the entire active area, but also for the simpler signal processing it allows.

Figure 2 shows the circuit diagram for the two-stage amplifier circuit. First, the currents from the photodiode are amplified using a transimpedance amplifier. A Dallas Semiconductor digital potentiometer is used in the second stage voltage amplifier to allow adjustment of the gain to match the voltage range to the analog to digital converters. Finally, the voltages are converted using 24-bit analog to digital converters before they leave the amplifier boards. In this way, performance degradation due to noise pickup is reduced relative to designs in which the analog signals travel through wires for long distances.

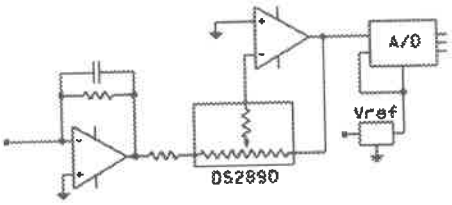

Figure 2 Circuit diagram for the 2-stage amplifier.

A completed circuit board can be seen in Figure 3. Each photodiode requires two circuit boards, one for each axis of measurement. The center of the circuit board contains a monolithic quad operational amplifier. This helps minimize variances in noise and gain characteristics caused by thermal gradients between amplifiers.

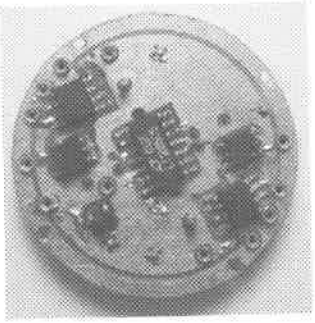

Figure 3 Circuit board for photodiode.

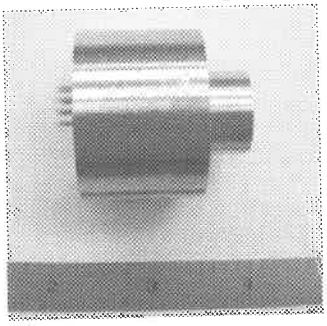

Figure 4 Complete photodiode assembly.

Figure 4 shows the completed diode assembly including two amplifier boards and a connector board. The connector board routes all the signals, power and ground lines to standard connectors on the back of the assembly. The smaller diameter section acts as a light pipe to help shield the diode from ambient light while testing. The entire assembly is 1.5 inches in diameter and 2 inches long. All low level signals are completely contained in the housing, with only digital signals and power at the connector.

Position Error Analysis

For the duo-lateral photodiodes to meet the system resolution requirements, they need to perform near their noise limit. The position error is then dominated by the shot noise of the detector, as shown in figure 5. The calculated worst-case theoretical noise limit is just below the required resolution for the system at an input power of 20 microwatts.

The curves in figure 6 show the detector shot noise, the theoretical noise limit of the diode and electronics and some experimental results of the noise measurements plotted versus the input light power. The current photodiode with electronics exhibits noise 10 dB above the theoretical limit. For the photodiode assembly to meet the system requirements, the input beam power must be 85 microwatts.

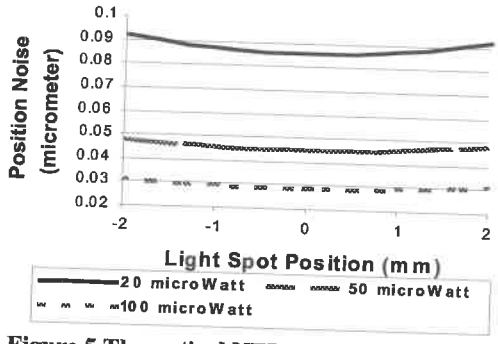

Figure 5 Theoretical NEP of the diode and electronics.

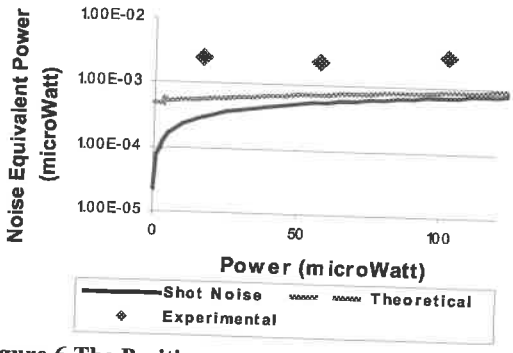

Figure 6 The Position error versus light spot position.

References

1. Kiridena V.S.B., Ferreira P.M., 1994, Parameter Estimation and Model Verification of First Order Quasistatic Error Model for Three-Axis Machining Centers, *Int. J. Mach. Tools Manufact.*, 34(1), 101-125
2. Shimizu S., Lee H., Imai N., 1994, Simultaneous measuring of table motion errors in 6 degrees of freedom, *Int. J. Japan Soc. Prec. Eng.*, **28**(3), 273-274
3. Ni J., Wu S.M., 1987, A New On-Line Measurement System for Machine Tool Geometric Errors, *NAMRC XV, Int. J. Mach. Tools Manufact.*, 573-577
4. Ni J., Huang P.S., Wu S.M., 1992, A Multi-Degree-of Freedom Measuring System for CMM Geometric Errors, *Transactions of the ASME,* **114**, 362-369
5. Feng Qibo, Hocken R.J., Miller, J.A., 2000, Quick and dynamic measurements of geometric errors of CNC machines, *Proc SPIE Int Soc Opt Eng*, v4222, 110-113
6. Patterson S.R., Schmidt D.M., 1994, Precision roll measurement using a polarization reference, *Proc. ASPE*, **10**, 80-83

Visual Based Motion Error Compensation for Precise Versatile Micro Robot

O. Fuchiwaki and H. Aoyama

Applied Micro Systems
Dept. of Mechanical Engineering and Intelligent Systems,
University of Electro-Communications,Chofu, Tokyo 182-8585
Japan
[URL http://www.aolab.mce.uec.ac.jp]

1. Introduction

In the field of micro system and precision engineering, there are many reports concerning micro robotics and its trial applications. Some of them are based on the advanced technology including micro battery, micro motor and tiny computational facility[1], the others are made by the sophisticated precision machining techniques[2-4] However it is still very important to find the industrial applications where such micro robots can provide effective benefits. It is well known that the *Desk top Factory* [5] has the potential application not only for the production engineering but also for the chemical and biotechnology. For years, our group has developed insect size robots equipped with various micro tools and instruments[6]. Particularly the in-situ micro processing in the scanning electron microscope can be one of feasible applications although it needs much of cost to install the fine positioning mechanism into the small chamber[7]. For the period of research, we have proposed the flexible micro-processing system organized by multiple miniature robots in SEM vacuum chamber as depicted in Fig.1[8]. In previous experiments for years, we concluded that we need the arc trajectory motion with facing center to keep its tip end within the microscopic monitoring area as well as XY orthogonal motions as shown Fig.2. Moreover we designed and controlled the newly developed versatile micro robot which can move any directions as shown in Fig.3[9]. In this paper, visual based motion error compensation system for this precise versatile micro robot will be discussed.

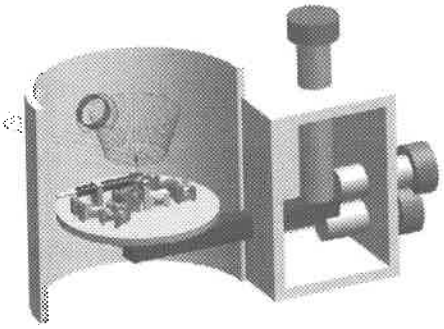

Fig.1 Flexible micro processing system by micro robots in SEM vacuum chamber

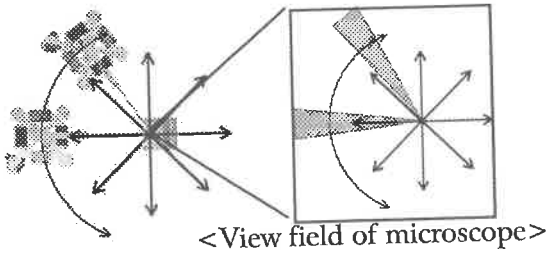

Fig.2 Motion pattern required at microscopic operation

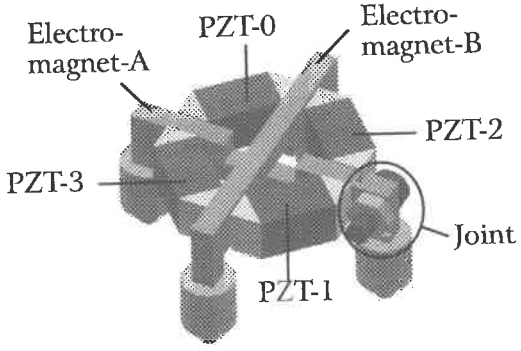

Fig.3 Structure of versatile micro robot

2 System Configuration

Fig.3 shows overview of the micro robot's structure. Where two closed loop electromagnets which are arranged to cross each other as like X character are connected by four piezo elements so that it can move in any directions with the manner of inch worm as depicted in Fig.2. Also we design the special joint at one of legs to get 4 legs smooth contact on the surface simultaneously.

Fig.4 shows the overview of whole system of this compensation system. We attached two LEDs on the robot to measure the position and direction of the robot by the CCD camera based microscope image tracking system.

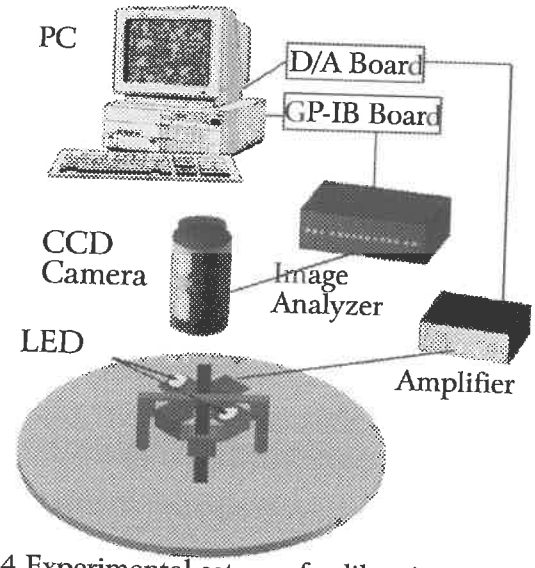

Fig.4 Experimental set up of calibration system

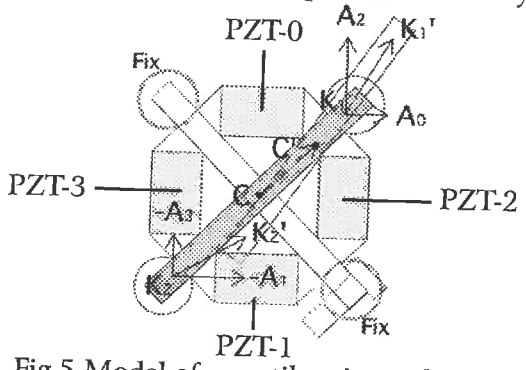

Fig.5 Model of versatile micro robot

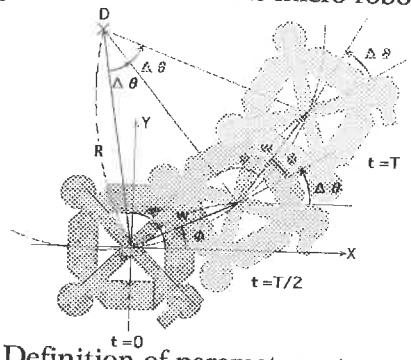

Fig.6 Definition of parameters at a step

3 Compensation Sequence

First of all, we analyse the robot's motion mechanism at a half step to investigate relationship between 4 piezo elements' displacements and motion as Fig.5 and FIg.6. Fig.5 shows schematic structure model of this small robot actuated by piezo elements. In this figure, we consider that the displacement of each PZT element A0, A1, A2, and A3 make the specified points K1, K2 on the free magnet move to the K1', K2'. Fig.6 shows the definition of parameters at a step motion. Then, the robot motion are measured by the CCD camera based microscope image tracking system. We calculate 4 piezo elements' experimental displacements as shown in Fig.7. Finally, we apply the compensation formula to compensate the robot motion as depicted

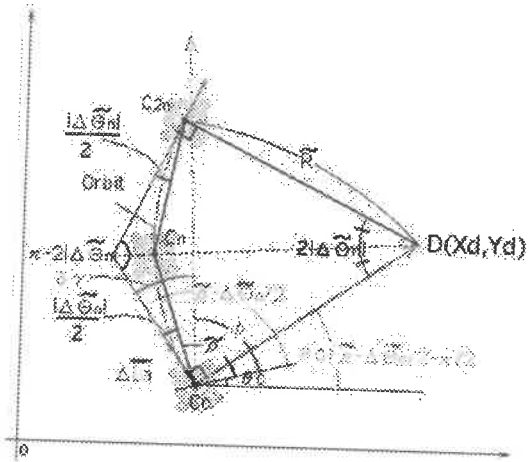

Fig.7 Geometric analysis of robot motion

$$PGain[k]' = PGain[k] \times \frac{Ak'}{Ak} \qquad (k = 0,1,2,3)$$

Ak': Ideal displacement of PZT-k

Ak: Experimental displacement of PZT-k

PGain[k]': Sinwave's amplitude of PZT-k after compensation

PGain[k]: Sinwave's amplitude of PZT-k at experiment

Fig.8 Compensation equation

in Fig.8. The robot can move more precisely with repetitive these procedures. The best calculation results are stored in PC as unique parameters.

4. Experimental Results

4.1 Round-trip movement in 8 directions

Fig.9 shows the experimental results of round-trip movement in 8 directions. Fig.10 shows the results of angle alternation in the robot's back and forth movement. In the experiment, we used the microscope with CCD based image analyzer to measure its motion accuracy. We confirm that we can compensate the robot motion in both the orthogonal and the diagonal directions.

4.2 Rotation and Arc Trajectory Motion

(1) Rotation

As shown in Fig.11, we attach the two LEDs to the robot to measure its rotational motion accuracy. Fig.12 shows the results of the experiment. If we compensate values of amplitude of 4 PZT elements' sine wave control signal, we can improve the rotational accuracy of the robot dramatically.

(2) Arc Trajectory Motion

In another experiment, we attach the two LEDs to the center of the robot and the ideal rotation center of the arc trajectory to measure its accuracy as shown in Fig.13. Fig.14 shows the results of the experiment. If we compensate values of amplitude of 4 PZT elements' sine wave control signal, we can improve the motion accuracy as well as rotation. This performance can be useful when we manipulate small objects in the focused area, such as microscope.

5. Conclusion & Future Works

Visual based motion error compensation system for precise versatile micro robot is proposed and developed. We confirm that the robot can move more precisely by this compensation system automatically. Furthermore, in order to develop the motion performance, improvement of the whole system by both side of hardware and software is required. In addition, development the PC controlled system with the help of the visual

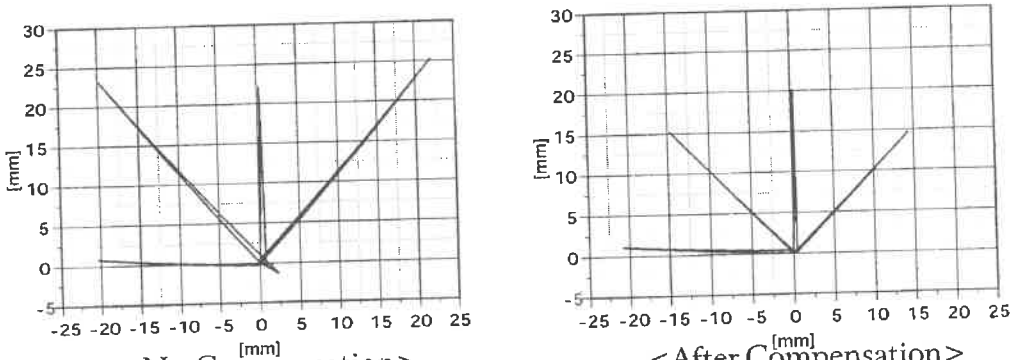

<No Compensation> <After Compensation>

Fig.9 Experimental result of round-trip movement in 8 directions(100Hz)

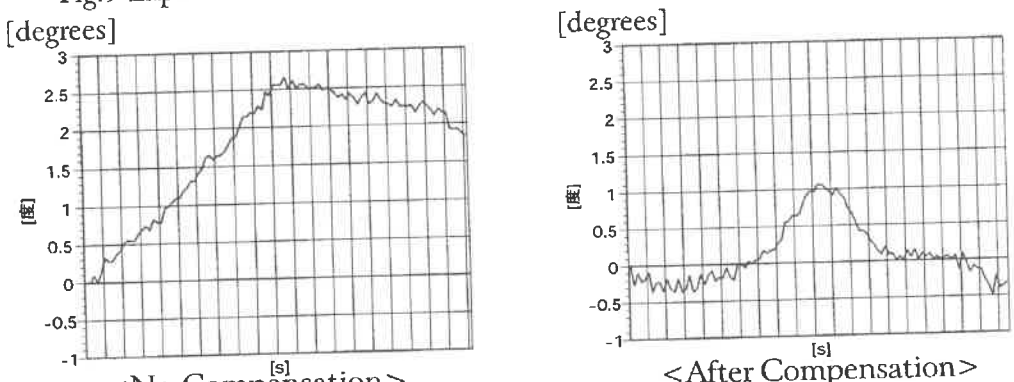

<No Compensation> <After Compensation>

Fig.10 Experimental result of the robot's directions at forward-back movement

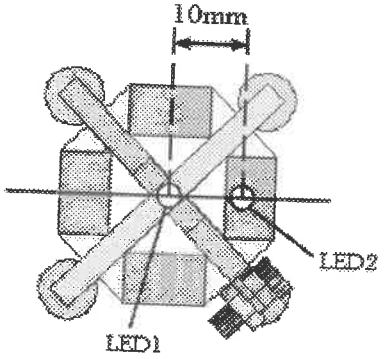

Fig.11 Arramgement of two LEDs in the rotational experiment

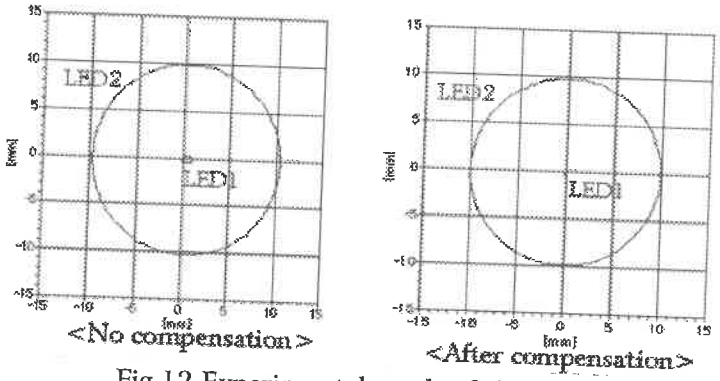

Fig.12 Experimental result of the rotation

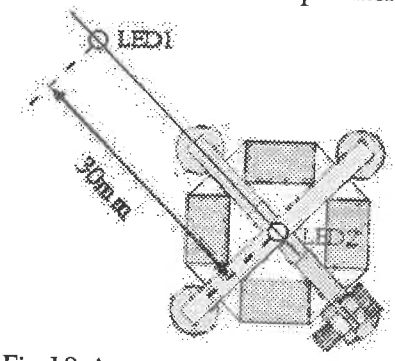

Fig.13 Arrangement of two LEDs in the arc trajectory's experiment

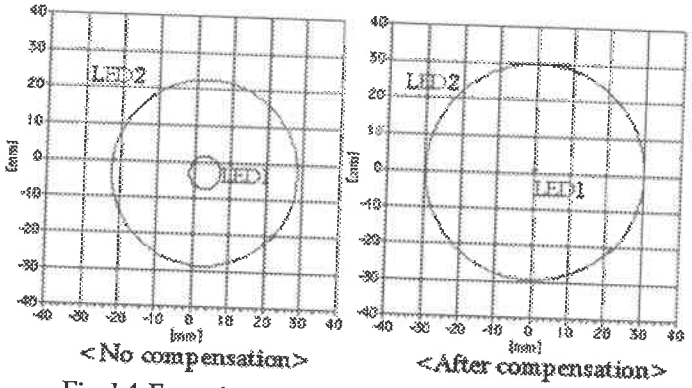

Fig.14 Experimental result of the arc trajectory

feedback system is also required. Moreover, micro tools which can be implemented on this robot to achieve the flexible micro processing under the collaboration by this versatile micro robots have been developing.

References

(1)H. Ishihara, T. Fukuda: Miniaturized Autonomous Robot, Proc. of SPIE, Vol.3202,(1997)pp.191-196

(2)S. Martel, K. Doyle, G. Martinez, I. Hunter, and S.Lafontaine: Integrating a complex electronic system in a small scale autonomous instrumented robot:the NanoWaker Project, Proc. of SPIE, Vol.3834(1999)pp.63-73

(3)S.Fatikow: Automated micromanipulation desftop-station based on mobile piezoelectric microrobots,Proc. of SPIE, Vol.2906, (1996) pp.66-77

(4)N. Kawahara, T. Shibata, T. Sasaya: Inpipe Wireless Micro Robot, Proc. of SPIE, Vol.3834(1999)pp.166-171

(5)T.Kitahara,K.Ashida,M.Tanaka,Y.Ishikawa,N.Oyama and Y.Nakazawa;Microfactory and Microlathe, Proc.of Int. Workshop on Microfactories,(1999)pp.1-8

(6)H. Aoyama, F. Iwata, and A. Sasaki: Desk top flexible manufacturing system by mova ble miniature robots,Proc. of Int.Conf .on Robotics and Automation(1995) pp.660-665

(7)Y.Hatamura,M.Nakao and T.Sato: Con struction of Nano Manufacturing World as a Desk-top Factory,Microsystem technologies 1, (1995)pp.155-162

(8)H.Aoyama and O.Fuchiwaki: Flexible Micro Processing by Multiple Micro Robots in SEM, 2001 IEEE International Conference on Robotics & Automation, (2001)FP04

(9)O.Fuchiwaki and H.Aoyama: Design and Control of Versatile Micro Robot for Microscopic Manipulation, American Society for Precision Engineering, (2001)pp.204-207

2 DOF DYNAMIC ACCURACY MONITORING FOR ROBOT AND MACHINE TOOL MANIPULATORS

Thomas R. Hanak, Oliver Zirn, Wolfgang Ruoff
University of Applied Sciences (FHTE), D-73728 Esslingen

Abstract

Trajectory monitoring at high speed is an important precondition for dynamic performance identification as well as dynamic modeling of robot and machine tool manipulators. In this contribution, a planar parallel measurement system for two dimensional trajectory monitoring is shown that combines accuracy and speed with robust design and low manufacturing costs. Due to the manufacturing, component and assembly errors a suitable calibration method is required that allows error identification and compensation of the parallel mechanism with respect to the rough machine tool or industrial robot environment. The work reported in this paper deals with the calibration of planar parallel measurement systems. Therefore, the high absolute precision of the lattice grid plate in the range of one micrometer is used to identify the errors of the parallel mechanisms. A nonlinear least-squares fit analysis using the Levenberg-Marquardt-Method yields a very robust error identification algorithm that requires only a few minutes of calibration time using state-of-the-art computing software. Exemplary manipulator measurements at machine tools elucidate the performance of this new measurement system that allows high precision measurements in the range of 3 micrometers even with path velocities of 60m/min.

1 Introduction

Up to the early 90's acceptance tests of machine tool and robot manipulators have been realized by static positioning accuracy measurements, e.g. using laser interferometers. With the increasing demand for higher manipulator performance dynamic trajectory monitoring became important.

The most sophisticated inspection tool for arbitrary trajectories (e.g. [1]) is the Lattice Grid Plate [2]. It yields high precision (ca. 1 μm) as well as high resolution (ca. 5 nm) path monitoring at velocities up to 0.5 m/s. The Lattice Grid Plate consists of a steel substrate with a grid of pattern squares. A scanning unit that has no mechanical contact to the plate measures the position with two degrees of freedom (2 DOF). The air gap between plate and scanning unit is in the range of 0.5 - 1 mm.

Inspection devices to measure 3 and more DOF movements are subject of further developments [3]. These high precision systems require careful use, especially in the rough manufacturing environment. Operator or path errors rectangular to the measurement plane as well as falling screws, tools, etc. can cause severe damages to the inspection devices. Especially robot inspection devices require adequate robustness against path errors. On the other hand, the measurement precision for robot acceptance tests is much smaller than the required precision for machine tools.

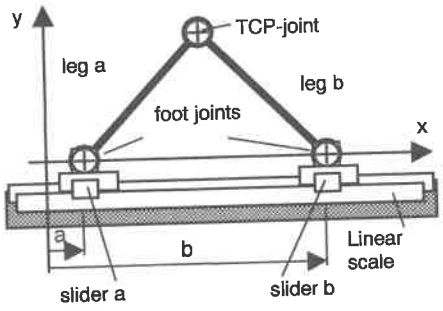

Figure 1: Principle sketch of a parallel 2DOF inspection system.

Experiences gained with parallel manipulators show that these kinematic principles yield very high repeatability with moderate effort [4]. Based on these experiences and the growing need to inspect robot manipulators a parallel 2 DOF inspection device was developed (see Fig. 1 and Fig. 2). The end effector of the robot or the tool center point (**TCP**) of the machine tool is attached at the top joint. The foot joints are guided on a straight line. Their position is measured by a standard linear encoder with two scanning units. For convenience the parallel 2DOF inspection device is from now on called 2DOF-System.

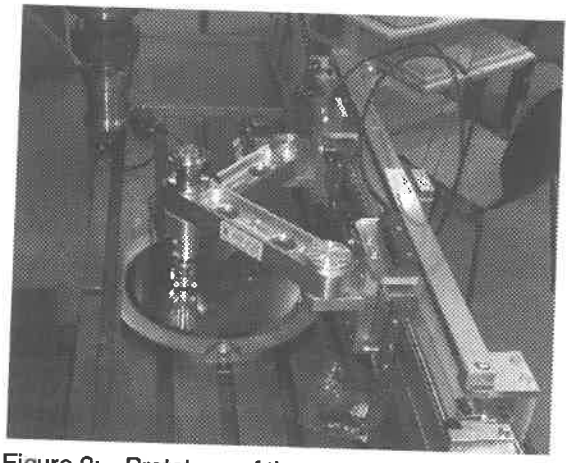

Figure 2: Prototype of the parallel 2 DOF inspection system in the FHTE machine tool laboratory - arranged above the Lattice Grid Plate [2]

2 Requirements and design

The mechanical and operational requirements for the parallel 2 DOF inspection device are:

- circular measurement area (100 mm radius)
- 10μm absolute precision in the measurement area
- 1 m/s resp. 60 m/min maximum path velocity
- robustness against operator errors
- low cost design
- easy to use calibration method

For the recommended circular measurement face the ratio of device size to measurement range is high. Prolongation of the measurement area in the preferred direction parallel to the linear encoder yields better ratios. Thus the system is scalable without any changes to the here shown principle. Especially for large measurement ranges, the „inverse Dinosaur effect" [4] of parallel manipulators leads to increasing system performance of the concept. The mechanical design of the inspection device is based on standard components. The sliders on the guideway support the foot joints of the legs. The scanning units of the linear encoder are connected to the sliders as well. The backlash free and stiff joints with one rotary DOF are realized with angular contact ball bearings. To avoid mechanical stress caused by operator errors (exceeding the measurement range, movements rectangular to the measurement plane) the mechanical interface to the tool center point (TCP) is equipped with a magnetic joint. Braking of a machine tool spindle is not necessary [3].
A PC interface board captures the linear encoder positions. Real time measurement and data recording is implemented in C. Forward transformation and error compensation requires no real time programming. Thus it is integrated in a postprocessor step as well as the graphical display of the inspection result. The application of standard components reduces the costs for the parallel inspection device to a fraction of the Lattice Grid Plate system price. Scaling up the measurement range will cause minor additional costs.

3 Calibration

Neglecting all geometric errors, the forward transformation to calculate the x,y-coordinates of the Tool Center Point (TCP) from the scanning unit positions (a,b) is given by

$$x = \frac{L_a^2 - L_b^2 + b^2 - a^2}{2 \cdot (b - a)}, \quad y = \sqrt{L_b^2 - (x - b)^2}, \tag{1}$$

where $L_{a,b}$ are the leg lengths of the device. If the four variables L_a, L_b, a and b are known, then the exact position of the TCP in the x,y-coordinate system can be calculated. However, due to the manufacturing, component and assembly errors shown in Fig. 3 this is not possible.

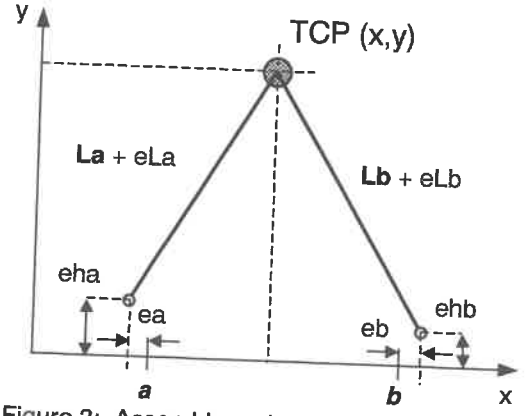

Figure 3: Assembly and manufacturing errors

In order to calculate the TCP coordinates including the possible errors a more general approach has been chosen. With the help of Fig. 4 the x,y-coordinates of the TCP can be related to the four vectors $\vec{r}_a$, $\vec{r}_b$ $\vec{L}_a$ and $\vec{L}_b$.

With $\vec{r}_a = \begin{pmatrix} a_1 \\ a_2 \end{pmatrix}$, $\vec{r}_b = \begin{pmatrix} b_1 \\ b_2 \end{pmatrix}$, $\vec{r} = \begin{pmatrix} x \\ y \end{pmatrix}$ and the relationships $\vec{L}_a = \vec{r} - \vec{r}_a$ and $\vec{L}_b = \vec{r} - \vec{r}_b$, the following set of two equations can be obtained.

$L_a^2 = (x - a_1)^2 + (y - a_2)^2$ and

$L_b^2 = (x - b_1)^2 + (y - b_2)^2$.

The solution of this set of equations will lead the x,y-coordinates of the TCP position in the coordinate system of Fig. 4.

$$x = f(a_1, a_2, b_1, b_2, L_a, L_b) \quad (2a)$$

$$y = f(a_1, a_2, b_1, b_2, L_a, L_b) \quad (2b)$$

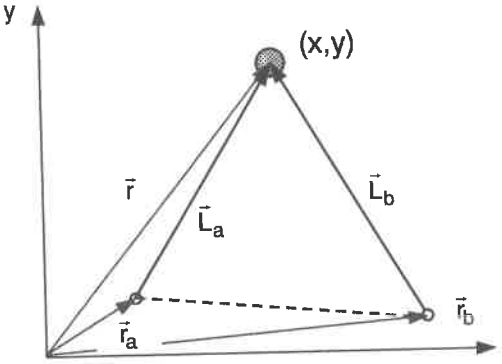

Figure 4: Vector analysis of the TCP position.

The analytic solution is calculated with the help of the computer algebra program MAPLE, but due to the size of the equations the results are not shown here. The six error possibilities of Fig. 3 related to the leg lengths (L_a, L_b) and the scanning positions (a,b) are documented in Table 1.

Variable Name	Comments	Error Variables
L_a	Manufactured leg length $L_a \approx 250$ mm.	eLa
L_b	Manufactured leg length $L_b \approx 250$ mm.	eLb
a_1	Scanning position of the left measuring head.	ea
a_2	a_2 = eha (see Fig. 3)	eha
b_1	Scanning position of the right measuring head.	eb
b_2	b_2 = ehb (see Fig. 3)	ehb

Table 1: Error classification

For the actual calibration measurement the TCP is brought to some arbitrary point in the x,y-plane (the starting point). The measurement software will simultaneously record the x,y-coordinates of the lattice grid plate (LGP) and the two scanning unit positions a_1 and b_1 of the 2DOF inspection device. Then the machine will move the TCP to the next point and the measurement procedure is repeated. Altogether a set of 25 data points from a (40 mm x 40 mm) square were recorded (s. Fig. 5).

Until now the data has been recorded in two different coordinate systems. For comparison a common reference point must be chosen, which

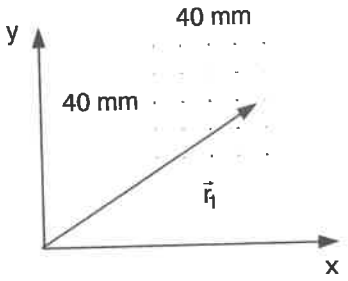

Figure 5: Shape, size and pattern of the measurement area.

will be defined to be the origin of a new mutual coordinate system (This reference point could be any of the 25 data points).

With this definition the new data vectors for the remaining 24 points are calculated for the 2DOF-System as well as for the LGP. Now, if the variables L_a, L_b, a_1, a_2, b_1 and b_2 were known precisely, the calculated x,y-position of the data points in the 2DOF coordinate system should coincide exactly within the accuracy of the LGP coordinate system (As mentioned before, the precision of the LGP in x or y direction is about 1 µm).

A direct comparison of the two data sets after the coordinate transformation with the assumptions $L_a = L_b = 250$ mm (manufacturing specification) and all errors of Table 5 set equal to zero is shown in Fig. 6.

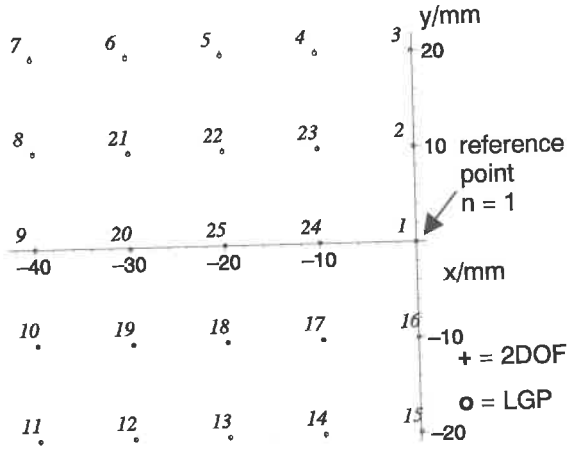

Figure 6: Data points of the LGP and the 2DOF-System after the coordinate transformation (reference point n = 1).

The numbers in Fig. 6 represent the sequence in which the data points were taken and despite the large scale on x and y-axis the deviation between the two data sets can be seen quite well for a number of data points (e.g. n = 5, 6, 7,...). The individual differences in position can

be demonstrated much better by calculating the absolute values dL of the difference vector for each data pair (see Fig. 7)

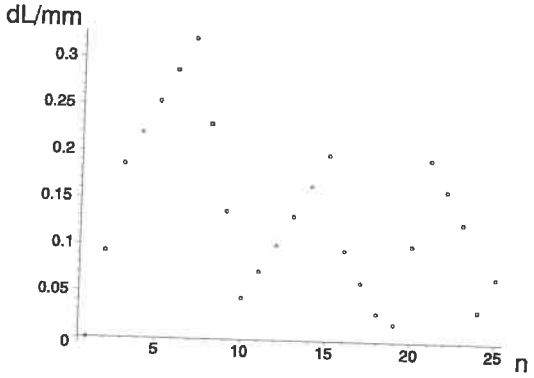

Figure 7: Individual deviations of the two data sets.

From Fig. 7 it can be seen that the maximum deviation is about 320 µm. Notice that the reference point (here n = 1) has no deviation by definition. The average value of all 25 data points comes out to be about 134 µm, which is not an acceptable value compared to the desired precision of at least 10 µm.
It must also be mentioned that another assumption had to be made before plotting the Data in Fig. 7. The x-axis of the LGP was aligned carefully with the x-axis of the 2DOF-System (track in which the scanning positions a and b run). This, however, doesn't guarantee that $\varphi = 0$ and the actual value for φ at this point is unknown (s. Fig. 8).

In general the angle φ must be added to the list

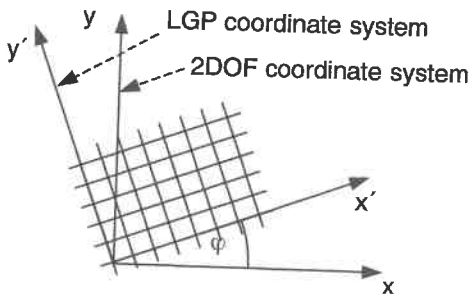

Figure 8: Alignment of the LGP relative to the 2DOF coordinate system.

of error possibilities, because small deviations from a perfect alignment will lead to a wrong calibration. At first it seems, that including the angle φ in the list of unknowns makes the task more difficult. However, if the calibration algorithm works despite the additional variable φ, then the LGP can simply be put in the x,y-plane without a tedious and time consuming alignment. With the angle φ, a comparison of the two data sets requires an additional rotation of one of the two data sets by the rotation matrix

$$\vec{r}' = \begin{pmatrix} \cos\varphi & \sin\varphi \\ -\sin\varphi & \cos\varphi \end{pmatrix} \vec{r} .$$

Before discussing the details of the calibration procedure jet another difficulty must be pointed out. As mentioned above, a common reference point was chosen with the assumption, that the TCP and the LGP coordinate systems are fixed in space when the data is acquired. However, due to inevitable vibrations of the running machine there is always some random movement in the order of a few µm (This variation can be estimated in a static position from the digital reading of the LGP positions). Therefore, we cannot assume that the measurement of the reference point in the LGP coordinate system would always give the exact same readings. In fact this has to be compensated for by two more fit-parameters exK and eyK, the random errors in the x,y-positions of the LGP at the instantaneous moment of the data acquisition. In summary this leaves us with the problem of how to find the best estimates for the possible errors eLa, eLb, ea, eha, eb, ehb, φ, exK and eyK in order to find the lowest average deviation.
By closer examination two of the 9 variables can be omitted right away. If we go back to Fig. 3 one can see, that in principle it takes 6 degrees of freedom to determine the absolute position of the triangle (a, b, TCP) in space. Choosing a common reference point in space for the two coordinate systems eliminates two degrees of freedom, because the absolute position in space of the triangle becomes unimportant. Relevant now, is only the shape and orientation of the triangle and for that 4 parameters are sufficient. Our choice was to set eb and ehb equal to zero and work only with the variables eLa, eLb, ea and eha in addition to φ, exK and eyK. This leaves us with the problem of adjusting 7 parameters for a best result. The main idea how to accomplish this is task is shown in Fig. 9.

For each data point the length of the difference vector dL_i should be as small as possible. It is therefore reasonable to define a function F as the sum of all quadratic errors

$$F = \sum_i (d\vec{L}_i)^2 ,$$

which should also be as small as possible.

Because each $d\vec{L}_i$ is a function of eLa, eLb, ea, eha, φ, exK and eyK this function needs to be

minimized with respect to the above parameters. With the definition of the parameter vector

$\vec{u} = (u_1,\ldots,u_m) = (eLa, eLb, ea, eha, \varphi, exK, eyK)$

the minimum of the scalar function F can be found by setting the gradient of F equal to zero, so that the condition $\nabla F(\vec{u}) = 0$ must be solved for the desired calibration parameters.

In order to solve this problem we adapted a nonlinear least squares fit algorithm which can be found in the book by Hörhager [5]. In the

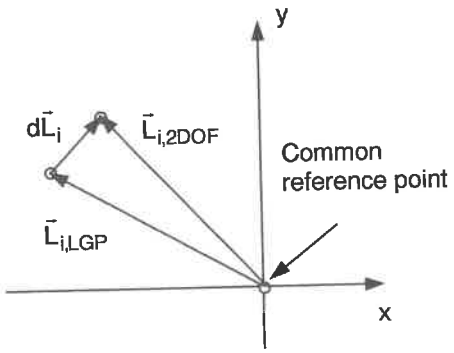

Figure 9: Difference Vector $d\vec{L}_i$ between the LGP and the 2DOF-System.

same book there is also a brief discussion of the Levenberg-Marquardt method, which is the basis of this program. Unfortunately this program only returns the optimized parameters $(u_1 \ldots u_m)$ without the uncertainties in the parameters. This, however, is an essential information for a good calibration routine. A more detailed explanation of the Levenberg-Marquardt method can be found in the book by Bevington and Robinson [6]. There it is also explained how to retrieve the standard deviations $(s_1 \ldots s_m)$ and the covariances $(c_{12}, c_{13}, \ldots c_{m,m-1})$ of the optimized parameters from the error matrix.

Before running the procedure not only the function $F(\vec{u})$, but also a starting vector $\vec{u}_0$ needs to be passed on to the program. The starting vector and the results of the optimized parameters for the first measurement are shown in the Table 2.

With seven fit-parameters the calibration routine takes about 3 min for conversion using a Pentium 4 processor with 1024 MB RAM. Using the optimized values the individual deviations were calculated and displayed in Fig. 10.

In comparison to Fig. 7, a significant reduction of the individual deviation has been achieved.

Parameters	Starting values	Optimized values	Standard deviation s_i
eLa	0.1 mm	0.30 mm	0.18 mm
eLb	0.1 mm	0.10 mm	0.18 mm
ea	1.0 mm	1.53 mm	0.18 mm
eha	0.1 mm	0.13 mm	0.18 mm
φ	0.057°	-0.184°	0.003°
exK	3 µm	-2.1 µm	1.0 µm
eyK	3 µm	0.7 µm	1.4 µm

Table 2: Starting values and optimized values for the best fit.

Almost all deviations between the 2DOF-System and the LGP are less than 5 µm. The worst data point (n = 11), gives about 6 µm and about 20% of the data pairs are less than 1 µm apart. Please note also, that the deviation for data point n = 1 (reference point) is not zero. From Fig. 10 it can be seen that the deviation for n = 1 is about 2.2 µm, which is nothing else then the numerical value of $\sqrt{exK^2 + eyK^2}$ using the data of Table 2. As a matter of fact, the determined values of exK and eyK mirrors the expected vibrational amplitudes of the machine movement. The average value of all 25 data points has been calculated to 2.3 µm. It might be pointed out, that the choice of a reference point other than n = 1 would lead to a different graph then Fig. 10, but the average value of all data points would always be the same. This outcome for different reference points was verified numerically, which is an important validation of this calibration algorithm.

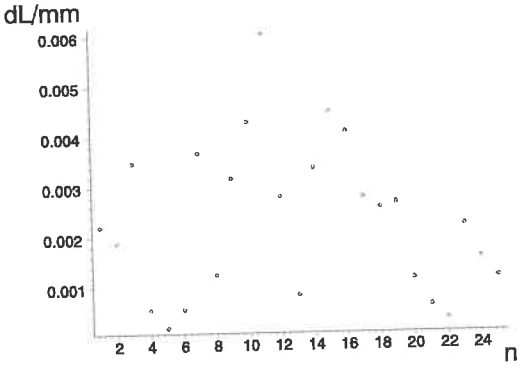

Figure 10: Individual deviation with optimized fit parameters

It might be emphasized that the average deviation of 2.3 µm for different reference points could not be achieved if the two fitting

parameters exK and eyK were excluded from the fit. In this case the average value could be significantly larger (up to 70%) in comparison to the minimum value. The mere fact that the optimized parameters in Table 2 produce the graph in Fig. 10 is sufficient evidence, that the calibration routine works extremely well to achieve an excellent precision. A number of other verifications for the validity of the procedure will be given below.

It might also be remarked that the determined angle $\varphi = -0.184°$ (see Table 2) indicates a fairly good alignment between the 2DOF-System and the LGP. However, if the fit is performed without the angle φ (i.e. $\varphi = 0$ assumed), the best average value for the above data set would be about 43 μm. In comparison to the actually achieved 2.3 μm this indicates how crucial it is to include the angle φ in the calibration routine.

The low average deviation was verified by calculating the standard deviation s_r of the position vector $\vec{r}$.

$$s_r = \sqrt{(\frac{\partial r}{\partial u_1})^2 s_1^2 + (\frac{\partial r}{\partial u_2})^2 s_2^2 + \ldots + 2\, c_{12} (\frac{\partial r}{\partial u_1})(\frac{\partial r}{\partial u_2}) + \ldots}$$

Including all standard deviations and covariances of the fit variables s_r was calculated to be 2.0 μm which is in excellent agreement of 2.3 μm.

In addition the straight leg position of the TCP was measured directly by the positions a_1 and b_1 of the 2DOF-System

$$L_0 = b_1 - a_1 = (501.768 \pm 0.002)\ \text{mm}$$

and was calculated from the determined fit parameters of Table 2

$$L_0 = ea + L_a + L_b = (501.93 \pm 0.11\ \text{mm}).$$

One can see, that the directly measured value of 501.768 mm lies within two standard deviations of the calculated result, which represents a 95 % confidence level.

In order to show reproducibility the measurement of the 25 data points was repeated three times. First the LGP was left in place, but a different location in absolute space was chosen for the square of the data points (Data set 2). Then two more measurements were performed, where the LGP was rotated by about an angle of 30° (Data set 3 and 4). It was our goal to show, that the calibration routine works equally well for arbitrary angles between LGP and 2DOF coordinate systems (s. Fig. 8). The result for the average deviation of all four measurements is shown in Fig. 11.

All measurement show reproducible average values around 3 μm. The standard deviation for each measurement is about 1.6 μm, so that one can conclude that a precision of less than 6.2 μm can be assumed for any data point with a 95 % confidence level.

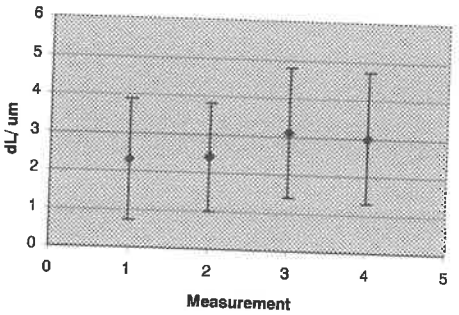

Figure 11: Average deviation between LGP and 2DOF for four different measurements (25 data points each).

5 Summary

The parallel 2 DOF inspection device is an easy to use trajectory monitoring tool for machine tool and robot manipulators. The high repeatability of parallel mechanisms and suitable error compensation yield sufficient accuracy in the range of 3 μm. As the amplitudes of the mechanical vibrations of the machine are also in the order of a few μm, this accuracy represents a result close to the lowest possible limiting values.

The system has a simple and low cost mechanical design. It is robust against operator and path errors as well as manufacturing environment influences. The new inspection tool will be used at the FHTE for machine tool diagnosis as well as for dynamic robot manipulator measurements to validate simulation models.

References

[1] N.N.: *ISO 230-1..4 – Test code for machine tools* International Organization of Standardization, 1996.
[2] Zirn, O.; Weikert, S.: *Dynamic Accuracy Monitoring for the Comparison and Optimization of Fast Axis Feed Drives.* Proceedings ASPE 12th Annual Meeting, , Norfolk, 1997.
[3] Weikert, S.: *Dynamic Accuracy Monitoring.* Proceedings ASPE 14th Annual Meeting, 1999.
[4] Zirn, O.; Treib, T.: *Similarity Laws of Parallel and Serial Manipulators for Machine Tools.* Proceedings, MOVIC'98, IfR ETH Zürich, 1998.
[5] M. Hörhager, *Maple in Technik und Wissenschaft,* (Addison-Wesley, 1996)
[6] P. R. Bevington and K. D. Robinson, *Data Reduction and Error Analysis for the Physical Sciences* (McGraw-Hill, 1992).
[7] J. R. Taylor, *An Introduction to Error Analysis* (University Science Books, 1997).

KINEMATIC COUPLING INTERCHANGEABILITY

A. John Hart (ajhart@mit.edu), Alexander H. Slocum
Precision Engineering Research Group
Massachusetts Institute of Technology, Cambridge, MA

I. Introduction

Traditional studies of kinematic couplings, such as those by Slocum, Mullenheld, and Poovey [1,2,3], have focused on the need for high interface repeatability; however, modular machines and instruments require rapid, accurate interchangeability. Interchangeability of a kinematic coupling is the tendency of the centroidal frame of the top half of the interface to return to the same position and orientation relative to the centroidal frames of different bottom halves when switched between them [4,5].

When a kinematic coupling is used to mount a machine or component, the mounting error arises from irregularities in the surface and preload conditions, manufacturing variation in the interface geometry, and environmental influences such as temperature changes. The translational and rotational components of these errors are reflected through the structural path of the machine by geometric transformations, giving the error contribution from the kinematic coupling at a point of measurement interest, such as the tool tip. The goal here is to model interchangeability and to determine if measurement of kinematic coupling contacts before interface mating can be used to decrease interchangeability error. The results are applied to kinematic coupling designs for the base and wrist of an industrial robot.

II. Kinematic Coupling Designs

A typical kinematic coupling mates a triangular configuration of three hemispheres on one interface plate to three "vee" grooves on another interface plate, thus enabling essentially exact constraint of the six-degrees of freedom between the two bodies by Hertzian surface contact at six small regions. The main caveat to traditional ball/groove couplings, where the sphere diameters are approximately the widths of the vee grooves to which they mount, is that their load capacity is limited to that of the small contact regions.

To achieve greater load capacity yet maintain repeatability, the "canoe ball" shape (named as such because it looks like the bottom of a canoe) evolved to include an integrated tooling ball for calibration as shown in Figure 1. The "canoe", made by precision contour grinding, emulates the contact region of a ball as large as one meter in diameter in an element as small as twenty-five millimeters across.

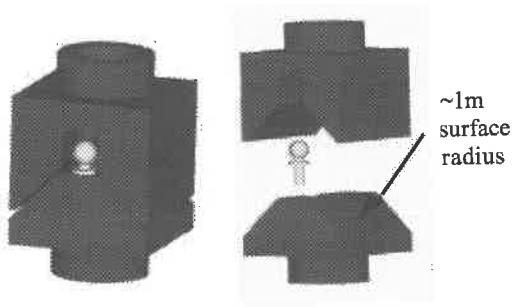

Figure 1: Canoe ball coupling elements.

III. Interchangeability Model

Neglecting the small variations in repeatability that may occur from relatively larger errors in the coupling geometry, a first-order estimate of the total mounting error for a kinematic coupling is the sum of the repeatability and the interchangeability errors. Repeatability of typical ball-groove and canoe ball kinematic couplings has been measured at one micron and better under well-controlled mounting conditions [1,2].

Interchangeability, on the other hand, is a deterministic geometric error. The kinematic behavior of a triangular coupling layout reduces the interchangeability error at the center of stiffness (the coupling centroid) to about one-third of the error of the coupling placements. The remaining error can be reduced by mapping the geometric errors based on the measured positions and orientations of each of the balls and grooves.

To model the interchangeability, first consider a general machine design application in which two

modules mate through an interface of ball-groove kinematic couplings, shown for an industrial robot in Figure 2. The grooves sit on a plate fixed to the floor and the mating balls are attached to the foot of the robot. Reference coordinate frames are placed centroidally on the groove set (A_{groove}) and the ball set (A_{ball}), and the couplings are secured using a sufficient (e.g. bolted) preload. The tool center point (TCP) and co-located coordinate frame (A_{TCP}) are offset from the ball coordinate frame by a translation and rotation described by the homogeneous transformation matrix (HTM), ${}^{TCP}T_{Ball}$. When the coupling balls and grooves are placed nominally, A_{ball} and A_{groove} are coincident.

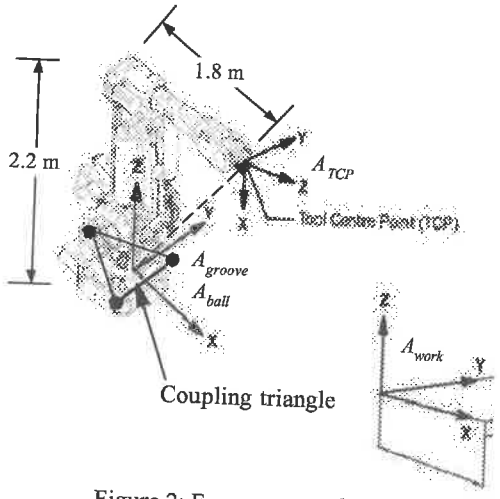

Figure 2: Frame nomenclature.

When error in the kinematic couplings is present, the total error at the TCP is the sum (average of worst-case and RSS) of the component errors at each of the contact points, expressed as a transformation matrix between the nominal and true centroidal frames of each interface half. These matrices, calculated using measurements of the contact points before the interface halves are mated, are denoted ${}^{Ball-true}T_{Ball-nom}$ and ${}^{Groove-true}T_{Groove-nom}$, and are specified to a model of the kinematic constraints between the balls and grooves. The output of the model, ${}^{Ball-true}T_{Groove-true}$, represents the mating error between the centroidal frames

The interface transformation, ${}^{Ball-nom}T_{Grv-nom}$, accounts for the total interchangeability error between the kinematic coupling balls and grooves:

$$ {}^{Ball-nom}T_{Grv-nom} = ({}^{Ball-true}T_{Ball-nom})^{-1} \cdots \cdots {}^{Ball-true}T_{Groove-true} \; {}^{Groove-true}T_{Groove-nom} \quad (1) $$

This is added to the machine's forward kinematics to reduce the interchangeability error at the TCP, giving the residual error transformation at the TCP:

$$ {}^{TCP-corr}T_{TCP-nom} = (T_{interface} \cdot {}^{TCP-true}T_{Grv-nom})^{-1} \cdots \cdots {}^{Work}T_{Grv-nom} \quad (2) $$

IV. Interchangeability Solution Method

When contact surfaces or offset features such as tooling balls of kinematic couplings are measured, the geometric mating relationship between the centroidal frames of the interface halves is found by solving a system of twenty-four linear equations. Specifically, measurement of the canoe ball interface gives location estimates for the following features of the balls and grooves, shown in Figure 3:

1. $[R_1, ..., R_6]$: The radii of the six spherical contact surfaces.
2. $[\hat{q}_{S,1}, ..., \hat{q}_{S,6}]$: Position vectors directed from each sphere center to the centroid of the ball interface.
3. $[b_1, ..., b_6]$: The base points of the six groove flats, relative to the measurement frame (A_{MS}).
4. $[\hat{N}_1, ..., \hat{N}_6]$: Normal vectors to the six groove flats, in A_{MS}.

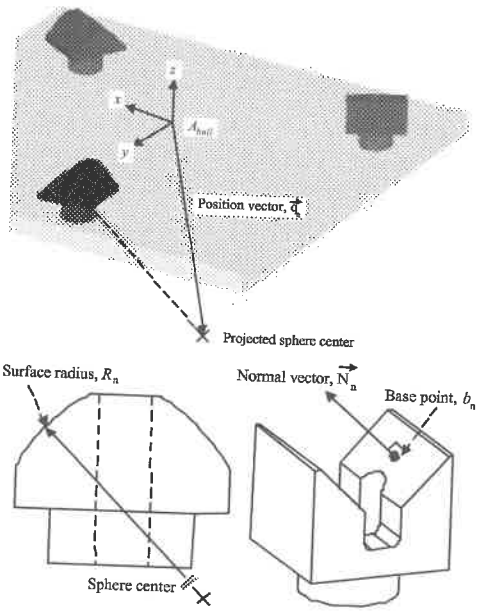

Figure 3: Canoe ball and groove measured features.

The eighteen unknown rest positions of the sphere centers are denoted $[p_{S,1}, \ldots, p_{S,6}] = [(x_{S,1},y_{S,1},z_{S,1}), \ldots, (x_{S,6},y_{S,6},z_{S,6})]$. The remaining six unknowns are the six error offsets between the centroidal frames of the interface plates, $[\varepsilon_x, \varepsilon_y, \varepsilon_z, \theta_x, \theta_y, \theta_z]$.

Separating variable and constant coefficients, the system has form $AX = B$, where X is the 24-element vector containing the unknown final positions of the spheres with respect to the measurement system and the six error motions of the interface. After inverting A and multiplying the result by B, the six error motions between the centroidal frames are elements of X. With small angle approximations, the transformation between centroidal frames is

$$ {}^{Ball-true}T_{Grv-true} = \begin{bmatrix} 1 & -\theta_{z_c} & \theta_{y_c} & \varepsilon_{x_c} \\ \theta_{z_c} & 1 & -\theta_{x_c} & \varepsilon_{y_c} \\ -\theta_{y_c} & \theta_{x_c} & 1 & \varepsilon_{z_c} \\ 0 & 0 & 0 & 1 \end{bmatrix}. \quad (3) $$

To construct the system of equations, first consider that when the interface is seated, the projected center of each spherical surface will be as close as possible to its mating groove. Hence, the line passing through the projected center of the each sphere and the contact point between the sphere and its mating groove flat will be normal to the flat. Then, the distance between the projected sphere center and the groove flat is equal to the measured radius of the spherical surface. For example, the mathematical constraint between the first sphere and mating flat for the first canoe ball to groove pair, with unknown p_1, is

$$ \frac{(p_1 - b_1) \cdot \hat{\mathbf{N}}_1}{\|\hat{\mathbf{N}}_1\|} = R_1 . \quad (4) $$

A group of six similar equations, one for each sphere/flat pair, contains the eighteen final coordinates of the sphere centers as unknowns.

Second, the measured distances between the sphere centers, calculated using $[q_{S,1}, \ldots, q_{S,6}]$, must not change. The motions $[\varepsilon_x, \varepsilon_y, \varepsilon_z, \theta_x, \theta_y, \theta_z]$ of the centroidal frame of the ball interface (A_{ball}) with respect to the centroidal frame of the groove interface (A_{groove}), can be expressed in terms of the final positions of the sphere centers. In order to calculate the matrices A and B, small angle approximations must be made such that:

$$ x_{S,1} = \delta_{x_c} + u_{S,1} - v_{S,1}\theta_{z_c} + w_{S,1}\theta_{y_c}, \quad (5) $$

$$ y_{S,1} = \delta_{y_c} + u_{S,1}\theta_{z_c} + v_{S,1} - w_{S,1}\theta_{x_c}, \quad (6) $$

$$ z_{S,1} = \delta_{y_c} - u_{S,1}\theta_{y_c} + v_{S,1}\theta_{x_c} + w_{S,1}. \quad (7) $$

Taken for the position of each sphere, these are the final eighteen equations of the system.

V. Model Validation

The canoe ball interchangeability model was validated by building a series of small prototype models and measuring the error in the positions and orientations of their centroidal frames over all possible combinations of ball sets and groove sets. A large baseplate with two arrangements of six grooves at equal 60-degree angles around a center point, and ten smaller top pallets each with an equilateral canoe ball arrangement, were manufactured. To ensure statistical confidence in the calibration-interchangeability relationship, the locations of the coupling mounting and alignment hole pairs on each plate were intentionally perturbed within circular tolerances zones of 3-sigma diameter 0.64 mm from their nominal positions.

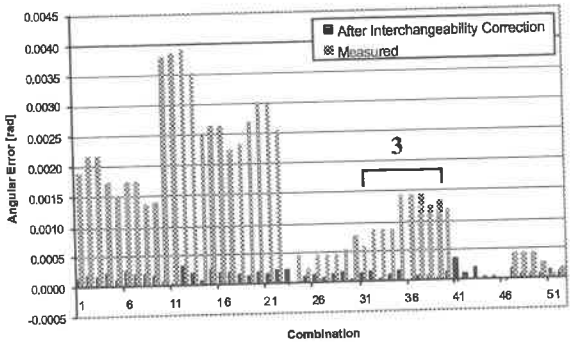

Figure 4: In-plane error of canoe ball pallets.

Figure 4 plots the in-plane angular error of each interface combination (choice of a pallet, groove set on the baseplate, and relative orientation), as measured between the centroidal frames, and after the transformation correction was applied. The combinations are grouped for each of the five pallets. The fifth pallet, for which the interchangeability correction actually increases the error for some trials, was machined with no more than 0.01 mm deviation from the nominal mounting hole locations. Over all trials, applying the interface transformation reduced the placement error by an average of 92%.

VI. Application to Industrial Robots

Kinematic couplings were designed for the base and wrist interfaces of an ABB IRB6400R six-axis industrial robot manipulator, shown in Figure 5. The base is normally restrained with eight 20 mm diameter bolts. The new three-bolt base alternatives are a canoe ball interface, a three-pin interface (see [6, 7] for details), and a groove-cylinder interface (see [4] for details). The new wrist mountings used canoe ball couplings, or a three-pin coupling.

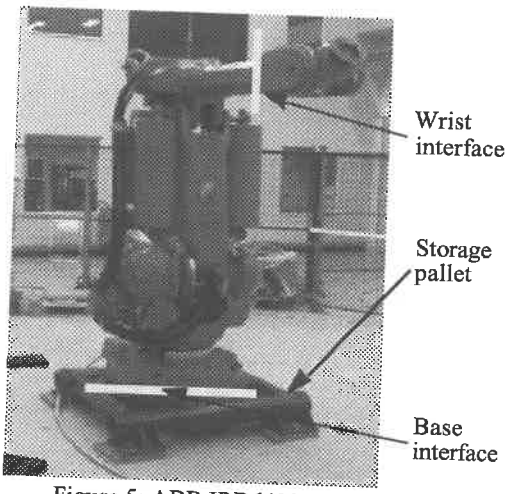

Figure 5: ABB IRB6400R industrial robot.

Interchangeability simulations specified the geometry of the manufactured prototypes and manufacturing and assembly tolerances representative of high volume production. 10,000 iterations were conducted for each level of calibration complexity (from no measurement, to measurement of two points per mount).

For the base interface, the interchangeability model predicts that the interface transformation accounts for approximately 50% or 0.11 mm of the 0.22 mm average total interchangeability error when full calibration is performed relative to offset measurement features. Similar results were obtained for the wrist interface. When the contact surfaces are measured directly, the interchangeability analysis reduces the tool point error by 88% to 0.02 mm. In the latter case, the remaining error is solely from measurement error; in the former case, variation in the dimension and placement of the measurement feature is also a factor. Negligible accuracy is gained by knowledge of the relative orientations of the balls and grooves. Hence, unless the process of mounting the couplings to the plates is poorly controlled, only measurement of a single feature is needed for very good performance when offset measurement is performed.

VII. Conclusions

Direct measurement of the contact points on the halves of a kinematic interface can greatly reduce the effect of tolerance errors on mounting accuracy, with the residual interchangeability error based only on the error of the measurement procedure. In production, by making the contact surface measurements ahead of time, calculation of the interface transformation would be a step of the machine calibration routine. Ideally, the software would take the measurement values for the components, calculate the interface HTM, and apply it to the machine kinematics. The pre-measured placements of the contacts could be written to an identification tag on the interface, or the interface serial number could serve as a database key to the calibration data.

Acknowledgements

This work was supported by grants from ABB Corporate Research and the Ford-MIT Alliance.

References

[1] Slocum, A.H. and Donmez, A. "Kinematic Couplings for Precision Fixturing, Experimental Determination of Repeatability and Stiffness", Precision Engg, 1988, 10(3), 115-122.

[2] Mullenheld, B. "Application of Kinematic Couplings to a Grinding Wheel Interface", S.M. Thesis, University of Aachen, 1999.

[3] Poovey, et al. "A Kinematically-Coupled Magnetic Bearing Test Fixture," Precision Engg, 1994, 16(2), 99-108.

[4] Hart, A. J. "Design and Analysis of Kinematic Couplings for Modular Machine and Instrumentation Structures", SM Thesis, MIT, 2001.

[5] Slocum, A.H. Precision Machine Design, Society of Manufacturing Engineers, 1992.

[6] Slocum, A.H. and Braunstein, D. "Kinematic Coupling for Thin Plates and Sheets and the Like," U.S. Patent 5,915,768, June 29, 1999.

[7] Willoughby, P. "Kinematic Alignment of Precision Robotic Elements in Factory Environments," S.M. Thesis, MIT, 2002.

Novel Linear Motor for High Precision Stage of Semiconductor Lithography System

Moon G. Lee, K. H. Kim, and D.-G. Gweon

ME3265, Department of Mechanical Engineering, Korea Advanced Institute of Science and Technology

373-1 Kusung-Dong, Yusong-Gu, Taejon, 305-701, Korea

I. Introduction

Stages used in semiconductor lithography system must satisfy needs of high precision positioning. The needs are high speed and high accuracy. The accuracy is about several nm and the speed is about 100msec of settling time for 20mm step. In addition to the needs, the stage must be able to move over the long stroke of 300mm, which is wafer size of next generation. Typical configuration of the stages is presented in Fig. 1.

Brushless permanent magnet linear motors offer significant advantages that can satisfy the mentioned requirements. The linear motor inherently has infinite stroke and resolution if guide mechanism can be selected ideally. We construct the linear motor symmetrically and it is guided by air bearing as depicted in Fig 2. Translation motion of the motor is delivered directly. The air bearing enables the system move smoothly for it has no friction. In addition to the smoothness, the symmetry of the two motors in both side of the bearing makes the system robust to environment such as heat, humidity and etc. and the attracting force between the stator and the mover diminished. The guide mechanism and the linear motor makes the stage simple, light, and smooth so the system can be controlled simply and moved rapidly.

In this paper we propose a novel multi-pole permanent magnet array. The magnet array has trapezoidal magnets. To design the linear motor, we propose a modeling method that describe magnetic filed of magnets and coil of the motor more accurately and effectively. Using this method, accurate design will be obtained and batch process can be easily applicable to perform, for example, optimal design, dynamic simulation and etc.

III. Linear motor with multi-segmented trapezoidal magnet array

Conventionally, salient-poles are used to maximize magnetic flux density in air gap where stator coil is wounded, however, the saliency can cause force ripple originated from the variation of reluctance between stator and mover. The force ripple is detrimental to precision positioning of the motor. Non-salient stator can be adopted to remove the force ripple, however, actuation force of the motor is not sufficient for it has lower magnetic flux density than salient motor. The alternative to remove the ripple and to improve the actuation force of linear motor is introducing multi-segmented permanent magnet array. Using the magnet array, the magnetic flux density can be so highly confined to stator winging that actuation force of the motor can be high. The principle of the multi-segmented magnet array is shown in Fig. 3. [1,2]

In this paper we propose a novel multi-segmented permanent magnet array. The magnet array has trapezoidal magnets as depicted in Fig. 4. Magnetization of the magnets has equal magnitude and direction that advances by 180/N deg. from one magnet to the next. N is segment number of magnets per pole pitch of the array. Using the magnet array, the magnetic flux density can be highly confined to stator winding. Actuation force of the motor with proposed and conventional magnet array is compared under condition of same volume and power of motor.

III. Modeling and design of the motor

To design the linear motor, we propose a modeling method that describe magnetic filed of magnets and coil of the motor more accurately and effectively. We can model magnet array with more complicated shape and magnetization direction and account end effect of mover precisely.

Firstly, the filed due to a single magnet in free space has been calculated using the method proposed by Halbach in the following equation. [1] In the equation, z* means conjugate of z and integration path is along the surface of the magnet.

$$B^*(z_0) = -\frac{B_r}{4\pi i}\oint \frac{dz^*}{z_0 - z}$$
$$\text{where } B_r = B_m + iB_m,\ z_0 = x + iy \qquad (1)$$

If the stator has infinitely permeable, long and thick, the magnetic flux is normal to the upper surface of the stator. To meet this boundary condition, the image magnet with same magnitude of magnetization is introduced in the opposite side of the surface at same distance with the real magnet. The magnet has identical y-directional but opposite x-directional magnetization. Superposing the field by the real and image magnet, we can obtain the field due to a single magnet above the stator yoke. After obtaining the field of the each magnet in Fig. 4, the field by the magnet array can be calculated by superposing the field. For 2-segmented magnet array with trapezoidal magnet, the calculation is verified by the finite element method in Fig. 5. The field due to the stator coil can be calculated in similar way. Using the field, we can calculate the force, back emf or inductance of the motor.

This modeling can be used as a general design tool for non-salient brushless permanent magnet DC motor. Using this method, accurate design will be obtained and batch process can be easily applicable to perform, for example, optimal design, dynamic simulation and etc.

IV. Discussion and conclusion

We perform optimization of the motor to maximize the force per volume of the motor under the geometrical, electrical constraints. Usually, active constraint is the power of the electrical circuit. Investigating the optimization results, the 4-segmented magnet array can produce maximum force per volume of the motor. This is in contrast in Marinescu's results. Marinescu studied multi-segmented rectangular magnet array and insisted that the 3-segmeted

one can produce more force. [3] However, if the thickness of the magnet is not limited and the gap is large compare to magnet thickness, 4-segmeted one can produce more force for same volume of the motor. The optimization results are compared in Table 2.

To apply the system to stage of semiconductor lithography, the motor most be able to carry enough load and move with high speed. The motor can move the load 15 kg with acceleration of $2.5m/s^2$.

Reference

[1]. K. Halbach, "Design of Permanent Multipole Magnets with Oriented Rare Earth Cobalt material", Nuclear Instruments and Methods, Vol. 169, No. 1, pp. 1-10, 1980.

[2] J. Ofori-Tenkorang and J. H. Lang, "A Comparative Analysis of Torque Production in Halbach and conventional Surface-Mounted Permanent-Magnet Synchronous Motors", IEEE IAS Annual meeting, Oct. 8-12, 1995, pp. 657-663.

[3] M. Marinescu and N. Mrinescu, "New Concept of Permanent Magnet Excatiation for Electrical Machines. Analytical and Numerical Computation", IEEE Transactions on Magnetics, Vol. 28, No. 2, March 1992, pp.1390-1393.

Table 1 Constraint of optimization

Constraint 1	heat generation ≤ heat emission
Constraint 2	commutation ripple ≤ 5 % of actuation force
Constraint 3	operation current ≤ 1.7 A
Constraint 4	voltage of stor coil ≤ 82.5 V

Table 2 Comparison of optimization results

	2-segmented	3-segmented	4-segmented
Force per Volume (N/m^3)	2.54e4	3.36e4	3.70e4
Magnet thickness ($*L_t/8$)	1.04	1.51	2.00
Air gap (mm)	3.32	4.13	4.90

* L_t is pitch of the motor

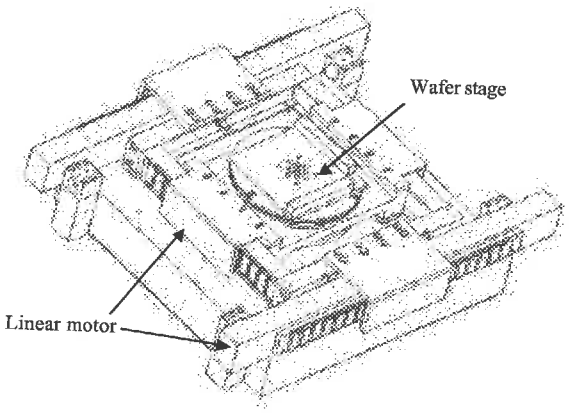

Fig. 1 A wafer stages of semiconductor lithography system

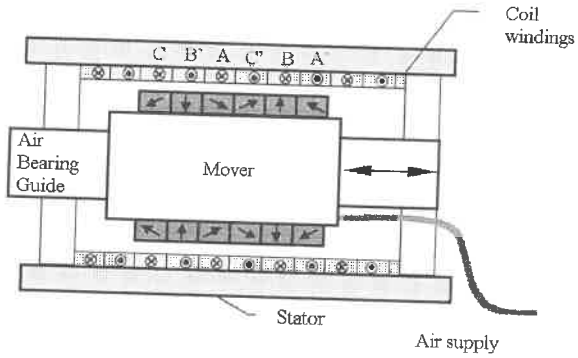

Fig. 2 Linear motor system guided by air bearing

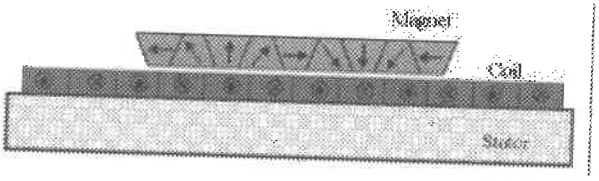

Fig. 4 Concerned model of a multi-segmented trapezoidal (MST) magnet array

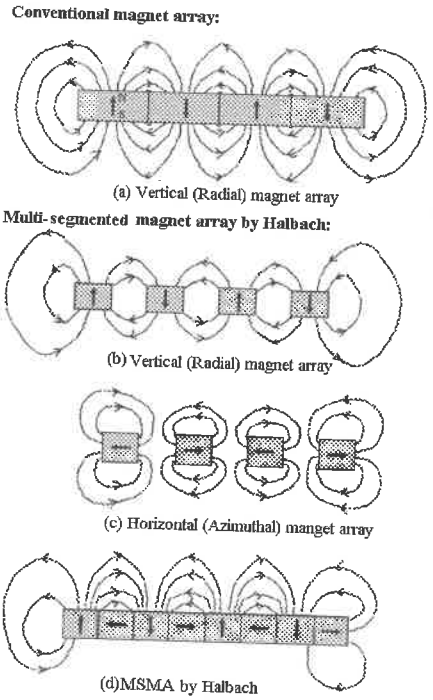
Conventional magnet array:
(a) Vertical (Radial) magnet array
Multi-segmented magnet array by Halbach:
(b) Vertical (Radial) magnet array
(c) Horizontal (Azimuthal) manget array
(d)MSMA by Halbach

Fig.3 Intuitive illustration of flux distribution in conventional magnets array and MSMA proposed by Halbach.

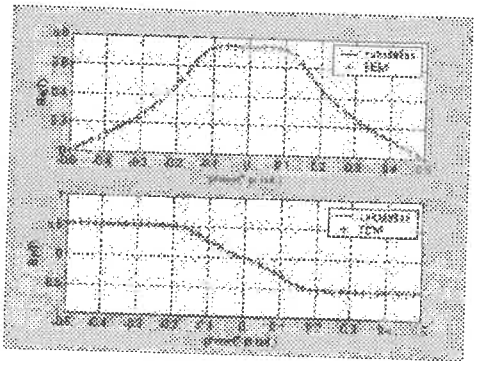

Fig. 5 Verification of the model using FEM: the flux density along coil surface.

CONSTRUCTION AND ALIGNMENT OF A KOLSKY BAR APPARATUS

Richard L. Rhorer, Matthew A. Davies*, Michael D. Kennedy, Brian S. Dutterer, and Timothy J. Burns
National Institute of Standards and Technology
Gaithersburg, MD 20899
*University of North Carolina, Charlotte, NC 28223-0001

Introduction

There is great interest in modeling machining processes to aid in the selection of optimum tooling and cutting parameters in modern manufacturing facilities. Implementing machining process models is often limited by not having appropriate material properties for the work piece material. This is complicated by the fact that most of the material data available is from tests performed at low strain rates and at room temperature, whereas the machining processes involve very high strain rates and very rapid heating of the material in the cutting zone. The relationship of stress to strain (how much a material deforms under a given load and often referred to as the stress-strain curve or constitutive material model) at high strain rates and high temperatures can often be very different from the normal "handbook" relationship. Therefore, a vital step in developing and implementing effective machining models is to provide appropriate stress-strain relationships for materials of interest to industry. In 2001, a project was started at NIST – Materials Data and Metrology for Machining Simulation — to obtain and provide to industry such data. The project includes building a unique facility using a traditional Kolsky bar apparatus, combined with a fast pulse-heating capability. The goal is to rapidly heat a material sample with an electrical pulse, and then immediately perform a Kolsky bar compression test, thereby providing high-strain-rate, pulse-heated material response data.

The most widely used method for obtaining high strain rate material data is the split Hopkinson pressure bar, often called a Kolsky bar. This dynamic testing method of impacting a long bar and studying the stress waves produced in the bar was pioneered by Bertram Hopkinson early in the 20th Century. By the middle of the century, H. Kolsky[1,2] developed enhancements of the Hopkinson method by splitting the bar into two parts, with the sample to be tested sandwiched in between. He demonstrated both analytically and experimentally that the apparatus could be used to obtain high-strain-rate stress-strain curves for materials. Many researchers have made significant contributions to further develop the method; a comprehensive article (including a list of 114 references) by Gray[3] summarizes much of this work.

Although many Kolsky bars have been built in research facilities, and the technique of constructing and operating the bars is fairly well documented, an interesting precision engineering aspect is the method for determining the straightness and alignment of the bars and their supports during construction of the apparatus. The alignment of the bars is important; for example Gray[4] states: "For proper Hopkinson bar operation, the bars must be physically straight, free to move without binding, and carefully mounted to ensure optimal axial alignment." However, to our knowledge, a quantitative specification for the alignment precision is not given in the literature. The purpose of this paper is to report the approach used at NIST to construct the Kolsky pressure bar system, with particular emphasis on the alignment of the bars. Measurement and documentation of the straightness of the NIST system will be valuable in assessing the effect of straightness on the performance of the system. An ongoing effort of the NIST project will be to correlate the straightness with the performance of the Kolsky bar apparatus.

Modeling Machining Processes

In the introduction to a 1938 paper, Hans Ernst[5], one of the pioneers in metal cutting research, said:

> **Over the past few hundred years we have slowly learned to use metal cutting tools without really knowing how they work. We have learned a lot about speeds and feeds, but, in order that we may meet the increasing demands of modern production for greater output and higher quality finish, it is necessary that we obtain a clear understanding of what is taking place at the cutting edge.**

We have learned a great deal about machining processes and the physics of what is "taking place at the cutting edge" since the 1930s, but there is still a great deal to learn. By the mid-twentieth century there was a broad effort, both in the U.S. and internationally, to conduct machining research and develop effective models that could guide

manufacturing planners to improved machining processes. With the advent of rapidly expanding digital computing capabilities in the late twentieth century, interest shifted to using modern analytical tools such as the finite element analysis (FEA) method to accurately model the machining process. However, efforts to use the FEA method to model machining processes have been hampered by the lack of adequate material properties data for the high strain rates and rapid heating encountered in machining processes. During the cutting of metals, i.e. machining, rapid heating occurs (on the order of 50,000 K s^{-1}) up to temperatures on the order of 1300 K at very high strain rates (in the range of 10^3 to 10^6 s^{-1})[6]. The new pulse-heated Kolsky bar apparatus at NIST has been designed and built to produce a high-strain-rate test, while simultaneously pulse-heating the sample with electric current, thereby providing data useful for machining simulations. The pulse-heating capability is part of an existing NIST facility for measuring thermophysical properties of materials. By placing the new Kolsky bar apparatus in the adjacent laboratory, we will take advantage of the sophisticated switching systems and large battery power supplies already in place to heat the sample to temperatures up to 1300 K in sub-second times, and accurately control the temperature prior to the strain wave impact. The system that will be used to pulse-heat and measure the temperature of the Kolsky bar sample is described by Basak, et al.[7]

Design, Fabrication, and Alignment of the NIST Kolsky Bar Apparatus

The NIST Kolsky bar apparatus was fabricated in the NIST Shops and assembled in the Special Projects Building. The design was based in part on discussions with researchers at Johns Hopkins University and the Army Research Laboratory*, along with published information, such as the articles in the American Society of Metals Handbook[8,9]. The completed Kolsky bar in the lab at NIST is shown in Figure 1. The apparatus consists of two long straight bars, called the incident and transmitted bars, with a material sample sandwiched between the two bars. The bars are mounted in bearings to allow only pure axial motion. The apparatus includes an air gun to accelerate a striker bar into the incident bar at velocities up to 40 m/s. In operation, the output of the system is the oscilloscope-recorded signals from strain gages (1000 ohm foil gages) mounted in the center of the incident and transmitted bars.

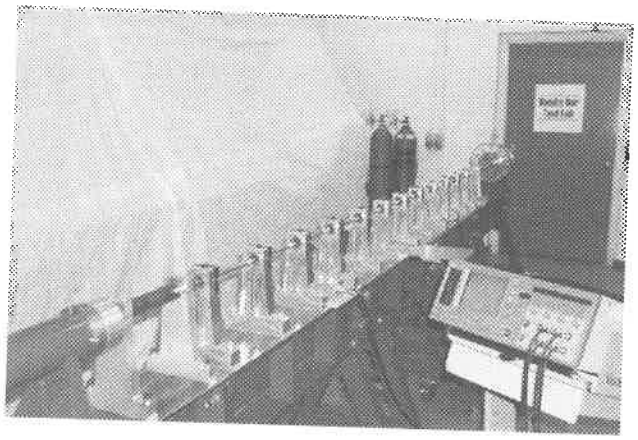

Fig. 1. NIST pulse heated Kolsky bar apparatus

The bar system is mounted on a precision base structure 5 m long, made in five sections. Each section consists of an H-beam (200 mm wide by 225 mm deep), with steel plates welded on the ends. Each section is precision machined on both ends and the top, then bolted together to form a long, straight, wide, flat surface for mounting the bar supports. Two A-frames that have casters and screw pads for leveling support each of the five base sections. The sections can be rolled into place and then bolted together to form the Kolsky bar base structure. The completed base structure can be seen in Figure1.Instead of using one long beam for the base structure, the base was made in sections that could be wheeled into place individually and then assembled in the laboratory next to the pulse-heating facility. At the time of the assembly, each base section was bolted in place and then the whole assembly precision leveled. After approximately one year, the base structure has

*Matthew Davies, Brian Dutterer, Richard Fields, Lyle Levine, Timothy Burns, and others from NIST met with K.T. Ramesh at The John Hopkins University, and with Wayne Chen of the University of Arizona and Tusit Weerasooriya at the U.S. Army Research Laboratory in Aberdeen, MD, prior to starting the design of the NIST Kolsky bar.

proven to be stable and remained level within the resolution of a precision machinist's level (approximately 40 μm/m.)

On top of the flat-machined surface of the base, 12 bearing support posts are mounted. These support and align the two 15 mm diameter by 1.5 m long bars. Each bearing support post contains an optical type x-y adjustable mount, so that the bearing in each post can be individually adjusted for alignment. The alignment was performed by carefully adjusting an optical tooling scope (K&E Model 71 2030 Alignment Telescope) for a line of sight determined by the air gun barrel using a target in each end of the barrel. This target is a precision brass cylinder machined to have a close fit to the inside bore of the barrel with a 1.5 mm hole drilled in the center. The scope mount adjustments for tip and yaw angle, plus vertical and horizontal motion, were used to bring the scope cross hairs in alignment with the target when placed alternately in each end of the barrel. After the line of sight was established using the targets in the barrel, the line of sight was then used to align each of the bearings in turn without touching the scope mount adjustments. For this alignment step, the scope cross hairs were focused on a precision target placed in each bearing. The bearing mount x-y screws were then used to bring the target center hole to a position centered on the scope cross hairs. This target was similar to the target placed in the barrel to establish the line of sight; however, the cylindrical surface was machined to fit closely into the bearing.

After the individual bearings were precision aligned, the 1.5 m long incident and transmitted bars were slid through the bearings into place. This optical tooling approach has an ultimate precision of "approximately one part in 200,000"[8], or a pointing uncertainty on the order of one arc second. This would translate into a ultimate straightness of about 25 μm for the support bearings. However, the overall deviation of the bearing centers from a perfect line has been estimated to be on the order of 100 μm when taking into consideration uncertainty sources such as the target fit into bearings and the ability to align crosshairs to the target center hole, plus air disturbances and optical distortions of the scope. The bearings are machined to have a clearance of 75 μm for the 15 mm diameter bars. The bars are fabricated from 350-maraging steel, hardened and centerless ground. The bars are straight within approximately 0.5 mm when placed on the flat surface of a coordinate measuring machine. The bearings of the Kolsky bar apparatus probably do some straightening of the bars and there is a slight drag of the bearings on the bars. We have not yet determined a quantitative way of measuring the effect of this straightening, but one of the ongoing efforts of the project will be to address this question.

Experimental Results to Date

A Kolsky bar compression test consists of holding a small sample of the material to be tested between two long steel bars. The first bar, called the incident bar, is impacted on the end with a striker bar fired from a small air gun. The impact produces a strain wave that moves down the incident bar, through the sample, and then into the second bar, called the transmitted bar. The deformations in the sample material affect the strain pulse in the transmitted bar and the strain pulse reflected back into the incident bar. A digital oscilloscope records signals from strain gages mounted in the centers of the incident and transmitted bars. The strain signals recorded as functions of time are then used to calculate a stress-strain curve for the sample material. Although the sample size can be varied, the initial testing has all been with 4-mm diameter by 2 mm thick specimens. Various metals are of interest and will eventually be tested. The initial work has been with AISI 1045 steel (because of its importance in the automotive industry) and copper samples for comparison to published results.

The results of a typical room temperature test are shown in Figure 2. The output from the strain gages is recorded on an oscilloscope (Nicolet model 440) and then transferred to a PC for data reduction and plotting. The strain gage output is calibrated in the normal way, using a precision parallel resistor (Vishay Measurements Group, Inc. gages and precision resistors have been used). The first pulse in Figure 2 is the compression wave arriving at the strain gage in the center of the incident bar. The reflected tension pulse arrives back at the same gage about 300 μs later, very close to the same time the transmitted pulse arrives at the transmitted bar gage. According to the theory underlying the experiment, the reflected pulse is directly proportional to the strain rate, and the transmitted pulse is directly proportional to the stress in the sample. Therefore, a stress-strain curve can be determined from these two signals. The details of the calculations are presented in Gray[3].

With respect to the alignment of the bars, the level of signal on the incident bar gage between the time of the end of the incident pulse and the return of the reflected pulse is of interest. If there were no constraint from the bearings, i.e. the bearings perfectly aligned and the bar perfectly straight, then there should be no reflections as a precursor to the

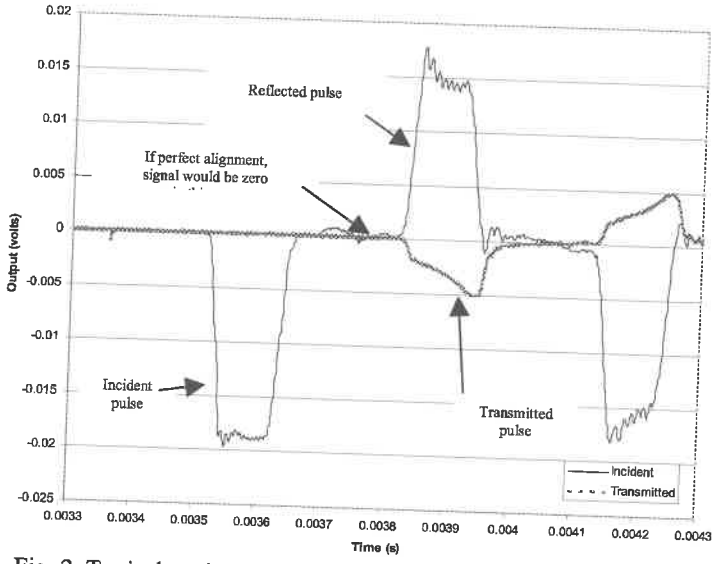

Fig. 2. Typical strain gage outputs from a Kolksy bar test

return pulse. Our signal indicates there is probably some reflection from the bearings supporting the bars, but this condition is difficult to quantify and there are possibly other sources of non-zero signal in this time period. Future work will involve purposely misaligning the bearings and comparing the strain gage output signals, thereby determining the magnitude of the effect of a known misalignment.

Conclusions

The construction of the NIST Kolsky bar apparatus is complete, and tests on several materials at room temperature have been completed. Preliminary pulse heating experiments have also been completed. However, tests using the combined system in which samples are pulse-heated prior to compression have not yet been completed. Preliminary results indicate that the bar alignment method was successful, but that there is still some problem with reflections from the bearings. Future work will involve special experiments to quantify the effects of any misalignment.

Disclaimer

Specific manufacturers have been mentioned to aid in the complete documentation of the equipment used for this project. This is not an endorsement or recommendation in any way for a particular manufacturer's equipment.

Acknowledgements

The authors acknowledge the support of NIST ATP intramural funding, Jack Boudreaux Program Manager, and the technical and administrative support of the NIST Predictive Process Engineering Program, Kevin Jurrens Program Manager. The authors also acknowledge the entire NIST Kolsky Bar Team for contributions to this project (Richard Fields, Howard Yoon, Debasis Basak, Lyle Levine, Eric Whitenton, Gerry Blessing, Robert Polvani, and others).

References

[1] H. Kolsky, "An Investigation of the Mechanical Properties of Materials at very High Rates of Loading", *Proc. Phys. Soc. (London)*, Vol 62B, 1949, p676-700.
[2] H. Kolsky, Stress Waves in Solids, Dover, New York, 1963.
[3] G.T. Gray III, "Classic Split-Hopkinson Pressure Bar Testing", ASM Handbook, Amer. Soc. Metals, Vol 8, 1998, p 462 – 476.
[4] Gray, ibid, pg. 464
[5] Hans Ernst, "Physics of Metal Cutting," *National Metal Congress*, American Society for Metals, October 17-21, 1938, Detroit.
[6] Kalpakjian S., *Manufacturing Processes for Engineering Materials*, 2nd Ed., Addison-Wesley, Reading, MA, 1991, p 46.
[7] D. Basak, H.W. Yoon, R. Rhorer, T. Burns, "Microsecond Time-Resolved Pyrometry During Rapid Resistive Heating of Samples in a Kolsky Bar Apparatus," submitted to the Proceedings of the 8th Symposium on Temperature, Its Measurement and Control in Science and Industry, October 21-24, 2002, Chicago, IL.
[8] P. Kissam, *Optical Tooling for Precise Manufacture and Alignment*, McGraw-Hill, New York, 1962, p 3.

NanoSlider Modeling and Waveform Adaptation for Positioning Control

Jong Y. Shim, Kihyun Kim and Dae-Gab Gweon
Department of Mechanical Engineering, Korea Advanced Institute of Science & Technology,
373-1 Kusong-Dong, Yusong-Gu, ME3265, Taejon 305-701, Korea

Introduction

Ultraprecision positioning mechanism with both long moving range and nanometer resolution is more and more required in the field of precision engineering (STM, AFM) and many efforts are made to meet these requirements such as inertial slider, inchworm etc. We have reported a nanopositioner which has long moving range and high resolution at the same time [1][2]. It uses inertial sliding principle and can move in the three-planar direction(XYθ). In the previous report only the experimental movement characteristics were presented. In this paper the dynamic modeling of the nanoslider and with that result input waveform to the piezoelectric actuator are discussed. With the assumption that the dynamic characteristic of the piezoelectric tube can be explained by the simple mass-spring-damper model the dynamic model of the nanoslider can be obtained. Dynamic equation formulation will be performed and its validity will be verified with the experiment. The experimental setup includes the three-axis laser interferometer and mirrors mounted to the body for reflecting laser beam(Fig. 1). With the model waveform shape of the input voltage can be determined to improve the performance. The considerations taken for waveform are the oscillation at the end of the actuation step and speed of the movement.

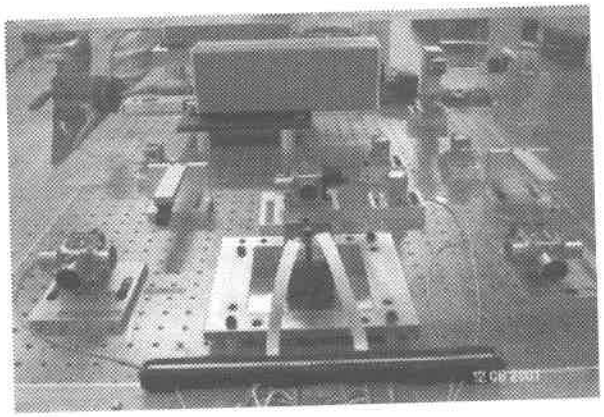

Fig. 1. Nanoslider and 3-axis interferometer view

Experimental investigation and friction uncertainty region

Many experiments with sawtooth input shows that under certain conditions there are significant friction condition uncertainties. The changes of the position of the nanoslider, moving path history and the motion direction(x and y) make the responses quite different and the resultant displacement is varied. This uncertain region is characterized by the input voltage and frequency : below certain voltage(about 2μm) and above certain frequency(200Hz). By the

small voltage input, the microscopic structure of the contacting surfaces becomes dominant and by the high frequency input (above natural frequency of the nanoslider in the motion direction) there exist so many sliding-conditions occurring and with the surface character generated by the sliding effect make the responses different (worst case is 100% error). However if the voltage is high enough and the frequency is low enough, the uncertainties become much lower(about 5%) and shows repeatable response characteristics. Therefore the modeling and simulation are based on the responses in this region and positioning control will be operated also.

Modeling and experimental results

The modeling of the nanoslider includes both the stick phase model and sliding phase model. The stick phase model will be used in the control when stick and theoretical aspects can assist in the controlling nanoslider such as gain tuning and control method (stick-control mode).

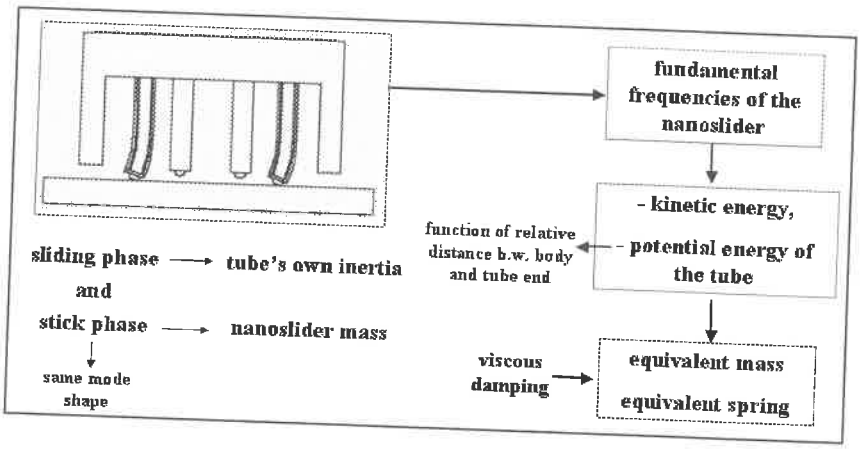

Fig. 2. Assumptions of the model

With some reasonable assumptions on the piezoelectric tube(Fig. 2), we can simplify the total nanoslider mechanism to a mass-spring-damper model as shown in Fig. 3. Large mass M is nanoslider, small mass m is tube equivalent mass(of which relative position is tube end relative position), k is tube equivalent stiffness and c is the damping coefficient. Fig. 3 shows the coordinate systems and schematic of the various components of the model. To make the dynamic equation of motion Lagrange's equation is used and first the sliding equation is formulated.

$$T = \frac{1}{2} M\, {}^{N}v_{M,G}^{2} + \frac{1}{2} I\, {}^{N}\omega_{G}^{2} + \frac{1}{2} \sum_{i=1}^{3} m_i\, {}^{N}v_{bi}^{2}$$

$$V = \frac{1}{2} \sum_{j=1}^{3} k_j \left({}^{N}\boldsymbol{r}_j - {}^{N}\boldsymbol{r}_{bj} \right) \cdot \left({}^{N}\boldsymbol{r}_j - {}^{N}\boldsymbol{r}_{bj} \right)$$
$$= \frac{1}{2} \sum_{j=1}^{3} k_j \left(x_{bj}^{2} + y_{bj}^{2} \right)$$

(1)

$$D = \frac{1}{2}\sum_{k=1}^{3} c_k \left({}^{k}\dot{r}_{pk} \cdot {}^{k}\dot{r}_{pk} \right)$$
$$= \frac{1}{2}\sum_{i=1}^{3} c_k \left(\dot{x}_{pk}^{2} + \dot{y}_{pk}^{2} \right)$$

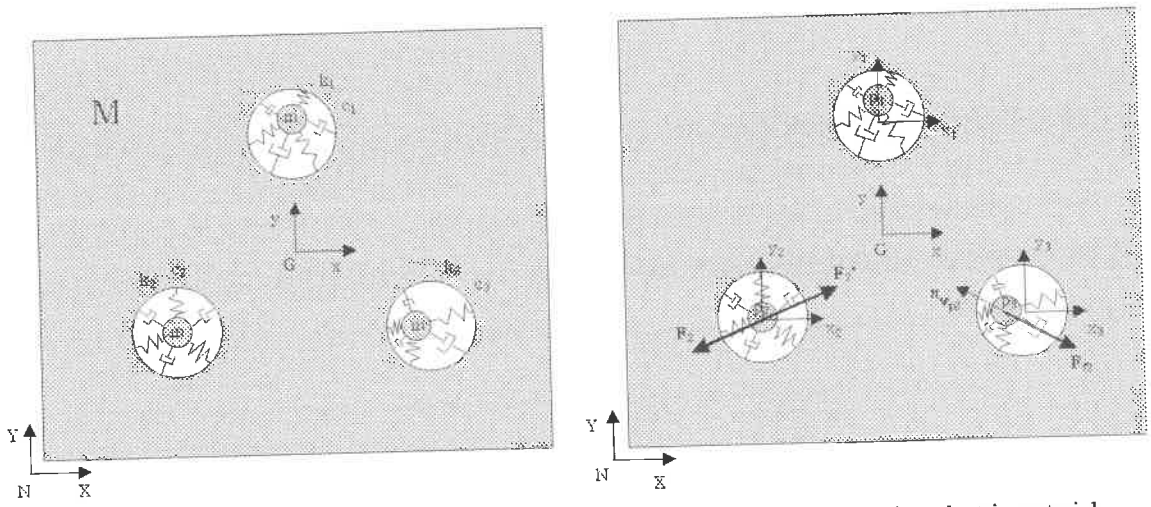

Fig. 3. Nanoslider model : m is mass, k is spring constant, c is damping of the tube piezoelectric material. Right hand figure shows the external and internal forces and coordinates used for model.

With the above equation and some labor, mass, spring and damping matrix can be obtained and shown below.

$$\boldsymbol{M} =$$

$$\begin{matrix}
M+\sum m_i & 0, & -\sum m_i\,{}^{G}y_i, & m_1, & 0, & m_2, & 0, & m_3, & 0 \\
0, & M+\sum m_i, & \sum m_i\,{}^{G}x_i, & 0, & m_1, & 0, & m_2, & 0, & m_3 \\
-\sum m_i\,{}^{G}y_i, & \sum m_i\,{}^{G}x_i, & I+\sum m_i({}^{G}x_i^2+{}^{G}y_i^2), & -m_1\,{}^{G}y_1, & m_1\,{}^{G}x_1, & -m_2\,{}^{G}y_2, & m_2\,{}^{G}x_2, & -m_3\,{}^{G}y_3, & m_3\,{}^{G}x_3 \\
m_1, & 0, & -m_1\,{}^{G}y_1, & m_1, & 0, & 0, & 0, & 0, & 0 \\
0, & m_1, & m_1\,{}^{G}x_1, & 0, & m_1, & 0, & 0, & 0, & 0 \\
m2, & 0, & -m_2\,{}^{G}y_2, & 0, & 0, & m2, & 0, & 0, & 0 \\
0, & m_2, & m_2\,{}^{G}x_2, & 0, & 0, & 0, & m_2, & 0, & 0 \\
m3, & 0, & -m_3\,{}^{G}y_3, & 0, & 0, & 0, & 0, & m_3, & 0 \\
0, & m_3, & m_3\,{}^{G}x_3, & 0, & 0, & 0, & 0, & 0, & m_3
\end{matrix}$$

$$K = \begin{bmatrix}
0, & 0, & 0, & 0, & 0, & 0, & 0, & 0, & 0 \\
0, & 0, & 0, & 0, & 0, & 0, & 0, & 0, & 0 \\
0, & 0, & 0, & 0, & 0, & 0, & 0, & 0, & 0 \\
0, & 0, & 0, & k_1, & 0, & 0, & 0, & 0, & 0 \\
0, & 0, & 0, & 0, & k_1, & 0, & 0, & 0, & 0 \\
0, & 0, & 0, & 0, & 0, & k_2, & 0, & 0, & 0 \\
0, & 0, & 0, & 0, & 0, & 0, & k_2, & 0, & 0 \\
0, & 0, & 0, & 0, & 0, & 0, & 0, & k_3, & 0 \\
0, & 0, & 0, & 0, & 0, & 0, & 0, & 0, & k_3
\end{bmatrix} \qquad C = \begin{bmatrix}
0, & 0, & 0, & 0, & 0, & 0, & 0, & 0, & 0 \\
0, & 0, & 0, & 0, & 0, & 0, & 0, & 0, & 0 \\
0, & 0, & 0, & 0, & 0, & 0, & 0, & 0, & 0 \\
0, & 0, & 0, & c_1, & 0, & 0, & 0, & 0, & 0 \\
0, & 0, & 0, & 0, & c_1, & 0, & 0, & 0, & 0 \\
0, & 0, & 0, & 0, & 0, & c_2, & 0, & 0, & 0 \\
0, & 0, & 0, & 0, & 0, & 0, & c_2, & 0, & 0 \\
0, & 0, & 0, & 0, & 0, & 0, & 0, & c_3, & 0 \\
0, & 0, & 0, & 0, & 0, & 0, & 0, & 0, & c_3
\end{bmatrix} \tag{2}$$

$$f = \begin{bmatrix} \sum_k F_{fkx} \\ \sum_k F_{fky} \\ \sum_k (-F_{fkx}\ {}^{G}y_k + F_{fky}\ {}^{G}x_k) \\ F_{1x}' + F_{f1x} \\ F_{1y}' + F_{f1y} \\ F_{2x}' + F_{f2x} \\ F_{2y}' + F_{f2y} \\ F_{3x}' + F_{f3x} \\ F_{3y}' + F_{f3y} \end{bmatrix}$$

And the total sliding equation is,

$$\boldsymbol{M}\ddot{\boldsymbol{q}} + \boldsymbol{C}\dot{\boldsymbol{q}} + \boldsymbol{K}\boldsymbol{q} = \boldsymbol{f} \tag{3}$$

When the contacting ball and surface is stick this equation holds : which says the absolute velocity of the ball end point is zero.

$$\begin{cases} \dot{q}_1 - {}^{G}y_1\,\dot{q}_3 + \dot{x}_{pi} = {}^{N}v_{pi,x} = 0 \\ \dot{q}_2 + {}^{G}x_1\,\dot{q}_3 + \dot{y}_{pi} = {}^{N}v_{pi,y} = 0 \end{cases} \tag{4}$$

And the stick equation is also derived from eq. (3) and (4). The dynamic model includes sliding and stick model and it is switched to each other, therefore the model is nonlinear. To simulate the response of the nanoslider the model equation is solved numerically using adaptive Runge-Kutta method. The parameters such as mass and damping are measured using FFT and step-responses and sinusoidal inputs. And the sliding friction coefficient is determined from the simulation comparing with the experimental result and error minimized method determines the value. Figure 5 shows the compared results with the experimental and simulation results. The input shape is sawtooth and the voltage is 80 V (total 160 V considering two opposite electrodes). The input frequency is varied from 100Hz to 200Hz. (a) and (b) is the x and y results repectively and (c) is the simulation results in the y-direction. The response characteristics and final displacement value are almost the same with respect to the tendency according to the input frequency. Thus the dynamics of the model can simulate the nanoslider adequately.

Waveform determination

With the model waveform shape of the input voltage can be determined to improve the performance. The considerations taken for waveform are the oscillation at the end of the actuation step and speed of the movement. The waveform is sectioned by the four segments and each segment is polynomial function or spline curve and the function parameter is varied and the movement performance is estimated numerically with the model. Therefore suitable waveform can be determined from the simulation process. However the nonlinearity and uncertainty exists

in the friction phenomena can make the real situation somewhat different from the simulation result, therefore the adaptation in the waveform should be made experimentally when applied to the real system.

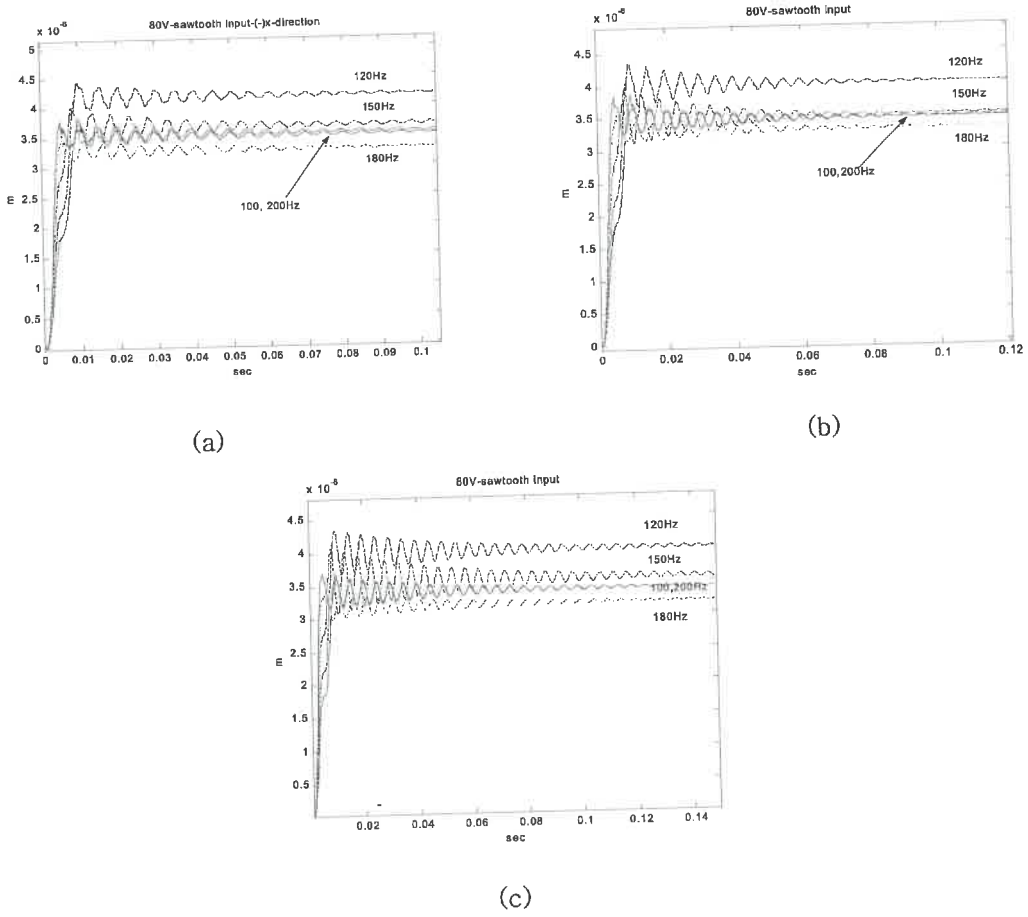

Fig. 5. Comparison between simulation and experiment : (a) and (b) is experiments and (c) is simulation

Conclusions

Through many experimental investigations, the uncertain region and repeatable region are known. And the modeling based on the repeatable region is performed and its validity is verified by comparison with the real phenomena. The further work will be launched by the waveform determination and follows the closed loop control of the nanoslider.

References

[1] J. Y. Shim, D. G. Gweon, Piezo-driven metrological multi-axis nanopositioner, Rev. Sci. Instrum, Vol 72, No 11, pp 4183-4187, 2001

[2] J. Y. Shim, H. Chung, D. G. Gweon, The New Long Range Multi-axis Nanopositioner using Inertial Slider/Walking Method, ASPE 2000 Annual Meeting

[3] D. W. Pohl, Rev. Sci. Instrum. 58, 54, 1987

[4] K. Besocke, Surface Sci., 181, 145, 1987

[5] J. W. Lyding, S. Skala, J.S. Hubacek, R. Brockenbrough, and G. Gammie, Rev. Sci. Instrum. 59, 1897, 1988

[6] Ch. Renner, Ph. Niedermann, A. D. Kent, and O. Fisher, J. Vac. Sci. and Technol. A 8, 330, 1990

[7] H. van der Wulp and P. V. Pistecky, J. Vac. Sci. Technol. B, 15, 566, 1997

Track/Focus control of cantilever type near field optical head for high density and fast data transfer rate data storage device

Sung-Q Lee, Ki-Bong Song, Jun-Ho Kim, Eun-Kyoung Kim, and Kang-Ho Park,
Basic Research Lab., Electronics and Telecommunications Research Institute, Korea

Abstract
A self-sensing cantilever is attached on the commercial optical disk drive system to verify feasibility of tracking and focusing optical recording head with a sub-wavelength aperture cantilever tip for the high areal density data recording and reading. In tracking control, a VCM head is controlled multi-offset by dividing photodiode signal into 16 levels. In focusing control, based on the frequency separation scheme, we controlled the VCM head to follow the low frequency surface profile and measured the gap between tip and sample at high modulation frequency, simultaneously.

Keyword : Track/Focus control, Near-field recording, Cantilever tip, Data storage.

1. Introduction

High-density data recording and fast data transfer rate are key issues in data storage devices [1-2]. One of the promising ways is optical recording with atomic force microscope (AFM) tip having a sub-wavelength aperture [3-4]. Through the aperture tip that is positioned in near field region, laser beam makes about 50~100 nm bit size data that matches more than 200 Gb/in^2 based on the principle of near field scanning optical microscopy (NSOM).

In the proposed system, a self-sensing cantilever (not aperture tip right now) is attached on the commercial optical disk drive system. This configuration takes the advantage of commercial optical pickup head for coarse tracking and focusing, and self-sensing cantilever tip for fine focusing to realize high areal data density.

The pickup head uses a voice coil motor (VCM) as an actuator and LD/PD optical tracking signal from land groove on the media. For one land-groove, only one tracking is possible. In this paper, we proposed multi-offset tracking control to achieve more tracks in each land-groove. The sinusoidal signal for a land-groove can be divided into several signal levels in order to make narrow track pitch in the point of cantilever tip.

In the optical pickup head, optical PD set cannot resolve under 1um along focus direction because of focal depth of the object lens. Above 1 μm, gap is controlled from focus signal of a DVD-ROM optical head set. Within 1 μm, with the self-sensing cantilever tip, we detect the atomic force between tip and the media surface and control the gap. In convention non-contact AFM gap control, oscillation PZT and gap control PZT is separated. However, the proposed frequency separation scheme, we apply the sum of modulation signal and gap profile signal .to VCM. VCM is mainly moves according to gap profile making cantilever resonated and the self-sensing cantilever sense the amplitude variation of modulation signal.

2. Principle and configuration of the system.

Figure 1 shows the schematic of the proposed system. A self-sensing cantilever is attached on the

commercial optical disk drive system. To read and write data densely, self-sensing cantilever approaches to the media until it gets close below 100nm (near field region, $d << \lambda$ [5]) and is controlled precisely in tracking direction. Through the aperture tip, laser makes the near field optical spot similar to aperture size on the media (Figure 2). In tracking control, VCM head is controlled multi-offset using photodiode signal. In focusing control, however, since photodiode is not sensitive below 1 μm, a self-sensing cantilever takes the place of distance sensor between media and cantilever tip.

3. Multi-offset tracking control

For about 50 nm bit size data, the cantilever tip should be controlled every 50 nm in tracking direction. If head is tracked by every 50 nm offset from the center of the track, data areal density would be 250 Gb/in^2. Since VCM, inherently, has a capability of controlling several-nm resolution, we try to control cantilever head by 50 nm using VCM only. In order to get the minimum positioning resolution, we performed a basic experiment using function generator and capacitive sensor with the commercial VCM in DVD head. Figure 3 shows a potential of VCM below 10nm resolution, in our case, even if input voltage is limited by noise. This result gives a clue to control cantilever head by 50nm or less using VCM only in focusing and even tracking direction. VCM is used as a tracking actuator in DVD system of which track pitch is about 800 nm. In order to control by 50nm multi-offset tracking, we divide the full range sensor signal by 16 levels. Figure 4 is the experimental result of two up and down 20 nm-steps. As VCM head goes farther from the track center, PD signal noise level becomes higher, so that we cannot use the full range land-groove.

4. Focusing control with frequency separation scheme.

A self-sensing cantilever is a good candidate for sensing the gap between tip and sample. It does not need optical alignment. Since near field data read/write is possible within 100nm tip-sample distance, gap control in case of data storage application could be coarser than AFM image application. . In convention non-contact AFM gap control, oscillation PZT and gap control PZT is separated. However, if we apply the sum of modulation signal and gap profile signal .to VCM, VCM is mainly moves to the low frequency gap profile making cantilever resonated at modulation frequency even with small movement of VCM. At the same time, the resonated self-sensing cantilever senses the amplitude variation of modulation signal. We call this 'frequency separation scheme'. In order to explain in detail, we make mathematical model of VCM with a cantilever tip (figure 5(a)). Followings are dynamic equation and transfer function of the system.

$$\begin{aligned} M\ddot{x}_v + b_v\dot{x}_v + k_v x_v + b_c(\dot{x}_v - \dot{x}_c) + k_c(x_v - x_c) &= F \\ m\ddot{x}_c + b_c(\dot{x}_c - \dot{x}_v) + k_c(x_c - x_v) &= 0 \end{aligned} \quad \cdots\cdots (1)$$

$$\begin{aligned} \frac{X_v(s)}{F(s)} &= \frac{ms^2 + b_c s + k_c}{mMs^4 + (Mb_c + m(b_c + b_v))s^3 + (Mk_c + b_v b_c + m(k_c + k_v))s^2 + (b_v k_c + k_v b_c)s + k_c k_v} \\ \frac{X_c(s)}{F(s)} &= \frac{b_c s + k_c}{mMs^4 + (Mb_c + m(b_c + b_v))s^3 + (Mk_c + b_v b_c + m(k_c + k_v))s^2 + (b_v k_c + k_v b_c)s + k_c k_v} \\ \frac{X_v(s) - X_c(s)}{X_v(s)} &= \frac{ms^2}{ms^2 + b_c s + k_c} \end{aligned} \quad \cdots\cdots (2)$$

where, F is applied force to VCM, x_v, M, b_v, k_v are displacement, mass, damping coefficient, spring constant of VCM, respectively and x_c, m, b_c, k_c are displacement, mass, damping coefficient, spring constant of cantilever, respectively.

In figure 5(b), frequency response function (FRF) shows that VCM motion is attenuated a lot at the cantilever resonance frequency, making cantilever resonated with small oscillation of VCM. Figure 5 (c),(d) verify the simulation result by experiment. Since VCM is suspended by four-wire guidance, it, in real, has more resonance at higher frequency, still having attenuated motion.

Based on the proposed frequency separation scheme, we can control VCM head to follow the surface profile and can measure the gap between tip and sample, simultaneously (Figure 6). With frequency separation scheme, we measure the gap distance and modulation frequency amplitude variation (Figure 7). As it is well known, the closer the tip approaches, the larger the amplitude variation is. And setting the regulation point, we control VCM head to stay at a constant height from sample with PI control algorithm. Figure 8 is the experimental result of gap control performance. Figure 8(a) is the z-directional sample motion of 150nm sinusoid. Figure 8(b)-(f) is the control performance according to the frequency of sample motion that simulate the scanning speed. Slow scanning gives more correct following than fast scanning. It depends on control speed. And slow scanning result shows errors because of low sensor sensitivity at this regulating point. In order to get more sensitive result, regulating point must be close to the sample that result harder gap control. Therefore, there is a room for improvement.

5. Conclusion

The idea of combining self-sensing and VCM head is proposed. Multi-offset tracking performance of 20nm gives insight to control multi-track with only one land-groove without changing commercial optical head. To control cantilever tip to follow the track with constant height, frequency separation scheme is applied. Small oscillation of VCM at cantilever resonance frequency makes the self-sensing cantilever sense the modulation amplitude according to the gap between tip and sample. Closed loop gap control is performed utilizing frequency separation schemed gap sensing. To give more precise and fast focusing performance, regulating point should be closer to the sample, and control gain should be higher to response to the sample height variation quickly.

References

[1] Youngho Seo and Wonho Jhe, Rev. Sci. Instr. Vol.73 No.5 (2002), pp. 2057-2059

[2] Hyung Bok Lee, Motonobu Kourogi, Takashi Yatsui, Kazuo Tsutsui, Nobufumi Atoda and Motoichi Ohtsu, Applied optics, Vol.38. No16.(1999), pp.3566-3571

[3] K. B. Song, J. Kim, and K. H. Park, Jpn. J. Appl. Phys., vol. 41 (2002) Part 1., pp. 1724-1727.

[4] J. Kim, K.-B. Song, and K.-H. Park, Jpn. J. Appl. Phys. vol. 41(2002), Part 1, pp. 1903-1904.

[5] Bert Hecht, Beate Sick, and Urs. P. wild, Volker Dechert and Renato Zenobi, Oilvier J.F. Martin, Dieter W. Pohl, J. Chemical physics, vol. 112, No. 18 (2000), pp.7761-7774.

Acknowledgements

Authors are pleased to acknowledge Woo-Sub Youm for helping experimental setup. This work has been supported by the Ministry of Informations and Communications, Korea

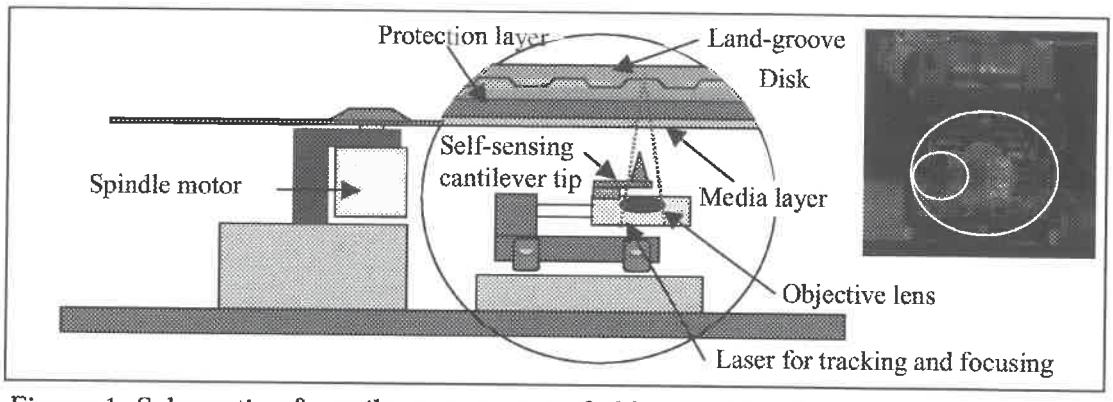

Figure 1. Schematic of cantilever type near field optical head

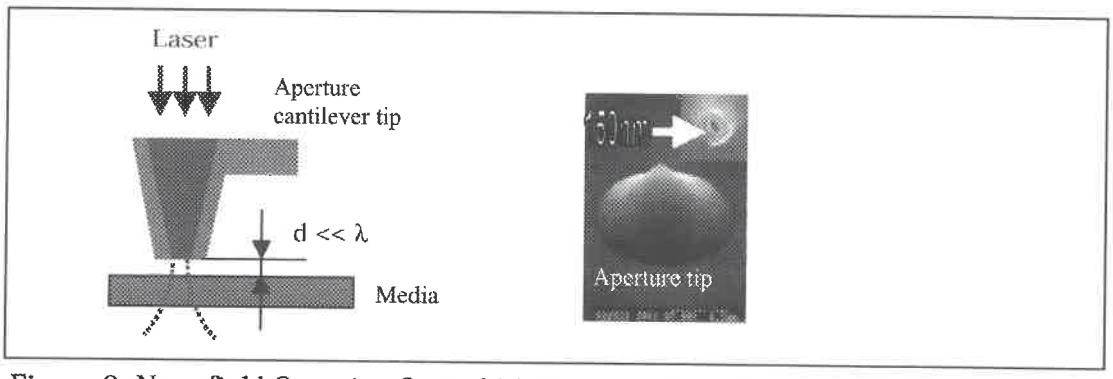

Figure 2. Near field Scanning Optical Microscope (NSOM)

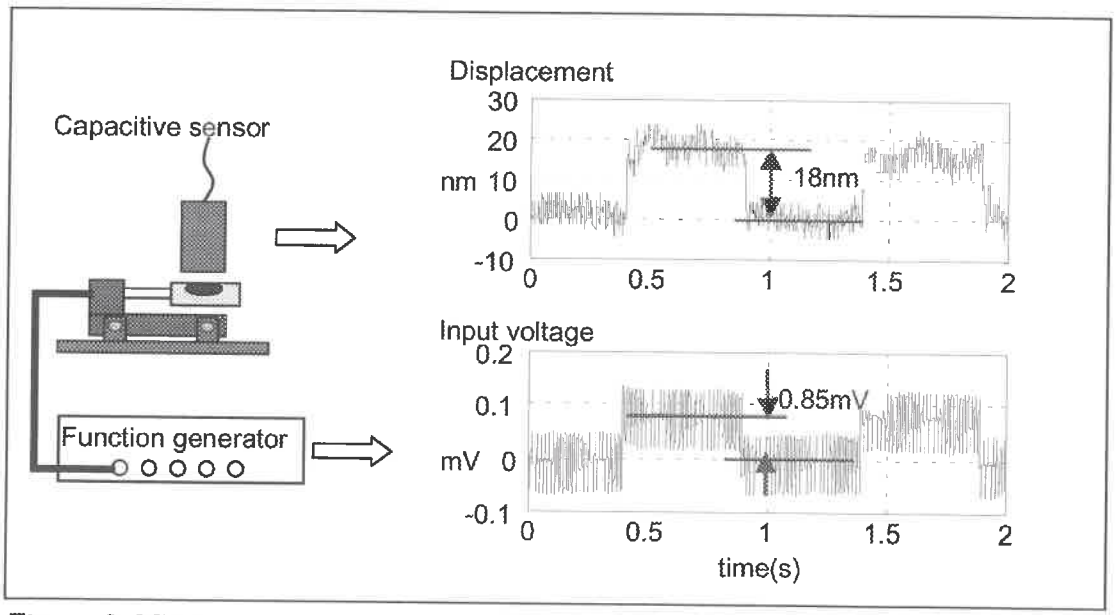

Figure 3. Minimum step motion of VCM (Resolution ~10nm)

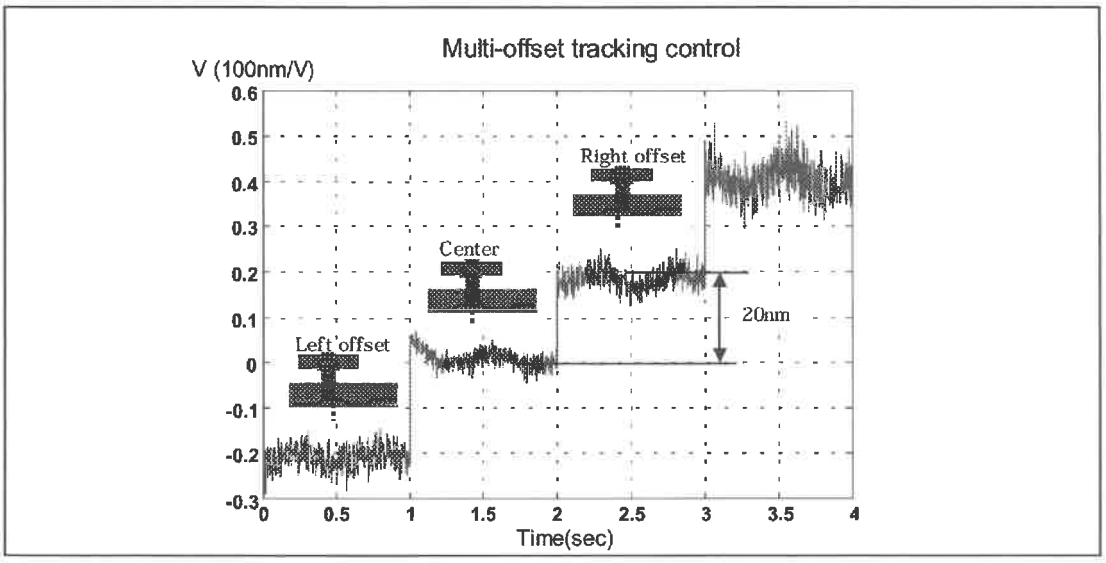

Figure 4. Experimental result of 20nm multi-offset tracking control

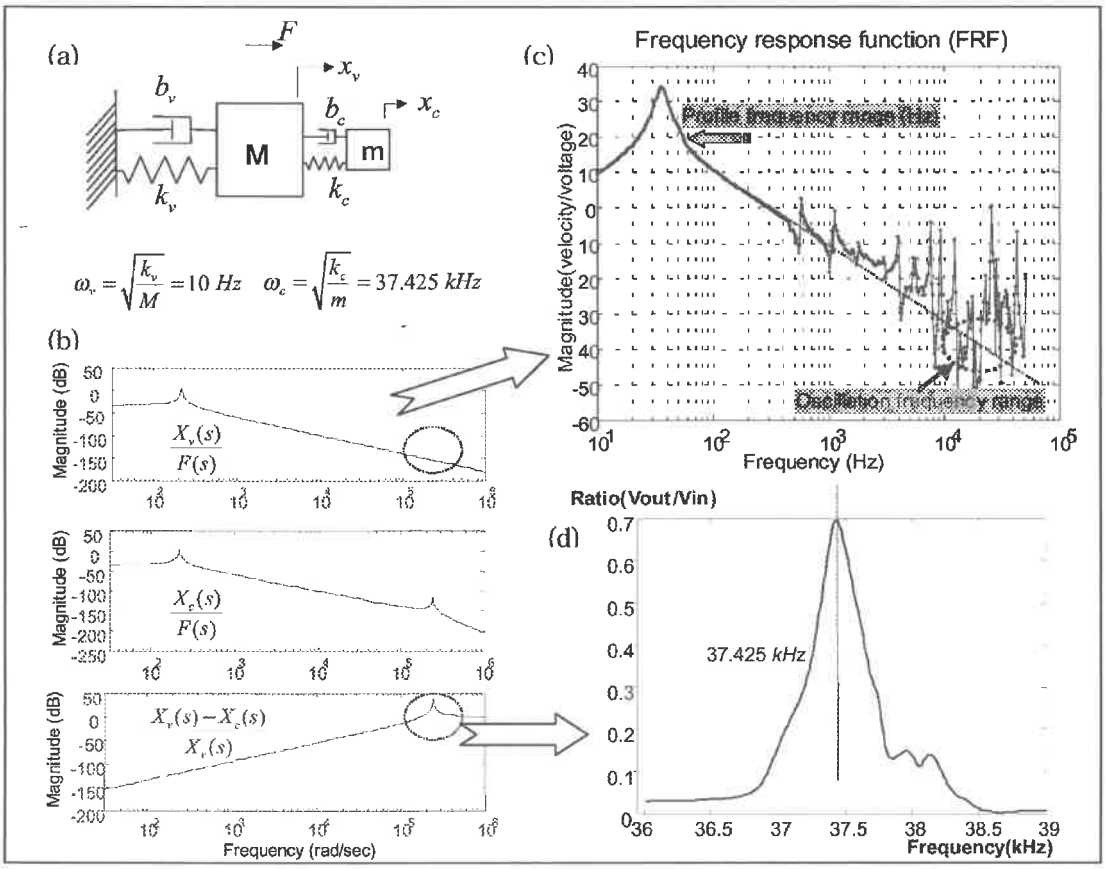

Figure 5. Modeling and frequency responses of VCM with cantilever
(a) dynamic modeling, (b) simulation (c-d) experimental result

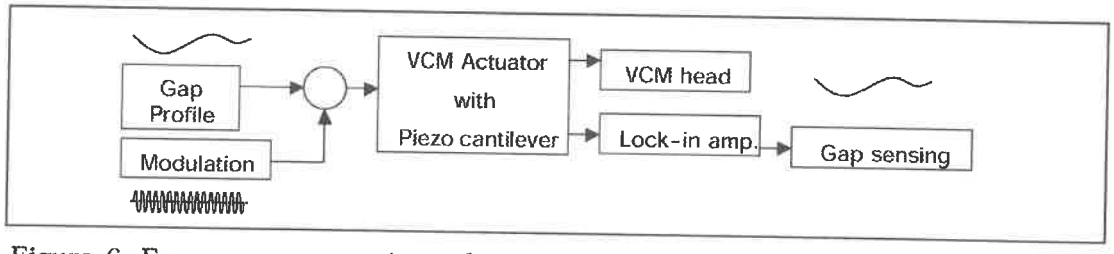

Figure 6. Frequency separation scheme: Gap profile and modulation signal is fed to VCM head, Lock in amp detect amplitude variation of modulation frequency

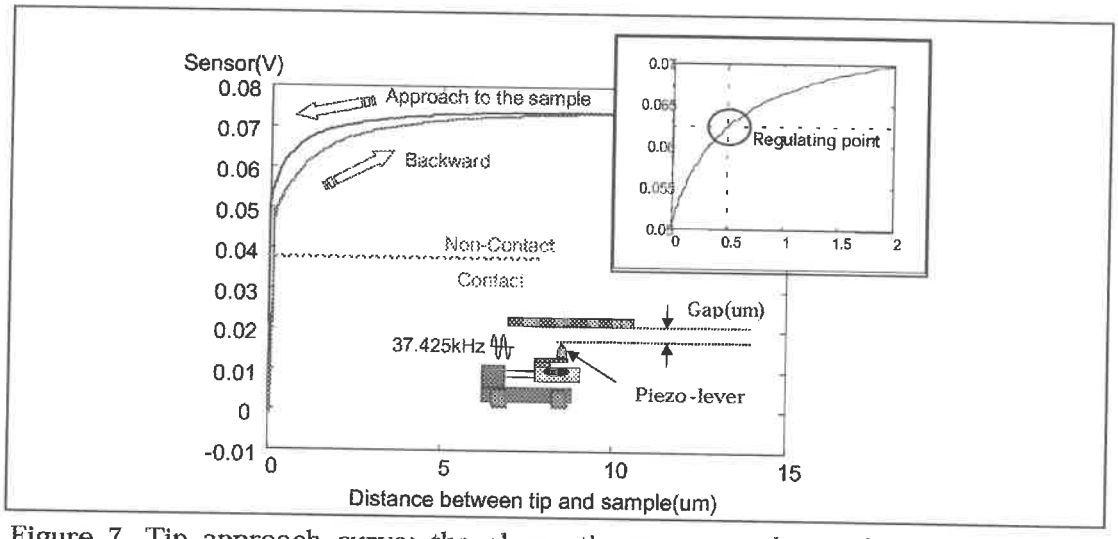

Figure 7. Tip approach curve: the closer tip moves to the surface, the more sensitive sensor is.

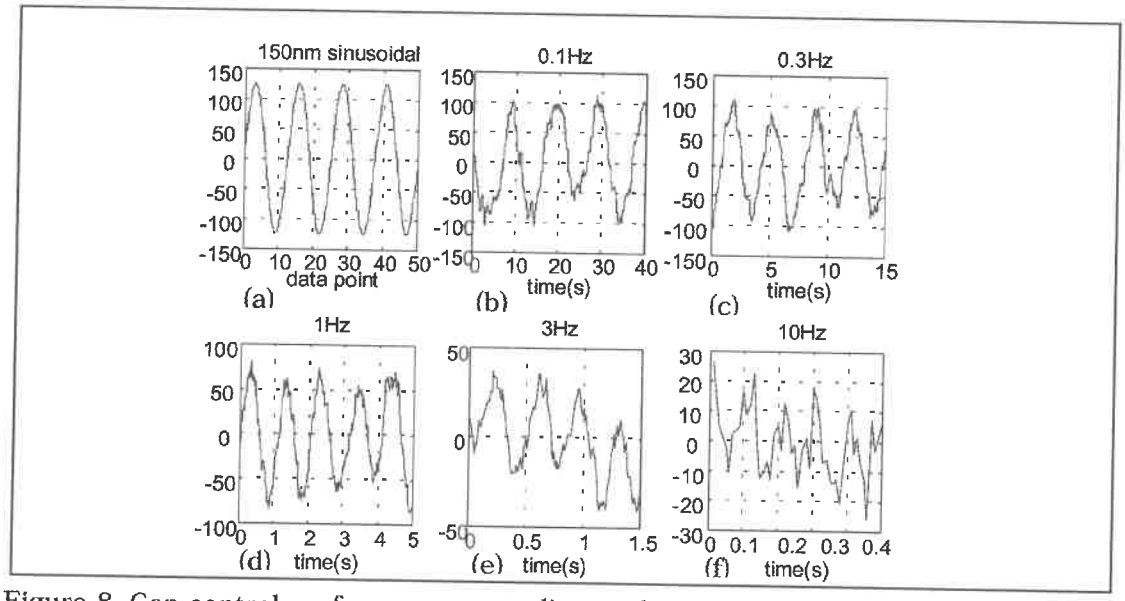

Figure 8. Gap control performance according to the scanning frequency

AN INSTRUMENT FOR CHARACTERIZING STIFFNESS OF PROTRUDING OPTICAL FIBERS

James A. Carter II, Shelby M. Shreve, and R. Ryan Vallance
Precision Systems Laboratory, University of Kentucky, Lexington, KY *

Sepehr Kiani and John Lehman
Teradyne Connection Systems, Nashua, NH †

Abstract

This paper presents the design of an instrument intended for measuring the stiffness of optical fibers terminated in MT ferrules. This paper describes the concept, detailed design of the instrument, details of major component analysis, and operation of the instrument. The instrument described in this paper will allow the operator to measure the stiffness of each optical fiber in the array of fibers in a ferrule.

Keywords: optical fiber, MT ferrule, fiber stiffness, protrusion length, flexure

Introduction

Optical fiber connectors consist of an array of optical fibers terminated within a ferrule that precisely aligns the fibers. Example types of ferrules include single-fiber ceramic, multi-fiber polymer, and multi-fiber silicon vee-grooves. Fig 1 illustrates a conventional MT ferrule and ribbon cable. Twelve single-mode optical fibers are terminated so that their ends protrude from the face of the ferrule (~1 μm). The termination process includes stripping away the cable cladding, bonding the fibers within the ferrule, and polishing the ferrule face. To minimize the signal loss within a connection, two ferrules are mated so that protruding fibers contact.

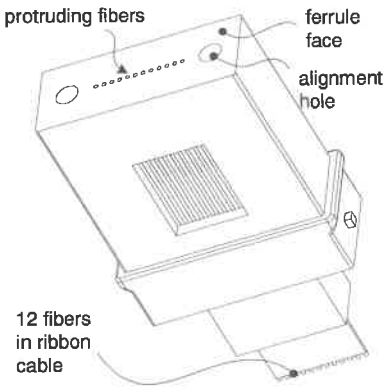

Fig 1: MT Ferrule and Terminated Fiber Array

Ensuring that mechanical contact exists between each fiber in the ferrule is crucial to effective fiber connections. Achieving mechanical contact depends upon the stiffness and amount of protrusion associated with each fiber. Fig 2 illustrates a set of hypothetical force-displacement relations for fibers terminated in a single ferrule. Each fiber has a unique curve resulting from variability in the adhesive joint, material properties, and compliance of the ferrule.

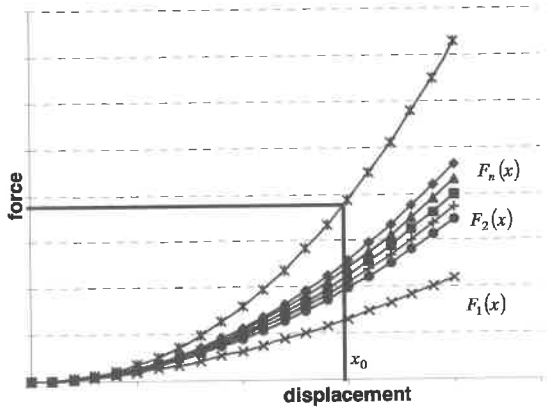

Fig 2: Force-Displacement Curves for Fibers Terminated in a Ferrule

Variability in the force-displacement curves requires that a sufficient preload force be established between two mating ferrules to ensure mechanical contact. The total force, F_{tot}, for compressing the

* *Precision Systems Laboratory, Mechanical Engineering, University of Kentucky, 210-A CRMS Building, Lexington, KY 40506. http://www.engr.uky.edu/psl.*
† *Teradyne Connection Systems, Nashua, NH. http://www.teradyne.com.*

fibers a distance, x_o, when mating a ferrule is then approximated with Eq (1).

$$F_{tot} \propto \sum_{i=1}^{n} F_i(x_0) \qquad (1)$$

The amount of force for mechanical contact depends upon a wide range of material and process variables that are difficult to predict and should therefore be characterized experimentally. This paper describes a new instrument, illustrated in Fig 3, for measuring the force-displacement relations fibers terminated in ferrules. The stiffness of each fiber, $k(x)$, can be determined by differentiating the force, $F(x)$, as shown in Eq (2). These relations can subsequently be used to assess the quality of the termination process.

$$k(x) = \frac{d}{dx} F(x) \qquad (2)$$

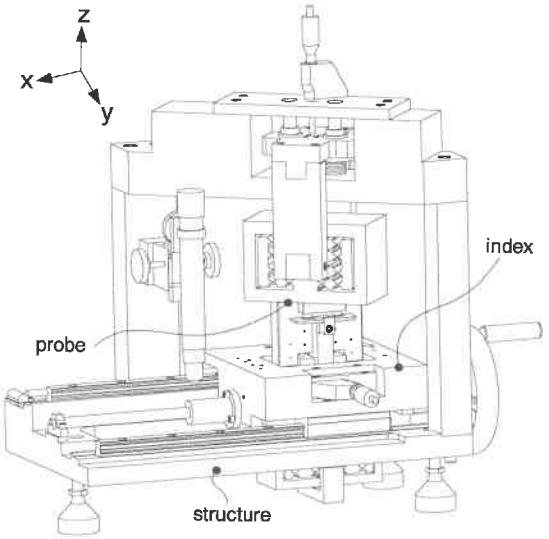

Fig 3: Instrument for Measuring Force-Displacement Relations for Optical Fibers

Conceptual Design of the Instrument

Fig 4 illustrates the conceptual principle of the instrument. A jewel probe with a flat face is displaced a distance, x_p, so that it pushes against the end of a single fiber. The fiber compresses a distance, δ_f, and the force is transmitted through the epoxy and ferrule to the ferrule base. The ferrule base floats on a compliant spring, so that the applied force can be inferred by measuring the compression within the spring. The compression of the fiber should be measured with respect to the face of the ferrule.

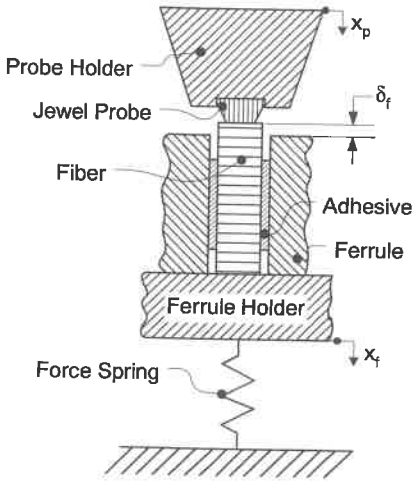

Fig 4: Concept for Measuring Fiber Stiffness

Since the displacements and compression of the fiber are only a few microns, flexural bearings [1] are used for the force spring and guide the probe holder. Fig 5 illustrates two double compound flexures that guide the probe and hold the ferrule. Flexural bearings provide maintenance-free, dirt-insensitive limited motion with very high stability and repeatability [2]. The displacement of the probe is controlled using a low-voltage PZT that actuates against flexure 1. The deformation in the fiber and the deflection of flexure 2 (force measurement) can be measured with capacitance displacement gages.

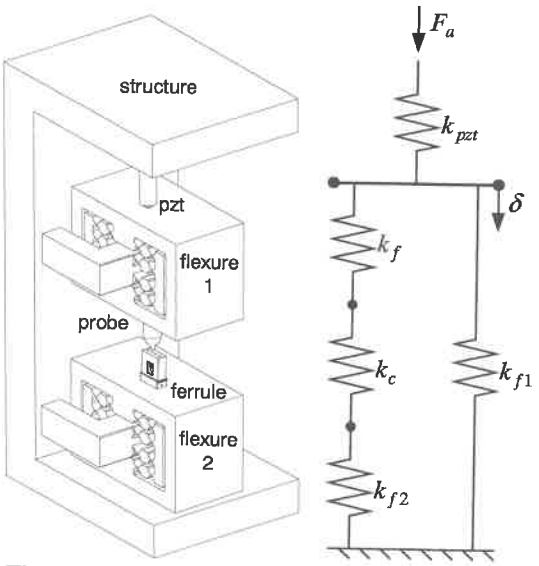

Fig 5: Flexural Bearings and Compliance Model

Detailed Design of the Stiffness Tester

Separate metrology loops limit the number of error sources, including structural deflections, thermal expansion, and alignment errors, near the ferrule face are illustrated in Fig 6. In order to measure the displacement of the fiber tip relative to the ferrule face, datum bars are implemented on either side of the optical fiber being analyzed.

The two independent datum bars have the same mass and center of gravity, which is coincident with the axis of the fiber being measured. Each datum bar contacts the ferrule face by way of a contact pin. The pin has a cylindrical surface, resulting in line contact in the vicinity of the fiber, preventing rotational errors and form errors from producing errors in the displacement measurement.

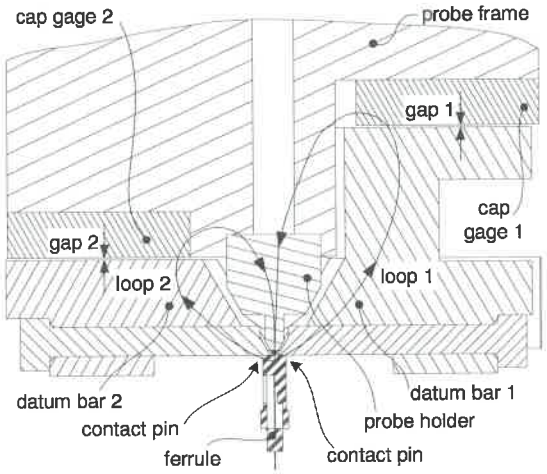

Fig 6: Ferrule Contact Region

The cap gages, mounted to the probe frame, measure the displacement of the datum bars relative to the cap gage surface. As the probe frame approaches the surface of the ferrule, the datum bars rest at a constant distance from the cap gage surface. When the datum bars touch the ferrule surface, the distance between the datum bars and the cap gages is reduced. In turn, the cap gages output a voltage that is proportional to displacement.

The probe frame, illustrated in Fig 7, functions as a housing for the air bushings, cap gages, and probe holder. The probe frame, mounted to flexure 1, travels vertically to allow the probe tip to push the tip of the optical fiber. Air bushings provide accurate linear motion without stiction. The air bushings are inserted into the probe frame and epoxy is forced into the space between the bushing o-rings and the frame to prevent movement. Bushing pins are pressed into the datum bars and translate vertically through the air bushings, allowing the datum bars to travel independently. Slots are ground into the bushing pins and the pin hard stop is inserted into the slots through the probe frame to control the total amount of displacement and prevent the datum bars from making contact with the cap gage surfaces.

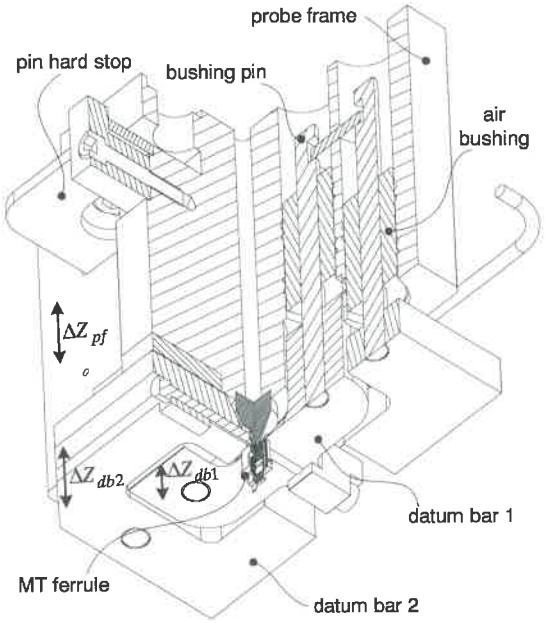

Fig 7: Probe Frame, Datum Bars, & MT Ferrule

The displacement for the loading of the optical fiber is provided by a PZT in conjunction with flexure 1. Together, they provide accurate linear motion with high resolution. The requirements for translation in the x direction led to the development of a z stage on the probe assembly, illustrated in Fig 8, where the micrometer head translates the components of the ferrule contacting region in the –z direction. The probe assembly is mounted to a gantry structure that is oriented at an angle to the x-axis.

The index assembly, illustrated in Fig 9, is comprised of components that enable translation in the x and y directions. The x-stage is mounted to a pair of recirculating linear ball bearings. These bearing rails provide accurate linear translation while withstanding a sufficient load. The rails are staggered to eliminate the effect of Abbe offsets in both the x and y stages. The x-stage is driven by a leadscrew and handwheel. The leadscrew provides repeatable positioning capabilities with no backdrive. One revolution of the handwheel translates the nut 1.58 mm. The y-stage rests upon a pair of crossed roller bearings and is driven by an absolute digital micrometer.

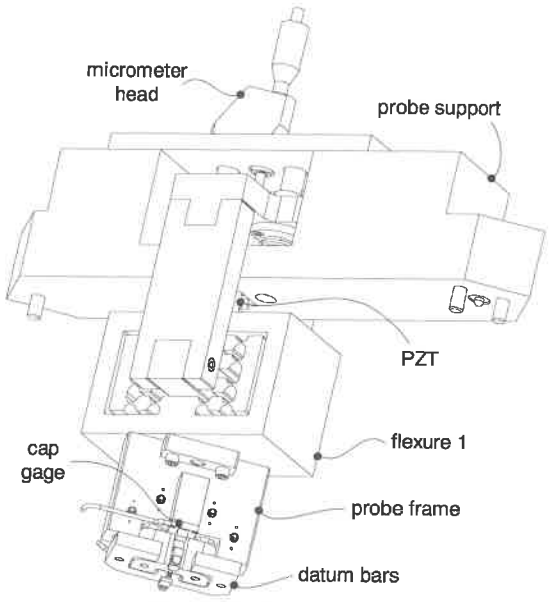

Fig 8: Probe Assembly

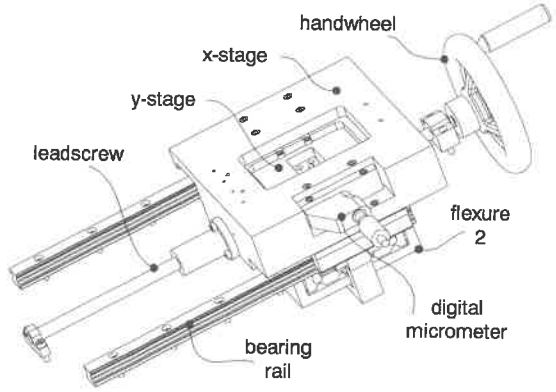

Fig 9: Index Assembly

Analysis of Flexures

The first step in the design of the flexures is to determine the force and displacement range expected in the fiber tip. A force of approximately 5 lb is required to properly mate two MT ferrules. The expected displacement for the fiber tip will be within the range of 0μm – 10 μm. Using Eq (2), the expected optical fiber stiffness, k_f, can be calculated.

The stiffness of the ferrule connector, k_c, is determined by finite element analysis. Using the known force and material properties, FEA gives an estimate for the displacement, from which the stiffness can be calculated using Eq (2).

The stiffness of flexure 2, k_{f2}, is governed by the capacitance gage that measures the force propagated between the connector and structure. The cap gage selected has a sensing range of 20 – 30 μm. This sensing range is the effective displacement range of flexure 2. The force through flexure 2 is the same as the fiber and ferrule connector. Therefore, k_{f2} is known by applying Eq (2).

The next step in the design is to select the PZT. Illustrated in Fig 5, both flexures as well as the PZT are attached to the structure. In the spring system diagram, the force from the PZT is equivalent to the combination of the forces from other components. The force balance equation for the spring system is given in Eq (3) where F_a is the effective PZT force, F_{f1} is the force from flexure 1, and F_s is the force that propagates through the fiber (F_f), ferrule connector (F_c), and flexure 2 (F_{f2}).

$$F_a = F_{f1} + F_s \tag{3}$$

The equivalent stiffness for the lower half of the spring system, k_s, is given in Eq (4) as a combination of springs in series and in parallel.

$$k_s = \left[\frac{1}{1/k_f + 1/k_c + 1/k_{f_2}} + k_{f_1} \right] \tag{4}$$

The PZT is selected by choosing the desired maximum displacement of the PZT without external loading, ΔL_o, and the stiffness of the PZT, k_{pzt}. The equivalent spring stiffness may then be related to the effective PZT force by using Eq (5) [3].

$$F_a \approx k_{pzt} * \Delta L_o \left(1 - \frac{k_{pzt}}{k_s + k_{pzt}} \right) \tag{5}$$

The stiffness of flexure 1 can be calculated by substituting Eq (4)-(5) into Eq (3) and using the relation $F_{f1} = k_{f1}*\delta$. Geometry for flexure 1 is designed around its stiffness and displacement, δ. The flexure geometry also depends upon other variables such as material properties and PZT positional errors. The parameters of the flexure geometry, illustrated in Fig 10, can be modeled with Eq (6)-(8) [4]. Θ is the hinge rotation, δ is the displacement, L is the length between hinges, E is the modulus of elasticity, b is the flexure depth, t is the hinge section thickness, R is the hinge section radius, and σ_{max} is the maximum allowable stress.

$$\Theta = \frac{\delta}{2L} \tag{6}$$

$$\Theta_{max} = \frac{4\left[.365\sqrt{t/R} + .166\right] R \sigma_{max}}{\left[\frac{2.7t + 5.4R}{8R + E} + .325 \right] Et} \tag{7}$$

$$k_{f1} = \left(\frac{4}{9\pi} \right) \left(\frac{Ebt^{5/2}}{L^2 R^{1/2}} \right) \tag{8}$$

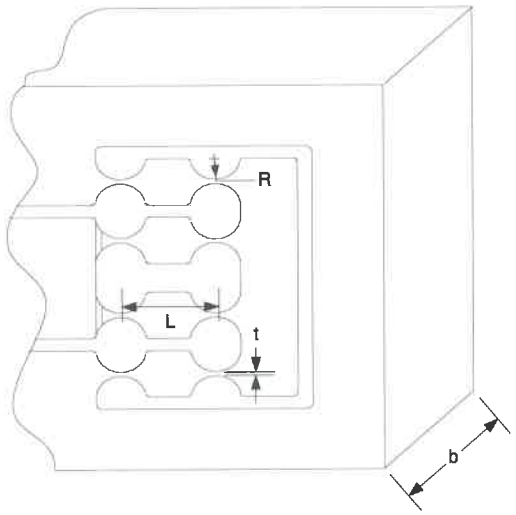

Fig 10: Flexure Dimensions

Operation of the Instrument

The stiffness tester will perform the task of measuring the stiffness of terminated optical fibers by following the procedure below. Fig 11 models the coordinates and vectors used in the procedure.

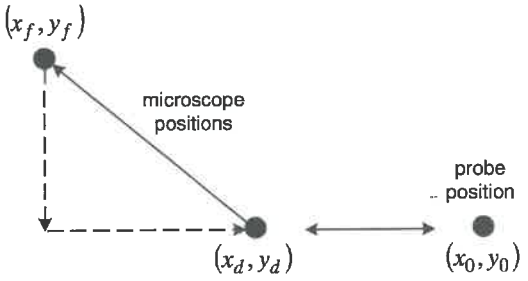

Fig 11: Positioning Vector Diagram

1. Align MT ferrule onto the ferrule mount by inserting the ferrule onto the alignment pins.

2. Translate the index assembly with the handwheel and position it under the probe assembly.

3. While monitoring the force from the resulting displacement in the flexure 2 cap gage, translate the probe assembly in the –z direction using the micrometer head until a force indicates that contact has been made. Null out the force by retracting the micrometer head. Actuate the PZT over the predefined range until a dimple is made at a random location on the ferrule surface. Record the x and y location of the index assembly (x_0,y_0) from the linear encoder and digital micrometer.

4. Translate the probe assembly in the +z direction to clear the index assembly. Translate index assembly along the x-axis with the handwheel and position it under the microscope.

5. Using the microscope, translate index assembly with handwheel and digital micrometer to locate the dimple and position it directly under the microscope reticle. Record the x and y dimple location (x_d,y_d).

6. Using the microscope, translate as in step 5 to locate the fiber to be analyzed and position it under the reticle. Record the x and y fiber location (x_f,y_f).

7. Translate index assembly to position (x_0,y_0). Position fiber under the probe by translating index assembly in y direction by the amount $y_f - y_d$ and in the x direction by the amount $x_f - x_d$.

8. One now knows that the fiber is positioned under the probe. Repeat the procedure in step 3 to apply a load to the optical fiber tip. Record the displacement of the datum bar cap gages, which is the displacement of the fiber. Using Eq (2), calculate the stiffness of the terminated optical fiber, δ_f.

Conclusions and Future Work

Currently, there is no instrument to experimentally determine the stiffness of optical fibers terminated in MT ferrules. This paper describes a concept, detailed design of the instrument, component designs, and operation of the fiber stiffness tester. Future work will include implementing control data acquisition systems. After assembly, experiments will be conducted to determine the stiffness of optical fibers terminated in MT ferrules. This design will benefit optical fiber connector manufacturers that are interested in fiber stiffness as a parameter to monitor and control.

References

[1] Smith, S.T. *Flexures: Elements of Elastic Mechanisms.* Taylor and Francis, Inc. 2000.

[2] Slocum, A. H. *Precision Machine Design.* SME Press. Dearborn, Michigan. 1992.

[3] Physik Instrumente (PI). *NanoPositioning 1998.* Germany. Cat 114, p. 4.23.

[4] Smith and Chetwynd. "Flexure Design for Positioning and Control". Ch. 4. in *Foundations of Ultraprecision Machine Design.* Gordon and Breach 1992.

[5] Higo, Y., Takashima, K., Shimojo, M., Sugiura, S., Pfister, B., Swain, M.V., "Fatigue Testing Machine of Micro-Sized Specimens for MEMS Applications", *Materials Research Society Symposium -Proceedings,* Vol 605, 2000 pp. 241-246

PRECISION INSTRUMENT FOR CHARACTERIZING CONTRACTION AND EXTENSION OF NITINOL WIRE

Sumanth Chikkamaranahalli and R. Ryan Vallance
Precision Systems Laboratory, University of Kentucky, Lexington, KY

Osamah A. Rawashdeh and James E. Lumpp
Embedded Systems Laboratory, University of Kentucky, Lexington, KY

Bruce L. Walcott
Control Systems Laboratory, University of Kentucky, Lexington, KY

Abstract

A large number of commercial applications could benefit from the properties of shape memory alloy (SMA) used in bias-spring actuators. These actuators often use nitinol wires that contract when heated above their transformation temperatures. During cooling, the wire relaxes and is elongated by a bias-spring. In this paper, we describe the conceptual and detailed design of a precision instrument to characterize the transient and steady-state contraction and relaxation of nitinol wires. Additional analyses of thermal and structural compliance conducted during the detailed design are presented. A variety of performance metrics such as the force, displacement, current and voltage can be determined using this instrument.

Keywords: Nitinol, Shape Memory Alloy, Bias-spring actuators, Instrument Design, Uncertainty

Introduction

Nickel Titanium (NiTi), commonly known as Nitinol, is a Shape Memory Alloy (SMA) that returns to a previously defined shape or size when subjected to appropriate thermal procedures [1]. At low temperatures, SMAs can be plastically deformed like other metal alloys, but this deformation can be recovered by subsequently increasing its temperature. This is known as the shape memory effect. The mechanism of this recovery is the transformation from a martensite phase to the parent austenite phase [2].

An important application of shape memory alloys is in actuators where repeated shape, geometry, or positions are required [3]. The important performance attributes in an SMA actuator are the amount of force and displacement produced as the alloy is thermally cycled. Fig 1 illustrates a typical cycle for a SMA actuator that consists of five time periods. During Periods 1, 3, and 5, the actuator is in a nearly steady-state or static condition. The SMA is heated during Period 2 producing a transient displacement when the wire contracts. During Period 4, the SMA wire cools and elongates to its original length. The response is plotted using a log time scale because the actuation period occurs quickly compared to the cooling period.

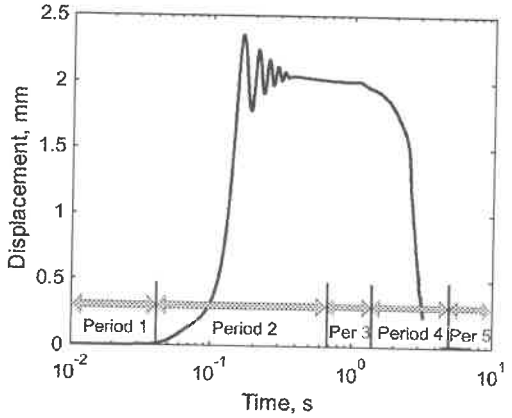

Fig 1: Transient Response of a NiTi Wire

This paper describes the conceptual and detailed design of a new instrument [4] for characterizing the response of NiTi wires. The material being tested is Flexinol™ wire of diameters 0.038 mm, 0.051 mm, 0.102 mm and 0.152 mm and various lengths. The material composition of the Flexinol™ wire is Ni (53%

by weight), Ti (Balance) and impurities (less than 0.03%). The contraction and the extension temperature under 100 MPa stress is 70°C ±15°C and 50°C ± 15 °C respectively [5].

Conceptual Design of the Instrument

The instrument employs a damped, spring-mass system supported by a linear bearing as illustrated in Fig 2. A single NiTi wire is attached between a translating mass and a force gage. A tension spring is attached between the mass and a micrometer so that extending or retracting the micrometer adjusts the preload force in the NiTi wire. The actuation cycle is initiated by resistively heating the NiTi wire by supplying a voltage, *V(t)*, across the NiTi wire. The current, *I(t)*, depends upon the resistance of the NiTi wire.

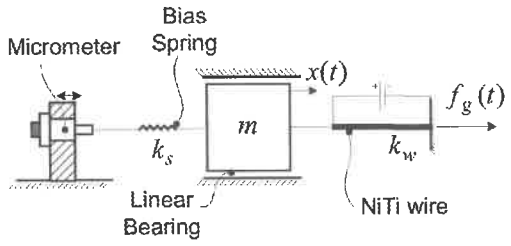

Fig 2: Conceptual Design

Idealized free-body diagrams of the mass during the five static and transient time periods are illustrated in Fig 3. Although the spring stiffness, k_s, remains nearly constant, the wire stiffness, k_w, and damping, c, likely vary with time since the NiTi's properties change with temperature.

Period-1 represents the state of the wire before actuation. The initial force exerted by the spring, ${}^{i}F_s$, equals the product of the spring stiffness, k_s, and preload position, x_p. Similarly, the initial force exerted by the NiTi wire, ${}^{i}F_w$, equals the product of the initial wire stiffness, ${}^{i}k_w$, and x_p. As shown in Eq (1), these forces equal the preload force measured by the gage, F_p, and set with the micrometer.

$$F_p = {}^{i}F_s = k_s x_p = {}^{i}F_w = {}^{i}k_w x_p \tag{1}$$

Period-2 represents the transient state of the wire during contraction of the wire. The wire generates an actuation force, ${}^{c}F_a(t)$, that causes the mass to displace by $x_c(t)$. The wire stiffness during contraction, ${}^{c}k_w$, and damping, ${}^{c}c$, likely vary as the material transitions from martensite to austenite. The equation of motion for Period 2 is then given in Eq (2).

$$\begin{aligned} {}^{c}F_a(t) &= m\ddot{x}_c(t) + {}^{c}c(t)\dot{x}_c(t) + \\ &[k_s + {}^{c}k_w(t)]x_c(t) \end{aligned} \tag{2}$$

Period-3 represents the static actuated state of the wire when the mass is held in position by the contracted wire. During this period, the free-body diagram reveals that the product of k_s and actuated displacement, x_a, equals the sum of the steady-state actuator force, ${}^{ss}F_a$, and the product of wire stiffness upon actuation, ${}^{a}k_w$, and x_a.

$$k_s x_a = {}^{a}k_w x_a + {}^{ss}F_a \tag{3}$$

Period–4 represents the transient state of the wire as it cools and elongates to its original length. The actuation force during extension, ${}^{e}F_a(t)$, decreases, and displacement, $x_e(t)$, results. Again, the damping and wire stiffness will likely vary with time, so that the equation of motion for Period 4 is given by Eq (4).

$$\begin{aligned} {}^{e}F_a(t) &= m\ddot{x}_e(t) + {}^{e}c(t)\dot{x}_e(t) + \\ &[k_s + {}^{e}k_w(t)]x_e(t) \end{aligned} \tag{4}$$

Period-5 represents the static or steady-state of the NiTi wire after the actuation cycle. During this state, the mass returns to its initial position. The final force exerted by the spring, ${}^{f}F_s$, equals the product of spring stiffness, k_s and the final position of the mass, x_f. Similarly, the final force exerted by the NiTi wire, ${}^{f}F_w$, equals the product of the final wire stiffness, ${}^{f}k_w$, and x_f. As shown in Eq (5), these two forces are equal.

$$ {}^{f}F_s = k_s x_f = {}^{f}k_w x_f = {}^{f}F_w \tag{5}$$

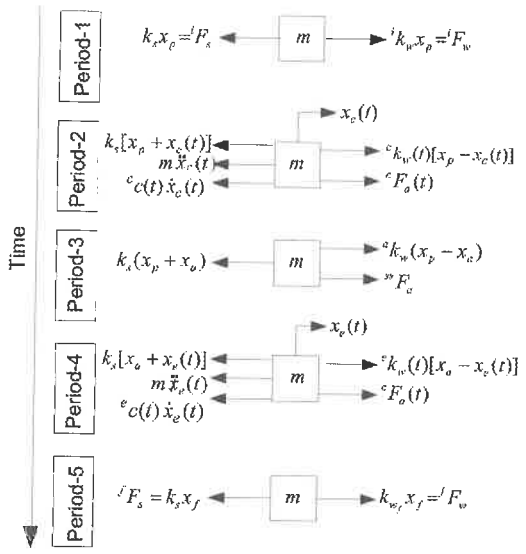

Fig 3: Idealized Static and Dynamic Periods During Characterization of NiTi Wire

Detailed Design of the Instrument

The entire setup is mounted on a base plate machined from cast iron (CI –30) as shown in Fig 4. The instrument consists of a linear motion stage supported by a porous-graphite air bearing (NewWay, S40400305). The bearing consists of a housing and an aluminum guide bar. An important advantage offered by air bearings is its low static and dynamic friction. This is vital since friction force would introduce significant uncertainty in the measurement of contraction forces. Nitinol wires of various lengths and diameters can be attached to one end of the linear motion stage by adjusting the position of the load cell mount.

The other end of the nitinol wire is attached to a stationary load cell (Sensotec, Model 31a, sensitive to tensile forces between 0- 445.0797N (0-100 lb) with a non linearity of ± 0.2% full scale) A tension spring connects to the opposite end of the guide bar to establish a preload force on the nitinol wire. The preload and length of the tension spring are adjusted using a micrometer, (Starrett, No.261L, with a displacement range of 0-12.7mm). This arrangement of the spring and the wire places the forces near the bearing's center of stiffness.

The displacement of the guide bar during the contraction and relaxation of the nitinol wire is measured using a Linear Variable Differential Transformer (LVDT). (Sentec, Model DCFS3/4 with a nominal linear range of 19 mm (0.76 inches), resolution of 0.001% full scale, and a non-linearity of 0.2%) housed within the air-bearing shaft. The output of the LVDT is a $\pm X$ V analog signal.

The transducer core is fastened to the end plate (Al-6061) by means of a threaded stud. The transducer body is held in its position by a clamp (Al-7075). This arrangement illustrated in Fig 5 places the LVDT in the center of stiffness of the air bearing and minimizes Abbe errors.

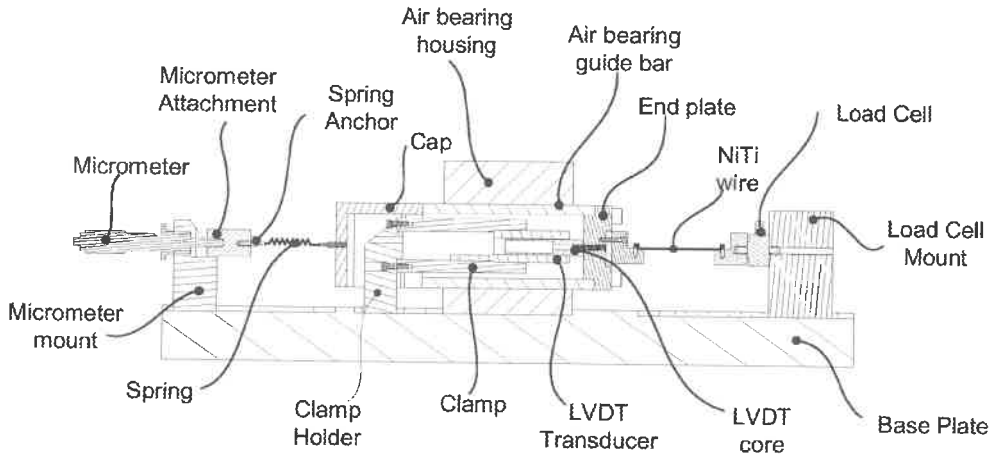

Fig 4: Cross-sectional View of Instrument

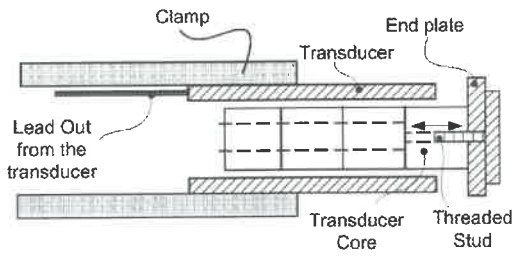

Fig 5: LVDT Setup

Control and Data Acquisition System

A block diagram of the approach to controlling and acquiring data is shown in Fig.6. The data acquisition system is based on a DaqBoard-2001™ by IOtech Inc. hosted in a generic personal computer. The DaqBoard-2001™ features a 200 kHz, 16 Bit A/D converter that is used to sample values from the load cell, LVDT, current meter and the voltmeter.

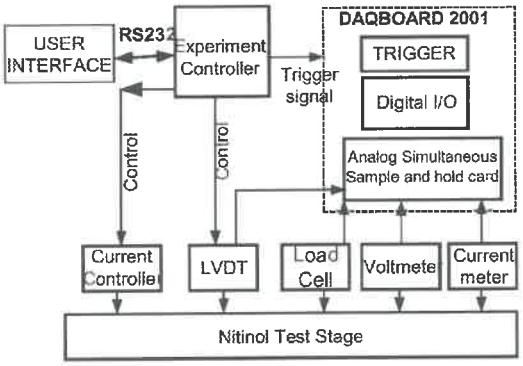

Fig 6: Block Diagram of Electrical Setup

A 4-channel simultaneous sample and hold card is used to sample the four analog signals simultaneously with the single A/D converter. A non-contact commercial current meter by F.W.Bell is used to measure the current running through the SMA wire sample. The mA-2000™ measures currents with a resolution of 0.1mA and an accuracy of 1% of the reading. A universal in-line amplifier conditions the signal from the load cell before being input into the DaqBoard-2001™. The voltage data combined with the current data will allow future studies of the variation in the resistance of shape memory alloys.

The Flexinol™ wire samples are driven by a commercial PWM power supply with variable voltage settings and variable current limitation allowing the freedom of adjusting arbitrary voltages. A trigger signal is generated by the experiment controller and received by the DaqBoard-2001™ to control start time of acquisition. The experiment controller is a micro controller based unit that communicates with a RS232 serial port on a PC. The experiment controller allows the user to set a number of experimental parameters such as the number of actuation cycles, the duration of actuation, and the cooling time between actuation cycles.

Error Analysis

In analyzing the errors within the instrument, one should consider the following error sources that affect the force or displacement measurements.

Thermal Expansion

Fig 7 illustrates the effect of thermal expansion in the instrument as a result of temperature fluctuation in the surrounding environment. One way to minimize this effect in the instrument is to match the axial expansion of the guide bar with that of the base plate.

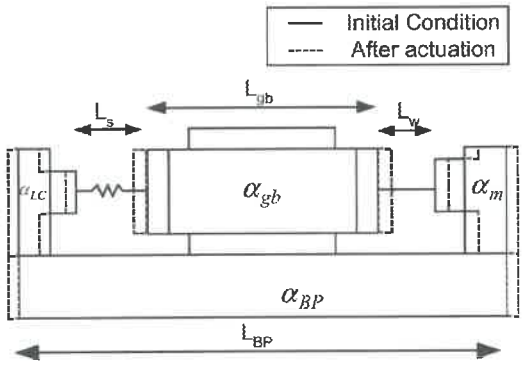

Fig 7: Thermal Expansion of Instrument

The axial expansion of the base plate, δ_{BP}, with a coefficient of thermal expansion, α_{BP}, length, L_{BP}, and a temperature fluctuation of, ΔT, is given in Eq (6).

$$\delta_{BP} = \alpha_{BP} L_{BP} \Delta T \qquad (6)$$

Similarly, the axial expansion in the guide bar material, δ_{gb}, with a coefficient of thermal

expansion, α_{gb}, length, L_{gb} and a temperature fluctuation of, ΔT is given in Eq. (7).

$$\delta_{gb} = \alpha_{gb} L_{gb} \Delta T \tag{7}$$

Since the lengths of the spring, L_s and the NiTi wire, L_w should be constant, the uncertainty [6] in the force measurement, U_F, that results from expansion is a function of, k_s, α_{BP}, α_{gb}, L_{BP}, L_{gb} and ΔT, and is given in Eq.(8).

$$U_F = k_s \Delta T(\alpha_{BP} L_{BP} - \alpha_{gb} L_{gb}) \tag{8}$$

To minimize UF, the expression parentheses should be nearly zero. Therefore, the ratio of the CTEs should be nearly equal to the ratio of the lengths as given in Eq (9). The guide bar is made of aluminum ($\alpha_{gb} \approx 23\text{x}10^{-6}$ 1/°C), and the base plate can be made of CI-30 cast iron ($\alpha_{BP} \approx 10.5\text{x}10^{-6}$ 1/°C). The appropriate length of the base plate that minimizes U_F is then about 400 mm.

$$\alpha_{BP} / \alpha_{gb} = L_{gb} / L_{BP} \tag{9}$$

Compliance of the Instrument

Compliance in structural components like the base plate, the load cell mount and the micrometer mount affect the uncertainty in displacement measurements. These parts need to be stiff to reduce the deflections and changes in geometry due to forces. The deformation in the geometry of the instrument is illustrated in Fig 8.

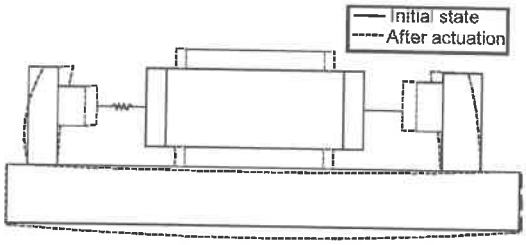

Fig 8: Deformation Due to Compliant Instrument

Fig. 10 illustrates the instrument as a combination of a mass and springs in series, whose stiffness can be predicted using finite element analyses. If the stiffness for each structural component, k_i, is combined using Eq (10), then the equivalent instrument stiffness, k_I, can be used in the simplified model of Fig. 9.

$$k_I = [\sum_{i=1}^{n} (1/k_i)]^{-1} \tag{10}$$

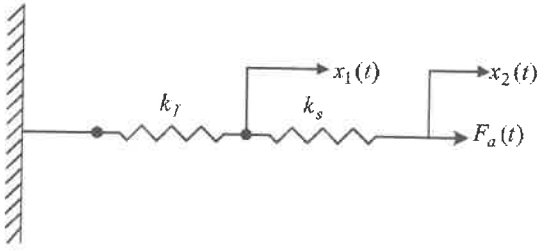

Fig. 9: Integrated Spring Model

The uncertainty in the displacement measurement, U_c, is approximately the ratio of the actuator force, F_a, and the instrument stiffness, k_I, given in Eq (11)

$$U_c = F_a / k_i \tag{11}$$

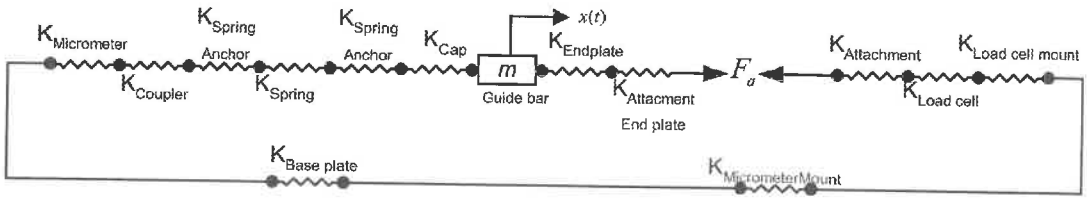

Fig. 10: Closed-loop Spring Model

Conclusion and Future Work

This paper describes the conceptual design, detailed design, and some error sources in a new instrument for characterizing Flexinol wires. The instrument uses a damped spring-mass system with an LVDT and force gage. A controller and data acquisition system enable force, displacement, current, and voltage to be measured as functions of time. Future experiments will characterize the variability in wire and actuator parameters, degradation of wire properties over many cycles, and optimization of control strategies.

Initially, the instrument will be used for investigating the transient displacement, steady-state actuation displacement, x_a, and actuation force, ${}^{ss}F_a$. Future work is necessary to characterize the transient actuation force produced by the wire. During the transient periods, the force recorded by the load cell is actually a combination of the wire's actuation force, the viscous damping forces, and inertial forces. Furthermore, the displacement of the mass is the convolution of the actuation force and the system's impulse response function. A method should be developed for separating these forces so that the transient actuation forces, ${}^{c}F_a(t)$ and ${}^{e}F_a(t)$ are obtained.

References

[1] Darel E. Hodgson, Shape Memory Applications Inc., Ming H.Wu, Memry Technologies, and Robert J.Biermann, Harrison Alloys, Inc. "Shape Memory Alloys.

[2] John A.Shaw and Stelios Kyraiakides, "Thermomechanical Aspects of NiTi", *Journal of Mech.Phys Solids, Volume 43 No.8, pp.1243-1281, 1995.*

[3] C.Liang, C.A.Rogers, "Design of Shape Memory Alloy Actuators", *Journal of Mechanical Design, June 1992, Vol.114/223*

[4] "Precision Machine Design" Slocum, A.. *Prentice Hall. Englewood Cliffs, New Jersey. 1992*

[5] Dynalloy Inc.,Costa Mesa, CA, "Material properties of Flexinol".

[6] "Test Uncertainty–Instruments and Apparatus", *ASME PTC 19.1.1988, American Society of Mechanical Engineers, 1998.*

SEGMENTED AND SHIELDED STRUCTURES FOR REDUCTION OF THERMAL EXPANSION-INDUCED TILT ERRORS

A. John Hart (ajhart@mit.edu), Alexander H. Slocum
Precision Engineering Research Group
Massachusetts Institute of Technology, Cambridge, MA

I. Introduction

Microscopes are now utilized for a wide variety of tasks in addition to imaging, requiring complex laser optics, metrology tools, and precision motion mechanisms in conjunction with the basic microscope structure. These technological advances have made single molecule detection and analysis possible, driving interest in measurements with subnanometer precision. However, structural designs of current microscopes, which have retained a similar cantilevered shape for decades, make such advanced setups cumbersome, difficult to reconfigure, and unacceptably sensitive to thermal and mechanical disturbances. Significant improvements in the flexibility, stability and resolution of the microscope are needed.

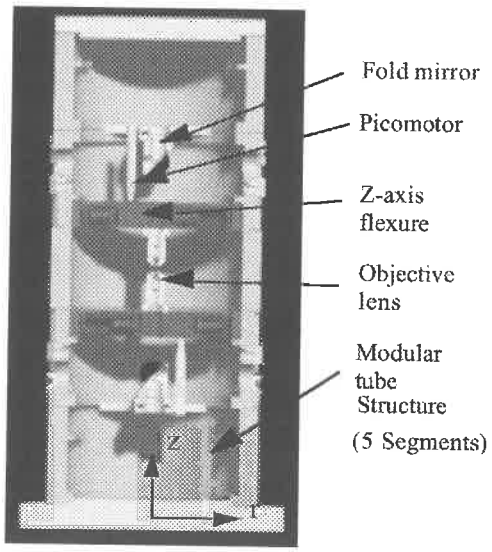

Figure 1: Segmented tube microscope structure.

The High Precision Microscope (HPM) project, headquartered at the University of Illinois Laboratory for Fluorescence Dynamics with the mechanical design and testing conducted by the MIT Precision Engineering Research Group, is developing a novel microscope system for single molecule experiments. The main feature, shown in Figures 1 and 2, is a series of five aluminum rings connected by kinematic couplings. The sample stage and lens optics are fastened to the inside surfaces of the ring modules, and the optical signals are transmitted to and from the lasers and signal processing equipment (placed away from the structure) by fiberoptic cables. This paper focuses on the thermal error modeling and testing of the HPM structure.

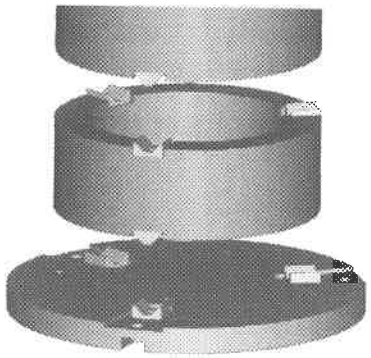

Figure 2: Tube interfaces using canoe ball kinematic couplings.

II. Structure Design

Compared to a traditional cantilevered microscope design or a single-tube structure, the segmented tube structure has two main performance advantages. First, as shown by the simulated isotherms in Figure 3, the gaps between the segments restrict heat flow parallel to the axis of the tube stack. As a result, the temperature distribution around the circumference of each tube under a thermal gradient in the ambient, characterized most simply by the difference in the surface temperature between opposite sides of the tube surface, is more uniform with a segmented design. Increasing the angular uniformity of the temperature distribution decreases the tilt error of the structure. Furthermore,

infinity corrective objectives used in microscopy are not sensitive to uniform axial expansion, and radial expansion is not an issue as long as the center point where the objectives reside remains in the same radial position as the elements along the optical path.

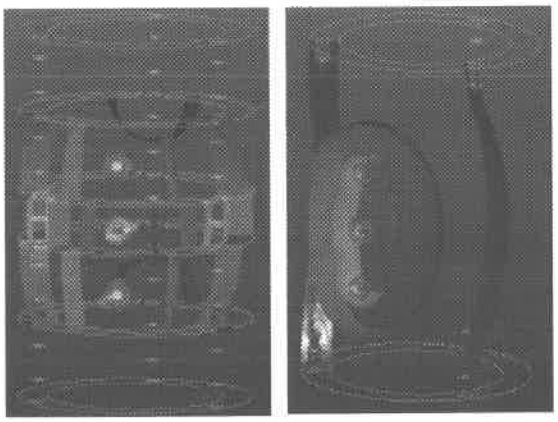

Figure 3: Steady-state isotherms on segmented and one-piece tube structures

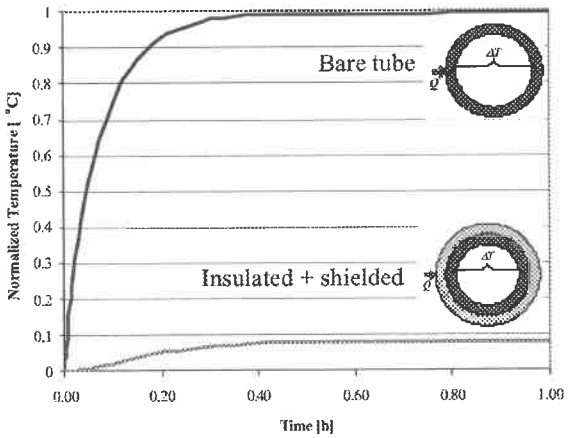

Figure 4: Simulated performance of shielded and insulated tubes under step heat input.

Each tube segment can be further thermally stabilized by insulating and shielding its outside surfaces. Here, the inner structural ring is covered by a layer of fiberglass insulation, and held in place by a thin shield having high thermal conductivity (e.g. aluminum or copper). The shield quickly dissipates temperature differences around its circumference [1], and the insulation increases the thermal resistance between the outside shield and the load transmission points on the inner ring. Figure 4 compares the simulated performance of a bare tube cross section to that of an insulated and shielded tube cross section. For the dimensions chosen, the shielding and insulation more than doubles the response time to a step input, and the steady-state temperature difference across the shielded and insulated tube is one-tenth of that across the bare tube. Similar results are noted when an oscillating input is tested; the shielding and insulation both delay and significantly reduce the magnitude of the disturbance on the structural section.

Second, the HPM design benefits from precision mechanical alignment of the optical axes, enforced by the inherent repeatability of the precision-ground "canoe ball" (named as such because the large-radius spherical surfaces look like the bottom of a canoe) kinematic couplings between the segments. Several studies have demonstrated sub-micron repeatability of kinematic couplings [2,3,4,5], and the detailed analysis methods for considering effects such as nonrepeatability due to friction [6] and interchangeability errors due to manufacturing variation [7] are now well-known. The equal-angle groove arrangement of the kinematic coupling averages the radial thermal expansion errors of the tubes to minimize the drift of the central optical axis. Different optical modules can be attached to pre-calibrated "replacement" tube segments, and the segments can be interchanged to reconfigure thhe setup of the HPM without requiring coarse re-calibration of the instrument each time.

III. Approximation of Thermal Errors

A difference in axial thermal expansion induced by a circumferential temperature gradient around the tube structure causes the tilt error motion shown in Figure 5. In terms of the temperature profiles along the heated (T_h) and non-heated (T_n) sides, the material coefficient of thermal expansion (α_t), and the initial height of the stack (L_o), the differential expansion (δ) of the opposite sides of the stack is

$$\delta = \alpha_t L_o(\overline{T}_h - \overline{T}_n) = \alpha_t \left(\int_0^{L_o} (T_h(z) - T_n(z))\, dz \right). \quad (1)$$

Hence, the tilt angle (θ_{tilt}) of the top plate is

$$\theta_{tilt} = \operatorname{atan}\left(\frac{\alpha_t L_o(\overline{T}_h - \overline{T}_n)}{D_s} \right). \quad (2)$$

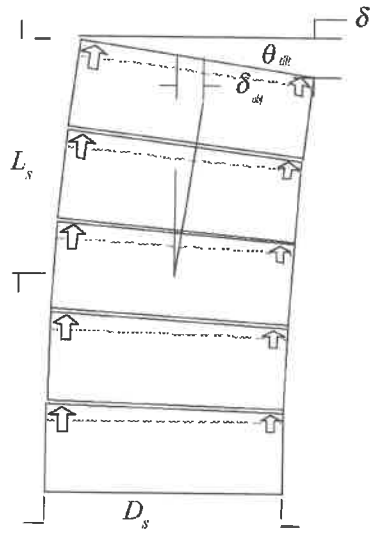

Figure 5: Tilt error motion of segmented structure.

The distance (δ_{obj}) by which the position of the sample moves with respect to the optical backplane (where the lasers are focused at the top of the structure) is

$$\delta_{obj} = L_S \frac{\alpha_t L_o (\overline{T}_h - \overline{T}_n)}{D_s} . \quad (3)$$

Treating the circumferential path of heat conduction around the structure as through a linear body with effective area A, effective length L, and material thermal conductivity k, the heat flow Q is

$$Q = \frac{(\overline{T}_h - \overline{T}_n)}{L} Ak. \quad (4)$$

Rearranging (3) and substituting into (2):

$$\delta_{obj} = L_S \frac{\alpha_t L_o L Q}{D_s A k} . \quad (5)$$

Therefore, with the goal to minimize δ_{obj} for a chosen structure geometry, the best material for steady-state performance is one with maximum thermal conductivity per unit of tendency to thermally expand, k/α_t.

In terms of transient performance, the penetration depth x of temperature change through the structure at time t after a constant thermal disturbance is applied is

$$x = \frac{\sqrt{\alpha t}}{\mathrm{Fo}} , \quad (6)$$

where Fo is the Fourier number based on the structure geometry [8], and α is the material thermal diffusivity. Assuming fixed geometry, the best structure material for transient performance is one with maximum α/α_t.

IV. Experiments

A. Setup and Procedure

The thermal stability of the microscope structure was evaluated by applying localized heat inputs to its outside surface, and measuring the resulting circumferential and axial temperature distributions around the tubes, as well as the tilt motion of a top reference plate. Two structures were tested: the five-segment aluminum structure shown in Figure 6, with 12" outside tube diameter, 1.5" wall thickness, 25" total height, and 250 mm radius stainless steel canoe ball couplings between the segments; and a structure with a single tube having equivalent dimensions to the stack of five segments. Later, each tube was covered with 1" of fiberglass insulation (k = 0.03 W/m-K) and a 1/16" aluminum shield.

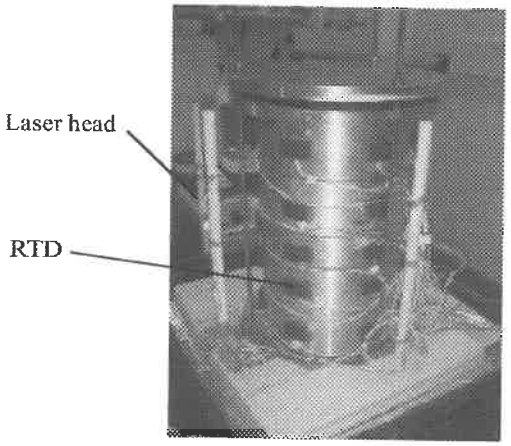

Figure 6: Prototype segmented structure, instrumented for thermal error measurements.

The temperature distribution on the structures and in the surrounding air was monitored using three-wire platinum RTD's (resistive temperature detectors). The RTD's were wired to a National Instruments LabView Data Acquisition System with 16-bit D/A conversion of the measured voltage giving resolution of 0.009 °C.

Angular drift was measured using a Zygo differential plane mirror interrometer (DPMI) [5], mounted to a 5" diameter aluminum column placed

within the stack assembly. The DPMI sensed the tilt of a reference mirror mounted to a horizontal reference plate attached to the top of the tube set. Temperature readings from the surface of the central column showed that it was sufficiently isolated from thermal gradients in the tube structure to be a reference mounting for the interferometer.

Thermal disturbances were applied to the structure using Minco copper thin film heating elements, each measuring 1/2" x 1/2". Three sources were mounted directly to the structure, one each at the vertical midpoints of the three center tubes, aligned vertically parallel to the single axis of the interferometer. The sources were wired in a parallel circuit.

The test apparatus (excluding the laser source) was placed in an insulated chamber constructed of 4" thick extruded polystyrene (Styrofoam), and mounted on an air-shock isolation table. Single-point readings from the interferometer and each RTD were taken once per minute, with a six-hour-long 3W (5V, 0.6A) step input starting one hour after data acquisition began. Real heat inputs to a microscope structure may be as small as 0.1 W from low heat-dissipation actuators, or as high as 30 W caused by an operator standing close to a bare structure [1].

In addition to the experimental setup, finite element models of the two structures were built in Pro/MECHANICA™. As a simplification, the kinematic coupling balls and grooves between the segments were replaced by sets of square (a very liberal estimate given the true nearly point contact) contacts between the tube-to-tube gaps. Derived from thermobuoyant convection relations for vertical cylinders and horizontal plates [9], a uniform steady-state loss coefficient was defined on each external surface of the model. The tilt angle of the structure was calculated using the results of the thermal analysis as a temperature boundary condition for a structural analysis.

B. Results

Figure 7 compares the measured tilt error of the single-tube structure, the segmented structure, and the segmented structure with insulation and shielding on the three heated segments. At steady-state, the bare segmented structure drifts approximately 40% less than the one-piece structure (0.61 arcsec vs. 0.86 arcsec). Insulation and shielding reduce the maximum drift to only 0.24 arcsec, a 75% overall improvement. The differences in the rates of drift are also significant; the drift of the segmented structure within the first hour of heating (a typical duration of an experiment with the HTM) is 60% less than of the single-tube design, due to the shorter time it takes for heat to reach the axial conduction constraints imposed by the gaps between the tube segments. This initial rapid drift is not seen with the shielded and insulated structure because the insulation delays penetration of the disturbance to the inner tube until well after the disturbance has propagated fully around the circumference of the shield.

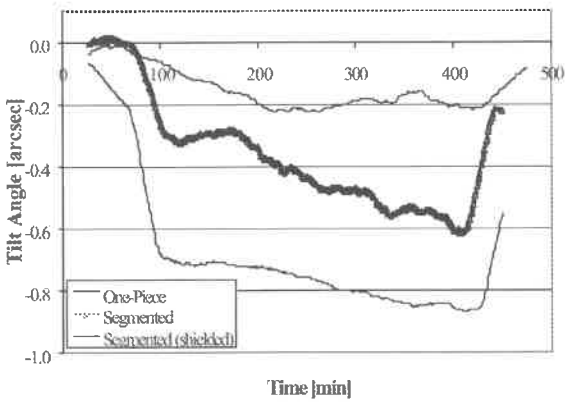

Figure 7: Measured tilt error (15-minute moving average of interferometer readings)

Level	Seg *FEA*	Seg *Meas.*	OnePc *FEA*	OnePc *Meas.*
1	0.01	0.00	0.07	0.06
2	0.12	0.13	0.12	0.09
3	0.18	0.21	0.12	0.12
4	0.12	0.12	0.12	0.09
5	0.01	0.00	0.07	0.06

Table 1: Simulated and measured circumferential temperature differences [°C] (level 1 = bottom).

Table 1 compares the measured steady-state temperature differences at the centerline level of each tube to those simulated by FEA. These differences are 0.03 °C or less at all levels of both structures, within reasonable tolerances for validation of the finite element model as a tool for design optimization. Discrepancies arise because the simulation is a steady-state calculation only, the coupling coupling

contacts are idealized, and the convection coefficient on the outer surface of the models is uniform. The FEA model predicts tilt of the segmented and one-piece designs of 0.50 and 0.75 arcsec, both approximately 15% less than the measured values taken after 450 minutes of testing.

V. Design Studies

Validation of the finite element models permitted their use for design optimization. First, a performance comparison between materials gave the tilt values listed in Table 2, showing copper to be the best traditional metal for the structure. Investigation of ceramics and other low-expansion materials (e.g. Invar) is also worthwhile.

Material	Tilt
Aluminum (6061)	1.00
Copper	0.35
Brass	1.40
Stainless (1040)	4.20

Table 2: Simulated tilt errors for common structural metals, normalized relative to value for Aluminum.

Next, keeping the total tube length and the inside diameter as packaging constraints, the tube thickness of both structures was varied within reasonable bounds of 1.0" and 2.5". Then, for the segmented structure, total length, inside diameter, and thickness were held constant and the number of segments was varied. For simplicity of the analysis, one 3W heat source was applied at the horizontal centerline of the structure.

Figure 8 shows that the error motion monotically decreases with increasing tube thickness for the one-piece structure and for the structure with five segments. Hence, a better design is one with five thick segments, and a structure with five segments always outperforms a one-piece structure of the same thickness. The data series marked by triangles shows the error motion with thickness fixed at 1.5", with the number of segments varying (in increments of two) from one to nine. When the results with varying thickness and with varying number of segments are collapsed onto the same plot in terms of the segment height to thickness ratio, Figure 9 results. Here, the (square- and diamond-marked) curves for when thickness is varied are similar in shape (within the convergence confidence of the simulation), and are simple translations along the triangle-marked curve for when the number of segments is varied. These results demonstrate that constraining the axial flow using a shorter segment is advantageous only until the effect of the decreased thermal capacitance of the segment takes over, after which the greater overall heating of the segment increases the magnitude of the thermal expansion.

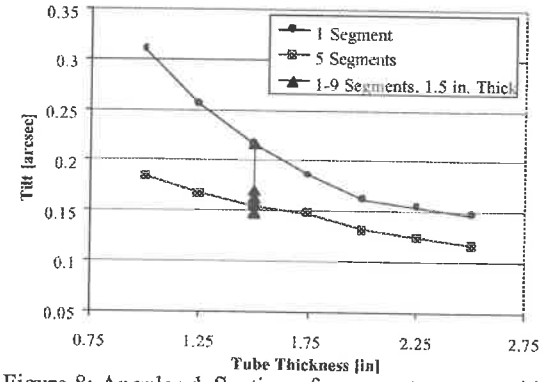

Figure 8: Angular deflection of copper structures with varying tube thickness

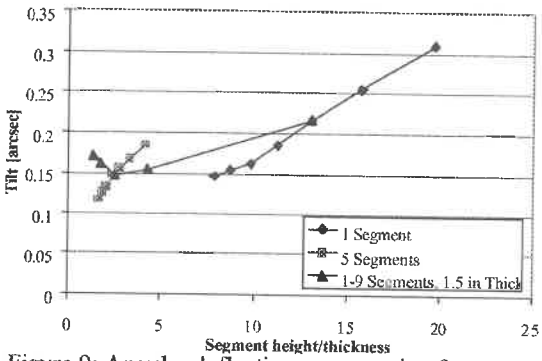

Figure 9: Angular deflection versus ratio of segment height to segment thickness

Design	Drift [nm]
One-segment Al (measured)	533
Five-segment Al (measured)	376
Five-segment Cu (FEA)	133
Five-segment 2.5" thick Cu (FEA)	99
Five-segment 2.5" thick Cu, 2" insulation. 1/16" shield.	26

Table 3: Predicted linear drift of several designs.

Finally, Table 3 compares the performance of various designs considered throughout the study, in terms of the translational error at the optical backplane, computed according to Eq. 3. Simulation predicts that a five-segment copper structure, with 2.5" thick segments covered by 2" of insulation and 1/16" copper shielding will drift nm over several hours, a 20-fold improvement over the initial aluminum segmented structure design

VI. Conclusions

The results of the thermal study of the HPM structure demonstrate the feasibility of a segmented design for modular serial assemblies, such as instrumentation structures including microscopes and high-precision reconfigurable industrial equipment such as large coordinate measuring machines or assembly robots. The design significantly reduces the thermal sensitivity of a tubular structure, while maintaining structural integrity and offering the flexibility of disassembly, reconfiguration, and reassembly using kinematic couplings. Insulation and shielding is shown to significantly reduce steady state thermal errors. Experimental results validate use of sequential thermal and structural finite element simulations for design optimization of segmented structures based on steady-state drift approximations. Measurement and modeling of the performance of the structure designs under fluctuating heat inputs will be performed next, after which a new structure will be built and tested in operation as a high-precision microscope.

Acknowledgements

John Hart gratefully acknowledges the support of a National Science Foundation Graduate Research Fellowship and a Fannie and John Hertz Foundation Fellowship. Philip Loiselle and Way Luu helped machine, assemble, wire, and test the prototype structures. Way's work was supported by the Ralph L. Evans (1948) Endowment Fund for undergraduate research (UROP) at MIT. Jason Sutin of the University of Illinois Laboratory for Fluorescence Dynamics guided the design requirements for the HPM structure.

References

[1] Ruiji, Theo. "Ultraprecision Coordinate Measuring Machine", Ph.D. Thesis, Eindhoven, The Netherlands, 2001.

[2] Slocum, A. H. and A. Donmez. "Kinematic Couplings for Precision Fixturing - Part 2: Experimental Determination of Repeatability and Stiffness", *Precision Engg*, vol. 10, No. 3, July 1988.

[3] Mullenheld, B. "Application of kinematic couplings to a grinding wheel interface", S.M. Thesis, University of Aachen (Germany), 1999.

[4] Poovey, T., et al. "A Kinematically-Coupled Magnetic Bearing Test Fixture," *Precision Engg*, Vol. 16, No. 2, April 1994.

[5] Slocum, A.H. Precision Machine Design, Society of Manufacturing Engineers, 1992.

[6] Hale, L. and Slocum, A.H. "Optimal Design Techniques for Kinematic Couplings", *Precision Engg*, 2000, 25(2), 114-127.

[7] Hart, A. J. "Design and Analysis of Kinematic Couplings for Modular Machine and Instrumentation Structures", S.M. Thesis, Massachusetts Institute of Technology, 2001.

[8] Leinhard, J.H. IV, and J.H. Leinhard V. A Heat Transfer Textbook, Phlogiston Press, 2001.

[9] Kaviany, M. Principles of Heat Transfer, Course Reader for Mechanical Engineering 370, University of Michigan at Ann Arbor, 1999.

Design of a Dual Servo XYtheta Stage using double H frame

K. H. Kim, M. G. Lee, D. M. Kim, and D. G. Gweon
Korea Advanced Institute of Science and Technology, Daejeon, Korea

Key words: Dual Servo, Decoupling mechanism, Precision stage, Double H frame, I-bar

1. Introduction

Dual servo actuator is very frequently used for ultraprecision stages requiring long travel and ultra fine resolution: from hundreds mm to nm. Especially, in recent year CMM and a high precision machine tool need it. It is composed of a coarse and a fine actuator. And, they have to carry out respectively long travel in XY and fine motion in XYtheta. In addition, a few requirements of it are decoupling mechanism between a Coarse and a Fine actuator, high speed and high power.

2. Conceptual Design of Dual Servo XYtheta Stage

A. Fine Actuator

At first, decoupling mechanism between a Coarse and a Fine comes from VCM(Voice Coil Motor) concept that a force is generated by a energized coil and magnetic field induced by magnet without contact with coil as shown in Fig. 1. [1] That is to say, as three coils of Coarse are energized in magnetic filed, Fine with three magnet pairs moves without physical contact between Coarse and Fine. And by adjusting three inputs through coils, Fine is able to have fine motions in XYtheta from millimeters to nanometers. Coils and magnets are located triangularly and respectively on frames of Coarse and Fine for symmetric structure to decrease thermal effect as shown in Fig. 2. [2] And then, Fine uses preloaded air bearings such as bearings of *New Way Machine Component. INC.* bottom magnet pairs in a frame of Fine on a granite plate with a triangular shape such like a location of three magnet pairs as a guide mechanism. So that, Fine actuator may be called as a tracking actuator.

B. Coarse Actuator

Second, Coarse actuator following Fine consists of double H-frame with four linear motors, a coil jig with three coils to drive Fine and several air bearings for guide mechanism The advantages of Double H-frame are symmetric structure and to induce higher force. And this actuator system uses 'I-bar' for composing of double H-frame to have higher rigidity, lighter, more compact. It is composed of two linear guides with rectangular granites and a window frame respectively with two linear motors, namely, that two motors are used for one axis movement with higher force. The linear motor is a moving coil type that has fixed magnet arrays and yoke bar and moves sustaining a distance on magnet arrays. In here, magnet arrays with a yoke bar are put on an optical table in a state of being able

to be moved by a reaction force and coils in the window frame. Coarse actuator might be called a follower because it follows fine actuator.

C. Guide system and Dual Servo XYtheta Stage

As above mentioned, Coarse has two axis motions that a window frame moves in one axis and a coil jig in other.

The window frame slides along two rectangular granites and on a granite plate. At that time, it uses several air bearings that some is on two rectangular and others on a granite plate. Especially, four air bearings are along two rectangular granites. Two are vacuum preload types and others not preloaded but flexure system. This system uses a rectangular granite bar with three bearings with two preloaded bearings and a general flat bearing as a reference of guide system in one axis that the window frame moves along, and other granite bar with a remaining as an adjusting guide.

And the coil jig with three coils moves in window frame composed of '?bars' and on a granite plate by using force from two linear motors that are composed of magnet arrays fixed at the window frame and coils fixed at coil jig and operated as above mentioned and a guide mechanism with several air bearings using like it of the above window frame.

3. Design of Dual Servo XYtheta Stage

A. Fine actuator

(1)XYtheta Stage

As shown in Fig. 3, Actuating Forces for XYtheta motions of Fine actuator are generated from Lorentz motor with magnets(NdFe40), yoke systems(steel1010), and coils. To design Lorentz motor for fine actuator, permeance method is used. With the method, in the limit of size, power, current, and so forth, the optimal design has been carried out. Results are shown in Fig. 4. Especially, this Lorentz motor generates a force to actuate fine actuator with its acceleration above 5(m/sec^2) in 0.53(T) between magnets. This XYtheta Stage includes leveling actuator for leveling and focusing due to the tightness in depth of focus on the decrease of lateral resolution – that is the shrink of an optical source, for example DUV. The actuator force is governed by flux change between a solenoid and a permanent magnet [3][4]. That is located on the triangular such as Lorentz motor for XYtheta Stage. Fine actuator is presented in Fig. 5.

B. Coarse Actuator

(1)Linear Motor using Halbach Magnet Array

As mentioned above and shown in Fig. 6, Linear motors with Halbach magnet array are designed for actuating coarse actuator. We calculate Maxell equations to have optimal design values for linear motors – especially in coarse actuator [5].

In detail, a linear motor for x-axis has magnets(75mm*12mm*11.25mm), coils connected to a window frame, and so forth, and for y-axis magnets(45mm*12mm*12.9mm). Optimal values happen as shown in Fig. 7. So that, a force for x-axis is 220N with induced current 2A and for y-axis 150N that respectively generates above 5(m/sec^2) with a safe factor –1.5.

C. Design of Dual Servo XYtheta Stage

According to be mentioned above, we design and assembly a noble actuator. This actuator is presented in Fig. 8. The size of this system is about 600mm*600mm*100mm to have a stroke range above 150mm. And frames are made of AL7076, total mass of fine actuator about 10kg, and of coarse actuator below 30kg. At last, this actuator system may have 6inch wafers.

Conclusion

This paper presents the design of each parts and assembled double H frame stage with them for Xytheta motions. Actuator system consists of fine and coarse actuator, respectively with Lorentz motor, three preloaded air bearings and mirrors, and with linear motors, several air bearings, and guide systems. And we designed a noble actuator system with above 5(m/sec^2) and with above 150mm moving range by using SQP of MATLAB program for optimal design of this actuator system.

References

1. Hans Butler, R. A. George and J. Baselmans, *Microlithography World*, pp. 8~16, Spring(1999)

2. D. M. Kim, K. H. Kim and D. G. Gweon, *ICCAS 2001*, October(2001).

3. Bruno Lequesne, "Fast-Acting, Long-Stroke Solenoids with Two Springs," *IEEE Trans. Ind. Appl.*, vol. 26, no. 5, pp. 848-856, Sept./Oct. 1990.

4. K. H. Kim, D. M. Kim and D. G. Gweon, *ICCAS 2001*, October(2001).

5. John T. Reitz, et al., *Foundations of Electromagnetic Theory* 4th edition, Addison-Wesley Publishing Company,1993.

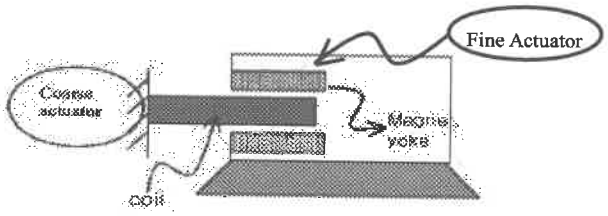

Fig. 1 Concept of Fine actuator

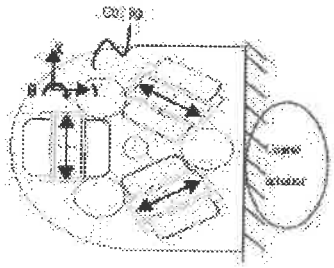

Fig. 2 Symmetric structure of fine actuator

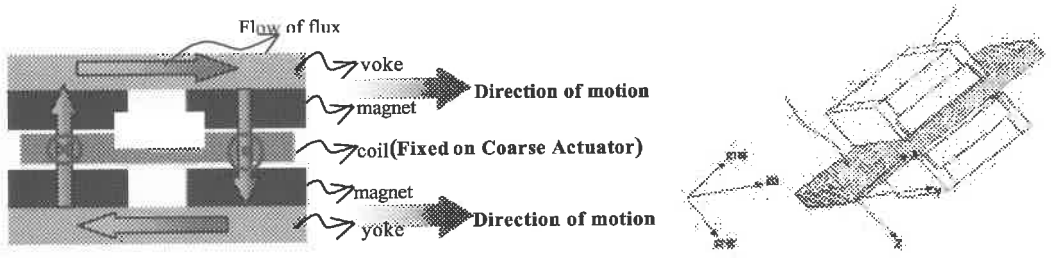

(a) Section of a Lorentz motor (b) Structure of a Lorentz motor in 3-D

Fig. 3 Lorentz motor for fine actuator

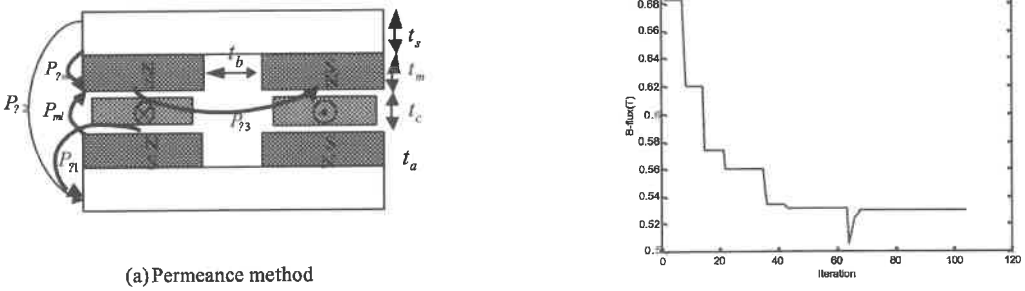

(a) Permeance method

(b) Optimal Value in B-flux(0.53T)

Fig. 4 Permeance method and optimal value of B-Flux for fine actuator

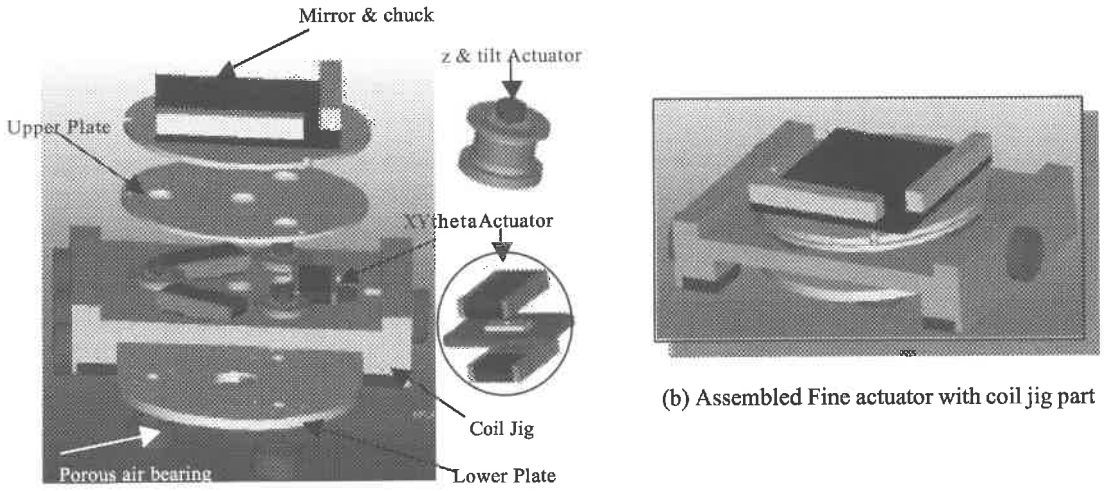

(a) Exploded Fine actuator with coil jig part

(b) Assembled Fine actuator with coil jig part

Fig. 5 Fine actuator for a noble Dual servo system

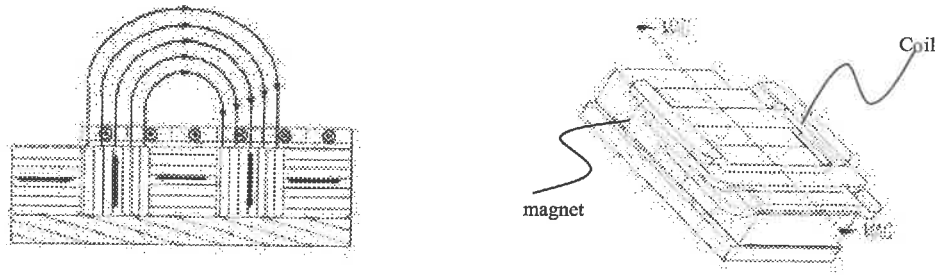

Fig. 6 Halbach Magnet Array for XY linear motors

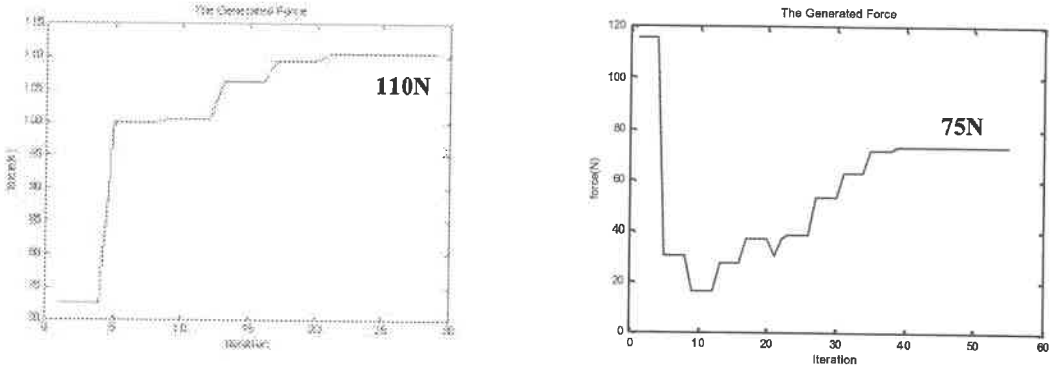

(a) Optimal Value of X-linear motor in one side

(b) Optimal Value of Y-linear motor in one side

Fig. 7 Optimal Values for XY linear motors

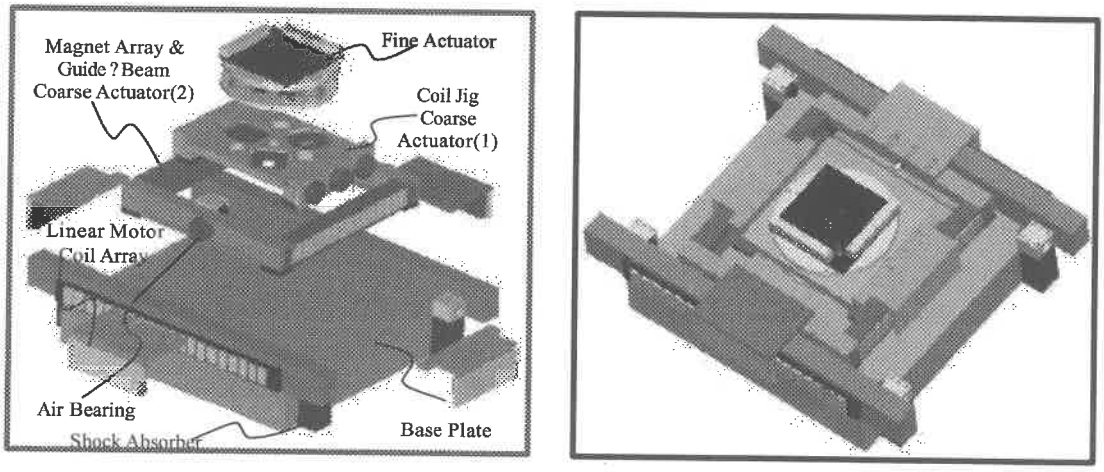

(a) Exploded actuator system

(b)Assembled actuator system

Fig. 8 Noble Dual Servo XYtheta Stage using Double H frame

System Design Methodology for Precision Layout Machines

Min-Seok Kim and Sung-Chong Chung

HYbrid Systems Design and Control LABoratory
School of Mechanical Engineering
Hanyang University, SungdongGu, Seoul 133-791, Korea

Abstract

This paper describes the development of a layout machine using an open architecture controller satisfying various needs of end-users. Driving motors of the layout machine are optimally selected by minimizing the heat dissipation of motors subjected to the constraints of torque and speed. Control parameters of each axis are tuned simultaneously through a heuristic approach. By using Taguchi method, optimal and robust control parameters are obtained. Performance of the developed layout machine is verified through several kinds of experimental work.

Keywords: Flexible measurement, Layout machine, Minimum heat dissipation, Optimum motor, Open architecture controller, Optimum control parameters, Taguchi method

1. Introduction

A horizontal arm type coordinate measuring machine is often called a layout machine. As it is simple in construction, inexpensive and convenient to use, it has been widely used in the manufacturing industry. However, because of the structural limitation, this type of coordinate measuring machine cannot give high accuracy [1, 2]. Layout machines are composed of machine structure, mechanical driving parts and sensors as well as motion controllers. Performance of a layout machine is determined according to their characteristics and interaction. Therefore, a system design method based on the integration of various components is required to develop a high precision layout machine. In addition, a layout machine cannot be used various kinds of measuring applications because the measuring performance depends upon the size of measuring targets, the quality of measuring accuracy and measuring speeds. In order to adapt various measuring tasks, a flexible measuring system providing convenient modification performance of measuring parameters or operating conditions without the extensive knowledge about the measuring system is required as an open architecture system.

However, it is difficult to implement these requirements, the integration of various components and the flexibility in measuring tasks, through existing control systems that have been designed for a dedicated purpose [3]. In this paper, a precision layout machine is studied by using an open architecture control system. Modules performing basic functions are designed and implemented to provide the flexibility and functionality.

In order to increase measuring accuracy and performance of the layout machine, electro-mechanical parts of the machine must be designed under the optimal conception. After constructing mechanical parts of the layout machine, driving motors satisfying the specified constraints such as a peak and rated torque, speed, and rotor inertia are optimally selected by minimizing heat losses of the motor.

Industrial motion control systems are essentially based on the three-term PID controller due to the effective and reliable characteristics. While the characteristics are appealing, PID controllers may be poorly tuned because traditional tuning methods need a closed-form mathematical model of the system and controller dynamics [4, 5].

In this paper, a heuristic optimum selection method is studied in tuning process of control parameters for layout machines. In this process, mathematical models of the system and additional devices are not needed. During this heuristic approach, the errors are measured through the error analysis module implemented by the open architecture control system. All of 12 controller gains of three driving motors are tuned simultaneously.

Through several kinds of experimental work, performance of the developed open architecture control system is verified.

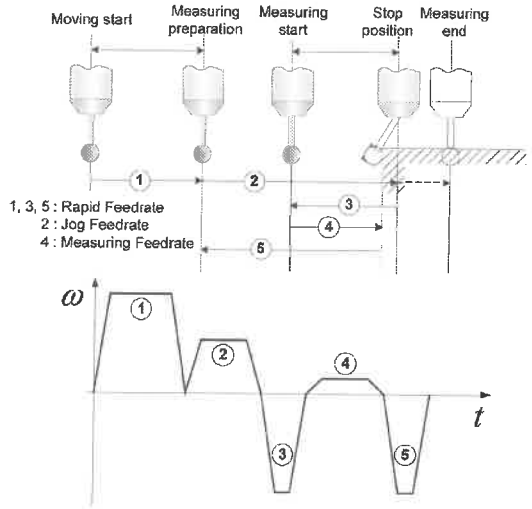

Fig.1 A duty cycle in measuring operation

2. Design of driving system

After selecting components of driving mechanism, designers have to select driving motors according to the specified performance of the system [6, 7]. In this paper, racks and pinions are used for the driving mechanisms. Driving motors satisfying the specified peak and rated torque, speed as well as rotor inertia are optimally selected by minimizing heat losses of the motors.

Torque requirements used in the selection of driving motors may be suitably expressed in the form of a duty cycle. A duty cycle used to measuring operations is specified by a series of trapezoidal speed profile as illustrated in Fig. 1. When a duty cycle is given, the torque and speed requirements on the motor to be selected may be derived. The motor torque T is determined as

$$T = J\alpha + T_L = (J_L + J_m)\alpha + T_L \tag{1}$$

in which, T_L is the friction torque due to external load, α is the acceleration of motor, and J_L is the load inertia expressed as

$$J_L = \left\{ J_W + J_G + \frac{J_P}{R^2} \right\} \left(\frac{l}{2\pi R} \right)^2 \tag{2}$$

$$\alpha = \left(\frac{2\pi R}{l} \right) \alpha_L \tag{3}$$

in which J_W is the inertia of moving part , J_G is the inertia of reduction gears and coupling, J_P is the inertia of pinion, $1/R$ is the reduction ratio, l is the lead, and α_L is the linear acceleration of moving part.

It is noted that the motor torque varies with the angular acceleration during the duty cycle. In specifying torque requirements of a motor, the peak torque T_P of the motor to be chosen should be higher than the maximum required torque T_P^* and its rated torque T_R should also be higher than the maximum required torque T_R^*. Besides the torque constraints, the maximum allowed speed of the motor ω_h to be chosen should not be less than the required maximum motor speed ω_h^*. Therefore, constraints for selecting the optimum motor can be formulated as

$$\begin{aligned} T_P^* &= T_L^{\max} + T_J = J\left(\frac{2\pi R}{l} \right) \alpha_L^{\max} + \frac{\mu \cdot M \cdot l}{2\pi \cdot \eta} \left(\frac{1}{R} \right) \le T_P \\ T_R^* &= T_J = \frac{\mu \cdot M \cdot l}{2\pi \cdot \eta} \left(\frac{1}{R} \right) \le T_R \quad , \omega_h^* \le \omega_h \end{aligned} \tag{4}$$

where, M is mass of a moving part, D is diameter of a pinion, ρ is density of a pinion($7.87 \times 10^3\ kg/m^3$), t is thickness of a pinion, μ is friction coefficient, η is efficiency of the rack and pinion mechanism and α_L is linear acceleration of the moving part.

The motor is an energy-converting component, but its efficiency is not ideal and some losses are inevitable [6]. Among various losses, heat dissipation represents the efficiency directly related with given duty cycle.

$$\begin{aligned} W_d &= \int_0^{t_c} \left(I_a^2 R_a \right) dt = \int_0^{t_c} \left(\frac{T}{K_t} \right)^2 R_a \, dt \\ &= \int_0^{t_c} \left[(J_L + J_m) \left(\frac{2\pi R}{l} \right) \alpha_L + \frac{\mu \cdot M \cdot l}{2\pi \cdot \eta} \left(\frac{1}{R} \right) \right]^2 \left(\frac{R_a}{K_t^2} \right) dt \end{aligned} \tag{5}$$

where, I_a is the armature current of the motor, R_a is the resistance of the armature coil, and K_t is the motor torque constant, and t_c is total duty cycle time.

Using the above equations, optimum driving motors of

Table1. Specification of selected motors

Specification	X-axis	Y, Z-axis
Power(W)	*100*	*200*
Rated torque (Nm)	*0.32*	*0.64*
Max. torque (Nm)	*0.95*	*1.91*
Torque constant(Nm/A)	*0.39*	*0.49*
Rotor inertia (kgm^2)	*0.04E-4*	*0.2E-4*

the layout machine are selected. The specification of selected motors is listed in Table 1.

3. Design of control system

Layout machines are composed of a machine structure, mechanical driving parts, a motion controller, and sensors. The design and optimization of those components is done separately, and designers (or makers) only assemble those into a layout machine in laboratory (or factory). Therefore, the integration of those components from various energy domains is important to achieve desired performance [8-10]. The system design based on the integration of those components can be performed in two kinds: through the integration of hardware components and through the software integration (see Fig.2).

The integration of hardware components can be accomplished by imbedding sensors, actuators, and a motion controller into the mechanical plant. The achievable performance of the system implemented through this hardware integration may be limited one of the individual components. The microcomputers can be integrated with the actuator, the mechanical plant, or sensor, or be arranged at several ways. Therefore, there are several possibilities to build up an integrated overall system by proper integration of the hardware.

The system design through software integration is mostly based on advanced additional control functions and an information processing. The schematic diagram of the design process for the layout machine through software integration is illustrated in Fig3. Besides a

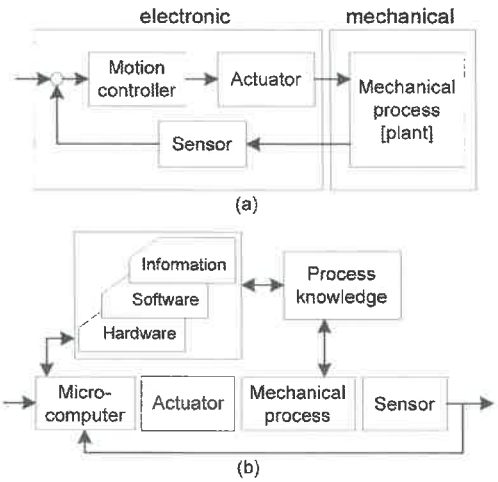

Fig.2 Ways of integration;
(a) hardware integration. (b) software integration

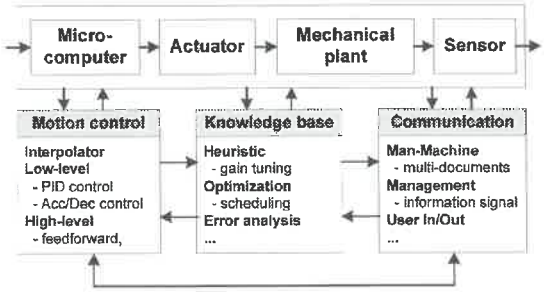

Fig.3 Software integration of layout machine

basic feedback PID control function, additional functions may take place through the knowledge of system and corresponding system information. This means that the system based on the software integration can make use of all of the available system information in higher levels, and easily compensate for the limitation of compon-ents by using additional functions.

However, it is difficult to implement those requirements through the existing control systems that have been designed for a specified purpose [3]. Even if some designers want to develop new functions or modules, they cannot easily add or modify system functions. The system suitable for providing the flexibility and functionality is known as open architecture control system. In this paper, a precision layout machine is studied by using such an open architecture controller. The open architecture controller used in this study is embodied in personal computers. Modules described below are designed and implemented in terms of "object-oriented" to provide the flexibility and functionality.

A. Motion control module: The measuring performance and the control accuracy depend upon this module. It consists of an interpolator, a lower-level controller and a higher-level controller. In the lower-level controller, a PID control is used as the basic feedback control term. In order to compensate for friction forces or contouring errors, a feedforward control is used in the higher-level controller.

B. Knowledge base module: This module has heuristic function, optimization function, error analysis function, and so on. This module provides intelligent functions through blending of system information. In order to determine control parameters of lower-level and higher-level controllers, designers and users can use various functions of this module. In addition, to maintain desired performance of measuring tasks, users can implement this module to

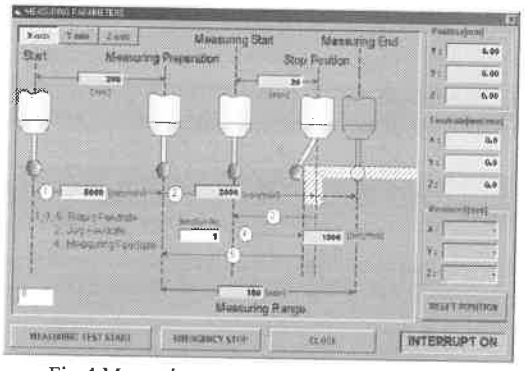

Fig.4 Measuring parameter setting function

Fig.5 Circular error analysis function

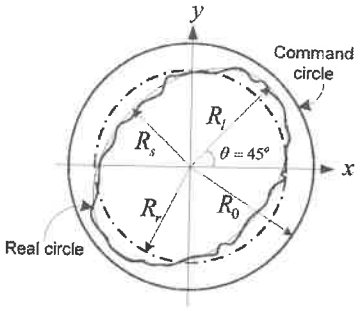

Fig.6 Errors in circular motion

check the accuracy of the layout machine periodically.

C. Communication module: In the software integration process, the control and management of available system information is essential to achieve desired performance. To communicate between the different modules and functions, as well as to manage information a user-friendly Man-Machine-Interface (MMI) module has been developed. Using this MMI, for example, users can conveniently modify and/or determine measuring parameters such as measuring preparation point, measuring speed (Fig.4), and so on.

4. Control parameter tuning

In spite of the advances in control theory, industrial motion control systems are still essentially based on the three-term PID controller due to the effective and reliable characteristics in most situations. While the characteristics are appealing, PID controllers may be poorly tuned because traditional tuning methods need a closed-form mathematical model of the system and controller dynamics [4, 5]. Since mathematical models of the layout machine cannot exactly represent dynamic characteristics of the system because of modeling

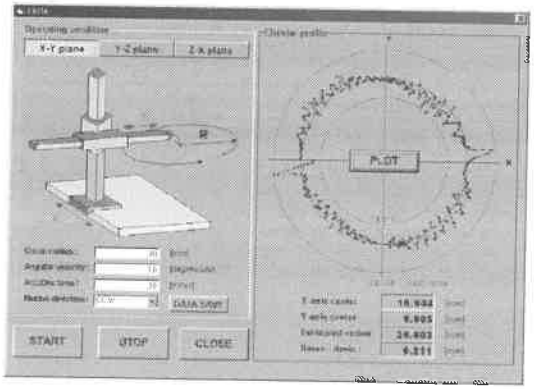

uncertainty, control parameters of each axis must be manipulated according to frequency responses of other axes in multi-axis driving systems. In order to overcome this sort of difficulty Taguchi method [11] is used to select optimal control parameters. In this process, mathematical models of the plant and additional devices are not required. Errors used for the tuning process are measured through the error analysis module implemented by the open architecture control system shown in Fig.5. Using this process, 12 controller gains of three driving motors are tuned simultaneously. Followings describe Taguchi method for the tuning of control parameters.

A. Object function: Fig.6 shows errors of the circular motion when there are gain mismatch of the feed drive axes and the radius reduction error. Objective functions to reduce the circular error are given by

$$e_R = \frac{R_o - R_r}{R_o} = \frac{\sqrt{a^2+b^2-c}}{R_o}, \quad e_M = \frac{R_l - R_s}{R_o}$$

$$\begin{Bmatrix} a \\ b \\ c \end{Bmatrix} = \begin{bmatrix} \sum_i^n 2x_i^2 & \sum_i^n x_i y_i & \sum_i^n x_i \\ \sum_i^n 2x_i y_i & \sum_i^n 2y_i^2 & \sum_i^n y_i \\ \sum_i^n 2x_i & \sum_i^n 2y_i & n \end{bmatrix}^{-1} \begin{Bmatrix} \sum_i^n -x_i\left(x_i^2+y_i^2\right) \\ \sum_i^n -y_i\left(x_i^2+y_i^2\right) \\ \sum_i^n -\left(x_i^2+y_i^2\right) \end{Bmatrix} \quad (6)$$

where, R_o is the command radius, R_r is the actual radius, (x_i, y_i) is the i th coordinates in circular motion, and n is total number of data point along the circular path.

B. Determine the quality characteristics: Quality characteristics mean the 'better' the control performance when the 'smaller' radius-decrease errors and gain-mismatch errors are obtained.

Table2. Levels of controllable and noise factors

Factor	Parameter	Level		
		a	b	c
Controllable factors	K_P	120	170	300
	K_I	3	7	13
	K_D	100	200	300
	K_F	500	1000	2000
Noise factors	f	3000	5000	10000

C. Selection of controllable factors and noise factors: Controllable factors have to be selected to desired values, while noise factors are those that may not be controlled. The selection procedure of the factors is important in Taguchi method [11]. In this paper, controller gains are used as the controllable factors and the linear velocity in a circular motion is used as the noise factor. After selecting factors, their desired number of levels is determined. Three levels of controller gains and noise factors are selected in this study. Table2 shows physical values for them.

D. Orthogonal array and experiment: Table 3 shows the orthogonal array $L_9(3^4)$. A total of 27 experiments are performed.

E. Analysis: Signal-to-noise ratio (S/N ratio, ξ) is used for the analysis of experiments [11]. Quality characteristics is defined by S/N ratio,

$$\xi_i = -10\log\left(\frac{1}{3}\sum_{j=1}^{3} e_{ij}^2\right) \qquad (7)$$

where, e_{ij} is the index of dimensionless object function for experiment number i=1~9 and levels of the noise factor j =1,2,3. The smaller the ξ the better quality characteristics can be obtained.

Table3. Orthogonal array of experimental sets

No.	Controllable factor				Noise factor
	K_P	K_I	K_D	K_F	f
1	a	a	a	a	a, b, c
2	a	b	b	b	a, b, c
3	a	c	c	c	a, b, c
4	b	c	a	b	a, b, c
5	b	a	b	c	a, b, c
6	b	b	c	a	a, b, c
7	c	b	a	c	a, b, c
8	c	c	b	a	a, b, c
9	c	a	c	c	a, b, c

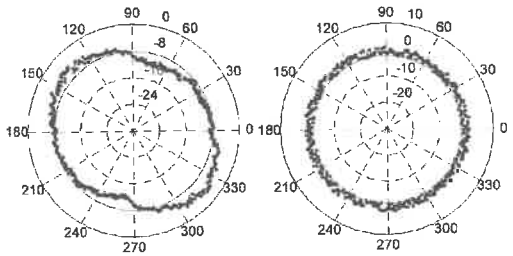

Fig.7 Result of parameter tuning

Analysis also includes determination of the most important controllable factors, which can maximize the S/N ratio, and selecting the optimal levels for those factors.

By successfully applying this procedure based on Taguchi method, it is possible to determine the controller gains producing minimum velocity and position errors while minimizing the effect of the noise factors. Fig.7 shows a result obtained through the parameter tuning procedure.

5. Implementation and measuring experiments

An Experimental setup for measuring a small sphere, ring gauge and model automobile is represented in Fig.8, 9. The layout machine with the open architecture control system embedded in a personal computer can combine a measuring task and other works in one machine, which gives both high efficiency and economic effect. For example, one can use a commercial software package such as CAD while a measuring is carried out (Fig.8). It is a useful tool in reverse engineering.

6. Conclusion

The development of the precision layout machine using open architecture controller has been presented. The optimum motor is selected so as to minimize the heat dissipation and satisfy the torque constraints. The integration can be performed by two kinds, through the integration of hardware components and through the software integration with open architecture controller. The systematic integration concept plays a crucial role in the further development of other electromechanical systems. A gain tuning technique using the Taguchi method is induced, which can tune control parameters for PID and feedforward controller optimally, robustly and simultaneously. The developed layout machine can carry out a measuring task and other works in one machine at a time.

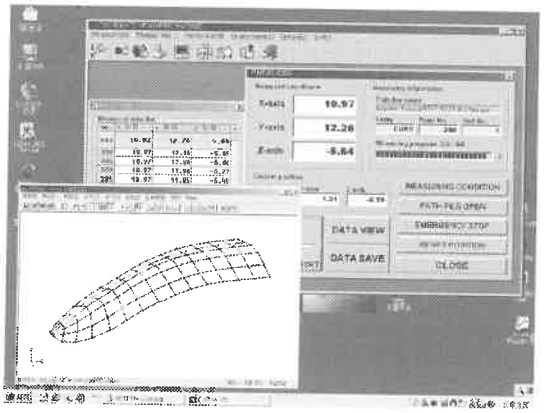

Fig.8 Operating environment on personal computer

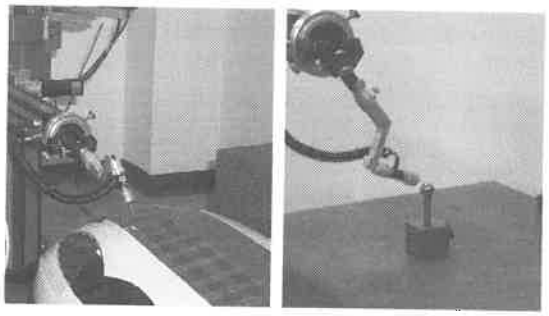

(a) (b)

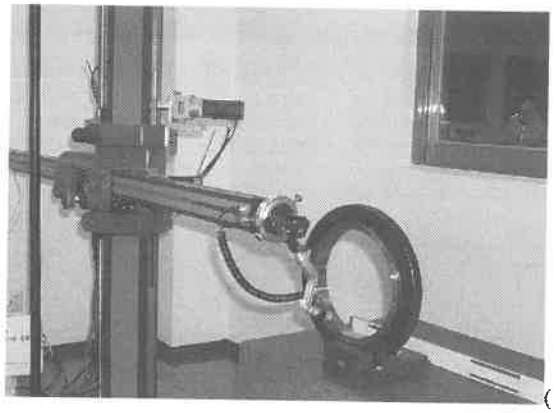

c)

Fig.9 Experimental setup for (a) model automobile, (b) small sphere, and (c) ring gauge

References

[1] A.John, Bosch, "Coordinate Measuring Machine and Systems", Marcel Dekker, Inc., 1995.

[2] A.M. Higginson and S.handley, "The modeling and Automatic commissioning of a High Precision Co-ordinate Measuring Machine", Mechatronics, Vol. 6, No. 3, pp. 261~281, 1997.

[3] H.A.Barker, M.Chen, P.W.Grant, C.P.Jobling, and P.Townsend, "Open Architecture for Computer-Aided Control Engineering", IEEE Trans. pp. 17~27, April. 1993.

[4] J.G.Ziegler and N.Nichols, "Optimum setting for automatic controllers", ASME Trans., 64, 759~768, 1942

[5] K.J.Astrom, C.C.Hang, P.Persson and W.K.Ho, "Towards intelligent PID control", *Automatica*, *28*(1), 1~9, 1992

[6] S. W. Kim and J. S. Park, "Computer aided optimum motor selection for D.C. servo drive system," Int. J. Mach. Tools Manufact. vol. 30, no. 2, pp. 227~236, 1990.

[7] Herman J. Van de Straete, Joris De Schutter, "An efficient procedure for checking performance limits in servo drive selection and optimization," IEEE/ASME Trans.On Mechatronics, vol. 4, no. 4, pp. 378~386, 1999.

[8] K.Y.Toumi, "Modeling, Design, and Control Integration: A Necessary Step in Mechatronics", IEEE/ASME Trans.On Mechatronics, vol.1, no.1, pp. 29~38, 1996.

[9] N.Kyura and H.Oho, "Mechatronics- An industrial perspective", IEEE/ASME Trans.On Mechatronics, vol. 1, no. 1, pp. 10~14, 1996.

[10] R.Isermann, "Modeling and design methodology for mechatronic systems", IEEE/ASME Trans.On Mechatronics, vol. 1, no. 1, pp. 16~28, March. 1996.

[11] G.Taguchi, *Taguchi on robust technology development*. New York, USA: ASME Press, 1993

[12] Samsung Electronics Co., *Manual for multi-motion control*. Seoul, Korea, 1996

A Study on Evaluation of Conceptual Designs of Machine tools

Nozomu MISHIMA
Fine Manufacturing System Group,
Institute of Mechanical Systems Engineering,
National Institute of Advanced Industrial Science and Technology,
1-2 Namiki, Tsukuba, Ibaraki, Japan

1. Introduction

In terms of energy efficiency, a large machine represents considerable waste. Miniaturization of machine tools to size compatible to the target products without compromising machining tolerance lead to enormous savings in energy, space, and resources. Recent years have seen the proposal of a factory comprised of such miniaturized machine tools. "Microfactory" [1] demonstrated a prototype ultra-miniature manufacturing system. However, the design of those miniature machine tools did not involve an in-depth evaluation of the required size and structure. Because machine tool design is rather experience basis, a fundamental design change is often difficult. Machine tool designers will need a general guideline to appropriately reduce the size of machine tools or determine the structure. In the former research [2], the author proposed and have examined a new design tool for machine tools combining the form-shaping theory [3] of machine tools; an analytical procedure representing the machining motions, with the Taguchi method [4]; a well-known robust tool to optimize processes or design parameters. Using the design tool, machine tool designers can evaluate how design parameters, local error factors and structures affect the machine performances without prototyping. The design tool was applied to the two designs of miniature mills for the aforementioned microfactory, and predicted that the design with distributed degrees of freedom (DOF) had better machining tolerances than the other. Although, in the former study, the design tool can evaluate and compare existing designs, was not helpful enough to create a new design concept. As the next step, the design tool is required to show general design guidelines and aid conceptual design stage of a machine tool. The design tool will be helpful to shorten the time-to-market of machine tools and create a new design strategy to meet various design requirements.

2. Basics of the proposed design tool, and former applications

2.1 Form-shaping theory

A machine tool structure can be considered as a chain of directly linked rigid components extending from a product through a cutting tool. Defining local coordinate system to each component, transformation between two next coordinates can be represented by a homogeneous transformation matrix. Calculating the transformation consecutively from the product towards the cutting tool, it is possible to express the relative displacement or motion between the product and the tool. The result of the matrices calculation is the definition of the form-shaping function that expresses the cutting motions of machine tools mathematically. However, actual machine tools have many error sources. In order to describe actual cutting motions, one must consider these errors. Such errors can be treated as errors in transformations between elements. The form-shaping error function, indicating the shift from the target value of the machine tool motion, is defined as the difference between the form-shaping function not containing errors and that containing errors. By defining the design parameters, error factors and product dimensions, the form-shaping theory can calculate the form-shaping error function of the machine tool.

2.2 Application of a robust design tool

The next step is to evaluate the calculated function by using a robust design method. When all variables of the form-shaping error function are known, the value of the error function can be easily calculated. However, when only the overall machining tolerance is specified, the inverse problem cannot be solved. Hence, the equation indicates the degree of machining error anticipated, given known local errors, but one cannot readily use it to estimate in advance the machining errors or assembly errors of component elements at the time of design. On the other hand, in order to obtain machining tolerance that is stable under a variety of machining conditions, a method is needed for obtaining a design that is robust with respect to unknown local errors. The Taguchi method is widely used in the fields of experimental design and quality engineering, and provides an environment for robust design. The design evaluation procedure uses the Taguchi method to evaluate the dimensional effect imposed on machining errors by the design parameters of the machine tool, when local errors are unknown. Simulations were performed applying the method to the form-shaping error function.

2.3 Examples of former applications

Microfactory is a name of a super miniature manufacturing system consists of miniature machine tools and manipulators, which has benefits to reduce energy consumption and space occupied by the machines The first microfactory was prototyped by author's research group in 1999. The system shown in fig.1 contains three machine tools including the micro-lathe [5] and the micro mill. In trying to find a general design guideline for miniature machine tools, the micro-lathe and the micro mill of the microfactory have been analyzed as examples. [6] As the result, the design tool concluded that among five defined design parameters of the micro-lathe, some had larger effects on its performance and some didn't. The tool also clarified which of the two design candidates of the micro mill had better theoretical performance than the other.

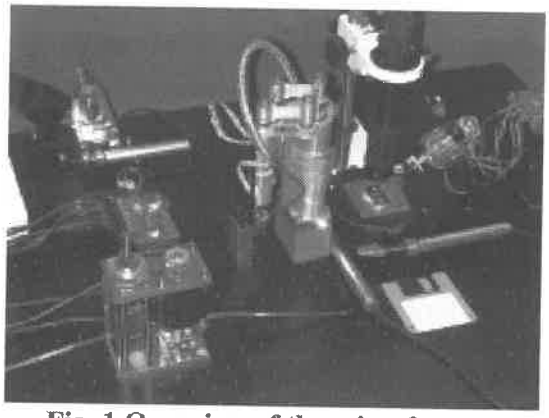

Fig. 1 Overview of the microfactory

3. Evaluation of a new machine tool design

3.1 Listing of possible design configurations

By using the form-shaping theory and the Taguchi method, it was possible to evaluate the effects of design parameters of an existing design. However, the tool did not provide a design suggestion to choose one design from design candidates, or to create an alternative design when the performance of the old design is insufficient. This stage of a design procedure is often called "Conceptual design". The Taguchi method does not mention about the conceptual design and some researchers created another design method for conceptual stages. [7] Though, one can compare performance of several designs by the Taguchi method with some assumptions. In creating a new design concept, there are many possible structures that have different sequences of motion axes. The issue is to applying the above-mentioned design tool to create a design concept of a machine tool. Assuming to create a new design concept of a miniature lathe, the paper tried to make the use of the design tool to evaluate a few design concepts. Basically, a lathe must have three motion axes. And as the definition of a lathe, following a link of components from a

product towards a cutting tool, a main spindle must come first. To express configurations of machine tools clearly, we often use "1" for transitional motion along X axis, "2" for motion along Y and "3" for Z. Under this expression rule rotational motion around X, Y and Z axes are written as "4", "5" and "6", respectively. Using this expression, structure of machine tools can be expressed by those numbers from 1 to 6 focusing on the sequence of the motion axes. Expressing a static component of a machine tool by "0", the structure of the micro-lathe used in the microfactory can be written as 6310. Using this expression, possible structures of a lathe are categorized into 6 types; those are 6013, 6031, 6301, 6103, 6310 and 6130. Further, assuming the x-axis and the z-axis would have the same characteristics, those 6 will be integrated to 3, shown in fig. 2. Following the machine tool elements from the main spindle towards the cutting tool, the first design has two linear motions after the base. The second one has one linear motion before and the other motion after, whereas the last design has two linear motions and the main spindle concentrated.

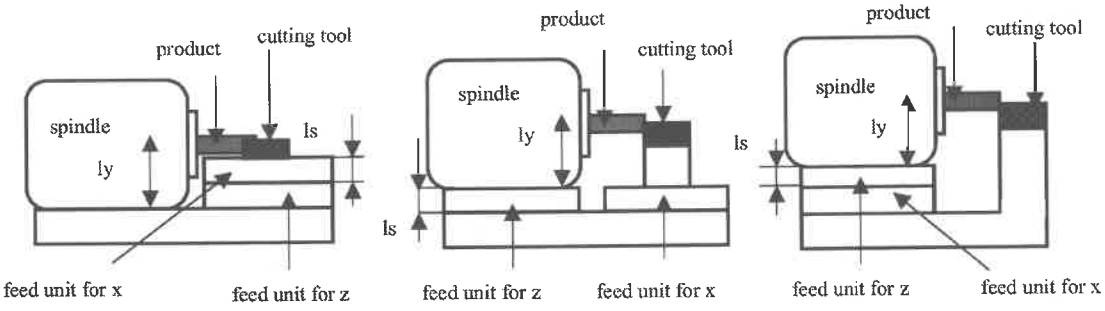

a) type 6031 **b) type 6301** **c) type 6310**

Fig. 2 Three different configurations of lathes

3.2 Comparison of design candidates of a lathe

Using the proposed design evaluation method, it was possible to predict the mean positioning error of each configuration. Table 1 and 2 are the defined error factors and the design parameters for the calculation. To isolate the effect of configurations only, these parameters have to be defined commonly to the three configurations. The nominal value of the design parameters came from the specification of sliders, the spindle and so on, that are used in the miniature-lathe model for measurement. Error factors in table 2 are from the catalog data of those sliders and the spindle. Just the axial expansion of the spindle is from measured data. Fig. 3 is the theoretical performance comparison, based on the calculation. The figure shows how the positioning error of the machines changes when the design parameters are changed along the value shown in table 1. The error

Table 1 Design parameters

Name of the factors	Ranges
Radius of the work-piece	0.1~0.4mm
Height of the work-piece	0.1~0.4mm
Height of the spindle center	15~60mm
Feed unit thickness	7.5~30mm
Cutting tool length	20mm

Table 2 Error factors

Parameter	Ranges
Angular inclination of the spindle axis	±0.005deg.
Radial eccentricity of the spindle	±3μm
Axial expansion of the spindle	0~3μm
Pitching angular error of the sliders	±10"
Towing angular error of the Z sliders	±10"
Rolling angular error of the Z sliders	±5"
Straightness error of the sliders (horizontal)	±2μm
Straightness error of the sliders (vertical)	±2μm
Scale error of the sliders	±2μm

factors vary within the ranges defined in table 2. The vertical axis of the view graph indicates the mean positioning error, and the horizontal axis shows how each parameter affects the overall positioning error. A steep line tells that the corresponding parameter strongly affects the performance and a shallow line does not. Three series of lines in the figure corresponds to the performance of the three configurations, respectively. Comparing the results, the figure clarifies that type 6031 evidently has the smallest positioning error, and type 6301 has the next best performance.

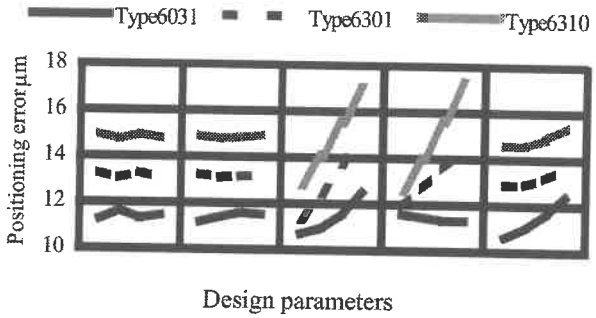

Fig. 3 Machining error comparison

3.3 Measurement of positioning errors

Since, the analytical results shown in fig. 3 depend on some assumptions made in determining the ranges of error factors, it is necessary to measure the positioning error directly and prove that the prediction made by the design tool was reasonable. For the purpose, relative positioning errors between the products and the cutting tools for three configurations were measured, using laser displacement sensors fixed to the table on which products are usually placed. Upper half of fig. 4 shows the comparison between measured and calculated value of errors to z-direction when coordinate value of z are fixed and x are changed. The lower half also indicates when x are fixed and z are changed. In the both figures most of the measured value except a few points of "type 6310" distribute under the lines express the calculated value. It also shows that measured errors of type 6310 are more scattered than that of type 6031 and 6301, as the calculation forecasts. Since, the calculated value means that the positioning error will be smaller than the value, one cannot predict the error itself, though, most of the measured error value exist beneath the calculated lines and the accuracy of the prediction seemed enough for the purpose to aid conceptual design. Since typical design requirement of a machine tool is to assure tolerance, a worst-case-analysis is useful for a designer. The design tool also simulates the performance difference of the structure types, well. The proposed design tool was helpful in determining which of several designs has better performance.

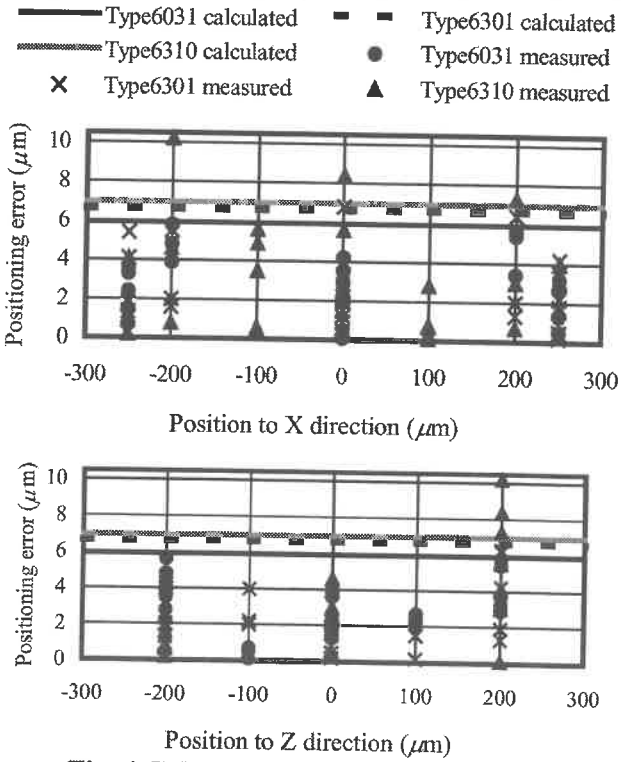

Fig. 4 Calculated and measured errors

4. Conclusions and future work

By applying the proposed design tool to a virtual design procedure of a lathe, following points have been concluded.

A) Typical design variations of a lathe are categorized to three types and the type 6031 has the best theoretical performance.

B) Above-mentioned result was followed by the measurement, and the prediction accuracy was enough for usage in the conceptual design stages.

However, to ensure the effectiveness of the design tool, further examination is necessary. Applying the conclusions indicated by the design tool to actual machine tools design will be the future work. Packaging the tool to interactive software will be also useful. The final goal is to supply a design procedure which will be easily operated by a non-experienced machine tool designer.

References

1. Mishima, N., Asida, K., Tanikawa, T., Maekawa, H., Kaneko, K. and Tanaka, M., *Micro-factory and a design evaluation method for miniature machine tools*, Proc. for ASPE 15th Annual Meeting, Phoenix, Oct. 2000, pp. 567-570.
2. Mishima, N. and Ishii K., *Robustness Evaluation of a Miniaturized Machine Tool*, Proc. for ASME Design Engineering Technology Conference, Las Vegas, Sept. 1999, DETC/DAC-8579.
3. Reshtov, D.N., and Portman, V.T. (1998). Accuracy of Machine Tools, ASME Press, New York
4. Taguchi, G. and Konishi, S. (1994) *Quality Engineering Series* Vol.1-4, ASI Press.
5. Kitahara, T., Ishikawa, Y., Terada, K., Nakajima, N., and Furuta, K. (1996). *Development of Micro-lathe,* Journal of Mechanical Engineering Lab., Vol. 50, No. 5, p. 117-123.
6. Mishima, N, *Development of a Design Tool for conceptual Design Stages of Machine Tools*, Proc. for ASPE 16th Annual Meeting, Arlington, Nov. 2001, pp. 184-187.
7. Ford, R.B. and Barkan, P. (1995). *Beyond Parameter Design --A Methodology Addressing Product Robustness at the Concept Formation Stage,* Proceedings of ASME National Design Engineering Conference

SPINDLE MOTOR DRIVEN BY FLUID ENERGY FOR ULTRA-PRECISION MACHINE TOOL

Yohichi NAKAO, Masato MIMURA
Department of Mechanical Engineering, Faculty of Engineering
Kanagawa University
3-27-1, Rokkakubashi, Kanagawa-ku, Yokohama 221-8686, JAPAN
(E-mail: nakao@cc.kanagawa-u.ac.jp)

1. Introduction

The present paper describes a high-speed motor driven by fluid power, primarily fluid flow energy. The motor can be effectively built into spindles for an ultra-precision machine tool and a micro-manufacturing system. Conventional spindle motors are driven by electric power, whereas the proposed motor is driven by fluid energy. Pure water, which is used in semi-conductor manufacturing plants, can be used as a working fluid for the motor. Therefore, the motor can be also used as an actuator for the semi-conductor plants as well as the ultra-precision machine tools.

The spindle devices used by dentists are the high-speed motors driven by fluid energy. In manufacturing fields, similar spindles have been designed to create small drilling holes, such as 0.6 mm in diameter [1]. An air-turbine is formed on the outer surface of the spindle and it is used as a motor. In this case, the air-turbine spins the spindle in excess of 100,000 rpm. However, making turbine structure for the spindle is relatively difficult, which is a disadvantage of the motor. In contrast, the spindle of the proposed motor has simple channels, which replace the turbine, in the spindle. Consequently, the structure of the proposed motor becomes rather simple than that of conventional high-speed motors using the air-turbine.

In the present paper, we first introduce the motor structure and the principle of the motor operation. We then derive a mathematical model of the motor to represent motor characteristics. A motor design procedure is established based on the derived mathematical model. Example of optimum parameters determined by the design procedure is shown and then the calculated performances of the designed motor are illustrated.

2. Proposed Motor

Figure 1 illustrates the schematic drawing of a cross section of the spindle, where a small and bend channel called a flow-out channel is present. The flow-out channels are located at two cross sections of the spindle. The working fluid in the flow-out channels flows from the center of the spindle to the outside of the spindle. The bend shaped-channels change significantly the fluid flow directions in the flow-out channels. Consequently, the torque used to spin the spindle is generated by the large change in angular momentum of the fluid flow.

Figure 2 illustrates the structure of the motor proposed in the present study. The spindle is supported by appropriate bearings. The working fluid, such as water or air, is supplied to a supply port in the casing of the motor. In order to lead the working fluid into the spindle, relatively large channels are present in the middle of the spindle. The working fluid flows inside the spindle because

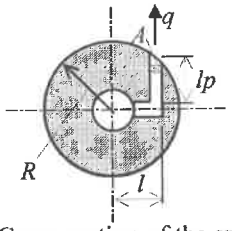

Fig. 1 Cross section of the spindle

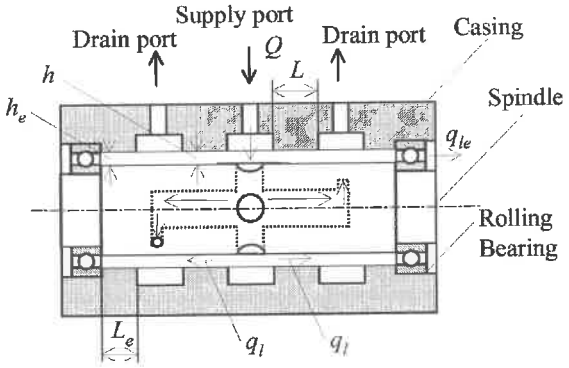

Fig. 2 Structure of proposed motor

the main channel passes through the center of the spindle in the axial direction. At both ends of the main channel, the flow-out channels are located between the main channel and the outside of the spindle. The working fluid in the flow-out channels flows through drain ports in the casing.

As show in Fig. 2, the proposed motor has an extremely simple structure. In addition, since no large mechanical frictional force acts on any of the moving parts of the motor, the motor can be driven by water flow by selecting appropriate materials for the motor elements. Particularly, the proposed motor can also be driven by pure water used in semi conductor manufacturing plants. Therefore, we can also design the high-speed motor for the actuators for machines in the semi conductor manufacturing plants as well as the spindle motor of the ultra-precision machine tools.

3. Mathematical Model

In order to design the proposed motor, a mathematical model is needed to determine optimum dimensions of the motor elements. Therefore, a mathematical model to establish design procedure for the motor is derived in this section. As described in the previous section, the flow-out channels are created in the cross sections of the spindle. The flow rate in each channel is then expressed as q, and the angular velocity of the rotor is expressed as ω. If the pressure at the outlet port of the casing is assumed to be zero, the output torque, T, generated by the fluid flow through the flow-out channels can be expressed as

$$T = 2n\rho q\left(\frac{l}{A}q - R^2\omega\right) \tag{1}$$

where n, A and ρ are the number of the flow-out channels in a cross section, the area of the cross section of the flow-out channel and the density of the fluid, respectively.

The negative torque due to fluid viscosity becomes significant as the rotational speed of the spindle increases due to the presence of fluid in the small gap between the casing and the spindle. If a Newtonian fluid is used for the motor, this negative torque can also be represented as

$$T_{f1} = \frac{2\mu\pi LR^3}{h}\omega \tag{2}$$

$$T_{f2} = \frac{2\mu\pi L_e R^3}{h_e}\omega \tag{3}$$

where μ is the coefficient of viscosity of the fluid. T_{f1} and T_{f2} represent the negative torques acting on the spindle between the inlet port and the outlet ports and at the end of the spindle, respectively.

If we consider the steady state of the motor, the motor torque can be expressed as

$$T_l = 2n\rho q\left(\frac{4cR}{\pi d^2}q - R^2\omega\right) - 2\frac{2\mu\pi LR^3}{h}\omega - \frac{2\mu\pi L_e R^3}{h_e}\omega \tag{4}$$

where $l = cR\ (0 < c < 1)$.

When the fluid flows into the motor, a pressure

drop is produced primarily by the flow in the flow-out channels. Assuming that the flow channels from the inlet port to two outlet ports are designed symmetrically. Then, the supply pressure for the motor can be represented as

$$p_s = \left(1 + \lambda \frac{l_p}{d} + \zeta_1 + \zeta_2\right) \frac{\rho q^2}{2A^2} \quad (5)$$

where λ is the friction factor of the flow-out channels and ζ_1 and ζ_2 are the resistance coefficients[2] for flow in bends and for flow in the sudden contraction at the flow-out channels. If we write

$$\kappa = 1 + \lambda \frac{l_p}{d} + \zeta_1 + \zeta_2 \quad (6)$$

Eq. (5) becomes

$$p_s = \frac{8\kappa\rho q^2}{\pi^2 d^4} \quad (7)$$

The second term in Eq. (6) is neglected in the calculations for the design of the motor described in the following section, because this term is negligible compared to the other terms.

The leakage flow in the gap between the casing and the spindle can be described as follows

$$q_l = \frac{\pi h^3 R}{6\mu L} p_s \quad (8)$$

Thus, the total flow rate is given by

$$Q = 2(nq + q_l) \quad (9)$$

4. Motor Design

The mathematical model derived in the previous section shows that the torque of the proposed motor can be controlled by the flow rate q in the flow-out channel. From the Eqs. (4), (7) and (8), it is found that the motor characteristics are extremely influenced by the following parameters; (1) the radius of the spindle, (2) the gap size between the casing and the spindle and (3) the diameter of the flow-out channels.

Since a large radius of the spindle makes the magnitude of the first term in Eq. (4), which represents the positive torque of the motor, increase, whereas the negative torque in the other terms also increases. Large gap sizes, h and h_e, are effective to reduce negative torque due to the viscosity of the fluid between the spindle and the casing. However, the leakage flow q_l in the gap increases as the gap size becomes large. The small diameter of the flow-out channels increases the positive torque, however, it decreases the efficiency of the motor due to the loss of the fluid flow energy. Therefore, optimum values for these parameters must be exist. Determination of the parameters is essential in designing a motor. In the present study, based on the derived mathematical model, we develop software to determine the optimum parameters so as to maximize the efficiency of the motor.

As an example of the design, the motor of the rated rotational speed of 20,000 rpm are designed. In this design, the maximum flow rate of the pump supplying the water to the motor was assumed to be 20 *l*/min. Determined optimum conditions for various output power of the motor are shown in Fig. 3. Figure 4 shows the torque characteristics of the designed motor with the rated power of 40 W. Characteristics of the power and the total efficiency of the motor are given in Figs. 5 and 6, respectively. The total efficiency of the motor is approximately 12 % at maximum. The maximum efficiency of the motor is less than that of the conventional electric motors. However, the magnitude of the energy loss is less than 300 W because the motor output is small.

The viscosity of the fluid in the gap and the loss of the fluid flow energy in the flow-out channels are the primary reasons for the low efficiency of the motor. Since the small gap is inevitable to reduce the leakage flow in the gap, it is difficult to reduce significantly the negative torque due to the fluid viscosity. In contrast, we can reduce the energy loss

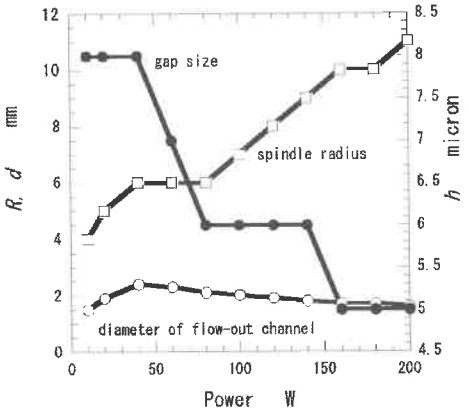

Fig. 3 Optimum parameters
(Rated rotational speed : 20,000 rpm)

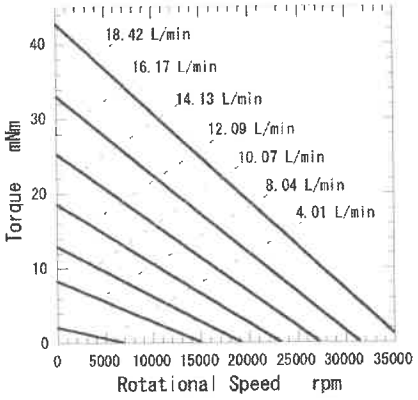

Fig. 4 Torque characteristics

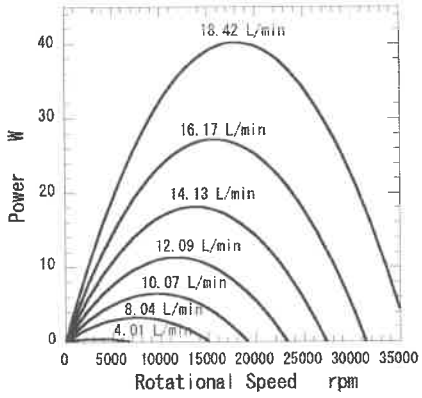

Fig. 5 Motor power

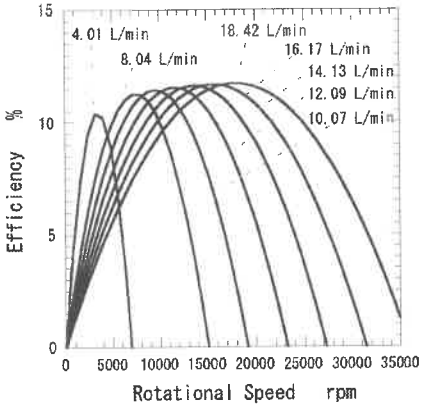

Fig. 6 Motor efficiency

of the working fluid flow in the flow-out channels by designing optimum geometry of the channels.

5. Summary

In this paper, a high-speed motor driven by various fluids such as water and air was proposed. The motor can be effectively built into the spindle of ultra-precision machine tools and the micro-manufacturing systems. In addition, since pure water can be used to drive the motor as the working fluid, the motor can be applied as the actuators used in semi-conductor manufacturing plants.

In order to determine the optimum parameters of the motor, a mathematical model was derived and then designed example was presented. A calculated motor efficiency was approximately 12 % at maximum. In order to improve the efficiency of the motor, the influence of geometry of a flow-out channel on energy loss will be considered in future work.

Acknowledgement

This research work is financially supported by the Grant-in-Aid for Scientific Research (C) of Japan Society for the Promotion of Science.

References

[1] S. Koda et al, Preprint of the Spring Meeting of JSPE, pp.649-650, 1985.

[2] JSME Data Book: Hydraulic losses in pipes and ducts.

New Die Design System for Injection Molding using Multivariate Analysis

Shinnosuke NITOH
Computer Science, Graduate School, College of Engineering, Nihon University
Yoshikazu KOBAYASHI and Kenji SHIRAI
College of Engineering, Nihon University

Abstract

Past injection mold shape data and processing data are often used in injection mold design. In these cases, the building of a database on past examples and retrieval of similar data shorten design time. The evaluation method multivariate analysis is used to calculate the similarity level between data input by the designer and data in the databases related to the injection mold composition parts that the designer intends to build and past design data. In this system, the designer edits corrections, changes, etc. using a list of injection mold composition parts and list of shape features, which have been retrieved as the most similar by calculating the similarity level, and a 3D model of the injection mold, which can be displayed and processed by DirectX on the web.Even users with only a slight knowledge of injection mold design can design injection molds efficiently using this system, and at design times about 50% shorter than conventional methods.

1. Introduction

In recent years, injection molds are designed using the three-dimension solid system[1)2)]. Generally past design data is used in most injection mold design jobs[3)]. However, it is difficult to search for data stored on computer quickly. For such knowledge succession problems in the manufacturing industry, the formation process of knowledge is theorized or formulized as in artificial engineering[4)]and TRIZ[5)]. Based on this, attempts are being made to construct mechanisms which support engineers. With the system introduced in this report, first parts composing injection molds designed in the past or processed parts were registered[6)]. Next, the data of parts composing injection molds was compared. In the comparison, the degree of similarity such as types of mold parts, part size, and number of parts, etc. were taken as parameters. Since there were multiple parameters, we prototyped a computer-aided design system for injection molds which can retrieve data by multi-variate analysis[7)].

2. System Configuration

The system proposed in this study mainly consists of three subsystems; an injection mold information input unit as shown in Figure 1, a similarity evaluation unit, and a knowledge base unit. The knowledge base unit stores information on the components of injection molds, features of injection mold structures, and injection mold 3D model data. The design information input unit inputs parameters on basic parts, additional features, etc. composing the injection mold designed using dialog. The similarity evaluation unit on the other hand evaluates similarities between input data and the data of tables in the knowledge base unit. The knowledge base unit was classified into 111 kinds of form features, including 180 kinds of parts, such as guide pin constituting an injection mold, ejector rod, sprue bush, hole and slot machining parts, special parts, and unit mechanism. The main injection mold composition data stored in the knowledge base unit are data on additional machining, inclusion of parts, injection mold features, design features, mold-base, mechanism data, standard mold-base specification changes, etc. There are also integrated data consolidating these seven data. Retrieval results are displayed in dialog form as shown in Figure 2. 3D models of retrieval results are displayed in four parts. Displays include list-displays of components of molds searched, inventory information on parts, machining information, part price, part name of selection parts, machining time, prices, total machining time and total prices, and displays of 3D models of retrieval results. In the 3D models displayed, parts are differentiated by color. Designers are able to change to any viewpoint using the mouse.

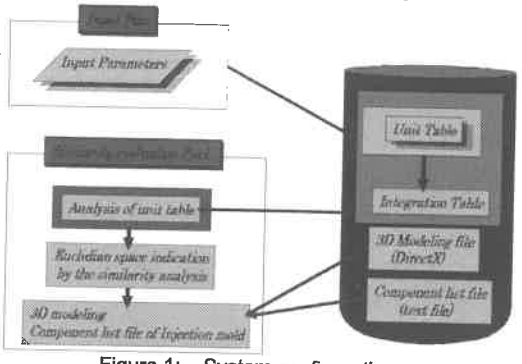
Input Parameters
Unit Table
Integration Table
3D Modeling file (DirectX)
Component list file (text file)
Analysis of unit table
Euclidian space indication by the similarity analysis
3D modeling Component list file of injection mold

Figure 1: System configuration

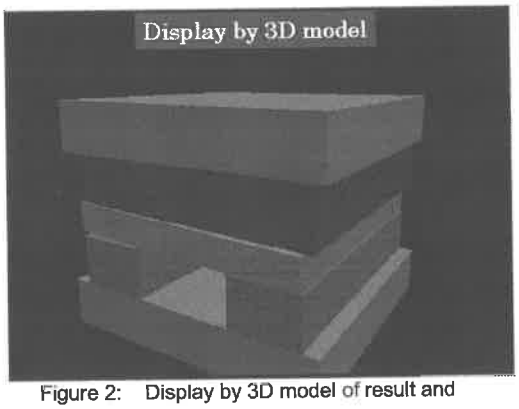

Figure 2: Display by 3D model of result and mold parts information

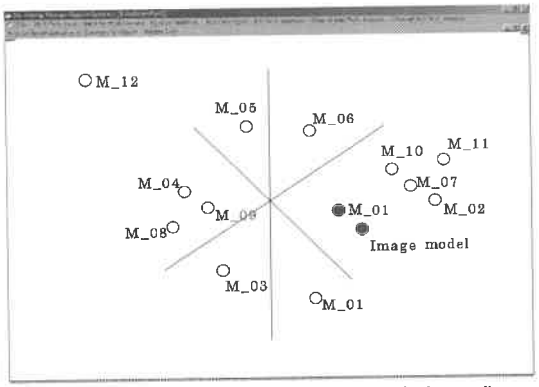

Figure 3: Display by Euclid space of an analysis result

3. Similarity Evaluation

This system was designed to evaluate similarities between composition data of injection molds designed in the past and composition data of injection molds visualized by the designer and search for data. Similarities are evaluated by quantification of multi-variate analysis and analysis of main components which are statistical techniques. Quantification is the method of spatially classifying qualitative variables while the analysis of main components is the method of spatially classifying quantitative variables. Since similar molds can be designed using past injection mold composition data the knowledge of experts play an important role in such past design data, the knowledge of which is composed of certain patterns. Moreover, injection molds are composed by combining form features. Components and injection mold structures are therefore similar. But there exist no two same molds. As parts which constitute an injection mold can be treated as qualitative data, the Euclid distance from the image data is calculated by the quantification method to evaluate similarity. The results are displayed on the Euclid space as shown in Figure 3. Because the numerical data of injection mold components are quantitative data, similarity evaluation of component size, quality, and attached position, etc. is performed using the analysis of main components.

4. Comparison of Analysis Results

4.1 Comparison of Mold Component Plate and Size

An example of analysis results by this system are described here. The input data of the analysis result example are parameters on injection mold features, hole and slot machining, types of parts, and unit mechanism. The output results are the Model of the overall image of the mold as shown in Figure 4 and hole and slot machining, and injection mold components as shown in Figures 5, 6, 7, 8, 9, and 10. Model A is the Model visualized by the designer. Model B is the result of retrieval of similar injection molds using all four parameters which injection mold features, hole and slot machining, types of parts, and unit mechanism as the input data. Model C is the result of retrieval of similar injection molds using injection mold feature as the input data.

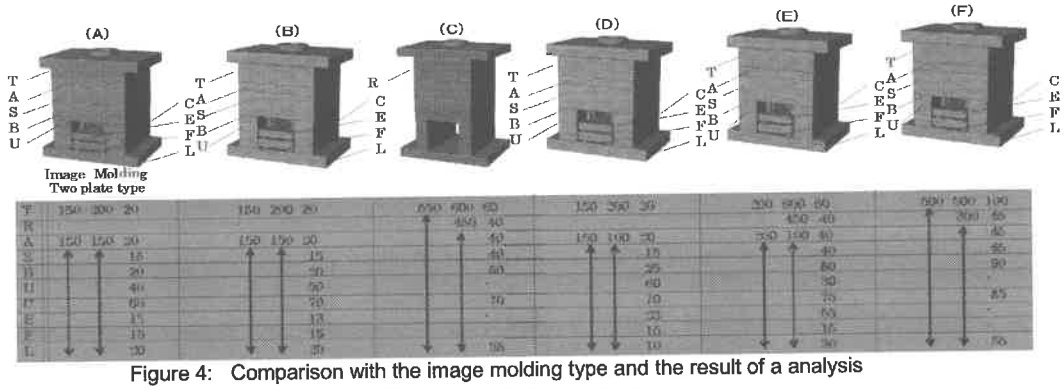

Figure 4: Comparison with the image molding type and the result of a analysis (Molding composition and dimension)

Figure 5: Designer's image of molding (Additional machining and installation parts (Model A))

Figure 6: The comparison of the additional machining characteristics as a result of an analysis (Model B)

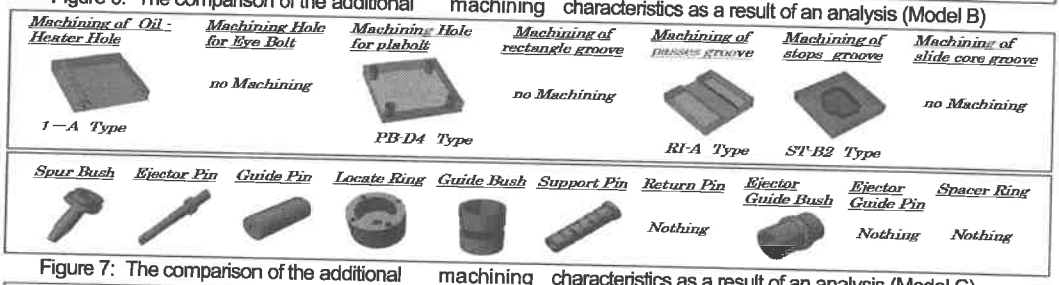

Figure 7: The comparison of the additional machining characteristics as a result of an analysis (Model C)

Figure 8: The comparison of the additional machining characteristics as a result of an analysis (Model D)

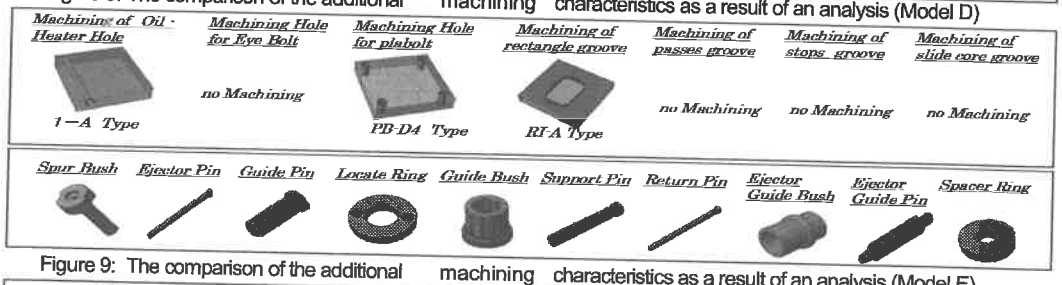

Figure 9: The comparison of the additional machining characteristics as a result of an analysis (Model E)

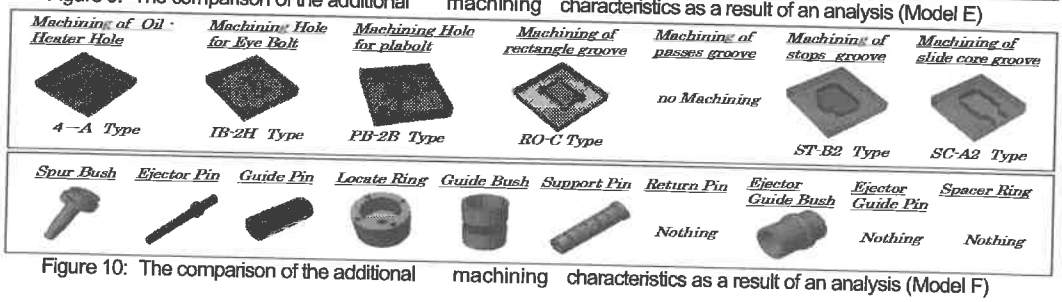

Figure 10: The comparison of the additional machining characteristics as a result of an analysis (Model F)

Model D is the result of retrieval of similar injection molds using hole and slot machining as the input data. Model E is the result of retrieval of similar injection molds using types of parts as the input data. Model F is the result of retrieval of similar injection molds using unit mechanism as the input data. If each Model is compared visually, Model C is not similar while Models B, D, E, and F are. Next, the plate size of each Model is compared. Models C and F are completely different plates while Models B, D, and E are comparatively of the same size. This is based on the difference in built-in parts and internal structure.

4.2 Comparison of Form Feature and Built-in Parts

Next, the hole and slot machining and types of parts of each Model are compared. Figure 6 shows the hole and slot machining, and types of parts visualized by the designer. There are seven types of hole and slot machining and ten types of parts. In the example of Model B, there are five types of the same hole and slot machining, and eight types of parts. The same comparison was performed for Models C, D, E, and F. In the example of Model C, there are two kinds of the same hole and slot machining, and no types of part were the same. In the example of Model D, there were six kinds of the same hole and slot machining, and seven types of parts. In the example of Model E, there were five kinds of the same hole and slot machining, and nine types of parts. In the example of Model F, there were three kinds of the same hole and slot machining, and two types of parts. These results indicate that importance given to mold structure by input data which injection mold features, hole and slot machining, type of part, and unit mechanism. Consequently, injection mold size and hole and slot machining are correlated with built-in parts and internal structure, and the size of the whole injection mold and the kind of hole and slot machining can be determined from built-in part and internal structure. However, although Models D and E must search for data with all the same elements as the injection mold components visualized by the designer, different data is searched in some cases. This is considered to be search of data containing some wrong information, where a part of a mold designed in the past was processed at an unintended area. For Models C and F, since the data is about the internal structure of an injection mold component, hole and slot machining, and parts corresponding to the mechanism were searched.

5. Conclusion

An injection mold design system applying multi-variate analysis was prototyped, and the following conclusions were obtained.

(1) Since retrieval reflecting data composing injection molds designed in the past can be performed, even users with little experience in injection mold design can design easily. Moreover, design time is about half that of conventional methods.

(2) Injection mold components such as components, design data, etc. of past injection molds, are managed into seven parts, and the data which the designer needs from this point can be searched quickly.

In future studies, the authors plan to construct knowledge base systems added with functions which can perform searches taking into consideration special parts composing the mold and special structures or knowledge base systems taking into consideration prioritization based on designer instructions, as well as to investigate retrieval methods.

References

1)O.J Canciglieri, R.I.M. Young: A Multi-Viewpoint Reasoning System in Design for Injection Moulding, 1997, Conference Proceedings of International Conference and Exhibition on Design and Production of Dies and Molds, Molding, p21-26

2)J. P. Kruth, R. Willems, D. Lecluse: A Design System using High Level Mould Objects, 1997, Conference Proceedings of International Conference and Exhibition on Design and Production of Dies and Molds, Molding, p39-44

3) Shuji KUBO, Masayuki ASAI, Yoshiro KASHIWABARA, Kauai TSHUKAHARA: Construction of the BPR concept of a product factory, 1999, Die & Mould Technology, vol14, no.7.

4) Toshiharu TAURA: Knowledge in engineering, artificial thing engineering, 1995.4, the Japan Society for Precision Engineering, p61.

5) Victor R. Fey, Eugene, I. Riving, Yoder HATAYAMA: 1997, A guide to TRIZ, Nikon Kogyo Shim bun Ltd.

6) Shinnosuke NITOH, Yoshikazu KOBAYASHI and Kenji SHIRAI: Development of the form similarity evaluation system 2001, and the injection mold design, the collection of the Japan Society for Precision Engineering spring convention academic lecture meeting treatises in the 2001 fiscal year, p147.

7) Koichi SUGIYAMA: A guide to multi- variable data analysis, 1983.4, Asakura Publishing Co., Ltd.

Measurement and Calibration of High Accuracy Spherical Joints

Alec Robertson, Adam Rzepniewski, Alexander Slocum
Massachusetts Institute of Technology, Cambridge, MA

1. Introduction

High accuracy robotic manipulators are required for numerous industrial applications; such as inline inspection of assembly lines; laser cutting; and precision pick and place operations. Parallel kinematic machines [1] offer benefits, compared to serial manipulators, due to their high stiffness and inherently superior accuracy. Many parallel robot implementations utilize two and three degree-of-freedom joints to connect the robot arms, with universal joints commonly used for the two degree-of-freedom joints. Significant research has led to practical implementations of three degree-of-freedom joints based on a modified universal joint concept. Whereas this simplifies joint construction, it introduces singularities and mechanical tolerances that degrade the overall robot accuracy. The goal of this research is to develop a high-stiffness spherical joint capable of a large, singularity-free workspace with accuracy on the order of several micrometers.

Spherical joints have been developed based on the ball and socket concept, wherein a spherical ball sits in a hemi-spherical cavity. Three designs are implemented; based on point and surface contact mechanisms. The first joint (point contact) is achieved by kinematically mounting the ball on three smaller spheres embedded in the socket, as per ball bar mechanisms [2]. The second joint (rolling contact) uses ball transfers instead of fixed spheres to significantly reduce friction. The third prototype implements surface contact through replication of the ball with a teflon-laced epoxy, to achieve a high accuracy and low-friction ball to socket mating surface [3]. Each joint design incorporates a magnetic preload wherein the socket is populated with various configurations of permanent magnets that attract the solid steel ball.

Each spherical joint prototype is tested using a spherical kinematic test rig that allows the independent actuation of each of the joints' degrees of freedom: roll (rotation about a nominal x-axis), pitch (y- axis rotation), and yaw (z-axis rotation). Each prototype is measured by affixing a tooling ball to a shaft attached to the ball and mounting the joint in the test rig, which itself is mounted in a coordinate measurement machine (CMM). The test rig actuates the joint to various positions in its working space and the CMM measures the position of the center of the tooling ball.

Joint accuracy is characterized using a geometric sphere-fit algorithm to fit the measurement data to a standard sphere through the calculation of the best-fit sphere center and radius. The final (sphere-fit) error is the deviation of each measurement position from the best-fit radius. Additionally, a kinematic parameter estimation algorithm has been developed to characterize the individual error parameters within the joint, such as the eccentricity of the axes of rotation. The passive joint is treated as a three degree-of-freedom mechanism and the error parameters determined through a numerical Jacobian-based technique [4]. As the joint prototypes have no angular feedback and the test rig is relatively inaccurate, joint angle positions are not accurately known and needed to be re-calculated for each measurement location. The calibration sequence involves the initial estimation of kinematic error parameters (based on the current joint angles) followed by the update of the joint angles (based on the updated error parameters and the measurement location). This "leap-frog" algorithm continues until both the error parameters and the joint angles converge; the final (calibrated) error is the difference between the predicted and the measured joint position.

Measurements of the rolling contact prototype joint indicate a maximum sphere-fit error of twelve micrometers (12μm) and a calibrated maximum error of eight micrometers (8μm). The error of the CMM is estimated to be two micrometers (2μm).

2. Design of Prototype Joints

The spherical joint is required to have a singularity-free working range of 180° and accuracy of the order of several micrometers. Three prototypes have been implemented, each comprising an aluminum socket machined from 3.5in stock and a 2in diameter solid steel ball bearing (Figure 1). Separation between ball and socket is prevented by a magnetic preload force supplied by a ring of magnets about the circumference of the socket. Three primary contact mechanisms have been investigated: point, rolling and surface contact.

The point contact prototype locates the ball kinematically upon three spheres embedded within the socket. Given minimal Hertz deformation due to the relatively low preload forces, the primary source of error for this type of joint is the accuracy of the ball (typically 5 micron). The main problem with this design is the friction inherent in the point contact region. The rolling sphere point contact prototype seeks to alleviate this friction problem by utilizing rolling ball transfers mounted in the socket in place of the solid steel spheres. This dramatically reduces the friction but potentially increases the errors due to the additional influence of the ball transfer accuracy. The full surface contact prototype creates an accurate mounting surface through replication with a Teflon-laced epoxy. This provides a larger contact region to minimize contact stresses with minimal friction due to the Teflon contact surface. Despite the potential accuracy of such a joint, the friction is still significant.

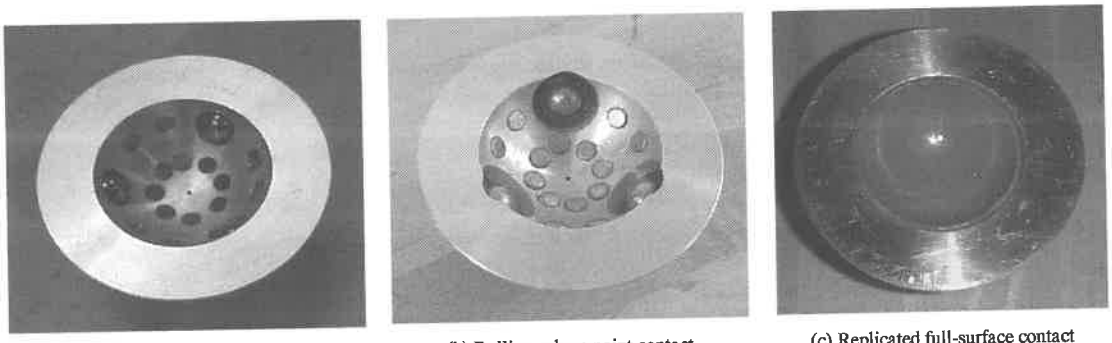

(a) Fixed sphere point contact (b) Rolling sphere point contact (c) Replicated full-surface contact

Figure 1 – Spherical Joint Prototypes

3. Design of Spherical Kinematic Test Rig

The spherical kinematic test rig (Figure 2) allows the actuation of each of the spherical joint's degrees of freedom for the purpose of measurement in a coordinate measurement machine (CMM). It comprises three concentric rings that are actuated by radio-control servomotors: the x-axis motor is mounted on the base; the y-axis motor is mounted on the x-axis ring; and the z-axis motor is mounted on the y-axis ring. The z-axis motor is connected to the spherical joint via a velcro clutch-plate and a tooling ball is mounted on the joint shaft to allow measurements by the CMM probe. The test rig stiffness is designed to be significantly less than the joint stiffness in order to avoid deformation of the joint during measurements. The test rig can be manually actuated with a radio control unit and automated via a commercially available controller. The test rig is mounted in the CMM and then run through a set of approximately 30 poses, distributed evenly about the joint workspace. For each pose, the tooling ball center is measured, and the set of joint poses and measured positions compiled for analysis.

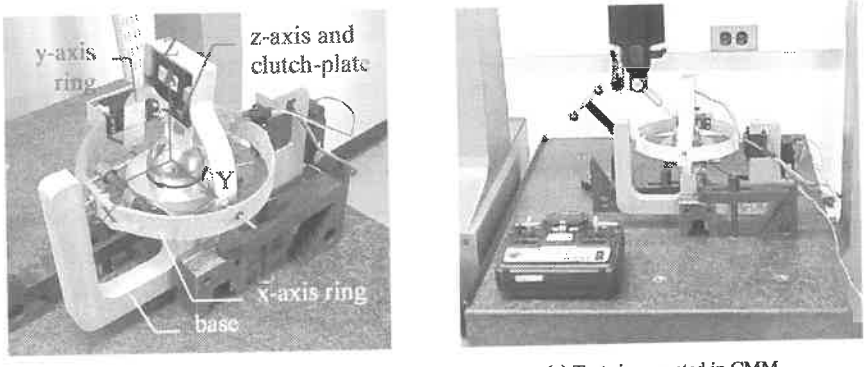

(a) Test rig and spherical joint (a) Test rig mounted in CMM

Figure 2 - Spherical kinematic test rig

4. Modeling of Spherical Joint

Each spherical joint prototype is modeled as a simple three degree-of-freedom mechanism, with three orthogonal axes: roll (rotation about the joint x-axis); pitch (y-axis rotation); and yaw (z-axis rotation). This allows each of the joint prototypes to be modeled and measured in the same fashion and the final accuracy characteristics compared. Two key models have been developed; a sphere fit model and a kinematic model. The sphere fit model assumes all axes intersect at a common location and fits a sphere center and radius to the measurement data by minimizing the residual error between the predicted tooling ball location and the measured position (Figure 3). The remaining residual error represents the accuracy of the joint.

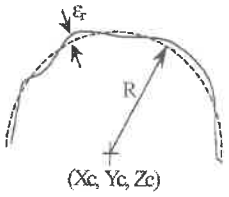

$$\varepsilon_r = R - \sqrt{(x_i - x_c)^2 + (y_i - y_c)^2 + (z_i - z_c)^2}$$

$$F(x_c, y_c, z_c, R) = \min\left(\sum_i (\varepsilon_r{}^2)\right)$$

Figure 3 – Spherical joint sphere fit model

The kinematic model extends the sphere-fit model by introducing a nominal forward kinematic model between the measurement system and the tooling ball (Figure 4). Six frames are introduced to describe the joint center in relation to the CMM coordinate frame; the roll, pitch and yaw joint angles; and the tooling ball center in relation to the joint center. The spherical joint angles are used as input to the kinematic model to determine the position of the tooling ball center. In a similar error minimization process as the sphere-fit, the nominal forward kinematic model attempts to fit the joint center and tooling ball location (radius) to the measurement data.

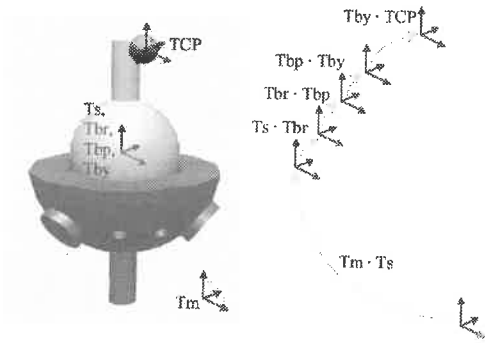

Frame descriptions:

1. Tm — measurement system frame
2. Ts — socket frame
3. Tbr — ball roll frame (θ_1)
4. Tbp — ball pitch frame (θ_2)
5. Tby — ball yaw frame (θ_3)
6. TCP — tooling ball frame

Nominal Forward Kinematics:

$$X(x,y,z) = F(\theta_1, \theta_2, \theta_3)$$
$$= Tm \cdot Ts \cdot Tbr \cdot Tbp \cdot Tby \cdot TCP$$

Figure 4 – Spherical joint structural loop and kinematic model

The error forward kinematics introduces position and orientation errors between each of the nominal kinematic frames (Figure 5) in order to characterize the location and magnitude of the joint errors. A numerical Jacobian matrix is computed from a sequence of joint positions, this matrix may be singular if too many parameters are included in the error kinematics. Through a process of elimination, the offending parameters are removed until the Jacobian is numerically well defined. In addition to the joint center and tooling ball location, six parameters are found to be significant: three orientation and three position errors representing the position and orientation of the actual joint center. A linear regression solver, utilizing the singular value decomposition of the Jacobian matrix, is then used to determine the error parameters by comparing the error forward kinematics with the measured positions. This process is derived from robot calibration applications [5], however in this case the input joint angles are not well known due to the inaccuracies of the spherical kinematic test rig. Using a "leap-frog" approach the joint angles are updated using a numerical inverse kinematics algorithm and the Jacobian and error parameters recomputed until

convergence is achieved. If the error parameters are set to zero (only the joint center and radius are calibrated), then the error forward kinematics becomes equivalent to both the nominal kinematic and sphere fit models.

Error Forward Kinematics:

$$X(x,y,z) = F(\theta,\varepsilon)$$

Jacobian:

$$J = \begin{pmatrix} \frac{\partial F_x(\theta_1)}{\partial \varepsilon_1} & \frac{\partial F_x(\theta_1)}{\partial \varepsilon_2} & \cdots & \frac{\partial F_x}{\partial \varepsilon_{nn}} \\ \frac{\partial F_y(\theta_1)}{\partial \varepsilon_1} & & & \\ \frac{\partial F_z(\theta_1)}{\partial \varepsilon_1} & & & \\ \vdots & & \ddots & \vdots \\ \frac{\partial F_z(\theta_M)}{\partial \varepsilon_1} & & \cdots & \frac{\partial F_z(\theta_M)}{\partial \varepsilon_{n1}} \end{pmatrix}$$

Singular Value Decomposition:

$$J = U \cdot S \cdot V^T$$

Measurement:

$$M(x,y,z) = \textit{Measured Positions}$$

$$E = M - F = \textit{Error Vector}$$

Calibration:

$$\partial\varepsilon = \textit{parameter update vector}$$

$$J \cdot \partial\varepsilon = E$$

$$U \cdot S \cdot V^T \cdot \partial\varepsilon = E$$

$$\partial\varepsilon = V \cdot \left(\frac{1}{S}\right) \cdot U^T \cdot E$$

Leap Frog Solver:

$$\theta_{new} = F^{-1}(X,\theta,\varepsilon)$$

Significant parameters:

1. pitch error Ts → Tbr
2. yaw error Ts → Tbr
3. y error Tbr → Tbp
4. z error Tbr → Tbp
5. x error Tbp → Tby
6. roll error Tbp → Tby

Figure 5 – Singular value decomposition and calibration

5. Measurement and Calibration

The rolling-sphere spherical joint is measured in a CMM with an accuracy of 2 micron in the working range of the test rig. The accuracy distribution is presented in Figure 6: the sphere fit model results in a maximum error of approximately 12 micrometers (μm); the kinematic model reduces this error to 8μm. The mean and standard deviation of both models is of the order of 3μm. This indicates that the uncalibrated joint is accurate to within 12μm within its working range, and this can be further improved to 8μm with the addition of the position and orientation error parameters.

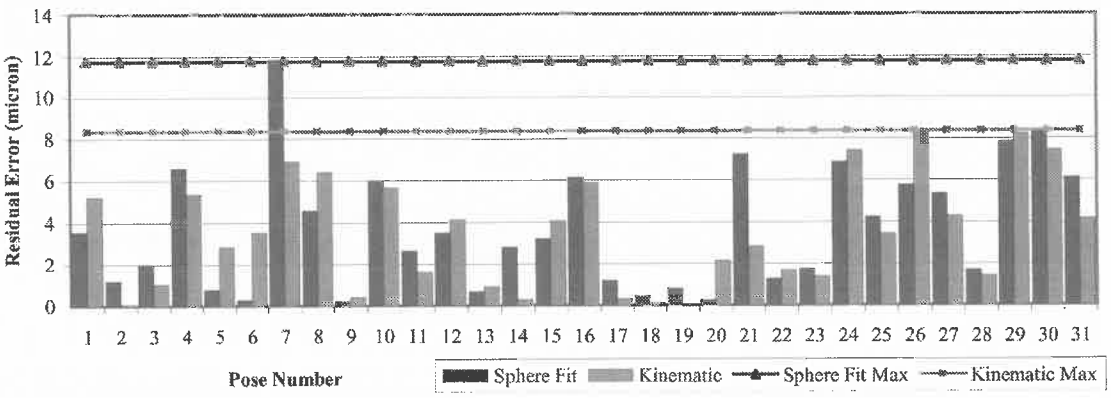

Figure 6 -- Accuracy distribution of rolling-sphere point contact prototype

6. Conclusions and Future Work

Three spherical joint prototypes have been developed for parallel robot applications. Each joint comprises an aluminum socket and a solid steel ball, preloaded by permanent magnets. The point contact prototype mounts the ball kinematically in the socket. The rolling contact joint significantly reduces friction by kinematically mounting the ball on rolling ball-transfers. The surface contact prototype uses replication to achieve a high-accuracy mating surface. A spherical kinematic test rig is used to actuate each joint to a predefined position, which is measured by a

coordinate measurement machine. The resultant uncalibrated accuracy of the rolling contact joint was 12 micron, which is reduced to 8 micron through calibration.

A fourth prototype is currently being investigated, based on a fluid contact mechanism. The replicated full-surface design is extended to include three orifices placed around the socket to create a thin film of air between the ball and the socket. This should significantly reduce the friction inherent in the replicated prototype while maintaining the high accuracy expected of a replicated joint. The residual error distribution remaining after the kinematic calibration has a large discrepancy between maximum and minimum residuals. This indicates that the simple kinematic error model insufficiently describes the physical phenomena underlying the measured joint. An improved model will be investigated with the goal of achieving a maximum error of the order of 2 micron.

7. References

[1] Clavel, R. Device for the movement and positioning of an element in space. U.S. Patent 4,976,582, 1989.
[2] Bryan, J. B. *Telescoping magnetic ball bar test gage*. U.S. Patent 4,435,905, 1982.
[3] Slocum, A.H. *Precision Machine Design*, Society of Manufacturing Engineers, 1992.
[4] Bernhardht, H. R et al. *Robot Calibration*. Chapman and Hall, 1993.
[5] Hayati, S., Mirmirani, M., *Improving the Absolute positioning Accuracy of Robot Manipulators*, Journal of Robotic Systems, 1985.

Keywords: spherical joint, calibration, metrology, parallel kinematic machines

GUIDELINES FOR DESIGN LOW COST MICROMECHANICS

L. Ruiz-Huerta, A. Caballero Ruiz, E. Kussul

Center of Applied Sciences and Technological Development, UNAM

Laboratory of Mechatronics and Micromechanics, Center of Applied Sciences and Technological Development, National Autonomous University of Mexico. Circuito Exterior s/n, Cd. Universitaria, Coyoacán, 04510, A.P. 70-186 México, D.F. Tel. +52-55-5622-8602 to 07 ext 115 e-Mail: leoruiz@servidor.unam.mx

I. Abstract

The problem of development microequipment is discussed. This paper contains description of the main problems connected with micro mechanical equipment developing, requirements to the micro machine tools properties, design and control systems of the prototypes of first generation machine tools, and applications of micro equipment. The mayor idea of this paper is to show the experience of the Laboratory of Mechatronics and Micromechanics in Center of Applied Sciences and Technological Development, UNAM, in development of different kinds of microequipment that include prototypes and models of CNC machines, manipulators for micromechanics, grippers and motors.

II. Introduction

At present in the world new technology direction is formed: creation of microfactories [1-8]. Micro devices are necessary for different field of production, for example, in watch industry, in automotive industry, in medical facilities, in biology investigation etc. Mechanical parts will become smaller in the future. It is possible to produce microcomponents with ordinary equipment but it is very difficult to provide high level of precision. We propose that micro mechanical equipment is to be made as a sequential generations of micro machine tools and micro assembly devices. Each next generation must have smaller sizes than previous one and must be produced by the equipment of previous generation [8].

In Japan the conception was proposed how to reduce the size of small parts production equipment to a level comparable with the size of the parts to be produced for the purpose of drastically saving energy, space and resources throughout the production plant [1]. It is simpler to provide high precision with micro devices, than with conventional ones.

Now exists the approach to manufacture the low cost micro components of sub millimeter sizes with using modern micro electronic technology. This approach is used very widely for manufacturing micro sensors and micro actuators, but it has some limitations connected with the problems of 3-D components manufacturing. This technology makes it possible to produce flat components. So it is very difficult to make automatic assembly of micro devices, because of 2-Dimensions. Our approach has no such problems, but demands low cost micro equipment, which is absent at present. In the article [8] main principles of such equipment creation are proposed.

III. The Main Requirements to the Micro Machine Tools (MMT)

At first, the micro machine tools (MMT) must be sufficiently precise. This characteristic must be considered always in relation with the cost of MMT. We develop and produce the first generation of MMT. The equipment for producing components having overall sizes from some hundred microns to some millimeters must provide accuracy of some microns [1, 5].

Developed MMT, at least the machine tools of first generation, must be multifunctional. The simplest multifunctional MMT must have four or five degrees of freedom (DOF) 3-translation axes and one or two rotary axes. MMT must use the simplest types of stepping motors and the contact sensors. It's preferable not use industrial motors and sensors because the next generation of micro equipment will demand the technology of producing of all micro equipment components using the same micro equipment.

It's important to ensure the simplicity of manufacturing and assembly of MMT. For this purpose all the complementary components of the machine tool must be as simple as possible. For mass parallel manufacturing process it's necessary to develop such a system of sensors and such adaptive control system, which facilitate combining of huge number of MMT in the frame of desktop micro factory, controlled by one operator.

IV. State of the Arts in the MMT Development

Mechatronics Laboratory (CCADET, UNAM) had developed and tested some prototypes of first generation machine tools. The main idea was to make prototypes as simple as possible, and to use minimum of industrial components, for scaling down developed micro machine tool in future generations.

CNC Prototype

The prototype is shown in the figure 1. On the base (1) the guides (2), (4), (6), for 3 carriages (3), (5), (7) are installed by the sequential scheme, i.e. each subsequent guide is installed on the previous carriage for to provide translation movements along the axis X, Y, Z. The spindle case (10) with spindle (11) also are installed on the base. The drives for carriages and for spindle use stepping motors (8) with gearboxes (9). The spindle has clamp for to grip workpiece by turning, drill by drilling or mill by milling. Support (12) has the cutter and two parallels metal pins for measurement of turned work piece diameter. For milling and drilling special gripper for workpiece should be installed on the carriage (7). The major part of the components of the MMT is made in brass and aluminum.

Components

The main components of the prototype are:

1. Stepping motors. We make our stepping motors with 4 steps per revolution and they can be forced to make 8 half steps. They are used in the mode of high-speed rotation.
2. Carriage. The guides for carriage were made as the round bars. It simplifies the manufacturing, assembly and scaling down processes. For reasons of robustness we decided to include some balls to compensate errors of guide's adjustment.

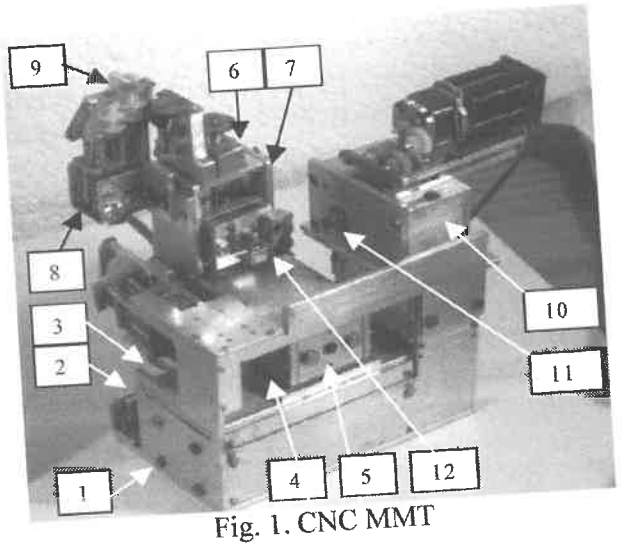

Fig. 1. CNC MMT

3. Transmission. It includes leading screws and gearboxes to reduce the speed of motors and increase the torque. All translation axes have the same configuration (gearbox, screw, stepping motor).

CONTROL

The feedback from the machine tool to the personal computer was realized on the base of four contact sensors, three of them are used to determine initial position of the carriages, and one is used to determine the moment of the contact of any tool with workpiece. This contact we used for determining relative positions of different instruments needed for the whole manufacturing process, and for measurements in the manufacturing process. We use electrical contact sensor and could have the feedback only from metal workpiece. If we need to make details from plastic, we made at first the same detail from metal, and then repeated the manufacturing process with plastic workpiesces. In principle it is possible to use other types of contact sensors (for example, acoustical contact sensor) to treatment the workpieces from any materials.
The control system, acquire the signals from sensors, using the PC's parallel port. In order to realize the control of the MMT, we assigned a specific task for the A port (sends data form PC to MMT); the B port (receives data form sensors and motors); and, finally the C port (gives the control signals to the system).

DESCRIPTION

The MMT has 130×160×85mm, and is controlled by PC. The MMT has three translation axes (X, Y, and Z), and one rotational. The axis X and Z, have 20 mm of displacement, and Y-axis has 35 mm. All of them have the same configuration. The resolution is 1.87μm per step of the motor.

TEST PIECES

Examples of the pieces that were manufactured with this MMT are showed in Fig. 2. Those photos are compared with a match head.

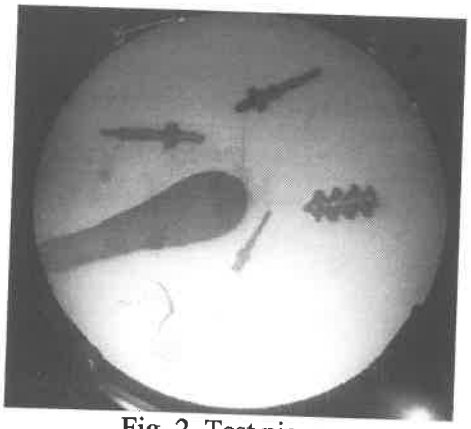

Fig. 2. Test pieces

V. Guidelines

On base of our experience with the showed machine, we propose some guidelines for develop low cost micromechanics. Most of all depends of the simplicity of the design. The simplicity was very important part to reduce the time of develop, and increase the viability of use same parts in many different parts of the machine. We used CAD software to improve and plan all the general schemes for new prototypes. We recommended the use of the same material in many parts of the prototypes for reduce problems associates with different thermal expansions.

In order to reduce the time of develop, we propose to include in the design processes, elements who could be reduced in sizes, and could have general applications in machines. We recommend to use simple elements for smooth displacements that require special attention to scalability and assembly.

We could resume the ideas in the next list:

1. Use of CAD Software
2. Use of same material in all parts as possible.
3. Design of pieces with general purpose
4. Simplicity of fix and assembly
5. Use of simple smooth elements (spheres and bars)
6. Use of simple elements to reduce backlash.

VI. Case of study

In order to prove our guidelines for low cost micromechanics, we design a new prototype of MMT. This new prototype includes similar specifications, that the previous, but use the experience in design and test. First of all, we decide to change the main material to brass, in all parts as possible. With this change we propose to reduce the thermal variations of the machine. Then, we consider to use a new design with bars and spheres. This mechanism pretend reduce alignment and backlash problems.

The mayor idea consist in use a single bar with different points of fix. With that points we could use the bar like a converter of low velocity and high torque. In the figure 3 we show a general schema of this mechanism.

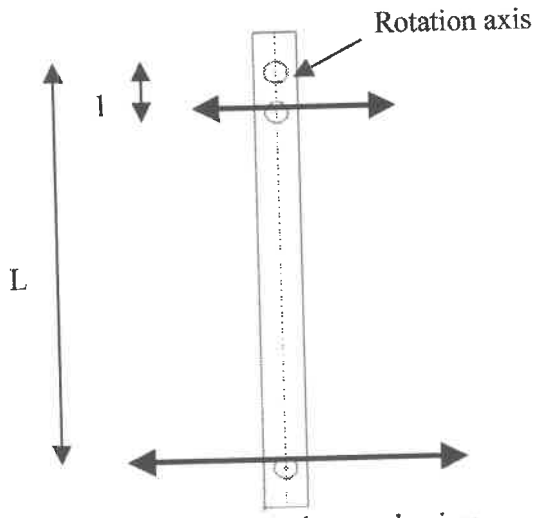

Fig 3. New power bar mechanism.

The new proposal system, consider common elements, (motors and power screws), but the operation is very different. Our new design include three bars parallelogram mechanism, to operate the three new axis (X, Y, Z). That's because this design allow us to have smooth movements. In figure 4 we show a general schema of the new axis displacement.

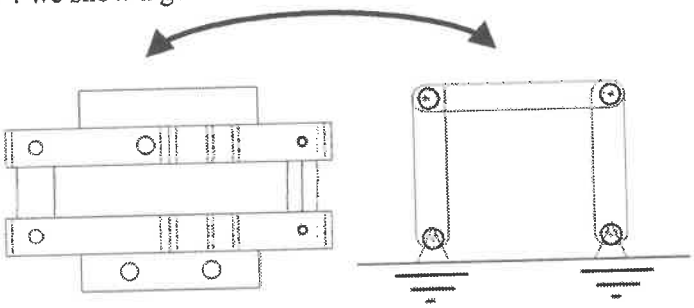

Figure 4. New axis displacement.

The new design for MMT, showed in fig 5), represents a new configuration to obtain low cost microdevices. The MMT has 180×210×135mm, and will be controlled by PC. The MMT will have three translation axes (X, Y, and Z), and one rotational. The axis X, Y and Z, have 20 mm of displacement. All of them have the same configuration. The theoretical resolution is less than 1.00μm per step of the motor. With this new mechanism, the mayor problem consist in control problem, but this new machine permit us to increase the rigidity and reduce the problems of assembly, discovered in the previous one. Actually we are manufacturing the parts to report in future their characteristics.

CONCLUSIONS

We presented a new MMT design that will reduce problems of rigidity and assembly. In order to improve these factors, we increase the size of the machine tool and the same time we increase the theoretical resolution. This new machine tool will require a new control system that includes new adjustment technique and bimodal motors. The new machine tool includes more parts, but most of all are similar. That reduces the manufacturing time.

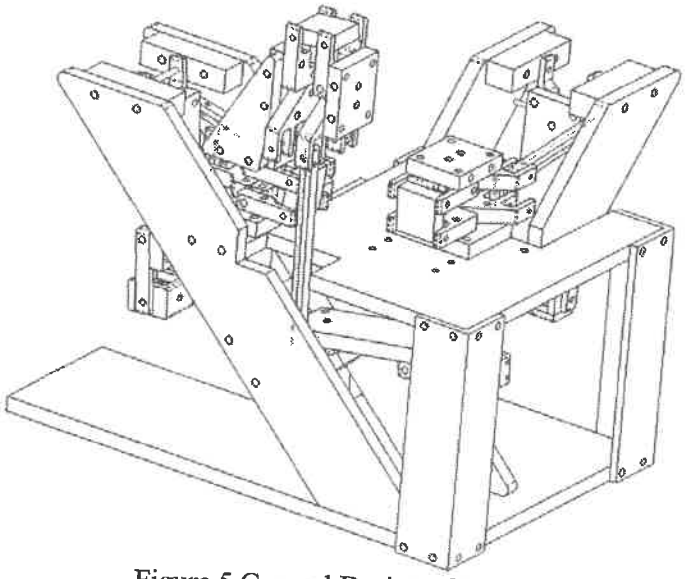

Figure 5 General Design of Machine.

ACKNOWLEDGEMENTS

This work was supported by CONACyT project 339944-U.

REFERENCES:

[1] Ishikawa Yu., Kitahara T. Present and Future of Micromechatronics. *1997 International Symposium on Micromechatronics and Human Science*, pp.13-20.

[2] Naotake Ooyama, Shigeru Kokaji, Makoto Tanaka and others. Desktop Machining Microfactory. *Proceedings of the 2-nd International Workshop on Microfactories*, Switzerland, Oct.9-10, 2000, pp.14-17.

[3] Bleuler H., Clavel R., Breguet J-M., Langen H., Pernette E. Issues in Precision Motion Control and Microhandling. *Proceedings of the 2000 IEEE International Conference On Robotics & Automation*, San Francisco, pp.959-964.

[4] Okazaki Yuichi, Kitahara Tokio. Micro-Lathe Equipped with Closed-Loop Numerical Control. *Proceedings of the 2-nd International Workshop on Microfactories*, Switzerland, Oct.9-10, 2000, pp.87- 90.

[5] Kussul E., Ruiz L., Caballero A., Kasatkina l., Baydyk T. CNC Machine Tools for Low Cost Micro Devices Manufacturing. *The First International Conference on Mechatronics and Robotics*; St.-Petesburg, Russia; 2000, Vol.1, pp.98-103

[6] Maekawa H., Komoriya K. Development of a Micro Transfer Arm for a Microfactory. *Proceedings of the 2001 IEEE International Conference on Robotics & Automat*ion, Seoul, Korea, May 2001, pp. 1444-1451.

[7] Mishima N., Ashida K., Tanaka M. Development of Machine Tools for the Microfactory. *Proceedings of International Workshop on Microfactories*, 2000, pp.137-140.

[8] Kussul E., Rachkovski D., Baidyk T. and Talayev S.. Micromechanical Engineering: a Basis for the Low Cost Manufacturing of Mechanical Microdevices Using Microequipment, *J. Micromech. Microeng.*, 1996, 6, pp. 410-425.

DYNAMIC DISPLACEMENT MEASUREMENT OF PZN-PT UNIMORPH MICROACTUATORS USING ATOMIC FORCE MICROSCOPY

Kee S. Moon*, Miguel Levy**, Yong K. Hong* and Shankar Ghimire**
*Dept. of Physics, Michigan Tech. University, Houghton, MI
**Dept. of ME-EM, Michigan Tech. University, Houghton, MI

Abstract

A measuring system was developed to test the piezoelectric response of $Pb(Zn_{1/3}Nb_{2/3})O_3$-$PbTiO_3$ (PZN-PT) film unimorph actuators. PZN-PT has been shown to exhibit piezoelectric coefficients and electromechanical coupling responses significantly larger than conventional ceramics. Their electromechanical coupling and large strain levels are much superior to $Pb(ZrTi)O_3$ (PZT). In addition PZN-PT also exhibit very low hysteresis. An atomic force microscope- (AFM) based measurement system was used to monitor and record the motion of the new microactuator. In this paper, we report on the experimental measurement of electrically induced strain. The results demonstrate the potential use of the unimorph actuator in micro-electromechanical systems (MEMS).

Introduction

Numerous atomic force microscope- (AFM) designs have been developed to study surfaces with nanometer-scale resolution. With the ongoing progress in scanning probe techniques, nanometer- and even atomic-scale imaging has become possible on a variety of different samples. [1-5] The AFM provides direct, high-resolution visualization of surface morphology. Using an AFM-based system, described below, we have monitored the motion of a novel PZN-PT film microactuator developed in our laboratories.

PZN-PT ($Pb(Zn_{1/3}Nb_{2/3})O_3$-$PbTiO_3$) is a piezoelectric material with superior piezoelectric response to conventional ferroelectric ceramics such as PZT. PZN-PT solid solutions exhibit piezoelectric coefficients (d_{33}) higher than 2,000 pm/V (a significant increase over PZT's d_{33} ~ 300-600 pm/V), excellent electromechanical coupling coefficients, and very low strain hysteresis, which are important characteristics for reproducible micro-mechanical performance. [6, 7] Here we report on the performance of unimorph microactuators based on freestanding single-crystal films of PZN-PT.

Sample design and fabrication

The fabrication of single-crystal microscopic (1 to 10μm thick) PZN-PT films for this research relies on a novel technique known as crystal ion slicing. [8, 9] The films are obtained from single-crystal PZN-PT bulk samples by slicing a thin layer off the top of the sample flat. This technique relies on the formation of a sacrificial layer below the surface with the aid of energetic (~4 MeV) helium ions implanted at near-normal incidence to the surface. The implantation energy controls the thickness of the films, allowing thinner films to be made at lower biases. After implantation, the sample is annealed and immersed in hydrochloric acid to detach the thin films. These are then used to fabricate stand-alone actuators, 0.5 x 1 mm^2 in lateral dimension. Two different actuator designs were fabricated with a micromanipulator. Figure 1 shows the two designs.

Measurement system

The actuator deflection is measured using the optical detection system shown in Fig. 2. Its main components comprise the following: an optical microscope, a PZT-based 3-D stage with a sample holder, a commercially available AFM probe, a helium neon laser, a segmented photodiode, a computer controller, a vibration isolation table, a data acquisition device, a CCD camera with a monitor, and a signal generator. The measuring system is designed to place an AFM tip between the objective lens and the specimen holder of an optical microscope. This system is capable of displaying microscopic images of the unimorph surface for AFM tip positioning to a specific location. Contact mode is used while maintaining a constant force between tip end and the surface of the microactuator.

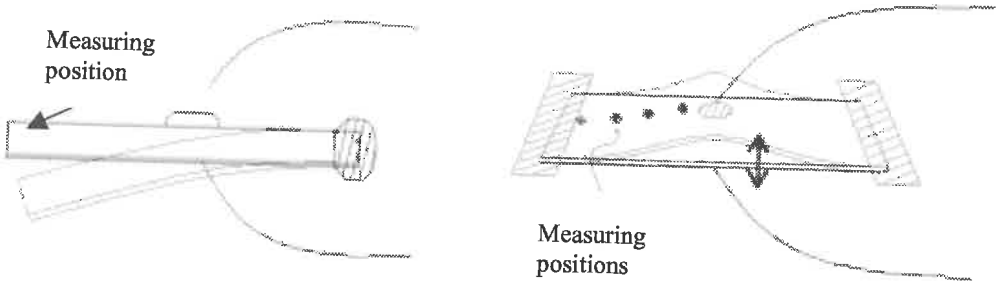

Figure 1: Unimorph micro-actuators based on freestanding single-crystal films of PZN-PT (left figure: cantilever-bending motion, right figure: bowing actuation)

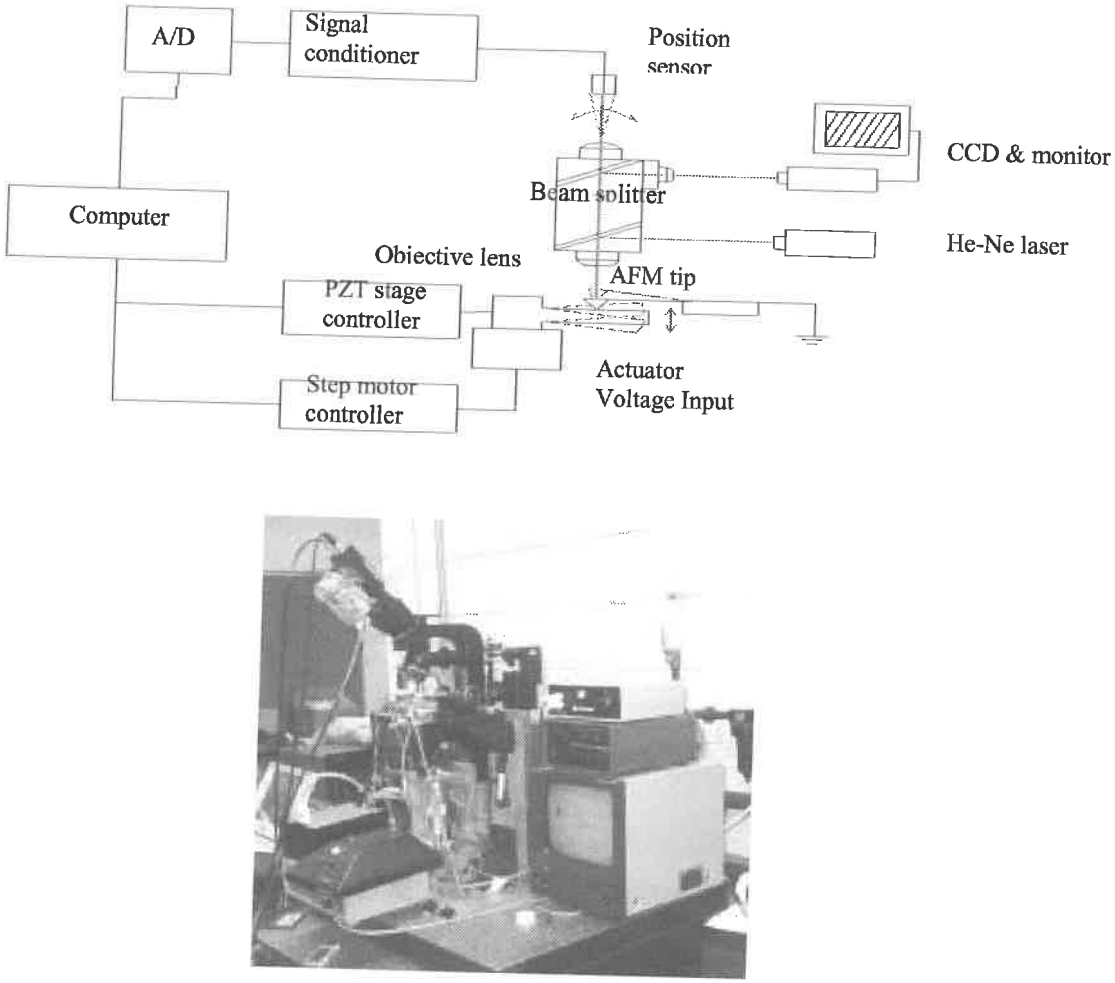

Figure 2: Experimental measurement setup.

The actuator motion is then transmitted to the AFM tip and the vertical displacement is detected by a double-cell photodiode. Data acquisition is synchronized with a signal generator to control the unimorph actuation motion. A PC-based real-time A/D board was used for collecting the displacement data.

Experimental results

Due to the small actuator size the flapping speed can reach very high values. Figure 3 shows the frequency response of the actuator at 50 kHz. Furthermore, the actuation voltage is relatively low as compared with the PZT actuation voltage (~100V). The actuator displacement is typically 1 micrometer with an applied voltage of 30V at relatively low frequencies, whereas the high frequency response requires higher voltages (~80V) for similar deflection due to loading. A detected output signal from the sensor and a typical hysteresis loop are shown in Fig. 4, respectively.

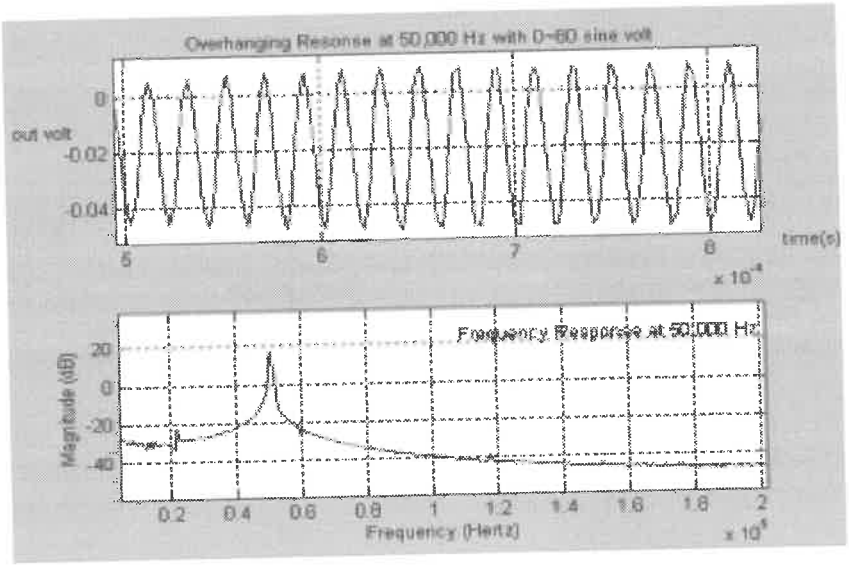

Figure 3: A high frequency response of a cantilever-bending motion actuator at 50 kHz.

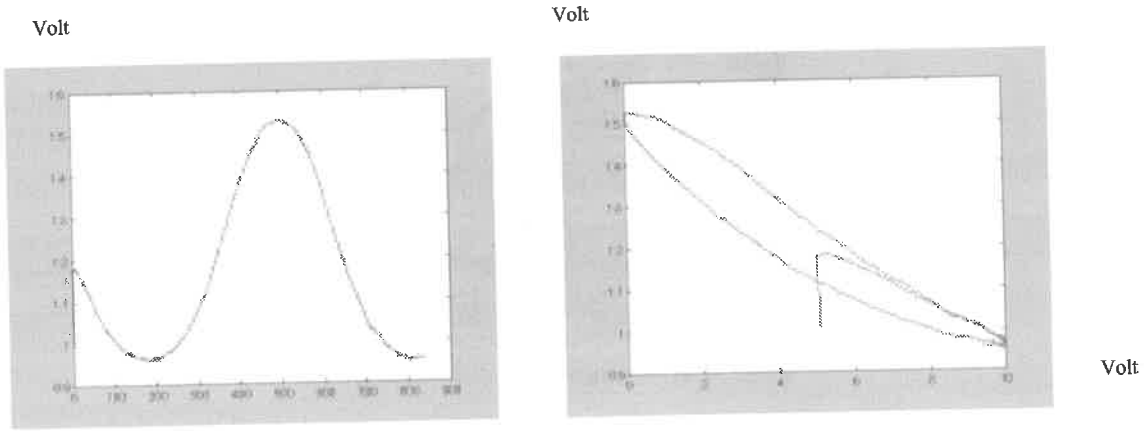

Figure 4: A detected output signal from the sensor (left figure) and a typical hysteresis loop (right figure) for a cantilever-bending motion actuator.

With this system we have also studied the displacement profile through point-wise scanning of the film's vertical position for a bow-bending motion actuator. (Fig 5 (a)) A typical hysteresis loop of the type is shown in Fig. 5(b) for the actuator examined in the 0 to 150 V range. The measurement results demonstrate that the PZN-PT unimorph samples fabricated in our lab can produce large (micron-scale) deflections.

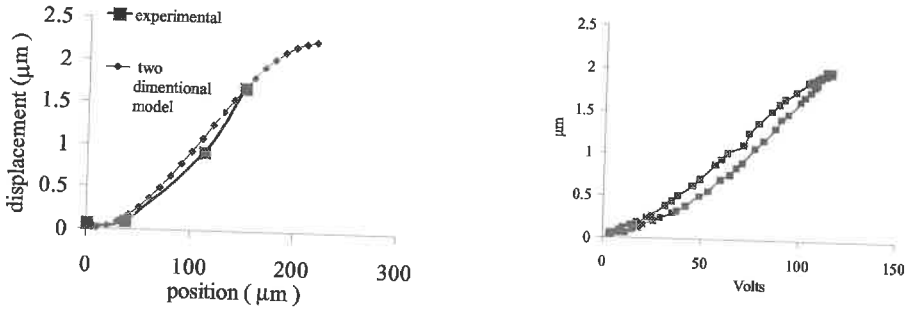

Figure 5: (a) Displacement profile in a bow-bending motion actuator (b) Hysteresis loop.

Conclusions

An AFM based measurement technique was applied to a novel PZN-PT unimorph actuator. Microactuator piezoelectric-response was measured using this technique. It was demonstrated that the PZN-PT unimorph samples fabricated in our lab could produce very large displacements and high frequency motion. ML gratefully acknowledges support from NSF grant ECS-9980828.

References

1. Hansma, P. K., V. B. Eling, O. Marti, and C. E. Bracker, "Scanning Tunneling Microscopy and Atomic Force Microscopy: Application to Biology and Technology," Science, vol. 242, 209-216 (1988).
2. Mate, C. M., M. R. Lorenz, and V. J. Novotny, "Atomic force Microscopy of Polymetric Liquid Films," J. Chem. Phys., vol. 90, no. 12, 7550-7555 (1989).
3. Bhusan, B. and G. S. Blackman, "Atomic Force Microscopy of Magnetic Rigid Disks and Sliders and Its Applications to Tribology," Transactions of the ASME, Journal of Tribology, 90-Trib-5, 1-6 (1990).
4. Ho, F., A. S. Hou, and D. M. Bloom, "High-speed Integrated Circuit Probing Using A Scanning Force Microscope Sampler," Electronics Letters, vol. 30, no. 7, 560-562 (1994).
5. Shaffer, O. L., R. Baghei, J. Y. Qian, V. Dimonie, R. A. Pearson and M. S. El-Aasser, "Characterization of the Particle-matrix Interfacing Rubber Modified Epoxy by Atomic Force Microscopy," J. of Appl. Polymer Sci., vol. 58, no. 2, 465 – 484 (1995).
6. Park, S.E. and T. R. Shrout, "Ultrahigh Strain and Piezoelectric Behavior in Relaxor Based Ferroelectric Single Crystals," J. Appl. Phys., vol.82, no.4, 1804-1811 (1997).
7. Fu, H. and R. E. Cohen, "Polarization Rotation Mechanism for Ultrahigh Electromechanical Response in Single-Crystal Piezoelectrics," Nature, vol.403, no.20, 281-283, Jan. (2000).
8. Levy, M., R. M. Osgood, Jr., A. S. Bhalla, R. Guo, L. E. Cross, A. Kumar, and H. Bakhru, "Stress Tuning in Crystal Ion Slicing to Form Single-Crystal Potassium Tantalate Films," Appl. Phys. Lett., vol..77, 2124 (2000).
9. Levy, M., R. M. Osgood, Jr., R. Liu, L. E. Cross, G. S. Cargill III, A. Kumar, and H. Bakhru, "Fabrication of Single-Crystal Lithium Niobate Films by Crystal Ion Slicing," Appl. Phys. Lett., vol..73, 2293 (1998).

A 2D OPTICAL DISPLACEMENT TRANSDUCER TO MEASURE NANOMETRIC ERRORS IN PRECISION MACHINES

A. Albertazzi Jr., A. R. Sousa, C. Veiga, D.P. Willemann
UFSC - Federal University of Santa Catarina
PHOTONITA – Photonical Instruments for Technical Applications Inc.
Rod. SC 401 km 1 - Parque Tecnologico Alfa
Florianopolis, SC – 88030-000 – Brazil
albertazzi@labmetro.ufsc.br - www.photonita.com.br

Abstract

This work presents an innovative and portable optical measurement system based on a radial ESPI interferometer, capable to measure small displacements with a nanometric uncertainty. The system is fully automated, very portable and light weighted (~0.6 kg). Almost no surface preparation is required for 2D displacement measurement, what makes it very convenient for measuring directly on the work piece surface. In the current configuration, the system has a measurement range of ± 2 μm, and its calibration using a modified Michelson interferometer has showed an uncertainty $U_{95} = \pm 0.008$ μm. The experiments revealed that the optical system is reliable and time efficient, having a strong potential to be applied in other situations where it is necessary to measure small displacements, with very low uncertainties. By combining three of those devices it is possible to measure all the six rigid body displacement and rotation components. Here, it is demonstrated its performance to measure the instalilities the the air bearings of a coordinate measuring machine. Its application to measure strain and stress in materials are also related in this work.

1. INTRODUCTION

Special machine tools and measuring machines must present very high positioning repeatability to assure that special parts (lenses, mirrors, ...) and very accurate measurement can be obtained from these machines. In order to accomplish such tasks, the machines must present sub-micron repeatability that is influenced mainly by thermal factors, mechanic hysteresis, control limitations and, to some special machines, instabilities in the air bearings.

Air bearings are widely used in special machines when it is necessary to assure low friction, high stability and high displacement velocities. Ultra precision lathes for diamond turning and coordinate measuring machines are some examples of machines with air bearings. In these machines, the manufacturers expect that the bearings have a very good position stability to assure accurate parts and measurement results. Some manufacturers stand that a rotational and axial stability of 0,050 μm is achieved with air bearings and that this accuracy remains constant over time as there is no wear due to metal to metal contact between the rotating and static parts.

In order to assure such accuracy, the air bearing must be accurately designed, manufactured and installed on the machine. Under operation, it is necessary that air pressure is stable and that the bearing holes are clean to not block the air flow. Only under these conditions, its accuracy will be assured. To verify if the bearing is working properly it is necessary to measure its position stability and the measurement of air bearing stability is a very difficult task. Because of the very small displacements, it is necessary a measurement system with nanometer resolution and very low uncertainty to detect instabilities in the

fluctuation of the machine parts over the air bearings. Classical instrumentation as mechanical gages, laser interferometers, etc., are not anymore suitable, because its uncertainty and operational limitations.

In this work, it is presented an innovative and portable system capable to measure nanometric displacements in moving parts, with very good time efficiency. The system, based on a radial interferometer, is very portable, light weighted and fully automated, having a resolution of 0,001 μm and an uncertainty of ± 0,008 μm. Its performance is demonstrated in the measurement of the instability of an air bearing of a coordinate measuring machine.

2. AN INNOVATIVE SYSTEM TO MEASURE SUB-MICRON DISPLACEMENTS

An innovative and portable optical measurement system based on a radial ESPI interferometer has been developed at the Federal University of Santa Catarina [1] to measure nanometric 2D displacements. The system can be seen in figure 3 and consists of an interferometer with conical mirrors to produce a double illuminated area from a single laser source. A diode laser and a CCD camera integrate the systems, that is fully automated and managed by a dedicated software

This double illumination makes possible to measure radial in plane displacements applying the principle of Electronic Holography or ESPI (Electronic Speckle Pattern Interferometry). The double illuminated area produces a speckle pattern that is acquired by the image processing system, producing a reference image. As the illuminated surface moves, the speckle pattern changes and new images are acquired and subtracted from the reference image, producing interference fringes and, after computer processing, phase maps. From these phase maps are measured the displacements of the illuminated region [2].

This innovative configuration made possible to build a compact measurement unit, capable to characterize in plane displacements in the illuminated surface, with metrological reliability, operational and economical advantages over classical methods.

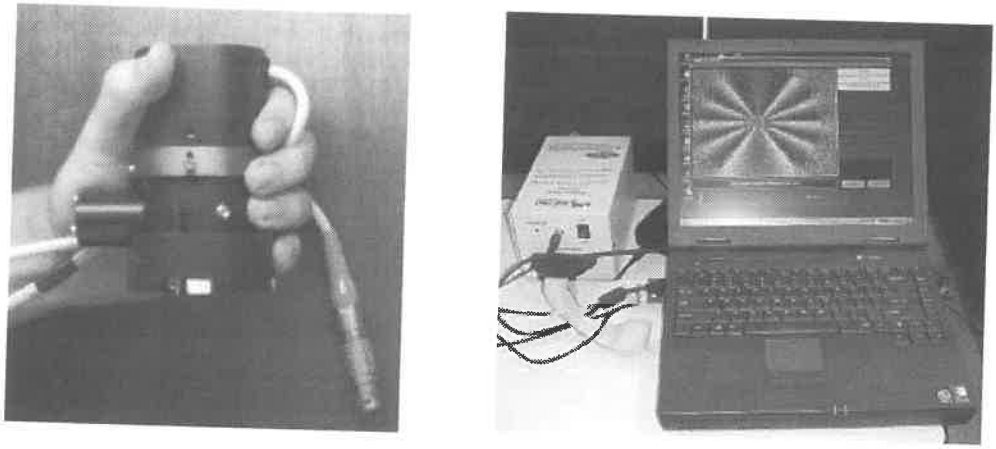

Figure 1 - Radial interferometer, drive control and software

The system was calibrated with an amplified Michelson interferometer using He-Ne laser and the results have a close concordance [3]. Some of then can be seen in figure 3. Its measuring range can be modified

according the application. It the current configuration the system has a 2 μm range with 0,001 μm resolution. From this calibration, an uncertainty of ± 0,008 μm was estimated. Lower uncertainty can be obtained with a more accurate reference.

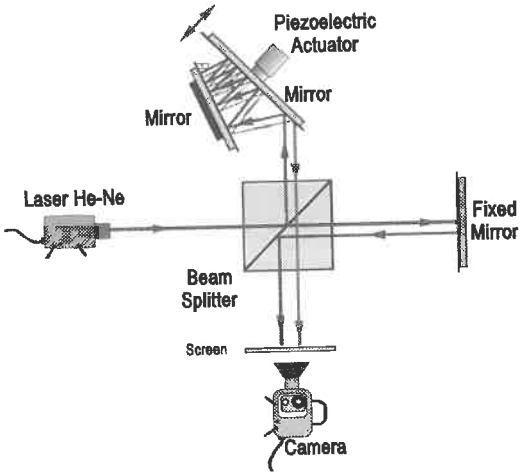

RUN	MICHELSON (μm)	SYSTEM (μm)
01	1.480	1.486
02	1.481	1.480
03	1.482	1.485
04	1.485	1.479
05	1.481	1.478
Mean	1.482	1.482
St Deviation	0.002	0.004

Figure 2 – Calibration with a modified michelson intereferometer

This same system can also be applied to measure stresses/strains and residual stresses in materials under load. For this operation, two dedicated and fully automated systems (***Optical Rousette*** and ***M-TRES***) were developed. Numerical and graphical results are obtained from the measurements enabling to know the stress state of mechanical components and structures in work conditions.

Comparisons with classical strain gages to measure stress and residual stresses have been done and the results were very close, but with ***Optical Rousette*** [4] and ***M-TRES*** [5, 6] systems this operation is done in 10% of the measurement time using strain gages and without the necessity of consumables. Figure 3 shows the ***Optical Rousette*** being applied to measure the stress in the rear suspension of a truck, after a 150 kg mass has been put over the vehicle. On the right side, there is an example of graphical and numerical result.

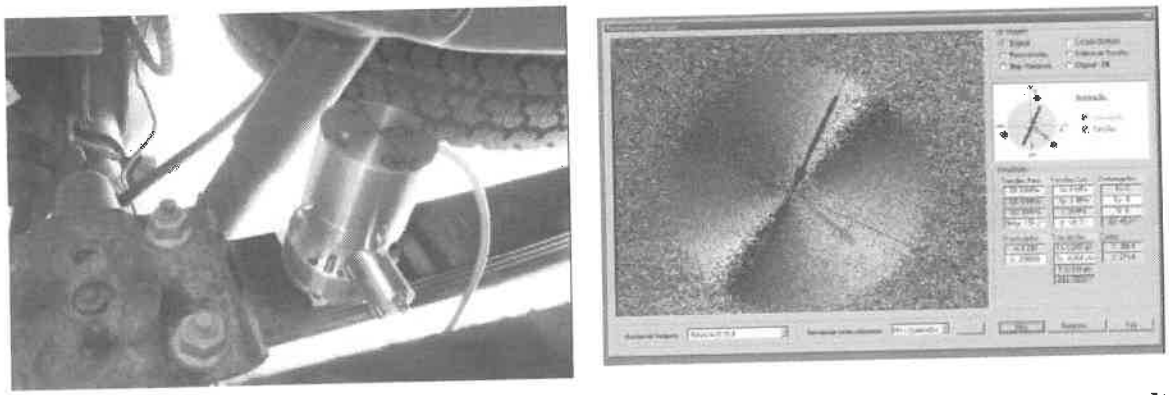

Figure 3 – Optical Rousette measuring the stress/strain in a truck suspension and a software result

3. MEASURING 2D DISPLACEMENTS OF AN AIR BEARING

As described in the introduction, air bearings are widely used in special machines when it is necessary to assure low friction, high stability and high displacement velocities. In these machines, the manufacturers expect that the bearings have a very good position stability to assure accurate parts and measurement results. In order to assure stability around 0,050 μm, the air bearings must be accurately designed, manufactured and installed on the machine. Under operation, it is necessary that the air pressure is stable and that the bearing holes are clean to not block the air flow.

In this work, the system was applied to measure the vertical bearing inslatibilty of an air bearing of a coordinate measuring machine (CMM). Under operation, the bearings of CMMs must present high stability to assure accurate results. Any instability will cause relative movement between the CMM touch probe and the workpiece to be measured.

In the experiments, the system was positioned in front of the right column of the CMM, 3 mm distant from the surface (figure 4). No surface preparation was done on the machine. The machine motors were turned off in order to measure movements only due to the air bearings. About 10 minutes after opened the air to the bearings, a first image was acquired and its phase map calculated. Other images were acquired with an interval of 1 minute between consecutive acquisitions. During the experiments, real time instabilities could be seen observing the real time fringes. This is as important tool to verify internal and external vibrations and/or quick variations in the bearings.

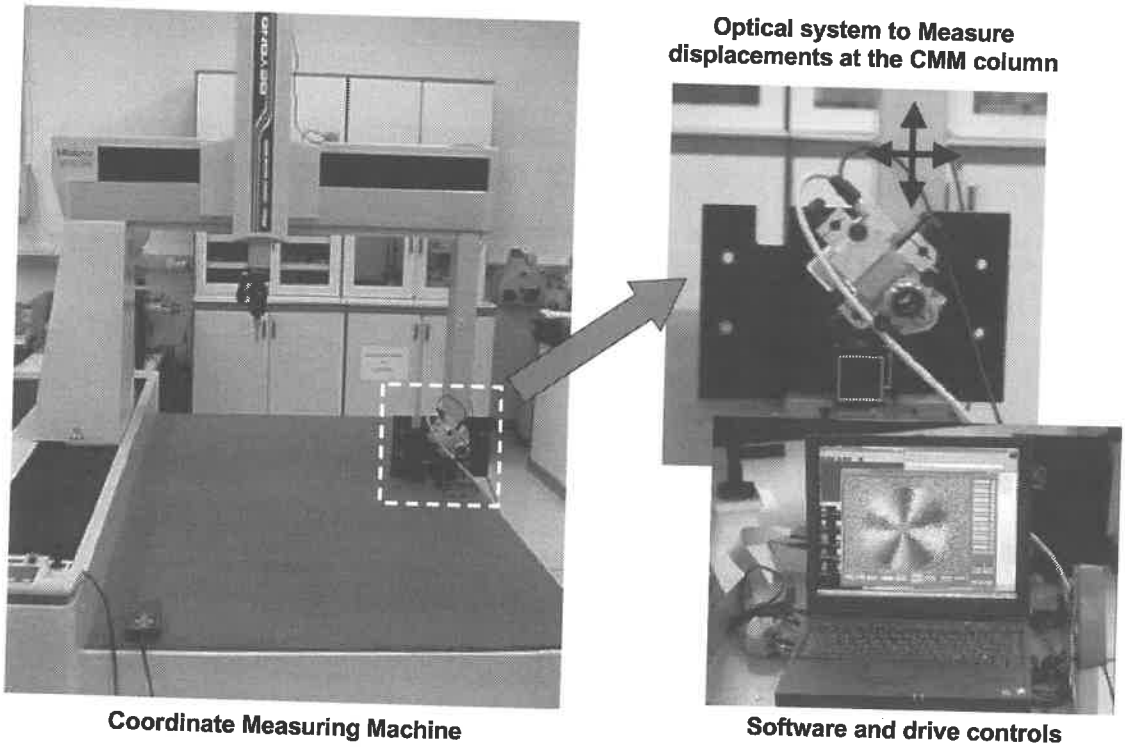

Figure 4 – Experimental setup to measure instabilities in the air bearing

The phase maps calculated for each image acquisition were combined and fringe patterns resulted, as a consequence of the displacementS caused by instabilities in the air bearing under the column of the CMM. The processing of these fringe patterns revealed the displacements. The image acquisition and processing is fully automated by software. The whole test was done in 25 minutes. Figure 5 shows some resultant images, as well as the bearing displacements along the period of test.

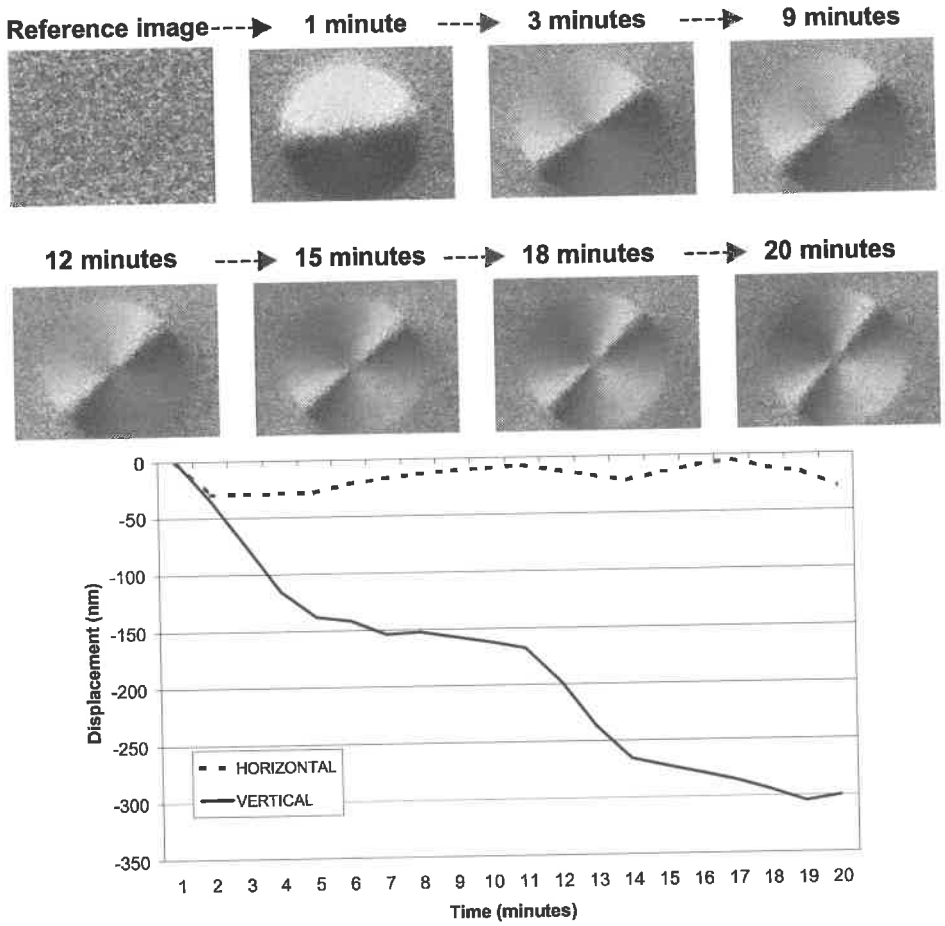

Figure 5 – 2D displacements measured on the CMM column

The results revealed that the air bearings had a vertical displacement of 0,305μm and 0,029μm horizontally, over a period of 20 minutes. Considering that the measuring uncertainty of this CMM starts from ± 3 μm, the bearing tested showed to be reliable to this application but for an ultra precision CMM this displacement level would be critical.

4. CONCLUSIONS

The konwledge of the performance of precision machines is a difficult task because it is necessary to measure very small errors with sub-micron uncertatinty. The measurement systems used to these experiments are usually very expensive or not reliable or have operational limitations.

This work presented an innovative and portable optical measurement system based on a radial interferometer using Electronic Speckle Pattern Interferometry, capable to measure very small displacements with a nanometric uncertainty. Based on this radial interferometer, different systems have been developed to test precision machines and also to measure stress/strain and residual stresses in materials.

For all these applications, an experimental setup is already complete. The radial interferometer, the diode laser and the CCD camera are integrated in one part. A control driver and a notebook complete the experimental setup, that it is configured and managed by a sofware test, making the system fully automated. These devices make the experiments to measure displacements, stress/strain and residual stresses very easy and quick.

Some evaluations comparing the ***Optical Rousette*** (stress/strain) and ***M-TRES (residual stresses)*** systems to classical instrumentation showed a similar uncertainty but strong operational advantages over classical systems [3]. Table 1 below shows one of these evaluations.

Cost [1]	Optical Rousette	Strain Gage
Man power [2]	US$ 1.50	US$ 22.50
Consumable	US$ 0.06	US$ 45.00
Total	US$ 1.56	US$ 67.50

[1] 1 measurement point [2] US$ 30.00/h

TABLE 1 – Economical comparison between Optical Rousette and strain gage for stress measurement.

The systems are very flexible and can be easily configured to specific applications. Developments have continuosly been implemented to make the systems even more reliable, time efficient and cost effective. All of them were developed at the Federal University of Santa Catarina and are produced and comercialized by Photonita - Photonical Instruments for Technical Applications – Inc (www.photonita.com.br).

5. REFERENCES

[1] **Albertazzi, A.** *Adequação de um interferômetro radial para a medição de tensões radiais por meio da holografia eletrônica.* **Brazilian Symposium on Experimental Stress Analisys – Brazil, 1995.**

[2] **Albertazzi, A.** *A robust hybrid phase unwrapping technique by block processing and sucessive approximation to a mathematical model.* **Fringe, 2001 – The 4th International Workshop on automatic processing of fringe patterns. Elsevier Science Publishers. Paris, 2001.**

[3] **Willemann, D.** Desenvolvimento de uma roseta óptica para a medição de tensões e deformações utilizando holografia eletrônica. **Master Program in Scientific and Industrial Metrology - Federal University of Santa Catarina – Brazil, 2002.**

[4] **Willemann, D.; Veiga, C.; Albertazzi, A.** *Desenvolvimento de um dispositivo interferométrico para a medição de tensões e deformações com holografia eletrônica.* **Brazilian Congress of Mechanical Engineering. Brazil, 2001.**

[5] **Boettger, J.** *Desenvolvimento de um sistema portátil para a medição de tensões residuais em campo utilizando a holografia eletrônica.* **Master Program in Mechanical Engineering - Federal University of Santa Catarina – Brazil, 1998.**

[6] **Ronsani, M.** *Otimização de um medidor portátil de tensões residuais.* **Master Program in Mechanical Engineering - Federal University of Santa Catarina – Brazil, 2000.**

Precision Assembly and Metrology of X-ray Foil Optics

Craig R. Forest[1], Matthew Spenko, Yanxia Sun, Michael McGuirk, Alexander H. Slocum, Mark L. Schattenburg
Massachusetts Institute of Technology, Cambridge, MA 02139

Keywords: x-ray telescopes, x-ray optics, Constellation-X, mirror alignment, precision assembly, MEMS, Shack-Hartmann, metrology, wavefront sensing

1 Introduction

Achieving arcsecond angular resolution in a grazing-incidence foil optic x-ray telescope such as the segmented mirror approach being considered for the NASA Constellation-X mission requires accurate and repeatable placement of thousands of individual foils. We are developing a method for assembling nested, segmented foil optics with sub-micron accuracy and repeatability using lithographically manufactured silicon alignment microstructures, called microcombs [1]. A system of assembly tooling incorporating the silicon microstructures, called an assembly truss, is used to position the foils that are then bonded to a spaceflight module. The advantage of this procedure is that the flight module has relaxed tolerance requirements while the precision assembly tooling can be reused. Previous work [5] has demonstrated that the microcombs can provide accurate and repeatable reference surfaces for the optic foils; current research has developed a device that makes progress towards actual flight module assembly. Key features include flexure bearings for frictionless motion of the microcombs, kinematic couplings to ensure repeatable alignment of successive flight modules, and flight module integration.

Metrology of the foil optics is critical to meeting the telescope performance goals. In addition to the sub-micron assembly tolerances, individual foils must be manufactured with figure error less than 500 nm over their 140×100 mm^2 surface area. A deep-UV Shack-Hartmann surface mapping tool has been created to determine whether the foils meet these manufacturing requirements and to provide active metrological feedback during the assembly procedure.

2 Design

2.1 Assembly truss

To accurately and repeatably assemble thin optic foils, an assembly truss has been designed and manufactured (Figure 1). In operation, optic foils are inserted into the device parallel to a reference flat. The foils' positions are constrained by two microcomb sets on the base and one microcomb set on the lid. Three flexure bearing assemblies, each containing a microcomb set (a spring microcomb and a reference microcomb), work in conjunction to position the optic foils. Figure 1 inset shows their design. To align the foils, a reference comb atop its flexure bearing is driven by a micrometer into contact with the polished reference flat, thereby aligning each of its "teeth." The spring comb is then actuated using a micrometer to force the optic foil into position against the reference comb's teeth. The flexure bearings provide hysteresis-free, friction-free support for reference combs to make contact with the reference flat and for the spring combs to impart forces to the foil.

The monolithic flexures have been manufactured from stress relieved aluminum 6061-T651 to prevent warping due to the release of internal stresses during manufacture. The four bar linkage design of the flexure bearings allows parallel motion between the top and bottom members. In fact, a parasitic pitch error in this motion is virtually eliminated with proper selection of the position of the driving point [6]. The flexures are actuated at half of their height by differential screw micrometers (Mitutoyo Model 110-102) which have a resolution of 0.1 μm. This resolution is necessary to achieve the microcomb placement accuracy of 1 μm. Force sensors (Honeywell, sold by Cooper Instruments Model LPM 560, LPM 562) are placed in between the micrometers and the flexure bearings to detect when contact with the reference flat occurs, since then the stiffness of the system changes. Before contact, the force per unit displacement is a function of the stiffness of the flexure bearings, force sensors, micrometers, and micrometer holders. After contact, there is

[1]email: cforest@mit.edu.

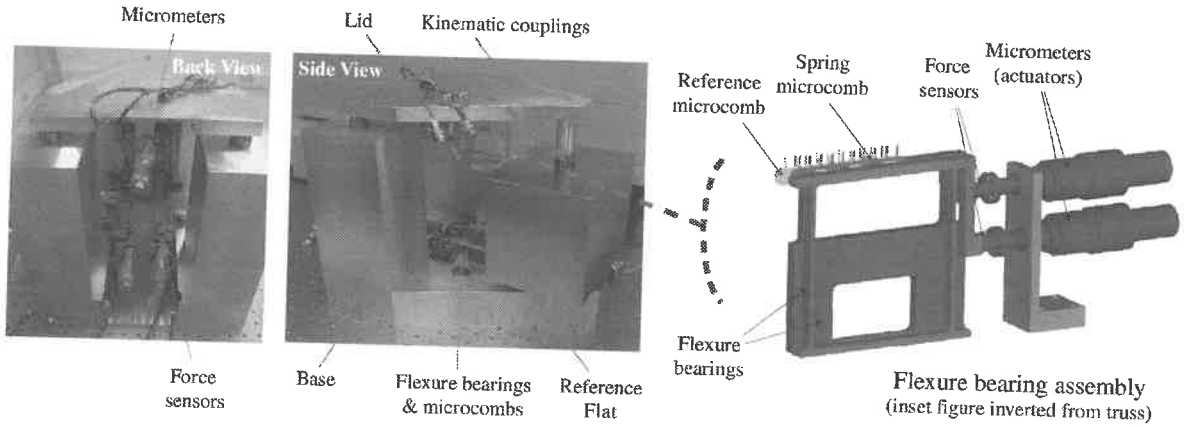

Figure 1: X-ray foil optic assembly truss. *Inset:* Flexure bearing assembly.

an additional stiffness component due to the Hertzian deformation of the microcomb. The force sensors are relatively insensitive to off-center plunger loading and have force ranges of 500 and 1500 grams-force for the reference and spring flexure bearings, respectively.

The structural parts of the assembly truss are stacked up with ball/v-block kinematic couplings at their interfaces. The ball and v-block design of these kinematic couplings theoretically allows repeatable assembly of the structure to less than 0.5 μm [2]. Fortunately, this error only impacts the foil assembly tolerances as a cosine term after flexure bearing actuation. The v-blocks are arranged such that the lines formed by the intersection of their respective faces intersect at the centroid of the triangle whose vertices are formed by the v-blocks themselves. This ensures uniform load distribution and prevents the faces from over-constraining the parts from misalignment.

The reference flat used as an alignment plane for the microcombs is a solid block of Aluminum 6061-T6 with 0.005 inches of electroless-plated nickel on its surface. The nickel is much harder than the aluminum to resist scratching during use. One face of the block is lapped and optically polished to 1 μm flatness peak-to-valley (P-V). Polished nickel was selected for a reference flat due to its low cost, hardness, and ease of machining.

A flight module containing the optic foils was incorporated into the design of the assembly tool. Prior to assembly, thirty foils are loosely held in this module by a set of "coarse combs." The entire structure is then loading into the precision assembly tool. The microcombs manipulate the foils into their aligned locations within the oversized slots of these coarse combs. Glue is then injected into holes on the coarse combs to secure the aligned foils in place. The flight module, containing the foils, is then removed and installed in the telescope. The flight module includes kinematic balls for the repeatable alignment with the base.

2.2 Shack-Hartmann surface metrology tool

The optical design for the deep-UV Shack Hartmann metrology tool is shown in Figure 2. The layout is similar to a Keplerian telescope design, where collimated input from the foil optic is demagnified to a collimated input to the wavefront sensor. This is accomplished using a large (200 mm diameter) off-axis parabolic mirror in conjunction with a relay lens. The magnification of the system and the advantage of this layout can be derived from the system matrix:

$$\begin{bmatrix} A & B \\ C & D \end{bmatrix} = \overbrace{\begin{bmatrix} 1 & 0 \\ L_2 & 1 \end{bmatrix}}^{\text{Propagation to } 2^{nd} \text{ lens from sensor}} \underbrace{\begin{bmatrix} 1 & -\frac{1}{f_2} \\ 0 & 1 \end{bmatrix}}_{\text{Refraction from } 2^{nd} \text{ lens}} \overbrace{\begin{bmatrix} 1 & 0 \\ f_1+f_2 & 1 \end{bmatrix}}^{\text{Propagation between lenses}} \underbrace{\begin{bmatrix} 1 & -\frac{1}{f_1} \\ 0 & 1 \end{bmatrix}}_{\text{Refraction from } 1^{st} \text{ lens}} \overbrace{\begin{bmatrix} 1 & 0 \\ L_1 & 1 \end{bmatrix}}^{\text{Propagation to } 1^{st} \text{ lens from foil}} = \begin{bmatrix} \frac{1}{M} & 0 \\ 0 & M \end{bmatrix} \quad (1)$$

where the 1^{st} lens is replaced by a parabolic mirror and the 2^{nd} is the relay lens. Choosing $L_1 = f_1 = 755.5$ mm and $L_2 = f_2 = 75.0$ mm, the system magnification M, given by matrix element D, reduces to

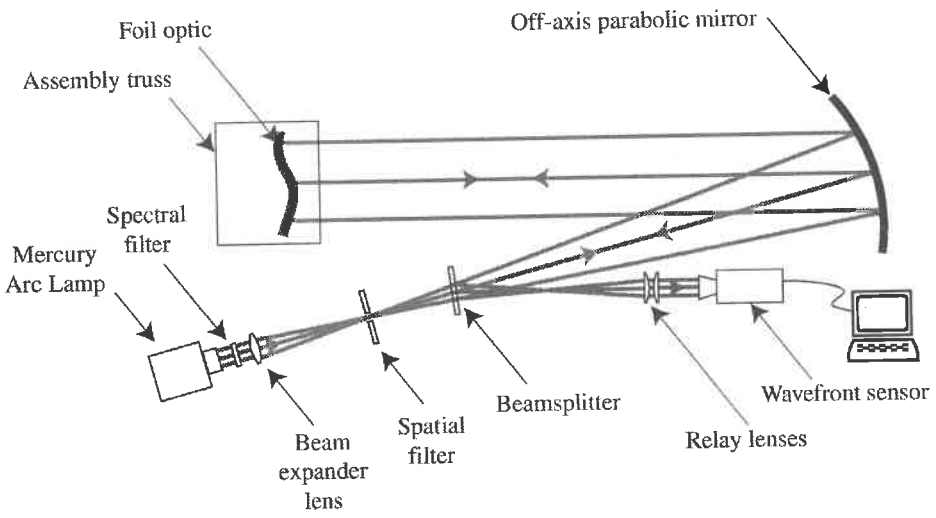

Figure 2: Shack-Hartmann metrology tool.

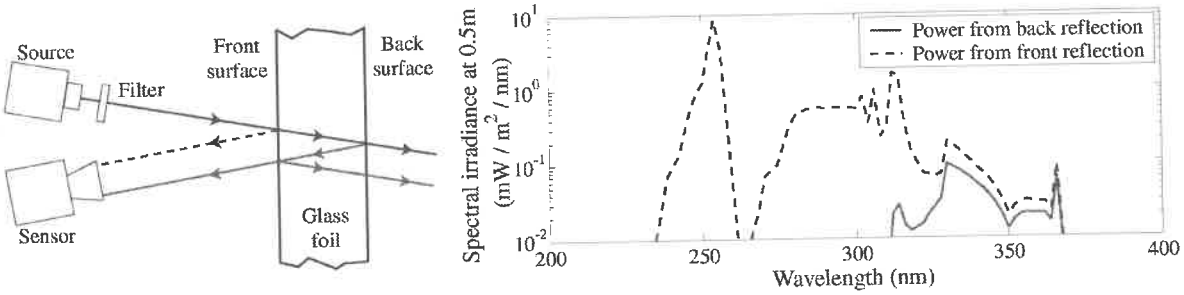

Figure 3: Irradiance from the glass sheets into wavefront sensor as a function of wavelength.

$-\frac{f_2}{f_1} = 0.1$. The system has no effective optical power as indicated by the B element. Element C shows that effective propagation distance is zero—the effects of diffraction are minimized at the image plane. The system matrix is diagonal, revealing that position and tilt are decoupled.

Deep-UV light is the most novel characteristic of the system. A 200 Watt broadband mercury arc lamp is spectrally filtered to allow mostly sub-visible wavelengths. Deep-UV light is exclusively required due to the optical transmission properties of the borosilicate glass foils (Schott, model D-263) proposed for the Constellation-X telescope optics. Light incident on the glass foil at wavelengths greater than 300 nm will partially transmit through the substrate and reflect off of its back surface. This will result in a doubled set of data on the wavefront sensor which will corrupt the wavefront reconstruction. The non-ideal spectral filter on the arc lamp does permit some longer wavelength radiation to reflect off of the foil optic, as shown in Figure 3. The theoretically computed irradiances take into consideration the spectral output of the arc lamp, the transmission curve of the spectral filter, and the optical properties of the glass to be tested. The ratio of the power into the camera from the front reflection to the back, calculated from the respective areas under the curves, is approximately 34.3. This back reflection power is below the sensor noise floor, making the error signal negligible. For comparison, if a higher wavelength HeNe laser were used for illumination, the ratio of the power from the front to back reflection would be 1.3. This would make the wavefront reconstruction erroneous.

A Shack-Hartmann [8] wavefront sensor (Wavefront Sciences, model CLAS-2D SMD) is used to image the optic under test. A key feature of this instrument is the lenslet array which dissects the incoming wavefront into 64×64 segments. Each of these segments is focused onto a detector located at the lenslet focal plane.

single slot repeatability test	displacement error, one σ (μm)			
	silicon wafer		fused silica plate	
	pitch	yaw	pitch	yaw
fixed lid and combs	0.26	0.39	0.59	0.23
dynamic lid, fixed combs	0.83	0.93	0.47	0.40
dynamic lid and combs	0.34	0.36	0.33	0.30

Table 1: Assembly truss slot alignment repeatability results.

The engineering tradeoffs with the performance of this instrument have been studied by Greivenkamp et al [4]. By comparing the focal spot locations on the detector with a reference surface to those from an aberrated surface, a difference map is calculated. Spatially integrating the slopes of this map allows the wavefront shape to be reconstructed. The instrument's sensitivity hinges on its ability to accurately centroid the focal spots. To do this, the focal spot should cover at least 10 pixels. The angular range of measurement involves the detector area allocated to each lenslet (area of interest or AOI). When the focal spot behind a lenslet appears near the edge of its AOI, crosstalk occurs and wavefront reconstruction is compromised, thereby limiting the angular range. The angular range for this camera can be estimated from the lenslet diameter of 0.224 mm and operating focal length of 17.904 mm to be approximately ± 6 mrad. The focal spot radius further reduces this range to ± 5.1 mrad. The sensitivity, a function of the pixel size, centroid estimation error, and focal length, can be calculated to be around ± 1 μrad. Over a 10 mm lateral distance in the magnified object plane, this corresponds to a theoretically measurable P-V height of ± 5 μm with a resolution of ± 1 nm. Previous surface mapping of stock silicon wafers indicate spatial distortion of this frequency and magnitude, so this instrument will be able to track subsequent flatness improvements from the original stock material.

3 Procedure and results

3.1 Assembly Truss

Numerous tests have been performed on the assembly truss to determine its ability to meet repeatability foil alignment goals of 1 μm. An autocollimator (Newport, model LAE500H) was used to measured the angular error of a foil located in a "slot," which was then converted to displacements. Previous experiments performed on a static breadboard test assembly system have demonstrated a 1 σ mounting slot repeatability error of about 0.11 μm in both axes [3]. This previous research defined repeatability as the standard deviation of a set of measurement collected by successively measuring, lifting, and replacing an optic foil against the reference microcomb teeth. This test was repeated with the new design and the data shows less than 0.05 μm for both pitch and yaw.

The current research involves a dynamic assembly truss, which strives to mimic the actual telescope foil alignment procedures. A static test was performed to obtain a baseline for repeatability. In this test, an optic foil was inserted into a slot, measured, then completely removed from the truss, reinserted, and remeasured. All mechanical parts on the truss were static. To test dynamic slot repeatability, two tests were performed. In the first test, the truss lid was removed and replaced as would be required for actual flight module assembly. The combs were not moved relative to the lid or base. The second dynamic test, which comes closest to actual flight module assembly, includes microcomb actuation to the planar reference flat in addition to lid reinstallation. These tests were conducted with both a 0.4 mm thick silicon wafer and a 3 mm thick fused silica plate coated with a reflective aluminum surface. Both materials were studied to understand the repercussions of thin foil deformation. Results from these tests are summarized in Table 1.

The results from the static test indicate that the repeatability of fully replacing an optic foil on the microcombs is approximately 0.3 μm in both axes. The second test includes the lid kinematic coupling repeatability error in addition. The final test effectively cancels out the kinematic coupling error by actuating the combs to the reference flat. Hence, in the final test, the optic foil placement repeatability appears to

dominate. Comparing the difference in results for the different foil thicknesses, thin foil deformation does not appear to be a significant contributor to the overall error.

3.2 Shack-Hartmann surface metrology tool

The surface metrology instrument has been successfully used to generate surface maps of large $\frac{\lambda}{30}$ reference flats, 0.45×100 mm diameter polished silicon wafers as commonly used in semiconductor industry, and 100×140×0.4 mm glass sheets. A sample image is shown in Figure 4.

The repeatability of the measurements has been primarily limited by random variations in the arc lamp caused by arc migration on the electrodes and convection currents inside the lamp [7]. Averaging 100 successive images has mitigated the effects of these variations, reducing the range of P-V surface maps to 5.0 nm (0.5 nm root-mean-squared (RMS)) over a minimum 100 mm diameter object size while the setup is unchanged. To determine the repeatability of the instrument for a human-in-the-loop environment, specimens were measured, physically removed from the metrology station, replaced and remeasured. Both the reference surface and the silicon wafer specimens were studied; results were similar. Repeatability measurements ranged 35.6 nm P-V with a 13.2 nm standard deviation. RMS surface variations ranged 14.0 nm with a 5.1 nm standard deviation.

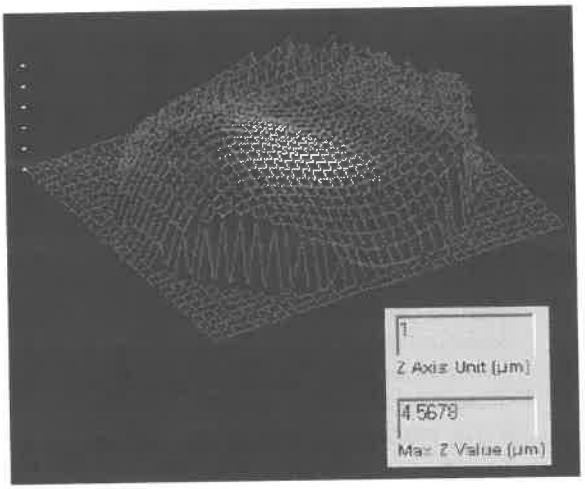

Figure 4: Reconstructed wavefront equivalent to a surface map at the object plane.

The accuracy of the system is difficult to quantify since aberrations in the lenses will contribute different angular errors to measurements at different spatial locations. To roughly estimate the overall accuracy of the system, two flats with factory-provided interferograms were measured. These interferograms reveal non-flatnesses of 2.6 nm RMS and 4.9 nm RMS, respectively. Comparing the two flats with the Shack-Hartmann system shows an average RMS surface difference of 17.6 nm. Overlapping the interferograms, the RMS deviation can be estimated to be $\sqrt{2.6^2 + 4.9^2} = 5.5$ nm. The difference between the Shack-Hartmann and interferometric data provides a crude estimation of the accuracy of the tool. Assuming root-sum-squared (RSS) stacking of errors, a conservative estimate of the accuracy yields $\sqrt{17.6^2 - 5.5^2} = 16.7$ nm RMS. Many factors contribute to the difference between the interferograms and Shack-Hartmann measurements. The mirrors are subjected to different temperatures and mounting forces between the instruments. Additionally, the uncertainty in the interferometric measurements is estimated to be $\frac{\lambda}{50}$ P-V.

In operation, the user will make a reference image with a flat, then substitute the optic under test. Based on the above analysis, the test measurement will be accurate to ~17 nm and repeatable to ~5 nm, RMS.

Results from glass metrology show no indication of back reflections in the raw data. The array of focal spots is regular and the frequency of spots is as expected, one per AOI. Large warp in pre-figured stock glass sheets makes their entire surface unmeasurable. A sample of this raw data is shown in Figure 5. Subset regions of the figure have been successfully measured to the accuracy and repeatability previously described.

4 Conclusions

Using a precision assembly truss, slot repeatability has been studied in an environment which closely matches that of the actual telescope optics assembly. This work has demonstrated that the assembly technology can meet the 1 μm Constellation-X foil placement repeatability requirement. Future work will include study of the accuracy of the microcombs.

A Shack-Hartmann surface metrology tool has been developed that permits metrological feedback of optic foils under consideration for the Constellation-X mission. This feedback is crucial during the assembly procedure since gravity, friction, and other forces can distort the wafers beyond the assembly tolerance.

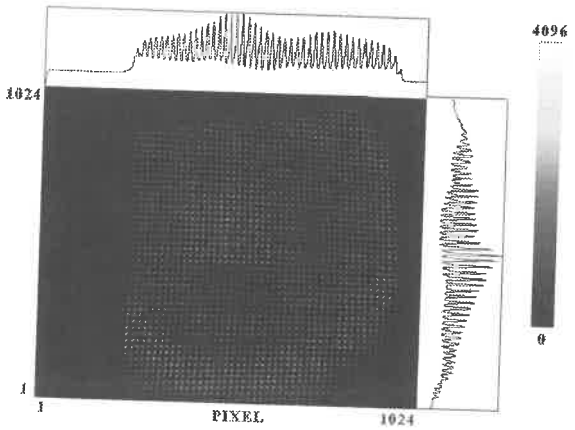

Figure 5: Raw data onto wavefront sensor from Schott D-263 glass sheet.

This instrument can be used to determine if a surface is meeting the current 500 nm global flatness manufacturing requirement. The surface mapping data is accurate to ~17 nm and repeatable to ~5 nm, RMS. Non-flat figures can also be studied up to a dynamic range of ± 250 μrad at the object plane. The 200 mm diameter viewing range can accommodate the proposed 140×100 mm^2 foil optic surface area.

5 Acknowledgments

We gratefully acknowledge the support of the students, staff, and facilities from the Space Nanotechnology Laboratory. This work is supported by NASA Grants NAG5-5271 and NCC5-633.

References

[1] C. G. Chen, R. K. Heilmann, P. T. Konkola, O. Mongrard, G. P. Monnelly, and M. L. Schattenburg. Microcomb design and fabrication for high accuracy optical assembly. *J. Vac. Sci. Technol. B*, 18:3272–3276, 2000.

[2] M. L. Culpepper, A. H. Slocum, and F. Z. Shaikh. Compliant kinematic couplings for use in manufacturing and assembly. In *International Mechanical Engineering Congress and Exposition*, Anaheim, CA, November 1998.

[3] Olivier Mongrard et al. High precision assembly and metrology of x-ray foil optics. In *Proc. Sixteenth Annual ASPE*, Crystal City, Virginia, November 2001.

[4] John E. Greivenkamp, Daniel G. Smith, Robert O. Gappinger, and Gregory A Williby. Optical testing using shack-hartmann wavefront sensors. In *Proc. SPIE*, number 4416, pages 260–263, Boston, 2001.

[5] Olivier Mongrard. High accuracy foil optics for x-ray astronomy. Master's project, Massachusetss Institute of Technology, Department of Aeronautics and Astronautics, September 2001.

[6] Yoichi Muranaka, Makato Inaba, Takeo Asano, and Eiichi Furukawa. Parasitic rotations in parallel spring movements. *Int. J. Japan Society of Precision Engineering*, 25(3), 1991.

[7] Oriel Instruments, http://www.oriel.com. *The Book of Photon Tools*, 2001.

[8] Ben C. Platt and Roland Shack. History and principles of shack-hartmann wavefront sensing. *Journal of Refractive Surgery*, 17:573–577, 2001.

DEVELOPMENT OF THIN FILM ACTUATOR USING ELECTROSTRICTIVE PHENOMENA

[a]Youngdae Jung, [b]Eunsoo Jeong, [a]Haedo Jeong, [c]Hansoo Park, [c]Namju Jo

[a]Department of Precision Mechanical Engineering, Pusan National University, Pusan, Korea

[b]MEMS Center, Pusan National University, Pusan, Korea

[c]Department of Polymer Science & Engineering, Pusan National University, Pusan, Korea

ABSTRACT

Micro-actuator have been developed using poly-urethane (PU) with electro-strictive phenomena and RTV silicon rubber. For the purpose of applying to micro-actuator, thermal properties and displacement of electro-strictive PU elastomers and RTV silicon rubber have been measured. If the PU film became thicker, higher driving voltage was required for the displacement. In this study, we classified actuator's characteristics into two factors, driving force and displacement and select a film thickness as a key parameter which affects driving force and input voltage of electro-strictive micro-actuators. We also evaluated electro-strictive effects according to thickness of thin film actuators such as membrane or uni-morph type actuator.

To spread PU and RTV rubber which both have high viscosity, content of solvent and cross-linking agent were controlled. Spin coater made polymer film thin and uniform. From the experiment, we could get better performance of displacement, lower input voltage and observe a driving force variation. So we finally optimized the film thickness depending on its desired requirements

Key Words: Poly-urethane(PU), Electrostriction, Micro-actuator, Real-Time Vulcanizing(RTV), Maximum Displacement, Recovery time, Median Filter, Artificial Muscle, Spin coating

1. Introduction

Advanced MEMS technologies has realized miniaturization, high-performance and multi-functional micro actuator to satisfy needs of various fields, especially HDD, DMD(Digital mirror device), AFM, DNA chip, artificial muscle. Micro actuator can be driven by piezo-electricity, pyro-electricity, electrostriction, and so on. Fig 1 shows comparison between strain and actuation pressure/density of various materials. [1]

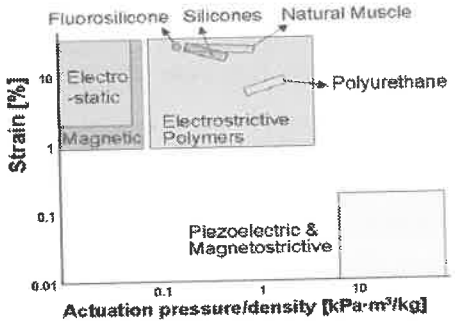

Fig 1. Comparison of high-speed actuator technology

Recently, new synthetic method and industrial needs lead to the development of functional polymer with piezo-electricity, pyro-electricity and etc. Generally, Lead Zirconate(PZT) and Barium Titanate($BaTiO_3$) are known as typical piezo-electric inorganic materials. As for the organic materials, polyvinylidene fluoride (PVDF or PVF2:β-

phase) and vinylidene fluoride copolymer can be also used as piezoelectric materials. Also, it is confirmed that PU has both piezo-electricity and electrostriction by the electrostatic interactions among molecules. [2][3]

Both PU and Silicon rubber have electro-strictive characteristic and these material are positively researched in polymer electrolyte, insulation film, body-friendly polymer for high displacement under high voltage and also show a merits, that is high-speed response & easiness of forming & flexibility and low price. We developed membrane and uni-morph type actuator using flexible electrode. [4]

2. Theoretical Background

2.1 Principle of Electrostriction

During last 10 years, Electro-active polymer (EAP) for artificial muscle, micro-actuator, robot etc have been widely researched. By classification of EAP, ionic gel, ionomeric polymer-metal composite (IPMC), conductive polymers, nano-tubes, electro-strictive polymer (dielectric EAP), ferroelectric (piezoelectric, ferroelectric) polymer, graft elastomer, PU is one of electro-strictive polymer and has high actuation density under high voltage. [5][6]

Electrostriction can be observed in PU and silicon rubber, is a phenomenon, occurrence of strain or stress under electric field. Fig 2 shows electrostriction between two electrodes in this paper.

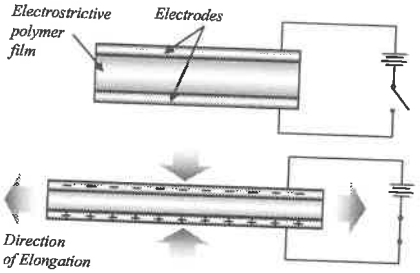

Fig. 2 Operation principle of polyurethane

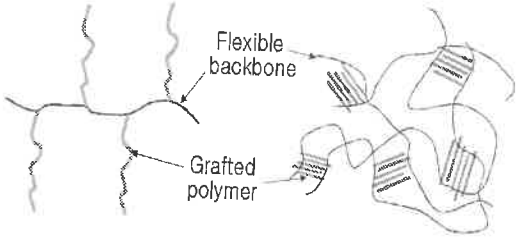

(a) Structure **(b) Morphology**

Fig. 3 Grafted elastomer

PU, electro-strictive material was synthesized by conventional prepolymer method. Generally, PU is composed of iso-cyanates, chain extender and polyols. Morphologically, PU is divided into hard segment by di-isocyanate, chain extender and soft segment by polyols. Iso-cyanates are made from 4,4'-diphenlymethanedissocyanate(MDI), and chain extenders can be made from 1,4'butanediol and so on. Polyols are formed from poly-tetramethelene adipatediol (PTAd) and polycarbonate diol (PCD). For the purpose of understanding the effect of hard segment, diisocyanate and chain extender are controlled. And in order to reduce a viscosity, content of the solvent as dimethyl acetamide (DMAc) was controlled.

PU is classified as a grafted elastomer but as a result of precedent research [7], it has both electro-striction and piezo-electricity despite of crystallization of grafted polymer. [8][9]

2.2 The Purpose of this Paper

At first, this paper describes dynamic characteristics, maximum displacement and recovery time according to contents of component and film thickness and shows a membrane type and unimorph type actuators using PU. In order to improve an actuator's performance, thin film actuator is manufactured using spin coater. For this, PU prepolymer needs more amount of solvents because of its low viscosity

3. Experiment and Measurement

3.1 PU Film Manufacturing

In this paper, PU film is cast by 60mm diameter teflon mold. Fig. 4 shows film process, mold, acrylic holder and final produced PU elastomer.

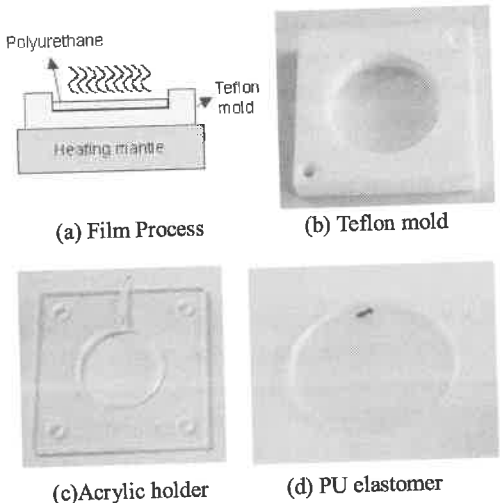

(a) Film Process (b) Teflon mold

(c)Acrylic holder (d) PU elastomer

Fig.4 Film process and component of measurement system

Sample	PU weight (㎖)	Thickness (㎜)	Sym-bol
PTMG - crosslinking agent (0.5wt%)	5	0.418	11-5
	9	0.760	11-9
	13	1.119	11-13
PTMG	5	0.503	12-5
	9	0.859	12-9
	13	1.147	12-13
PTMG - NaOH	5	0.392	13-5
	9	0.694	13-9
	13	0.943	13-13
PTMG - crosslinking agent (1wt%)	5	0.615	14-5
	9	0.835	14-9
	13	1.234	14-13

Table 1 Casting weight, thickness and symbol of samples

3.2 Measurement System

In order to trace a movement of PU actuator, Non contact measurement as laser sensor, OMRON Z4M-S40R was used. Z4M-S40R is semiconductor type sensor and measurement parameter is 40±10mm as maximum displacement and 60ms as sampling time and 3μm as resolution. In order to reduce a noise, vibration was isolated.

Acrylic holder was used for whole constraint except electrode coated surface and in order to prevent from leakage of high voltage, Poly-ethylene (PE) plate is used under the acrylic holder. As a standard electrode, we used CircuitWorks^{R} silver grease and Fig 5 shows configuration of displacement measurement system for membrane type micro-actuators

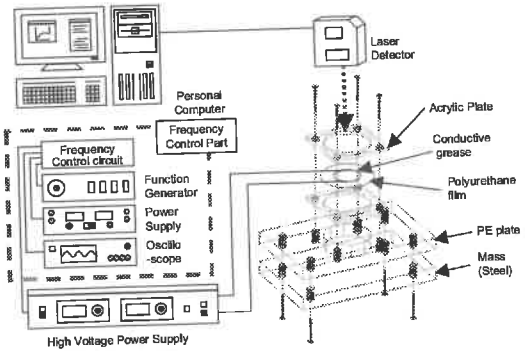

Fig. 5 Displacement measurement system

4. Result

Hydrophilic characteristics can make physical properties of PU film changed well. Naturally, measurement may include a couple of noises, resulting from the physical property change or accuracy of sensor itself. So displacement was filtered two times through median filters for noise reduction

Fig 6 shows a displacement according to samples and thickness. Maximum displacement is 698.1 ㎛ at 14-5 films as best result. The thicker a film became, the higher the driving voltage was required. 13-5 film could be measured by insulation failure because of an effect of NaOH under 4KV. Recovery time of 13 films was taken about

twice as long as those of 11 films.

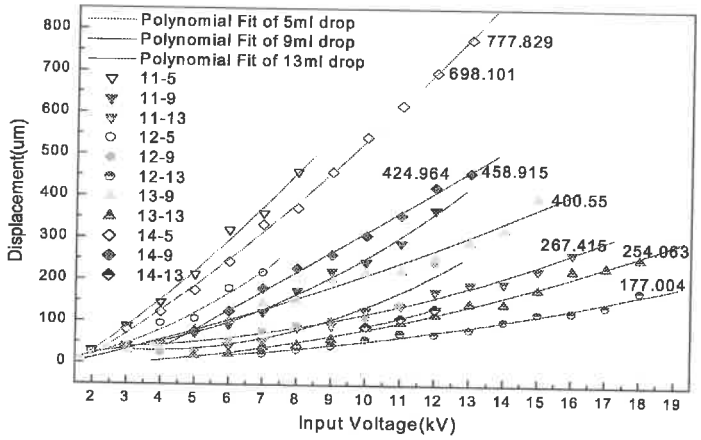

Fig. 6 Displacement of various type of PU and thickness

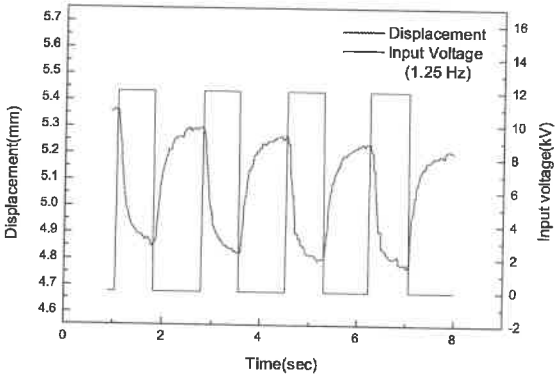

Fig. 7 Response to step function with 12kV

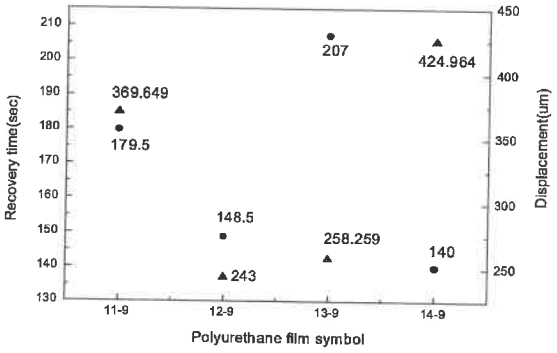

Fig. 8 Recovery time and displacement of 9ml of each sample.

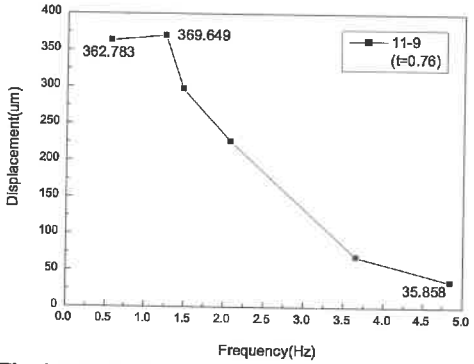

Fig. 9 Results of according to frequency with 12kV

Fig. 7 shows frequency response to step function with 12KV, 1.25Hz. PU films almost recovered its length within tens of seconds but the rest recover slowly. Consequently, errors due to repetition were increased gradually during input voltage is loaded. These caused by visco-elastic behavior, may result badly in position control and can be overcome by increasing the hard segment content of PU film and making it more plastic.

Displacement and recovery time of 11-9, 12-9, 13-9, 14-9 films at 12KV in 3 seconds is shown as Fig 8.

Recovery time of 14-9 films with 1% cross-linking agent was decreased about 39.5 seconds and displacement of 14-9 is increased about 55 ㎛ when 11-9 films with 0.5wt% is used. In case of 13-9 film with Na^+, only recovery time was increased because elasticity of films was decreased by Na^+ compared with 12-9 film without cross-linking agent

Fig 9 shows maximum displacement according to frequency with 12KV. Displacement was decreased suddenly above 1.25Hz. This can be caused by natural frequency according to volume or density of film. To improve performance, thin film process is required.

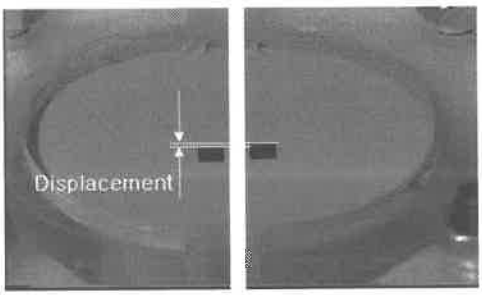

Fig. 10 Displacement of 11-9 with black point

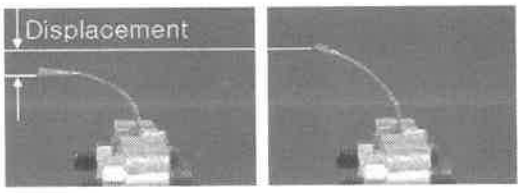

Fig. 11 Displacement of uni-morph 11-9 sample

Fig.10 shows displacement of 11-9 with black point. In case of loading force, recovery time increase about 15 seconds. Fig.11 shows displacement of uni-morph type 11-9 film. Al is used as upper electrode and conductive grease is used as lower electrode and its displacement is about 14mm.

For better performance to input voltage, PU film was manufactured by spin coater about 200μm thickness. Fig. 12 shows a appearance of spinner used in this paper and Table 2 is experiment conditions and results are as follows.

Fig.12 Spinner (5 step)

Sample	*PTMG cross-linking agent (1wt%) 180㎛*
Displacement	*376㎛ at 3KV load*
Spin Speed	*300RPM in 10sec, 1000RPM in 30sec*
Viscosity	*2300 CPS (Brookfield Viscometer)*
Mold Base	*Silicon Wafer (6")*
Solvent Content	*15% PU :85% DMAc(solvent)*

Table 2 PU film manufacturing condition using spinner

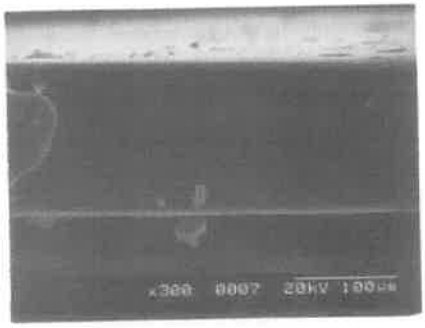

Fig 13 SEM Photograph of cross-sectional view of PU film

5. Conclusion

In this paper, thin film type micro-actuator using electro-strictive phenomena of PU was developed and its mechanical property was measured and evaluated. maximum displacement of PU films is 698.1 ㎛ when 13KV was loaded at 14-5 films. It means that an amount of cross-linking agent affected maximum displacement and thickness of film affected input driving voltage. On the other hand, Na^+ ion affected elasticity of film so maximum displacement was decreased as a result.

And thin film actuator was manufactured by spin coater about 200 microns thickness so we could acknowledge the possibility of practical use when under 100 micron thickness PU film is made.

Polymer actuator using PU has some demerits to recovery time, high input voltage, flexible electrode. But in next several years, this can be overcome. So it is positively possible to apply it to micro-pump, ink jet pump, artificial muscle, artificial blood vessel and so on.

Reference

1 Ron Pelrine, Roy Kornbluh, Jose Joseph, and Seiki Chiba, "*Electrostriction of polymer films for micro-actuator*" IEEE 97, pp. 238 - 243 (1997)

2 T. Ueda, et. al., "*Polyurethane Elastomer Actuator*", Synthetic Metals 85, 1997, pp. 1415~1416

3 J. Kyokane, Research et.al., "*Electro-Striction Effect of Polyurthane Elastomer(PUE) and Its Application to Actuator*", Synthetic Metals 103, 1999, pp. 2366~2367

4 J. Park, K. Park, Y. Bae, "*PDMS-based polyurethane with MPEG grafts: synthesis, characterization and platelet adhesion study*", Biomaterials, Vol 20, pp 943-953, 2000

5 R. Heydt, R. Kornbluh, R. Pelrine, V. Mason, "*Design and performance of an electrostrictive-polymer-film acoustic actuator*", Journal of Sound and Vibration, pp 297 – 311, 1998

6 Q.M.Zhang, J.Su, Chy Hyung Kim, "*An experimental investigation of electromechanical responses in a polyurethane elastomer*", Journal of Applied Physics. Vol 81, pp 2770 – 2776, 1997

7 Eun-soo Jeong, Han-soo Park, Hae-Do Jeong, Nam-Ju Jo, "*Development of electrostrictive polyurethane(PU) films and its characterization*", 10th ICPE , pp 406 – 410 (2001)

8 Yoseph Bar Cohen, "*Electroactive Polymer Actuators as Artificial Muscle*", SPIE Press, 2001

9 Mchran Mojarrad, Mohsen Shahinpoor, "*Biomimetic Robotic Propulsion using polymeric artificial muscles*", International conference on Robotics & Automation, pp. 2152 - 2157, 1997.

Mesoscale Piezo-Motors: Scaling Issues and Performance Measurement

J T Leinvuo, S A Wilson, R W Whatmore and A E Gee,
School of Industrial and Manufacturing Science Cranfield University Cranfield, UK MK43 0AL

Keywords: Piezoelectrics, piezo-motors, steppers, measurement, fine-mechanisms.

Abstract
A novel (~10mm track diameter) piezoelectric/leg motor employed vibrating/standing wave indexing principles to generate arcuate step-motions of the order of 1μm. Measurements were needed for step-actions, speed, acceleration and torque of the order of 500rev/min, 100rad/s^2 and 0.001Nm (1Nmm) respectively. This placed the work in an interesting scale range where large-scale mechanisms might be scaled down but few demonstrations of this were available.

Motor
The standing wave type piezomotor shown in figure 1 converts contour vibrations of a piezoelectric plate to vertical oscillations of the principal response mode of a beryllium-copper disc 'cymbal' analogously to the musical instrument [1,2]. An elastic-fin rotor converts this to rotary actuation, via three inclined spring legs, the whole having been micromachined from beryllium-copper. The tip of each fin is held in contact with the cymbal surface via a vertical bias force. The fins act as levers and the rotor is propelled about its axis of rotation by the horizontal component of the reactive force. When the vibrating cymbal moves downwards the tips of the fins slip across its surface and the cycle progresses. The fin exhibits Lissajou-type motion components when engaging with the cymbal. Because of the leg-inclination, the motion and friction have greatest effect when the leg slope is 'leading' with higher contact force reduced contact when trailing with lower contact force on the return part of the cycle. Speed and torque are adjusted by varying the frequency and amplitude of the (single-phase) sinusoidal supply voltage. In operation the vertical displacement of the cymbal is proportional to the lateral displacement of the PZT plate. The motor design assumes that the fins act as rigid struts [1,3].

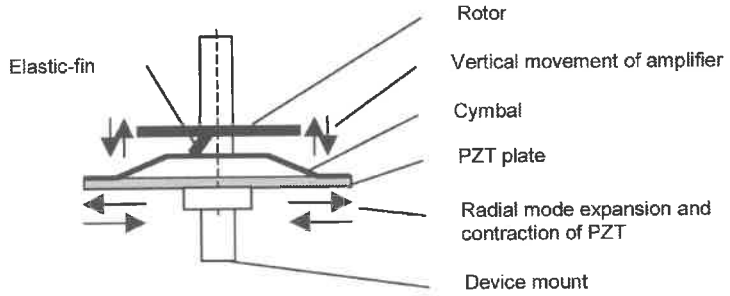

Figure 1. Side profile of pzt-flexural motor.

Speed and torque characterization stage
The stage employs force through two spring-strip flexures/sensors shown in figure 2. One (Type LCL-816G [4]) is used to measure the frictional force between rotor and stator. Another (LCL-113G) is used to measure torque in the motor. Since the measured voltages are relatively small (~20 mV) compared with actuation voltages (50 V_{rms}) noise protection for signals was provided. In order to increase signal to noise level signals were amplified 24 times with CM015 signal conditioning modules with signal conditioning adapter CM001 [5].

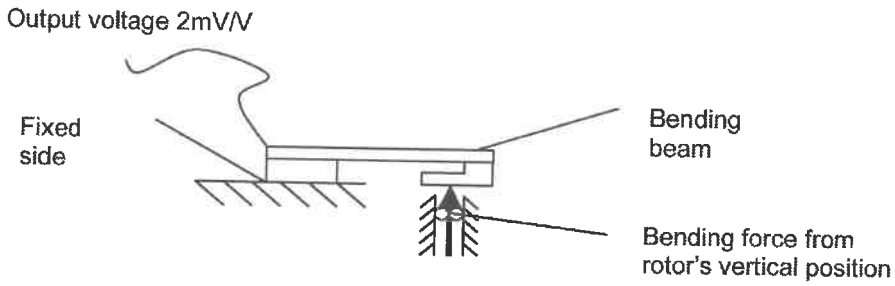

Figure 2. Structure of force and torque sensing element.

For torque measurements, a capstan pulley brake technique was employed. In this method the load is measured from sliding nylon monofilament line wound once around the rotor with one end attached to a known weight. Alternatively, two flexure force generator-cum-sensors could be used as shown in figure 3 with force sensed by strain-gauges and a bridge. When the rotation commences against the additional frictional force (F_μ), this adds tension to one side of the line and reduces it at the other. Continuous operation requires that line frictional force is in proportion to pulley (bearing) surface length with kinetic friction coefficient (μ_k). Holding torque is determined from the static frictional coefficient (μ_s).

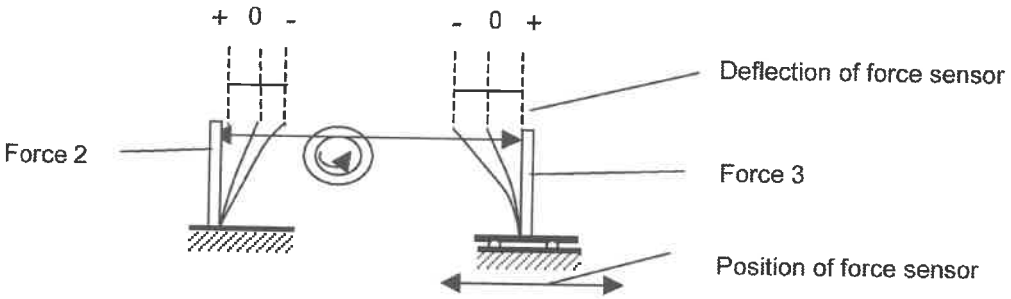

Figure 3. Capstan brake torque measurement using two flexure force sensors.

Speed measurement was made by counting pulses from a fibre optic probe mounted on the test stage, which sensed an angular encoder on the shaft. The sensor (FU-20, FS-V11P [6]) can detect targets as small as 0.01 mm. Achieved pulses (20 pulse /round) were converted to rotational speed information after capture using the high-speed counter of the I/O card (PCI-6023E [7]).

The motor drive was from the signal generator integrated with the PC (PCI-5401 [7]). Since the output signal of the card is ± 5 V there was a need to amplify the signal current and voltage to be suitable for the motor. For this purpose an APEX high power operational amplifier module (PA-90) was used specially designed for driving piezoelectric loads with adequate bandwidth and voltage ranges (± 200 V, 200 mA, slew rate 300 V/μs [8]).

In order to measure the electrical energy supplied to the motor, it was necessary to measure current, voltage and phase difference. Voltage was measured using a voltage divider since the input voltage range of the PC integrated digital scope (PCI-5102 [7]) employed was ± 50V. When calculating motor power it was important to apply power factor compensation in respect of the phase difference between voltage and current (cosΦ) to take account of capacitive and inductive load components. In addition losses caused by resistance in the high voltage circuit were taken into an account. The power factor was calculated from current and phase difference between input current and voltage signal. The phase difference was measured with reference to he unloaded amplifier set up for the same voltage and frequency as for the speed/torque measurements.

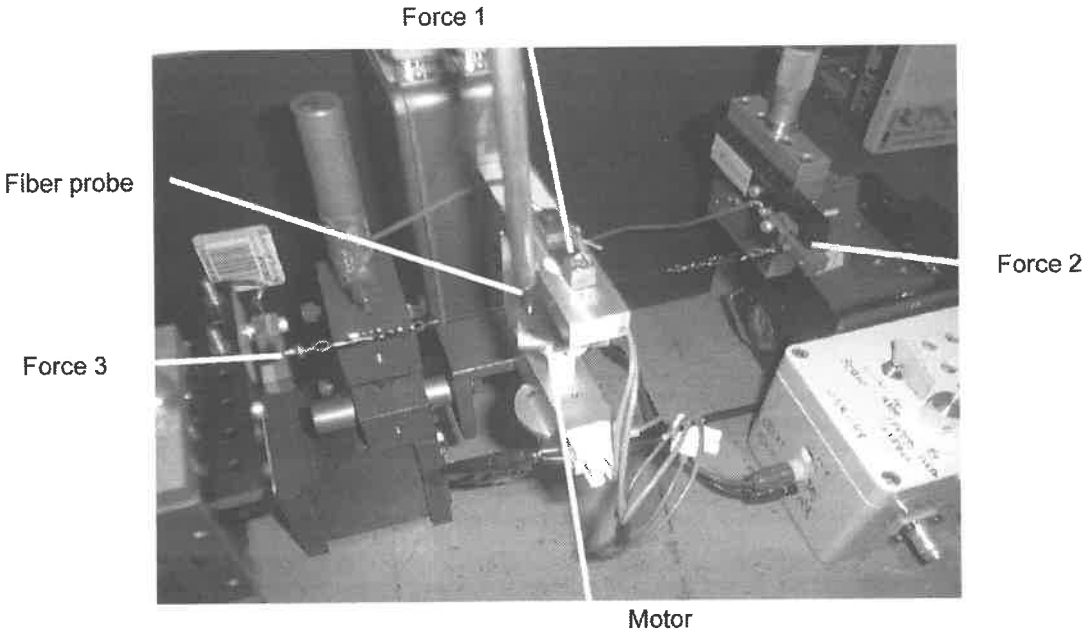

Figure 4. The photo of the speed torque characterization layout.

Test procedure and results

Referring to Figures 3 and 4, the test motor was mounted between an axial force sensor (force 1) and a micrometer screw slideway. With polymer monofilament line Ø 0.16 mm wound around the outer radius of bearing the axial force (frictional force) was adjusted to the desired level and the force 3 sensor adjusted to zero position with the precision micrometer to take up slack in the line. Another force sensor (force 2) was mounted also to a micrometer slide held stationary while adjusting frictional force via force 3.

Zero values of the sensor-readings were recorded in order to compensate possible offsets in measurements. The motor was driven from PC using specific user interface for the signal generator. The measurement data was collected with a Labview written program. Speed, current, voltage and force sensors were all monitored simultaneously on the screen.

The test was carried out adjusting the force 2 flexure settings until no rotation was detected, indicating stall torque. Columns in the recorded text file present measured data in a 10s time period [speed (rpm), Force 1 (V), Force 2 (V), Force 3 (V), Frequency (Voltage probe)(kHz) Frequency (Current probe) (kHz), Voltage (V_{rms}) and Current (V_{rms})]. Once all data were collected to the text file it was converted, filtered and responses plotted using MATLAB. The force, voltage and current measurements were filtered using averaging. The result of speed measurement was filtered using media. The test stage allowed relatively easy evaluation of motor speed torque behaviour with different axial load conditions as has been demonstrated [1].

Figure 5 presents the graph achieved from the hard PZT (Morgan Electroceramics™, PC-4 material), 25X25X2 mm motor with $\cos(\Phi)=0.4$, U_{in}= 50 V_{rms}, I_{in}=47 mA_{rms}, f=66 kHz and force 1= 740 mN. The graph indicates that maximum speed is achieved in no load conditions (450 rpm) and stall torque in zero speed (~0.47 Nmm).

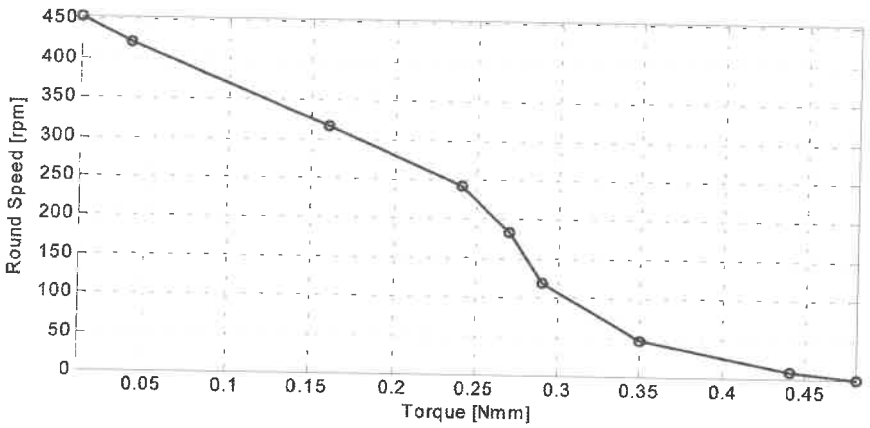

Figure 5. Speed torque characteristics of piezoelectric motor.

Figure 6 presents achieved data of power output/input and efficiency. It can be seen that power output reaches its saturation point at 250 rpm i.e. about half maximum speed. This same trend was achieved with other tested combinations. The variation in power input values is practically stable with 8 mW variation shown, only 1% of the mean values. The last graph describes the obtained efficiency of power input and output which is calculated using following equation (1):

$$\mu = \frac{P_{out}}{P_{in}} = \frac{T_m \omega_r}{U_{in} I_{in} \cos(\phi)} \qquad (1)$$

where T_m is the torque of the motor and ω_r the angular velocity. U_{in} and I_{in} are RMS voltage and current supplied to motor. CosΦ is power factor where Φ is the phase difference between the voltage and current signals.

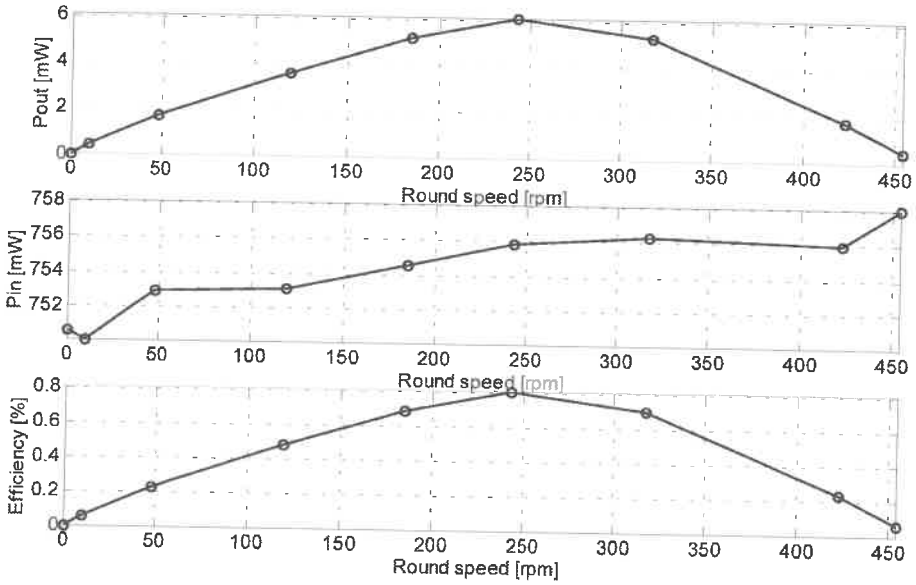

Figure 6. Power output/input and efficiency characteristics of piezoelectric motor.

Conclusions

This paper describes a successful demonstration of the capstan pulley brake torque measurement principle and fibre-optic speed measurement at mesa-scale on piezoelectric flexure-motors to measure torque, speed and power efficiency. It is foreseen that considerable further reduction in scale may be possible.

Acknowledgements

The authors gratefully acknowledge the financial support of the Engineering and Physical Sciences Research Council (EPSRC) grant number GR/N 34017 and BAe Systems (Sowerby Research Centre).

References

[1] Leinvuo J.T., Wilson S. A., and Whatmore R.W. "Experimental analysis of a new type of flextensional ultrasonic piezoelectric motor," *8th International conference on new actuators, ACTUATOR 2002,* Bremen, Germany, proceedings pp. 489-492.

[2] Rayner P, Piezoelectric Ultrasonic Motors and Micromotors PhD Thesis, Cranfield University 2000

[3] Uchiki T., Nakazawa T., Nakamura K., Kurosawa M., and Ueha S. "Ultrasonic motor utilizing elastic fin rotor," *Ultrasonics Symposium, 1991. Proceedings., IEEE Conf,* Orlando, FL, pp. 929-931, 1991

[4] OMEGA Complete Pressure, Strain, and Force Measurement Handbook & Encyclopedia. Omega Engineering Inc., Stamford, CT, 2000

[5] PICO Technology Ltd, *Signal conditioning*, Web Page, http://www.picotech.com/sigcond.html. as at 28/07/2002

[6] 'Sensors Vision Systems & Measuring Instruments 2001-2002' catalogue, ref.no. G2001-UK-2-0700, Keyence (UK) Ltd, Milton Keynes, 2000

[7] 'The Measurement and Automation catalog' National Instruments, Austin, TX, 2001

[8] 'Power Integrated Circuits Data Book Volume 9' CD-ROM 2000. Apex Microtechnology Corp. Tucson, AZ, 2000

Precision microcomb design and fabrication for Constellation-X spectroscopy x-ray telescope segmented optic assembly

Yanxia Sun*, R. K. Heilmann, C. G. Chen, M. J. Spenko, C. R. Forest, and M. L.Schattenburg
Massachusetts Institute of Technology, Cambridge, MA 02139

Keywords: X-ray telescopes, x-ray optics, Constellation-X, Spectroscopy X-ray telescope, Wolter-I type, Segmented optic assembly, Abbé error, Precision silicon microcombs, MEMS, TMDRIE

I. INTRODUCTION

The Constellation-X mission is the next major NASA x-ray observatory [1], which expands on the capabilities of the current Chandra and XMM missions. For its Spectroscopy X-Ray telescope (SXT) to meet the mission requirement of 15 arcsec (HPD) resolution, thousands of segmented cylinder-like foil mirrors must all be aligned at grazing incidence to the focal plane to a tolerance in the neighborhood of 1 micrometer (μm). A typical optic resembles a 60 degree partial cylinder of 200 mm length, and a wall thickness of 440 μm [2]. Precision silicon microcombs [3] developed at MIT, have previously been used to assemble sub-millimeter-thick flat substrates to achieve submicron-level assembly repeatability and accuracy [4, 5]. Their design is modified here to hold cylindrical Wolter−I type optics for Constellation-X to improve the total assembly accuracy.

II. DESIGN OF MICROCOMBS

The focusing Wolter−I optic used in the SXT design consists of two subsequent 20 cm modules, each containing concentric shells of approximately conical segments, radially spaced a few millimeters apart, from an innermost radius of ~ 150 mm to an outermost radius of ~ 800 mm. Mirrors in the first module (P – module) follow a parabolic shape in the axial direction with slope angles on the order of 1 degree. Mirrors in the secondary module (H – module) have a hyperbolic shape and three times the slope angle of the optics in the P-module (Figure 1) [2].

Four different sets of precision silicon mircocombs are designed to align the mirrors within the telescope. The current comb generation is designed to allow assembly of P-type and H-type mirrors at five different radial positions (Figure 2), and each mirror's position is defined by ten microcombs, five combs on the top and five on the bottom. The reference combs are aligned to a high-precision reference cylinder via spacer, and mirrors are registered at comb's teeth.

The design for a set of microcombs includes two types of combs: Reference combs provide highly accurate single-point contacts against which mirrors are registered, and spring combs provide the mechanical actuation needed to properly position the mirrors (Figure 3). For the reference combs, if the foil-to-tooth's contact point's axial position is different from the comb-to-reference surface's

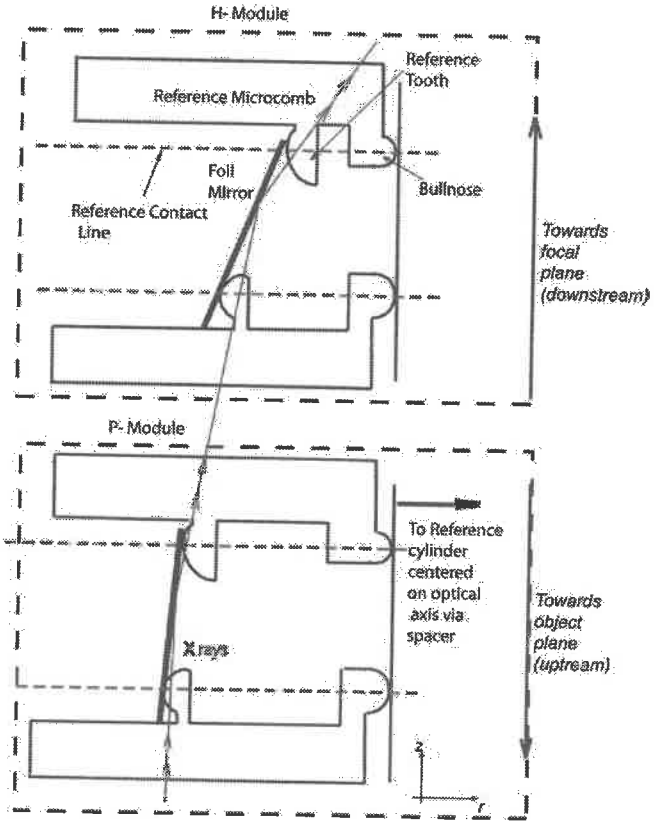

Figure 1: Schematic of mirror position in H and P modules for SXT design (not to scale). The optical axis, z, is an axis of cylindrical symmetry.

* email: yxsun@mit.edu

contact point, the contact offset, *d*, will introduce an extra sin error for assembly (Figure 4). The entire error budget shows that this Abbé error contributes 10 ~ 30% of total error budget. A new, raised-up nose-like feature (so-called bullnose) is added to reference combs to remove this misalignment pitch error source.

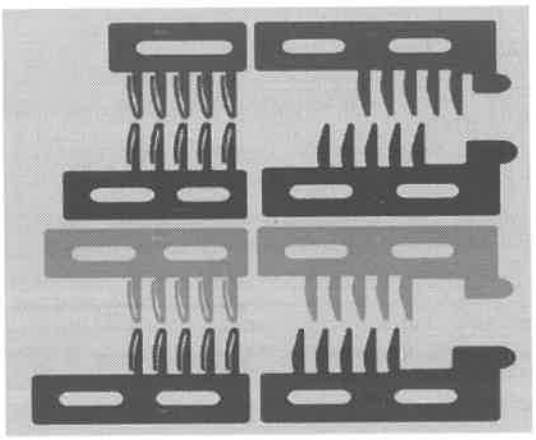

Figure 2: CAD drawing for four different sets of microcombs (Top two sets for H module, bottom two sets for P module).

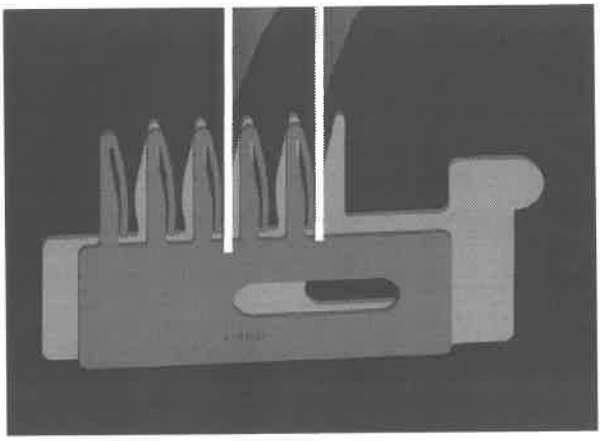

Figure 3: CAD model shows a close view of a set of microcombs holding cylindrical optic foils (only two foils shown).

The teeth are positioned radially to define the mirrors' radial distance to the spacer, *x*. The foil's slope angle, β, is defined by the radial positions of upper tooth and lower tooth which hold the foil together, as well as the foil's length. The teeth's shape is designed as a round curve to achieve point contact with foils. Since the axially parabolic or hyperbolic curvature of foil is much smaller than the curvature of mircocomb's tooth, the mirror can be approximated as a flat surface at the point of contact with the mircocomb's tooth. The reference tooth's radial positions are adjusted to accommodate the mirror slope angle requirement and align all the reference contact points in the same line. At the same time, the spring tooth shift axially also, such that the contact force from spring tooth, *F1*, and the force from reference tooth, *F2* appose each other, so that no rotational moment is applied to the foil (Figure 5).

If the combs are perfectly aligned with the reference cylinder, and if both reference cylinder and the mirror are perfectly shaped, the point-contact mechanism of microcombs defines every mirror's registering position and achieves better than half μm accuracy. The limit on the accuracy is then determined by the manufacturing tolerances for the microcombs.

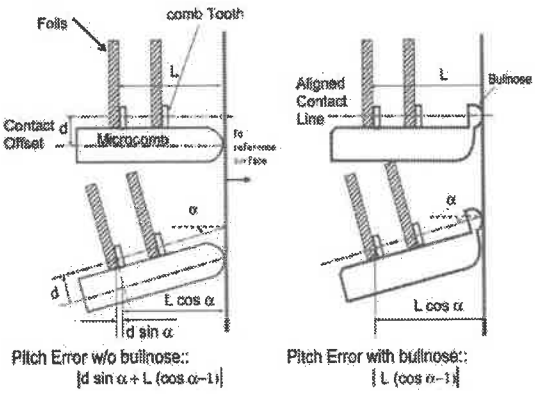

Figure 4: The bullnose feature reduces the assembly misalignment pitch error by $d * \sin\alpha$, where *d* is the previous contact offset, α is the misalignment pitch angle between comb and reference surface.

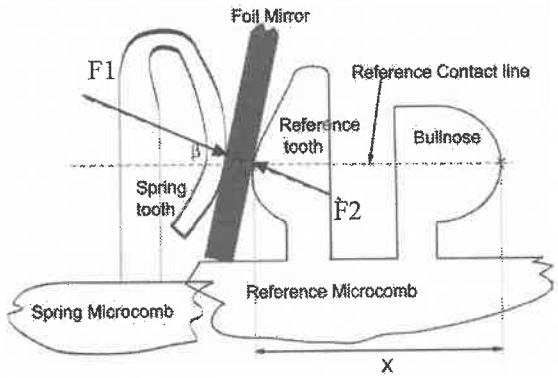

Figure 5: The contact force from spring tooth, *F1* is aligned to the force from reference tooth, *F2*, by spring tooth's position to avoid application of rotational moment on the foil mirror.

III. MEMS FABRICATION

Micro-combs are fabricated with micro-electro-mechanical systems (MEMS) technology [4]. The process starts from 150 mm diameter double-side-polished silicon wafers with an average thickness of 475 μm and flatness of 6 μm. The chrome-on-quartz photomask is produced by Image Technology Inc., with a pattern accuracy of 50 nm. Both photoresist (PR) and the silicon dioxide serve as etch masks during the Time-multiplexed Deep Reactive Ion Etch (TMDRIE) process, which plasma-etches through the entire silicon wafer. The manner in which photoresist and silicon dioxide are patterned contributes to the Critical Dimension (CD) loss, and the etching uniformity and accuracy of the DRIE process determine the final manufacturing accuracy. However, we are presently only interested in the relative placement of the tooth-to-mirror contact points, and their relative placement to the bullnose tip, what we call global accuracy. That is, as long as the CD loss is repeatable and uniform over the entire wafer, the combs will have perfect global accuracy. We have demonstrated better than 0.5 μm global accuracy by the following process (Figure 6).

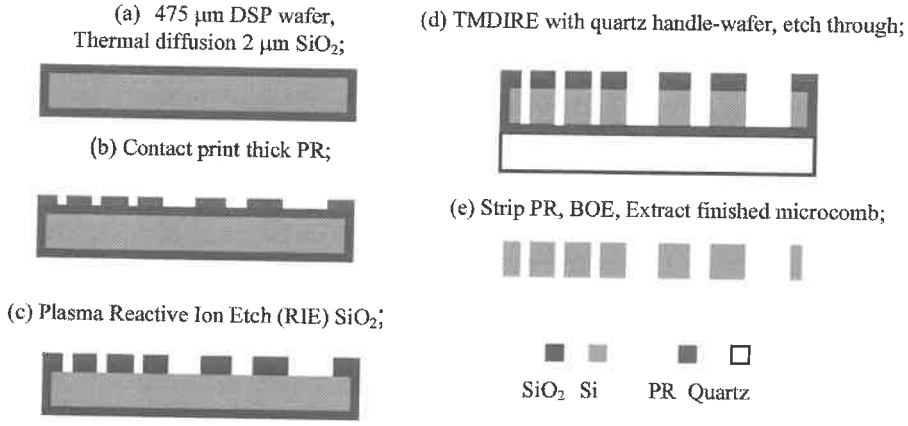
(a) 475 μm DSP wafer, Thermal diffusion 2 μm SiO_2;
(b) Contact print thick PR;
(c) Plasma Reactive Ion Etch (RIE) SiO_2;
(d) TMDIRE with quartz handle-wafer, etch through;
(e) Strip PR, BOE, Extract finished microcomb;
SiO_2 Si PR Quartz

Figure 6: Mircocomb fabrication

i. Oxide growth

Thermal silicon oxide is used as hard mask to protect features during the TMDRIE. The growth of 2 μm thermal oxide is done with a wet oxidation recipe running at 1150°C.

ii. Photolithography

The photolithographic principles are similar to those used for IC semiconductor fabrication, but there are some important differences, since the patterning material must stand up to plasma etch that can last for several hours. Two types of thick resist, AZ4620 and AZ9260, manufactured by Clariant, are tested. Though both have similar Photoresist to silicon selectivity (about 1:50 to 1:100) during Deep Reactive Ion Etch, the later one gives better accuracy especially for long-term etching, and gives better vertical-like resist profile (Figure 7).

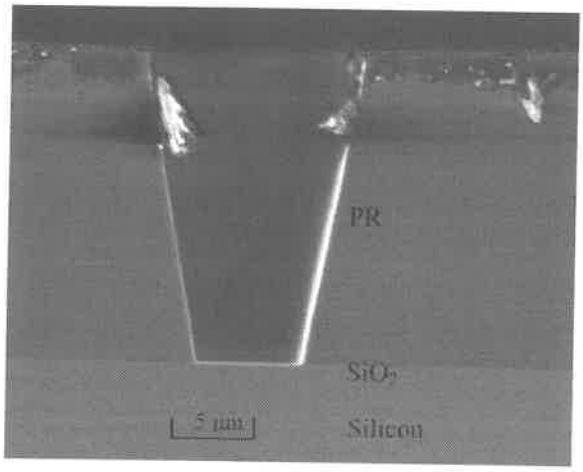

Figure 7: SEM images of 20 μm PR profile, the sidewall angle is about 19° from the normal.

The required 20 μm thick photoresist is deposited by double-coating and contact photolithography. The recipe consists of the following six steps:1) Hexamethyldisilazane (HMDS) vapor prime. HMDS acts as an adhesion promoter. One monolayer of HMDS bonds readily with the surface of the wafer, the other side bonds readily with the resist; 2) dispense resist using a Solitec Model 5110 photoresist coater, first coat while wafer spinning at speed of 1500 rounds per minute (RPM); 3) softbake at 90°C for 30 minutes in a convection oven; 4) dispense second layer resist while wafer spinning at speed of 2000 RPM ; 5) softbake at 90°C for another 60 minutes; 6) contact exposure of resist for 120 seconds using the Electronic Visions Model EV620 Mask Aligner (wavelength of 365-405 nm, the flux setting of 10mW/cm^2/sec). Since the required exposure time is long, interval exposures are used, with a cool down time between exposures to prevent the resist from bubbling; 7) develop resist with Clariant AZ300 MIF developer; 8) hardbake at 90°C for 60 minutes.

iii. Oxide Etch

For oxide etch, both dry etch and wet etch are tested. Wet etch (Buffered-Oxide-Etch, H_2O:HF=7:1 buffered with NH_4F) gives less than 1% uniformity but shows approximately 70 degree undercut (Figure 8). Unfortunately, the oxide tip will degrade during DRIE so that the feature's linewidth is enlarged. The typical etching results show 4 μm ± 1 μm SiO_2 tip erosion after 4.5 hour DRIE, which does not meet our sub-micrometer global accuracy requirement.

Plasma dry etch using CHF3 can achieve straight-like sidewall profile with the selectivity from PR to SiO_2 being about 1:2. Approximately 7 degree undercutting is observed (Figure 9). However, the plasma etch rate is higher at the edge than in the center of the wafer, so that about half μm over-etching to silicon can not be avoided in some places. Furthermore, the sidewall profile's angle of SiO_2 will continue into silicon. The experimental result shows the effect to global accuracy is not significant (less than 50 nm).

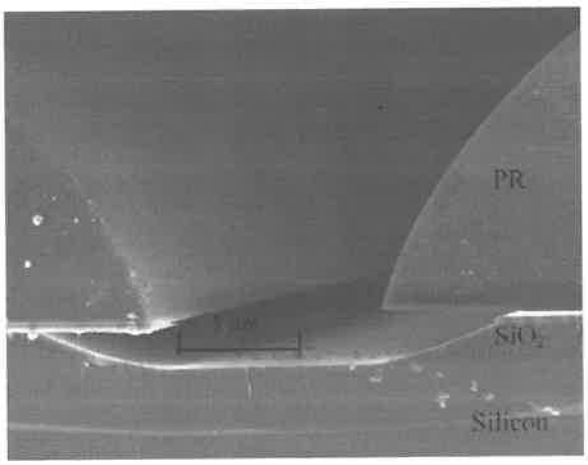

Figure 8: SEM images for Silicon oxide profile after BOE, 70 degree undercut. PR was deveoped with Clariant AZ440 MIF developer, softbake at 105 °C.

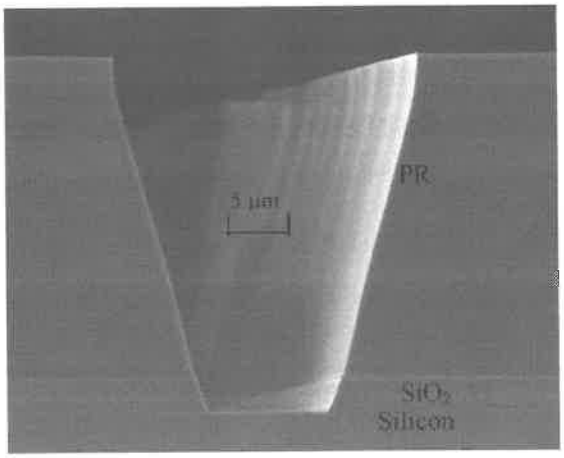

Figure 9: SEM images for Silicon oxide profile after plasma etch, showing approximately sidewall angle of seven degree. PR was deveoped with Clariant AZ300 MIF developer, softbake at 90 °C .

iv. TMDRIE

TMDRIE etching results show a negative taper sidewall profile (the trench is wider on the bottom than on the top), which can provide point-like contact for X-ray telescope optics assembly (Figure 10). Quartz handle wafers are attached to the back of the device wafer during TMDRIE to help loading and unloading the wafer. The CD loss during TMDRIE includes the effects of silicon undercut and hard mask (silicon oxide) erosion. And once again, as long as they are uniform and repeatable, that CD loss will not affect the global accuracy of the microcomb. The DRIE etching uniformity highly depends on the aspect ratio of the trench. Experimental results show the uniformity during the first-hour etching and during the fourth-hour are 1% and 4% respectively. It's argued that a reduction of the ion flux due to the ion angular distribution

causes a reduction of the depassivation rate of the trench bottom. The accuracy and repeatability of the etching result are under investigation using SEM and other metrology. The result will be presented during the meeting. Figure 11 shows the spring comb pattern a on silicon wafer after four hours TMDRIE.

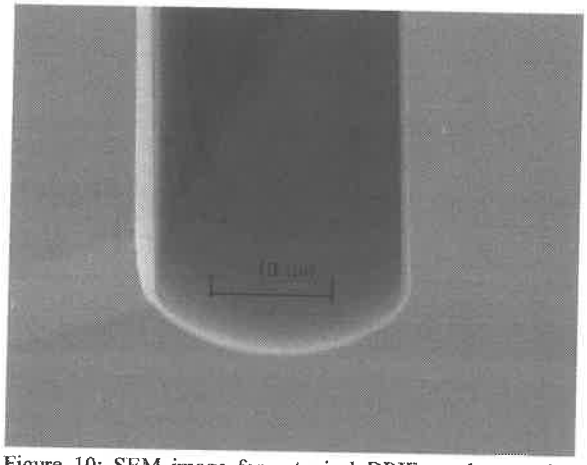

Figure 10: SEM image for a typical DRIE result: negative taper sidewall profile.

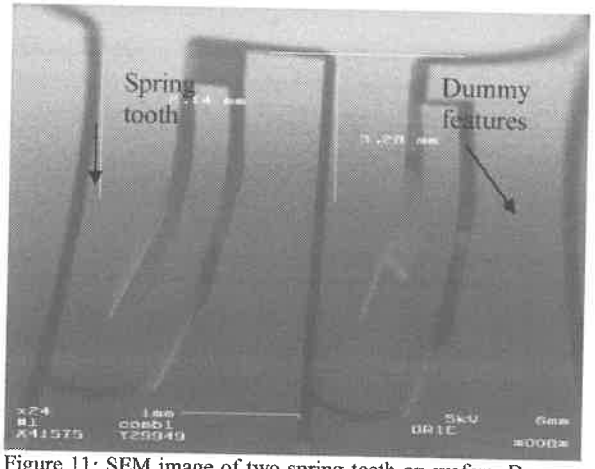

Figure 11: SEM image of two spring teeth on wafers. Dummy features are added to the pattern for uniform etching trench linewidth.

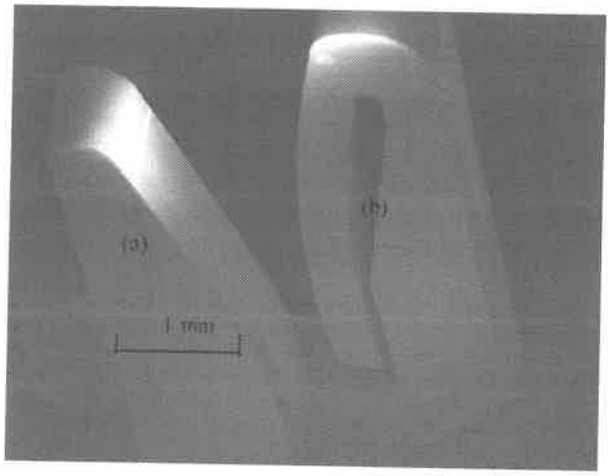

Figure 12: SEM image of a pair of microcomb teeth:
(a) Reference tooth; (b) Spring tooth.

IV. FUTURE WORK

Current microcombs demonstrate better than 1 μm global accuracy [4]. The point-like contact is achieved due to the negative taper sidewall profiles. We are investigating a two-masks etch process to reduce the accurate frontside TMDIRE etch depth to 50 μm ~ 100 μm. The process is illustrated in figure 13. The current mask aligner in the Microsystems Technology Laboratory (MTL) at MIT, has 2 μm alignment accuracy for top-to-bottom alignment, which is enough for our application. For 50 ~ 100 μm TMDRIE etch, oxide alone can serve as protection mask, and advanced lithography such as E-beam lithography could be used to pattern oxide so that better lithography results can be achieved, which in turn give better accuracy, uniformity and repeatability. We believe we can achieve 100 nm global accuracy for microcombs using current facilities in MTL after those process improvements.

V. ACKNOWLEDGEMENTS

We greatly acknowledge the outstanding student, staff and facility supports from the Space Nanotechnology Laboratory, the Nanostructures Laboratory, and the Microsystems Technology Laboratory, all at MIT. This work is supported by NASA grants NAG5-5271 and NCC5-633.

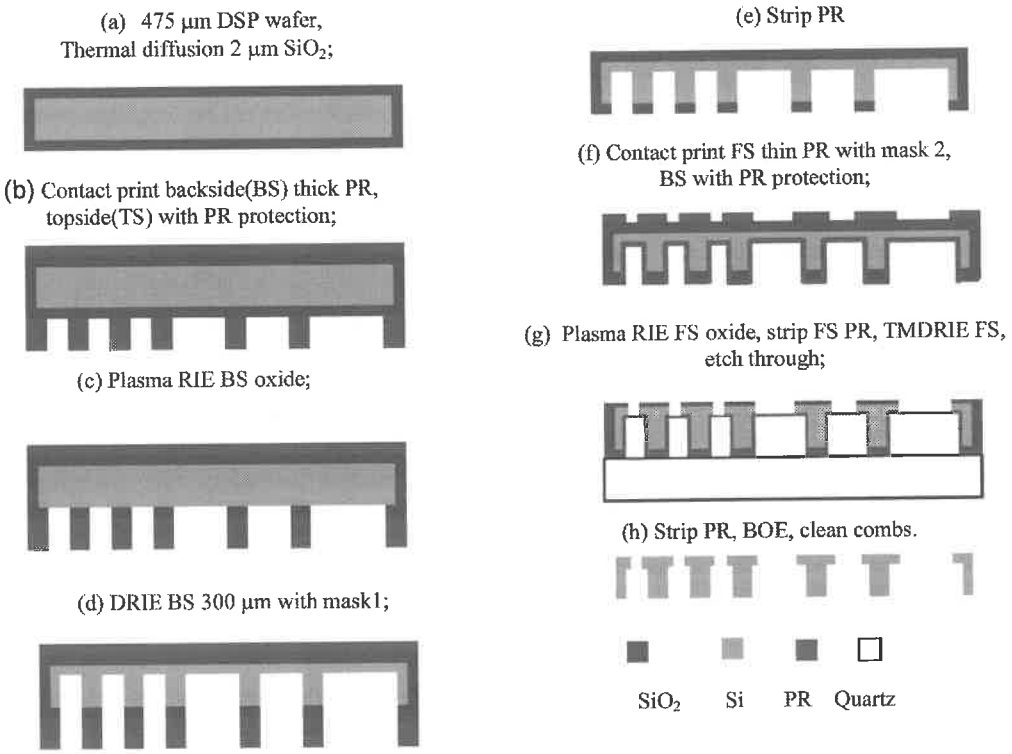
(a) 475 μm DSP wafer,
Thermal diffusion 2 μm SiO_2;
(b) Contact print backside(BS) thick PR,
topside(TS) with PR protection;
(c) Plasma RIE BS oxide;
(d) DRIE BS 300 μm with mask1;
(e) Strip PR
(f) Contact print FS thin PR with mask 2,
BS with PR protection;
(g) Plasma RIE FS oxide, strip FS PR, TMDRIE FS,
etch through;
(h) Strip PR, BOE, clean combs.
SiO_2
Si
PR
Quartz

Figure 13: Mircocomb two-masks fabrication process.

REFERENCES

1. R. Petre, W.W. Zhang, D. A. Content, .T. T. Saha, J. Stewart, J. H. Hair, D. Nguyen, W. A. Podgorski, W. R. Davis, Jr., M. D. Freeman, L. M. Cohen, M. L. Schattenburg, R. K. Heilmann, Y. Sun, C. Forest, "Constellation-X Spectroscopy X-ray Telescope (SXT)", *SPIE* 4851 – 50
2. W.A. Podgorski, D. Content, P.Glenn, J. Hair, R. Petre, T. Saha, M. Schatternburg, J. Stewart, W. Zhang, "Constellation – X Spectroscopy X-ray Telescope Assembly and Alignment", *SPIE* 4851 – 57
3. C. G. Chen, R. K. Heilmann, P. T. Konkola, O. Mongrard, G. P. Monnelly, and M. L. Schattenburg, "Mirco-Comb Design and Fabrication for High-Accuracy Optical Assembly", *J. Vac. Sci. Technol. B* **18**, 3272-3276 (2000).
4. G. P. Monnelly, D. Breslau, N. Butler, C. G. Chen, L. M. Cohen, W. Gu, R K. Heilmann, P. T. Konkola, O. Mongrad, G.R. Ricker Jr., and M. L. Schattenburg, "High-Accuracy X-Ray Foil Optic Assembly", *Proc. SPIE* 4138, 164 (2000).
5. O. Mongrard, *High-Accuracy Foil Optics for X-ray Astronomy.* Master's thesis, Massachusetts Institute of Technology, 2001.
6. C. R. Forest, M. Spenko, Y. Sun, M. Mcguirk, A. H. Slocum, M. L. Schatternburg, "Precision Assembly and Metrology of X-ray Foil Optics", *ASPE 2002 annual meeting proceedings*
7. C.G.Chen, *Microcomb Fabrication for High Accuracy Foil X-ray Telescope Assembly and Vector Gaussian Beam Moldling,* Master's thesis, Massachusetts Institute of Technology, 2000.

Thermal Energy Conversion using a Microfabricated Shape Memory Alloy Structure

Yi Zhang and Hy D. Tran[1]
Department of Mechanical Engineering
University of New Mexico
Albuquerque, NM87131

Abstract:
In this paper we present the conversion of fluctuations in ambient temperature to mechanical energy (strain energy). The design is based on the phase transformation of shape memory alloy (TiNi; e.g. Nitinol). Ambient temperature fluctuation instead of current is used to drive the alloy. Compared with aluminum/polysilicon bimorphs, which are based on the difference between the thermal expansion coefficients of Al and polysilicon, larger displacement can be achieved by a free standing TiNi/polysilicon bimorph with in-plane motion. Optimization analysis of the geometry is applied and optimal scaling is determined with consideration of fabrication limitations. A novel fabrication process and low-cost but reliable mask making method are also described.

Introduction:

A conventional bimorph consists of two different materials bonded together. As the temperature changes, both materials undergo different strains. Therefore, a large deflection is achieved by the difference between the thermal expansion coefficients of two materials.

A shape memory alloy (SMA) bimorph consists of a layer of TiNi film bonded with a supporting structure (polysilicon), which acts as a bias spring. At low temperature, the TiNi film is easily deformed. Upon heating over the austenitic transformation temperature A_s, the TiNi film recovers its memorized shape and transforms to austenite phase. When cooled below the martensitic transformation temperature M_s, the TiNi film transforms to martensite phase and the bimorph returns to original shape.

Fig.1 Bimorph Layout

Commonly used bimorphs are layer-by-layer structure, which means the actuator layer is on the top of the bias layer. Therefore the motion is restricted only at out of plane. In order to achieve in plane motion, a side-by-side design is necessary[1]. In this paper we present a novel side-by-side SMA bimorph that can convert of fluctuations in ambient temperature to mechanical energy (strain energy).

Geometry Optimization:

The SMA bimorph can be modeled as follows[2]:

$$\delta = \frac{3 \cdot \sigma_{rec} / E_b \cdot (t_a + t_b)}{t_b^{\,2} \cdot KI} \cdot l^2 \qquad (1)$$

[1] Hy D. Tran: tran@me.unm.edu. This work was funded by NSF ECS0093966.

where the effective stiffness factor KI is given by:

$$KI = 4 + 6 \cdot \frac{t_a}{t_b} + 4\left(\frac{t_a}{t_b}\right)^2 + \frac{E_a}{E_b} \cdot \left(\frac{t_a}{t_b}\right)^3 + \frac{E_b \cdot t_b}{E_a \cdot t_a} \qquad (2)$$

where t_a and t_b are the thickness of the two materials; E_a and E_b are the Young's moduli of the bias spring and austenitic TiNi; and l is the length of the bimorph;

$\frac{\sigma_{rec}}{E_b}$ is the recoverable strain; (recoverable stress σ_{rec}, measured by substrate curvature, we set 200MPa, divided by the Young's modulus of austenitic TiNi)

Table 1 shows that a 0.529μm deflection is achieved by an Al/polysilicon bimorph with a 40K temperature fluctuation, but 1.75μm deflection is achieved by a SMA bimorph of the same size. The major advantage of a SMA bimorph over a normal thermal bimorph is the large deflection for small temperature changes.

	Al / Polysilicon	TiNi / Polysilicon
Temperature Difference	40K	N.A.
Thickness of two materials	20μm both	20μm both
Bimorph Length	200μm	200μm
Young's Moduli	77GPa / 165GPa	83GPa / 165GPa
Thermal Expansion Coefficients	23×10^{-6}/ °C; 4.7×10^{-6}/ °C	N.A.
Recoverable Stress	N.A.	200MPa
Tip Displacement	0.529μm	1.75μm

Table 1 Comparison of Al/polysilicon bimorph with TiNi/polysilicon bimorph

From equations (1) and (2) above, we understand that the tip deflection is the function of multiple parameters, like the thickness of two layers, Young's moduli of two materials, length of the bimorph and the recoverable strain. Due to the fabrication factors, the following parameters are fixed: Young's moduli of TiNi and polysilicon. Therefore only three parameters can be modified to achieve the maximum tip deflection.

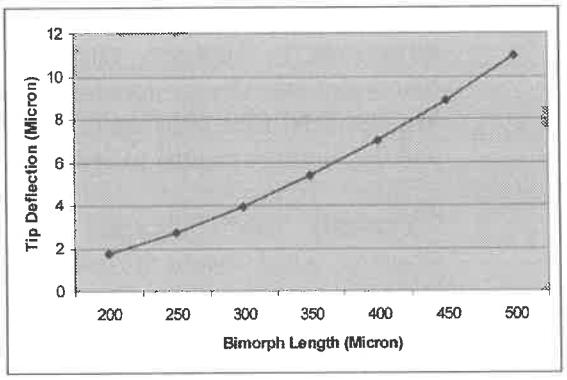

Fig.2 Tip deflection Vs. Bimorph length

We fix the thickness of TiNi and polysilicon at 20μm, and increase the length of bimorph from 200μm to 500μm. Fig.2 indicates clearly that greater tip deflection increases while the bimorph is getting longer.

We fix the bimorph length at 200μm and thickness of polysilicon at 20μm. Meanwhile we increase the thickness of TiNi from 1μm to 40μm. Fig.3 indicates that the tip deflection will reach maximum when the ratio of thickness of TiNi to polysilicon is around 0.675.

We fix the bimorph length at 200μm and the thickness ratio at 0.675 and increase the thickness of TiNi from 2μm to 40μm. From Fig.4 we understand that the tip deflection decreases while the material layers are getting thicker.

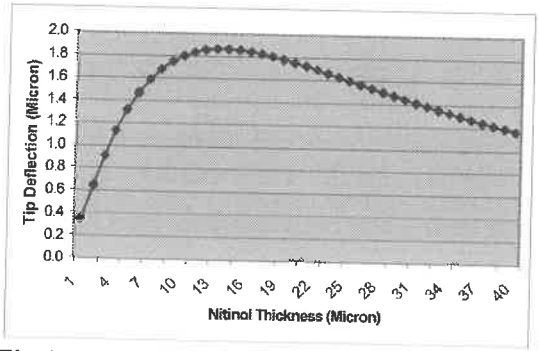

Fig.3 Tip Deflection Vs. Thickness Ratio

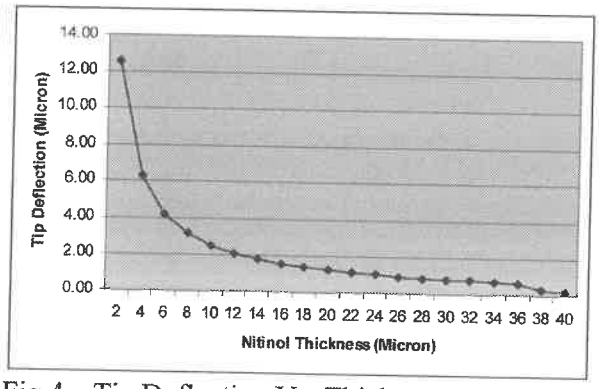

Fig.4 Tip Deflection Vs. Thickness at Fixed Ratio

Actually due to the fabrication limitations, we cannot make a structure with an optimal thickness ratio. Structure widths below 20μm are beyond our current facility capacity. Therefore we design the thickness of material at 20μm.

Fabrication Process:

In this paper, a new surface micromaching process is designed for fabricating the side-by-side bimorph. In a normal SMA bimorph, the SMA depositions were made by blanket depositions on top of the bias spring, which was in line with the deposition and patterning. In order to make side by side effect, one more patterning of the bias spring before the deposition of SMA is necessary. Fig.5 shows the cross section and top view at different stages of our process. (1) A 0.5μm silicon nitride is deposited on the silicon substrate as the protection layer. A 2μm sacrificial silicon dioxide layer is deposited onto the silicon nitride. (2) The sacrificial layer is patterned to make the anchor of bimorph. (3) A 2μm polysilicon is deposited as the structure layer. (4) The polysilicon is patterned to make the bias spring. (5) A SMA blanket deposition is sputtered and then patterned by photolithography. The alloy on the bias spring is etched away by SMA etchant and the alloy beside the bias spring is left. (6) Finally the whole structure is released from the substrate.

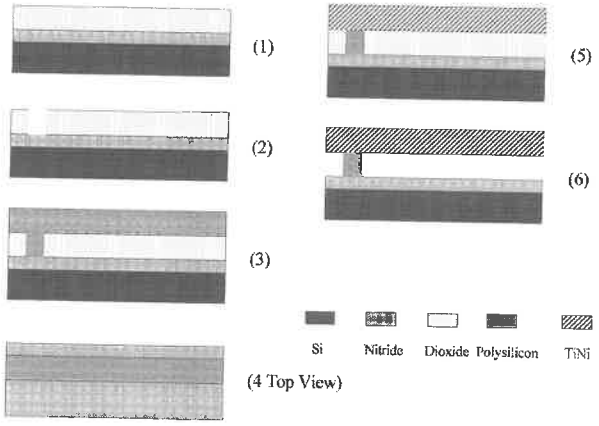

Fig.5 Fabrication Process Chart

Mask Making:
In previous papers, several alternatives to standard chrome masks have been discussed[3][4]. In this paper, the mask pattern has been printed on transparency films using a high-resolution printer first. Then the pattern on the transparency films will be transferred to the soda-lime glass through contact lithography. A commercially available polished soda-lime glass coated with iron oxide (4×4 inch, Nanofilm, CA) has been used. Prior to mask making, the soda-lime glass must be cleaned by acetone, methanol, isopropanol and DI water consecutively. A Karl Suss mask aligner and the standard procedure of AZ5214 has been used. The iron oxide was etched by a $3HCl:1H_2O$ etchant.

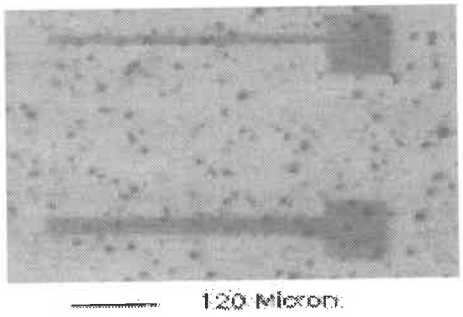

Fig.6 Pattern on the Transparency Film

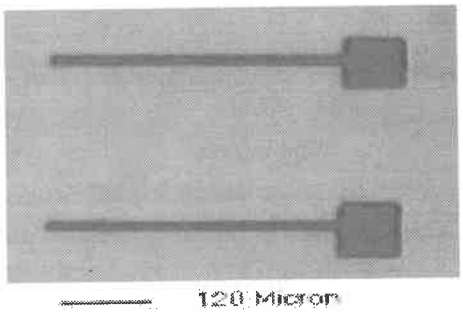

Fig.7 Pattern on the Soda-lime Glass

From Fig.6 and 7 we observe that most dust and ink dots on the transparency film can be removed via the photolithography process. Finally the iron oxide has the permanent mask pattern. Therefore a satisfactory hard mask can be made reliably and inexpensively through this method. This will be used in contact photolithography to pattern the structures designed to verify TiNi/polysilicon bimorphs, together with finite element simulations.

Conclusion:
Larger tip deflection can be achieved by using a SMA bimorph rather than normal Al/polysilicon bimorph from theoretical calculations. Geometry optimization has been discussed. A novel surface micromachining has been designed to fabricate side-by-side bimorph. A reliable and low cost mask making method has been proved by experiment.

References:
(1) Sehr H et.al; Fabrication and test of thermal vertical bimorph actuators for movement in the wafer plane, J. Micromech. Microeng. V11 pp306-310 2001
(2) Krulevitch P et.al; Thin film shape memory alloy microactuators, J. Micro Electro Mechanical Systems, V5, No.4 pp270-282 1996
(3) Lin C H et.al; A fast prototyping process for fabrication of microfluidic systems on soda-lime glass, J. Micromech. Microeng. V11 pp726-732 2001
(4) Deng T et.al; Prototyping of masks, masters, and stamps/molds for soft lithography using an office printer and photographic reduction, Anal.Chem. V72 pp3176-3180 2000

Artificial Insemination System by Male and Female Micro Robots

Hisayuki Aoyama and Hideharu Takubo

Applied Micro Systems, Robotics Div.
Dept. of Mechanical Engineering & Intelligent Systems,
University of Electro-Communications, Tokyo 182-8585
Japan
[URL http://www.aolab.mce.uec.ac.jp]

1.Introduction

In the biomedical field, the precise operation is required to achieve cell injection and genome analysis. To enhance these technologies, the special instrument with higher accuracy can provide the solution to these requirement. Several sophisticated instruments have been developed and some of them are equipped with the advanced sensor and actuator. In the meantime, the micro robotics has the potential application to many fields such the biomedical engineering as well as micro-engineering. For these years, our group have developed many small robots for the application to the precision engineering[1),2),3)].

In this report, the unique artificial insemination system operated by male and female micro robots is proposed and the successful experimental results are described. The small robot, which is approximately 1 cubic inch, is composed of piezo element and electromagnet to move precisely with the manner of an inch worm[4)]. And one small robot has the micro pipette actuated by the micro pump while another one has the special micro capillary which can incubate the fertilized egg. In the experiment, the egg and the spermatozoon of fish are implemented into the micro injector and the micro incubator on these small robots. Two small robots can navigate each other to inseminate by using acoustic, optical and mechanical touch trigger switch sensors and reactive based sequential manner. And the fertilized egg in the micro incubator was successfully hatched after two weeks later under the temperature and water condition control instrument.

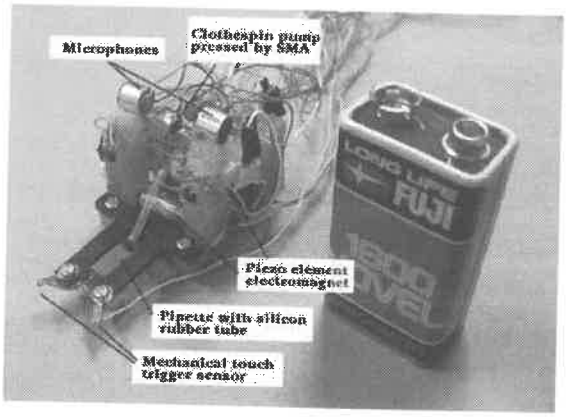

Fig.1 Male micro robot with a pipette, a pump and three range sensors for autonavigation to the female robot

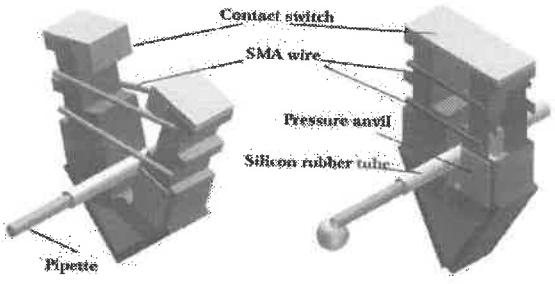

Fig.2 Illustration of the one-shot clothespin pump pressed by the SMA wire

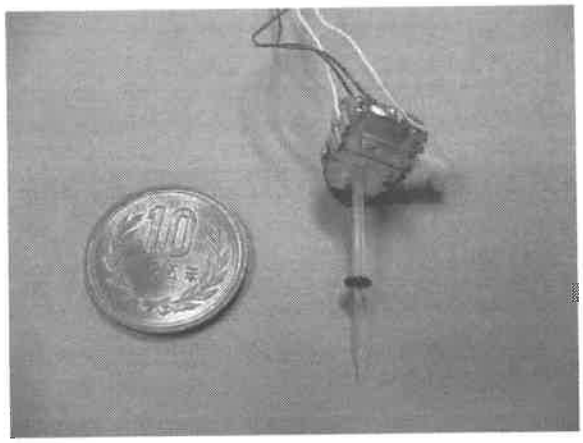

Fig.3 Photograph of the simple active pipette and clothespin pump

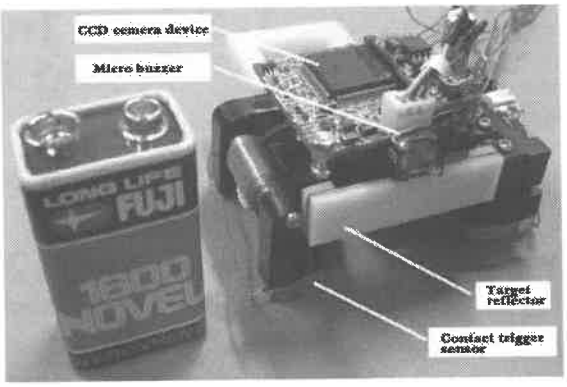

Fig.4 Female small robot with CCD image device and capillary incubator.

2. System Configuration

2.1 Male Micro Robot

The small male robot with a micro pipette, a micro pump as well as several sensory elements is shown in Fig.1. It has piezo elements and electromagnet legs to provide an inchworm step locomotion although the electricity and control signal are still supplied via several wires.

For the male to head, approach and align to the female one, three kinds of range sensors are implemented on the small robot. A pair of microphones is used to detect the direction of acoustic source on the female robot. Twin micro infrared optical sensors can measure the approaching angle and the mechanical touch sensor on the feeler can contact with the guide bar of the female robot. The component of a pipette with a one-shot SMA driven clothespin pump which is incorporated with the male robot is developed as shown in Fig.2 and Fig.3. The silicon rubber tube is connected with the end of the pipette and can be compressed by the clothespin actuated by SMA wire. Then the small amount of the liquid in the tube can be easily pushed out by the simple electric signal while the higher resolution can not be expected.

2.2 Female Micro Robot

Female micro robot with a micro capillary incubator, a CCD camera element, a target reflector and a small buzzer as an acoustic invitation signal is shown in Fig. 4. As shown

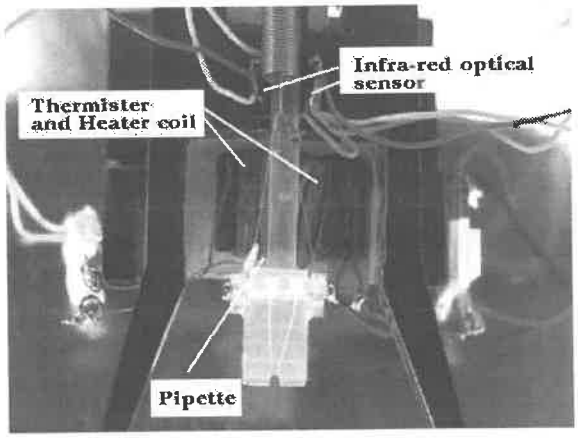

Fig.5 Close up view of small incubator with sensor, heater and shutter.

in Fig.5, the unique micro capillary which is equipped with the optical infrared sensor for checking the egg movement, the thermistor and heater coil for controlling the temperature is fixed at the center of body to incubate and the focus point of CCD image device is set at the end of capillary to monitor the egg status visually after the insemination.

3. Precise Navigation for Insemination

As shown in Fig.6, the sequence of insemination is illustrated. At first, a pair of microphones on the male robot can detect the

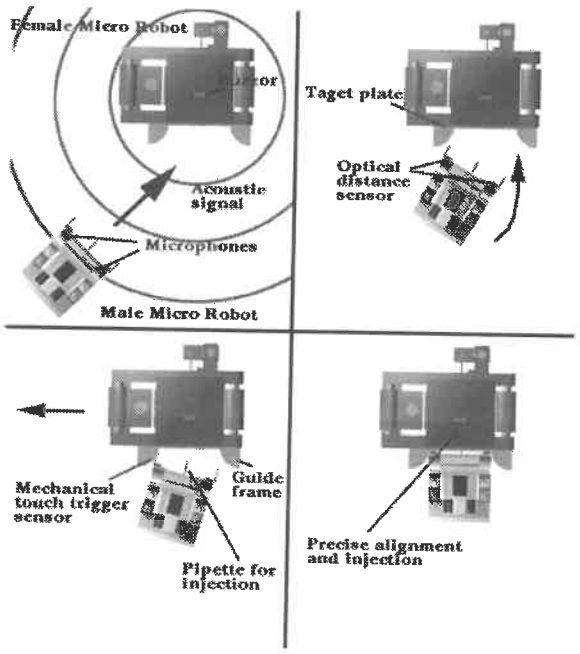

direction of acoustic source generated by the buzzer on the female robot. The differential amplitude of detected signals causes the alternative activation of piezo elements to head itself to the signal source. When the male robot comes to close the female one, twin micro infrared optical sensors can measure its approaching angle to keep itself at right angle to the female one. At last the mechanical touch trigger sensor on the feeler can contact with the guide bar of the female robot to generate the control signal that causes the female one to move forward or backward to align the micro pipette into the incubation capillary precisely. Then the spermatozoon in the male small robot can be injected into the egg of female robot. This precise rendezvous action is based on "insect like behavior" rather than engineering procedure with global positioning system.

Fig.6 Sequence of two robots navigation

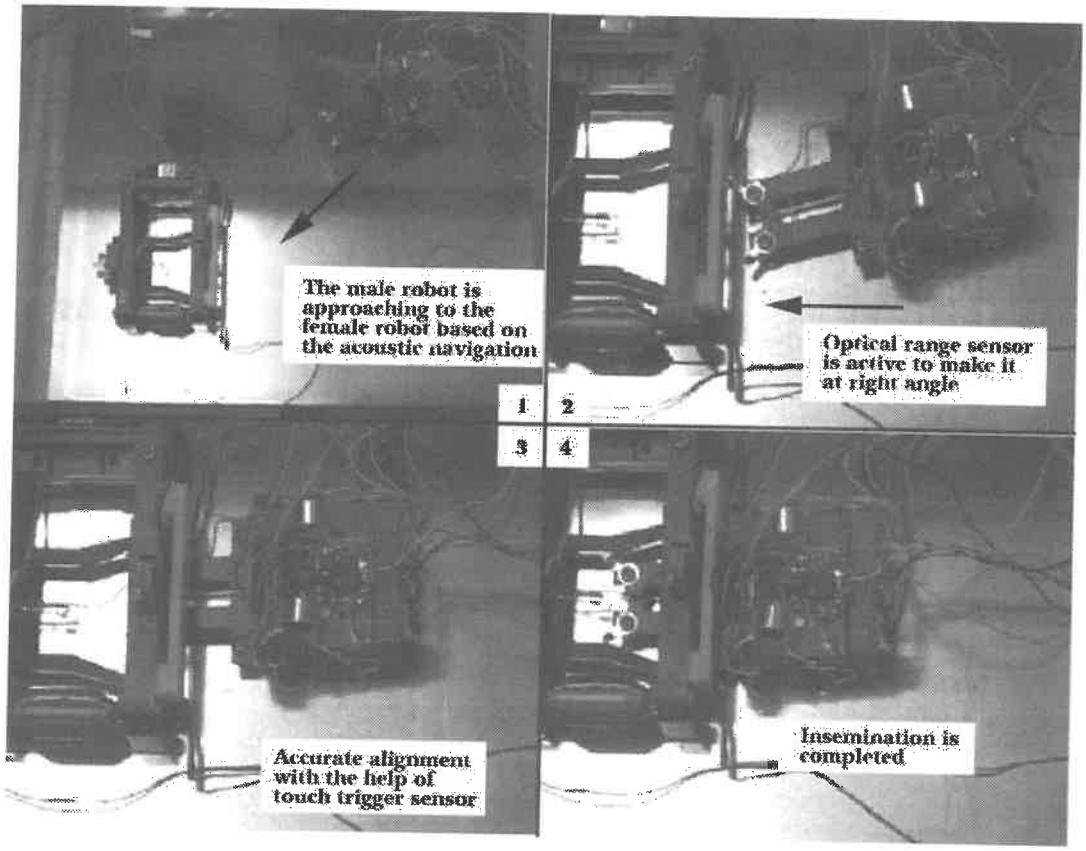
The male robot is approaching to the female robot based on the acoustic navigation
Optical range sensor is active to make it at right angle
1
2
3
4
Accurate alignment with the help of touch trigger sensor
Insemination is completed

Fig.7 Expermental result of automatic navigation for insemination performed by two small robots.

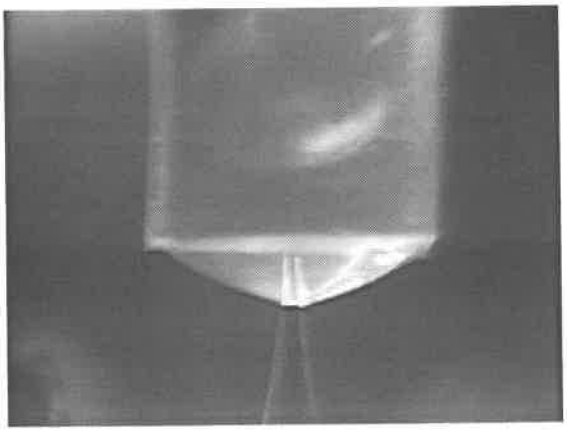

Fig.8 Close up view of precise injection to the egg in the tube on the female robot

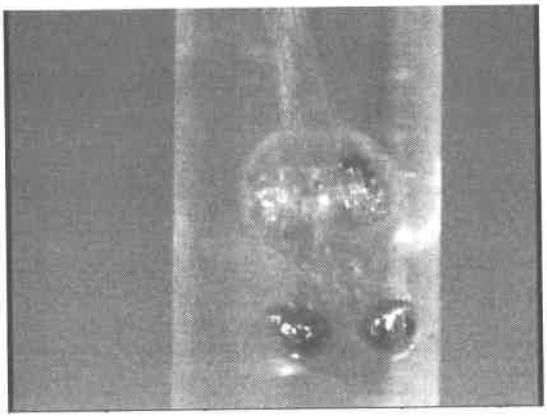

Fig.9 A tiny fry succeeded in hatching after 12 days

4. Experiment of Insemination and Incubation

The sequential photo of the actual experiment is shown in Fig.7 as well as the close up view of injection is in Fig.8. In this experiment, the egg and the spermatozoon of killifish are used for artificial insemination. This active pipette pumped by the SMA driven clothespin can control of the small amount of the liquid at the resolution of 0.35 microliter The two small robots succeeded in approaching each other automatically and making fine positioning based on three range sensors with the repeatability of 20 micron. After the tool alignment is completed, the spermatozoon was injected into the egg cell. In the female small robot, the fertilized egg can be incubated under the temperature control system and water monitoring instrument. As shown in Fig.9, the tiny fry succeeded in hatching in the tube after12 days later when the water temperature is kept at 25 degree.

5. Conclusions

In this report, an artificial insemination system performed by the piezo drive micro robots. These robots can navigate automatically each other by using acoustic, optical and touch trigger sensors to make accurate alignment and injection. As the primary experiment, the artificial insemination was successfully conducted by using the egg and the spermatozoon of killifish.

References

[1]P.Sooraksa and Hisayuki Aoyama; A Low-Cost Passive Acoustic Resonator for Insect-Like Micro Robotic System,Proc. of 16th IAARA/IFAC/IEEE Int. Symp. on Automation and Robotics in Cobstruction, pp.725-729(1999)

[2]Hisayuki Aoyama et.al; Automatic precise micro-drilling system by distributed insect robots, Proc. of 1999 ASPE Annl.Meeting, pp.238-286(1999)

[3]Hisayuki Aoyama and Satoshi Miyamoto; Automatic Surface Damage Exploring and Repairing System by Precise Micro Robots, Proc. of 2000 ASPE Annl. Meeting, pp.332-335(2000)

[4]Ohmi Fuchiwaki and Hisayuki Aoyama; Design and control of versatile micro robot for microscopic manipulation, Proc. of 2002 ASPE Annl.Meeting,pp.204 -204(2001)

Precision Machining of Steel with Ultrasonically Driven Chilled Diamond Tools

E. Brinksmeier, R. Gläbe

LFM Laboratory for Precision Machining, University of Bremen, Germany

Abstract

Several papers have been published concerning precision machining of steel with monocrystalline diamond tools. In order to prevent catastrophic tool wear, different types of process modification have been investigated. Although some of them - like cryogenic cutting and elliptical vibration cutting - offer definite advantages, there is still a potential for improvement. In this investigation cryogenic cutting and elliptical vibration cutting were combined in machining of Ck45N carbon steel. Compared to cryogenic cutting or elliptical vibration cutting alone, the combination yields an improved surface finish. However, a further reduction of tool wear could not be observed.

Introduction

A thorough discussion of diamond tool wear in single point diamond turning is given in [1]. Regarding diamond turning of steel alloys several approaches for reducing tool wear have been published. By coating the diamond with TiN a wear reduction up to 40% could be achieved [2]. Evans has investigated cryogenic cooling of the tool and the workpiece consisting of a special steel alloy with a ductile material response at low temperatures [3]. Ultrasonic tool vibration, providing an intermitted contact between the tool and the workpiece, was presented by Moriwaki [4].

The achieved wear reduction of these process modifications under almost identical experimental conditions was studied in [5]. It was found, that cryogenic cutting could increase tool life up to one order of magnitude and that elliptical vibration cutting could increase tool life up to two orders of magnitude. In this work we have investigated the combination of both process modifications.

Experimental setup

Several face turning experiments have been performed using the experimental set-up shown in Figure 1. A 40 kHz ultrasonic generator (BRANSON) and a piezoelectric converter were used for vibrating the tool with an amplitude of 1.7 µm. Elliptical vibration cutting with an amplitude ratio of approx. 1:10 was achieved by displacing the center of mass of the tool with respect of the symmetry axis of the resonator [5].

Two types of heat sinks for cooling the diamond tool were employed:

a) liquid nitrogen cooling

b) Peltier element cooling

Liquid nitrogen was lead from a nitrogen tank through a steel pipe with an inner diameter of 0.6 mm which was soldered beneath the diamond tool. The temperature was monitored by a thermocouple soldered to the base of the diamond. The lowest temperature that could be achieved by liquid nitrogen cooling before starting the experiment was -180°C.

A 300 W Peltier element was positioned near the cutting tool (cf. Figure 1). A 30 mm long copper bar was glued to the Peltier element and the rake face of the diamond tool. The lowest temperature that could be achieved by cooling with the Peltier element was -10°C.

The workpiece itself was kept at ambient temperature.

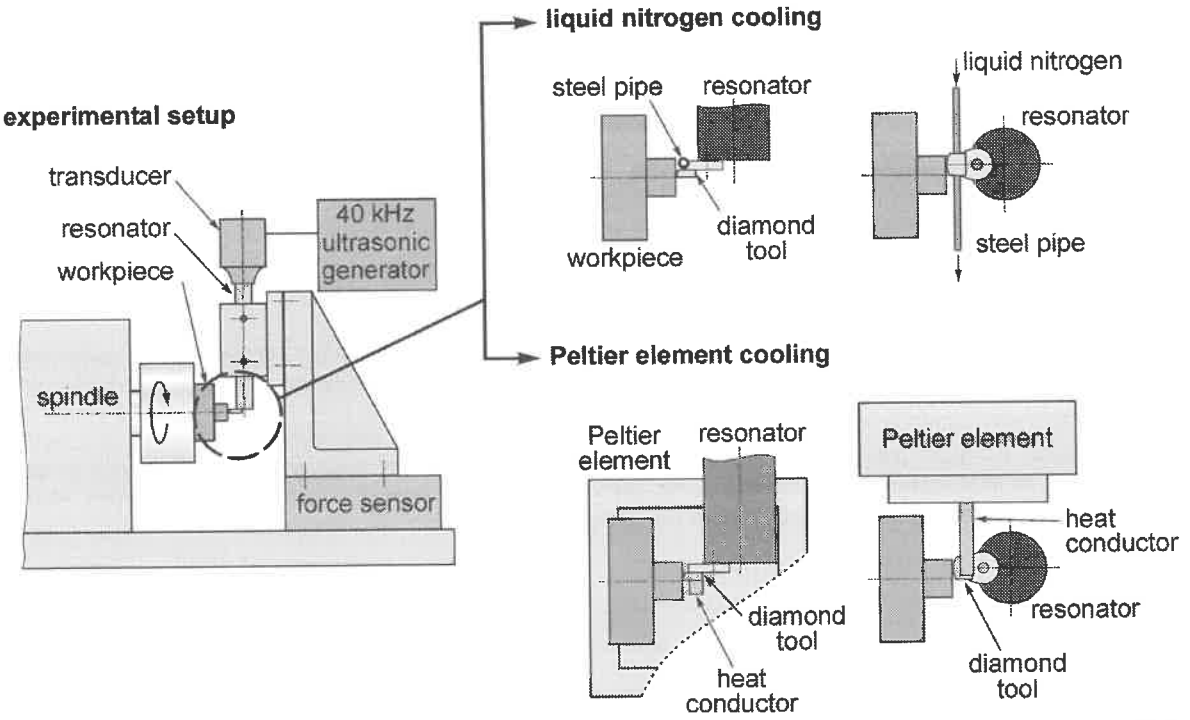

Figure 1: Experimental set-up for turning of steel with ultrasonically driven monocrystalline diamond tools with different chilling devices

The face turning experiments were carried out on a precision lathe Hembrug Super-Mikroturn CNC using monocrystalline diamond tools with a nose radius of 3 mm, a rake angle of 0° and a clearance angle of 6°. The outer diameter of the Ck45N (0.45 % C) carbon steel workpiece was 18 mm. The spindle speed was 60 rpm, the feed 5 µm and the depth of cut 10 µm. The face turning process was repeated five times in order to achieve a total cutting distance of 1000 m. The thrust forces were recorded with a piezoelectric sensor Kistler 9257B. The surface roughness at different cutting distances was determined by taking a plastic replica which was evaluated with a white-light interferometer. After a cutting distance of 1000 m the wear land width was determined with a Nomarski microscope.

Results

In Figure 2 the dependence of the wear land width of the diamond tool on tool temperature is shown. For comparison some data from experiments without tool vibration are added. A significant difference between the wear land widths of vibrating and non-vibrating tools could not be observed. The wear land width increases roughly exponentially with tool temperature. The same applies to the thrust forces which correlate with the wear land width.

As can be seen in the Nomarski micrographs shown in Figure 3, there is an appreciable reduction of tool wear at cryogenic temperatures. The wear land width and cutting edge radius of the diamond tool used at -120°C, as measured with a scanning force microscope, was 400 nm and 50 nm, respectively.

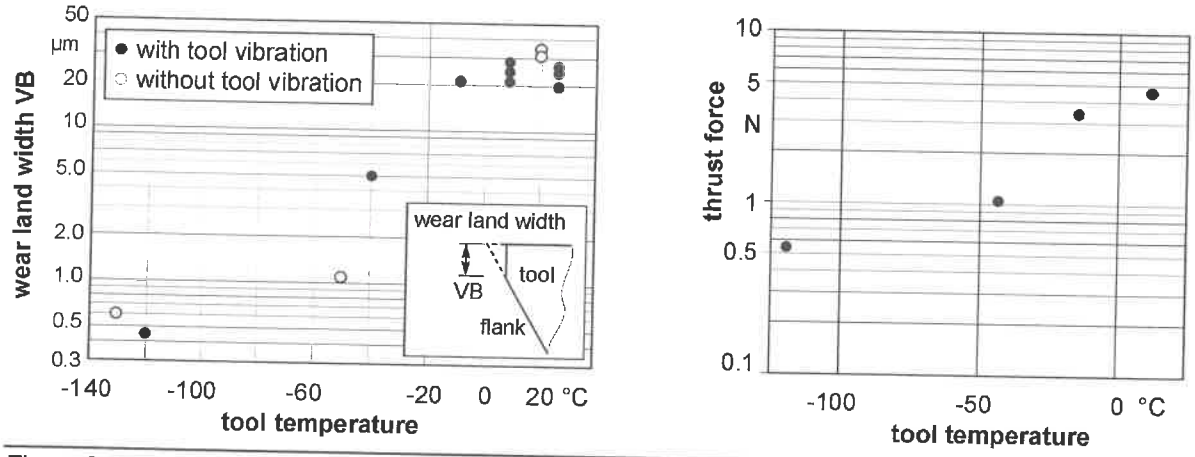

Figure 2: Temperature dependence of wear land width and thrust forces after a cutting distance of 1000 m

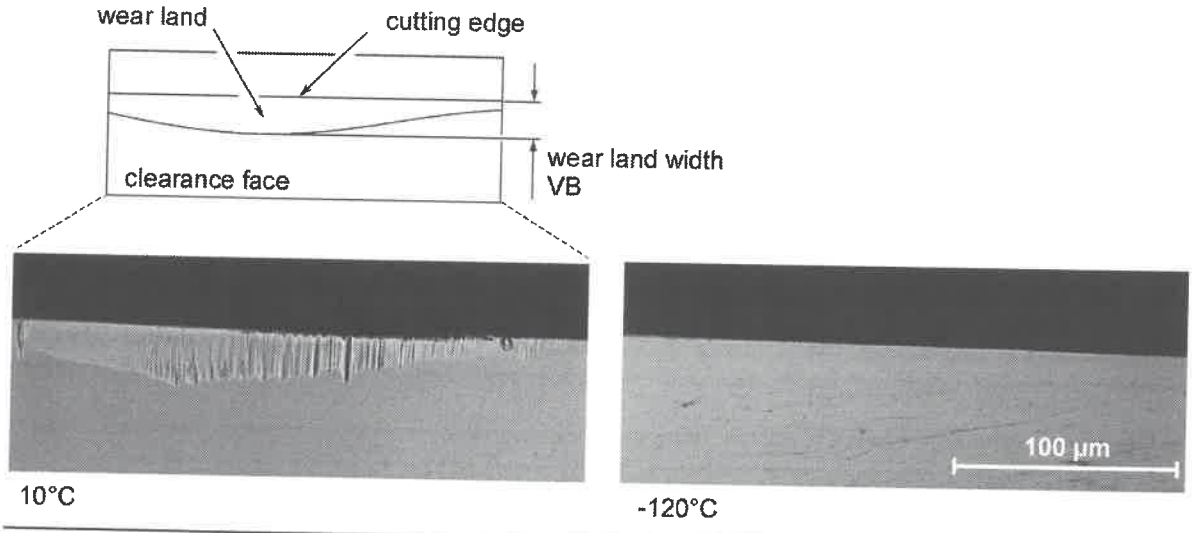

Figure 3: Wear land of monocrystalline diamond tools after a cutting distance of 1000 m obtained in elliptical vibration cutting at 10°C and -120°C

As shown in Figure 4 thrust forces increase approximately linearly with cutting distance. The measured roughness values are much lower than in experiments without vibration. At a tool temperature of -120°C and a cutting distance of 1000 m a Ra roughness of 30 nm could be achieved. Although thrust forces and wear land widths increase with cutting distance, the roughness of the vibration cut surfaces does not depend on cutting distance. Rather the topography of the elliptical vibration cut surfaces mainly seems to be determined by the nature of the cutting process [5].

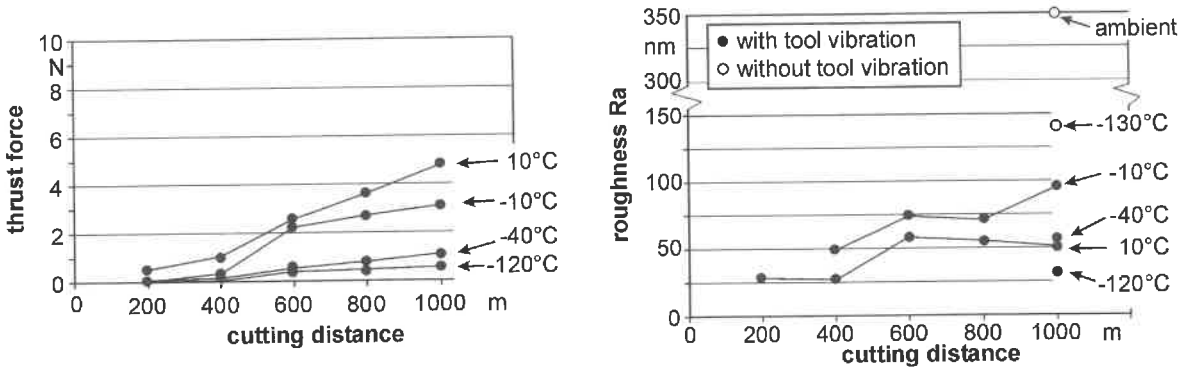

Figure 4: Dependence of surface roughness Ra and thrust forces on cutting distance at different temperatures

In Table 1 a comparison is made between the tool wear and surface roughness achieved in conventional diamond cutting of steel, cryogenic cutting, elliptical vibration cutting and its combination. As is evident form the experimental results, only a combination of cryogenic and elliptical vibration cutting yields both a substantial reduction of tool wear and a low surface roughness.

	temperature	wear land width VB	roughness Ra
without tool vibration	ambient	≈ 40 µm	≈ 350 nm
with tool vibration	ambient	≈ 20 µm	≈ 80 nm
without tool vibration	-130°C	≈ 0.6 µm	≈ 140 nm
with tool vibration	-120°C	< 0.5 µm	≈ 30 nm

Table 1: Comparison of the wear land width of monocrystalline diamond tools and the surface roughness after a cutting distance of 1000 m at ambient and cryogenic temperatures with and without tool vibration

Acknowledgement

The authors like to thank the German Research Foundation (DFG) for the support of this work (grant no. Br 825/22).

References

[1] Evans, C.J.; Paul, E.; Mangamelli, A.; Mc Glauflin, M.L.: "Chemical Aspects of Tool Wear in Single Point Diamond Turning", Prec. Eng. 18(1996)1, p. 4-19.

[2] Brinksmeier, E.; Gläbe, R.: "Advanced Cutting Tools for Precision Machining of Steel". Proc. 2nd International euspen Conference, Turin, Italy, May 27 - 31, 2001, p. 628-631.

[3] Evans, C.: "Cryogenic Diamond Turning of Stainless Steel", Annals of the CIRP, Vol. 40, 1 (1991), p. 571-575.

[4] Moriwaki, T.; Shamoto, E.: "Ultraprecision Diamond Cutting of Hardened Steel by Applying Elliptical Vibration Cutting", Annals of the CIRP, 48(1999)1, p. 441-444.

[5] Brinksmeier, E.; Gläbe, R.: "Advances in Precision Machining of Steel". Annals of the CIRP Vol. 50/1/2001, p. 385 - 388.

DESIGN OF ACCURATE AND REPEATABLE KINEMATIC COUPLINGS

Martin L. Culpepper, Carlos Araque and Marcos Rodriguez

Massachusetts Institute of Technology, Cambridge, MA

Keywords: Kinematic coupling, accuracy, repeatability, fixture, compensation

1. INTRODUCTION

Kinematic couplings (KCs) are exact constraint devices that rely on point contacts to constrain components. Figure 1A shows a common three groove kinematic coupling that constrains six degrees of freedom when mated. Most research on kinematic couplings has concentrated on developing designs to achieve better repeatability [1, 2, 3]. Although repeatability is necessary for precision fixtures, it is not always sufficient. Fixture designers should also consider methods for improving the accuracy of these couplings.

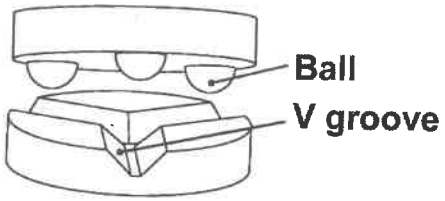

A: Three groove kinematic coupling

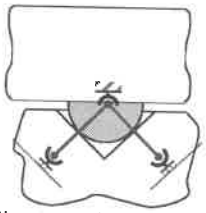

B: Analogy of ball-groove joint to a mechanism

Figure 1: Kinematic coupling geometry

The accuracy of a kinematic coupling is a function of systematic errors (e.g. errors in ball-groove size and placement) and other errors that may (e.g. wear) or may not (e.g. friction and surface finish effects) be measured and compensated for. Achieving accuracy in kinematic couplings requires careful attention to all of these error sources.

From a design/decision making standpoint, analytic tools that model the effect of some errors have recently been developed [4]. Other related work has addressed developing coupling designs capable of error compensation via adjustment in two [5] and three [6] axes. However; as kinematic couplings are generally used to constrain six DOF, we would like to be able to adjust in six axes. In addition, six-axis adjustability is beneficial as it enables one to control parasitic motions in other axes.

The purpose of this paper is to present a novel kinematic interface that can be used to make small displacement adjustments in six axes. This ability can be used to ensure a level of fixture accuracy that is limited primarily by the repeatability of the coupling. Subsequent sections present the concept for the new coupling, the theory used to model the adjustable kinematics of the device and the correlation between the adjustable kinematic theory and experimental data.

2. CONCEPT FOR ADJUSTABLE KINEMATIC COUPLING

One can think of the constraints between balls and grooves as "legs" of a Stewart platform (see Fig. 1B). From the analogy one can see that displacement between top and bottom platforms in Fig. 2A can be obtained by selectively changing the relative location of the balls with respect to the top platform. The figure shows a simple means[1] to accomplish this where the balls are attached to a shaft. The shaft axis is eccentric to the center of the ball, by distance E. All shafts are constrained within one of the mated components by bearings and a dual motion actuator. Using the actuators, any or all of the ball-shaft assemblies may be held rigid, or allowed to rotate and/or translate along the shaft's axis.

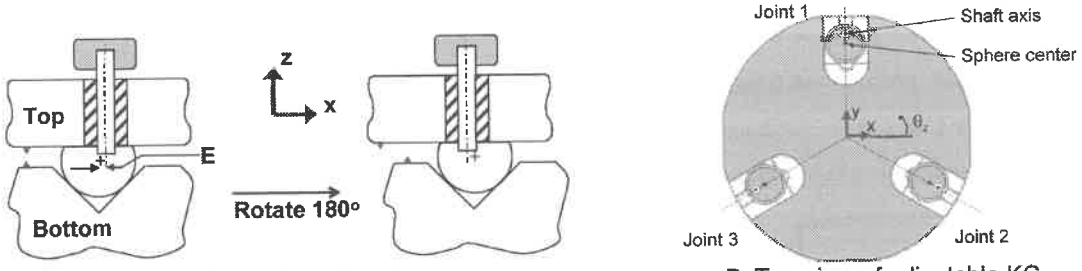

A: Adjustable KC joint
[Top and bottom platform displaced locally by 2E]

B: Top view of adjustable KC
[Top platform removed for clarity]

Figure 2: Concept for spatially adjustable kinematic coupling

When one or more shafts are revolved, the pattern of ball centers changes and the relative x, y, and θ_z position of the coupled components changes to maintain geometric compatibility between the grooves and the new ball pattern. For instance, if we assume a 120° coupling and common eccentricity between all balls, rotating balls 2 and 3 equal amounts from a homed position, but in opposite directions will result in pure y translation between the components. These positions may be deterministically controlled by selectively rotating the three shafts. This design has the advantage that the eccentric mechanism can provide small transmission ratios for in-plane displacements. For instance, if the eccentricity between ball center and shaft axis is 125 microns, it is theoretically possible to achieve in-plane position resolution better than ~ 1.5 $^{\text{micron}}/_{\text{degree of shaft rotation}}$ (when one ball is rotated). A small value of eccentricity also makes it difficult to back drive the coupling as the back drive torque on the shaft is proportional to the contact forces and eccentricity. In general, friction forces between the balls and grooves are sufficient to resist the back driving torque when the eccentricity is on the order of a few hundred microns.

We now consider out –of –plane displacements. When any shaft translates along its axis, relative displacement in z and rotation about the x and y axes may be controlled. This non-planar method is similar to three point adjustable mounts used in optical fixtures and three-axis adjustable kinematic mounts [6].

---

[1] Patent pending, Culpepper, 2001

3. ADJUSTABLE KINEMATIC ANALYSIS

The following in-plane and out-of-plane analyses have been verified via simulation with a solid model of an adjustable kinematic coupling. A comparison of experimental data and theory will be presented in section 5.

3.1. In-plane adjustable kinematics

In-plane modeling of adjustable kinematics is based upon vector loops through the structure of the coupling as shown in Fig. 3. Assuming small angle approximations of coupling rotations, we can use the projections of these vectors on the coupling plane in our in-plane analysis. Subsequent discussions of vectors are based on the projection of these vectors onto the plane of coupling unless otherwise stated. The path of one loop (for ball-groove $i = 1$) is explained via legend in Fig. 3.

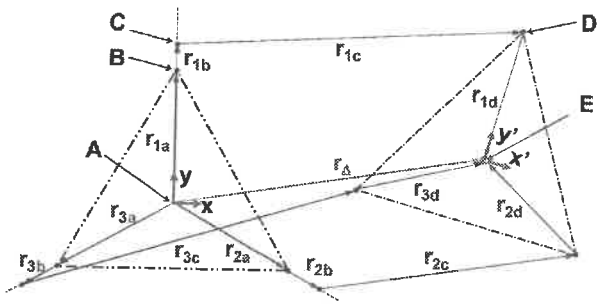

Legend for vector loop 1 (e.g. ball 1)

A. Static coupling centroid [bottom component with grooves]
B. Ball center at home position
C. Ball center displaced from home
D. Shaft axis
E. Mobile coupling centroid [top component with balls]

Figure 3: Vector based model for in-plane adjustable kinematic analysis

The three vector loops are coupled together by vector r_{Δ}. Two equations (one in x and one in y) are extracted from each vector loop and combined to produce Eq. (1). In our kinematic analysis, $s[\theta]$ and $c[\theta]$ are used as abbreviation for sine[θ] and cosine[θ] respectively. Subscripts denote variables associated with specific vectors, for instance, θ_{1a} denotes the direction of vector r_{1a} with respect to the x-y coordinate system Variables of the form L_{ij} signifiy the magnitude of vector r_{ij}'s projection on the plane of coupling.

When all vectors r_{ic} are aligned with their respective groove's plane of symmetry, e.g. $\theta_{ic} = \theta_{ia}$, the coupling lies in its home position and coordinate systems x-y and x'-y' are coincident (see Fig. 2 as well). Vectors r_{ia} lie along the plane of symmetry of grooves ia and all r_{id} lie along the angle bisectors of a triangle formed by the intersection of the shaft axes with the homed plane of coupling. In developing this set of equations we have assumed small angle rotations (on the order of 1000 μradians) about the z axis and therefore have linearized θ_z. Given the coupling geometry, Eq. (1) can be solved for approximate values of in-plane displacements from a homed/calibrated position.

$$\begin{bmatrix} c[\theta_{1b}] & 0 & 0 & -1 & 0 & L_{1d}\cdot s[\theta_{1a}] \\ s[\theta_{1b}] & 0 & 0 & 0 & -1 & -L_{1d}\cdot c[\theta_{1a}] \\ 0 & c[\theta_{2b}] & 0 & -1 & 0 & L_{2d}\cdot s[\theta_{2a}] \\ 0 & s[\theta_{2b}] & 0 & 0 & -1 & -L_{2d}\cdot c[\theta_{2a}] \\ 0 & 0 & c[\theta_{3b}] & -1 & 0 & L_{3d}\cdot s[\theta_{3a}] \\ 0 & 0 & s[\theta_{3b}] & 0 & -1 & -L_{3d}\cdot c[\theta_{3a}] \end{bmatrix} \cdot \begin{pmatrix} L_{1b} \\ L_{2b} \\ L_{3b} \\ x \\ y \\ \theta_z \end{pmatrix} \approx \begin{pmatrix} (L_{1d}-L_{1a})\cdot c[\theta_{1a}]-L_{1c}\cdot c[\theta_{1c}] \\ (L_{1d}-L_{1a})\cdot s[\theta_{1a}]-L_{1c}\cdot s[\theta_{1c}] \\ (L_{2d}-L_{2a})\cdot c[\theta_{2a}]-L_{2c}\cdot c[\theta_{2c}] \\ (L_{2d}-L_{2a})\cdot s[\theta_{2a}]-L_{2c}\cdot s[\theta_{2c}] \\ (L_{3d}-L_{3a})\cdot c[\theta_{3a}]-L_{3c}\cdot c[\theta_{3c}] \\ (L_{3d}-L_{3a})\cdot s[\theta_{3a}]-L_{3c}\cdot s[\theta_{3c}] \end{pmatrix} \quad (1)$$

3.2. Out-of-plane adjustable kinematics

Starting from an initial calibrated position and given the translation of each shaft, it is possible to calculate out-of-plane changes in position. In our analyses, out-of-plane position changes occur with respect to a homed position where:

- Balls are located the same distance from the component they are attached to
- Opposing faces of coupled components are parallel and separated by a given gap

The z position of each ball is set to 0.0 and a plane containing the centers of the balls is defined in this position. Out-of-plane position changes are captured using the translations of the balls with respect to the top platform to define a new plane. Given the equation of each plane, we find the difference in out-of-plane position between the initial and displaced coupling configurations. Assuming small angle approximations and neglecting second order terms, out-of-plane displacements can be approximated via Eqs. (2) - (4).

$$\theta_x \approx -\frac{L_{1d}\cdot(s[\theta_{1a}]\cdot\theta_z - c[\theta_{1a}])\cdot(z_2-z_3)+L_{2d}\cdot(s[\theta_{2a}]\cdot\theta_z - c[\theta_{2a}])\cdot(z_3-z_1)+L_{3d}\cdot(s[\theta_{3a}]\cdot\theta_z - c[\theta_{3a}])\cdot(z_1-z_2)}{L_{1d}\cdot L_{2d}\cdot s[\theta_{2a}-\theta_{1a}]+L_{2d}\cdot L_{3d}\cdot s[\theta_{3a}-\theta_{2a}]+L_{3d}\cdot L_{1d}\cdot s[\theta_{1a}-\theta_{3a}]} \quad (2)$$

$$\theta_y \approx \frac{L_{1d}\cdot(s[\theta_{1a}]+c[\theta_{1a}]\cdot\theta_z)\cdot(z_2-z_3)+L_{2d}\cdot(s[\theta_{2a}]+c[\theta_{2a}]\cdot\theta_z)\cdot(z_3-z_1)+L_{3d}\cdot(s[\theta_{3a}]+c[\theta_{3a}]\cdot\theta_z)\cdot(z_1-z_2)}{L_{1d}\cdot L_{2d}\cdot s[\theta_{2a}-\theta_{1a}]+L_{2d}\cdot L_{3d}\cdot s[\theta_{3a}-\theta_{2a}]+L_{3d}\cdot L_{1d}\cdot s[\theta_{1a}-\theta_{3a}]} \quad (3)$$

$$z_c \approx L_{1d}\cdot(\theta_y\cdot c[\theta_{1a}]-\theta_x\cdot s[\theta_{1a}])+z_1 \quad (4)$$

In Eqs. (2) – (4), z_i denotes the displacement of the center of ball ***i*** from its out-of-plane home position.

4. PROTOTYPE AND EXPERIMENTAL SETUP

The prototype and experimental setup used to test the concept are shown in Fig. 4A and Fig. 4B respectively. Critical prototype design characteristics are given in Table 1. To minimize the risk associated with wear, friction hysteresis and surface irregularities, the balls and grooves were polished then coated with a 5 μm TiN layer followed by a 1 micron thick WS_2 layer (for lubrication). These surface treatments provided a 90 nm rms surface, surface hardness of 88 RC and static friction coefficient of 0.1. When a position change was desired, the coupling was decoupled, actuation was performed, then the coupling was re-engaged. This cycle was used to prevent relative sliding between ball and groove that would lead to wear at the ball-groove contacts.

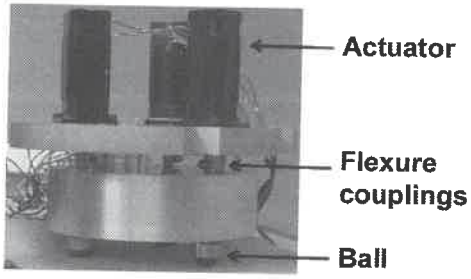

A: Prototype
[grooved component removed for clarity]

B: Prototype with supporting experimental hardware

Figure 4: Prototype and experimental set up

Table 1: Characteristics of prototype coupling

Coupling diameter	152.4 mm	**Ball/groove material**	304L Stainless
Ball radii of curvature	63.5 mm and 31.75 mm	**Included groove angle**	90 degrees
Eccentricity	Ball 1 = 165 microns	Ball 2 = 318 microns	Ball 3 = 363 microns

The coupling is driven by three dual-motion actuators with 0.225 degree rotary resolution and 10 microns linear resolution. Run-out of the actuators (measured at 25 microns) was decoupled from rotary ball motion by two sets of flexures. The actuators are connected to the kinematic coupling via flexures and coupled to the ball-shaft assemblies by flexural couplings. To increase radial stiffness and eliminate clearance error between bearings and shafts, a radial interference of 1.5 microns was specified between each shaft and its linear-rotary bearing. After extensive testing, we found that this level of interference increases the rolling friction somewhat, but has otherwise not adversely affected bearing performance. The prototype was mounted in a test fixture which houses six capacitance probes and provides 550 N nesting preload through the coupling centroid.

5. EXPERIMENTAL RESULTS

Figure 5 shows a comparison of theoretical predictions for in-plane displacement tests. The independent variable is the angle vector r_{ic}'s projection makes on the plane of coupling. This vector points from the i^{th} ball center to the respective shaft axis. Systematic errors for the in-plane data sets in Fig. 5 show maximum error of 13% between theory and experiment. Data sets for out-of-plane displacements show similar results, but are not included due to space limitations. Random errors due to friction and surface irregularities were quantified at less than 2 micron via repeatability tests. Bearing run-out contributes to random errors and was measured at 1.5 microns. Due to the limitations of the capacitance probe's measurement range, we were not able to take data over the fully actuated range for each ball (+/- 90° from home position). A planned reduction of eccentricity will allow us to measure performance over the entire work volume. Systematic errors were less than 13% and likely due to error in the measurement of eccentricities and ball-groove size and placement. Fortunately, the systematic errors can be mapped and eliminated through compensation techniques.

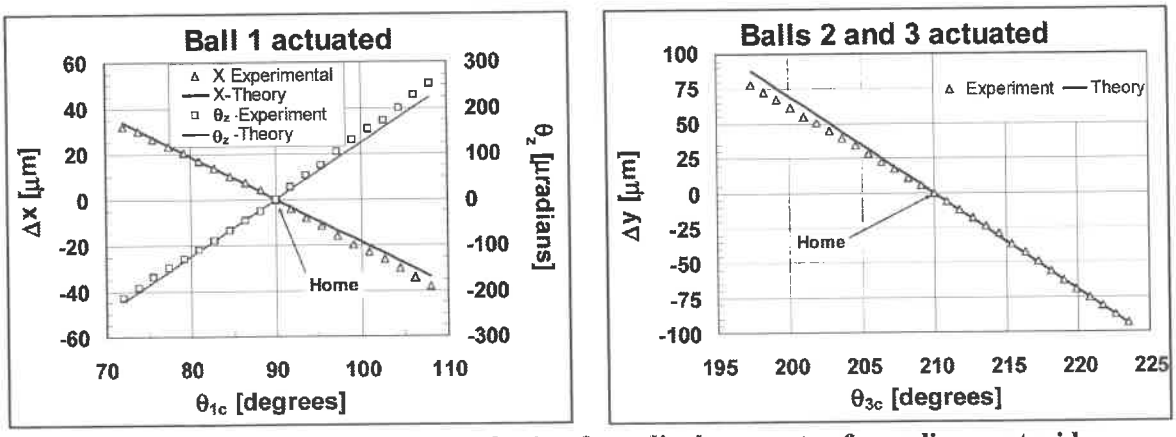

Figure 5: Experimental data vs. theory for in-plane displacements of coupling centroid

6. CONCLUSIONS

The systematic error between the adjustable kinematic theory and experimental is about 13%. Subsequent work will concentrate on mapping these errors and modifying the model to compensate for them. The maximum error occurs near the edge of our data acquisition ability, and must be further investigated over the full range of ball motions (+/- 90° from home position). Random errors limit the repeatability and accuracy of the current design to approximately 2 - 3 microns. Subsequent work will seek to improve coupling calibration and reduce the magnitude of random errors.

7. ACKNOWLEDGEMENTS

We would like to thank BryCoat for their technical support and generous donation of coating services for the balls and grooves used in our experiment.

8. REFERENCES

[1] Slocum A. Design of Three-Groove Kinematic Couplings. Prec Eng 1992;14;67-73.

[2] Schouten CH, Rosielle PCJN, Schellekens PHJ. Design of a kinematic coupling for precision applications. Prec Eng;20;46-52.

[3] Hale LC, Slocum AH. Optimal Design Techniques for Kinematic Couplings. Prec Eng;25;114-27.

[4] Barraja, M. and Vallance, R. Tolerance Allocation for Kinematic Couplings, draft article for the 2002 ASPE Summer Conference, July 2002.

[5] Taylor, J. B., and Tu, J. F. Precision X-Y Microstage With Maneuverable Kinematic Coupling Mechanism, Precision Engineering, April, 1996, vol. 18, No. 2, p.85 – 94.

[6] Conversations with Eugene Gleason of Bal-tech with regard to three axis adjustable kinematic mounts, December 2001.

HEXFLEX: A PLANAR MECHANISM FOR SIX-AXIS MANIPULATION AND ALIGNMENT

Martin L. Culpepper, Gordon Anderson and Patrick Petri
Massachusetts Institute of Technology, Cambridge, MA

Keywords: Compliant mechanism, photonics alignment, assembly, micro-manipulation, optics

1. INTRODUCTION

The need for multi-axis micromanipulation in MEMS and photonics has driven the development of novel designs [1 – 3] that use three dimensional structures (e.g. hexapods) to achieve spatial position control. Simplicity of design and ease of manufacture/integration into MEMS devices would be improved if such devices were based on planar structures. The structure of the HexFlex™ [1], shown in Fig. 1, is entirely planar and capable of six-axis alignment. This paper presents the experimental validation of the theory used to design a low-cost micro-positioning stage using the HexFlex. The knowledge gained from this experiment will then be used to design small-scale versions of the HexFlex for MEMS and Microphotonic alignment/manipulation.

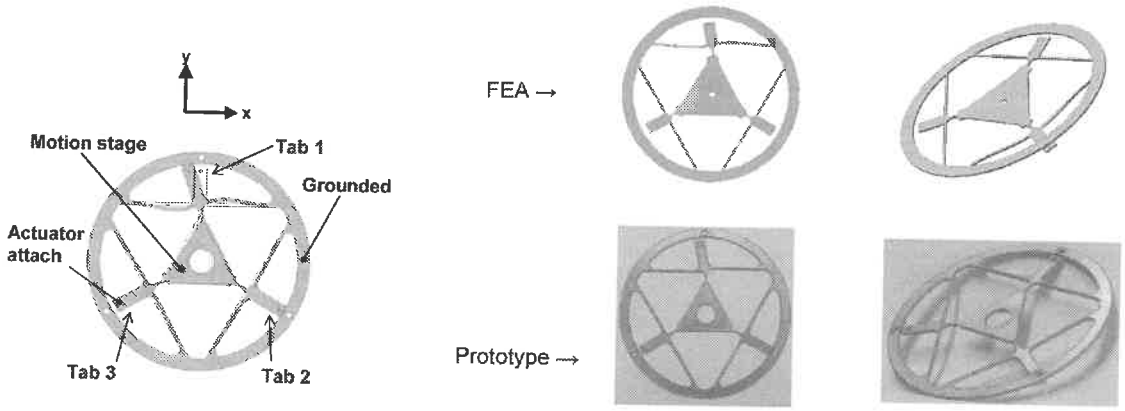

Figure 1: Generic HexFlex geometry and deformation response

2. MOTIVATION FOR DEVELOPMENT OF THE HEXFLEX SYSTEM

Ideally, one would like to have alignment manipulators integrated into Microsystems so that they can perform initial assembly positioning as well as in-service alignment corrections. Unfortunately, few small-

[1] Patent pending, Culpepper, 2001

scale spatial manipulators exist. As a result, six-axis alignment of Microsystems is generally achieved with manipulators that are roughly three orders of magnitude larger than the assembled components [2, 3]. Although recent efforts have produced novel small-scale versions of common macro-scale manipulators (e.g. MEMS hexapods) [1], friction at segmented joints poses a reliability problem for these machines. Some commercial products use MEMS thermal actuators to align components (in three axes) and then fix the alignment with temporary adhesive bonds [4]. Unfortunately, they do not present a comprehensive six-axis alignment solution and the dynamic response is limited by the time required to melt/solidify the adhesive. On the other hand, the HexFlex provides limited six axis motion without rubbing surfaces. The planar nature of the device and tensegrity-like structure offer improved dynamic response over three dimensional, segmented mechanisms.

The subsequent sections of this paper present the concept for the HexFlex, provide a brief overview of the means used to model the mechanism, and compare theoretical predictions with experimental data generated from tests on a low-cost, "proof of concept" prototype.

3. HEXFLEX CONCEPT

As shown in Fig. 1, six beams act as legs that connect the stage (triangle) to a grounded structure (shown as a ring). Three "tabs" are provided to interface the actuators with the HexFlex stage. In our example, one actuator drives a tab in-plane (for planar motion) while another actuates the end of a tab in the z direction (for out-of-plane motions). Ideally, planar and non-planar actuation motions would be decoupled with flexural bearings between the actuators and tabs; however for the purpose of constructing a low-cost prototype we opted to utilize a ball on flat contact between actuator and tab. As will be seen in section 6, this rough design is sufficient to obtain less than 5% error between experimental data and theory for the stage's centroid displacement. The "rough" nature of this tab-actuator interface will however be recognized when we examine parasitic errors.

Combinations of in-plane tab actuations may be used to position the stage in x, y, and θ_z. Out-of-plane tab actuations position the stage in z, θ_x, and θ_y. The curious reader may skip ahead to Fig. 4 to view intuitive examples of motions that are generated by simple displacements. Planar and non-planar displacements may be produced simultaneously.

4. MODELING HEXFLEX MOTIONS

The HexFlex was modeled using CoMeT™ (Compliant Mechanism Tool) developed by the Precision Systems Design and Manufacturing Research Lab at MIT. CoMeT is written in Matlab, fully utilizing its matrix manipulation capabilities. Given user inputs that define the compliant mechanism geometry, material, and constraints, CoMeT develops the global stiffness and compliance matrices via the direct

stiffness approach [5]. The analytic model developed by CoMeT is fully parametric and therefore amenable to a wide range of optimization routines within Matlab. This enables the designer to rapidly converge on an optimum design solution. The compliant mechanism design process is over an order of magnitude faster than design by FEA. Figure 2 shows screen shots of CoMeT during in-plane and out-of-plane simulations.

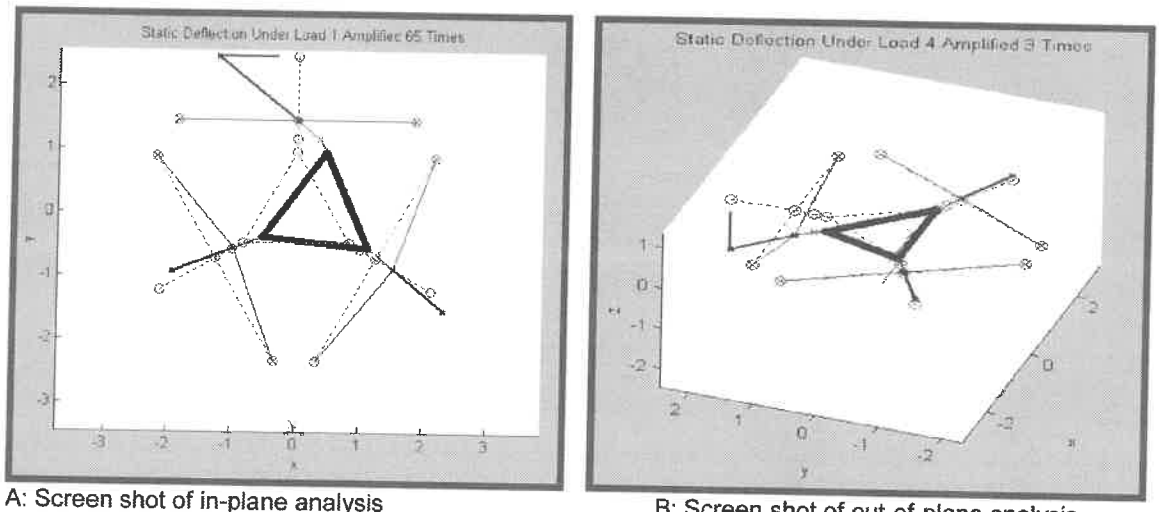

A: Screen shot of in-plane analysis B: Screen shot of out-of-plane analysis

Figure 2: CoMeT – Compliant mechanism design tool interface/GUI

5. EXPERIMENTAL PROTOTYPE

The experimental prototype and test fixture used to verify concept and theory are shown in Fig. 3. The HexFlex structure was designed and optimized using CoMeT. Critical prototype design characteristics are given in Table 1. Note that one of the advantages of the HexFlex concept is the potential to alter the transmission ratio between actuator and stage by changing the geometry and/or compliance of the respective tab. In some cases, near zero or negative transmission ratios may be obtained. For instance actuating the tabs in the negative z direction can result in stage displacement in the positive z direction if the structure is tuned properly.

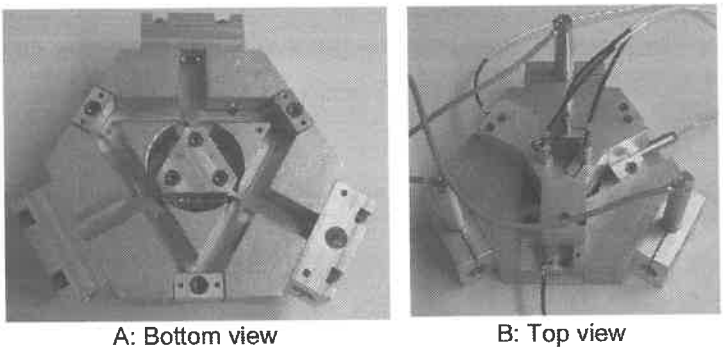

A: Bottom view B: Top view C: Exploded CAD view

Figure 3: Prototype HexFlex in test fixture

Table 1: Characteristics of prototype HexFlex mechanism	
Diameter of circle that encompasses the HexFlex	180 mm
HexFlex material	6061 Aluminum
Tab length / width / thickness	55 mm/5 mm/3.1 mm
Transmission ratio achieved via tabs	In-plane: $^{1}/_{15}$ and out-of-plane $^{1}/_{44}$

The main component of the test fixture is a monolithic aluminum base with a thru-hole at its center. Six piezoelectric actuators (40 micron stroke), six capacitance probes, and grounded portions of the HexFlex mechanism are rigidly attached to the base. HexFlex stage displacement is extracted from capacitance probe measurements of the target position (see Fig. 3, target is rigidly attached to the HexFlex stage).

6. EXPERIMENTAL RESULTS

Experimental data for three motion paths is compared to CoMeT predictions in Fig. 4. Note that the maximum linear displacement is less than 5 microns, however one hundred micron displacement has been obtained in preliminary tests with actuators that posses longer strokes. Experimental results show the maximum error between theoretical and experimental displacements is less than 5%. The largest parasitic motions of the stage centroid during all tests were 90 nm and 5 μradians. The "rough" design of the tab-actuator interface and the "as machined" surfaces used to align actuators to the tab are likely causes of the parasitic motions. Manufacturing errors in the HexFlex geometry that are not captured in the CoMeT model are another likely source of error.

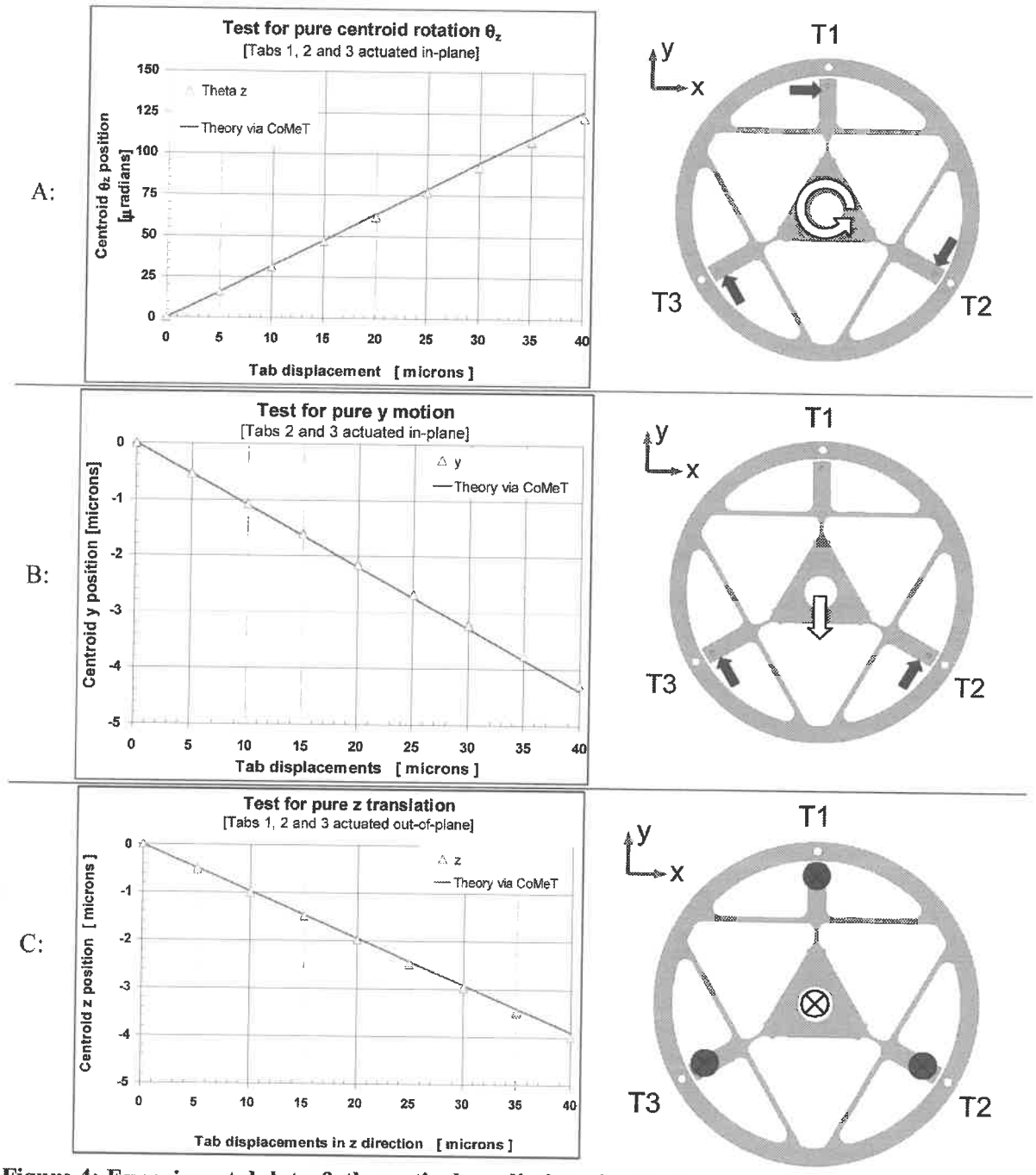

Figure 4: Experimental data & theoretical predictions for HexFlex displacements

Note: Solid arrows represent direction of positive actuation (● signifies away from viewer). Centroid displacements/positions are referenced with respect to the global coordinate system given in the respective legend sketch.

7. CONCLUSIONS AND NEXT STEPS

Although parasitic errors are large for a precision micromanipulation stage, the accuracy of the actuated displacements provides confidence in the CoMeT model. Future efforts will address reducing the parasitic errors by redesigning the tab-actuator interface. The design of HexFlex stages for active alignment tasks in Microphotonic and MEMS are presently underway.

8. REFERENCES

[1] Bernhard, J., Benavides, L., and Allen, J., "Planar and Spatial Three-Degree-of-Freedom Micro-stages in Silicon MEMS", Proceedings of the 16th Annual ASPE Meeting, November, 2001.

[2] Dagalakis, N., and Amatucci, E., "Kinematic Modeling of a 6 Degree of Freedom Tri-stage Micro-Positioner", Proceedings of the 16th Annual ASPE Meeting, November, 2001.

[3] Kota, Sridhar, "Exploiting Elasticity in Engineering Design: Synthesis and Applications", Invited Lecture at MIT Fall 2001 Mechanical Engineering Seminars, September 28, 2001.

[4] US Patent 6,253,011, "Micro-aligner for precisely aligning an optical fiber and an associated fabrication method".

[5] Kurtis R. Gurley, Direct Stiffness: Beam application, CES4141 Lecture Notes, Summer1998, www.CE.UFL.EDU/~KGURL/.

[6] Petri, P., "A Continuum Mechanic Design Aid for Non-planar Compliant Mechanisms," Masters Thesis, MIT, Cambridge, MA, September 2002.

Kinematic and Stiffness Analysis of a Novel Ortho-Guided Tripod Machine Tool

Wei-Yao Hsu*and Jenq-Shyong Chen**
National Chung Cheng University, Department of Mechanical Engineering
* Ph.D. Student, **Professor

Abstract

This paper introduces a novel parallel kinematic machine (PKM) called Ortho-Guided Tripod (OGT) which is constrained to move in X, Y, and Z-directions by using an orthogonal guiding system. This paper analyzes the kinematic and stiffness of the OGT machine. It shows that the OGT machine has more consistence and higher stiffness over the workspace. The position of the OGT machine is directly measured along the unforced orthogonal guiding system which is separated from driving system, it means joint location and deformation, and thermal expansion of the OGT can be neglected, and the OGT has higher accuracy.

Keywords: Tripod, parallel kinematic machine

Introduction

The development of the parallel kinematic machines (PKMs) has been moved from six parallel-links to three parallel-links [1], for six parallel-links structure has some disadvantages: 1. poor ratio of workspace to machine size, 2. singularity problems, 3. complicated solutions of kinematic model, and 4. high cost of servo control system [2][3].

There are some commercial three parallel-links machines such as Tricept from Neos Robotics AB which is constrained by linear central tube and universal joint, Delta C300 form Hitachi, Ltd. which is constrained by the universal joints of one end of the links, and SKM400 form Heckert GmbH which is constrained by the rotary parallel 4-bar linkages.

We introduce a new kind of three parallel-links machines called Ortho-Guided Tripod (OGT) which is constrained by three orthogonal linear guides, as shown in the Fig. 1. OGT machine used ball joint of the link end attached moving platform and universal joint of the other end, and used the orthogonal linear guides, so that the OGT machine has three degree of freedoms. By using the orthogonal linear guide way system, we should put the position sensors on the guide ways, and the high precision of the moving platform can be expected.

It is well known that parallel kinematic machine has high rigidity due to its strut construction. But there are some different opinions [5] [6], for the components such as ball joints and universal joint used in the PKMs have poor rigidity. The static stiffness analysis of the parallel kinematic machine which can be represented by Jacobian matrix has been studied by many researchers [7] [8] [9]. We drive Jaocbian matrix from kinematic constraint equations of the new kind machine and evaluate the stiffness map.

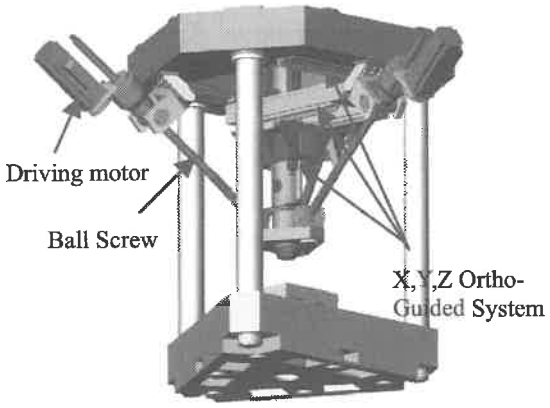

Fig. 1 Ortho-Guided Tripod Machine Tool

Inverse kinematic

The inverse kinematic problem is to find the limb lengths q_1, q_2, and q_3, when the moving coordinates X are given. That is

$q = Inv(\rho, X)$, where ρ is the kinematic parameters of tripod machine.

The inverse kinematic model can be obtained through vector loop analysis. As shown in fig. 2, the closed vector loop of each limb can be described as

$$B_i + Q_i = X + RP_i, \quad i = 1 \sim 3 \qquad (1),$$

where,

$B_i = [B_{ix} \;\; B_{iy} \;\; B_{iz}]^T$: base-joint location vector related to global coordinate,

$Q_i = [Q_{ix} \;\; Q_{iy} \;\; Q_{iz}]^T$: leg vector related to global coordinate,

$X = [x \;\; y \;\; z]^T$: platform position vector related to global coordinate,

$P_i = [P_{ix} \;\; P_{iy} \;\; P_{iz}]^T$: platform-joint location vector related to moving platform,

R: rotation matrix of moving platform related to global coordinate,

q_i: limb length.

The length of each leg is determined as:

$$q_i = \|Q_i\| = \|X + RP_i - B_i\|, i = 1 \sim 3 \qquad (2).$$

Since the orientation of the platform is constraint by orthogonal three slides, the rotation matrix **R** in the equation (2) is an identity matrix.

Forward Kinematic

The forward kinematic problem is to determine the position of the moving platform, i.e. $X = for(\rho, q)$.

If we arrange the coordinates of the three base-joints and three platform-joints as P1 $\left(-r_p\sqrt{3}/2,-r_p/2,0\right)$, P2 $\left(r_p\sqrt{3}/2,-r_p/2,0\right)$, P3 $(0,r_p,0)$, B1 $\left(-r_b\sqrt{3}/2,-r_b/2,0\right)$, B2 $\left(r_b\sqrt{3}/2,-r_b/2,0\right)$, and B3 $(0,r_b,0)$, and substitute these coordinated into the Eq. *2*, the forward kinematic model can be determined as:

$$x=\frac{q_1^{\,2}-q_2^{\,2}}{2\sqrt{3}\left(r_b-r_p\right)} \qquad (3a),$$

$$y=\frac{q_1^{\,2}+q_2^{\,2}-2q_3^{\,2}}{6\left(r_b-r_p\right)} \qquad (3b),$$

$$z=-\left(q_3^{\,2}-\left(\frac{q_1^{\,2}-q_2^{\,2}}{2\sqrt{3}\left(r_b-r_p\right)}\right)^2-\left(\frac{q_1^{\,2}+q_2^{\,2}-2q_3^{\,2}}{6\left(r_b-r_p\right)}-\left(r_b-r_p\right)\right)^2\right)^{1/2} \qquad (3c).$$

Notice that the forward kinematic model of the innovative tripod machine is a closed form solution. The time-consuming and iterated numerical analysis of the forward kinematic solution is eliminated.

Stiffness Analysis

In this section we develop methods for representing static forces acting on a tripod machine tool and for transforming them to the Cartesian-coordinates system.

First, let the stiffness matrix of each actuate link be defined as:

$\tau = K_s \cdot \Delta q$ (4),

where $K_s = diag[k_{s1},k_{s2},k_{s3}]$: the stiffness matrix of the actuator space,

$\tau = [\tau_1 \ \tau_2 \ \tau_3]^T$: forces applied at the actuate link,

$\Delta q = [q_1 \ q_2 \ q_3]^T$: deformations of each link.

The deformations of the actuate links have the geometric relationship as follow:

$\Delta q = J\Delta X$ (5),

in which $J=\left[\frac{X+RP_1-B_1}{\|X+RP_1-B_1\|} \ \frac{X+RP_2-B_2}{\|X+RP_2-B_2\|} \ \frac{X+RP_3-B_3}{\|X+RP_3-B_3\|}\right]^T$ is found by differentiating Eq. 2.

Using the potential energy principle, we have the following relationship:

$$V_s=\frac{1}{2}\Delta X^T K_d \Delta X=\frac{1}{2}\Delta q^T K_s \Delta q \qquad (6),$$

where K_d is the stiffness matrix of the tripod machine tool transformed to Cartesian-coordinates system. Substituting Eq.5 into Eq. 6, we have:

$$K_d = J^T K_s J \qquad (7).$$

Eq. 7 implies that the external force applied on the end-effector is related to its deformation by the stiffness matrix K_d. Assume each actuate link have the same stiffness. Then Eq. 7 can be rewritten as:

$$K_d = k_s J^T J \qquad (8).$$

In eq.8 k_s is the combination stiffness of each actuate link including the universal-joint, ball-

screw/nut, and ball-joint. As an example of a workspace 400mm_400mm_300mm (X_Y_Z), Table 1 shows the computer simulation results of the stiffness of each type OGT machines for different link horizontal angles.

Table 1 Stiffness OGT machines

horizontal angle	Stiffness range Kxx/Kyy/Kzz (100N/μm)
45°	1.2~2.6/1.3~2.6/2.7~4.3
60°	0.6~1.4/0.7~1.5/4.5~5.8

Conclusion

In this paper, we present a new kind of Tripod machine that the moving platform is guided by the three orthogonal linear guide ways. By putting the position sensors on the guide way system, the volumetric error of OGT machine is determined by accuracy of the guide way system but no the link and joint errors. We also show that the stiffness of the Tripod machine is higher and more consistent over the workspace than the conventional serial machines.

Reference

1. Volker Maier, The parallel universe, American Machinist, The International Magazine of Manufacturing Technology, August, 2001, pp.74-77
2. Günter Pritshow, Parallel Kinematic Machines (PKM)-Limitation and New Solutions, Annals of the CIRP Vol. 49/1/2000, pp. 275-280.
3. F. Rehsteiner, R. Neugebauer, S. Spiewak, and F. Wieland, Putting Parallel Kinematics Machines (PKM) to Productive Work, Annals of the CIRP, Vol. 48/1/1999, pp. 345-350.
4. G.. Q. Cai., M. Hu, C. Guo, B. Li, and Q. M. Wang, Development and Study of a New Kind of 3-DOF Tripod, Annals of the CIRP Vol. 48/1/1999, pp. 333-336..
5. Jiri Tlusty, John Ziegert, Shanon, Ridgeway, Fundamental Comparison of the Use of Serial and Parallel Kinematics for Machine Tools, CIRP, Vol. 48/1/1999, pp. 351-356.
6. Jiri Tlusty, John Ziegert, Shanon, Ridgeway, A Comparison of Stiffness Characteristics of Serial and Parallel Machine Tools, Journal of Manufacturing Processes, Vol. 2, No. 1, 2000, pp. 67-76
7. Gossslin. C., Stiffness Mapping for Parallel Manipulators, IEEE Trans. Robot. Autom. Vol. 6, pp. 377-382.
8. Lung-Wen Tsai, Robot Analysis – The Mechanics of Serial and Parallel Manipulator, John Wiley & Sons, Inc. 1999.
9. Tian Huang, Xingyu, Zhao, and David J. Whitehouse, Stiffness Estimation of a Tripod-Based Parallel Kinematic Machine, IEEE Transaction on Robotics and Automation , Vol. 18, No. 1, Feb. 2002.

Micro Turning System: A Super Small CNC Precision Lathe for Microfactories

Sumio Ito*, Daisuke Iijima*, Akira Hayashi*, Hisayuki Aoyama**, and Masashi Yamanaka***
*Nano Corporation, Tokyo, Japan
**University of Electro-Communication, Tokyo, Japan
***Tohoku University, Sendai, Japan

Introduction

Micro Turning System (MTS) is a palm-top precision lathe that has a machine base size of 150 x 100 mm (postcard size) and PC (personal computer) based CNC (computerized numerical control) with linear/circular interpolation. The machine was developed to be a substitute for conventional NC lathes: heavy, huge, high-powered machines even for manufacturing very small parts. MTS is capable of machining brass with a surface roughness of 0.20 μm and a circularity of 0.19 μm.

Figure1: MTS packaged in a suitcase

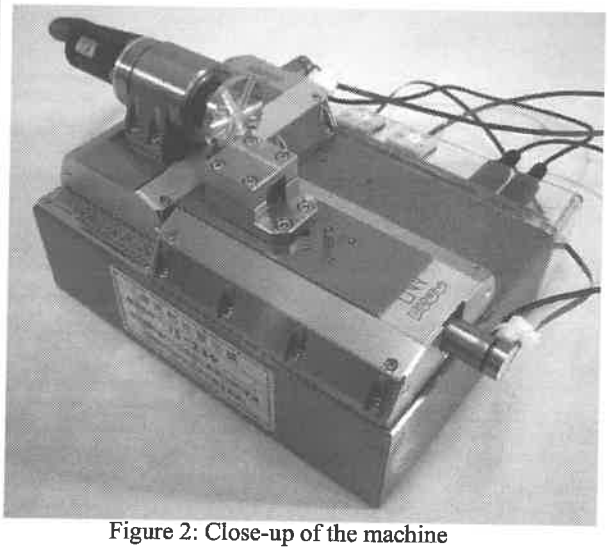

Figure 2: Close-up of the machine

Background

The use of over-sized machines for small parts results an over consumption of energy that have been ignored in today's mass production systems; however, the market demands further efficient ways of manufacturing. Lower energy consumption will be obtained by utilizing smaller machines with the parts' size becomes smaller. Small machines will also let manufacturers have more flexible factory layout that will be fit for a "large item small volume production" method. Such idea led to the concept of *Microfactories*, a production system that is constructed only with *micro machines* [1]. Several engineering colleges and institutions have already developed some prototypes of Microfactories but not yet for practical applications. One reason that prevents the micro machines from practical use is lack of accuracy; that is, precision machining is necessary for most of the small parts that are to be machined with such micro machines. While conventional precision machines have large and heavy components to obtain higher rigidity and fewer vibrations, miniaturized machines may have less rigidity and more vibrations; consequently,

the accuracy of products machined with micro machines will get worse. If the micro machines could obtain enough accuracy, the Microfactories will be practical.

Main Features of MTS

MTS is consisted with a postcard-sized machine bed, X and Z-axis for main spindle and tool holder respectively, and motor control system. The machine is designed to have high rigidity and less vibration for precision machining of practical parts at lower cost in the smallest machine size we've ever had. The specifications of MTS are listed on the table below.

Machine Base Size		150 x 100 mm
Maximum Cutting Length		10 mm
Maximum Chucking Diameter		5 mm
Main Spindle	Reducer Type	Traction Drive
	Maximum Speeds	10,000 rpm
	Radial Rigidity	2.8 N/μm
	Axial Rigidity	2.3 N/μm
	Run-Out	1.0 μm
X/Z-Axes	Slide Type	Cross Roller
	Feed Type	Slide Screw (0.2 mm pitch)
	Table Stroke	12 mm
	Rapid Traverse	2.4 m/min
	Smallest Feed	0.2 μm
	Radial Rigidity	8.9 N/μm
	Thrust Rigidity	1.1 N/μm
	Positioning Accuracy	1.0 μm
Motors for Axes	Type	Brushless DC Servo
	Rated Output	10 W
	Rated Torque	2.5 mNm
	Max. Torque	11 mNm
Motors for Axes	Type	Micro AC Servo
	Encoder Resolution	1024 pulse/rev
	Rated Output	2 W
	Rated Torque	1.9 mNm
	Max. Torque	3.8 mNm

Table 1: Specifications of MTS

X and Z-Axis

Both X and Z-axes are driven by 0.2-mm-pitch threads and have cross-roller ways for their slide. The cross roller is preferred over the other types of slide, such as static air/oil slide that has higher rigidity and fewer vibrations, because the cross roller has relatively high rigidity and no need of extra power or extra cost. Each motor for the axes is Yaskawa Electric's AC servo that has a diameter of 10 mm, a power consumption of 2 W, and a 1024-pulse-per-revolution encoder [2]. The encoder signal is feed backed in semi-closed loop to control each axis with a smallest feed of 0.195 μm. The picture of the X/Z-axis is shown on Figure 2. Figure 3 shows the deviation of positioning for 1-pulse feed (0.195 μm): the error is within 0.6 μm from a desired value for about 20-μm feed.

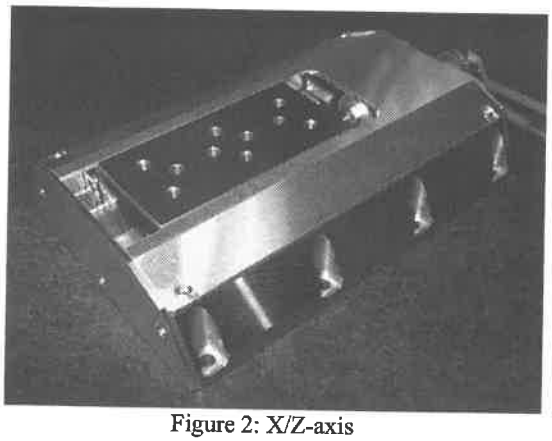

Figure 2: X/Z-axis

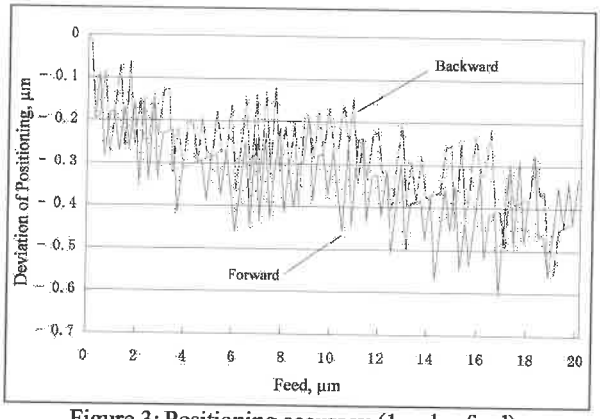

Figure 3: Positioning accuracy (1-pulse feed)

Main Spindle

The main spindle has a motor, a traction-drive planetary roller reducer, a set of angular ball bearings, and a collet-chuck that has the maximum chucking diameter of 5 mm. The ball bearings are chosen because of the same reason with the slides—no need of any extra power. The planetary roller reducer, which has a speed reduction ratio of 4:1, is installed to increase the motor torque. The traction drive is used instead of micro planetary gears, because the traction drive makes fewer vibrations and is fabricated at lower cost. The size of the spindle is 27 mm in diameter and the maximum speed is 10,000 rpm.

Figure 4: Main spindle

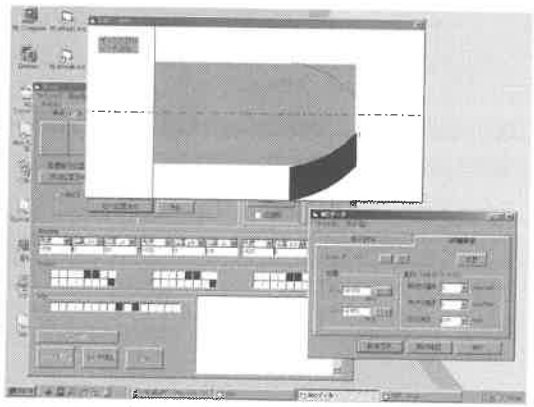

Figure 5: NC controller

Control System

The motor control system is consisted with a set of motor driver and controller, sensor amplifiers, a 12-volt-DC power source, a PC, and a NC program. The NC program, that has linear/circular interpolation, runs on the PC with Windows 98/2000, and the NC data is transmitted to the motor controllers via Arcnet interface. The program is based on a motor controller for the Micro AC Servo provided by Yaskawa Electric Co., and modified as the NC program using Visual Basic by Nano Corp. Users can create the NC data either using drawing feature of the program or directly inputting coordinate data. The NC control panels on the PC screen is shown on Figure 5.

Test Cutting and Results

Several materials (Brass, Aluminum, Steel, and Stainless Steel) were turned and brass (C3604) was appeared to be

the best finished. Turning a 5-mm-diameter cylinder with a cutting speed of 23.6 m/min, we obtained a surface roughness of 0.03 μm (Ra) and circularity of 0.19 μm. Shape accuracy was 5 μm that was caused by an error occurred in a censor installed in the axes. The results above show the MTS has an enough ability to be a precision lathe and micro machines have potential to construct Microfactories.

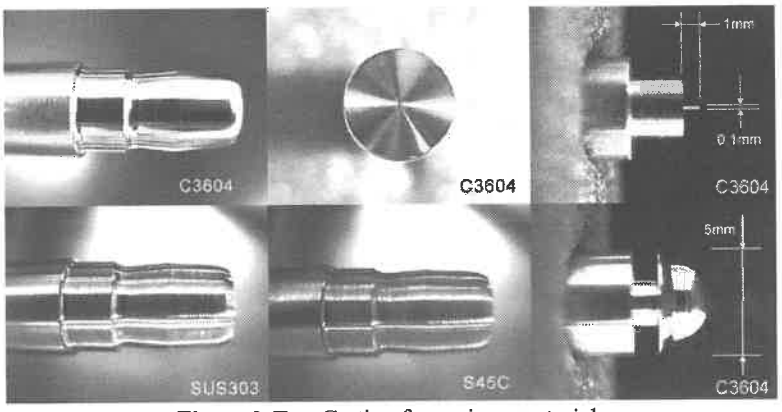

Figure 6: Test Cutting for various materials

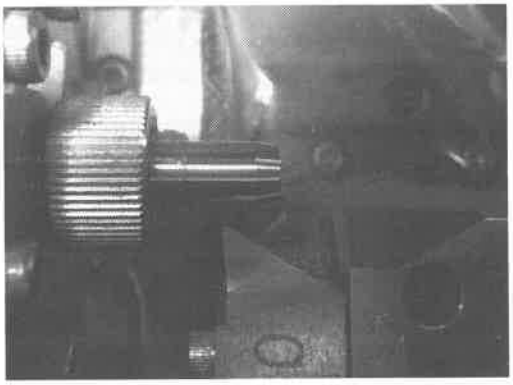

Figure 7: Turning stainless steel

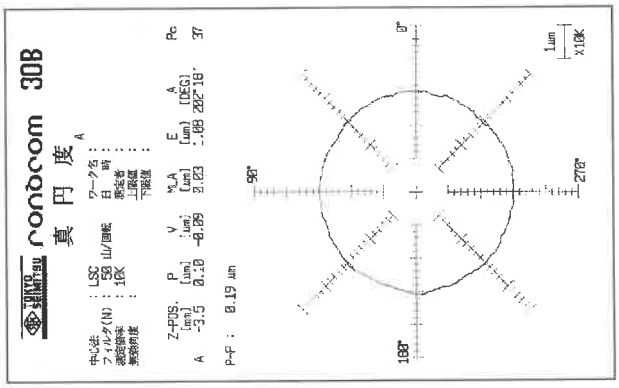

Figure 8: Circularity for turned brass

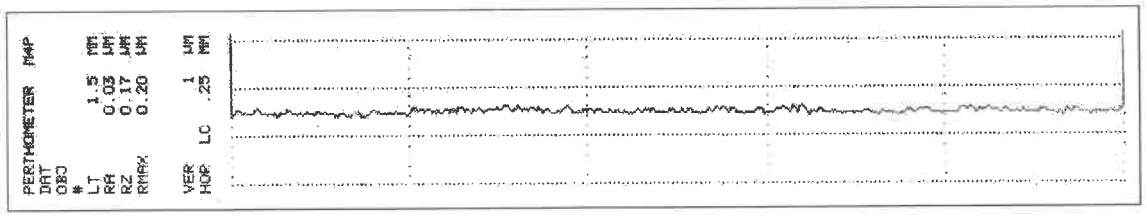

Figure 9: Surface roughness for turned brass

References

[1] Y. Okazaki, T. Kitahara, *Development and Evaluation of a Micro-Lathe Equipped with Numerical Control,* Journal of the JSPE 67, 11 (2001) p.1878.

[2] H. Nakamura, T. Matsuo, K. Matsuzaki, K. Uemura, T. Kabashima of Yaskawa Electric Corporation, *Development of Micro Servo Actuators,* Proc. 2nd International Workshop on Microfactories, p.133.

OPERATION AND ANALYSIS OF A NANOPOSITIONING AND NANOMEASURING MACHINE

Gerd Jäger, Eberhard Manske, Tino Hausotte and Walter Schott
Technische Universität Ilmenau, Germany, 98684 Ilmenau, P.O. Box 100 565

Key words: nanomeasuring, nanopositioning, interferometers, nanometer-accuracy

1 Introduction

Nanopositioning and nanomeasuring machines (NPM machines) are technological means of positioning, measurement, scan, treatment and manipulation of objects with nanometer precision. Current and future high technologies such as microelectronics, micromechanics, optics, molecular biology and material engineering demand increasing ranges of motion, extreme precision and high positioning speeds. Furthermore, novel probe systems and nanotools have to be integrated into these machines to make them suitable for various tasks such as nanostructuring, mask and wafer inspection, large-area scanning probe microscopy, biotechnology and genetic engineering as well as measuring mechanical precision workpieces, precision treatment and assembly in the field of micro- and nanotechnology or for engineering new materials.

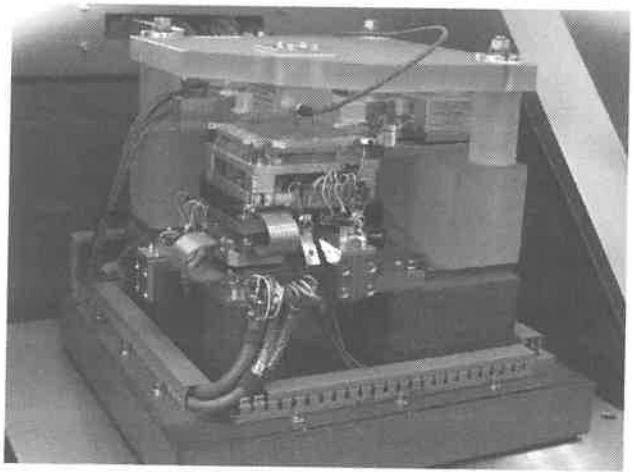

Figure 1: Nanopositioning and nanomeasuring machine with a optical probe system

At the Institute of Process Measurement and Sensor Technology of the *Technische Universität Ilmenau*, an NPM machine with the following parameters has been developed and succesfully tested: positioning and measuring range 25 mm x 25 mm x 5 mm, resolution 1.24 nm and 0.1 nm, respectively, positioning uncertainty < 10 nm. The outstanding precision has been obtained by realizing the Abbe comparator principle in all three measuring axes and applying a new concept for compensating systematic errors resulting from mechanical guide systems. The machines have been manufactured by the *SIOS Messtechnik GmbH* company, Ilmenau. Up to now, three NPM machines have been built. They are operating successfully in several German research institutes. This paper deals with basic information on our NPM machines, explains their mode of operation and discusses their performance and efficiency based on an exemplary error analysis.

2 Design and operation

An Abbe offset free design (see figure 2) with three miniature interferometers, a user selectable surface-sensing probe and two angular sensors provides extraordinary accuracy [1], [2], [3], [4]. The intersection of all measuring axes of the length measuring systems is the point of contact of the probe with the sample. The measuring object is placed on a moveable mirror corner that is positioned by a three-axis electromagnetic drive system. The position is recorded by three firmly arranged plane mirror interferometers. Translatory errors of the linear guide elements have no influence on the measuring result. Angular errors of the drive system are also measured at the mirror corner by means of optical sensors and used for angular control. Guide error compensation of the linear stages is achieved by a closed loop control system. The data acquisition and control system uses a digital signal processor and specific signal conversion electronics. The possibility to apply different appropriate surface-

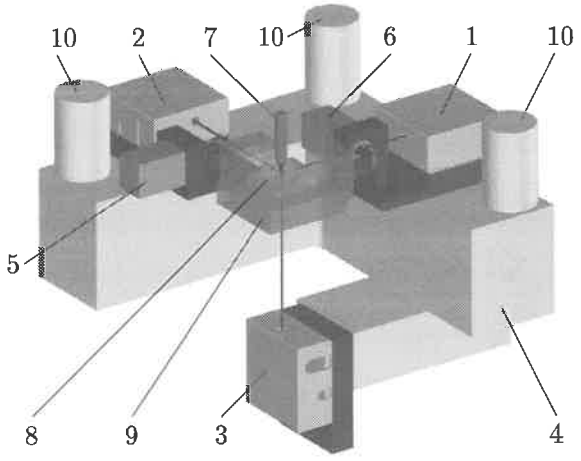

Figure 2: Principle design of the nanomeasuring machine: 1 x-interferometer, 2 y-interferometer, 3 z-interferometer, 4 metrology frame made by Zerodur, 5 roll and yaw angular sensor, 6 pitch and yaw angular sensor, 7 surface-sensing probe, 8 sample, 9 mirror corner, 10 fixing points for probe system

sensing probes allows a wide spectrum of applications. By the use of AFM or STM probes, long range scanning probe microscopy becomes possible.

3 Performance and uncertainty

The small uncertainty is achieved by a design following the Abbe comparator principle in combination with the accurate reference coordinate system defined by the mirror corner. Traceability to the national length standard is possible as interferometers based on stabilized HeNe-lasers serve as length measurement systems. The uncertainty of length measurements performed by the NPM machines depends on various uncertainty components [1]. Contributing components are:

- wavelength of frequency stabilized HeNe-Lasers,
- offset, amplitude and phase uncertainty of analog interference signals,
- quantization and rounding errors during the demodulation of interference signals,
- uncertainty of reference coordinate system of the mirror corner,
- uncertainty by calculated refractive index of air,
- thermal expansion of metrology frame, interferometers and probe system and
- uncertainty of length by angular errors (Abbe offset and cosine errors).

The mirror corner of our NPM machine is moved by combination of electromagnetic drives and linear guides in all three linear axes. While there is one drive for each x- and y-axis there are four drives for the z-axis. Therefore the angular errors φ_x and φ_y can be compensated. Looking at one of the three interferometers (figure 3), just two of the three angular errors have an influence on the measuring result as the rotation around the measuring axis is

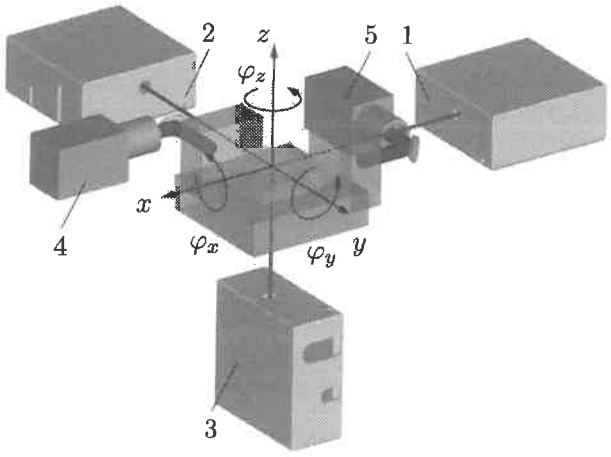

Figure 3: Axes and angle definition of the nanomeasuring machine: 1 x-interferometer, 2 y-interferometer, 3 z-interferometer, 4 roll and yaw angular sensor, 5 pitch and yaw angular sensor

without consequence. For instance, the measuring result of the x-interferometer depends on the rotations φ_y and φ_z where only φ_y can be compensated.

As the interferometers have only one measuring beam with a small diameter, the alignment of the measuring axes on one point can be done with a tilted circular aperture and an optical power meter. This results in residual Abbe offsets of less than 0.1 mm.

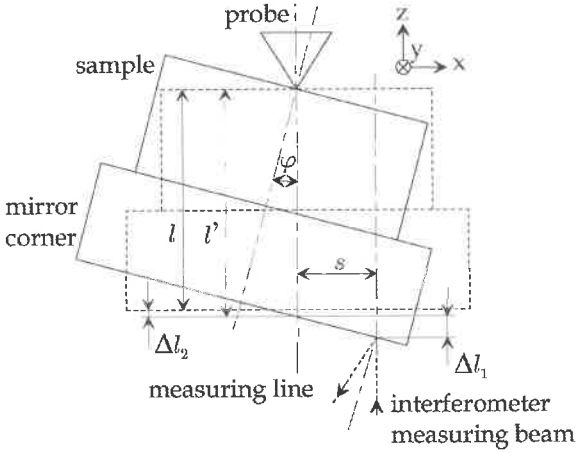

Figure 4: Abbe offset and cosine errors

Figure 4 shows the Abbe offset s, the Abbe offset error Δl_1 and the cosine error Δl_2 examplarily for the z-axis. The angular control systems cause angular uncertainties of x- and y-axis $u(\varphi_x) = u(\varphi_y) = 0.05''$, while the rotatory guide errors of the z-axis $u(\varphi_z) = 5.2''$. Resulting measurement uncertainties are shown for the x-axis examplarily in equations 1 to 4. The cosine error depends on displacement l_x and constructional offset l_{x0}.

$$u_{1.Ord1}(l_x) = s \cdot \tan\left(u(\varphi_y)\right) = 0{,}03\,\text{nm} \tag{1}$$

$$u_{1.Ord2}(l_x) = s \cdot \tan\left(u(\varphi_z)\right) = 1{,}46\,\text{nm} \tag{2}$$

$$u_{2.Ord1}(l_x) = (l_{x0} - l_x) \cdot \left(\frac{1}{\cos\left(u(\varphi_y)\right)} - 1\right) \leq 2{,}06 \cdot 10^{-6}\,\text{nm} \tag{3}$$

$$u_{2.Ord2}(l_x) = (l_{x0} - l_x) \cdot \left(\frac{1}{\cos\left(u(\varphi_z)\right)} - 1\right) \leq 7{,}4 \cdot 10^{-3}\,\text{nm} \tag{4}$$

A second type of uncertainty is caused by measurement beam deflection as shown in figure 5. Optical interference signals are converted into electrical signals after passing through a circular aperture. Only axial parts of measurement and reference wavefronts will pass this aperture. Thus a length shortened by Δl_{geo} is measured, resulting in an error Δl.

$$\Delta l_{geo} = a \cdot \left(\cos\left(2 \cdot \varphi\right) - 1\right) \tag{5}$$

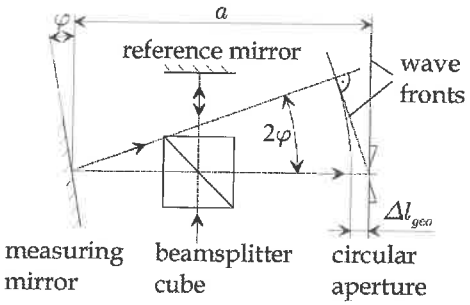

Figure 5: Cosine error of the interferometer

$$\Delta l = \frac{\Delta l_{geo}}{2} = \frac{a \cdot (\cos(2 \cdot \varphi) - 1)}{2} \tag{6}$$

With the angular uncertainties and the system measurement lengths the following uncertainties can be calculated.

$$u_{Int1}(l_x) = \left| \frac{(l_{x1} + l_x)}{2} \cdot (\cos(2 \cdot u(\varphi_y)) - 1) \right| \leq 6{,}2 \cdot 10^{-6}\,\text{nm} \tag{7}$$

$$u_{Int2}(l_x) = \left| \frac{(l_{x1} + l_x)}{2} \cdot (\cos(2 \cdot u(\varphi_z)) - 1) \right| \leq 2{,}3 \cdot 10^{-2}\,\text{nm} \tag{8}$$

The third type of uncertainty to be discussed here is caused by the measuring mirror surface topography. It contributes to the total measurement uncertainty in the way of a cosine error with an angular uncertainty $u(\varphi_s) = 1.3''$ and leads to the contribution calculated in equation 9.

$$u_{Int3}(l_x) = \left| \frac{(l_{x1} + l_x)}{2} \cdot (\cos(2 \cdot u(\varphi_s)) - 1) \right| \leq 4{,}0 \cdot 10^{-3}\,\text{nm} \tag{9}$$

The discussed uncertainties referred to the x-axis. Uncertainties can be calculated for the y- and z-axis as well. When summed up according to their respective dependencies according to equation 10, they result in the combined uncertainties shown in table 1.

$$\begin{aligned} u^2(l_x) \;=\; & (u_{1.Ord1}(lx) + u_{2.Ord1}(lx) + u_{Int1}(lx))^2 \\ & + (u_{1.Ord2}(lx) + u_{2.Ord2}(lx) + u_{Int2}(lx))^2 \\ & + 2 \cdot (u_{Int3}(lx))^2 \end{aligned} \tag{10}$$

With its design according to the Abbe comparator principle and its angular control systems, the NPM machine shows an extraordinary accuracy.

As thermal expansion has the largest influence on uncertainty, the design of the interferometers is currently revised. The new design uses material with a smaller thermal expansion coefficient for certain parts of the interferometers and adapts their reference beam length to the NPM machine needs. These changes also reduce the contribution of the uncertainty of

	x- and y-axis		z-axis	
Minimum	$u(l_{xy}) = 1.48\,\text{nm}$	for $l_x = l_y = 0$	$u(l_z) = 0.035\,\text{nm}$	for $l_z = 0$
Maximum	$u(l_{xy}) = 1.49\,\text{nm}$	for $l_x = l_y = 25\,\text{mm}$	$u(l_z) = 0.036\,\text{nm}$	for $l_z = 5\,\text{mm}$

Table 1: Uncertainties of length by angular errors ($k_{0,6827} = 1$)

the calculated index of refraction of air and thus the wavelength of the laser light. Another improvement of the machines has been achieved in the last year by replacing the electronical interferometer signal demodulation modules. The new version features reduced quantization and rounding errors below 0.1 nm. By future implementation of a real-time elliptical regression based on direct signal measurement, the modules will allow fast and accurate correction for nonlinearities caused by offset, amplitude and phase errors of the analog interference signals as well. Our improved NPM machines will have an estimated combined uncertainty of less than 10 nm.

4 Acknowledgements

The development of the nanopositioning and nanomeasuring machine is supported by the Thuringian Ministry of Science, Research and Arts. The authors wish to thank all those colleagues who have contributed to the developments described.

References

[1] Tino Hausotte. *Nanopositionier- und Nanomessmaschine.* PhD thesis, Technische Universität Ilmenau, 2002.

[2] G. Jäger, E. Manske, T. Hausotte, and H.-J. Büchner. Laserinterferometrische Nanomeßmaschinen. In *VDI Berichte Nr. 1530 Sensoren und Meßsysteme 2000*, pages 271–278. VDI/VDE-Gesellschaft Meß- und Automatisierungstechnik, März 2000.

[3] G. Jäger, E. Manske, T. Hausotte, and H.-J. Büchner. Nanomeßmaschinen zur abbefehlerfreien Koordinatenmessung. *Technisches Messen*, 67(7-8):319–323, Juli/August 2000.

[4] G. Jäger, E. Manske, T. Hausotte, H.-J. Büchner, R. Grünwald, and W. Schott. Nanomeasuring technology - nanomeasuring machine. In *The Sixteenth Annual Meeting*, pages 23–27, Crystal City, Arlington, Virginia, 10.-15. November 2001. American Society for Precision Engineering.

Linear Motion Carriage Driven and Guided by Elastically Supported and Preloaded Lead Screw Nuts

Alexander H. Slocum, Ahmed Elmouelhi, Tyson Lawrence, Peter How, Joe Cattell
Massachusetts Institute of Technology
77 Massachusetts Ave., Room 3-445, Cambridge, MA 02139 slocum@mit.edu fax 617.258.6427

Abstract -
The quest for low cost precision machinery benefits developing nations and can open new markets. The principles of elastic averaging can fulfill the need for low cost precision machinery while maintaining a large degree of accuracy and repeatability. In this paper, a linear carriage was constructed, built, and tested using readily available industrial construction supplies. Elastic averaging was achieved by two hex nuts preloaded via flexures on a threaded rod. The prototype maintained accuracy and repeatability to better than 25 microns in the carriage's six degrees of freedom. These results are consistent with the postulations of a kinematic error model performed on the carriage design and suggest a wide variety of applications for the concept.

keywords – *linear motion, elastic averaging, low cost, lead screw*

Introduction

The first precision machines used lead screws whose nuts were preloaded either with a split nut or by using a leather nut, and the straightness error in the screw shaft was isolated from the carriage by means of a coupling [1]. Since then, the goal has been similar: use preload to minimize the effects of backlash, and isolate the nuts from the carriage. However, the task of creating preloaded precision linear motion bearings still remains. In the quest for lower cost precision machines, for use by small shops or the developing world, we can return to fundamental principles of elastic averaging [2] and use these to enable the creation of low cost precision machines. In such applications an accuracy one-half millimeter or better is desirable. Accordingly, this paper introduces the concept of using two low cost rolled threaded rods as the guidance rails and actuators for a linear motion axis. Preloaded nuts are mounted on the rods. One nut serves as the master against which all others are preloaded using flexural bearings. Due to the angled geometry of the threads on the rod, this means that all six degrees of freedom are in effect preloaded, and a high degree of repeatability is obtained. Furthermore, by using additional nuts preloaded against the master nut by flexures, a greater degree of accuracy could be obtained through the mechanism of elastic averaging.

Figure 1 shows the prototype system that was designed, built, and tested. This single axis apparatus consists of a precision linear carriage actuated by two RH 1"-14 threaded rods coupled to each other with pulleys and a timing belt. Using two threaded rods eliminates the need for costly bearings and places the actuation forces along the centers of stiffness. This configuration helps reduce binding and load-induced errors. The linear carriage is coupled

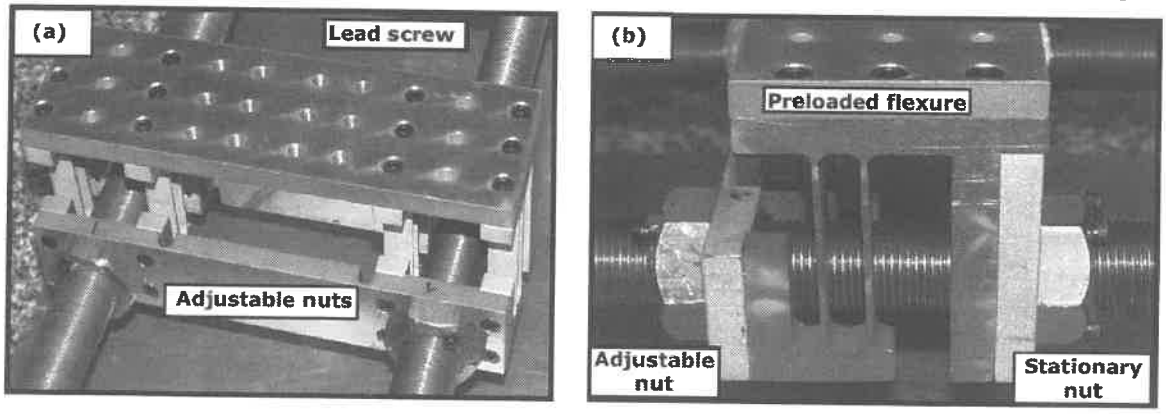

Figure 1 (a) Prototype system built using simple construction materials **(b)** Nuts preloaded via flexures

to the threaded rods through four brass hex nuts, two per rod. Preload is provided by flexures between the nuts. The rolled threaded rods were obtained from a construction supply vendor, and are typical of threaded rod used the world over in construction projects. The brass nuts were turned on one end to form a round section, which fit into a bore in the end plates of the carriage. The flexures are preloaded by rotating and then locking the nuts in place using socket head cap screws. The flexures were cut using an OMAX 2626 abrasive waterjet machining center [3]. This simple system cost less than $50 in materials and represents a cost savings of two orders of magnitude or more over conventional precision carriages.

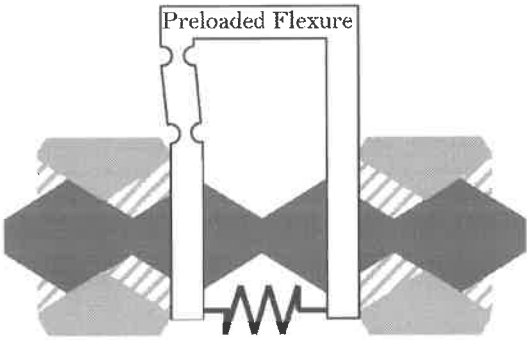

Figure 2 Concept of self-centering nuts under preload

Besides cost advantages, the industrial grade components used provide the necessary tolerances to allow for self-adjustment. In normal applications, the clearance inherent in these components is undesirable, if not detrimental, to the system. Our design uses this clearance to its advantage. By preloading the hex nuts on the threaded rods, they self-center against the 60-degree thread form, resulting in more accurate and more repeatable carriage control. This self-centering action continues until the flexures find their lowest energy states; a state which occurs at the minimum deflection of the flexure as shown in Figure 2. The clearance between the rods and the nuts also reduces the possibility of binding.

For the experiment contained in this paper, only two nuts per rod were used to obtain the desired elastic averaging effects. However, as more flexured nuts are added to the mechanism, the accuracy and repeatability will increase [2]. In this configuration, the master nut anchors the position of the carriage, while the flexured nut provides the preload.

To ensure elastic averaging, the preload exerted on the nuts must be larger than opposing counter forces. Thus, the weight of the carriage must be controlled. A simple balance of forces at the interface of the nut and the threaded rod, including frictional effects, can be summarized as

$$F_{preload}\cos\theta > w\sin\theta + \mu\left(w\cos\theta + F_{preload}\sin\theta\right), \tag{1}$$

or alternatively,

$$F_{preload} > \left(\frac{\mu\cos\theta + \sin\theta}{\cos\theta - \mu\sin\theta}\right)w. \tag{2}$$

Here w represents the weight of the carriage applied to each nut, $F_{preload}$ is the preload force, θ the incline angle of the threaded form, and μ the coefficient of friction between the steel rod and the brass nuts. The outcome of Equation (2) as applied to the experimental system in this paper is

$$F_{preload} > 2.865w. \tag{3}$$

Consequently, a preload of 100N was applied to the hex nuts to overcome the weight of the carriage (14.6N). The 100N preload was more than sufficient because the weight of the carriage is spread over four preloaded nuts.

Kinematic Error Model

A kinematic error model was developed to estimate the accuracy and repeatability of the prototype system. The proposed experimental design, shown in Figure 3, forms a closed structural loop between the support frame and the rolled threaded rods with the linear carriage stacked on top of this loop. In order to simplify the model, the entire

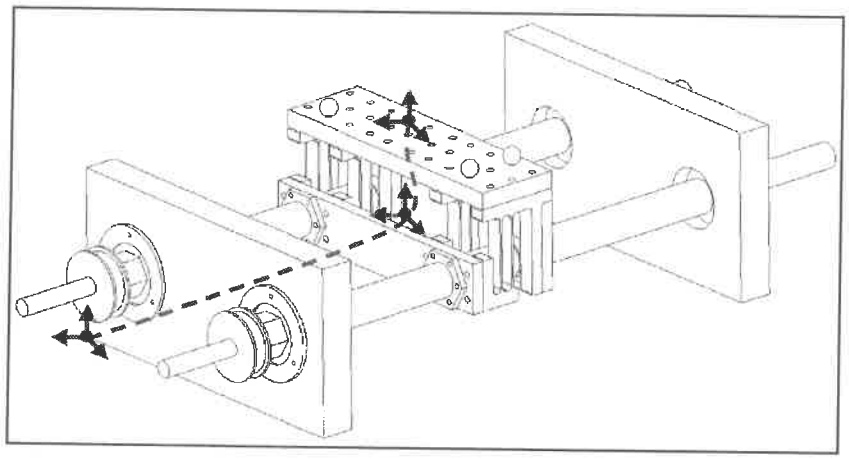

Figure 3 Proposed design illustrating error budget coordinate reference frames

system was analyzed in an open structural loop form. A coordinate system reference frame placed in the middle of the threaded rods with estimated translation and rotation errors takes into account the aforementioned closed structural loop. Prominent errors included in this error budget analysis were radial and axial play in the threaded rod bearings, manufacturing errors in the threaded rods and brass hex nuts, machining errors in the prototype system components and misalignment of assembled pieces. The estimated errors and coordinates of the component reference frames were placed into an error gain matrix spreadsheet in order to calculate the resulting accuracy and repeatability of the carriage's 6 degrees of freedom [4]. All of the manufactured components were machined using the OMAX 2626 abrasive waterjet machining center and a Bridgeport EZTRAK I CNC milling machine [5]. This resulted in machining tolerances to within +/- 76 microns, which were used as a guideline for calculating the systematic errors in the kinematic error model.

Experimental Setup

In order to evaluate the performance of the prototype, an experiment was designed and conducted using a coordinate measurement machine (CMM), which is accurate to approximately 5 microns [6]. The linear motion axis was clamped to the CMM table and measurements were taken at intervals of fourteen rotations (approximately 25.4mm or 1" of linear travel). Three spheres were bonded to the motion carriage and measured at each position to calculate both translational and rotational error motions. All measurements were taken in a static condition with the threaded rods rotated to exactly the same position, give or take one degree, or about two ten thousandths of an inch error motion in the axial direction. This testing configuration eliminated the effect of several of the prototype's systematic errors.

Measurements were taken at eleven locations with the carriage moving in the positive axial direction (forward) and then taken at the same eleven locations with the carriage moving in the negative axial direction (backwards). Each of these locations was fourteen turns apart resulting in approximately 25.4cm or 10" of total travel.

Results

The experimental results of the prototype were extremely encouraging. The original goal of an accuracy and repeatability of around one-half millimeter was easily met. At worst, the prototype was accurate to approximately 10 microns in the transverse (x) (Figure 4) and axial (y) directions (Figure 5), and to within 25 microns in the vertical (z) direction (Figure 6).

The repeatability was equally impressive with error in the vertical direction of less than 15 microns, and error in the transverse and axial directions of less than 10 microns. Table 1 lists the accuracy and repeatability measures at each position along the threaded rod. Additionally, all rotational error motions were less than five ten thousandths of a radian.

It is important to note that the accuracy is computed after taking into account a best linear fit calibration of the individual data sets relative to the reference frame.

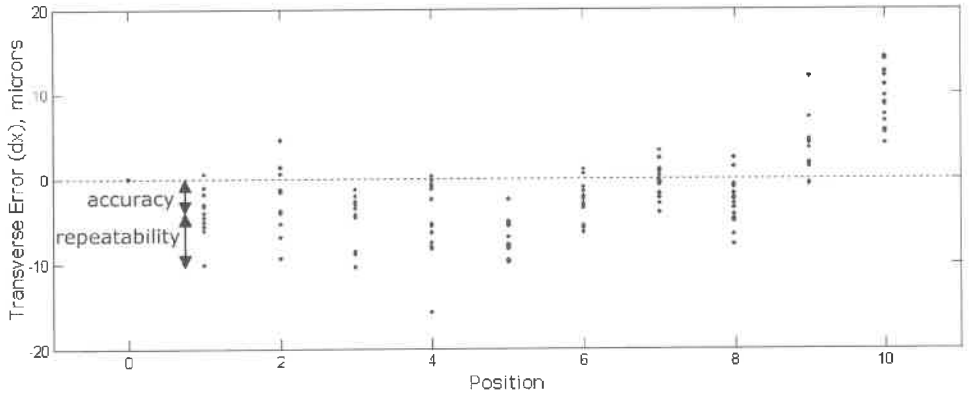

Figure 4 Linear fit of transverse error vs. position (position markers spaced 25.4mm apart)

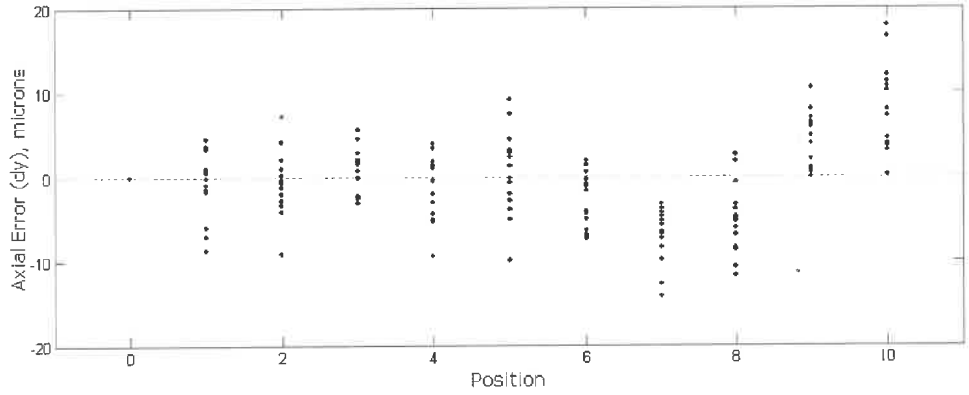

Figure 5 Linear fit of transverse error vs. position (position markers spaced 25.4mm apart)

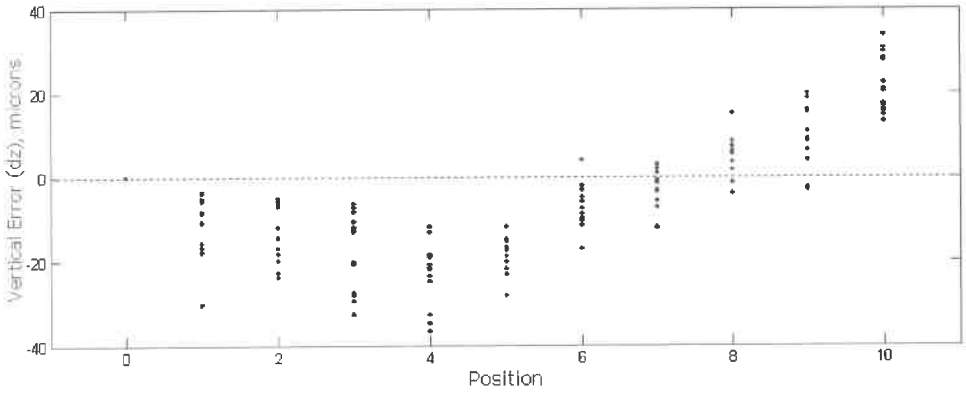

Figure 6 Linear fit of vertical error vs. position (position markers spaced 25.4mm apart)

The original data showed clear linear trends indicating that the measurement axes and the actual motion were not aligned. A simple linear correction was applied to obtain the above data, simulating a calibration movement aligning the motion axes to the reference frame. In the transverse and vertical directions this was a rotation of the reference frame due to misalignment. In the axial direction the linear correction was for thread inaccuracy

(approximately 1.00145" per 14 turns). The remaining error is most likely due to bearing error motions, straightness and other manufacturing errors in the threaded rod, as well as deflection of the threaded rod in the center of the range of motion. This deflection error can be clearly seen in Figure 6. Unlike the accuracy error, the repeatability error did not display many clear trends.

Position	Accuracy			Repeatability		
	dx transverse	dy axial	dz vertical	dx transverse	dy axial	dz vertical
0	-	-	-	-	-	-
1	-3.8	-1.4	-11.3	5.4	6.5	13.4
2	-2.8	-0.8	-12.9	7.1	8.1	9.2
3	-6.1	1	-18.4	4.7	4.2	13
4	-4.9	-1.5	-23.3	8	6.7	12.5
5	-7.1	0.4	-18.7	3.7	9.5	8
6	-2.8	-3	-7.1	3.7	4.6	10.5
7	-0.5	-7.7	-2.2	3.7	5.5	7.3
8	-2.8	-5.1	3.7	5.2	7.1	9.5
9	3.5	4	9.9	6.4	5.3	11.3
10	9.4	8	21.9	5.1	8.8	10.2

Table 1 Accuracy and repeatability at each position (in microns)

Conclusions

The results of the prototype prove that low cost rolled threaded rods can be used to drive a repeatable linear axis using preloaded, elastically averaged nuts. Table 2 compares the results of the kinematic error model and the experimental results to the original functional requirements. The implications of these results lend themselves to many applications where ultra high precision is not necessary. In these cases a low cost alternative would be most viable. Small shops, developing countries, and non-traditional industries may most benefit from this technology in the immediate future.

		Functional Requirement	Prototype Kinematic Error Model	Prototype Experimental Results
Accuracy	dx	500	(±) 58	+9.4/-7.1
	dy	500	(±) 37	+8.0/-7.7
	dz	500	(±) 25	+21.9/-23.3
Repeatability	dx	±500	±30	±8.0
	dy	±500	±22	±9.5
	dz	±500	±16	±13.4

Table 2 Error budget and experimental results for worst cases (all units in microns)

Further improvements can be made using one LH threaded rod and one RH threaded rod for actuation to cancel torques created on the carriage. Similarly, lining up the natural bow of the threaded rod can lead to improved accuracy and repeatability. Other variants include elasticity within the nut threads themselves as suggested by an engineer at Polaroid or elasticity in the nut diameter.

References:

[1] C. Evans *Precision Engineering: an Evolutionary View*, Cranfield Press. Bedford, UK. 1989.
[2] A. Slocum, *Precision Machine Design*, SME, 1992.
[3] http://www.omax.com
[4] http://pergatory.mit.edu/2.75/ErrorGainSpreadsheet-master.xls
[5] http://www.bpt.com/
[6] http://www.brownandsharpe.com/

Development of a Micro Cutting and Deforming System for Glass Materials

Shin'ichi WARISAWA, Takashi KARINO, Pairat Tangpornprasert, Mamoru MITSUISHI
Department of Engineering Synthesis, School of Engineering, The University of Tokyo
7-3-1 Hongo, Bunkyo-ku, Tokyo 113-8656, Japan
warisawa@nml.t.u-tokyo.ac.jp

1. Introduction

Many papers have been reported concerning the ductile mode cutting. Yoshino et al. have reported that the critical depth of cut became larger in case of cutting a single crystal silicon under the high hydro static pressure condition [1]. The atmosphere dependency of the cutting mode for an optical glass has been investigated [2]. By the way, it has been reported that brittle materials, especially a glass material, present a plastic deformation manner at the nano to micro scale as well as a ductile cutting mode [3,4]. The characteristic feature has been verified mainly by the Vickers indentation or scratching test. A development of a system that can realize ductile mode cutting and deformation at the nano to micro scale will contribute very much to produce nano/micro optical devices or modify a part of geometry of optical parts. The paper deals with the micro cutting and deforming system for brittle materials.

First, the paper explains the configuration of the developed system to be a shaper which can realize a nano-meter order depth of cut. Especially, the mechanism and method to determine the depth of cut in nano-meter order is explained. Using the system, some cutting experiments conducted are presented. Experiments with the small inclination of the workpiece to give a gradual increase of the depth of cut show that there are three characteristic phases during the cutting. These are characterized as follows; (i) only the thrust component of cutting force is measured, (ii) the principal and thrust components of cutting force are measured and (iii) the variance of cutting force becomes larger. Machined surface conditions observed by a laser micro scope and a surface profiler corresponding to the three phases are examined. Especially, the phase (i) seems to be deformation by densification of a glass. In the last of the paper, an application cutting using the phase (i) to make a groove is presented.

2. Experimental setup

Figure 1 shows the experimental setup. The developed system consists of a linear motor driven tool feed system, a hybrid-type tool positioning unit, a workpiece alignment unit, a piezoelectric type three-axis force sensor (model type 9256A1, Kistler Ltd.).

The hybrid-type tool positioning unit consists of coarse and fine positioning units, a capacitance type displacement sensor (model type 5401, Japan ADE Ltd.) and a laser displacement sensor (model type LC2430, Keyence Ltd.) shown in Fig.1(b). The coarse

positioning unit using a ball screw with 1mm lead is installed for tool setup and rough approaching.

The fine positioning unit with a piezo-electric actuator and a capacitance type displacement sensor determines the depth of cut. The displacement sensor is installed to detect the displacement of the cutting toot. In order to determine the depth of cut, the position of the workpiece surface should be measured. To this end, the coarse and fine positioning units and the force sensor are used. Simply speaking, (i) approaching the cutting tool to the workpiece using the coarse positioning unit, (ii) when the force reaction is measured, retracting the cutting tool once using the fine positioning unit in finer step, (iii) approaching the cutting tool to the workpiece again using the fine positioning unit, (iv) when the force reaction is measured, the position can be estimated as the position of the workpiece surface.

The laser displacement sensor is used to check the inclination of the workpiece, scanning the workpiece by the laser displacement sensor. The stage can control the orientation of a workpiece by adjusting four screws installed at each corner of the table.

Rigidity of the workpiece alignment unit and tool positioning unit in cutting depth direction are 10.03N/um and 2.20N/um respectively.

3. Experimental results

Cutting experiments using the developed system have been conducted. The workpiece material is soda-lime glass. Specification of the cutting tool used in the experiments is shown in Table 1. Various feed speeds are examined from 1mm/s to 500mm/s.

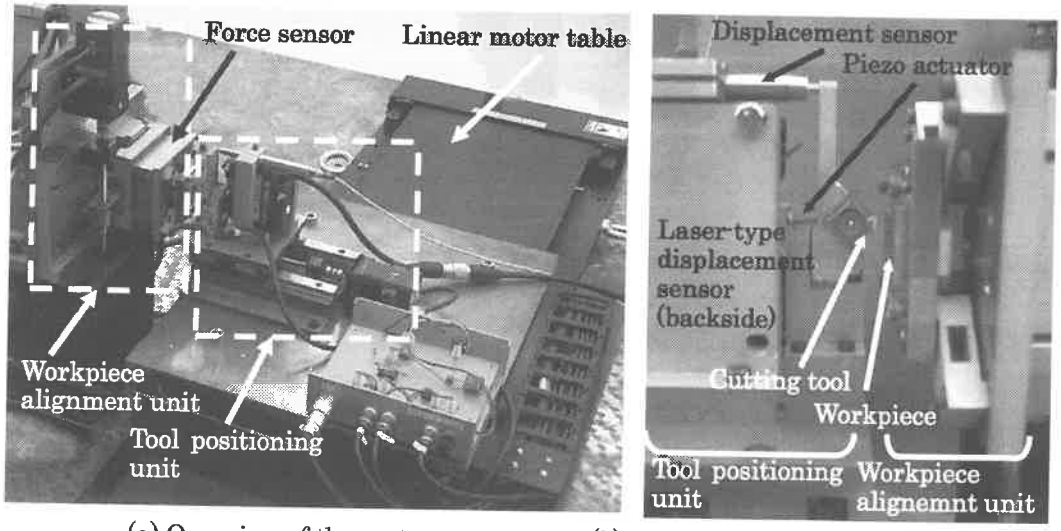

(a) Overview of the system (b) Macrograph around the cutting tool

Fig.1 Experimental setup

Table 1 Specifications of the cutting tool

Tool angle	118 deg.
Rake angle	-30 deg.
Nose radius	1.5mm
Edge radius	less than 80nm
Material	Single crystal diamond

3.1 Deformation and ductile to brittle transition in various feed speeds

A workpiece is set with the inclination as 1um per 20mm in feed direction on the alignment unit in order to realize a gradual increase of the depth of cut. Figure 2 shows a principal (Fx) and thrust (Fz) components of the cutting force measured by the force sensor and their variance. It is observed in Figure 2 that there are three characteristic phases during the increase of the depth of cut. These are characterized as follows; (i) only the thrust component of cutting force is measured, (ii) the principal and thrust components of cutting force are measured and (iii) the variance of cutting force becomes larger. The characteristics seem to be common even if the feed speeds are different. After the thrust component becomes larger than 500mN, the principal component can be measured in any cases. The increase ratio of the thrust component in the phase (i) is smaller than that in the phase (ii).

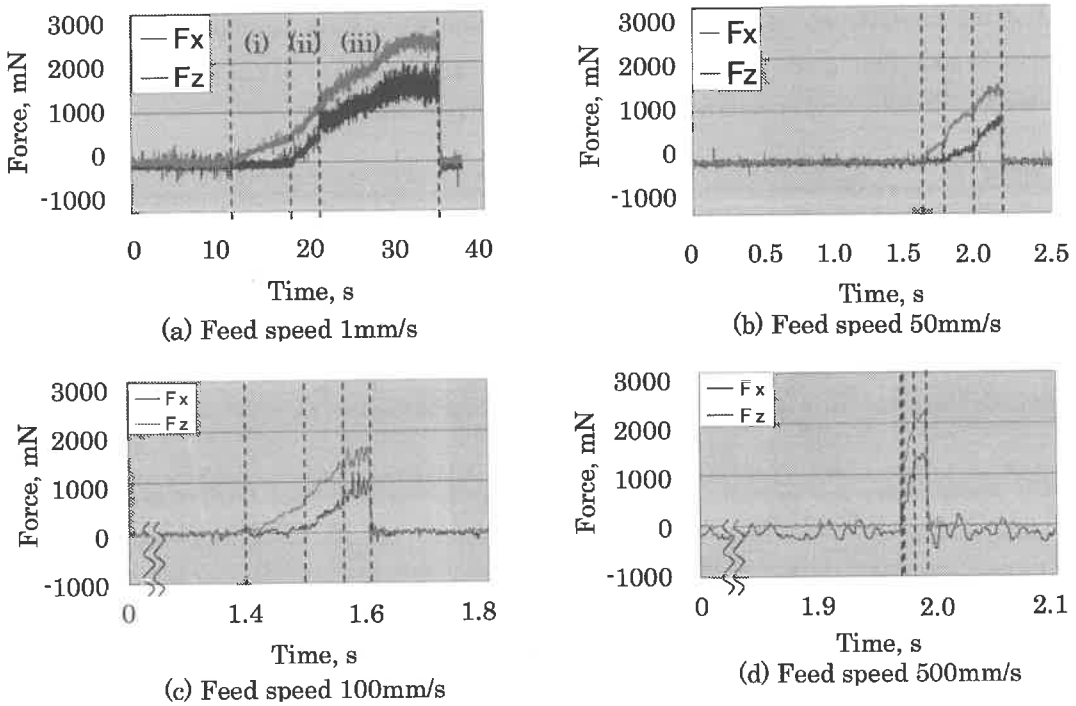

Fig.2 Cutting force (Rake angle -30deg.)

Figure 3 shows the machined surface profiles in case of the feed speed 1mm/s as a representative case. The machined surface profiles are observed by a laser microscope (model type VK-8550, Keyence Corp.) and a surface profiler (model type SURFCOM 570A, Tokyo Seimitsu Ltd.) corresponding to the three phases. From the figure, the phase (iii) represents brittle mode cutting clearly. The phase (i) seems not to have any crack observed on the machined surface although it should be examined by means of etching tests. The machined surface in the phase (ii) has some bosses on it which are observed by the laser microscope.

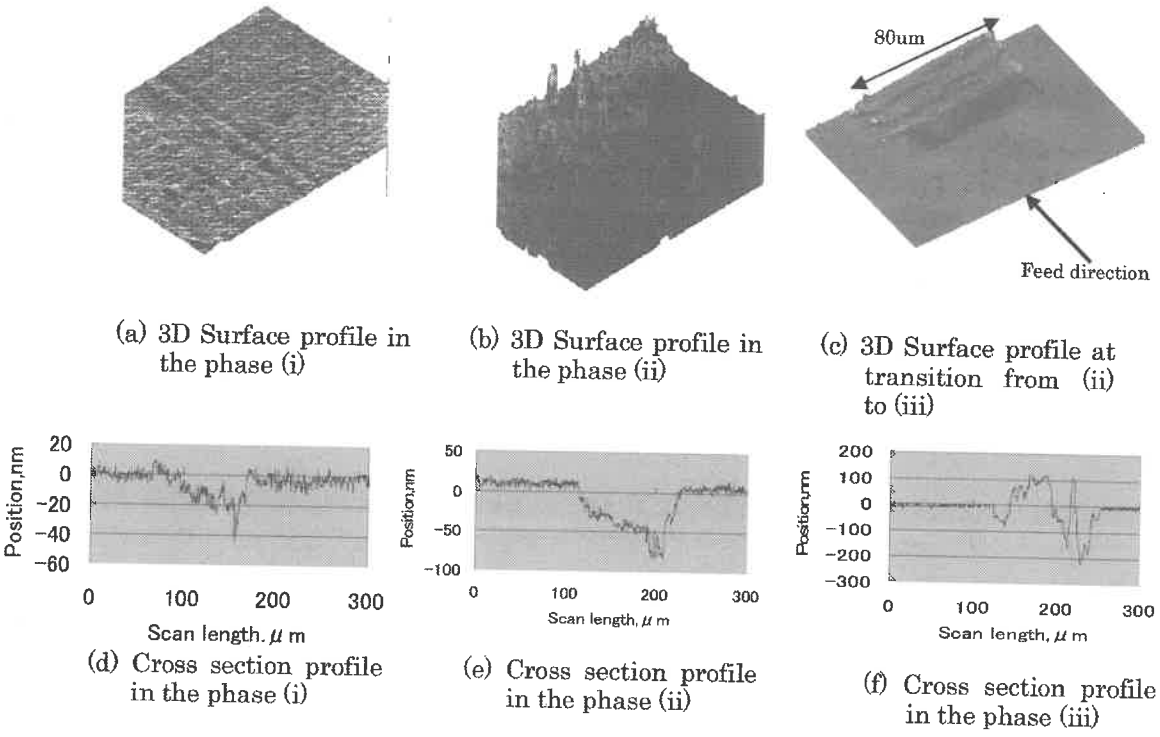

(a) 3D Surface profile in the phase (i)

(b) 3D Surface profile in the phase (ii)

(c) 3D Surface profile at transition from (ii) to (iii)

(d) Cross section profile in the phase (i)

(e) Cross section profile in the phase (ii)

(f) Cross section profile in the phase (iii)

Fig.3 Machined surface profile (Feed speed 1mm/s, Rake angle -30deg.)

3.2 Deformation and ductile to brittle transition in various rake angles

The influence of rake angles of the cutting tool on the phases observed in 3.1 has been also examined. Figure 4 shows the cutting forces acquired in the experiments in which various rake angles of the cutting tool are taken as -15, 0, 5 deg. In case of -15 deg., it can be observed that there is a small region corresponding to the phase (i). However, in case of other rake angles, the phase (i) cannot be observed. From the results, it can be said that the emergence of the phase (i) would be strongly influence by the rake angle of the cutting tool not by the feed speed.

3.3 Application by means of the first phase

We tried to make deeper groove applying the first phase repeatedly. Specifically, the feed speed was 1mm/s and the cutting tool with the rake angle -30 deg. in 3.1 was used. The grooving was repeated five times. Figure 5 shows the cutting results. It can be observed that the realized depth of cut is 200nm and the cross section of the groove is very smooth.

3.4 Discussions

It is very interesting that there are three phases during the increase of the depth of cut characterized by the cutting force and surface profile. Among the three phases, the first phase in which only the thrust force can be measured should be very important for nano-micro machining for glass materials. Whether the first phase is categorized into deformation or ductile mode cutting should be discussed carefully by taking material analyses. However, it can be suggested that the first phase may be deformation, because the emergence of the phase depends on the rake angle and the principal component cannot be measured. If the cutting chip is generated, both components of cutting force should be measured. Another measure to make it sure is to use video camera observing the cutting chip generation in real time. It will be a future topic. To discuss whether plastic flow or densification produces the deformation [3] is also interesting to understand the phase in deep.

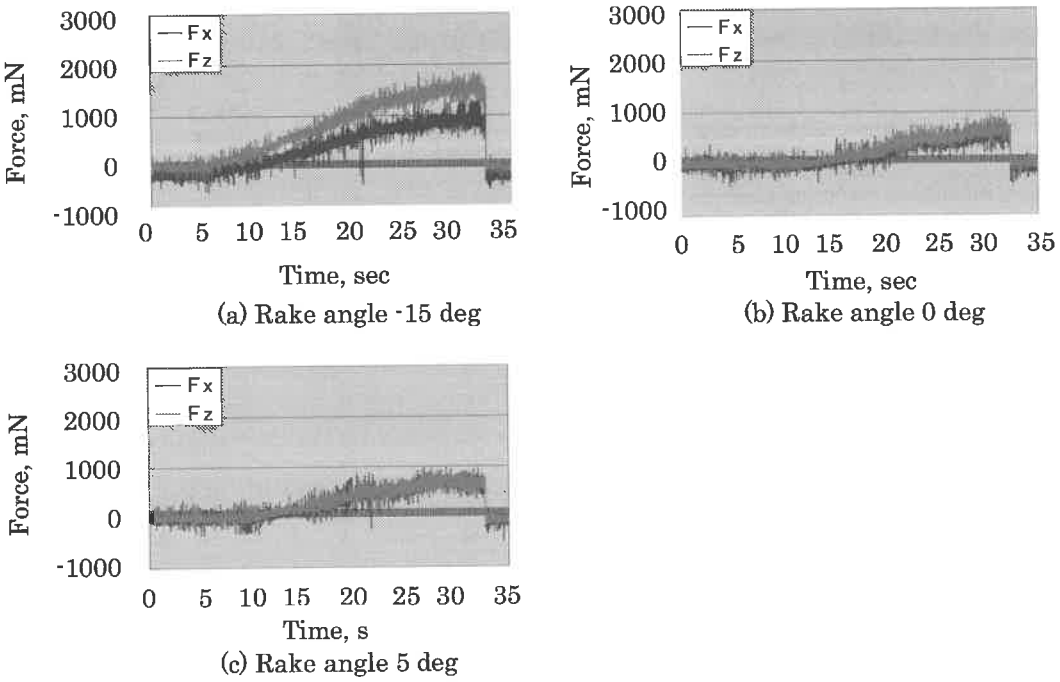

Fig.4 Cutting force in various rake angles(Feed speed 1mm/s)

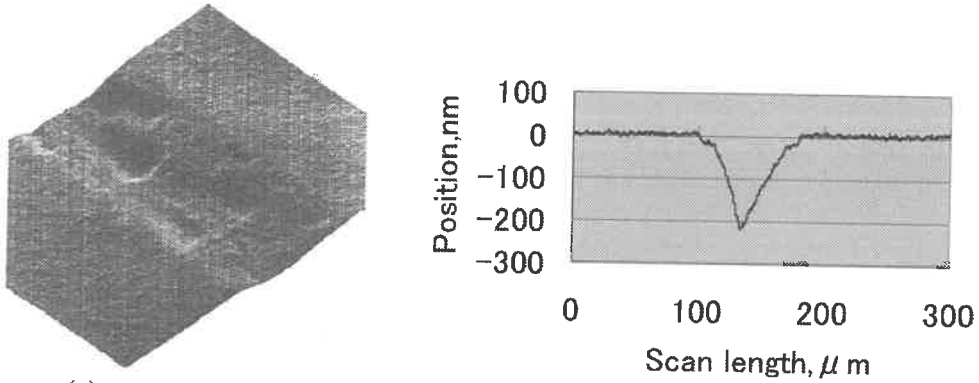

(a) 3D Surface profile (b) Cross section profile

Fig.5 Machined surface profile of five times repeat cutting by the phase (i)

4. Conclusions

A micro cutting and deforming system has been developed. Through some cutting experiments and observation of cutting force and machined surface profile, it was found that there are three phases during the increase of depth of cut in nano-meter order. Especially, the first phase was very interesting because only the thrust component could be measured and the machined surface was very smooth. Although further analyses should be conducted, the phase would be important to make nano-micro structure of glass materials.

Acknowledgement

This work was supported in part by Digital New Deal of Research Institute of Economy, Trade and Industry and in part by Machine Tool Engineering Foundation. The supports are appreciated. The authors also thank to Asahi Glass Co. Ltd. for their discussions and glass supply. Finally, the authors also thank to Keyence Corp. for their support of laser displacement sensor and laser microscope.

References

[1] M. Yoshino, T. Aoki, T. Sugishima and T. Shirakashi, "Scratching Test on Hard-brittle Materials under High Hydrostatic Pressure," J.JSPE, 65-10, pp.1481-1485 (1999).

[2] Jon A. Patten,Sherman V.Mumford, "The effects of Fluids on the Deformation and Ductile-to-Brittle Transition of Silicon," Proceedings ASPE 2000 Annual Meeting, 22, pp.604-607 (2000).

[3] J. Sehgal, S. Ito, "Brittleness of glass," J. of Non-Crystalline Solids, 253, pp.126-132 (1999).

[4] M.C.Shaw, "Precision Finishing," Annals of the CIRP, 44/1, pp.343-348 (1995).

DESIGN AND ANALYSIS OF A NANO-STEPPING DEVICE

Y. Gao *, X. Liu, K. Yuen

Department of Mechanical Engineering, Hong Kong University of Science and Technology
Clear Water Bay, Kowloon, Hong Kong
* E-mail: meygao@ust.hk

Introduction

As the development of manufacturing technology is shifting its focus to the nanometer level resolution, many research and development facilities and applications are demanding low cost and convenient to use displacement measurement and calibration facilities at the nanometer level resolution. Current measurement and calibration devices, that are capable to achieve nanometer level precision, mainly rely on the techniques utilizing the heterodyne interference [1-2], the Fabry-Perot (F-P) interference [3-4], the swept-frequency interference [5], and the differential interference principle [6-8]. The devices can be complex and expensive, and sensitive to external environmental influences, with a very limited measurement range.

To address the above issues, a new nanometer level stepping displacement measurement and calibration device is proposed. The device is based on the multi-beam interference principle and photoelectronic sensors. The working principle of the proposed device is introduced, key design parameters are analyzed. The expected resolution is 0.2nm and displacement range 100μm. Simulations and numerical analysis are performed to demonstrate the characteristics of the device.

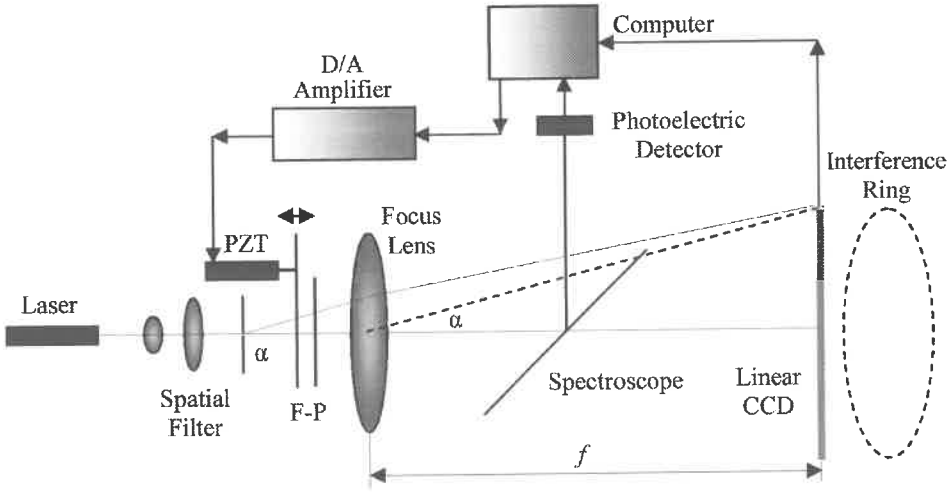

Fig. 1 Schematic diagram of the nano-stepping device

Working Principle

The proposed nano-stepping device (Fig. 1) consists of a laser with a stablized frequency, a spatial filter, a F-P etalon as the multi-beam interference cavity, which consists of two plane mirrors with reflective index of more than 90%, a focus lens, a linear CCD detector, a PZT

driver, and data sampling and control circuits. According to the multi-beam interference principle [9], when a group of rays from the pin hole of the spatial filter incident onto the first mirror at an angle α, multiple beams are generated behind the second mirror with a parallel propagation direction. The beams are focused by the focus lens on to the focus plane for interference. The obtained interference patterns correspond to the optical path difference between the beams, which can be expressed as $2d\cos\alpha$ [9], d is the distance between the two mirrors.

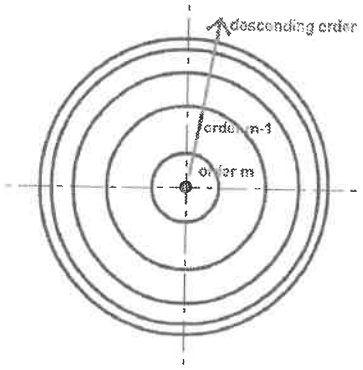

Fig. 2 Interference rings on CCD

The ray angle corresponding to the mth order bright interference ring behind the focus lens satisfies $2d\cos\alpha=m\lambda$. According to the lens focusing principle, the ring diameter corresponding to the incidence angle α is $D=2f\tan\alpha$, where f denotes the focal length of the focus lens. The obtained interference ring distribution on the whole focus surface, also the CCD plane, is shown in Fig. 2.

When the distance between the two mirrors in the F-P etalon is changed, the diameters of all orders of interference rings on the focus plane will vary. The zero order ring shrinks into, or come out, of the center on the photoelectric detector surface. Thus the displacement related with the relative movement of the two mirrors can be obtained through interference ring acquisition and analysis. If the intensity at the center is examined through the photoelectric detector, it will help to achieve a large displacement range that corresponds to integer multiples of $\lambda/2$. For the design, we can calibrate the displacement of the PZT that drives one of the mirrors to change the distance between them. The stepping displacement for calibration is to be realized through driving one mirror by the PZT to generate a stepping displacement which is accurately monitored by the CCD and the photoelectric detector. If the ratio between the interference ring diameter change and the distance change of the two mirrors is sufficiently large, the displacement measurement of a very high resolution can be achieved. To achieve a large measurement range, the interference ring order will be counted through the use of the photoelectric detector at the center. The device can be compact in size. The Abbe principle and the shorted link rule for precision mechanism design can be easily satisfied to achieve good stability and immunity to environmental disturbances for ease of use and reliability under laboratory conditions.

Design Analysis

For the proposed design, for the objective of a displacement range of 100μm and a resolution of 0.2nm, suitable design parameters should be determined to ensure a larger ratio. This means that, when the distance d of the two mirrors varies in the whole scope of 100um by 0.2nm, the CCD detector is able to distinguish the diameter change of the interference ring on the surface. Other parameters are selected. The length of the linear CCD is 48mm. Its resolution, or the distance of two neighboring pixels, is 7μm. The wavelength of the laser is 632.8nm. The main parameters that affect the resolution and range of the displacement stepping device are the focus length of lens f, the distance range of the two mirrors d, and the wavelength drift $\delta\lambda$, caused by the laser instability.

Preliminarily, the distance between the mirrors is 250μm±50μm. Close to the distance of 200μm, the order number of the interference ring corresponding to 0 incidence angle is m_0, where m_0 can be obtained as m_0=fix($2d/\lambda$)=632. From the above, $2d=m_0\lambda$. Similarly, close to the distance of 300μm, the order number m_1 can be obtained as m_1=fix($2d/\lambda$)=948. Based on the analysis,

$$2d\frac{2f}{\sqrt{D^2+4f^2}}=m\lambda, \text{ and } d=\frac{m\lambda}{2}\sqrt{\left(\frac{D}{2f}\right)^2+1}. \tag{1}$$

Therefore,

$$\frac{\partial D}{\partial d}=\frac{16fd}{m\lambda\sqrt{4d^2-m^2\lambda^2}}, \frac{\partial d}{\partial f}=-\frac{4m\lambda D^2}{f^2\sqrt{D^2+4f^2}} \text{ and } \frac{\partial d}{\partial \lambda}=\frac{m}{2}\sqrt{\left(\frac{D}{2f}\right)^2+1}. \tag{2}$$

The linear CCD can discern the change of distance d only when the change of ring diameter D caused by the d change is larger than the CCD resolution of 7μm. In an optical design, the error of f is usually controlled under 0.1mm. The measurement error of displacement induced by the error of focus length should be less than the required resolution of 0.2nm. Thus the two conditions

$$\frac{\partial D}{\partial d}>\frac{7000}{0.2}, \text{ and } \left|\frac{\partial d}{\partial f}\right|<\frac{0.2}{100000}, \tag{3}$$

should be satisfied.

From the initial setting of the distance between the two mirrors, m_0, m_1, Eq. (2), and the condition (3), it can be seen that, for the expected properties of the proposed design, the focus length should be $f>$ 391mm, and the displacement range can be d=200-300μm, the monitored range for the CCD is 10-40mm. Similarly, based on Eq. (1), the limitation on the wavelength drift of laser source is obtained as

$$\partial d=\frac{m}{2}\sqrt{\left(\frac{D}{2f}\right)^2+1}\times\partial\lambda<0.2. \tag{4}$$

Therefore,

$$\partial\lambda<0.421\mu m. \tag{5}$$

The design should have f=400mm, d=200-300μm, and $\delta\lambda$<0.421μm.

Testing and Discussion

Using the above design parameters, computational testing through simulations were performed to demonstrate the characteristics of the proposed design. The ring diameter D, ring diameter change ΔD, related to 0.2nm displacement against the expected displacement range, were obtained (Fig. 3). It can be seen that the ring diameter changes is larger than 0.01mm for the whole displacement range of d=200-300μm. Since the linear CCD resolution is 0.007mm, the

resolution for the displacement measurement in the whole expected displacement range should be sufficient.

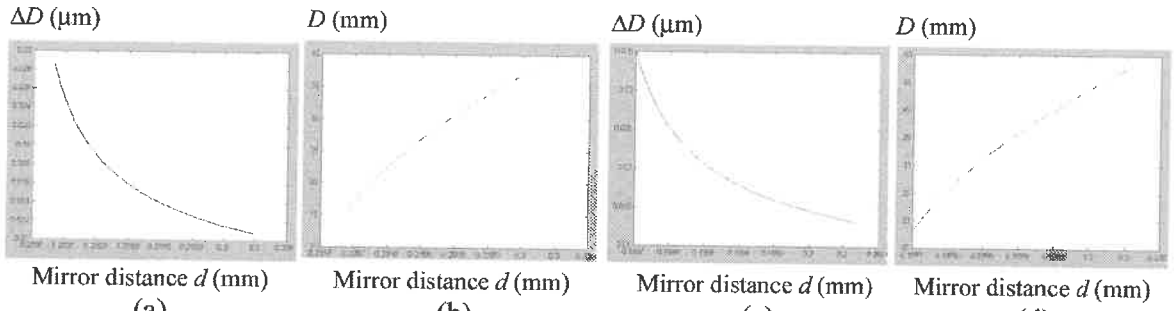

Fig. 3 D and ΔD for the 0.2nm mirror distance change in the range of 0.2-0.3mm±λ/2 and f=400mm

Conclusions

For low cost and ease of use displacement measurement and calibration at the resolution of nanometer level, a new nano-stepping device design for nanometer displacement measurement and calibration is proposed. The design is based on the F-P cavity and the multi-beam interference principle. The analysis shows the device is to have a resolution of 0.2nm and a range better than 100μm. The device is compact in size. From the Abbe principle and the shortest link rule, it should be stable and immune to environmental disturbances.

References

[1] Dai, X., and Seta, Katuo, High-accuracy absolute distance measurement by means of wavelength scanning heterodyne interferometry, Measurement Science and Technology, **9**, 1998, pp. 1031-1035.

[2] Guo, G., Ji, X., Qin, Y., Du, J., and Wang, Z., Mach-zehnder heterodyne interferometer for high-precision displacement measurement, Optical Technique, **6**, 1997, pp. 19-22.

[3] Gao, F., and Xu, Y., A study of folded cavity Fabry-Perot interferometer and its transmitting light phase changes, Opto-electronic Engineering, **20**(3), 1993, pp. 30-33.

[4] Han, Haitjema, Rosielle, N., Kotte, G., and Steijaert, H., Design and calibration of a parallel-moving displacement generator for nano-metrology, Measurement Science and Technology, **9**, 1998, pp. 1098-1104.

[5] Barwood, G., Gill, P., and Rowley, W., High-accuracy length metrology using multiple-stage swept-frequency interferometry with laser diodes, Measurement Science and Technology, **9**, 1998, pp. 1036-1041.

[6] Heymann, G., and Reed, C., Laser interferometry to evaluate the performance of local displacement transducers, Geotechnique, **47**(3), 1997, pp. 399-405.

[7] Hiyono, Satoshi, and Ge, Z., Subnanometric calibration of a differential interferometer, Procision Engineering, **19**, pp. 187-197, 1996.

[8] Hosoe, Shigeru, and Yoshida, Takashi, Applied measurements of multipurpose precise interferometer (AMOS-1), Nanotechnology, **4**(4), 1993, pp. 206-212.

[9] Vaughan, J. M., The Fabry-Perot interferometer: history, theory, practice, and applications, Hilger, Bristol, 1989.

GROSS MEASUREMENT ERROR IDENTIFICATION USING THE GREY SYSTEM THEORY

Z. Wang [a], Y. Gao [b,*], S. Tse [b], P. Qin [c]

[a] Henan University of Science and Technology, Luoyang, 471039, China
[b] Hong Kong University of Science and Technology, Clear Water Bay, Kowloon, Hong Kong
[c] Xi'an Jiaotong University, Xi'an, 710049, China
* E-mail: meygao@ust.hk

Introduction

In a measurement process, measurement data may involve gross errors, which significantly exceed true values, when a measurement quantity is measured repeatedly without significant changes in measurement conditions. If the suspicious data remained during data processing, it will cause incorrect assessment on measurement accuracy due to the distorted measurement results have been used. Correct identification of gross measurement errors is an important issue to achieve reliable measurement results.

Gross errors may be reduced by using suitable measurement devices and under appropriate physical conditions. However, it would be quite difficult to avoid gross errors in measurement processes having large quantities of data.

Gross error identification has been based on statistics. A number of criteria have been used such as the 3σ criterion, the Chauvenet criterion, the Grubbs criterion, and the Dixon criterion [1]. The existing methods [2-10] have been based on a typical distribution such as the Gaussian distribution and require prior knowledge on the data that the measurement data conform to the Gauss distribution or conform approximately to it. In a practical measurement, it may be difficult to have a large quantity of data. Furthermore, the distribution may be found not conforming to the typical distribution. These may make the statistical methods [2-10] not applicable for gross error identification and removal.

In order to address the above issues to proceed with gross error identification and subsequently removal, a new method using the grey system theory is proposed. The advantages of the proposed new method is that the measurement data is not required to conform to a particular probability density distribution and the sampling size of the data does not need to be large. The principle of the gross error identification is presented and an identification criterion proposed. A case study is provided to demonstrate the effectiveness of the proposed grey system method. The proposed method should be a convenient and useful tool to identify gross errors in a precision measurement process.

Working Principle

The grey system method relies on the geometric features of the measurement data, instead of the probability density distribution and the sample size. In order to apply the grey system method, a measurement system is considered as a grey system and the measurement data is therefore a grey number within a particular interval [11].

To establish a complete grey area (Fig. 1), the distance between the data accumulation curve of the sorted data series, $x^{(0)}(k)$, $k=1,2,\ldots, n$, and the reference line, noted as $\Delta(k)$, $k=1,2,\ldots n$, is considered. In a measurement process, as the measurement proceeds, the number of

measurement k would increase, and in the meantime the distance $\Delta(k)$ would increase, and would approach to the maximum distance Δ_{max}. After this point, $\Delta(k)$ would decrease and approaches zero at the last measurement point, where $k=n$.

To simplify the analysis, the medium point of the measurement number n is used as the turning point A to establish the 2-segment line, indicated as Line 2 in Fig. 1. The distance between the point A and the reference line would be h times of the maximum distance Δ_{max}. It can be seen that the 2-segment line (Line 2) is obtained by link up the origin of the coordinate, the turning point A and the end point of the data accumulation. The reference line (Line 3) and the 2-segment line (Line 2) would constitute the grey area that contains the data accumulation curve. It is considered that if there were no gross errors in the measurement data, the data accumulation curve would be restrained in the grey area, between Line 2 and Line 3. If the data accumulation curve cannot be restrained in the grey area, gross errors would exist. Therefore, if only random errors are involved, the data accumulation curve would be restrained within the grey area. Based on this, a criterion for the identification of gross errors can be established.

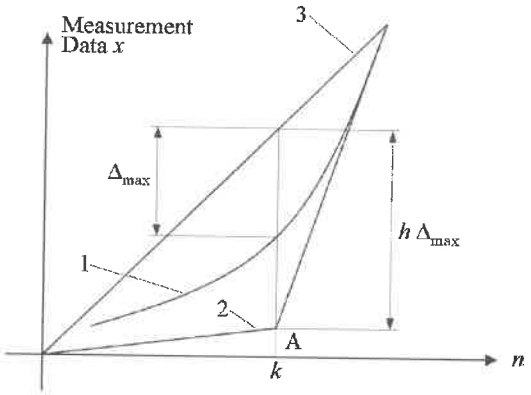

Fig. 1 Data processing using the grey system theory

Firstly, the original data series prior to the accumulation is sorted in an ascending order, noted as $x^{(0)}$. Therefore, $x^{(0)} = [\, x^{(0)}(1), x^{(0)}(2), \ldots, x^{(0)}(n) \,]$. Secondly, applying the 1-AGO algorithm to obtain an accumulated data series, noted as $x^{(1)}$ (Fig. 1). The turning point A of the 2-segment line is the pth measurement point and can be obtained as $p=n/2$ for an even n and $p=(n+1)/2$ for an odd n. The upper side of the grey area can be determined based on the reference line Line 3 (Fig. 1). The linear equation to describe the reference line is as

$$x^{(1)}_{max}(k) = \frac{1}{n} x^{(1)}(n)k = [\frac{1}{n}\sum_{i=1}^{n} x^{(0)}(i)]k = \bar{x}k \quad , \tag{1}$$

where $k=1,2,\ldots,n$, and $\bar{x}$ is the arithmetic mean of the measurement data. The lower side of the grey area can be determined based on the 2-segment line. The linear equation to describe the 2-segment line is as

$$x_{\min}^{(1)}(k)=\begin{cases}(\bar{x}-\dfrac{h\Delta_{\max}}{p})k, & 1\le k\le p\\ \bar{x}k-\dfrac{h\Delta_{\max}}{n-p}(n-k), & p<k\le n\end{cases}. \tag{2}$$

Thirdly, the parameter h is used to define the lower side of the grey area. Through the analysis of many practical examples, h=3.75 seems appropriate. Finally, the criterion can be expressed mathematically as (a) if

$$x_{\min}^{(1)}(k)\le x^{(1)}(k)\le x_{\max}^{(1)}(k), \tag{3}$$

there would be no gross errors. This is due to the accumulated data points being within the grey area. Due to $x^{(1)}(i)<x^{(1)}(i+1)$, the above criterion could be simplified as $x^{(1)}(k)\le x_{\max}^{(1)}(k)$; (b) if

$$x^{(1)}(k)<x_{\min}^{(1)}(k), \tag{4}$$

there would be gross errors. This is due to the accumulated data points being outside the grey area (Fig. 1).

The data point identified to have gross errors should be removed and the remaining measurement data should be rearranged and re-assessed using the above criterion to identify and remove any suspicious data points. This process should be repeated until no gross error is identified in the data series.

Experimental Testing and Discussion

In the experimental testing of the errors of a measurement instrument, 20 repeated measurements were obtained [12]. The systematic errors were identified and compensated. The measurement data series, with the unit of mm, were obtained as

20.002, 20.000, 20.000, 20.001, 20.000, 19.998, 19.998, 20.000, 20.001, 19.998,
20.002, 20.002, 20.000, 20.004, 20.000, 20.002, 19.992, 19.998, 20.002, 19.998.

For the above measurement data, the turning point A of the lower side of the grey area was at p=10, the maximum distance $\Delta_{\max}$=0.0174mm. The arithmetic mean of the data $\bar{x}$=19.999mm. Therefore,

$$x_{\min}^{(1)}=\bar{x}-3.75\frac{\Delta_{\max}}{p}=19.999-3.75\frac{\Delta_{\max}}{7}=19.9934.$$

The first data point and the last one could have higher possibilities in having gross errors, after re-arranging the original sequence into an ascending order. For the first data point k=1, $x^{(0)}(1)$=19.992mm, and $x^{(1)}(1)$=19.992mm. $x^{(1)}(1)$=19.992mm was smaller than $x^{(1)}_{\min}$=19.9934mm. Therefore, it could be concluded that the data point was suspicious of having

gross errors. For the last data point k=20, $x^{(0)}(20)$=20.004mm, $x^{(1)}(20\text{-}1)$=379.994, and

$$x^{(1)}_{\min} = (n-1)\bar{x} - 3.75\frac{\Delta_{\max}}{n-p}[n-(n-1)] = 379.9916.$$

It was greater than $x^{(1)}_{\min}$ =379.9916. Therefore, it was concluded that the last data point was not a suspicious one. Once the data point was identified to have gross errors, it should be removed. As a result, 19 data points remained in the data series. Using the proposed procedure, the remaining 19 data points were subject to the same identification process. It was found that no data point was suspicious of having gross errors.

If a statistics method is used, the data point 19.992mm was also treated as a suspicious one. This shows that the proposed method is more effective in the gross error identification. In general, the statistics methods [2-10] require that the data series conform to the normal distribution. The grey system method does not have such requirement. It is noted that the results from the use of the grey system criterion could be affected by the actual selection of the coefficient h. A systematic examination of the effect should be a topic of further investigation.

Conclusions

The grey system theory can be successfully applied in the identification of gross errors involved in a measurement process. In the proposed method, geometric aspects in the measurement data series plots are considered in the gross error identification criterion. The advantages of the new method are that the probability density distribution of the data series can be unknown and the sampling size small, thus suitable for both statistical and non-statistical measurement. The effectiveness of the proposed method is demonstrated in the experimental testing.

References

[1] Fei, Y., Error theory and data processing, China Mechanical Industry Press, 1995, Beijing.
[2] Bagajewicz, M. J., Gross error modeling and detection in plant linear dynamic reconciliation, Computers and Chemical Engineering, **22**(12), 1998, pp. 1789-809.
[3] Mangalvedekar, H. A., Gross error identification in current measurements, Electric Machines and Power Systems, **25**(8), 1997, pp. 907-16.
[4] Kim, I. W., Robust data reconciliation and gross error detection, the modified MIMT using NLP, Computers and Chemical Engineering, **21**(7), 1997, pp. 775-82.
[5] Sanchez, M., Gross measurement error detection/identification for an industrial ethylene reactor, Computers and Chemical Engineering, **20**, Pt. B, 1996, pp. S1559-64.
[6] Tong, H., Detecting persistent gross errors by sequential analysis of principal components, Computers and Chemical Engineering, **20**, Pt. A, 1996, pp. S733-8.
[7] Yang, Y., A study of gross error detection and data reconciliation in process industries, Computers and Chemical Engineering, **19**, 1995, pp. S217-22.
[8] Kaminski, W., The method of growing rigor for the adjustment of geodetic observations contaminated by gross errors, Manuscripta Geodaetica, **19**(2), 1994, pp. 55-61.
[9] Harikumar, P., A method to incorporate bounds in data reconciliation and gross error detection, Computers & Chemical Engineering, **17**(11), 1993, pp. 1121-8.
[10] Falcao, D. M., Linear programming state estimation: error analysis and gross error identification, IEEE Transactions on Power Systems, **3**(3), 1988, pp. 809-15.
[11] Lin, Y., and Wang, Z., Grey assessing the measurement uncertainty, Journal of Grey System, 2001, **14**(2), pp. 161-164.
[12] Zhu, J., Bin, H., and Wang, Z., Non-statistical distinguish of gross errors in measurement values, Journal of Huazhong University of Science and Technology, 2000, **28**(4), pp.17-19.

Large array thermal machine monitor

Shuqing Zhang and Steven R. Patterson
Department of Mechanical Engineering and Engineering Science
University of North Carolina at Charlotte
Charlotte, NC28223

Abstract

A low cost temperature measurement system is described in this paper. A thermal model, which accommodates the failure of thermal sensors, is developed. The model can correct up to 80% of the thermal growth errors of the spindle in Z-axis.

Keywords: error correction, temperature measurement, thermal model.

1. Introduction

Thermal errors are generally considered one of the major machining errors in computer numerical control (CNC) Machining centers; in some cases thermal errors can contribute more than 50% of the total machining errors [1]. In particular, spindle thermal drifts are often the dominant source of errors among thermally induced errors. The solutions for reducing thermal errors are of two main types: improving the machine tool design and error compensation techniques [2]. In spite of the machine tools manufacturer's effort, there are always some residual thermal displacements, because it is very hard to optimize the design for different kind of operation conditions [3]. In recent years more research has been directed to the control of the CNC machining center; and several techniques have been reported for the correction and compensation of the thermal growth. To be effective in a production environment, a compensation system that corrects thermal errors must be both low-cost and robust.

There are two main techniques for compensating thermal growth of CNC machining center: the finite element calculation and empirical modeling [4]. It is often difficult to estimate boundary conditions and heat dissipation throughout the machine structure. As a result finite element techniques are used only for trend prediction rather than as a precise prediction method.

Thermal error prediction based on the empirical model approach is based on the measurement of the actual thermal state of the machining and requires an effective temperature measurement system to measure the temperature at key points on the machining center.

2. Temperature measurement system

In this paper a low-cost temperature measurement system is represented. It comprises an IC-based temperature measurement system, a micro-controller interface to a PC-based real-time data acquisition system. This temperature measurement system can drive a large array of thermal sensors. Figure 1 shows the block diagram of the temperature measurement system.

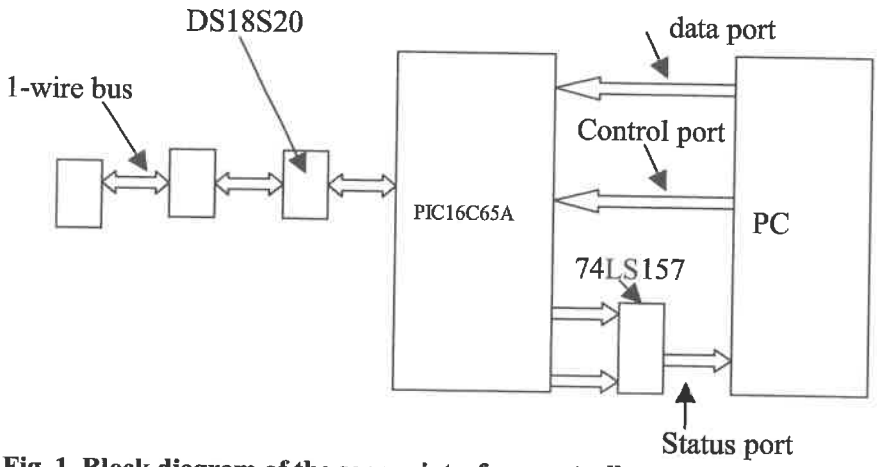

Fig. 1. Block diagram of the sensor interface controller

The high-precision 1-wire digital thermometer DS18S20 is used as the thermal sensor in the temperature measurement system. Each DS18S20 sensor communicates with a central microprocessor over a "1-wire" bus. Each DS18S20 sensor has a unique 64-bit serial code, and multiple sensors can coexist on the same "1-wire" bus. Thus it is straightforward to use one microprocessor to control many sensors distributed over a large area. A PIC16C65A is used as the central microprocessor, it communicates with the sensors over the "1-wire" bus and with the PC through the printer port. The PIC16C65A sends commands received from the PC to the DS18S20, and sends the temperature results from each sensor to the PC.

3. Modeling and evaluation

To test the systems on a machining center, 31 thermal sensors have been mounted on a Monarch VMC45 machining center. Because one of the major heat sources that influences the spindle growth is the spindle system and its bearings, the thermal sensors for the initial testing are mainly mounted around the spindle, gearbox and X-, Y-, W- and Z-slide scale.

Modeling and evaluation was conducted in three steps: (1) data collection on the Monarch VMC45, (2) data processing and modeling, (3) model evaluation on the same machining center. The data collection tests consist of: (1) a Warm-up run test (2) various spindle speed run test (3) a production cycle run test and (4) a cool-down run test of the spindle. A linear least squares regression thermal model has been developed based on the initial data. Because the VMC-45 is a "C" frame vertical machining center, the spindle thermal growth is mainly along the Z-axis. All data reported here refers to motion along the Z-axis.

Twenty-five thermal sensors have been used in the model. The correlation coefficients between the thermal sensors and the spindle-axis growths have been calculated in order to find the key locations of the heat sensors. Then the thermal sensors are ordered by the values of the correlation coefficients.

The thermal growth of the spindle has been modeled as

$$Z = a_0 + a_1(T_1 - 20) + a_2(T_2 - 20) + \cdots + a_{25}(T_{25} - 20) \qquad (1)$$

where
Z -- thermal growth errors predicted along Z-axis
T_i -- the value of thermal sensors, i=1,2,..., 25
a_i -- the parameters of the model, i=1,2,...,25

The covariance matrix of the parameters shows the parameters a_i are not statistically independent and their errors are correlated. In this paper the model is modified. If Vector A is the original parameters, vector B is the modified parameters and matrix C is the eigenvector matrix of the covariance matrix, then

$$B = C^{-1} * A \qquad (2)$$

After the modification the parameters in vector B are statistically independent and their errors are not correlated. So if one sensor fails, it will not affect other parameters in the model.

Thermal models developed by data from different operational conditions have been evaluated. Figure 2-4 shows the evaluations of the thermal model under three different operational conditions: warm-up run, cool down run, and production cycle run.

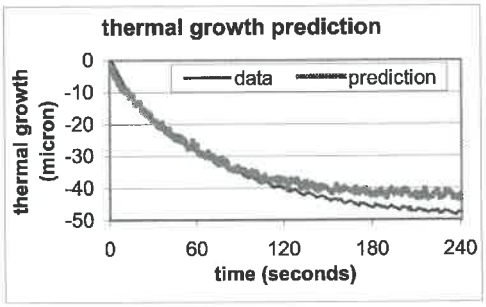

Fig. 2 Thermal growth prediction during Warm up run test with speed of 1500rpm

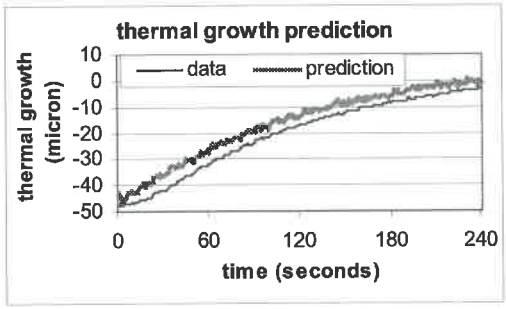

Fig. 3 Thermal growth prediction during cool down run test

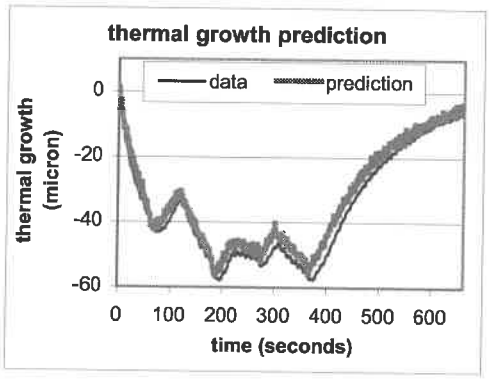

Fig. 4 Thermal growth prediction during production cycle run test

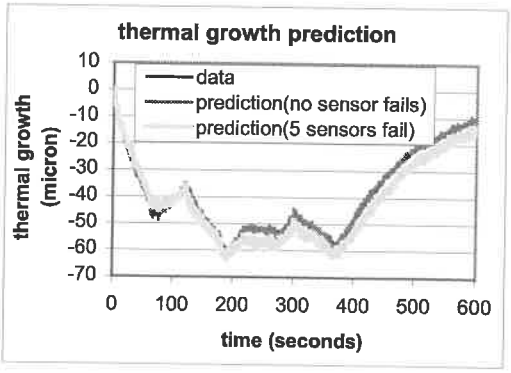

Fig. 5 Thermal growth prediction by model when 5 thermal sensors fail

A thermal model that gracefully accommodates the failure of thermal sensors has been developed. Because the thermal model is based on the temperature and spindle thermal growth measurement, it will be affected by the failure of thermal sensors. The experiment results show that if one thermal sensor fails, the uncorrected thermal growth prediction error of the model is up to 2 mm; if five thermal sensors fail, the uncorrected thermal growth prediction error is more than 5mm. The correlation coefficient between the thermal sensors is calculated, and then a failed sensor can be replaced by a linear combination of other sensors that have high correlation coefficient with it. The resulting corrected thermal growth prediction is minimally affected by the failure of a small number of thermal sensors. Figure 5 shows the comparison of thermal growth prediction by the model with and without thermal sensor's failure.

References

[1] M.Weck, P. Mckeown, 1995, Reduction and Compensation of thermal Errors in Machine tools. Annals of the CIRP, Vol. 44.

[2] J.S.Chen, J.X.Yuan, etc, 1993, Real-time Compensation for time-variant Volumetric Errors on a Machining Center. Transactions of the ASME, November, Vol. 115.

[3] S.Fraser, M. H. Attia, M. O. M. Osman, 1998, Modeling, Identification and Control of Thermal Deformation of Machine Tool Structures, Part 1: Concept of Generalized Modeling, Journal of Manufacturing Science and Engineering, Aug., vol. 120.

[4] K. C. Lau, 1993, Development of A Spindle Thermal Error Characterization and Compensation Senor System for Machining Center Accuracy Enhancement.

Cutting Error Measurement of Harmonic Drive Gears Using Laser Probes

Masaru Furukawa[1], Wei Gao[1], Satoshi Kiyono[1], Hiroshi Yamazaki[2]
1 Department of Mechatronics and Precision Engineering,
Graduate School of Engineering, Tohoku University, Sendai, 980-8579 Japan
Phone & Fax: +81-22-217-6953, E-mail: masaru@nano.mech.tohoku.ac.jp
2 Harmonic Drive Systems Incorporated,
1856-1 Maki, Hotaka-machi, Minamiazumi-gun, Nagano, 399-8305 Japan

1. Introduction

The harmonic drive is a precision mechanism that has a high reduction ratio with low backlash[1]. The dimensional tolerances required for the precision gears used in the harmonic drive are getting tighter and tighter[2]. To assure the quality of the machined gears, it is necessary to accurately measure cutting errors of hobbing machines for cut of the gears. It is also desired to perform the measurement efficiently so that the machining efficiency can be improved[3].

In this paper, we develop a new system of cutting error measurement for the flexspline(FS) gear of the harmonic drive. Two laser probes[4] are used in the measurement. The non-contact measurement avoids deforming the gear geometries, and leads to a high-speed measurement.

2. Principle of measurement

In the case of measuring the radial cutting error component, two laser displacement probes are employed to replace the conventional method of using Van Kuven wires and a micrometer[5]. Fig.1 shows a schematic comparison between the conventional method and the new method. In the conventional measurement method of using wires and micrometers, the wire is placed between two adjacent gear teeth, and the measurement over wires is obtained by the micrometer. If the teeth are over-cut, the tooth thickness decreases and the space interval between the gears increases. As a result, the contact points of the wire will move toward the gear center. The radial cutting error component can then be evaluated from the measurement over wires.

In the developed laser probe-based measurement system, the two laser beams are projected onto different tooth surfaces.

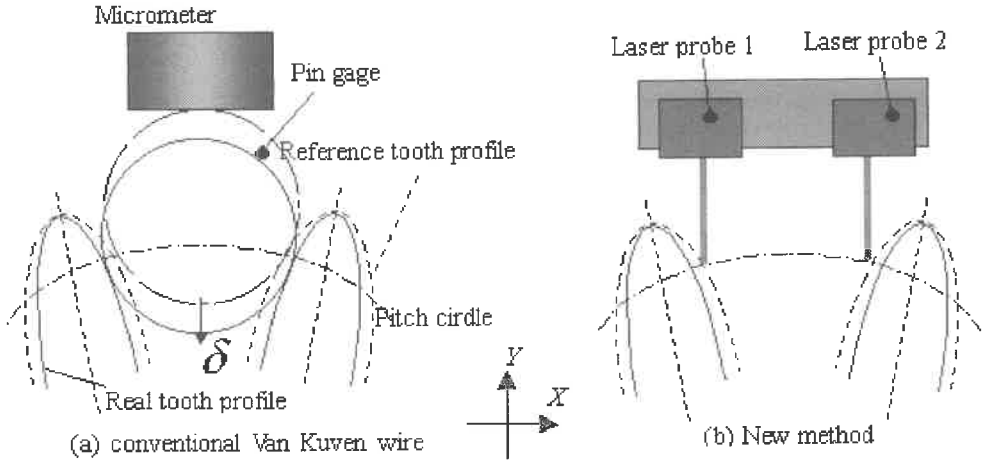

Fig.1 A comparison between the conventional Van Kuven wire method and the new method

The incident light spots on the tooth surfaces function as the contact points of the wire on the tooth surfaces. The radial cutting error component can be obtained from the probe outputs. The measurement uncertainty can be greatly reduced through rotating the gear and performing the measurement over the entire teeth. The influences of the alignment errors as well as the rotational errors of the rotary gear stage can be removed by a differential data processing technique described as follows.

Fig.2 shows the measurement model taking eccentricity error of alignment and rotation error of the gear stage into consideration. Assume that the eccentricity error of the when FS attached is d ,and X-, and Y-directional components of the rotation error are $e_x(\theta_i)$, $e_y(\theta_i)$, respectively. The probe outputs $D_1(\theta_i)$, $D_2(\theta_i)$ can be expressed as :

$$D_1(\theta_i) = g_1(\theta_i) - \{d\cos\theta_i + e_x(\theta_i)\}\tan\phi_1(\theta_i) + d\sin\theta_i + e_y(\theta_i) \quad (1)$$

$$D_2(\theta_i) = g_2(\theta_i) + \{d\cos\theta_i + e_x(\theta_i)\}\tan\phi_2(\theta_i) + d\sin\theta_i + e_y(\theta_i) \quad (2)$$

where $g_1(\theta_i)$, $g_2(\theta_i)$ are the probe optputs when eccentricity and rotation errors don't exist.

Subtracting (2) from (1), the differential output ΔD becomes

$$\begin{aligned}\Delta D &= D_1(\theta_i) - D_2(\theta_i) \\ &= g_1(\theta_i) - g_2(\theta_i) - \{d\cos\theta_i + e_x(\theta_i)\}(\tan\phi_1(\theta_i) + \tan\phi_1(\theta_i)) \end{aligned} \quad (3)$$

It can be seen that the Y-directional components of eccentricity and rotation errors are removed. To reduce the influence of the X-directional error components, an average of the data over one rotation is carried out. The averaged result $\overline{\Delta D}$ can be denoted as :

$$\begin{aligned}\overline{\Delta D} &= \sum_{i=1}^{N}\frac{\Delta D}{N} = \sum_{i=1}^{N}\frac{g_1(\theta_i) - g_2(\theta_i)}{N} - \sum_{i=1}^{N}\frac{\{d\cos\theta_i + e_x(\theta_i)\}\{\tan\phi_1(\theta_i) + \tan\phi_2(\theta_i)\}}{N} \\ &= \Delta G + \Delta E_X \end{aligned} \quad (4)$$

where, N is a sampling number over one rotation.

The residual error term ΔE_X, which is caused by non-synchronous rotation components of the X-directional rotation error, is expected to be smaller than ΔG. Average of data over multiple rotations can also be carried out to reduce ΔE_X furthermore. As a result, the cutting error, which is a function of ΔG, can be evaluated from $\overline{\Delta D}$ accurately.

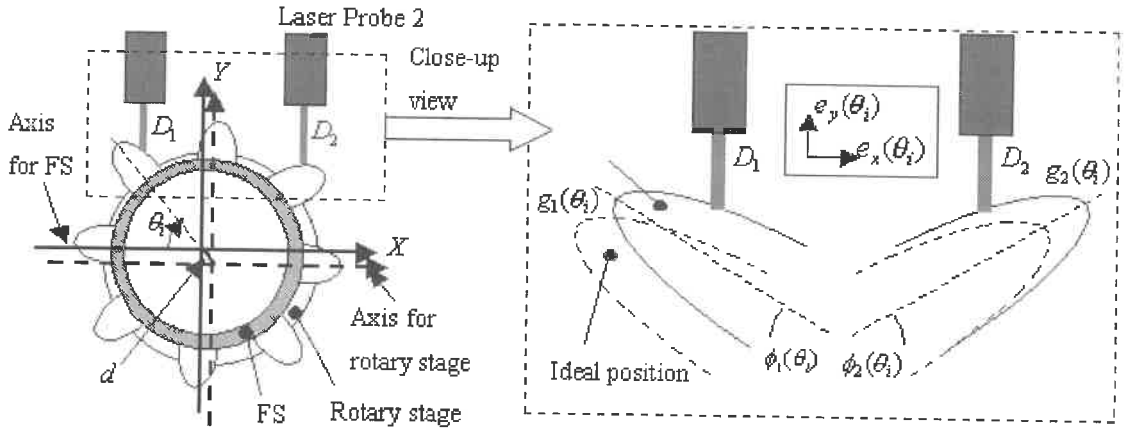

Fig.2 Geometric model for analyzing the new method when rotation

3. Experiments

Fig.3 shows a schematic of the measurement system. The system consists of two laser probes and a rotary stage on which the gear is mounted. Resolution of the laser probe is 10 nm. The displacement interval L was approximately 35mm. The probe outputs were taken into a personal computer through an AD board. The rotary stage is driven by a stepping motor. The radial error motion of the stage is approximately 5 μm. The time for the measurement of one rotation is 60 seconds. The eccentricity of the FS center is approximately 5 μm.

Three FS samples with cutting errors of 0, -5, +5μm were used in the experiment. The samples are referred to as standard FS, -5μmFS and +5μmFS, respectively. The cutting errors were generated by adjusting the depth of cut when the samples were machined on the hobbing machine. Measurements were made after the laser probes and the rotary stage had been powered for an hour. The FS samples were cleaned by ethanol before the measurement. The temperature of the measurement room was approximately 23℃ and the humidity was under 30%.

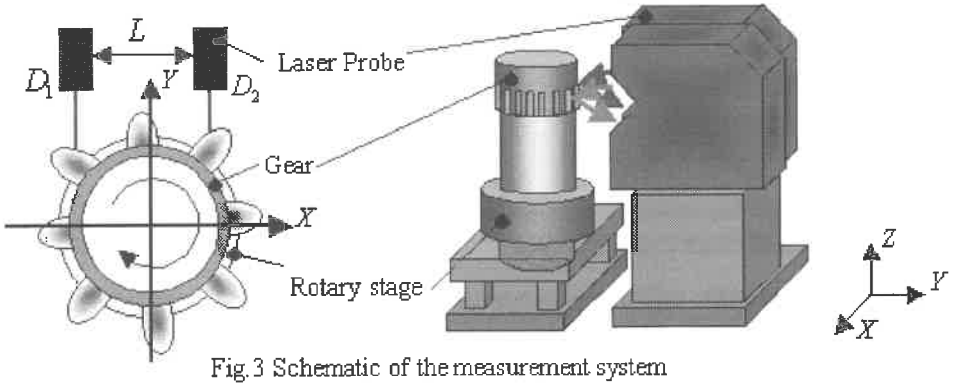

Fig.3 Schematic of the measurement system

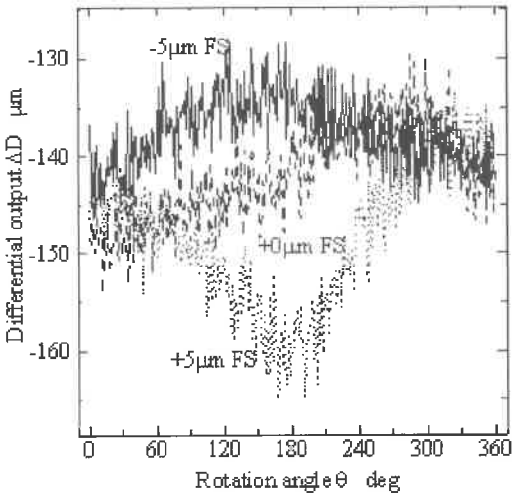

Fig.4 Differential output ΔD

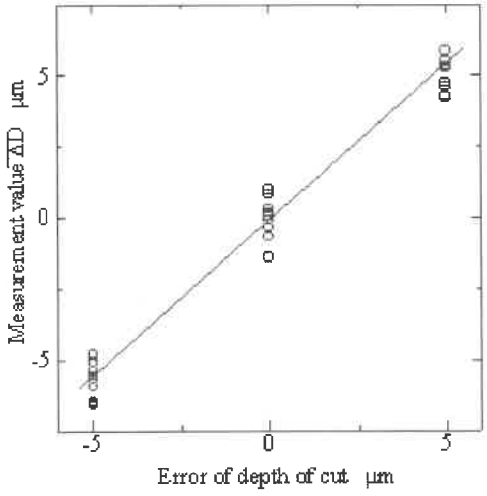

Fig.5 Measurement results

Fig.4 shows the measurement results of ΔD defined in Eq.(3) for different FS samples. The data of one rotation are shown in figure. The horizontal axis shows the rotary angle of the stage and the vertical axis shows the differential output ΔD. It can be seen that influences of the eccentricity and rotation errors are included in the differential output ΔD. The eccentricity errors were not constant for different FS samples since they were

mounted on the stage at different times.

Fig.5 shows $\overline{\Delta D}$ defined in Eq.(3), which is the average of the differential output ΔD over one rotation. The horizontal axis of figure shows the applied FS cutting error and the vertical axis shows $\overline{\Delta D}$. It can be seen that the cutting errors have a good correlation with $\overline{\Delta D}$, which indicates the feasibility of the developed measurement method.

Measurements were also made when a layer of cutting oils remained on the FS surface. Fig.6 shows the probe output with oils on the surface. The result after the oil was removed from the surface by compressed air is also shown in the fig.6. The horizontal axis shows the rotary angle of the rotary stage and the vertical axis shows one of the laser probe outputs. It can be seen that the laser probe did not function well for the sample with oil on its surface. However, the laser probe was able to measure the sample when the surface was cleaned by compressed air. This indicates that blowing off cutting oil from the sample surface with compressed air is an efficient method for cleaning the sample surface in practical use.

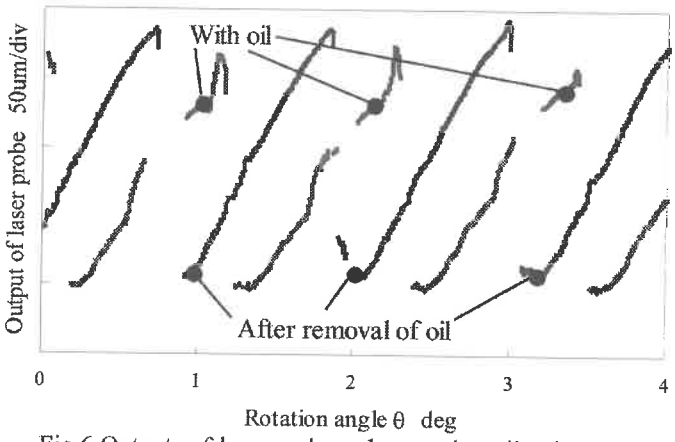

Fig.6 Outputs of laser probes when cutting oil exists on the surface, and after the surface was cleaned with compressed air, and cutting oil don't exist.

4. Conclusions

A new method has been developed for measurement of cutting errors of flexspline gears of the harmonic drive through using two laser displacement probe instead of a Van Kuven wires and a micrometer. An averaging operation of the data over one rotation of the gear stage removes the influence of eccentricity and rotation errors. The effectiveness of using compressed air to remove the oil from the gear surface, which enables the measurement of laser probes, has also been confirmed.

References

[1] Dennis P. Townsend, et al., Dudley's Gear Handbook, McGraw-Hill, Inc, New York.

[2] Fathi H. Ghorbel, Prasanna S. Gandhi, Friedhelm Aalpeter, On the Kinematic Error in Harmonic Drive Gears, Journal of Mechanical Design, Transactions of the ASME, Vol.123, MARCH (2001).

[2] Heui Jae Pahk, Young Min Hwang, et al., Vision based Precision Inspection System for Profile and Performance of Small and Micro Gears Using the Intelligent Image Processing Techniques and Virtual Master Gears, Proceedings of SPIE Vol.4222, (2000), 48.

[3] Hirohito Matsuoka, Shinji Kasei et al., Application of optical cutting method to measurement of tooth-profile error of minute module gears, J.JSPE, 66,8 (2000), 1226.

[4] Keyence Laser Probe, LC-2420, http://www.keyence.com/

[5] J.R. Walker, Machining Fundamentals, The Goodheat-Willcox Company Inc. (1998).

In-process Measurement of Topography of Grinding Wheel by Using Hydrodynamic Pressure

Katsushi Furutani, Noriyuki Ohguro[1], Nguyen Trong Hieu[2] and Takashi Nakamura[3]
Department of Advanced Science and Technology, Faculty of Engineering, Toyota Technological Institute
12-1, Hisakata 2-chome, Tempaku-ku, Nagoya 468-8511 Japan
Phone: +81-52-809-1796, Fax: +81-52-809-7121, e-mail: furutani@toyota-ti.ac.jp

1. Introduction

Wet grinding is one of the major ways of high-precision machining. An error factor in grinding is wear of a grinding wheel. In order to reduce machining error, in-process measurement of the grinding wheel wear is required.

Loading and dulling on a grinding wheel frequently occur under inappropriate grinding conditions. Eventually, the surface of a workpiece is burned. The working surface of a grinding wheel is dressed at a certain interval to avoid the burning. Therefore, it is very important to measure both wear amount and topography change of the grinding wheel during grinding process.

Grinding fluid, which causes the difficulty of the in-process measurement, is often used to cool a workpiece. Some in-process measurement methods of wear of a grinding wheel have been proposed for both dry and wet grinding [1][2].

Some methods to detect or measure loading, dulling and shedding of a grinding wheel have been also proposed by using a triangulation displacement sensor [3] for dry grinding. Because the grinding fluid disturbs light, it must be removed in wet grinding. Sensing acoustics [4] or vibration [5] has been also proposed for both dry and wet grinding. However, they are indirect methods.

Some measurement methods by measuring static pressure caused by applying fluid to a grinding wheel have been proposed [6]-[8]. Because these methods are similar to an air micrometer, superfluous grinding fluid must be removed for accurate measurement. The authors have proposed a measurement method using hydrodynamic pressure [9][10]. This method actively uses the grinding fluid to generate the pressure. The topography of the working surface of a grinding wheel affects the flow of the grinding fluid. Therefore, it is expected that the topography change can be measured by analyzing the pressure.

In this paper, the in-process measurement method of a grinding wheel in wet condition is introduced. Then the relationship between the topography and the pressure during grinding is discussed.

2. Principle of measurement

Fig. 1 shows the measurement principle in the case of applying to a surface grinding process [9][10]. A pressure sensor is set beside a grinding wheel. Additional grinding fluid is poured near the gap between the grinding wheel and a pressure sensor. Grinding fluid is dragged by the rotation of the grinding wheel into the gap. Hydrodynamic pressure is generated in the gap. Then the pressure change caused by the hydrodynamic pressure is measured with the sensor. The hydrodynamic pressure decreases with an increase of the gap distance between the sensor and the working surface of the grinding wheel. After a relationship between the gap and the pressure is calibrated, the gap can be predicted by measuring the pressure. The electromagnetic properties of the grinding wheel, a workpiece and grinding fluid do not affect the pressure. Viscosity of the grinding fluid seldom changes during grinding even if the temperature of the working fluid is slightly changed or debris is mixed. The diameter

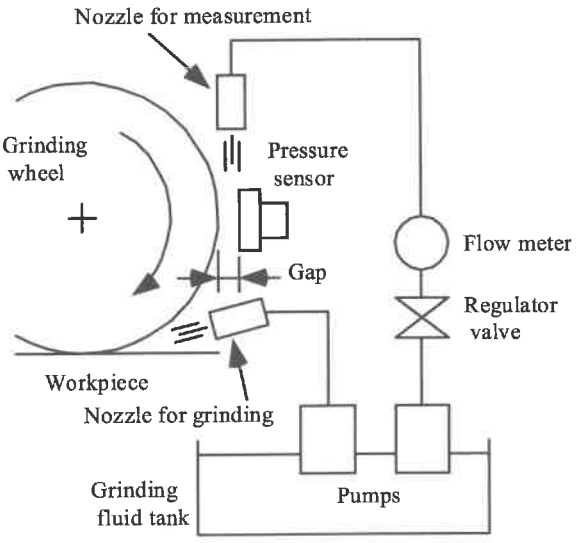

Fig. 1 Measurement principle by using pressure.

[1] Daikin Industries, Ltd. at present
[2] Nagoya Institute of Technology at present
[3] Nagoya Institute of Technology

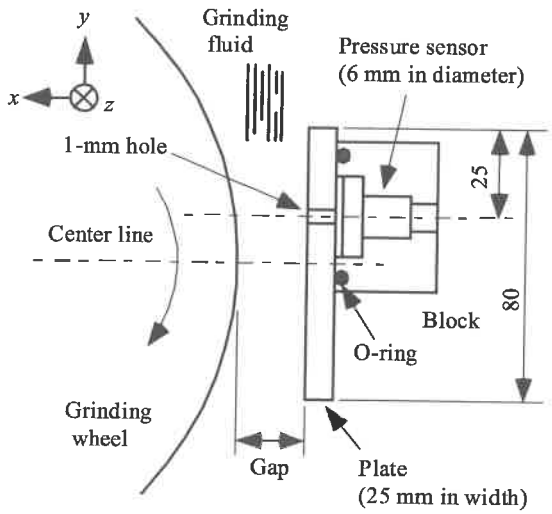

Fig. 2 Arrangement of pressure sensor.

change by the wear seldom affects the peripheral speed of the grinding wheel because the ratio of the wear to the diameter is negligible. Therefore, the measurement process by this method becomes easier and more accurate than the measurement process with other noncontact sensors. Because the grinding fluid is actively used, no other additional device is needed.

A roughness of the working surface of a grinding wheel changes because of loading, dulling and shedding during grinding, and affects flow in the gap. As a surface becomes rougher, flow is separated earlier in general and becomes more turbulent. It is expected that its frequency components change. The influence of the roughness is investigated by frequency analysis.

3. Experimental setup

An external cylindrical grinding machine was used in the following experiments. Table 1 shows specifications of the grinding machine and a grinding wheel. The grinding wheel was composed of grains made from white fused alumina with an average diameter of 250 μm.

Fig. 2 shows an arrangement of a pressure sensor. The sensor was covered with a plate with a hole of 1 mm to avoid the direct contact with the grinding wheel. The surface roughness of the plate is 1.7 μmR_z. Table 2 shows specifications of the pressure sensor. The sensor with a diaphragm of 6 mm in diameter was a strain gauge type. The sensitivity of the pressure sensor was 10 kPa/V at the output of the strain amplifier.

The sensor unit was mounted on the table of the grinding machine with a combination of an xyz and a rotational stages, which can be mounted and dismounted with a magnet chuck. The maximum pressure was at 5

Table 1 Specifications of grinding machine

Cylindrical grinding machine	Revolution of grinding wheel	26.8 s^{-1}
	Maximum peripheral speed	29.9 m/s
Grinding wheel	Type	JIS-WA60J7V
	Grain	White fused alumina
	Average grain size	250 μm
	Bond	Vitrified
	Diameter	355 mm
	Width	50 mm

Table 2 Specifications of pressure sensor

Pressure sensor	Type	Strain gauge (diaphragm)
	Nominal pressure	100 kPa
	Diameter of diaphragm	6 mm
	Natural frequency	22 kHz
	Linearity	1 %
Strain amplifier	Band width	DC-200 kHz
	Accuracy	±0.1 % of FS
	Linearity	±0.01 % of FS

FS: full scale

mm above the contact point of the grinding wheel with a workpiece. Because the sensor unit was removed during grinding, the pressure sensor must be exactly put back after grinding process by adjusting the position with the stage. The gap was measured with an eddy current displacement sensor with a measurement range of 1 mm and a resolution of 0.4 μm.

Soluble-type grinding fluid containing surfactant was diluted 70 times with water. The grinding fluid was supplied at the maximum flow rate of 1.3×10^{-4} m^3/s through a regulator.

4. Experiment

4.1 Adjustment of gap distance

The gap distance between the grinding wheel and the plate mounting the sensor must be adjusted before the experiments.

Fig. 3 shows the adjustment process of the gap distance. The sensor was arranged in parallel to the working surface of the grinding wheel. When the grinding wheel contacts with the plate detecting by a spark on the plate, this distance of the gap was defined as zero. Then, the spindle was moved backward to change the gap. The gap distance is measured as the displacement of the spindle. The removed depth in the zero detection procedure is measured with a

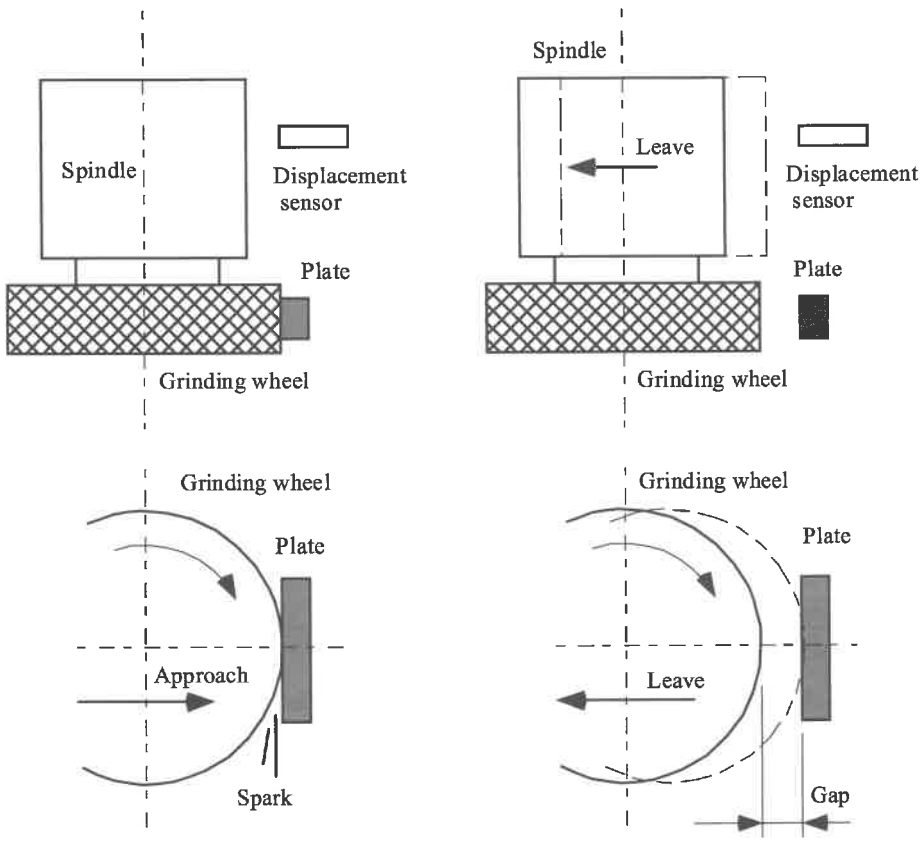

(a) Setting zero-gap distance. (b) Measurement of gap distance.

Fig. 3 Gap adjustment process.

profilometer to compensate the gap distance after the experiments.

4.2 Influence of supplying direction of grinding fluid for measurement

A flow rate of the grinding fluid and a nozzle position affect conditions in the gap [11]. Their influence on the pressure is investigated.

Fig. 4 shows two arrangements of a nozzle. The grinding fluid was supplied from the 20° or tangential directions. The pressure sensitively changed below a flow rate of 6×10^{-5} m^3/s with the inclined nozzle. The grinding fluid was frothed with the rough surface of the grinding wheel. This trend grew as the flow rate was increased with the inclined nozzle. However, the pressure was almost flat with the tangential nozzle. The supply from the tangential direction makes the pressure robuster against the ripple of the grinding fluid. The grinding fluid was applied from the tangential direction in the following experiments.

4.3 Relationship between pressure and gap distance

The relationship between the pressure and the gap distance must be calibrated for each grinding wheel before actual measurement.

Fig. 5 shows a relationship between the pressure and the gap distance in the case of using the grinding wheel shown in Table 1. The spindle was driven to change the gap. The grinding fluid was applied at a flow rate of 4.2×10^{-5} m^3/s. The peripheral speed of the grinding wheel was set to 26 m/s. The pressure was linearly decreased with a sensitivity of 150 Pa/μm from 5 to 30 μm in gap distance. The pressure changes in the same way in both the cases of changing the diameter of the grinding wheel by dressing and of adjusting the spindle position because the diameter change affects its peripheral speed little.

4.4 Pressure change caused by loading

Table 3 shows grinding conditions to accelerate loading of the working surface. Mild material, aluminum, was used for a workpiece. Against the general grinding conditions for aluminum, the structure of the grinding wheel was porous and the peripheral speed of the workpiece was slow to deposit debris on the grinding wheel by the accumulated heat.

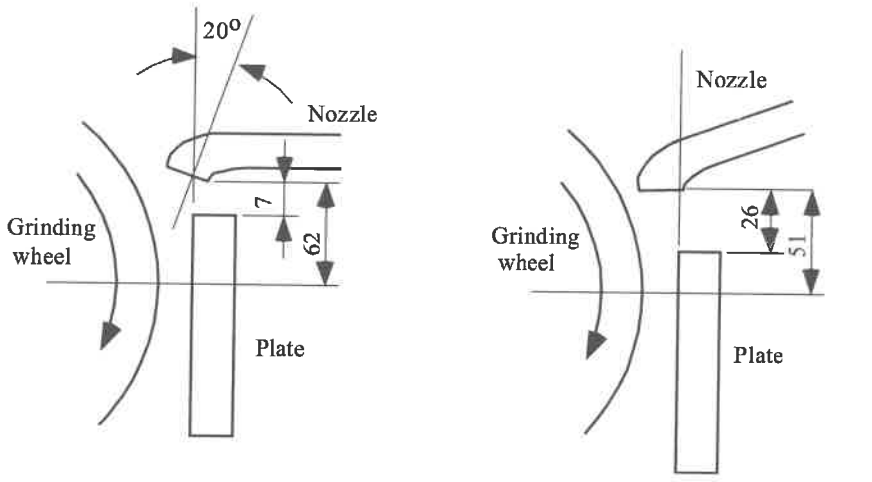

(a) 20°-direction. (b) Tangential direction.

Fig. 4 Arrangement of nozzle.

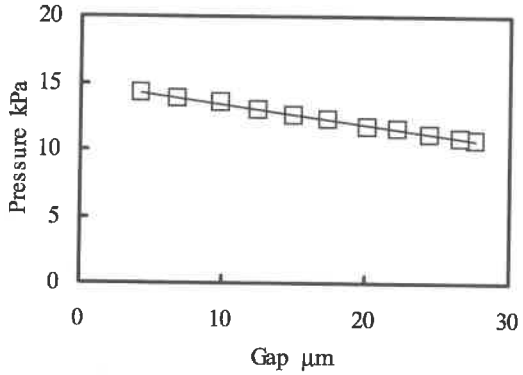

Fig. 5 Relationship between pressure and gap distance.

Table 3 Grinding conditions to accelerate loading

Grinding wheel	Type	JIS-WA60J7V
	Peripheral speed	26 m/s
Dressing conditions	Depth of dressing	10 μm
	Feed speed	5 μm/s
Grinding conditions	Method	Plunge grinding
	Depth of grinding	2.5 μm
Workpiece	Material	Aluminum (JIS-A2014, ASTM-2014), ϕ30 mm
	Peripheral speed	0.13 m/s
	Rotational direction	Reverse of grinding wheel

Total amount of grinding was 208 mm^2 after grinding to a thickness of 50 μm. The wear of the grinding wheel was too small to measure it. Frequency components were observed with a Fast Fourier Transform (FFT) analyzer. Fig. 6 shows an example of spectra of the pressure, which is the average of 50 measurements to avoid random errors. The initial gap was set to 20 μm. As the gap between the sensor and the grinding wheel increased with the progress of grinding, total pressure becomes smaller. However, some components, a frequency of 350 Hz mainly in this case, were increased after grinding. The roughness of the working surface of the grinding wheel is decreased from 285 to 191 μmR_z and from 13 to 9 μmR_a because of loading. No diameter change was measured. This trend was clearly observed at higher flow rate.

Fig. 7 shows a change of the spectra of the pressure with a progress of grinding. The horizontal lines

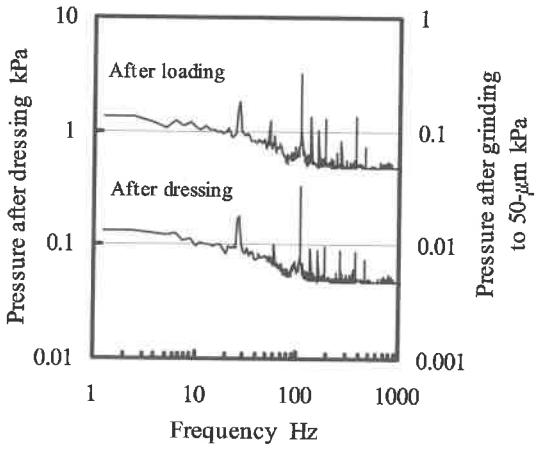

Fig. 6 Example of pressure spectra before and after loading.

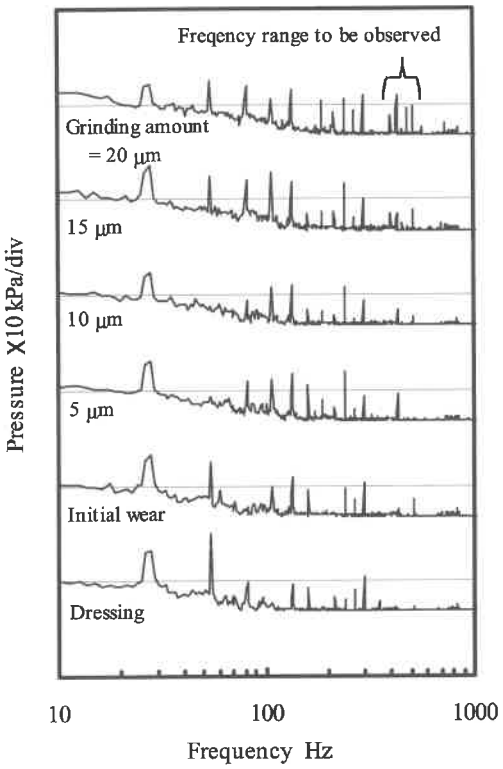

Fig. 7 Change of pressure spectra with progress of loading.

indicate 0.1 kPa in each set of spectra. Table 4 shows grinding conditions. Bearing steel (JIS-SUJ2, ASTM-52100) is ground to a thickness of 10 μm to remove cracked part of grains just after dressing. Then the pressure was observed during grinding aluminum. Though the spectra from 400 to 500 Hz were observed very little after dressing and the initial wear by grinding bearing steel, they were increased with a progress of grinding. This band depends on the structure of the grinding wheel.

Fig. 8 shows a dependency of frequency components of the pressure on the gap distance. Higher components decreased with an increase of the gap distance. Smaller gap is preferable to detect the topography change.

4.5 Pressure change caused by dulling

The working surface becomes flatter also by dulling. In-process measurement of dulling was also tried.

After grinding a tungsten carbide rod with a diameter of 40 mm to a thickness of 50 μm with a depth of cut less than 1 μm, the working surface of the grinding wheel was dulled.

Fig. 9 shows examples of the spectra of the pressure before and after dulling under the grinding conditions shown in Table 5. The spectra in a higher frequency

Table 4 Experimental conditions for progress of loading

Grinding wheel	Grinding wheel	JIS-WA60J7V
	Peripheral speed	26 m/s
Dressing conditions	Depth of dressing	10 μm
	Feed of table	5.2 mm/s
Initial wear	Workpiece	Bearing steel (JIS-SUJ2, ASTM-52100)
	Peripheral speed	0.27 m/s
	Depth of grinding	2.5 μm
	Amount	40 mm^2
Loading	Workpiece	Aluminum (JIS-A2014, ASTM-2014), ϕ30 mm
	Peripheral speed	0.13 m/s
	Depth of grinding	2.5 μm
	Amount	14 mm^2
Pressure measurement	Initial gap	10 μm
	Flow rate	8.3×10^{-5} m^3/s

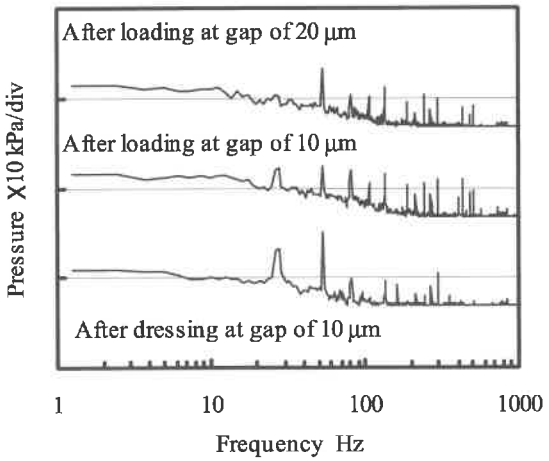

Fig. 8 Comparison of spectra with respect to the gap distance.

range are increased as well as loading. Therefore, dulling can be detected by this method.

The discrimination among loading, dulling and shedding should be considered for detail analysis of the topography of the grinding wheel. However, it is enough to detect the necessity of dressing.

5. Conclusions

In this paper, the topography change of a grinding wheel was observed using hydrodynamic pressure. The conclusions can be drawn as follows.

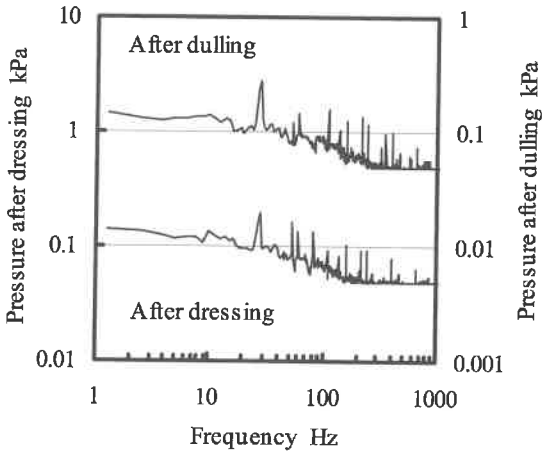

Fig. 9 Example of pressure spectra before and after dulling.

(1) Spectra of the pressure in higher frequency were increased with the progress of loading and dulling.
(2) Not only the flow rate but also turbulent flow of the grinding fluid and air affected the measured pressure.
(3) The pressure was decreased with an increase of the gap distance in the case of a narrow gap.

A measured diameter of the grinding wheel by this method changes by the wear and topography changes caused by loading, dulling and shedding. Their influence should be discriminated in the measurement process in future.

Table 5 Grinding conditions for measurement of dulling

Grinding wheel	Grinding wheel	JIS-WA60J7V
	Peripheral speed	26 m/s
Dressing conditions	Depth of dressing	10 μm
	Feed of table	5.2 mm/s
Grinding conditions	Method	Plunge grinding
	Workpiece	Tungsten carbide ϕ40 mm
	Peripheral speed	0.33 m/s
	Depth of grinding	less than 1 μm

Acknowledgement

The authors wish to thank Mr. Masaru Ohta for his helpful cooperation. This study is financially supported by Osawa Scientific Grant (OSG Fund), Fluid Power Technology Foundation and Grant-in-Aid for High-tech Research Center " Space Robotics Research Center" and Academic Frontier Center for "Future Data Storage Materials" by Ministry of Education, Culture, Sports, Science and Technology, Japan.

References

[1] W. P. Dong, L. Annecchino and J. A. Webser: On-Line Measurement of Grinding wheel Wear Using Acoustic Emission, Proc. Ann. Meet. Am. Soc. Precis. Eng., Monterey, California, USA, pp. 566-571 (1996).

[2] G. Spur and F. Leonards: Sensoren zur Erfassung von Prozesskenngrössen bei der Drehbearbeitung, Ann. CIRP, 24, 1, pp. 349-355 (1975).

[3] E. Brinksmeier and F. Werner: Monitoring of Grinding Wheel Wear, Ann. CIRP, 41, 1, pp. 373-376 (1992).

[4] S. Hagiwara, T. Obikawa, M. Gomi, T. Matsumura, T. Iizuna, A. Yui: Prediction of Grinding Status Based on Dressing Sounds - Approaches by Linear Prediction Method and Neural Network -, J. Jpn. Soc. Precis. Eng., 67, 1, pp. 137-141 (2001) [in Japanese].

[5] A. Hosokawa, K. Sakuma, and T. Ueda: In situ Characterization of Grinding Wheel Surface, Proc. 14th Ann. Meet. Am. Soc. Precis. Eng., Monterey, CA, USA, pp. 99-102 (1999).

[6] H. J. Schreitmüller and M. Dederichs: Pneumatisches Meßverfahren zur Ermittlung des Schleif-scheibenverschleißes, Industrie-Anzeiger, 93, 68, 1733-1734 (1971).

[7] T. M. A. Maksoud, A. A. Mokbel, and J. E. Morgan: In-process Detection of Grinding Wheel Truing and Dressing Conditions Using a Flapper Nozzle Arrangement, Proc. Insttn. Mech. Engrs., J. Eng. Manufact., 211, Pt. B(5), pp. 335-343 (1997).

[8] J. F. Rahman, V. Radhakrishnan: Measurement of Grinding Wheel Surface Topography Using Electro-Pneumatic Turbulence Amplifier System, Int. J. Mach. Tool Des. Res., 20, 3/4, pp. 189-196 (1980).

[9] K. Furutani, T. Katoh and N. Mohri: In-process Measurement of Wear of Grinding Wheel by Using Hydrodynamic Pressure in Wet Grinding Condition (1st Report) - Measurement Principle -, J. Jpn. Soc. Precis. Eng., 66, 1, pp. 127-131 (2000) [in Japanese].

[10] K. Furutani, T. Katoh and N. Mohri: In-process Measurement of Wear of Grinding Wheel by Hydrodynamic Pressure, Proc. 14th Ann. Meet. Am. Soc. Precis. Eng., Monterey, CA, USA, pp. 610-613 (1999).

[11] S. Ebbrell, N. H. Woolley, Y. D. Tridimas, D. R. Allanson and W. B. Rowe: The Effects of Cutting Fluid Application Methods on the Grinding Process, Int. J. Mach. Tools Manufact., 40, 2, pp. 209-223 (2000).

Precision Measurement of Aircraft Control Surface Axis Alignment over 1-3m Scales

A.E.Gee, SIMS50, Cranfield University Cranfield, Bedford MK43 0AL, UK

Keywords: Mechanisms, optical measurements, mechanical metrology

Rotational control of an aircraft about its three principal axes is effected by hinged offset control-surfaces about axes lying within the three orthogonal flying surfaces (wing, fin and tailplane). Rotational deflection of any one control surface deflects the airflow normally and the resulting reaction force and torque causes rolling, yawing or pitching, arcuate motions normal to the three respective flying surfaces. To minimise the likelihood of flutter (spontaneous oscillation due to a control surface interacting inertially with airframe flexing) inertia and therefore weight of the control surface needs to be kept low. As a result, these control surfaces are generally 'floppy' plane-spring flexures with stiffness in only three (in-plane) degrees of freedom

The hinge mechanism definitively has one principal (rotational) degree of freedom plus some axial end-float. Dimensional changes in the airframe can be accommodated by the hinge and control surface flexure other than bending about any axis normal to the control surface. In this bending mode, the control surface has considerable structural beam 'depth' and therefore stiffness making it vulnerable to structural failure due to imposed bending. This may arise through in-flight flexing and any prior misalignment of the hinge bearings. The latter in turn can arise through parallel or angular misalignment of one hinge pin with respect to others.

Typical control surfaces measured had ~1m span, ~0.1m chord and ~10mm mean section thickness (eg 18mm tapering to 2mm) with five equispaced hinges at 0.2m axial separation (and 0.1m overhang either end). Simple parallel misalignment of any one hinge with respect to its neighbors results in offset X in the intermediate hinge-line. When transmitted as bending of the control surface, this results in ~0.5X strain over the 0.1m chord.

With improving aerodynamic efficiency leading to increased air-speeds, hinge misalignments had become increasingly significant requiring jigs for alignment curing of the FRP material. In the context of previous misalignments of ~1mm measured over 0.2m hinge-spacing, (net angle 5mrad), reductions by an order of magnitude to 0.1mm (0.5mrad) were sought with appropriate metrology capability to a further order of magnitude performance to 10micrometres (50μrad).

A long-path optical-lever measuring arrangement was devised combining circular Moire gratings with an autocollimator. With the optical axis set parallel to the hinge axis, hinge-pins formed an *in situ* optical bench and hinge components were measured by rotating mirrors on them without need for the mirrors to be accurately normal to the hinge-pins. The angularly offset mirrors returned a laser beam which prescribed a circle whose centre was the position of the beam had the mirror not been offset. The sensitivity of this rotating optical lever arrangement was proportional to the optical path length and this could be readily arranged to be twice the length of the hangar (100m or more). These instrumental arrangements were readily capable of measuring the required further improvement to within 10micrometres (50μrad) misalignment.

Special considerations arose in making measurements on necessarily 'floppy' lightweight metre scale components. These do not arise in the machine development lab. or high precision manufacturing environment where components are definitively stiff.

DEVELOPMENT OF SPHERICAL FORM ERRORS MEASURING SYSTEM
--- DESIGN AND SOME EXPERIMENTAL RESULTS ---

Hiroyuki Kawa, Tohru Kanada and Takahiro Watanabe
Dept. Mech. Eng., Kanto Gakuin University,
1-50-1 Mutsuura-higashi, Kanazawa-ku, Yokohama-city, 236-8501 Japan

Introduction

Recent high-performance mechanical system requires high precision profile measuring techniques for mechanical parts. Especially, form errors of spherical parts, which are important in rotational mechanism, three-dimensional measurement and evaluation are needed. For example, sphericity of a steel ball, which is one of the elements for ball bearing applied in computer hard disk or aerospace device, is approaching to 1nm.

Some developments on spherical form profiles measuring techniques by means of original systems have been reported[1],[2]. Those systems have some merits and demerits such as (i) restriction on measurable range and sphere diameter and (ii) long measuring time due to manual operation. Furthermore, it is difficult to evaluate the three-dimensional spherical form by a few two-dimensional data. This report deals with the development of a three-dimensional measuring system for spherical profiles.

Target specifications

Measuring mechanism whose principle is radial method with rotating detector is designed and developed in the viewpoints as follows.

(1) Measuring accuracy of up to several 10nm can be achieved for various diametrical spheres.
(2) Measuring time, labor and errors due to human operation can be reduced by means of full automatic operation.
(3) Improvement and prediction of performance for the device using spherical parts can be presented by the evaluation of obtained three-dimensional data.

Principle of measurement

After searching the position of the maximum diametrical cross section of a spherical specimen with contacting detector, as shown in Fig.1(a), the profile of the cross section is measured. Next, the specimen is rotated by a virtual center axis passing through the two poles as shown in Fig.1(b). Two rotating axes perform self-rotation of the sphere specimen.

Repeating the self-rotation and measurement of profile makes the measured points distributed correctly in longitudinal and latitudinal directions. Fig.2 shows the positions of measuring points and self-rotation axis. Therefore, the three-dimensional data can be expressed in polar coordinate (r - θ - ϕ) system. This will be helpful for further analytical evaluation[3].

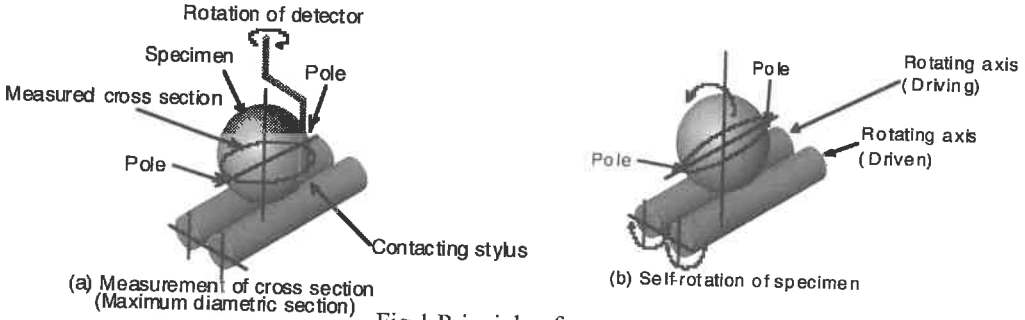

Fig.1 Principle of measurement

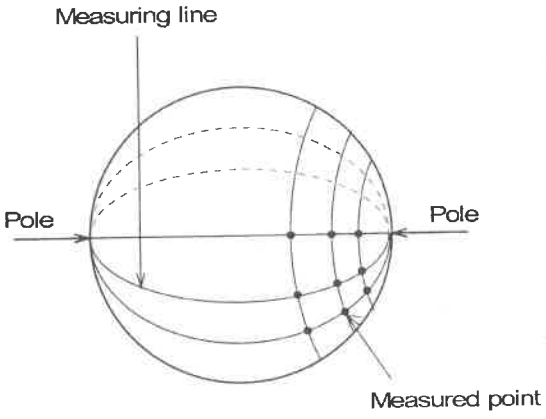

Fig.2 Measuring lines on the specimen

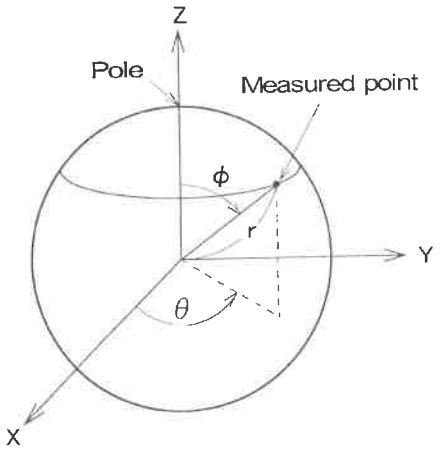

Fig.3 Polar coordinate system for spherical surface specimen

Outline of the system

The developed machine consists of the following four systems as shown in Fig.4 and Fig.5.

(1) Specimen stage system: The specimen set on the stage can be positioned in X-, Y-, Z- and θ -directions. X- and Y-stages are for correcting the eccentricity of the specimen. Z-stage is for searching the position of the maximum diametrical cross section. θ -stage is for rotating the specimen around the vertical axis in the experiment of systematic rotational error by using reversal method. Stroke of X- and Y-directional movement is 10mm with the resolution of 0.0174 μm. Z-directional stroke and positioning accuracy are respectively 10mm and 1 μm. θ -directional movement can be positioned by 200000 separations for 360 degrees.

(2) Specimen rotation system: The specimen is set between two axes. Then, ϕ -directional movement of the specimen is realized by means of friction drive mechanism. ϕ -axis is for changing the longitude of the specimen sphere surface. Fig.6 represents a measuring cross section changing device. The diameter of driving and driven axes with grooves is 15mm. Four contacting points between the specimen surface and the groove surface support the specimen. In order to restrict the run-out of the two axes, wave washers are used to apply preload to the axes. A pulse motor drives the driving axis and the driven axis is rotated by O-ring belt drive mechanism.

(3) Z-axis and detector rotation system: Two detectors are fixed to an air spindle, which is rotated by a DC servomotor. Its revolution speed is from 0.5rpm to 6rpm. The systematic rotational error is nominally 0.04 μm. The rotation angle of the detector is measured by an incremental rotary encoder pulse signal (81000 pulse/revolution). In proportion to the various diameter of the specimen, Z-directional movement of the detector is enabled. Two contacting detectors (wireless signal transmission) are prepared to the profile measurement. The maximum measuring ranges of the two detectors are 600 μm and 60 μm. The maximum resolutions, 0.1 μm and 0.01 μm.

(4) Peripheral system: The above-mentioned three systems are controlled by a personal computer. Peripheral system includes the interface circuits between the personal computer and the other three systems.

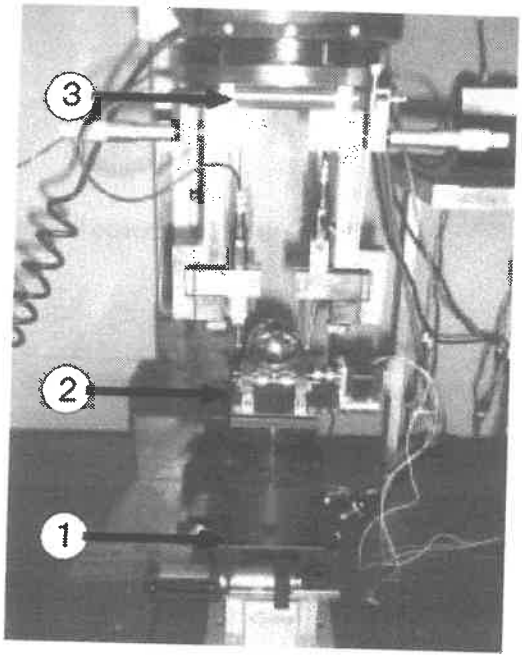

①Specimen stage system
②Specimen rotation system
③Z-axis/detector rotation system

Fig.4 Outview of the developed system

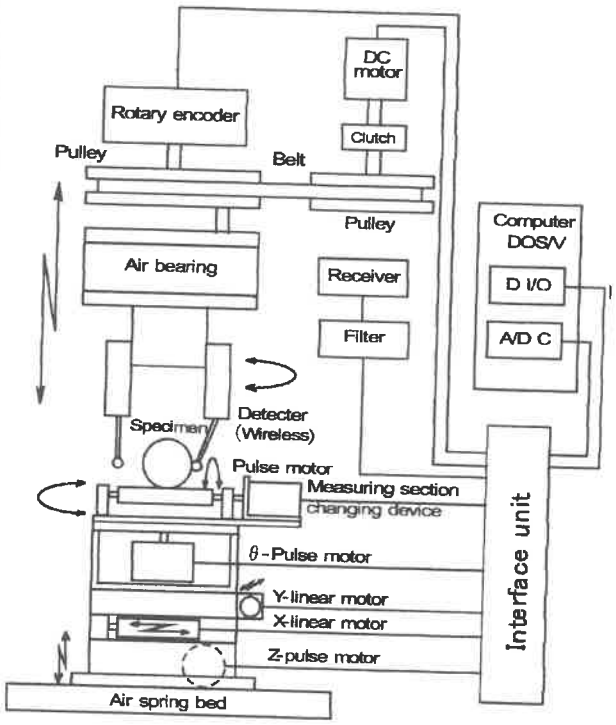

Fig.5 Schematic diagram of the system

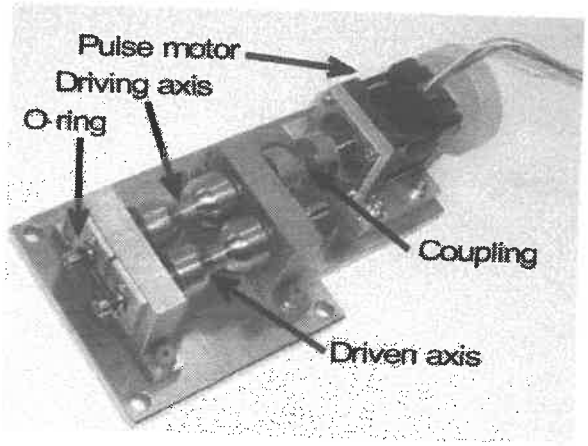

Fig.6 Outview of measuring cross section changing device

Experimental results

(1) Systematic rotational error separation using reversal method

Reversal method can clarify the systematic error and the specimen form error in a certain condition. Fig.7 shows an example of experimental results. Magnitude (peak-to-valley value) of the systematic rotational error is 1.5 μ m. This is considerably large and should be investigated.

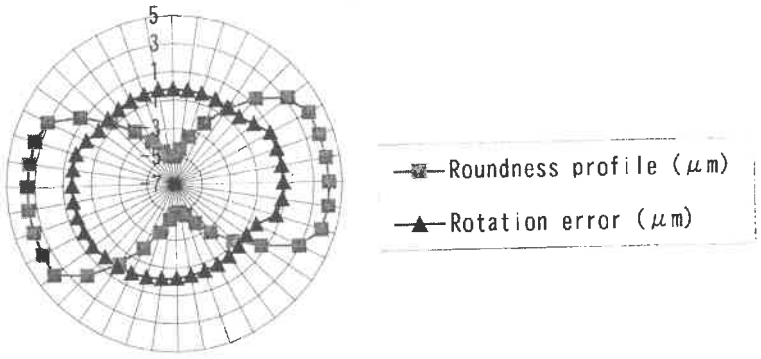

Fig.7 Result of systematic error separation

(2) Searching the position of the maximum diametrical cross section
In order to confirm the appropriateness of the computer control program for searching the position of the maximum diametrical cross section, Fig.8 was drawn. This result shows that searching procedure is completed before the real position of the maximum diametrical cross section is found. The difference between the real position and the recognized position by the computer program is from 70 μm to 100 μm. This is also rather remarkable value and the algorithm should be inspected.

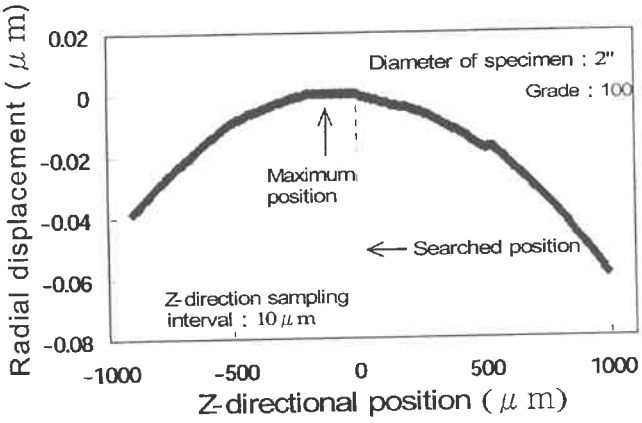

Fig.8 Result of maximum diametric section search

Conclusions

Three-dimensional spherical form measuring system is designed and developed. However, reduction and repeatability of the systematic rotational error should be investigated in near future. Furthermore, searching algorithm for the position of the maximum diametrical cross section should be improved in order to guarantee the three-dimensional positioning accuracy.

References

[1] J.A.Lipa and G.J.Siddall: High precision measurement of gyro rotor sphericity, Precision Engineering, 2-3, (1980), 123-128
[2] T.S.R.Murthy, B.R.Rao and S.Z.Abdin: Evaluation of spherical surfaces, Wear, 57, (1979), 167-184.
[3] T.Kanada: Estimation of Sphericity by means of Statistical Processing for Roundness of Spherical Parts Precision Engineering, 20-2, (1997), 117-122

Development of Measuring Method for 3D Shapes and Dimensions of Micro-components

Kimiyuki MITSUI, Toshiya SHIRAMATSU,
and Masayoshi KAWADA
Department of Mechanical Engineering, Keio University,
3-14-1 Hiyoshi, Kohoku-ku, Yokohama, 223-8522 JAPAN

1. Introduction

In order to facilitate the advancement of micromachine technology and to encourage its use across a wider range of industrial fields, measuring technology appears to be essential. For the development of micromachines and microfabrication technologies, it is necessary to devise a technique to measure both shapes and dimensions of micro-components.

Some researches on measuring methods for microparts have been reported [1]-[9]. However, general-purpose CMM for both form and dimensional metrology on micro-system components has not been realized yet. To this end, one of the authors tried to develop a small three dimensional shapes measuring apparatus which has non-contact probe detecting proximity to measuring object through tunneling effect, and the results has already been reported [6]. In this report, measurement not only shapes but also dimensions of micro-components are tried.

As for probe system, which is a major factor for this kind of measurements, we propose new probe system using quartz oscillators, in addition to STM type probing system. Modified measuring device including probe over-travel protection mechanism and the calibration technique for micro-probes are explained in detail, and then several measuring results are shown.

2. Structure and elements of measuring apparatus

The configuration of the apparatus is shown in Fig.1. The trial apparatus is composed of X-Y-Z precision stages with linear encoders resolution of 0.1 μm, θ (rotating) stage with rotary encoder and a personal computer controlling these stages through GP-IB interface. The probe is mounted to Z stage

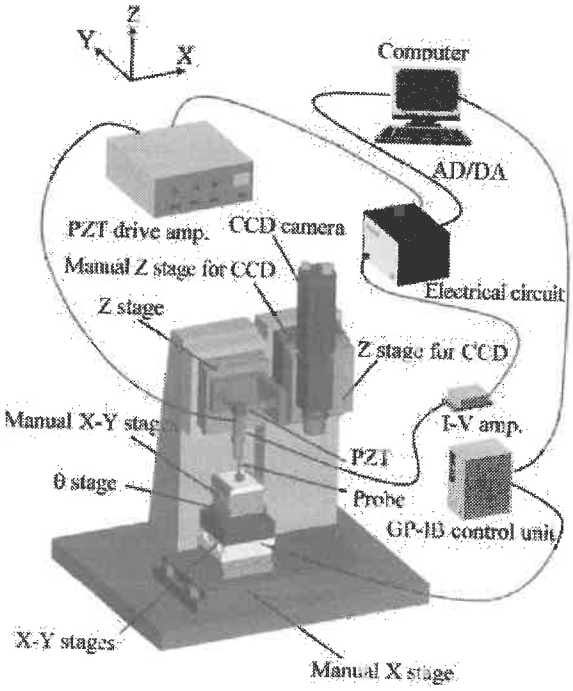

Fig.1 Configuration of measuring apparatus

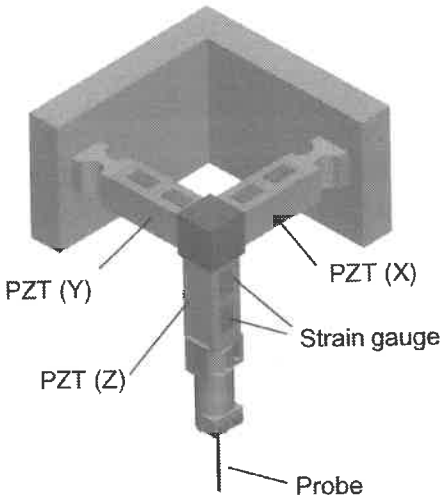

Fig. 2 Probe over travel protection mechanism

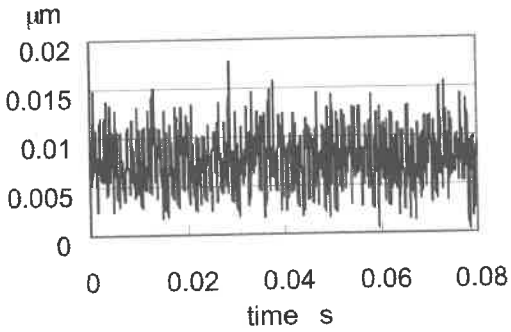

Fig.3 Output signal of strain amplifier

by flexure hinge with PZT actuators. The flexure hinge equipped with piezoelectric actuators, as shown in Fig.2, works not only as the probe over travel protection mechanism but also can be used for the precise and high speed mode measurements. For example, when the probe approaches to the measurement sample from +Z direction, the PZT (Z) is fully expanded. The PZT (Z) shrinks when tunnel current is detected to avoid collision with the measurement sample before Z micro-stage stops.

As the flexure hinge can be moved to three directions, the mechanism allows positive and negative approach of the probe to measurement sample. The displacement of the flexure hinge is measured by strain gauges with great precision. Figure 3 shows the output signal of the strain amplifier. The electrical noise corresponding to the PZT displacement of 15nm is observed.

3. Measurement of small internal thread

Figure 4 shows the measured shape of internal thread, the major diameter of 1mm. The probe used is also shown in Fig. 4. Probes suitable for each measurement samples are fabricated by micro electro discharge machining [10]. Measured area is 20μm in Z, 10μm in Y. The pitch and height of the thread are measured as approximately 250μm and 100μm respectively. Any other measuring method is not available at the moment, however the height of the thread is slightly smaller than the value specified in the

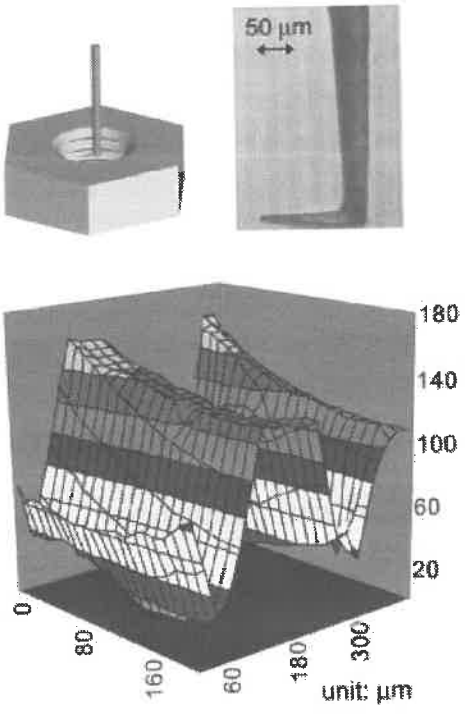

Fig. 4 Measurement results from a M1 nut

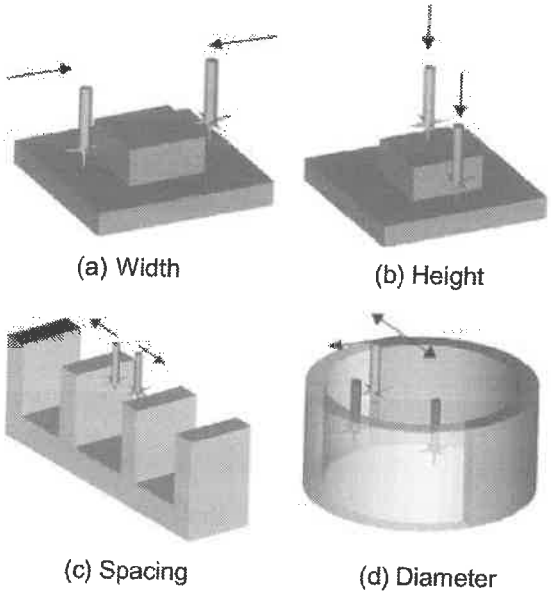

Fig. 5 Probe shape and measuring functions

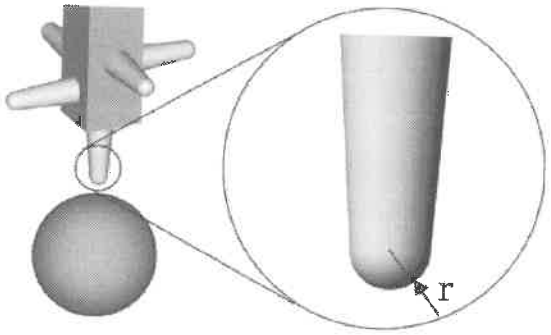

Fig. 6 Master ball for probe calibration

JIS standard.

4. Dimensional metrology on micro parts

4.1 Calibration of probes

Calibration of probes must be carried out before the probes are used for dimensional metrology on micro system components. If relative positions between projections of a probe are known, the probe can be used for various dimensional measurements as shown in Fig. 5. In the following, probe calibration procedure using master test ball with known diameter is described.

It is assumed that the tip of all projections is spherical as shown in Fig. 6. More than five points on the master test ball are measured by each projection. Using the least squares method, the coordinates of the master ball center corresponding to each projection and each tip radius are measured.

(X_i,Y_i,Z_i) : coordinates of the master ball center measured by projection i (i=1,2,3,4,5)

r_i : tip radius of projection *i*

Position vector of projection j (j=2,3,4,5) against projection 1 is given by equation (1).

$$\overrightarrow{L_{j1}} = \left(X_j - X_1, Y_j - Y_1, Z_j - Z_1\right) \qquad (1)$$

Hence, tip position of other projections against projection 1 can be measured.

After calibration of a probe, width of a block gauge was measured to examine how accurately the calibration was carried out. The calibration of the probe was done using a steel ball sample that was 0.5 mm in diameter.

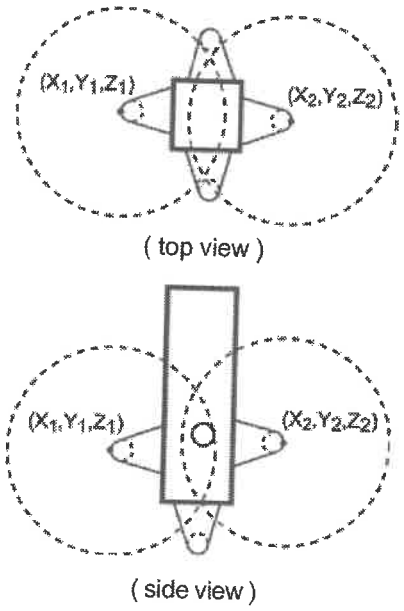

Fig. 7 Probe calibration procedure

The probe fabricated by micro electro discharge machining is X-X type probe that has two projections in horizontal direction. The tip radius of the probe is 1 to 2 μm, sharp enough to assume the tip radius is zero.

Five points on the master test ball were measured by each projection. Then the positional relationship between the projection 1 and 2 was calculated.

Nine points on one side of the 1.5 mm thick block gauge was measured, and the inclination of the block gauge surface was compensated using a regression surface. Then, nine points on another side of the block gauge surface was measured to obtain the thickness of the block gauge. Table 1 shows the results of three consecutive measurements through calibration of the probe to thickness of the block gauge. Table 1 also shows position vector of projection 2 against projection 1.

Experiments	$\overrightarrow{L_{12}}$ (μm)	Measured width for gage block (mm)
1	(184.4, -9.8, 10.3)	1.5012
2	(185.7, -9.6, 10.2)	1.4993
3	(183.8, -9.9, 8.5)	1.5007

Table 1 Evaluation of the probe calibration method

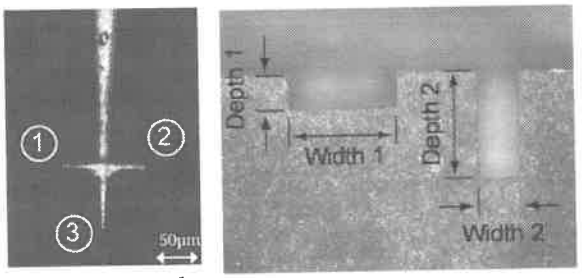

X-Z-X type probe

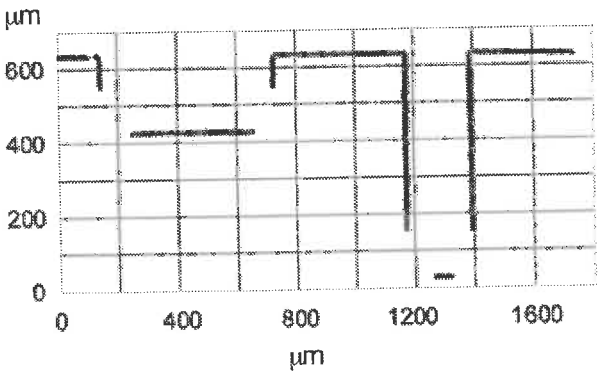

Fig. 8 Dimensional measurements of width and depth of grooved surface

4.2 Measurements of micro grooves

The probe calibration procedure, already described in the previous section, has been applied to the X-Z-X type probe shown in Fig. 8. The shape and dimension of the measurement sample, micro-groves in Figure 8, which was fabricated by micro electro discharge machining, was measured. Figure 8 (upper right) is showing grooves observed by laser microscope, and Fig. 8 (lower) is the shape of the grooves measured by our proposed method. Using X-Z-X type probe, upper surface, vertical wall and bottom surface can be measured continuously.

Dimensions of depth and width for micro grooves are shown in Table 2. In the table, dimensions measured by laser microscope are also shown for comparison.

5. Development of the probes using quartz oscillators

Although the non-contact probes detecting proximity to measuring sample through tunneling effect are useful for micro parts metrology, the drawback of the probe system is

that they can not be used for non-conductive measurement samples. Thus, quartz oscillator type probe was developed.

The resonant frequency of quartz oscillators for watches is 32768 Hz. The resonant frequency drops certain amount when they vibrate in the air due to resistance of the air. Fig. 9 shows resonance amplitude change due to contact of the probe to measurement sample. Signal change is observed by the contact.

Fig. 10 shows the measuring result using a quartz oscillator probe. The measurement sample is a glass sphere diameter of 1 mm. Probing ball diameter of 0.3 mm are put to the tip of the quartz oscillator probe. Four points on the glass sphere sample were measured, and diameter was calculated. Twenty repetitive measurements are performed, and average diameter is 1.002 mm.

6. Conclusion

The main conclusion obtained from this study are summarized as follows:

(1) The flexure hinge equipped with piezoelectric actuators works not only as the probe over travel protection mechanism but also can be used for the precise and high-speed mode measurements. As the flexure hinge can be moved to three directions, the mechanism allows positive and negative approach of the probe to measurement sample. The displacement of the flexure hinge is

	Width 1 (μm)	Width 2 (μm)	Depth 1 (μm)	Depth 1 (μm)
Proposed method	586.0	218.7	205.9	604.5
Laser microscope	588.9	220.8	203.7	602.0

Table 2 Width and depth measurements of the grooves

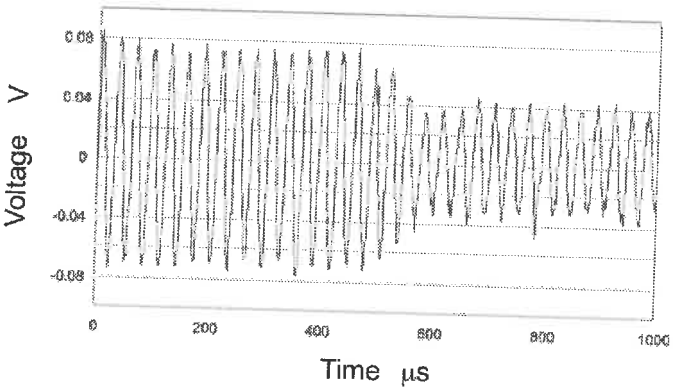

Fig. 9 Resonance amplitude change due to contact

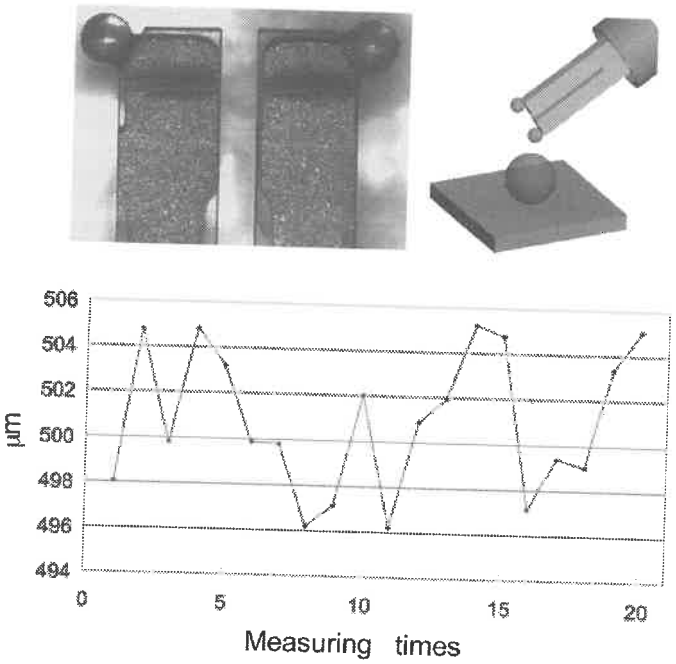

Fig. 10 Radius measurement of sphere by quartz oscillator probe

measured by strain gauges.
(2) For dimensional metrology on micro system components, calibration of the probe used is an essential part of the measurements. In this study probe calibration procedure using master test ball with known diameter was described in detail, and depth and width for the micro grooves were measured.
(3) Quartz oscillators for watches were applied to the probe system, which can be used for non-conductive measurement samples. A glass sphere diameter of 1 mm is used for the measurement sample, and the result shows the validity of the new quartz oscillator probing system.

References

1) R. Kokawa and H. Sato: Profile Measurement of Aspheric Lenses Using a Scanning Electron Microscope, Trans. of the JSME, 55-515 (1989) 1777. (in Japanese)
2) T. Masuzawa, Y. Hamasaki and M. Fujino: Vibroscanning Method for Nondestructive Measurement of Small Holes, Ann. CIRP, 42/1 (1993) 589.
3) K. Mitsui and T.Goto: Development of Dual Servo STM, Proc. of ASPE Annual Meeting (1996) 146.
4) T.Masuzawa et al. :Twin-Probe Vibroscanning Method for Dimensional Measurement of Microholes, Ann. CIRP, 46/1(1997) 437.
5) T. Shiraishi and K. Mitsui: Development of Three Dimensional Profile Measuring Apparatus for Microparts -Measuring Principle and Measuring Results-, J. of the JSPE, 64-9 (1998) 1395. (in Japanese)
6) K. Mitsui: Development of Three-Dimensional Profile Measuring Method for Microparts, ASPE Proceedings Vol.20 (1999) 320.
7) M. Yamamoto, I. Kanno and S. Aoki: Profile Measurement of High Aspect Ratio Structure using a Tungsten Carbide Micro Cantilever Coated with PZT Thin Films, Proc. of The 13th Annual Int. Conf. on Micro Electro Mechanical Systems (2000) 217.
8) Y. Takaya, S. Takahashi and T. Miyoshi: Nano-Positional Detection Using Laser Trapping Probe For Microparts, ASPE Proceedings Vol.22 (2000) 584.
9) H. Schwenke et al.: Opto-Tactile Sensor for 2D and 3D Measurement of Small Structures on Coordinate Measuring Machines, Annals of the CIRP Vol. 50/1(2001) 361.
10)H. Tanimura, T. Yamaguchi and K. Mitsui: Fabrication of Probes for Profile Measurement of Microparts by Micro Die-sinking EDM - Fabrication of X-Y and X-Z Type Probes -, J. of the JSPE, 65-9 (1999) 1296. (in Japanese)

Development of micro probe for micro-CMM

Ichiro Ogura, Yuichi Okazaki
Fine Manufacturing System Group
Institute of Mechanical Systems Engineering
National Institute of Advanced Industrial Science and Technology (AIST),
Tsukuba 305-8564, Japan

1. Introduction

This study describes the development of a probe for a micro coordinate measuring machine (micro CMM).

In order to guarantee the accuracy of products, a profile measurement evaluation process is indispensable. A CMM (Coordinate Measuring Machine) is generally used to measure product profiles. Although it can make various product measurements, such as the diameter of holes or complicated profiles, the measurement scale of a CMM is usually several tens of millimeters or more, and it is not suitable for measuring small parts of submillimeter order.

To measure micro-parts in nanometric order, the concepts of a nano-CMM[1] and an ultra precision CMM[2] have been proposed, and there have been many interesting studies on novel probe development [3]-[5].

We conducted the basic research on a micro probe for a micro-CMM. As the first step, we developed a two-dimensional measurement probe. The actual probe for the CMM will be realized by extending our proposal to three dimensions. The probe is a contact type, and is also made to rotate on the detection side by an actuator. By comparing the signal at the time of contact with the phase of the circular motion, it is possible to detect the contact direction within a field.

In this research, we developed a prototype probe system, and conducted a preliminary experiment to verify the proposed principle. The results showed that accurate evaluation of profiles is possible.

2. Measurement principle

Fig. 1 (a) and (b) show the measurement principle of the proposed system. A contact type probe is rotated in a circular motion within several micrometers in the measuring plane. Fig. 1 (a) is a schematic of the rotating probe. In this system, most contact type probes could be selected such as the electrical touch type, optical type, or strain gage type. However the this probe must be able to detect contact from all directions in the measuring plane.

The circular rotation is applied by two right-angled actuators or a tube piezo actuator that can move in the x and y directions. As sine and cosine wave motion signals are applied to the x and y actuators, respectively, the probe is rotated in a circular motion.

A x-y stage moves the profile to be measured until the probe contacts the profile. When the probe contacts profile, a series of data as shown in Fig. 1 (b) can be acquired. These signals are generated by the movement of the x and y actuators and a periodi contact signal.

From the x-y stage coordinates, the two-dimensional position of the contact point can be detected. The length of the contact signal Δt depends on the displacement between the center of rotation and the contact point r. The phase of this contact signal ϕ varies with the contact angle θ, and can be calculated by Fourier analysis. Thus, the system can simultaneously detect the contact position and contact angle.

To obtain an equal response from all contact directions, the rotating motion should ideally be

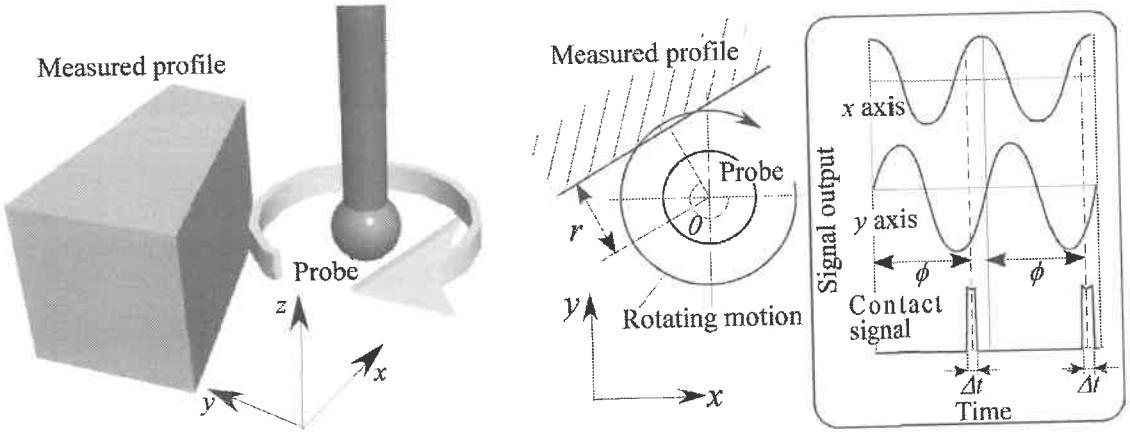

Fig. 1 Principle of measurement

perfectly circular and the probe should have a high-precision circular profile. However, if the probe motion or probe profile have some error, measurement accuracy can be confirmed by a calibration technique.

3. Development of prototype probe system

Using the MEMS technique, a small probe system for measuring micro machine devices or micro holes can be obtained. Our final goal is to develop such probes and a micro CMM. Before that however, we developed a prototype probe system to demonstrate our method and evaluate its accuracy.

Fig. 2 shows a schematic of the prototype probe system, and Fig. 3 shows a photograph of the system. The probe used is an electrical touch type.

A 0.7 mm-diameter ball bearing is attached to the tip of this probe, and a 5 V contact voltage is applied to the probe. When the probe contacts the target, a computer detects the contact signal. The target in our experiment was a 2.5 mm-diameter ball bearing. This target was fixed to an aluminum base that was mounted on the precision stage. Conductive glue was used to fix the bearing to the probe and also to fix the target in place.

Feedback controllers move two piezoelectric actuators using two displacement sensors. The displacement sensors are of the optical fiber type. The measurement range of these sensors is 20 μm,

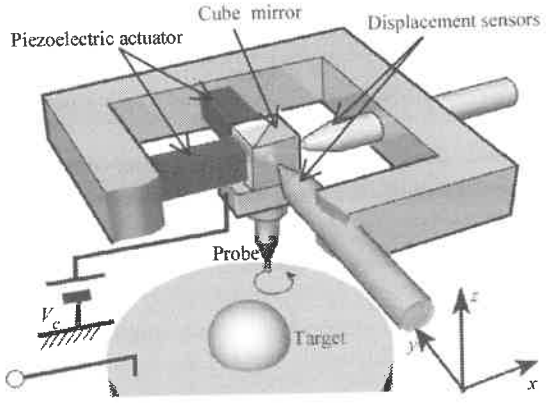

Fig. 2 Prototype probe system

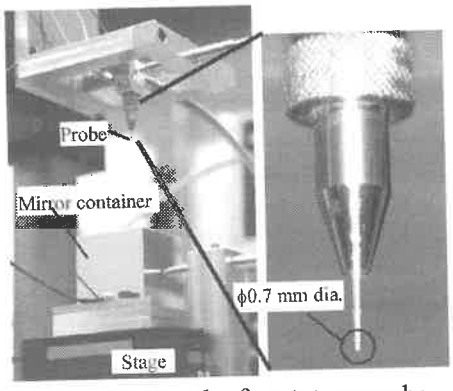

Fig. 3 Photograph of prototype probe

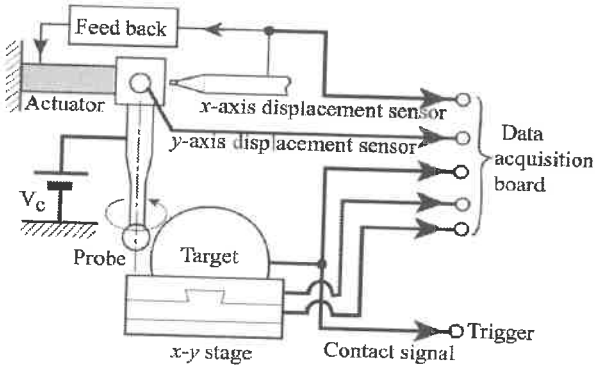

Fig. 4 Diagram of signal process

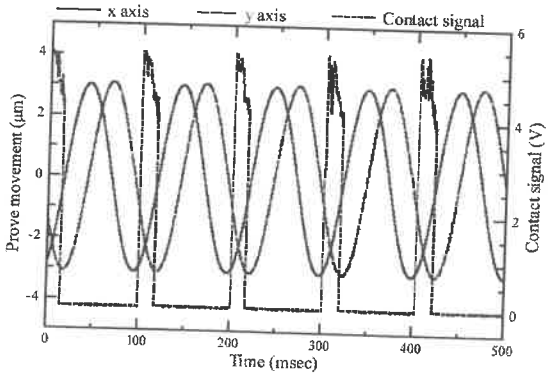

Fig. 5 Contact signal and probe movement

and their resolution is of nanometric order. These sensors measure the movement of each actuator through the cube mirror. A two-output type function generator applies sine and cosine command signals to the feedback controllers, then the probe rotates. In this study, we set that the amplitude of each axis at 3 μm and the frequency at 10 Hz.

The precision stage has a 400 μm range in the *x-y* plane. This stage is controlled by a feedback system using an optical fiber type probe and a mirror container. When contact between the probe and target is detected, the stage is stopped. The precision stage is attached to a manual stage for rough positioning. In future studies, a stepping motor type *x-y* stage will take the place of this manual stage. An interferometer measures the movements of the precision and stepping motor stages.

Fig. 4 shows a diagram of the signal process. This figure omits the *y*-axis feedback system of the probe and the *x-y* stage feedback system for simplicity of description. The computer moves the *x-y* stage and detects the contact signal as a trigger. When contact is detected, the computer stops the *x-y* stage and begins to acquire the movement signals of the *x* and *y* actuators, the contact signals, and the coordinates of *x-y* stage. After acquiring these data, the computer moves the *x-y* stage again to measure the next point. The data acquisition board can measure the synchronizing data of the *x* and *y* actuators and the contact signals. The internal clock of this board is used for the sampling time.

4. Experimental results

A preliminary experiment was performed to verify our probe system.

Fig. 5 shows typical output of the contact probe. A total of 512 points were sampled in 1 cycle. In this figure, the *x* and *y* actuators move in a sinusoidal curve without any deformation, and their phase difference is $\pi/2$. This output shows that the probe is moving circularly.

The periodic contact signal indicates the probe is repeatedly contacting the target and releasing from it. The time of each contact is almost the same, indicating that contact with the target does not affect the actual displacement between the center of the rotating probe and the surface of the target.

In the contact signal, the center point between the rising up point and setting down point is the contact direction. From 3 periodic data, the phase angle was calculated to be 233.1°. This result was confirmed from the actual experimental condition.

A profile measurement experiment was performed on the target. Fig. 6 shows a schematic of this experiment. The *x-y* stage moves in the *y* direction and detects the contact point. After making contact, the stage shifts 0.25 mm in the *x* direction, and moves the *y* axis of the stage to make contact again. Because of the diameter and rotating motion of the probe, the actual contact points are different from

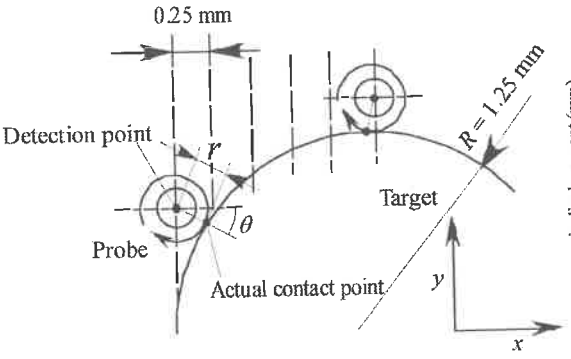

Fig. 6 Profile measurement experiment

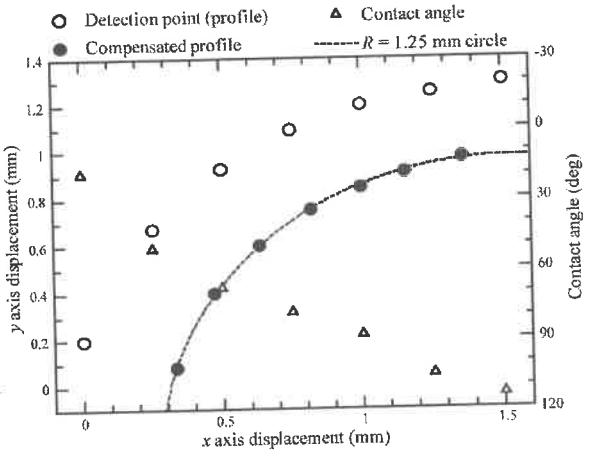

Fig. 7 Result of profile measurement

the detection points. The actual contact point (x_t, y_t) can be calculated from the detection point (x_d, y_d) and contact angle θ as follows:

$$x_t = x_d + r\cos\theta$$
$$y_t = y_d - r\sin\theta$$

Here, r is the displacement between the center point of the probe and the envelope of the rotating probe. More precisely, r changes with the contact time Δt shown in Fig. 1 (b), but in the present experiment we did not take this into account. Thus, r is the radius of the probe (0.35 mm) + the probe movement amplitude (3 μm).

Fig. 7 shows the result of the profile measurement experiment in terms of the detection point, the contact angle of each point, and the compensated contact point. The contact angle was calculated from each contact signal phase. The compensated profile means the actual contact point. This graph also shows the R = 1.25 mm circle. This circle represents the ideal profile of the target. The center point of this circle was selected from the least square error to fit the compensated profile. From this figure, we can see good agreement with the compensated profile and the R = 1.25 mm circle. This result indicates that the system could measure the actual contact angle and actual contact point, and confirms the validity of our measurement method.

5 Conclusion

We have proposed a new probe for a micro CMM that can simultaneously detect the contact point and contact direction. A prototype probe system was developed and a preliminary experiment was performed. The results of the experiment confirmed the validity of our method.

References

1) K. Takamasu, et al.: Basic Concepts of Nano-CMM (Coordinate Measuring Machine with Nanometer Resolution)., Proc. of Japan-China Bilateral Symposium on Advanced Manufacturing Engineering (1996) 155.
2) T. Ruijl, et al.: Ultra Precision CMM Aiming for the Ultimate Concept., Proc. of 2nd euspen International Conference (2001) 234.
3) U. Brand, et al.: Development of a special CMM for dimensional metrology on microsystem components., Proc. of ASPE 2000 (2000) 542.
4) T. Masuzawa, et al.: Twin-Probe Vibroscannning Method for Dimensional Measurement of Microholes., Annals of the CIRP 46, 1 (1997) 437.
5) Y. Takaya, et al.: Nano-Positional Detection Using Laser Trapping Probe for Microparts, Proc. of ASPE 2000 (2000) 584.

Dimensional Stability of 17-7 Stainless Steel Springs

Steven R. Patterson, Kevin M. Lawton, Dongmei Ren
Center for Precision Metrology
University of North Carolina at Charlotte, Charlotte, NC 28223

keywords: *dimensional stability, springs, optical metrology*

Introduction

The use of precision formed springs presents a challenge to the designer of fine mechanisms. The forming process by its nature introduces stress in excess of the yield stress of the material used, and relaxation after forming leaves substantial residual stress. Subsequent heat treatment must be limited to those processes which preserve the necessary high yield strength of the spring material. This limitation results in residual stress levels which have the potential to drive dimensional instability mechanisms. The present study was motivated by the observation that a group of 6 mm U-shaped 17-7 stainless steel springs had changed free state dimension after several years of storage. Fifty-three springs from this lot have been examined at the Center for Precision Metrology at the University of North Carolina at Charlotte in an attempt to determine the magnitude and nature of the underlying dimensional instability mechanism. While the initial dimensional instability of the springs is unknown, the level of continuing dimensional change in the springs provides a bound on the behavior at early times. Dimensional instability as well as temperature dependence of the instability mechanism have been observed in the springs.

OCMM Measurement

Spring dimensional measurements were carried out using an Optical CMM in the metrology lab of the UNCC Center for Precision Metrology. Through lighting illumination and an objective lens with magnification of 20 were used to analyze machine repeatability. To assess the repeatability of measurement independent of the actual spring geometry, a series of repeated measurements were made of a precision coated glass reference artifact with scales in the x- and y-directions. The distances between the scale lines were measured and used to evaluate short-term measurement repeatability. In each measurement, the scale was measured along +x (or +y) direction and then along –x (or –y) direction to reduce the effect of any backlash in the system. The average of the measurements in the two reverse directions is used as the result of a single measurement. The process was repeated several times and the standard deviation of 14 groups of measurements was 75 nm for the x-direction and 240 nm for the y-direction.

The long-term stability of the OCMM measurements was assessed by repeating the initial repeatability tests after six months had elapsed. The measurement instrument, measurement object, measurement procedures and data processing method were the same as those in the original tests. The standard deviation of 14 groups of measurements for this data was 77 nm for the x-direction and 250 nm for the y-direction. The result of this measurement series shows that both the value and uncertainty of measurements are essentially independent of the measurement date. No statistically significant linear drift was apparent.

To assess the underlying uncertainty of the spring measurement process, a series of experiments was carried out to assess the repeatability of the optical measurement of spring opening. The spring dimension was measured 30 times along both +x and –x directions. The entire cycle of steps, including removal and replacement of the spring from the machine was repeated 14 times. The test shows that the most repeatable measurement that characterizes the spring dimension is that of the median opening as determined from the average of the measurements in both +x and –x directions. The average of the standard deviation of the 30 measurements in each group is 53 nm. The standard deviation of 14 groups

of measurements that were made over the period of a week is 192 nm, which is taken to be the estimate of the uncertainty for each spring dimension measurement.

Spring Data Summary

The dimensional stability of 53 springs has been analyzed for approximately sixteen months. The 53 springs were separated into two groups: untreated springs and temperature treated springs. 17 springs were subjected to heat treatments at several elevated temperatures or chilled to liquid nitrogen temperature. The remaining 36 springs were measured in an undisturbed state. It should be noted that the 36 undisturbed springs may not be representative of the entire lot because the 17 springs removed for thermal treatment typically had relatively large drift rates when compared to the rest of the lot. Springs that were thermally treated were heated or cooled at a maximum rate of 4° F per minute in order to avoid thermal stresses. The springs were heat treated in a vacuum oven with a custom digital temperature controller with cascaded thermocouple feedback loops. Temperature uncertainty is approximately 0.5° F for a range of 125° F to 400° F.

The average of the observed best-fit linear drift rates of the 36 untreated springs is 0.22 nm/day. The standard deviation of the best-fit drift rates is 1.22 nm/day, and the uncertainty of a single spring drift rate measurement is 0.38 nm/day. The average drift rate is statistically significant. 32 of the 36 springs have drift rates with larger magnitude than their drift rate uncertainties, which suggests that a large percentage of the springs may have significant drift rates. The standard deviation of the drift rates is significantly larger than the drift rate measurement uncertainty, which suggests there is a statistically significant distribution of the drift rates. A chi-square test verifies this hypothesis with greater than 99.99% certainty. The histogram data shown in Figure 1-1 (bin size is 0.5 nm/day) suggests that the lot of springs does not have a very normal distribution of drift rates. Three springs have high drift rates near 5 nm/day that prevent the measured distribution from tailing off like the Gaussian distribution. Also, a relatively large number of springs have drift rates of approximately 2 nm/day.

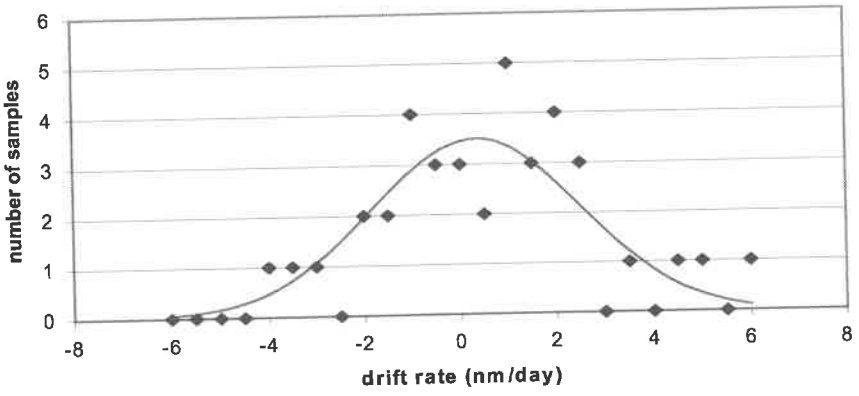

Figure 1-1: Untreated spring drift rate distribution with overlayed Gaussian distribution with standard deviation equal to that estimated from the population of samples

Of the 17 thermally treated springs, 15 springs were subjected to heat treatments at elevated temperatures to test the correlation of spring opening and drift rate to thermal cycling. It should be noted that the springs used for the heat treatment tests were chosen because of their relatively large drift rates and

should not be viewed as a random sample from the lot. The statistics of the fitted linear drift rates of the 15 heat treated springs, prior to and after treatment, were:

- average drift rate, nm/day: Prior: 1.87 ±0.72 After: 0.11 ±0.36
- standard deviation of drift rate, nm/day: Prior: 2.78 After: 1.40
- drift rate measurement uncertainty, nm/day: Prior: 1.49 After: 0.60

The larger uncertainty in the initial drift rate of the treated springs (compared to the untreated springs) is attributable to the lower measurement time and the associated smaller number of data points used to estimate the slope through the spring drift data.

The average drift rate decreased from a statistically significant amount prior to treatment to a statistically insignificant value after treatment, suggesting that the heat treatments help to relieve stress or cause some other change in the springs to reduce their average drift rate. Since the measurement uncertainty of the post-treatment drift rates is larger than the standard deviation of the drift rates, it is unclear whether the heat treatments reduced the variability of the drift rates about the mean.

Figure 1-2 shows the change in spring opening versus the initial drift rate for three temperature treatments. Linear trend lines are plotted with the measured points to show correlation of the change in opening with initial drift rate. A spring treated at 93.3 °C (200 °F) with the change in opening of approximately 5 microns appears to be an outlier from the other points and was not used to fit the linear trend line. The slopes of the linear fit lines suggest that the higher the heat treatment temperature, the greater the sensitivity of the change in opening to initial drift rate. Additional tests and data at intermediate heat treatment temperatures could help to verify this theory.

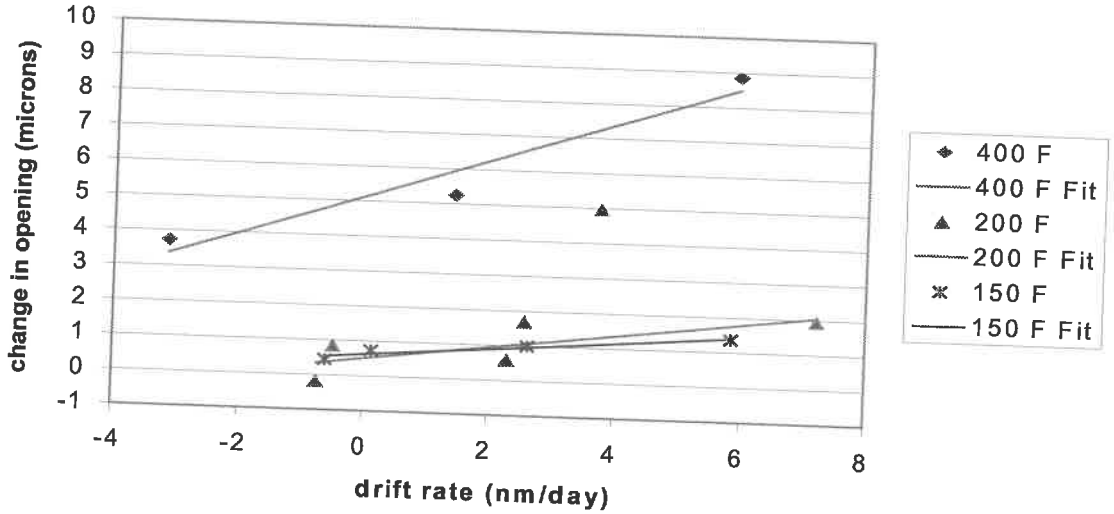

Figure 1-2: Change in spring opening versus initial drift rate for the springs heat treated at 150, 200, and 400 °F, with associated linear fits

Of the 17 heat treated springs, 6 were heat treated a second time. Three springs reheated to 204.4 °C (400 °F) showed no significant change in opening, in contrast to the change detected after the first heat treatment (average of 5.95 ± 1.24 μm). This may suggest that the first treatment relieved most or all of the unstable residual stress in the springs.

Three springs reheated to 93.3 °C (200° F for 12 hours) showed significant changes to both heat treatments. Statistics prior to and after the second treatment were:

- average drift rate: Prior: 0.05 ±3.24 nm/day After: 0.52 ±0.66 nm/day
- standard deviation of drift rate: Prior: 5.61 nm/day After: 1.14 nm/day
- drift rate uncertainty: Prior: 6.92 nm/day After: 2.26 nm/day
- average change in opening: Prior: 1.78 ±1.60 μm After: 0.24 ±0.28 μm

The average drift rates before and after treatment were both statistically insignificant, so a possible conclusion is that the heat treatment did not change the average drift rate. The same can be said of the standard deviation of the drift rates since both, before and after treatment, were statistically insignificant (ie. less than measurement uncertainty). The average change in spring opening was much lower for the second treatment than for the first treatment, which may suggest that the first treatment removed a significant amount of residual stress, but did not fully relieve the spring material.

To test for possible room temperature phase transition from residual metastable states, two springs were subjected to cryogenic temperatures by submersion (within a package insulated to limit cooling rate) into liquid nitrogen. The average drift rate of the two springs increased from 1.01 ±1.59 nm/day to 4.12 ± 1.50 nm/day, which suggests that cryogenically treating the springs caused increased drift rates.

The activation energy associated with a simple creep mechanism has been estimated from the slope of a plot of the logarithm of creep rate versus inverse absolute. Figure 1-3 shows the three points, based on the average logarithmic creep rate caused by the heat treatments described above, used for fitting a line. The slope of this fitted line is $-1435\ K^{-1}$, which gives an activation energy of 0.12 eV. Performing additional heat treatments at intermediate temperatures could help verify both the applicability of the simple activation energy model as well as the activation energy of the process.

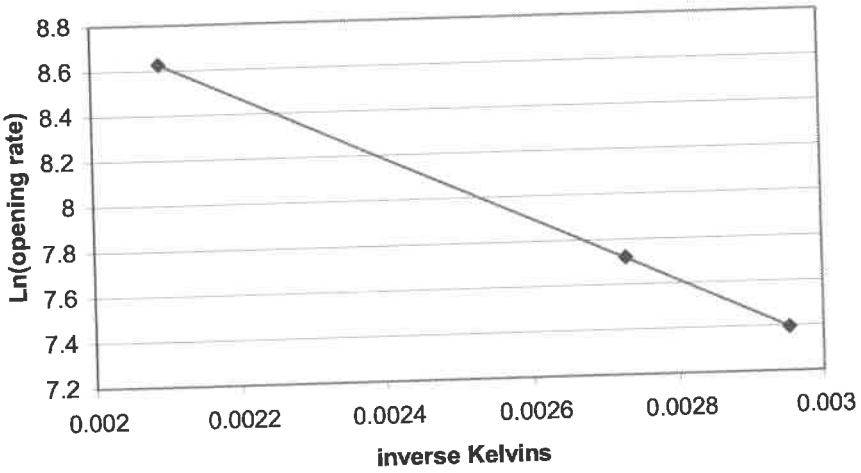

Figure 1-3: Average logarithmic creep rate from heat treatment versus inverse absolute temperature

STYLUS PROFILOMETRY TO QUALIFY VEE-GROOVES FOR OPTICAL FIBER ALIGNMENT

P. Rachakonda, and R. R.Vallance,
Precision Systems Laboratory, University of Kentucky, Lexington, KY *

S. Kiani, B. Hunsaker, J. Lehman
Teradyne Connection Systems, Nashua, NH †

Abstract

Precise alignment of optical fibers is necessary while terminating fibers to devices such as lasers, diodes, and switches or connectors. Manufacturing processes necessary to achieve highly precise and parallel vee-grooves to align optical fibers must be repeatable and accurate. Surface profiling is suitable to qualify vee-grooves through the measurement of surface topography and post processing techniques. This paper discusses aspects of this application, including process, fixturing with 3-2-1 supports, and post-processing techniques. The centers of fiber cores are compared to ideal locations with visualization techniques and geometric approaches that yield the resting position of fibers in a filtered profile. Vee-grooves are qualified by assessing the maximum signal loss expected for fiber alignment [1].

Keywords: Stylus Profilometry, Vee Grooves, Metrology, Quality Assessment, Optical Fibers

Introduction

Optical fibers are traditionally packaged in a set of micro machined structures. These fibers are produced by anisotropically etching silicon [2] or material removal processes. Manufacturing processes necessary to achieve such highly precise and parallel vee-grooves must be repeatable and accurate. Manufacturers design vee grooves for the purpose of aligning the vee grooves perfectly with another set of fibers in vee grooves. For the alignment to be nearly perfect with little transmission losses, these vee grooves need to be parallel to each other and have uniform cross section. But each vee groove actually has numerous manufacturing variations. The vee grooves may not be parallel, consistent in their cross section along the groove, or incorrect dimensions.

Measurement of vee grooves precedes the process of qualifying them. Accurately measuring the 3D geometry and variation is extremely challenging but is necessary to compare the process capabilities of alternative manufacturing processes. Of the many surface-profiling methods available, we chose stylus profilometry for our analysis. The following sections discuss the reasons for selecting this technique and the methodology involved in qualifying the vee grooves.

Stylus Profilometry

Stylus profilometry is a technique in which a contact, skidless stylus measures its displacement relative to an external datum. The stylus traverses over the surface in a raster fashion. The displacements of the stylus are linearly proportional to the heights of features contained on the surface. The pickup of the profilometer comprises a stylus, a stylus holding mechanism, a measuring transducer and any signal conditioning associated with the measuring transducer. As the stylus is traversed across the measurand, z-axis displacements of the stylus are measured by the transducer, thus generating a 2D or 3D profile of the surface topography, relative to the reference datum [3].

* *Precision Systems Laboratory, Mechanical Engineering, University of Kentucky, 210-A CRMS Building, Lexington, KY 40506. http://www.engr.uky.edu/psl.*
† *Teradyne Connection Systems, Nashua, NH. http://www.teradyne.com.*

Stylus profilometry offers sufficient capability for qualifying the large vee grooves area with appropriate resolution. Table 1 lists the desired capability of the stylus profilometer for profiling the vee grooves.

Vertical Resolution	<50nm
Vertical Range	>1mm
Lateral Resolution	0.1μm
Lateral/Longitudinal Resolution	Sub-Micron

Table 1: Measurement Requirements

Figure 1 illustrates an amplitude-wavelength plot of various surface profiling instruments, and compares their working ranges. This plot, initially presented by Stout and Blunt [4], illustrates that stylus profilometers have a large working range and hence are best suitable to measure the vee-grooves.

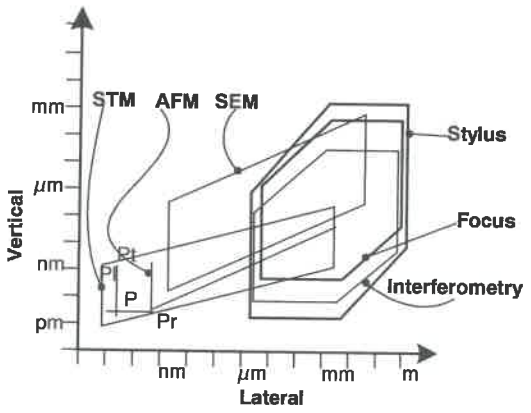

Figure 1: Amplitude-wavelength Plot

Due to the wide range of applicability of the stylus profilometers, it may be used to measure the vee grooves. Qualification of vee grooves can then be done by post processing the data obtained from the stylus profilometers.

Measurement Process

To better understand the post processing process, a coordinate system is assigned to the vee grooves, and is illustrated in Figure 2. The measurement process is affected by the orientation of the vee groove pattern to the path of the stylus. Figure 3 illustrates a typical measurement procedure, where the vee grooves are perpendicular to the direction of the stylus's traverse path.

Ideally, the stylus should travel perpendicular to the vee grooves, without any elevation as the stylus steps in a raster fashion to measure. That is, the vee grooves' y-axis and the direction in which the stylus traverses should be perpendicular.

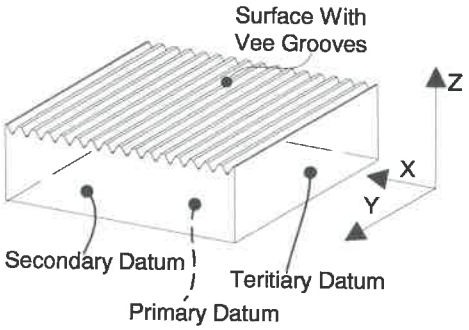

Figure 2: Coordinate system and fixturing datum planes of the vee grooves' structure

If there is any rotational error about the x-axis, the vee grooves appear deeper. If there is any rotational error about the z-axis, the vee grooves appear wider. The effect of any rotation about y-axis can be removed during the post processing procedure.

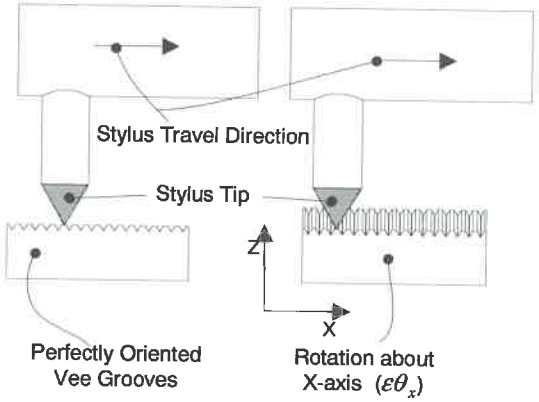

Figure 3: Orientation Errors during Measurement

The effect of rotations about x and z axes can be estimated. Consider r to be the fiber radius, w to be the width of the vee groove in which the fiber rests and h to be the distance from the top of the vee groove to its apex. Equations (1) and (2) give the distances (d_x and

d_z) by which the location of the fiber varies with the angle between the stylus travel direction and the vee grooves about the x-axis (ϕ_x) and z-axis (ϕ_z).

$$d_x = \frac{r}{\sin\left(\tan^{-1}\left(\frac{w\cos(\phi_x)}{2h}\right)\right)} \quad (1)$$

$$d_z = \frac{r}{\sin\left(\tan^{-1}\left(\frac{w}{2h\cos(\phi_z)}\right)\right)} \quad (2)$$

Figure 4 illustrates the effect of the rotational angle on the location of the fiber in a particular vee groove. Within a 1 degree error, the location of the fiber may be shifted by ~ 15 nm. Therefore a mechanism for aligning the vee grooves to the instrument coordinate system is necessary.

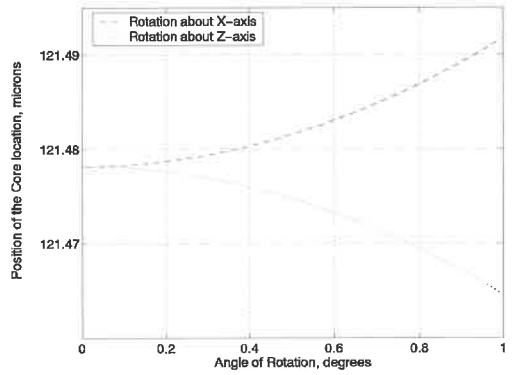

Figure 4: Dependency of Core location on the angles of rotation.

FIXTURING

Fixturing is a complex issue, but it is important since it plays a significant role in accurate measurements. A fixture to precisely hold the measurand (vee grooves in this case) is necessary for repeatable surface profile measurements. The fixture should enable accurate and repeatable surface profile measurements. Hence, the fixture needs two mechanisms, one for adjusting the orientation by tipping-tilting and rotating and another mechanism for repeatable holding of the vee grooves. For the adjusting mechanism, an Aerotech tip-tilt (ATT-185-5) and a rotate stage (ARS301) with micrometer drive and cross-roller bearings is employed.

The second part of the design of fixture, which positions the vee grooves, is divided into two steps [5]. The first consists of a scheme for locating the vee grooves by making contact with it at a fixed number of contact points on its surface. The second concerns the preloads, which constrain the vee groove and immobilize it against external forces and disturbances.

Location Scheme

The 3-2-1 principle is one of the most widely used principles for locating schemes. Following this principle, three surface datums, illustrated in Figure 2, are selected to locate the part. On the first surface F_1, or primary datum, three positions are selected for making locator contact with the part. Similarly, two positions are selected on the second surface F_2 or the secondary datum, and one on the third surface F_3 or tertiary datum. This location scheme provides a deterministic location [6] for the part, which means that the part cannot move without losing contact with at least one locator.

Based on this principle, we have a placement block that has 3 datums with 6 bored holes for press fitting spherical ruby jewel bearings (φ 2 mm). 3 jewels are on the primary datum, 2 on the secondary and 1 one the tertiary datum. These jewel bearings form an exact constraint device that restricts the motion of the part with respect to the block, in all six degrees of freedom.

Preloading Method

Permanent magnets are used to preload the vee grooves against the jewel bearings. The magnets are glued to setscrews, which can be adjusted to increase or decrease the preload on the three datums of the vee groove. Appropriately balancing these forces is necessary for reliable positioning. The preload force can be changed by varying the distance of the setscrews from the surface of the vee grooves. For a particular configuration, we need to change this location of the setscrew-magnet only once.

Figure 5 illustrates the 3-2-1 locating scheme and also the permanent magnets used for preloading. Silicon vee grooves can be held with wax in a ferro-magnetic carrier. In this case, the carrier should allow the jewel bearings to contact the measurand and establish the datums.

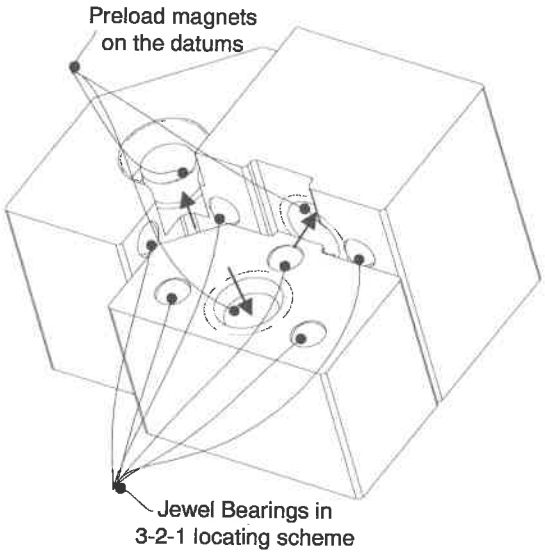

Figure 5: Preloading of the vee grooves by permanent magnets

ELASTIC DEFORMATION OF VEE GROOVES

Elastic deformation due to fixturing can affect the accuracy and repeatability of surface topography measurements. The amount of deformation associated with a 3-2-1 scheme can be analyzed a priori using finite element analyses. The following is a list of test cases to study the elastic deformation occurring in the vee groove structure.

1. Load due to gravity on the vee grooves constrained at 6 locations in the 3-2-1 scheme.
2. Load due to gravity on the vee groove placed on 6 springs with stiffness equal to Hertzian contact stiffness as given in Eq (3). P is the reaction force at the contact point when the measurand is loaded by gravity and preload forces, E_e is the equivalent elastic modulus, and R is the radius of the jewel bearing.

$$k = \left[6PRE_e^{\,2}\right]^{1/3} \tag{3}$$

3. Maximum magnetic preload, which exerts a pressure over a circular area on the primary datum, when the vee groove is placed on 6 springs with same stiffnesses.
4. A sufficient magnetic preload, which exerts a pressure over a circular area on the primary datum, when the vee groove is placed on 6 springs with same stiffnesses.

Since the preload force is magnetic, it is inversely proportional to the square of the distance between the magnet and the vee groove surface. A Gaussmeter was used to measure the flux density at the vee groove surface, due to the magnet. This flux density is proportional to the force exerted by the magnet on the surface. The magnetic force for varying positions of the preloads was calculated from these measured flux densities.

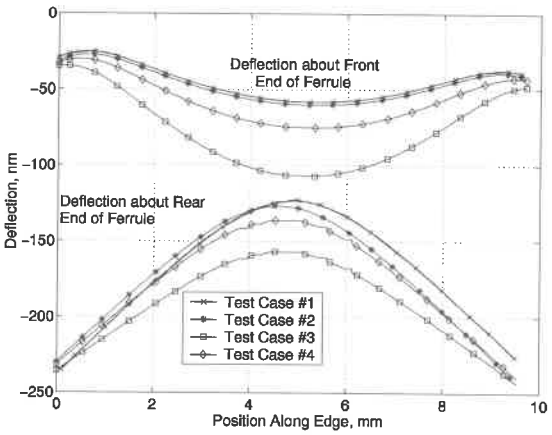

Figure 6: Deflection at the front and the rear edges of the vee groove

Figure 6 illustrates the amount of deflection (calculated with FEA) that occurs along the front and the rear edges of the vee groove, for all four test cases. It can be observed that the vee groove deflects more on the rear edge compared to the front edge. Therefore, the placement of the vee grooves on the primary datum should be in such a way that the critical edges are supported above the 2 contact points (on the primary datum) on the jewel bearings to minimize the deflections

due to gravity and preload forces. It can be observed from Figure 6 that the maximum deflection at the end of the ferrule, for normal gravity and preload forces is comparable to the vertical resolution of the stylus profilometer.

To ensure the repeatability of the measurements, the fixture has to be designed and tested for its repeatability.

Post Processing Techniques

A key problem in surface-related research is choosing parameters that characterize surface properties in such a way that they correlate with surface formation mechanisms or functional behavior in a fundamental way. Literature presents a range of characterization techniques, such as statistics, spectral analysis, autocorrelation analysis, time-series modeling, fractals and function-specific methods. Generally the properties of surface topography are assessed in accordance with visual images and parameter values of the surface [7,8].

Once the measurement data is obtained, the analysis depends on the post processing technique and the functionality of the measurand. A function-specific method is most appropriate for considering the alignment of optical fibers in vee grooves. Table 2 illustrates a flow chart that is used in this characterization process. This algorithm accounts for problems with bad data or insufficient data for the analyses. Error checks determine if there are major deviations in the cross section of the vee grooves. This way, the analysis is performed quickly by sorting the good and the bad data and proceeding with the analyses.

The algorithm locates the resting positions of ideal fibers in the vee groove and hence their position can be compared with their ideal position to qualify the vee grooves. The same procedure is adaptable to all the scans of the surface data. Figure 7 is an illustration of one vee groove, which is out-of-spec. It is observed that the resting location of the fiber is very different from its ideal location. This shows that the vee groove is not good and there is an adjustment needed in the manufacturing process.

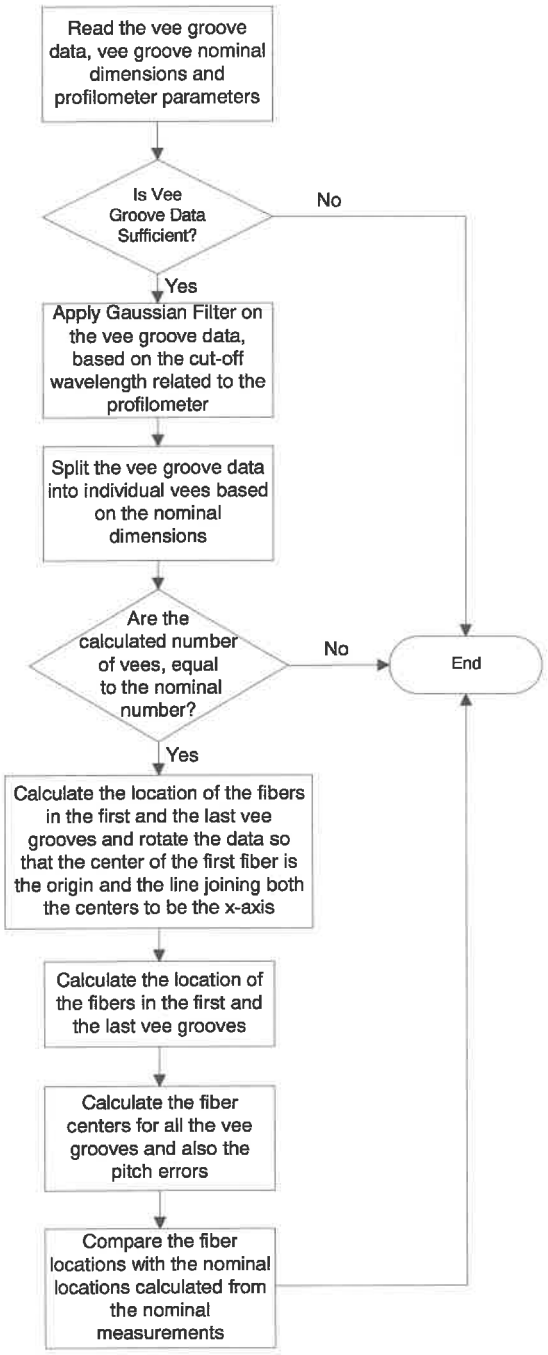
Read the vee groove data, vee groove nominal dimensions and profilometer parameters
Is Vee Groove Data Sufficient?
No
Yes
Apply Gaussian Filter on the vee groove data, based on the cut-off wavelength related to the profilometer
Split the vee groove data into individual vees based on the nominal dimensions
Are the calculated number of vees, equal to the nominal number?
No
End
Yes
Calculate the location of the fibers in the first and the last vee grooves and rotate the data so that the center of the first fiber is the origin and the line joining both the centers to be the x-axis
Calculate the location of the fibers in the first and the last vee grooves
Calculate the fiber centers for all the vee grooves and also the pitch errors
Compare the fiber locations with the nominal locations calculated from the nominal measurements

Table 2: Procedure of Characterization of Vee Groove Data

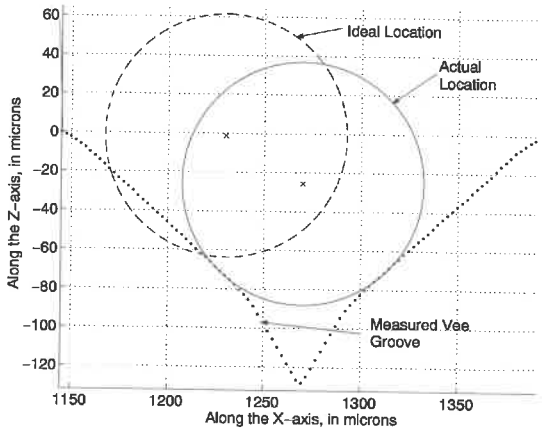

Figure 7: Comparison of the ideal and the actual fiber resting locations in the vee groove

Conclusions

This method of qualifying vee grooves for aligning optical fibers requires accurate profilometry measurements. A 3-2-1 fixturing method employing jewel bearings and magnetic preload helps provide repeatable positioning of the measurand, and a micrometer tip-tilt-rotate stage assists with aligning the vee-grooves to the stylus. The resting position of an ideal circular fiber in a measured vee-groove is used to calculate the actual location of a fiber. Deviations between the actual and ideal centers of the fiber give an indicate problems with the manufacturing process.

References

[1] Rachakonda, P., Barraja, M., Vallance, R.R., Kiani, S., Lehman, J., *"2D Error Models and Monte Carlo Simulations for Budgeting Variation in Optical Fiber Array Connectors"*, Proceedings of the American Society for Precision Engineering, Annual Conference, Crystal City, Virginia, November 10-15, 2001, pp.509-512.

[2] Strandman, C., Backlund, Y., *"Bulk silicon holding structures for mounting of optical fibers in v-grooves"*, Journal of Microelectromechanical Systems, Vol.6, No.2, March 1997, pp.35-40

[3] ASME B46.1-1995, *Surface Texture (Surface Roughness, Waviness, and Lay)*, 1995.

[4] Stout, K.J., Blunt, L., *"Thee Dimensional Surface Topography"*, Penton Press, London, Second Edition, pp. 12.

[5] Marin, R.A., and Ferreira, P.M., *"Kinematic Analysis and Synthesis of Deterministic 3-2-1 Locator Schemes for Machining Fixtures"*, ASME Journal of Manufacturing Science and Engineering, Vol.123, No. 4, November 2001, pp.708-719.

[6] Asada,H., and By, A.B., *"Kinematic Analysis of Workpart Fixturing for Flexible Assembly with Automatically Reconfigurable Fixtures"*, IEEE Journal of Robotics and Automation, RA-1, No.2, 1985, pp.86-94.

[7]Stout, K.J., Sullivan, P.J., Dong, W.P., Mainsah, E., Luo, N., Mathia, T., and Zahouani, H., *"The Development of Methods for the Characterization of Roughness in 3 Dimensions"*, Commission of the European Communities, (BCR-3374/1/0/170/90/2), (1993).

[8] Stout, K.J., Sullivan, P.J., Dong, W.P., Mainsah, E., Subari, K., and Mathia, T., *"The development of methods for the characterization of roughness in 3 dimensions"*, Interim Report No.1, EC Contract NO. 3374/1/0/170/90/2 (March 1991), First EC workshop on 3-D surface topography measurement and characterization (September 1991)

A Self-calibration Method for Coordinate Measuring Machines

Hiroki Shimizu, Satoshi Kiyono, Wei Gao
Department of Mechatronics and Precision Engineering, Tohoku University
Aza Aoba01, Aramaki, Aoba-ku Sendai 980-8579 Japan

1. Introduction

Nowadays, Coordinate Measuring Machines (CMM) are widely used not only in temperature controlled measuring rooms, but also in manufacturing lines, which are severe environments for CMMs. Temperature variation, vibration, and so on will make it difficult to keep CMMs to be accurate; accordingly, frequent calibration is required. However, conventional calibration method of using ball-plates is not easy to setup and takes long time. Moreover, calibrated artifact like a ball plate is expensive and it is difficult to use many artifacts. Although, self-calibration methods of using uncalibrated ball plate have been proposed[1], these methods also require complex calibration procedure. Here, we propose a calibration technique for CMMs based on the self-calibration concept[2) 3)]. This method is simple, takes only short time and there is no need to use expensive artifact like ball-plates. It is therefore suitable for frequent calibration of CMMs.

In this paper, the authors show the principle and some experimental results of the self-calibration methods. In addition, unequal pitch calibration methods, which can use the parts that are measured in manufacturing lines as the artifacts, are also proposed.

2. Principle

Errors of a CMM are classified into the mean sensitivity error and the linearity error. At first, before calibrating the linearity error, the mean sensitivity error is calibrated by a reference artifact or a calibrated gauge like a gage block.

Next, the linearity error calibration is carried out without using any calibrated artifact. In Fig. 1, the vertical axis shows real coordinate x, the lateral axis shows output value of CMM m, $h(m)$ shows the calibration curve. The object placed at left of the vertical axis shows an artifact that has some measuring points indicated with circles. First, coordinates of the measuring points are measured and values $a[1],a[2],...,a[n]$ are obtained. Relation between x_i and $a[i]$ is expressed by the following equation.

$$x_i = h(a[i]) \qquad i=1,2,...,n \tag{1}$$

After shifting the artifact parallelly with a distance D, measurement is carried out again and values $b[1],b[2],...,b[n]$ are obtained to establish the next equation.

$$x_i + D = h(b[i]) \qquad i=1,2,...,n \tag{2}$$

If the linearity error is 0, difference between output values at the same measuring point before and after the shift (cf. $b[1]$-$a[1]$) becomes D. However, if there is the linearity error, the difference between output values becomes slightly different from D. In other word, it is possible to obtain the local derivative of calibration curve $h'(m)$ from the difference between output values as follows:

$$h'[i] = \frac{D}{b[i]-a[i]} \qquad i=1,2,...,n \tag{3}$$

where, D is obtained by equation (4).

$$D = \frac{1}{n}\sum_{k=1}^{n}(a[k]-b[k]) \tag{4}$$

In using equation (3) position of $a[i]$ can be compensated for and the compensated position $a_c[i]$ is obtained by equation (5)

$$a_c[i+1] = a[i] + h'[i](a[i+1]-a[i]) \qquad i=1,2,...,n \tag{5}$$

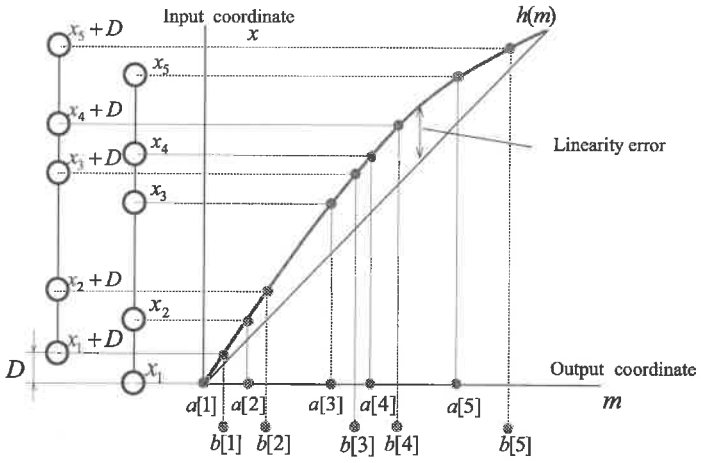

Fig.1 Calibration curve and calibration procedure

On the other hand, it is possible to obtain the calibration curve *h(m)* by integrating the derivative in equation (3).

$$h[i]=\sum_{k=2}^{i} h'[k-1](a[k]-a[k-1]), \qquad h[1]=0 \qquad i=2,3,\ldots,n \qquad (6)$$

As described above, this method is very simple and there is no need to use calibrated artifacts like the ball-plates in the linearity calibration process. It can be applied to two-dimensional calibration with using an uncalibrated two-dimensional ball plate or hole plate. Moreover, measuring points are not required to have equal pitch. Therefore, unequal pitch calibration can be realized and workpieces themselves can also be used as artifacts for calibration.

3. Equal pitch self-calibration experiments

To confirm effectiveness of the proposed method, one-dimensional calibration experiments were carried out. A prototype of a CMM "m-job" by Dai-Ichi Sokuhan Works Co. is used as a target for calibration. This CMM has a good repeatability of 1.1μm in the standard deviation, but relatively large errors at the end of measuring range. As an artifact, a commercial available step gauge was used. The step gauge consists of 22 gauge blocks with a length of 10mm, aligned with an equal interval of 10mm (total length of the step gauge was 450mm). The calibrated values of this gauge ware not used in the experiments. As a reference CMM, a commercially available one (Mitutoyo Corp. Model: Bright Apex504, accuracy: 2.9+4L/1000μm) was adopted.

Data correction was carried out by the following sequence. First, the left side position of the gauge surface and positions of all gage blocks were sampled to obtain 23 position data with a pitch of 20mm. In addition, to reduce the affect of dispersion, the measurements were carried out 10 times sequentially and the averaged value was adopted as *a[i]*. Next, the artifact was shifted by approximately 20mm parallel along the gauge axis. Though the shifting distance can be arbitrarily selected, the shift distance was selected to be equal to the pitch of the measuring points. After that, the same sampling process was carried out again and *b[i]* was obtained. At this time, the mean sensitivity error was compensated for by comparing the distance between the positions of the left-side surface of the gauge and the gage block at 440mm. In the next process, the self-calibration method mentioned in section 2 was applied. The result is shown in Fig.2. The lateral axis shows the positions of gage blocks and vertical axis shows the linearity error of the CMM. Before calibration, the CMM has a linearity error of maximum 27μm. In contrast, the residual error after calibration was reduced to 3.4μm peak-to-valley. This was almost the same as the level of the measurement repeatability of the CMM. From this result, the effectiveness of proposed method, which does not need any calibrated artifacts as references, has been confirmed. In other words, handmaid uncalibrated artifacts can be used for calibration. This is a large merit for frequent calibrations in manufacturing lines.

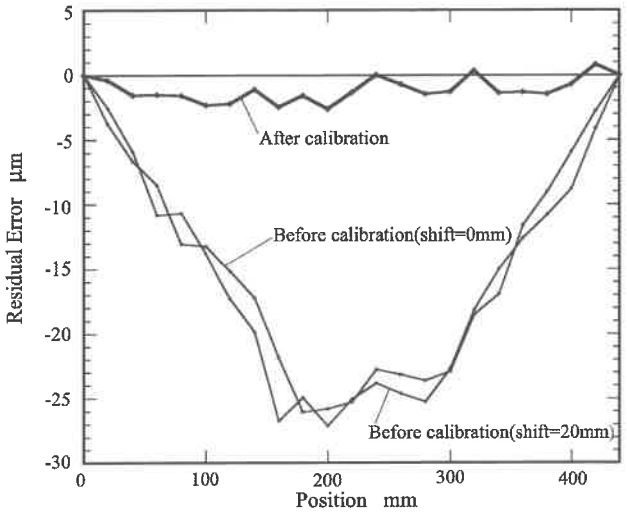

Fig.2 Calibration result of equal pitch self-calibration method

4. Unequal pitch self-calibration experiments

In the next step, we consider to use the parts themselves that are measured in the manufacturing line as artifacts for calibration. In many cases, measuring points of the parts, however, are with unequal pitches. Because pitch equality of measuring points is not required in the self-calibration method as shown in equations (5) and (6), basic experiments of unequal pitch self-calibration were carried out.

As the unequal pitch coordinate data, we chose coordinate data of 12 positions with unequal pitches from the coordinate data obtained in the experiment in section 3, which were data of 0, 40, 60, 120, 140, 180, 220, 240, 320, 340, 400, 440mm. In this case, pitches of measuring points varied from 20mm to 80mm. For comparison, calibration experiments of 12 data with an equal pitch of 40mm were also carried out.

The results of calibration experiments are shown in Fig. 3. In the case of equal pitch calibration, the residual error was reduced to maximum 9.9μm. On the other hand, in the case of unequal pitch calibration, the residual error was reduced to 8.9μm peak-to-valley. This results shows that the error reduction effects were approximately the same in both cases.

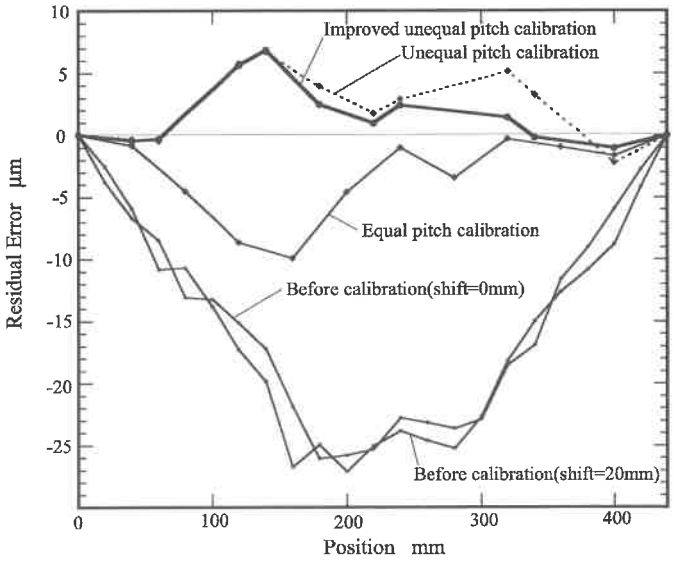

Fig.3 Residual errors of each calibration method

5. Improved unequal pitch self-calibration

In section 4, it is shown that compensation of linearity error by unequal pitch self-calibration is accomplished. However, in the unequal pitch calibration, the shift distance and pitches are sometimes quite different. Therefore, it can be predicted that deviation between *a[i+1]* and *a[i]* is quite different from that between *b[i]* and *a[i]*. To reduce the calculation error caused from the difference mentioned above, we propose an improved unequal pitch calibration technique. This method uses both deviations of near *a[i]* and near *a[i+1]* in integration when compensating linearity errors. In this method, compensated coordinate and calibration curve are described as follows:

$$a_c[i+1]=a[i]+h'[i](b[i]-a[i])+\frac{h'[i]+h'[i+1]}{2}(a[i+1]-b[i]) \qquad i=1,2,\ldots,n \tag{7}$$

$$h[i]=\sum_{k=2}^{i}h'[k-1](b[k-1]-a[k-1])+\frac{h'[k-1]-h'[k]}{2}(a[k]-b[k-1]), \quad h[1]=0 \qquad i=2,3,\ldots,n \tag{8}$$

A broad line in Fig.3 shows the result of applying the improved method. The residual error was reduced to 7.9μm peak-to-valley and the sum of residual errors at each point was also reduced comparing with the unequal pitch calibration shown in section 4. From this result, efficiency of the improved unequal pitch calibration was confirmed.

6. Conclusions

1) A new self-calibration method for CMMs was proposed. From the results of basic experiments, it is confirmed that this method can reduce the linearity error to the level of repeatability without using calibrated gauges.
2) Instead of equal pitch calibration that is conventionally performed, an unequal pitch calibration of self-calibration method is proposed and the effectiveness was confirmed from the experimental result. This method has the feasibility of using the parts in measurement for calibration.
3) To reduce the error of unequal pitch self-calibration, an improved technique was proposed and the efficiency was confirmed by experiments.

Acknowledgement

This research was supported by a Grant-in-Aid from Mitutoyo Association for Science and Technology. The authors also thank Dai-Ichi Sokuhan Works Co. for providing the prototype CMM.

References

1) L. De Jonge, J. P. Kruth: Self-Calibration Method for Three Dimensional Coordinate Measuring Machines Using a Ball Plate, Proc. 7th IPES, Kobe, Japan May (1993) 402.
2) Michael Takac: Self-cailbration in one dimension, SPIE Vol. 2087 Photomask Technology and Management, (1993) 80.
3) Satoshi Kiyono, Wei Gao, Shizhou Zhang, and Toru Aramaki: elf-calibration of a scanning white light interference microscope, Optical Engineering 39, 10 (2000) 2720.

THE MICROPROBE FOR NANO-POSITIONAL DETECTION USING OPTICALLY FORCED VIBRATION METHOD

Y. TAKAYA, M. NISHIKAWA, S. TAKAHASHI and T. MIYOSHI
Osaka University, 2-1 Yamadaoka Suita, 565-0871 Osaka, JAPAN

1. INTRODUCTION

As seen in various type of microsystems such as micromechanical system, microoptical system, three-dimensional LSI, MEMS(Micro-Electo-Mechanical System), MOEMS(Micro-Opto-Electro-Mechanical System), technical trends of microfabrication include increasing diversification and complexity of processes, combination of different processes, and multifunction. In contrast, quantitative evaluation technique of geometrical quantities such as size, dimensions, and tolerances has not been established yet. The establishment of assessment technologies for three-dimensional micromachining accuracy is an urgent issue.

To assess geometrical quantities of micromachined 3-D shape based on coordinate metrology with nanometer order accuracy, nano-CMM [1] as a three dimensional coordinate measuring machine with the measuring range of mm and accuracy of nm order. As the microprobe satisfying harsh requirements for nano-CMM, we have been developed the laser trapping probe [2] [3] whose principle is based on the single-beam gradient-force optical trapping technique [4] and the Linnik type microscope interferometer. We employ an optically trapped 8μm spacer silica particle as the probe sphere, which has a low spring constant of about 10^{-5}N/m. In the previous system, interferometric sensing is not robust to complex motions of the probe sphere resulting from dynamical effects in microscopic region, for example, electro static effect, adsorption, heat fluctuation, Brownian motion, etc. Therefore, it is difficult to decrease measurement uncertainty in positional sensing. To overcome this problem, we propose a vibrational microprobe driven by radiation pressure as an active sensing method.

The work reported in this paper deals with fundamental characteristics of the newly developed laser trapping probe introducing an optically forced vibration method. The experimental system is developed and fundamental experiments are performed to investigate characteristics of the vibrational microprobe. An optically trapped silica particle in air is used as a microprobe sphere with the diameter of 8.0μm. Frequency response to external excitation is obtained in 2 kHz. The spring constant of the probe is estimated by measuring frequency response. Finally, we demonstrated approach to a glass microsphere with 168 μm diameter.

2. PRINCIPLE OF OPTICALLY FORCED VIBRATION METHOD

Fig. 1 shows the principle of the laser trapping probe for nano-CMM using optically forced vibration method. An optically trapped small dielectric particle in air is used as a microprobe sphere. It is sensitive to external force generated by interactions with a workpiece and has the same dynamical properties as a positional detection probe. As the source of the trapping beam, Nd:YAG laser light formed annular is used. The probe sphere retains a stable position against gravity when applied with trapping force (Fig.1(a)). Improving the stability of the trap using annular beam trapping technique, a probe sphere can be forced to oscillate by the driving force exerted by radiation pressure. As the source of the driving beam, the light from the laser diode (LD) traveling through the center of the annular beam is used (Fig.1(b)). The driving force is changed by modulating the intensity of LD emission. An optically trapped small dielectric particle in forced oscillation state is useful for the positional detection probe (Fig.1(c)). Consequently, a position can be detected based on changes of oscillating frequency (Fig.1(d)).

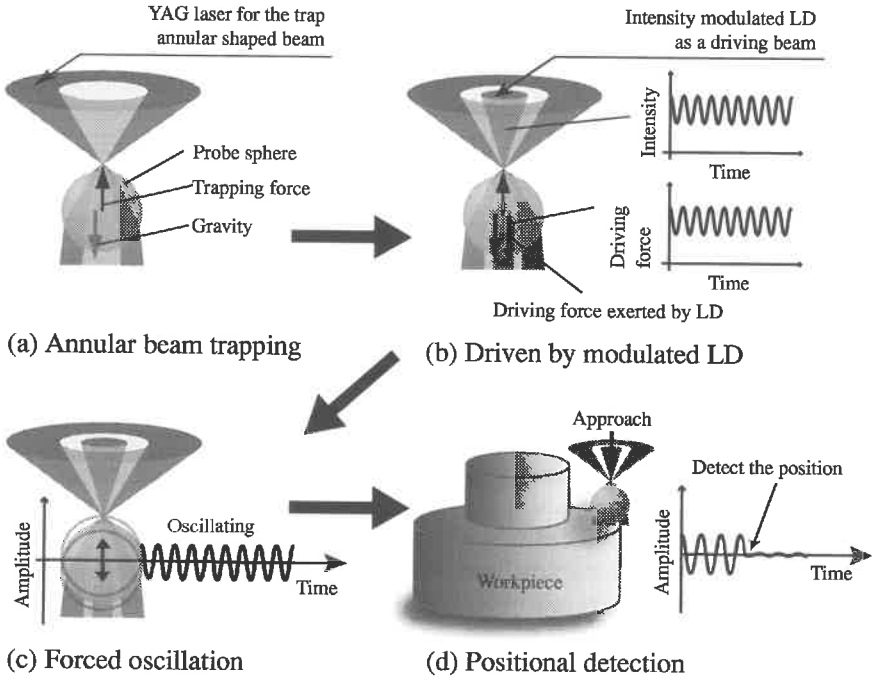

Fig. 1 The principle of the laser trapping probe for nano-CMM using optically forced vibration method.

3. EXPERIMENTAL SETUP

Schematic diagram of the laser trapping probe system based on the optically forced vibration technique is illustrated in Fig.2. The system is composed of a trapping optical system, a driving optical system for optically forced oscillation of a probe sphere, a detecting optical system for monitoring the oscillating status.

The light with wavelength of 1064nm is emitted from Q-switch/Nd:YAG laser and is annular shaped by an obstruction. The laser beam is deflected by polarized beam splitter (PBS2), after through PBS1, then focused by an objective with N.A. of 0.95 on a silica particle with 8μm diameter. The silica particle on the glass plate can only be levitated in air with the concentration of the high energy of the Q-switch pulse emission, after which the probe sphere can be maintained at a stable position in the CW emission mode with a low power of less than 100mW. The modulated light with wavelength of 687nm from LD is joined with the YAG laser light at PBS1 and travels through the center of the annular beam. Then it is focused on a silica particle after deflected by PBS2. The backscattered YAG laser light from a trapped particle passes through IRTF with eliminating LD light. The light deflected by DM is collected by a lens, then detected using PD. Oscillating condition is monitored by output signal from PD. Positioning of a workpiece is performed using an xyz-stage with positioning accuracy of 5nm, which is driven by PZT actuators.

4. FUNDAMENTAL EXPERIMENTS

4.1 Annular beam trapping

Fig. 3 shows annular beam generation for stable trapping. Trapping force is the resulting force of a pulling component and a pushing component, as indicated in Fig. 3(a). A pulling component is exerted by the light with a large incident angle and a pushing component by the light with a small incident angle, that is, the light around the optical axis in the focused beam. A pulling component in the trapping force is more dominant for annular beam than Gaussian beam, therefore, annu-

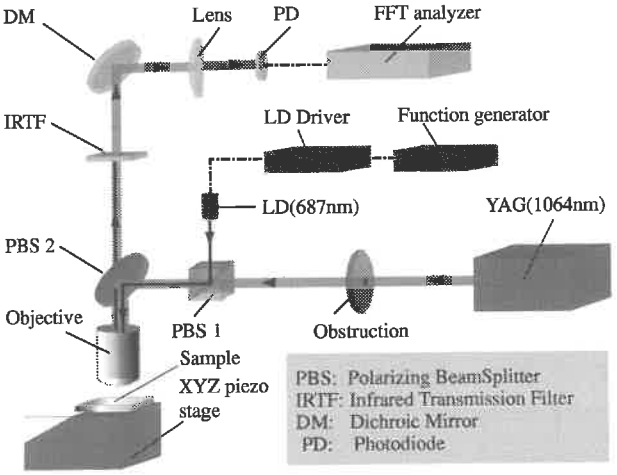

Fig. 2 Schematic diagram of the laser trapping probe system based on optically forced vibration technique.

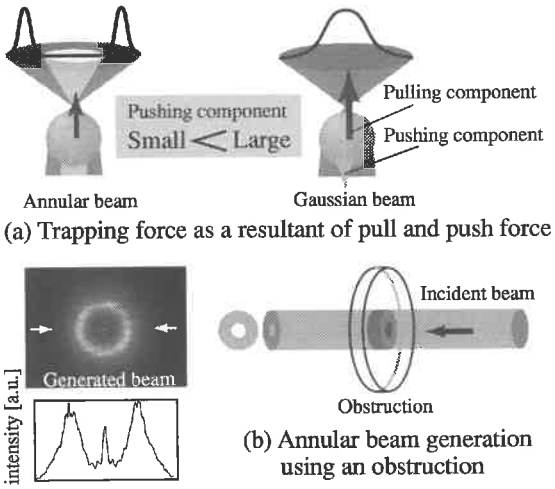

Fig. 3 Annular beam generation for stable trapping.

lar beam enables more stable trap. Moreover, annular beam is advantageous for driving the trapped particle in the condition that the pushing component in annular beam is smaller than Gaussian beam. Methods to generate annular beam and it's intensity profile are shown in Fig.3(b). Incident beam from YAG laser is obstructed using a circular opaque disk[5]. This method makes it possible to simplify the system. Transforming efficiency is low, however the annular beam is obviously more effective to trap a particle than Gaussian beam. The bright spot seen in the center of the generated annular beam is caused by diffraction. This diffraction spot has so small size and low intensity that trapping stability is not influenced. As indicated in Fig.3(b), the intensity profile has good rotation symmetry, this beam property is important to trap stably.

4.2 Vibration properties of the probe

The probe sphere is driven by modulated LD light in addition to annular beam trapping to confirm vibration of the trapped probe sphere in air. Fig. 4 shows measurement results of oscillating behavior of the probe sphere. The LD laser light is given the sinusoidal modulation at the amplitude of 12mW and the frequency of 23Hz. The voltage output from the photodetector is obtained by detecting the backscattered light from the probe sphere. And the voltage output is reflecting the Z directional displacement of the probe sphere, when the axis of the trapping beam is in the Z direction. We can recognize the periodical signal resulting from vibration of the probe sphere in Fig. 4 (a). The voltage output from the photodetector is processed using a FFT analyzer in real time to analyze the vibration in the spectral domain. The power spectral density for the voltage output from the photodetector is obtained as Fig.4(b). From the peak at 23.75 Hz in the power spectral density distribution, we can confirm that the frequency response corresponding to the sinusoidal modulation of LD laser light is obtained. This is supported by no response seen in the power spectral density distribution without modulation also.

The optically trapped particle can be modeled as a mass in a three-dimensional harmonic potential[6]. The laser trapping probe has two spring constants, one is the axial and the other in the radial direction. For the axial movement of the trapped particle, a differential equation modeling is given by,

$$m\ddot{z} + D\dot{z} + k_z z = F \tag{1}$$

where k_z is the spring constant in the axial direction, m is the mass of the particle, D is the viscous

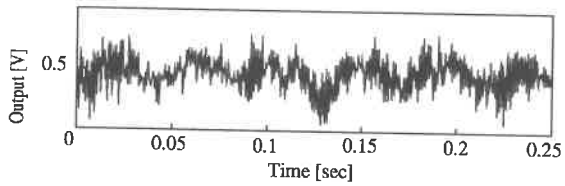

(a) Voltage output from the photodetector

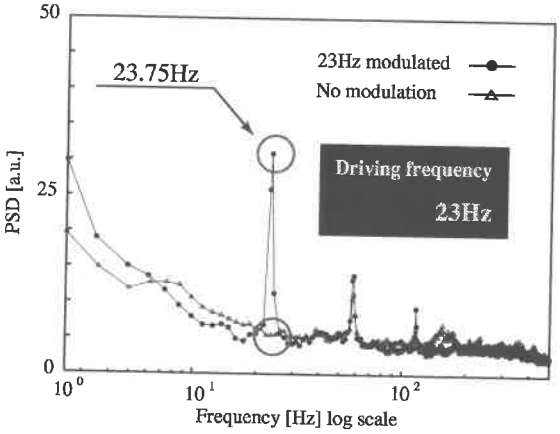

(b) Power spectral densities

Fig. 4 Measurement results of oscillation of the probe sphere driven by radiation pressure of modulated LD laser light.

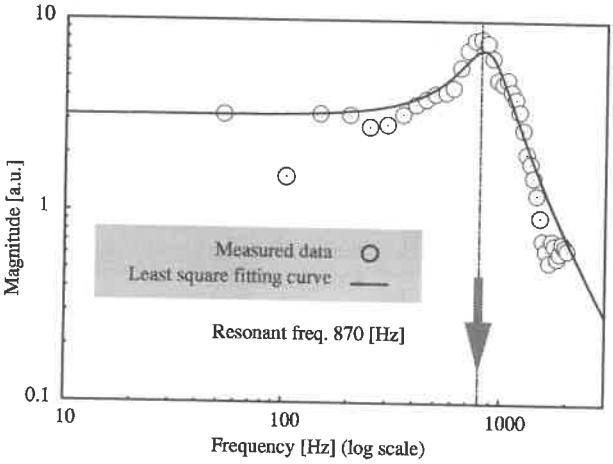

Fig. 5 The measured amplitude response for the sinusoidal modulation at frequencies ranging from 50Hz to 2kHz and the least-squares fitting curve.

drag coefficient of the surrounding medium, and F is the external driving force. According to the Stokes Law, a spherical particle that moves in air at low velocity undergoes a viscous drag, and its Stokes drag coefficient is given by,

$$D = 6\pi\eta r \tag{2}$$

where η is the viscosity of the surrounding medium, and r is the radius of the particle. The following amplitude response $|\hat{R}|$ is deduced from Eq. (1).

$$|\hat{R}| = \frac{Const.}{\sqrt{\left\{1-\left(f/f_n\right)^2\right\}^2 + \left(2\zeta f/f_n\right)^2}} \tag{3}$$

Here, f_n is the resonance frequency without viscous damping and ζ is the viscous damping term. Using $\zeta = D/\left(2\sqrt{m k_z}\right)$, by measuring the frequency response of the oscillating amplitude and performing a least-squares fitting according to Eq. (3),we can determine the term f_n and further obtain the axial spring constant k_z using the relation,

$$f_n = \frac{\sqrt{k_z/m}}{2\pi} \tag{4}$$

Fig. 5 indicates the measured amplitude response for the sinusoidal modulation at frequencies ranging from 50Hz to 2kHz and the least-squares fitting curve. The least-squares fitting of the

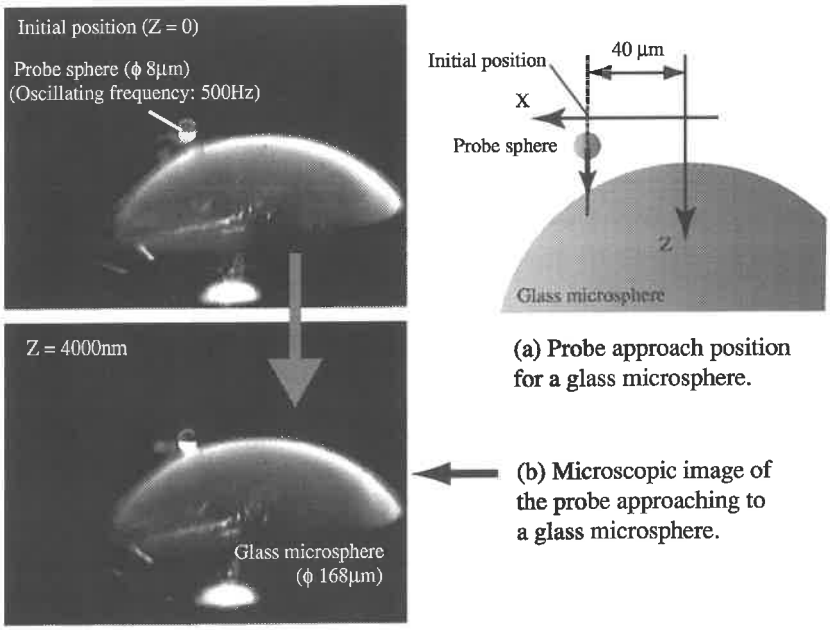

Fig. 6 Investigation of positional detection using the change of vibrational status of the probe sphere by approaching it to a glass microsphere.

measured data is performed by employing constant values according to the experimental conditions: the radius of the probe sphere $r = 4.0 \times 10^{-6}$ m, the mass of the probe sphere $m = 5.0 \times 10^{-13}$ kg, the viscosity of air $\propto = 1.81 \times 10^{-5}$ Pa·s and the viscous drag coefficient of air $D = 1.36 \times 10^{-9}$ N·s/m. Substituting the deduced value of the resonant frequency f_n=870Hz from the least-squares fitting into Eq.(4), we obtain the axial spring constant $k_z = 1.6 \times 10^{-5}$ N/m.

4.3 Positional detection

In order to verify the performance of the vibrational microprobe as a positional sensitive probe, we conducted an experiment to approach the probe sphere to a glass microsphere with 168∝m in diameter. Fig. 6 shows investigation of positional detection using the change of vibrational status of the probe sphere by approaching it to a glass microsphere. In this experiment, the probe particle is forced to vibrate at a frequency of 500Hz. The probe sphere is moved toward the glass microsphere in the Z direction at the X position of about 40∝m from the center of the sphere (Fig.6(a)). The microscopic images of the probe sphere at the initial position and reaching at Z=4000nm are indicated in Fig.6(b). Relative displacement between the probe sphere and the glass microsphere is given by moving the sample stage.

Fig. 7 shows measurement results of the peak power in Fourier spectra of the voltage output from the photodetector changing with the vibration status for verifying positional detection principle. Fourier spectra of a monitoring signal of vibrating probe sphere are measured while approaching it to the glass microsphere. While the probe sphare is moving from z=0nm to z=4900nm, the spectra keeps a peak at the modulating frequency of 500Hz. However, we can recognize that the peak vanishes at z=4925nm. On the other hand, the probe sphere returns to z=4900nm, then the peak appears again. This means that the probe comes in contact with the work surface in 25nm. We confirmed that the chane of spectrum changes has high repeatability and is independent of an inclination angle of the work surface. These results show that our method has the possibility to have positional sensing accuracy of less than 25nm.

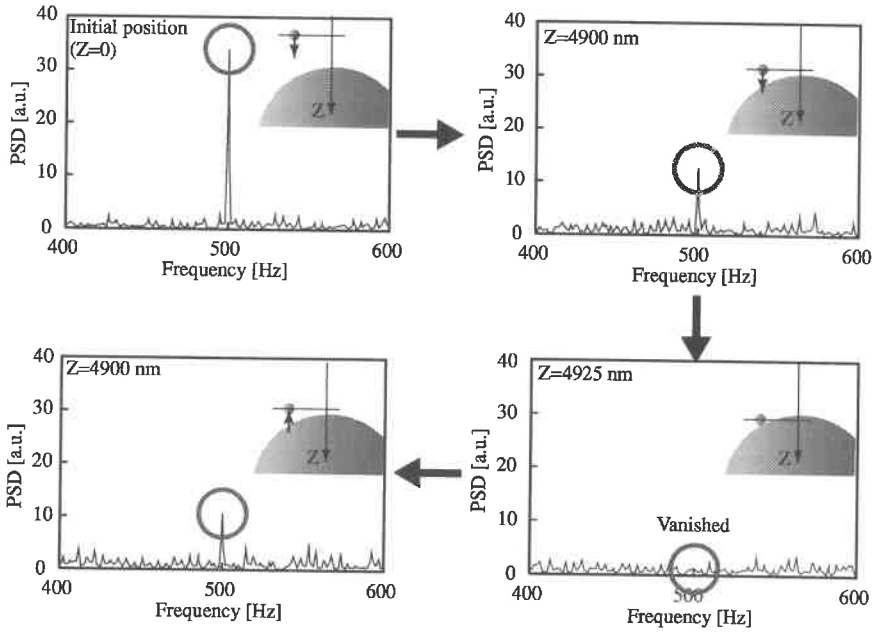

Fig. 7 Measurement results of the peak power in Fourier spectra of the voltage output from the photodetector changing with the vibration status for verifying positional detection principle.

5. CONCLUSIONS

Fundamental characteristics of the newly developed laser trapping probe introducing an optically forced vibration method were experimentally investigated. We have achieved three dimensional trapping of a microprobe sphere in air with the annular beam generated by using an obstruction. The probe sphere in annular beam trapping was oscillated using the LD laser light with the sinusoidal modulation. We confirmed it by measuring the voltage output from the photodetector detecting the backscattered light from the probe sphere. Amplitude response for the sinusoidal driving force at frequencies ranging from 50Hz to 2kHz were measured. From the obtained resonant frequency, we could estimate the axial spring constant k_z of the laser trappping probe as 1.6 X 10^{-5} N/m. Finally, we suggested that our method has the possibility to have an accuracy of less than 25nm from the measurements of the vibrational status while the probe sphere is approaching to the glass microsphere.

REFERENCES

[1] K. Takamasu, et al.,"Basic Concept of Nano-CMM", Proc. of The Japan-China Bilateral Symposium on Advanced Manufacturing Engineering, pp.155(1996).

[2] Y. Takaya, S. Takahashi, T. Miyoshi, "Nano-Positional Detection Using Laser Trapping Probe For Microparts", Proc. of ASPE 2000 annual Meeting, pp. 584(2000).

[3] Y. Takaya, S. Takahashi, T. Miyoshi and K. Saito(2), "Development of The Nano-CMM Probe based on Laser Trapping Technology", CIRP ANNALS , **48**/1, pp.421(1999).

[4] A. Ashkin, J. M. Dziedzic, J. E. Bjorkholm and S. Chu, "Observation of a single-beam gradient force optical trap for dielectric particles", Opt. Lett.,11, pp.288(1986).

[5] M. Nishikawa, Y. Takaya, S. Takahashi, M. Uekita and T. Miyoshi, "Probing technique for microparts using optically trapped particle by annular beam", Proc. of International Symposiun on Photonics in Measurement, pp.103(2002).

[6] M. E. J. Friese, A. G. Truscott, H. R. Dunlop, N. R. Heckenberg, "Determination of the force constant of a single-beam gradient trap by measurement of backscattered light", Appl. Opt., **35**/36, pp.7112(1996).

Direct measurement of lattice spacing on crystalline surface using scanning tunneling microscope and laser interferometry

Masato AKETAGAWA*, Pongpun RERKKUMSUP, Koji TAKADA
Tomonori WATANABE, Shin SADAKATA
Department of Mechanical Engineering, Nagaoka University of Technology
Kamitomioka 1603-1, Nagaoka, Niigata, 940-2188 JAPAN
Fax: +81-258-47-9770, *E-mail: masatoaa@vos.nagaokaut.ac.jp

I. INTRODUCTION

Since research activities in precision engineering and nanotechnology have progressed rapidly, a new length-measurement method with sub-nanometer resolution is required. Nowadays, laser interferometry is of industrial length standard. A lot of commercial interferometer are widely used in the industry. However, it is very difficult to determine arbitrary length with nanometer accuracy using the commercial interferometer, because it suffers from the nonlinearity problem of fringe interpolation[1,2]. On the other hand, a phase modulation homodyne interferometer, which can determine the optical path difference of wavelength times integer ($\lambda \times n$) with the accuracy of 10 pm or less, has been proposed[3].

The lattice spacing of approximately 0.2 nm for some regular crystalline lattices is uniform and stable over a long range when the crystals are stress free. These crystals can be used as reference scales with sub-nanometer resolution instead of laser interferometry. X-ray interferometry (XRI) utilizing silicon crystal has been developed to determine the lattice spacing of silicon[4]. And it can be used for length measurement with sub-nanometer resolution[5]. However, XRIs are not commonly used in the industry, because they are special and relatively large instruments, and it is difficult to adjust it for obtaining sufficiently contrast x-ray fringes. On the other hand, the scanning tunneling microscope (STM)[6] is becoming a popular tool in surface engineering fields and can be used to obtain images of atoms on regular crystalline surfaces in air. It is, therefore, expected that such crystalline surfaces can be used as the "crystalline lattice scale" with sub-nanometer resolution by combining them with the STM as a detector[7-9]. We have shown the feasibility of the "crystalline lattice scale" using the crystal and a dual-tunneling-unit STM[9]. In order to realize a length measurement method using a crystalline surface[10], the lattice spacing on a regular crystalline surface, e.g. highly oriented pyrolytic graphite (HOPG), has to be measured and verified first. In this paper, a design and performance results for measuring the lattice spacing on a HOPG crystalline surface are discussed.

II. INSTRUMENT DESIGN AND OPERATION PRINCIPLE

Figures 1 shows a photograph of the instrument developed for measurement of lattice spacings on crystalline surfaces. The operations include; 1) three-dimensional atomic STM imaging of the crystalline surface of interest using a STM head with a *YZ*-axes tip scanner and an *X*-axis sample stage, 2) measurement of sample stage displacement along the *X*-axis (= measurement axis) with a phase modulation homodyne interferometer. If the number N of lattice spacings along measurement axis on the atomic STM image of the crystal and the sample stage displacement L along the measurement axis are determined, the lattice spacing d can be written as L/N. A low linear thermal expansion cast iron, whose coefficient less than 0.8×10^{-6} /K at room temperature, is selected for the material of the STM head and the base plate for the sake of a reduction of the thermal deformation effect. A tube-type PZT actuator is used for the *YZ*-axes tip scanner of the STM head. The STM head itself is supported with three precision screws. A

coarse approach of the STM tip into a tunneling region is performed by the *Z*-axis motion of the back precision screw which is attached to the base plate and a precise stepping motor. To enhance lateral and vertical rigidities of the STM head to the base plate, two springs are utilized. Four parallel springs are fabricated at the center of the base plate using a wire-cut method. The center part of the base plate is used as the *X*-axis sample stage with fine straight motion and high stiffness by combining the parallel springs and a stacked-type piezo actuator. The first resonance frequency of the parallel spring stage is over 2 kHz. The maximum travel of the stage is approximately 10 μm (applied voltage is 1 kV) with a maximum pitching or yawing error of less than 1.0 μrad. To adjust the sample surface to be parallel to the *X*-axis, a tilting sample adjuster, on which the sample should be placed, is set on the *X*-axis sample stage just beneath the STM tip. Three-dimensional STM imaging can be performed by combining the motions of the *X*-axis sample stage and the *YZ*-axes tip scanner. In order to reduce thermal drift error, the *X*-axis is selected as the measurement and fast scanning axis[11]. The instrument is also set in the thermo-stabilized cell[9], whose temperature stability is better than 0.05 K, to reduce the thermal drift. In the cell, calibrated thermo-, pressure- and humidity-meters are installed to determine the refractive index of air during the lattice measurement.

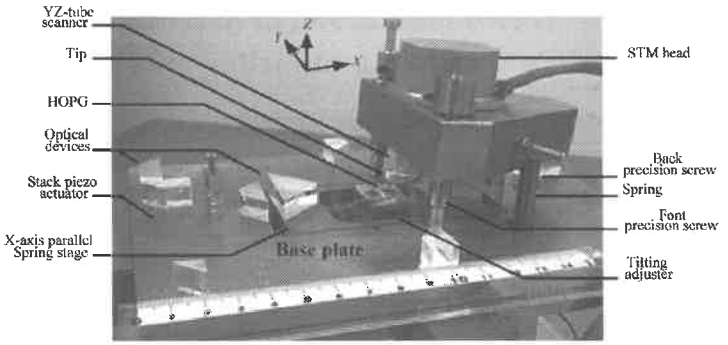

FIG. 1. The instrument for direct measurement of lattice spacing on crystalline surface. Dimensions (in mm) of the base plate and parallel spring stage are 200 (W) × 150 (D) ×25 (T) and 96 (W) ×52 (D) × 25 (T), respectively.

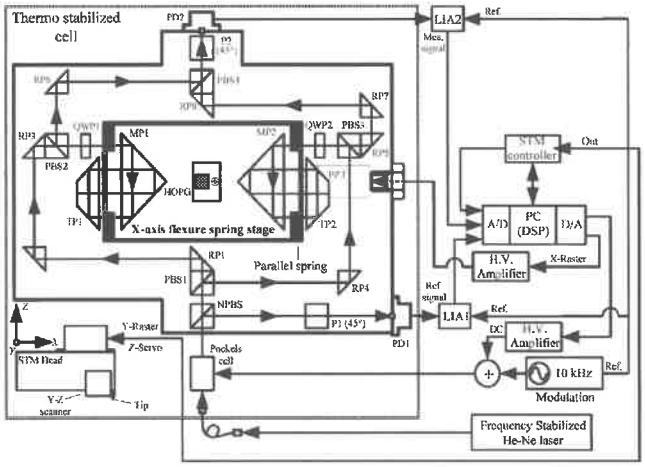

FIG. 2. Top schematic view of the instrument for direct measurement of lattice spacing on crystalline surface. NPBS: Non-polarizing beam splitter, PBS: Polarizing beam splitter, P: 45° polarizer, PD: Photodiode, RP: Right angle prism, QWP: Quarter wave plate, TP: Trapezoid prism, MP: Moving prism, LIA: Lock in amplifier.

Figure 2 shows the top schematic view of the measurement system. A linearly polarized beam, whose polarization angle is 45° from the vertical axis, is emitted form the frequency-stabilized He-Ne laser. The beam is introduced into the single mode polarization preserving fiber and led into the thermo-stabilized cell in order to reduce beam pointing instability and heating effect. The output beam from the end of the fiber passes through the Pockels cell. Two $LiNbO_3$ crystals of 5 mm × 5 mm × 20 mm size are utilized as the Pockels cell with a thermal-compensation configuration. The Pockels cell results in a phase modulation of a 10 kHz sinusoidal wave and bias-phase shift between the two polarization states *p* and *s*. The output beam from the Pockels cell passes through the non-polarizing beam splitter (NPBS), and a part

of the beam is split into the photodiode 1 (PD1) through polarizer 1 (P1; polarization angle = 45°) for the reference phase detection with the lock-in amplifier 1 (LIA1). The beam incident on the polarized beam splitter 1 (PBS1) is divided into two components, *p* and *s*. The output signal of LIA1 is used to control the bias-phase shift (= DC voltage) to the Pockels cell using 16 bit ADC and DAC with DSP so that the amplitudes of the *s* and *p* components at the PBS1 should be the same. The two beam components, *s* and *p*, travel along the two arms of the interferometer via PBS2/3, quarter wave plates 1 and 2 (QWP1/2), moving prisms 1 and 2 (MP1/2) on the *X*-axis stage and trapezoid prisms 1 and 2 (TP1/2). The beams travel back and forth four times between MP1/2 and TP1/2. The two beams which again pass through QWP1/2 and PBS2/3 are recombined at PBS4. The output beam from the PBS4 travels to PD2 via P2 (polarization angle = 45°). The PD2 signal is fed into LIA2 to determine the phase shift corresponding to the travel of the *X*-axis stage. The output signal of LIA2 should be a sine function of the optical path difference. The travel of the *X*-axis stage can be measured at the null points (= dark fringes) in the LIA2 signal with picometer resolution. In our design, the displacement for one fringe should be λ/16. The 16 bit ADC and DAC with DSP are also used for the recording of the LIA2 and tunneling current signals and the feed of the precise *X*-axis raster signal. The STM controller is used for the *Z*-axis servo control and the feed of the *Y*-axis raster signal.

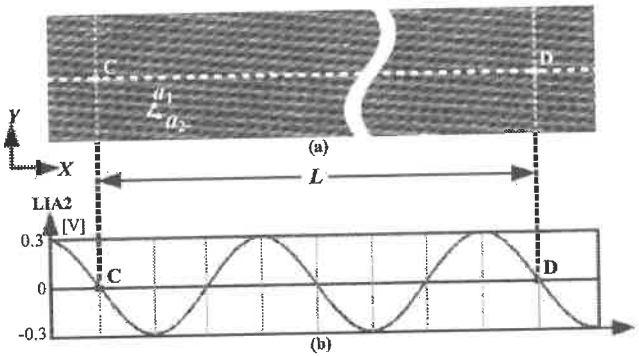

FIG.3. (a) A part of an approximately 100-nm-long atomic STM image of the HOPG crystal, (b) Output of LIA2 shown in Fig.2. One fringe equals λ/16. The complete 2 fringes of LIA2 output are compared with the number of crystalline lattices.

Table I. Experimental results for lattice spacing of HOPG.

No.	No. of atoms m_1 (atoms)	No. of atoms m_2 (atoms)	No. of atoms in scanning direction (atoms)	No. of fringes (cycles)	Calculated lattice spacing (nm)
1	204.5	164.3	320.0	2	0.247
2	205.8	165.7	322.4	2	0.245
3	205.3	165.2	321.5	2	0.246
4	204.3	164.9	320.3	2	0.247
Average					0.246 ± 0.002 (2σ)

III. PERFORMANCE EVALUATION AND RESULTS

The HOPG crystal is one of the candidate crystals for the "crystalline lattice scale". Therefore, the HOPG crystal was imaged and the lattice spacing on its surface was measured with the proposed instrument. Figures 3(a) and (b) show one of the results of the determination of the lattice spacing. Figure 3(a) shows the atomic STM image whose length along the *X*-axis (= measurement axis) was approximately 100 nm. Figure 3(b) shows the interferometer signal (LIA2) recorded for the center-line A-B parallel to the *X*-axis shown in Fig 3(a). In Fig. 3(b), the distance $\boldsymbol{L}$ between null points C and D corresponds to two fringes (≈ 80 nm). In Fig 3(a), two unit crystalline lattice vectors $\boldsymbol{a}_1$ and $\boldsymbol{a}_2$ are shown. In the case of the HOPG crystal, $|\boldsymbol{a}_1| = |\boldsymbol{a}_2| = d$ and the angle θ_{12} between $\boldsymbol{a}_1$ and $\boldsymbol{a}_2$ is 60°. Therefore, the number N of lattice spacings between null points C and D can be determined using vector calculation. The lattice spacing d, therefore, can be expressed as,

$$d = \frac{|\mathbf{CD}|}{N} = \frac{L}{\sqrt{m_1^2 + m_2^2 + 2m_1 m_2 \cos 60°}}, \quad (1)$$

where m_1 and m_2 are constants in ***CD*** vector. The refractive index of air was determined from temperature, air pressure, humidity and the concentration of CO_2[12] using the modified Edlen method[13]. Table I summarized the measurements for the lattice spacing on the HOPG crystalline surface. Measurements were repeated four times within 2 hours. The mean value of the lattice spacing was very close to that in another reference[14]. The measurement uncertainty of d is come from the measurement uncertainties of L and N. From the uncertainty analysis, the expanded uncertainty (k = 2) for the measurement was 7 pm. Major contributors to measurement uncertainties from L include the Abbe offset error, deadpath error and reading error of LIA2 signal. Careful alignment when setting the sample and interferometer optics can reduce the Abbe offset and deadpath errors. The S/N ratio of the LIA2 signal was relatively low because we could not achieve better energy efficiency of the light in front of the fiber input due to a reflectance light effect. However, we will improve the S/N ratio 20-fold from the current one via accurate adjustment of the fiber and optical isolator. For N, although the thermal drift was relatively large in the measurement, the degree of uncertainty from it was not significant, because the fast scanning axis (X-axis) was selected as the measurement axis.

IV. CONCLUSION

In order to realize a length measurement method using a regular crystalline lattice as a reference scale, an instrument for direct measurement of the lattice spacing on regular crystalline surfaces using a STM and a phase modulation homodyne interferometer was developed. To demonstrate the performance of the proposed instrument, the lattice spacing on HOPG surface was measured, and the measurement uncertainty was evaluated. The experimental results show that the proposed method has high capability for lattice spacing measurement with high accuracy.

ACKNOWLEDGEMENTS

The partial financial support from the Scientific Research Fund of the Japanese Ministry of Education, Culture, Sports, Science and Technology is gratefully acknowledged. The partial financial support from Saneyoshi Scholarship Foundation and Mitutoyo Association for Science and Technology are also acknowledged.

REFERENCES

[1] C.M. Wu, and R.D. Deslattes, Appl. Opt. **37**, 28(1998), pp. 6696.
[2] F. Petru, and O. Cip, Prec. Eng., **23**, 1999, pp. 39.
[3] G. Basile, A. Bergamin, G. Cavagnero, and G. Mana, Metrologia, **28**, 1991/92, pp. 455.
[4] P. Becker, J. Stumpel, Metrologia, **27**, 1990, pp. 127
[5] G. Basile, P. Becker *et al.*, Proc. R. Soc. Lond. A, **456**, 2000, pp. 701
[6] G. Binnig, H. Rohrer, Ch. Gerber, and E. Weibel, Appl. Phys. Lett. **40**, 1982, pp. 178
[7] H. Kawakatsu, and T. Higuchi, J. Vac. Sci. Technol. A, **8**(1), Jan/Feb 1990, pp. 319.
[8] S. Gonda, H. Zhou, J. Fu, R.M. Silver, Proc. SPIE nanotechnology workshop, NIST, Oct, 2001.
[9] M. Aketagawa, K. Takada *et al.*, Meas. Sci. Technol. **9** (1998), pp. 1076.
[10] M. Aketagawa, P. Rerkkumsup *et al.*, Proc. of the 16th Annual Meeting, ASPE, Nov 2001, pp. 107.
[11] M. Aketagawa, K. Takada *et al.*, Rev. Sci. Instrument., **70**, 1(1999), pp. 133.
[12] J. Res. Natl. Inst. Stand. Technol. **104**, 225 (1999), pp. 225.
[13] K.P. Birch, and M.J. Downs, Metrologia, 1994, **31**, pp. 315.
[14] Sang-Il Park, and C.F. Quate, Appl. Phys. Lett. **48** (2), 1986, pp. 112.

MICROMACHINE TOOL: MEASUREMENT AND CONTROL

A. Caballero-Ruiz, L. Ruiz-Huerta, E. Kussul, T. Baidyk, G. Velasco
Laboratory of Mechatronics, CCADET, UNAM(Center of Applied Sciences and Technological Development, National Autonomous University of Mexico). Circuito Exterior s/n, Cd. Universitaria, Coyoacán, 04510, A.P. 70-186 México, D.F.
Tel. (+52) 5622-8602 to 07 ext 115 E-mail. albcaru@servidor.unam.mx

1. INTRODUCTION

Microfactories can help to reduce the consumption of resources (energy, materials and space); and can help to increase productivity. The major problems with CNC machines tools are related with adaptive control accuracy and precision.

The micromachine tools (MMT) must be sufficiently precise. This characteristic must be considered always in relation with the cost of MMT. We develop and produce the first generation of MMT. The equipments for producing components having overall sizes from some hundred microns to some millimeters must provide accuracy of some microns [1, 2].

Beside to development of MMT raises the need of generate the technology that allow us to learn its behavior for development systems to minimize error and increase the precision of these. At this moment, those needed technologies are too specific and expensive. In the past we worked in the characterization of micromachine tools by indirect method [3], the results obtained with this method permitted us to know the behavior of this MMT, but these results are not offer us sufficiently information about the specific geometrical errors to development correction methods.

In this work we propose low cost special algorithms to determine geometrical errors on each guide way of a the MMT by two balls; and the adaptive control to reduce these errors in the MMT is proposed.

2. STATE OF THE ARTS IN THE MMT DEVELOPMENT

Mechatronics Laboratory (CCADET, UNAM) had developed and tested some prototypes of first generation machine tools. The main idea was to make prototypes as simple as possible, and to use minimum of industrial components, for scaling down developed micro machine tool in future generations [3]. One of these prototypes is shown in the figure 1.

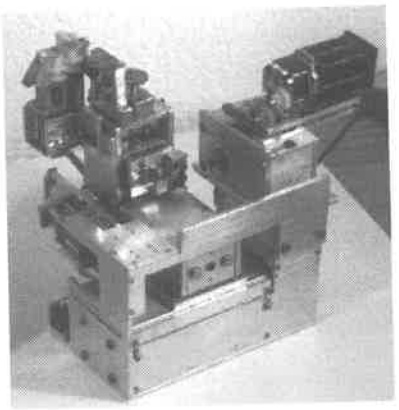

Figure 1. CNC prototype.

This prototype has 130×160×85mm, and is controlled by PC. The MMT has three translation axes (X, Y, and Z), and one rotational. The axis X and Z, have 20 mm displacement, and Y-axis has 35 mm. All of them have the same configuration. The resolution is 1.87μm per step of the motor.

2. CONVENTIONAL METHODS TO EVALUATE CNC´s.

There ere many methods to detect and correct errors in CNC´s, some of these are developed to apply single dimension tests, such as interferometers and graduated standard; and multi-dimensional tests, such as the Double Ball Bars and the Lattice Grid Plate [4]. The results obtained with these methods are employed to design electronic systems and software to compensate the errors.

All of these methods to evaluate conventional CNC´s are difficult to put in practice within micromachine world where the overall sizes of a micromachinetool is less than 20x20x20 cm.

3. METROLOGY PROCESS TO EVALUATE MMT´s

To determine the real characteristics of micromachine tool, we proposed a method based on to employ tow balls: one ball (B1) is fixed in a point within the workspace of the MMT, another ball (B2) is fixed on the tool support. In the figure 2, the balls are shown.

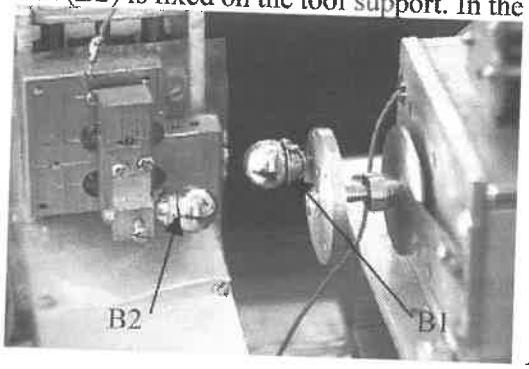

Figure 2. Placement of the balls in the MMT. (The balls have a diameter of 9.11 mm with deviations less than 0.5 μm.)

With the help of the ball B1 is possible to measure many positions of the ball B2, the measures are made by electric contact. The measurements are divided in three groups: each one, contains one axis constant. The first measurements group will have the "X" axis in a constant position and the ball B1 will move in the "Y","Z" axes to make the measures; the second group will have "Y" axis position constant; and the third will have "Z" axis position constant. By a computer program, the process of measurements is made automatically as follows (we only explain the procedure to the first group of measures, all the procedure are similar, only changes the movement axes) :

1) At first the MMT goes to its home position.
2) The ball B2 moves to a position under B1, then B2 moves forward along "Y" axis until makes electric contact with de ball B1. The measure is recorded in a text file.
3) B2 moves back along "Y" axis a distance dY (with this distance we assure to eliminate the error generates by the backlash). It moves up dZ.
4) B2 moves forward again along "Y" axis until makes electric contact with de ball B1 and the programs records the measure.
5) This steps are repeated along the "Z" axis (see figure 3).

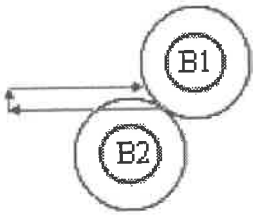

Figure 3. Measurement of B2.

The files with the measurements are read by algorithm based in genetic algorithms, this algorithm finds the center of the associated sphere with the experimental measurements by an error equation,

$$err = \sum_{i=1}^{k} (r_i - r_m)^2. \qquad (1)$$

where *err* is the quadratic error; r_i is the distance between an arbitrary selected point X_0, Y_0,Z_0 (that we consider as a center of the approximation sphere) and the experimental points X_i, Y_i Z_i (see equation 2); and r_m is the real distance between ball centers.

$$r_i = \sqrt{(X_i - X_0)^2 + (Y_i - Y_0)^2 + (Z_i - Z_0)^2}\ ; \qquad (2)$$

The algorithm searches the values X_0, Y_0 and Z_0 where the equation of error began to be minimal, then this point is the theorical center of B1. In the figure 4 and 5 some results are presented.

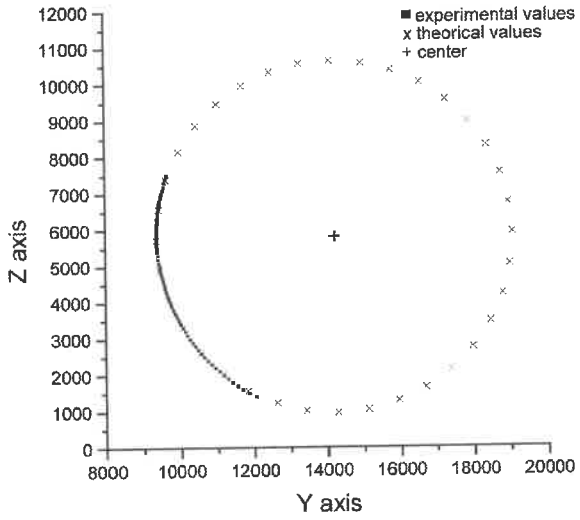

Figure 4. Coordinates of the experimental points[1]

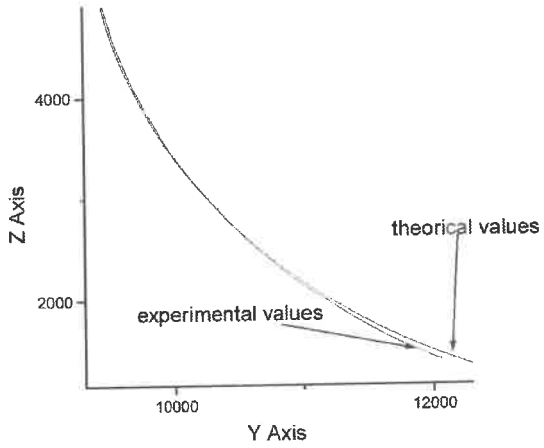

Figure 5. Measurement errors

In the figure 5 is possible to see the difference between the experimental values and the theorical values. This difference represents the error in the MMT. The sources of errors in the machine tools can be associated with the mechanical parts and its characteristics[5]. In the case of MMT,

[1] All the measures are in steps of motor, each step is equal to 1.88μm

the errors sources are associated with: the non squareness between all the axes; the non straightness of each axis; the rotation of axis; the not linear behavior of leadscrew, etc. Many error sources can be represented by mathematical functions. A general decomposition of the errors in the MMT is shown bellow,

$$\delta_x = f_1(x) + y\cos\alpha_{xy} + z\cos\alpha_{xz} \quad (3)$$

$$\delta_y = f_2(y) + x\cos\alpha_{yx} + z\cos\alpha_{yz} \quad (4)$$

$$\delta_z = f_3(z) + x\cos\alpha_{zx} + y\cos\alpha_{zy} \quad (5)$$

$$\alpha_{xy} = \varphi_1(x,y) \quad (6)$$

$$\alpha_{xz} = \varphi_2(x,z) \quad (7)$$

$$\alpha_{yz} = \varphi_2(y,z) \quad (8)$$

Where δ represents the error associate to each axis, f is the function error of leadscrew, and φ is the function error of straightness, rotation and squareness.

An other algorithm introduces the error equations into the experimental measures to compensate the error found in the previous algorithm.. The errors equations employed in this algorithm are presented below,

$$\delta_x = C_1 + C_2x + C_3x^2 + y\cos(\frac{\pi}{2} + \alpha_1) + z\cos(\frac{\pi}{2} + \alpha_2) \quad (9)$$

$$\delta_y = C_4 + C_5y + C_6y^2 + x\cos(\frac{\pi}{2} + \alpha_1) + z\cos(\frac{\pi}{2} + \alpha_3) \quad (10)$$

$$\delta_z = C_7 + C_8z + C_9z^2 + x\cos(\frac{\pi}{2} + \alpha_2) + y\cos(\frac{\pi}{2} + \alpha_3) \quad (11)$$

Where the constants C_1, C_4, C_7 represent some errors produced by parts of MMT such as gear boxes, home position, randomly errors, etc.; the constants C_2, C_5, C_8, C_3, C_6, C_9 represent some errors related with the leadscrews and the non straightness of each axis; finally, the constants α_1, α_2, α_3 represent the deviation angle between all axes.

At first it's proposed random values for the constants of the error equations. Then, the experimental values are compensated with the values δ_x, δ_y and δ_z, then the algorithm creates a new file with the experimental values compensated.

The compensated values are introduced in an algorithm to find the new center employing the equation (1). This algorithm changes the constants according the genetic principles, searches and finds the optimum values to the constants of error equations.

The figures presented bellow show the results obtained whit the compensation algorithm.

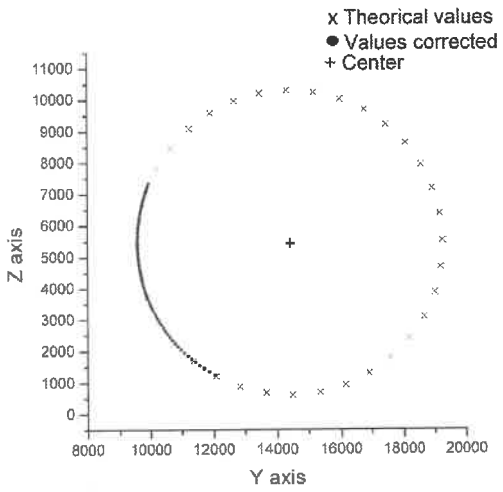

Figure 6. Coordinates of the compensated points

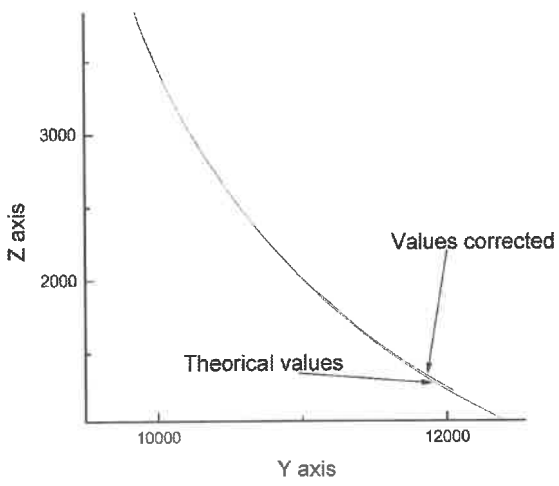

Figure 7. Measurement of compensated errors

3.1 Results

The algorithm have demonstrated to be stable, in some experiments developed the algorithm can reduce the errors six times the initial errors. In the figures presented up, at the beginning the software found the center with an error maximum of 158 steps (282 μm) after the compensation, the error maximum decrease till 32 steps (57 μm). The values of the constants are shown bellow,

C_1=14.76, C_4=0, C_7=10.26, C_2=0.0013, C_5=0.00066, C_8=0.0012, C_3= -1.20x10^{-7}, C_6= -8.29x10^{-8}, C_9= -1.8x10^{-7}, α_1=0.013, α_2=0.006, α_3=0.051

4. CONTROL

The information generated with the help of the previously algorithms will help us to reconstruct the work space of the MMT and find the associated errors to each point of this space. It is difficult to sample all the work space of the MMT. To cover all the work space we propose to develop a software based in neural networks to generate an adaptive control. At this time we are working on this algorithm.

CONCLUSIONS

An method to find and compensate errors in a MMT was presented, the results obtained at this moment are satisfactory, but it is necessary to make more researches about the error equations to reduce the error even more and increase de accuracy in the MMT's. This method represents an alternative low cost method to assess not only MMT's. The obtained results will help us to increase the actual accuracy of MMT (±18 μm).

ACKNOWLEDGEMENTS

This work was supported by CONACyT 339944-U.

REFERENCES

[1] Ishikawa Yu., Kitahara T. Present and Future of Micromechatronics. 1997 International Symposium on Micromechatronics and Human Science, pp.13-20.

[2] Kussul E., Ruiz L., Caballero A., Kasatkina l., Baydyk T. CNC Machine Tools for Low Cost Micro Devices Manufacturing. The First International Conference on Mechatronics and Robotics; St.-Petesburg, Russia; 2000, Vol.1, pp.98-103

[3] A. Caballero-Ruiz, FIRST GENERATION MICROMACHINE TOOL CHARACTERIZATION, ASPE´s (American Society for Precision Engineering), 16th Annual Meeting , Criytal City, Virginia, Washintong DC, USA.

[4]Machine Tool inspection by Rick Glos, Heidenhan corporation (www.heidehain.com/INSPECTN.HTM)

[5] Kussul E., Rachkovski D., Baidyk T. and Talayev S.. Micromechanical Engineering: a Basis for the Low Cost Manufacturing of Mechanical Microdevices Using Microequipment, J. Micromech. Microeng., 1996, 6, pp. 410-425.

[6] G.H.J. Florussen, F.L.M. Delbressine, M.J.G. van de Molengraft, P.H.J. Schellekens. Assessing geometrical errors of multi-axis machine by three-dimensional length measurement. Journal of measurement, Elsevier edited, 2001

Geometrically Compensated Measurement with a Laser Digitizer Equipped CMM

John O. Harris and Allan D. Spence*
McMaster University, Hamilton, Ontario, Canada

1. Introduction: Industrial designers frequently sculpt conceptual freeform shapes in wood or clay. The model is then digitized to create a Computer-Aided Design (CAD) model. During manufacturing, there is an industrial need to measure parts such as automotive sheet metal body panels for dimensional conformance. Because of their high data collection rates, laser digitizers are commonly chosen as the digitizing device. The digitizer is attached to a Coordinate Measuring Machine (CMM) in place of the conventional touch trigger probe, and reoriented as required to cover the large and complex part surface. High accuracy is required so that the geometric data collected from each orientation can be merged into a common part coordinate system.

Currently, the accuracy of such systems is limited by the lack of an integrated geometric error compensation system. That is, there is no correction of the laser digitizer point coordinates to compensate for the varying geometric errors encountered at different locations within the CMM volume. This paper reports progress towards achieving such as integrated system.

2. Laser Digitizer Description: The laser digitizer used in this paper is a Hymarc Hyscan 45C [1]. A real-time microprocessor system obtains points from the sensor in the local digitizer $[U \quad V \quad W]^T$ coordinate system (Figure 1). Simultaneously, uncompensated CMM $[D \quad E \quad F]^T$ axis coordinates are obtained using opto-isolators connected to the scale electronics. These six coordinates are recorded to a data file for later offline geometric error compensation.

3. Position Error: A conventional CMM has three carriages mounted in orthogonal directions. For this research, a moving bridge style Z on Y on X configuration was used. To obtain the volumetric error parameters of a CMM, the linear, straightness, and angular errors of a CMM are typically obtained using a laser interferometer, and squareness errors are obtained using a double ball bar. The error map and correction scheme followed herein is based on Kunzman [2]. At a given scale position relative to the home position $[D \quad E \quad F]^T$, the geometric error equations are:

$$\begin{aligned} e_X &= \delta_X(D)+\delta_X(E)+\delta_X(F)-E\cdot\varepsilon_Z(D)+F\cdot\varepsilon_Y(D)+F\cdot\varepsilon_Y(E)-E\cdot S_{XY}-F\cdot S_{XZ} \\ e_Y &= \delta_Y(D)+\delta_Y(E)+\delta_Y(F)-F\cdot\varepsilon_X(E)-F\cdot\varepsilon_X(D)-F\cdot S_{YZ} \\ e_Z &= \delta_Z(D)+\delta_Z(E)+\delta_Z(F)+E\cdot\varepsilon_X(D) \end{aligned} \tag{1}$$

where the error factor terms are obtained from Table 1.

4. Orientation Error: Unlike single point acquisition touch trigger probes, the laser digitizer collects line data in a local scan plane. As the sensor is translated, the scan plane orientation varies due to the CMM volumetric errors. Including this effect when correcting the uncompensated digitizer data is the primary goal of the reported research. The initial step, for every intended laser digitizer orientation, is to calibrate with respect to a reference optical sphere. This Hymarc defined procedure establishes the transformation

* Corresponding author: adspence@mcmaster.ca, Department of Mechanical Engineering, McMaster University, Hamilton, Ontario, Canada L8S 4L7

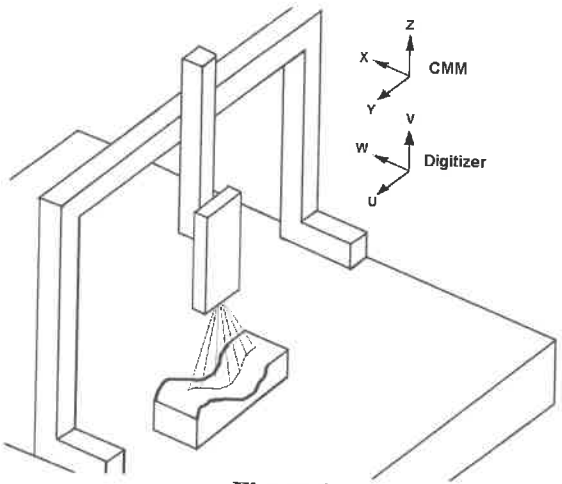

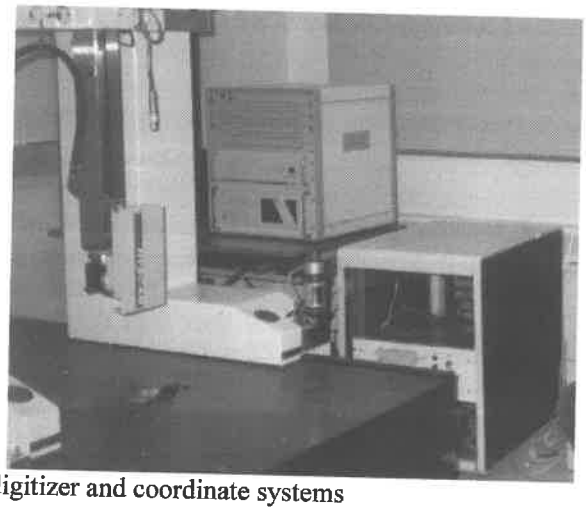

Figure 1: Hyscan 45C laser digitizer and coordinate systems

Table 1: CMM error table

X axis	Position Error (μm)			Orientation Error (arc-seconds)			Squareness Errors (arc-seconds)
D scale (mm)	$\delta_X(D)$	$\delta_Y(D)$	$\delta_Z(D)$	$\varepsilon_X(D)$	$\varepsilon_Y(D)$	$\varepsilon_Z(D)$	
0	0	0	0	0	-0.6	-0.1	S_{XY} =-169.397
100	3	0	0	0	-0.8	0.5	
200	2	0	0	0	-0.95	0.25	S_{YZ} =33.979
300	5	0	0	0	-0.5	0.1	
400	8	0	0	0	0.15	-0.1	S_{ZX} =-25.984
500	11	2	0	0	0.65	0.55	
600	11	-1	0	0	0.6	0.95	
700	11	2	0	0	0.95	1.55	
800	12	0	0	0	1.45	1.75	
900	12	0	0	0	1.4	2	
Y axis	Position Error (μm)			Rotational Error (arc-seconds)			
E scale (mm)	$\delta_X(E)$	$\delta_Y(E)$	$\delta_Z(E)$	$\varepsilon_X(E)$	$\varepsilon_Y(E)$	$\varepsilon_Z(E)$	
0	0	0	0	-0.35	0	-0.2	
100	0	11	0	-1.15	0	0.1	
200	-7	16	1	-0.7	0	0.05	
300	-11	25	1	-1.05	0	0.1	
400	-7	33	-1	-1.45	0	0.4	
500	2	38	-1	-1.6	0	0.95	
Z axis	Position Error (μm)			Rotational Error (arc-seconds)			
F scale (mm)	$\delta_X(F)$	$\delta_Y(F)$	$\delta_Z(F)$	$\varepsilon_X(F)$	$\varepsilon_Y(F)$	$\varepsilon_Z(F)$	
-500	0	0	0	-1.5	-0.15	0	
-400	0	0	0	-2.4	0.55	0	
-300	0	0	-4	-1.05	0.4	0	
-200	0	0	-2	-3.3	-0.45	0	
-100	0	-2	-2	-3.7	-1.6	0	
0	0	0	-5	-3.8	-3.2	0	

Note: Data was collected at 25 mm increments. Only the 100 mm increments are shown.

$$ {}^{R}\begin{bmatrix} X \\ Y \\ Z \\ 1 \end{bmatrix} = \begin{bmatrix} & [R] & & \begin{matrix} D-D_0 \\ E-E_0 \\ F-F_0 \end{matrix} \\ 0 & 0 & 0 & 1 \end{bmatrix} \cdot \begin{bmatrix} U \\ V \\ W \\ 1 \end{bmatrix} \tag{2} $$

that relates $[U \quad V \quad W]^T$ to the uncompensated position ${}^{R}[X \quad Y \quad Z]^T$. The rotation matrix $[R]$ corrects for the misalignment between $[U \quad V \quad W]^T$ and the CMM axis directions at the location of the reference optical sphere, and $[D_0 \quad E_0 \quad F_0]^T$ is the scale reading when $[U \quad V \quad W]^T = [0]$. This information is automatically stored within the Hymarc data point file.

By using three separate digitizer orientations, the distance between the $[U \quad V \quad W]^T$ origin and the sensor (CMM geometric error compensation map) origin was determined to be $[U_1 \quad V_1 \quad W_1]^T = [2.196 \quad 265.320 \quad 129.826]^T$ mm. Using this information, the transformation

$$ {}^{P}\begin{bmatrix} X \\ Y \\ Z \\ 1 \end{bmatrix} = \begin{bmatrix} & [R] & & [R] \cdot \begin{bmatrix} -U_1 \\ -V_1 \\ -W_1 \end{bmatrix} \\ 0 & 0 & 0 & 1 \end{bmatrix} \cdot \begin{bmatrix} U \\ V \\ W \\ 1 \end{bmatrix} \tag{3} $$

establishes the digitized point position relative to the pose origin. Application of the transformation

$$ {}^{H}\begin{bmatrix} X \\ Y \\ Z \\ 1 \end{bmatrix} = \begin{bmatrix} [X_P] & [Y_P] & [Z_P] & \begin{matrix} D+e_X \\ E+e_Y \\ F+e_Z \end{matrix} \\ 0 & 0 & 0 & 1 \end{bmatrix} \cdot {}^{P}\begin{bmatrix} X \\ Y \\ Z \\ 1 \end{bmatrix} \tag{4} $$

where

$$ [Z_P] = \begin{bmatrix} \dfrac{\tan\varepsilon_Y}{\sqrt{1+\tan^2\varepsilon_X+\tan^2\varepsilon_Y}} \\ \dfrac{-\tan\varepsilon_X}{\sqrt{1+\tan^2\varepsilon_X+\tan^2\varepsilon_Y}} \\ \dfrac{1}{\sqrt{1+\tan^2\varepsilon_X+\tan^2\varepsilon_Y}} \end{bmatrix}; [X_P] = \begin{bmatrix} \dfrac{1}{\sqrt{1+\tan^2\varepsilon_Z+(\tan\varepsilon_X\cdot\tan\varepsilon_Z+\tan\varepsilon_Y)^2}} \\ \dfrac{-\tan\varepsilon_Z}{\sqrt{1+\tan^2\varepsilon_Z+(\tan\varepsilon_X\cdot\tan\varepsilon_Z+\tan\varepsilon_Y)^2}} \\ \dfrac{-(\tan\varepsilon_X\cdot\tan\varepsilon_Z+\tan\varepsilon_Y)}{\sqrt{1+\tan^2\varepsilon_Z+(\tan\varepsilon_X\cdot\tan\varepsilon_Z+\tan\varepsilon_Y)^2}} \end{bmatrix}; [Y_P] = [Z_P] \times [X_P] $$

and $\varepsilon_j = \sum_{i=D,E,F} \varepsilon_j(i); j = X,Y,Z$, provides the final, fully compensated digitized point position.

5. Measurements: To verify the correctness of the algorithms developed in Section 4, measurements were made with and without compensation on an ASME B89.4 [3] style optical ballbar. The spheres were 76.25 mm in diameter and the bar was approximately 404 mm between the sphere centers.

The CMM errors were previously measured and stored (Table 1). For each intended orientation, the laser digitizer was calibrated to obtain the equation (2) parameters. The ballbar was then measured at the 20 specified ASME B89.4 [3, Figure 26] positions. For each point, the $[U \quad V \quad W]^T$ and $[D \quad E \quad F]^T$ coordinates were collected. Approximately 17,000 sphere points were recorded at each end of the ballbar. The matrix procedure described in Section 4 was used to compensate each point, and the sphere centers were located using orthogonal least squares. Results are shown in Figure 2.

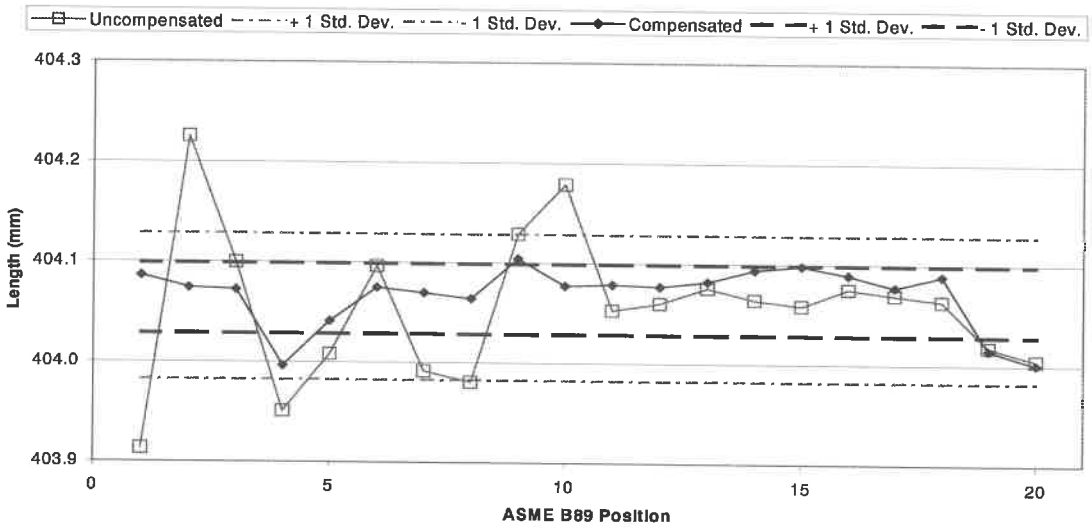

Figure 2: ASME B89 Figure 26 Ballbar Accuracy Test

6. Discussion: The most significant CMM flaw is the 160 arc second *XY* squareness error. This shows up particularly at positions 1 and 2. The compensation procedure handles this well. Positions 4, 19 and 20 give the smallest apparent corrected length of the ballbar.

The uncompensated measurements had a mean of 404.056 mm and a standard deviation of 73 μm. The compensated measurements had a mean of 404.068 mm and a standard deviation of 31 μm. Based on the published laser digitizer accuracy, and the measured CMM error, this 60% improvement in the data standard deviation is consistent with expectations.

7. Conclusions: To implement the integrated error compensation, the scan plane coordinates and the CMM axis scale positions were recorded simultaneously in real time and compensated for pose position and attitude. There is a 60% improvement in the accuracy of the data.

As well as error compensation algorithms, good operator technique in careful camera alignment calibration and scanning path planning are important to obtaining improved accuracy using a laser digitizer on a CMM.

This paper has shown an error compensation technique for laser digitizer measurements that will benefit CAD applications and quality assurance.

8. Acknowledgements: The authors are grateful to NCE-Auto 21 for financial support, CFI/OIT for equipment, and to Omni-Tech CMM Services for their support in measuring the CMM errors.

9. References:

[1] "Hyscan 45C 3-D Laser Digitizer", Hymarc 3D Vision Systems, Nepean, ON.

[2] Kunzman, H.; Ni, J.; Waldele, F. "Accuracy Enhancement", Coordinate Measuring Machines and Systems, Bosch, John A.(ed.), Marcel Dekker, Inc., New York., 1995.

[3] ASME B89.4.1 "Methods for Performance Evaluation of Coordinate Measuring Machines", An American National Standard., 1997.

2-D Self-Calibration for Scale Based Metrology in Nanolithography

Xiaoming Lu & Hy. D Tran[1]
Department of Mechanical Engineering
University of New Mexico
Albuquerque, NM 87131

Abstract

Two-dimensional precision stages for semiconductor lithography require sub-nm-level accuracy. Current ultraprecision stage metrology based on heterodyne laser interferometers with a 632.8-nm HeNe laser and interpolation to λ/2048 provide resolution of 0.3 nm. Unfortunately, the refractive index of air varies with CO_2 and water vapor content, as well as with air turbulence. Without expensive atmospheric compensation, the actual accuracy may only be sub-μm for operation in air.

In our approach two scale based metrology system (OPTRA NanoGrid) are used. The NanoGrid greatly reduces possible effects from air turbulence and Abbe offsets from using separate X and Y scales. However, the metrology is based on an physical artifact, and the accuracy of the metrology is limited to the accuracy of the grid artifact itself: about 1μm. Physical scales may provide greater precision, but not always greater accuracy. Real-time self-calibration is implemented to improve the accuracy of stage to the level limited by repeatability of stage.

Fourier transform is used to decouple the distortion of artifact metrology and stage metrology at sampling points from 3 measurement view. Based on feedback principle high accuracy translation and rotation is implemented to minimize misalignment error. Square reversal is used to calculate rotation error δγ. Iterative algorithm is developed to isolate the rotation error δγ in self-calibration.

Keywords: Self-Calibration ,Nanolithography, two-dimensional stage, scale based metrology

1.Introduction

The key issues in self-calibration is how to solve measurement equations. In other words, isolate the scale and stage distortion from measurement equations when there are misalignment errors during translation and rotation. In a previous approach, Ye, Pease et al. (1997) developed a discrete Fourier transform-based algorithm by approximating A(x,y) and S(x,y) with Fourier series, which is numerically robust to measurement noise. The alignment error is isolated in the statistical meaning by using least square method under several assumption, which is effective when the measurement noise has a normal distribution and required space sample interval is big enough. Second, translation and rotation error will affect the sample position. This will be problematic when space sample interval is small e.g sub-μm. Third, because the x and y translation and rotation values of the stage point set can not be given by the algorithm or known before the self-calibration, it is difficult to find the origin and the axis orientation which meet the assumptions. Thus the stage error map obtained from this method has an unknown coordinate system, which might not be directly related to the machine coordinate system.

[1] luxm@unm.edu; tran@me.unm.edu This work is supported by DOD/ARO DAAD-19-99-0196

2.Testbed physical realization of an X-Y stage for Nanolithography

The testbed is an air-bearing ,capstan drive interferometric lithography stepper, with HP laser interferometers for feedback. This stage is configured as a stacked-slide X-Y stage. The moving stage is supported by air bearings on the granite surface plate. Two scale based metrology systems are mounted on the same plane of moving stage to implement real-time self-calibration. The configuration in the plane is shown in Figure 1.

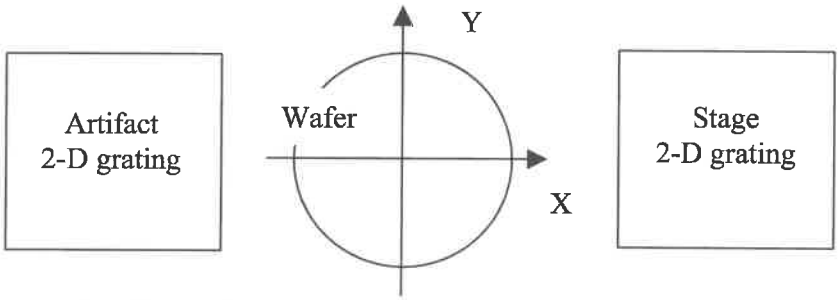

Figure 1 Configuration of 2-D real-time self-calibration

Scale based metrology system is a 2-D ultra-high resolution diffraction interferometer. It can measure X and Y plane motion simultaneously with 0.3 nm resolution and to detect small angle motion around Z axis.

One of the main error source in nanolithography come from the disturbance of guideway. The translation error of guideway in X and Y direction will be canceled by feedback of accurate stage metrology. The disturbance from the rotation error of guideway around Z axis will be minimized based on Abbe principle in X direction. For 1 nm accuracy, compare with traditional configuration, the tolerance of rotation error will increase from 1 μrad to 80 μrad. In Y direction the rotation error of guideway around Z axis will be measured by two scale based metrology system and compensated with software. So the accuracy of nanolithography mainly depends on the accuracy of metrology.

3. Mathematical model and Self-Calibration Algorithm

3.1 Decouple 2-D grating distortion when there is no alignment error

Two scale based metrology system are used to generate measurement view. One is stage metrology .The other is artifact metrology. The distortion s(x,y) of stage grating and distortion a(x,y) of artifact grating at sampling points (x_m,y_n) can be expressed as

$$\begin{aligned} s(x_m,y_n) &= s_x(x_m,y_n)e_x + s_y(x_m,y_n)e_y \\ a(x_m,y_n) &= a_x(x_m,y_n)e_x + a_y(x_m,y_n)e_y \end{aligned} \qquad (1)$$

We need 3 measurement views to solve $s(x_m,y_n)$ and $a(x_m,y_n)$. In View 0 or home view, two metrology system is aligned with the air bearing of the stage by minimizing the angle between the moving direction of air bearing and X-axis of the metrology. $s(x_m,y_n)$ and $a(x_m,y_n)$ is compared at sampling points, so

$$v_x 0(x_m,y_n) = s_x(x_m,y_n) - a_x(x_m,y_n) \qquad (1a)$$

$$v_y 0(x_m,y_n) = s_y(x_m,y_n) - a_y(x_m,y_n) \qquad (1b)$$

In View 1, the sensor head is translated from View 0 by one sample site interval relative to the artifact grating, yield the measurement equations

$$x_x 1(x_m, y_n) = s_x(x_m, y_n) - a_x(x_{m+1}, y_n) \quad (2a)$$

$$v_y 1(x_m, y_n) = s_y(x_m, y_n) - a_y(x_{m+1}, y_n) \quad (2b)$$

Based on translation property of 2-D discrete Fourier transform to solve $A_x(u,v)$ from equation (1) and (2)

$$A_x(u,v) = \frac{V_x(u,v)}{1 - e^{j2\pi\frac{u}{M}}} \quad (3)$$

where

$$A_x(u,v) = \frac{1}{MN} \sum_{x_m=-\frac{N-1}{2}}^{\frac{N-1}{2}} \sum_{y_n=-\frac{M-1}{2}}^{\frac{M-1}{2}} a_x(x_m, y_n) e^{-j(\frac{2\pi}{M}ux_m + \frac{2\pi}{N}vy_n)}$$

$$V_x(u,v) = \frac{1}{MN} \sum_{x_m=-\frac{N-1}{2}}^{\frac{N-1}{2}} \sum_{y_n=-\frac{M-1}{2}}^{\frac{M-1}{2}} (v_x 0(x_m, y_n) - v_x 1(x_m, y_n)) e^{-j(\frac{2\pi}{M}ux_m + \frac{2\pi}{N}vy_n)} \quad (4)$$

Equation (3) only gives solution at $u \neq 0$. Based on the rotation property of 2-D Fourier transform $A_x(0,v)$ will be solved from equation (5) in View2 where artifact grating is counterclockwise rotated 90^0 relative to View 0.

$$V_x 2(x_m, y_n) = s_x(x_m, y_n) - ROT90(a_y(x_m, y_n)) \quad (5a)$$

$$V_y 2(x_m, y_n) = s_y(x_m, y_n) - ROT90(a_x(x_m, y_n)) \quad (5b)$$

where ROT90 denotes "90^0 rotation."

3.2 Minimize the misalignment error based on feedback and iterative algorithm

The sensor head is mounted on 6 degree kinematics stage. The direction and location of sensor head relative to the 2-D grating are determined by the 6 balls on the kinematics stage. A picomotor is used to drive the relative movement of sensor head relative to the 2-D grating with 30 nm resolution . The sensor head is aligned with the 2-D grating stage by minimizing the angle between the moving direction of 6 degree kinematics stage and X-axis of the metrology. The relative translation between sensor head and 2-D grating will be measured by 2-D metrology system itself. The feedback is used to guarantee required one sample site interval translation accuracy determined by sampling requirement.

A 2-D grating is mounted on the bearing and rotation can be driven by a picomotor with 30″ resolution. Square reversal is used to measure the 90^0 rotation error $\Delta\gamma$ which will be reduced by feedback to the level limited by the picomotor resolution.

The accuracy to implement translation and rotation depends on the accuracy of 2-D grating. The translation error can be minimized by implement 1-D self-calibration in X axis first.

The 2-D self-calibration error due to 90^0 rotation error $\Delta\gamma$ can be compensated if $\Delta\gamma$ is accurately measured when $\Delta\gamma$ is tiny. From experiment and computer simulation the measurement accuracy of $\Delta\gamma$ is insensitive to the accuracy of metrology which means error transfer coefficient is less than 1. This will guarantee that an iterative algorithm will be convergent. So an iterative algorithm is developed to minimize disturbance from measurement accuracy of rotation error $\delta\gamma$.

4. Experiment results and summary

Real-time calibration was implemented on the Nanolithography testbed. Dynamic data sampling methodology was developed to minimizes effects of quasi-static disturbance from measurement environment change, such as temperature. The repeatability of scale based metrology is about 8.5 nm (see Fig 2). The initial calibration result is shown in Fig 3. The distortion of 2-D Grating is about 1μm . Real time self-calibration will increase the accuracy of scale based metrology from 1 μm to the level limited by the measurement noise.

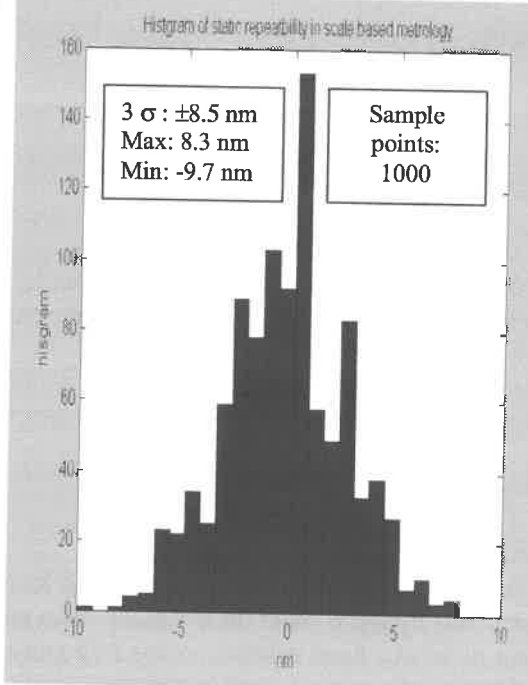

Figure 2 Short term repeatability of scale based metrology

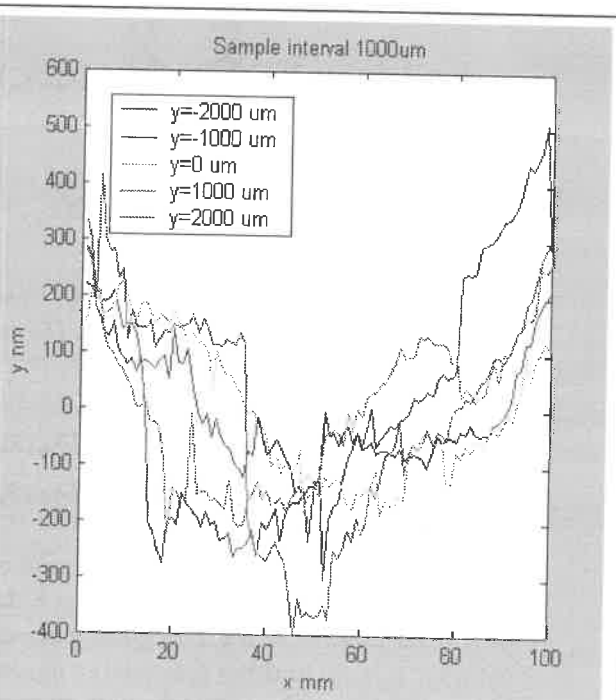

Figure 3 Distortion of 2-D grating

References

Evans,C,J.,Hocken,R,J., and Estler,W.T.,"Self-calibration:reversal, redundancy,error separation, and 'absolute testing,'" CIRP annals,Vol45(2),1996.

Ye,J.,Takac,M.,Berglund,C.N.,Owen,G.,and Pease,R.F.,"An exact algorithm for self-calibration of two-dimensional precision metrology stages," Prec Eng vol.20(1),p.163-32,1997.

KINEMATIC SPINDLES FOR PORTABLE ROUNDNESS INSTRUMENTS

Eric Wolsing, King-Fu Hii, R Ryan Vallance
Precision Systems Laboratory, University of Kentucky, Lexington, KY

Abstract

This paper describes the design and analysis of a kinematic spindle for a rotating sensitive direction portable roundness instrument. The instrument will employ contact profilometry and reversal techniques with a kinematically coupled spindle for an application such as quality assurance in the production- of engine bores. Reversal requires a spindle configuration exhibiting low asynchronous errors. The spindle uses exact constraint principles (kinematic) by establishing one axial contact point and four radial contact points. Explanation of the spindle drive arrangement is provided including (1) experiments for measuring magnetic preload, and (2) a demonstration of the relationship between z-axis magnetic preloading and radial preloading on the spindle's four radial contact points.

Keywords: Kinematic, spindle, exact constraint, roundness, metrology

Introduction

Roundness is a critical geometric tolerance in precision machines and products [1]. Any precision product utilizing cylindrical bores is likely concerned with form errors in the manufactured cylindrical surface. For instance, piston bores in engine blocks require tight roundness and cylindricity tolerances to generate maximum power and operate efficiently. A precise, robust, but inexpensive method for measuring the roundness of engine bores on the production line could therefore benefit engine manufacturers.

Instruments used for measuring roundness require spindles with low asynchronous errors in the axis of rotation. If synchronous errors are present in the axis of rotation or artifact, they may be separated from the measured profile using reversal techniques as described by Donaldson [2] and by Estler and Hocken [3]. Therefore, a kinematic spindle, which exhibits low asynchronous error but higher synchronous errors, can be used in conjunction with a reversal technique.

This paper presents some aspects of designing a portable prototype instrument suitable for measuring roundness profiles. The instrument employs a kinematically constrained spindle shaft as illustrated in Fig 1. The spindle is exactly constrained [4] using an arrangement of four radial constraints and one axial constraint. Curvature matching at the contact points is achieved with hemispheres contacting the surface of a bored hole. Preload in the axial direction is by permanent magnets (not shown in Fig 1) and by a flexure in the radial direction.

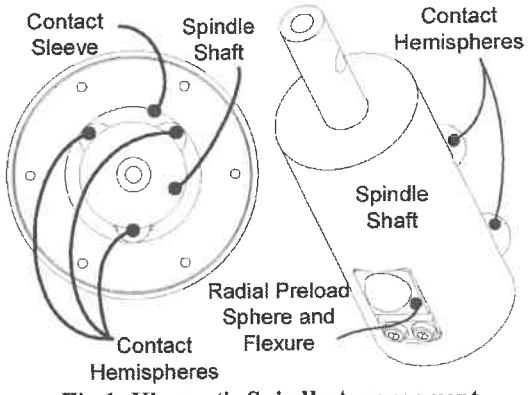

Fig 1: Kinematic Spindle Arrangement

Hii [5] investigated a kinematically constrained spindle shafts (without curvature matching) and demonstrated that they are capable of low asynchronous errors (~ 25-50 nm). The synchronous errors are repeatable and directly related to the roundness profile of the spindle shaft and bore. Hii et al. [6] rotated the kinematically constrained shaft using a lightly tensioned belt wrapped around the spindle's shaft and driven with a pulley. This approach introduced errors associated with compliancy at the radial contact points and fluctuations in the belt tension.

In this paper, we describe an alternative embodiment using curvature matching and analyze a method for rotating the shaft by applying nearly pure torque though the axial contact point. This is achieved by friction-based surface tractions within the contact area at the axial constraint. Since permanent magnets preload the axial contact point, the normal force producing friction depends upon the magnitude of the magnetic force minus the weight of the spindle shaft. Therefore, experiments quantifying

the magnetic preload as a function of the distance between an array of magnets and a steel plate are presented.

To prevent slipping at the axial contact point while rotating the shaft, the peak transmissible torque must exceed the torque due to friction at the radial contact points. Possible designs are analyzed by integrating data from the magnetic preload measurements with an analytical model. This determines a suitable preload force in the radial direction that does not produce exceedingly high friction and lead to slipping at the axial constraint.

Description of the Prototype Instrument

A cross section of the prototype instrument is illustrated in Fig 2. The drive arrangement is clearly depicted in the upper portion of Fig 2 at the Z-axis contact. A knurled wheel is turned by hand, and torque is transmitted via surface tractions between the Z-axis contact hemisphere and the steel plate. The kinematically constrained shaft rotates within the spindle bore. The radial contact spheres preferably slide on a low-friction contact sleeve. A contact probe (not shown) would be affixed to the bottom of the shaft to reside within the test bore.

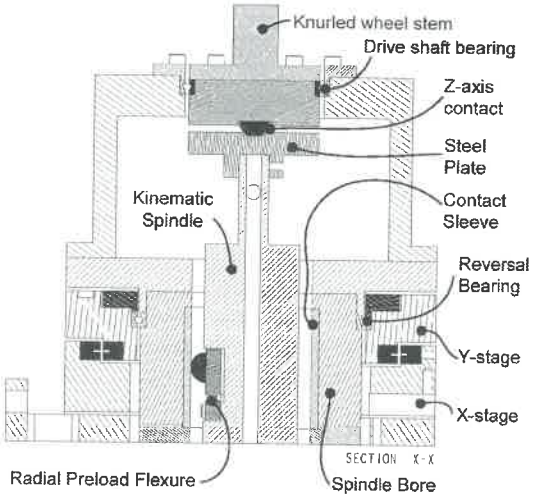

Fig 2: Cross Section of Spindle and Drive System

Two linear translation stages, X-stage and Y-stage, provide a method to align the instrument's axis of rotation with the axis of the test bore. The stages travel a maximum of 6.35 mm on crossed roller bearings. Micrometers allow precise positioning of both stages. A gothic-arch rolling element bearing accommodates reversal by enabling a 180-degree angular rotation of the spindle's support structure (contact sleeve, spindle bore, and Z-axis contact).

Reversal and Error Separation

Conventional, fixed sensitive direction, roundness testers require reversing sensor orientation [7]. A rotating sensitive direction roundness tester, however, relies upon reversing the orientation of the tester (but not the sensor) in relation to the bore.

Reversal retains applicability for rotating sensitive direction roundness testing if it can be shown that reversing one set-up orientation eliminates one set of errors via addition or subtraction of gauge expressions. Fig 3 illustrates the reversal method for the prototype instrument. It is necessary that the probe's starting position be the same for both initial and reversal orientations.

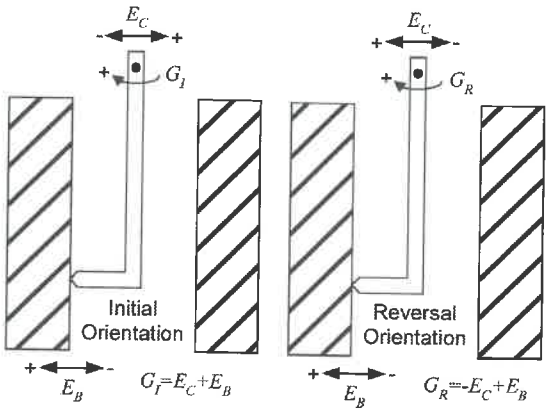

Fig 3: Reversal for Rotating Sensitive Direction

The reversal procedure inverts the spindle's error motion, E_C, while the orientation of the test bore and its roundness errors, E_B, remain constant. The gauge reading before reversal, G_I , and after reversal, G_R, are given in Eqs (1) and (2).

$$G_I = E_C + E_B \quad (1)$$

$$G_R = -E_C + E_B \quad (2)$$

Adding and subtracting the gauge readings gives the separated error expressions for E_B and E_C shown in Eqs (3) and (4).

$$E_B = \tfrac{1}{2}(G_I + G_R) \quad (3)$$

$$E_C = \tfrac{1}{2}(G_I - G_R) \quad (4)$$

Kinematic Spindle Arrangement

The kinematic spindle relies upon exact constraint to position and orient its axis of rotation in space. Only five contacts are used, thereby allowing one degree of freedom in the spindle: rotation about its axis. As illustrated in Fig 4, P_{C1} is defined as the Z-axis constraint and is located on the spindle's axis of rotation. Four other contact points (P_{C2}, P_{C3}, P_{C4}, P_{C5}) are placed in high and low contact planes (HCP

and LCP). In each contact plane, two spheres are separated by 90 degrees, on the shaft's cylindrical surface.

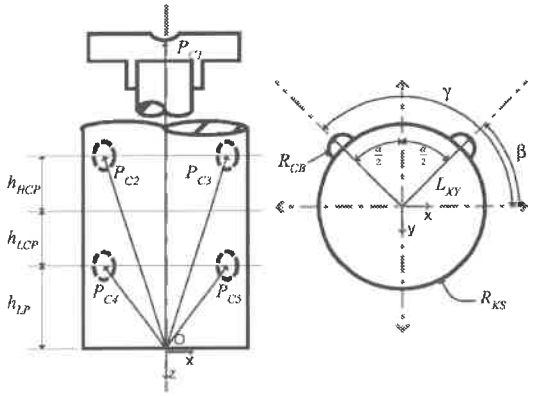

Fig 4: Contact Locations on Kinematic Spindle

The shaft rotates within a sleeve, creating a point-contact bearing. Tungsten carbide will likely be used for both the sleeve and contact hemispheres P_{C2} though P_{C5} due to its beneficial wear properties, low coefficient of friction, and high stiffness. The axial contact P_{C1} is a steel hemisphere contacting a steel plate for two reasons: 1) a larger coefficient of friction for steel on steel and 2) the ferromagnetic properties for the Z-axis preload. A radial compressive preload is established on contacts P_{C2} through P_{C5} using a flexure equipped with a contact hemisphere as seen in Fig 1. The contact between the preload flexure's hemisphere and the contact sleeve is termed P_{C6}, and it is centered between the contact planes and is aligned with the Y-axis.

Spindle Drive Arrangement

Torque transmitted through the shaft's Z-axis constraint rotates the kinematic spindle. This arrangement, illustrated in Fig 5, is preferable to belt-drive since it does not impart radial forces, which are a source of error motion [5].

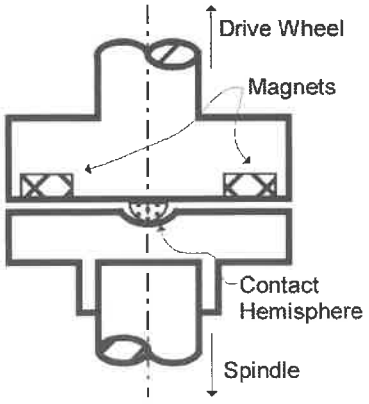

Fig 5: Z-axis Contact and Drive Arrangement

The maximum transmissible torque is derived from the surface traction between the axial contact hemisphere and the steel plate. The peak traction depends upon the radius of the contact area, the coefficient of friction, and the magnetic preload between the plates. The drive arrangement is successful when the transmitted torque is greater than the opposing moment generated by friction at the radial contact hemispheres P_{C2} through P_{C5} and P_{C6} against the contact sleeve.

Magnetic Force Experiment

The magnetic force for a given separation between plates was empirically tested using the setup shown in Fig 6. An array of 3 and an array of 6 evenly spaced neodymium magnets (ϕ12.7 mm x 6.35 mm) were fixed in an aluminum plate matching the configuration in the instrument. A 1018 carbon steel plate was attached to a Sensotec model 31 load-cell. The plate and load cell assembly were bolted to vertical translation stages.

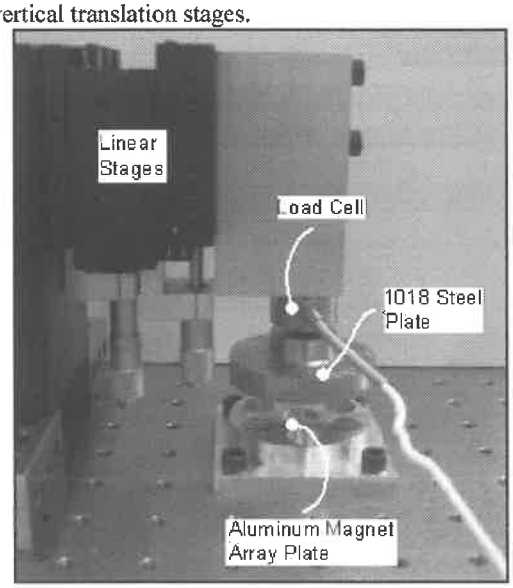

Fig 6: Magnetic Force Experiment Setup

Using a 1.27 mm (0.050") gauge block to establish parallelism, the steel plate was lowered to a known distance away from the magnetic plate. The load cell subsequently measured the force acting on the steel plate by the magnets at 0.5 mm increments up to 32mm. The experiment was executed thrice for each magnet array.

The mean of the three measurements are plotted in Fig 7 for the 3 and 6 magnet arrangements. Three magnets produced roughly 44 N and six magnets doubled the force to 88 N at the minimum offset of 1.27 mm. Dividing the six-magnet force curve by

two and plotting the result against the three-magnet force curve validated this relation.

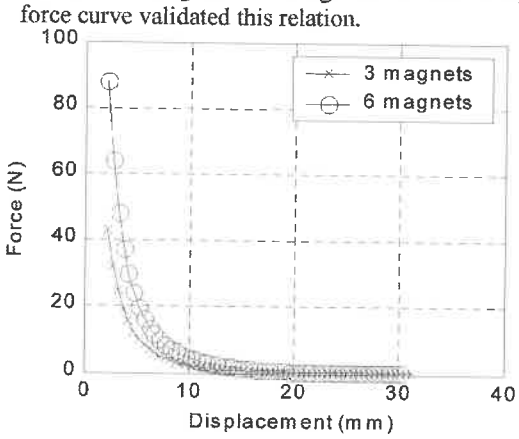

Fig 7: Magnet Force as Function of Displacement

Analysis of Surface Traction

Hertzian contact analysis [8] provides a value for the contact radius, a, as a function of normal force, P, chosen from data gathered in the mag2netic force experiment. The analysis is based on the method described by Johnson [8]. Eq (5) gives the rotation angle, β, as a function the contact radius, a, shear moduli of the contacting materials, G_1 and G_2, and the applied moment M_z.

$$\beta = \tfrac{3}{16}\left(\frac{1}{G_1}+\frac{1}{G_2}\right)\frac{M_Z}{a^3} \qquad (5)$$

Once β is known, the radius of the slip annulus region, c, may be calculated using Eq (6a). $K(k)$ and $E(k)$ are elliptical integrals of the first and second kind, respectively, evaluated for k given in Eq (6b). MATLAB or another computational method is helpful in solving for c.

$$\frac{3}{4\pi}\left(1-\frac{c^2}{a^2}\right)\left(\frac{1}{G_1}+\frac{1}{G_2}\right)\left[K(k)-E(k)\right]=\frac{a^2\beta}{\mu P} \qquad (6a)$$

$$k=\left(1-c^2/a^2\right)^{1/2} \qquad (6b)$$

Two functions exist for the traction between contacting bodies: 1) the region of no-slip from the center of the contact area to the slip annulus, and 2) the region between the slip annulus and the perimeter of the contact area. Within the slip annulus, the traction, $q(r)$, is given by Eq (7), and beyond the annulus, the traction is given by Eq (8).

$$q(r)=\frac{3M_Z r}{4\pi a^3}\left(a^2-r^2\right)^{-1/2} \text{ for } 0\le r<c \qquad (7)$$

$$q(r)=\frac{3\mu P}{2\pi a^3}\left(a^2-r^2\right)^{1/2} \text{ for } c\le r\le a \qquad (8)$$

The plot in Fig 8 illustrates the form of these functions for a particular preload. The traction increases until the slip annulus, c, is reached. It then jumps to a peak value and quickly decays to zero at the contact boundary, a. Increasing the magnetic preload, P, increases a, and the jump at c diminishes slightly.

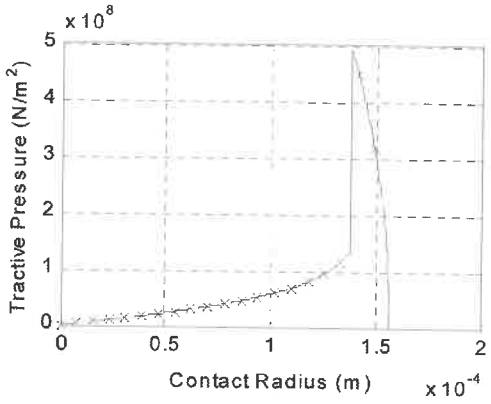

Fig 8: Surface Traction

Magnetic Preload versus Critical Flexure Preload

The spindle's radial preload, supplied by a flexure, should be sized such that frictional forces acting at the contacts P_{C2} through P_{C6} do not create a moment greater than the drive arrangement can overcome. The flexure preload at which the drive arrangement begins to freely slide is defined as the critical flexure preload.

Johnson's expression for the maximum moment, M_Z, transmissible through the drive arrangement is given in Eq (9) [8]. This expression shows that the torque is directly proportional to the coefficient of friction, μ, and the preload force, P.

$$M_Z = 3\pi\mu Pa/16 \qquad (9)$$

Eq (9) is used with an expression for spindle contact frictional forces to create a function of the radial preload imparted by the flexure. Using a MATLAB optimization routine, the critical flexure preload may be calculated as a function of the magnetic Z-axis preload.

Fig 9 plots the critical flexure preload versus the magnetic preload on the Z-axis contact. The coefficient of friction between P_{C1} though P_{C5} and P_{C6} and the spindle sleeve is varied to demonstrate the advantages of choosing a low-friction material for this application.

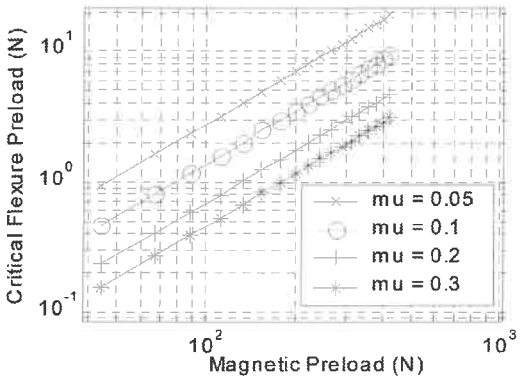

Fig 9: Critical Flexure Preload as Function of Magnetic Axial Preload Force

Conclusions and Future Work

Since Hii demonstrated that kinematic spindles could achieve low asynchronous error but higher synchronous error, they may be applied with a reversal technique to construct a portable roundness instrument. Because it is necessary to maintain low asynchronous error for successful reversal, it is crucial to drive the spindle in a manner that introduces little or no disturbance forces to the shaft. This can be achieved with a point-contact drive system.

From this work, a number of generalizations are made regarding the design of such a drive system. A critical design aspect is the amount of torque transmissible through P_{C1} and its steel-plate companion. Increasing the magnetic preload on the steel plate and increasing the coefficient of friction at the radial contact points increase this transmitted torque. Increasing the magnetic preload causes the area beneath the surface traction curve to increase, and hence the moment that may be passed through the contact point.

The magnetic preload could be increased though several methods:

1. Increase the number of magnets in the array to achieve the desired preload,
2. Increase the size of the magnets used,
3. Custom manufacture a neodymium ring to match the diameter of the 1018 steel plate.

The P_{C1} contact hemisphere will likely be steel rather than tungsten carbide. The coefficient of friction for steel on steel contact is fairly high (~0.80).

For near point contact drive of a kinematic spindle, the friction at the radial contact points, P_{C1} through P_{C5} and P_{C6}, must be minimized to allow maximum radial preload. Maximized radial preload is desirable for a robust construction and a stable spindle. Materials with low coefficients of friction, such as tungsten carbide (μ=0.25), may be a suitable choice for the contact hemispheres and contact sleeve.

Since spindle repeatability is necessary for reversal techniques to function properly, a wear study of the tungsten carbide contact hemispheres and sleeve will be undertaken. Wearing in either of these surfaces changes the spindle's asynchronous error pattern. In addition, characterization of the proposed contact probe (Mitutoyo SurfTest SJ-400) is required.

Acknowledgements

The authors acknowledge encouragement from Bob Wasilesky at Mitutoyo for considering the application of kinematic spindles in roundness metrology.

References

[1] "Measurement of Out-of-Roundness". ASME B89.3.1–1972. American Society of Mechanical Engineers. 1972.

[2] Donaldson, R.R. "A Simple Method for Separating Spindle Error From Test Ball Roundness" *CIRP Annals*. V. 21. 1972.

[3] Evans, Chris J. and J. Robert Hocken. "Self-Calibration: Reversal, Redundancy, Error Separation, and Absolute Testing." *CIRP Annals*, V.45, N.2. 1996.

[4] Blanding, D.L. Exact Constraint: Machine Design Using Kinematics Principles. ASME Press. New York. 1999.

[5] Hii, King-Fu. *Kinematically Constrained Spindles*. M.S. Thesis. University of Kentucky. 2002.

[6] K-F. Hii, E. Wolsing, R. Vallance, "Design of a Kinematic Spindle for Low-Force, Low-Speed Applications," *Proceedings of 16th Annual Meeting of the American Society for Precision Engineering*. ASPE. Crystal City, VA. November 10th – 15th, 2001.

[7] "Axes of Rotation – Methods for Specifying and Testing". ASME 89.3.4-1985. American Society of Mechanical Engineers. 1985.

[8] Johnson, K.L. *Contact Mechanics*. Cambridge University Press. Cambridge. 1985.

Effective Measurement Method of Thermal Deformation of Machine Tools Caused by Linear Axis Motion

Shinji Shimizu, Noboru Imai
Department of Mechanical Engineering, Sophia University, Tokyo

1. Introduction

The spindles speed and feed rate of machine tools increase greatly to realize high-productivity with high accuracy. This leads to exceeding increase in heat generation and then the thermal deformation of the machine tools become serious problems. Therefore it makes necessary to measure and evaluate the thermal deformation. With these points as background, measuring methods for thermal deformation of machine tools were standardized in the international standard ISO 230-3 in March 2001[1]. In this standard, the measurement methods of thermal deformation caused by environmental temperature variation, spindle rotation and linear axis motion were provided. For measuring thermal deformation caused by environmental temperature variation and spindle rotation, the methods to measure simultaneously five degrees of freedom components of the thermal deformation are specified in the standard. In this standard, the measurement method proposed by us for high-speed spindle is adopted as a recommended method[2]. In addition, we have proposed more effective evaluation method with our method[3].

On the other hand, in ISO, for measuring thermal deformation caused by linear axis motion, the only thermal deviation in positioning direction is measured. However, it is pointed out that the thermal deviations in other five directions also occurs and influence on the machining accuracy[4]. Then many measurement and compensating methods have been studied[5,6]. However, there are no simple and effective measurement methods for measuring the thermal deformations with linear axis motion.

Therefore, in this paper, we propose a new measurement method to measure simultaneously six degrees of freedom components of the thermal deviation caused by linear axis motion in machine tools and shows its effectiveness.

2. Proposition of an effective measurement method and device

2.1 Measurement methods under ISO230-3 and its problems

Figure 1 shows a measurement method of thermal deviations in ISO230-3[1]. This is a case of measurement test for X axis motion of a vertical machining center.

In this method, displacement sensors are fixed on the nose end of the spindle and two targets are located on the table. The spindle head is moved relatively to the table between the targets and only the change of the positioning accuracy is measured. However, the problems of thermal expansion of the ball screw tend to be resolved by the adoption of a linear encoder or a cooling system.Then the importance of the thermal deviations in the positioning direction shifts to the other directions to achieve the higher machining accuracy. This tendency becomes stronger with the great increase of heat generation accompanied by the speeding-up of the recent machine tools. Therefore the universal measurement and evaluation methods of thermal deviations with the six degrees of freedom are getting to be demanded.

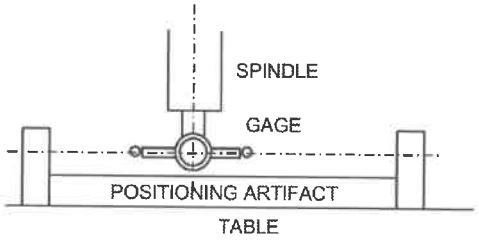

Fig.1 The measuring method of thermal deviations under ISO230-3[1]

2.2 Proposition of an effective measuring device and method

(1) Measuring device

In this study, we propose a new simultaneous measuring method of six components of the thermal displacement consisting of a component in positional direction, two components orthogonal to the positioning direction, three angular components around these three directions.

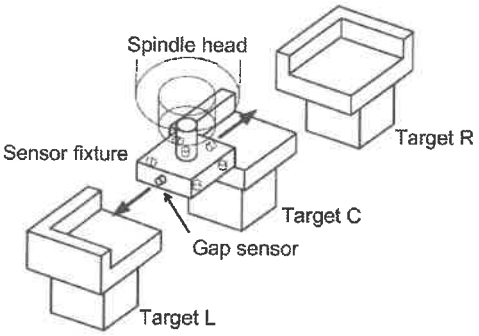

Fig.2 Setup of proposed measuring device

Figure 2 shows the proposed measuring device. The device consists of a sensor fixture to hold seven non-contact type displacement sensors and three targets. The details of the sensor fixture and targets are shown in figure 3 and 4. The sensor fixture is fixed on the spindle nose with a tool holder. The three targets are located on the table in a straight line parallel to the feed direction. In the measurement test, the following cycles are continued for a prescribed hours. The sensor fixture moves back and forth between the target L and R several times and stops at a target, the gap changes between target and sensors are detected to measure the thermal deviations.

Equations to calculate thermal deviations are shown as follows. Δg_i (i :1-7) is the gap change at sensor S_i. The direction increasing the gap to the target is the plus direction of the sensor output . L_{ij} is the distance between sensor S_i and S_j.

Translational deviations: $X = \begin{cases} \Delta g_1 & (at\ L) \\ -\Delta g_2 & (at\ R) \end{cases}$, $Y = -\dfrac{\Delta g_3 + \Delta g_4}{2}$, $Z = \dfrac{\Delta g_5 + \Delta g_6}{2}$

Angular deviations: $\theta_X = \dfrac{\Delta g_5 - \Delta g_7}{L_{57}}$, $\theta_Y = \dfrac{\Delta g_6 - \Delta g_7}{L_{67}}$, $\theta_Z = \dfrac{\Delta g_3 - \Delta g_4}{L_{34}}$

In this method, the measurement is carried out also at the center of the linear motion, unlike the method in ISO. Therefore the change of the straightness by the thermal effect can be evaluated from the measurement results of thermal translational deviations at each three targets.

Another advantage of the proposed measuring method is that the machining error can be predicted more accurately. For example, when angular deviation around Y axis occurs, the value of positioning deviation is different according to Z position. Then, if a thermal deviation for only one direction is measured, the machining error can not be estimated accurately even in its direction.

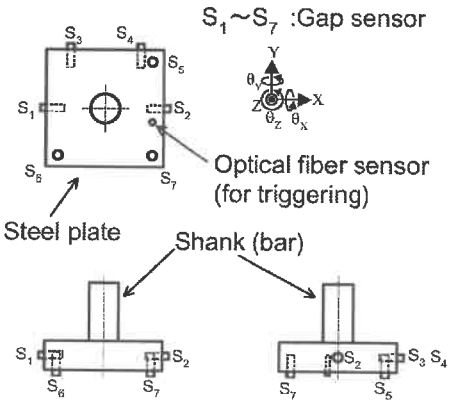

Fig.3 Sensor fixture

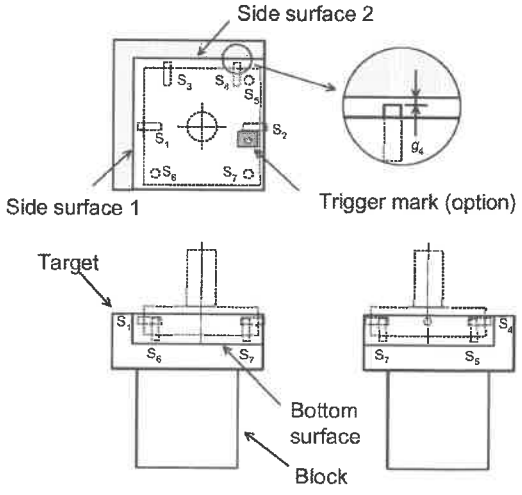

Fig.4 Target (L)

The other feature of the proposed measuring device is that all sensors are held on a sensor fixture to makes the reference point of the device determinate. For example, if the sensors are located on the table side, the deformation of the table causes to change the positions of sensors, and to shift the reference point of the device. Moreover, when the thermal drift of sensor occurs, it is easy to resolve this problem by correcting the sensors' outputs with the temperature of the fixture, since all sensors are fixed on the fixture.

In addition, the construction of the measurement system is very simple, easy to be carried and suitable to use in machine shops. Then the system proposed here can be accepted for the standardization in ISO.

A prototype measuring device based on the proposed method was made. Table 1 shows main specifications of the prototype system. Eddy current sensors are used. The mild steel is used for the material of the sensor fixture and targets. The reason for this is that the jigs and fixtures of the device should be the same material as the workpieces to evaluate the effect of the thermal deviations on the machining error. In this study, the workpieces are assumed to be made of mild steel.

(2) Measuring method

Figure 5 shows the top view of the paths of axis motion for the test of thermal deviations. After the spindle head moves back and forth for a prescribed times on the path 1, the measurement is carried out at three targets with dwell along the path 2 at a distance d from the path 1. This cycle is repeated for prescribed hours. The influence of shifting distance d to measure seams to be small, if the distance is small and the frequency of the measurement is few.

3. The measurement results of the test with the proposed measuring device and the efficiency of the device

3.1 Test method and conditions of the thermal measurement test

Figure 6 shows the setup of the experimental device to verify the effectiveness of the proposed measuring method. The measurement test was carried out on the X axis of a double column type machining center. The X axis motion of the machining center is carried out by the spindle head traverse from side to side and the table is fixed. The thermal expansion of the ball screw effects greatly on the positioning accuracy, since X axis control is a semi-closed type with a rotary encoder.

In this figure, the points of temperature measurement at the environment, the sensor fixture, the targets and the bed of machine are also drawn. Table 2 shows the conditions of the test.

3.2 The results of temperature measurement

Figure 7 shows the change of the temperature from the start of the test. From the figure, it seems that the heat generation caused by X axis motion does not effect on measurement system and the sensor fixture becomes cool down slightly by the fall of the environmental temperature. Therefore, the effects of the temperature change in the measurement test can be ignored.

Table 1 Specifications of the prototype measuring system

Type of sensors	Eddy current sensor
Angular resolution	0.1 μm
Translational resolution	1 arc-sec
Size of sinsor's fixture	120 x 120 x 20 mm
Size of target	140 x 140 x 120 mm
Material of fixure & target	mild steel

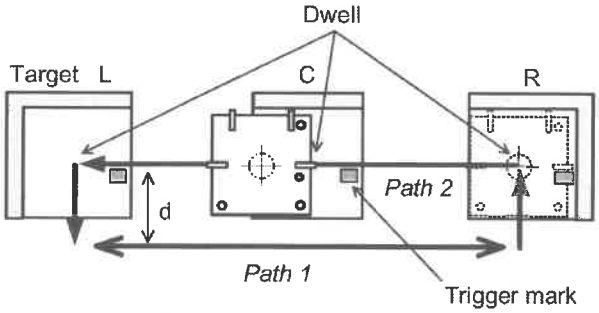

Fig.5 Paths for measurement

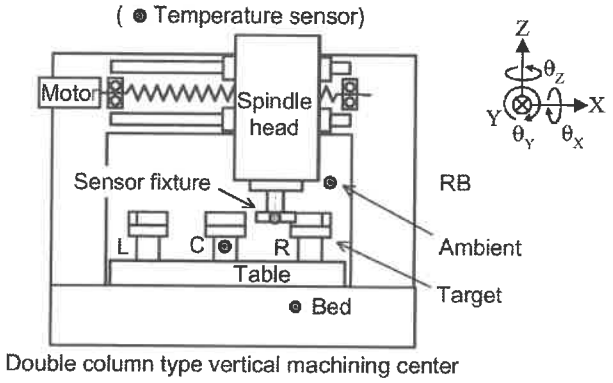

Fig.6 Experimental setup

Table 2 Conditions of the measurement test

Feed rate	1700 mm/min
Transverse length	500 mm
Offset d	5 mm
Dwell	2 s
Measuring cycle	1 / 10 round trips

3.3 The results of the positional thermal deviation measurement

Figure 8 shows the measurement results of the thermal deviation along the positioning direction. The thermal deviation X at target R tends to increase with the time passed and shows the characteristic like a first order lag system. The thermal deviation X at target L decreases slightly once, then increases gently. The difference between R and L indicates the typical characteristic of thermal deviation caused by the thermal expansion of a ball screw. This results shows that the proposed measuring method can get the equivalent results with the method standardized in ISO230-3.

3.4 The results of the translational thermal deviation measurement

The measurement results of the thermal deviations in Y and Z direction orthogonal to the positioning direction are shown in figure 9 and 10. The deviation in Y tends to degrease and in Z tends to increase monotonously. These results are smaller than in X direction, but the order can not be ignored. The thermal deviation in Y at target C is lager than the deviation at the other targets in the minus direction. The reason seems that the temperature rises on the front side of the cross-rail fixing guide ways, and then the cross-rail is warped to the operator's side like a convex curve. The difference of the deviations in Z direction at all targets can not be observed. Therefore, the result seems to originate from the thermal expansions of two columns in Z direction and/or from the angular deviation around the axis X with the warp deformations of the columns.

3.5 The results of the angular deviation

Figure11 shows the measurement results of the thermal angular deviation θ_X. θ_X increases only just after the start of the test in plus direction and increases monotonously in minus direction. It is reasonable to think that the monotonous increasing tendency originates from column's warping caused by the temperature difference between the front and back of column as mentioned above or the thermal deformation of the spindle head or saddle. Pointing out the cause of the

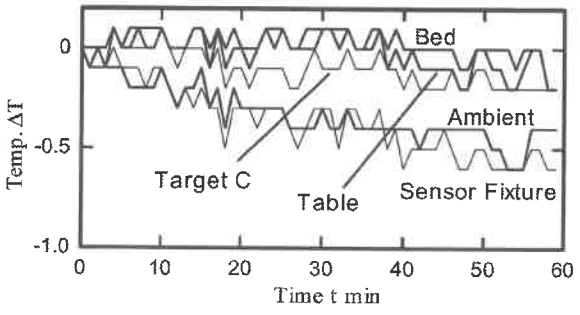

Fig.7 Temperature change

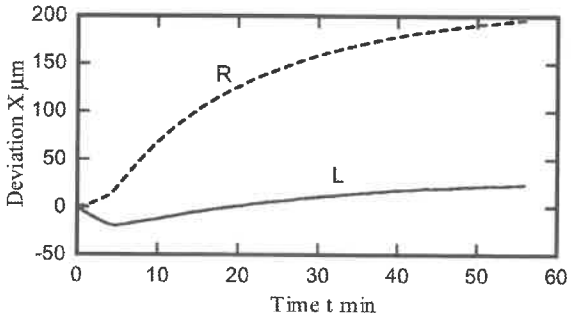

Fig.8 Thermal deviation X

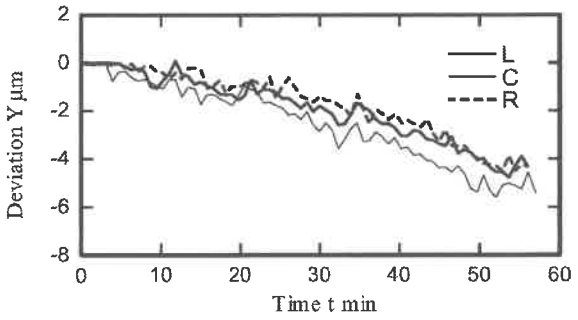

Fig.9 Thermal deviation Y

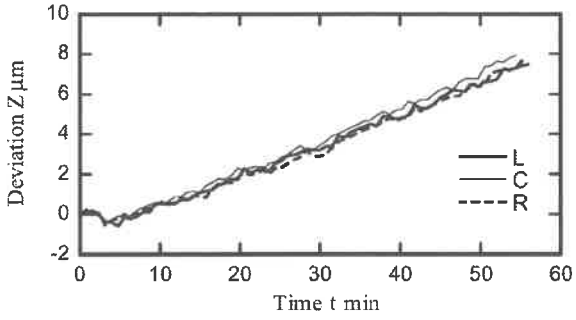

Fig.10 Thermal deviation Z

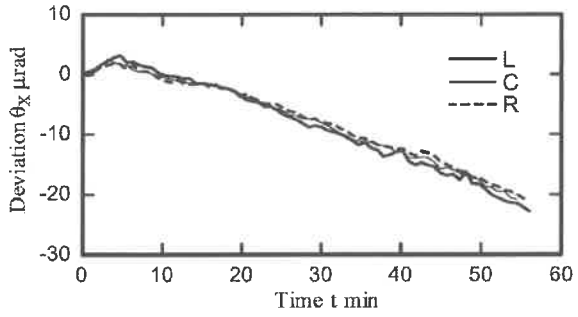

Fig.11 Thermal deviation θ_X

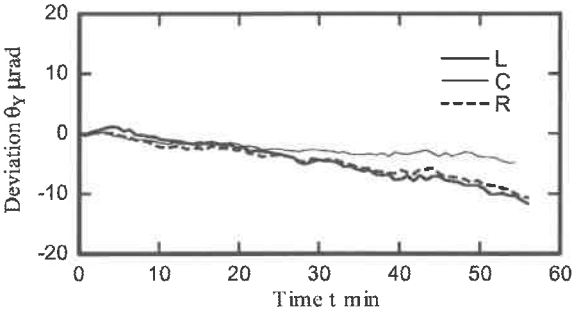

Fig.12 Thermal deviation θ_Y

warping is impossible from the result of this measurement only, but it can be realized by measuring simultaneously the temperatures of the machine structures. The effect of θ_X must be included in the results shown in figure 9 and 10, since θ_X influences on the displacement in Y and Z direction,

Figure 12 shows the thermal angular deviations around axis Y (θ_Y). θ_Y at the target C changes a little, but tend to decrease at target L and R. From this results, it is reasonable to think that the cross-rail curves up like S character. Generally θ_Y effects on X directional deviation. However, this effect can not be recognized in this results, since the deviation caused by the thermal expansion of the ball screw is the dominant cause of X directional deviation.

Figure 13 shows the measurement results of thermal angular deviation θ_Z. θ_Z value at right target is larger than at left one. This seams to be caused by the warping of the cross-rail as mentioned above to generate the deviation in Y direction. If the cross-rail is warped completely symmetrically, then θ_Z at target C becomes zero, and θ_Z at target R should displace to plus direction and θ_Z at target L should displace to minus direction. However, θ_Z at all targets displace actually to plus direction. The reason is this that the upper side of the machine structure than the table occurs twist deformation and/or the saddle or the spindle head deforms in this direction. The thermal deformation predicted from the above results is shown in figure 14.

3.6 Efficiency of the proposed measuring method and device

As mentioned in the above section, the five components of the thermal deviation except for the positioning are also remarkably generated in the same way as the positioning. The combination of these results enables to predict the behavior of the thermal deformation of the machine tool. Moreover, thermal deviations at any points in the work area seams to be estimated more accurately from the measurement results. In addition, the proposed method has great possibility to search the cause of the thermal deformation accurately in a short time more than in the past.

As described above, it was made clear that the proposed simpler measuring device can measure simultaneously six degrees of freedom components of thermal deviations with the compatible characteristics of ISO230-3 and can evaluate thermal deviations more effectively.

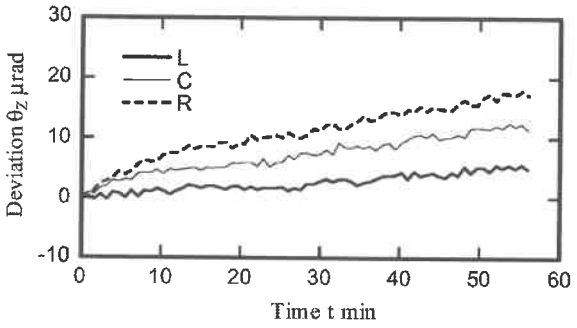

Fig.13 Thermal deviation θ_Z

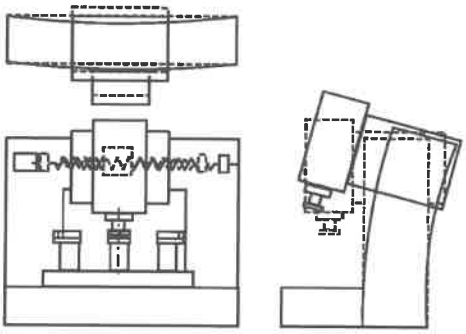

Fig.14 Deformation of machine structure

4. Conclusion

A new effective measurement method was proposed to measure simultaneously the six degrees of freedom components of the thermal deviation of machine tools caused by linear axis motion. The measurement test for the X axis motion was carried out with the prototype measurement system on the machining center. From the results, the effectivness of the proposed measurement method was made clear.

References

1) ISO, Test code for machine tools part 3: Determination of thermal effects, ISO 230-3 (2001).
2) X. Qi, S. Shimizu and N. Imai, Measuring method of thermal displacement for machine tools at high-speed spindle motion, Journal of the Japan Society for Precision Engineering, 65, 3 (2001) 396.
3) S. Shimizu and N. Imai, Evaluation method of thermal displacement of machine tools, I. Inasaki ed. Initiatives of precision engineering at the beginning of a millennium, Kluwer Academic Publishers, (2001) 639.
4) M. Weck, Handbook of machine tools: Metrological analysis and performance tests, Vol.4, John Wiley and Sons, (1984) 43.
5) R. Ramesh, M. A. Mannan and A. N. Poo, Error compensation in machine tools – a review Part II: thermal errors, Int. J. Mach. Tools Manuf., 40, 9 (2000) 1257.
6) H. J. Pahk, S. W. Lee, Thermal error measurement and real time compensation system for the CNC machine tools, Proc. Int. 33rd Matador Conf., 33, (2000) 249.

THE VIRTUAL-SHAPE APPROACH FOR MODELING VOLUMETRIC ERRORS OF MACHINE TOOLS

Kyung-Don Kim and Sung-Chong Chung
Hybrid Systems Design and Control LABoratory, School of Mechanical Engineering
Hanyang University, Seoul 133-791, Korea

Abstract: A modeling method of volumetric errors of machine tools through the concept of a virtual-shape element is proposed. The virtual-shape element is introduced to exclude problems occurred owing to Abbe offsets. Hypothetical elements without having real dimensions are used for the virtual-shape elements. An equivalent diagram for error propagation through the virtual-shape element is studied as well. The proposed modeling approach can include both geometric and thermal errors. The derived error model requires no dimensional information of machine tools due to elimination of the Abbe error terms that are unavoidable in the previous method. Introducing the virtual-shape element can also solve the difficulties in the parameter identification process.

Keywords: Abbe error, Error synthesis, Equivalent vector approach, Geometric error, Machine tools, Separated element approach, Thermal error, Virtual-shape approach, Volumetric error

1. Introduction

Machining accuracy depends upon deviation from the planned relative movement between the tool and the workpiece. For three-axis machine tools and coordinate measuring machines, this relative error is called the volumetric error. Among the machine error sources, geometric and thermal errors are known to be key contributors [1,2]. In general, the error synthesis method using the homogeneous coordinate transformation is widely used to derive a volumetric error model [3].

The error synthesis method can be classified into two approaches with or without thermal errors: the equivalent vector approach and the separated element approach. The equivalent vector approach represents the configuration of machine tools or coordinate measuring machines with three equivalent vectors [4-6]. Each vector is modeled as a joint transformation matrix. Therefore, thermal errors of shape elements such as spindle errors cannot be properly incorporated into the model. The equivalent vector approach has been mainly used for modeling geometric errors. On the other hand, the separated element approach analyses the configuration of machine tools as a sequence of shape elements connected by joint elements [7-9]. Each shape and joint is modeled as a shape and joint transformation matrix, respectively. Therefore, both geometric and thermal errors can be modeled explicitly.

Although the separated element approach is able to incorporate into thermal errors, volumetric error models derived by using this approach have several weak points: (1) The measuring line of laser interferometers for identification of model parameters has to be aligned on the same axes of ball screws because the setup positions of measuring instruments are restricted to the positions of local coordinate frames defined at the model building stage. However, it is difficult or impossible to fulfill the above-mentioned requirement practically. (2) The volumetric error model is more complex than that derived by using the equivalent vector approach because of the Abbe error terms expressed as multiplication of the rotational errors of joint elements by the real dimensions of shape elements. The reason why the Abbe error terms are intervened is that joint transformation matrices are defined as the errors along ball screws. (3) The volumetric error model requires dimensional information of machine tools for error compensation. It is not easy for users to obtain exact dimensional information of machine tools. All the above disadvantages are resulted from the fact that shape elements have actual size.

In this paper, a new concept of a virtual-shape element is introduced to compensate for disadvantages concerning both approaches. An equivalent diagram for error propagation through the virtual-shape element is studied as well. A volumetric error model for the C-shaped vertical machining center is derived by using the proposed method and compared with that derived

by using the previous methods.

2. The virtual-shape approach

As shown in Fig. 1, a shape element has translational and rotational error terms due to thermal errors. A shape transformation matrix that transforms the coordinate of a point in the $X_2'Y_2'Z_2'$ coordinate frame into the $X_1Y_1Z_1$ reference frame can be represented as follows:

$$S_{actual} = \begin{bmatrix} 1 & -\alpha(t) & \beta(t) & a+\Delta a(t) \\ \alpha(t) & 1 & -\gamma(t) & b+\Delta b(t) \\ -\beta(t) & \gamma(t) & 1 & c+\Delta c(t) \\ 0 & 0 & 0 & 1 \end{bmatrix} \quad (1)$$

where, $\alpha(t)$, $\beta(t)$ and $\gamma(t)$ are rotational errors around Z-, Y- and X-axis, respectively. $\Delta a(t)$, $\Delta b(t)$ and $\Delta c(t)$ are translational errors in X-, Y- and Z-axis directions. a, b and c are dimensions of the ideal shape element in X-, Y- and Z-axis direction. All of the error terms are usually modeled as a function of time or temperature, t.

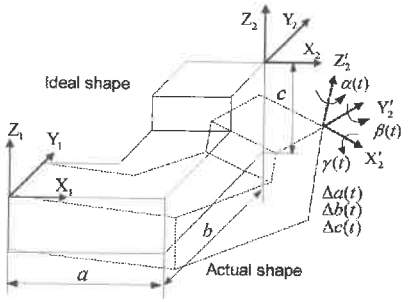

Fig. 1 Relative position of two coordinate systems established on a real shape element.

A virtual-shape element is defined as the hypothetical element that has no real dimensions. But, it is assumed that the hypothetical element can have shape errors such as translational and rotational errors as follows:

$$V_{actual} = \begin{bmatrix} 1 & -\alpha(t) & \beta(t) & \Delta a(t) \\ \alpha(t) & 1 & -\gamma(t) & \Delta b(t) \\ -\beta(t) & \gamma(t) & 1 & \Delta c(t) \\ 0 & 0 & 0 & 1 \end{bmatrix} \quad (2)$$

If there is no error, the virtual-shape transformation matrix could become an identity matrix. Note that a prerequisite for Eq. (2) is coincident with the position of $X_2Y_2Z_2$ coordinate frame as that of $X_1Y_1Z_1$ coordinate frame.

Fig. 2 shows an equivalent diagram for modeling volumetric errors of a C-shaped vertical machining center by using virtual-shape elements. The reference coordinate system is established at the position where the origin of the workspace is joined with that of the spindle. The kinematic chain from the reference coordinate system to the tool is as follows: A virtual-shape element for Z-axis, V_Z, exists between the origin of reference coordinate system, O_R, and the joint element for Z-axis, J_Z. A virtual-shape element for a spindle, V_S, exists between the joint element for Z-axis, J_Z, and the spindle origin, O_S. The kinematic chain from the reference coordinate system to the workpiece is determined in a similar way.

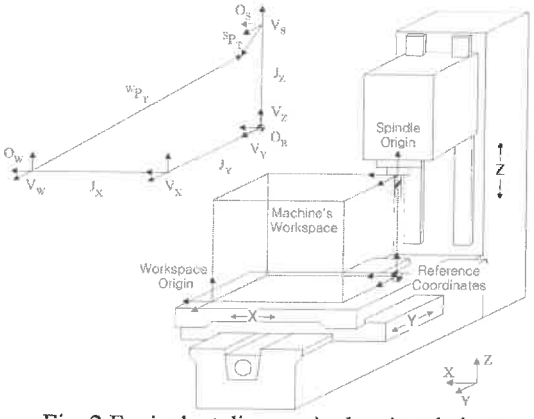

Fig. 2 Equivalent diagram in the virtual-shape approach.

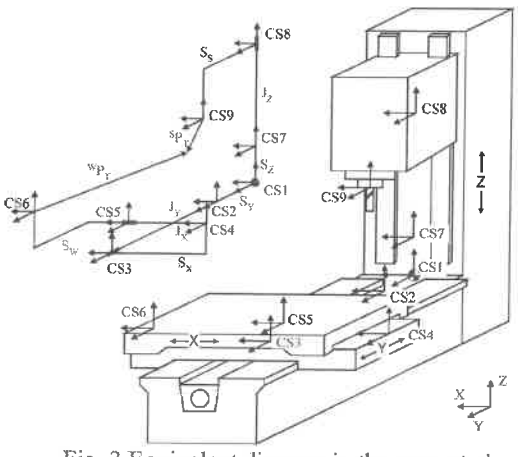

Fig. 3 Equivalent diagram in the separated element approach

Positions and roles of virtual-shape elements can be explained more easily by comparing two equivalent diagrams shown in Fig. 2 and Fig. 3. Fig. 3 shows an equivalent diagram for modeling volumetric errors of the same machining center by using the separated

element approach. The reference coordinate system, CS1, is established at the intersection point between Y- and Z-axis ball screws. A local coordinate frame CS7 is located at the lower mount of the Z-axis ball screw. CS8 is established at the nut of the Z-axis ball screw, CS9 is at the tool grasp point, and so on. So, a joint transformation matrix is defined with translational and rotational error terms along a ball screw axis in this separated element approach.

The equivalent diagram shown in Fig. 2 is acquired by moving the coordinate frame CS1 in Fig. 3 to the position where O_R in Fig. 2 is established, and substituting the virtual-shape elements for the real shape elements. Since the virtual-shape element has no real dimensions, CS7, CS9, CS2, CS4 and CS6 coordinate frames are transferred to CS1, CS8, CS1, CS3 and CS5 coordinate frames, respectively. And, since the reference coordinate frame is transferred from CS1 to O_R, the joint transformation matrix shown in Fig. 3 is redefined at the equivalent diagram shown in Fig. 2 with translational and rotational error terms along an axis of the reference coordinate frame O_R.

The tool position with respect to the origin of the workspace, ${}^{W}P_{T}$, can be derived from the equivalent diagram shown in Fig. 2 as follows:

$$\begin{aligned} {}^{W}P_{T\ actual} &= [X+dX \quad Y+dY \quad Z+dZ \quad 1]^{T} \\ &= [V_{W}]^{-1}_{actual}[J_{X}]^{-1}_{actual}[V_{X}]^{-1}_{actual}[J_{Y}]^{-1}_{actual}[V_{Y}]^{-1}_{actual} \\ &\quad \times [V_{Z}]_{actual}[J_{Z}]_{actual}[V_{S}]_{actual}\,{}^{S}P_{T} \end{aligned} \tag{3}$$

where, ${}^{S}P_{T} = [t_x \quad t_y \quad t_z \quad 1]^{T}$ is a tool offset vector. dX, dY and dZ are volumetric error terms in X-, Y- and Z-axis directions, respectively.

3. Case study

In a vertical machining center, the dominant thermal error sources are the thermal drift and tilt of a spindle, the thermal drift and expansion of three ball screws, and the thermal distortion of C-shaped machine frames. Joint errors are divided into stationary geometric errors and time-variant thermal errors.

Considering the prescribed dominant error sources, the joint and virtual-shape transformation matrices can be expressed as follows:

$$[J_X]_{actual} = \begin{bmatrix} 1 & -\varepsilon_z(x) & \varepsilon_y(x) & x+\delta_x(x)+P_x(t)x \\ \varepsilon_z(x) & 1 & -\varepsilon_x(x) & \delta_y(x)+S_{xy}x+\Delta S_{xy}(t)x \\ -\varepsilon_y(x) & \varepsilon_x(x) & 1 & \delta_z(x) \\ 0 & 0 & 0 & 1 \end{bmatrix} \tag{4}$$

$$[J_Y]_{actual} = \begin{bmatrix} 1 & -\varepsilon_z(y) & \varepsilon_y(y) & \delta_x(y) \\ \varepsilon_z(y) & 1 & -\varepsilon_x(y) & y+\delta_y(y)+P_y(t)y \\ -\varepsilon_y(y) & \varepsilon_x(y) & 1 & \delta_z(y) \\ 0 & 0 & 0 & 1 \end{bmatrix} \tag{5}$$

$$[J_Z]_{actual} = \begin{bmatrix} 1 & -\varepsilon_z(z) & \varepsilon_y(z) & \delta_x(z)+S_{zx}z+\Delta S_{zx}(t)z \\ \varepsilon_z(z) & 1 & -\varepsilon_x(z) & \delta_y(z)-S_{yz}z-\Delta S_{yz}(t)z \\ -\varepsilon_y(z) & \varepsilon_x(z) & 1 & z+\delta_z(z)+P_z(t)z \\ 0 & 0 & 0 & 1 \end{bmatrix} \tag{6}$$

$$[V_X]_{actual} = \begin{bmatrix} 1 & 0 & 0 & \Delta a_x(t) \\ 0 & 1 & 0 & 0 \\ 0 & 0 & 1 & 0 \\ 0 & 0 & 0 & 1 \end{bmatrix} \tag{7}$$

$$[V_Y]_{actual} = \begin{bmatrix} 1 & 0 & 0 & 0 \\ 0 & 1 & 0 & \Delta b_y(t) \\ 0 & 0 & 1 & 0 \\ 0 & 0 & 0 & 1 \end{bmatrix} \tag{8}$$

$$[V_Z]_{actual} = \begin{bmatrix} 1 & 0 & 0 & 0 \\ 0 & 1 & 0 & 0 \\ 0 & 0 & 1 & \Delta c_z(t) \\ 0 & 0 & 0 & 1 \end{bmatrix} \tag{9}$$

$$[V_W]_{actual\ ideal} = \begin{bmatrix} 1 & 0 & 0 & 0 \\ 0 & 1 & 0 & 0 \\ 0 & 0 & 1 & 0 \\ 0 & 0 & 0 & 1 \end{bmatrix} \tag{10}$$

$$[V_S]_{actual} = \begin{bmatrix} 1 & 0 & \beta_s(t) & \Delta a_s(t) \\ 0 & 1 & -\gamma_s(t) & \Delta b_s(t) \\ -\beta_s(t) & \gamma_s(t) & 1 & \Delta c_s(t) \\ 0 & 0 & 0 & 1 \end{bmatrix} \tag{11}$$

where, $\delta_i(j)$ and $\varepsilon_i(j)$ are translational and rotational error terms along an axis of the reference coordinate system, i represents error direction and j represents moving direction. x, y and z are travel distances. S_{ij} is a squareness error between i- and j-axis of the reference coordinate system. $P_x(t)$, $P_y(t)$ and $P_z(t)$ represent linear thermal expansions of X-, Y- and Z-axis, respectively. $\Delta a_s(t)$, $\Delta b_s(t)$ and $\Delta c_s(t)$ are thermal drifts of a spindle in X-, Y- and Z-axis directions, respectively. $\beta_s(t)$ and $\gamma_s(t)$ are tilt motions of a spindle. $\Delta a_x(t)$, $\Delta b_y(t)$ and $\Delta c_z(t)$ represent thermal drifts of each axis origin. $\Delta S_{xy}(t)$, $\Delta S_{yz}(t)$ and $\Delta S_{zx}(t)$ are thermal distortions of C-shaped machine frames.

Substituting Eqs. (4)~(11) into Eq. (3), and neglecting higher order terms, volumetric errors are derived as follows:

$$\begin{aligned} dX &= -\delta_x(x)-\delta_x(y)+\delta_x(z)-P_x(t)x+\Delta a_s(t)-\Delta a_x(t) \\ &\quad +\{\varepsilon_z(x)+\varepsilon_z(y)-\varepsilon_z(z)\}t_y-\{\varepsilon_y(x)+\varepsilon_y(y)-\varepsilon_y(z)-\beta_s(t)\}t_z \\ &\quad -\{\varepsilon_z(x)+\varepsilon_z(y)\}y-\{\varepsilon_y(x)+\varepsilon_y(y)-S_{zx}-\Delta S_{zx}(t)\}z \\ dY &= -\delta_y(x)-\delta_y(y)+\delta_y(z)-P_y(t)y+\Delta b_s(t)-\Delta b_y(t) \\ &\quad -\{\varepsilon_z(x)+\varepsilon_z(y)-\varepsilon_z(z)\}t_x+\{\varepsilon_x(x)+\varepsilon_x(y)-\varepsilon_x(z)-\gamma_s(t)\}t_z \\ &\quad +\{\varepsilon_z(x)-S_{xy}-\Delta S_{xy}(t)\}x+\{\varepsilon_x(x)+\varepsilon_x(y)-S_{yz}-\Delta S_{yz}(t)\}z \\ dZ &= -\delta_z(x)-\delta_z(y)+\delta_z(z)+P_z(t)z+\Delta c_s(t)+\Delta c_z(t) \\ &\quad +\{\varepsilon_y(x)+\varepsilon_y(y)-\varepsilon_y(z)-\beta_s(t)\}t_x-\{\varepsilon_x(x)+\varepsilon_x(y)-\varepsilon_x(z)-\gamma_s(t)\}t_y \\ &\quad -\{\varepsilon_y(x)\}x+\{\varepsilon_x(x)+\varepsilon_x(y)\}y \end{aligned} \tag{12}$$

4. Comparison with traditional approaches

Measuring devices such as a laser interferometer or other mechanical methods can identify the well-known 21 geometric errors. Fig. 4 shows two setup locations for identification of model parameters. The choice of

setup location for the laser and optics is usually determined according to what information is desired [10]. If the translational error along the tool path is the desired information, the optics should be positioned to the axis of tool path. However, if the translational error along the axis of ball screw is the desired information, the optical components should be positioned to the axis of ball screw. It should be remembered that these two setups are not equivalent and, in general, will not yield the same error results owing to Abbe offset. In the separated element approach, since the joint transformation matrix is defined along the axis of ball screw, the optics should be positioned to the axis of ball screw. However, it is difficult or impossible to fulfill this requirement practically. Lo et al. [11] have been proposed the flexible error synthesis model to acquire correct error values from measurements taken at different spatial positions.

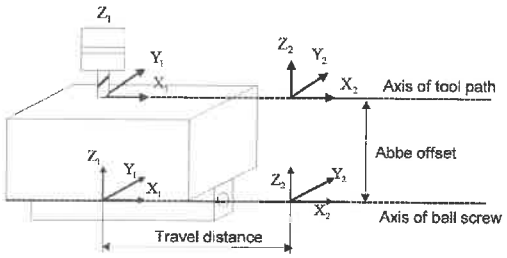

Fig. 4 Setup configuration of the laser and optics.

On the contrary, by introducing the virtual-shape element, a joint transformation matrix is redefined with errors along an axis of the reference coordinate frame established at the vertex of the workspace. Therefore, the error terms of each joint transformation matrix can be identified accurately through positioning the optical components at the origin of the reference coordinate system and measuring the errors during the movement along the axis of the reference coordinate system corresponding to the edge of the workspace.

A laser interferometer or dial gauges can also measure thermal drifts and expansions of three ball screws [12]. Measurement of thermal drift and tilt motions of a spindle is usually performed with a test mandrel and the fixture in which five displacement transducers are mounted [12]. The fixture should be set up at the origin of reference coordinate system even though the test is carried out on machines with rotating spindles. Heat generated by spindle rotation is transferred to the surrounding structure and mainly causes a variation of the column temperature distribution. Time-variant thermal distortions of machine frames affect the volumetric error as shown in Eg. (12). Therefore, in order to measure accurate drift data, the fixture should be securely fixed at the origin of the reference coordinate system.

In the equivalent vector approach, since the reference coordinate frame is established at the same position with the virtual-shape approach, the choice of setup location for the laser and optics is identical with the above-mentioned measuring method. However, the equivalent vector approach can't be applied to model thermal errors of machine tools, because the equivalent vector approach represents the configuration of three-axis machine tool as three joint transformation matrices. That is, shape elements such as a spindle are ignored in the model building process. Therefore, thermal errors of shape elements such as the spindle drift or the tilt motion can't be properly and explicitly incorporated into the volumetric error model. Hence, the equivalent vector approach mainly applied to modeling geometric errors of machine tools or coordinate measuring machines.

Since the separated element approach recognizes shape elements as with real dimensions, joint elements are defined as ball screws. Although thermal errors of shape elements are incorporated into a volumetric error model successfully, the volumetric error model derived by using the separated element approach is more complex than the Eq. (12) because of Abbe error terms expressed as multiplication of the rotational errors of joint elements by the real dimensions of shape elements. The reason why the Abbe error terms are intervened can be explained as follows: As shown in Fig. 3, local coordinate systems and ball screws are located at the outside of the workspace. The distance between the ball screw axis and the workspace can be represented as dimensional information of shape elements. Therefore, in order to represent the volumetric errors within the workspace with joint errors along ball screw axes, the Abbe error terms are additionally intervened. And, the derived volumetric error model requires dimensional information of machine tools for error compensation.

Since the virtual-shape approach recognizes shape elements as hypothetical elements that have only shape errors without real dimensions, all the above disadvantages of traditional approaches are improved by introducing the virtual-shape element.

5. Conclusions

A method for modeling volumetric errors of machine tools using the virtual-shape element is proposed. Following conclusions are obtained:

1. Traditional error synthesis methods can be classified into two approaches: the equivalent vector approach and the separated element approach. Both approaches have several conflicting good and bad points in model building and parameter identification processes.

2. In order to improve the problems of the previous modeling techniques, a concept of a virtual-shape element is proposed. The virtual-shape element is defined as a hypothetical element that has only shape errors without real dimensions and expressed as the virtual-shape transformation matrix.

3. A volumetric error model for the C-shaped vertical machining center is derived on the basis of the equivalent diagram that consists of joint elements and virtual-shape elements. The derived error model includes both geometric and dominant thermal error terms explicitly.

4. In order to incorporate thermal errors of shape elements into a volumetric error model, the Abbe error terms expressed as multiplication of the rotational errors of joint elements by the real dimensions of shape elements are unavoidable in the previous method. These errors make the model building process more complex. However, by introducing the virtual-shape element, the Abbe error terms do not exist in the derived volumetric error model.

5. Since three joint transformation matrices are redefined with the errors along three axes of the reference coordinate frame by introducing the virtual-shape element, the setup location of measuring instruments for parameter identification is coincided with the origin of the reference coordinate frame established at the vertex of the workspace. This solves the difficulties in the parameter identification process.

References

[1] Weck, M., McKeown, P., Bonse, R. and Herbst, U., 1995, "Reduction and Compensation of Thermal Errors in Machine Tools," *Annals of the CIRP*, Vol. 44, No. 2, pp. 589~598.

[2] Sartori, S. and Zhang, G. X., 1995, "Geometric Error Measurement and Compensation of Machines," *Annals of the CIRP*, Vol. 44, No. 2, pp. 599~609.

[3] Ni, J., 1997, "CNC Machine Accuracy Enhancement Through Real-time Error Compensation," *Journal of Manufacturing Science and Engineering*, Vol. 119, pp. 717~725.

[4] Schultschik, R., 1977, "The Components of the Volumetric Accuracy," *Annals of the CIRP*, Vol. 25, No. 1, pp. 223~227.

[5] Zhang, G., Ouyang, R., Lu, B., Hocken, R., Veale, R. and Donmez, A., 1988, "A Displacement Method for Machine Geometry Calibration," *Annals of the CIRP*, Vol. 37, No. 1, pp. 515~518.

[6] Elshennawy, A. K. and Ham, I., 1990, "Performance Improvement in Coordinate Measuring Machines by Error Compensation," *Journal of Manufacturing Systems*, Vol. 9, No. 2, pp. 151~158.

[7] Donmez, M. A., Blomquist, D. S., Hocken, R. J., Liu, C. R. and Barash, M. M., 1986, "A General Methodology for Machine Tool Accuracy Enhancement by Error Compensation", *Precision Engineering*, Vol. 8, pp. 187~195.

[8] Ferreira, P. M. and Liu, C. R., 1993, "A Method for Estimating and Compensating Quasistatic Errors of Machine Tools," *Journal of Engineering for Industry*, Vol. 115, pp. 149~159.

[9] Chen, J. S., Yuan, J. X., Ni, J. and Wu, S. M., 1993, "Real-time Compensation for Time-variant Volumetric Errors on a Machining Center," *Journal of Engineering for Industry*, Vol. 115, pp. 472~479.

[10] Hewlett Packard, 1989, *Application Note 325-2 Machine Tool Calibration Using the HP 5528A Laser Measurement System*, Hewlett Packard, U.S.A.

[11] Lo, C. H., Yuan, J and Ni, J., 1994, "Error Link Metrology and Flexible Error Synthesis Model for Correcting Quasi-Static Machine Errors," *Transactions of NAMRI/SME*, pp. 267~273.

[12] ISO/FDIS 230-3, 2000, *Test Code for Machine Tools – Part 3 : Determination of Thermal Effects.*

IMPLEMENTATION OF THE ESTLER FACE MOTION REVERSAL TECHNIQUE USING A SINGLE PROBE

James G. Salsbury
Mitutoyo America Corporation, Aurora, IL

Abstract

An implementation of the Estler face motion reversal technique [1] is presented that allows for the separation of the axial and tilt error motions of an axis of rotation from the circular flatness of a measured part. A single probe method is used that has practical applications in testing spindle type roundness measuring instruments. The method and experimental results are presented.

Keywords: Reversal method, self-calibration, error separation, axis of rotation, surface metrology, form error, roundness measuring machine

1. Introduction

Self-calibration techniques have been shown to be effective in performing precision measurements [1]. Since new international standards are requiring the inclusion of uncertainty when demonstrating product conformance to specification [2], the application of self-calibration techniques may expand in industry. One type of self-calibration is error separation via reversal, and we have been exploring the larger role that reversal techniques may have in the general testing of the error motions of commercial metrology instruments. While the straightedge [1,3-5] and the Donaldson ball reversal [1,6-9] methods are well developed in the literature, there has been little attention given to similar reversal techniques for measuring the face motion of an axis of rotation [6,9]. In [1], the Estler face motion reversal is introduced that allows the separation of tilt and axial error motions from the circular flatness of a test part. This technique is only briefly summarized, however, and no experimental implementation is presented. In this paper, we present a practical implementation of the Estler reversal using a three setup, single probe, approach. The method is specifically applied to the testing of spindle-type roundness measuring machines.

2. Approach

The Estler face reversal described in [1] uses two measurement setups and two indicators in each setup. In our implementation only a single indicator is used. As shown in Figure 1, three setups are required with the single indicator approach. The first setup, Fig. 1(a), is the normal position measurement. In the second setup, Fig. 1(b), the reversal position, the measured part is rotated 180° about the axis of rotation and relative to the first setup. The third setup, Fig. 1(c), is the on-axis measurement. For the on-axis measurement, which measures only axial error, the orientation of the measured part is unimportant. Furthermore, the on-axis measurement is not directly involved with the reversal part of this technique but is still required for the analysis. This measurement, therefore, does not necessarily need to be done at the same time or on the same measured part as the normal and reversal measurements. This feature of the Estler face reversal differs for other common reversals, such as straightedge and Donaldson ball reversal, and presents some opportunities when reducing the technique to practice, as is discussed in the next section of this paper.

Following an analysis similar to that presented in [1], we define:

$P(R,\theta)$: circular flatness of the test part as a function of the radial (R) and angular (θ) positions.

$F(R,\theta)$: face motion of the axis of rotation.

$I_j(\theta)$: deviations measured by indicator j.

It can be shown that the part error and the face motion error can therefore be determined by:

$$P(R,\theta) = \tfrac{1}{2}\,[I_1(\theta) + I_2(\theta)] - I_3(\theta) \quad (1)$$

$$F(R,\theta) = \tfrac{1}{2}\,[I_1(\theta) - I_2(\theta)] + I_3(\theta) \quad (2)$$

The reversal method always yields both part and machine results, Eqs. (1) and (2) respectively. Our concern is specifically with testing the face motion of the measuring machine axis of rotation, and therefore we are more interested in the machine results, $F(R,\theta)$. The measured part errors, $P(R,\theta)$, are of interest when the objective is a measurement of the circular flatness of the part independent of the machine errors. We will include all results here for completeness and to demonstrate the capabilities of the technique.

3. Experiment

We used the single probe implementation of the Estler reversal to measure the face motion error of a precision roundness machine. A common, off-the-shelf, precision roundness machine might have a specification such as 20+0.4R nm (R in mm) for the maximum face motion error. We performed the reversal measurements using this class of machine in a good environment.

An uncalibrated optical flat was used as the measured part for the normal and reverse positions, Figs. 2(a) and 2(b) respectively. For the on-axis measurement, a hemisphere was used as shown in Fig. 2(c). By precisely centering the hemisphere to the axis of rotation and then crowning the indicator, measuring close to the axis of rotation (R=0) is easily possible. This ensures that axial error motion is measured with no contribution from tilt motion. Typical measurement results are shown in Figure 3.

Reversal procedures are commonly done using an average of a number of measurements to reduce variation from asynchronous motion. The results in Figure 3, however, are only a single rotational trace using a Gaussian filter with a 15 undulations per revolution (UPR) low pass cut-off. Since the measuring machine specifications are for any single measurement, additional averaging of results when testing for conformance to the specifications is not normally allowed.

For reversal techniques, the measurement uncertainty is typically dominated by the long-term reproducibility of the measurement process (for example, see [10]). The only other potentially significant source of uncertainty is the indicator and its calibration, which is the source of traceability to the unit of length for the measurement. Additional face motion tests determined the reproducibility (1σ) of the measurements is about 2 nm. This reproducibility represents the variation of any single point at a defined R and θ position.

4. Conclusions

With the increased attention to uncertainty in industrial metrology, we may start seeing more self-calibration techniques moving from the calibration laboratories to the shop floor. A practical

single probe implementation of the Estler face reversal technique was presented that has application in testing spindle-type roundness machines. The primary advantage to the technique is that uncertainty can be achieved that approaches the repeatability of the machine under test.

5. References

[1] Evans CJ, Hocken RJ, Estler WT. Self-calibration: reversal, redundancy, error separation, and absolute testing. CIRP Annals 1996;45(2):483-92.

[2] ISO 14253-1:1998, Inspection by measurement of workpieces and measuring equipment – Part 1: Decision rules for proving conformance or non-conformance with specification. International Organization for Standardization. Geneva, 1998.

[3] Estler WT. Calibration and use of optical straightedges in the metrology of precision machines. Optical Engineering 1985;24(3):372-9.

[4] Bryan JB, Carter DL. How straight is straight. American Machinist 1989;133(12):61-5.

[5] Campbell A. Measurement of lathe Z-slide straightness and parallelism using a flat land. Prec Eng 1995;17(3):207-10.

[6] Bryan J, Clouser R, Holland E. Spindle accuracy. American Machinist. Special Report No. 612. December 4, 1967.

[7] Donaldson RR. A simple method for separating spindle error from test ball roundness. CIRP Annals 1972;21:125-6.

[8] Chetwynd DG, Siddall GJ. Improving the accuracy of roundness measurement. J Physics E: Sci Instruments 1976;9:537-44.

[9] ANSI/ASME B89.3.4M-1985. Axes of Rotation. American Society of Mechanical Engineers. New York, 1985.

[10] Doiron T, Stoup J. Uncertainty and Dimensional Calibrations. J Res NIST 1997;102(6):647.

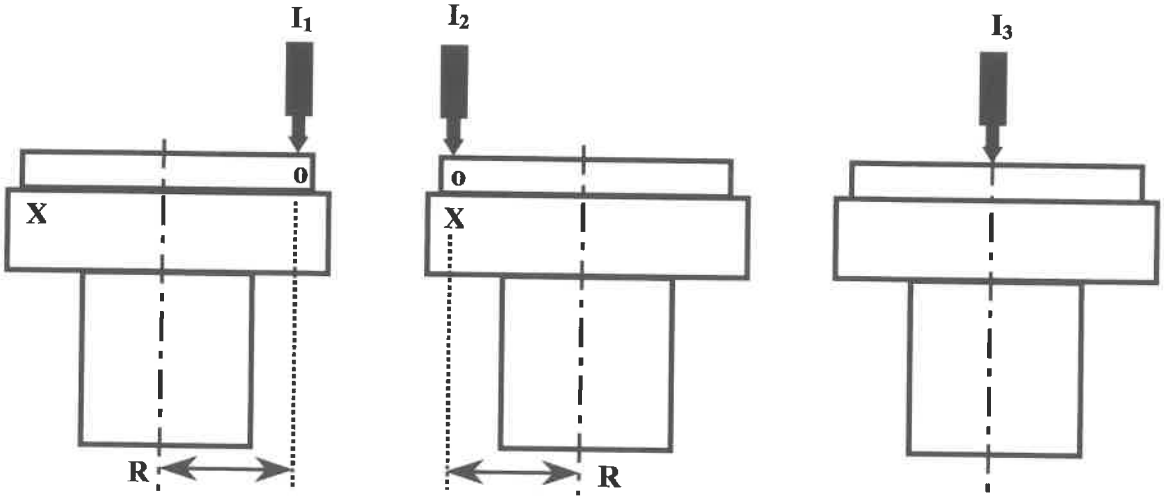

(a) normal position (b) reverse position (c) on-axis measurement

Figure 1: Estler face motion reversal implemented using three setups and a single probe.

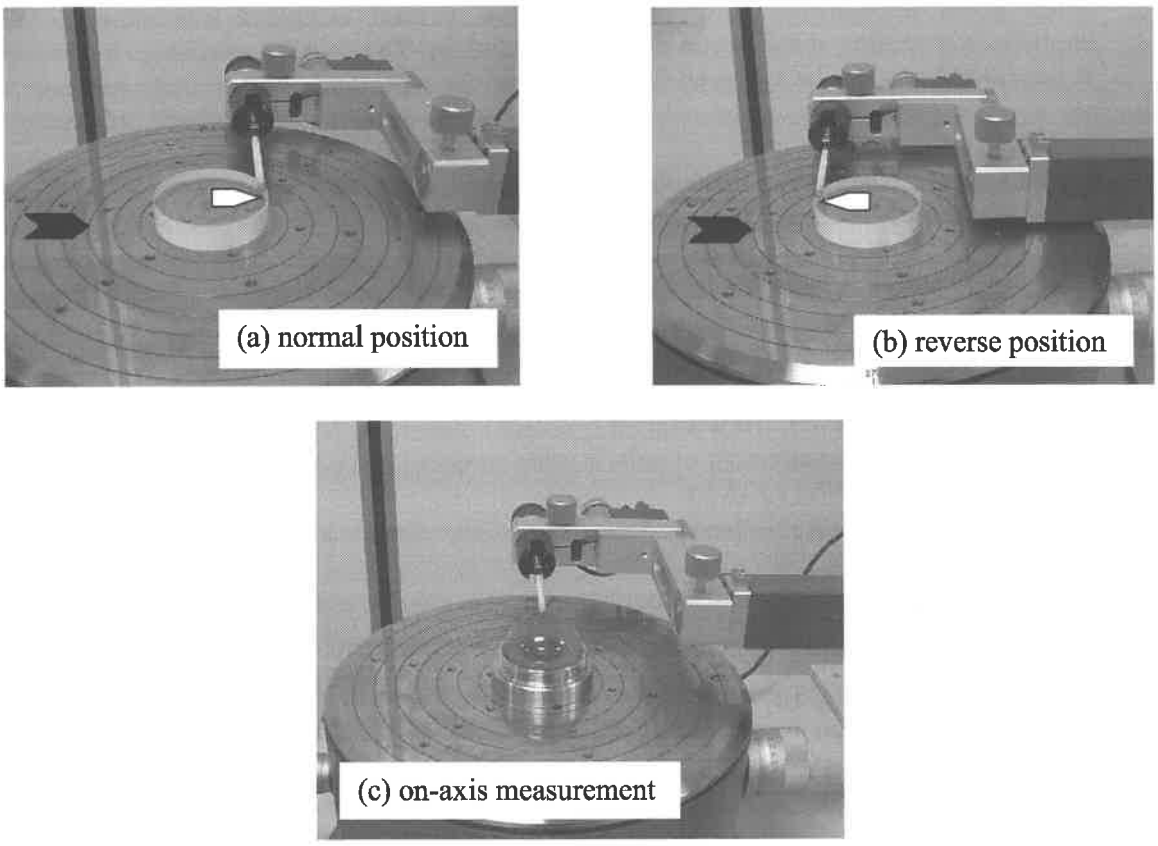

Figure 2: Example measurement setups for the single probe Estler face reversal.

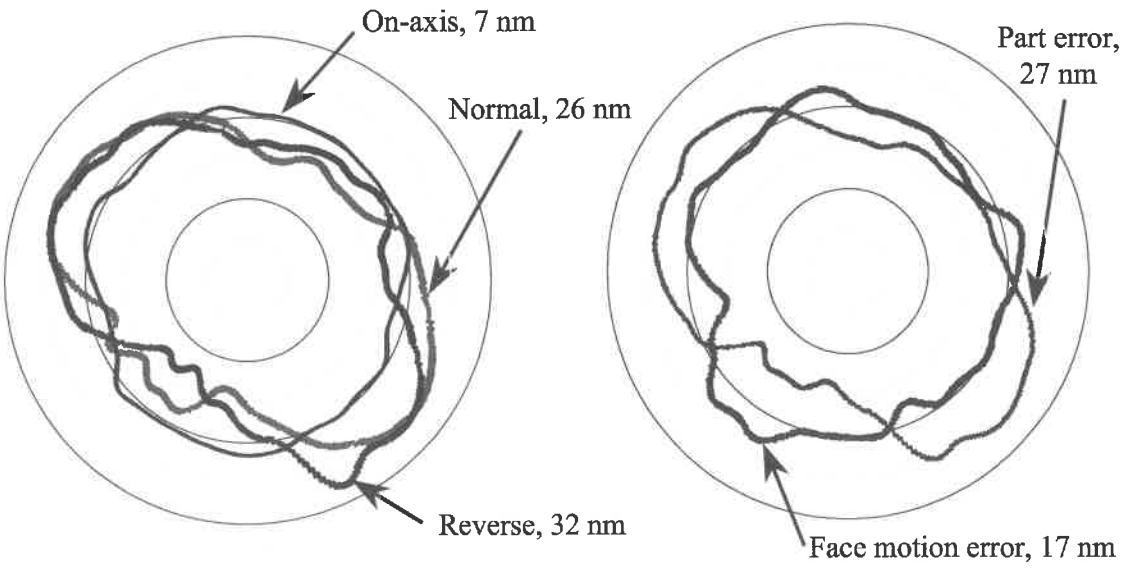

Figure 3: Typical measurement results using the single probe Estler face reversal.

Phase-measuring volumetric interferometer for three-dimensional coordinate metrology

Seung-Woo Kim*, Hyug-Gyo Rhee, Ji-Young Chu
Department of Mechanical Engineering
Korea Advanced Institute of Science and Technology
Science Town, Daejeon, 305-701, KOREA
*: Who is responsible for correspondence.
Tel: ++82-42-869-3217; Fax: ++82-42-869-3210; E-mail: swk@kaist.ac.kr

1. Introduction

In designing precision machines, it is required that displacement transducers be installed with as small Abbe offsets as possible [1]. However, the requirement is usually not satisfactorily met with widely used optical encoders and laser interferometers especially for three-dimensional coordinate measuring machines. To address the problem, the authors have recently proposed the new concept of phase-measuring volumetric interferometer that enables to accurately measure the xyz-coordinates of the probe without metrology frames [2,3]. The interferometer is composed of a movable target and a fixed photo-detector array. The target is made of point diffraction sources to emit two spherical wavefronts, whose interference is monitored by an array of photo-detectors. Phase shifting is applied to obtain the precise phase values of the photo-detectors [4,5]. Then the measured phases are fitted to a geometric model of multilateration so as to determine the xyz-location of the target by minimizing least square errors [6,7]. For description of the interferometer's geometric configuration, the global xyz-coordinate system is set so that its origin is positioned right on one of the photo-detectors as illustrated in Figure 1. The two point diffraction sources on the target are given the coordinates as (x_1, y_1, z_1) and (x_2, y_2, z_2), respectively, which are to be determined to find out the xyz-location of the target. The proposed interferometer has been designed and built with a volumetric uncertainty of less than 1.0 μm within a cubic working volume of side 100 mm. Here, in this paper we also present error sources, an evaluated uncertainty, and test results from the prototype system. Self-calibration concept of two-dimensional precision metrology stages [8,9] is applied to prove the performance of the interferometer.

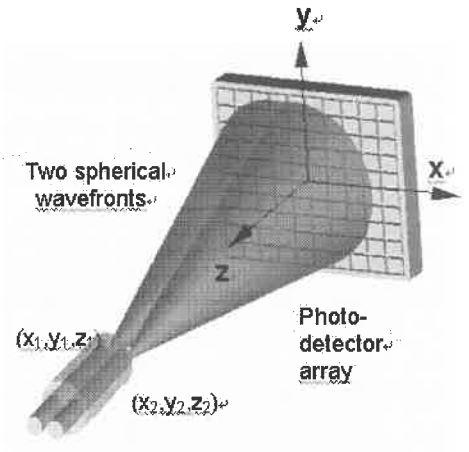

Figure 1. Geometry of the proposed volumetric interferometer.

2. Phase-measuring volumetric interferometry

The interferometric intensity field from two spherical wavefronts, referred to as u_1 and u_2, respectively, is derived as

$$I = |u_1 + u_2|^2 = \Pi + \Gamma\cos(\Phi + \Delta\phi)$$
$$\text{where } \Pi \equiv \frac{U_1^2}{r_1^2} + \frac{U_2^2}{r_2^2},\ \Gamma \equiv \frac{2U_1U_2}{r_1r_2},\ \Phi \equiv \frac{2\pi}{\lambda}(r_1 - r_2),\ \text{and } \Delta\phi \equiv (\phi_1 - \phi_2) \quad (1)$$

where U is the source strength, λ is the wavelength, φ is the initial phase, and r is the diagonal distance from the source. The subscripts 1 and 2 affixed to the variables introduced in the above derivation correspond to u_1 and u_2, respectively. The mean intensity Π, the visibility Γ, and the phase Φ of the intensity field vary with the diagonal distances, while the initial phase difference Δφ remains constant. Among the variables, the phase Φ relates to the diagonal distances most simply with the relationship of

$$\Phi(x,y,z) = \frac{2\pi}{\lambda}[r_1(x,y,z) - r_2(x,y,z)]$$
$$= \frac{2\pi}{\lambda}\{[(x_1-x)^2 + (y_1-y)^2 + (z_1-z)^2]^{1/2} - [(x_2-x)^2 + (y_2-y)^2 + (z_2-z)^2]^{1/2}\} \quad (2)$$

Eq.(2) indicates that the six unknowns (x_1, y_1, z_1) and (x_2, y_2, z_2) can be determined by solving inverse kinematics if the absolute value of Φ is provided from more than six different locations. For that, a two-dimensional array of photo-detectors is deployed to capture the interferometric intensity I at multiple locations. From the measured intensity, the phase $\Phi+\Delta\phi$ of Eq.(1) is computed by applying the well-established phase measuring technique with phase shifting. For description, let us introduce the superscript k so that Φ^k refers to the computed value of Φ at the location of (x^k, y^k, z^k). Now, all the measured values of Φ^k are processed to be unwrapped, starting from a particular reference principal phase value that is for convenience designated as Φ^0 at location (x^0, y^0, z^0). Then, a new variable Λ^k is defined such as

$$\Lambda^k = \frac{\lambda}{2\pi}[(\Phi^k + \Delta\phi) - (\Phi^0 + \Delta\phi)] = \frac{\lambda}{2\pi}[\Phi^k - \Phi^0] \tag{3}$$

Now, as the final step for absolute distance measurements, using the relationship of Eq.(3), the six unknowns (x_1, y_1, z_1) and (x_2, y_2, z_2) are determined so as to minimize the cost function that is defined as

$$E = \sum_k [\frac{\lambda}{2\pi}(\Phi^k - \Phi^0) - \hat{\Lambda}^k]^2 \tag{4}$$

Note that the summation over k in the above expression is performed all over the photo-detectors to be considered, and $\hat{\Lambda}^k$ represents the actually measured value of Λ^k. The cost function E is so highly nonlinear in terms of the unknowns (x_1, y_1, z_1) and (x_2, y_2, z_2) that no explicit solutions exist for the minimization. Thus, numerical technique is used to search for the global minimum of the cost function[2],[3].

3. Error analysis

For the estimation of measurement uncertainty, a thorough analysis has been made following the ISO's guide to the expression of measurement uncertainty [10]. The major sources of errors considered are listed in Table 1 along with their individual contributions determined through appropriate error models or experiments. All the error sources in Table 1 are divided into two groups according to whether their individual influences are directed to phase or displacement. All the listed uncertainties represent the worst cases that could possibly occur over the whole working volume and they are given in terms of standard deviation. The total uncertainty is worked out to be 420 nm for x-, 550 nm for y-, and 9.7 nm for z-directions when we use a 640 × 480 CCD as a photo-detector array. The CCD array used for the evaluation has an overall dimension of 6.4 mm in the x-direction and 4.8 mm in the y-direction, so the larger x-dimension takes more phase information resulting in better uncertainty in the x-direction. The z-direction has the best result as the cost function defined in Eq.(4) turns out to be most sensitive to the z-coordinate.

Table 1. Error sources and their contributions to the overall uncertainty of the absolute distance interferometer.

Classification	Error sources	Input condition	Output uncertainty
Phase errors	Laser intensity stability	≤ 0.07% of Π	0.0071 rad.
	Temperature variation in the fiber	≤ 0.01K	0.0084 rad.
	Low frequency pressure variation in the fiber	≤ 8×10^{-4} rad.	5×10^{-5} rad.
	Nonlinearity of fiber elongation & PZT	≤ 0.15 rad.	0.009 rad.
	Electrical noise	≤ 0.7% of Π	0.005 rad.
	Detector nonlinearity	≤ 0.8% of Π	0.023 rad.
Displacement errors	Sphericity of the spherical wave	≤ 1×10^{-5} rad.	4×10^{-3} nm
	Laser frequency stability	≤ 1 MHz	1.3×10^{-6} nm
	Air refractive index variation	≤ 10^{-7}	6.3×10^{-5} nm
	Detector position error	≤ 100 nm	8×10^{-2}nm

This uncertainty analysis also reveals an important fact that from the viewpoint of the system design, the size of the CCD array is one of the most influencing parameters. The uncertainty especially in the x- and y-directions drastically improves as the size of the CCD arrays is enlarged. For instance, if a 2048 × 2048

array is used, the uncertainty in the x- and y-directions reaches 20 nm, almost the same level of the z-direction.

4. Measurement results

A prototype volumetric interferometer has been set up on a two-dimensional precision stage as illustrated in Figure 2. For testing, the target emitting two spherical wavefronts is fixed on the granite table and the CCD photo-detector

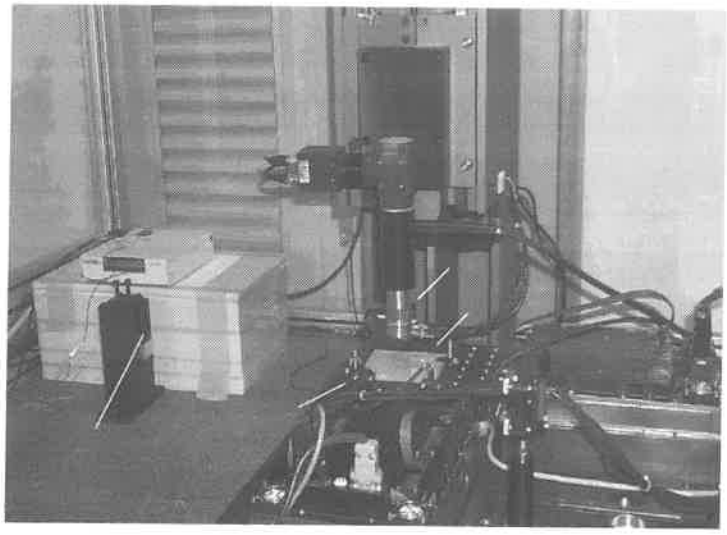

Figure 2. Photographic view of the two-dimensional stage with the volumetric interferometer.

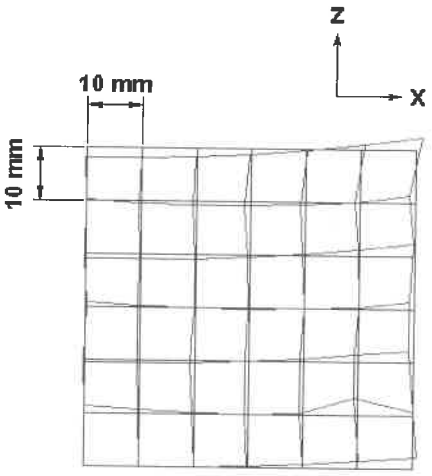

Figure 3. Deviation map between the optical scale reading and the volumetric interferometer result.

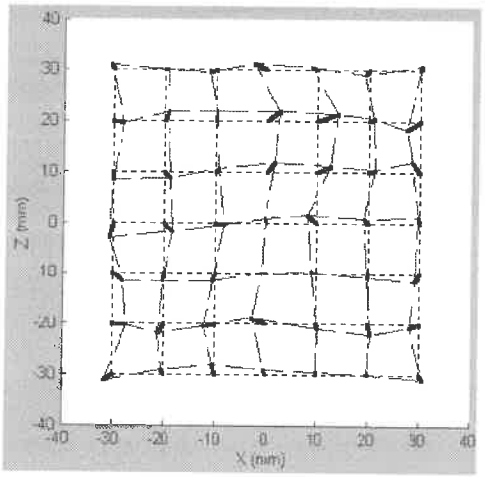

(a) The systematic error of the two-dimensional optical scale.

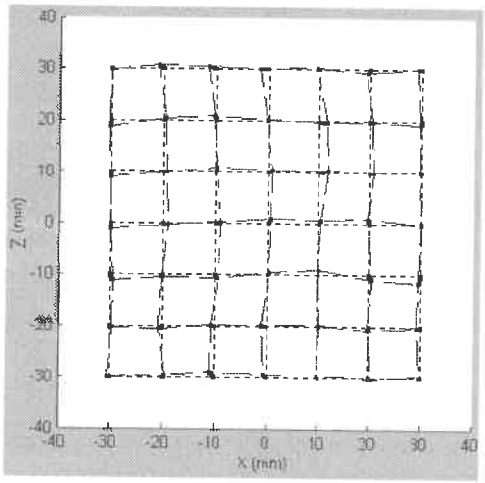

(b) The systematic error of the volumetric interferometer.

Figure 4. The reconstructed systematic error using the Fourier self-calibration algorithm.

array is attached to the moving stage. An artifact made of glass plate We also use the 7×7 array made by an electron beam lithograph system as. The readings of the optical linear scales installed on the measurement axes of the stage

are taken as the initial values of the numerical search of the interferometer, so the convergence to true xyz-coordinates can be accelerated. Figure 3 shows the differences between the readings of the optical scale and the results of the interferometer at each node point of the artifact plate. Test results was obtained within 60mm × 60mm working area, in which the maximum deviations were measured 0.48 μm for x- and 1.3 μm for z-direction. However this deviation map does not mean the error of the volumetric interferometer because it includes many error sources such as the alignment error between two metrology frame, the optical scale's systematic error, scale factor, and random measurement noise.

To remove these effects and extract the systematic error of the proposed interferometer, we applied the Fourier self-calibration algorithm[9]. When we obtained the coordinates of each node for calibration, we used averaging technique to reduce the random noise effect. Figure 4 (a) shows the systematic error of the two-dimensional optical scale, in which the absolute values of the maximum error were measured 2.0 μm for x- and 1.5 μm for z-direction. On the other hand, Figure 4 (b) shows the systematic error of the interferometer, in which the absolute values of the maximum error were measured 0.87 μm for x- and 0.82 μm for z-direction. Through a repeat test of self-calibration, we confirm that the reconstructed systematic error has reasonable repeatability.

5. Summary

A volumetric interferometer has been developed and tested. The interferometer consists of two optical fibers held on the target to emit two identical monochromatic spherical wavefronts with a lateral offset and a two-dimensional array of photo-detectors to monitor the interference of the two spherical wavefronts. The xyz-coordinates of each fiber's end are determined by fitting the measured phase values to a geometric model of multilateration so as to minimize least square errors. A prototype demonstrates that the proposed interferometry is capable of measuring the xyz-coordinates of the target with a volumetric uncertainty of less than 1 μm, which will be further improved to a level of 0.1 μm if large size photo-detector arrays are used. In addition, the systematic errors of the interferometer have been identified adopting the concept of self-calibration, and the maximum error was 870 nm within a working area of 60 mm x 60 mm x 20 mm.

6. Acknowledgment

The work published here has been conducted as part of the national Creative Research Initiatives program sponsored by the Ministry of Science and Technology of the Republic of Korea.

References

[1] J. B. Bryan, "The Abbe principle revisited," An updated interpretation, Prec. Eng., **1**(3), 129(1979).
[2] S.W. Kim and H.G. Rhee, "Phase measuring volumetric interferometry for three-dimensional coordinate metrology, " Proc. of 2nd euspen international conference, **1**, 230(2001).
[3] S.W. Kim, "New Design of Precision CMM based upon Volumetric Phase-Measuring Interferometry," Ann. CIRP, **51**(1), 357(2001).
[4] J.C. Wyant, "Interferometric optical metrology: basic principles and new systems," Laser Focus, **18**, 65(1982).
[5] P. de Groot, "Deviation of algorithms for phase-shifting interferometry using the concept of a data-sampling window," Appl. Opt., **34**, 4723(1995).
[6] O. Nakamura and M. Goto, "Four-beam laser interferometry for three-dimensional microscopic coordinate measurement," Appl. Opt., **33**(1), 31(1994).
[7] E. B. Hughes, A Wilson, and G. N. Peggs, "Design of a high-accuracy CMM based on multi-lateration techniques," Ann. CIRP, **49**(1), 391(2000).
[8] M. R. Raugh, "Absolute two-dimensional sub-micron metrology for electron beam lithography : A theory of calibration with applications," Prec. Eng. **7**(1), 3(1985).
[9] J. Ye, M. Takac, C. N. Berglund, G. Owen, and R. F. Pease, "An exact algorithm for self-calibration of two-dimensional precision metrology stages," Prec. Eng., **20**(1), 16(1997).
[10] ISO, "Guide to the expression of uncertainty in measurement," International vocabulary of basic and general terms in metrology, 2nd edition, (1993).

Finite Element and Experimental Validation of Stiffness Analysis of Precision Feedback Spring and Flexure Tube of Jet Pipe Electrohydraulic Servovalve

M. Singaperumal*, Somashekhar. S. Hiremath* R. Krishna Kumar**
*Precision Engineering and Instrumentation Laboratory
**Manufacturing Engineering Section
Indian Institute of Technology Madras
Chennai - 6000 36 (India).

Abstract Electrohydraulic servovalve has a major part to play in feedback control system. The feedback spring and flexure tube elements are identified as more critical spring elements in servovalve operation. If these elements are properly designed with respect to stiffness, automatically dynamic performance of the servovalve is improved. Hence an attempt has been made to predict the stiffness of these elements by finite element method. The solid model of these components are carried out in IDEAS-Master module and simulated with appropriate boundary conditions. Also an experimental prototype model is designed and fabricated to test these precise components .The obtained results are validated with FEM results. The FEM gives complete behavior of these components. Results related to stress concentration areas due to loading are also included in the paper.

Key words: jet pipe, servovalve, solid model, stiffness and simulation.

1. INTRODUCTION

Fluid power control, that is the transmission and control of energy by means of a pressurized fluid, is an old and well recognized discipline. The growth of fluid power has accelerated with our desires to control ever increasing quantities of power and mass with higher speeds and greater precision. More specifically, where precise motion control is desired and space and weight are limited, the convenience of high power-to-weight ratio makes hydraulic servomechanisms the ideal control elements. The demand to achieve more accurate and faster control at high power levels, especially in the areas of machine tools, primary flight controls, and automatic fire control produced an ideal marriage of hydraulic servomechanisms with electronic signal processing. Information could be transuded, generated, and processed more easily in the electronic medium than as pure mechanical or fluid signals, while the delivery of power at high speeds could be accomplished best by the hydraulic servo. This marriage of electronics and hydraulics into electrohydraulic servomechanisms created both a solution to an existing class of control problems and a demand for a whole new strain of components [1]. An electrohydraulic servo valve is a transducer. It transforms an electrical signal into hydraulic power. This is not done directly. An intermediate conversion to mechanical motion is first made by means of an electromagnetic torque motor and this is then used to stroke the mechanical control element of the valve. Originally, solenoids were used to directly move the spool, but this requires a relatively long stroke. It also requires large forces to overcome friction and flow forces. In order to ensure sufficiently low time constants, except for very small systems, therefore, it is necessary to use the torque motor to drive the pilot stage or hydraulic amplifier which in turn strokes the power spool [2]. A very wide range electrohydraulic flow control valves have been employed and comprehensive reviews been published by Shute and Turnbull [3] and [4]. A varied range of designs have been described by Himmler [5]. The modern valve is a two-stage device, invariably employing feedback from the second stage to the first stage, which is controlled by an electric torque motor. The analyzed valve is a two-stage jet pipe electrohydraulic flow control servovalve, converts an electrical signal to precise proportional hydraulic flow. The jet pipe servo valve serves to convert pressure energy into the kinetic energy of a jet and directs this jet towards two closely spaced receiver holes in the receiver block [6]. When the jet of oil strikes the flat receiver block, its kinetic energy is recovered in the form of pressure. If the stream is directed exactly halfway between the receiver holes, the pressure in the two holes will be equal; the differential pressure, therefore, is zero. As the jet pipe is deflected, more oil will be directed at one hole than the

other, raising the pressure in that hole and decreasing the pressure on the other, and thus creating a differential-pressure output. Due to this differential pressure, the spool moves and opens pressure port 'P' to one control port 'C1'; opens other control port 'C2' to return line 'R'. During spool movement, it pushes the end of a feedback spring, creating a restoring torque on jet pipe. As the feedback torque becomes equal to torque from magnetic forces, jet pipe moves back to centered position (null position).Spool stops at a position where feedback spring torque equals torque due to input current. Therefore, spool position is proportional to input current.

The static recovery pressure in receiving holes is a function of jet pipe nozzle displacement relative to receiver plate. The recovery pressure depends on web thickness, jet pipe nozzle diameter, receivers hole diameter, nozzle offset and nozzle stand-of distance. A detailed static recovery pressure analysis of a two stage, four-way, closed ports electrohydraulic flow control valve considering the effect of web thickness, nozzle diameter, receiver hole diameter and offset parameters and also the effect of supply pressure on recovery pressure are presented in the paper [7].

The servovalve can be separated into two stages:

- The first stage pilot includes the torque motor, jet pipe, flexure tube and receiver holes.
- The second stage body includes the spool and sleeve assembly.

The schematic view of jet pipe electrohydraulic servovalve is shown in Figure 1.

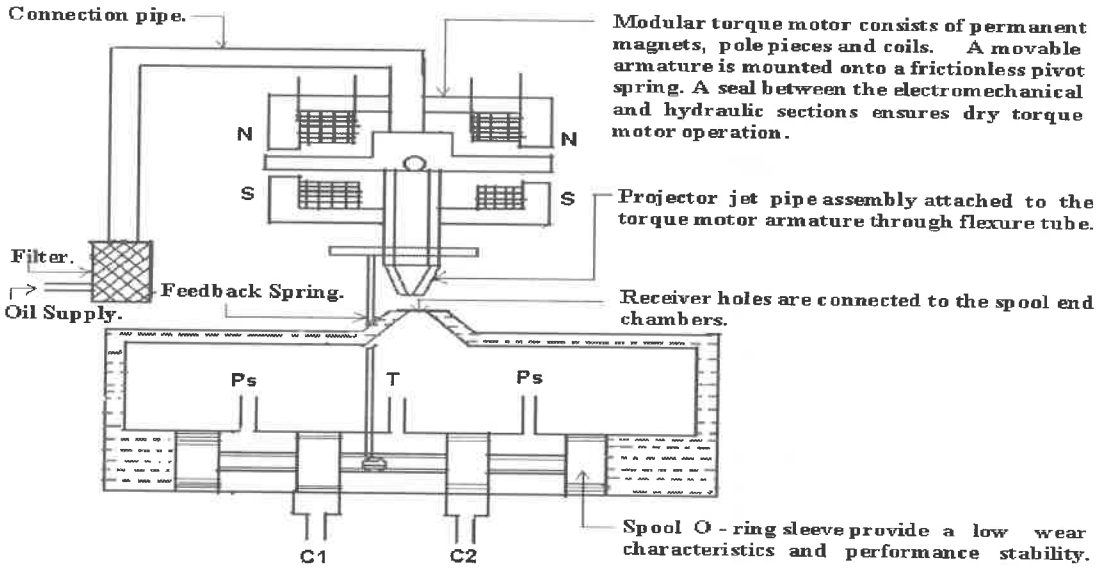
Connection pipe.
Modular torque motor consists of permanent magnets, pole pieces and coils. A movable armature is mounted onto a frictionless pivot spring. A seal between the electromechanical and hydraulic sections ensures dry torque motor operation.
N
N
S
S
Projector jet pipe assembly attached to the torque motor armature through flexure tube.
Filter.
Feedback Spring.
Oil Supply.
Receiver holes are connected to the spool end chambers.
Ps
T
Ps
Spool O - ring sleeve provide a low wear characteristics and performance stability.
C1
C2

Figure 1: Schematic view of jet pipe servovalve.

2.0 FINITE ELEMENT METHOD

Complete solid model of the servovalve was created in SDRC IDEAS and simulated with suitable materials, boundary and loading conditions.

2.1 Finite element method for finding the feedback spring stiffness

Feedback spring is a more critical element in the servo valve operation. Its stiffness plays a dominant role in establishing the static and dynamic valve characteristics. So an attempt has been made to predict the stiffness and stress distribution in the feedback spring. The FE analysis is carried out with suitable assumptions for the material property, boundary and loading conditions.

Material properties:

AISI Type 440C $\rho = 7.8E03\ kg/m^3$ $\upsilon = 0.27$ & $E = 2.0E11\ N/m^2$

Boundary and Loading Conditions:

All degrees of freedom on the surface of spring guide are arrested since it is press fitted with nozzle. A maximum nodal force of 0.27 N such that the free end of the feedback spring deflects by 0.85 mm. This corresponds to the desired maximum spool displacement in the valve assembly.

Element type:

Beam elements of varying cross sections are used for feedback spring, due to its cantilever type of operation. Thin shell elements are used for spring support and spring guide, since they are very thin compared to other dimensions. Multipoint constraints are used to connect shell element nodes to beam element.

Number of Elements generated: 311 Number of Nodes generated : 361.

The finite element mesh, loading and boundary conditions are as shown in Figure 2. The deformed FE model and stress distribution model are as shown in Figure 3. The stresses are highest at the plate corners, bush sides and feedback spring end where it is fixed to the feedback spring plate.

Figure 2: Finite Element model of Feedback spring assembly.

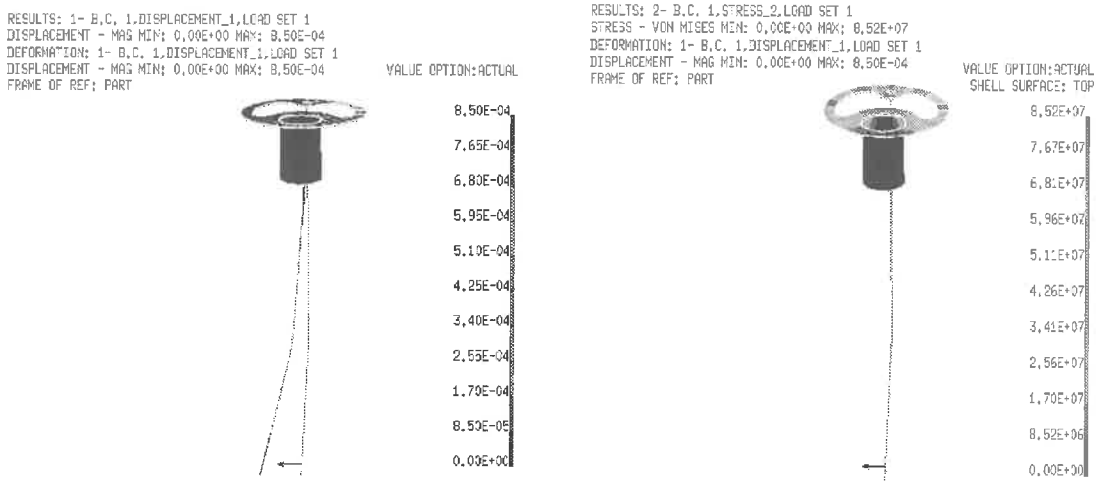

Figure 3: Deformed FE model showing the displacement (meter) and von-misses stress contour (N/m^2).

Since the load required deflecting the feedback spring to the desired deflection of 0.85 mm as 0.27N, the stiffness of the spring is found to be 0.3176 N/mm.

2.1 Finite Element Method for finding the Flexure tube Stiffness in jet pipe assembly

The jet pipe is supported by a thin flexure tube element and flexure tube acts as a seal between the electromagnetic and hydraulic sections of the servovalve. Its stiffness also plays a dominant role in servovalve operation. The applied motion (force) is transmitted from armature to armature bush to flexure tube to jet pipe. Similarly the restoring torque, from jet pipe through flexure tube to armature bush and armature. If the flexure tube is not properly designed with regard to stiffness, the servovalve operation is affected. The FE analysis gives us the stiffness as well as failure areas during operation.

Material properties

Flexure tube: Beryllium copper $\rho = 8.8E03$ kg/m^3 $\upsilon = 0.34$ & $E = 1.17E11$ N/m^2

Jet pipe: AISI 316: $\rho = 8.0E03$ kg/m^3 $\upsilon = 0.27$ & $E = 1.93E11$ N/m^2

Armature, Connection pipe and support spring: AISI 440 C

Armature bush: Brass IS 319: $\rho = 7.820E03$ kg/m^3 $\upsilon = 0.34$ & $E = 1E11$ N/m^2

Boundary and Loading Conditions

All degrees of freedom on the bottom surface of flexure tube, connection pipe and support spring are clamped

A force of ± 2.7818 N is applied on armature to get required jet pipe deflection as 0.1775 mm.

Element type

Beam elements of varying cross sections are used for jet pipe due to its cantilever type of operation. Thin shell elements are used for armature, armature bush, flexure tube. Multipoint constraints are used to connect shell element node to beam element nodes.

The complete FE model, with all boundary conditions is as shown in Figure 4. The deformed FE model and stress distribution is shown in Figure 5.

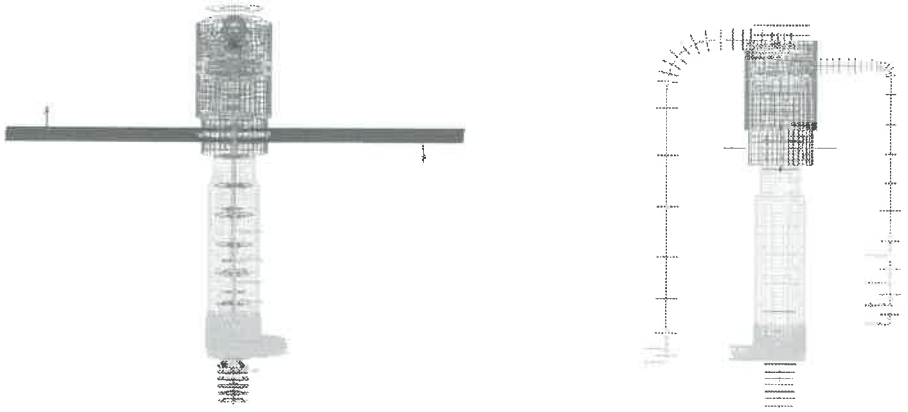

Figure 4 : Finite element model of jet pipe assembly.

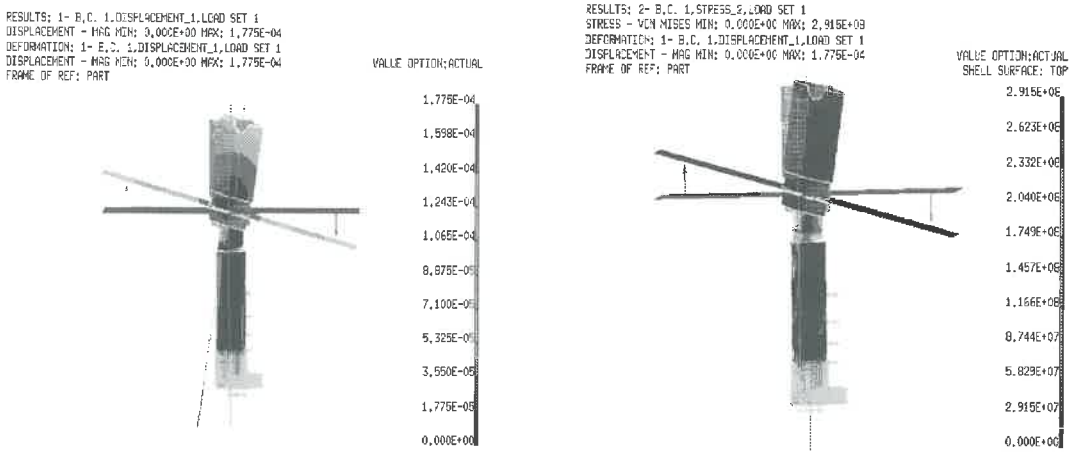

Figure 5 : Deformed FE model showing the displacement (meter) and von-misses stress contour (N/m^2).

Since a force of 2.7818 N is required to deflect the jet pipe through 0.1775 mm, the stiffness of the flexure tube is 15.672112 N/mm.

3.0 EXPERIMENTATION

The Finite element results as obtained above are validated with experimentation by designing and fabricating precise test rigs and conducted the experiments with great care regarding the application of load using the load cell and measuring the deflections with non contact displacement transducers.

3.1 Feed back spring stiffness

Figure 6 shows the experimental prototype model, fixture is designed with very careful consideration to hold the feedback spring and allow the movement in one direction (in the loading direction). The load was increased and decreased gradually and several trials were conducted.

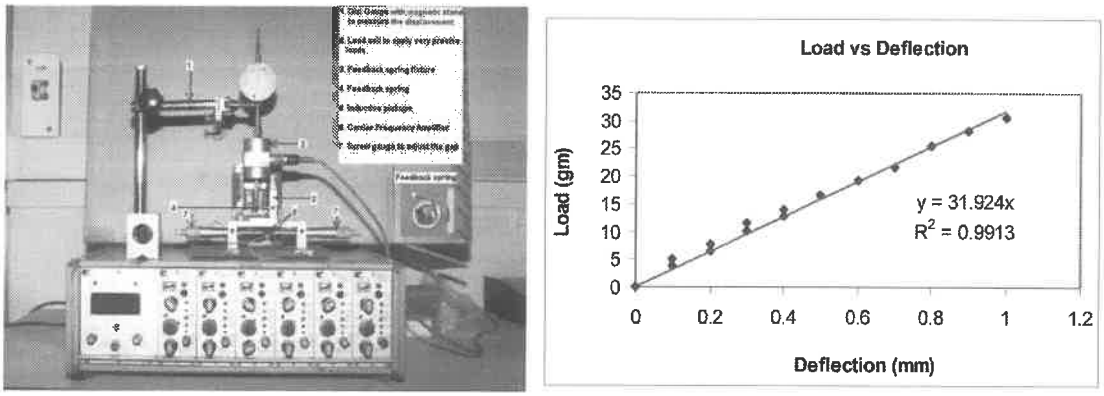

Figure 6: Experimental setup and obtained results during loading of the feedback spring.

So from the experimentation, it was found that the load required deflecting the feedback spring to 1 mm as 31.7 gm = 0.317 N and hence the stiffness of the spring was found to be 0.317 N/mm.

3.2 Jet pipe assembly testing

The test bench is designed with great consideration regarding the sensing of the jet pipe deflection using inductive pickups and point load application exactly at the required position on the armature. Figure 7 shows the photographic view of test bench. Several trials were conducted.

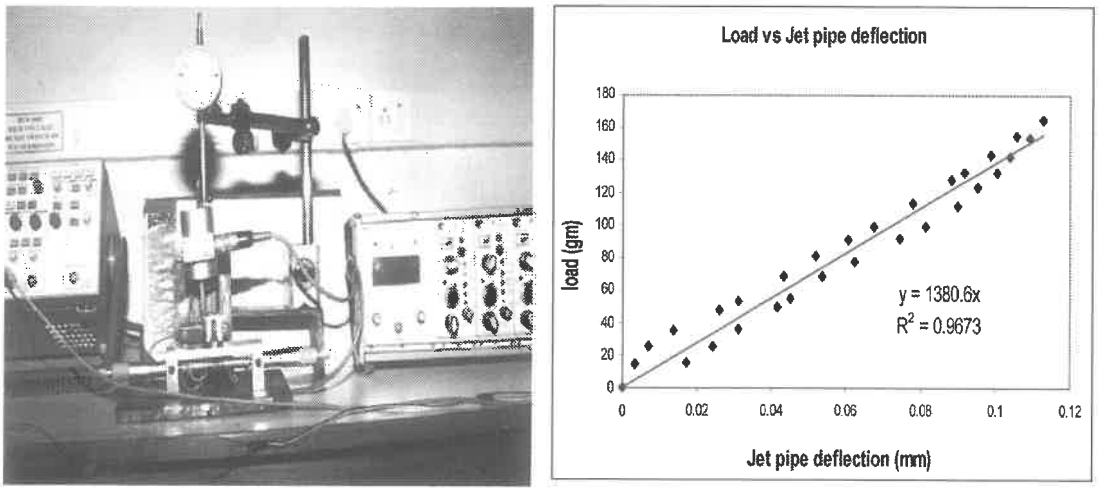

Figure 7: Experimental setup and obtained results during loading of the jet pipe assembly.

One set of obtained results are shown in Figure 7. The scattered points show the experimentally obtained values. Finally the best line is fitted to these obtained results.

The load required deflecting the jet pipe (δ) to 0.1085mm as 165.9492 gm =1.659492 N and hence the stiffness of the flexure tube was found to be 15.29 N/mm.

The comparative statement of FEM and experimentally obtained values are as shown in Table 1.

Table 1: Comparison of FEM and Experimental Results.

Components	Parameter	FEM	Experimental	Error (%)
Feedback Spring	Stiffness (N/mm)	0.3176	0.317	0.1889
Flexure Tube	Stiffness (N/mm)	15.67	15.29	2.425

CONCLUSIONS

From the analysis made, the following conclusions may be drawn concerning the adequacy of the finite element model and laboratory model for predicting stiffness of critical components:

- The stiffness of the feedback spring estimated by FEM model agreed well with the experimentally tested spring. From the stress distribution result it was found the more stress concentration areas are at curved areas at the spring plate, spring bottom side where it is fixed to the spring plate and sides of the spring guide due to its cantilever action.
- The FEM and experimental value of the stiffness of flexure tube was also found to be in good agreement. Stresses are very high where cross section change occurs. Flexure tube thickness plays a dominant role in operation.
- The developed laboratory model can also be used for dynamic testing of the servovalve.

REFERENCES

[1] Maskrey, R. H, Thayer, W.J, A brief history of electrohydraulic servomechanisms, Transactions of the ASME, June 1978, volume 100, page 110-116.

[2] Allen, C. M., Electrohydraulic Servomechanisms, McGraw-Hill, New York (1963).

[3] Shute, N.. A and Turnbull, D. E. " A review of some of the characteristics of current American electrohydraulic and electropneumatic servovalves", BHRA Report TN 650, 1960 (January).

[4] Guillon, M. Hydraulic servosystems-Analysis and design, Butterworths, London (1969).

[5] Himmler, C. R. Electrohydraulische Steuersysteme , Krausskopf-Verlag, Mainz (1969).

[6] Somashekhar. S. H, Singaperumal. M. and Krishna Kumar R, Solid modeling and parametric evaluation of two stage jet pipe flow control valve, Proceeding of the Seventh Scandinavian International Conference on Fluid Power, Linking, Sweden, May 30- June 1, 2001, volume 1, page 67-75.

[7] Somashekhar. S. H., Singaperumal. M., Krishna Kumar. R, Design parameters and their optimization to get maximum pressure recovery in two stage jet pipe electrohydraulic servovalve, Proceedings of the 49th National conference on Fluid Power, March 19-21, 2002, NCFP I02-27.6/ SAE OH 2002-01-1462, pp. 725-730.

EVALUATION OF TASK SPECIFIC UNCERTAINTY FOR CMM MEASUREMENTS

Siva Venkatachalam, Babu Uppiliappan and Jay Raja
Center for Precision Metrology
Department of Mechanical Engineering and Engineering Science
The University of North Carolina at Charlotte
Charlotte, NC 28223.

Introduction

The evaluation of measurement uncertainty is complex as there are a variety of sources of errors and variation. The task of combining all the sources of errors, according to the guidelines in GUM [1], to come up with an uncertainty budget is not an easy one. There is no single uncertainty statement that can be generally applied to all CMMs. The uncertainty for every individual CMM is specific to a particular task and depends on various issues like sampling strategies, probe errors, residual systematic errors, fitting algorithms used and the ambient conditions.

There are a couple of approaches to evaluate measurement uncertainty for a CMM that are currently in use. The first method involves extracting all possible information from the performance evaluation of a CMM to estimate the measurement uncertainty. This method is however not always feasible for the reason that the performance evaluation is done for the total working volume of the machine. The measurement, however, is done at a certain location within the working volume, which is why the evaluation results cannot be translated into uncertainty estimates. The second method involves the comparison of the part under study to a well-calibrated artifact. The selected artifact must be, in reasonable measures, identical to the part under study. The ambient conditions for measurement of the artifact and the part under study must be identical to the extent possible. This method can give good estimates of measurement uncertainty if the artifact corresponding to the part is available. The obvious drawback to this method is the non-availability of well-calibrated artifacts for every part manufactured.

Virtual CMM and Computer Simulation

The work presented in this paper demonstrates the use of computer simulation to determine the measurement uncertainty for CMM measurements. The idea behind this approach is to simulate the conditions of measurement identical to the actual measurement conditions to a reasonable degree. Fig. 1 shows the schematic of the approach adopted.

Initial set-up

The implementation of the virtual simulation has been done with the aid of Matlab®. The initial task is to set-up the working volume of the measuring machine. The maximum possible travel by the X, Y and the Z axis make up the working volume of the coordinate measuring machine. All the measurements are made within the working volume of the CMM. The machine zero is fixed and this will constitute the machine coordinate system for the measurements. The virtual part is

simulated based on the part drawing and placed on the virtual CMM. This is done by first setting up the part zero with reference to the machine origin. The bounding values of the various elements constituting the part are established and so are the datum planes. The part, in general, is constituted of elements like lines, planes circles, cylinders, cones and spheres.

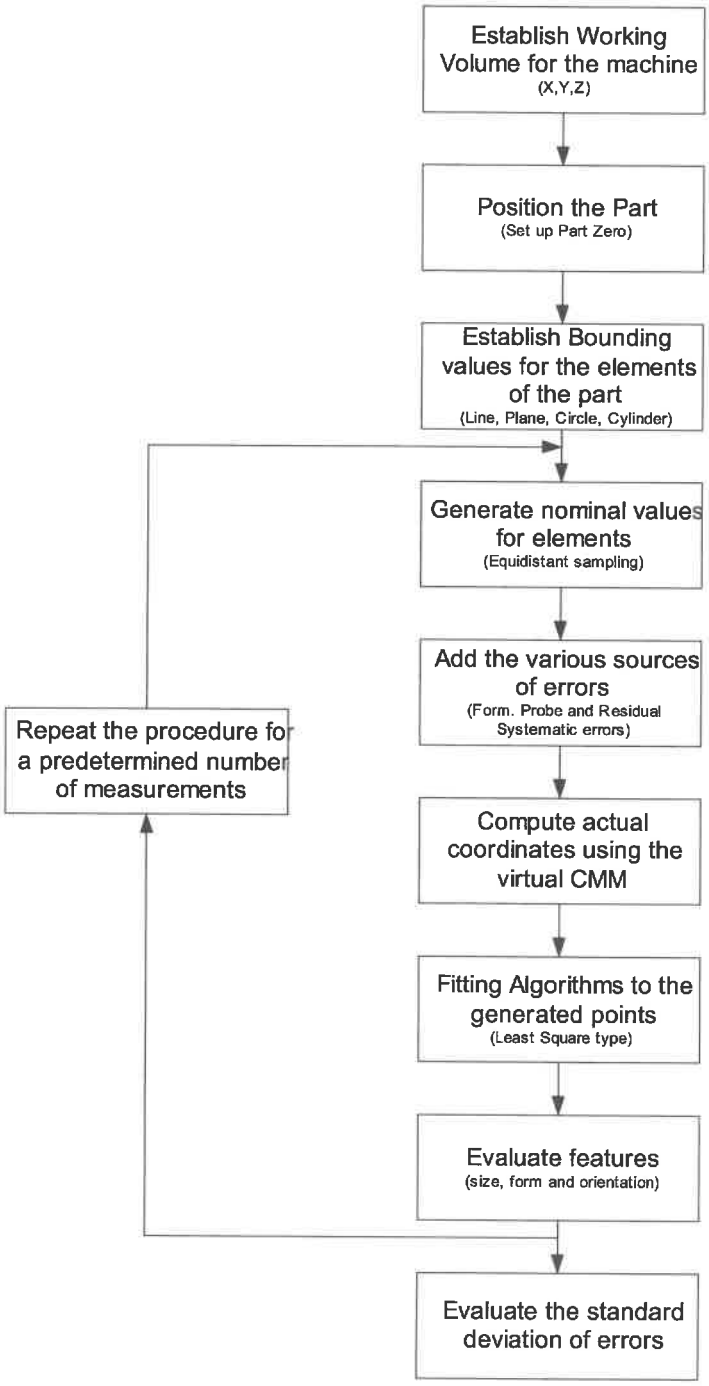
Establish Working Volume for the machine (X,Y,Z)
Position the Part (Set up Part Zero)
Establish Bounding values for the elements of the part (Line, Plane, Circle, Cylinder)
Generate nominal values for elements (Equidistant sampling)
Add the various sources of errors (Form. Probe and Residual Systematic errors)
Compute actual coordinates using the virtual CMM
Fitting Algorithms to the generated points (Least Square type)
Evaluate features (size, form and orientation)
Evaluate the standard deviation of errors
Repeat the procedure for a predetermined number of measurements

Fig. 1 The Virtual CMM approach

Virtual measurement

The measurement process starts by generating the nominal values using equidistant sampling. There are other techniques of sampling like the random sampling, stratified sampling etc. that could be used. The various errors are then modeled based on the nature of errors. The form error on the part is modeled as a sine wave with the required amplitude and the no. of cycles. The probe error is modeled as a uniform distribution with the required amplitude of the density function. Noise is added according to a Gaussian distribution with the required confidence level and the amplitude of the density function.

The virtual CMM developed by Babu [2] was used for the determination of measurement uncertainty in measuring features on the virtual part. The parametric errors were determined by using a calibrated ball step gage which is a 1-D array of precision spheres. The function of the virtual CMM is to determine the coordinates of a point as if it were measured on an actual CMM.

The nominal values of the measurements with the form, probe, systematic and random errors are fed into the virtual CMM. The resulting values are the actual values of the measurement. The substitute geometry for each of the elements is then determined by appropriate fitting algorithms. Least square fitting algorithms [3] were used for the purpose of this research since these algorithms are very well established and also easy for implementation. Once the elements are established, various features can be measured either in a single element or a combination of elements. Various features like perpendicularity, parallelism and angularity (orientation), circularity, flatness, straightness and cylindricity (form) could be determined. The diameter of a circle (size) or the distance between two points (length) could also be evaluated.

The procedure described above is repeated for a predetermined number of measurements and the resulting errors are analyzed by statistical tools to get an estimate of the standard deviation. The results are plotted and the measurement uncertainty is reported with a coverage factor.

Results and Conclusion

The above procedure to estimate the measurement uncertainty is used to evaluate the diameter and form measurement of a circular feature measured on the CMM.

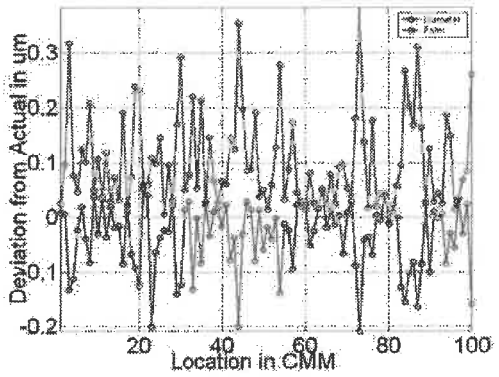

Fig. 2 Measurement Uncertainty for a circle measured at 100 locations in the XY plane
Uncertainty in Diameter: 50mm (nom) – 0.379 μm (2σ) Form – 1.002 μm (2σ)

First the nominal circle is generated with inputs being the specified diameter, measurement plane and the center point (x_0, y_0, z_0). The actual coordinates are then obtained by feeding the nominal values to the Virtual CMM. A least squares circle is fitted to the actual coordinates obtained and the diameter and form error are computed. The errors indicate the deviation from the nominal values of measurement. This procedure is repeated for a specified number of measurements (in this case, 100) and the values are plotted as shown in Fig. 2. The measurement uncertainty is reported as a standard deviation of the parameters measured namely, diameter and form errors. There is also an ongoing effort to include characteristics like size and orientation (perpendicularity, parallelism and angularity) for planar features.

The procedure for evaluating the measurement uncertainty using a Virtual CMM and computer simulation is a practical approach. However the various errors modeled here are simple and a more detailed error analysis should give better estimations. The errors can be modeled and plugged in to this routine by writing more detailed M-files to give the expected results.

References

1. ISO, 1993, Guide to Expression of Uncertainty in Measurement, International Organization for Standardization, Geneva.
2. Uppiliappan, B., "A Method to Estimate task Specific Uncertainty for Coordinate Measuring Machine (CMM) Measurements," PhD Thesis, University of North Carolina at Charlotte, 2001.
3. Forbes, B. A., "Least Squares Best Fir Geometric Elements," NPL report DITC 140/89, April 1989.

A Study on a Novel Tool Temperature Measurement Method in High-Speed Machining of Titanium

Xingquan Zhang, Kazuo Yamazaki, Yoshitaka Yamaguchi
IMS-Mechatronics Laboratory, Department of Mechanical and Aeronautical Engineering
University of California, Davis, CA 95616

INTRODUCTION

Due to their superior mechanical properties, heat resistance and exceptional corrosion resistance, titanium alloys are widely used in the aerospace, chemical and ship building industry [1]. However, during the machining of titanium alloy, tool wear progresses rapidly because of the high cutting temperature and strong adhesion between the tool and the work material owing to their low thermal conductivity and high chemical reactivity. Therefore, it is not easy to achieve productive machining with good cost performance rate of 400-600 cubic millimeters in roughing. But, when finishing, a long, small diameter cutting tool is needed, hence a low material removal rate of only 40-60 cubic millimeters. Since it is difficult to apply the heavy-duty cutting to a finishing operation because of its slender tool application, the high-speed cutting is expected to be an alternative approach to enhance the productivity of titanium cutting. There are many advantages to high-speed machining, however, cutting speed strongly affects the cutting temperature and high cutting temperature increases the excessive tool wear [2-4]. Therefore, it is important to measure and control the cutting temperature to enhance the efficiency in titanium machining.

On the other hand, end milling is intermittent cutting process, and tool engages both material and air during a single revolution. This cycle seems to be closely connected with tool wear. Several methods can be used to measure cutting temperature. Thermo-couple method is often used for cutting temperature measurement. Meanwhile, there are two types of methods using thermo-couple. One method is that thermo-couple is put into cutting tool or workpiece. For this method, a small hole must be drilled in the tool or workpiece. Another method is to use the tool-workpiece interface as a thermo-couple. This method is practical for measuring cutting temperature for turning process. However, it is difficult to build the measuring circuit of the thermo-couple in end milling.

The research focused on developing a novel method to measure the cutting temperature in high-speed end milling of titanium alloys by PCD (Polycrystalline Diamond) cutting tools. Meanwhile, it also tried to find some relation between machining conditions and cutting temperature. In the proposed method, the infrared radiation pyrometer was selected to measure the temperature under the various cutting conditions, which is able to measure the temperature without contact to measuring object. Through the experiments, we found the proposed method can meet the requirement of accuracy.

CONCEPTUAL AND MEASURING PRINCIPLE

End milling process

End milling process is one of typical intermittent process. In the process, since the cutting tool repeats cutting material and air cutting, the temperature of cutting tool repeats heat up and cooling down, shown in Figure 1.

Measuring principle and concept

Since it is difficult to directly measure the temperature of the contact point between the tool and the workpiece, we can use certain non-contact measurement method to measure the temperatures at different position of the tool during air cutting, like every other 90-degree of the whole cutting process. Then, based on the temperature tendency of the tool in the air cutting, we can estimate the actual cutting temperature of the tool. That is the major principle of the temperature measurement method.

As we know, all objects on the earth radiate infrared according to the temperature. By measuring the radiate infrared of an object using an infrared radiation pyrometer and converting it to voltage value by photo conductor, the temperature of an object can be measured. And one of the greatest merits of infrared radiation pyrometer is that temperature measurement can be carried out without contacting the measuring object.

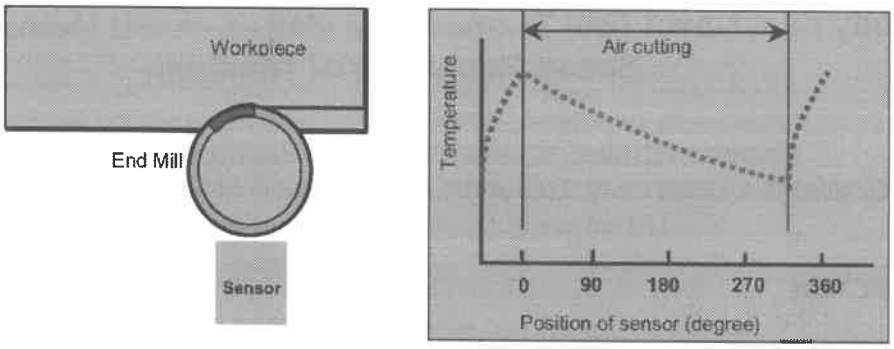

Fig.1: End mill process

Therefore, owing to the feature of end mill process, infrared radiation pyrometer was selected as a sensor to measure the temperature of tool. Thus tool temperature in air cutting can be measured in this method. After the temperatures are obtained, the temperature at cutting contact point can be derived through extending the temperature curve. The measuring system is easy to build compared to the thermo-couple method. This also means that the measuring system is flexible and applicable to actual manufacturing.

EXPERIMENT SETUP AND CONDITIONS

Figure 2 shows the schematic view of temperature measuring system with infrared radiation pyrometer. Sensor head of pyrometer is fixed on a spindle unit of machine tool with fixture. Infrared radiated from flank face of insert is caught by the sensor head and conveyed to the infrared radiation pyrometer through an optical fiber. The photo-conductor in the pyrometer converts radiation energy from the infrared to a voltage value. The output voltage is captured in the PC by way of A/D converter. Then the temperature data can be obtained by software designed for data processing.

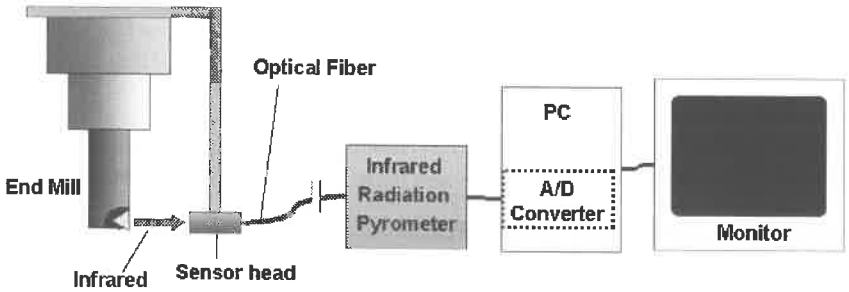

Fig.2 Schematic view of temperature measurement system

Specification of End Mill

The specification of end mill is shown in Table 1. Here, two different insert materials, Polycrystalline Diamond (PCD) and Cemented Carbide, have been utilized to compare the temperature of different tool insert materials. All the other parameters are the same.

Tab.1 Specification of end mill

Manufacturer	Sumitomo Electric Inc.
Type	Throw away end mill
Diameter	30 mm
Axial rake angle	15°
Radial rake angle	-3°
Insert materials	Polycrystalline Diamond (PCD) Cemented Carbide

Experiment conditions

Experiment conditions are shown in Table 2. A vertical machine tool was used for machining of titanium alloys and a software, Labview is used for data acquisition. Figure 3 shows the sensor head setup. The sensor head is rigidly attached to the spindle with a aluminum plate fixture. The sensor head can be fixed at three positions around end mill.

Tab. 2 Experiment conditions

Workpiece	Titanium Alloy (Ti-6Al-4V)
Machine Tool	Vertical type machine center
Cutting speed	300m/min, 400m/min, 500m/min
Feed rate	0.06-0.14mm/tooth
Radial depth of cut	0.06-0.14mm
Axial depth of cut	3.0mm
Measuring distance	50mm
Sensor position	90°, 180°, 270°
Cutting direction	Down cutting

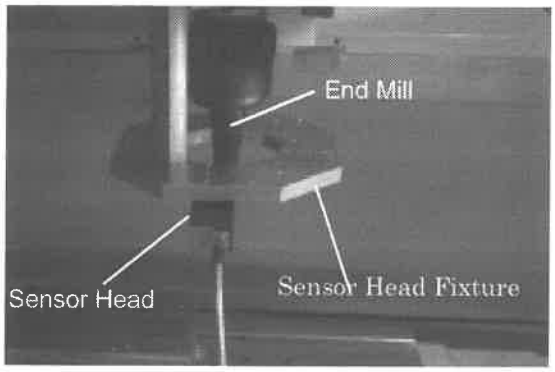

Fig.3: Setup of the sensor head

Measurement of emissivity

Since each object has different emissivity, the emissivity of cutting tools must be measured in advance. Figure 4 shows the measurement setup of emissivity of cutting tools. Cutting tool is put in electric furnace. And atmosphere is kept to particular temperature. Meantime, temperature of specimen was measured by infrared radiation pyrometer.

Thermal measuring method

Figure 5 shows the overview of thermal measurement method. A tool temperature was measured at three different positions during machining which are 90°, 180° degree and 270° around the end mill.

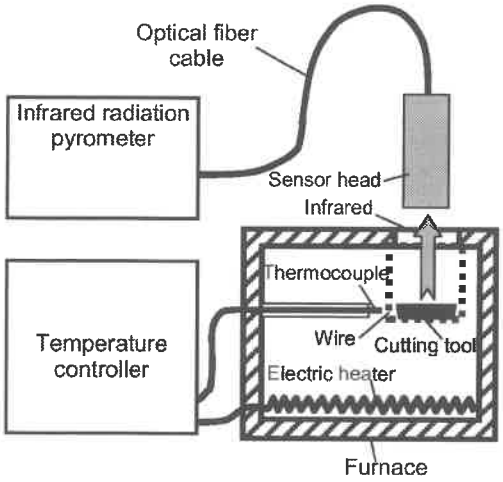

Fig.4: Measurement setup of emissivity of cutting tools

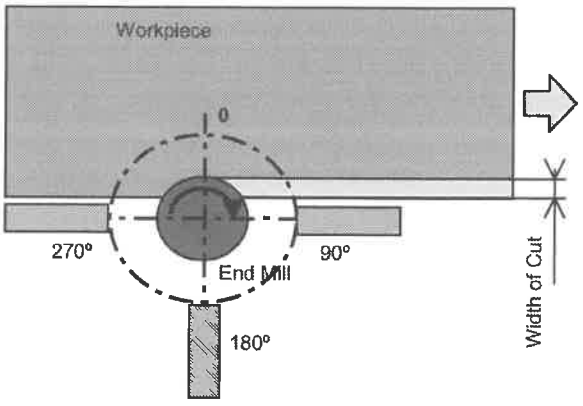

Fig.5: Experiment method

RESULTS AND DISCUSIONS

Figure 6 shows the data sample results from experiment. Figure 6 (a) shows the raw data gathered by computer system based on the basic setup. The data in Figure 6 (b) is the conversion from raw data to temperature. Figure 6 (c) is a cloud of peak points of the signal and the average value was defined as cutting temperature. Using the method, tool temperature with different cutting tools at different sensor positions can be obtained as shown in Figure 6 (d).

From Figure 6 (d), it can be seen that the tool temperature at high speed machining such as feed rate 0.1 mm/tool gradually decreases during air cut. The tool temperature at 90 degree is the highest and the tool temperature at 270 degree is the lowest. Though cutting the titanium by the PCD tools, the tendency of thermal variation during the air cut is almost same as that of thermal variation of the carbide tools. However, the absolute value of the tool temperature is 150~300 degree C lower compared with the tool temperature of carbide tools. This tendency shows the good thermal conductivity of PCD tools same as original [3]. From this result, it can be concluded that the new sensor system with infrared radiation pyrometer have a reasonable measurement accuracy for the purpose of easy-to-use in an actual machining in real time manner. Actually, experiments at different conditions have been conducted to investigate the relation between machining conditions and cutting temperature, but the results will not be presented because of page limit. Moreover, thermocouple method (tool-workpiece interface) is to be used to measure the temperature at the same condition for the comparison purpose.

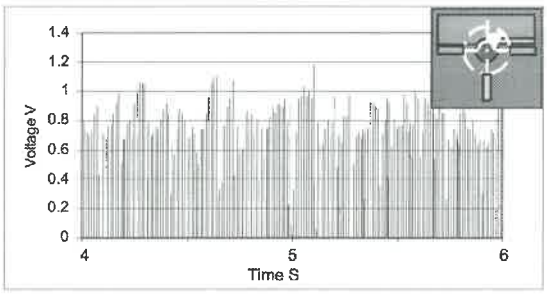

(a) Acquired data

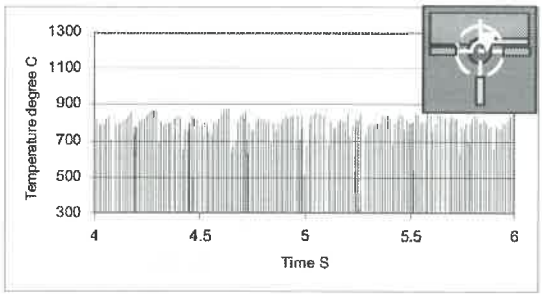

(b) Converted data from voltage to temperature

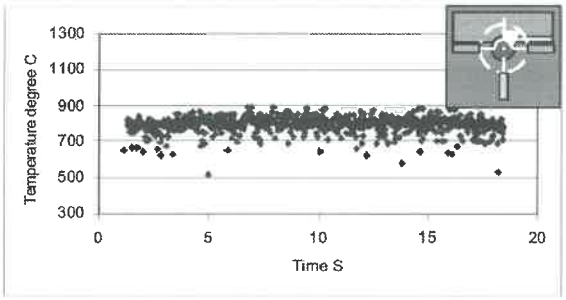

(c) Signal peaks

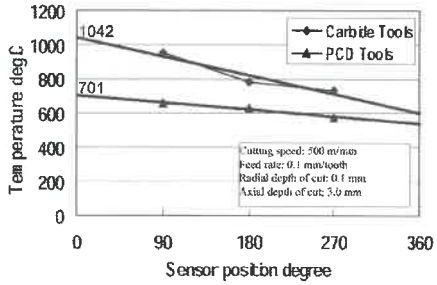

(d) Cutting temperature with different conditions

Fig. 6: Measurement results

CONCLUSIONS

(1) The novel temperature measurement method has been proposed based on the concept of the easy-to-use in an actual machining condition in order to investigate the high-speed machinability of titanium Ti-6Al-4V by polycrystalline diamond (PCD) cutting tools.

(2) The measurement results of the sensor system show the reasonable tendency of the thermal conductivity during air cutting. The Tool temperature of PCD tools is 150~300 degree C lower than that of carbide tools in titanium end milling.

REFERENCES

[1] Ezugwu E. O., Wang Z. M., 1995, "Titanium Alloys and Their Machinability – A Review", Journal of Materials Processing Technology Vol. 68, p. 262 – 274.

[2] Bhaumik S. K., Divakar C., Singh A. K., 1995, "Machining Ti-6Al-4V Alloy With a wBN-cBN Composite Tool", Materials & Design Vol. 16, No. 4, p. 221 – 226.

[3] Liu J., Yamazaki K., Nakai T., Fukaya T., Mori M., Furuta M., 1999, "High-Speed Machining of Titanium by New PCD Tools", Society of Automotive Engineers, Inc.

[4] Dowey S.J., Rahle, B., 1997, "Performance Analysis of Coated Tools in Real-life Industrial Experiments Using Statistical Techniques", Surface & Coating Technology Vol. 99, p.213 - 221.

Uncertainty Analysis in Integrated Measurement Processes

Xiaoping Zhao, Robert G. Wilhelm
Center for Precision Metrology and Intelligent Manufacturing
Department of Mechanical Engineering and Engineering Science
University of North Carolina at Charlotte
Charlotte, NC 28213

1. Introduction

The result of a measurement is only an approximation of the true value and thus is complete only when accompanied by a quantitative statement of uncertainty. Much research work has been conducted to identify uncertainty contributors and provide quantitative or qualitative analysis of measurement uncertainty. Among them, ISO GUM represents the current international view for expressing uncertainty in measurement based on the CIPM approach. It provides a general framework to express measurement uncertainty and suggests two ways ("Type A/Statistical" and "Type B/Expert") to quantify the individual measurement uncertainty that will be combined by RSS (root-sum-square) to form final combined and expanded uncertainty.

Often, the value of uncertainty can be calculated once all information about the measurement task is known. Such "task specific uncertainty" is dependent on the specific measurement plan used and specific features measured on specific measurement machines. Here, the measurement plan or process plays an important role. By choosing an appropriate inspection process, some individual uncertainty components can be decreased or even eliminated, which is the concern of an engineer in industrial practice.

An integrated measurement process (IMP) has the potential to dramatically improve measurement performance. When applied in industry, it promises the benefits of higher measurement efficiency and shared information among different application departments while also reducing measurement uncertainty.

In this paper, the importance of reducing measurement uncertainty is first discussed. A conceptual analysis of an integrated measurement process is then presented and examples are shown of how such a process can decrease measurement.

2. Uncertainty and Tolerance

ISO 14253-1 specifies the decision rules that suppliers and customers should use to accept or reject a part. Fig.1 illustrates this idea by defining conformance zone, non-conformance zone and uncertainty range.

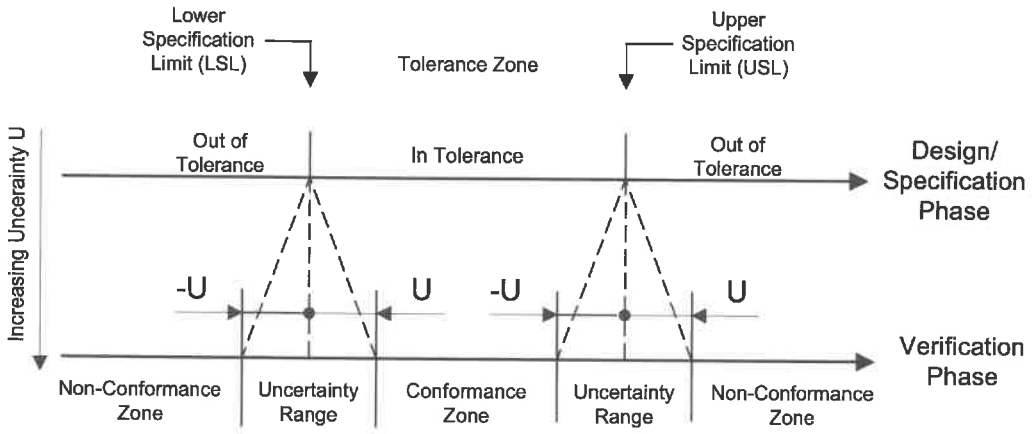

Figure 1 - the effect of measurement uncertainty on the conformance and non-conformance zone

where

$$U = k \times u_c$$

represents the expanded uncertainty whose value is based on the coverage factor k and combined standard uncertainty u_c. All of these values can be calculated according to ISO GUM.

It is clear from Fig.1 that two effects occur due to the existence of measurement uncertainty. First, the conformance zone during the verification phase is less than the tolerance zone specified during design phase. Second, if the result of a measurement falls within one of the uncertainty ranges, it will become ambiguous to accept or reject a part. Thus, the cost associated with accepting a bad part or rejecting a good part is unavoidable.

This situation is more severe in modern industry as tolerance specifications become more stringent. Hence measurement uncertainty now plays a much more important role in verification. Reducing uncertainty is economically important for industry because of the cost related to rejecting a good part or accepting a bad part. Both costs are due to the existence of an uncertainty range and the reduced conformance zone as compared to tolerance zone specified during design phase.

3. Effects on Conventional Uncertainty Model

Though the value of measurement uncertainty is tightly coupled to a specific measurement task, it is still meaningful to have a detailed list of all possible measurement uncertainty contributors. Practicing engineer can use this list to have a conceptual idea of what kind of uncertainties are included in a particular measurement process. By comparing different possible measurement processes, the engineer can choose one that has fewer measurement uncertainty sources and then use either a statistical method or expert opinion to quantify them based on ISO GUM to obtain estimates of combined and expanded measurement uncertainty.

Fig.2 shows a list of potential components that may bring uncertainty into a measurement result and their relationship. A one-way arrow " ⟶ " indicates that the left contributor has an effect on the right contributor.

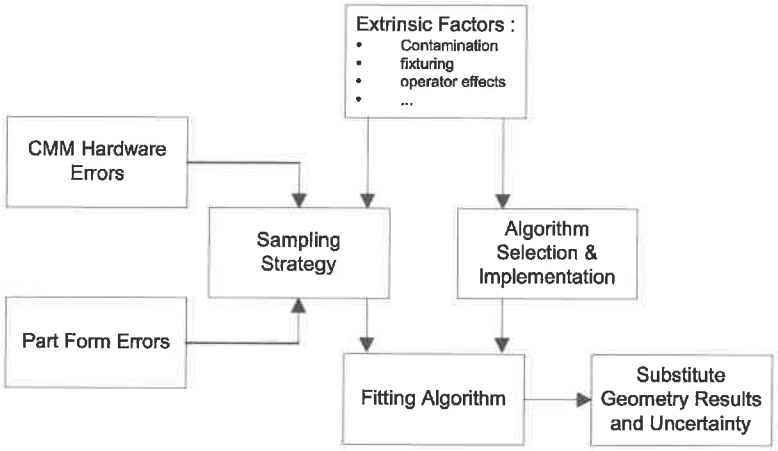

Fig 2 - measurement uncertainty contributors and their relationship

Many of these possible uncertainty contributors have been studied in detail by a variety of researchers. "Extrinsic Factors" have not been well characterized, however, because this component includes many factors and it is hard to find a systematic way to model all of the factors. An integrated measurement process can eliminate or decrease some of those factors because of its inherent features such as automatic sampling, high-speed measurement and so on.

The factors that can be improved most dramatically are mainly associated with operators and environment. As human beings, operators are inherently changing. They may generate errors during operating, recording or analysis due to their education, experience, physical ability and knowledge. Their experience may also have further effects on sampling strategy and algorithm selection. Environmental variation is also inherent in the measurement process. An IMP can implement and enforce standard measurement methods that span operators and account for environmental variation. In addition to eliminating or decreasing uncertainty caused by those factors, an IMP also allows different people associated with the product life cycle to share the same view-point on measurement results. These people may include designers, manufacturers, inspectors, customers, suppliers and so on.

4. Reduced Uncertainty based on a Bayesian Approach

In an IMP, engineers can easily access prior measurement data since all these measurement data are stored in a database. Furthermore, industrial production processes typically lend to batch manufacturing. Because of this, it is often reasonable to assume that historical product data embodies the characteristics of the current workpiece. This assumption matches the most important pre-condition of Bayesian theory. According to Bayesian theory, if both the measurement and workpiece have a Gaussian distribution, then, the new best estimate of the measurand and its associated uncertainty can be represented by the following equations:

$$y = y_m\left(\frac{\gamma^2}{1+\gamma^2}\right) + y_{pe}\left(\frac{1}{1+\gamma^2}\right) \qquad (1)$$

$$\text{Where} \qquad \gamma = \frac{u_{pe}}{u_{cm}}$$

$$\frac{1}{u_c^{\,2}} = \frac{1}{u_{cm}^{\,2}} + \frac{1}{u_{pe}^{\,2}} \qquad (2)$$

y – the best estimate of the measurand including prior information
y_m - the best estimate of the measurand without including prior information.
y_{pe} - the best estimate of the measurand based on prior information of the workpiece population.
u_c - the combined standard uncertainty associated with the measurement when prior information is included.
u_{cm} – the combined standard uncertainty of the measurement without using prior information.
u_{pe} – the standard deviation of the probability distribution which describes the measurand based on prior information.

Based on equation (1) and (2), it can be concluded that the best estimate of the measurand is shifted from y_m toward y_{pe} and the new combined uncertainty u_c decreases due to the use of historical data. Bayesian theory is also valid if the prior and measurement distributions are not Gaussian distributed, but more complex modifications to above two equations are required.

5. Conclusion

This paper presents the importance of reducing measurement uncertainty in industrial practice related to the cost of rejecting a good part and accepting a bad part. Based on this, this paper suggests the use of integrated measurement process in industry, not only because of its higher sampling efficiency and more convenient analysis of archived data, but also because of reduced measurement uncertainty. IMP can reduce measurement uncertainty by decreasing or removing some of the potential uncertainty contributors in conventional analysis. Also, it can reduce measurement uncertainty by applying historical data based on Bayesian theory.

Reference

1. R. G. Wilhelm, R.Hocken, H.Schwenke, "Task Specific Uncertainty in Coordinate Measurement", *Annals of the CIRP Vol.50*, Feb, 2001.
2. Zhao,X; Wilhelm,R.G.; Martin,O.A.; Bullock,J.B. "Software Frameworks for Integrated Measurement Processes", *Proceedings of the 16th of American Society for Precision Engineering*, November 10-15, 2001.

3. S.D.Phillips, B.Borchardt, G.Caskey, "Measurement Uncertainty Considerations for Coordinate Measuring Machines", *NISTIR 5170*, April 1993.
4. ISO/FDIS 14253-1, Geometrical Product Specifications(GPS) – Inspection by measurement of workpieces and measuring equipment - Part 1 : Decision rules for proving conformance or non-conformance with specifiction, 1998, Geneva, Switzerland.
5. ISO/FDIS 14253-2, Geometrical Product Specifications(GPS) – Inspection by measurement of workpieces and measuring equipment - Part 2 : Guide to the estimation of uncertainty of measurement, in calibration of measuring equipment and in product verification, 1998, Geneva, Switzerland.
6. ISO - GUM, Guide to the Expression of Uncertainty in Measurement, 1993, Geneva, Switzerland.
7. G.Box, G.Tiao, Bayesian Inference in Statistcal Analysis, John Wiley, 1992.

A proposal for a common language for sharing surface texture data

B. Muralikrishnan and J. Raja
Center for Precision Metrology
The University of North Carolina at Charlotte
Charlotte, NC 28223

1. Introduction

There is a large amount of metrology data along with associated information regarding the manufacturing process or function that needs to be transferred, stored or analyzed. As more data is being collected, there is a need for sharing data and associated information effectively to eliminate redundancy in data collection and analysis. While formats currently being used such as the SDF data format [1] cover the representation of discrete data points along with some header information, they do not convey information about the measurement operation, the manufacturing process or the functional requirements of the component.

This document is a proposal for the specification of a common language for expressing metrology data along with related process and functional data. The language being proposed is based on XML (Extensible Markup Language) [2]. XML is increasingly used in various areas as the medium of communication because it provides an intuitive, machine and human readable structure, it is hierarchical and flexible, accommodates industry leading data formats, supports freeware conversion and analysis tools. A similar information model has been developed at NIST [3] to describe the properties and results of machine-tool performance tests.

2. Metrology Markup Language

The proposed Metrology Markup Language is XML based, with user-defined tags that serve as attributes for the data. The tags form the basis for a Document Type Definition (DTD) that serves as the reference for all data files generated by any instrument. A sample DTD for the surface finish application is shown in Fig. 1. There are three major elements in the DTD – metrology, process and function. The 'metrology' DTD covers measurement and analysis aspects such as part (name, number, material), instrument (name, type), data file (name, number of points, spacing) and analysis (filter, cutoff, Ra, Wa). The 'process' DTD covers process information such as process name, number, tool (radius, speed, feed). Additional attributes include user-defined 'ProcessAtt' that stores any process related information that is gathered during measurement of part. This could include information on tool wear, force measurement etc. The 'function' DTD stores information about the functional intent of the component. The 'symbol' attribute provides broad information on the functional intent of the part such as two-body contact, hydrodynamic drag, etc. Additional attributes include user-defined 'FunctionAtt' that stores any function related information that is gathered during measurement of part such as torque measurement data, optical reflectivity etc.

```
<!DOCTYPE DATA[

<!ELEMENT DATA (METROLOGY+, PROCESS+,
FUNCTION+)>

<!ELEMENT METROLOGY (PART+,
MEASUREMENT+, DATAFILE+, ANALYSIS+)>
<!ELEMENT PART (NAME, NUMBER, MATERIAL)>
<!ELEMENT NAME (#PCDATA)>
<!ELEMENT NUMBER (#PCDATA)>
<!ELEMENT MATERIAL (#PCDATA)>

<!ELEMENT MEASUREMENT (DATE, TIME,
INSTNAME, INSTTYPE, PRBRNG, PRBRES)>
<!ELEMENT DATE (#PCDATA)>
<!ELEMENT TIME (#PCDATA)>
<!ELEMENT INSTNAME (#PCDATA)>
<!ELEMENT INSTTYPE (#PCDATA)>
<!ELEMENT PRBRNG (#PCDATA)>
<!ELEMENT PRBRES (#PCDATA)>

<!ELEMENT DATAFILE (FILENAME, NUMPTS,
SPACING, CLASS, DATAPOINTS)>
<!ELEMENT FILENAME (#PCDATA)>
<!ELEMENT NUMPTS (#PCDATA)>
<!ELEMENT SPACING (#PCDATA)>
<!ELEMENT CLASS (#PCDATA)>
<!ELEMENT DATAPOINTS (#PCDATA)>

<!ELEMENT ANALYSIS (FILTER, CUTOFF, PA, RA,
WA)>
<!ELEMENT FILTER (#PCDATA)>
<!ELEMENT CUTOFF (#PCDATA)>
<!ELEMENT PA (#PCDATA)>
<!ELEMENT RA (#PCDATA)>
<!ELEMENT WA (#PCDATA)>

<!ELEMENT PROCESS (NAME, SPEED, FEED,
DEPTHOFCUT, TOOLMATL, TOOLRAD,
PROCESSATT)>
<!ELEMENT NAME (#PCDATA)>
<!ELEMENT SPEED (#PCDATA)>
<!ELEMENT FEED (#PCDATA)>
<!ELEMENT DEPTHOFCUT (#PCDATA)>
<!ELEMENT TOOLMATL (#PCDATA)>
<!ELEMENT TOOLRAD (#PCDATA)>
<!ELEMENT PROCESSATT (#PCDATA)>

<!ELEMENT FUNCTION (SYMBOL, DESCRIPTION,
FUNCTIONATT)>
<!ELEMENT SYMBOL (#PCDATA)>
<!ELEMENT DESCRIPTION (#PCDATA)>
<!ELEMENT FUNCTIONATT (#PCDATA)>

]>
```

Fig. 1 Sample DTD

3. Process and functional toolbox for surface & form metrology

The proposed DTD has been implemented as part of a process and functional toolbox for surface and form metrology, that is currently being developed at UNCC. As current metrology analysis systems are not geared towards analyzing multiple profiles or in performing correlation analysis with functional or process data, they are limited in their capabilities. The toolbox being built is designed to understand the temporal relationships in the datasets and handles metrology, process and functional data in one framework. The toolbox is itself not discussed in this report, but the database is presented here to demonstrate the application of the proposed XML format. Because the toolbox is designed to handle both surface texture and associated process and functional data, the proposed XML format proves to be useful in describing the data, in inserting to, retrieving from, and querying the database, and also in transferring the data to another schema that understands the same DTD.

4. Entity-Relationship diagram for surface texture database

A database for storing surface texture and associated process and functional information has been built in Oracle. The database has been built as the backend for a process-specific and functional toolbox for surface metrology. The database schema is similar to that reported by Bui et al. [4], but with some modifications. A key addition to the schema is the attributes for the entity 'Datafile'. A 'class' attribute has been added to indicate some user knowledge about the class of the data file. Thus, a sequence of data files collected from a process could fall into one of many classes, depending on the process or the

function. Also, more user-defined attributes can be added, such as 'ProcessAtt' or 'FunctionAtt' that convey information about the process or the function. Examples of these include cutting force measurement data, tool wear information etc. The database schema is shown in Fig. 2. A sample data retrieved from the system is shown in Fig. 3 to illustrate the format and tags of the output. As mentioned before, the output conforms to the DTD specifications laid out earlier.

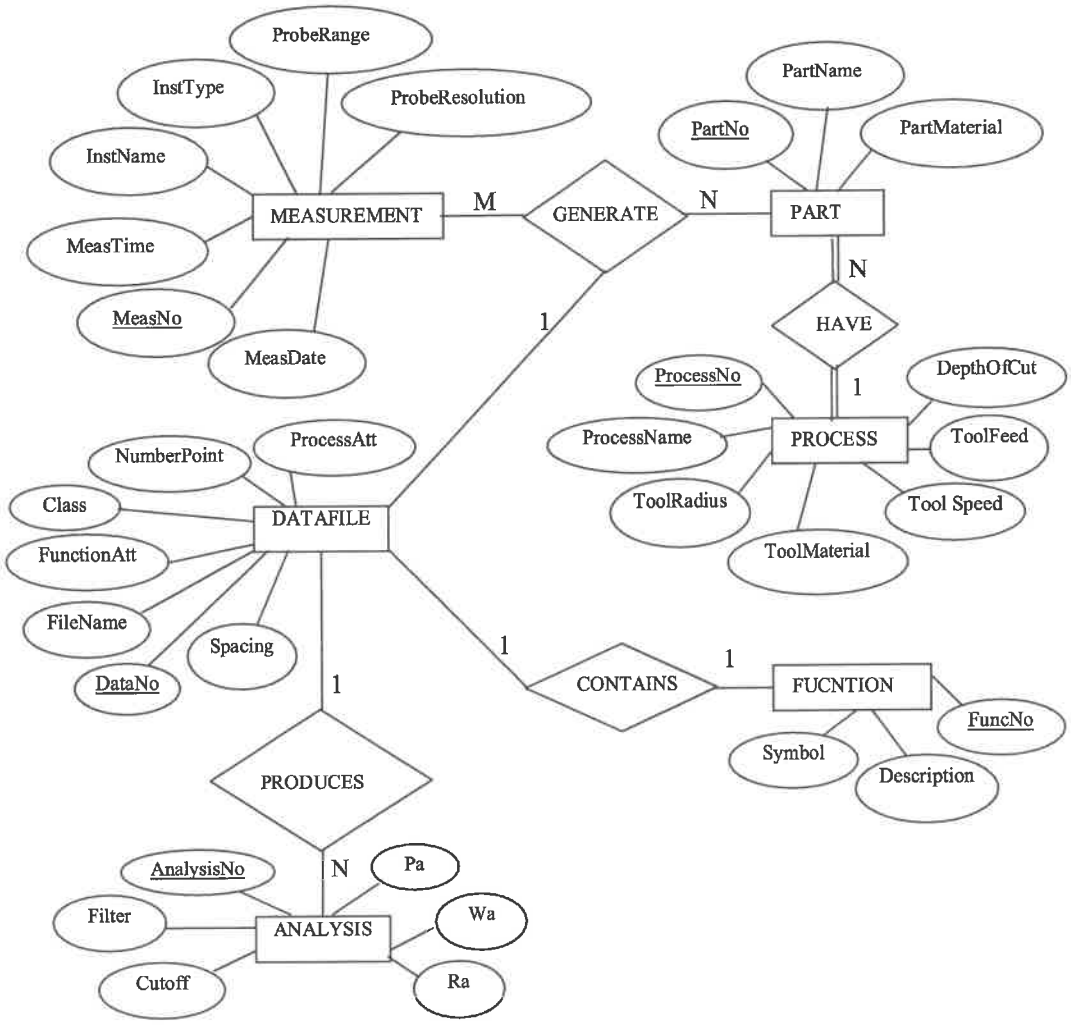

Fig. 2 Entity-Relationship diagram for surface texture database

5. Conclusions

This article has laid out a proposal for a common format for exchanging surface texture data across different platforms. There is no current industry wide standard format for transferring data and this leads to creation of several vendors specific and other data formats being used. XML based languages are increasingly becoming popular among the manufacturing and metrology community. Therefore, it is natural to consider an XML based language for sharing surface texture and form data as well. Currently, a process and functional toolbox for surface metrology is under development. The system recognizes and reports outputs in this XML format. The sample DTD shown in this report is not exhaustive. There is considerable room for additional tags; but the capability of this system to accept additions makes it remarkable in its utility and value.

```
<?xml version="1.0" encoding="ISO-8859-1"?>
<DATA>
<METROLOGY>

<PART>
<NAME>SHELL</NAME>
<NUMBER>TURN25</NUMBER>
<MATERIAL></MATERIAL>
</PART>

<MEASUREMENT>
<DATE>06-04-2002</DATE>
<TIME></TIME>
<INSTNAME>TAYLORHOBSON</INSTNAME>
<INSTTYPE>STYLUS</INSTTYPE>
<PRBRNG>6MM<PRBRNG>
<PRBRES>0.01UM<PRBRES>
</MEASUREMENT>

<DATAFILE>
<FILENAME>TUNR25-1.DAT</FILENAME>
<NUMPOINTS>20000</NUMPOINTS>
<SPACING>0.25UM</SPACING>
<CLASS>1</CLASS>
<DATAPOINTS>223.21,223.22,225.37,...,234.45,145.34
</DATAPOINTS>
</DATAFILE>

<ANALYSIS>
<FILTER>GAUSSIAN</FILTER>
<CUTOFF>0.8MM</CUTOFF>
<PA>24.5</PA>
<RA>12.3</RA.
<WA>16.4</WA>
</ANALYSIS>

<PROCESS>
<NAME>HARD TURNING</NAME>
<SPEED>300</SPEED>
<FEED>0.66</FEED>
<DEPTHOFCUT>21</DEPTHOFCUT>
<TOOLMATL>CAST IRON</TOOLMATL>
<TOOLRAD>23</TOOLRAD>
<PROCESSATT>0.234UM</PROCESSATT>
</PROCESS>

<FUNCTION>
<SYMBOL>TB</SYMBOL>
<DESCRIPTION></DESCRIPTION>
<FUNCTIONATT></FUNCTIONATT>
</FUNCTION>
```

Fig. 3 Sample output data format

6. References

1. P.J.Sullivan and K.J. Stout, The specification of a flexible file format for storage and retrieval of engineering topographic data, Proceedings of the ASPE 1992 Annual Meeting
2. http://www.w3.org/XML/
3. Y. Tina Lee, J A Soons, M A Donmez, Information model for machine-tool performance tests, Journal of Research of the NIST, 106, 2, March-April 2001
4. S. H. Bui, V. Gopalan, J. Raja, An internet based surface texture information system, International Journal of Machine Tools and Manufacture, 41 (2001) 2171-2177

A fast and accurate non-contact profiling instrument for assessing areal surface texture and flatness

Teruaki Saito*, Kazuhisa Yanagi*, Kazuhito Togawa **
* *Nagaoka University of Technology, School of Mechanical Engineering, Kamitomioka 1603-1, Nagaoka, Niigata 940-2188, Japan*
** *Nagaoka National College of Technology, Department of Electronic Control Engineering, Nishikatakai 888, Nagaoka, Niigata 940-8532, Japan*
e-mail:xitou@stn.nagaokaut.ac.jp http://orion.nagaokaut.ac.jp/

1. Introduction

Surface texture and surface form deviation of industrial products are significant geometrical specifications. Practical measuring instruments to measure and evaluate those specifications are expected to come onto the market. The surface form data is generally composed of discrete sampling points and so it is needed to trace a point- or spot-type displacement sensor relatively over an object surface. Although ISO/TC213 (Technical committee on dimensional and geometrical product specifications and verification) has discussed about the assessments of straightness, flatness and so on, the final agreements have not been attained due to the difficulties to guarantee their consistency. As to the areal surface texture, the official discussion has been just started.

In this study, the novel measurement principle for evaluating both flatness and surface texture of machined products is proposed. Their extraction and filtration procedures are developed in due consideration of utilized displacement sensors.

2. Measurement principle of developed instrument

The developed instrument is based on scanning method using a point-type displacement sensor. Its schematic view is shown in Figure 1. An object surface is set on the X-Y table and laterally moved by orthogonal linear motors. The displacement sensor for measuring geometrical deviation is attached to the bridge-type column made of granite. A super smooth optical flat of 140 mm diameter is attached to the backside of the X-Y table as the plane datum and the vertical motion error can be detected using an electric capacitance displacement sensor located below the optical flat.

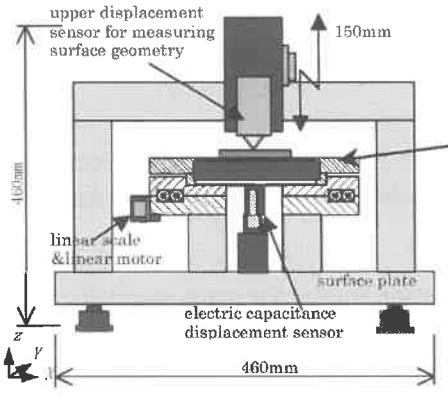

Fig.1 Schematic view of developed instrument

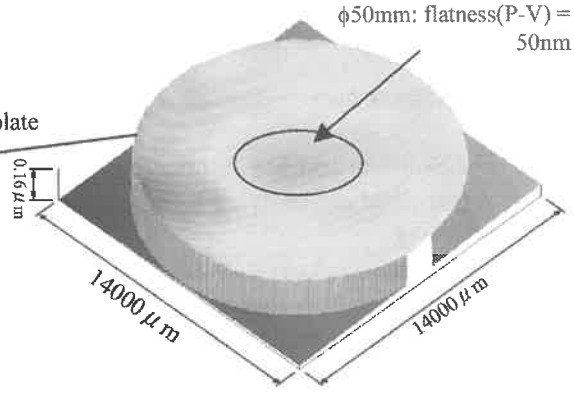

Fig.2 Flat plate

The principal specifications of the instrument are tabulated in Table 1. Its measurable area is limited to that of the plane datum. The measuring range and resolving power for surface form deviation depend on the upper sensor utilized.

Table 1 Principal specifications

External size (D x W x H)	460 x 460 x 370mm
Measurement area and height (X x Y x Z)	100 x 100 x 150mm
Positioning resolution in the X-Y plane (with linear scale)	0.1μm
Tracing speed	~30mm/s

3. Analytical model of measurement error

Measurement error of the instrument can be caused by location and orientation of its composing elements. Supposing that the work surface, X-Y motion plane and optical flat surface are ideally parallel to each other and the pitching motion center O of the X-Y table is below the work surface by h_1 and just on the displacement measuring axis of the upper sensor as shown in Figure 3, the measurement errors δ_{zh} and δ_x caused by rotational angle ϕ can be approximated by the following equations.

$$\delta_{zh} = h_1\left(\frac{1-\cos\phi}{\cos\phi}\right) \qquad (1)$$

$$\delta_x = (h_1 + \delta_{zh})\phi \approx h_1\phi \qquad (2)$$

There exists some misalignment a between measuring axes of the two sensors as shown in Figure 4. The measured displacement by the lower sensor is slightly changed due to the rotational angle ϕ and its radius of curvature h_2 in accordance with a. The vertical error for the lower sensor δ_{za} is expressed by equation (3)

$$\delta_{za} = a\tan\phi + \left(\frac{1-\cos\phi}{\cos\phi}\right)h_2 \qquad (3)$$

The total measurement error in the vertical direction δ_z becomes $\delta_{zh} + \delta_{za}$. In the case that h_1=50mm, h_2=20mm, a=1mm and ϕ=0.01°, δ_z can be roughly estimated at 0.18 μ m.

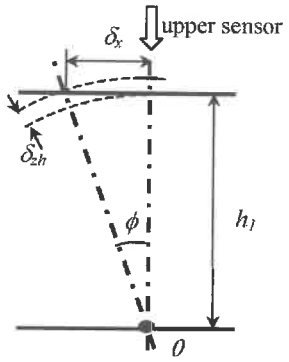

Fig. 3 Measurement error caused by table pitching

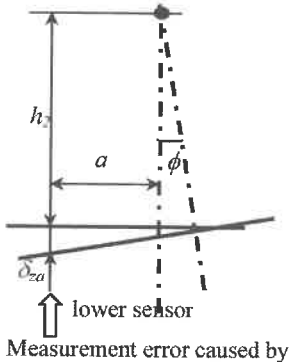

Fig. 4 Measurement error caused by misalignment of the two sensors

4. Fundamental performance test

One of the advantages of the developed instrument was experimentally verified using a smooth flat plate as a work surface. Figure 5 shows the measured profiles by following raster scan method for lower sensor as well as upper sensor. From the concaved hollow portion of the profiles for the two sensors, a certain motion error of the X-Y table can be identified. And it was made clear that the motion error was thoroughly corrected by the proposed measurement principle. This means that the compensated or subtracted final profile does not include any significant motion errors.

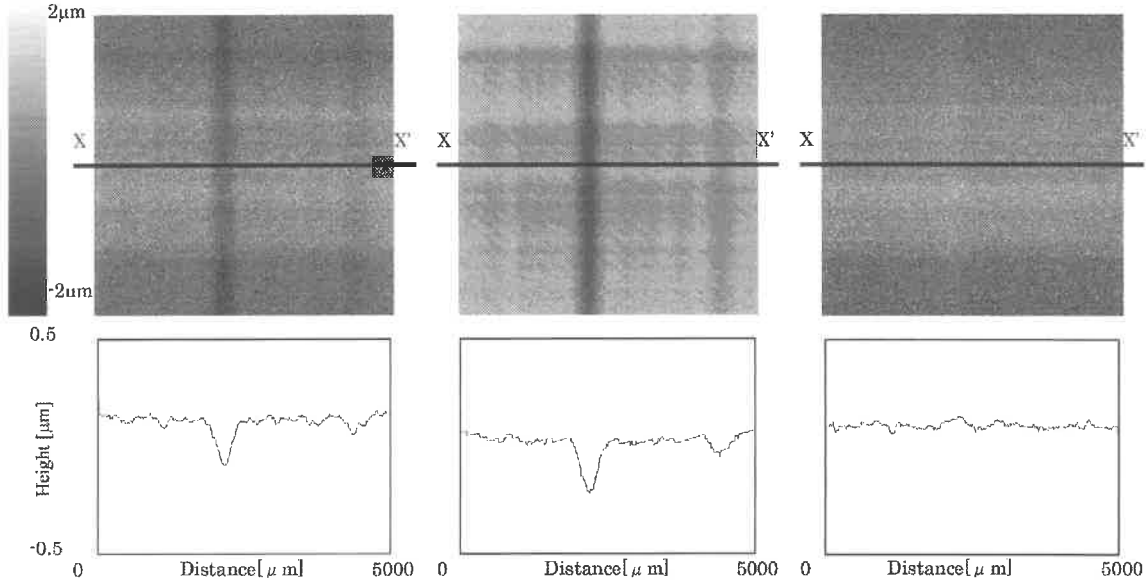

(a) Originally measured profile of the specimen(X-X')

(b) Profile of reference plate (Motion error)

(c) Corrected profile

Fig.5 Measurement result by using raster scanning method

5. Sampling conditions for flatness evaluation

ISO/TC213 has discussed about specification operators to evaluate flatness deviation and proposed the default measuring conditions shown in Table 2 when using a ball probe[1]. The ball radius tends to dominate the cut-off values λc and so the evaluation length ℓn. As an extraction method for the flatness evaluation, orthogonal grid sampling shown in Figure 7 is generally used. In that case, any adjacent sampling points have to be well correlated from a statistical point of view. Consequently it is necessary to select a reasonable displacement sensor in accordance with the work surface geometry. An auto-correlation curve for a real surface is suddenly attenuated as depicted in Figure 8 when short wavelength components are superimposed on the surface. In order to evaluate the flatness deviation, relatively shorter wavelength components have to be excluded to make the sampling distance much longer. The auto-correlation curve derived from a profile measured by either large ball probe or non-contact displacement sensor can be gently-sloping as shown in Figure 8.

For reference, amplitude transmission characteristics of electric capacitance sensors are shown in Figure 9. It is clearly seen that the shorter surface wavelength components can be excluded with such a sensor depending upon its probe diameter. The reasonable sampling distance for the electric capacitance sensor would be less than 1/6 of its diameter.

Table 2 ISO proposal for measuring flatness deviation [1]

dimensions in millimeters

L		λc	R
from	up to and including		ball radius
0.4	1.25	0.08	0.05
1.25	4	0.25	0.15
4	-	0.8	0.5

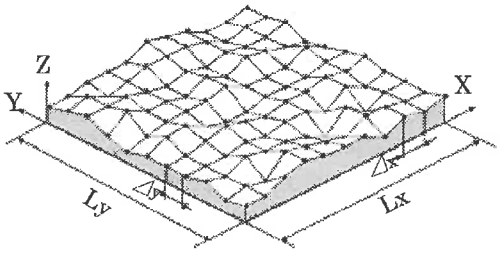

Fig. 7 Orthogonal grid sampling for flatness evaluation

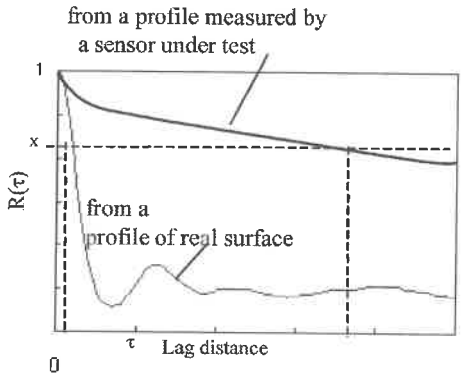

Fig. 8 Auto-correlation curves

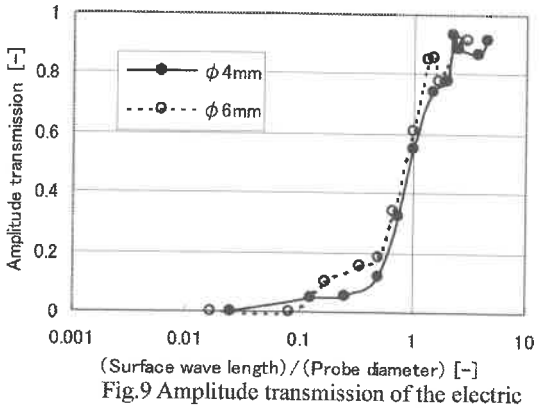

Fig.9 Amplitude transmission of the electric capacitance sensor

6. Areal surface texture measurement

As far as surface texture measurement using stylus instrument is concerned, the profile data is to be measured in accordance with the conditions shown in Table 3[2]. It should be noted that the evaluation length is five times of the cut-off length λc in the default case. However, actual sampling distance is likely to be taken much less than the values shown in Table 3 because of filtration at λs. In the case of areal 3D surface texture, extremely short sampling distance is inconvenient because the repetitive measurements in the orthogonal direction would become almost impossible. It is also to be desired that the cut-off values λs for the areal case should be much greater than those of the 2D case so that the maximum sampling distance could be nearly stylus tip radius or spot radius of optical stylus. In addition to that, measuring area or evaluation area should be taken into account

Table 3 Measuring condition for the case of 2D stylus instrument [2]

λc mm	λs μm	λc/ λs	Max r_{tip} μm	Max sampling distance μm
0.08	2.5	30	2	0.5 (to be changed to 0.41)
0.25	2.5	100	2	0.5 (to be changed to 0.41)
0.8	2.5	300	2	0.5 (to be changed to 0.41)

7. Concluding remarks

The developed instrument can realize the fast and accurate assessment of both areal surface texture and flatness deviation of mechanical products. Tentative sampling conditions for evaluating those geometrical specifications using non-contact displacement sensors were proposed in compliance with the committee drafts of ISO/TC213/WG1. A further study on the amplitude transmission characteristics of non-contact displacement sensors and the sampling scheme will be needed in the near future.

Reference

[1] ISO/DIS 12781-2: Geometrical product specification (GPS)-Flatness part 2 specification operators, (1999)
[2] ISO 3274: Geometrical product specification (GPS)-surface texture :Profile method- Nominal characteristics of contact (stylus) instruments, (1996)

A STUDY OF THE MEASUREMENT ERRORS FOR LASER BEAM PASSING THROUGH FLOWING PARALLEL LAYER FOR SURFACE PROFILE MEASUREMENT

Z. Tao, Y. Gao *

Department of Mechanical Engineering, Hong Kong University of Science and Technology
Clear Water Bay, Kowloon, Hong Kong
E-mail: * meygao@ust.hk

Introduction

An analysis of measurement errors for laser beam passing through flowing parallel layers for in-process surface profile measurement is presented. A model of the fluid dynamics aspects for in-process optical measurement under coolant conditions has been discussed [1]. With a transparent region generated [2], a laser beam can through flowing transparent layer and reach the surface of workpiece for measurement in our experiments. There are two transparent layers in the new measurement method [3]. One is a glass plate, in which the measurement error is constant because the thickness of the glass plate, the glass refraction index and others are stationary. The measurement errors caused by this layer can be corrected. Other one is the flowing water layer. The measurement errors caused by flowing layer are complex and inconstant because of the fluid flowing properties [4-6].

The flowing water layer is in the region between the glass plate and workpiece surface. As a kind of fluid, its form depends on the two walls included glass plate and workpiece surface. The flow pattern of this water layer is governed by many factors included gap h between glass plate and workpiece surface, velocity v of the water flow, speed of the workpiece movement V_w, and others. The propagation of the laser beam in the transparent window is not only affected by the static properties of the fluid layer, but also by its flowing properties. So the fluid flow patterns in the transparent window region and its effect on laser beam propagation should be studied.

Laser Beam Propagation through Different Fluids

In the new method [3], the laser beam passes through a fluid layer in a small area, named the measurement window. Fig. 1 shows the flow field of the transparent window, and Fig. 2 is a photo captured from a microscope image system. The fluid flow field patterns are complicated in the zone of the transparent window. Based on previous analysis [1-3], the region of the transparent window should be in the zone of the water flow. The characteristic size L of the flow, the characteristic flow velocity u, and the kinematic viscosity ν of the flowing fluid can be arranged in a dimensionless grouping, known as the Reynolds number, as

$$(Re)=uL/\nu. \tag{1}$$

The transition from laminar to turbulent flow occurs at a particular critical value (Re) of the Reynolds number.

The velocity u of water flow in the transparent window region is the range of 0.05~6.0 m/s. If we take the characteristic size of the flow in the layer of the transparent window, say h=1mm, and water kinematic viscosity ν=1.01 mm^2/s, then for the condition u=0.05~6.0 m/s, the Reynolds number is about 50~6000 ((Re)=50 ~6000). When the Reynolds number is low, i.e. (Re)=50, the flow should be a laminar flow. Fig. 2 is a typical image of this flow pattern. On the other hand, if the Reynolds number is high, i.e. (Re)=6000, the flow will be complicated. The resultant may be

a laminar flow or turbulent flow or others. For these reasons, we will discuss the laser beam propagation for laminar flow and turbulent flow, respectively.

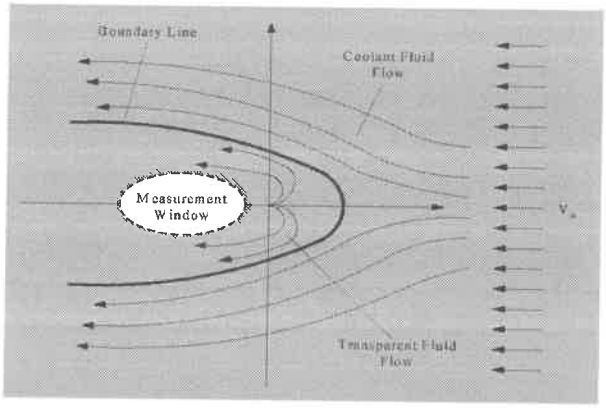

Fig. 1 Window for the in-process measurement

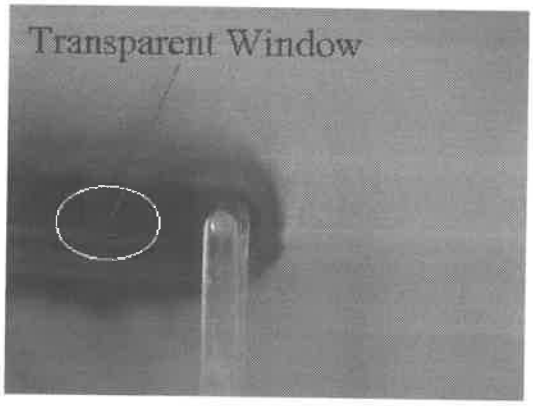

Fig. 2 Photo of the transparent window

a) Laminar flow condition

In the region near the nozzle, the water flow should be governed mainly by pressure drive. If we assume the workpiece surface is static, V_w=0, the flow velocity profile should be a parabolic curve as shown in Fig. 3.

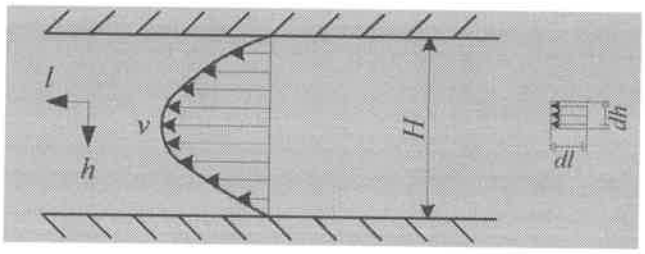

Fig. 3 Velocity profile in the laminar flow

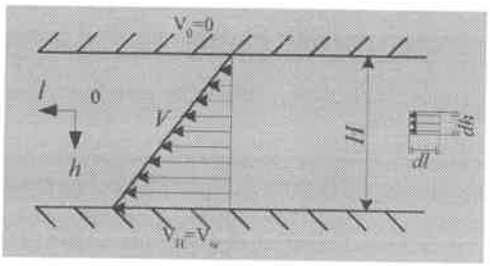

Fig. 4 Linear laminar flow

In a thin layer, the distance the light beam travels in the h direction is dl when the light travels a distance dh through the flow layer. Therefore,

$$dt=\frac{dh}{c},\ dl=v*dt,\ v=a*h,\ \text{and}\ V=V_0(1-(\frac{h}{H/2})^2),$$

where V_0 is the maximum velocity of the flow. Then, the deflection of laser beam is l, and

$$l=\int dl=\int vdt=\int V_0(1-(\frac{h}{H/2})^2)dt \quad = \int_{-H/2}^{H/2} V_0(1-(\frac{h}{H/2})^2)dh/c=\frac{V_0H}{c}(1-\frac{H}{6}). \qquad (2)$$

If the workpiece surface is moving at velocity V_w, the flow should be a laminar flow as shown in Fig. 4. Similar to the case of pressure driven laminar flow, the deflection of laser beam in this layer is obtained as

$$l = \int dl = \int v dt = \frac{V_w}{H} h\, dt \;\; = \int_0^H \frac{V_w}{H} h \frac{dh}{c} \;\; = \int_0^H \frac{V_w}{H\,c} h dh \;\; = \frac{1}{2}\frac{V_w}{H\,c}\int_0^H d(h^2) \;\; = \frac{1}{2}\frac{V_w H}{c}, \qquad (3)$$

where c is the velocity of light in water, $c=C_0/n_2$, n_2 is the refraction index, n_2=1.3330. c_0 is the velocity of light in vacuum, and c_0=3x10^8 m/s. If V_w=0, the effect of the propagation of the laser beam through the fluid can be evaluated by Eq. 2. When H=1 mm, V_0=1.0 m/s. Then,

$$2l = 1.3330\times10^{-3}\frac{1}{3\times10^8}(1-\frac{10^{-3}}{6})\ \text{(m)} = 0.444\times10^{-5}\ \text{(um)}.$$

If the workpiece is moving at a velocity V_w, the effect of the propagation of the laser beam through the fluid can be calculated using Eq. 3. When H=1 mm, V_w=1.0 m/s. Then,

$$2l = 1.3330\times10^{-3}\frac{1}{3\times10^8}\ \text{(m)} = 0.444\times10^{-5}\ \text{(um)}.$$

Therefore, if the gap is thin, as H=1mm, the deflection of laser beam through fluid flow is low under the given conditions.

b) Turbulent flow condition

In most cases, the characteristic size L of flow is h, which is about 1 mm in our experiment; the flow is a small scale one and should not be a turbulent flow. But if flow rate Q of the transparent fluid is high, its velocity will be high and the relative Reynolds number (Re) should be high as stated above. However, we still cannot determine a criterion based on the Reynolds number for deriving the flow to be laminar or turbulent.

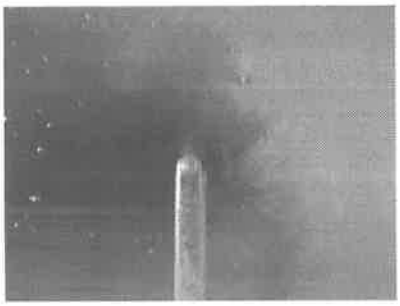

Fig. 5 Image of the turbulent flow

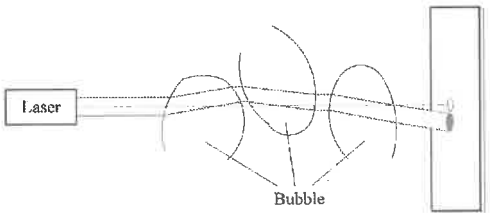

Fig. 6 Laser beam is deflected by the turbulence

Fig. 5 is an example of turbulent flow, in which the boundary of the transparent window becomes rough and unsteady. But the transparent window is still available although the form of the boundary line is changed. Because the velocity directions of the turbulent flow are different in different layers, the effect of laser beam propagation in this case should be low than in the case which direction of flow is at a special direction due to the bucking effect.

According to the analysis the above laminar flow case where flow is in a special direction, the effect of laser beam propagation in turbulent case can be ignored. However in the case of turbulent, air bubbles may exist in the water flow, which will cause considerable problem for laser beam propagation in the transparent window. The turbulence cells act as very weak lenses

that deflect the beam as a whole in a random way as shown in Fig. 6. The resulting beam displacement from the initial beam direction is known as beam wandering.

Experimental Testing and Discussion

In order to investigate this new method, we measured a test piece in Wyko optical profiler and our experimental rig. Fig. 7 shows the profile of test piece in the range of 70 mm measured by Wyko. Fig. 8 shows the profiles measured by our experimental rig. Compare these profiles, they are fit each other in whole range.

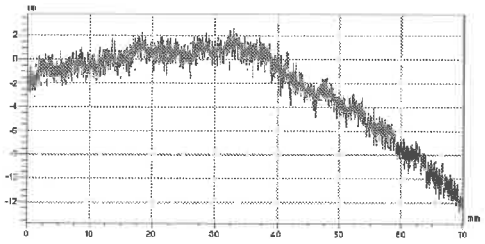

Fig. 7 Profile measured using the Wyko profiler

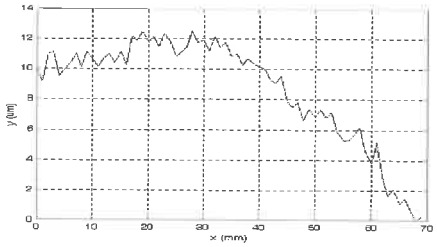

Fig. 8 Profile measured using the new method

Conclusions

The propagation of the laser beam in the transparent window is not affected by the static properties of the fluid layer, but also by the flowing properties. In the case of laminar flow, the deflection of the laser beam through the flowing layer can be computed and the values are low. If the flow is turbulent, the deflection of laser beam is also low depending on analysis. However, we have to pay special attention to the case of turbulent flow because air bubbles may exist in the water flow, which will cause serious problems for the laser beam propagation in the transparent window. The comparison of the measurement results by Wyko and the new method respectively has been performed, which shows that the two results are fit and the new method can be used to measure the surface profile under coolant condition.

Acknowledgement

This work has been supported by the Research Grants Council of Hong Kong SAR of China (Project no. HKUST6100/97E).

References

[1] Z. Tao, and Y. Gao, Modeling of the fluid dynamics aspects for in-process optical measurement under coolant conditions, Proc ASPE 2001, pp. 257-260.
[2] Y. Gao, and Z. Tao, Tests of flow patterns of grinding coolant interfered using an injection of stream, Proc EUSPEN 2001, **2**, pp. 684-687.
[3] Y. Gao, Use of fluid beams to establish a clean zone for in-process optical measurement, Proc ASPE 2001, pp. 329-332.
[4] Z. Tao, and Y. Gao, Analysis of transparent fluid patterns for optical in-process measurement, Proc ISMTII 2001, pp. 407-411.
[5] Z. Tao, and Y. Gao, Recognition of fluid images for in-process surface profile measurement, Proc ISMQC 2001, pp. 123-128.
[6] Y. Gao, and Z. Tao, Analysis of measurement errors for light passing through parallel layers, Proc EUSPEN 2002, pp. 707-710.

A METHOD FOR FAST GAUSSIAN FILTERING FOR 3D ROUGHNESS EVALUATION

W. Zeng [a], Y. Gao [b,*], K. O [b], T. Xie [a]

[a] Huazhong University of Science and Technology, Wuhan, Hubei, 430074, China
[b] Hong Kong University of Science and Technology, Clear Water Bay, Kowloon, Hong Kong
* E-mail: meygao@ust.hk

Introduction

In the assessment of engineering surfaces, it is fundamental to decide correctly a datum line or plane. The precision of datum line or plane directly influences the precision of the assessment of surface parameter.

In the assessment of parameters of surface roughness, the method of mean line assessment datum and the one of filtering are often to be used. The mean line assessment datum mainly includes the least square mean line and the arithmetic mean line. The mean line methods have two inherent disadvantages. Firstly, along the overall evaluation length, the assessment datum is not continuous. A step may appear at the crossover region of two adjacent sampling lengths. Naturally, the datum should be a smooth curve. Secondly, the datum greatly relies on the sampling length to extract surface roughness. Distortions in surface roughness assessment may occur if the sampling length is too long or too short.

The traditional filtering method mainly relied on 2RC filter. Many instruments of surface roughness in the earlier period use the 2RC filter in the electronic filtering. Due to the inherent nonlinear phase characteristics, the 2RC filter may lead to distortions in a reference datum plane. The 2RC filter has gradually been phased out in recent years.

The wavelet method has been widely applied in the areas of signal processing. In surface feature processing, the wavelet datum to be used as an assessment datum for surface feature assessment has produced some interesting results [1]. The option to use the wavelet datum also has a disadvantage such as the level of wavelet decomposition is uncertain.

The datum line of surface roughness assessment is required to be a Gaussian datum line in the current international standard ISO 11562. The sampling signal is to pass through a Gaussian low pass filter in order to obtain a datum line for roughness assessment. The main advantage of the Gaussian filter is the linear phase characteristics [2-3]. Currently, surface measurement and assessment is moving from 2D to 3D. The Gaussian filter has been accepted for both 2D and 3D surface roughness assessment.

However, in the post measurement data treatment, the filter is computationally intensive. A new algorithm is presented to provide a solution to the problem. The algorithm is based on the approach of direct and fast convolution. The essential technique in the algorithm is to utilize the iterative characteristics and the separable characteristics of the 2D Gaussian function to significantly reduce the number exponential computations. Numerical example shows that the

proposed algorithm is faster than the Fourier transform approach.

Filters and Datum Surface for 3D Surface Roughness Evaluation

A 3D surface f may be defined as

$$f(x,y) = s_1(x,y) + s_2(x,y), \tag{1}$$

where the Fourier transformation of s_1 and s_2, , noted as S_1 and S_2, respectively, satisfy

$$S_1(w_x, w_y) = \begin{matrix} F(w_x, w_y), & |w_x| \le w_{cx} \, |w_y| \le w_{cy} \\ 0, & |w_x| > w_{cx} \, |w_y| > w_{cy} \end{matrix} \tag{2}$$

and

$$S_2(w_x, w_y) = \begin{matrix} F(w_x, w_y), & |w_x| > w_{cx} \, |w_y| > w_{cy} \\ 0, & |w_x| \le w_{cx} \, |w_y| \le w_{cy} \end{matrix}, \tag{3}$$

where F is the Fourier transformation of $f(x,y)$, w_{cx} and w_{cy} are the cut-off frequencies in the x and y directions, respectively. Choosing suitable cut-off frequencies, s_1 includes the form and waviness errors of the 3D surface. It can be the datum surface. s_2 is the 3D roughness surface for the 3D roughness evaluation. It is clear that $s_2 = f - s_1$. In addition, s_2 can be obtained by using a low-pass filter $h(x, y)$ [4-5] as

$$\begin{aligned} s_1(x,y) &= f(x,y) * h(x,y) \\ S_1(w_x, w_y) &= F(w_x, w_y)\, H(w_x, w_y) \end{aligned}, \tag{4}$$

where H is the Fourier transformation of the function h. H may have either a square shape or a circle shape in the frequency domain (Fig. 1). For convenience in the digital implementation, the Gaussian low pass filter (Fig. 2), noted as g and its Fourier transformation as G, may be used to replace the idealized filter h (Eq. (2) and Eq. (4)). In this case, s_1 is noted w (Eq. 4).

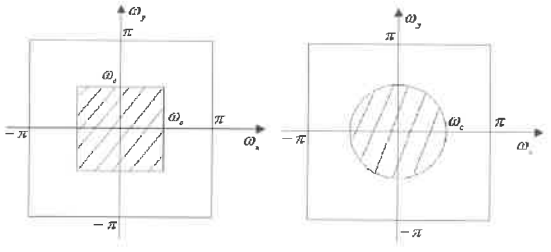

Fig. 1 Datum filter characteristics

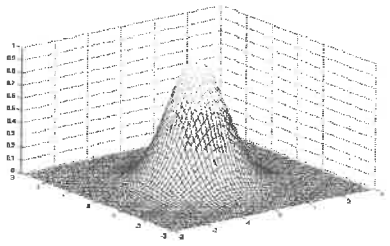

Fig. 2 Gaussian filter characteristics

Fast Estimation of Gaussian Filter and Datum Surface

The actually measured 3D surface f is typically discrete. w must be discrete as $w_{i,j}$. The sampled data of a 3D surface is noted as $z_{i,j}$. The datum surface $w_{i,j}$ can be obtained as

$$w_{i,j} = \sum_{k=-M}^{M} \sum_{l=-N}^{N} z_{i-k,j-l} g_{k,l} \Delta x \Delta y , \tag{5}$$

where $i=M,\ldots,LX-M, j=N,\ldots,LY-N$, LX and LY represent number of samples, and

$$g_{k,l} = \frac{1}{\alpha^2 \lambda_{cx} \lambda_{cy}} \exp\left[-\pi \left(\frac{k\Delta x}{\alpha \lambda_{cx}} \right)^2 - \pi \left(\frac{l\Delta y}{\alpha \lambda_{cy}} \right)^2 \right]. \tag{6}$$

Equation (5) may be done using two methods, FFT or direct convolution. The FFT method involves the Fourier transformation and the inverse transformation. The direct convolution method does not require the two complex computational operations. For both methods, extensive computations of the exponential function are involved. To reduce the computation time for high efficiency, this problem must be solved.

In the proposed method, the convolution method is utilized and the fast algorithm is based on the use of the symmetrical feature of the exponential function, noted as $g(-k)=g(k)$. The datum surface can be obtained as

$$w_{i-k} = z_{i-k,j-l}\, g(l=0) + \sum_{l=1}^{N} (z_{i-k,j-l} + z_{i-k,j+l})\, g(l)\, \Delta y , \tag{7}$$

and

$$w_{i,j} = w_{i-k}\, g(k=0) + \sum_{k=1}^{M} (w_{i-k} + w_{i+k})\, g(k)\, \Delta x . \tag{8}$$

The above equations have a similar structure, for which a reduction of 50% in the multiplication computations can be achieved for each of the cases. Therefore, a total reduction of 75% in the multiplication computations can be achieved.

In addition, a reduction in the number of computations of the exponential function can be realized to further improve the datum surface algorithm. This is illustrated as

$$g_0 = \frac{1}{\alpha \lambda_c}, \; g_k = p_{k-1} g_{k-1}, \; k=1,\ldots, M \text{ or } N, \tag{9}$$

where

$$p_0 = q,\ p_k = q^2 p_{k-1},\ p_k = q^{2k+1},\ q = \exp\left(-\pi\left(\frac{k\Delta}{\alpha\lambda_c}\right)^2\right),\ k=1,\ldots,M \text{ or } N. \tag{10}$$

The above algorithm indicates that the (2M+1)(2N+1) multiplications have been used to replace the (M+1)(N+1) exponential calculations. Thus the calculation has significantly been reduced and the proposed method is very fast.

Experimental Testing, Discussion, and Conclusion

The proposed algorithm has been realized using VC6 and Matlab5. The code has been tested experimentally (Fig. 3). In the example, the number of the 3D surface data points was 250x250. The calculation time on a Pentium III 450MHz PC was only 2s. The calculation time using the FFT method was 3s. The direct convolution took 6s approximately on the same PC. This shows that the proposed method is effective. In terms of computational efficiency, the proposed method is more advantageous than the other two methods.

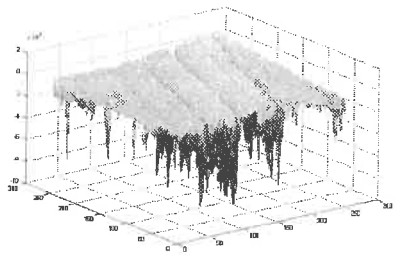

Fig. 3 Measured 3D surface f

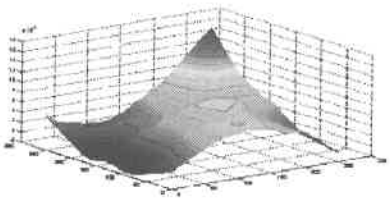

Fig. 4 3D datum surface w

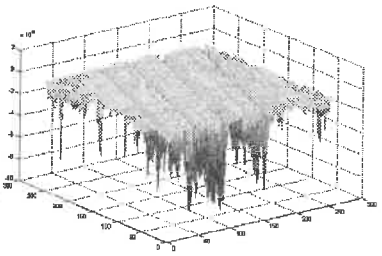

Fig. 5 3D roughness surface s_2

Acknowledgement

This work has been supported by the National Natural Science Foundation of China (Project No 50175037).

References

[1] Chen, Q., Surface roughness evaluation by using wavelets analysis, Precision Engineering, **23**, 1999, pp. 209-212.
[2] ISO/CD 11562-1993, Metrological characterization of phase correct filters and transmission bands for use in contact (stylus) instruments, ISO, Geneva, 1993.
[3] ISO 4287-1997, Geometrical product specification (GPS) - Surface texture: Profile method - Terms, definition and surface texture parameters, ISO, Geneva, 1997.
[4] Krystek, M., A fast Gauss filtering algorithm for roughness measurements, Precision Engineering, **19**, 1996, pp. 198-200.
[5] Stout, K. J., Development of methods for the characterization of roughness in three dimensions, Penton Press, London, 2000.

FLOAT POLISHING OF CALCIUM FLUORIDE SINGLE CRYSTALS FOR ULTRA VIOLET APPLICATIONS

Yoshiharu Namba, Naoyuki Ohnishi and Kazuaki Harada

Chubu University, Kasugai, Aichi 487-8501, Japan

Kunio Yoshida

Osaka Institute of Technology, Osaka 535-8585, Japan

Abstract

Calcium fluoride single crystals for ultra violet applications have been finished to flat by the float polishing process with 7nm-diameter silicon dioxide powder, pure water and a tin lap. The 42nm P-V and 5.81nm rms flatness were obtained on a sample of 100mm in diameter. Atomically-smooth surfaces were also obtained on the surface. The surfaces were measured with optical surface measuring apparatus, atomic force microscope and transmission electron microscope. There is no damage layer on float-polished surface due to machining.

Keywords: Calcium fluoride; Float polishing; Atomic surface structure; Lithography; Transmission electron microscopy

1. Introduction

The light sources for micro-lithography has been changed from the g-line, i-line of mercury lamp to excimer lasers of Deep Ultra Violet (DUV) region, and will be planed to use ArF excimer and F_2 excimer in Vacuum Ultra Violet (VUV) region. However, there are some problems on optical components for using such shorter wavelength lasers. The problems are listed as limitation of transparent materials for such regions, no established machining technology for such materials, lack of knowledge on interaction between the materials and lasers, and lack of data of laser induced damage thresholds on the materials. DUV/VUV lithography-grade calcium fluoride (CaF_2) is the only candidate for such applications. The demands on the surface are high precision in figure and smoother surface roughness, though the crystal is soft and relatively high thermal expansion coefficient, as well as higher laser-induced damage threshold, higher uniformity in index and higher transparency. The float polishing has being finished various single crystals and optical glasses ultra-finely without deformed layer [1-3]. We will try to use this technology to get DUV/VUV lithography-grade surface on CaF_2 single crystals. The finished surface geometry will be also measured in the range of macro to atomic scale.

2. Experimental Procedure

DUV-grade CaF_2 single crystal samples of 35mm × 35mm × 10mm in dimensions were cut oriented in the (111) plane. The samples were ground, optically polished and finally float-polished with SiO_2 powder of 7nm in nominal diameter and pure water on a tin lap as shown in Fig. 1. The float polishing machine [3] has a hydrostatic oil bearing of high rigidity and damping as well as high rotational accuracy. The tin lap having many concentric grooves of 2mm in pitch and 1mm in depth was cut into flat with a single point diamond tool. The temperature of polishing fluid was controlled in a range of ± 0.01K. Optically polished samples were also obtained from the market. One sample has dimensions of 100mm in diameter and 20mm in thickness. This sample was float-polished to get a large plane.

The finished surfaces were observed under a Nikon's Nomarski differential interference microscope, and measured with ZYGO's GPI-XP, WYKO's TOPO-2D, Seiko's Atomic Force Microscope (AFM). Subsurface damage was observed by an etching technology with the Nikon's Nomarski microscope.

The cross-sections of polished surfaces were observed with JEOL's JEM-2010 Transmission Electron Microscope (TEM) operated at 200kV. For the TEM observations, the optically polished and float-polished crystal samples were sectioned oriented normal to the (111) surface. The samples were then ground and polished with Al_2O_3 powder of about 50 nm in diameter. These samples were finally ion-polished with Fischione's Model-1010 ion mill.

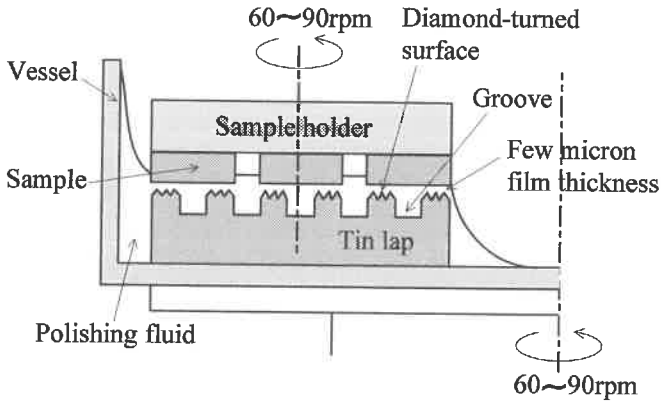

Fig. 1 Principle structure of a float polishing machine.

3. Experimental Results and Discussion

Figure 2 shows the flatness of the float-polished CaF_2 sample of 100mm in diameter and 20mm in thickness, measured with ZYGO's GPI-XP phase measuring interferometer system. The surface flatness of 5.81nm (λ/109;λ=633nm) rms and 42nm (λ/15) P-V was obtained on a float-polished CaF_2 sample of 100mm in diameter. By controlling polishing conditions, especially temperature, 3.16nm (λ/20) P-V flatness will be obtained very near future by using the float polishing

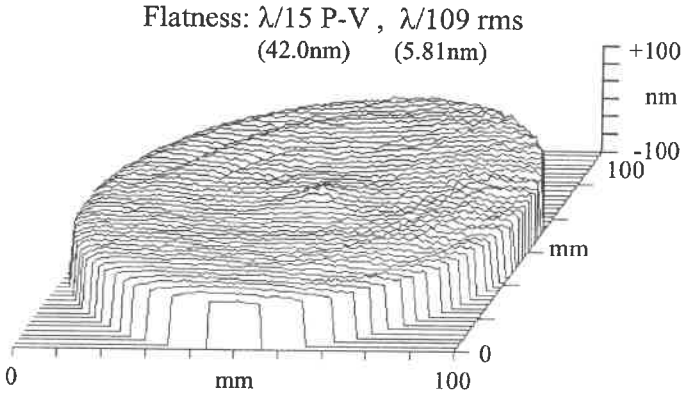

Fig. 2 Surface flatness of a float-polished CaF_2 sample of 100mm in diameter, measured with GPI-XP.

Figure 3 shows the surface roughness of a float-polished CaF_2 sample, measured with TOPO-2D at 40X. The surface roughness numbers are 0.228nm rms, 0.183nm Ra, 1.33nm P-V in the measuring length of 320μm. This number is about the same number in float-polished BK-7 and Zerodur [3], however this number is the smallest among many samples that we have measured optically polished CaF_2 samples from the market.

Figure 4 shows the surface roughness of a float-polished CaF_2 sample, measured with an AFM in 10μm by 10μm area. The surface roughness numbers are 0.162nm rms, 0.131nm Ra, 1.10nm P-V. In the case of polishing CaF_2 single crystals for infrared applications, the surface roughness of 0.235nm rms, 0.188nm Ra, 1.65nm P-V was obtained. From this result, it is clear that the polished surface roughness depends upon the purity of materials. From the simulation of 3D surface roughness on ideal atomic structure [4], the ideal surface roughness of CaF_2 may be estimated 0.033nm rms. Therefore, the surface roughness less than 0.1nm rms can be obtained on CaF_2 samples.

Various (111) CaF_2 samples such as float-polished, cleaved and ultra-precisely ground were prepared and etched with hydrochloric acid to reveal the dislocation on the surface. The float-polished sample shows etch pits of triangular pyramid in shape. The distribution density of such pits is same as those on well-cleaved surface. From the observation of etch pits, it is clear the float-polished surface is free from dislocation due to machining.

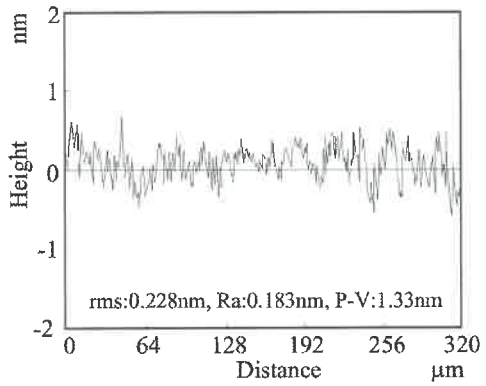

Fig. 3 Surface roughness of a float-polished CaF_2 sample, measured with TOPO-2D.

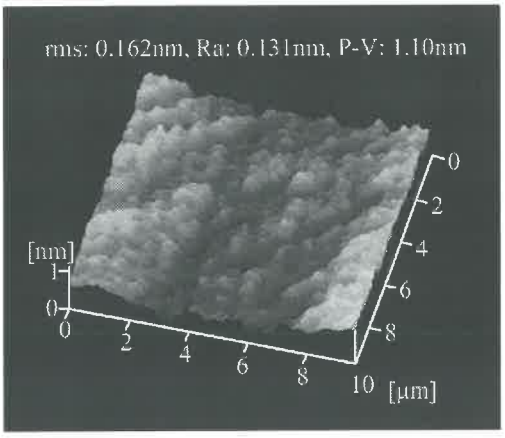

Fig. 4 Surface roughness of a float-polished CaF_2 sample, measured with SPA270.

Figure 5 shows cross-section TEM images of optically polished and float-polished CaF_2 crystal surface, obtained with an incident electron beam parallel to the (111) plane. The images show high-density strain field contrast at the subsurface of optically polished specimen. This indicates higher dislocation density exist at the subsurface of the sample. On the other hand, there is no such strain contrast attributed to dislocations due to machining on float-polished surfaces. These TEM observation results are consistent with those obtained by the etching experiments.

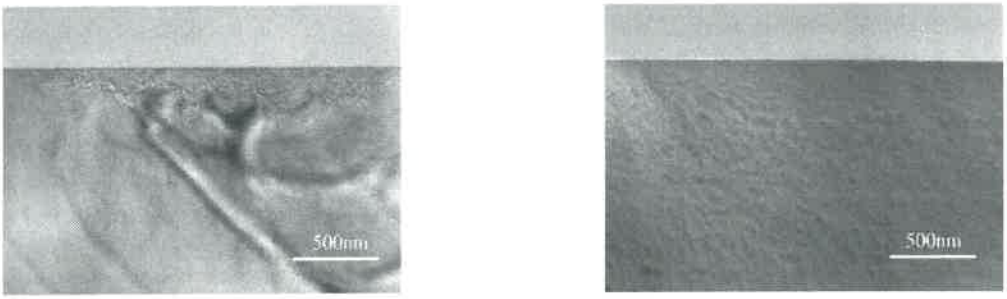

(a) Optically polished surface (b) Float polished surface

Fig. 5 Cross-section TEM images of polished CaF_2 samples.

Figure 6 is a high-resolution TEM image of float-polished surface taken with the same electron beam incidence as Figure 5. The image shows fine fringes of (111) plane with a lattice spacing of 0.32 nm. This profile-view image shows the float-polished surface consists of fine lattice steps of the (111) plane. In a small area on the terrace of the surface, an atomically smooth planes parallel to the (111) lattice are achieved, though the surface roughness derives from steps of a few nm between (111) planes. These step profiles are considered due to mismatch of the sample surface orientation from the (111) lattice plane. And thus, the result shows that if we can obtain a sample surface oriented parallel to the (111) plane in ultra high precision, the surface roughness less than 0.1nm rms may be obtained by float polishing.

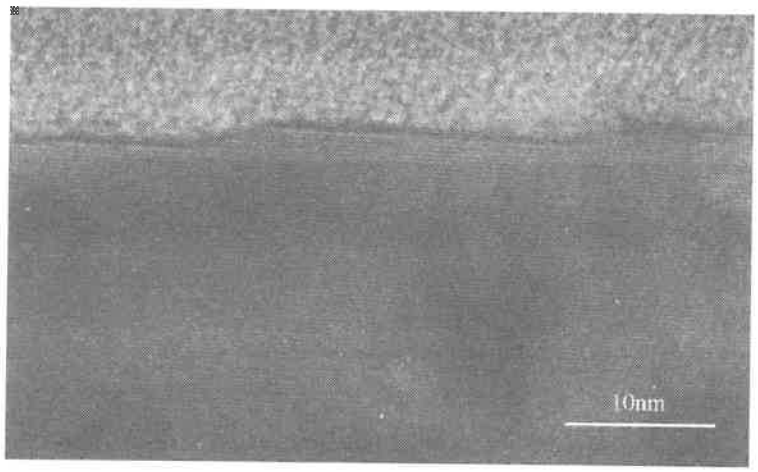

Fig. 6 TEM image of a float-polished CaF_2 surface, indicating the (111) lattice fringes.

4. Conclusions

Calcium fluoride single crystals were finished to flat by the float polishing process with 7nm-diameter silicon dioxide powder, pure water and a tin lap. The 42nm P-V and 5.81nm rms flatness were obtained on a sample of 100mm in diameter. Surface roughness of 0.235nm rms, 1.33nm P-V in measuring length of 0.32mm was obtained on the float-polished surface, measured with TOPO-2D at 40X. The surface roughness of 0.162nm rms, 1.10nm P-V was obtained on the float-polished sample, measured with an AFM in 10μm by 10μm area. The polished surface roughness depends upon the purity of materials. The etching technology makes clear that the float-polished surface is free from dislocation due to machining. Transmission electron microscopy shows the float-polished surface is atomically smooth on (111) surface, however there are lattice steps due to miss orientation of the sample from (111) surface.

Acknowledgements

A part of this work was supported by the Grants-in-Aid for Scientific Research (B) No.11450063 and No.13875030 of the Japan Society for the Promotion of Science.

References

1. Y. Namba and H. Tsuwa: "Ultra-Fine Finishing of Sapphire Single Crystal", Annals of the CIRP, **26/1** (1977)p.325-329.
2. J. M. Bennett, J. J. Shaffer, Y. Shibano and Y. Namba: "Float Polishing of Optical Materials", Appl. Opt., **26**, 4 (1987)p.696-703.
3. Y. Namba, H. Tsuwa and R. Wada: "Ultra-Precision Float Polishing Machine", Annals of the CIRP, **36/1** (1987)p.211-214.
4. Y. Namba, J. Yu, J. M. Bennett and K. Yamashita: Modeling and Measurements of Atomic Surface Roughness, Appl. Opt., **39**, 16 (2000)p.2705-2718.

COMPARISON OF TWO INSTRUMENT DESIGNS FOR NON-CONTACT MEASUREMENT OF GOSSAMER MIRRORS

Phil Smith and R. Ryan Vallance
Precision Systems Laboratory, University of Kentucky*

Abstract

Lightweight, large format mirrors are planned for the next generation of space-based telescopes to collect the maximum amount of light from faint sources. A second, less-demanding application for large format mirrors is for the collection of solar radiation. In either case, accurate measurements of the large-scale form of the surface of gossamer optics must be achieved. If the wavelength of light is in the visible region, then a useful measure should have accuracy on the order of 50 nm or less to be a useful indication of the quality of the optic. In this paper two machine designs are compared and contrasted to determine which machine offers the potential accuracy, while allowing sufficient flexibility for measuring a variety of mirror surfaces and curvatures.

Keywords

membrane optics, gossamer optics, ultra-lightweight mirrors, non-contact form measurement

Introduction

The traditional method of measuring the form of large optics is using an interferometric method [1]. Optics divert a plane wave to the idealized shape of the optic, then the fringe pattern on the surface is checked for areas that need further work. In many cases, a CCD camera captures the image of the fringe pattern for analysis.

Unfortunately, this method is limited in the surfaces it can easily evaluate. Some optics may require a customized, holographic grating to check for form errors. For different radii of curvature, a different optic would be required. Large deviations from the ideal form cannot be measured interferometrically, due to the overlap of fringes. Often for this reason the interferometer method is used only at the final evaluation step.

Another method of surface evaluation is to use contact profilometry to measure multiple points on an arc [2]. A pivoting arm is designed to trace a circular arc, and a gauge measures deviation in radius from sphericity. To access all points on the surface, a second rotational axis is required, either to rotate the measurement structure over the mirror surface, or to rotate the mirror surface under the measurement structure.

The proposed machines is designed to have both the non-contact benefit of interferometer techniques, as well as the flexibility of pivoting arms provide to measure a variety of near-spherical shapes with a minimum of specialized optics or extended setup.

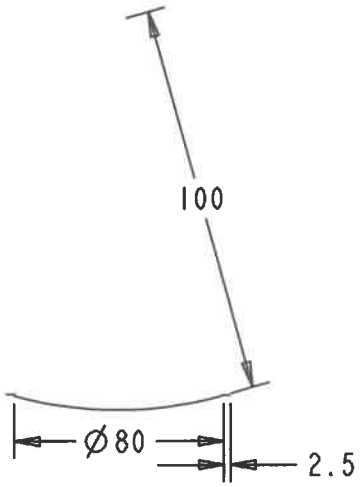

Figure 1. Initial target values for mirror dimensions, in mm

* *Precision Systems Laboratory, Mechanical Engineering Department, University of Kentucky, Lexington, KY 40506. http://www.engr.uky.edu/psl.*

Mirror Description

The initial target mirror dimensions for this application are shown in Figure 1. The surface has a radius of curvature of 100 cm and a diameter (circumference/pi) of 80 cm. The mirror is formed from a thin sheet of polymer with aluminum deposited on the concave side.

As with most gossamer optics, the mirror is designed to be supported only by its edges, so a "nest" has been designed that allows for uniform support of the edge of the mirror. The nest also has a series of holes around its upper surface that provide a slight vacuum to hold the film in place during measurement. This nest is shown in Figure 2. The mirror must be mounted horizontally to prevent it from collapsing under its own weight, due to lack of any significant stiffness of the polymer. Naturally, such a flexible surface can only be measured using a non-contact method. Since the mirror surface is aluminized, a capacitance gauge is chosen as the optimal non-contact sensor to be mounted on the end of the probe tip.

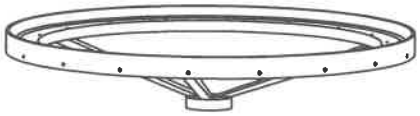

Figure 2. "Nest" for supporting thin flexible mirror

Radial Displacement Sensing

The proposed device for non-contact measurement of the mirror surface is a capacitive gauge sensor. These sensors have the advantage of an averaging effect over the active area of the sensor (typically ~2 mm^2), thus averaging out roughness and waviness wavelengths. This size is also compatible with the number of measurement points desired for analysis purposes.

Although a capacitive gauge such as that proposed herein can detect relatively large changes in distance (1 mm or more on lower sensitivity settings [3]), this extended range comes at the expense of a loss in resolution. It is proposed instead that the cap gauge be mounted on a small air bearing and kept at a constant distance from the surface using a voicecoil or linear motor and closed-loop feedback. This arrangement will also prove advantageous when analyzing systematic errors. The movement of the capacitive gauge in the radial direction will be measured by a laser interferometer. A similar scheme has been proposed previously using a commercially available CD optical head [4], but this does not have the averaging advantage provided by the capacitance gauge.

The primary limitation of standard commercial capacitance gauges is in the range of acceptable angles. Because of the small gap and relatively large flat surface (including guard ring structure), the maximum angle of one commercial gauge is calculated to be ~ 2.3 degrees at the highest sensitivity setting. Ultimately this range limits the mirror geometries that can be measured, and highlights the importance of proper alignment when setting up this machine.

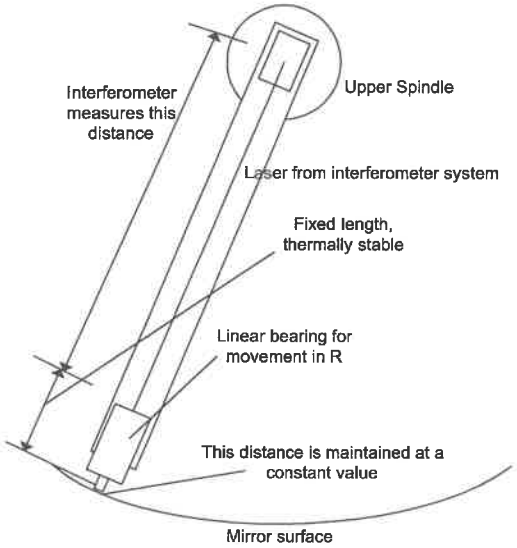
Interferometer measures this distance
Upper Spindle
Laser from interferometer system
Fixed length, thermally stable
Linear bearing for movement in R
This distance is maintained at a constant value
Mirror surface

Figure 3. "Pendulum" design

Two Competing Instrument Designs

The first instrument design considered for this measurement uses a "pendulum" geometry, with a radial arm pivoted at the nominal center of the mirror. The basic configuration of this system is shown in Figure 3. The nest is supported by a spindle that allows rotation around a vertical axis. The pendulum pivots on a second, horizontal axis to sweep across the surface of the mirror. The light path for the interferometer travels along the horizontal axis of the upper spindle, then is reflected downward

to the back side of the capacitance gauge sensor. For a perfectly spherical mirror with the upper axis of rotation intersecting the center of the mirror, the variation in radius and the tilt of the surface are naturally both zero.

The second design considered for this machine uses a "swingarm" to traverse the surface of the mirror. This design is shown in Figure 4. As in the first machine, the mirror is mounted horizontally on a rotating spindle. For optimal operation of the machine the tilted axis of the swingarm must intersect with the vertical axis of the mirror at the nominal center of the mirror.

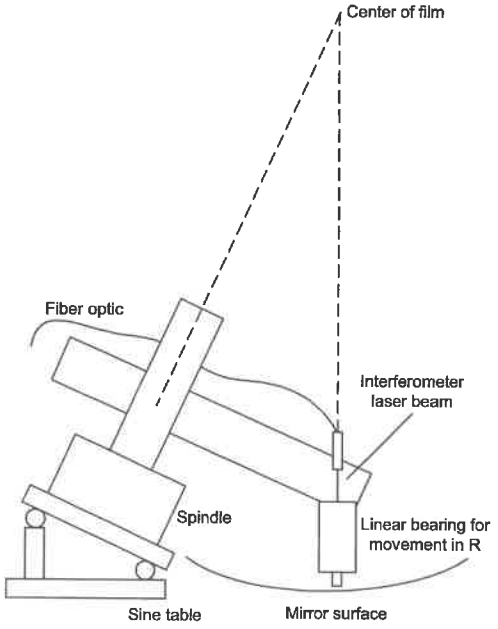

Figure 4. "Swingarm" design

First Design: The "Pendulum"

The pendulum design shown in Figure 3 is the most straightforward of the two designs. The upper spindle supports a stiff but lightweight arm that in turn supports the linear bearing and voicecoil. This spindle is mounted in a large overhead structure, possibly granite, which allows for multiple mounting locations of this spindle.

The laser for the interferometer passes through the center of this spindle, then is reflected downward, along the arm, to the back side of the capacitance gauge mount. This mount is to be made of zerodur or a similar low CTE material. The advantage of this light pathway is in its ability to include changes in the length of the overall arm due to gravity, temperature changes, etc. Temperature changes may affect the surrounding granite structures, but they have a much more significant thermal mass.

A final point in favor of this design is in the ease of calculating the angular location of the surface points. Figure 5 shows a plot of lines traversed by the capacitance gauge. For a given measured point it is only necessary to read the two angles from the two spindles. These angles, combined with the radius determined by the interferometer, specify the exact location in space of that point on the mirror.

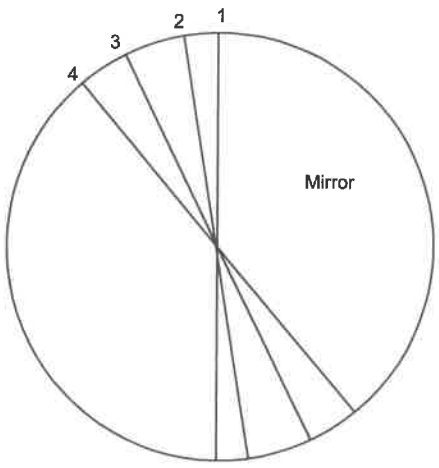

Figure 5. Downward-looking plot of lines traversed by pendulum design

The most fundamental limitation of the pendulum design is its inability to measure a wide range of different curvatures. Since the upper spindle must be aligned with the nominal center of curvature of the film, relatively flat mirrors require mounting the spindle high above the surface. Any offset between the spindle and this center results in added tilt between the capacitance gauge and the surface. A sample plot of this increase is shown in Figure 6.

As the radius of curvature of the mirror increases, the length and mass of the arm increases, with a third-order increase in the bending angle of the arm. Even given multiple mounting locations for the upper spindle, the final alignment must be achieved by raising/lowering the film, necessitating z-axis motion of the lower spindle. Alignment of the

center of the film under the zero position of the pendulum arm requires x and y axis control of the lower spindle as well.

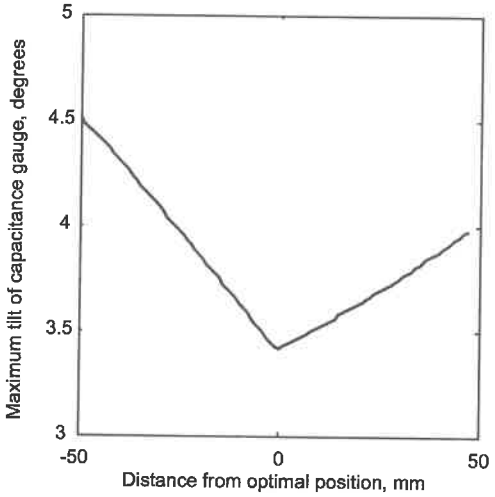

Figure 6. Tilt angle due to spindle offset from film center, pendulum design

Second Design: The "Swingarm"

The swingarm design of Figure 4 uses a different geometrical configuration to position the capacitance gauge over different points on the mirror surface. In this case a horizontal arm rotating on a tilted axis suspends the capacitance gauge mount above the surface. The capacitance gauge is moved in the radial direction by the same voicecoil arrangement described above. As can be seen from the figure, a huge advantage to this system is that the arm is only slightly larger than the radius of the mirror. For different radii of curvature, only the angle of the sine table changes. This geometrical relationship is given [2] by the equation

$$\sin\theta = \frac{L}{R} \qquad (1)$$

Where L is the perpendicular distance from probe tip to axis of rotation, and R is the nominal radius of the film. Once the approximate angle is set by adjusting the sine table, the mirror is moved to its final position using x and y axes. No z-axis motion of the mirror is required for alignment. As can be seen from the above equation, the swingarm design can even accommodate a mirror of infinite radius (flat surface). Finally, since this design locates the measurement equipment to one side of the surface, other equipment (e.g., optics) can be mounted overhead.

One downside of this swingarm arrangement is the difficulty in choosing the optical path for the interferometer. Current thinking is to bring the laser to the end of the arm using fiber optics, measuring just the travel of the capacitance gauge relative to the end of the arm. No longer can the laser pathway measure all vertical motions of the capacitance gauge mount. Instead, corrections due to arm bending and thermal drift must be added later, as described in the systematic errors section.

A second difficulty arises when calculating the location on the mirror surface of measured points. As can be seen in Figure 7, rotating the capacitance gauge causes arcs to be traced on the surface of the mirror. The position of these points is calculated from knowledge of the distance L of the machine and the angular information from the two spindles.

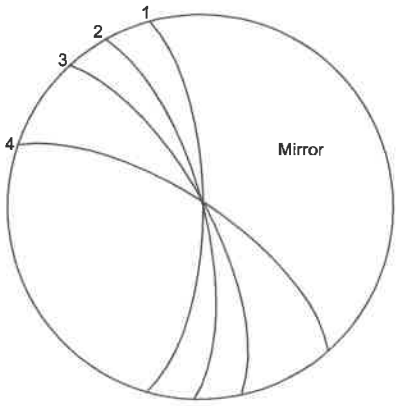

Figure 7. Downward-looking plot of arcs traversed by swingarm design

Systematic Errors

Several systematic errors of this machine are anticipated and are being analyzed. The temperature of the various parts of the machine changes the dimensions slightly; in both designs some of these changes will be in the sensitive direction. Once the measurement time is known (the number of minutes necessary to measure an entire surface) room temperature fluctuations over this time scale can be evaluated.

A second systematic error occurs whenever the capacitance gauge is tilted with respect to the

surface being measured. The capacitance gauge is factory-calibrated using a parallel reference flat at a known distance. Any tilt with respect to the surface being measured has the effect of the capacitance gauge perceiving the average distance as being closer than it actually is. Closed-form solutions to this capacitance problem exist for small angles [5], one such solution is as follows:

$$C = \frac{2\pi\varepsilon r^2 \cos\theta}{d_0}\left[\frac{1-\left(1-k^2\right)^{0.5}}{k^2}\right] \quad (2)$$

$$k = \frac{r\sin(2\theta)}{2d_0} \quad (3)$$

The plot in Figure 8 shows the percentage error in distance for a particular spacing and tilt angle. This correction can be added to radius values from either machine by simply calculating the gradient of the surface at each measurement point, then adding the appropriate value.

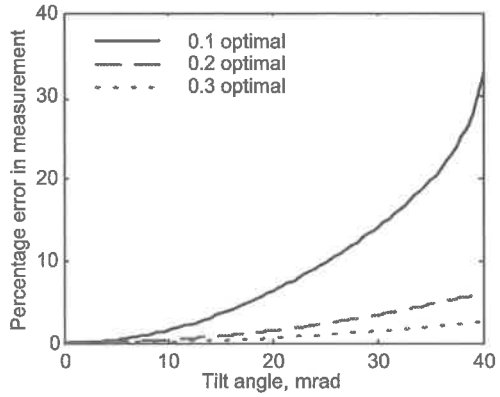

Figure 8. Plot of distance offset as a function of tilt angle, optimal spacing in mm

Another systematic error is due to structural bending or extension of the measurement arm. As discussed previously, in the pendulum design the extension of the arm is included in the measurement of the R value by the interferometer. At any position other than vertical there also exists bending in the arm, which is manifest in both deflection and tilt at the end of the arm. Tilt errors are most likely much smaller than the tilt encountered by the cap gauge simply due to the mirror surface being aspheric. Equations for deflection can be solved as a function of the arm angle, and these can be used to correct the location of the measurement point in postprocessing.

For the swingarm design, the arm is primarily in a bending mode, although the direction changes as a function of both sine table and spindle angle. For this reason it is advisable to use a hollow cylinder as the arm structure, since this geometry has a uniform moment of inertia for bending at any angle. As above, changes in capacitance gauge position as a function of angle can be added in postprocessing.

Setup and Measurement

The resolution goal of measurements along the surface of the mirror is 0.1 mm in any direction. To achieve this the arm must be set to zero and the mirror centered under this arm. All measured distances and angles will be from this point, so this alignment is crucial.

The first step in this alignment is the x-y adjustment of the mirror relative to the capacitance gauge. For this purpose a reference surface is ground into the nest holding the mirror. Checking the distance to the reference surface when the arm is at $\pm\theta_{max}$ ensures that the film is centered in the x and y directions.

The second step in this alignment is to locate the center of the mirror. To a certain level this can be done visually by spinning the mirror continuously and moving the capacitance gauge to the proper location. Next, the capacitance gauge is held fixed and the analog output voltage (proportional to distance) is viewed over time. When the mirror is exactly centered, the voltage of the gauge will be minimized. Since these two steps are somewhat dependent on each other, they may have to be repeated for optimal alignment.

Parametric Studies

To study the geometry of the swingarm model in greater detail, a skeleton model of the structural components was created in ProEngineer. This model, shown in Figure 9, was used to perform sensitivity studies as the arm traversed the surface. First, a spherical surface was created and the probe swept across its surface. As expected, with optimal alignment the probe surface remained equidistant and

parallel to the mirror surface at all angles. Of greater interest is the clearance of the main arm with respect to the edge of the film, as plotted in Figure 10. This information is helpful when designing the arm and nest structures.

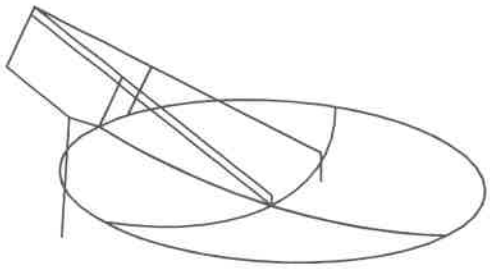

Figure 9. Skeleton model of swingarm design for parametric studies

A second study modeled a parabolic mirror surface with similar dimensions to the original, spherical surface. Figure 11 shows the radial travel such a surface would necessitate. This information is essential when designing the capacitance gauge support structures.

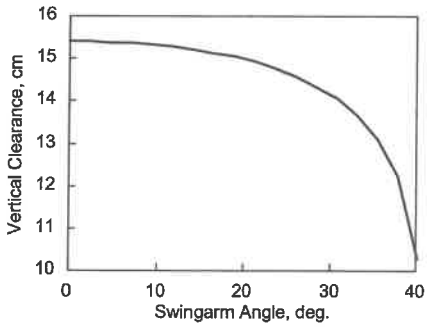

Figure 10. Clearance of swingarm over mirror edge as a function of arm angle.

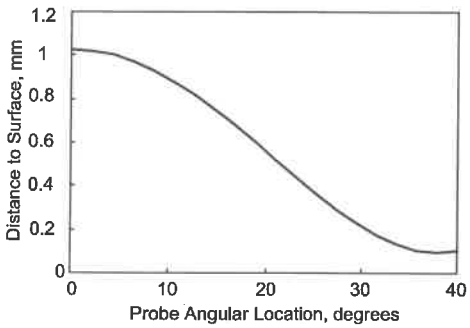

Figure 11. Travel distance required for probe for parabolic surface

Conclusions and Future Work

The swingarm design has been favored to this point due primarily to its greater flexibility in measuring a variety of surface curvatures and to its shorter arm length. Also, the lower profile of the equipment makes this design more easily built from existing machine structures. A solid model is shown in Figure 12.

A final decision on which design will be built and tested must wait until a complete error budget analysis is performed. Already it is apparent that the machine precision will be greatly affected by the choice of rotational bearings. It is likely that the final design will incorporate one or two air bearing spindles, selected for their low radial, axial, and tilt errors.

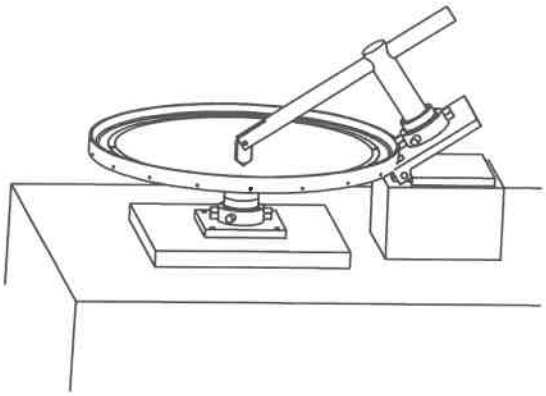

Figure 12. Solid model of final design

References

[1] Environmental Effects in the Testing of Large Astronomical Mirrors ASPE April 1992

[2] Swing-arm Profilometry of Aspherics SPIE Vol. 2536

[3] "3/8 inch cylindrical probes" www.lion precision.com/modular/3-8-cyl.html

[4] J.-H. Zhang, L. Cai, "Profilometry using an optical stylus with interferometric readout" *Meas. Sci. Tech.* **8** (1997) 546-549.

[5] S. Harb, D. G. Chetwynd, S. T. Smith, "Application and performance of capacitive micrometry as a super precision transfer standard" *ASPE Proceedings* **1991** (Santa Fe): 17-20.

Displacement sensor by a common-path interferometer

Kazuhide KAMIYA[*a], Takashi NOMURA[*a], Shinta HIDAKA[*a],
Hatsuzo TASHIRO[**b], Masayuki MINO[+c], Seiichi OKUDA[++d]
[a] Facility of Engineering, Toyama Prefectural University, [b]Facility of Engineering, Toyama University,
[c] Tokushima Bunri University, [d] Computer Engineering & Consulting LTD.
* Kurokawa, Kosugi-machi, Toyama 939-0398, Japan, ** Gofuku, Toyama, Toyama 930-8555, Japan
+ Shido, Shido-machi, Kagawa 769-2193, Japan, ++ Shibuya, Tokyo 150-0002, Japan

Keywords: displacement measurement, common-path interferometer, specular object

Introduction

In manufacturing process technologies, high-precise displacement measurements are one of the key requirements for upgrading of these technologies. For the high-precise displacement measurements, the use of an interferometer such as Twyman-Green is a common practice. However, the interferometers are affected by air turbulence.

A position sensing-grating (PSG) interferometer for a specular object was proposed in order to solve this problem.[1)] The PSG interferometer is a common-path interferometer. The setting for sensing is simple and analysis of the fringe pattern is easy. However, the aberrations of the focusing lens cause measurement error. Therefore, the analysis of measurement error considering the aberration of the lens was carried out and an optics configuration that canceled the aberration was determined. [2)] However, the problem of diffraction efficiency has not yet been solved.

In this paper, an improved common path interferometer is proposed to measure the displacement of a specular object. The proposed interferometer is based on the PSG interferometer but has no diffraction grating. The analysis method of interference fringes analysis for more precise is also described.

Displacement sensor

Figure 1 shows a schematic of the proposed interferometer. The interferometer consists of the beam splitter, the focusing lens and the plane mirror. The specular object is placed at the focus of the focusing lens in the interferometer. A schematic of the optical path is shown in Fig. 2. The incident light is divided into clockwise light and counterclockwise light by the beam splitter. Both types of light propagate in almost the same space in the interferometer. Therefore, the air disturbance dose not influence the measurement. In the interferometer, interference fringes are null fringes when there is no aberration of the focusing lens and the specular object is plased at the focus of the focusing lens. When the specular object is moved in the direction of

the z axis, the interference fringes become straight lines with equal intervals. As both optical paths in the interferometer are symmetrical, only the effect of a coma aberration contributes to the formation of the interference fringe, even if there are many other aberrations in the focusing lens. The interval narrows in proportion to an absolute value of the displacement of the specular object. Figure 3 shows interference fringes obtained by the proposed interferometer.

Analysis method of interference fringe

When the specular object is close to the focus of the focusing lens, there is a region where the number of interference fringes is less than one and it is possible to measure precisely a small displacement by analyzing the intensity of the interference fringe. The analysis of the interference fringe is carried out by integrating the intensity over the region where the interference fringe is obtained. A photodetector is used to integrate the intensity of the interference fringe. By acquiring the intensity with the photodetector, information of the interference fringe is converted into the displacement signal without the use of a computer. When the specular object is placed at the focus of the focusing lens in the interferometer, the interference fringe becomes null and the voltage of the displacement signal obtained by the photodetector is minimum. When one interference fringe is formed on the photodetector, the voltage of the displacement signal is maximum.

The relationship between the displacement of the specular object and displacement signal was simulated from the amount of coma aberrations of the focusing lens. A result of the simulation is shown in Fig. 4. The simulation was carried out under the following conditions: The wavelength and the diameter of the light source were 633 nm and 10 mm, respectively. The focal length of the focusing lens was 300 mm. The interval of the light on the lens was 80 mm.

Experimental results

The experiments were carried out in order to confirm the validity of the proposed interferometer. In the interferometer, the numerical aperture of the focusing lens was 0.25 and the light source was a He-Ne laser with a wavelength of 633 nm. In the experiments, the voltage of the displacement signal obtained by the photodetector was 6.49 V when the displacement of 50 μm was given. Therefore, the sensitivity was 7.7 nm/mV. When the mirror was displaced by 10 nm step, the displacement was detected by the proposed interferometer. Figure 5 shows the displacement signal obtained by the proposed interferometer.

Conclusions

In this paper, a simple common path interferometer was proposed to measure the displacement of a specular object. The analysis method of the interference fringe was also described. When the displacement of 10 nm was given, the displacement was measured by the proposed interferometer and the fringe analysis method.

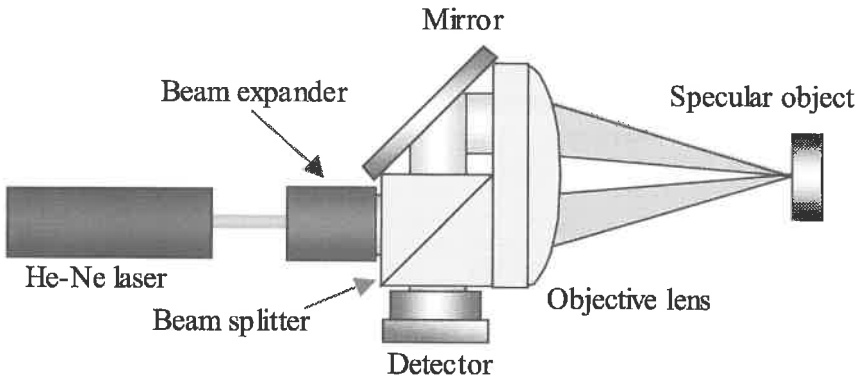

Fig. 1 Schematic of the displacement sensor

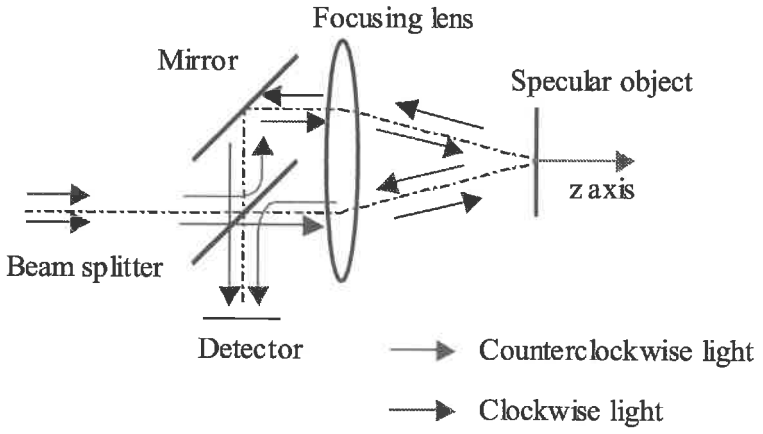

Fig. 2 Schematic of the optical path

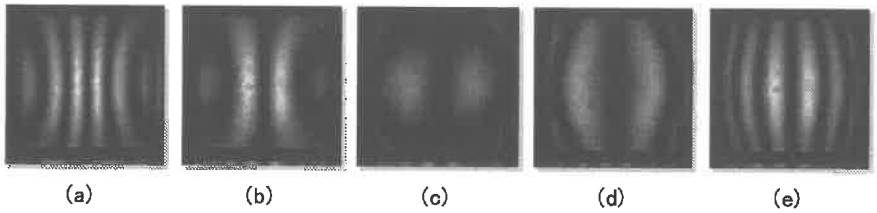

Fig.3 Interferograms obtained by the proposed interferometer in displacement z of a specular object; z=-0.2mm, (b) z=-0.1mm, (c) z=0.0mm, (d) z=0.1mm, (e) z=0.2mm

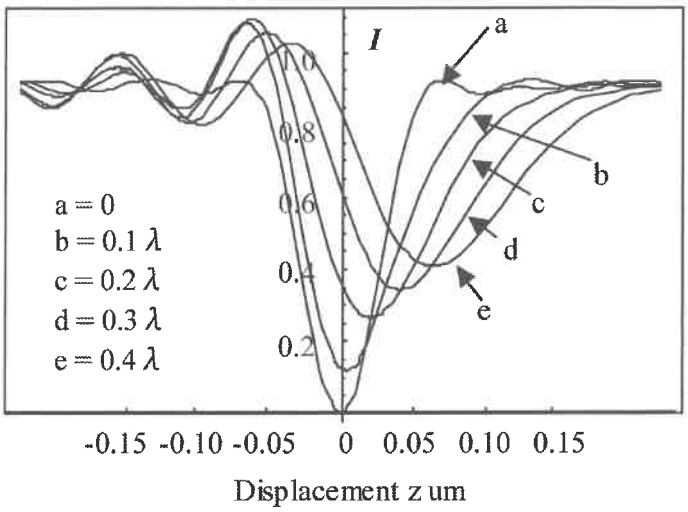

Fig. 4 Optical intensity integrated over the aperture of the sensor

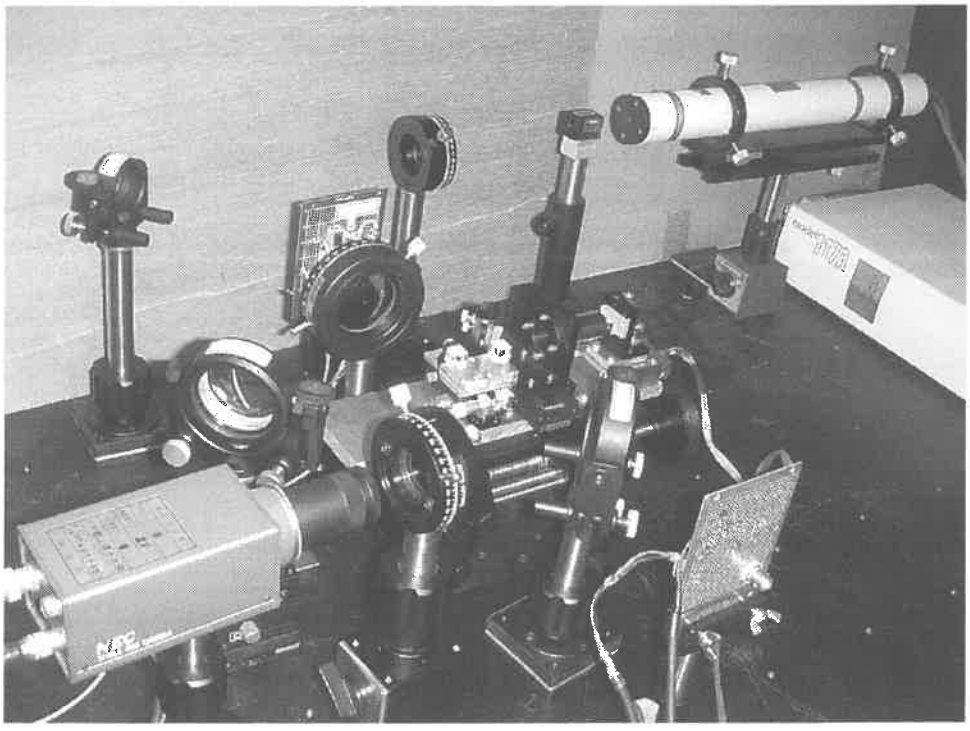

Fig. 5 Photograph of the proposed interferometer

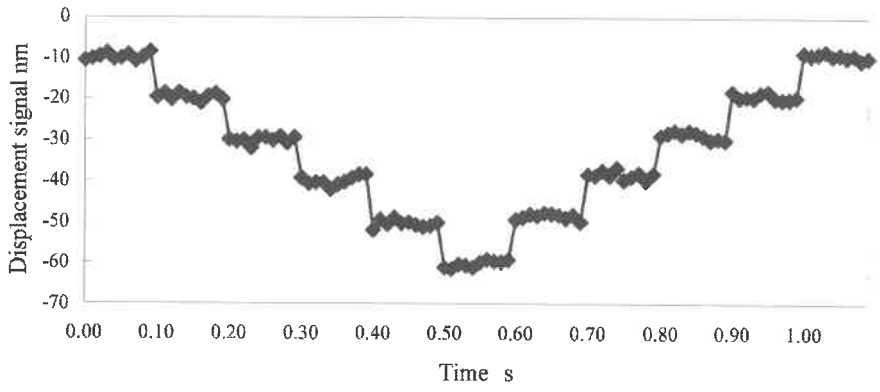

Fig. 6 Waveform of signal obtained by the proposed interferometer

Acknowledgment

This study is financially supported in part by a special grant in aid from the Toyama Prefectural University.

References

1. Masayuki Mino, "Position-Sensing Grating Interferometer for a Specular Object", Optical Review, Vol.5, No.3 (1998), pp.191-195.
2. Kazuhide Kamiya, Takashi Nomura, Seiichi Okuda, Hatsuzo Tashiro, Kazuo Yoshikawa, "Position-Sensing Grating Interferometer For a Specular Object - Analysis Considering the Aberration –", Proc. SPIE, Vol.4416 (2001), pp.416-419.

Development of shape measuring system using a line sensor in a lateral shearing interferometer

Takashi NOMURA*a, Kazuhide KAMIYA*a, Akiko NAGATA*a,
Hatsuzo TASHIRO **b, Seiichi OKUDA ***c
a Toyama Prefectural University, b Toyama University, c Computer Engineering &Consulting LTD.,
* Kurokawa, Kosugi-machi, Toyama 939-0398, Japan,
** Gofuku, Toyama, Toyama 930-8555, Japan,
*** Shibuya, Tokyo 150-0002, Japan

1. Introduction

Mirrors with spherical or aspherical shape are manufactured with ultraprecision lathes. In order to increase the accuracy of the mirrors and the efficiency of the manufacturing process, it is desired that the shapes of the mirrors be measured on the lathes themselves either after or during processing. In a noncommon-path interferometer such as the Fizeau interferometer, the fringes obtained are affected by mechanical vibrations and air turbulence, because the wavefront under test and the reference wavefront traverse in different spaces. Therefore, it is difficult to obtain interference fringes by the noncommon-path interferometer under such measurement conditions.[1] On the other hand, in a common-path interferometer, the fringes obtained by the interferometer are slightly affected by air turbulence, because the wavefront under test and the reference wavefront travel in the same space. A lateral shearing interferometer can be constructed as a common-path interferometer. Therefore, the shapes of the mirror can be measured by an interferometer constructed as a common-path one mounted on the lathe.[2] When the mirror under processing is measured by the interferometer, a cutting tool and a tool post obstruct a part of the measurement area of the surface under test. It is difficult to analyze the entire area of the surface due to defective fringes. To solve the problem, we propose a shape measuring system using a line sensor in a lateral shearing interferometer.

2. Lateral Shearing Interferometer

Figure 1 shows a lateral shearing interferometer. A laser beam is collimated by lenses L1 and L2. The collimated beam is diffracted by a zone plate, and the diffracted beam progresses perpendicularly onto the mirror surface under test. The beam reflects off the surface and is nominally collimated by the zone plate. When the surface of the mirror has errors, the wavefront of the reflected beam is deformed. The wavefront is incident upon the optical parallel glass plate and reflects off the front and back surfaces of that plate. The two reflected wavefronts are laterally sheared with respect to each other. Interference fringes are obtained from the area where the two wavefronts in the lateral shearing interferometer overlap, as shown in Fig. 2. When the mirror under processing is measured by the

interferometer, a cutting tool and a tool post obstruct a part of the measurement area of the surface under test.

3. Principle

A sensor is used to capture the interference fringes in every direction of shear. Because the surface under test rotates, some interference fringes are captured on the line. The line includes the central axis of the rotation. Shape error of the entire surface is obtained by analyzing some interference fringes. The wavefront under test is expressed as $W_\theta(x, y)$, where (x, y) are coordinates of a measurement point and θ is the angle of rotation. When this wavefront is sheared in the x-direction by an amount s, the sheared wavefront at the same points is $W_\theta(x\text{-}s, y)$. The optical path difference $\Delta W_\theta(x, y)$ between the original wavefront and the sheared one is $W_\theta(x\text{-}s, y)\text{-}W_\theta(x, y)$. When s is small, the optical path difference

$$\Delta W_\theta(x,y) = W_\theta(x-s,y) - W_\theta(x,y) \cong \left(\frac{\partial W_\theta}{\partial x}\right)s = n\lambda, \quad (1)$$

where λ is the wavelength of the light source, and n is the order of the interference fringe. The interference fringes obtained by the lateral shearing interferometer represent the derivative of the shape error in the sheared direction of the wavefront under test. By integrating the phase distribution, the shape error of the mirror under test in the sheared direction is obtained. When the fringes on the x axis are captured by the line sensor, the wavefront is

$$W_{\theta,x} = \frac{1}{s}\int_{x_0}^{x} \Delta W_{\theta,x}(x,y)dx + C_\theta. \quad (2)$$

To obtain three-dimensional shape error, the constant C_θ should be determined. Because the measurement values at the central axis of rotation are the same at all rotation angles, C_θ is defined as zero. As a consequence, the shape error of the mirror under test is reconstructed.

4. Simulation

We performed a simulation to evaluate the validity of the principle. A shape under test which was constructed by Zernike coefficients of the 4th item was used in the simulation as shown in Fig. 3. In the proposed method, some interference fringes obtained by the line sensor are used. Some fringes are analyzed in the radial direction, and these analyzed data are composed. The sampling number of interference fringes obtained by the line sensor is required to be more than twice the number of undulations in the circumferential direction at least. In this simulation, in order to reconstruct the wavefront correctly, a sampling angle of 1 degrees is used. The number of pixels of the line sensor is 512. The wavelength of the laser is 633 nm, and the shear ratio is 0.2 in the simulation.

The result of the simulation is shown in Fig. 4. The result agreed well with the original shape under test. The difference between the original shape and reconstructed one was 1 %.

5. Shape measuring system

A shape measuring system using a line sensor in a lateral shearing interferometer was developed as shown in Fig. 5. The optical arrangement is shown in Fig. 1. The mirror under test is attached to the spindle with an encoder. The angle is detected by the encoder. A personal computer counts the signals from the encoder, and sends a trigger signal to a CCD camera and a video grabber board. Interference fringes are obtained by the CCD camera with an aperture stop and are analyzed by the computer. In the developed measuring system, the angular simulation of the encoder is $2\pi/5000$ rad, and the number of pixels of the line sensor is 512. The wavelength of the laser is 633 nm, and the shear ratio is 0.2 in the simulation.

6. Conclusion

We proposed a shape measuring system using a line sensor in a lateral shearing interferometer. A shape under test constructed by Zernike coefficients of the 4th item was used in the simulation. A sampling angle of 1 degree was used in the simulation. The result obtained by the proposed method agreed well with the original shape under test. The difference between the original shape and reconstructed one was 1 %. A shape measuring system using a line sensor in a lateral shearing interferometer was developed.

[1] T. Nomura, K. Yoshikawa, H. Tashiro, K. Takeuchi, N. Ozawa, Y. Okazaki, M. Suzuki, F. Kobayashi and M. Usuki, "On-machine shape measurement of workpiece surface with Fizeau interferometer," Precision Engineering, 14, pp.155-159, 1992.

[2] T. Nomura, K Kamiya, H. Miyashiro, S. Okuda, H. Tashiro and K. Yoshikawa, "Shape measurements of mirror surfaces with a lateral shearing interferometer during machine running," Precision Engineering, 22, pp.185-189, 1998.

Keywords: on-machine shape measurement, common path interferometer, lateral shearing interferometer, shape measurements of a spherical surface

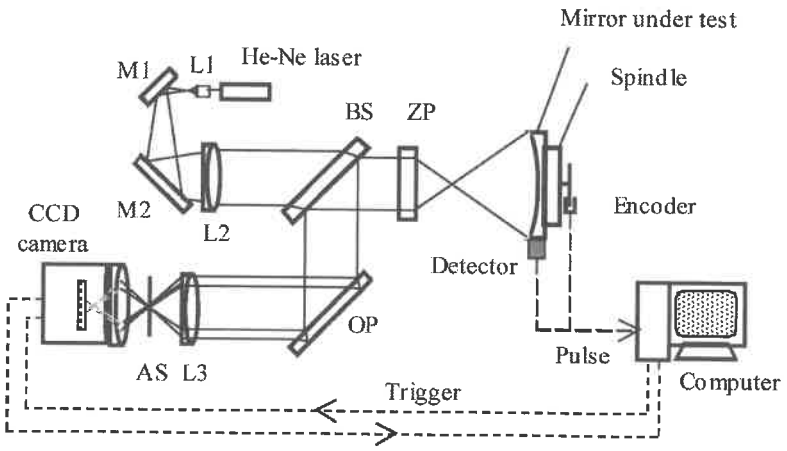

Fig. 1 Optical arrangement of a shape measuring system using a line sensor in a lateral shearing interferometer

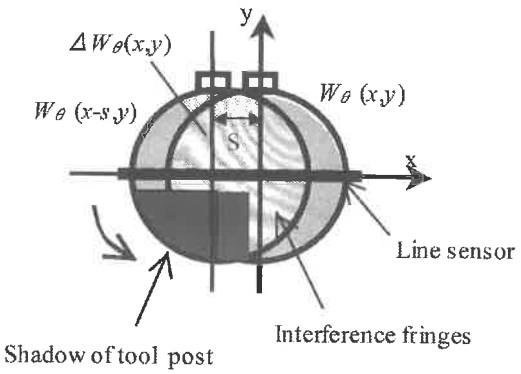

Fig. 2 Fringes obtained by the lateral shearing interferometer on the lathe

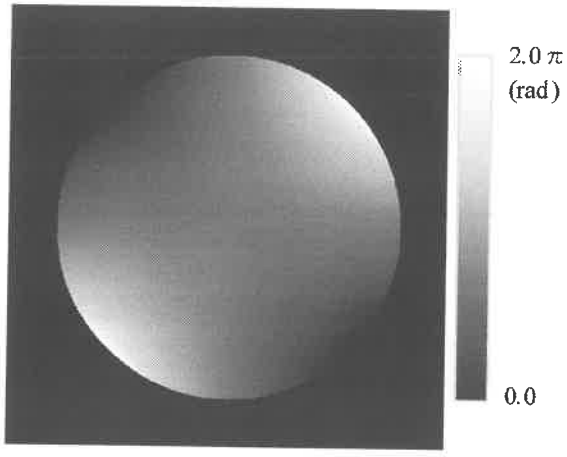

Fig. 3 Shape under test used in the simulation

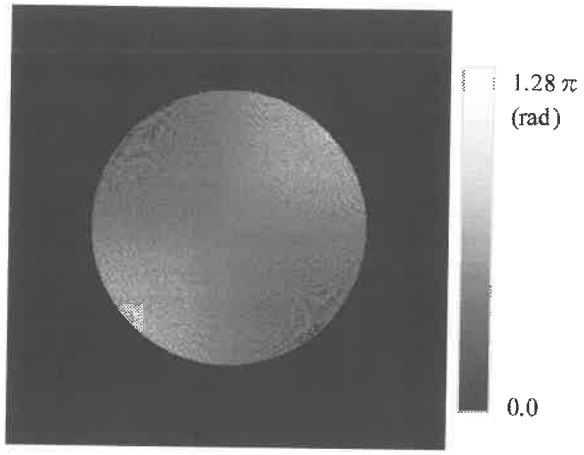

Fig. 4 Result of the simulation

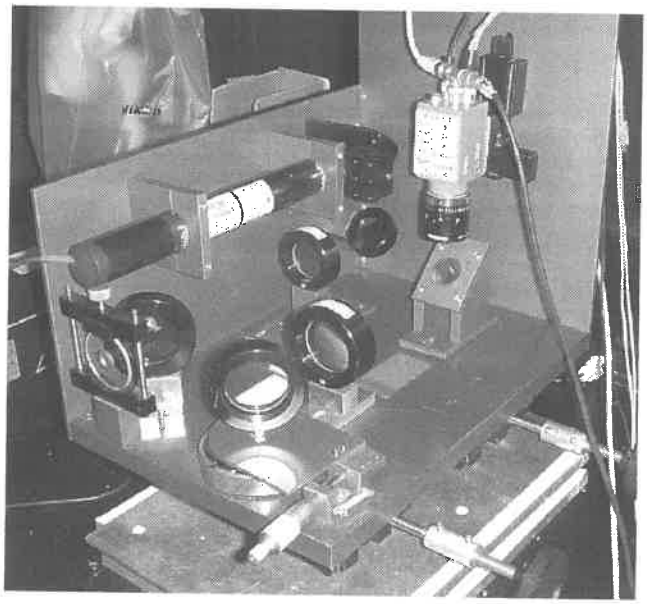

Fig. 5 Photograph of the developed interferometer

HIGH ACCURACY MEASUREMENT OF AIR REFRACTIVE INDEX IN REAL-TIME

Youjin Wang, Guangping Xie

Excel Precision Co., Santa Clara, CA, USA

Introduction

With the development of new technologies in semiconductor, aerospace and other industries requiring high resolution in dynamic environments, comes the need for higher measurement accuracy. Typically, a laser interferometer is used to meet these precision measurement requirements. Changes of air refractive index seriously affect accuracy in the measurement environment. With such systems, wavelength compensation for interferometer systems has become important.

There are many compensation methods, such as, Weather Station[1], Wavelength Tracker[2], etc. None of them can accurately compensate for changes in temperature, pressure, humidity and composition in the measuring environment. In order to bridge this gap, Excel Precision Co. designed and developed the REFRACTOMETER[3] (figure 1) to compensate for the effects of environmental changes.

Refractometer is used to determine in real-time absolute index of refraction of air within the measuring environment. The sealed vacuum cavity of Refractometer requires no re-pumping between measurements and allows Refractometer to function well in industrial applications. The Refractometer was designed for large-quantity production without loss of operating accuracy.

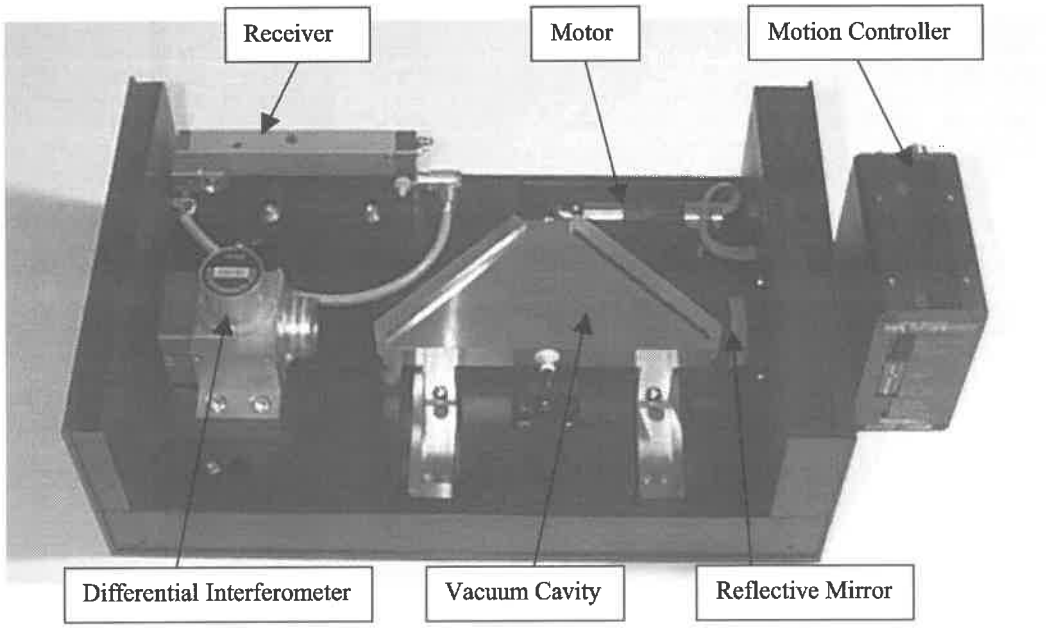

Figure 1. Refractometer

Principle of the measurement

When the laser interferometer performs measurement in air, the laser wavelength is shortened by a factor of n.

$$\lambda_{air} = \frac{\lambda_v}{n} \tag{1}$$

Where, n is air refractive index

λ_v is laser wavelength in vacuum

λ_{air} is laser wavelength in air

Measurement accuracy is improved by the refractometer by measuring the index of refraction of air and generating a correction factor that is applied to the original measurement data.

Refractometer measures the instantaneous index of refraction of air and provides compensation factor to the laser interferometer system. Measurement of instantaneous index of refraction is achieved by comparing two laser optical paths, one passing through a vacuum and the other through the measuring environment, from a differential interferometer to a reflective mirror, and back to a receiver. The vacuum optical path length is varied by moving a trapezoidal vacuum cavity through a known distance.

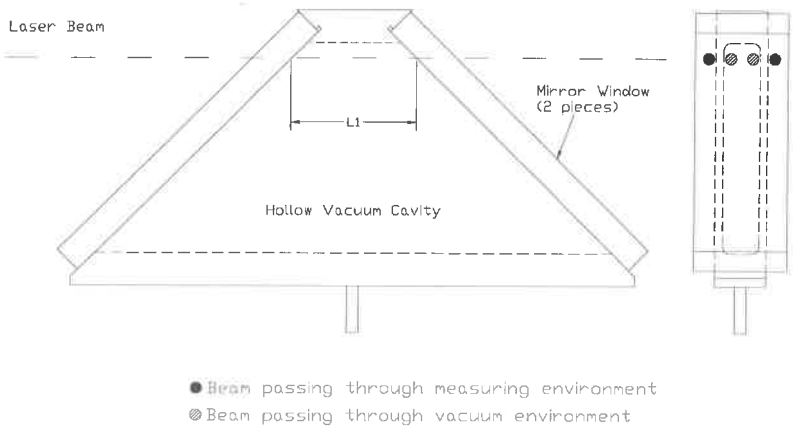

Figure 2. Laser beam goes through short path position

When laser beam goes through short path position (figure 2):

$$(n-1)\cdot L_1 = N_1 \cdot \frac{\lambda_v}{128} \tag{2}$$

When laser beam goes through long path position (figure 3):

$$(n-1)\cdot L_2 = N_2 \cdot \frac{\lambda_v}{128} \tag{3}$$

Eq. (3) subtracts Eq. (2), obtains:

$$(n-1)\cdot (L_2 - L_1) = (N_2 - N_1)\cdot \frac{\lambda_v}{128} \tag{4}$$

Let $N_2 - N_1 = \Delta N$, Eq. (4) becomes:

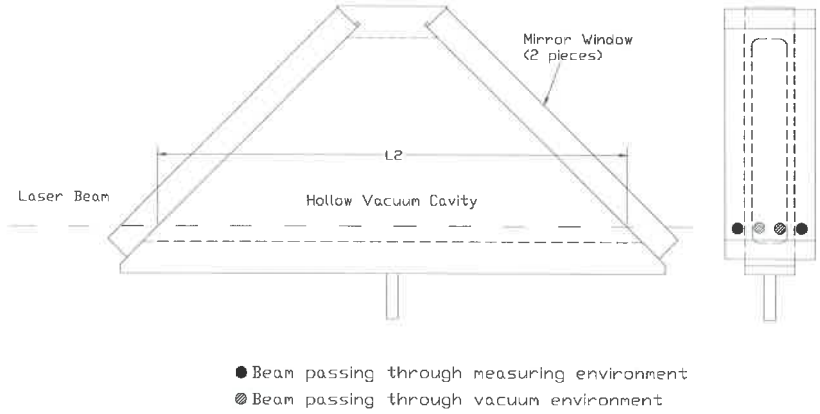

Figure 3. Laser beam goes through long path position

$$(n-1)\cdot(L_2-L_1)=\Delta N\cdot\frac{\lambda_v}{128} \tag{5}$$

Where,

n is air refractive index in measuring environment

ΔN is differential laser counts between short path position and long path position

L_2 is the physical beam path length at long path position in vacuum cavity

L_1 is the physical beam path length at short path position in vacuum cavity

L_2 and L_1 can be obtained exactly through precise calibration.

During field initialization of the refractometer, application software is used to drive the motor in order to move the vacuum cavity to the short path position, then back to long path position.

Initial ΔN(0) is obtained from computer based signal processing card. So initial n(0) is obtained from Eq. (5).

$$n(0)=1+\frac{\Delta N(0)\cdot\lambda_v}{128\cdot(L_2-L_1)} \tag{6}$$

While vacuum cavity stays at long path position, change of air refractive index can get from Eq. (3):

$$dn=\frac{\lambda_v}{128\cdot L_2}\cdot dN_2 \tag{7}$$

$dN_2=d(\Delta N)$, So

$$n(t)=n(0)+\Delta n=n(0)+\frac{\lambda_v}{128\cdot L_2}\cdot[\Delta N(t)-\Delta N(0)] \tag{8}$$

Eq. (8) is used for continuous measurement for air refractive index.

Experiments

2 units of refractometer were compared with a standard unit of refractometer in the measuring environment. The standard refractometer was the same as normal refractometer, except that its

physical displacement. The measurement process of this method is fairly fast (about one minute to obtain one measurement data point). Its setup is simple, and its cost is very low.

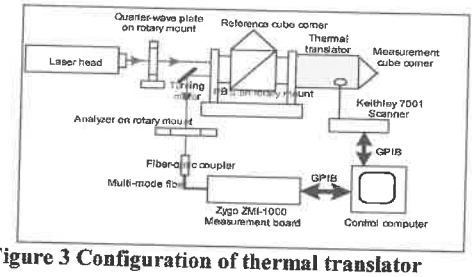

Figure 3 Configuration of thermal translator

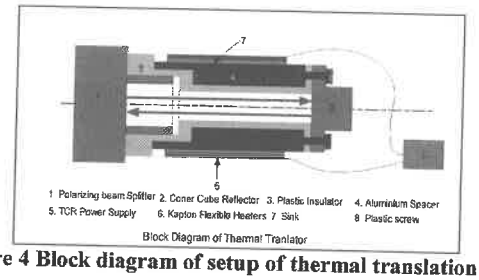
1 Polarizing beam Splitter 2. Corner Cube Reflector 3. Plastic Insulator 4. Aluminum Spacer
5. TCR Power Supply 6. Kapton Flexible Heaters 7 Sink 8 Plastic screw
Block Diagram of Thermal Tranlator

Figure 4 Block diagram of setup of thermal translation

The experimental setup is shown schematically in Fig.3. The interferometer is a heterodyne displacement measuring interferometer. A two-frequency He-Ne laser head emits two orthogonal linear polarized light components with the slightly different frequencies. A quarter-wave plate can be rotated to change the incident linearly polarized laser light into an elliptically polarized light. The interferometer consists of one polarization beam splitter (PBS) and two retroreflectors. One retroreflector is directly mounted on one face of the PBS in the reference arm, and the other retroreflector is mounted on one end of a thermal translator. The other end of thermal translator is mounted on the other face of the PBS in the measurement arm. The exit beam from the interferometer is turned toward an analyzer (Glan-Thompon polarizer) by a turning mirror. The light through the analyzer is focused into a multimode fiber by a fiber-coupler. The temperature variation of the thermal translator and other parts are monitored by thermistors.

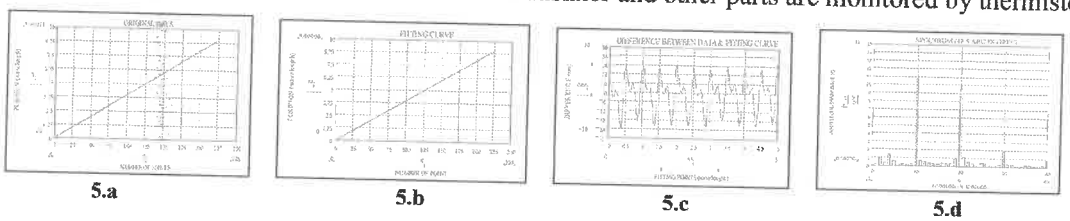

5.a 5.b 5.c 5.d

Figure 5 Data processing procedure

The configuration of the thermal translator is depicted in Fig.4. The active part of the translator is a 6 inch aluminum spacer. A plastic insulator is fitted into the spacer. A Kapton flexible heater surrounds the aluminum spacer; heat sink compound is used to promote heat conduction between the heater and the spacer. The cube-corner retroreflector is mounted to the aluminum spacer by two plastic screws. When voltage is applied, the heater warms the aluminum spacer and generates the desired thermal extension. Each thermal translation measured by the laser (Fig.5.a) is a combination of a nominal actual displacement and interferometer errors. Polynomial regression is employed to determine the nominal displacement (Fig.5.b). The difference between the measured displacement and the nominal displacement is the nonlinearity (Fig.5.c). The nonlinearity data is transformed into a frequency spectrum (Fig.5.d) in which two certain frequency components correspond to the first and second harmonic nonlinearity.

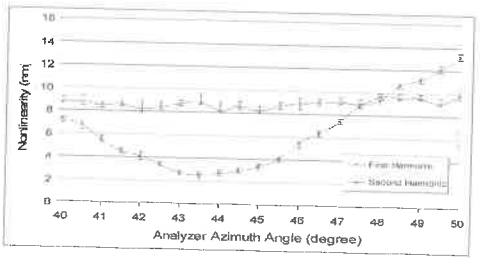

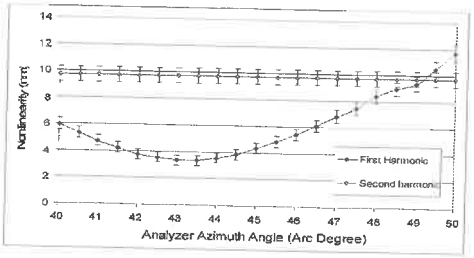

Figure 6 Experimental results using thermal translation **Figure 7 Experimental results using velocity scanning**

Using thermal translation technique, the relationship between the nonlinearity and the azimuthal angle of the analyzer can be measured. A typical measurement result is shown in Fig.6. This relationship was also measured using velocity scanning (Fig.7). These measurement results are in substantial agreement.

3. Fiber effects

The nonlinearity in the heterodyne interferometer has previously been investigated using Jones calculus [7]. In the following discussion, a modified form of Jones calculus [3] is employed to describe the fiber-optic coupled interferometer. Polarization maintenance in the fiber is achieved through high internal linear birefringence produced in the manufacturing process. In practice, the PM fiber suffers some kinds of external stresses when it is used in the optical system. Typically, the PM fiber is subjected to bending, twisting, or combination of these two external behaviors. The bending produces a linear birefringence in the fiber, and the twisting induces a rotary birefringence. These birefringent properties reduce the polarization-maintaining ability of the fiber.

The Jones matrix M for a bent PM fiber can be defined in terms of a modified differential "N matrix" [8]

$$M = \exp\left(\int_0^z \overline{N}\cdot dz\right) = \exp\left(\int_0^z \tfrac{1}{2}(N_m + N_b)dz\right) \tag{1}$$

The N matrix N_m corresponding to the manufacturing birefringence is expressed as

$$N_m = \frac{i\eta_m}{2}\begin{bmatrix} 1 & 0 & 0 & 0 \\ 0 & -1 & 0 & 0 \\ 0 & 0 & 1 & 0 \\ 0 & 0 & 0 & -1 \end{bmatrix} \tag{2}$$

where $\eta_m = 2\pi/L_B$ is the phase retardation per unit length introduced by manufacturing process, and L_B is the nominal beat length of the PM fiber. When the bending fiber is free of any axial tensile stress, the birefringence $\Delta\tilde{n}$ introduced by bending (Fig.8) can be expressed as [9]

$$\Delta\tilde{n} = C_e\frac{r^2}{R^2} \tag{3}$$

where C_e is the photo-elastic coefficient, r is the radius of a fiber, and R is the bending radius of curvature of the fiber. In general, the fast axis introduced by the bending does not overlap the fast axis introduced by manufacturing. Similarly, slow axes introduced by two processes don't align. When the angle between these two fast axes is α, the N matrix N_b introduced by bending can be expressed in the reference system of eigenaxes of manufacturing birefringence

$$N_b = \tfrac{i\eta_b}{2}\begin{bmatrix} \cos 2\alpha & \sin 2\alpha & 0 & 0 \\ \sin 2\alpha & -\cos 2\alpha & 0 & 0 \\ 0 & 0 & \cos 2\alpha & \sin 2\alpha \\ 0 & 0 & \sin 2\alpha & -\cos 2\alpha \end{bmatrix} \tag{4}$$

where $\eta_b = (\Delta\tilde{n}\cdot 2\pi)/\lambda$, is the phase retardation per unit length introduced by bending, and λ is the wavelength of light wave through the fiber.

The resultant ellipticity of the output light from a 1000 mm long circularly bent PM fiber is shown in Fig.9 as a function of bending radius for α=45°. The ellipticity of the output light from a fiber of equal length bent into an elliptical loop is a function of the minor axis diameter of the ellipse is shown in Fig.10. The peak-to-peak variation of ellipticity in Fig.10 corresponds to 2 nm nonlinearity.

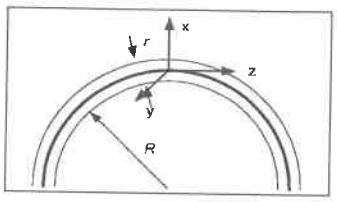

Figure 8 Bending of the fiber

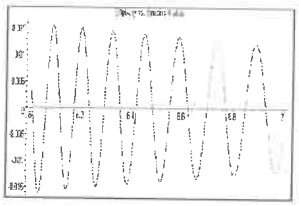

Figure 9 Ellipticity vs. bending radius

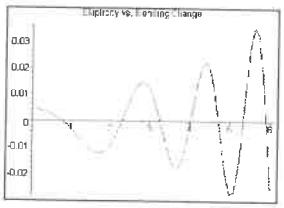

Figure 10 Ellipticity vs. bending change

This behavior provides a basis for the construction of an ellipticity adjuster that simulates the coupling present in practical FIDMI. A PM fiber is coiled in loops and inserted into the squeezer shown in Fig.11. The shape of the fiber coil becomes ellipse in the squeezer. When the micrometer of the squeezer is adjusted, the fiber coil is squeezed to change its shape into the desired ellipse with a certain length of the major and minor axes. The linear birefringence arising from the bending is changed correspondingly.

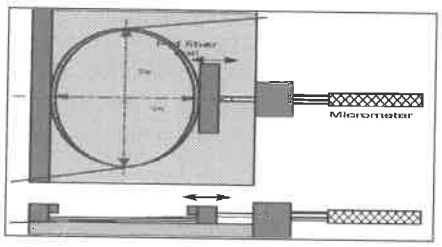

Figure 11 Fiber manipulator

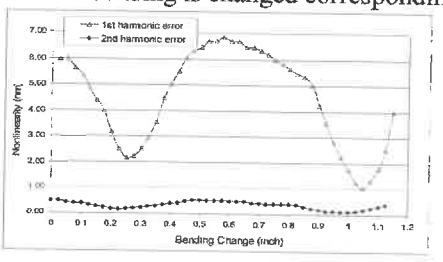

Figure 12 Nonlinearity vs. bending change

The experimental result is shown in Fig.12. The bending change in this graph represents the change of length of the minor axis of the PM fiber coil. The nonlinearities oscillate with the change of shape of coil ellipse. It indicates that the nonlinearity of the interferometer measurement is strongly dependent on the bending of the PM fiber.

Acknowledgements

The work repeated in this paper were supported by the affiliates of the Center of Precision Metrology (CPM) at the University of North Carolina at Charlotte (UNCC).

References

1. H. Kunzmann, "Scales vs. Laser Interferometers Performance and comparison of Two Measuring Systems", *Annals of the CIRP*, Vol.42/2/1993, pp. 753-767.
2. Juichi noda, Katsunari Okamoto, Yutaka Sasaki, "Polarization-Maintaining Fibers and Their Applications", *Journal of lightwave Technology*, Vol. LT-4 (8), pp.1071-1089.
3. Vivek Gopal Badami, "Investigation and compensation of periodic nonlinearities in heterodyne interferometry.", PhD dissertation in UNCC, 1999.
4. Sutton, C. M. "Non-linearity in length measurement using heterodyne laser Michelson interferometer", J. Phys. E: Sci. Instrum., 1987, 20, pp.1290-1292.
5. Steve Patterson, John Beckwith, "Reduction of systematic errors in heterodyne interferometric displacement measurement", 1995, *ASPE*.
6. V.G. Badami, S.R. Patterson, "A frequency domain method for the measurement of nonlinearity in heterodyne interferometry", *Precision Engineering*, 24(2000), pp. 41-49.
7. R. Clark Jones, "A new calculus for the treatment of optical systems I. Description and discussion of calculus", *J. Opt. Soc. Am.*, Vol.31, July 1941, pp.488-493.
8. R. Clark Jones, "A new calculus for the treatment of optical systems. VII. Properties of the N-matrices", *J. Opt. Soc. Am.*, Vol.38, No.8, Aug 1948, pp.671-685.
9. Serge Huard, "Polarization of Light", John Wiley & sons, 1997.

ALLOCATING TOLERANCES FOR VEE-GROOVE FIBER ALIGNMENT

Mathieu Barraja and R. Ryan Vallance
Precision Systems Laboratory, University of Kentucky, Lexington, KY *

S. Kiani, J. Lehman and Burke Hunsaker
Teradyne Connection Systems, Nashua, NH †

Abstract

This paper presents a method for allocating tolerances to dimensions in micro scale vee-grooves used to align optical fibers. The objective is to reduce the manufacturing cost without exceeding a limit on the misalignment between two mating fibers. The allocation procedure is performed on a 2D geometric model of a connector that aligns an array of multiple fibers. An analytical model of the connection, based upon statistics, is used for providing a relation between variation in manufactured dimensions and variation in the resulting misalignment of the fibers contained in the array. Optimal tolerances are determined using a non-linear constrained optimization algorithm that minimizes the manufacturing cost while satisfying constraints on the variation of the misalignment of any pair of fibers in the array. The method provides a useful tool when designing mass-produced connectors for multi-fiber cables, for which manufacturing cost and accuracy are critical parameters.

Keywords: tolerance allocation, vee-grooves, optical fibers, alignment, manufacturing cost

Introduction

Vee-grooves are widely used in microscale devices, especially for positioning cylindrical objects. A common application is to align optical fibers, which is of primary interest for communications [1]. When connecting two fibers, a lateral misalignment, due to the manufacturing errors of the vee-groove, generates a consequential amount of signal loss. Considering Marcuse's [2] model for signal loss due to lateral misalignment of single-mode fibers, the cores of two fibers should be aligned within about 1 μm to achieve ~ 0.21 dB signal loss. This is a challenging proposition for only two individual fibers, but the challenge is even greater for mass produced interconnects which join cables containing eight or more fibers, as shown in Fig 1.

Our objective is to select tolerances that are sufficient for aligning optical fibers without excessive loss, but simultaneously minimizing manufacturing costs that arise from excessively tight tolerances. Tolerance allocation is generally formulated as an optimization problem with an objective function and set of constraints. In this case, the objective is to minimize the manufacturing cost which is a function of the tolerances. Tolerance relations for etched silicon vee-grooves are not available. However, for other materials like zirconium, a secondary material removal process like grinding may improve the tolerances. In this case, we employ relations developed by Chase [3] to relate manufacturing costs to tolerances. Both cost and signal loss can be defined as functions of the tolerances allocated by the designer. The optimization constraints are formulated as maximum tolerable signal loss within an entire connector.

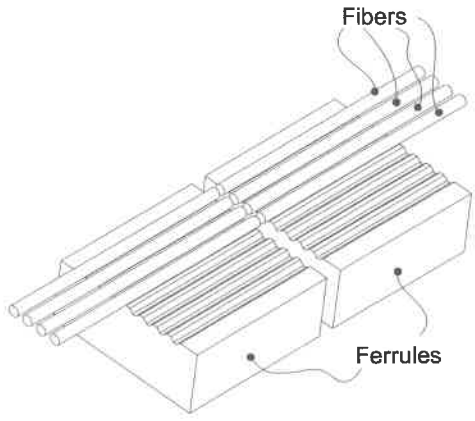

Fig 1: Multifiber Connector with Vee-Grooves

In formulating the optimization problem, the greatest challenge is determining a relationship

* *Precision Systems Laboratory, Mechanical Engineering, University of Kentucky, 210-A CRMS Building, Lexington, KY 40506. http://www.engr.uky.edu/psl.*
† *Teradyne Connection Systems, Nashua, NH. http://www.teradyne.com.*

between the tolerances and the performance criteria. For complex assemblies such as a fiber-optic connector, Monte Carlo simulations are effective means for relating final tolerance of an assembly to the tolerances of the components [4]. However, it may be difficult to implement Monte Carlo simulations within the optimization algorithm due to computational time. We instead use an alternative approach in which a few Monte Carlo simulations proved a mathematical model relating assembly tolerances to component tolerances. Knowing the geometry and the dimensions of the vee-groove, it is possible to define the signal loss of the fiber connection as a function of the tolerances of the vee-groove.

This paper presents a process to efficiently allocate the tolerances for vee-groove fiber alignment. The first step is to construct a mathematical model of the dimensions and geometry of vee-grooves. The second step is to define, through a statistical study, the misalignment of the fiber as a function of the tolerances in the vee-grooves. The third step is to estimate a relation between the tolerances and the manufacturing costs. Finally, tolerances are allocated with an optimization algorithm that minimizes the manufacturing cost for a given maximum limit on signal loss. An example illustrates the method.

Mathematical Model of the Dimensions and Geometry of a Vee-Groove

Fiber-to-fiber connections are a major source of optical loss. There exist three types of connection losses [1] that are directly related to the manufacturing errors within the connectors. The first one is caused by the lateral misalignment, due to the offset of the centerlines of the mating fibers. The second comes from the end-separation misalignment, which is the gap between the ends of the connected fibers. And finally, the third loss is generated by the angular misalignment, which occurs when there exists an angle between the two axes of the fibers.

The lateral misalignment is of most concern for connection loss since angular misalignment is negligible and end-separation is usually resolved by mechanical contact between the fibers or index-matching compounds. In considering only lateral misalignment, a 2D model of the vee-grooves is a reasonable approximation for representing the vee-groove geometry. The modeling plane is the *xz*-plane, *y* being the direction along the axes of the fibers. Geometry of a ferrule using vee-grooves is illustrated in the plane perpendicular to the axes of the fibers in Fig 2.

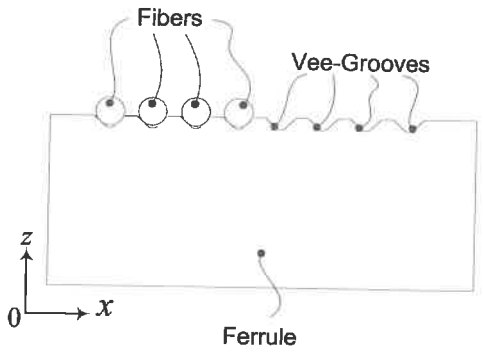

Fig 2: Connector in the *xz*-Plane

In the 2D configuration, it is possible to establish a mathematical relation between the variation of the dimensions in the ferrules and the lateral misalignment between two mating fibers.

As shown in Fig 3, the j[th] vee-groove of an array can be parametrically represented in two dimensions with four parameters and their manufacturing errors:

1. aperture angle, α_j, and angle error, δ_{α_j},
2. inclination angle, γ_j, which is the angle between the groove's bisector and a vertical line (ideally γ equals zero), and angle error, δ_{γ_j},
3. depth to the virtual vertex, h_j, and error, δ_{h_j}, and
4. radius of curvature, r_j, at the bottom of the groove and error, δ_{r_j}.

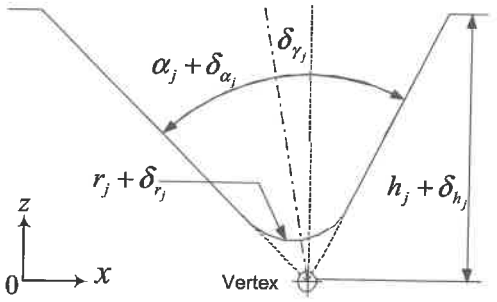

Fig 3: Manufacturing Errors in a Vee-Groove

Metrology applied to a ferrule cannot directly measure the value of the inclination angle, so it was decided to represent the aperture angle and the inclination angle as a combination of two half-angles: β_{Lj} on the left side and β_{Rj} one the right side. The aperture angle is defined as the sum of the two half-

angles while the inclination angle is calculated as half their difference.

The geometry of a single vee-groove is then defined by four dimensions (β_{Lj}, β_{Rj}, h_j, r_j) and their variations. Furthermore, variation in the pitch between two successive vee-grooves is also a critical parameter for aligning fibers. The pitch p_j is then a fifth dimension used for modeling the connector.

Variation Analysis by the Law of Error Propagation

Tolerance allocation requires a relation between dimensional variation and connection loss. Marcuse [2] presented a relation, given in Eq (1), for the connection loss, T_j, of single-mode fibers as a function of the lateral misalignment, d_j, and the width parameters, w_{j1} and w_{j2}, of the two fibers. The dimensions, d_j, w_{j1}, and w_{j2} are expressed in the same length unit, and T_j has no dimension. Usually, connection loss is expressed in decibels.

$$T_j = \left(\frac{2w_{j1}w_{j2}}{w_{j1}^2 + w_{j2}^2} \right)^2 \exp\left[-\frac{2d_j^2}{w_{j1}^2 + w_{j2}^2} \right] \qquad (1)$$

For multi-mode fibers experimental data are used to establish the relation between lateral misalignment and connection loss, as shown in Fig 4.

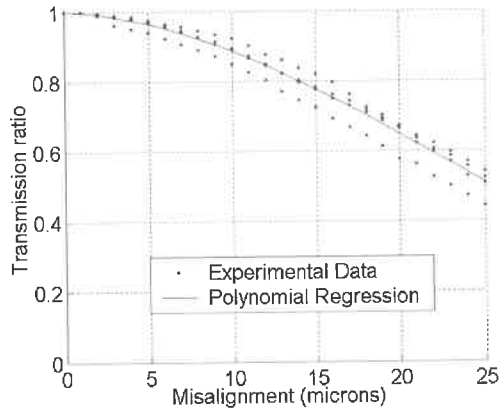

Fig 4: Experimental Determination of a Relation between Loss and Misalignment by Curve Fitting

For both single-mode and multi-mode cases, it is necessary to establish a relation between dimensional variation and lateral misalignment. This is done by applying the law of error propagation [5] on the mathematical model of the connectors. This method is computationally efficient when used in a tolerance allocation algorithm.

The geometric model of the vee-groove must be expressed in terms of statistics. Every dimension ξ_i is defined as a randomly distributed variable. Its mean μ_i equals the value of the nominal dimension, while its standard deviation σ_i is a third of the tolerance. For a complete representation of the connector, the same procedure is applied for the dimensions of the fibers and for the dimensions of the system that aligns the two ferrules. The distribution of errors between the two ferrules may be measured experimentally or predicted using another geometric/variation model.

The lateral misalignment d_j for the jth pair of fibers is modeled as a vector in the xz-plane. It is possible to define its coordinates, $\left(x_{d_j}, z_{d_j}\right)$, as a function of the dimensions of the vee-grooves, the fibers and the aligning system, as shown in Eqs (2)-(3).

$$x_{d_j} = f_{x_j}\left(\xi_1, \xi_2, \ldots, \xi_i, \ldots, \xi_n\right) \qquad (2)$$

$$z_{d_j} = f_{z_j}\left(\xi_1, \xi_2, \ldots, \xi_i, \ldots, \xi_n\right) \qquad (3)$$

n being the total number of assigned dimensions within the connector.

According to the law of error propagation, if the dimensions are independent (which is a reasonable assumption for most applications), then the standard deviation $\sigma_{x_{d_j}}$ of the lateral misalignment in the x-direction is given by Eq (4). A similar equation gives the lateral misalignment in the z-direction.

$$\sigma_{x_{d_j}}^2 \approx \sum_{i=1}^{n} \left(\frac{\partial f_{x_j}}{\partial \xi_i} \right)^2 \sigma_i^2 \qquad (4)$$

For perfect dimensions, the misalignment equals zero. Hence for random dimensions, its variation is directly related to its standard deviation. The law of propagation error then gives a direct analytical expression of the variance in lateral misalignment as function of the variances in the different dimensions of the connector.

Four dimensions, β_{Lj}, β_{Rj}, h_j and p_j, define the geometry of a vee-groove. Since the current study analyzes the sensitivity of the lateral misalignment to the geometry of the vee-grooves, the standard deviations of the components in the x and z directions for the lateral misalignment are expressed as shown in Eqs (5)-(6):

$$\sigma^2_{x_{d_j}} \approx \left(\frac{\partial f_{x_j}}{\partial \beta_{Lj}}\right)^2 \sigma^2_{\beta_{Lj}} + \left(\frac{\partial f_{x_j}}{\partial \beta_{Rj}}\right)^2 \sigma^2_{\beta_{Rj}} + \left(\frac{\partial f_{x_j}}{\partial h_j}\right)^2 \sigma^2_{h_j} + \left(\frac{\partial f_{x_j}}{\partial p_j}\right)^2 \sigma^2_{p_j} + Const_{x_j} \quad (5)$$

$$\sigma^2_{z_{d_j}} \approx \left(\frac{\partial f_{z_j}}{\partial \beta_{Lj}}\right)^2 \sigma^2_{\beta_{Lj}} + \left(\frac{\partial f_{z_j}}{\partial \beta_{Rj}}\right)^2 \sigma^2_{\beta_{Rj}} + \left(\frac{\partial f_{z_j}}{\partial h_j}\right)^2 \sigma^2_{h_j} + \left(\frac{\partial f_{z_j}}{\partial p_j}\right)^2 \sigma^2_{p_j} + Const_{z_j} \quad (6)$$

where the constant terms are due to the variations in the dimensions of the fibers and the aligning system.

Eqs (5)-(6) return the variances of the components in the x and z directions for the lateral misalignment, but Marcuse's model and Eq (1) require the magnitude of the misalignment, d_j. Its value could be expressed with a joint probability distribution for x_d and z_d, but an unknown correlation coefficient between the two components compromises the accuracy of the calculation. Therefore a Monte Carlo simulation of the connector is used to determine an empirical relation between the connection loss and the standard deviations of x_{d_j} and z_{d_j} by a two-step process.

The first step consists in collecting data from the Monte Carlo simulation. Its inputs are the nominal values and the tolerances of the different dimensions defining the geometry of a connector. A large number of connectors are virtually generated using the mathematical model previously presented. Their dimensions are normally distributed, with a mean equal to their nominal value and a standard deviation equal to one third of their tolerance. The algorithm calculates the misalignment of each randomly generated sample, then it performs a statistical treatment on the collected results. Finally, it returns the standard deviation of the components in x and z of the lateral misalignment, as well as a cumulative distribution function (cdf) of the connection loss (in dB) for every pair of fibers, as shown in Fig 5.

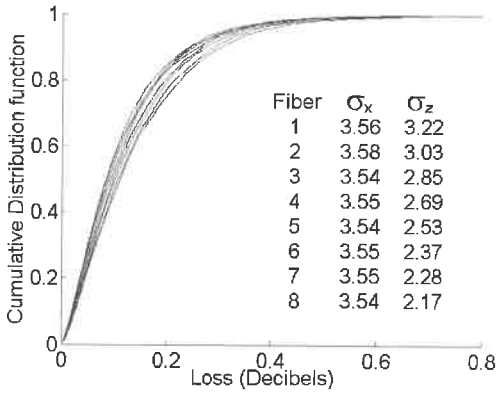

Fig 5: Outputs of Monte Carlo Simulation

Every cdf is curve fitted with a two-variable continuous function. Since the tolerance analysis focuses on the highest part of the cdf (beyond 90%), the curve fitting is performed exclusively on this part of the cdf, in order to get more reliable approximations. It has been found that for single-mode fibers, the cdf of a Weibull random variable is a good approximation, while a Gamma incomplete function fits well the cdf of the multi-mode fibers.

The simulation is run many times, with different input tolerances. The resulting cdf's are reduced to two parameters defining the fitted curve. Hence the first step of the process returns a set of values for the two fitting parameters, in function of the standard deviations of x_{d_j} and z_{d_j}.

The second step is a new curve fitting procedure. This time, one of the fitting parameters is plotted in function of the standard deviations of x_{d_j} and z_{d_j}, and it is curve fitted. The resulting relations are finally compared to new Monte Carlo simulations, and it has appeared that they were extremely reliable. These functions are used as empirical models of the connection loss.

Thereby a variation analysis based upon the law of propagation error, followed by an empirical yet accurate model of the connector performance, provides a relation between the connection loss and the tolerances of the vee-grooves.

Cost-Tolerance Relations

The cost of a manufactured part depends upon the selected manufacturing process and dimensional tolerances. The cost of achieving a particular tolerance depends upon both the dimension's nominal value and tolerance. The manufacturing cost generally increases if the tolerance is tightened, and it

is more expensive to make a given tolerance on a large nominal dimension. Based on this, Chase [3] recommends expressing tolerances as reciprocal power functions for material removal processes. Eq (7) expresses the tolerance for the i^{th} dimension, t_i, as a function of cost, C_i, range, R_i, and three constants a_i, b_i, and c_i. The values of the three constants depend upon the range and the manufacturing process. Although a constant term would be necessary for accuracy, it is practically impossible to evaluate and doesn't affect the tolerance allocation.

$$t_i = c_i \times \frac{R_i^{a_i}}{C_i^{b_i}} \tag{7}$$

Similar functions are not available for etching processes commonly used with silicon.

Knowing the range and the manufacturing process of every dimension enables generating the cost-tolerance functions required to estimate the manufacturing cost of a connector in function of the tolerances assigned to its different dimensions. The portion of the total manufacturing cost that is attributable to vee-groove tolerancing is then the sum of the costs for the four dimensions, β_{Lj}, β_{Rj}, h_j and p_j, as shown in Eq (8).

$$Cost = \left(\frac{c_{\beta_{Lj}} \cdot R_{\beta_{Lj}}^{\ a_{\beta_{Lj}}}}{t_{\beta_{Lj}}} \right)^{1/b_{\beta_{Lj}}} + \left(\frac{c_{\beta_{Rj}} \cdot R_{\beta_{Rj}}^{\ a_{\beta_{Rj}}}}{t_{\beta_{Rj}}} \right)^{1/b_{\beta_{Rj}}} + \left(\frac{c_{h_j} \cdot R_{h_j}^{\ a_{h_j}}}{t_{h_j}} \right)^{1/b_{h_j}} + \left(\frac{c_{p_j} \cdot R_{p_j}^{\ a_{p_j}}}{t_{p_j}} \right)^{1/b_{p_j}} \tag{8}$$

When tolerancing the connector, only one tolerance is assigned to a nominal dimension, even if this feature is repeated several times in the product. That is the reason why the manufacturing cost depends upon the dimensions of one single vee-groove, instead of the complete array of grooves.

Tolerance Allocation by Optimization

Optimal tolerances for the dimensions are determined using nonlinear constrained optimization. The problem is formulated as a minimization subject to constraints. The function to minimize is the manufacturing cost of the connector with respect to its tolerances, as defined in the previous section. Constraints are formulated by specifying that the standard deviation of the lateral misalignment, σ_{d_j}, for every pair of fibers within the connector must be positive yet below a critical value. Additional bounds can be specified to prevent the optimization from driving the assigned tolerances to unreasonably high or low values.

Since this optimization only deals with allocating tolerances to the vee-grooves, it is assumed that the tolerances for the fibers and the system that aligns the ferrules is already known empirically or predicted by another analysis. The variables of the optimization problem are then the tolerances for the four dimensions (β_{Lj}, β_{Rj}, h_j, p_j) defining the vee-grooves. The radius of curvature is not included, since it doesn't affect the positioning of the fiber.

This method was used to allocate tolerances to an exemplary connector. The objective was to minimize the manufacturing cost of an 8-fiber connector while the connection loss of every pair of single-mode fibers should be less than 0.5 dB. The calculated connection losses along the connectors are displayed in Fig 6, and the resulting tolerances allocated by the optimization procedure are listed in Table 1.

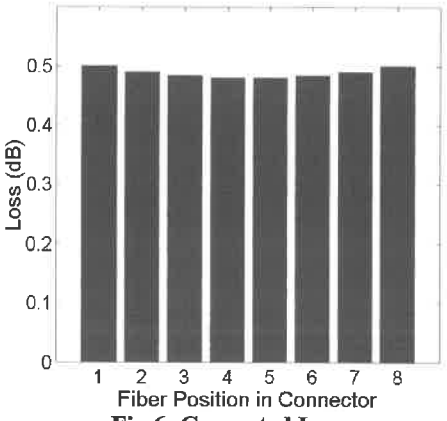

Fig 6: Computed Losses

Table 1: Computed Tolerances

Dimension	Assigned Tolerance
Left Angle	5.76×10^{-3} radians
Right Angle	5.76×10^{-3} radians
Depth of the Vertex	0.519 microns
Pitch between Vees	0.594 microns

Conclusions

Manufacturing cost is a critical parameter for mass-produced features. On the other hand, accurate devices need low variation in their dimensions. Mass-produced multi-fiber connectors using vee-grooves

face both problems. Their design can be optimized by a tolerance allocation method.

This paper presents a method for allocating tolerances to the dimensions of the vee-grooves. A mathematical model of the geometry is constructed and used in a statistical analysis. Applying the law of error propagation allows derivation of a relation between dimensional variance and variance in signal loss. Optimal tolerances of the vee-grooves are computed by minimizing the relative manufacturing cost while respecting constraints on maximum loss acceptable for every pair of mating fibers. The method is demonstrated for an exemplary 8-fiber vee-groove alignment system.

References

[1] Zanger, H. & Zanger, C., *Fiber Optics, Communication and Other Applications*, Macmillan Publishing Company, New York, 1991.

[2] Marcuse, D., "Loss Analysis of Single-Mode Fiber Splices". *The Bell System Technical Journal.* May- June 1977. pp. 703-718.

[3] Chase, K. W., "Tolerance Allocation Methods for Designers", ADCATS Report No. 99-6, Brigham Young University, 1999.

[4] Rachakonda, P., Barraja, M., Vallance, R.R., Kiani, S. & Lehman, J., "2D Error Models and Monte Carlo Simulations for Budgeting Variation in Optical-Fiber Array Connectors", *Proceedings of the ASPE 2001 Annual Meeting*, pp. 509-512

[5] Arenberg, J. W., "On the Origins of the Law of Error Propagation and its Uses", *Proceedings of the ASPE 2002 Summer Topical Meeting*, pp. 80-84.

The Application of an Empirical Tool Force Model on Vibration Assisted Cutting

Xiaorui Fan and Michele H. Miller
Michigan Technological University, Houghton, MI

Introduction

Many experiments have demonstrated that vibration assistance can make machining forces decrease. Several researchers have presented force models for single point cutting with vibration. Astashev presents a model for cutting with tool vibration parallel to the cutting direction [1]. Dow et al. describe a force model for elliptical cutting [2]. In this paper we develop a force model for cutting with vibration in the thrust direction. We modify an empirical tool force model incorporating elastic and plastic material properties that was developed for diamond turning [3].

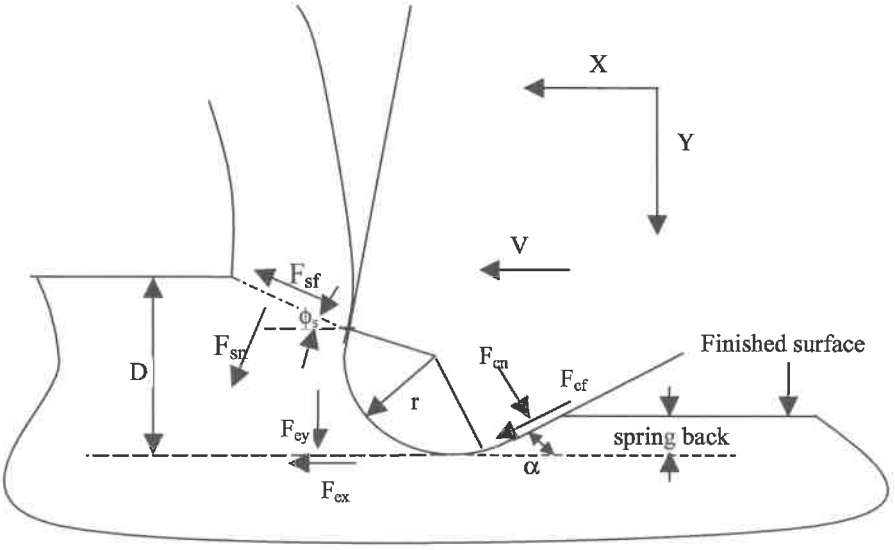

Fig.1 2D view of chip formation process showing three sets of cutting forces

Figure 1 shows a 2-dimensional view of the orthogonal cutting process. Key parameters include depth of cut (D), cutting speed (V), tool tip radius(r), shear angle (ϕ_s), clearance angle (α), spring back(s) and rake angle (γ_{ne}). Some of these parameters are prescribed: depth of cut, cutting speed, clearance angle and rake angle. The figure also shows three sets of forces: shear plane(F_{sf} and F_{sn}), tool edge(F_{ex} and F_{ey}) and clearance face(F_{cf} and F_{cn}). The shear plane forces can be represented as rake face forces with a coordinate transformation. Tool forces are thus divided into three zones: rake face, tool edge, and clearance face.

Introducing high frequency vibration in the vertical direction (applied to tool or workpiece) causes most parameters to change during the machining process. These changes affect the forces on the three tool zones. For example, the relative cutting speed between tool and workpiece changes in amplitude and direction. This results in the possibility of a friction force direction

change on the rake face. Also, vibration changes the contact length between the tool edge and workpiece so that the cutting and thrust force on the tool edge area differ from the forces without vibration. Meanwhile, the contact length between the clearance face and workpiece changes, as does the effective clearance angle. This makes the normal force and friction force on this cutting zone different from the situation without vibration. The machining forces on these three zones can be investigated separately as described below.

Forces on the Rake Face

Some assumptions need to be made in order to calculate the normal force and friction force on the rake face [3]. First, the workpiece material is regarded as elastic-perfectly plastic. Second, the normal stress on the shear zone is the uni-axial material flow stress, i.e. $\sigma_s=H/3$. Third, Von Mises failure criterion is employed so that shear stress is

$$\tau_s = \sigma_s / \sqrt{3} = H / 3\sqrt{3} \tag{1}$$

Finally, the shear plane angle with respect to a fixed coordinate system remains constant and consequently the shear angle with respect to the cutting direction varies [4]. The normal force and shear force on the shear plane should be:

$$F_{sn} = \sigma_s A_s = \frac{H}{3}\frac{A_c}{\sin\phi_s} = \frac{HL}{3\sin\phi_s}(D - a\sin\omega t) \tag{2}$$

$$F_{sf} = \tau_s A_s = \frac{HL}{3\sin\phi_s}\frac{D - a\sin\omega t}{\sqrt{3}} \tag{3}$$

where A_c=uncut chip area, L=tool/chip contact length projected onto surface of workpiece, A_s=shear plane area, a=vibration amplitude and ω=vibration angular velocity.

With respect to the rake face, these forces can be rewritten as[5][6]:

$$F_{rf} = F_{sn}\cos(\phi_s - \gamma_{ne}) - F_{sf}\sin(\phi_s - \gamma_{ne}) \tag{4}$$

$$F_{rn} = F_{sn}\sin(\phi_s - \gamma_{ne}) + F_{sf}\cos(\phi_s - \gamma_{ne}) \tag{5}$$

where F_{rf}=friction force on the rake face, and F_{rn}=normal force on the rake face.

The direction of the rake face friction force depends on the relative velocity between the chip and tool. Under certain conditions, it is possible for the vibration velocity (V_a) to exceed the chip velocity (V_c). At these times, the friction force between the chip and tool changes direction. Consequently, when averaged over many cycles, the friction force is less than its nominal value.

Figure 2 shows an example of a case where the friction force points up the rake face between t_0 and t_1, down the rake face between t_1 and t_2, and back up the rake face between t_2 and t_3.

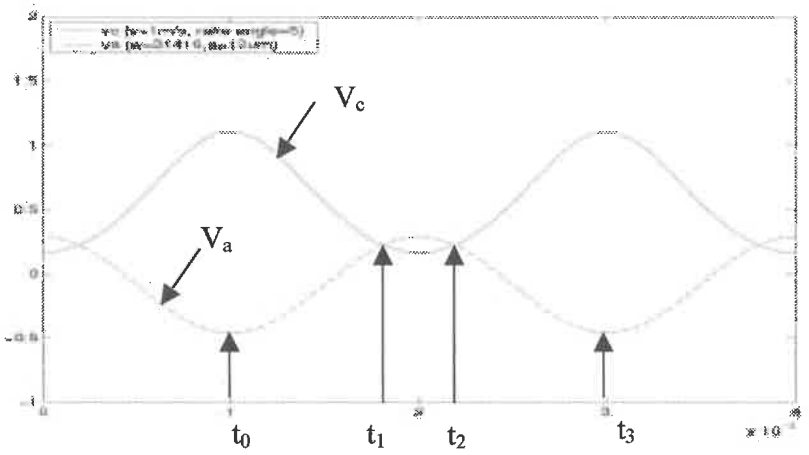

Fig. 2: Comparison of V_a and V_c

In these three regions, the time weighted friction force is:

$$F_{rfv1} = \frac{HL}{3\sin\phi_s}\frac{1}{T}\int_0^{t_1}(D - a\sin\omega t)\cos(\phi_s - \gamma_{ne}) - \frac{1}{\sqrt{3}}(D - a\sin\omega t)\sin(\phi_s - \gamma_{ne})dt \quad (6)$$

$$F_{rfv2} = \frac{HL}{3\sin\phi_s}\frac{1}{T}\int_{t_1}^{t_2}(D - a\sin\omega t)\cos(\phi_s - \gamma_{ne}) - \frac{1}{\sqrt{3}}(D - a\sin\omega t)\sin(\phi_s - \gamma_{ne})dt \quad (7)$$

$$F_{rfv3} = \frac{HL}{3\sin\phi_s}\frac{1}{T}\int_{t_2}^{t_3}(D - a\sin\omega t)\cos(\phi_s - \gamma_{ne}) - \frac{1}{\sqrt{3}}(D - a\sin\omega t)\sin(\phi_s - \gamma_{ne})dt \quad (8)$$

We define "time weighted force" as $F_{weighted}=F_{actual}\Delta t/T$ where Δt is the time over which the force acts and T is the vibration period. The average friction force on the rake face is

$$F_{rfv} = F_{rfv1} - F_{rfv2} + F_{rfv3}$$

Without vibration, the friction force on the rake face is:

$$F_{rf} = \frac{HL}{3\sin\phi_s}\left[D\cos(\phi_s - \gamma_{ne}) - \frac{1}{\sqrt{3}}\sin(\phi_s - \gamma_{ne})\right] \quad (9)$$

To illustrate the effect of vibration on the rake face forces, we consider the following cutting condition: V=1m/s, γ_{ne}=5°, f=5000Hz, a=12μm, D=20μm, ϕ_s=30°, α=8°, r=5μm, H=5.3GPa, and L=0.01m. In this case, F_{rfv1}=104.25N, F_{rfv2}=34.5N, and F_{rfv3}=41.45 N. The friction force on the rake face with vibration is therefore F_{rfv}=112 N. The friction force without vibration F_{rf}=180.2 N However, the normal force keeps constant with vibration, i.e. $F_{rnv}=F_{rn}$=397.84 N

Force on the Tool Edge

Figure 3 shows the interface stress (σ_f) acting on the tool edge. The forces F_{ex} and F_{ey} can be computed based on σ_f, the edge contact length l_e, and the tool width (into the paper) L.

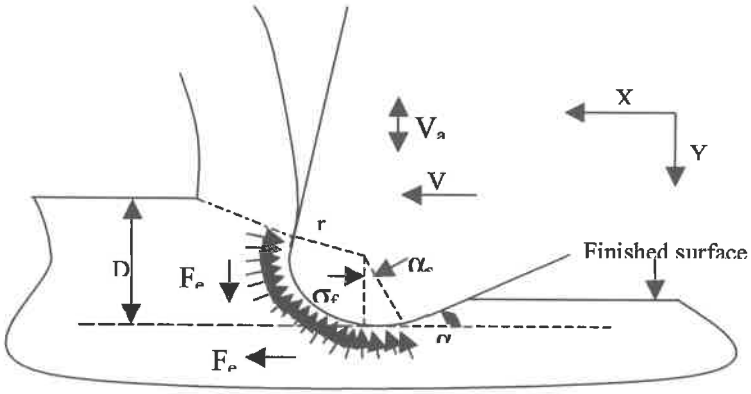

Fig.3: Normal stress distribution on the

An empirical formula for the tool/workpiece interface stress σ_f, is given by [3]:

$$\sigma_f = K_2 H\sqrt{\frac{H}{E}} \quad \text{where } K_2 \text{ is a constant} \tag{10}$$

The endpoint of l_e is tangential to the resultant tool velocity. Without vibration, the contact length between the tool edge and workpiece is

$$l_e = (\frac{\pi}{2} + \gamma_{ne})r \tag{11}$$

The total force in the horizontal and vertical directions are given by:

$$F_{ex} = \sigma_f L l_e \left[\sin\left(\frac{\pi}{4} + \frac{\gamma_{ne}}{2}\right) + \mu\cos\left(\frac{\pi}{4} + \frac{\gamma_{ne}}{2}\right)\right] \tag{12}$$

$$F_{ey} = \sigma_f L l_e \left[\cos\left(\frac{\pi}{4} + \frac{\gamma_{ne}}{2}\right) - \mu\sin\left(\frac{\pi}{4} + \frac{\gamma_{ne}}{2}\right)\right] \tag{13}$$

With vibration: $l_e = (\frac{\pi}{2} + \gamma_{ne} + \alpha_s)r$ (14)

where α_s is defined as an angle between the tangential point of resultant cutting speed and the beginning of the straight flank area. Under the same conditions mentioned previously and with μ=0.9, the maximal absolute value $|\alpha_s|$=atan(ωa/V)=20.66°

We define the time weighted forces F_{exv1} and F_{exv2} as follows. In the half vibration cycle, from t_0=0 to t_1=6.2158×10^{-5}sec, α_s increases from –20.66° to 8°,

$$F_{exv1} = \frac{2}{T}\sigma_f L \int_0^{t_1} l_e \left[\sin\left(\frac{\pi}{4} + \frac{\beta}{2} - \frac{a\tan\frac{\omega a\cos\omega t}{V}}{2}\right) + \mu\cos\left(\frac{\pi}{4} + \frac{\beta}{2} - \frac{a\tan\frac{\omega a\cos\omega t}{V}}{2}\right)\right] dt \tag{15}$$

Then α_s remains at 8° until t_2=1×10^{-4}sec (end of the half vibration cycle) due to the clearance angle limitation. The limitation is because the resultant speed could vary from –20.66° to 20.66°. However, because the clearance angle is smaller than 20.66°, the variation of α_s is from –20.66 to 8°.

For the second half of the vibration cycle:

$$F_{exv2} = \frac{2}{T}\sigma_f L\left(\frac{\pi}{2} + \gamma_{ne} + \alpha\right) r(t_2 - t_1)\left[\sin\left(\frac{\pi}{4} + \frac{\gamma_{ne}}{2} - \frac{\alpha}{2}\right) + \mu\cos\left(\frac{\pi}{4} + \frac{\gamma_{ne}}{2} - \frac{\alpha}{2}\right)\right] \quad (16)$$

So the cutting force is $F_{exv} = F_{exv1} + F_{exv2}$. Introducing a value for interface stress σ_f=3.54GPa The cutting and thrust force without vibration are F_{ex}=394.82 N and F_{ey}=3.52 N. With vibration, F_{exv1}=222.3 N, F_{exv2}=161.49 N, and F_{exv}=383.79 N. Because F_{ey} is very small compared to F_{ex}, it was not calculated.

Force on the Clearance Face

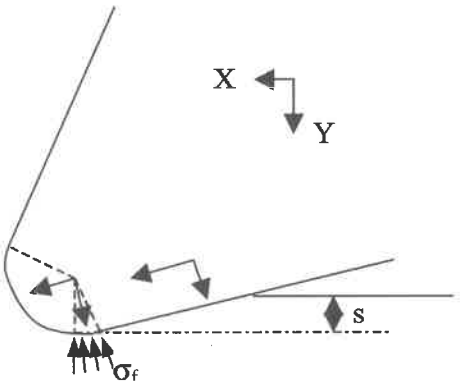

Fig.4: Force distribution on the clearance face (no vib.)

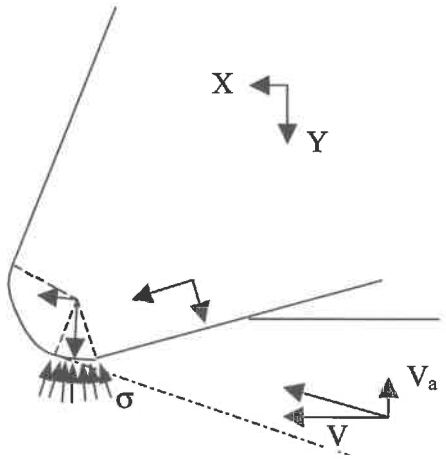

Fig.5: Force distribution on the clearance face (with vib.)

The analysis on the clearance face includes two parts: the straight flank area and a small arc where the direction of normal stress σ_f is not constant. In Figures 4 and 5, the left starting point of the small arc is defined by the tangential point of the resultant cutting speed and the right ending point of the small arc is the beginning of the straight flank area. Suppose spring back(s) is 6 μm, the machining forces on the clearance face without vibration are:

$$F_{cx} = \sigma_f Lr\alpha\left[\sin\left(\frac{\alpha}{2}\right) - \mu\cos\left(\frac{\alpha}{2}\right)\right] + \sigma_f L[s - r(1-\cos\alpha)](\sin\alpha - \mu\cos\alpha) \quad (17)$$

$$F_{cy} = \sigma_f Lr\alpha\left[\cos\left(\frac{\alpha}{2}\right) + \mu\sin\left(\frac{\alpha}{2}\right)\right] + \sigma_f L[s - r(1-\cos\alpha)](\cos\alpha + \mu\sin\alpha) \quad (18)$$

With vibration, we determine the time weighted forces F_{cxv1} and F_{cxv2}. In the half vibration cycle, from t_0=0 to t_1=6.2158×10^{-5}sec, α_s increases from –20.66° to 8°, and

$$F_{cxv1} = \int_0^{t_1}(\alpha + \alpha_s)r\left[\sin\left(\frac{\alpha_s}{2} - \frac{\alpha}{2}\right) + \mu\cos\left(\frac{\alpha_s}{2} - \frac{\alpha}{2}\right)\right]dt \quad (19)$$

$$F_{cyv1} = \int_0^{t_1}(\alpha + a\alpha_s)r\left[\cos\left(\frac{\alpha_s}{2} - \frac{\alpha}{2}\right) - \mu\sin\left(\frac{\alpha_s}{2} - \frac{\alpha}{2}\right)\right]dt \quad (20)$$

Then α_s remains at 8° until t_2=1×10^{-4}sec, and

$$F_{cxv2} = \int_0^{t_2} [s - r(1-\cos\alpha)](\sin\alpha - \mu\cos\alpha)dt \quad (21)$$

$$F_{cyv2} = \int_0^{t_2} [s - r(1-\cos\alpha)](\cos\alpha + \mu\sin\alpha)dt \quad (22)$$

So, the cutting force is $F_{cxv} = F_{cxv1} + F_{cxv2}$, and the thrust force is $F_{cyv} = F_{cyv1} + F_{cyv2}$. Using the same conditions described previously, the cutting and thrust forces without vibration are F_{cx}=184.59 N and F_{cy}=222.92 N. With vibration, F_{cxv1}=24.72 N , F_{cxv2}=171.37 N and F_{cxv}=196.09 N. And F_{cyv1}=25.35 N, F_{cyv2}=227.53 N and F_{cyv}=252.88 N.

Combined Force

Summing the forces from the three zones, the cutting and thrust forces without vibration are:

$$F_x = F_{rf}\sin\gamma_{ne} + F_{rn}\cos\gamma_{ne} + F_{ex} + F_{cx} = 991.44N \quad (23)$$

$$F_y = F_{rf}\cos\gamma_{ne} - F_{rn}\sin\gamma_{ne} + F_{ey} + F_{cy} = 371.28N \quad (24)$$

With vibration, the forces would be:

$$F_{xv} = F_{rfv}\sin\gamma_{ne} + F_{rnv}\cos\gamma_{ne} + F_{exv} + F_{cxv} = 985.97N \quad (25)$$

$$F_{yv} = F_{rfv}\cos\gamma_{ne} - F_{rnv}\sin\gamma_{ne} + F_{eyv} + F_{cyv} = 333.3N \quad (26)$$

For this case, the cutting force decreases by 0.55%, and thrust force decreases by 10.2%.

Conclusions

Using an existing empirical tool force model, together with a simple geometric assumption about the shear angle, we can predict that moderately high vibration frequencies (thousands of Hertz) can produce significant force reductions, especially on the thrust force. Experiments will be done to validate the theoretical results. Future work will also investigate the effect of vibration parameters and tool geometry on the total force reduction.

Acknowledgments

This work was supported in part by NSF grant number 9875251.

References

[1] Astashev, V. K. "Effect of Ultrasonic Vibration of a Single-point Tool on the Process of Cutting," *Journal of Machinery Manufacture and Reliability*, No. 3, 1992, pp. 65-70.

[2] Dow, T. A., Cerniway, M. A. and Sohn, A., "Vibration Assisted Diamond Turning Using Elliptical Tool Motion," *Proc. of the 2001 ASPE Annual Meeting*, pp. 92-97.

[3] Arcona, C. and Dow, T. A., "An Empirical Tool Force Model for Precision Machining," *Journal of Manufacturing Science and Engineering*, Vol. 120, No. 4, Nov, 1998, pp. 700-707.

[4] Fan, X and Miller, M. H. "Force Modeling in Vibration Assisted Cutting," *Proc. of the 2001 ASPE Annual Meeting*, p 409-412.

[5] Merchant, M. E., "Mechanics of the Metal Cutting Process," *J. Appl. Phys.*, Vol. 16, No. 5, 1945, p. 267.

[6] Lee, E. H., and B. W. Shaffer, "The Theory of Plasticity Applied to a Problem of Machining," *J. Appl. Mech.*, Vol. 18, No. 4, 1951, p. 405.

Grinding of Microstructures in Hardened Steel with CBN Tools

Hans-Werner Hoffmeister, Marcus Hlavac
Institute of Machine Tools and Production Technology
Technical University of Braunschweig, Germany

Abstract

Considering the mass production of micro parts, injection moulding or micro forming processes are of high cost efficiency. High resistance against wear and high dimensional and shape stability are demands for these moulding tools. For this application hardened steel is used to an increasing degree in conventional moulding tool manufacturing [1]. But the production of microstructures with high quality in steel proves to be difficult.

Micro grinding with CBN tools is a new possibility of manufacturing microstructures in steel. The Institute of Machine Tools and Production Technology of the Technical University Braunschweig, Germany, examines the potential and applications of the micro grinding technology with CBN tools.

State of the art in micro machining of steel

To manufacture microstructures in hardened steel the machining can only be done by micro electro-discharge machining or micro cutting processes. A high structure quality and a high aspect ratio up to 80:1 are characteristics of micro electro-discharge machining [1]. However, the process times are very long and in addition to that it the spark discharge results in a thermal damaging of the surface layer. Shorter process times and a minimal thermal surface layer damage are the advantages of micro cutting processes. Other advantages are a high quality of the microstructures and a high flexibility of the manufacturing process. The chemical wear of the used diamond tools during micro milling and micro turning is the reason for a low efficiency of these processes. By ultrasonic assisted diamond turning the short life of the diamond tool could be increased [3]. Alternatively tools made of sintered carbide are used for micro cutting of steel. Unfortunately, these tools are exposed to a high abrasive wear so that their life is very short and the reproduceable aspect ratio is only at 5:1 [2]. The machinability of steel becomes more difficult by increasing the hardness of this material. Processes with a geometrically defined cutting edge come near their limits. In contrast to that grinding processes are suitable for cutting hard materials. Microstructures were already successfully produced in hard and brittle materials by micro grinding. Diamond abrasive penciles and dicing blades proved to be suitable for machining microstructures [4]. For machining hardened steel micro grinding with CBN tools is now available as a new micro cutting process.

Micro grinding with CBN tools

Grinding with CBN tools has proved to be an efficient machining process of hardened steel. A low tool wear, the chemical resistance and a material removal rate are well-known characteristics of grinding hardened steel with CBN tools. Adapted into the dimensions of the world of micro-

structures micro grinding with CBN tools is being developed to a highly efficient machining process with short process times and material removal rates in a current research project*.

For the manufacturing of microstructures in steel dicing blades with CBN abrasives were used. Usually dicing blades are only available with diamond grains because these tools are principal used to separate silicon wafers. Dicing blades are available in a large range of diamond grain sizes, wheel thicknesses, diameters and bonding types. Compared to that the range of CBN dicing blades is very small. These tools are available with a minimum thickness of 100 µm and a standard diameter of 56 mm.

Grinding with dicing blades allows the manufacturing of straight-line structures only, e.g. grooves, the minimum width of which are determined by the thickness of the micro grinding wheel. The tools have an accuracy of thickness of 1...5 µm. The varying thickness results of the grinding wheel production process. Moreover it the accuracy of the machine tool and the tool deflection, caused by the cutting pressure, take effect on the ground groove width (figure 1). These effects have to be considered when manufacturing microstructures by micro grinding to obtain the required accuracy of shape and dimension.

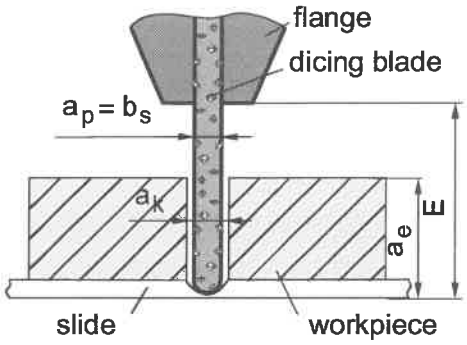

excess length (range): $E = (20 \ldots 30) \cdot b_s$

operation depth (range): $a_e = (10 \ldots 15) \cdot b_s$

actual operation width: $a_k \approx 1{,}1 \cdot b_s$

© IWF 392-68-00

Figure 1: General guidelines for the adjustment of dicing processes

In experiments, we tested commercially available CBN micro grinding wheels to study their periphery. The micro grinding wheels are resin bonded with CBN grain sizes of 1, 15 and 46 µm. The machined steels were 90 MnCrV 8, X 90 CrMoV 18, X and X 155 CrVMo 1 2 1. These materials are used for moulds and stamping tools. The hardness of the three different hardened steels was HRC 58. By varying the process parameters (cutting speed, infeed, depth of cut), we measured the process forces and the surface quality of the ground surface. The experiments showed that generally higher cutting speeds are suited for micro cutting of hardened steels. At a low cutting speed of $v_c = 40$ m/s the process forces increase fast by rising the cutting volume. The typical process forces were in the range of a few Newton. Micro grinding with CBN allows material removal rates up to $Q'_w = 0.7\ mm^3/(mm\ s)$ for the machining of hardened steel. Microstructures with an aspect ratio of 40:1 can be ground within short process times. Figure 2 shows some possible micro ground structures. The strength of the used steels allowed the grinding of microstructures with the minimal dimension of 10 µm and the limits have not yet been reached. Micro grinding of hardened steel has the potential of machining smaller structures and obtaining a higher efficiency of the cutting process. The development of this technology has just begun. As further advantages of micro grinding the very small wear of the tool and the constant machining quality have to be mentioned.

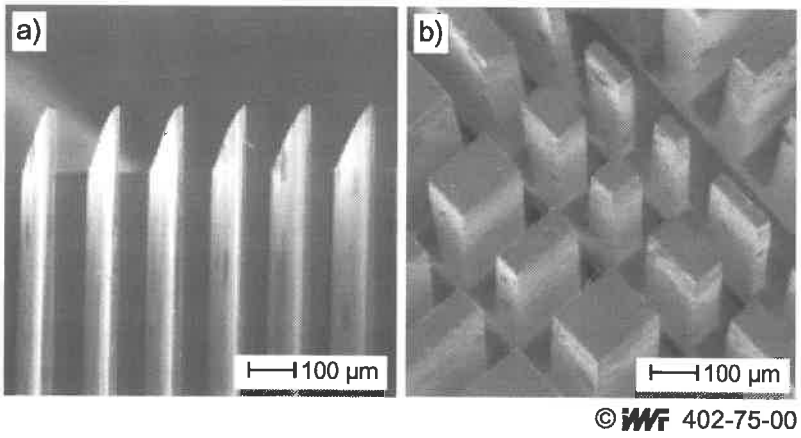

Figure 2: Ground micro structures in X 90 CrMoV 18 (a) and X 155 CrVMo 1 2 1 (b)

The measurement of the surface roughness showed that small CBN grains produce a very good surface quality. The best surface roughness obtained was $S_a = 47$ nm by using a superfine CBN grain size of 1 µm. Micro grinding wheels with larger grains allow high material removal rates, but a lower surface quality is obtained with these tools. Especially the type of micro grinding wheels with the large grain size of 46 µm causes deep machining traces through several, widely outstanding CBN grains (figure 3). Here the surface roughness is about $S_a = 0.4 - 0.6$ µm.

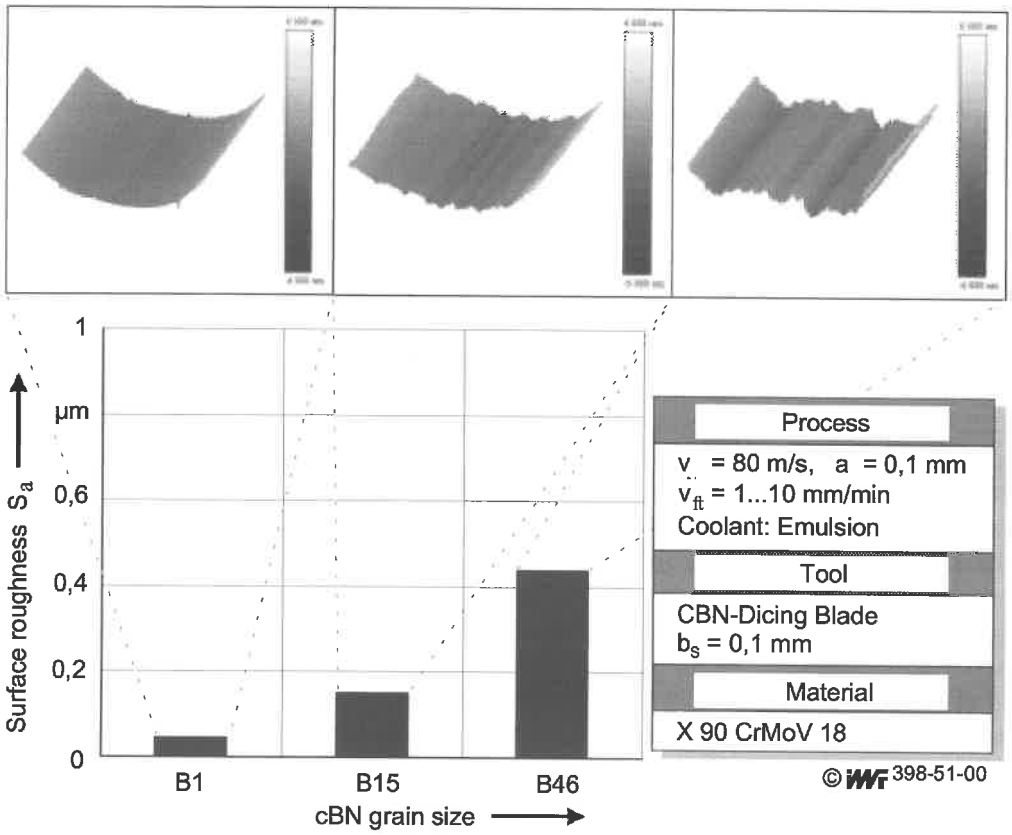

Figure 3: Surface roughness dependent on the CBN grain size

The size of the chipping space, which is given by the grain size, determines the possible maximum material removal rate of the micro grinding wheel. CBN dicing blades with a superfine grain size are only suited for polishing surfaces, whereas grinding wheels with a grain size of 15 µm cut high volumes and produce a good surface quality of about S_a = 0,1 µm. Through dressing of micro grinding wheels a reduction of the machined surface roughness is planed.

Not only the grain size has an influence on the machining results, but also different geometric dimensions of the micro grinding wheel. Depending on the grinding wheel thickness and the machined material the results are varying. The comparison of the process forces by varying the grinding wheel thickness showed a precise difference between the three materials. Clearly higher process forces were measured on micro grinding wheels with a thickness of 100 µm as on a micro grinding wheel with a thickness of 300 µm during the machining of 90 MnCrV 8. In contrast to this result the difference between the thickness of micro grinding wheels is minimal when machining of X 90 CrMoV 18 (figure 4). These differences are attributed to the material structure.

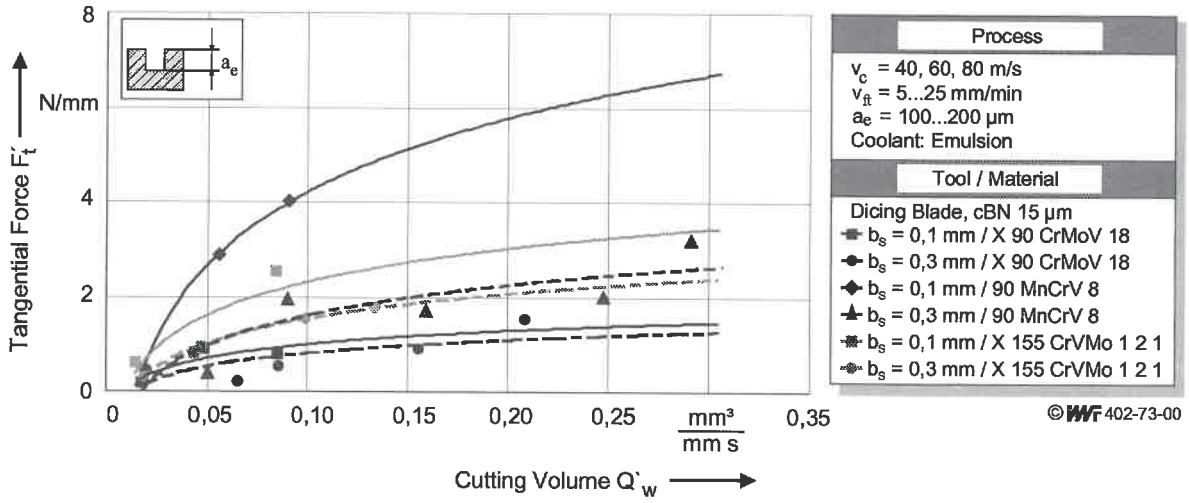

Figure 4: Dependency of process force and thickness of micro grinding wheels at different hardened steels

Beside the process forces also an influence of the grinding wheel thickness on the manufactured surface roughness was determined. Differences between the machined materials could be seen again. Wide micro grinding wheels produce a medium surface quality of S_a = 0,2 µm for the both steels X 90 CrMoV 18 and 90 MnCrV 8. The measured surface roughness was better up to the factor 2, when small micro grinding wheels were used. With the material X 155 CrVMo 1 2 1 this connection is directly opposite. Here better surface qualities are produced by using wide micro grinding wheels. The analysis of the experiments shows that beside the grinding tool the material, too, has an effect on the machining result. Further studies will examine the size of this effect.

The burr could not be completely prevented during the micro cutting of the ductile material steel. However, a connection between the grain size and the size of the burr was found. A smaller grain size causes a lower burr. We measured a burr smaller than 1 µm when using of micro grinding wheels with a superfine grain size of 1 µm. In contrast to that often a burr is often existing of

2 - 4 µm when grinding with large CBN grains, unattached by varying the process parameters. In all experiments the burr adhered strongly at the edges of the structure and results in the plastic deformation of the steel during the ductile cutting process.

Summary and Outlook

The experiments showed that the machining of microstructures in hardened steel can carried out well by micro grinding with CBN tools. This production technology allows the manufacturing of microstructures with a high aspect ratio and a high quality.

In new experiments we will aim at varying the bonding system of the micro grinding wheels and optimizing the process parameters to fully exploit the potential of this micro machining process and to fully develop this technology for the manufacturing of micro structures in hardened steel. A further miniaturization and quality increase is planned. The influences of the material structure on the micro grinding process will be studied through further experiments and metallographical analyses. An analysis of a possible thermal damage of the surface layer caused by the grinding process will be carried out, too.

Also if there is a thermal damage of the surface layer caused by the grinding process will be analyzed.

Following these experiments our aim is to dress micro grinding wheels in order to obtain better surface qualities and to profile micro grinding wheels for machining surfaces with special micro profiles.

* The work presented here is financially funded by the Deutsche Forschungsgemeinschaft DFG ("German Society for Research").

References

[1] Michel, F.; Ehrfeld, W.; Koch, O.; Gruber, H.-P.: *EDM for Micro Fabrication Technology and Applications.* Euspen, 1st International Conference, Turin (Italy), 2001.

[2] Schmidt, J.; Hüntrup, V.; Tritschler, H.: *Microcutting of steel molds.* In: wt Werkstattstechnik 89 (1999), 11/12, pp. 495 - 498

[3] Klocke, F.; Rübenach, O.: *Ultrasonic Assisted Diamond Turning of Steel and Glas.* In: Proceedings of international seminar on precision engineering and micro technology (EUSPEN), July 19th/20th 2000, Aachen, Germany, pp. 3-12

[4] Hoffmeister, H.-W. ; Wenda, A.: *Novel grinding tools for machining precision micro parts of hard and brittle materials.* In: Proceedings of the 15th annual meeting of the ASPE, October 22th/27th 2000, Scottsdale, Arizona, USA, pp. 152-155

DEVELOPMENT OF CHILLED AIR COOLING TECHNOLOGY FOR PRECISION GRINDING: AN ECO-FRIENDLY ALTERNATIVE

H. Huang*+, K. Ramesh+, L. Yin+ and A. Yui++

+Singapore Institute of Manufacturing Technology, Singapore 638075
++National Defense Academy, Yokosuka, Japan
*email: hhuang@SIMTech.a-star.edu.sg

ABSTRACT

The presence of hazardous chemical additives in a liquid-base coolant causes environmental problems. Increasingly, stringent government legislations are being imposed on coolant use and disposal, which could result in an expense of up to 20% of the total machining cost. This paper reports on the development of an ecologically friendly cooling technology that uses chilled air with a biodegradable oil and air mist to replace the conventional liquid-base coolant. It is found that when the material removal rate is below a critical value, the chilled air/oil mist can replace the liquid-base coolant in terms of grinding surface quality.

INTRODUCTION

A liquid-base coolant is often used in a grinding process to avoid thermal damage and to achieve better surface integrity and longer tool life. However, the presence of chemical additives, such as sulfur, phosphorous and chlorine, in the coolant introduces a health hazard to operators [1]. Disposal of a used chemical coolant involves incineration, which partially contributes to global warming [2]. As a result, stringent government legislations are being imposed on coolant use and disposal. It has been reported by the German automobile manufacturer's association that about 17% of the manufacturing related cost is due to coolant related issues and 94.5% of coolant related cost is attributed to the maintenance disposal and plant investment [3]. In view of this, studies of "green" machining have gained increasing significance. This paper reports on the development of an ecologically friendly grinding technology that uses chilled air with a biodegradable oil and air mist to replace the conventional liquid-base coolant.

CHILLED AIR COOLING SYSTEM

The chilled air/oil mist (or chilled air, in short) cooling system consists of an air compressor, an air chiller, an oil-air mist generator and a nozzle, as shown in Figure 1. The air is first compressed and then released to the chilling and mixing systems. During air chilling, a two-

stage vapor compression refrigeration cycle is adopted to produce a chilled air with a temperature of -30 °C, a pressure of 0.3 MPa and a flow rate of 0.4 m^3/min. The chilled air and the oil-air mist are supplied through two separate paths and then combined using a specially designed twin compartment nozzle (Figure 2b). The twin compartment nozzle has circular holes in the middle as an outlet for the chilled air and square holes surrounding the circular holes for the oil-air mist.

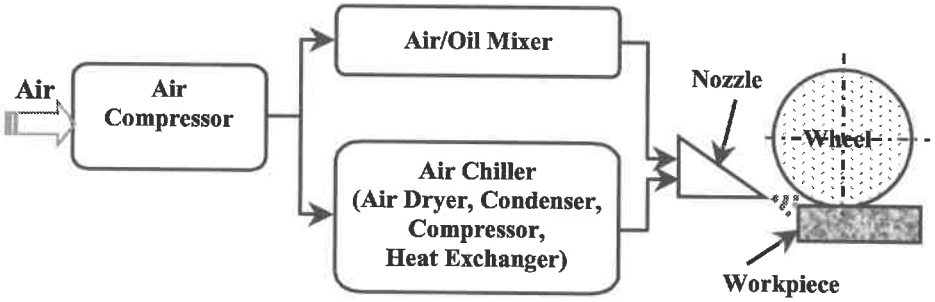

Figure 1: Illustration of the chilled air cooling system.

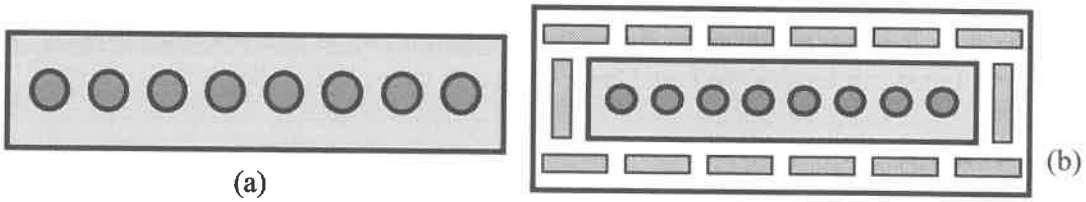

Figure 2: Sectional view of (a) conventional nozzle and (b) twin compartment nozzle.

Coming out from the twin compartment nozzle, the oil-air mist functions as a carrier for maximizing the chilled air penetration into the grinding zone and preventing the air temperature from rising. It also behaves as a lubricant for reducing the wheel-workpiece friction. Figure 3 shows the effect of the air travelling distance on the air temperature for the two nozzles. Compared with the conventional nozzle (Figure 2a), the twin compartment nozzle has a much better performance in terms of cooling effect.

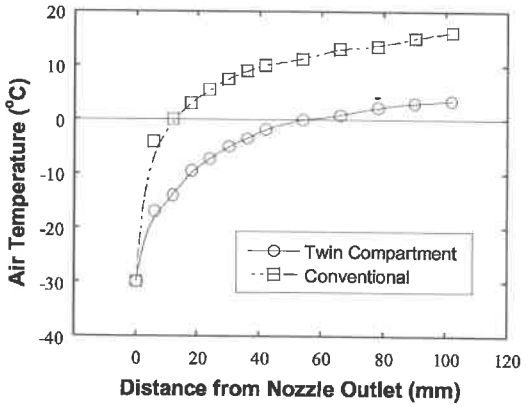

Figure 3: Effect of air travel distance on air temperature.

GRINDING EXPERIMENTS

Grinding experiments were carried out to evaluate the performance of the chilled air cooling on an Okamoto surface grinder, by comparing with the water-base coolant. S45C and SS304 steels were used as workpiece materials. A vitrified CBN wheel (B91N100V) was employed. Grinding velocity and table feed were fixed at 33 m/s and 17.35 m/min., respectively. Depth of cut was varied from 1 to 20 μm. The twin compartment nozzle was used to supply a chilled air with a temperature of -30 °C, a pressure of 0.3 MPa and a flow rate of 0.4 m^3/min. wrapped by an oil-air mist. The water-base coolant flow rate was approximately 4 liter/min.

Grinding force measurements revealed that when the specific material removal rate (MRR) was below a critical value the chilled air grinding of either S45C or SS304 steel resulted in a grinding force with a similar magnitude to that caused using the water-base coolant, as shown in Figure 4. When specific MRR was above the critical value, the increase in grinding force for the chilled air was more significant than for the water-base coolant. This indicates that the cooling effect of the chilled air might be insufficient to remove the grinding heat when the specific MRR was relatively high. From Figure 4, it can be estimated that the critical values for S45C or SS304 are 2 and 1.5, respectively. Increasing the chilled air pressure would result in a better cooling effect, which could enable an increase in the specific MRR.

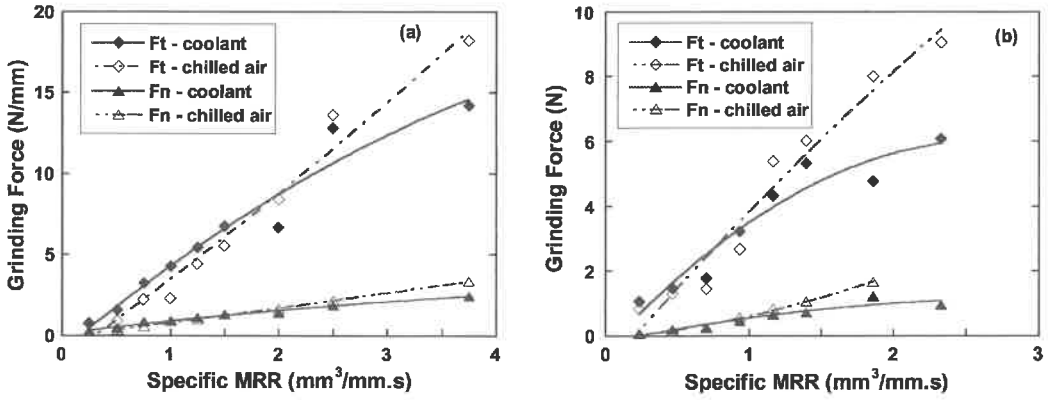

Figure 4: Effect of specific MRR on grinding forces for (a) S45C and (b) SS 304 steels.

A simplified thermal energy equilibrium model that relates to grinding energy, heat transfer and internal energy rise can be used to predict the critical specific MRR. In the model, it is assumed that all the grinding power (per grain), E_g, is transformed into grinding heat, Q_g. The grinding heat is transferred through the cooling media only via convection and evaporation. E_g is computed as

$$E_g = F_t.v/n \qquad (1)$$

where F_t is the tangential grinding force, v the wheel velocity and n the number of active cutting grains. F_t and normal grinding force, F_n, can be computed using the following equations [4],

$$F_t = C_p.f.d.b / v + \mu.F_n \quad (2)$$

$$F_n = C_p.\pi.f.d.b.\tan\alpha / (2v) \quad (3)$$

where C_p is the specific grinding energy, f the table feed, d the depth of cut, μ the friction coefficient, b the wheel width and α the semi-included angle of a grain. The convective heat transfer, Q_c, is determined by [5]

$$Q_c = h.A.\Delta T \quad (4)$$

where h is the convection heat transfer coefficient (kW/ Km^2), A the contact surface area of the cooling media and ΔT the temperature difference between the cooling media and the average grinding zone temperature. The heat transfer due to evaporation, Q_e, is written as

$$Q_e = \varepsilon.g_m.w_m.\rho.u.L \quad (5)$$

where ε is the evaporation factor, ρ the cooling media density, g_m the abrasive grit depth of cut, w_m the distance between the two active cutting edges, u the cooling media velocity and L the latent heat of evaporation.

Q_g is the sum of Q_c and Q_e and can be computed using Equations (4) and (5) under the same experimental conditions. E_g can also be calculated using Equations (1) to (3). Values of the coefficients and properties of the chilled air, the water-base coolant and the workpiece materials in the equations can be found elsewhere [4-5]. Using S45C as an example, values of Q_g and E_g were calculated and are plotted as a function of the specific MRR in Figure 5. The cross points of Q_g and E_g indicate the equilibrium status for using the two different cooling media. The critical specific MRR for the chilled air is 2.2 mm^3/mm s, which is in agreement with the experimental result in Figure 4a. When the MRR is greater than 2, the measured force for the chilled air deviates from that for the water- base coolant.

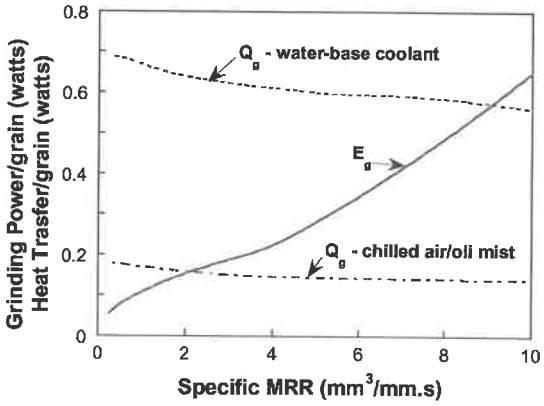

Figure 5: Computed grinding energy per grain and heat transfer per grain for water-base coolant and chilled air/ as a function of the specific material removal rate.

As can be seen in Figure 5 using the water-base coolant the critical specific MRR can reach 9. Apparently, the current chilled air cooling system is competitive to the water-base coolant only at a low specific MRR. To achieve a larger MRR, a greater air pressure or lower air temperature should be supplied to increase the cooling effect. This requires a larger capacity of air chiller or air compressor.

The surface roughness measurements showed that the chilled air grinding led to a similar surface finish for both S45C and SS304 steels, as shown in Figure 6.

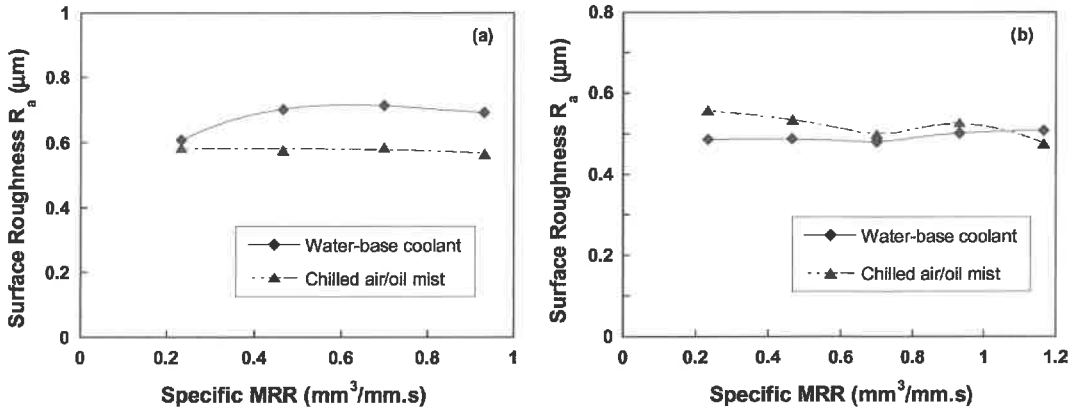

Figure 6: Surface roughness of ground specimens of (a) S45C and (b) SS 304 steels.

However, detailed SEM examinations revealed that the SS304 steel surface generated by the wet grinding (Figure 7c) exhibits slightly more deformed grinding grooves than those caused by the chilled air grinding (Figure 7d), but the ground surface characteristics are similar for S45C (Figure 7a and 7b). The possible explanation is because the air/oil mist which penetrated into the grinding zone significantly reduced the friction between the wheel and the workpiece. Therefore, a smaller work hardening resulted when using the air/oil mist than using the water-base coolant. These effects could have more impact on the SS304 steel than the S45C steel possibly because the SS304 steel is much softer. Further investigations are still needed to verify this conjecture.

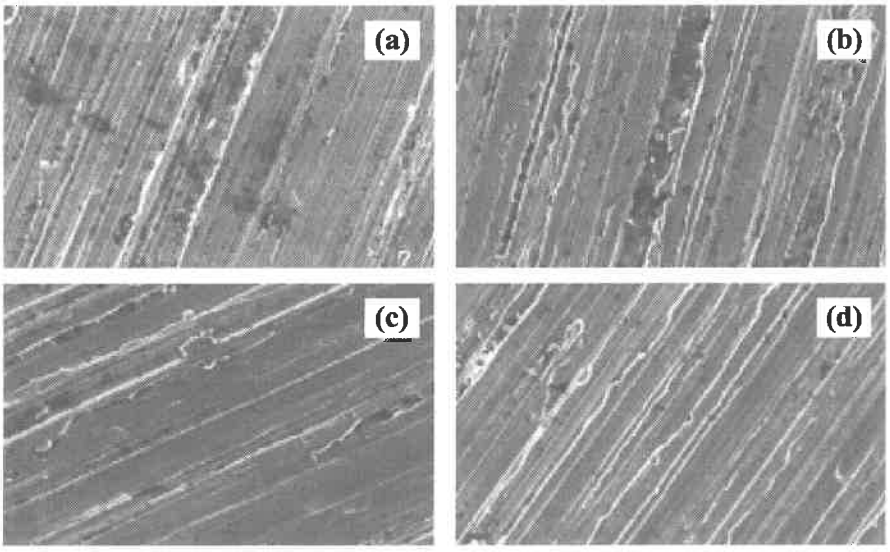

Figure 7: SEM photos (x1000) of ground surfaces for (a) wet grinding of S45C, (b) chilled air grinding of S45C, (c) wet grinding of SS304 and (d) chilled air grinding of SS304.

The residual stress of a ground SS304 surface was measured using x-ray at three different locations and the data are plotted in Figure 8. For either the water-base coolant or the chilled air used, the residual stresses left on the ground surface measured along the grinding marks are tensile and those measured perpendicular to the grinding marks are compressive. There are little differences between the two cooling methods except for the largest MRR used. In this case, the chilled air grinding produced a greater compressive stress and a smaller tensile stress than the water-base coolant. Studies to clarify this point are still under way.

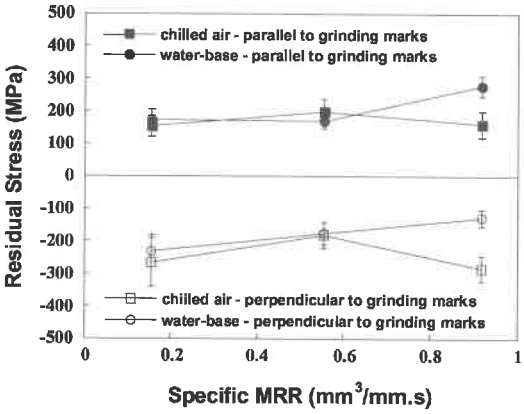

Figure 8: Residual stresses left on the ground SS304 workpiece.

The average surface temperature rise in the grinding zone was also measured using thermal couples for SS304. Using the chilled air cooling, the measured temperature rise varied from 15 °C to 70 °C for the specific material removal rates ranging from 0.15 to 0.9 $mm^3/mm.s$, which was only slightly higher than those using the water-base coolant (from 10°C to 50°C).

CONCLUSIONS

An eco-friendly cooling system was established. This system produced a similar cooling effect to the water-base coolant when the material removal rate is not high. This was explained using a thermal energy equilibrium model. The current system could be applied in fine grinding processes, which require small material removals. To apply the chilled air cooling to grinding processes with large material removals, the chilled air temperature must be further lowered and the air pressure needs to be increased.

ACKNOWLEDGEMENT:

The authors would like to thank Ms. Y.C. Liu & Ms. P.L. Teo for experimental assistance.

REFERENCES:

[1] H.K. Tonshoff, B. Karpuschewski and T. Glatzel, Particle emission and immision in dry grinding, Annals of the CIRP, 46(2) 1997, p693-695.
[2] F. Klocke, A. Schultz, K. Gerschwiler and M. Rehse, Clean manufacturing technology – The competitive edge of tomorrow, Inter. J. of Manufact. Sci. and Tech., 1(2) 1998, p77-86.
[3] F. Klocke, Dry cutting, Annals of the CIRP, 46(2) 1997, p519-526.
[4] S. Matsui,K. Shoji, Estimation of wear process of grinding wheels, JSPE, 35(4), 1969, p235-240.
[5] A. Bejan, Convection Heat Transfer, Wiley Publications, New York, 1984, p351-354.

A Basic Study on Processing Characteristics of OD-Blade Saw Using Ultrasonic Vibration

Ken-ichi ISHIKAWA, Hitoshi SUWABE, Ken-ichi NOKURA, and Michio UNEDA
Kanazawa Institute of Technology : 7-1 Ohgigaoka, Nonoichi, Ishikawa 921-8501 Japan
e-mail : suwabe@neptune.kanazawa-it.ac.jp
Yoshihiro TAKE
Takesho Co. : 6-149-2 Sukuminami, Kasuga, Fukuoka 816-0863 Japan

1. Introduction

The OD-blade saw is one of the cutting or the dicing methods for silicon wafers, ceramics and magnetic materials. This processing system uses the blade tool of disk type that fixes the diamond or cBN grains on contour of the disk. This blade tool brings about the blade deflection in the spindle shaft direction during the processing [1], [2]. Therefore, this processing method is pointed out the many problems concerning the processing ability and accuracy.

The authors tried to develop a new processing system using ultrasonic vibration to clear the several problems of OD-blade saw. This processing system has the unique spindle system to generate the ultrasonic vibration on the NC micro-slicer. The ultrasonic vibration generated by means of the exciter built in the ultrasonic spindle system is transmitted to the blade tool through the spindle shaft, and the blade tool is oscillated by ultrasonic vibration in the radius direction.

This study aims to evaluate the possibility of practical use of this newly developed processing system using ultrasonic vibration. This report describes the mechanism of this newly developed processing apparatus and the results experimented processing characteristics and processing accuracy under a series of the experimental conditions.

2. Experimental apparatus and methods

Figure 1 shows the outline of the experimental apparatus. Figure 2 shows the schematic illustration of ultrasonic vibration exciter. This ultrasonic exciter was made by Takesho Co. This exciter generates ultrasonic vibration of 40kHz at

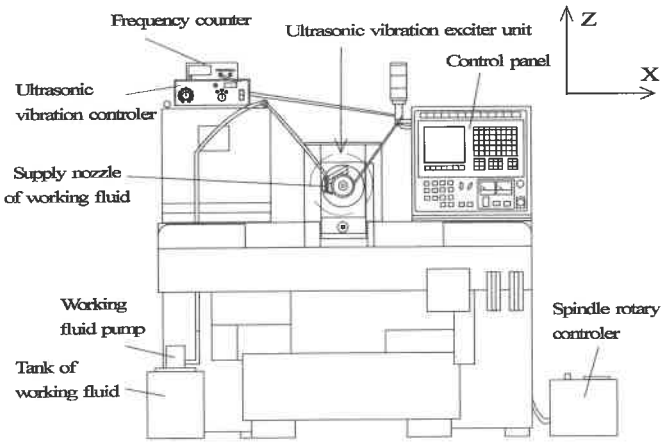

Fig. 1 Model of experimental apparatus

the vibration element. The generated vibration transmits to the top of spindle shaft through the ultrasonic vibration hone. Figure 3 shows the outline of OD-blade tool for ultrasonic vibration slicing. The top of spindle shaft fixes this tool by titanium bolt. The transmitted ultrasonic vibration from the element is changed to the vibration of radius direction of blade tool at this

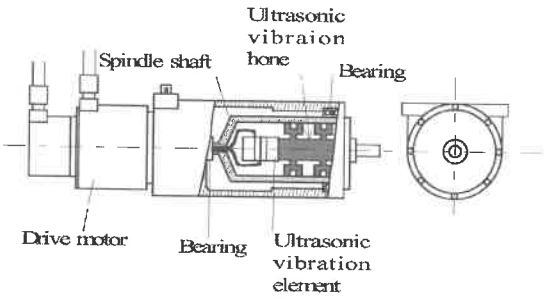

Fig. 2 Ultrasonic vibration exciter

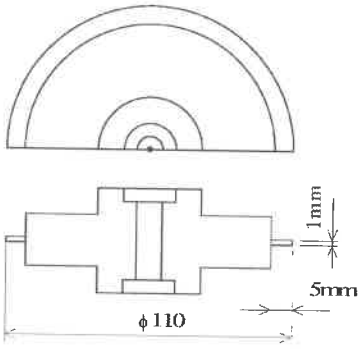

Fig. 3 Outline of OD-blade tool

Table 1 Experimental conditions

Blade:Outer diameter	D	ϕ110
Thickness of grain parts	T_g	1.0mm
Blade type		Electroplated , SD#200
Blade peripheral speed	V_B	1037m/min(3000rpm)
Cutting mode		Down
Depth of cut	c	1.1mm
Feed speed of workpiece	$\dot{X}$	20mm/min
Frequency	f	40kHz
Workpiece, Size		Soda glass, 60×50×1 mm
Working fluid		Water soluble coolant(1/50) JIS - K2241

tool body. The cutting depth is 1.1 mm in the each experimental conditions. Therefore, the cutting forces in the experiment are evaluated by the measurement of load voltage of spindle motor. Table 1 shows the experimental conditions.

3. Processing characteristics in ultrasonic vibration slicing

3.1 Behavior of processing force

Figure 4 shows the relationship between amplitude and load voltage of spindle motor. The load voltages of spindle motor in the ultrasonic vibration processing are smaller than the voltage of normal processing. And, when the amplitude of ultrasonic vibration is 3 μm, the load voltage in ultrasonic vibration shows the decrease of 50% to compare with the normal processing. In case of the non-vibration processing, the OD-blade contacts with the workpiece at all processing time. Therefore, the removal of cutting debris is not so good, and the large cutting force acts on the blade tool. On the other hand, the ultrasonic vibration processing has the phenomena of contact and non-contact during the each vibration cycle. The diamond grains on blade tool can grind the bottom surface of processing kerf by very small cracking of these vibration phenomena. And, the

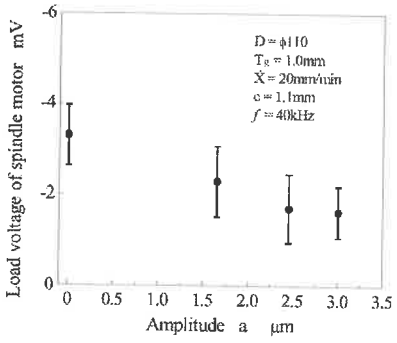

Fig. 4 Behavior of load voltage

removal of cutting debris improves in this non-contact phenomenon in one vibration cycle. As these results, the processing force shows the small value.

Figure 5 shows the SEM photos and surface roughness curves at the bottom surface of processing kerf. As shown in this figure, the bottom surface in ultrasonic vibration processing has large depression to be compared with the surface in non-vibration processing. In case of ultrasonic vibration processing, the diamond grains have a hammering effect to the processing surface caused by contact and non-contact phenomena in one vibration cycle. Therefore, the ultrasonic vibration processing brings out small crack of workpiece.

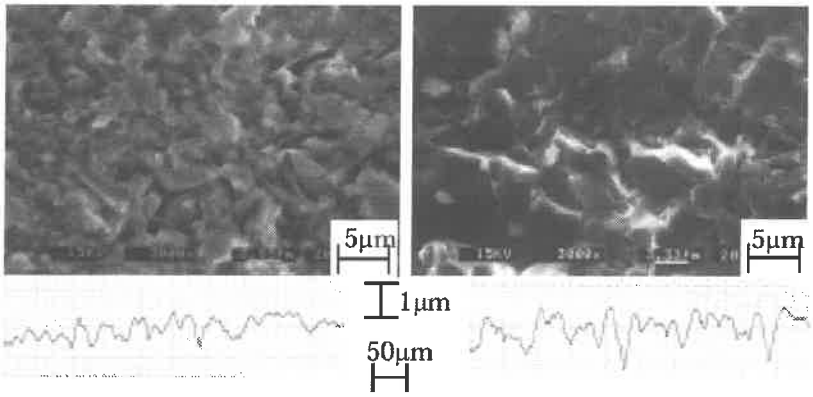

(a) Non-vibration processing (b) Ultrasonic vibration processing

Fig. 5 SEM observations of bottom surface of processing kerf

3.2 Behavior of processing accuracy

Figure 6 shows the relationship between roughness on the processing surface and amplitude of the ultrasonic vibration. As shown in this figure, the surface roughness in ultrasonic vibration are larger than the roughness in non-vibration processing. And, when the amplitude of ultrasonic vibration increases, the surface roughness shows large value. This blade tool has very small vibration in the spindle shaft direction. As the diamond grains on the side surface of blade tool hit the processing surface by this small vibration, the surface roughness in vibration processing shows large value.

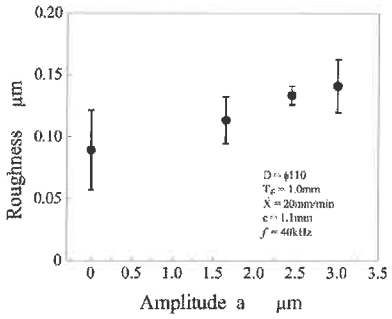

Fig. 6 Behavior of surface roughness

Figure 7 shows the measurement results of processing surface waviness. The surface waviness in vibration processing are two-thirds of the waviness in non-vibration processing, and the dispersions of surface waviness in the vibration processing are smaller than the dispersion in the non-vibration processing. In case of non-vibration processing, the blade tool has the

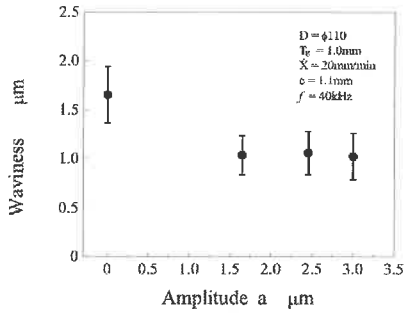

Fig. 7 Behavior of surface waviness

deflection due to processing load, and the surface waviness is influenced by this tool deflection. On the other hand, the processing loads in the vibration processing decrease resulted contact and non-contact phenomena during one vibration cycle, and the surface waviness in the vibration processing decrease caused by the decrease of blade tool deflection.

Figure 8 shows the observation results of edge chipping. The (a) in figure 8 shows the position of observations and definition of chipping amount. The chipping amount defines

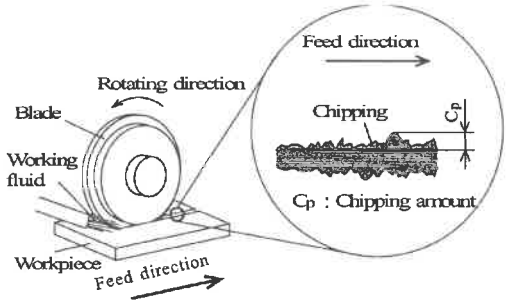

(a) Definition of edge chipping

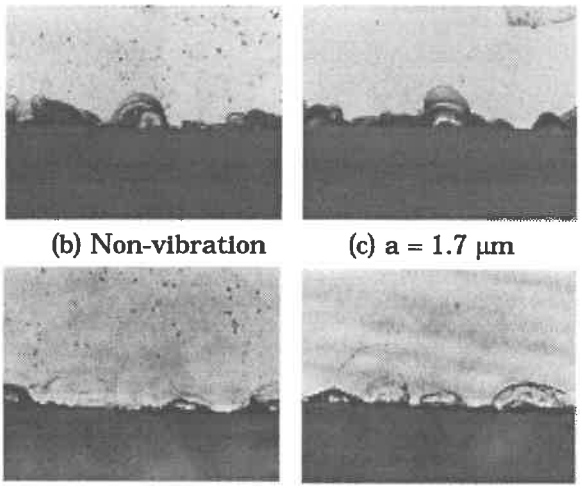

(b) Non-vibration (c) a = 1.7 μm (d) a = 2.5 μm (e) a = 3.0 μm

Fig. 8 Edge chipping

the maximum size observed by microscope. As shown in the observation photos, the chipping amounts in the ultrasonic vibration processing are larger than the amount of non-vibration processing, and the chipping amounts in the vibration processing show the large value with increase of amplitude. The small vibration of blade tool in the spindle shaft direction increases with the change of amplitude in the radial direction. Therefore, the edge chipping is influenced by this small vibration of blade tool.

4. Conclusions

The OD-blade saw using ultrasonic vibration is developed, and the processing characteristics and processing mechanism are studied, and the followings are clear.

1. When the amplitude is 3 μm, the processing loads in ultrasonic vibration show the decrease of 50% by contact and non-contact phenomena in one vibration cycle. And, in case of ultrasonic vibration processing, it is clear that the bottom surface of processing kerf has many depressions by vibrated diamond grains.
2. The diamond grains on side surface of blade tool hit the processing surface by small tool vibration in the spindle shaft direction. And, the surface roughness and the edge chipping in vibration processing show large value.
3. The surface waviness and the dispersions in vibration processing are smaller than them in non-vibration.

The references are omitted.

STUDY ON THE MACHINING ACCURACY OF ROUND-OFF TRUING METHOD
- EXPERIMENTAL ANALYSIS OF ERROR FACTORS -

Takayuki Kitajima, Shigeki Okuyama, Toshihiro Wakatomo and Akinori Yui
National Defense Academy, Yokosuka, Kanagawa, Japan

Hirofumi Suzuki
Toyohashi University of Technology, Toyohashi, Aichi, Japan

Shinsaku Hanasaki
Osaka University, Suita, Osaka, Japan

Abstract

The round-off truing method of a grinding wheel for a precision form grinding, where the circular motion of a CNC grinding machine and an abrasive stick are utilized, was proposed by the authors. In the previous studies, experiments and simulations were performed to clarify the mechanism and appropriateness of this method. Truing accuracy for a precision form grinding, however, could not be realized through these studies. In this study, truing experiments have been performed to realize the effects of geometrical and motional errors on the truing accuracy. The distribution of wear ratio of the abrasive stick, α, directly affects the truing accuracy. Compensation method of the maldistribution of α is then proposed, and the proposed method results in the improvement in truing accuracy.
Key words: form grinding, round-off truing, abrasive stick, brake truer, truing accuracy, form error, wear ratio

1. Introduction

A spherical wheel or a straight wheel with round-off (toroidal shape) is usually employed to fabricate non-axisymmetric aspherical lenses and their dies. In these cases, form error of the grinding wheel directly affects the form accuracy of the generated shape.

The authors proposed a simple round-off-truing method utilizing the circular motion of a CNC grinding machine as shown in **Figure 1** [1]. In this method, an abrasive stick (or a brake truer) is set on the machine table, and the grinding wheel is moved around the stick along the circular path. Effects of the circular motion radius, G, thickness of the grinding wheel and the abrasive stick, Tg, Ts, and initial curvature radii of their profiles, $Rg(I)$, $Rs(I)$, on the generated curvature radius of the grinding-wheel profile, Rg_2 were investigated [1]. The factors which affect the truing accuracy were also examined by computer simulations and truing experiments [2-4]. As a result, Rg_2 settles to the value which can be derived by the equation, $1/Rg_2=\{(Ts/Tg)+1\}/G$. Truing accuracy for the precision form grinding, however, could not be realized through these examinations.

In this study, truing experiments have been performed to realize the effects of geometrical and motional errors, such as set-up error, Δx, inclination of the brake truer, θz, and wear ratio of the abrasive stick, α, on the truing accuracy.

2. Method and Conditions of the Experiment

In the truing experiment, the high-precision CNC surface-grinding machine, Kuroda SPG-25, is used. The machine has hydrostatic oil bearings for horizontal motion and precision ball bearings for vertical motion. Each slide has a scale-feed-back system with a minimum feed of 0.1μm. The ultra-accurate 3-D profilometer, National UA3P-4, is used to evaluate the form accuracy of the trued grinding-wheel surface. This system has an atomic-force probe with a minimum position-resolution of 10nm.

In the experiment, a brake truer is set on the machine table. The grinding wheel is, then, down-fed and moved around the truer along the circular pass. Following the first pass, the wheel is down-fed again and circularly moved in the reverse direction. After a certain number of truing passes, the profile of the wheel

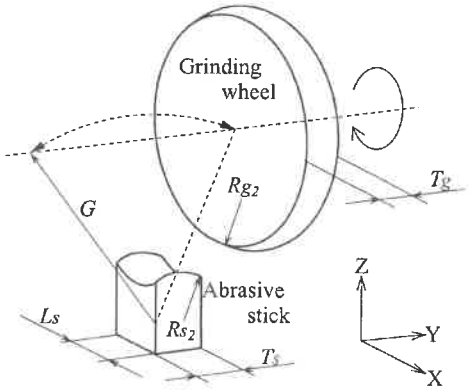

Fig.1 Schematic diagram of the round-off truing method

Table 1 Conditions for the truing experiment

<Grinding wheel>		
Type		GC120H
Dimension		Straight wheel (D_g180×T_g25.4)
Initial radius	$R_{g2}(I)$	90 mm
Objective radius	R_{g2}	90 mm
<Brake truer>		
Type		C150K (D_s100×T_s25.4)
Initial radius	$R_{s2}(I)$	90 mm
<Abrasive stick>		
Type		GC120H (L_s25×T_s25.4)
Initial radius	$R_{s2}(I)$	90 mm
Wheel speed	V	1500 min^{-1}
Cross feed speed	v_{cf}	300 mm/min
Down feed	t	10 μm
Grinding fluid		W-2 type 3, 50 times dilution

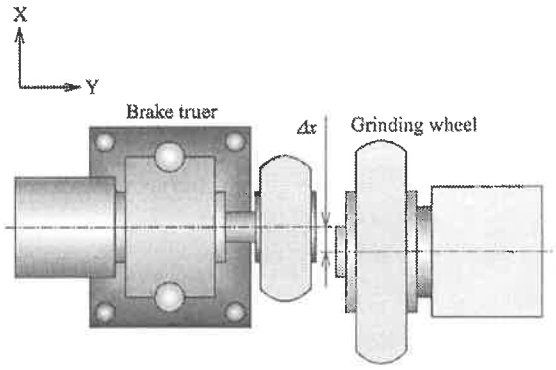

Fig.2 Set-up error, Δx, of the brake truer

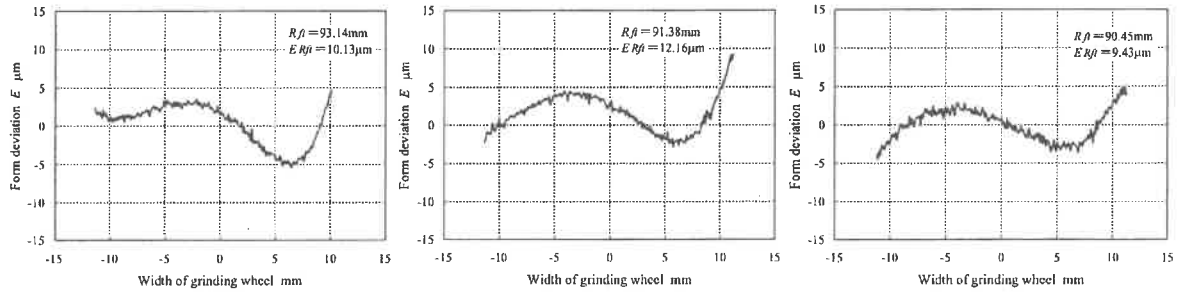

(a) Δx=0mm (b) Δx=5mm (c) Δx=10mm

Fig.3 Form deviation caused by the set-up error, Δx

surface is transferred to a graphite plate. The edge of the plate is traced by the atomic-force probe of the profilometer. Radius of the best-fit circle, Rfi, form error, E_R, and form error from the circle of the minimum square, E_{Rfi} are then evaluated. Experimental conditions are shown in **Table 1**.

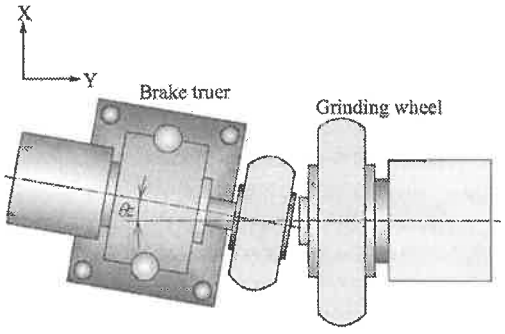

Fig.4 Inclination, θz, of brake truer

3. Results and Discussions

3.1 Effects of error factors

Set-up error in the direction of table feed, Δx, may occur when the brake truer is set on the machine table as shown in **Figure 2**. **Figure 3** shows the experimented results of the form deviation, E, when Δx=0, 5 and 10mm. Rfi decreases with the increase of Δx. The reason of this can be geometrically considered that the shape of the vertical section of the grinding-wheel surface which contains the grinding point shifts from circle to ellipse with increase of Δx. Thus, it would be necessary to enlarge the value of G when there is a set-up error, Δx.

Inclination, θz, shown in **Figure 4** may occur when the brake truer is set on the machine table. **Figure 5** shows the results of the truing experiments when θz is set at 5 and 10 degrees. E_{Rfi} obviously decreases with the increase of θz. The reason of this will be theoretically investigated in the successive paper.

When the grinding-wheel is trued by the brake truer, the form deviation curves often appears as a letter S as shown in Fig.3. When the truing wheel is reset upside-down and the truing experiment is performed again, the form deviation curve changes to the reverse shape. This means that the distribution of α directly affects the truing accuracy and it is necessary to unify the distribution to improve the truing accuracy.

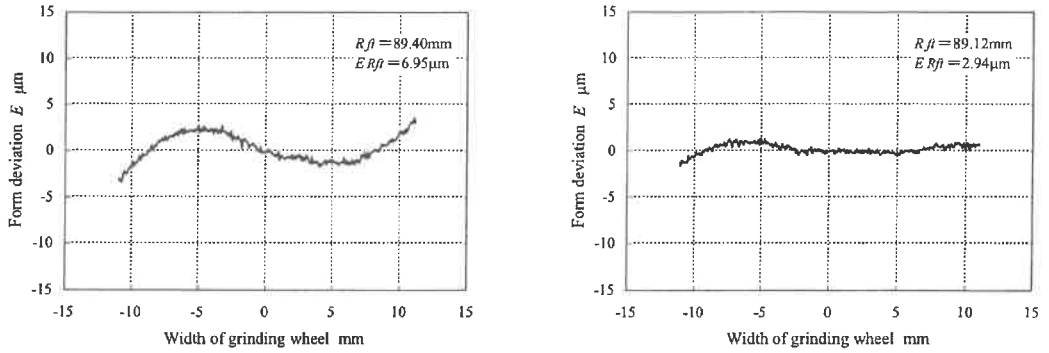

(a) $\theta z=5°$ (b) $\theta z=10°$

Fig.5 Form deviation caused by the relative inclination, θz

3.2 Compensation of the maldistribution of α

Homogeneity of an abrasive stick and a truing wheel has been checked through the infeed-grinding tests as shown in **Figure 6**. In the experiment for the brake truer, free end of the truer spindle was supported by the tailstock to avoid the inclination of the truer spindle due to vertical truing force as shown in Fig.6(b). **Figure 7(a)** and **(b)** show the experimental results for the abrasive stick and brake truer respectively. When total depth of cut, T, is at 3mm, form deviation becomes as big as 40μm for the abrasive stick. These results show that the value of α is not constant and form deviation increases with T.

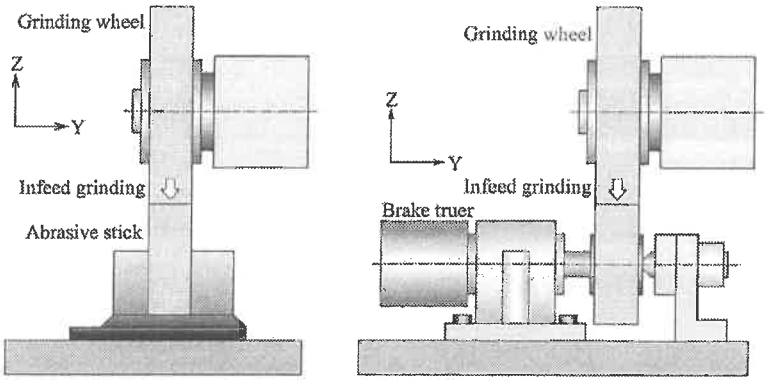

(a) Abrasive stick (b) Brake truer

Fig.6 Observation of the distribution of α by infeed grinding

Figure 8 shows an example of the measured form deviation of a trued wheel surface by an abrasive stick. In this case, large wear occurs at both ends of the trued wheel. It can be said that α of both ends of the truing wheel are

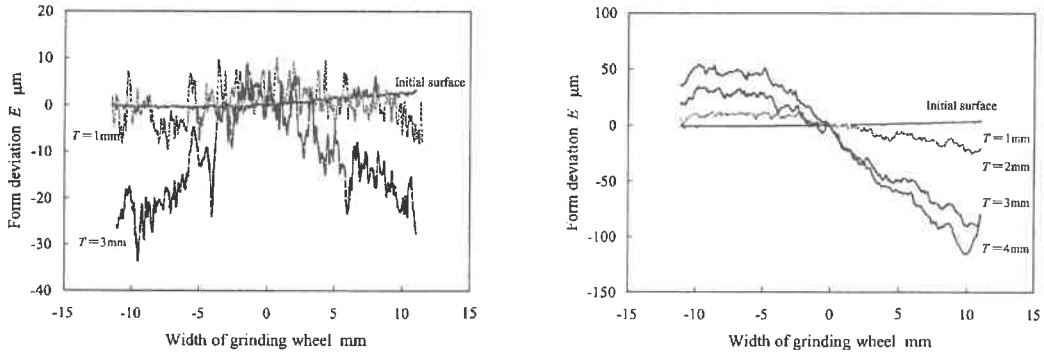

(a) Grinding wheel vs. abrasive stick (b) Grinding wheel vs. brake truer

Fig.7 Form deviation due to unevenness of α

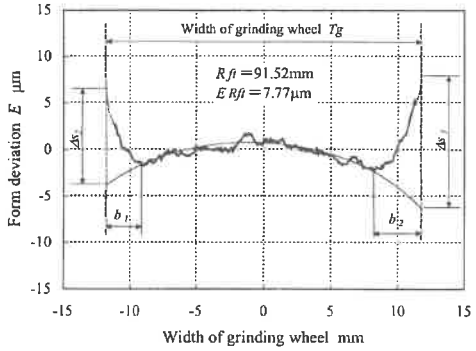

Fig.8 Form deviation of a trued wheel surface when an abrasive stick is used

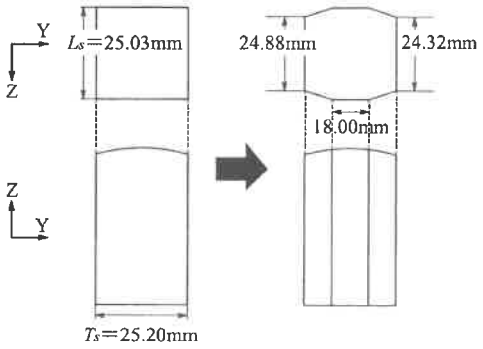

Fig.9 Trimming method of abrasive stick

relatively small than that of middle part. In order to unify the distribution of α, thickness of the abrasive stick in the direction of the wheel rotation, Ls, must be controlled according to the following procedure. (1) Since middle part of the grinding wheel surface is trued almost circularly, the form deviation at both ends can be regarded as Δs_1 and Δs_2 as shown in Fig.8. (2) α in the central part and total depth of cut, T, are given by the following equations: $\alpha=\Delta s/(\Delta g+\Delta s)$; and $T=\Delta g+\Delta s$, where Δs and Δg are total amount of wear of the abrasive stick and the grinding wheel respectively. Thus, wear ratio of right end of the abrasive stick, α', can be given by the equation: $\alpha'=\alpha-(\Delta s_1/\Delta g+\Delta s)$. (3) In order to unify the distribution of α, thickness of the right end of the abrasive stick in the direction of the wheel rotation, Ls', must be controlled according to the following equation: $\gamma=Tg\cdot\pi Dg\cdot(1-\alpha')\cdot T/(Ts\cdot Ls'\cdot\alpha'\cdot T)$, where γ is grinding ratio and Dg is diameter of the grinding wheel. (4) To simplify the trimming process, end of the abrasive stick is trimmed along the straight line as shown in **Figure 9**.

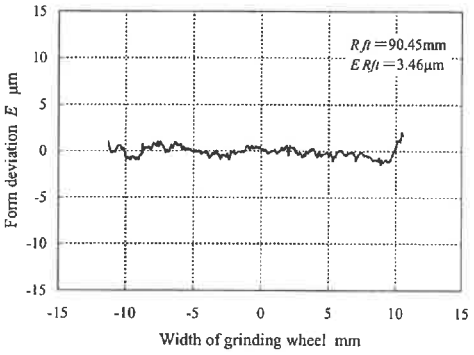

Fig.10 Form deviation when trimmed abrasive stick is used

Figure 10 shows the form deviation curve of the trued wheel surface by the trimmed abrasive stick. Form deviation is satisfactory compensated through the proposed trimming process.

4. Conclusions

Round-off truing experiments have been performed to realize the effects of setting errors and wear ratio of the abrasive stick, α, on the truing accuracy. The main results obtained are as follows:

(1) When inclination of the brake truer, θz, is set at 10 degrees, truing accuracy can be obviously improved.
(2) The distribution of α directly affects the truing accuracy.
(3) Trimming of an abrasive stick so as to unify the distribution of α results in the improvement of truing accuracy.

References

[1] S.Okuyama, T.Iwaya, T.Kitajima, H.Suzuki and A.Une, "Theoretical investigation of a new round-off truing method" *Proc. of the 3rd Int'l ABTEC*, 243-250. (1999)
[2] S.Okuyama, T.Kitajima, T.Iwaya and H.Suzuki, "Experimental study on the new round-off truing method utilizing the circular motion of a CNC machine and an abrasive stick" *Proc. of the 3rd Int'l ABTEC*, 251-257. (1999)
[3] T.Kitajima, T.Iwaya, T.Wakatomo, S.Okuyama and H.Suzuki, "Study on the round-off truing method utilizing the circular motion – Method for improving the process efficiency" *Proc. of the ISAAT2000*, 379-384. (2000)
[4] T.Kitajima, S.Okuyama, T.Wakatomo, A.Yui and H.Suzuki, "Study on the machining accuracy of the round-off truing method - Theoretical analysis of error factors" *Proc. of the ISAAT2001*, 79-84. (2001)

A Study on the Micro Tool Fabrication using Electrolytic In-process Dressing

Hyunwoo Lee[1], Jaeyoung Choi[1], Haedo Jeong[1]
Seokwoo Lee[2], Honzong Choi[2]
[1] Department of Precision Mechanical Engineering, Pusan National University
San 30, Changjeon-Dong, Kumjeong-Ku, Pusan, 609-735, Korea
[2] Korea Institute of Industrial Technology 35-3, Hongchon-Ri, Ibjang-Myum, Chonan, 330-825Korea

Abstract. In this study, micro tools(WC) to produce micro-structures and parts, were fabricateded on a cylindrical grinding machine using ELID(Electrolytic In-process Dressing) technique. The shape of the micro-carbide tool was circle, square, corn, rounded square, rectangular and ellipse. The size of the micro-carbide tool was measured less than 100μm respectively and minimum 3μm by SEM(Scanning Electron Microscope). Surface roughness was measured Ra 55nm-94nm by AFM(Atomic Force Microscope). Furthermore, We have studied on the characteristics of micro-drilling by the micro-carbide tools. We have also compared normal micro-machining with ultrasonic micro machining using a vibration table. It was confirmed that the micro-carbide tool fabricated by ELID grinding, can be broadly used in a variety of micro-machining field.

Keywords: Micro Tool(WC), ELID(Electrolytic In-process Dressing), Micro Drilling, Ultrasonic.

1. Introduction

With increased demand for micro and precision parts, micro mechanical fabrication methods like cutting and grinding are considered more important than before, because they are methods by which the products of the 3D complicated form and of materials having various physical and mechanical properties can be machined efficiently and accurately. Concerning tool materials, single crystalline diamond and cemented carbide have been applied to machining of micro structures and parts. To make these hard brittle micro tools, EDM and grinding have been used. Although in the former method machining force is negligibly small, it is not so efficient and leaves electric discharge marks on work surface. On the other hand, in making micro tools by grinding it is necessary to reduce the grinding forces. Also, according as down sizing of micro tools, the tool easily breaks away on machining or results in poor dimensional accuracy. Surface cracks or scratches are also one of the reasons why micro tools are easily broken down.[1]

The purpose of this study is to examine micro tools with less than 100μm tips, by applying ELID grinding method to reduce the grinding force and scratches on tool surface. Another goal is to evaluate the characteristics of micro-drilling on Si wafer using the developed micro-carbide tool. To improve the workability, ultrasonic vibration was introduced and compared to general micro-machining.

2. The mechanism of ELID process

Fig.1 shows the flow chart of the ELID process. After truing, the wheel surface has a flat face (Fig.1①). A pre-dressing process using the electrolytic dressing is required to maintain the protrusion of the diamond abrasive on the wheel surface (Fig.1②). Since insulation is formed on the wheel surface during the electrolytic dressing as a result of hydration or oxidation of the bonded

material, the electrolytic effect is gradually reduced and finally stabilized (Fig.1③). Excessive electrolysis is prevented by the above mentioned formation of the insulating layer and thus the pre-dressing stage ends. After grinding with the pre-dressed wheel begins, the grains are worn and the insulating layer on the wheel surface is removed (Fig.1④,⑤).[2-4]

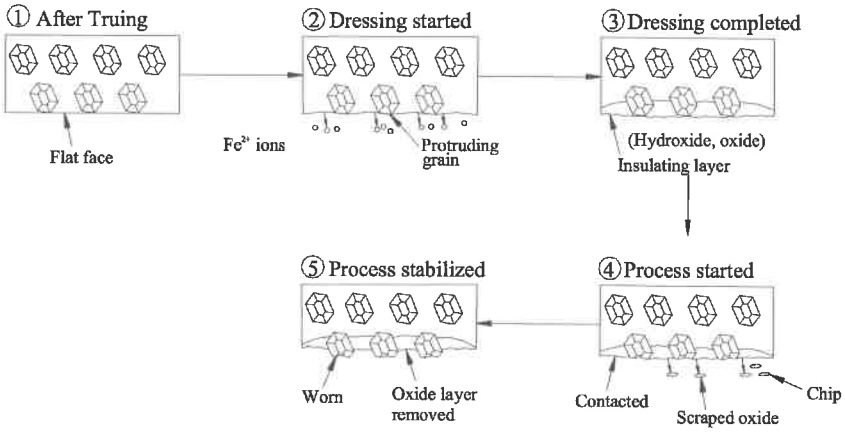

Fig.1 ELID grinding flow chart

3. Experimental method

3.1 Experimental system

Fig.2 shows the cylindrical grinding machine with the ELID system. Fig.3 shows the process flow chart. The grinding machine has three axes: X, Y and Z. All linear axes are supported by a rolling contact bearing a cross a roller guide, and are driven by a step motor. The accuracy of X, Y and Z axes positioning is 0.25μm (semiclosed-loop control is used). The positioning step of the X, Y, Z axes is within 0.5μm. The main spindle is driven with a brushless motor for better rigidity. The maximum speed of the main spindle is 40,000rpm. The ultrasonic vibration table was installed for ultrasonic machining. The frequency and amplitude were 20kHz and 5μm, respectively. A PC-based NC unit was used for the control of the linear axes movement.

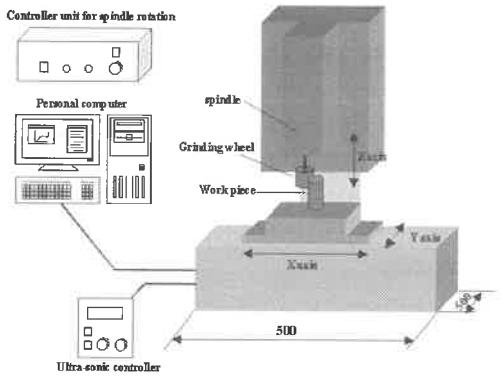

Fig. 2 Grinding machine chart

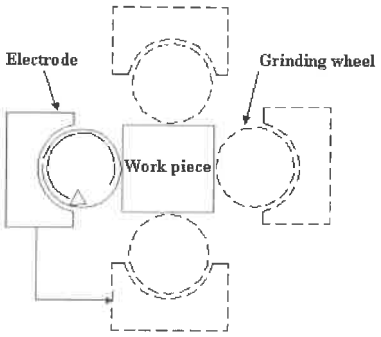

Fig.3 Process flow chart

3.2 Experimental method and machining condition

Before grinding, the grinding wheel must be trued and electrically pre-dressed. Fig.4 shows the ELID grinding system and the change of current and voltage during the pre-dressing of a wheel. The grinding wheel becomes a positive pole, and the truing wheel becomes a negative electrode. Mist-type grinding fluid is supplied for cooling. The graph showed that the current sharply decreases after 30 seconds, whereas the voltage goes up. After 160 seconds, both the current and the voltage become constant. These changes are due to the oxidized layers being formed during the dressing time. Table 1 shows the experimental conditions.

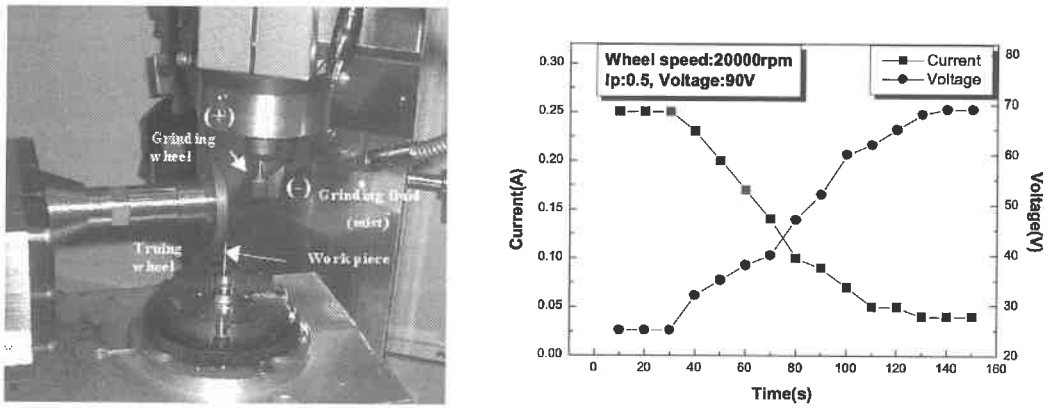

(a) ELID Grinding System (b) Electrical characteristics

Fig.4 Truing and Dressing process in ELID system

Table 1 Experimental conditions

Raw material	Cemented carbide (200μm)
Grinding wheel	#2000
Cutting depth	1μm
Rotation speed	20000rpm
Grinding fluid	Solution type (50:1)

4. Experimental results

4.1 The machining experiments on the micro tool

Fig.5 shows an overview of differently shaped micro tools. The dimension of the tool was measured using SEM. The measurement results show good shape accuracy with high straightness and high dimensional accuracy. Also, we have measured surface roughness using an AFM. The measurement results show the surface roughness of 55nm-94nm. Therefore, the ELID grinding method was confirmed to reduce the grinding force and the scratching of the tool surface. Fig.6 shows surface roughness of the micro tool.

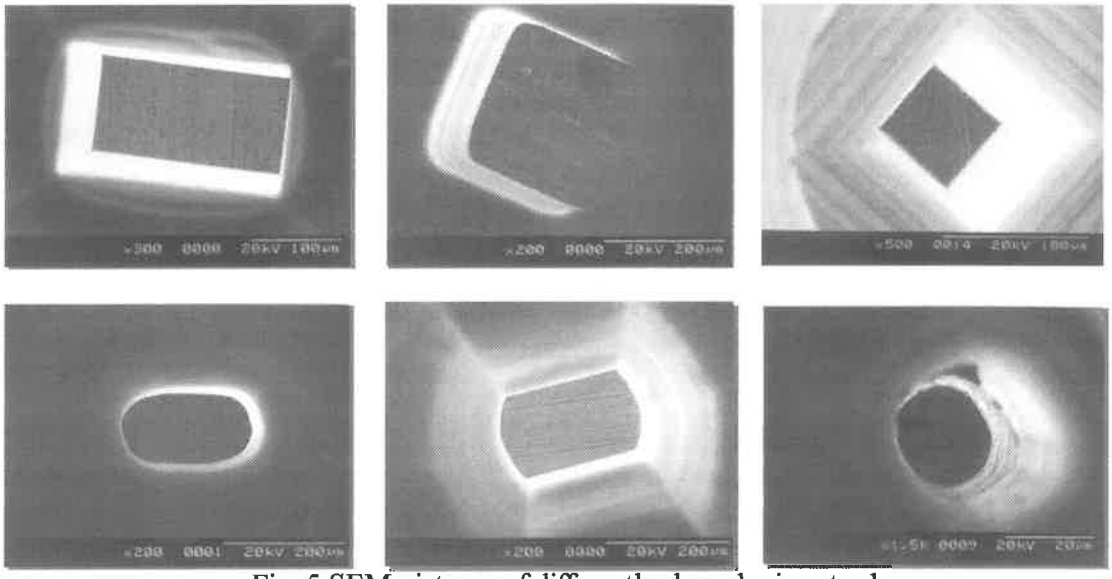

Fig. 5 SEM pictures of differently shaped micro tools

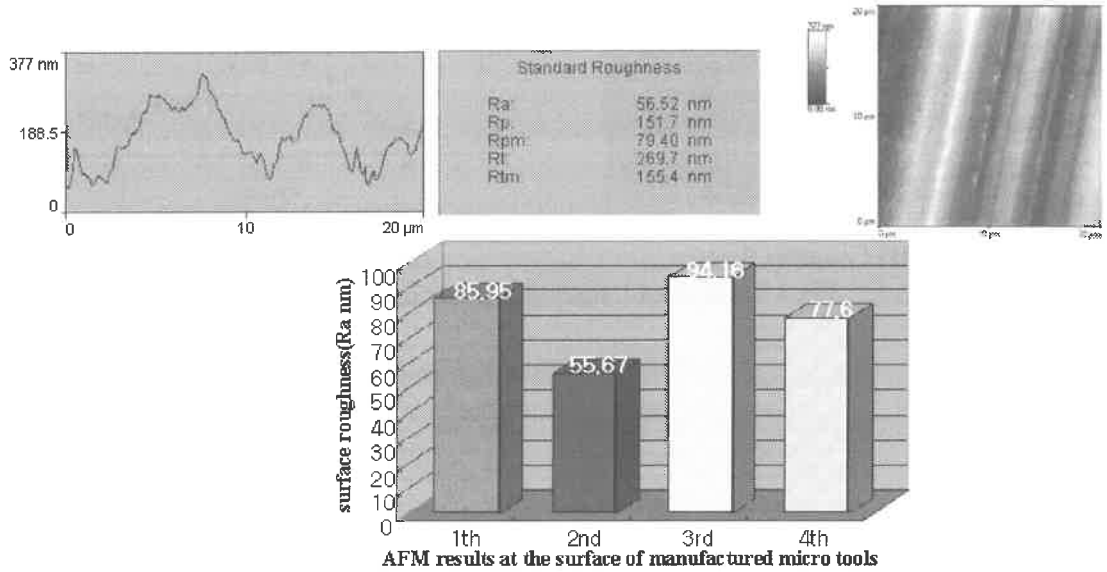

Fig.6 AFM measurement results of surface roughness of micro tool

Fig.7 shows a view of a conically-shaped micro tool. The measurement shows that the endpoint of the micro tool is 3μm wide. This is because of the worn corner of the grinding wheel. The corner of wheel was not absolutely vertical. Because it has a slope, this section was used.

Fig.8 shows micro-structures fabricated by different processing methods on the desk top cylindrical grinding machine. The measurement shows that the endpoint of micro-structure is 50×50μm.

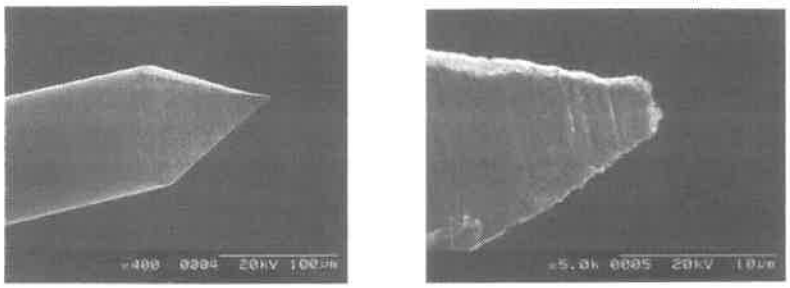

Fig.7 SEM picture of a cone micro tool

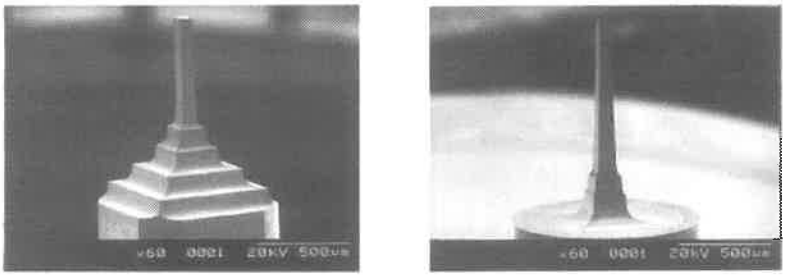

Fig.8 SEM picture of the manufactured micro structures

4.2 The machining experiments on micro drilling

We applied the micro tool to the micro drilling of the brittle material. When the micro tool goes down to Si substrate, machining characteristics are compared for the normal machining and the ultrasonic micro machining using the vibration table. Fig.9 shows a view of the micro tool applied to micro drilling. Table 2 also shows the micro drilling test conditions.

Fig.10 shows the result of micro drilling on the Si substrate. The Si substrate is a representative hard brittle material. So the result of pure mechanical micro drilling shows that silicon is difficult-to-drill. Finally, the tool was broken in drilling. But by adding of ultrasonic vibration, the hole was clearly removed with high roundness without chipping.[5]

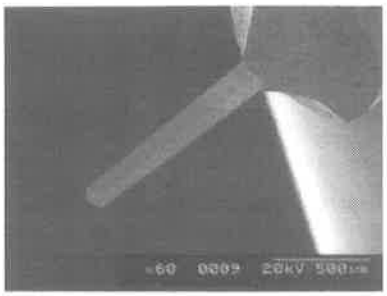

Fig.9 SEM picture of micro tool applied to micro drilling

Table 2 Drilling Test Conditions

Micro tool	Square (W: 80μm, H: 80μm)
Rotation speed	20000rpm
Feed rate	10μm/s
Dwell time	500μs
Drilling depth	250μm
Workpiece	Si wafer
Cutting fluid	Water
Vibration table	Frequency (20kHz), Amplitude (5μm)

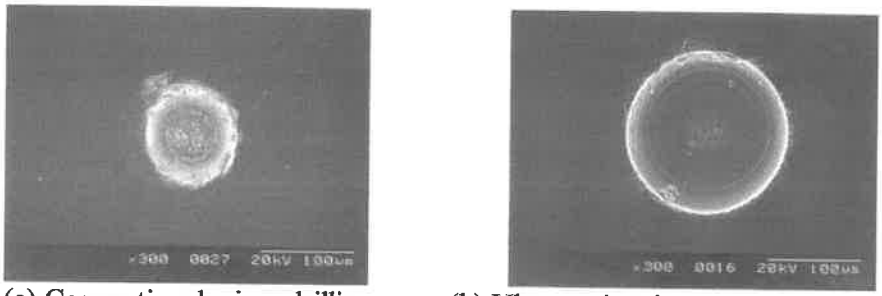

(a) Conventional micro drilling (b) Ultra sonic micro pattern machining

Fig.10 Compare conventional with ultrasonic machining in micro drilling(Si substrate)

5. Conclusion

In this study, we have made a number of differently shaped micro tools and micro-structures using cylindrical grinding with ELID. The surface roughness was Ra 55nm ~ 94nm by AFM measurement. The ELID is thought to reduce the grinding force and the surface roughness. Next, the micro tool was used for micro-drilling. In micro-drilling, ultrasonic vibration improved the form accuracy on the hard brittle Si substrate. The results confirmed that the micro tool fabricated by ELID grinding could be used for micro machining field.

References

[1] H.Onikura,O.Ohnishi,Y.Take, On Annals of the CIRP Vol.49,(2000)p.257
[2] Masuzawa T, Fujino M., Kobayashi, K, On Annals of the CIRP, Vol.34/1, (1985), p431.
[3] Yeo, S. H, Balon, S. A. P, On Proc. of the EuSpen, (1999), p155
[4] H.Ohmori, T.Nakagawa, On Annals of the CIRP, Vol. 39, (1990),p329
[5] Bong Gu Lee, Heon Zong Choi, On Spring Conference of KSPE, pp988-992, 2002

Force and Temperature Measurements in Vibration Assisted Grinding

Prasanna M. Mahaddalkar, Michele M. Miller
Michigan Technological University, Houghton, MI

Introduction

Grinding is a high-energy process where a substantial amount of heat is generated due to friction and plastic deformation in the region where the wheel interacts with the workpiece. The heat generated in the grinding zone either enters the workpiece and wheel or is carried away by the chips and the grinding fluid. The heat entering the workpiece is of primary importance because it causes thermal damage to the workpiece and degrades the quality of the finished part. Excessive temperatures lead to distortion of workpiece dimensions, changes in metallurgical structure and residual stress distribution in the finished part. High temperatures also accelerate the wheel wear, which abets further heat generation.

Numerous research studies [1-8] in the past have shown that the superposition of high frequency vibration to the workpiece over the regular kinematics of a grinding process reduces forces and temperatures and affects tool wear, surface quality and sub-surface properties (residual stress and bending stresses) of the workpiece. While grinding steel, Colwell [1] observed that high frequency vibration could improve the surface finish and reduce the incidence of thermal cracking. Ulhmann et al. [2, 7] and Warnecke et al. [3] have published extensive literature on the effects high frequency modulations to the grinding tool on the forces, surface quality and residual stress distribution in ceramics. Markov [4] observed that modulation to the workpiece improved coolant penetration in the cutting zone.

This paper focuses on evaluating the effect of vibration frequency and amplitude on the temperatures in grinding.

Experimental Setup

Figure 1 shows the grinding test set up. A 50 x 9.5 x 9.5 mm steel workpiece is attached to an aluminum workpiece holder that is threaded to the tip of a magneto-strictive actuator. A flexure that is sandwiched between the actuator and the workpiece holder serves to contain the displacement of the workpiece in the x-y plane. The actuator vibrates the workpiece sinusoidally in the z direction. E Type thermocouples are threaded to the bottom of the workpiece. The tip of the thermocouple is at distance of 1-2 mm from the top surface. The actuator holder is attached to a tri-axial force transducer. The force and temperature signals are recorder simultaneously using a data acquisition system.

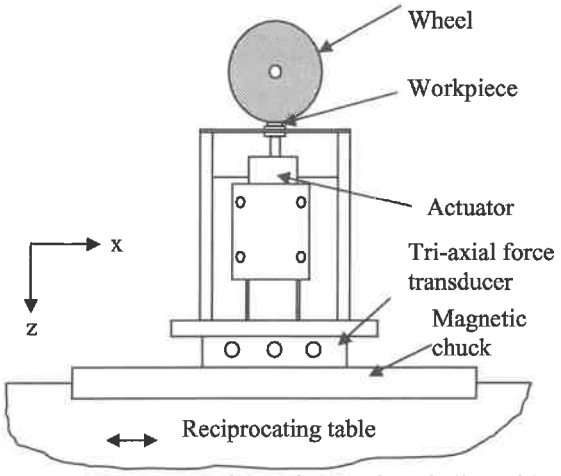

Figure 1: Experimental Setup for grinding with modulation to the workpiece

Grinding Runs at Moderate Frequency Modulation (0-2.65 kHz)

Table 1: Grinding Conditions – Moderate Frequency

Workpiece Material	4140 Steel 50 x 9.5 x 9.5 mm
Grinding Wheel	Aluminum oxide 32AR46-JV60 178 mm dia. x 12.7 mm
Wheel Speed	27.0 m/s
Feed Rate	0.05 m/s
Depth of Cut	15 μm
Vibration amplitude	5 μm, 7.5 μm (p-v)
Vibration frequency	0, 1.039, 1.727, 2.65 kHz.

Table 1 lists the test conditions for moderate frequency dry (no coolant), down grinding tests. The tests were performed within a frequency range of 0 kHz to 2.65 kHz. These particular frequencies were

chosen because actuator amplitude of 7.5μm could be readily achieved at these frequencies. Three observations were recorded corresponding to each frequency and amplitude. Before the first test a pre-pass was done under the same grinding conditions to ensure that the depth of cut remains alike for all the consecutive passes. Without the pre-pass the material removal rate for the first pass would be more than successive passes as indicated in figure 2. The wheel was trued before every pre-pass to ensure sharp cutting properties of the abrasive grit during the test passes.

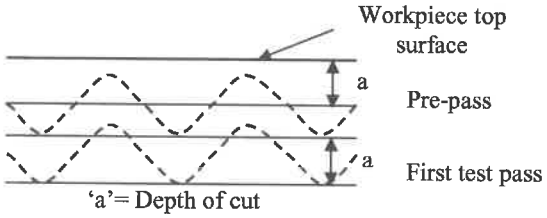

Figure 2: Grinding pre-pass

Figure 3 & 4 compare the tangential force and the normal force at 0, 1.039, 1.729 and 2.65 kHz due to modulation at 7.5μm amplitude and a depth of cut of 15μm. The dotted smooth line shown in the figures passes through the average data point at corresponding frequencies.

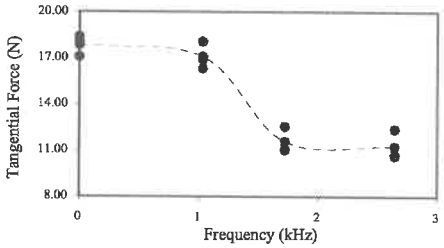

Figure 3: Tangential force at 7.5 μm amplitude and 15μm depth of cut

The force results are summarized in Table 2 and 3. We observed that with the increase in frequency from 0 kHz to 2.65 kHz a substantial drop in force occurred. The tangential force decreased by 36.84% and the normal force by 32.09%. The reduction of force may be attributed to the disturbance in the adhesive wear mechanism between the abrasive grit and the workpiece and the presence of splintered sharp grits due to hammering effect of the wheel as observed by Uhlmamm [2].

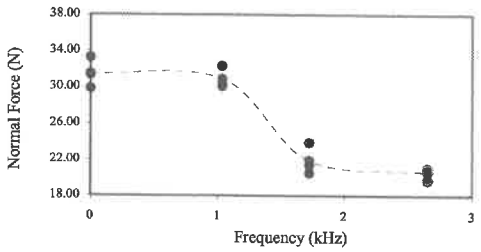

Figure 4: Normal force at 7.5 μm amplitude and 15μm depth of cut

Table 2: Summary of Tangential Forces with 7.5μm amplitude

Vibration Frequency (kHz)	Average Tangential Force (N)	% Reduction when Compared to no Vibration
0	17.82	-
1.039	17.08	4.15
1.727	11.58	35.03
2.65	11.26	36.84

Table 3: Summary of Normal Forces with 7.5μm amplitude

Vibration Frequency (kHz)	Average Normal Force (N)	% Reduction when Compared to no Vibration
0	31.46	-
1.039	30.89	1.79
1.727	21.91	30.35
2.65	21.36	32.09

To investigate the influence of amplitude the experiments were repeated with modulation of 5μm (p-v) within the same frequency range. Figure 5 & 6 compare the tangential forces and the normal forces at 0, 1.039, 1.729 and 2.65 kHz with 5μm amplitude. The results are tabulated in Table 4 & 5. The average cutting force and normal force decreased by 30.28% & 21.65%, respectively, from 0 kHz to 2.65 kHz. From Tables 2 and 4 one might conclude that the percentage reductions in forces at 5μm amplitude are lower when compared to 7.5μm. However a careful analysis by performing a two factor ANOVA on the cutting force data indicates that the effect of vibration amplitude within the given data range is not significant. In fact the analysis indicates that the vibration frequency of vibration and the interaction between frequency and amplitude are the only significant factors. The analysis was performed assuming 95% confidence interval.

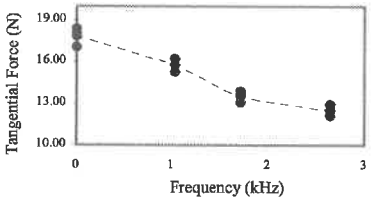

Figure 5: Tangential force at 5 μm amplitude and 15μm depth of cut

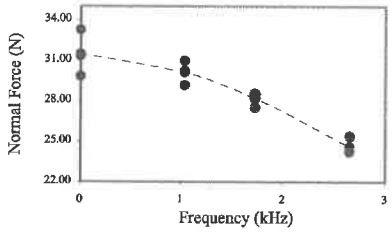

Figure 6: Normal force at 5 μm amplitude and 15μm depth of cut

Table 4: Summary of Tangential Force with 5μm amplitude

Vibration Frequency (kHz)	Average Tangential Force (N)	% Reduction when Compared to no Vibration
0	17.82	-
1.039	15.67	12.06
1.727	13.24	25.72
2.65	12.43	30.28

Table 5: Summary of Normal Force with 5μm amplitude.

Vibration Frequency (kHz)	Average Normal Force (N)	% Reduction when Compared to no Vibration
0	31.46	-
1.039	30.07	4.42
1.727	27.83	11.54
2.65	24.65	21.65

For all the tests, temperature rise above the ambient was recorded by a thermocouple at known spatial location in the workpiece. The temperature rise depends upon the distance of the thermocouple tip from the heat source. This distance however, changes for consecutive test runs. Therefore the temperature rise is not a true indicator of the thermal loads on the workpiece. However, the heat entering the workpiece is independent of the thermocouple distance from the heat source and would truly represent the effect of thermal load on the workpiece.

Estimation of Heat Source Strength and the Energy Partition Coefficient

The net power required for removing material in grinding is given by:

$$P_{net} = F_t v \quad (1)$$

where 'F_t' is the tangential force and 'v'is the peripheral wheel speed.

The heat source strength per unit length at the workpiece surface is given by:

$$q' = P_{w/p} / b \quad (2)$$

where '$P_{w/p}$' is the heat entering the workpiece and 'b' is the width of the workpiece. The heat source is assumed to be an infinite line of constant heat strength parallel to y-axis traversing at a constant velocity 'v' over a semi-infinite body. Due to the small depth of cut in our experiments we have assumed that the line source is a reasonable approximation. Also the contact width 'b' is much less than the length of the workpiece. Therefore the assumption of semi-infinite body is also reasonable. Carslaw and Jaeger's model [8] was used to estimate the temperature rise at a desired spatial coordinate (x,z). The temperature rise above ambient is given by:

$$\theta = \frac{q'}{\pi k} e^{\frac{vx}{2\alpha}} K_0[v\frac{(x^2+z^2)^{1/2}}{2\alpha}] \quad (3)$$

where 'k' & 'α' are the thermal conductivity and thermal diffusivity of the workpiece material and 'K_0' is the modified Bessel function of the second kind. The temperature rise for a known depth is recorded during the test and is used to back calculate q' by matching the recorded peak temperatures with the modeled value. The energy partition coefficient, i.e. the ratio of '$P_{w/p}$' and 'P_{net}' is then estimated.

Figure 7 & 8 show the effect of frequency on the heat entering the workpiece and the energy partition coefficient for tests with 7.5μm amplitude. The percentage heat drop and the average energy partition coefficient are listed in Tables 6 & 7. The results indicate a huge drop of 63.82% in the heat entering the workpiece per unit length from 0 kHz to 2.65 kHz. The observed drop in the heat entering the workpiece is not only due to the reduction in the cutting forces but also due to the decrease in the energy partition coefficient symbolizing effective transfer of heat away from the grinding zone. The energy partition coefficient steadily reduced from

0.30 to 0.18 signifying a reduction of almost 40% from 0 kHz to 2.65 kHz.

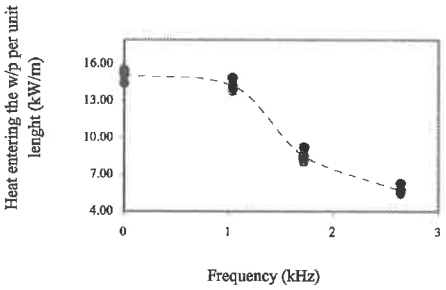

Figure 7: Average heat entering the w/p per unit length - 7.5μm amplitude

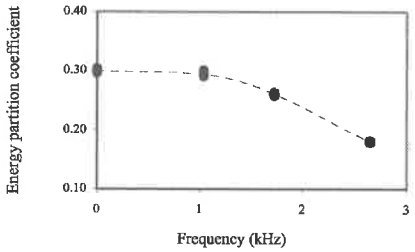

Figure 8: Effect of frequency on energy partition coefficient - 7.5μm amplitude

Table 6: Summary of heat entering the workpiece with 7.5μm amplitude

Vibration Frequency (kHz)	Avg. heat entering the w/p per unit length (kW/m)	% Reduction when Compared to no Vibration
0	15.13	-
1.039	14.29	5.89
1.727	13.56	43.46
2.65	9.13	62.05

Table 7: Summary of the energy partition coefficient with 7.5μm amplitude

Vibration Frequency (kHz)	Avg. energy partition coefficient	% Reduction when Compared to no Vibration
0	0.30	-
1.039	0.29	1.94
1.727	0.26	13.10
2.65	0.18	40.00

Figures 9 & 10 show the effect on the heat entering the workpiece and the energy partition coefficient for 5μm amplitude. The heat and the energy partition results are tabulated in Table 8 & 9.

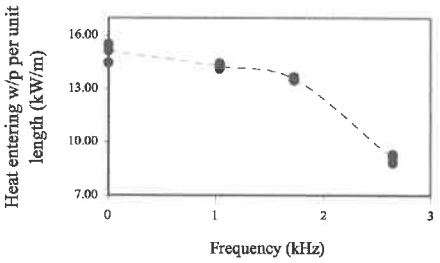

Figure 9: Average heat entering the w/p per unit length– 5μm amplitude

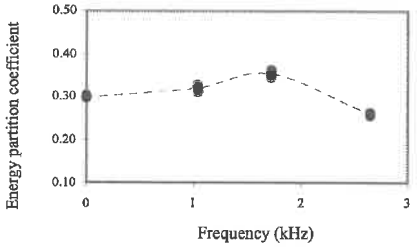

Figure 10: Effect of frequency on energy partition coefficient-– 5μm amplitude

Table 8: Summary of heat entering the workpiece with 5μm amplitude

Vibration Frequency (kHz)	Avg. heat entering the w/p per unit length (kW/m)	% Reduction when Compared to no Vibration
0	15.13	-
1.039	14.29	5.55
1.727	13.56	10.37
2.65	9.13	39.66

Table 9: Summary of the energy partition coefficient with 5μm amplitude

Vibration Frequency (kHz)	Avg. energy partition coefficient	% Reduction when Compared to no Vibration
0	0.30	-
1.039	0.32	-7.26
1.727	0.35	-17.82
2.65	0.26	13.60

The results indicate a gradual reduction in the heat entering the workpiece from 15.13 (kW/m) to 9.13

(kW/m), a reduction of almost 40% over a frequency range of 0 kHz to 2.65 kHz. On the other hand, the energy partition coefficient increases slightly at 1.309 & 1.727 kHz frequency. (Negative values in the percentage reduction column indicate increase in magnitude above corresponding no vibration test.)

Grinding Runs at Very High Frequency Modulation (up to 12.63 kHz)

To investigate avenues for further force and heat reduction, grinding tests were performed at 3.21, 6.25 and 12.63 kHz frequencies. However, the workpiece could not be modulated at amplitudes higher than 1.57μm due to limitations of the actuator. The depth of cut was also reduced to 5μm so as to maintain an acceptable S/N ratio. The test parameters are summarized in Table 10.

Table 10: Grinding Conditions – Higher Frequencies

Workpiece Material	4140 Steel 50 x 9.5mm x 9.5 mm
Grinding Wheel	Aluminum oxide 32AR46-JV60 178 mm dia. x 12.7 mm
Wheel Speed	27.0 m/s
Feed Rate	0.05 m/s
Depth of Cut	5μm
Vibration amplitude	1.57μm (p-v)
Vibration frequency	0, 3.21, 6.25, 12.63kHz.

Three test runs were performed at each frequency after a pre-pass. The force results of the tests are shown in Figures 11 and 12 and are tabulated in Tables 11 and 12.

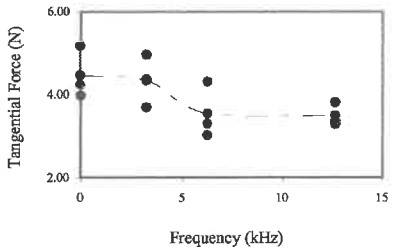

Figure 11: Tangential force at 1.57 μm amplitude and 5μm depth of cut

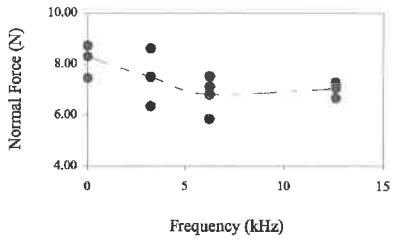

Figure 12: Normal force at 1.57 μm amplitude and 5μm depth of cut

Table 11: Summary of Cutting Forces with 5μm amplitude

Vibration Frequency (kHz)	Average Tangential Force (N)	% Reduction when Compared to no Vibration
0	4.47	-
3.21	4.35	2.68
6.25	3.55	20.51
12.63	3.50	21.77

Table 12: Summary of Normal Forces with 5μm amplitude.

Vibration Frequency (kHz)	Average Normal Force (N)	% Reduction when Compared to no Vibration
0	8.30	-
3.21	7.47	9.96
6.25	6.82	17.87
12.63	7.04	15.22

Although the force data show a downward trend, any conclusive inference cannot be made due to the variation associated with the data.

Figures 13 & 14 indicate the effect of high frequency modulation on the heat entering the workpiece and on the energy partition coefficient. The results are tabulated in Tables 13 & 14. The heat entering the workpiece dropped by almost 14.46% from 0 kHz to 12.63 kHz. However, the energy partition coefficient increased above the no-vibration condition by almost 12% indicating that the workpiece retained more heat at very high frequencies.

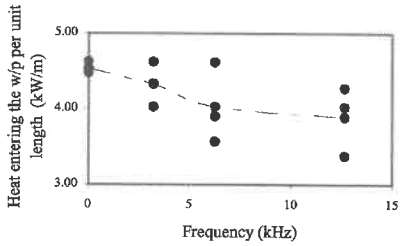

Figure 13: Average heat entering the w/p per unit length– 1.57μm amplitude

Table 13: Summary of heat entering the workpiece with 1.57μm amplitude

Vibration Frequency (kHz)	Avg. heat entering the w/p per unit length (kW/m)	% Reduction when Compared to no Vibration
0	4.54	-
1.039	4.32	4.85
1.727	4.02	11.42
2.65	3.88	14.46

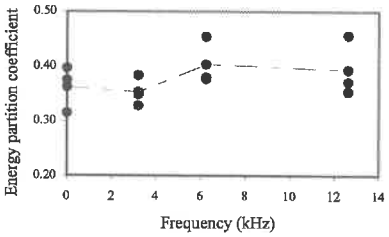

Figure 14: Effect of Frequency on energy partition coefficient– 1.57μm amplitude

Table 14: Summary of the energy partition coefficient with 1.57μm amplitude

Vibration Frequency (kHz)	Energy partition coefficient	% Reduction when Compared to no Vibration
0	0.36	-
1.039	0.35	1.92
1.727	0.40	-11.98
2.65	0.39	-9.21

Conclusions

Modulation of the workpiece at moderate frequencies has shown to reduce forces and temperatures in grinding. Vibration at moderate frequencies and 7.5μm amplitude reduced the forces by almost 37% and reduced the thermal load by almost 62%. In addition the energy partition coefficient decreased by 40%. Tests at higher frequencies with smaller amplitudes are less conclusive due to variation in the results. A decrease in force and heat flux with increasing frequency is apparent. However contrary to the low frequency results, the energy partition coefficient appears to increase with frequency. Development of a thermal model to predict effects of vibration on temperature is underway.

Acknowledgment

This work was supported in part by NSF Grant No. 9875251.

References

1. Colwell, L., "Effects of High Frequency Vibrations in Grinding," *Transactions of the ASME*, May 1956, pp. 124-131.
2. Ulhmann, E., Spur, G., Holl, S., "Machining of Complex Contours by Ultrasonic Assisted Grinding," *SME Technical Paper-MR99-284*, 3rd International Machining and Grinding Conference, Cincinnati, Ohio, Oct. 1999.
3. Warnecke, G., Zapp, M., "Ultrasonic Superimposed Grinding of Advanced Ceramics," *SME Technical Paper–MR95-169*, 1st International Machining and Grinding Conference, Dearborn, Michigan, September 1995.
4. Markov, A., "Ultrasonic Drilling of Hard Non-Metallic Materials with Diamond Tools," *Stanki I Instrument*, Vol. 48, No. 9, 1977.
5. Khanna, N., Pei, Z., Ferreira, P., "An Experimental Investigation of Rotary Ultrasonic Grinding of Ceramic Disks," *SME Technical Paper-MR95-141*, NAMRC XXIII Conference, Houghton, Michigan, May 1995.
6. Suzuki, K., Mishiro, S., Tochinai, H., Uematso, T., "A New Grinding Method for Ceramics Using Biaxially Vibrated Non-Rotational Ultrasonic Tool," *Annals of CIRP*, Vol. 42/1, 1993, pp. 375-378.
7. Uhlmann, E., Holl, S. E. and Daus, N. A., "Ultrasonic Assisted Grinding – Part 1," *Abrasives*, Oct. – Nov., 2000, pp. 16-25.
8. Jaeger, J. C., Carslaw, H. S., "*Conduction of Heat in Solids*," Oxford University Press, London, 1947.

Identification of the Static Stiffness of Grinding Wheels with Resin Bond

Takazo YAMADA, Hwa-Soo LEE, Takeshi SHIKAUCHI, Hiroyuki MATSUSHITA

Department of Mechanical Engineering, College of Science & Technology, Nihon University, 1-8-14 Kanda-Surugadai, Chiyoda-ku, Tokyo 101-8308 Japan

Abstract: In this study, a mathematical model consisting of rigid abrasive grains and bonds as spring elements is proposed. As the results of analysis using the proposed model, it is clarified that the elasticity of grinding wheel can be evaluated based on the static stiffness of bond connecting successive two grains.

1. Introduction

In grinding operation, machining accuracies are affected by elastic deformations of grinding wheels in the contact area with workpieces and/or the deformations due to the centrifugal forces. These wheel deformations have been analyzed by applying the theory of Hertz's contact and by using elastic modulus and Poisson's ratio under the assumption that wheel is a uniform continuous body so far. However, it is well known that grinding wheels consisting of abrasive grains, bonds and voids are not actually uniform continuous body. Consequently, when analyzing the elastic deformations of grinding wheels, grinding wheels should be assumed to be non-uniform continuous body.

In this study, in order to analyze the dynamic phenomena of grinding wheels under grinding operations, a mathematical model of grinding wheels consisting of rigid abrasive grains and bonds as spring elements with stiffness k is proposed [1]. The amount of static stiffness of bond k used in the proposed model can be obtained by FEM analysis and the bending test of abrasive sticks. In such a way, the static stiffness of bond k in grinding wheels with vitrified bond has been analyzed in the previous study [1]. As the analyzing results, it has been clarified that the elastic modulus of whole abrasive wheels changes depending on the geometrical shape of grinding wheels, however the static stiffness k of basic unit of abrasive wheels is constant independent from the geometrical shape.

In this paper, the same analysis for the grinding wheel with resin bond is carried out, and the result is compared with the wheel with vitrified bond.

2. Analytical approach

A mathematical model in which bond is connecting successive two grains as shown in Figure 1 is proposed. In this model, a basic unit is uniformly arranged in body centered lattice structure with nine rigid bodies and sixteen spring elements with stiffness k. By arranging this basic unit, any grinding wheels shapes can be modeled.

When an external load is applying to this model, a relation between load F and displacement δ is shown with a spring constant k as follows.

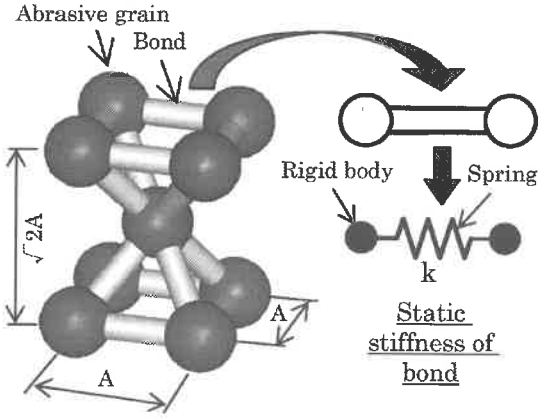

Fig.1 Unit of kinetic model of grain

$$F = k\alpha\delta \quad (1)$$

Where, α is called a geometrical coefficient in this study. α is a characteristic value of grinding wheel model. This α can be calculated as follows. First, assuming a certain spring constant k, displacement δ corresponding to this k is calculated by FEM. Second, substituting F, δ and k into the next equation, actual α is obtained.

$$\alpha = \frac{1}{k}\frac{F}{\delta} \quad (2)$$

The static stiffness k is calculated as follows. In the method shown above, α was calculated under an assumption that k=1 [N/μm]. Of course, actual k is not 1.

Actual amount of k is obtained by substituting the load F and measured δ into next equation.

$$k = \frac{1}{\alpha}\frac{F}{\delta} \quad (3)$$

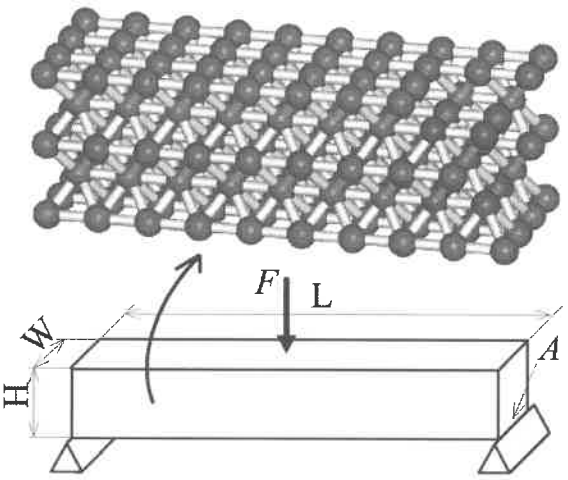

Stick	Width [mm]	Height [mm]	Length [mm]
1	8.0	5.7	60
2	4.0	5.7	60
3	5.0	7.1	60

Fig.2 Abrasive sticks used in experiment

3. Experiments and results

Bending tests for grain size #60, #80, #100 and #120 are carried out. The sizes of used abrasive sticks are shown in Figure 2. Figure 3 shows α for the grain volume percentage 20~60% obtained in the method shown above respectively. The amount of α is determined depending on the abrasive stick shapes. It is known that this tendency means that α is the value corresponding to the geometrical shape of abrasive sticks. Table 1 shows the amount of α for the grain volume percentage 50% in each grain size. α is determined only by the geometrical shape, which is independent from bond materials.

Static stiffness of bond k is calculated from the results of three points bending test. Figure 4 shows a schematic diagram of three points bending test. An external force is loaded by a screw and is measured by a force sensor. Displacement is measured with an electric micrometer in the opposite side of the loading face. Since it is difficult to identify the initial contact point of loading bar to abrasive stick,

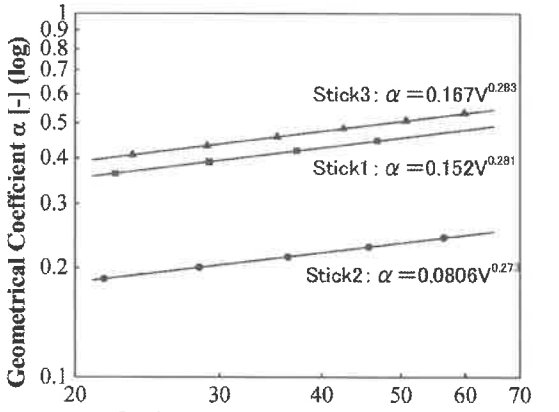

Fig.3 Analyzed results of geometrical coefficient

Table 1 Geometrical coefficient α (V=50%)

Stick	#60	#80	#100	#120
1	0.455	0.610	0.826	0.943
2	0.236	0.311	0.420	0.474
3	0.505	0.676	0.901	1.05

relative load and displacement are monitored.

Figure 5 shows results of the three points test, in which #60 and 50% vitrified bond and resin bond are used. Ten times bending test are carried out for each condition. From the result of the vitrified bond shown in Figure 5(a), it is known that a relation between load and displacement is linear. On the other hand, in case of the resin bond shown in Figure 5(b), it is known that the relation is non-linear. This result may be caused by that the resin bond is using phenolic resin. From these results, a ratio of the relative load to the relative displacement F/δ is calculated. For the resin bond, since the relation between load and displacement is non-linear, 50% data from the start point is used. Each ratio of F/δ is shown in Figure 6. From the F/δ and the α, the static stiffness k is obtained by using equation (3). Figure 6 shows the relations between the static stiffness k and the grain size # for vitrified and resin bonds. The relation between grain size # and static stiffness k of each bond can be shown as k_v=470/# for vitrified and k_b=130/# for resin bond.

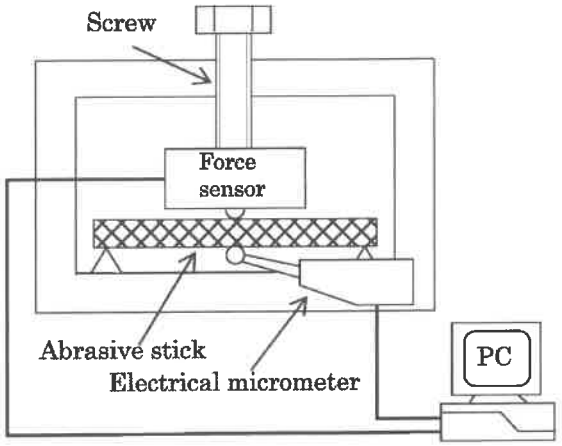

Fig.4 Schematic diagram of three points bending test

From these results of analysis, it is known that k decreases with the increase of the grain size. This tendency may be caused by the size effect of bond explained in the previous study [1]. That is, since the size of bond may be considered to be changed with the grain size, the length of bond in #60 is two times longer than one in #120 and the sectional area of bond in #60 is four times larger than one in #120 as shown in Figure 7. It means that the amount of static stiffness k in #60 may be two times larger that one in #120. Table 2 shows the amounts of stiffness corresponding to the grain size. As shown in this table, size effect of the bond stiffness can be observed in the resin bond as same as the vitrified bond. And, from Figure 6, it is known that the static stiffness of vitrified bond is 3.6 times larger than

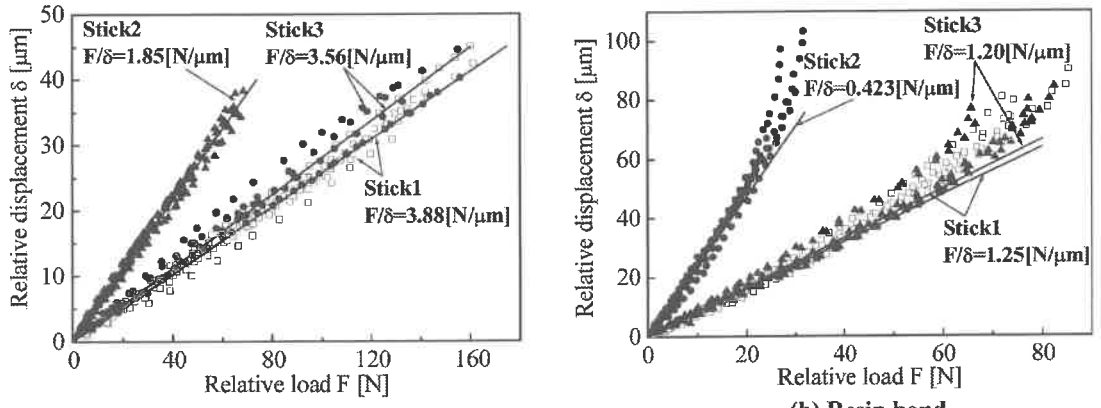

(a) Vitrified bond **(b) Resin bond**

Fig.5 Results of bending tests in #60

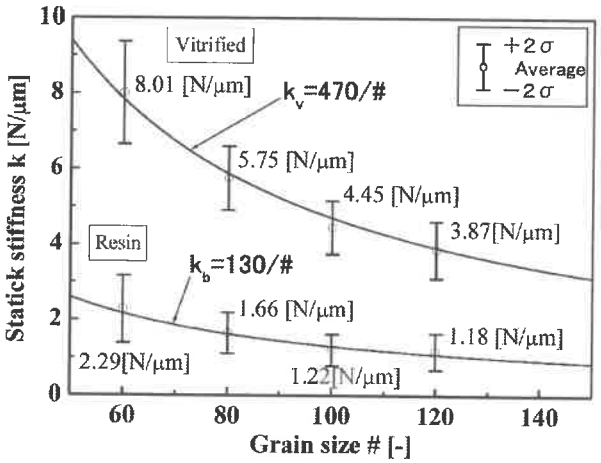

Fig.6 Relation between stiffness and grain size

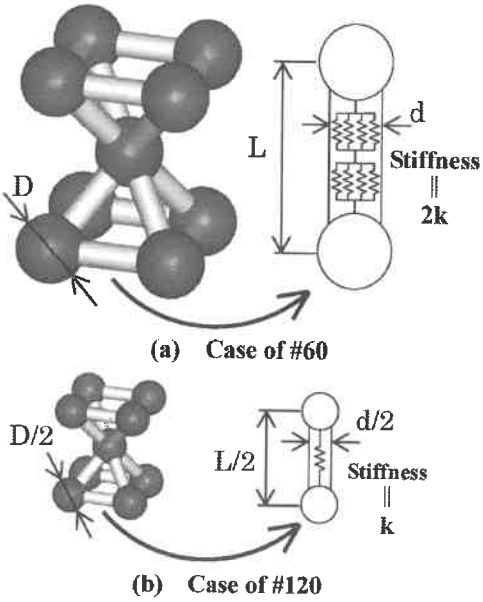

Fig.7 Spring model of bond

the resin bond. In the same way, it is well known that the elastic modulus of the whole grinding wheels of vitrified bond is almost 3.0 times larger than the elastic modulus of resin bond [2].

According to the results shown above, it is known that the model proposed in this study can be used to calculate the static stiffness to bond. Therefore, utilizing the bond stiffness proposed in this study, elastic deformation of grinding wheel in the contact area with workpiece and/or variation of geometrical shape due to centrifugal forces can be analyzed quantitatively.

Table 2 Amount of stiffness corresponding to the grain size

Grain size	#60	#80	#100	#120
Geometry	1	0.75	0.60	0.50
Vitrified bond	1	0.73	0.56	0.48
Resin bond	1	0.73	0.53	0.52

4. Conclusions

It is clarified that the elastic phenomena of resinoid wheel can be explained by using the static stiffness of bond as same as in the case of vitrified wheel.

Acknowledgement

The authors would like to appreciate to the Science and Research Foundation of the Japanese Ministry of Education for financial supporting of this research (C 12650125).

References

[1] Hwa-Soo LEE, Kojiro SADASUE, Yujiro ITO and Tadashi WAKABAYASHI, Static Modeling of Grinding Wheel, Proceeding of The 15th Annual Meeting, ASPE(2000-10), p.99-101.

[2] Handbook of Precision Machining, (in Japanese), Corona Publishing, (1992), p.306.

Relationship between Stiffness of Grinding Systems and Depth of Affected Layers

Sakari YOKOYAMA, Hwa-Soo LEE and Takazo YAMADA

Department of Mechanical Engineering, College of Science & Technology, Nihon University,

1-8-14 Kanda-Surugadai, Chiyoda-ku, Tokyo 101-8308, Japan.

Abstract: In this study, the relationship between the stiffness of grinding systems and the depth of generated surface affected layers are discussed experimentally. As the results, under the condition of low stiffness, surface affected layers generated in the grinding process have a tendency to be smaller.

Key words :Affected layers, Elastic deformations, Static stiffness

1. Introduction

Since grinding is a machining used in finishing process, high quality workpiece surfaces have to be obtained in this process. From such a viewpoint, it is very important to determine the machining condition without any affected layers. The generating mechanism of affected layers have been studied so far[1)], however the effect of stiffness in grinding system on the generating mechanism of surface affected layers have not been discussed yet. In this study, the relationship between the stiffness of grinding systems and the depth of generated surface affected layers are discussed experimentally.

According to the conventional studies, it is known that the surface affected layers are generated by the effect of the grinding force and the heat at the grinding point[2)] . At the first step of the present study, the effect of the stiffness of grinding system on the grinding force is studied experimentally. As such an experimental results, it is made clear that grinding force is determined only by the machining condition independent from the stiffness of grinding systems. In the conventional sense, the depth of surface affected layers depending on the grinding force is constant independently from the stiffness. However, in the present experimental discussion, it is clarified that the depth of surface affected layers are depending on the stiffness of grinding system.

2. Amount of elastic deformations and surface affected layers

2.1. Surface affected layers

Using a newly designed grinding simulator, which can set the static stiffness of grinding system, external plunge grinding operations are carried out. Machining condition used in this experiment is shown in Table 1. In order to monitor the generating process of surface affected layers, spark-out grindings are not carried out. In this experiment, the depths of affected layers are evaluated by the

Table 1 Machining condition

Material		S50C Hardened and tempered
Infeed speed	[μm/rev]	5, 15, 30
Wheel speed	[m/min]	1800
Work speed	[m/min]	10
Grinding wheel		WA60JV
Machine stiffness(Km)	[N/μm]	0.7, 1.8, 4.5, 5.8, 7.6

distribution of the workpiece hardness in the depth direction from surfaces.

Two measured examples of the distributions of workpiece hardness are shown in Fig.1. In these figures, workpiece hardness are shown in normalized amounts by the previously measured hardness of workpiece part independent from grinding operations. In case of low stiffness condition shown in Fig.1(a), the hardness in the surface area slightly decreased, however any large variation of hardness cannot be observed. On the other hand, in case of Fig.1(b), where stiffness is high, it can be observed that the hardness is obviously decreased in the surface area. Machining condition in these two grinding is constant and the normal and tangential grinding resistances, which are not shown in this paper, are same. Therefore, it can be supposed that the difference of generated surface affected layers is depending on the effect of the difference of the stiffness of grinding system.

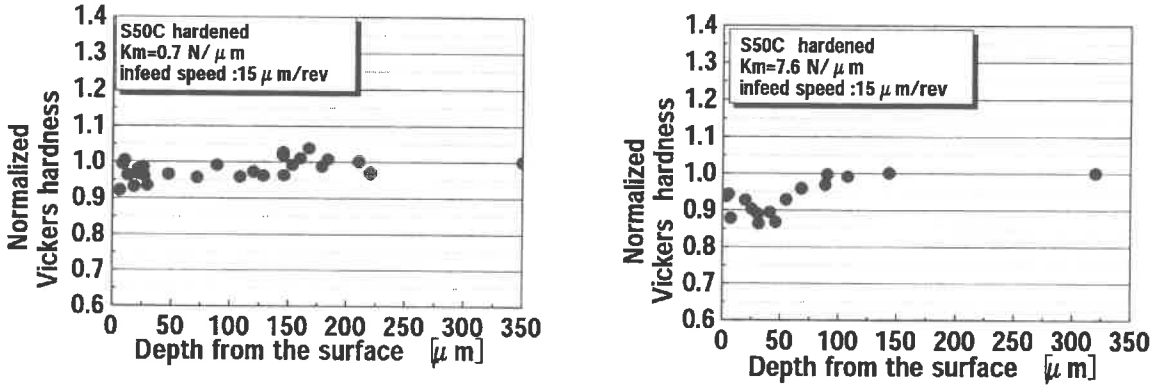

(a) Km=0.7 N/μm (b) Km=7.6 N/μm

Fig.1 Measured hardness

2.2. Stiffness and elastic deformations

As well known, elastic deformation in the grinding operation takes place due to the grinding force.

Fig.2 shows a schematic diagram of the wheel head infeeding and decreasing process of workpiece size in plunge grinding process.In case when stiffness of grinding system is low, large elastic deformation takes place and the workpiece size decreases with a huge time lag. On the other hand, since the amount of elastic deformation becomes small and the time lag is also smaller[3] .It is well known that the amount of grinding force is determined in a certain value depending on the machinability of grinding wheel [4] . However, it can be considered that actual machinability is continually varying in grinding operation depending on the distribution of cutting edges in the grinding wheel surface and on the change of hardness of machined workpiece. Although such a variation of grindability is difficult to be monitored experimentally, the action of grinding wheel to the workpiece

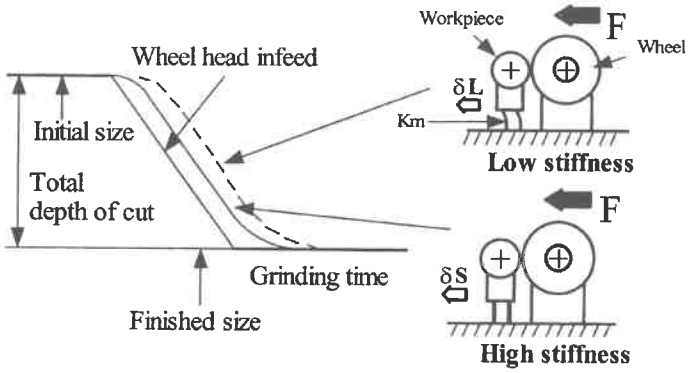

Fig.2 Elastic deformation

surfaces may also continually changes. That is, when the stiffness of grinding system is low, grinding wheel can be deformed easily depending the variation of grindability, and then the grinding wheel may acts to workpiece softly. However, under the condition that the static stiffness is high, grinding wheel may acts to workpiece hardly. As shown above, the difference of the action of grinding wheel to the workpiece may make the difference of the generating process of affected layers.

3. The difference of elastic deformation due to stiffness

3.1. Experiment

Using a workpiece shown in Fig.3, external plunge grinding is carried out. In this workpiece, a half part of width is 10 mm and the other is 5 mm. Using such a workpiece in external grinding, the amount of elastic deformation varies in grinding process due to the change of grinding width, and consequently the similar effect with the change of grindability may be observed experimentally. In order to easily monitor the grinding phenomenon depending on the variation of grindability, experiment is carried out under low workpiece speed as shown in Table 2.

Table 2 Machining condition

Material		S50C Tempered
Infeed speed	[μm/rev]	15
Wheel speed	[m/min]	30
Work speed	[m/min]	2
Machine stiffness (Km)	[N/μm]	0.7, 7.6

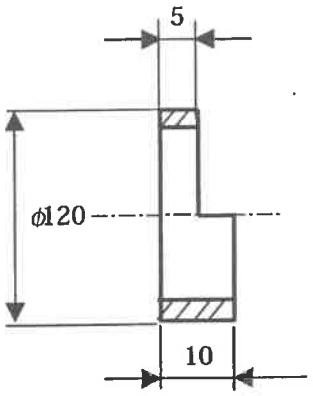

Fig.3 Used workpiece

3.2. Experimental results

Fig.4 and Fig.5 show the grinding force and the process of workpiece size generations. Where Fig.4 shows the case that stiffness is low and Fig.5 shows the case that stiffness is high respectively. In these experiments, grinding resistance is same.

However, the processes of workpiece size generation are different. The results of these experiments are shown in Table 3. As shown in this table, the amount of elastic deformation due to the difference of grindability depends on the stiffness of grinding system. From such experimental results, when stiffness is low, the grinding wheel can deform easily and then the action of grinding wheel to workpiece may be soft. However, when stiffness is high, wheel action becomes harder and then this action may make large surfaces affected layers.

Table 3 Difference of elastic deformation

Thickness of workpiece	Kres(Resultant stiffness)	Fn(Normal force)	δ (Fn/Kres)	Difference of elastic deformation	
				Theoretically	Measured
mm	N/μm	N	μm	μm	μm
10	1.1	34	30.9	16.4	18
5		16	14.5		
10	7.6	32	4.2	2.6	3
5		12	1.6		

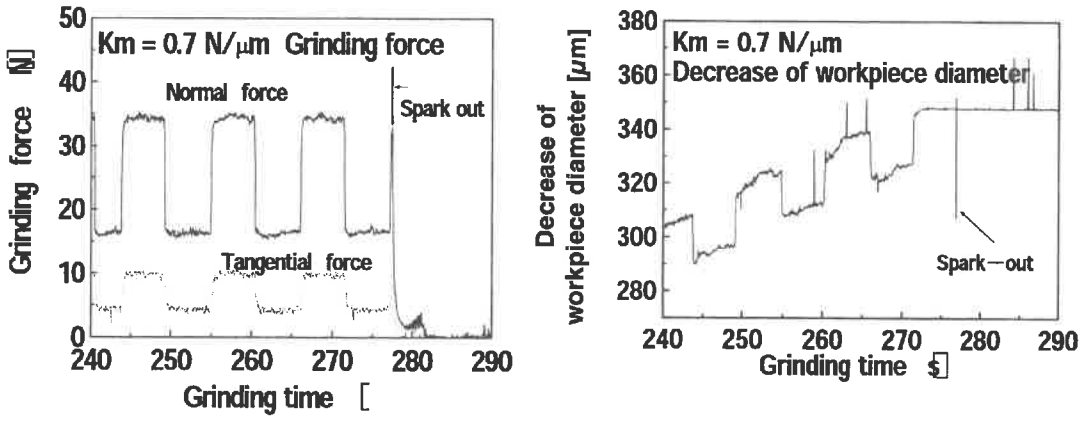

(a) Grinding force (b) Workpiece radius reduction

Fig.4 Measured value (Km = 0.7 N/μm)

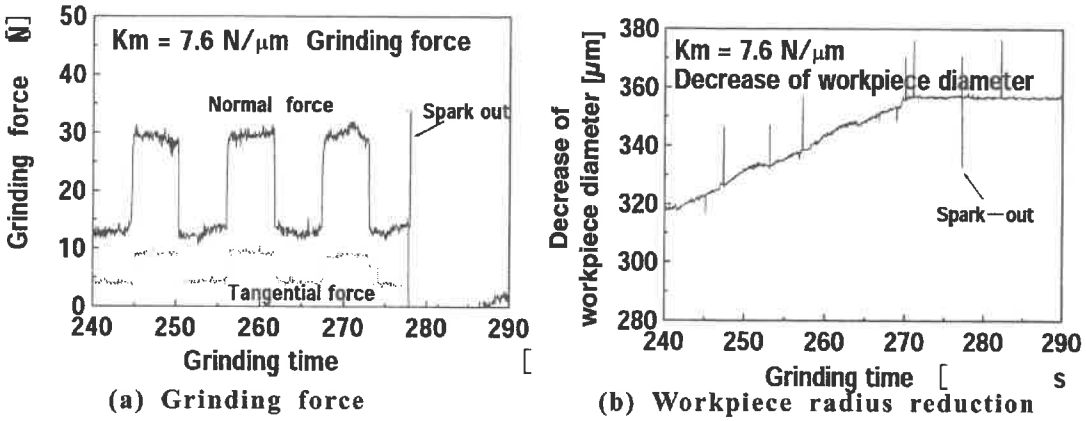

(a) Grinding force (b) Workpiece radius reduction

Fig.5 Measured value (Km = 7.6 N/μm)

4. Conclusions

It has been considered that grinding resistance is determined only the machining condition independently from the stiffness of grinding systems. Consequently, the generating processes of surface affected layers are independent from the stiffness of grinding system. However, under the condition that stiffness is low, grinding wheel can easily deform due to the variation of grinding force and wheel acts workpiece softly. As the results, surface affected layers generated in the grinding process have a tendency to be smaller.

Reference

1) Hiroshi EDA et al:Trans.JSME,408,46(1977),970.
2) Koji Ono :Kensaku shiage ,makishoten(1962), 121.
3) Hwa-soo Lee et al:Stiffness Design Method of Grinding Machine, Bul.of JSPE,24,2(1990), 136.
4) Hwa-soo Lee et al:On the Method to Determine the Stiffness of Grinding Machines ,Bul.of JSPE,22,2(1988), 127.

Grinding Wheel Condition Prediction and Improvement

Ping Zhang, Michele H. Miller
Michigan Technological University, Houghton, MI

Introduction

Grinding is regarded as a good way to do ceramics machining due to its multiple abrasive cutting particles. While a single point tool may dull and require re-sharpening, a grinding wheel distributes wear over many cutters and is capable of replenishing itself. However, the quality of the finished workpiece greatly depends on the constantly changing condition of the grinding wheel. Individual grits dull, and some fracture or pull out of the binder. Other grits at different locations with different shapes and sizes replace the lost grits as cutting grits. Chips accumulate in the spaces between grits thus removing clearance for subsequent chips. Chip accumulation (or loading) is particularly problematic with the fine grit wheels used in fine grinding of ceramics.

Wheel loading occurs when workpiece chips either adhere to the grits or embed in the space between grits.[1] Wheel loading affects the efficiency of the grinding process as well as the lifetime of the grinding wheel in fine grinding.[2] With wheel loading, forces and temperatures can increase to levels that cause poor surface finish, reduced material removal rate, and high wheel wear rate.

To maintain the grinding wheel condition with little chip loading, dressing is usually used. Traditionally, the grinding operation is interrupted to dress grinding wheels using methods such as stick or wire brush dressing. Several in-process dressing methods have been developed such as mechanical in-process dressing, electrolytic in-process dressing, electro-contact discharge dressing and waterjet in-process dressing. These offer the advantages of consistent wheel condition over time as well as uninterrupted operation. In order to make better use of the various dressing methods, our research seeks to understand the factors leading to wheel condition deterioration. We focus specifically on chip loading and study how factors such as chip size, wheel characteristics, work material, temperature, and coolant influence the rate of chip accumulation.

Computer Modeling

The literature indicates that the main cause of chip (or wheel) loading is adhesion between the active grits and the workpiece material deformed in the form of chips. [2] Chips accumulate in the

spaces between grits. Thus the relationship between chip volume and volume between grits is likely to influence the tendency for wheel loading. These quantities were investigated using a kinematic based simulation.[3] The wheel/work interface for the surface grinding geometry shown in Fig. 1 was modeled.

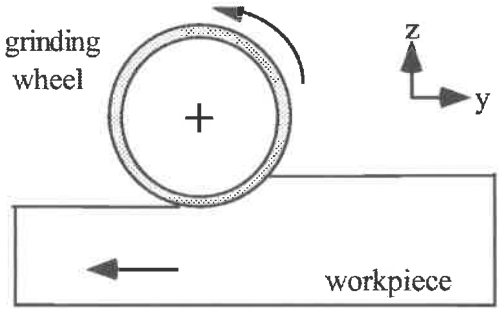

Figure 1: Surface grinding geometry

Based on the grinding conditions and wheel characteristics, the simulation program calculates chip volumes. The volume between grits $_{Vbetweengrits}$ is assumed as the binder volume per grit. It can be calculated from the grit size and abrasive volume fraction f_v. Approximating the grits as spheres with radius r_g, the grit volume is:

$$V_{grit} = \frac{4}{3}\pi r_g^{\,3} \tag{1}$$

The abrasive volume fraction of the grinding wheel is defined as:

$$f_v = \frac{V_{grit}}{V_{grit} + V_{betweengrits}} \tag{2}$$

Solving for the volume between grits:

$$V_{betweengrits} = V_{grit}\frac{1 - f_v}{f_v} \tag{3}$$

Combining (1) and (3),

$$V_{betweengrits} = \frac{4}{3}\pi r_g^{\,3}\frac{1 - f_v}{f_v} \tag{4}$$

Fig. 2 shows the relationship of chip volume and volume between grits for grit radii ranging from 25 μm to 175 μm and volume fractions ranging from 12.5% to 37.5%. Though not shown in the figure, both volumes increase with increasing grit size and decreasing volume fraction. The figure indicates that the volume between grits grows more quickly than the volume of chips as the grit size increases and/or volume fraction decreases. A higher ratio of $V_{betweengrits}/V_{chip}$ would reduce the tendency for chip accumulation. This result seems to validate the common observation that fine grit wheels experience more chip loading than coarse grit wheels.

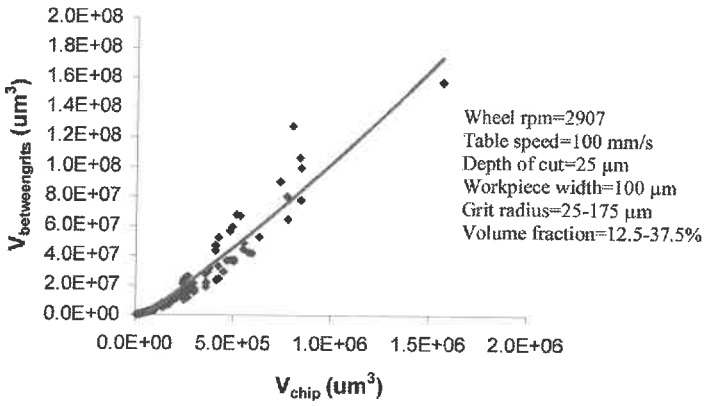

Fig 2: Relationship of chip volume to volume between grits

Equation (4) describes the effect of grit radius and volume fraction on volume between grits. In summary, the volume between grits is proportional to r_g^3 and approximately proportional to f_v^{-1}. We must use the simulation to determine the effect of grit radius and volume fraction on chip volume. Fig. 3 shows chip volume results as a function of volume fraction for 4 different grit sizes. Fitting trend lines to these points indicates that

$$V_{chip} \propto f_v^{-0.8} \qquad (5)$$

Fig. 4 shows chip volume results as a function of grit radius for 4 different volume fractions. After adding trend lines for these points, we get the following equation:

$$V_{chip} \propto r_g^{2.17} \qquad (6)$$

The ratio of volume between grits to chip volume is thus approximately:

$$\frac{V_{betweengrits}}{V_{chip}} \propto \frac{f_v^{-1} r_g^{3}}{f_v^{-0.8} r_g^{2.17}} = f_v^{-0.2} r_g^{0.83} \qquad (7)$$

This ratio can be increased (and the tendency for wheel loading reduced) by increasing grit size or decreasing volume fraction. The ratio is much more sensitive to changes in grit size than to changes in volume fraction.

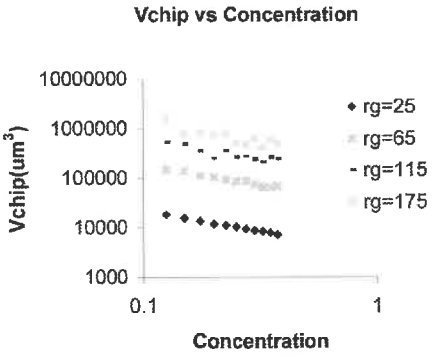

Fig 3: Relationship between chip volume and wheel concentration

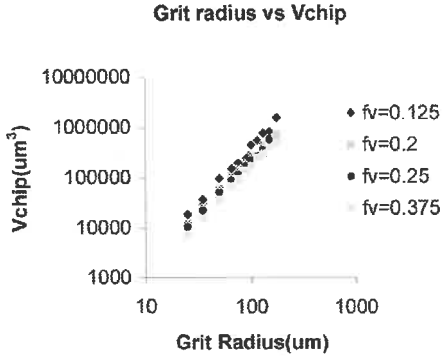

Fig 4: Relationship between chip volume and grit radius

Experimental Method

We have begun experiments to test our conclusions about the effects of grit size and concentration on wheel loading. Other researchers have used chemical detection, calorimetry, spectroscopy, eddy current sensing, magnetization, radiotracing, and x-ray fluorescence to evaluate wheel loading. We have adopted a simple approach for quantifying wheel loading that uses microscope images and image analysis software.[4]

Before the experiment, we set the workpiece, a truing wheel, and an optical microscope on the worktable of the grinding machine. After regular intervals we take several microscope images at different locations on the grinding wheel. Figure 5 shows a sample image of an aluminum oxide wheel after grinding steel. We then use Scion Image software to convert the image to black and white (shown in Figure 6) and to compute the percentage of black area. This percentage is our measurement of wheel loading. Next, we average the values from the different locations.

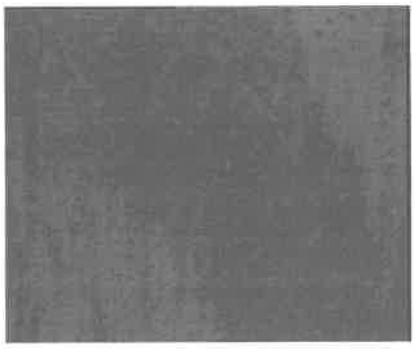

Fig 5: Microscope image of the grinding wheel

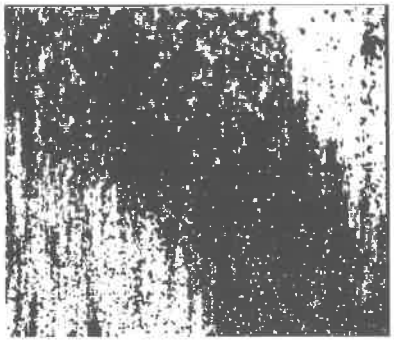

Fig 6: Black and white image

In our first experiments, we used this method to study the loading of aluminum oxide wheels grinding steel. Next, we plan to use the microscope and image analysis software to study the loading condition of diamond wheels grinding ceramic workpieces.

Conclusion

Our computer modeling results validate the common observation that fine grit wheels experience more chip loading than coarse grit wheels. We also get equations to predict chip volume based on wheel concentration and grit radius. Our current plans are to analyze wheel loading using a microscope and image analysis software. The final goal for this research is to study how chip size, wheel characteristics, work material, temperature, and coolant affect the rate of chip accumulation, and then use these results to improve dressing techniques.

References

1. Nagaraj, A. P. and A. K. Chattopadhyay, "On Some Aspects of Wheel Loading," *Wear*, Vol. 135, pp. 41-52, 1989.
2. Srivastava, A.K., K. Sriram and G.K. Lal, "A Simple Analysis for Evaluating Grinding Wheel Loading," *Int. J. Mach. Tool Des. Res.* Vol. 28, No. 2, pp. 181-190, 1988.
3. Miller, M. H. and K. S. Moon, "The Effect of Workpiece Modulation on Grinding Kinematics," *Proc. of the ASPE Spring Topical Meeting*, pp. 70-75, 1996.
4. Srivastava, A. K., K. Sriram and G. K. Lal, "A New Technique for Evaluating Wheel Loading," *Int. J. Mach. Tool Des. Res.*, Vol. 25, No. 1, pp. 33-38, 1985.

3D KINEMATICAL ANALYSIS OF LARGE SCALE SUBSTRATE SURFACE GRINDING

Libo ZHOU, Jun SHIMIZU, Kazuhiro SHINOHARA, Hiroshi EDA
Ibaraki University, Nakanarusawa 4-12-1, Hitachi-shi, JAPAN 316-8511

1. Introduction

In the previous report [1], an advanced grinding machine with the capability of one-stop finishing for ϕ300mm Si wafer has been developed. The core technology is the GMM actuated positioning/alignment device which is able to position half a ton of payload at the resolution of 5 Å and align tilt angle of α, β at the resolution of 0.1". Use of state-of-the-art technologies developed for the grinding system have made it possible to precisely control the motion of each cutting edge, for example, to achieve the ductile mode machining. The behavior of each grain and its effect on surface generation become mathematically analytical in 2D or 3D manner. Taking one step further, this paper has developed a 3D model for infeed grinding which is often used in grinding systems for silicon wafer and other large scale substrates, and mathematically described the cutting path and its density. Being associated with the achievable surface roughness and global flatness, the simulation results are discussed and compared with the experimental results.

2. Infeed grinding Model

Most wafer grinding system utilizes the plunge (infeed) method [2] to keep the contact area unchanged and thereby to deliver a stable grinding performance throughout the grinding process. **Fig.1** shows a typical arrangement of the wheel and the wafer, where the wheel is half overlapped with the wafer. The grinding wheel is often shaped in a segmented ring with several millimeter thicknesses. When the wheel axis is aligned to be parallel to the wafer axis, the interaction between the wheel and wafer is made in X-Y plane. The two dimensional grinding model is schematically shown in **Fig.2**, where the relevant parameters are labeled. Corresponding to the alignment, in the 3D model, the tilts of wafer axis are defined as α and β respectively around X-axis and Y-axis. The other parameters used for analysis are listed in **Table 1**.

In a coordinate system that the origin is fixed at the center of the wafer, the three position components $[x(t), y(t), z(t)]$ of a grain, which is initially located at (r_1, θ_1) on the wheel, is specified as;

$$\begin{bmatrix} x(t) \\ y(t) \\ z(t) \end{bmatrix} = A \cdot B \cdot C \cdot D \begin{bmatrix} r_1 \\ L \\ -f \cdot t \end{bmatrix} \quad (1)$$

where the matrix A , D respectively represent the rotations of wafer and wheel, and are given as;

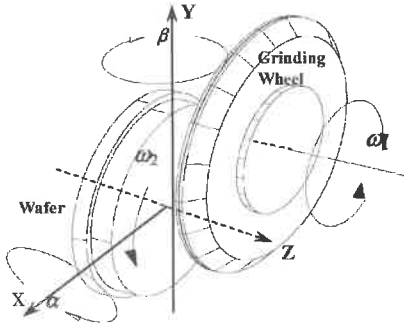

Fig.1 Grinding wheel/wafer arrangement

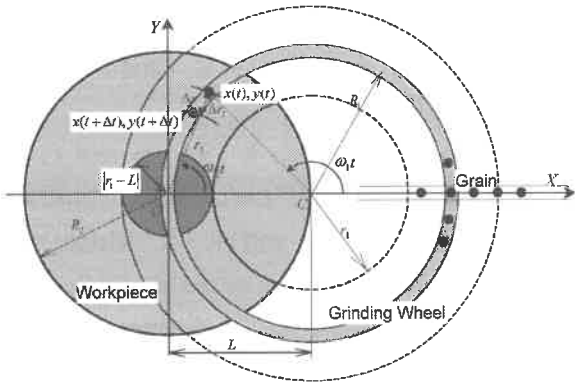

Fig.2 Grinding model

Table 1 Parameter list

R_1	Wheel radius, 150mm or indicated otherwise
R_2	Wafer radius, 150mm or indicated otherwise
(r_1, θ_1)	Grain initial position ($0 \le r_1 \le R_1, 0 \le \theta_1 \le 2\pi$)
r_2	Position of machining point ($0 \le r_2 \le R_2$)
L	Offset between wheel axis and wafer axis
n_1	Wheel rotational speed (+: CCW, -: CW)
n_2	Wafer rotational speed (+: CCW, -: CW)
ω_1	Wheel angular speed ($=2\pi \cdot n_1$)
ω_2	Wafer angular speed ($=2\pi \cdot n_2$)
f	Infeed rate
t	Grinding time
Z_1	Infeed ($Z_1 = f \cdot t$)
α	Wheel axis tilt around X-axis
β	Wheel axis tilt around Y-axis

$$A=\begin{bmatrix}\cos\omega_2 t & \sin\omega_2 t & 0\\ -\sin\omega_2 t & \cos\omega_2 t & 0\\ 0 & 0 & 1\end{bmatrix}$$

$$D=\begin{bmatrix}\cos\omega_1 t & 1 & 0\\ \sin\omega_1 t & 0 & 0\\ 0 & 0 & 1\end{bmatrix}$$

while matrix B, C respectively express the tilts of wheel around X-axis and Y-axis, and are given as;

$$B=\begin{bmatrix}1 & 0 & 0\\ 0 & \cos\alpha & -\sin\alpha\\ 0 & \sin\alpha & \cos\alpha\end{bmatrix}$$

$$C=\begin{bmatrix}\cos\beta & 0 & \sin\beta\\ 0 & 1 & 0\\ -\sin\beta & 0 & \cos\beta\end{bmatrix}$$

L is the offset between axes of the wafer and wheel and f represents the infeed rate. A grain which is initially located at (150, 0) is chosen for the case study of ϕ300mm Si wafer. Shown in **Fig.3** is its cutting path made at different speed ratio n_2/n_1 and projected in X-Y plane. When $n_2/n_1=0.5$ the cutting path formed is a straight line. Other than that, lines are curved. It is important to note that the $n_2/n_1=1/3$ and $n_2/n_1=500/1500$ share the same pattern regardless of difference in each rotational speed. It is meant that the cutting path pattern is only determined by the speed ratio n_2/n_1 of the wafer against the wheel, not the individual revolution speed.

Since the matrix A, D are the periodic functions with respective period of $2\pi/\omega_2$ and $2\pi/\omega_1$. The least common period is then given as $2\pi\cdot k\cdot m\cdot n$. k, m, n should fulfill the following equation.

$$\frac{n_2}{n_1}=\frac{\omega_2}{\omega_1}=\frac{k\cdot n}{k\cdot m} \quad (k, m, n\text{: natural number}) \quad (2)$$

where k is the greatest divisor of ω_1 and ω_2, while n/m is their irreducible fraction. It means within the first common period that one grain cuts the wafer once every rotation. From the second period onwards, the grain repeatedly goes through the same path so that the number of the cutting path formed is no longer increased. This is defined as the stable state. Comparing the stable states respectively made by $n_2/n_1=50/1500$ (or 1/30) and $n_2/n_1=40/1500$ (or 2/75), it is able to conclude that the number of the cutting path is determined by the denominator m.

3. Cutting path density and surface roughness

By examining the cutting path pattern shown in Fig.3, it

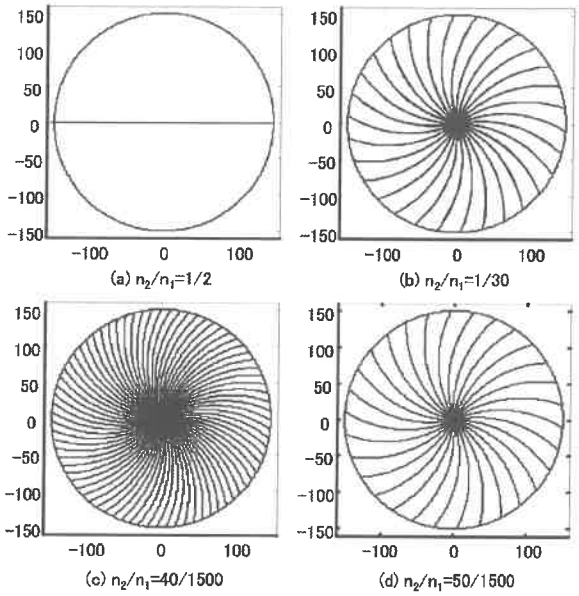

Fig. 3 Cutting path pattern

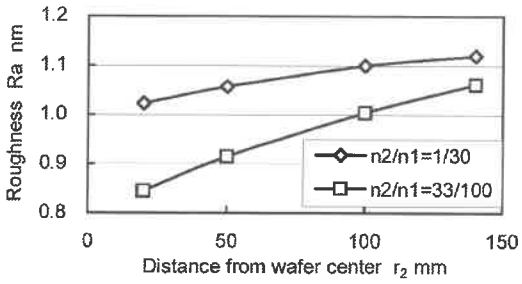

Fig. 4 Effect of cutting path density on Ra

is easily understood that the density of cutting path is higher in the wafer center than that at its fringe, and increases by increasing the denominator m. From the viewpoint of surface roughness, a large denominator m is preferable. **Fig.4** compares the surface roughness obtained from the different rotational speed combination. The cutting path at $n_2/n_1=495/1500$ (or 33/100) is about three times denser than that at $n_2/n_1=50/1500$ (or 1/30). It is clearly proven that the density of cutting path contributes to improvement in the surface roughness. In the meantime, an excessive m takes a long time to reach the stable state, which often leads to severe burn marks on the wafer surface. The result in Fig.4 also addresses a fact that the roughness obtained is inconsistent over the wafer surface, corresponding to the change in the density of cutting path.

Therefore, it is impartment to know the variation of the cutting path density at different radius r_2. Form t

to $t+\Delta t$, the grain changes its position from $x(t), y(t)$ to $x(t+\Delta t), y(t+\Delta t)$ in X-Y plane. The increments in position are as;

$$\begin{cases} \Delta x = x(t+\Delta t) - x(t) \\ \Delta y = y(t+\Delta t) - y(t) \end{cases} \quad (3)$$

if the Δt is small enough, then the length of the cutting path formed in such short period is given as;

$$\Delta s \approx \sqrt{\Delta x^2 + \Delta y^2} \quad (4)$$

The change in the radius of the wafer is expressed as;

$$\Delta r_2 = \sqrt{x^2(t+\Delta t) + y^2(t+\Delta t)} - \sqrt{x^2(t) + y^2(t)} \quad (5)$$

Therefore, the cutting path density $d(r_2)$ at a specific wafer area is stated as;

$$d(r_2) = \lim_{t \to 0} \frac{m \cdot \Delta s}{2\pi r_2 \cdot \Delta r_2} = \frac{m}{2\pi} \cdot \frac{ds}{r_2 dr_2} \quad (6)$$

Fig.5 is the results calculated at different speed ratio, showing the density $ds / r_2 dr_2$ and the length change rate ds / dr_2 of the cutting path. No matter how the speed ratio changes, the cutting path density sharply increases toward to the wafer center and becomes infinite as radius r_2 takes zero. Mathematically, the center is a singular point for cutting path density. With such condition, the interference between wafer and wheel becomes irregular and creates an undesirable surface.

4. Cutting path density and flatness

The inconsistency of the cutting path density affects not only affects the surface roughness, but also the global flatness. As long as the loop stiffness of the machine tool is not infinite, higher cutting path density always leads to a higher removal of the material and results in a concave profile.

The 3D profile, which is obtained at grinding with a #3000 diamond wheel of 3mm thick segment, is shown in **Fig.6**. It is found that the profile at the wafer center is concaved as deep as 0.5μm. The diameter of the hollow is approximately 3mm, exactly agrees with the wheel thickness. This problem remains unsolved as long as the wheel takes a ring shape.

More precisely, a ring type wheel can be considered as cutting edges uniformly distributing between external and internal radii. Therefore, its cutting path density is given in Eq.(7) by integrating the cutting path made by every grain which is located inbetween.

$$D(r_2) = \frac{m}{2\pi} \cdot \int_{r_i}^{R_i} \frac{ds}{r_2 dr_2} dr_1 \quad (7)$$

Fig.7 shows the density variation calculated on basis of the actual wheel dimension of $148.5 < r_1 < 151.5$. It is found that the density exactly takes a reverse form of Fig.6. This fact indicates that the material removal depth $h(r_2)$ is proportional to the cutting path density.

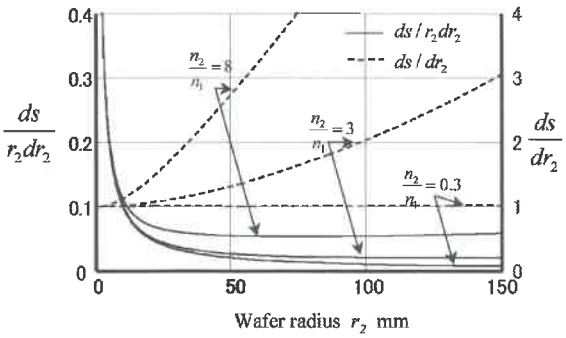

Fig. 5 Cutting path density and length ratio

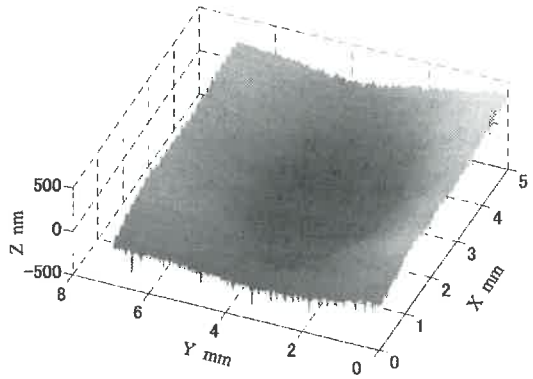

Fig. 6 Concave profile in wafer center

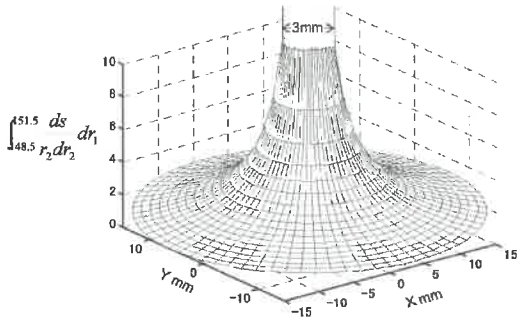

Fig. 7 3D cutting path density

A practical solution for solving the flatness problem is to tilt the axis of the wafer (or wheel) slightly inclining against the axis of the wafer [3], to offset the effect of unevenness of cutting path density. **Fig.8** is the cutting path, re-calculated at $\alpha = \pm 0.1^\circ$ and presented in 2D/3D graphs according to the Eq.(1). When the tilt is made around X-axis only, the profile takes a circular cone shape regardless of the direction of tilt. 0.1° in α creates a variation of profile in Z direction of about 0.2mm over 300mm. **Fig.9** shows the results when the wheel axis inclines around Y-axis. A positive β makes the profile convex, while a

negative β makes the profile concave. The effect of β on the global flatness is about half that of α.

From the results shown in Fig.6 ~ Fig.9, it is easy to understand that choosing an appropriate alignment α, β is able to counterbalance the profile error created by unevenness in the cutting path density. Taking in account of the geometrical form $z(r_2)$ made by alignment, when the removal depth $h(r_2)$ meet the following condition, a flat surface is achievable.

$$h(r_2) = z(r_2) - \lambda \cdot D(r_2) = \text{constant} \qquad (8)$$

where λ is a constant associating the removal depth with the cutting path density. As described in the previous report, the grinding machine developed in this project is equipped with a GMM alignment plate, able to tilt 0.1 second over the range of ±1.5 degrees around both X- and Y-axis. For this particular case of ϕ300mm Si wafer, the wafer axis is aligned at $\alpha = 0.001^\circ$ and $\beta = -0.001^\circ$. After grinding, as shown in Fig.10, the global flatness is significantly improved up to 0.2μm/300mm. This result demonstrates how important the alignment mechanism is for infeed grinding to improve the global flatness.

5. Conclusion

In this report, a 2D/3D grinding model is developed to address the kinematics of each abrasive in infeed grinding process for ϕ300mm silicon wafer. The cutting path and density is mathematically investigated and experimentally associated with the achievable surface roughness and the global flatness. The results are summarized as follows;

1) The cutting path pattern is only determined by the speed ratio n_2/n_1 of the wafer against the wheel, not the individual speed.
2) When $n_2/n_1 = 0.5$ the cutting path formed is a straight line. Other than that, lines are curved.
3) The cutting path density in the wafer center is higher than that at the fringe. The achieved surface roughness is inconsistent over the whole wafer.
4) The removal depth into the wafer is proportional to the cutting path density. The variation in the cutting path density leads the ground wafer to a concaved profile.
5) A proper tilt (alignment) between the wheel and wafer is able offset the effect of the cutting path density.

Acknowledgement

This research was partially sponsored by the Regional Consortium from New Energy and Industrial Technology Development Organization, the Grand-in-Aid for Exploratory Research (No.10875029) and the Regional Joint Research (No. 11792007) from the Ministry of Education, Science and Culture of Japan.

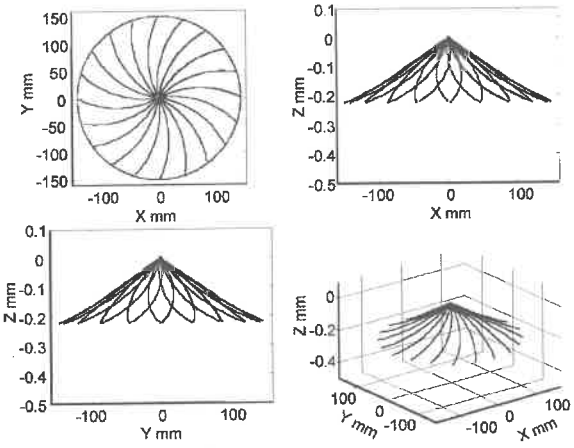

Fig. 8 $\alpha = \pm 0.1^\circ$

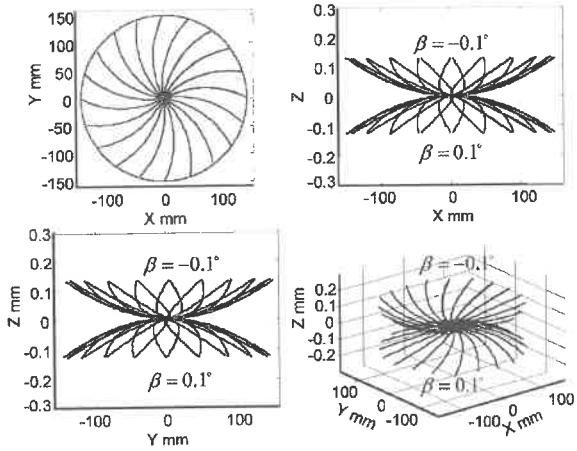

Fig. 9 $\beta = 0.1^\circ$, $\beta = -0.1^\circ$

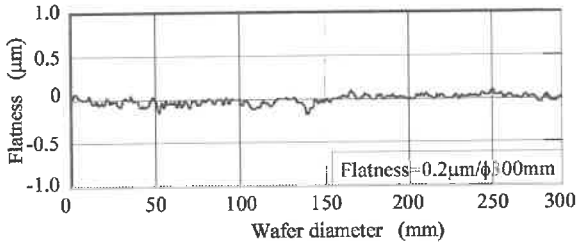

Fig. 10 Achieved flatness

References

[1] L.ZHOU, H. EDA, et.al.: "Development of One-stop Machining System for ϕ300mm Silicon Wafer, Proc. of ASPE 2000, 140-143.

[2] K. Kimura, et.al.: Characteristics of CMP Using Hard Wheel Pad, Proc. of JSPE 1988, 245.

[3] Töshoff H.K., Schmieden W.V., Inasaki I., König W. and Spur G., 1990, Abrasive Machining of Silicon, Annals of CIRP, 39/2, 621-635.

Generation of large-area microstructured surface by diamond turning with a fast tool servo

Takeshi Araki* , Wei Gao* , Satoshi Kiyono* , Masasyu Sudoh** and Masami Mito*

* Department of Mechatronics and Precision Engineering, Faculty of Engineering, Tohoku University, Aramaki Aza Aoba 01, Sendai, 980-8579 Japan
** Nissan Motor Co.,Ltd.

1. Introduction

The authors have proposed a new surface encoder for detecting multi-degree-of-freedom (MDOF) translational and tilt motions of precision stages [1]. The surface encoder consists of two fundamental elements: a sinusoidal grid, which is referred to as the angle grid, and a two-dimensional (2D) slope sensor.

The angle grid has a 2D micro-grid surface, which is a superposition of sinusoidal waves in the X- and Y-directions. Since the angle grid surface is used as the reference of position measurement, it is necessary to fabricate the sinusoidal surface accurately over a large area. Considering the specifications of the angle grid surface, the authors decided to apply the single-point diamond turning with fast tool servo to fabricate the angle grid surface. It has the advantage of producing difficult geometries with high form accuracy and good surface finish with the assistance of the fast tool servo technique [2-4]. In the wavelength range of tens of microns to hundreds of microns, diamond turning is superior to the electronic and optical methods, especially for fabrication of precision micro-structured surfaces.

In this paper, the constructed fabrication system together with several evaluation and compensation techniques for improvement of the fabrication accuracy are presented.

2. Fabrication system for angle grid surfaces

Figure 1 shows a schematic of the surface encoder consisting of a two-dimensional slope sensor and an angle grid. The height profile of the angle grid surface at point P, which is a superposition of sinusoidal waves in the X and Y directions, can be expressed as:

$$f(x,y) = A_X \sin(\frac{2\pi}{\lambda_X}x) + A_Y \sin(\frac{2\pi}{\lambda_Y}y) \qquad (1)$$

where, A_X and A_Y are the amplitudes of the sine functions in the X direction and Y direction, respectively. λ_X and λ_Y are the corresponding spatial wavelengths. These values are designed to be A_X, A_Y=100 nm and λ_X, λ_Y=100 μm based on the specifications of the slope sensor. The fabrication area is determined to be 150 mm in diameter.

Figure 2 presents the principle of the fabrication method. The workpiece is mounted on the spindle with its axis along Z-direction and the single point diamond tool is mounted on the X-slide of a diamond turning machine. The displacement of the tool along Z-direction (the depth of cut) is controlled by a fast tool servo. Assume that the rotation of the spindle and the feed of the X-slide are synchronized, the polar coordinates

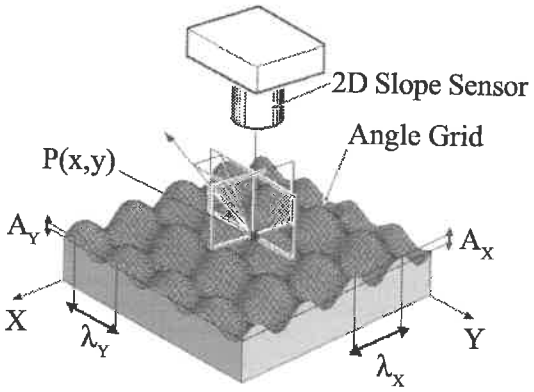

Figure 1 Schematic of the surface encoder

of the position of the tool tip in the XY plane can be expressed by

$$(r_i, \theta_i) = (r_0 - \frac{Fi}{PT}, 2\pi\frac{i}{P}) \qquad \text{i=0, 1, N-1} \qquad (2)$$

where F, P, T, and i are the feed rate of the X-slide, pulse number of the rotary encoder of the spindle in each rotation, rotational speed of the spindle, and i-th rotary encoder pulse, respectively. To generate the sinusoidal grid surface shown in Eq. (1), the depth of cut at each point is calculated as follows and stored in a personal computer before the fabrication.

$$\begin{aligned} z(i) &= f(r_i\cos\theta_i, r_i\sin\theta_i) \\ &= f((r_0 - \frac{Fi}{PT})\cos(2\pi\frac{i}{P}), (r_0 - \frac{Fi}{PT})\sin(2\pi\frac{i}{P})) \end{aligned} \qquad (3)$$

The system is composed of a commercially available CNC ultra-precision diamond turning machine (Table 1 summarizes the specifications), a personal computer in which the data of depth of cut are stored, and a fast tool servo for fast and accurate tool positioning.

The data shown in Eq. (3) are stored in the hard disk of the personal computer as a data file before fabrication. When the fabrication starts, the data are then output to the controller of the fast tool servo one by one responding to the trigger signals from the rotary encoder of the spindle. By using the technique of DMA ring buffer [4], data exceeding the memory capacity can also be output continuously.

Figure 3 shows a schematic of the designed and constructed fast tool servo. A piezoelectric tube actuator (PZT) is used to control the depth of cut. A round-shape tool cap flexure is employed to transmit only the PZT displacement along Z-directions to the diamond tool. A capacitance probe is installed inside the PZT tube to monitor the displacement of the PZT. An analog PID controller is con-

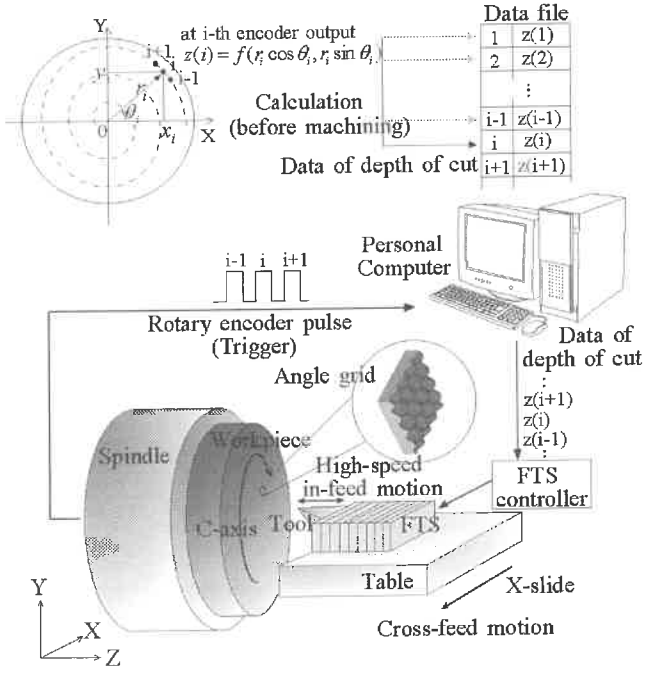

Figure 2 Principle of the fabrication method

Table 1 Specifications of the ultra-precision diamond turning machine

Model	Ultra-precision CNC diamond turning machine ULC-100A (HC) TOSHIBA MACHINE CO.,LTD.
Slides	Movement range: 220mm (X), 150mm (Z) Straightness: 0.5μm/full measurement range Positioning repeatability: ± 0.05μm Resolution: 0.01μm
Air Spindle	Rotational speed: 1~1500rpm Pulse number of the rotary encoder: 180000Pulse/rev Spindle errors: 0.05μm (radial and axial motions) Resolution: 0.001deg

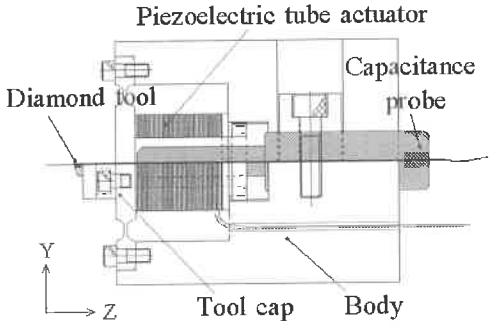

Figure 3 Schematic of the fast tool servo

structed to feedback control the PZT displacement. The bandwidth is approximately 2.5 kHz.

In the fabrication experiments, an aluminum alloy workpiece was used as the workpiece. The rotation speed of the spindle and the feed rate of the X-slide were set to be 20 rpm and 5 μm/rev.

3. Sub-micrometer center-adjustment

The first effort in the fabrication experiment was made to position the tool origin to the center of the spindle (center-adjustment) since it is important to fabricate the sinusoidal grid surface accurately.

Figure 4 shows a schematic of the center-adjustment in Y-direction. Assume that $O_{spindle}$ is the origin of the spindle axis and O_{NC} is that of the tool. A facing cut was made after O_{NC} was set slightly below $O_{spindle}$. Since the radius of the residual part in the center of the workpiece corresponds to the Y-component δ_Y of the center-adjustment error, it can be identified by imaging and measuring the residual part. As a result of measurement and adjustment using the AFM, δ_Y was evaluated to be smaller than 0.1 μm.

The center-adjustment in X-direction was carried out after that in Y-direction was accomplished. The X-directional center-adjustment is to identify the relative distance δ_X between O_{NC} and $O_{spindle}$. As shown in Figure 5, the tool was set at a position on the X-axis with a distance of D_A from O_{NC} to turn a circular groove on the workpiece surface. δ_X can thus be evaluated from taking the difference of D_A and D_B. As a result of measurement and adjustment using the interference microscope, δ_X was evaluated to have an uncertainty of 0.094 μm (2σ).

4. Fabrication and evaluation results of angle grid surfaces

Another great challenge in the fabrication experiment was how to evaluate the profile errors of the fabricated angle grid surface. Figure 6 shows the fabrication and evaluation results. Profiles of several parts along the radial direction are imaged by the interference microscope, which can be treated as representative parts for evaluation of profile errors. The spatial spectrum of each part is evaluated by the spectrum analysis through the two-dimensional discrete Fourier transform (DFT) technique. Here, the f_X and f_Y axes show the X-directional and Y-directional spatial frequencies, respectively. X- and Y-directions correspond to cross-feed direction of the X-slide and cutting direction of the workpiece, respectively. The vertical axis shows the amplitude of the spectrum. The four largest components at wavelengths of 100 μm show those of desired sinusoidal surface profile. Other components are error-components. The large error-component at wavelength of 50 μm in the f_X axis, which was caused by the round nose geometry of the diamond tool, was successfully reduced to approximately 4 nm through the compensation using the local radius of the diamond tool.

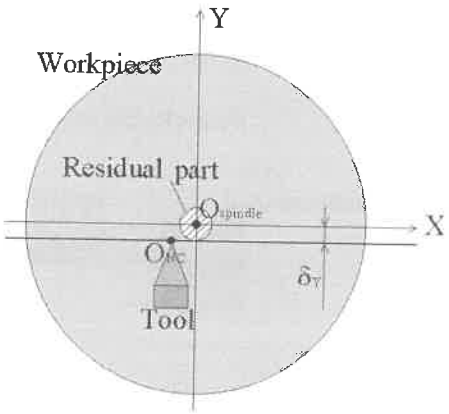

Figure 4 Center-adjustment in Y-direction

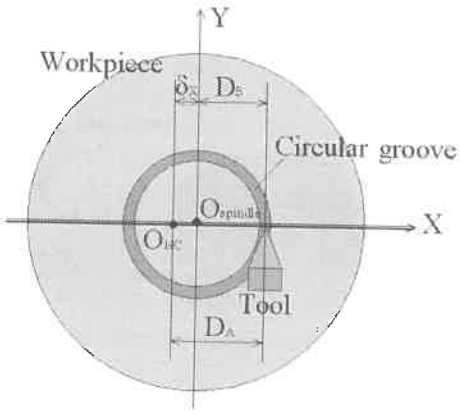

Figure 5 Center-adjustment in X-direction

5. Conclusions

(1) A fabrication system consisting of ultra-precision diamond turning machine and fast tool servo has been constructed for an angle grid surface. The sinusoidal waves have been successfully fabricated on the entire grid surface.

(2) Center-adjustment has been accomplished to the sub-micrometer level with the aid of an AFM and an interference microscope.

(3) An efficient evaluation technique based on two-dimensional DFT has been developed for the fabricated surfaces. The error-component caused by the round nose geometry of the diamond tool has been identified and the error has also been reduced to 4 nm through a compensation procedure.

Acknowledgements

This work was financially supported by a grant from Ministry of Education, Culture, Sports, Science and Technology of Japan (MEXT). The authors thank Dr. Y. Okazaki of AIST for his valuable suggestions on building the FTS. The support and suggestions from Toshiba Machine Co.,Ltd. especially on the center-adjustment were greatly appreciated.

References

[1] S. Kiyono, P. Cai and W. Gao, An angle-based position detection method for precision machines, JSME Int. J., 42-1, (1999), 44-48.

[2] S. R. Patterson and E. B. Magrab, Design and testing of a fast tool servo for diamond turning, Precision Engineering, 7-3, (1985), 123-128.

[3] T. A. Dow, M. H. Miller and P. J. Falter, Application of a fast tool servo for diamond turning of nonrotationally symmetric surfaces, Precision Engineering, 13-4, (1991), 233-250.

[4] Y. Okazaki, Fast tool servo system and its application to three dimensional fine figures, Proc. of 13th ASPE, (1998), 100-103.

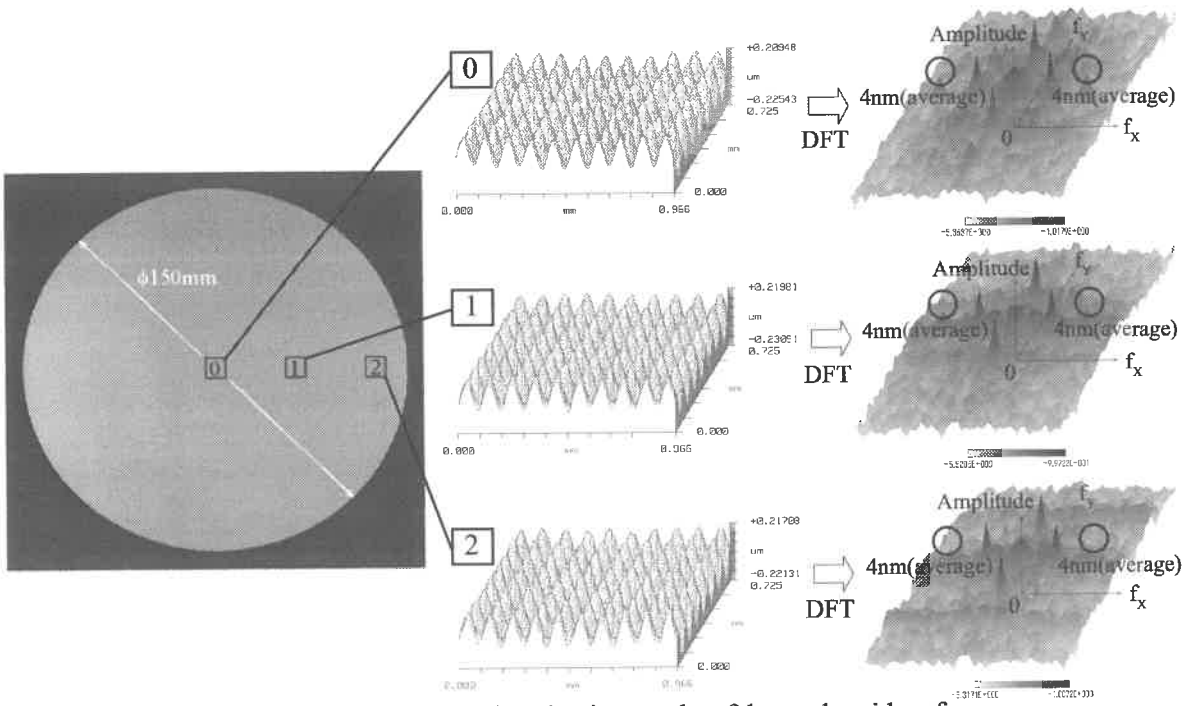

Figure 6 Fabrication and evaluation results of the angle grid surface

Generation of Freeform Surfaces by Diamond Machining

E. Brinksmeier, D. Grimme, W. Preuss

LFM Laboratory for Precision Machining, University of Bremen, Germany

Introduction

Freeform surfaces, i.e. surfaces without rotational symmetry, are gaining increasing importance in optical systems design. With the advent of multi-axis ultra-precision machines, manufacturing of such surfaces in optical quality by a deterministic micro-cutting process has become a promising alternative to prohibitively expensive iterative measuring and polishing techniques.

In this paper we are discussing machining processes suitable for the generation of freeform surfaces which require at least three numerically controlled axes, operating either in Cartesian or polar coordinates:

- line contact fly-cutting with three degrees of freedom
- raster fly-cutting and raster grinding
- asymmetric contour milling

Interestingly, many important applications of these processes refer to modern telescopes and their instrumentation.

Monolithic mirror arrays

Diamond fly-cutting is a classical method for generating concave toroidal surfaces with radii r_1 and r_2 in two mutually perpendicular cross-sections, where r_1 equals the fly-cut radius r_f, and r_2 must be larger than the tool nose radius r_ε (cf. Fig.1). Eventually, if $r_1=r_2$, or $r_2= \infty$, spherical or cylindrical surfaces may result. If the midpoint **M** of the fly-cutter can be moved in all three spacial coordinates x,y,z with respect to the workpiece (the angular orientation of the fly-cut plane being fixed), one- and two-dimensional arrays can be created with the following geometrical options:

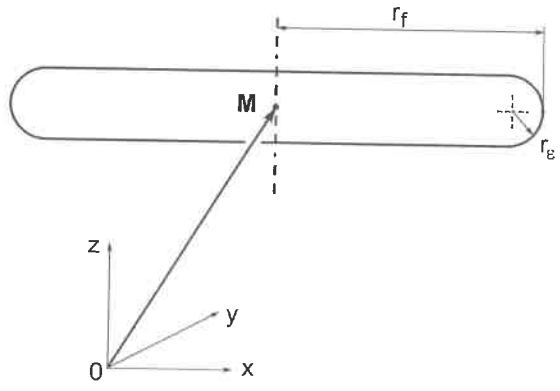

Fig.1 A fly-cutter has an effective toric shape with fly-cut radius r_f and tool nose radius r_ε

- radius r_2 variable from facet to facet
- in case of spherical facets, variable centerpoint coordinates
- arbitrary envelop contours (within certain limits)

Such arrays are the key components of so-called Integral Field Units (IFUs) now being designed and tested by various groups of astronomers for implementation in a new generation of optical and near infrared spectrographs. IFUs allow a spectrum to be obtained from many sub-sections of the telescope image simultaneously by optically splitting the image into rectangular segments and rearranging them along the entrance slit of the spectrometer [1].

We have machined different types of arrays for IFUs to be installed in the Gemini North

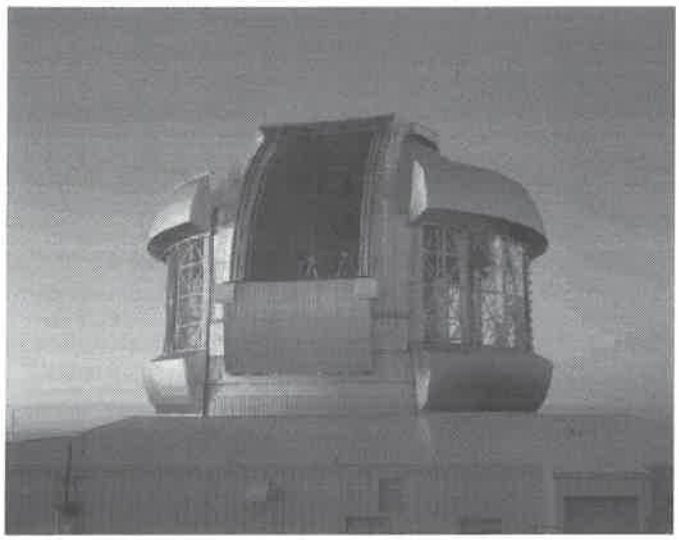

Fig.2 View of the Gemini North Observatory, Mauna Kea, Hawaii

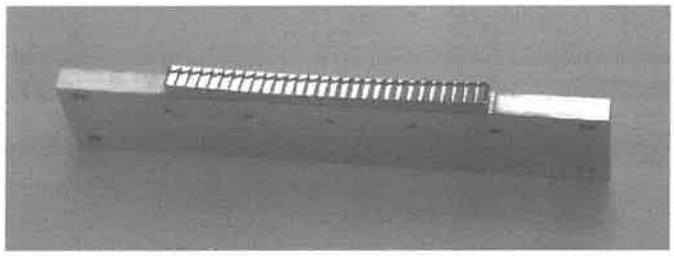

Fig.3 Pupil mirror array for the Near Infrared Integral Field Spectrograph for the Gemini South Observatory (cf. text for details)

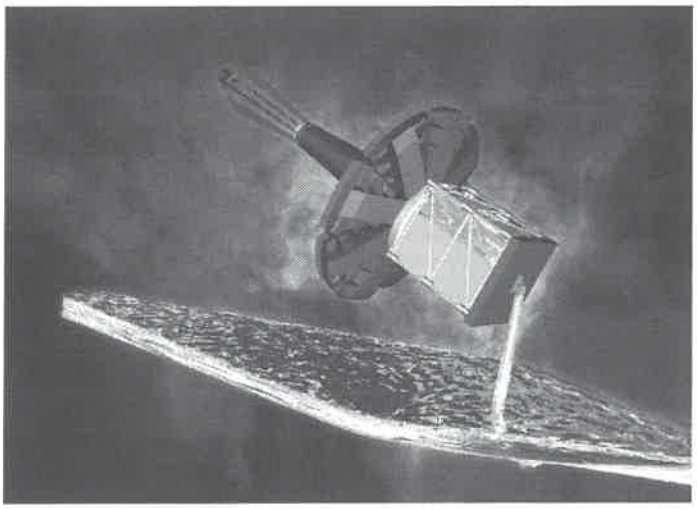

Fig.4 Artist's conception of the Next Generation Space Telescope (NGST)

(Fig.2) and South Observatories. Fig.3 shows a pupil mirror array for the Near Infrared Integral Field Spectrograph for Gemini South consisting of 29 toroidal facets 4.5mm x 2mm in size with radii r_1=52.71mm and r_2=53.17mm arranged along a circular envelop with a radius of 448mm. The array was fly-cut on a Precitech Freeform 3000 multi-axis ultra-precision machine into an electroless nickel plated aluminum substrate. The surface roughness, measured with a white-light interferometer over an area of 0.8mm x 0.6mm, is 2.9nm Ra (3.7nm rms). The figure accuracy of the toroidal facets is better than 50nm peak-to-valley. The key for achieving this surface quality is a precise determination of the fly-cut geometry (r_f, r_ε and midpoint location **M** with respect to the mirror body) as well as careful balancing and excellent thermal stability.

Grinding studies, carried out on a Nanotech 500 Freeform Generator, are under way for a proof-of-concept mirror array with spherical surfaces and varying centerpoints generated by ductile grinding of a block of Zerodur. First results show that figure accuracy and surface finish of the ground glass surfaces are comparable to those obtained in fly-cutting of metal substrates.

Freeform surfaces

A different approach for accomplishing spectroscopy of multiple objects simultaneously is the utilization of so-called digital micro-mirror devices composed of over half a million mirrorlets, of which any desired subset can be tilted by approx. +/- 10°. Since the direction of tilt is along a diagonal, a distorted focal plane results which must be corrected with aspheric optics including non-axisymmetric surfaces. This approach is adopted in the Infrared Multi-Object Spectrometer (IRMOS) [2]

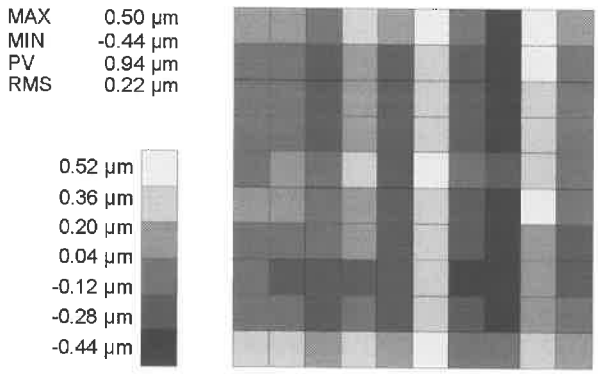

Fig.5 Contour error plot of the IRMOS bi-conical mirror obtained with a Moore M18 coordinate measuring machine

Fig.6 Stratospheric Observatory for Infrared Astronomy (SOFIA)

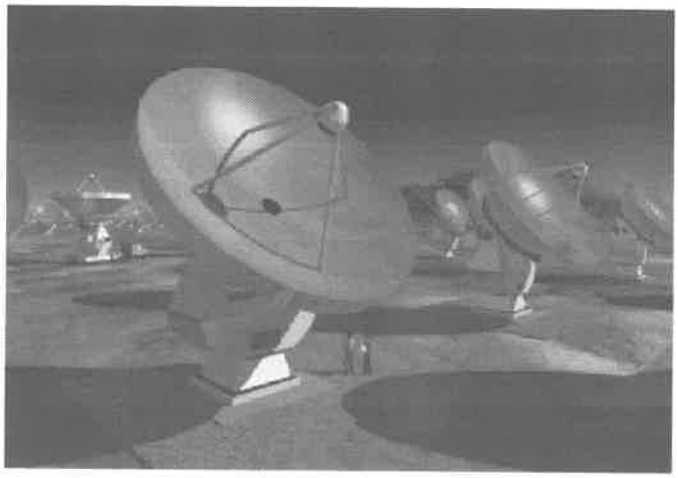

Fig.7 Atacama Large Millimeter-Submillimeter Array (ALMA)

for the Next Generation Space Telescope (NGST) (Fig. 4).

One of the crucial IRMOS mirrors is a concave off-axis elliptical toroid with two different conical constants which - from a manufacturing point of view - is a freeform surface. We have generated the bi-conical mirror surface, approx. 94mm x 76mm in size, by raster fly-cutting a premachined T6061 aluminum blank. Machining was performed on a Precitech Freeform 3000 machine with a fly-cut geometry r_f=63mm and r_ε=10mm in the down milling mode. Machining time for one complete cut was 16 hours. Fig.5 shows a contour error plot of the machined surface obtained with a Moore M18 coordinate measuring machine. The peak-to-valley figure error is below 1µm. The achieved surface roughness is less than 8nm Ra (11nm rms), measured with a white-light interferometer over an area of 1.3mm x 1.0mm. Raster fly-cutting of several bi-conical mirrors employed in the Far Infrared Spectrometer of the Stratospheric Observatory for Infrared Astronomy (SOFIA) (Fig.6) was performed with similar results.

Besides the a.m. requirements on alignment, balancing and thermal stability, raster fly-cutting of freeform surfaces involves a toric cutter compensation and cutting of test parts with simpler geometry which is accessible to interferometry without the use of computer generated holograms. If the figure evaluation of a freeform surface with a coordinate measuring machine yields good results, this is indicative of correct programming of the machining code, since probe radius compensation is mathematically different from toric cutter compensation.

Large segmented reflectors

Another challenge for multi-axis precision machining is the fabrication of off-axis segments of large parabolic reflectors needed for millimeter and submillimeter radio telescopes. Typi-

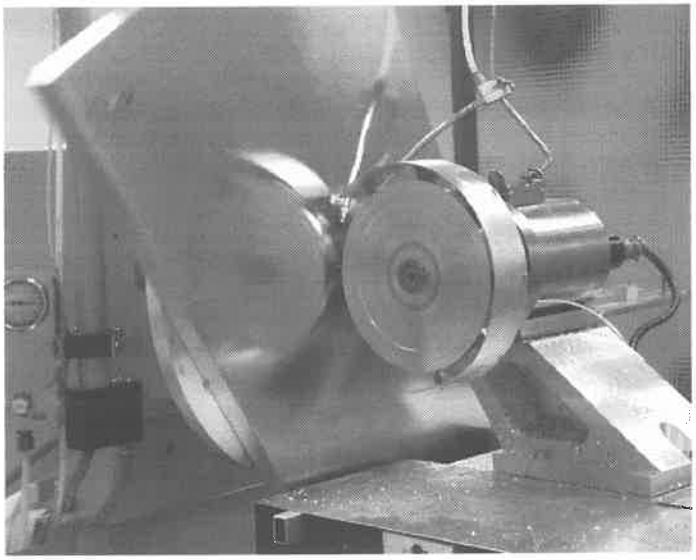

Fig.8 Machining of panels for the first ALMA prototype reflector on a modified Moore M18 Aspheric Generator

cally, such segments consist of weight-relieved aluminum panels with a thickness of only 2mm. We have described an asymmetric contour milling process developed for machining the 3m reflector of the KOSMA submillimeter telescope in [3]. In contrast to raster milling, where the workpiece is stationary, in asymmetric contour milling the mirror is rotating on the workpiece spindle, while the fly-cutter is moved back and forth as a function of angular position in order to keep track with the changing sag of the surface being cut.

The process has been improved and automated for the fabrication of the first 12m prototype reflector for the Atacama Large Millimeter-Submillimeter Array (ALMA) (Fig.7) consisting of 264 panels arranged in 8 tiers. Machining is performed on a modified Moore M18 Aspheric Generator with a motorized Professional Instruments 4R fly-cut spindle (Fig.8). Fly-cutting is performed at a spindle speed of 3600rpm with four half-arc polycrystalline diamond tools with a nose radius of 12mm yielding 240 point contacts per second. Rough and finish cuts are carried out in sequence without the operator's attention. One panel is completed within 3h 45'. Figure accuracy of the machined surface is measured in situ on the machine with a PC controlled LVDT probe held in kinematic mounts. The achieved figure accuracy mainly depends on the amount of relieved residual stress and is typically between 2.5µm and 5µm rms. Total production time for the 12m reflector is five months.

Acknowledgement

The authors like to thank many dedicated individuals of the Astronomical Instrumentation Group / University of Durham, UK, the Mt. Stromlo and Siding Spring Observatories / Australian National University, the Space Telescope Science Institute / Goddard Space Flight Center, USA, the Max-Planck-Institute for Extraterrestial Physics, Germany, and Vertex RSI, USA and Germany, for excellent cooperation.

Literature

[1] C.M. Dubbledam, R. Content, J.R. Allington-Smith, S. Pokrovsky, and D.J. Robertson: „An Integral Field Unit for the Gemini Near InfraRed Spectrograph", SPIE Proceedings Vol. 4008

[2] R. Winsor, J.W. MacKenty, M. Stiavelli, M. Greenhouse, E. Mentzell, R. Ohl, R. Green: „Optical Design for an Infrared Multi-Object Spectrometer (IRMOS)", SPIE Proceedings Vol. 4092

[3] E. Brinksmeier, W. Preuss: „Diamond Machining of the 3m Reflector of the KOSMA Submillimeter Telescope by a Single-point Fly-cutting Process", Proceedings of the ASPE, Monterey 1996

A FRAMEWORK OF A KNOWLEDGE-BASED SYSTEM FOR PREDICTIVE CHARACTERIZATION IN ULTRA-PRECISION DIAMOND TURNING

C.F. Cheung and W.B. Lee
Advanced Optics Manufacturing Centre, Department of Industrial and Systems Engineering, The Hong Kong Polytechnic University, Hung Hom, Kowloon, Hong Kong

Abstract: Most of the current methods of surface characterization provide only measures, parameters and patterns of the data without any prediction of useful information or recommendations for the improvement of surface quality in ultra-precision diamond turning. In this paper, a framework of a knowledge-based system (KBS) is proposed for predictive characterization of surface generation in ultra-precision diamond turning. The development of the KBS provides an essential means for the optimization of cutting strategy and diagnosis of process faults in ultra-precision diamond turning.

Keywords: knowledge-based system, predictive characterization, process optimization, faults diagnosis, surface generation, ultra-precision diamond turning.

1 Introduction

The methodology for the characterization of surface generation in ultra-precision diamond turning has been the subject of many theoretical and practical studies. This is due to the increasing demand for better surface finish, as exemplified by the reflection mirror for lasers in terms of longer life. Many methods have been developed for the measurement and the characterization of surface generation, ranging from the most widely used stylus method of determining the surface roughness parameters [1] to more recent methods based on optical principles in connection with 2D Fourier analysis [2]. However, most of the methods focus on static measures of surface roughness parameters, information and patterns of data. Relative little research was found in establishing dynamic and predictive measures which can be used to improve and optimize the cutting processes.

Ultra-precision diamond turning is an expensive process. Nowadays, the surface quality of diamond turned surface is still relied largely on empirical procedures and the technical skills of the operators. Numerous trial cutting tests are usually needed to establish optimal cutting strategy when new materials and new machines are used. They are not only time-consuming but also expensive. On the other hand, the skill and techniques incurred in ultra-precision diamond turning are complex which is composed of various tacit knowledge elements. There is a need for developing predictive measures and strategy for predicting cutting performance as well as assimilation of the tacit practice of the operators so as to optimize the surface quality in diamond turning. In this paper, the concept, the theoretical basis and the underlying assumptions in the development and the implementation of a knowledge-based system (KBS) for predictive characterization are discussed.

2 Predictive Characterization

The surface roughness profile of a diamond turned surface provides a faithful signature of the cutting process and the variation of material properties. In addition, an imprint of all static as well as dynamic forces, stresses, strains, material swelling and tool interference is left in the

surface roughness profile. The properties of the surface roughness profiles have been reported to be highly correlated to different surface generation mechanisms [3].

Predictive characterization makes use of data mining and model-based simulation techniques for the dynamic deduction and prediction of useful information and facts of cutting performance from the surface roughness profile data obtained in a test cutting. The implicit experience, tacit knowledge and skill of the machine operators as well as the implicit characteristics of machining system are captured by a case-based reasoning (CBR) algorithm. Hence, optimal cutting strategies such as optimum cutting conditions and the selection of cutting tools are derived by an inference engine for driving continuous improvement of surface quality as well as diagnosis of process faults in diamond turning.

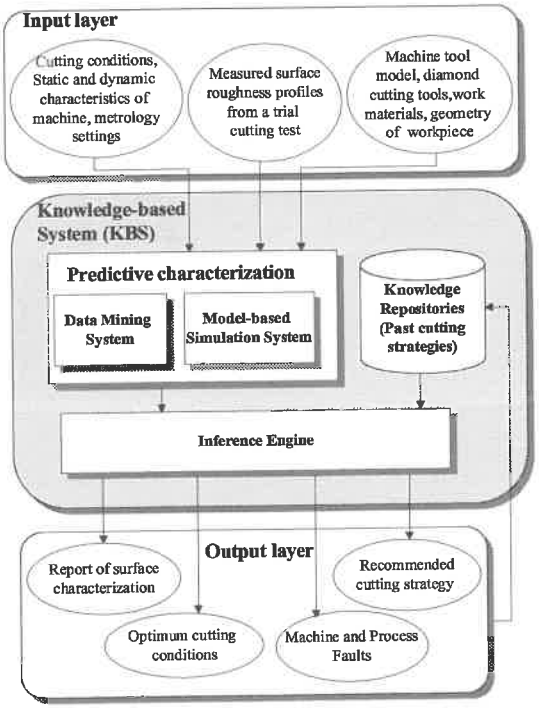
Input layer
Cutting conditions, Static and dynamic characteristics of machine, metrology settings
Measured surface roughness profiles from a trial cutting test
Machine tool model, diamond cutting tools, work materials, geometry of workpiece
Knowledge-based System (KBS)
Predictive characterization
Data Mining System
Model-based Simulation System
Knowledge Repositories (Past cutting strategies)
Inference Engine
Output layer
Report of surface characterization
Recommended cutting strategy
Optimum cutting conditions
Machine and Process Faults

Fig. 1 Schematic diagram of the framework of the KBS for predictive characterization

3 Framework of the KBS

The underlying design concept of the KBS for the predictive characterization is shown in Fig. 1. Basically, the KBS is composed of four components which are a knowledge repository, a data mining system, a model-based simulation system and an inference engine, respectively. The knowledge repository is built based on previous recommended cutting strategies. The surface roughness profile obtained in a trial cutting is analyzed by the data mining system and the model-based simulation system. The patterns, correlation and patterns discovered by the data mining system together with the optimum cutting conditions derived by the model-based simulation system are fed into an inference engine.

3.1 Data mining system

As shown in Fig. 2, the data mining system consists of two data mining models which are multi-spectrum analysis method [4] and multiple data dependent systems (MDDS) method [5], respectively. The multi-spectrum analysis of surface roughness profiles has been demonstrated to be useful for characterizing the influence of materials swelling [6], materials induced vibration [7], crystallographic orientation [8] and other factors such as spindle error motions and relative tool-workpiece vibration [9] upon the surface generation in diamond turning. For the MDDS method, it provides a parsimonious mathematical model for correlating the cutting dynamics and the factors affecting surface generation with their respective contributions to the total surface roughness of a diamond turned surface. Individual components composed of the surface roughness profiles and their contributions can be quantitative determined.

3.2 Model-based simulation system

A model-based simulation system has been built based on a surface topography model developed by the authors [10]. Fig. 3 shows a schematic diagram of the model-based simulation

system. The system is composed of the input module, the simulation module, the application module and the output module, respectively. The input module allows the inputs of the information of tool geometry, workpiece dimensions, process parameters, relative tool-work vibration as well as the metrology settings of the measuring instrument.

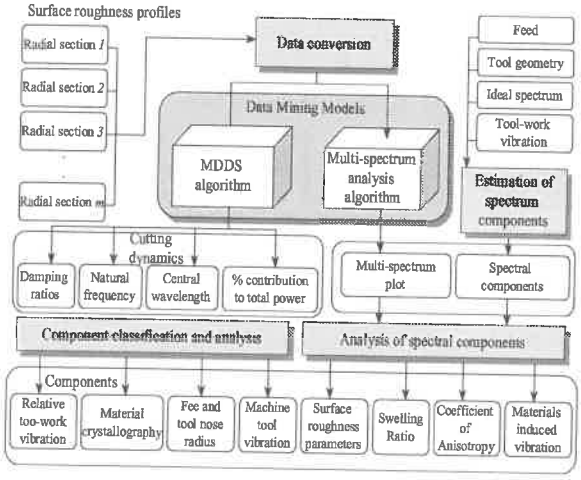

Fig. 2 A block diagram of the data mining system

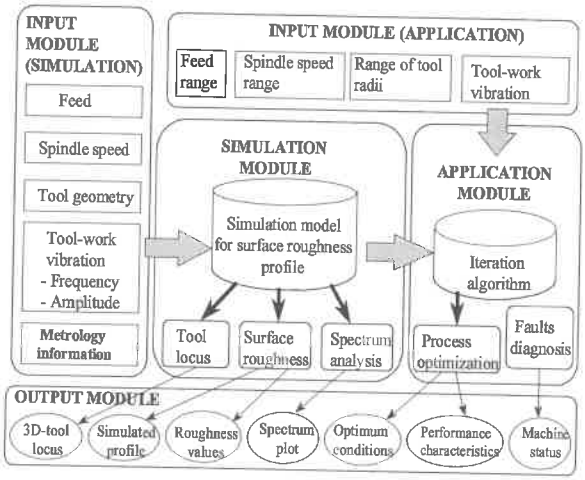

Fig. 3 A schematic diagram of the model-based simulation system [10]

The simulation module is capable of simulating the surface roughness profile and its power spectrum based on the kinematics of the cutting process. The application module is purposely built for the process optimization and the diagnosis of machine faults. Process optimization is done by an iterative algorithm which searches linearly for the optimum cutting conditions with an incremental step size within a pre-defined range of process and vibration parameters. The iterative algorithm is based on the surface roughness simulation model and the minimum surface roughness criterion. The outputs are the suggested optimum cutting conditions and the projected performance characteristic diagrams which depicts the variation of surface roughness with the process parameters being investigated. For the diagnosis of machine faults, a synthetic spectrum is firstly generated as a norm spectrum which is compared with the measured spectrum. Any outstanding components or significant differences between the synthetic and the measured spectra could be identified and checked for any abnormal states of the machining process. Based on the numerical data obtained from the simulation model and the spectrum analysis, the output module generates the results of the surface roughness analysis to the inference engine for further analysis.

3.3 Inference Engine

Inferencing is the central of reasoning for the knowledge-based system. Fig. 4 shows the conceptual design of the inference engine. In the present study, the inference engine is built based on a case-based reasoning (CBR) algorithm and the forward chaining rules are used to deduce the cutting strategy. A rule is in the form of "If PREMISE then CONCLUSION". Where PREMISE is a collection of conditions. For example, if "Power Spectral Density (PSD) of the feed components decrease (condition 1) and frequencies of the feed components shift to a lower frequency range (condition 2)" then "the presence of tool interference (conclusion)". According to the inputs from the data mining system and the model-based simulation system, the CBR cycle

starts with the retrieval of the closely matched cases based on a similarity function. The matched cutting strategy is reused and recommended for conducting the machining job. Then the recommended strategy is verified through a trial cutting test and the verified case is either revised or retained as a new case in the knowledge repository. Fig. 5 shows a snapshot of the recommended optimum cutting conditions by the inference engine of the KBS.

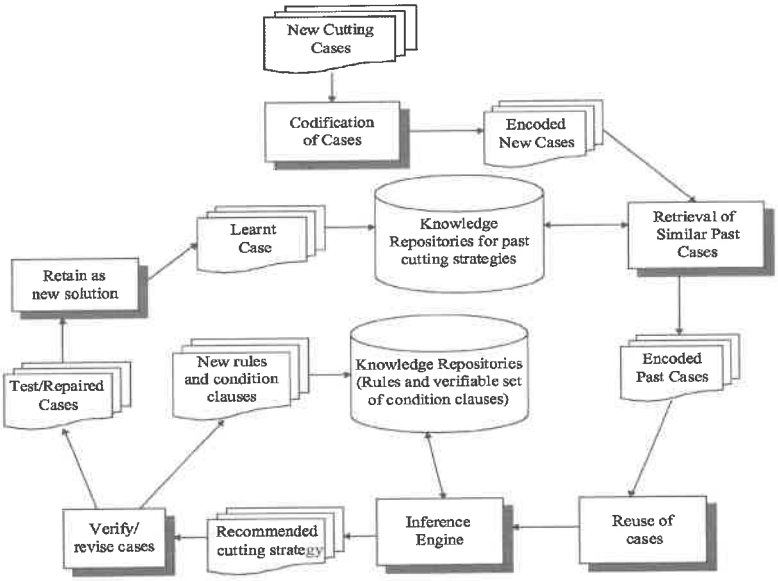

Fig. 4 Conceptual design of the inference engine

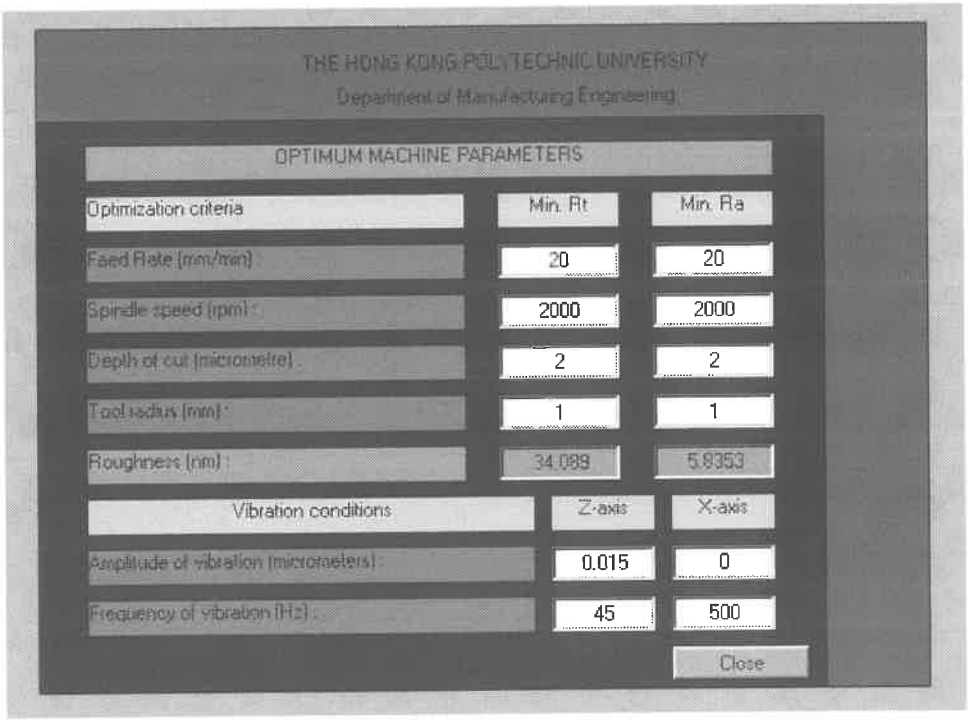

Fig. 5 Recommended optimum cutting conditions by the KBS

4 Concluding Remarks

Nowadays, the achievement of a super mirror surface finish in many industrial applications of ultra-precision diamond turning still depends much on the experience and skills of a machine operator through an expensive trial and error approach when new machine tools, new cutting setup and new materials are used. By integrating data mining, artificial intelligence and computer simulation technologies, a framework towards the building of a KBS for predictive characterization is presented. The successful development of the KBS will contribute to the identification of factors affecting surface generation as well as the prediction of the best cutting strategy for the optimization of surface quality in ultra-precision diamond turning.

Acknowledgements

The authors would like to express their sincere thanks to the Research Grants Council of the Hong Kong Special Administrative Region of the People's Republic of China for financial support of the research work under the project no. PolyU5188/01E.

References

[1] Thomas, T.R., Characterization of Surface Roughness," *Precision Engineering*, Vol. 3, p. 97-104 (1981).

[2] Sato, H. and O-Hori, M. "Characteristics of Two Dimensional Surface Roughness – Taking Self-excited Chatter Marks as Objective, *Annals of the CIRP*, Vol. 30, p.481-486 (1981).

[3] Cheung, C.F. and Lee, W.B. "Characterization of Nano-surface Generation in Single-Point Diamond Turning," *International Journal of Machine Tools and Manufacture,* Vol. 41, No. 6, p.851-875 (2001).

[4] Cheung, C.F. and Lee, W.B. "A Multi-spectrum Analysis of Surface Roughness Formation in Ultra-precision Machining," *Precision Engineering*, Vol. 24, No.1, p.77-87 (2000).

[5] Cheung, C.F. and Lee, W.B. "An Investigation of Cutting Dynamics in Single Point Diamond Turning," *JSME International Journal-Series C: Mechanical Systems, Machine Elements and Manufacturing*, Vol. 43, No.1, p.116-126 (2000).

[6] To, S., Cheung, C.F. and Lee, W.B. "Influence of Material Swelling Upon Surface Roughness in Diamond Turning of Single Crystals," *Materials Science and Technology*, Vol. 17, No. 1, p.102-108 (2001).

[7] Lee, W.B., Cheung, C.F. and To, S. "Materials Induced Vibration in Ultra-precision Machining," *Journal of Materials Processing Technology*, Vol.89-90, p.318-325 (1999).

[8] Lee, W.B., To, S. and Cheung, C.F. "Effect of Crystallographic Orientation in Diamond Turning of Copper Single Crystals," *Scripta Materialia*, Vol. 42, No. 10, p.937-945 (2000).

[9] Pandit S.M. and Revach, S. "A Data Dependent Systems Approach to Dynamics of Surface Generation in Turning," *Transactions of ASME, Journal of Engineering for Industry*, Vol. 103, p.437-445 (1981).

[10] Cheung, C.F. and Lee, W.B. "A Theoretical and Experimental Investigation of Surface Roughness Formation in Ultra-precision Diamond Turning," *International Journal of Machine Tools and Manufacture*, Vol. 40, No. 7, p.979-1002 (2000).

CHIPPING MINIMIZATION DURING DICING AND SLICING

Hans H. Gatzen[1], Gordon M. Jones[2], Alexey Karyazin[1]
[1]Institute for Microtechnology, Hanover University, Germany
[2]Seagate Technology, Bloomington, MN, U.S.A.

Key Words: Chamfering, Dicing, Slicing, V-shaped wheel

Abstract: Dicing and slicing are standard technologies for fabricating components for micro-electromechanical systems (MEMS). The dicing process influences the components' quality with respect to physical dimensions, surface quality, grinding induced subsurface damages as well as residual stresses, and edge chipping. For components in sliding contact with others, optimal edge quality is required to not risk failure of these parts during operation. This paper presents investigations aiming at the improvement of the edge quality during dicing of hard and brittle materials by utilizing V-shaped profiling wheels.

1. Introduction

The investigations were performed aiming at the improvement of the edge quality of a dicing cut by the use of V-shaped dicing diamond wheels (Slicing before V-grooving). Dicing and slicing of hard and brittle materials is accomplished by outside diameter high precision grinding [1,2]. As probe material for the investigations Al_2O_3-TiC ceramic was chosen. This ceramic has excellent mechanical properties and is also the material of choice for read-write heads in hard disk drives (HDD) [3].
For reducing edge chipping, the approach taken was to chamfer the right angled edge created by dicing by making a second cut with a V-shaped wheel. For the investigations, a metal bonded wheel with a 45° angle was used. In a second step, experiments were performed to examine the dependence of the chipping width on the cut length. Further tests focused on the deformation of the wheel profile due to wear using white light interferometry. This method proved to be well suited for monitoring the effect of wheel wear on the wheel shape and showed a linear increase of the wheel wear as a function of the cut length. To investigate which chamfer angle yields the best results, chamfering was also done at angles of 15° and 30°, respectively. For these tests, an edge quality analysis was performed on both transitions between upper surface and chamfer and between chamfer and kerf sidewall, although the main interest was focused on the chipping between the probe surface and the chamfer. In a following step, slicing tests were executed using dicing wheels with rectangular profile and V-shaped profile (V-grooving before Slicing). The experiments were performed with a rectangular profiled metal bonded wheel, choosing the parameters of the V-shaped wheel. For quantitative analysis the edge quality was developed a new measuring method. The method is based on analyzing edge images with a suitable software.

2. Experimental Procedure and Results

2.1. Relationship between Edge Chipping, Kerf Width, and Feed Rate for V-shaped Wheels

Experimental Procedure

For the investigations two types of dicing wheels were used: a rectangular profiled resin bonded wheel and a V-shaped metal bonded wheel. First the ceramic substrates were prepared with 300 µm deep rectangular cuts. The kerf width was approx. 80 µm. Chamfering was performed with the V-shaped wheel such that the chamfer width was 10 µm. This resulted in a kerf width of 100 µm including the chamfer on both sides. In order to examine the influence of the feed rate of the V-wheel on the edge quality and the kerf width, the feed rate was varied within a range from 1.0 mm/s to 40 mm/s.

Chipping Analysis

Kerf width and edge chipping were measured by optical microscopy. The following method was applied: the kerf was divided into five inspection intervals of 10 mm, with the first one beginning 25 mm off the work piece edge. In top view, the minimum kerf width (i.e. the width without chipping) and maximum kerf width (i.e. width inclusive chipping) were measured. For each pass, for both minimal and maximal kerf width, five measurements were taken and the average was determined. From these values, the amount of edge chipping can be calculated using the following equation:

$$w_C = \frac{w_{Kmax} - w_{Kmin}}{2} \qquad (2.1)$$

w_C is the chipping width, w_{Kmin} minimum and w_{Kmax} maximum kerf width, respectively.

Results

The left picture in Figure 1 shows the dependence of the kerf width on the feed rate of the V-shaped wheel. The kerf width remained constant up to a feed rate of 15 mm/s and increased substantially with higher feed rates. A potential reason for this effect was the rising load of the wheel resulting in increased vibrations. The right picture in Figure 1 depicts the chipping width as a function of the feed rate. On the diagram a slight increase of the chipping width over feed rates from 1 mm/s to 25 mm/s is visible. The further increase of the feed rate leads to a higher increase of the chipping. This effect is associated with the increasing kerf width due to higher wheel load. For the next phase, a feed rate of 10 mm/s was selected. At this feed rate kerf width and chipping were constant.

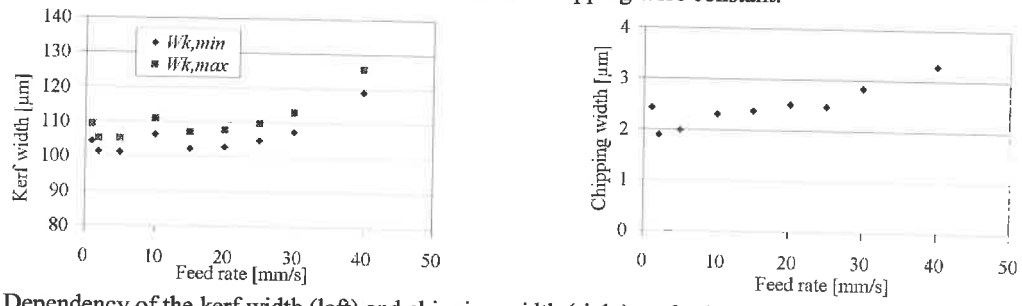

Fig. 1 Dependency of the kerf width (left) and chipping width (right) on feed rate of the V-shaped wheel

2.2. Long Term Test Observing Chipping and Wheel Wear by Using a 45° V-shaped Wheel

Experimental Procedure

After the feed rate variation, investigations for determining the dependence of the chipping width and the profile of the wheel on the cut length were executed with a constant feed rate of 10 mm/s. The measurements of the wheels' profile were performed with a white-light scanning interferometer. Measurements were executed on the new wheel and after 3,450, 6,900, 10,350, and 11,500 mm cut length. For each cut length, the average value of 4 measurements on every wheel side was calculated. The measuring field at the edge of the V-wheel was 140 µm (Fig. 2).

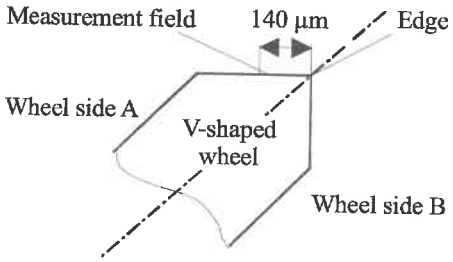

Fig. 2. Measurement field for the determination of the wheel wear

Wheel Wear Results

The measurements of the wheel revealed that the wear of the wheel with the rising cut length increases. Figure 3 depicts the wear at the two sides of the V-wheel as a function of the cut length.

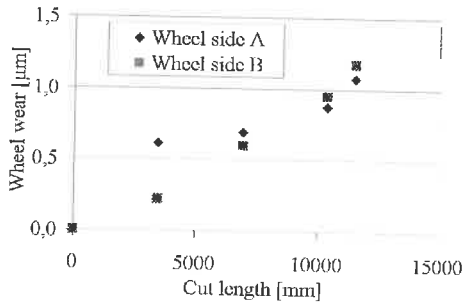

Fig. 3 Wear as function of cut length

Chipping Results

After dicing with the rectangular profiled wheel, edge chipping was determined. The chipping width remained at a constant average level but varied from 2.5 µm to 3.6 µm with an average value of 3.1 µm. Figure 4 shows SEM pictures of the edges after dicing with a rectangular profiled wheel.

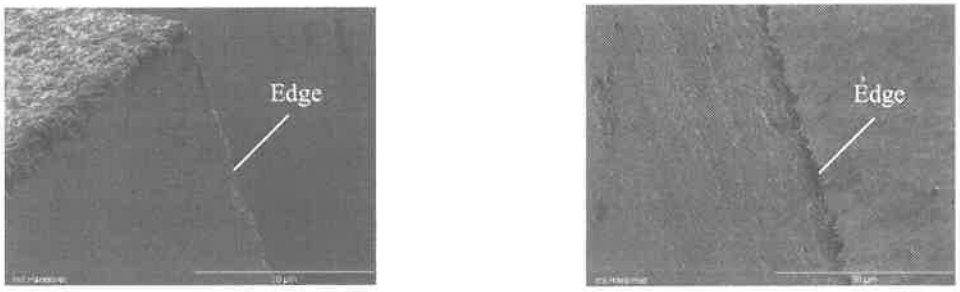

Fig. 4 Edges without chamfer

The chamfering cut with the V-shaped wheel was performed with a feed rate of 10 mm/s. The analysis of the chipping width showed an improvement of the edge quality. The average chipping width was 2.7 µm. The chipping width in the examining area was constant. Figure 5 shows SEM images of the cut with the chamfer machined with a V-shaped wheel. The chamfer angle is 45°.

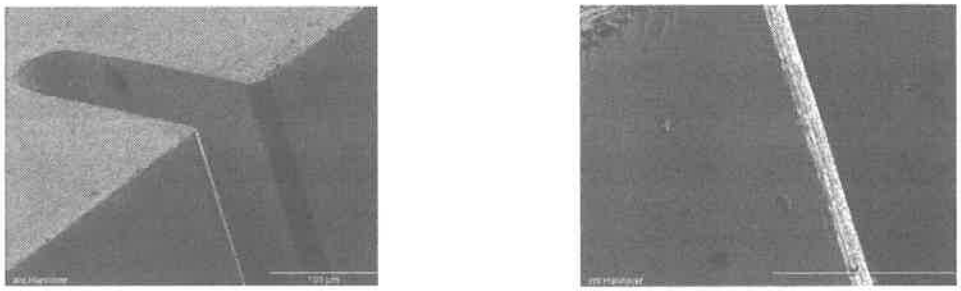

Fig. 5 Edges with 45° chamfer (left) and left edge after 6,900 mm cut (right)

The SEM figures visualize the quality of the chamfered edges which is substantially better than the unchamfered cuts (Fig. 4). Chipping occurs rarely and irregularly. Chip sizes are rather small, but occasional clusters of bigger chips are visible (Fig. 5 right).

2.3. Chamfer Angle Variation

Experimental Procedure

The influence of the chamfer angles on the edge quality was examined. Tests with chamfer angles of 45° (described in chapter 2.2), 30°, and 15° were performed (see Fig. 6).

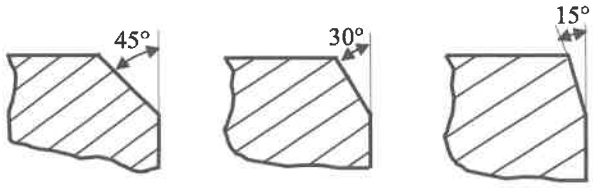

Fig. 6 Chamfer angle

Results

Figure 7 shows the chipping width in dependence of the chamfer angles and compares both edges between upper sample surface, chamfer, and kerf sidewall. As depicted in Fig. 7, the chipping width was minimal on the edge between chamfer and substrate surface at a chamfer angle of 45°. For chamfer angles of 30° and 15° the chipping

width of the two edges (edge between chamfer and sidewall and the edge between chamfer and substrate respectively) did not differ significantly. For the 45° angle the difference between both edges was 0.7 µm.

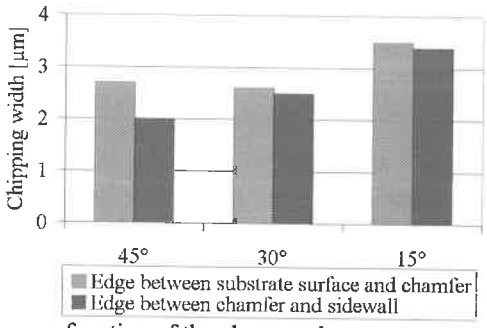

Fig. 7 Chipping width of the edge as a function of the phase angle

Fig. 8 shows high resolution SEM images of the edge between work piece surface and chamfer for the different angles investigated. Larger chipping width and longer chipping areas were typical for the edges with chamfer angles of 15°. The edge quality for a chamfer angle of 30° is clearly better than the 15° chamfer, and very similar to the edge quality of the 45° chamfer.

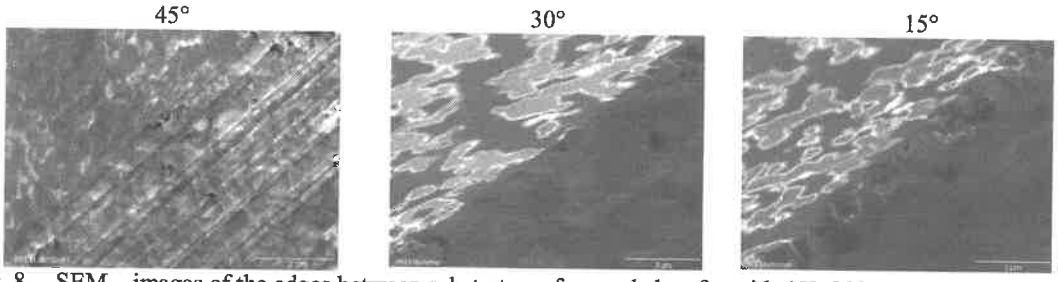

Fig. 8 SEM – images of the edges between substrate surface and chamfer with 45°, 30°, and 15° chamfer angles

Comparing all results led to the conclusion that a chamfer angle of 45° yielded the best results with regard to edge chipping.
V-grooving proved to be extremely sensitive to height variations of the substrate. At a 45° chamfer angle every µm height deviation caused a widening of the chamfer of 1 µm. To avoid this influence, the substrate needed to be mounted with minimum height variation. This refered to the chuck as well as the work piece mounted on the carrier (lava).

2.4. Slicing Tests Using Dicing Wheels with a Rectangular Profile and V-shaped Profile (V-grooving before Slicing)

Experimental Procedure

First the ceramic substrates were prepared with V-shaped wheel cuts. The width of the V-groove was approx. 100 µm. In the second step the slicing was executed with the rectangularly profiled wheel. The chamfer width was 10 µm. This resulted in a kerf width of 100 µm including the chamfer on both sides. The feed rate was 1.0 mm/s. The higher feed rate leads to very strong noises and too much chipping width. The feed rate of the rectangular profiled wheel was 0.3 mm/s. The test cuts were executed with a metal bonded rectangular profiled wheel with the same parameters than that of the V-shaped wheel. Before the tests the metal bonded wheels were dressed with a dressing stick.

Chipping Results

After dicing with the V-shaped wheel edge chipping was determined. The average chipping width of the edge between substrate surface and chamfer was 2.5 µm. This was smaller than the chipping results of chamfering fabrication process with chamfering after slicing. It can be attributed to the substantially smaller feed rate than that

of V-grooving before slicing. The chipping width of the edge between chamfer and sidewall was 2 µm. The greater feed rate of 10 mm/s leads to a larger chipping width of up to 200 µm.

2.5. Quantity Method of the Chipping Characterization

Experimental procedure

The analysis of the edge quality executed up to now gave us information regarding the chipping width for different dicing parameters. In order to quantitatively describe the edge quality, a special method was developed. It is based on the analysis of bitmap images taken by the CCD camera of a microscope. The value calculated is the chipping area in relation to the edge length (in the following called fiducial chipping area) according to the following equation:

$$Fiducial\ \ chipping\ \ area\left[\frac{\mu m^2}{\mu m}\right] = \frac{Chipping\ \ area\left[\mu m^2\right]}{Measurment\ \ field\ \ length\left[\mu m\right]} \qquad (2.2)$$

Results

The executed analysis of the edge images showed that the chipping surface was rising both for the edge between substrate surface and chamfer (upper edges), as well as for edges between chamfer and sidewall (lower edges) with a decreasing chamfer angle (Fig. 9). The fiducial chipping area of the lower edges for chamfer angles of 45° or 30° was smaller than the fiducial chipping area for the upper edges. For the chamfer angle 15° the fiducial chipping area values of the lower edge are higher than for the upper edge. A comparison of different processes for the phase fabrication showed that the fiducial chipping surfaces are smaller when applying the 'Slicing before V-grooving' process (Fig.10).

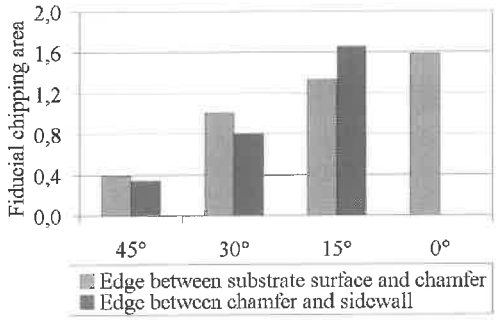

Fig. 9 Fiducial chipping area in $\mu m^2/\mu m$ as a function of the chamfer angle with the chamfer production with the 'Slicing before Chamfering' process

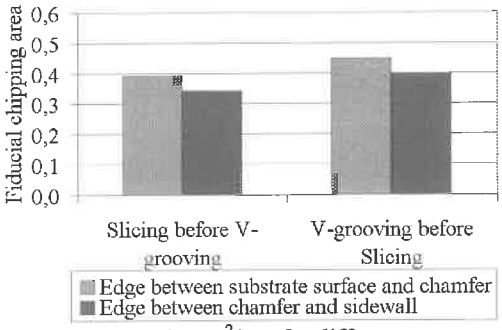

Fig. 10 Comparison of the fiducial chipping area in $\mu m^2/\mu m$ for different processes for the phase fabrication

3. Conclusions

The executed investigations showed that the chipping results for dicing with V-shaped wheels (chamfer 45°) were better than those obtained with a rectangular profiled wheel. The kerf width and chipping width of the chamfered cut rise with increasing feed rate. The chipping width of the edge between chamfer and sidewall was higher for a

chamfer angle of 15° than for chamfer angles of 30° and 45°. For these edges the chipping width also decreased with increasing chamfer angle. A chamfer angle of 45° yielded the best results with regard to edge chipping. V-grooving was extremely sensitive to height variations of the substrate. Due to the angle of the chamfer height variation directly translated into variations of the chamfer width. A comparison of different processes for the chamfering showed that the fiducial chipping area of the 'Slicing before V-grooving' process were smaller than for other processes.

Acknowledgement

Conference attendance was sponsored in part by the Cray Foundation.

References

[1] Komanduri, R.; Lucca, D.A.; Tani, Y.: Technological Advances in Fine Abrasive Processes. Annals of the CIRP Vol. 46 (1997) No. 2, pp. 545-596

[2] Beltrao, P.A.; Gee, A.E.; Corbett, J.; Whatmore, R.: Ductile Mode Machining of Commercial PZT Ceramics. Annals of the CIRP Vol. 48 (1999) No. 1, pp. 437-440

[3] Gatzen, H.H., Maetzig, J.C., Schwabe, M.: Precision Machining of Rigid Disk Head Sliders, IEEE Transcations of Magnetics, Vol. 32, No. 3, May 1996

Dicing of Ultra-thin Silicon Wafers

Hans H. Gatzen, Gerald Guenzel
Institute for Microtechnology, Hanover University, Germany

Keywords: dicing, ultra thin wafers, silicon, chipping, machining

Abstract: One of the most recent semiconductor technology mass products are very thin devices like smart cards and smart labels. These devices require ultra thin wafers, while cost reasons dictate a high packaging density. For wafer separation, a combination of minimal street width and a maximal feed rate is required. For developing an optimized dicing process, dicing investigations were conducted. For the investigations, five different electroplated dicing wheels with various grain size and concentration of diamond grit and with a wheel thickness varying between 15 and 100 µm were used. The feed rate was varied from 10 mm/s to 100 mm/s. As a result, chipping and feed rate showed a non-linear dependency with a clear local minimum of chipping.

1. Introduction

Smart cards and smart labels are thin plastic devices containing a computer chip holding for instance information for medical, financial or insurance use. As smart cards are twistable, credit card sized plastic artifacts, the smart labels are made of a thin polymer film laminated in-between paper sheets or plastic foils.
Smart cards and smart labels require ultra thin wafers, while cost reasons dictate a high packaging density in conjunction with an optimal usage of the wafer real estate, i.e. the accumulative kerf and chipping width, called street width, between individual devices has to be as small as possible. At the same time a high feed rate is required for an economic execution of the separating process [1]. Investigations were conducted for determining the best combination of cutting parameters for the separation of 50 µm thin silicon wafers. The challenge was to find cutting conditions with both a maximal feed rate and a minimal chipping for separating very thin silicon wafers with a thickness of only 50 µm.

2. Experimental Setup

For the experiments with the thin wafers a precision dicing machine was used. This machine was equipped with an air-bearing spindle designed for accepting dicing wheels with an outer diameter of approx. 2 inches. To minimize the environmental influences, the experiments were carried out in a temperature controlled room at 20 °C (±1 °C) [2]. In order to conduct the investigations, the wheels had to be conditioned. First, the dicing wheels were trued to insure that the dicing wheel is rotating concentrically around the spindle. To do so, the dicing wheel was mounted on the spindle; afterwards, the wheel circumference was ground by a SiC cup wheel. In a next step, the dicing wheel was dressed by cutting a couple of dozen times into a SiC block to exposure the diamond grains by recessing the softer metal bond [3].

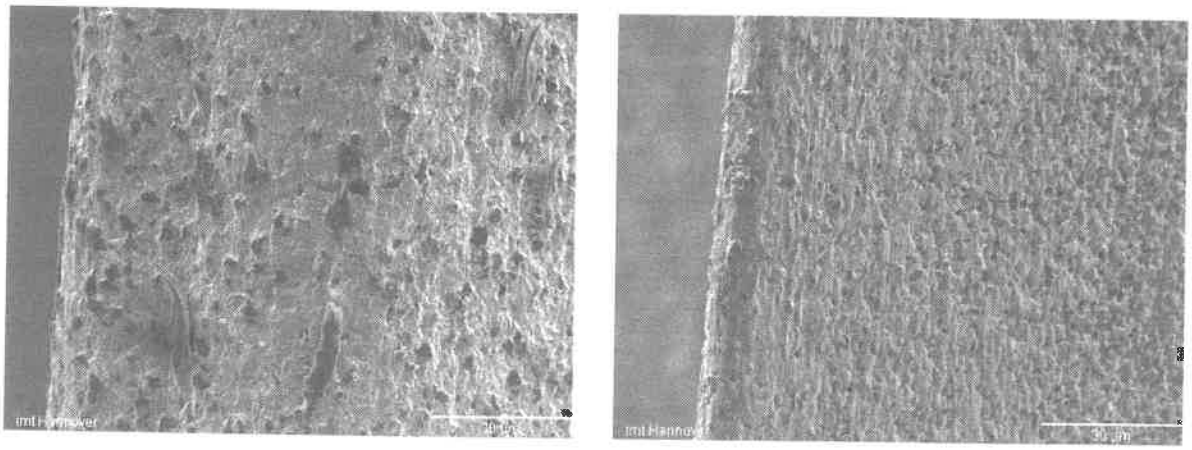

Fig. 1: SEM pictures of dicing wheels 2.187 4-5 NiF (left) and MCT Q 241540(right)

For the investigations, 50 µm thick silicon wafers with a diameter of 6 in were used. They were attached to a rigid substrate by a double sided adhesive tape. This sandwich was mounted directly on the vacuum chuck of the dicing machine. For each combination of wheel and feed rate, three cuts were made. The cut depth was 70 µm, with the tape scribed at a depth of 20 µm. The kerf to kerf spacing was 500 µm. Due to the low hardness of the silicon the diamonds of the dicing wheel became blunt very slow. Therefor in-process dressing wasn't needed

For the evaluation and to compare the dicing results, every cut kerf was divided into 6 sections. Every section had a length of 5 mm. The size of the biggest chipping at both kerf edges was measured separately. With the measurements obtained, the arithmetic average C_m and the standard deviation S were calculated. By using the values C_m and S the cut quality between different cuts was compared. For these investigations, a microscope with a magnification of 1000x was used.

The grain concentration was determined with scanning electron microscopy (SEM), taking advantage of its great depth of focus and the wide magnification range of this metrology. The cutting area of all dicing wheels under investigations consisted of a homogenous diamond-metal-matrix. There were no differences in diamond concentration between the circumference and the wheel's sidewall. As a consequence, the investigations were conducted on the wheel's side wall since measurements were easier than at the circumference. For each dicing wheel under investigation, three micrographs from different areas of the sidewall were taken.

In a second step, the areal grain concentration was determined. By dividing the average number of grains by the size of the measured area, this value was calculated. The average grain exposure was determined with atomic force microscopy (AFM). On each dicing wheel, three areas with a size of 100 µm x 100 µm each were measured and for each area five profile cuts with a distance of 25 µm from each other were established.

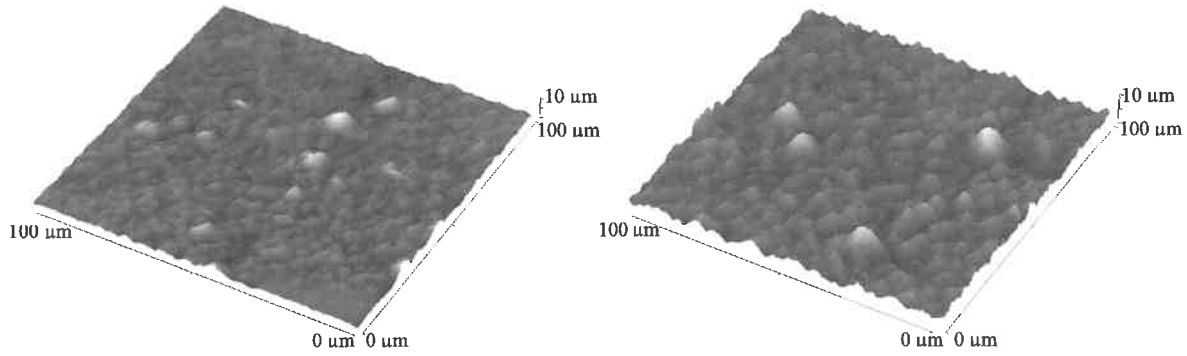

Fig 2: AFM scans from MCT Q 241540 (left) and MCT Q 461540 (right)

For each profile cut a reference line was found. This line divided the measured profile such that the squares of the deviations on both sides was the same. The greatest deviation from this reference line was asumed to be the grain exposure. This measurement coinsides with value R_p as defined by ISO 4287/1 [4]. The value for average grain exposure was the average taken off the 15 values of each dicing wheel.

3. Machining Parameters

The experiments were carried out with metal bonded dicing wheels with different grain sizes from various manufacturers. Table I provides an overview over the dicing wheels used for the investigations.

TABLE I
DICING WHEELS USED FOR THE INVESTIGATIONS

Wheels	Manufacturers	Wheel width	Grain size
MCT Q 241540	Mitsubishi	15 µm	2-4 µm
MCT Q 461540	Mitsubishi	15 µm	4-6 µm
55.8 x 0.16 x 40 PD3/6 Mic	Norton	16 µm	3-6 µm
2.187 4-5 NiF	microkerf	100 µm	5 µm
2.187 4-10 NiF	microkerf	100 µm	10 µm

The dicing wheels from Mitsubishi were hub-type. For this wheel type the dicing wheel is bonded to an aluminum hub serving as a carrier. The hub was mounted directly on the spindle of the dicing machine. Since all other dicing

wheels were hubless, they had to be mounted on the spindle with a precision pair of flanges. The 50 µm thick silicon substrate was mounted on a rigid carrier using a double sided adhesive tape. This carrier, a simple blank silicon wafer, made the handling much easier. The whole package was held directly by a vacuum table on the dicing machine.
The cutting speed was v_c= 105 m/s (approx. 36,000 rpm). The cut depth was d_c= 70 µm, and the feed rates were varied in six steps by 10 / 30 / 50 / 64 / 80/ 100 mm/s.

4. Results

The evaluation of the cutting experiments are demonstrated in Fig. 3.

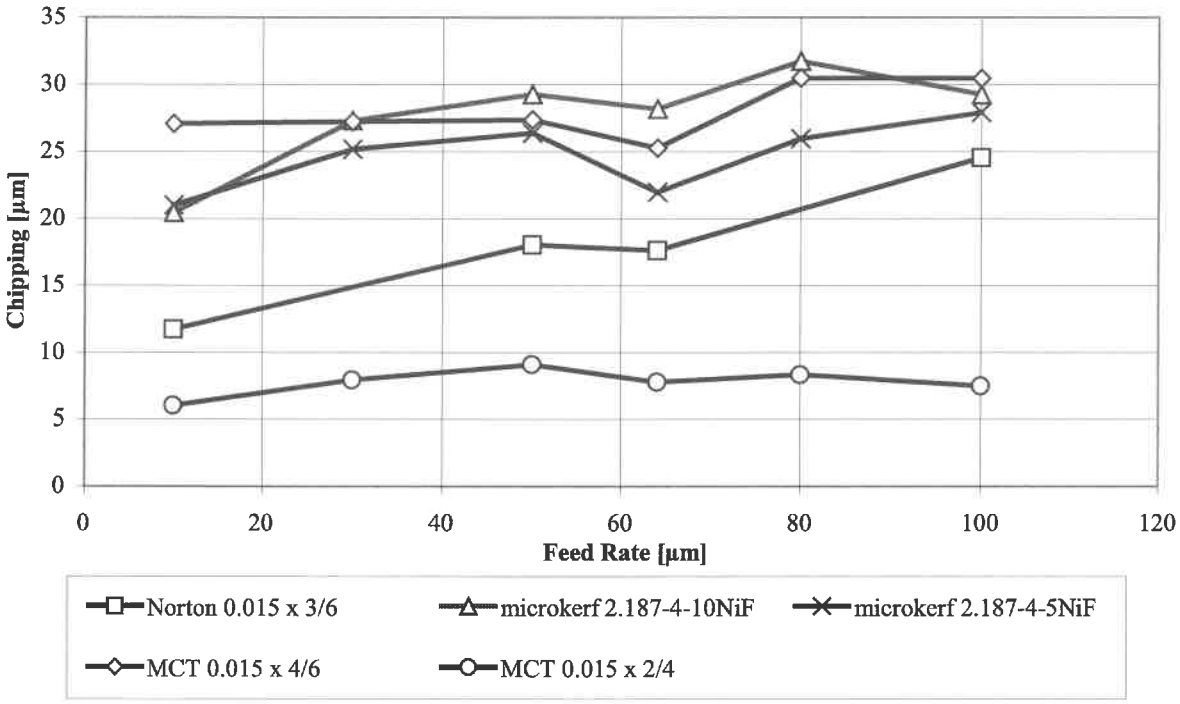

Fig. 3: Results of chipping evaluation

When machining thin wafers, the dependence of the chipping on the feed rate for the investigated dicing wheels can be easily deducted. For the hubtype Mitsubishi wheels, the influence of the feed rate on the chipping is weak. However, the grain size effects chipping quite strongly. For the remaining wheels, all of them hubless, the chipping depends much stronger on the feed rate and is less inflicted by the grain size.
Interestingly, there is a distinctive local minimum in chipping at a feed rate of v_f= 64 mm/s for most dicing wheels. The respective ratio of v_c / v_f is 1640 at a cutting speed of v_c= 105 m/s (≈36,000 rpm). This effect can be observed independently from wheel width, mounting system (hub type or hub less), and grain size. Only the dicing wheel with the grain size of 2 to 4 µm does not exhibit this effect, but at a feed rate of v_f= 64 mm/s the chipping decreases as well. In the graph of the microkerf 1.187-4-5 NiF (grain size 5 µm) in Fig. 3 the local minimum is very strong. The wheel by Norton with approx. the same grain size of 4.5 µm shows a much weaker effect.

TABLE II
GRAIN CONCENTRATION, GRAIN EXPOSURE, GRAIN SIZE

Dicing Wheel	Grain Concentration	Grain Exposure	Grain Size
MCT 0.015 x 2/4	4.03 grains / 100 µm²	1.01 µm	3 µm
MCT 0.015 x 4/6	2.22 grains / 100 µm²	1.21 µm	5 µm
Norton 0.015 x 3/6	4.62 grains / 100 µm²	2.03 µm	4.5 µm
2.187 4-5 NiF	2.26 grains / 100 µm²	2.53 µm	5 µm
2.187 4-10 NiF	0.84 grains / 100 µm²	4.76 µm	10 µm

In Table II the average grain concentration and the average grain exposure are evaluated. There is a linear dependency between grain size and grain concentration. The larger the grain size, the lower the grain concentration.

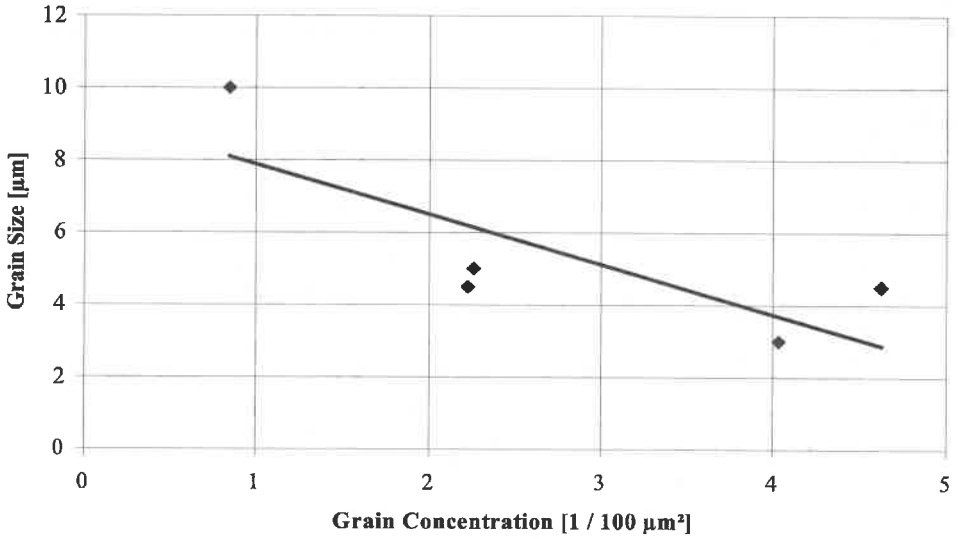

Fig. 4: Dependency between grain concentration and grain size

The influence of the wheel parameter grain concentration, grain exposure and grain size wheel on the chipping are quite similar. For the investigation the average of the chipping size of all feed rates was taken. The average chipping size is not proportional to the average grain size and to the average grain concentration. Figure 5 shows the dependence between average grain size and average chipping.

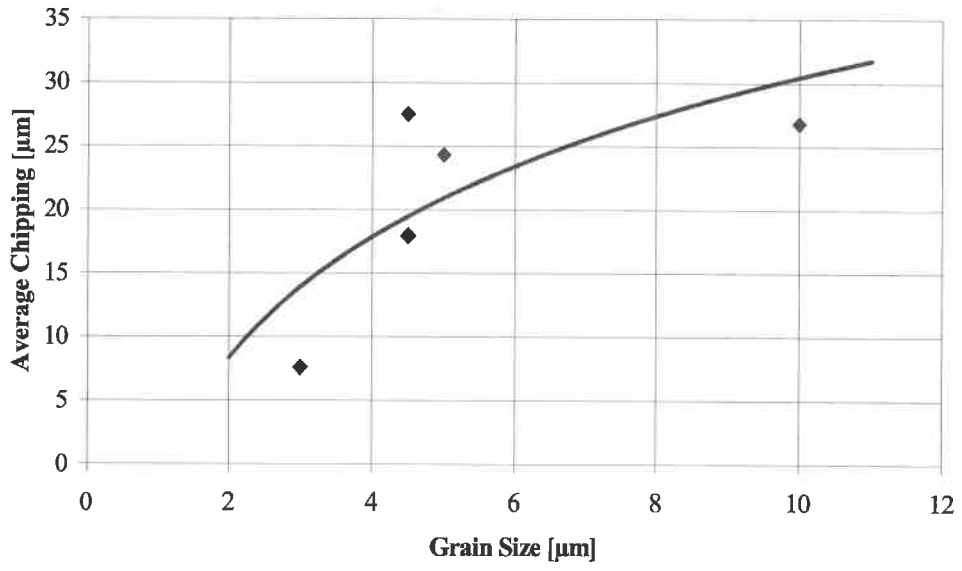

Fig. 5: Influence of the grain size on chipping

Since there is a linear dependency between grain size and grain concentration (Fig. 4) the influence of the grain concentration on the average chipping is similar. Figure 6 shows the influence of the average grain exposure to the average chipping. The cut quality decreased with an increasing in grain exposure.

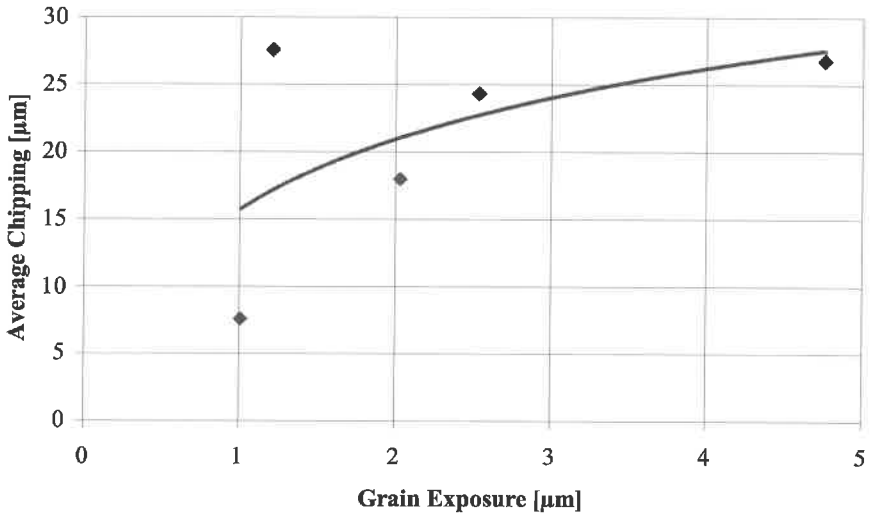

Fig 6: Influence of the grain exposure on chipping

5. Conclusion

To achieve an economic dicing process for ultra–thin silicon wafers, several cutting parameters had to be co-ordinated. On the one hand, the wheel parameters has to be optimized. For achieving minimal chipping, the dicing wheels should have high grain concentration, small grain size and low grain exposure. Due to this parameter combination the removal per grain is low and hence the chipping is low as well. On the other hand, the cutting parameters of the dicing machine had to be optimized. The experiments demonstrated the independence of the cutting parameter from the wheel parameters. For all wheels the best cutting quality resulted at a feed rate of v_f=64 mm/s with a a cutting speed of v_c= 105 m/s. This is a ratio of v_c /v_f = 1640. In combination of all this coordinated parameters a street width of less than 32 µm was achieved.

Acknowledgement

This research is sponsored by the 5th framework „Competitive and Sustainable Growth“ of the European Commission. Attendance for the conference was sponsored in part by the Cray Foundation, Hanover, Germany.

References

[1] Inasaki, I.: Dicing Of Silicon Wafers. Abstracts MicroMat 2000, Berlin, Germany, Apr. 2000, p. 154
[2] Gatzen H.H: Mikrobearbeitung sprödharter Kermikwerkstoffe mittels Trenn- und Profilschleifen. 59. Jahresband Schleifen Honen, Läppen und Polieren, 1999
[3] Gatzen, H.H.; Jones, G.M.; Morsbach, C.: Investigations on the Wear Profile of Dicing Wheels. Proc. ASPE 14th Ann. Meet., Monterey, USA, Oct.-Nov. 1999, pp. 67-70
[4] ISO 4287, Terms, definitions and surface texture parameters, 1997

MECHANICAL MICROMACHINING OF HIGH ASPECT RATIO MICRO-STRUCTURES

Hans H. Gatzen, Caspar Morsbach, Alexey Karyazin
Institute for Microtechnology, Hanover University, Germany

Key Words: precision machining, ductile machining, dicing, profiling, high aspect ratio microparts

Abstract: The investigations presented in this paper focused on the potentials of precision outside diameter grinding for the fabrication of high aspect ratio microparts. The material used was a two phase polycrystalene advanced ceramic. The goal was to create high aspect ratio parts standing freely, allowing to study how to optimize the fabrication process. Since structures with a minimal cross-section and a maximum length were desirable for the investigations, obelisk structures (i.e. columns with a square cross-section and an pyramidal tip) were selected for demonstrating the process capabilities. Subsurface damages as well as lateral cutting forces may cause a breakage of the parts therefore, the challenge was to minimize both. As cutting tools, 200 µm wide resin bonded diamond wheels were selected, their diamond grit was varied between 5 µm and 45 µm. The technology study revealed the machining capabilities of high aspect ratio outside diameter grinding. The aspect ratio achieved during the study was 27 to 1. The creation of pointed tips also shows that the process, although within stringent imitations, is capable of creating 3-D parts.

1. Introduction

Due to its high performance in regard of precision, as well as edge and surface quality, outside diameter grinding is an ideal technology for machining hard and brittle materials. An important application of this technology is the separation (or "dicing") of microelectronic components fabricated on silicon substrates. It is also used for machining glass as well as mono- and polycrystalline ceramics utilized as wafer for micro electro-mechanical systems (MEMS). For this purpose, highly accurate machines are available which allow the machining of separation cuts with a submicrometer accuracy. Dicing wheels consist of a resinoid or metallic binder which holds a matrix of abrasive grains and range from 15 µm to 1 mm in thickness. Since wafer materials usually are hard and brittle, diamond grain is the abrasive of choice. Typical grain sizes for dicing wheels are between 2 µm and 45 µm. In order to evaluate the potential of this technology for the fabrication of three-dimensional microparts, investigations were performed with the goal to maximize the aspect ratio of small footprint structures. Previous efforts centered on fabricating high aspect ratio microparts by first creating membranes and then slicing them to create resonator type structures by mechanical micromachining [1]. The work presented in this paper focused on the fabrication of column-like structures. Two factors limit the achievable aspect ratio: lateral forces exerted from the dicing wheel which cause breakage of the parts during machining and grinding induced subsurface damages. Breakage may be reduced by appropriately choosing the wheel parameters. A minimization of subsurface damages is achieved by machining in a ductile mode. Ductile machining takes advantage of the phenomenon that it is possible to plastically deform brittle materials under certain conditions. By selecting machining conditions resulting in a predominantly ductile mode machining, the formation of subsurface microcracks is minimized. As a result microstructures with very small lateral dimensions on the order of some ten micrometers may be created. Factors promoting a plastic flow during abrasive machining are a small depth of cut of the single diamond grain and a great hydrostativ pressur caused by the negative rake ankle of the cutting tool [2, 3]. A low depth of cut can be achieved by choosing suitable process parameters; while a negative rake angle is present due to the shape of the blocky shape of diamond grains. The goal of the work performed was to find process parameters to reduce both the lateral forces subsurface and the subsurface damages. To do so, a compromise between reduced forces and a ductile grinding mode had to be found.

2. Experimental Procedure and Results

2.1. Machine and Workpiece Material

For the investigations a commercial dicing machine was used. It is equipped with a precision air bearing spindle, air bearing guides of the feed axis and a highly rigid machine body. The spindle's rotational velocity is up to 40,000 RPM. A feed rate between 0.01 mm/s and 100 mm/s was chosen. The machine's pitch accuracy, i.e. the accuracy of two parallel dicing cuts, is 0.2 µm. The material for the dicing experiments was Al_2O_3-TiC (Altic), a dual phase, advanced ceramic which is commonly used for the manufacture of read/write heads in rigid disk drives. The composition of the material is 64% Al_2O_3 and 36% TiC. Due to its high density, the fine dispersion of the two

phases, and the small average grain size of below 1 µm it has a rather high fracture toughness index of 4.1 MPa $m^{-1/2}$ [4]. These properties make Altic an ideal material for the fabrication of microstructures, since it exhibits a, compared to other ceramics, high resistance against brittle fracture propagation.

2.2. Minimizing the Structure Width

As mentioned above, two factors limit the dimensions of high aspect ratio parts: the extent of microcracks, that weaken the part and the grinding wheel's axial forces. In order to investigate the lower limit of structural cross section achievabe by a dicing process, the following approach was chosen: by grinding parallel slots with a regressive pitch (distance between two slots), walls were created with decreasing thickness. The distance between two cuts decreased with an increment of 5 µm from 100 µm down to 30 µm. This way, the limit in wall width that was achievable with the parameters and wheels used could be identified. Based on the results of former investigations, all parameters except the diamond grain size were kept constant. Table 1 summarizes the process parameters. By grinding a kerf in two depth steps with a depth of cut of 0.4 µm in each step, the total depth of the kerfs added up to 0.8 mm.

TABLE 1
PROCESS PARAMETERS

Parameter	Unit	Value
Wheel Parameters		
Binder		Resin
Diameter	mm	55.6
Width	mm	0.2
Diamond grain size d_g	µm	5, 15, 30, 45
Dicing Parameters		
Feed rate v_f	mm/s	0.4
Depth of cut a_e	mm	0.4
Cutting speed v_c	m/s	55
Coolant flow rate V'	l/min	1

The variation of the diamond grain size revealed a dependency of he achievable minimum structure of the grit size. The 5 µm grit wheel failed in the second depth step due to destruction. The best result in respect to wall width were achieved with a 45 µm diamond size wheel. The minimal wall width was 30 µm. The other two wheels, with a width of 15 µm and 30 µm, respectively, led to a destruction of the walls at thicknesses above 30 µm. Figure 1 shows a SEM image of the walls created using a 45 µm diamond grit. With a thickness of 30 µm and a height of 0.8 µm the aspect ratio is 27 to 1.

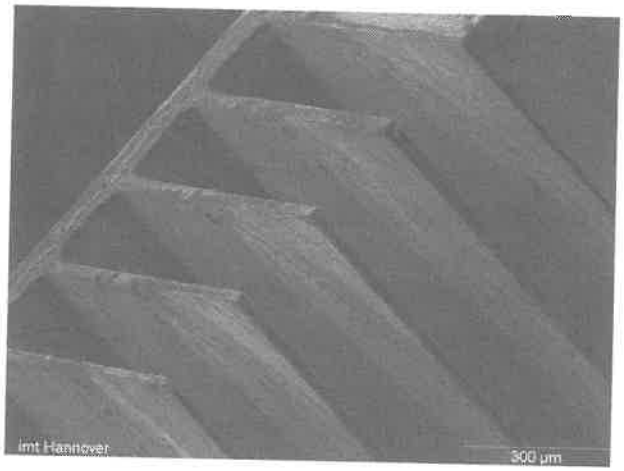

Fig. 1 Test structures machined with a 45 µm diamond grit resinoid bonded dicing wheel

The fact that a coarser grit leads to better results in regard of wall width may seem surprising, since it is known that finer grits usually yield better surface quality and reduced subsurface damages. In order to take a closer look at the damages caused by the abrasive action on the workpiece surface, investigations of the kerfs' sidewalls where performed, as described in the following chapter.

2.3. Grinding Mode Considerations

An investigation of the workpieces' sidewalls showed the diamond grit's influence on the surface roughness. Investigations were performed using a white light interferometer. The dicing parameters were the same as documented in Table 1 but due to the early failure of the 5 µm diamond size wheel only one depth step was realized with this wheel. Therefore, in this case the total depth of cut was only 0.4 mm. The surface roughness was measured parallel and perpendicular to the feed direction. The two values vary slightly, since grooves on the sidewalls, formed by the interaction the workpiece and diamonds protruding from the wheel's sidewall have a prevailing orientation parallel to the feed direction. Therefore, the roughness value perpendicular to the feed direction was always greater than parallel to it. Figure 2 depicts the sidewall roughness as a function of the diamond grain size, with R_{ay} the roughness perpendicular and R_{ax} parallel to the feed direction.

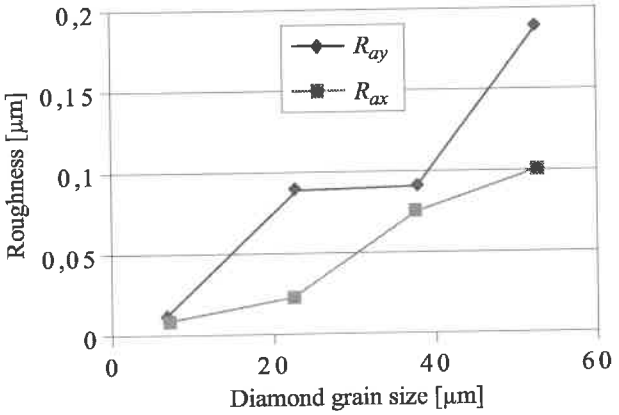

Fig. 2 Sidewall roughness as a function of the diamond grain size

The increase of the sidewall roughness is obvious. But the total values, ranging from 0.01 µm for a 5 µm grit to 0.1 µm for the 45 µm grit are indications for a predominantly ductile cutting mode. In order to verify this assumption, an analysis of the chips produced during grinding was performed. Therefore, the coolant was collected in the machine's coolant drain, and filtered with a paper fine filter with a pore size of 0.3 µm. Each filter was dried and subjected to a scanning electron microscopy (SEM). Figure 3 shows Altic chips produced by dicing with a 45 µm diamond grain size resin bonded wheel.

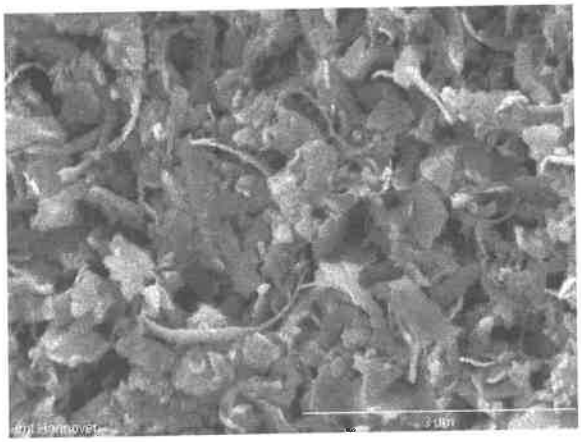

Fig. 3 SEM micrograph of Altic chips collected during machining with a 45 µm diamond grit dicing wheel.

The spectrum of chip shapes indicated a cutting mode at the transition from ductile to brittle fracture. Two types of chips could be detected: blocky chips, which are a result of a brittle fracture propagation as well as long and long and narrow chips formed by plastic deformation. The ratio in the number of both types of chips rather pointed towards a that the cutting mode was predominant brittle. Nevertheless, the partially ductile cutting mode, as indicated by the glossy surface and the presence of plastically deformed chips provided an explanation for the capability of the dicing wheel to machine rather fragile structures. On the other hand, it did not explain why the poor finer grit wheels (< 45 μm) were inferior in fabricating high aspect ratio microstructures. A potential reason was the forces exerted from the wheels on the workpiece during machining. Due to the high aspect ratio, the structures were extremely sensitive to lateral forces. These forces were a result of the stress field induced by the interaction between tool and workpiece. The stress field originated from the point of engagement of the diamond grains in the cutting zone and from frictional forces between workpiece and abrasive products squeezed in between wheel binder and workpiece surface. With respect to the latter phenomenon, wheels with a coarse grit are superior to fine grit wheels, as they provide more space between single abrasive grains due to a wider distance and larger grain protrusion. Therefore the stress field induced by coarse wheels is much lower then the one induced by fine grit wheels.

2.4. Fabrication of Microcolumns

In order to demonstrate the potential of the process described above, obelisk shaped columns with a square cross-section and pyramid like tips were manufactured applying the following process sequence. First, a desired cross section was selected. Since 30 μm was the minimum value achieved during the machining of walls, and columns yield a lower resistance against axial forces, a 40 μm x 40 μm footprint was chosen. Next, a shallow waffle pattern was ground to create the pyramid tips. The cut depth was 50 μm and a wheel with rounded edge profile was used, creating the slopes of the tips. In a third step, 800 μm deep grooves in x-direction were formed by a dual cut of 400 μm depth each, creating walls of a thickness of the desired cross section. For creating the columns, it was found necessary to backfill the grooves. This was mainly necessary due to the coolant jet directed tangentially to the wheel into the grinding zone. The forces from the coolant jet were destroying the structures during machining if they are not stabilised by backfilling. As material, the same hot glue used for mounting the workpieces to carriers was chosen. Cutting the grooves in y-direction followed the same fabrication sequence previously applied for generating the x-grooves. Removing the hot glue with acetone completed the fabrication sequence. Figure 4 depicts an array of the columns fabricated that way.

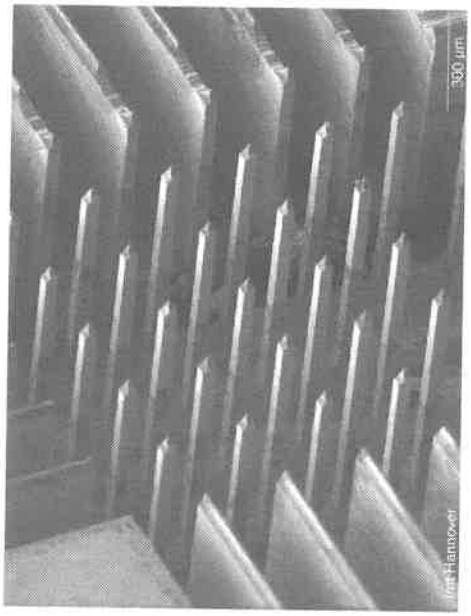

Fig. 4 SEM micrograph micro-columns with a pyramidal tip

3. Summary and Conclusions

The work presented in this paper demonstrates the potential of a modified dicing process to fabricate three-dimensional, high aspect ratio micro-parts. By using a resinoid wheel with a rather coarse grit of 45 µm, walls with a minimum thickness of 30 µm and an aspect ratio of 27 to 1 could be created. Investigations of the workpieces' sidewalls and of the abrasive product revealed, that the process parameters resulted in a partially ductile machining mode. A coarse grit proved to be advantageous because it offered sufficient space for the removal of abrasive products from the machining zone and therefore minimizes the effect of friction between tool and workpiece, which subsequently leads to high axial forces. As a for instance of high aspect ratio three-dimensional parts, obelik shaped columns with a pyramidal tip were manufactured applying the above the beforehand developed process. The footprint of these columns was 40 µm x 40 µm and with a height of 800 µm the aspect ratio is 20 to 1. For the manufacture of the columns a technique was developed to support the structures during the last machining step in order to prevent destruction caused by the impact of coolant.

Acknowledgement

The research presented in this paper was in part sponsored by the German Research Foundation (DFG) in the priority program "Micro Mechanical Production Technology". Furthermore, the authors would like to acknowledge the Cray Foundation, Hanover, Germany, providing support for attending the conference. Attendance for the conference was sponsored in part by the Cray Foundation.

References

[1] Gatzen, H.H., Beck, M., Zeadan, J.: Technological Challanges in Ultraprecision Grinding of Flexural Resonators. Proc. 1st euspen Intern. Conf., Vol 1, Bremen, (1999).

[2] Ngoi, B.K.A.; Sreejith, P.S.: Ductile Regime Finish Machining - A Review. Int. J. Adv. Manuf. Techn. (2000), pp. 574-550

[3] Patten, J.A.; Gao, W.: Extreme Negative Rake Angle Technique for Single Point Diamond Nano-cutting of Silicon. Prec. Eng. Vol. 25 (2001), pp: 165-167

[4] Sumitomo Special Metals product information

Cutting Conditions of an Engineered Tool with the Ultrasonic Excitation

Hiroshi Hashimoto, Kenichiro Imai

Kanagawa Institute of Technology

Shimo-Ogino 1030, Atugi-shi, 243-0292 Japan

Fax 81-463-93-5440

e-mail hasimoto@me.kanagawa-it.ac.jp

Keywords: engineered tool, ultrasonic machining, brittle materials, critical depth of cut、total depth of cut

1 Introduction

The laser machined diamond has many posts which correspond to the diamond grits on a grinding wheel. Post motion by ultrasonic excitation achieves an intermittent removal mechanism for a critical depth of cut and, as a result, depending on the number of posts, makes it possible to make a very large total depth of cut in brittle material machining.

.2 An "Successive Grit Point Spacing" Model and Ultrasonic Vibration assisted Shear-mode Grinding

The main points demonstrated previously by our experimental results(1,2) are:

1) The grinding force showed almost no fluctuation. The reproducibility was as high as ±2N. 2) Flat top grits were observed to cut material and found to be flat as if they had been abraded. 3)During the experiment no dressing was performed.

Distribution and resultant function (averaging effect) of abrasives have been explained statistically. Abrasives of grinding wheel surface have a Gaussian distribution (3).

The successive grit point spacing (p) is give by the following, P=w2/b,

Here, w is the average grit point spacing and b is the average width of the groove.

When the wheel is excited with ultrasonic vibration of frequency f and amplitude a, the motion of the grits can be expressed by a sinusoidal function and each grit has a phase shift of $(2\pi/\lambda)\cdot P$, $f(x) = a/2\cdot\sin[(2\pi/\lambda)\cdot\{x-n\cdot p\}]$ Here, λ is the wave length. Thus distributed grits are presumed to remove material at a depth lower than the critical depth of cut under certain machining conditions depending on the feed velocity and the ultrasonic frequency and amplitude.

Figure 1 shows the normal grinding force. When the silicon material is ground, chip-loading peculiar to the material accelerates an increase in the force.

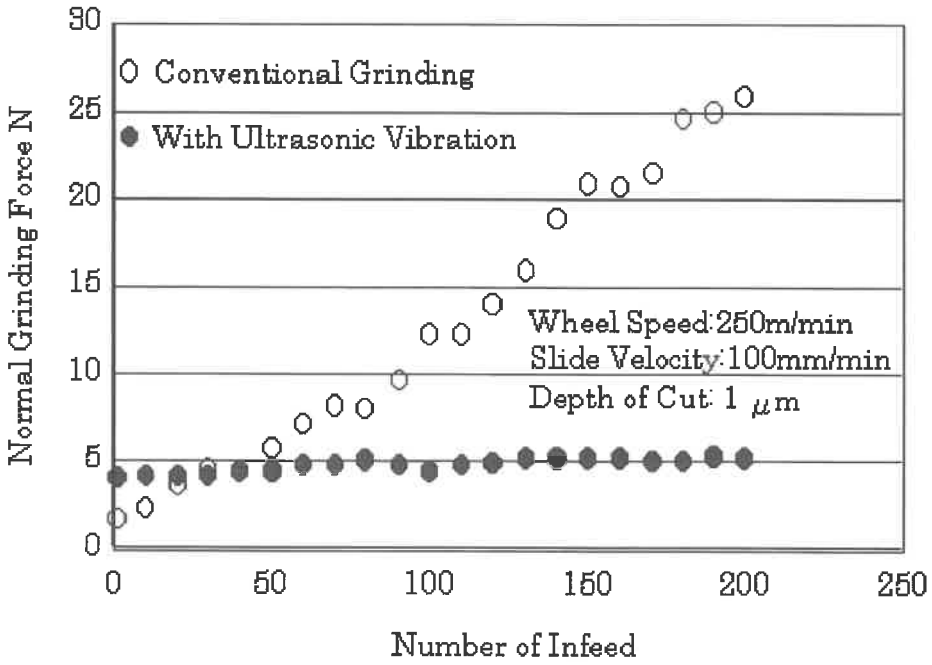

Fig.1 Normal grinding force with the ultrasonic excitatio

However, when ultrasonic vibrations were applied, the grinding force remained almost constant. Although the cup-type grinding wheel had a greater contact area than the straight one, it was assumed that the cup-type grinding wheel used in this case allowed the inflow of relatively more grinding fluid. Furthermore, the problem of chip-loading could also be solved.

3 The Removal Mechanism and the Critical Depth of Cut of an Engineered Tool

To overcome the disadvantages of using a grinding wheel for ultrasonic vibration assisted grinding, that is, the excessive deviation of the continuous abrasive spacing from the average abrasive spacing, and the shedding, etc., an engineered tool chip (ET chip) was developed. This is composed of a large diamond chip (about 2mmx2mm square and about 0.5mm thick), which has been excimer laser-machined to leave 10 μm high posts that are about 3 to 5 μm square. Figure 2 shows details of the cutting edge of a single post. The ET chip characteristics are: a) high grain distribution density and b) uniform cutting edge; c) uniform grain projection height and d) uniform grain crystallographic orientation; and no contamination, because of no heavy metal. (4)

. The engineered tool has two parts, a rake surface and a flank one. The rake angle θ of the tool can be determined, so that the height difference of each adjacent post is lower than the critical depth of the cut [dc].

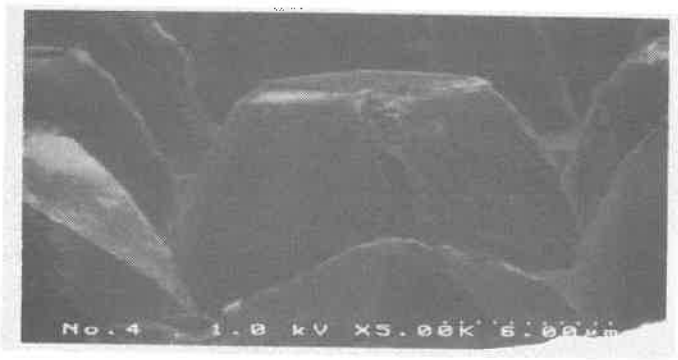

Fig.2 Details of a Single Post Machined by the Excimer Laser

The post motion is determined by the cutting speed v, ultrasonic frequency f, ultrasonic amplitude a, and the post pitch P(s+w). Equations 1) and 2) give the post motions of the rake and flank surfaces, respectively. Intermittent removal is possible by designing the post pitch to

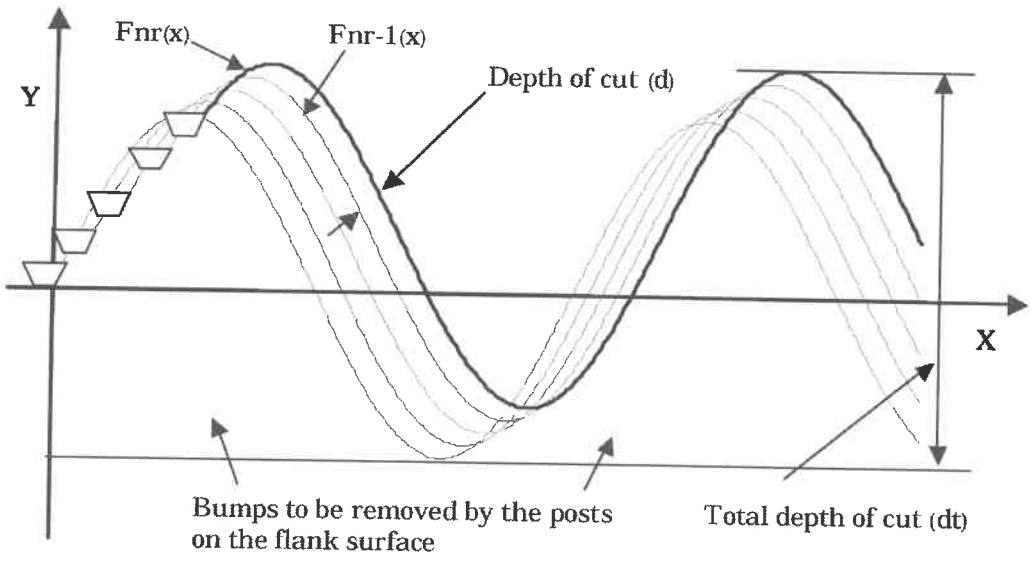

have an adequate phase shift, as shown by the hatched part of Fig.3.

Fig.3 Intermittent Removal Mechanism with the Ultrasonic Excitation

Motion of Post on Rake Surface :

$$fnr(x) = nr \times P(s+w) \times \tan\theta + \frac{a}{2} \times \sin\left[\frac{2\pi}{\lambda} \times \{x - nr \times P(s+w)\}\right] \quad 1)$$

Motion of Post on Flank Surface :

$$fnf(x) = \frac{a}{2} \times \sin\left[\frac{2\pi}{\lambda} \times \{x + nf \times P(s+w)\}\right] \quad 2)$$

Here , nr, nf are the numbers of posts on the rake and the flank surfaces, P(s+w)is the Post pitch, Ps is the post spacing. The total depth of cut [dt] and the post height difference on

the rake surface (d) are given by the following;

$$dt = a + nr \times dc \quad 3)$$

$$d = P(s+w) \times \tan(90 - \theta) \quad 4)$$

4. Conclusions

1) With tremendous cutting edges on the rake surface, that are aligned so that the vertical spacing is lower than the critical depth, making it possible to give a large total depth of cut.

2) The phase shift in the design of the cutting edge pitch means the cutting edges remove the material intermittently. This is expected to minimize cutting edge wear and subsurface damage.

References

[1] H.Hashimoto, J.Takeda, K.Imai and K.Blaedel: Shear-mode Grinding of Brittle Materials and Surface Characteristics, International Journal of The Japan Society for Precision Engineering, Vol.27, No.2, pp95-99, 1993.

[2] Y.Yoshida, P.Nan, K.Imai, I.Iida, N.Tsuda and H.Hashimoto: Shear-Mode Grinding Force Criteria in Grinding Silicon Wafers with Cup Wheels, Proceedings of the 11th Annual Meeting, The American Society for Precision Engineering, Monterey, CA, pp.602-605, 1996.

[3]E. Usui : Cutting and Grinding, Kyouritu Publishing Co., p.25, 1971.(in Japanese)

[4]H.Hashimoto, K.Imai, D.Dornfeld, and K.Blaedel: Speculation on Ultrasonic-Assisted Grinding with an Engineered Wheel, 1998 OSA Technical Digest Series Volume12, Optical Fabrication and Testing, Conference Edition, Hawaii, OMB3-1, June, p20, 1998.

Lubrication at Tool-chip Interface by Oil Injection

Toshiaki Kaneeda and Satoshi Matushita

Department of Mechanical Engineering, Okayama University of Science
1-1 Ridai-cho, Okayama city, Okayama 700-0005, Japan

Keywords: oil injrction cutting, lubricant applying effect, oil-submerged cutting, lubrication, applied material, work hardened layer, work hardening-capacity, pre-cut surface, machinability, pure aluminum

1. Introduction

Applying large quantity of cutting fluid during cutting is characterized by problems in the immediate working environment and in waste disposal. These problems result in a large number of ecological problems and in a climate of increasingly strict work safety and environmental legislation. To reduce the quantities of cutting fluid, dry cutting and near-dry cutting should be replaced conventional oil supplying method. In performing dry or near-dry machining, the same machinability as conventional machining using enough quantity of cutting fluid should be maintained. However, role of cutting fluid has not been analyzed precisely. Cutting fluid have two major roles in cutting. One is lubrication, and the other is cooling effect. However, the extent of the lubrication has yet to be determined. The reasons are as follows: First, there are three directions from which the operator can supply the cutting fluid to the cutting process. As yet there is no agreement on which direction should be standard, and so the results of lubrication cannot easily be compared among them. Second, the lubrication is affected by the supply pressure, the amount of cutting fluid, the cutting conditions, and the operator. Kaneeda et al. developed oil-submerged cutting which presents a steady and constant cuting fluid supply method to determine the extent of lubrication.[1] They also found that applying materials on the pre-cut surface in ductile metal cuttings could improve the machinability, which was called lubricant applying effect. [2] However, in some conditions, the oil-submerged cutting could provide not only the lubricant applying effect but also other lubrication. It is reasonable that the cutting fluid infiltrate into and lubricate the interface between the chip and tool rake face. However, considering the high normal stress on the tool rake face and chip flow direction, the cutting fluid cannot infiltrate into the interface. It has been reported by M.C.Shaw that the cutting fluid lubricated the rake face by pumping action.

Therefore we have developed direct lubrication to the rake face, namely oil injection cutting which enables the cutting fluid to lubricate the interface between the chip and the rake face. The purpose of this paper is to determine the performance in the lubrication in the oil injection cutting.

2. Experimental Procedures

Cutting experiments were conducted on an NC orthogonal precision cutting apparatus. A large-work hardening-capacity ductile metal, pure aluminum(A1050, 1/2) was used as the work material. Dimensions of the work material was 300 × 35 × 3 mm. Cemented carbide (WC+Co) K10 was selected as the tool material. The rake angle was a constant 0° . Depth of cut in the last-pre cutting t_L, being able to control the rate of work hardening in the region to be cut, was 10μm and 100μm.[1] Depth of cut t_1 was 10μm. Cutting speed is a constant 25.7 m/min.

The tool for the oil injection cutting is shown in Fig.1. The cutting fluids with high pressures (0.4MPa) was supplied from the small hole that passed through the tool, and then can lubricate the tool rake face. A quartz force transducer (Kistler Co. type 9251A) was employed to measure the cutting forces. Table 1 summarizes the cutting conditions.

Table 1 Cutting conditions

Work material			Pure aluminum (Al050-H24)
Tool material			Cemented carbide K10
Tool	Rake angle	α °	0
	Relief angle	ε °	7
Cutting form			Orthogonal
Cutting speed	V	m/min	25.7
Last pre- cutting	t_L	μm	10, 100
Depth of cut	t_1	μm	10, 30, 50
Lubricant			Oleic acid

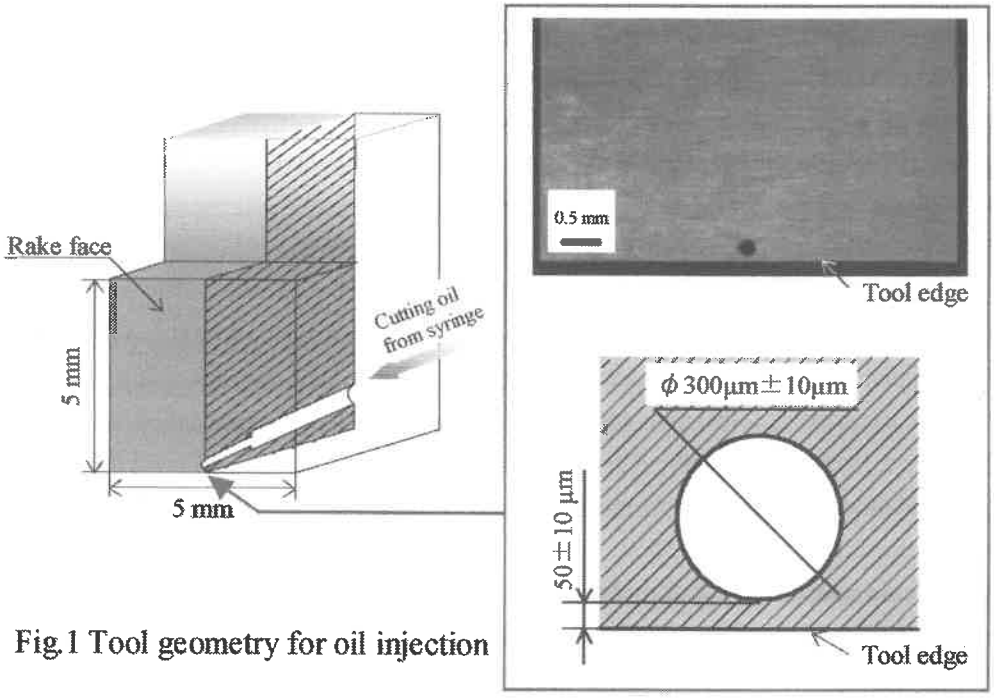

Fig.1 Tool geometry for oil injection

3. Results

3.1. Cutting force

Fig.2 shows the depth of cut in the last-pre cutting t_L effects on the tangential cutting forces F_T in dry cutting, lubricant applying effect, oil-submerged cutting [1] and oil injection cutting (0.4MPa). The normal cutting forces in all the cutting experiments showed the same trend as for the tangential forces, so the tangential cutting forces were focused on in the discussion. From the results in Fig.2, it can be seen that the oil injection cutting reduced the cutting forces as well as the oil-submerged cutting, although the reduction in the lubricant applying effect cutting depends on the depth of cut in the last pre-cutting t_L.

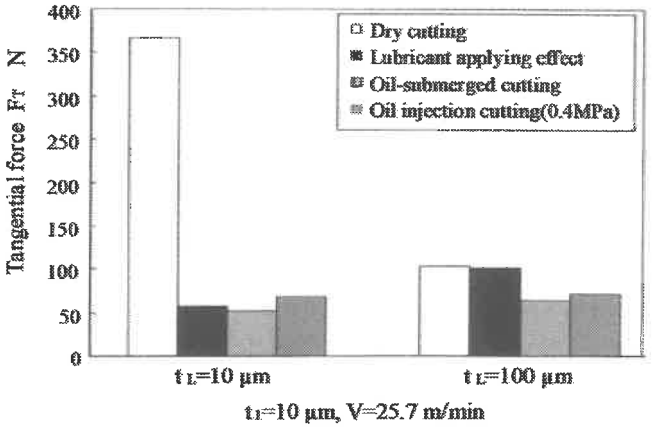

Fig.2 Tangential cutting forces

3.2. Adhesion on rake face

Adhesion on the rake face after the cutting experiments is shown in Fig.3. The adhesion showing a white layer from the tool edge along the chip flow direction can be defined as a contact length between the chip and the rake face in this paper. The measured values of contact length are shown in table 2.

In the case of t_L=10μm as shown in table 2, the contact length increase in this order: the oil-submerged cutting, the lubricant applying effect, the oil injection cutting and dry cutting. The contact length corresponds to extent of the tangential cutting forces shown in Fig.2.

On the other hand, in the case of t_L=100μm, the oil injection cutting could reduce the contact length as well as the oil-submerged cutting, however the lubricant applying effect could not reduce the contact length. The length in the lubricant applying effect was almost the same as in the dry cutting shown as in table 2.

Fig.3 (a) and (b) suggested that the oil injection cutting could not provide enough lubrication at the rake face, because much of adhesion left on the both side of the rake face. That is to say, the cutting fluid could lubricate around the hole in the oil injection cutting.

Table 2 Contact lengths (mm)

	t_L=10 μm	t_L=100 μm
Dry cutting	1.16	0.77
Lubricant applying effect	0.18	0.60
Oil-submerged cutting	0.17	0.23
Oil injection cutting(0.4MPa)	0.23	0.33

If the cutting fluid was injected through the many holes and by higher than 0.4MPa pressure, the oil injection cutting would be a more powerful lubrication system. In the case of larger t_1 and t_L, the oil injection cutting would provide better performance in lubrication, in other words, the lubrication at the interface appears to be more important. However, in that case the cutting forces are relatively small compare to in the case of smaller t_1 and t_L, then larger reduction of the cutting forces due to the lubrication could not be obtained.

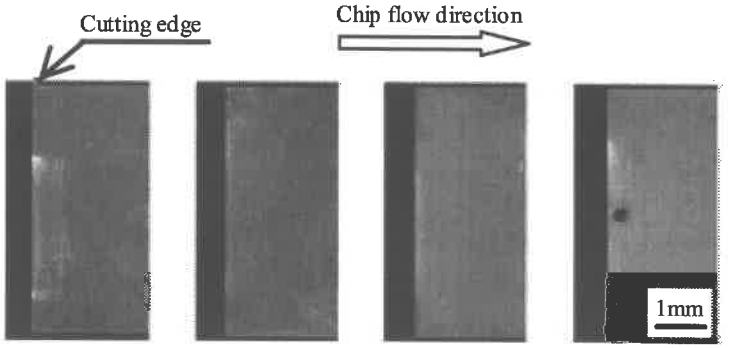

(a) V=25.7 m/min, t_1=10μm (t_L=10μm)

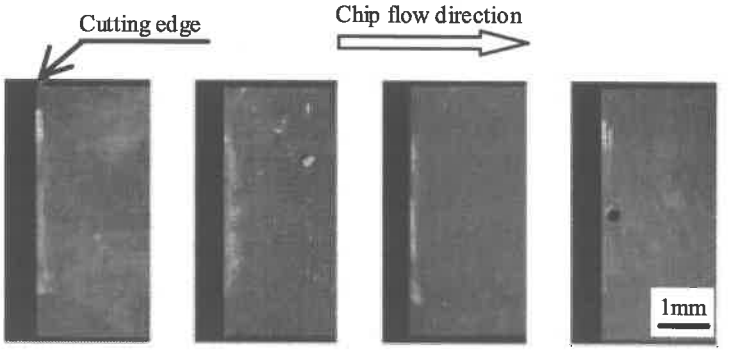

(b) V=25.7 m/min, t_1=10μm (t_L=100μm)

Fig.3 Adhesion on rake face

4. Conclusion

1) The oil injection cutting presented nearly the same performance as the lubricant applying effect cutting and the oil-submerged cutting in lubrication.
2) The oil injection cutting will provide a higher performance if the cutting fluid is injected from many holes and by higher pressures.

References

[1] T. Kaneed, and Y. Oe : J. of Japan Soc. Prec. Engng. 66 (2000) 78.

[2] T. Kaneed; In advancement of Intelligent Production, Elsevier Science B. V., (1994) 385.

Evaluation of machining characteristics of the micro grooving machine for the mold of PDP barrier rib

Nam-Hun Kim*, Eun-Sang Lee**, Deug-Woo Lee***

* Department of Mechanical and Precision Engineering, Pusan National University, Busan, Korea

** Mechanical Engineering Division, Inha University, Incheon, Korea

*** Mechanical Engineering Division, Pusan National University, Busan, Korea

Abstract

This paper describes the machining characteristics of developed micro grooving machine. Experiments have been conducted on the various grooving condition such as spindle revolution speed, infeed rates and depth of groove with a blade designed according to the shape of groove. And acoustic emission (AE) sensor was examined by the in-process monitoring of groove machining. As a result, this study represented optimized grooving condition and possibility of application of AE technique in groove machining.

Keywords: Micro grooving, Blade, Acoustic emission

1. Introduction

Increasing demand for higher quality of multimedia industry, plasma display panel (PDP) will open a new market for display in 2005 year. PDP is the next generation multimedia display device combing techniques of TV, computer and Internet. In 2005 year, CRT, large LCD, LCD and PDP will occupy 44%, 34%, 11% and 11% respectively. The demand for home PDP will occupy 80% of the PDP market.

PDP is a display device using the plasma generated by the electric discharge of gas and consists of the glass coated with the dielectric and many electrodes. In general, the PDP has partitions having a height of about 100-200μm provide periodically for partitioning the display space. For example, in a PDP of a surface discharge type suitable for fluorescent color display, barrier ribs that are rectilinear as seen in a plan are equidistantly arranged along data electrode lines. The barrier ribs prevent the interference of discharge and the cross talk of colors.

In many process of the PDP production, forming of barrier rib is the most difficult process. Various methods for forming barrier ribs have been proposed and carried out. Typical examples include a screen-printing method, a sand blasting method and an additive method etc. But these methods are excessive time and materials consuming. Hence these defects make the PDP expensive. To overcome these defects, the direct molding technique after mixing barrier rib material and binder has been studied [1].

Most of the current micro grooving techniques is based on chemical etching that provides an excellent accuracy, but they have a few defeats. For example, photolithography process or LIGA(Lithographie & Galvanoformung & Abformung) process requires extensive capital investment and process time. Another method for micro grooving is single point diamond tool machining. But single point diamond bite is fragile, so it is unsuitable for machining of hard and brittle material. Accordingly, copper and aluminum have been used for shaping using single point diamond tool [2].

In this research, 3 axis controlled micro grooving system was developed for machining of PDP barrier rib mold. To improve capability in operation and precision, the structure of system used the method that fixes the table and feeds tool considered large size of workpiece and vibration. Each axises applied ultra precision LM guide system, which set on polished granite. The machining tool with micro grain diamond and CBN blade each according to the shape of groove was fixed to

high-speed air spindle. To evaluate the developed micro grooving machine, STD11 was used, AE signal obtained from each experimental condition was analyzed, and cutting stability was compared with the surface topography.

2. Estimation of AE signal

On-line monitoring technique for processing characteristic estimation is the technique to be solved in the manufacturing field. Fig. 1 shows the surface damage due to blade breakage in grooving process. To identify whether there is blade malfunction in large-sized mold machining or not is very important. Because the manufacturing price of large-sized mold materials is too expensive. Hence, to reduce the cost of re-machining from machining failure, it is necessary to monitor and control the grooving process.

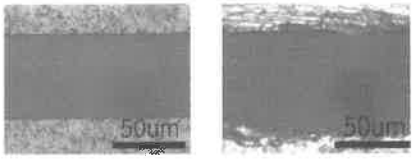

Fig. 1. Comparison of the shape of groove under steady & unsteady state.

Owing to the development of sensing technique, AE is widely used in monitoring the machining state of ultra-precision process [3]. In this paper, frequency analysis and root mean square (RMS) was used to identify the AE signal characteristics during micro grooving process,. The correlation between results from material deformation and fracture was discussed using frequency analysis, and the relation between the amplitude of AE signal and physical variation in experiment was studied using RMS.

Kannatey-Asibu interpreted AE signal energy-quantity with the work-quantity of generating source in the cutting, and the RMS of AE AC wave as an energy criterion was defined like the following [4]

$$RMS = [(1/\Delta T)\int_0^{\Delta T} V^2(t)dt]^{1/2} \qquad (1)$$

where V(t) is raw AE signal, ΔT is the integration time constant.

3. Experiments

Fig. 2 shows the developed micro grooving machine. To test the machining ability of developed system, the grooving characteristic was examined. The workpiece of STD11 that is alloy tool material was used. The shape of micro groove according to various conditions was observed using diamond and CBN blade tools.

To obtain the optimized grooving conditions, machining parameters of spindle revolution speed (25,000-40,000rpm), infeed rate (0.4-0.8 mm/sec), depth of groove (100-300μm), etc. were took into consideration. The generated whether the burr is constructed or not is the main target to examine.

AE sensor was attached using grease on the side of workpiece to obtain the AE signals that is generated during grooving process. The type of AE sensor is a wide band that has uniform sensitivity at the wide frequency range. The signal was amplified (52db) and filtered (100~1200KHz) using the pre-amp[1220A(PAC)] and main-amp[AE1A(PAC)]. The digital signal obtained from AE sensor at sampling speed of 5MHz was digitalized and stored using the A/D converter (Gagescope CS1012) that has a 12 bit-resolution. And the characteristic of AE signal in accordance with groove machining was analyzed.

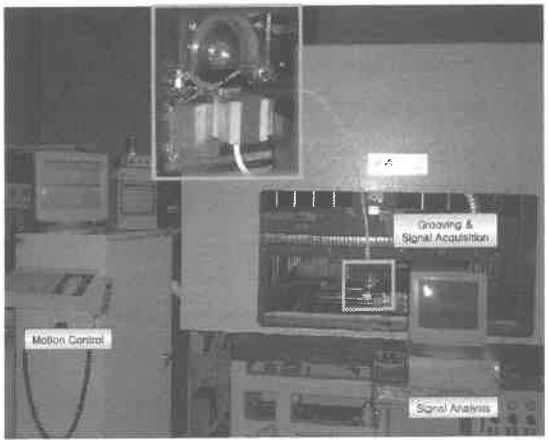

Fig. 2. Monitoring system of grooving process.

4. Experimental results and discussion

4.1 Evaluation of characteristics of micro grooving machine

Fig. 3 shows the grooving results with diamond blade. From the grooving result of STD11, in all the conditions but 40,000rpm, a burr on the border-surface was observed severely. This means that ductile fracture cutting process has been occurred, according to the material characteristics. In the case of 40,000rpm of ultra-high speed cutting, stable processing was executed due to low temperature. However, in the case of air spindle that used in this research, the noise and load at 40,000rpm became much higher and showed some limitations of machining.

In General, CBN is a tool showing an excellent machining ability to high-hardness and difficult-to-cut material. As shown in Fig. 4, groove machining with CBN blade showed outstanding decrease in burr and ductile fracture than with diamond blade. And, the experimental result represented that spindle revolution speed within 30,000-35,000rpm, depth of groove below 200μm and feed rate of 0.6mm/sec were the optimum machining condition for the developed micro grooving machine.

Fig. 5 shows the cross sectional picture of mold that machined in each condition. To improve the mold release, the mold was machined having 9 degrees of tilt angel.

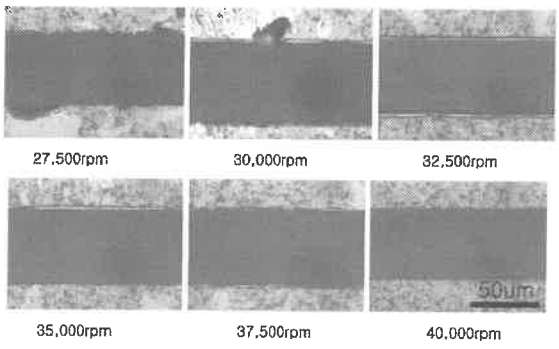

Fig. 3. Micrographs of groove. (With diamond blade)
(Feed rate : 0.6mm/sec, Depth of groove : 150μm)

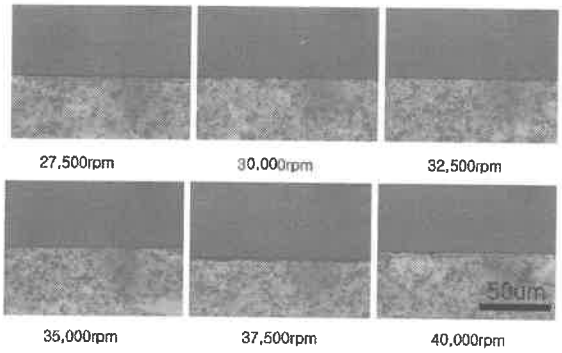

Fig. 4. Micrographs of groove. (With CBN blade)
(Feed rate : 0.6mm/sec, Depth of groove : 150μm)

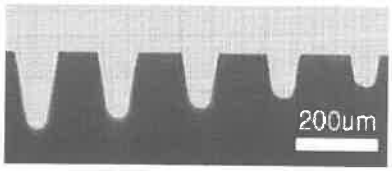

Fig. 5. Cross sectional micrograph of mold.

4.2 Evaluation of grooving process using the RMS

Fig. 6 shows the tendency of variation of RMS according to grooving time. After acquiring raw AE signal at constant time intervals and making RMS conversion in order to figure out relationship in time domain signal and to machining tendency. And then after getting the average value of the converted RMS, the graph according to grooving time was indicated. From the RMS tendency, groove machining in the stable processing state started after initial high peak. This phenomenon, in accordance with conventional grinding process, groove machining using the blade reflects well the usual cutting process mechanism [5].

If the initial high peak can be controlled, the better results of groove machining will be able to be estimated.

Fig. 7 shows RMS signal characteristic according to depth of groove. The depth of groove is proportional to the AE-RMS signal. This means that AE signal reflects well the normal characteristic of grooving process.

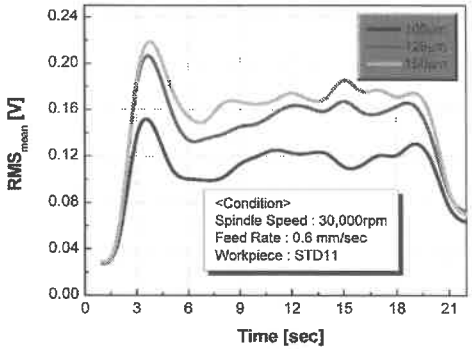

Fig. 6. RMS characteristics in accordance with grooving time.

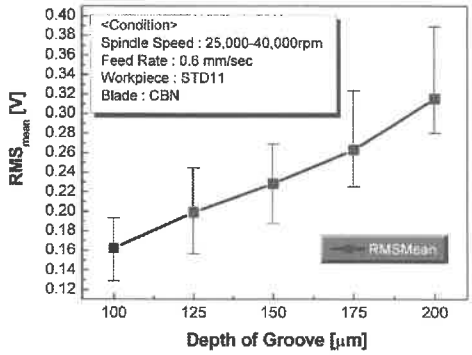

Fig. 7. RMS characteristics in accordance with depth of groove.

4.3 Monitoring of grooving process through frequency analysis

As mentioned above, in-process monitoring technique of large-sized PDP machining is very important in view of machining efficiency and cost. In this study, after the sampled signals in the time domain were transformed into frequency domain signal with FFT analyzer, they were compared the relation with generated physical phenomenon during grooving process. And the possibility of in-process monitoring technique was investigated. Fig. 8, Fig 9, Fig. 10 shows the frequency characteristic according to experiment results. Fig. 8 and Fig. 9 indicates the sensitivity at certain frequency levels (100KHz) regardless of grooving condition. Fig. 10 shows the frequency characteristic analyzed from the signal of workpiece with burr. In this case, frequency characteristic is irregular; it is possible to predict abnormal state grooving process.

Accordingly, based on the signal consequences from this experiment, it is possible that in-process measurement using AE to monitor the abnormal state in grooving process.

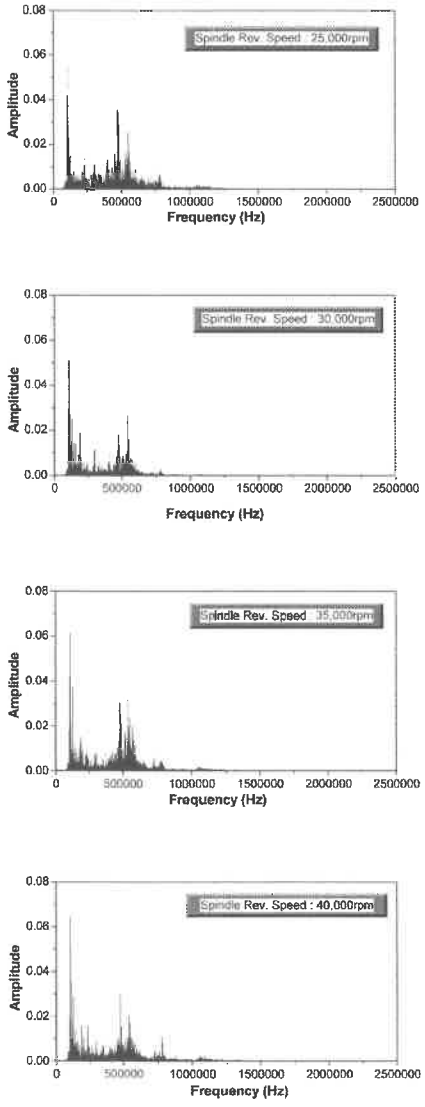

Fig. 8. AE frequency characteristics in accordance with grooving condition.

(Feed rate : 0.6, Depth of groove : 150μm)

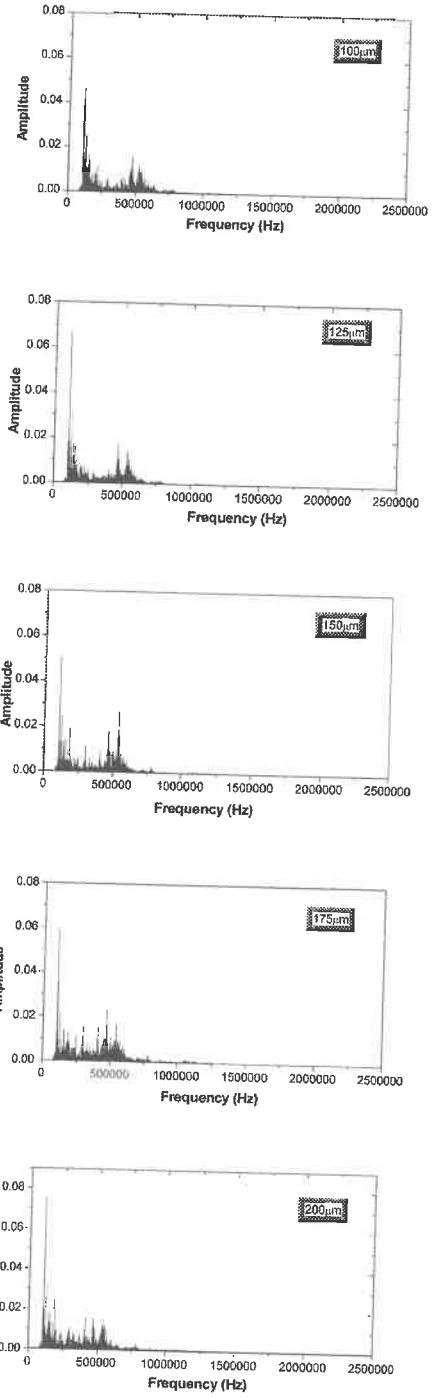

Fig. 9. AE frequency characteristics in accordance with grooving condition.

(Spindle revolution speed : 30,000rpm, Feed rate : 0.6mm/sec)

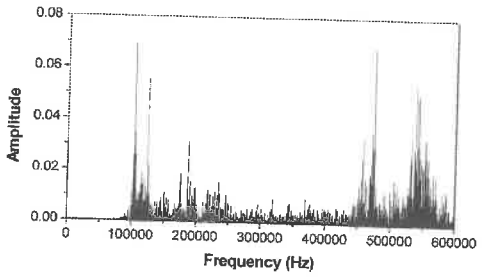

Fig. 10. AE frequency characteristics in accordance with unsteady state grooving.

(Spindle revolution speed: 27,500rpm,

Feed rate: 0.6mm/sec, Depth of groove: 150μm)

5. Conclusion

Based on the evaluation of machining characteristics, the monitoring process of grooving machine for forming PDP barrier rib using blade and defining the possibility of application of AE to abnormality diagnosis, the following was drawn

1. From the experimental results of machining characteristic of micro grooving machine developed in this research, it is known by comparing the burr-generated rate using CBN blade, that the depth of groove below 200μm, spindle revolution speed of 30,000 to 35,000rpm and feed rate of 0.6mm/sec is the optimum grooving condition.
2. From the RMS analysis of raw AE signal, it is known that AE signals reflect well the mechanism of general cutting process according to the change of condition in grooving process.
3. AE signal of frequency domain shows the uniform sensitivity regardless of process condition in the stable processing, but indicates the unstable frequency characteristic in the abnormality process. Accordingly, the utilization for monitoring abnormality is expected using AE frequency characteristic in groove machining.

Reference

1. In-Ho Cho, Sang-Cheol Jeong, Jun-Min Park, Hae-Do Jeong, "The application of micro-groove machining for the mold of PDP barrier ribs", Journal of Materials Processing Technology, 113, pp.355-359, 2001.
2. H.S.Lim, J.H.Ahn, "A Study on the Cutting Conditions of Self-Induced Chattering in Micro Shaping with Diamond Tool" Journal of the Korean Society of Precision Engineering, Vol 15, No. 3, pp.141-149, March, 1998.
3. H.K. Tönshoff, M. Jung, S. Männel, W.Rietz "Using acoustic emission signals for monitoring of production processes", Ultrasonics, 37, pp681-686, 2000.
4. Elijah Kannatey-Asibu, Jr. and D. A. Dornfeld, "Quantitative relationships for acoustic emission from orthogonal metal cutting", Trans. ASME. Ser. B. 103. 3. 330, 1981.
5. S. Malkin, " Grinding Mechanisms ", Grinding Technology, pp. 107-142.

PREDICTION AND SIMULATION ON THE MACHINING DYNAMICS AND INSTABILITY IN PERIPHERAL MILLING

Xiong-Wei Liu, Kai Cheng, Dave Webb
School of Engineering, Leeds Metropolitan University, Calverley Street, Leeds LS1 3HE, UK

Abstract

Based on an improved dynamic cutting force model proposed by the authors and the 2D vibratory model of peripheral milling, this paper presented a closed-loop simulation model for studying the machining dynamics. The modal parameters of the machining dynamics system were identified with the experimental modal analysis using the real-time measured dynamic cutting force and the cutter vibration. The simulation results give us a more comprehensive and in-depth understanding on the machining dynamics and instability. The simulation results also reveal that the proposed approach is feasible for shop floor implementation.

Keywords: Machining dynamics, machining instability, peripheral milling, chatter.

1. Introduction

The machining dynamics of a cutting process has a direct influence on the machining instability, which in turn significantly determines the surface quality of the finished part, the productivity, and even the life of the machine tool and the cutter. Although the machining dynamics of the milling process has been investigated by quite a few of researchers, the process is rather complex and further research is required for a thorough understanding of its physics. Due to using of more powerful mathematics software toolkits, such as Matlab and Simulink, the precision modelling and simulation of the machining dynamics is becoming possible.

The machining dynamics involves the dynamic cutting force, the structural dynamics of the machine tool/cutter system and the workpiece. The dynamic cutting force acting on the cutter and workpiece, which significantly determines the self-excited chatter vibration of the cutting process, is dependent on the cutting conditions, the behaviours of the cutter and work materials. In peripheral milling, with its periodically interrupted cutting process, the dynamic cutting force changes periodically, which excites relative vibration between the cutter and workpiece, which in turn leads to time-varying chip thickness. Under chatter conditions, the vibration developed is sometimes so strong that the amplitude of the vibration between the tool and workpiece is larger than the nominal chip thickness, so that the chip becomes dissected, and the machined surface is spoiled by chatter marks [10]. This phenomenon is called machining instability. The manufacturing industry requires qualified machined surfaces, and so violent chatter or machining instability must be avoided.

The machining dynamics of peripheral milling has been investigated by numerous researchers in the past. Among them Tlusty is the pioneer, who had contributed to the understanding of the machining dynamics, chatter vibration and machining stability in general milling [9-11]. In recent years, Altintas contributed to the further understanding of the machining mechanics (dynamic cutting force modelling), machining dynamics and chatter stability in milling [1-6,12]. The model used for the machining dynamics analysis by the previous researchers is a 2D spring-damper vibration model, in which the vibration of the cutter is excited by periodically changing cutting forces, resulting mainly from the discontinuous cutting process and the undulation left behind by the preceding cut. Of these the periodically interrupted cutting force is dominant and its frequency depends on the spindle speed and the teeth number of the cutter. Based on an improved dynamic cutting force model proposed by the authors [7] and the 2D vibratory model of the milling operation, a closed-loop simulation model was developed for studying the machining dynamics.

The reliability of the closed-loop simulation model depends on the accuracy of the modal parameters. Experimental modal analysis is broadly accepted for identifying modal parameters. However, one of the problems of the traditional experimental modal analysis is using an impulse hammer to excite the structure [1], which is very different from the practical cutting process. The identified modal parameters may differ very much from the practical modal parameters of the cutting process. In order to get the precise modal parameters and verify the effectiveness of the simulation model, a series of cutting tests were arranged. The dynamic cutting force and the cutter vibration were measured in real time. Based on the experimental results, the modal parameters of the cutting process were identified using the experimental modal analysis.

Using the identified modal parameters, a set of simulation was carried out to verify the effectiveness of the proposed machining dynamics model. The simulation results give us a more comprehensive and in-depth understanding on the machining instability. The simulation results also reveal that the proposed approach is feasible for shop floor implementation.

2. Machining Dynamics Model

The vibratory model used for machining dynamics modelling of peripheral milling is shown in Figure 1. The cutter is considered to be a two-degree-of-freedom spring-damper vibratory system in the two mutually perpendicular directions X and Y. The cutting forces excite vibrations in the normal (X) and feed (Y) directions, causing dynamic displacements x and y, respectively.

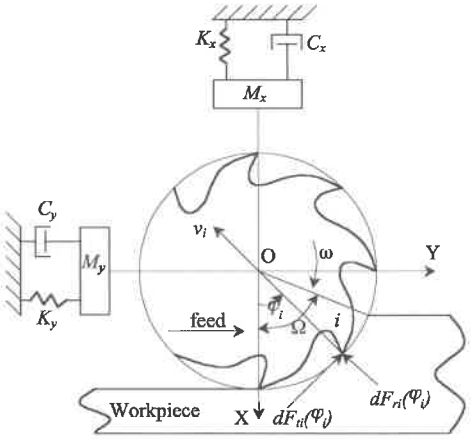

Fig. 1. The spring-damper vibratory model of milling

The authors developed a dynamic cutting force model, which is illustrated in the literature [7]. In Figure 1, the differential tangential and radial cutting forces acting on the ith helical flute's rake face are given by [8]:

$$dF_{ti}(\varphi_i) = K_s t_i(\varphi_i) dz, \quad (1)$$

$$dF_{ri}(\varphi_i) = c dF_{ti}(\varphi_i), \quad (2)$$

where K_s is the tangential cutting force coefficient, φ_i is the position angle of a point on the cutting edge of the ith helical flute, dz is the differential axial depth of cut, c is the force ratio, and $t_i(\varphi_i)$ is the undeformed chip thickness of the tooth element and can be calculated as follows:

$$t_i(\varphi_i) = \begin{cases} f_t \sin(\varphi_i) + (v_{i(-T)} - v_i), \text{if } 0 \le \varphi_i \le \Omega \\ 0 \qquad \text{else} \end{cases} \quad (3)$$

where f_t is the feed rate per tooth, v_i is the dynamic displacement of tooth i in the radial direction, which has the co-ordinate transformation of

$$v_i = -x\cos(\varphi_i) - y\sin(\varphi_i), \quad (4)$$

$v_{i(-T)}$ is the dynamic displacement of tooth i in previous tooth period, Ω is the cutter radial immersion angle within the radial depth of cut.

The contribution of the cutter run-out to the undeformed chip thickness is given by:

$$\delta t_i(\varphi_i) \approx |\overline{O'P}| - |OP|, \quad (5)$$

where $|OP|$ is the cutter radius, and

$$|\overline{O'P}| = \sqrt{|OP|^2 + \delta_e^2 - 2|OP|\delta_e \cos(\angle O'OP)} \quad (6)$$

$$\angle O'OP = \pi - |\varphi_i - \varphi_e|$$

where δ_e is the run-out value, O′ is the spindle centre, O is the cutter centre, and $\overline{OO'} = \delta_e$, as shown in Figure 2.

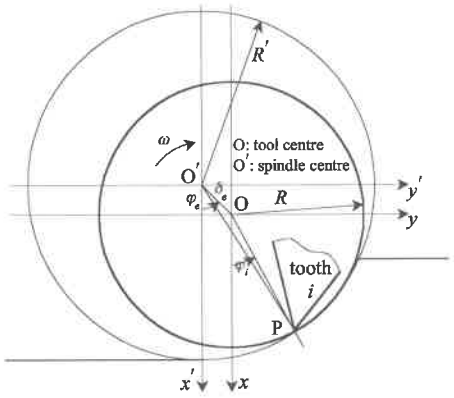

Fig. 2. The cutter run-out model

Integrating the differential cutting forces applied on the ith helical flute into the feed (y) and normal (x) directions, then summing up the cutting forces acting on all the m helical flutes, gives the total cutting force applied on the whole cutter

$$\begin{cases} F_x(t_{\text{ime}}) = \sum_{i=1}^{m} F_{ix} \\ F_y(t_{\text{ime}}) = \sum_{i=1}^{m} F_{iy} \end{cases} \quad (7)$$

The regenerative dynamic displacements (cutter vibration) can be expressed in the frequency domain as a product of the transfer function of the structure and the dynamic cutting force.

$$\begin{Bmatrix} x(i\omega) \\ y(i\omega) \end{Bmatrix} = (1 - e^{-i\omega T}) \begin{bmatrix} G_{xx}(i\omega) & G_{xy}(i\omega) \\ G_{yx}(i\omega) & G_{yy}(i\omega) \end{bmatrix} \begin{Bmatrix} F_x(i\omega) \\ F_y(i\omega) \end{Bmatrix} \quad (8)$$

where T is the tooth passing period, and G_{xx}, G_{xy}, G_{yx} and G_{yy} are the direct and cross transfer functions in the normal X and feed Y directions. The regenerative displacements $[x, y]^T$ and the dynamic cutting forces $[F_x, F_y]$ have a closed loop interaction as shown in Figure 3. Both of them grow exponentially when the operating condition is unstable, which leads to chatter vibration.

Experimental results reveal that the measured cross transfer functions were negligible, i.e. $G_{xy} = G_{yx} = 0$

[1,6]. So the frequency domain response function can be expressed as:

$$\begin{cases} x(i\omega) = (1 - e^{-i\omega T}) G_{xx}(i\omega) F_x(i\omega) \\ y(i\omega) = (1 - e^{-i\omega T}) G_{yy}(i\omega) F_y(i\omega) \end{cases} \quad (9)$$

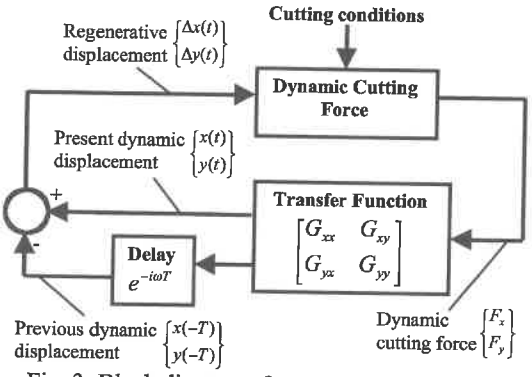
Cutting conditions
Regenerative displacement $\{\Delta x(t) \; \Delta y(t)\}$
Dynamic Cutting Force
Present dynamic displacement $\{x(t) \; y(t)\}$
Transfer Function
$\begin{bmatrix} G_{xx} & G_{xy} \\ G_{yx} & G_{yy} \end{bmatrix}$
Delay
$e^{-i\omega T}$
Previous dynamic displacement $\{x(-T) \; y(-T)\}$
Dynamic cutting force $\{F_x \; F_y\}$

Fig. 3. Block diagram of regenerative chatter in peripheral milling.

The measured transfer functions G_{xx} and G_{yy} in the Laplace domain can be expressed as:

$$G_{xx}(s) = \frac{x(s)}{F_x(s)} = \frac{\omega_{nx}^2}{k_x(s^2 + 2\xi_x\omega_{nx}s + \omega_{nx}^2)} \quad (10)$$

$$G_{yy}(s) = \frac{y(s)}{F_y(s)} = \frac{\omega_{ny}^2}{k_y(s^2 + 2\xi_y\omega_{ny}s + \omega_{ny}^2)} \quad (11)$$

where s is the Laplace operator, ω_n and ξ are the natural frequency and structural damping ratio respectively.

3. Experimental Modal Analysis and Simulation

The transfer functions of the machining dynamics system are identified generally by structural dynamic test. An impulse hammer equipped with a piezoelectric force transducer is used to excite the vibration of the cutter. The resulting vibrations are measured with displacement, velocity, or acceleration sensors. Then, both of the recorded dynamic force and vibration are input to a Fourier analyser (or modal analysis software) to get the modal parameters of the machining dynamics system (or the cutter, more precisely). The identified modal parameters of the machining dynamics system may differ very much from the practical modal parameters of a cutting process.

In order to get the precise modal parameters of the machining dynamics system and verify the effectiveness of the proposed simulation model, a series of cutting tests were carried out. The dynamic cutting forces and the cutter vibration were measured in real-time. Experimental modal analysis was used to identify the modal parameters of the cutting process using the real-time measured data.

Figure 4 illustrates the experimental configuration. The cutting test was carried out on the three axis vertical CNC machine centre, Cincinnati Arrow2-500. The workpiece, made of aluminium alloy Al-7075, is fixed with Microloc fixture system, Kit-75, which is mounted on the Kistler table dynamometer, 9257BA. The dynamometer, which in turn is mounted on the worktable of the machine centre, records the 3D dynamic cutting force in real-time. The cutter is a two-fluted solid carbide end mill with a helix angle $\beta = 30°$, a radial rake angle $\alpha_r = 5°$ and a diameter $\phi 20$ mm. Its overhang length is 58mm. The cutter vibration was measured with three accelerometers, which are linked to the signal analyser, SignalCalc Mobilyzer. The cutting conditions are: down milling, axial depth of cut $b_a = 11.36$ mm, radial depth of cut $d = 4$ mm, spindle speed $n = 3183$ rpm (cutting speed $V = 3333$ mm/s), feed rate $f_t = 0.08$ mm/tooth.

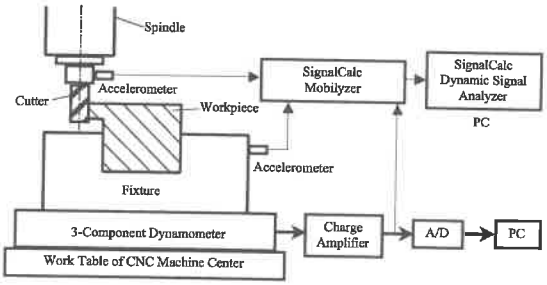

Fig. 4. Experimental configuration of cutting test.

The real-time measured dynamic cutting force and cutter vibration were input to the modal analysis module ARMAX of the Simulink (Matlab). Figure 5 gives the simulation result of experimental modal analysis for the peripheral milling process. The simulation result shows that the predicted model output (cutter vibration) agrees well with the actual output (measured cutter vibration in the X direction).

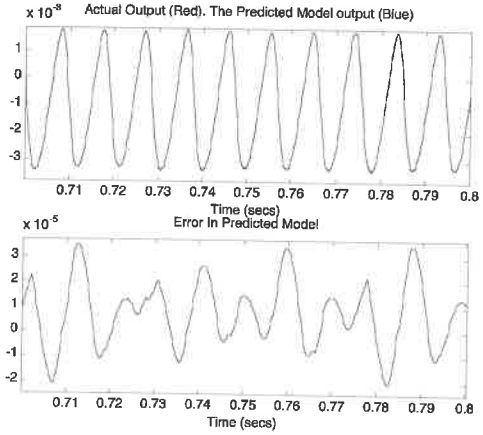

Fig. 5. Simulation of the experimental modal analysis.

Now let us investigate the system response of the machining dynamics model with the identified transfer function. It is assumed that the transfer function keeps constant provided different cutting parameters. Figure 6 gives a set of simulation result of the cutter vibration.

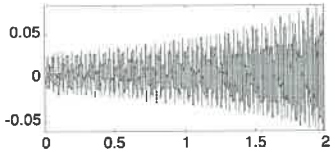

a) $n = 3183$, $b_a = 11.36$, $d = 8.1$, $f_t = 0.08$

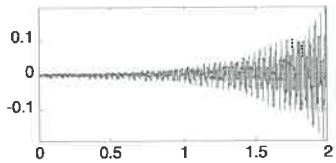

b) $n = 3183$, $b_a = 15.2$, $d = 4$, $f_t = 0.08$

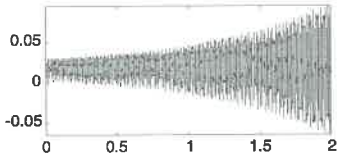

c) $n = 6950$, $b_a = 20$, $d = 10$, $f_t = 0.08$

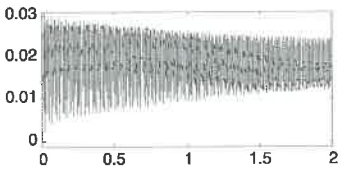

d) $n = 7000$, $b_a = 20$, $d = 10$, $f_t = 0.08$

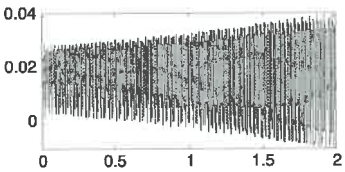

e) $n = 7000$, $b_a = 20$, $d = 10$, $f_t = 0.075$

Fig. 6. Simulation with different cutting conditions

The simulation result shows that all the cutting conditions, i.e. cutting speed, axial depth of cut, radial depth of cut and feed rate, have influence on the machining instability. The result indicates that the concept of machining stability lobes [4], which involves only the cutting speed and axial depth of cut, needs to be improved.

4. Conclusions

For the optimisation, which means high precision, high stability and meanwhile high productivity, of cutting process of high-speed milling, not only the cutting speed and axial depth of cut, but also the radial depth of cut and feed rate, must be considered.

The research work convinces us that the modal parameters of the machining dynamics system can be identified with the experimental modal analysis using the real-time measured dynamic cutting force and the cutter vibration, and the proposed approach is feasible for shop floor implementation.

Acknowledgements: The authors would like to give thanks to the EPSRC for grant support (EPSRC GR/R13395) and also to the collaborating partners, Ultra Precision Engineering Centre, University of Huddersfield, Cincinnati (UK) Ltd, Kistler Ltd, Renishaw plc and Siemens Ltd, for their financial support, advice and practical assistance.

References

[1] Altintas Y. Manufacturing Automation: Metal Cutting Mechanics, Machine Tool Vibrations, and CNC Design. Cambridge University Press, Cambridge, 2000.

[2] Altintas Y, Engin S. Generalized modeling of mechanics and dynamics of milling cutters. Annals of the CIRP 2001;50(1):25-30.

[3] Altintas Y. Analytical prediction of three dimensional chatter stability in milling. JSME Int J Series C 2001;44(3):717-23.

[4] Altintas Y, Budak E. Analytical prediction of stability lobes in milling. Annals of the CIRP 1995;44(1):357-62.

[5] Budak E, Altintas Y, Armarego EJA. Prediction of milling force coefficients from orthogonal cutting data. ASME Trans J Manufact Sci Eng 1996;118(2):216-24.

[6] Budak E, Altintas Y. Analytical prediction of chatter stability in milling. Part I: General formulation; Part II Application of the general formulation to common milling systems. ASME Trans J Dyn Syst Meas Control 1998;120(1):22-36.

[7] Liu XW, Cheng K, Webb D, Luo XC. Prediction of cutting force distribution and its influence on dimensional accuracy in peripheral milling. Int J Mach Tools Manufact 2002;42(7):791-800.

[8] Shaw MC. Metal Cutting Principles. Oxford University Press, Oxford, 1984.

[9] Smith S, Tlusty J. Efficient simulation programs for chatter in milling. Annals of the CIRP 1993;42(1):463-6.

[10] Tlusty J. Dynamics of high speed milling. ASME Trans J Eng Ind 1986;108(2):59-67.

[11] Tlusty J, Ismail F. Special aspects of chatter in milling. ASME Trans J Vibration, Acoustics, Stress, and Reliability in Design 1983;105(1):24-32.

[12] Yucesan GB, Altintas Y. Improved modelling of cutting force coefficients in peripheral milling. Int J Mach Tools Manufact 1994;34(4):473-87.

Machining Phenomena in EDM for Surface Modification with TiC Semi-sintered Electrode

Toshio Moro, Akihiro Goto, Nagao Saito
EDM system department, MITSUBISHI ELECTRIC CORP., Nagoya, Japan*
Naotake Mohri
Department of Precision Machinery Engineering, The University of Tokyo, Tokyo, Japan**
Koji Akamatsu, Hisashi Yamada
MC MACHINERY SYSTEMS, INC. Wood Dale, IL+
and Toshio Sata
Toyota Technological Institute, Nagoya, Japan++

Abstract

Electrical Discharge Coating (EDC) is one method of surface modification process for making a hard layer on the work piece, using the composite structure electrode made by metallic powder that forms carbide easily. In this research, semi-sintered product made of TiC powder is used as an electrode for surface modification. It is important to examine the electrode wear process because a large amount of powder from the worn electrode is expected to exist among the gap region and it becomes the source of generated layer on the work piece. As a result, the machine surface of the work piece is covered with TiC layer and it becomes functionally graded material. The wear length of semi-sintered electrode depends on electrode area. Especially, pulse duration does not affect on the amount of electrode wear in the same electrode area. The growth of the TiC layer on the work piece tends to stop at a certain thickness according to pulse duration but it dose not depend on the electrode area. From the hardness distribution of the machined surface, hardened region expands into the inside of original work piece. In this paper, some peculiarities in the surface modification phenomena by EDM with TiC semi-sintered electrode are discussed and the result of an application of the treatment to the tool edge of a punching die will be reported.

Keywords: Electrical discharge machining, Electrode, Surface modification, TiC, Hard layer

Introduction

During these past 10 years, crack less surface of a work piece has been realized by the finishing electrical discharge machining (EDM) in which specially made electrode or powder mixed working fluid is used. Corrosion resistance and wear resistance of the work piece improves more. Besides, the trial to implant the substance in the gap onto the work piece was going to appear prosperous, and it become to produce new characteristics on the work piece[1][2][4][5][7][8][9].

For the surface modification by EDM, it is necessary to move and accumulate the in the gap region onto the top of the work piece. The substance in the gap region might be the decomposition product from tool electrode, the powder mixed from outside or the cracked carbon from working oil. As for the polarity of electrode, machining is done minus in case of all. For the use of the substance produced from an electrode, the electrode should be worn much through EDM. The electrode can be made by press-forming or sintering of fine powder being implanted to overcome the constraint of thermo-physical prosperities of material [3][6].

*EDM system department,MITSUBISHI ELECTRIC CORPORATION, NAGOYA WORKS, 1-14,Yada-minami5-chome, Higashi-ku, Nagoya 461-8670,Japan. e-mail:moro@edm.mei.melco.co.jp
**Department of Precision Machinery Engineering, The University of Tokyo, Graduate School of Engineering, Hongo, 7-3-1, Bunkyou-ku, Tokyo 113-8656, Japan
+ MC MACHINERY SYSTEMS, INC. 1500 Michael Drive Suite C Wood Dale, IL 60191, U.S.A
++Toyota Technological Institute, 2-12-1 Hisakata, Tempaku-ku Nagoyga 468-8511, Japan

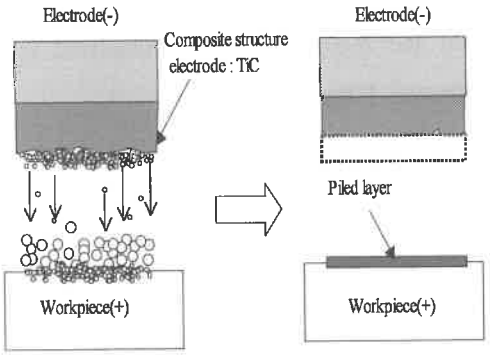

Fig 1: Principle of Surface Modification by EDM

Table 1: Specifications of composite structure electrode

Material	TiC powder
Purity	99.0 %
Diameter of powder	2-5μm
Forming and sintering conditions	Pressure forming 98.1N/mm^2 Sintering process 900°C×1hr
Size(mm)	60×60×60
Transverse-rupture strength	14.1N/mm^2

The surface layer of titanium carbide (TiC) gets possible to form on the face top of tungsten carbide (WC) if we use green compact of titanium hydride (TiH_2) as an electrode, and surface layer hardness reaches up to two thousand several hundred Hv. In this case the carbon in TiC which accumulated on the work surface, can be considered as the result of cracked carbon of working fluid which reacts with titanium. However, it is difficult to make large electrode because the compact was fragile even if it is made under high compacting pressure in use of Ti or TiH_2 powder. Besides, since these kinds of electrode wear too much, there is a tendency of generating rough surface on the work piece surface. Thermal conductivity of the electrode apparently falls, and, besides, bonding strength between particles is smaller than base material. On this account the electrode material leaves it by discharge easily as shown in Fig 1. The products of semi-sintered green compact of TiC can be used for stable and large scale electrodes which leads to practical use in the market.

Table 2: Machining conditions for Surface Modification by EDM

EDC conditions	No.1	No.2	No.3	No.4	No.5	No.6
Discharge current:i_e(A)	8	8	8	8	8	8
Discharge duration:t_e(μs)	2	2	8	8	16	16
Pulse interval time:t_o(μs)	64	32	256	128	512	256
Duty factor:τ(%)	3.0	5.9	3.0	5.9	3.0	5.9
Electrode polarity	(-)					
Workpiece	S45C					

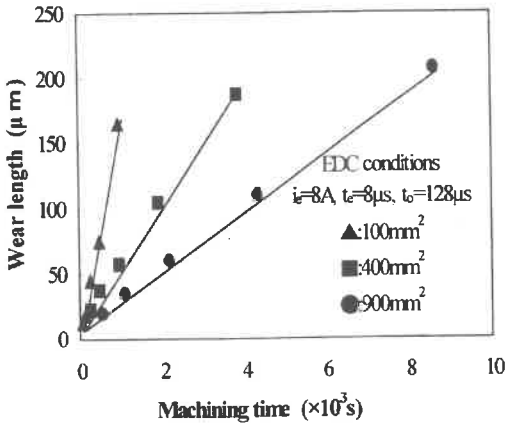

Fig 2: Relation between machining time and wear length

In this paper, some peculiarities in the surface modification phenomena by EDM with TiC semi-sintered electrode are discussed and the result of an application of the treatment to the tool edge of a punching die will be reported.

TiC Electrode Wear Phenomena

In this research, semi-sintered product made of TiC powder is used as an electrode for surface modification. It is important to examine the electrode wear process because a large amount of powder from the worn electrode is expected to exist among the gap region and it becomes the source of generated layer on the work piece. The electrode forming and sintering conditions with its transverse rupture strength are shown in Table 1. Table 2 shows the electrical machining conditions for surface modification. Under these conditions, we confirm in advance that TiC layer of several μm thickness can be provided on carbon steel under these machining conditions. And this coated layer has remarkable resistance to wear of die and cutting tool.

The electrode wear length against machining time is shown in Fig 2 for each electrode area. These data are acquired in the machining with the electrodes of 100, 400, 900mm^2 under the condition of No.4

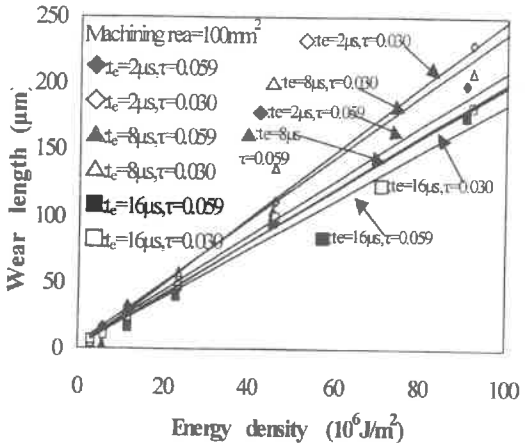

Fig 3: Wear length for different pulse duration vs. energy density

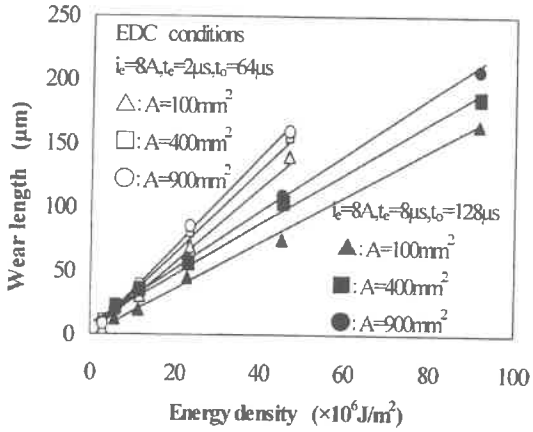

Fig 4: Wear length for different electrode area vs. energy density

in Table 1. The machining time is set so that the number of discharges per electrode area is the same. The wear of electrode increases in proportion to the machining time for each electrode with its own area. In order to evaluate the effect of the machining time and the electrode area, we introduce energy density which represents supplied energy per unit area into the gap region.

Energy density E(J/m²) is defined by the following equation,

$$E = e/n/A = U_e/i_e/\tau\ /t/A \qquad (1)$$

where, e: energy consumed in gap region for a single discharge, n: number of total discharges, A: electrode area, U_e: discharge voltage, i_e: discharge

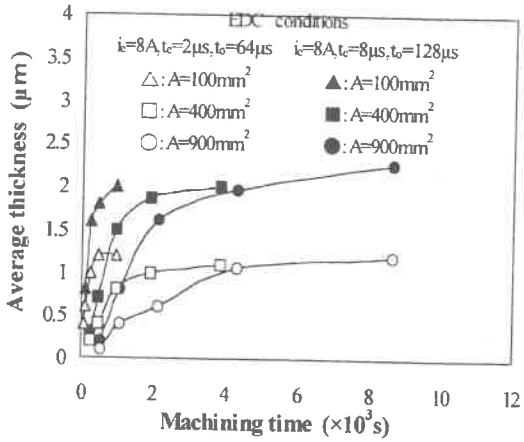

Fig 5: Relation between average thickness and machining time

current, τ : duty factor and t: machining time.

In removal or additive machining, the data for the amount of machining might lay almost on a straight line if these are represented against the energy density. In other words, in this case, discharge disperses uniformly over the whole area of work piece surface, and the unit amount of removal or additive machining by a single discharge shows a constant.

Fig 3 shows the electrode wear length against the energy density under the condition in Table 2 using sintered TiC electrode of 100mm². Electrode wear length increases in proportion to energy density and it means that the quantity of electrode wear increases according to the machining time as shown in Fig 2. Judging from this figure, the change of wear length seems less than 20% for the change of pulse duration te 2-16 μ s under same duty factor.

On the other hand, as for the generally used solid electrode or work piece, for example in the machining of steel with copper electrode, the removal rate of the steel (-) changes more than 200% for the change of pulse duration.

Therefore, the effect of pulse duration is extremely little on the electrode wear in surface modification. It is considered that the semi-sintered electrode is removed by the first impact force with the vaporization of working fluid owing to each discharge before it is affected by heat duration because the electrode material is so fragile.

Next, the relations between electrode wear length and energy density for different electrode

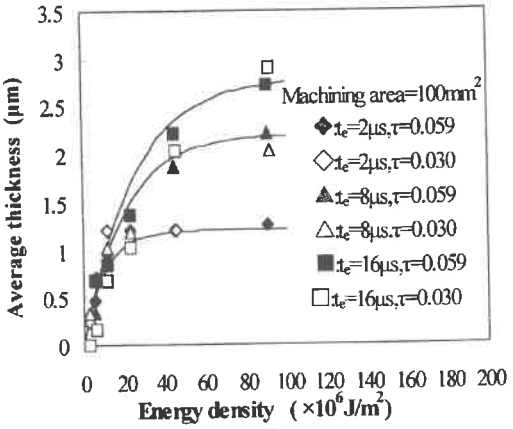

Fig 6: Relation between average thickness and energy density

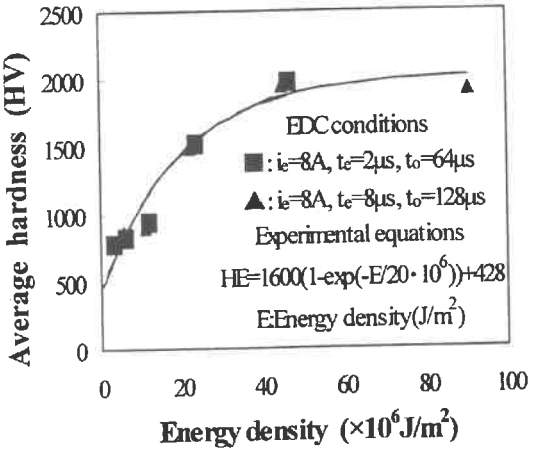

Fig 7: Relation between average hardness and energy density

area are shown in Fig 4. These data are acquired under the conditions of No.1 and No.4 in Table 1.

We can observe in this figure that the wear length for each energy density gets larger according to the electrode area and short pulse duration gets larger. This suggests us that the impact force which acts on the electrode depends on the dispersion of discharges and vanish time of bubble due to each discharge.

Thickness of Modified Layer

As for the thickness of the modified layer, we adopt average height from the profile curve measured by a roughness meter. The resultant thickness given under No.1 and No.4 conditions in Table 2 with 100, 400, 900mm² electrode is displayed in Fig 5 in relation to machining time. The average thickness that is the amount of the accumulation per electrode area increases up to the limit thickness according to each machining conditions . The relation between average thickness and energy density for all conditions in Table 2 with 100mm² is shown in Fig 6. This Figure tells us that the thickness of piled layer does not depend on the electrode area and duty factor but depends on the pulse duration.

In the surface modification by EDM the worn powder from the electrode is the main component of the piled layer on the work piece. The amount of electrode wear increases according to energy density as shown in Fig 3. It means that the amount of powder supplied into the gap region per unit time is constant through the machining process. On the contrary, the thickness of the layer depends on pulse duration. Consequently, it is considered that the generation of piled layer is strongly caused by the heat input due to each discharge. Furthermore, the fact that the thickness of generated layer reaches to a limit in spite of stationary supply of worn powder in the gap indicates a special feature of modification by EDM.

At the beginning of machining, the work piece is treated onto its virgin surface and the component of the surface gradually changes according to machining time. The top of the surface gets dense with TiC grains which are different from the original matrix of the work piece in thermal and mechanical properties. Therefore the thickness of piled layer reaches its limit in the machining process with constant conditions. Actually, piling does not occur onto the surface of complete sintered TiC under the same conditions in this research.

Hardness of Modified Layer

After machining at each time onto a plate of carbon steel (S45C) with a TiC semi-sintered electrode under the conditions of No.1, No.4, in Table 2, we measured the hardness of the work piece surface under 98mN of indentation force. The value of hardness averaged over 5 times are plotted in relation to energy density as shown in Fig 7. This graph shows that the data of the average hardness are on a curve gradually approaching the fixed value of about 2000HV. And it does not depend on any machining conditions and electrode area.

In order to evaluate the hardness of the inside

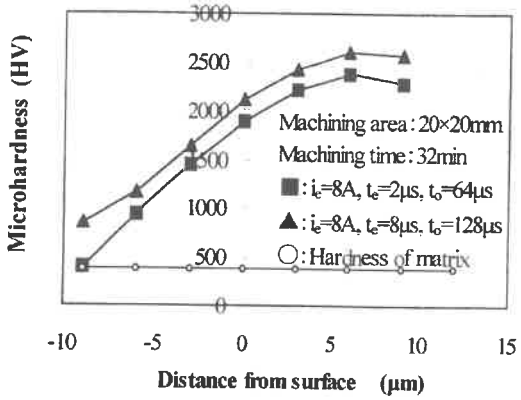

Fig 8: Microhardness distribution on the cross section of workpiece

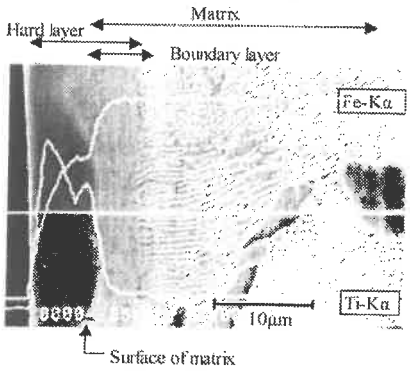

Fig 9: Result of EPMA on the cross section of hard layer

of the work piece, we grind the work piece from the top surface and measure the hardness of the ground face at each depth. The measured hardness distributions are illustrated in the Fig 8 which are obtained by machining a 400mm^2 work piece under conditions No.1, No.4 in Table 2. This Figure shows that the hardness changes against the distance from the surface and it reaches inside of the original work piece. Fig 9 shows the result of an elemental analysis on the cross section of the work piece by an EPMA (electron probe micro analyzer). The result of the line analysis on Ti and Fe tells us that the machined layer is functionally graded even inside of the original work piece. Ti diffuses into the work piece through the machining, and this material distribution corresponds to the hardness distribution of the work piece.

Effect of TiC Modified Layer on Press Die

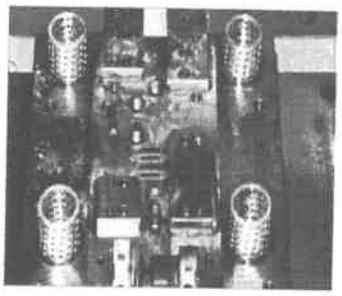

Fig 10: Press die set for test shot

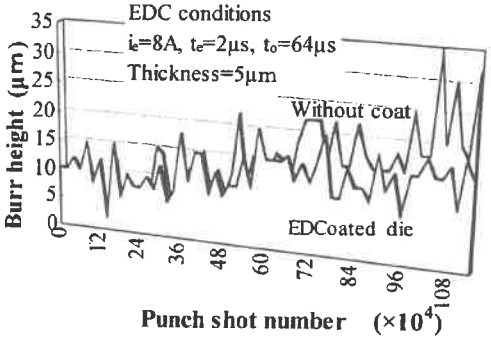

Fig 11: Burr height of punched product vs. punch shot number

We tried surface modification by EDM onto the surface of cutting edge of a press die and a punch made from hardened tool steel (SKD11) with the hardness of HRC 60. With TiC semi-sintered electrodes, the surfaces of the punch and die are treated by EDM with planetary motion for 20min. The electrode of 20mm diameter is scanned around the surface of edges. The machining conditions are i_e=8A, t_e= 2 μ s and t_o=128 μ s.

Fig 10 shows a photo of a part of the die set. 4 holes of ellipses (5mmx30mm) can be seen in the center of the photo. Treated hole and non-treated hole are arrayed alternately. Silicon steel plates of 0.5mm thickness are punched with this die and punch set. The height of burr of the punched products are measured for the evaluation of the die performance.

Fig 11 shows the relation between the burr height and shot number as the result of the punching test. While the burr height of the products made by non-treated die increases according to the increase of shot number , the products made by surface modified by EDM keep the same burr height after hundreds of thousands. It shows that the die life increases obviously.

Conclusions

Some experiments of electrical discharge machining for surface modification were carried out onto carbon steel plate with TiC semi-sintered electrode. Summarizing the data given in the experiments, the following conclusions can be drawn.

(1) The machine surface of the work piece is covered with TiC layer and it becomes functionally graded material.
(2) The removal or additive machining rate can be represented with energy density. This shows the division of the effects of machining conditions on the machining performance.
(3) The wear length of semi-sintered electrode depends on electrode area. Especially, pulse duration does not affect on the amount of removal in the same electrode area. It means that in the process of semi-sintered electrode wear, the electrode is removed mainly by the impact due to each discharge not by heating effect.
(4) The growth of the TiC layer on the work piece tends to stop at a certain thickness according to pulse duration but it dose not depend on the electrode area. It is important to concern the effect of heating by each discharge taking consideration of thermal properties of piled layer.
(5) From the hardness distribution of the machined surface, hardened region expands into the inside of original work piece. It corresponds to the distribution of Ti given by EPMA.
(6) It is confirmed that the life of the die treated by EDM with TiC electrode increases through punching test of silicon steel.

It is expected by applying this material coating method to die and cutting tool that we can industrialize this method as alternative technology of conventional PVD or CVD.

References

[1] H.Narumiya, et.al." EDM by Powder Suspended Working Fluid." *Proc.of ISEM-9*, (1989) 5.

[2] Y.Iino,et.al."Joining of Ceramic to Metal by use of an electric discharge machined surface." *J. Materials Science Letters* 8(1989) 493.

[3] N.Mohri, et.al." Metal Surface Modification by Electrical Discharge Machining with Composite Electrode." *Annals of CIRP*, 42,1,(1993) 219.

[4] K,Masui, et.al." Surface Modification of Tool Steels by Alloying Method Using EDM Process." *Proc. of ISEM-11*, (1995) 419.

[5] J.P.Kruth, et.al." Micro Structure Investigation and Metallographic Analysis of the White Layer of a Surface Machined by Electro Discharge Machining." *Proc. of ISEM-11*,(1995) 849.

[6] H.Miyake, et.al." Improvement of Tool Life through Surface Modification by Electrical Discharge Machining." *Proc. of ISEM-12*, (1998) 261.

[7] N.Mohri, et.al." Materials accretion by Electrical Discharge Machining with thin Electrodes." *Proc. of the International Seminar on Improving Machine Tool Performance*, (1998) 829.

[8] H.Takezawa, et.al." Precision Machining by Feedback of Shape Data." *Proc. of the 4th Japan- France Conference on Mechatronics*, Kitakyushu, Japan, 2 (1998) 732.

[9] N.Mohri, et al. "A New Process of Additive and Removal Machining by EDM with a Thin Electrode." *Annals of CIRP*, 49.1,(2000) 123.

Surface Quality and Tool Wear in Interrupted Hard Turning of 1137 Steel Shafts

Radu Pavel*, Keith Sinram, Dana Combs***,**
Michael Deis*, Ioan Marinescu***
* University of Toledo, MIME Department, Nitschke Hall 4005, MS312, Toledo, OH 43606
** Spicer Driveshaft Division, Dana Corporation, P.O. Box 955, Toledo, OH 43697-0955
*** Advanced Technology Resource Group, Dana Co., Technical Resource Park, 8000 Yankee Rd., Ottawa Lake, MI 49267

1. INTRODUCTION

The machining of hardened steel components with PcBN inserts having a geometrically defined cutting edge has gained substantially in importance due to improvements in the performance of such modern cutting tool materials. Hard turning is increasingly a profitable alternative to finish grinding. The objective is to remove workpiece material in a single cut rather than a lengthy grinding operation, thus reducing processing time and production costs.

Many studies have been carried out in the hard turning of continuous surfaces and the success of this method has encouraged in the recent years studies in the interrupted hard turning area [1], [2]. An interrupted cut occurs when the non-uniform shape of the workpiece disrupts the otherwise smooth removal of material. Consequently interrupted hard turning can be defined as a turning process of hardened parts (>45 HRC) having areas with interrupted surfaces.

The studies in the interrupted hard turning field have concentrated mostly on tool wear evolution or mechanism [1], [4]. For continuous hard turning the maximum tool wear land width (VB_{max}) shows a near linear increase with cutting distance after initial rapid wear [3]. The same effect has also been noticed for interrupted hard turning [1]. On the other hand, tool life has been found to be very sensitive to both cutting speed and frequency of interruption [4]. More recent studies [5] highlight that the low-content CBN tool is superior to a high–content CBN tool in terms of tool wear and surface integrity for intermittent hard turning. The cutting force decreases with the increase of the cutting speed while the thrust cutting force increases significantly with the increase of tool wear.

In terms of surface finish the roughness parameters taken into consideration are generally the average roughness R_a and average maximum height of the profile R_z [6], [7], [8]. Results come mostly from studies of continuous hard turning. According to some authors [9] the main factors that have a direct influence on surface quality are the corner radius of the cutting edge and the feed rate. Generally speaking, the greater the feed, the greater the value of R_a; however, this is still influenced by the occurrence of tool nose chipping or surface cratering [4].

When analyzing surface quality in hard turning, special attention was paid to metallurgical alterations in the superficial layer. Most common for hard turning is the occurrence of a white layer. White layer is a result of microstructural alteration. It is called "white" layer because it resists standard etchants and appears white under an optical microscope (or featureless in a scanning electron microscope). In addition the white layer has high hardness, often higher than the bulk [10]. Authors [10], [11] claim that the white layer has a mixed martensite and austenite structure.

Typical materials that are hard-turned are 5120 steel (62 HRC), 1050 steel (62 HRC), 9310 (60 HRC) and 4320 steel (60-62 HRC) [12]. However, other steels are constantly used on a large scale in industry and their behavior in terms of hard turning is still insufficiently explored.

This paper presents the results of an experimental study of hard turning of a spline shaft made of 1137 steel hardened to 47 - 50 HRC. The goal was to obtain a similar or better surface finish as in case of grinding for the external interrupted surface (OD turning) defined by ten splines. Two types of cutting tools were first analyzed from the viewpoint of tool wear and surface roughness. The wear of the cutting inserts was evaluated and recorded using optical and SEM microscopy. After choosing the most suitable insert for interrupted cutting, a mathematical model for average roughness prediction was determined using Response Surface Methodology. The response variable was the average surface roughness, R_a, and it was investigated as a function of the cutting regime (feed, cutting speed, and depth of cut) for a given geometry of the cutting tool. The workpieces used for wear trials were also analyzed from the viewpoint of superficial layer transformations, pre-eminently occurrence of white layer.

2. EXPERIMENTAL SETUP

The component parts considered for this study are spline shafts made of 1137 steel, induction hardened to 47 - 50 HRC. Figure 1 presents the component part and the surface (IS) that was machined.

This type of steel is widely used for parts where a large amount of machining is necessary, or where threads, splines or other operations offer special tooling problems. Table 1 presents the chemical composition of 1137 steel.

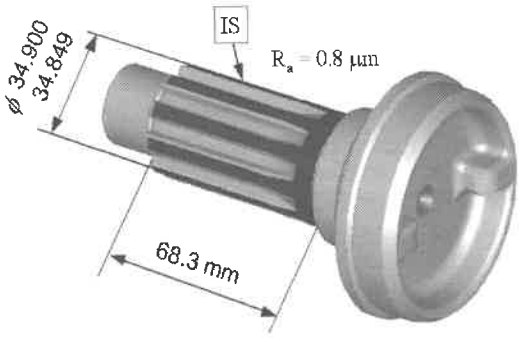

Figure 1. Spline shaft 1137 steel, 3D view

Table 1. Chemical composition of 1137 steel

%C	%Mn	%P (Max.)	%S (Max.)
0.32 - 0.39	1.35 – 1.65	0.040	0.08 – 0.13

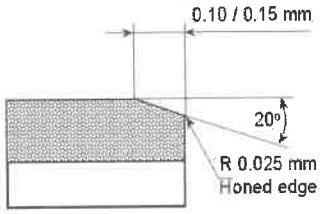

Figure 2. Edge preparation for PcBN inserts

The cutting tools considered for this research were specifically designed for hard turning applications and are relatively new on the profile market. One type of PcBN insert is AMBORITE DBC50 and the other type AMBORITE DBN45. Both types have the same nose radius, equal to 0.8 mm.

DBC50 is a low content, fine grain PcBN material on a tungsten carbide base. The CBN content is 50% by volume in a TiC binder phase, and the average CBN grain size is 2µm. DBN45 is a low content PcBN material (45% - CBN) with a sub-micron grain size integrally bonded with a titanium nitride (TiN) ceramic binder onto a tungsten carbide base. The cutting edge preparation is the same for DBC50 and DBN45 and consists of a chamfer at 20^0 from the rake face and a hone of the active edge. Figure 2 presents the edge preparation characteristics.

3. RESULTS AND DISCUSSIONS

3.1. Flank wear investigation

Maximum flank wear land width (VB_{max}) was monitored as a function of cutting length. The cutting regime considered was: depth of cut a = 0.18 mm, cutting speed V = 125 m/min, and feed f = 0.15 mm/rev. No coolant was used – dry turning. The number of passes between two measurements was chosen 8 for each type of component part. The wear analysis consisted in optical investigation (using a stereo microscope) of the inserts and measurement of the maximum flank wear land width, plus SEM observation of the worn area. Same number of passes has been done with each type of cutting insert. The wear experiments have been replicated (the same cutting parameters and mountings were used). An additional test has been performed for higher cutting speed, V = 175 m/min, the other parameters remaining unchanged (depth of cut a = 0.18 mm, feed f = 0.15 mm/rev). The preset tool life criterion was that when maximum flank wear land width becomes equal or greater than 0.2 mm, the tool life ends.

Figure 3 presents the VB_{max} versus cutting length for the first series of wear tests while figure 4 presents the results for the replicated wear tests. Figure 5 presents the wear evolution in case of high-speed tests, V = 175 m/min. It can be remarked for all tests that the flank wear in case of using DBC 50 is higher comparing to DBN45. However, in first two cases it is considered that the differences are not significant enough to specify with certitude which type of insert has a better behavior for interrupted hard turning. This situation is considered to be a result of the fact that the cutting process was interrupted to often in order to take measurements of the flank wear so a stable cutting regime could not be reached. The difference in the PcBN inserts behavior becomes more significant when the interval between two measurements of wear is increased to 16 and while the cutting regime is tougher – see last two measurements for the higher speed case (V = 175 m/min) on the chart from figure 5.

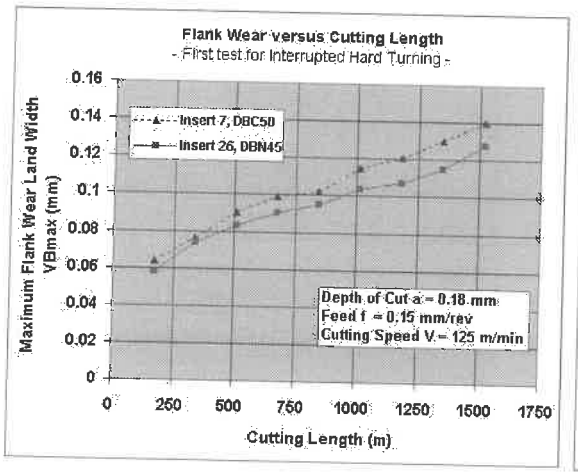
Flank Wear versus Cutting Length
- First test for Interrupted Hard Turning -
Maximum Flank Wear Land Width VBmax (mm)
Cutting Length (m)
Insert 7, DBC50
Insert 26, DBN45
Depth of Cut a = 0.18 mm
Feed f = 0.15 mm/rev
Cutting Speed V = 125 m/min

Figure 3. Initial wear tests

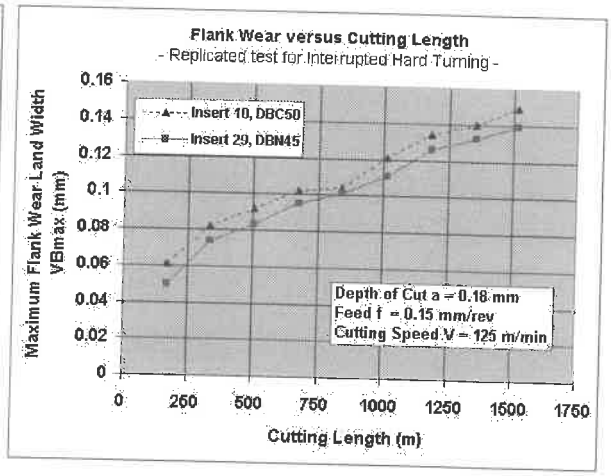
Flank Wear versus Cutting Length
- Replicated test for Interrupted Hard Turning -
Maximum Flank Wear Land Width VBmax (mm)
Cutting Length (m)
Insert 10, DBC50
Insert 29, DBN45
Depth of Cut a = 0.18 mm
Feed f = 0.15 mm/rev
Cutting Speed V = 125 m/min

Figure 4. Replicated wear tests

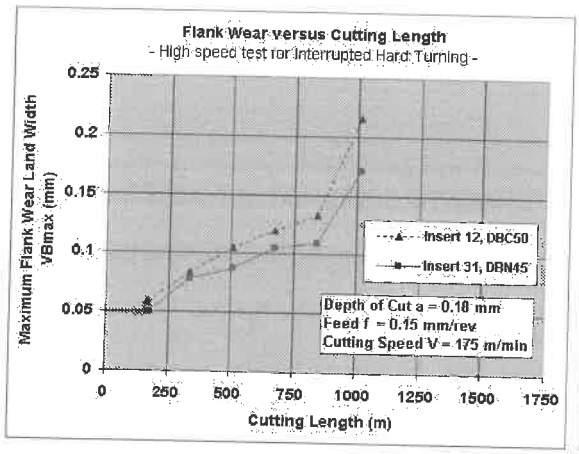
Flank Wear versus Cutting Length
- High speed test for Interrupted Hard Turning -
Maximum Flank Wear Land Width VBmax (mm)
Cutting Length (m)
Insert 12, DBC50
Insert 31, DBN45
Depth of Cut a = 0.18 mm
Feed f = 0.15 mm/rev
Cutting Speed V = 175 m/min

Figure 5. Initial wear tests

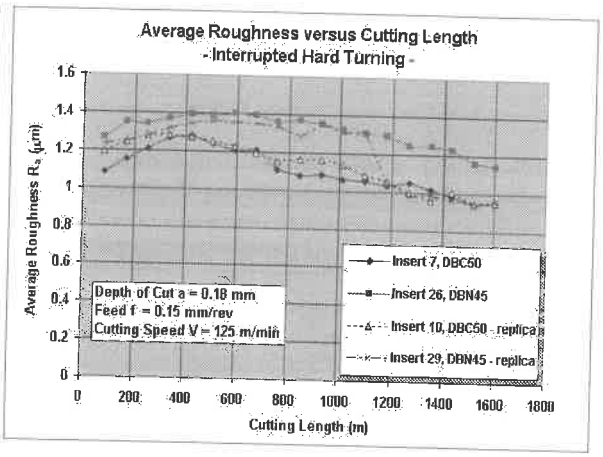
Average Roughness versus Cutting Length
- Interrupted Hard Turning -
Average Roughness Ra (µm)
Cutting Length (m)
Insert 7, DBC50
Insert 26, DBN45
Insert 10, DBC50 - replica
Insert 29, DBN45 - replica
Depth of Cut a = 0.18 mm
Feed f = 0.15 mm/rev
Cutting Speed V = 125 m/min

Figure 6. Replicated wear tests

Figure 6 presents the average roughness evolution for the component parts used for wear experiments. It can be remarked that for all the situations the roughness has an initial increase followed by a plateau stage and then by a slow decrease. This behavior of R_a is also encountered in common turning and it is explained by the fact that while the flank wear increases the cutting edge becomes 'dull' in the contact area. As a result, the depth of the tool traces on the workpiece surface tends to decrease and consequently the Ra decreases as the cutting edge accommodates the workpiece surface.

The SEM analysis performed in case of interrupted cutting revealed wear patterns similar to abrasion wear patterns. Grooves parallel to the movement of chip/workpiece material could be remarked. It is considered that these grooves are provoked by the hard particles from workpiece material and by the CBN grains pulled out through an attrition process and due to the removal of the ceramic binder through abrasion. Figure 8 presents the flank wear in case of DBN45 insert type; besides the fine vertical grooves that were remarked on the tool flank, traces of adhered layer could also be seen, mostly under the flank wear region. A much thicker adhered layer was also found on the rake face for both types of PcBN inserts. Figure 7 presents the chamfered edge of a DBC50 insert with such an adhered layer. EDS (Energy Dispersive Spectrometer) analyses confirmed that material from the workpiece adhered to the cutting insert. It is assumed that during cutting the adhered layer has a protective effect against abrasion mostly for the rake face and lesser for the flank of the insert.

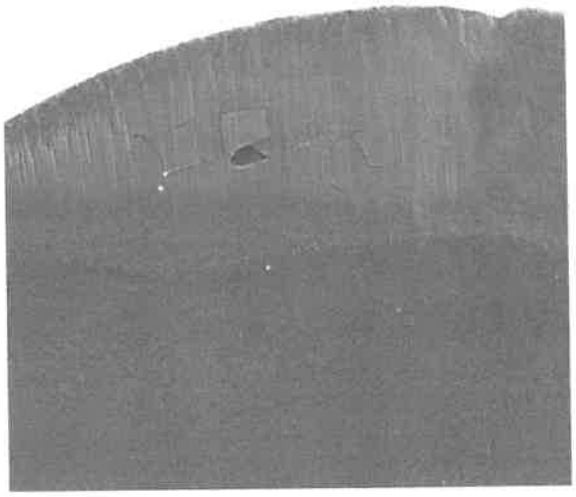

Figure 7. Adhered layer on hamfered cutting edge, Insert 7, DBC50, 250X

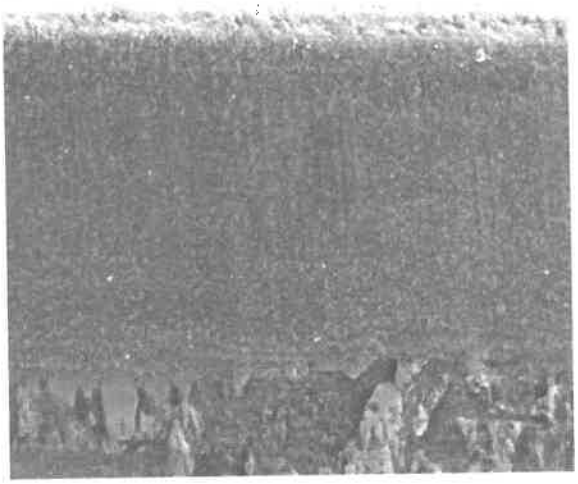

Figure 8. Flank wear pattern (DBN45, 250X)

3.2. Analysis of Surface Finish

The factorial technique was used to analyze the evolution of average surface roughness R_a versus the cutting regime. A preliminary experiment of mixed 3^2 factorial was first conducted varying only feed and cutting speed. Following the results obtained during the preliminary experiment, a replicated 3^3 factorial experiment was designed in order to determine an accurate predictive function for R_a versus the cutting regime. The intervals considered for the parameters of the cutting regime were chosen within the recommended operating values of the PcBN inserts: feed f = 0.025 to 0.229 mm/rev, cutting speed V = 100 to 150 m/min, and depth of cut a = 0.102 to 0.254 mm. The experimental matrix for the 3^3 design is presented in table 2. The factorial experiment was completely randomized. The dedicated software STATGRAPHICS *Plus* 5.0 was used as aid tool for statistical analysis of the recorded data.

Table 2 Experimental matrix for 3^3 design

Factors of influence / Levels	Feed (mm/rev)	Cutting Speed (m/min)	Depth of Cut (mm)
Low	0.025	100	0.102
Medium	0.127	125	0.178
High	0.229	150	0.254

According to [13] the terms containing third factor interactions can be neglected, as they do not have a physical interest. From this reason, only the second order factors were considered. The initial analysis of variance proved that feed is the most significant factor. Depth of cut was found to be also a significant factor but its influence is much lower comparing to the cutting feed. The effect of cutting speed can be neglected. However, in an initial approach the residuals versus predicted values chart suggested that a transformation of the response variable should be performed. Several transformation were tried for R_a and the solution considered best was found to be for the following conditions: maximum order effect considered for the analysis is 2, a normal logarithm transformation is applied to the response variable. The optimization of regression equation was made in terms of R-squared and the chart of residuals versus predicted values. Finally, the results of analysis of variance for this optimal case are presented in table 3.

Figure 9 presents the response surface for the transformed variable Log(Ra) while figure 17 presents the response surface for R_a versus feed and depth of cut. The predictive model was experimentally validated for cutting regimes different from those considered for the factorial design. Additionally, a study of optimum cutting parameters in terms of reaching and maintaining the prescribed surface roughness R_a = 0.8 μm was completed. It was obtained that the prescribed value of R_a can be easily achieved and

maintained while maintaining the dimensional accuracy of the workpiece. Considering a minimum cutting time criterion while applying a correction for tool wear, the optimum cutting regime was found: f = 0.102 mm/rev, a= 0.178 mm, and v = 125 m/min.

Table 3. Analysis of Variance for Log(Ra)

Source	Sum of Squares	DOF	Mean Square	F - Ratio	P -Value
A:Feed	65.9761	1	65.9761	3712.97	0.0000
C: Depth of Cut	0.245545	1	0.245545	13.82	0.0005
AA	3.26228	1	3.26228	183.59	0.0000
Lack-of-fit	0.140475	5	0.028095	1.58	0.1838
Pure error	0.835147	47	0.0177691		
Total	83.3842	55			
R^2 = 98.6153 % $R^2_{adjusted}$ = 98.5355 %	The equation of the fitted model is $LOG(R_a)$ = -2.44022 + 25.5698*Feed - 1.08668*Depth of Cut -48.4159*Feed^2				

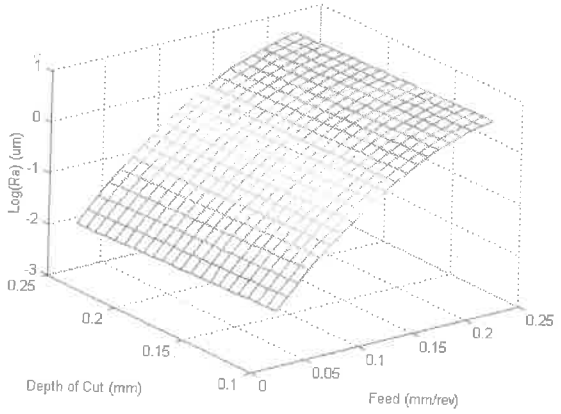

Figure 9. The response surface for Log(Ra)

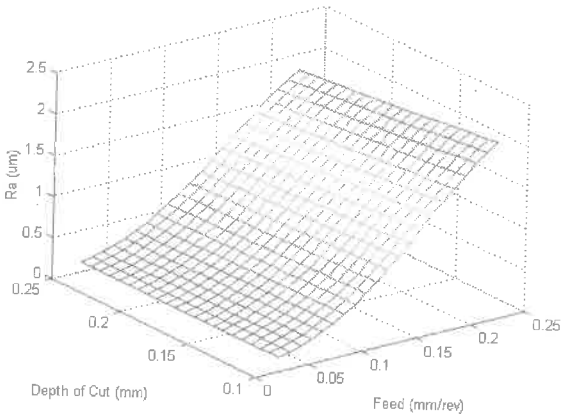

Figure 10. The response surface for Ra

A study of surface topography revealed a similar pattern of the machined surface as for common turning of steels, as long as the insert was not worn. Figure 11 shows such a pattern captured through a ZYGO instrument. While the cutting insert starts to wear off, the profile of surface changes from the classical helix shape (figure 11 – 1) towards a more and more irregular shape as in figure 11, 2) and 3). This change of profile with time is directly related to tool wear.

It can be remarked that while in terms of Ra hard turning can easily achieve surface finish comparable or better than grinding, in terms of other surface finish parameters, further investigations need to be performed.

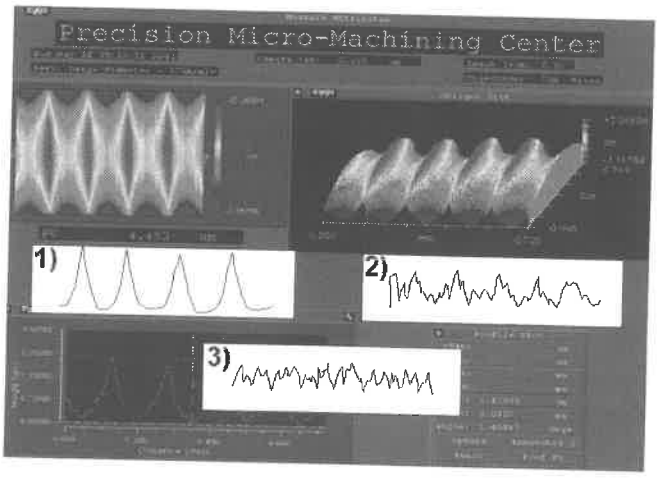

Figure 11. Topography of hard turned surface

3.3. White Layer investigation

The white layer evolution was investigated only as a function of flank wear of the insert. Samples were cut from workpieces involved in wear experiments. The samples were further nickel covered to avoid edge rounding during polishing. Both longitudinal and transversal areas of the machined surface

were investigated. It could be remarked that only for the highest values of VB_{max} (over 0.17 mm), the white layer starts to have a consistency, in all the other samples being no certitude for consistent white layer consideration. The maximum thickness of the white layer observed was found to be not bigger than 0.007 mm. A darker layer could be remarked under the observed white layer. It is inferred that the dark layer is overtempered martensite but more research has to be done in this area.

4. CONCLUSIONS

The hard turning of 1137 steel shafts has been successfully completed. The 1137 steel did not raise any specific problems to the PcBN inserts used for these experiments. AMBORITE DBN45 made proof of better performance in interrupted cutting.

The main wear mechanism for the PcBN inserts was found to be the abrasion of the binder material by the hard particles of the workpiece and the loose CBN grains pulled out during the cutting process. It is assumed that the CBN grains are pulled out due to a combined abrasive/attrition wear action. A protective layer made of workpiece material builds up mostly on the rake face. It is presumed that at higher speed the adhered layer becomes softer and it is easily scratched and penetrated by the hard particles thus accelerating the wear.

No consistent white layer was remarked but for high values of insert flank wear, closer to tool life limit.

A regression equation that predicts average roughness of the hard turned surface versus cutting regime was determined. Feed was found to be the most significant factor of influence followed by the depth of cut that, however, has a much lower influence. The lowest significance belongs to the cutting speed, which was not considered in the equation. An optimization of the cutting regime for the prescribed roughness was performed. The dimensional accuracy could be achieved and maintained throughout this study.

An investigation of surface topography showed a similar pattern of the machined surface as for common turning of steels as long as the insert was not worn. While the cutting insert starts to wear off, the profile of surface changes and becomes irregular. Further studies involving different roughness parameters becomes necessary in order to completely characterize the surface finish obtained through hard turning.

5. REFERENCES

[1] Chou, Y. K., Evans, C. J., *"Cubic boron nitride tool wear in interrupted hard cutting"*, Wear 225 – 229, (1999), pp. 234-245.

[2] Dawson, Ty G., Kurfess, R. T., *"Hard turning, tool life, and surface quality"*, Manufacturing Engineering, April 2000, pp. 88 – 98.

[3] Chou, Y. K., Evans, C. J., *"Tool wear mechanism in continuous cutting of hardened tool steels"*, Wear 212 (1997), pp. 59-65.

[4] Lin, Z. C., Chen, D. Y., *"A study of cutting with a CBN tool"*, Journal of Materials Processing Technology, 49 (1995), 149-164.

[5] Ko, J. T., Kim, S. H., *"Surface integrity and machineability in intermittent hard turning"*, The international Journal of Advanced Manufacturing Technology, No. 18, 2001, pp. 168 – 175.

[6] Knuefermann, M. M. W., Read, R. F. J., Nunn, R., Clark, I. E., Fleming, M. A., *"22 nm R_a surface finish achieved with AMBORITE DBN 45 in ultra-precision turning of hardened steel"*, Industrial Diamond Review, No. 2, 2001, pp. 87 – 92.

[7] Liu, C. R., Mittal, S., *"Single-Step Superfinishing Using Hard Machining Resulting in Superior Surface Integrity"*, Journal of Manufacturing Systems, Vol. 14/No. 2, 2001, pp.129 – 133.

[8] Sood, R., Guo, C., Malkin, S., *"Turning of Hardened Steel, Society of Manufacturing Engineers"*, MR99-241, 1999, pp.1-12.

[9] Klocke, F., Lung, D., Liermann, J., Rottger, K., *"Part quality in hard turning"*, 1997,pp. 389 – 400.

[10] Griffiths, B. J., Furze, D. C., *"Tribological advantages of white layers produced by machining"*, Transactions of ASME, 1987, 109, pp. 338 – 342.

[11] Chou, Y. K., Evans, C. J., *"White layers and thermal modeling of hard turned surfaces"*, International Journal of Machine Tools & Manufacture 39, 1999, pp. 1863 – 1881.

[12] Hasan, R., *"Why are you still grinding?"*, Manufacturing Engineering, February 1998, pp. 76-78.

[13] Montgomery, D. C., *"Design and Analysis of Experiments"*, John Wiley & Sons, Inc., 2001.

Ultra-Precision Cutting of Stainless Steel by Using Coated Carbide Bite

Shigehiko SAKAMOTO*, Heiji YASUI*, Akira Fujimori* and Sumihisa KONDO*

*: Dept. of Mechanical Engineering & Materials Science,
Kumamoto University,
2-39-1, Kurokami, Kumamoto 860-8555, Japan
Phone : 81-96-342-3758
Fax : 81-96-342-3764
E-mail : sak@mech.kumamoto-u.ac.jp

Keywords: ultra-precision cutting, cutting tool, stainless steel, surface roughness

1. Introduction

The technique of ultra-precision cutting using the diamond bite is well-established for soft materials such as aluminum, copper, plastic and so on in these days. However, there are not still much attempts on the ultra-precision cutting of difficult-to-cut metals such as titanium metals, stainless steel and so on. Because the diamond bite is worn quickly at very short cutting length, the diamond bite is not convenient for the ultra-precision cutting of difficult-to-cut metals. In our previous research[1] we found out the availability of ultra-precision cutting of titanium alloys using a commercial coated cemented carbide bite in no use of special equipment. This research describes on the possibility of the ultra-precision cutting of stainless steel SUS 316 using a coated cemented carbide bite under three kinds of cutting fluids.

2. Experimental procedure

The experiments are executed by face-turning the stainless steel SUS 316 with cutting tool set on the ultra-precision turning lathe. The overview of experimental setup is shown in Fig. 1. The experimental conditions are summarized in Table 1. The workpiece metal used is stainless steel SUS 316 (18Cr-12Ni-2.5Mo) and its shape is ϕ50mm in diameter and 10mm in thickness.

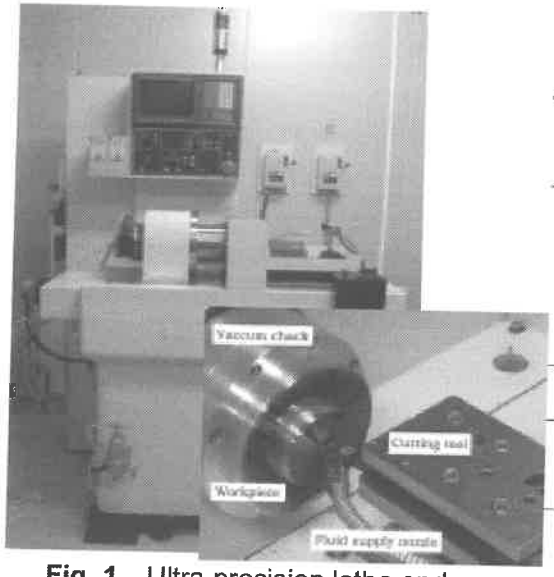

Fig. 1 Ultra-precision lathe and face-turning setup

Table 1 Experimental conditions

Machine tool:	Ultra-precision Lathe ULC-100A, Toshiba Machine CO.,LTD.
Cutting tool:	Cemented carbide bite Cermet bite Coated cemented carbide bite Nose radius: 0.4 mm Rake angle: 0 deg, Relief angle: 7 deg
Workpiece material:	SUS 316 (18Cr-12Ni-2.5Mo)
Cutting fluid:	Kerosene Oil type cutting fluid (Type B, Type Y)
Cutting conditions	Cutting speed: V = 90~125 m/min Depth of cut: d = 5 μm Feed rate: f = 2~10 μm/rev

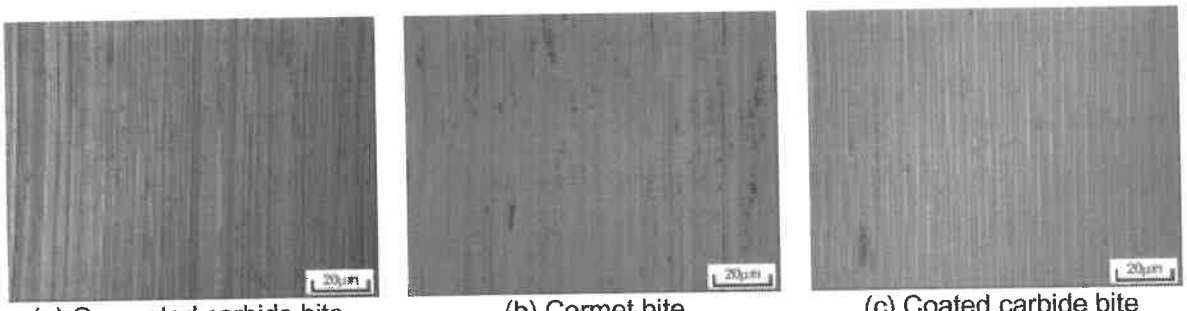

(a) Cemented carbide bite [Rz = 460nm(P-V)] (b) Cermet bite [Rz = 320nm(P-V)] (c) Coated carbide bite [Rz = 60nm(P-V)]

Fig. 2 Influence of cutting tool on face-turned SUS 316 surface
(f=2μm/rev, d=5μm, V=120m/s, L=100m, Oil type cutting fluid B)

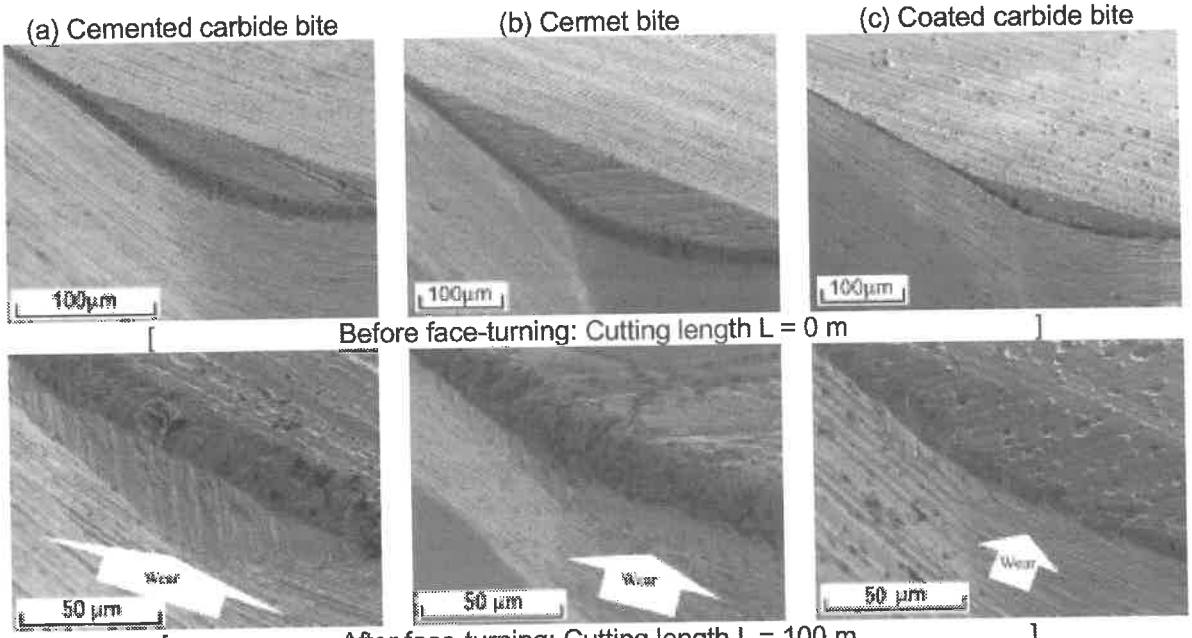
(a) Cemented carbide bite
(b) Cermet bite
(c) Coated carbide bite
100μm
Before face-turning: Cutting length L = 0 m
50 μm
After face-turning: Cutting length L = 100 m

Fig. 3 SEM photographs of cutting tool before/after face-tuning SUS 316
(f=2μm/rev, d=5μm, V=120m/s, L=100m, Oil type cutting fluid B)

Three kinds of commercial cutting tools which are cemented carbide bite, cermet bite and coated cemented carbide bite are used in this experiment. Cutting fluids used are kerosene and two kinds of oil type cutting fluids which are denoted by Type B and Type Y, respectively. The difference between these oil type cutting fluids is due to the different extreme additives included in the cutting fluid. The face-turned stainless steel SUS 316 surfaces are examined by observing with a Nomarski differential interference microscope and measuring with surface interferometer WYKO. The observation of cutting tools is done with SEM.

3. Results and Discussions

3.1 Influence of cutting tool upon surface roughness

First of all, the influence of different cutting tools on the surface roughness in the ultra-precision cutting of stainless steel SUS 316 is investigated. Three kinds of cutting tools which are a cemented carbide bite, a cermet bite and a coated cemented carbide bite is used in the

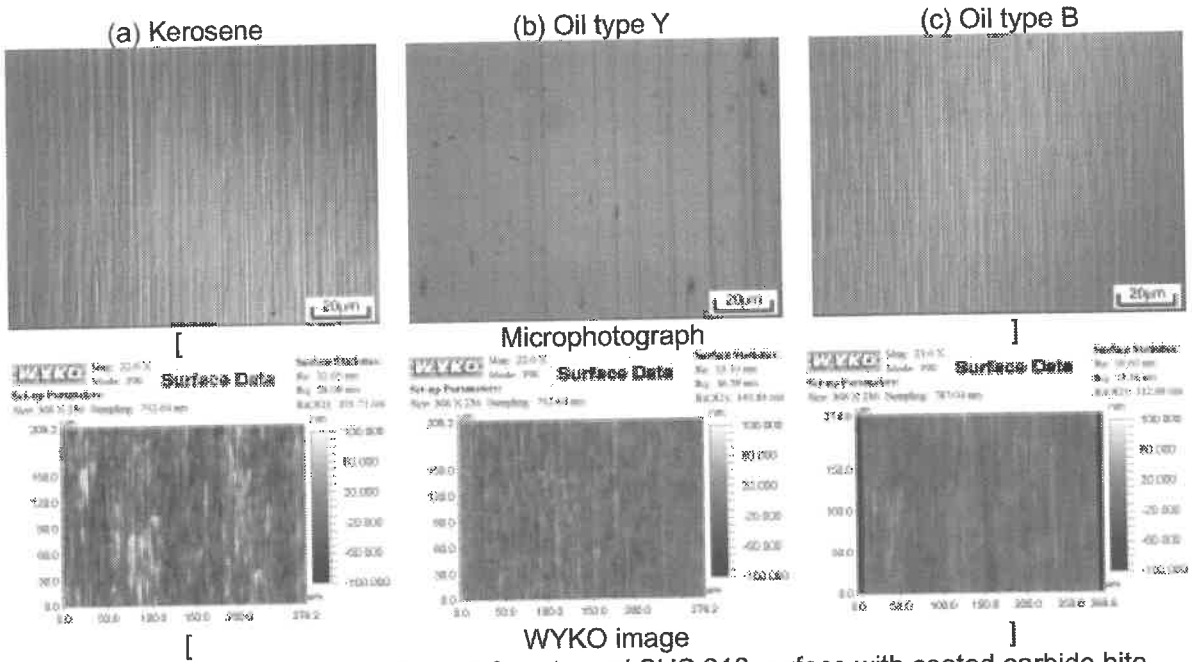

Fig. 4 Influence of cutting fluid on face-turned SUS 316 surface with coated carbide bite (f=2μm/rev, d=5μm, V=120m/s, L=100m)

experiment. Fig. 2 shows the microphotographs of face-turned SUS 316 surface with three kinds of cutting tools under using oil type cutting fluid Type B. It seems that surface of SUS 316 face-turned with coated cemented carbide bite is smoother than those with cemented carbide bite and cermet bite. The 2D surface roughness Rz in face-turning of SUS 316 is 460nm(P-V) for using cemented carbide bite, 320nm(P-V) for using cermet bite and 60nm(P-V) for using coated cemented carbide bite, respectively. Fig. 3 shows the cutting edge of three kinds of cutting tools before and after face-turning SUS 316 at cutting length of 100m. The enormous wear at even cutting length of 100m is found out on the cutting point of cemented carbide bite and cermet bite. Compared with those, on the other hand, the wear of coated cemented carbide bite is so small. The wear of cutting tool is concerned with the surface roughness of face-turned SUS 316. From the results, it is found that a cemented carbide bite and a cermet bite is not available because of their high bite wear rate. Then the coated cemented carbide bite is used in a series of following experiments for obtaining the surface roughness of SUS 316 below 100nm(P-V).

3.2 Influence of cutting fluids upon surface roughness

The microphotographs and WYKO images of face-turned SUS 316 surfaces with coated carbide bite under using each cutting fluid are shown in Fig. 4. According to the 3D measurement of the surface roughness $Rz_{(3D)}$ with WYKO, it is 190nm(P-V) under using kerosene, 140nm(P-V) under using oil type cutting fluid Type Y and 110nm(P-V) under using oil type cutting fluid Type B, respectively. Smooth cutting grooves are observed on the surface of SUS 316 face-turned under using oil type cutting fluid Type B. The both surfaces of SUS 316 face-turned under using kerosene and oil type cutting fluid Type Y, on the other hand, are formed by rough and irregular cutting grooves. The improvement in surface roughness is considered to be caused by the good additives contained in the oil type cutting fluid Type B. From the results, it is referred that the type of cutting fluid considerably effects on the ultra-precision turning characteristics of SUS 316. It is important that the most suitable cutting fluid for ultra-precision cutting of SUS 316 is selected.

3.3 Tool life of coated carbide bite in ultra-precision turning of SUS 316

The relationship between surface roughness Rz and feed rate f in the face-turning of SUS 316 with coated cemented carbide bite under using oil type cutting fluid Type B is shown Fig. 5. The surface roughness becomes smooth as the feed rate decreases. In this experiment, the smoothest SUS 316 surface is about 60nm(P-V) at the minimum feed rate of 2μm/rev. In the Fig. 6, the ultra-precision face-turned SUS 316 surface in two cutting length of 20m and 875m with coated cemented carbide bite under using oil type cutting fluid Type B are compared. At first short cutting length of 20m, the 3D surface roughness $Rz_{(3D)}$ and the 2D surface roughness Rz are 80nm(P-V) and 50nm(P-V), respectively. At the cutting length of 875m with coated cemented carbide bite under using oil type cutting fluid Type B, furthermore, the 2D surface roughness Rz is still 95nm(P-V). Tool damage of coated cemented carbide bite varies from Fig.7(a) to 7(f) according to cutting length L. While the 2D surface roughness Rz of face-turned SUS 316 is below 100nm(P-V) until the cutting length of 1,000m as shown in Fig.8. After cutting length of 1,000m, the flank face of coated cemented carbide bite is much worn as shown in Fig.7(f). At last the PVD layer coated on the cutting point of cutting tool is removed and basement of the cutting tool appears. As the result, the surface roughness of face-turned SUS 316 deteriorates rapidly.

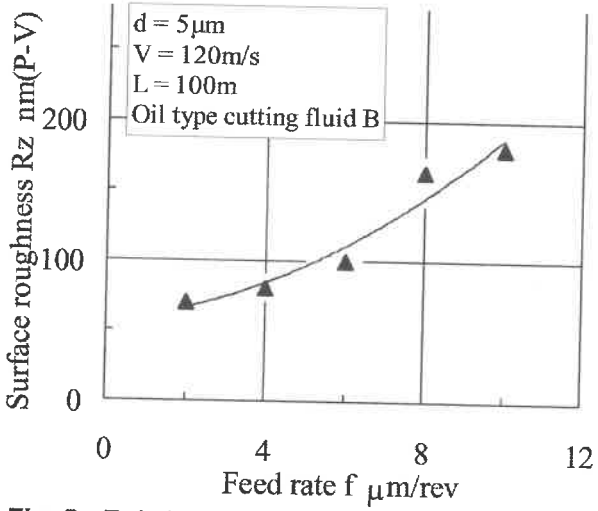

Fig. 5 Relationship between surface roughness and feed rate in the face-turning of SUS 316 with coated carbide bite

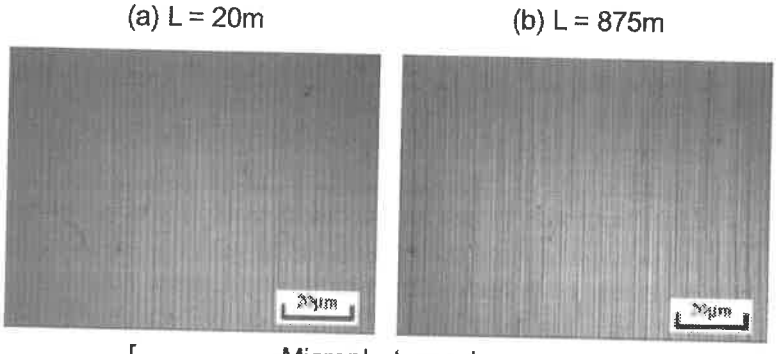

[Microphotograph]

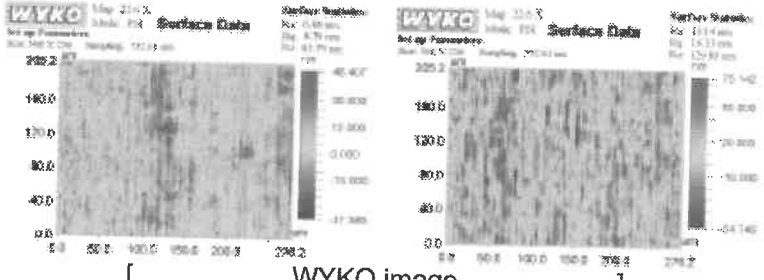

[WYKO image]

Fig. 6 Change of face-turned SUS 316 surface with cutting length using coated carbide bite (f=2μm/rev, d=5μm, V=120m/s, Oil type cutting fluid B)

4. Summary

To built the ultra-precision cutting technique of stainless steel for which the use of diamond bite is difficult due to its high wear rate, the possibility of coated cemented carbide bite is examined under using three kinds of cutting fluids. The main conclusions

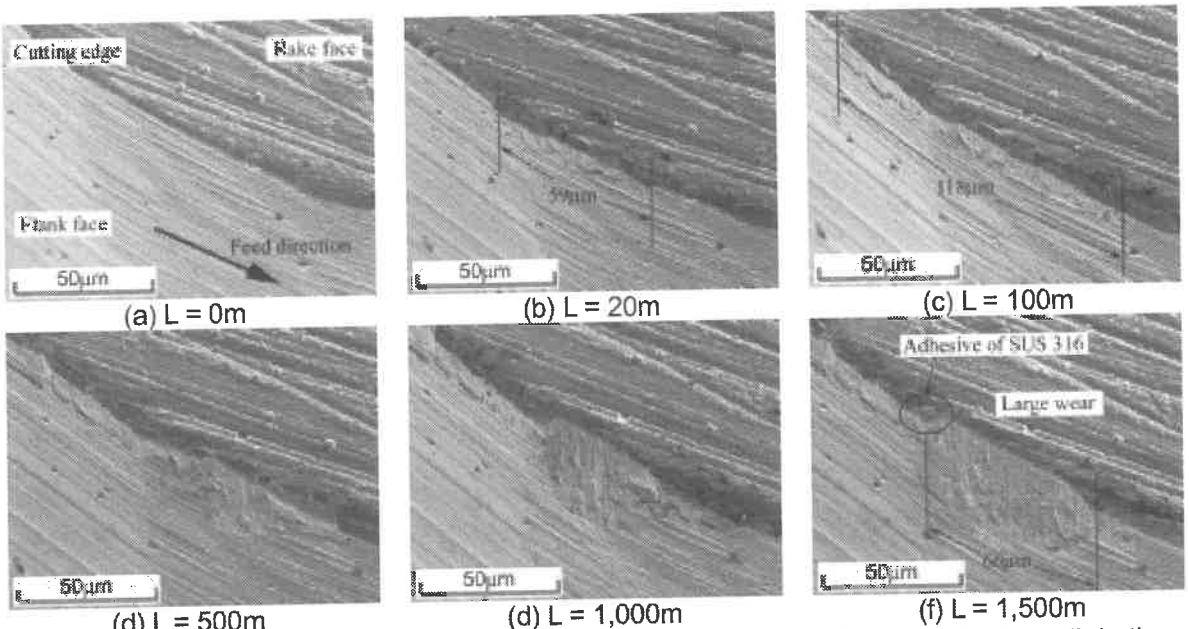

Fig. 7 Change of cutting point on the coated cemented carbide bite with cutting length in the face-turning of SUS 316 (f=2μm/rev, d=5μm, V=120m/s, Oil type cutting fluid B)

obtained are as follows;

1) In the case of kerosene used generally as the cutting fluid in ultra-precision cutting of aluminum, copper and so on, the surface roughness of SUS 316 is rougher than 200nm(P-V) at the first short cutting length of 100m by using coated cemented carbide bite.
2) In the case of oil type cutting fluid including the special additives, on the other hand, the surface roughness of SUS 316 face-turned with coated cemented carbide bite is smoother than 60nm(P-V).
3) The surface roughness of SUS 316 face-turned with coated cemented carbide bite under using oil type cutting fluid including the special additives is kept smoother than 100nm(P-V) until the cutting length of 1,000m.

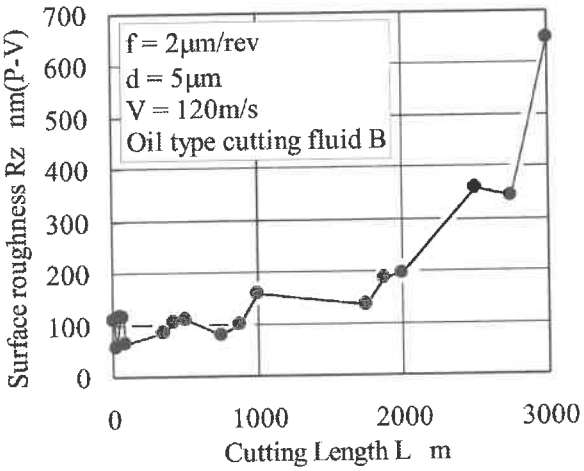

Fig. 8 Relationship between surface roughness and cutting length in the face-turning of SUS 316 with coated carbide bite

Acknowledgment

The authors would like to thank Toshiba Machine Co., Ltd., Osaka Diamond Industrial Co., Ltd., Yushiro Chemical Industry Co., Ltd., UEX Co., Ltd. and Daido Steel Co., Ltd for providing cutting fluids and stainless steel workpiece materials. A part of this research is supported by Grant-In-Aid for Scientific Research, 2000-2001, in Japan.

References

[1] H.YASUI, S.SAKAMOTO, M.KAWADA, S.KONDO and A.HOSOKAWA: Ultra-Smoothness Cutting of α–β Titanium Alloy, Proc. of 2000 Annual Meeting of ASPE, 2000, pp.70-73.

SPECTRAL ANALYSIS OF ACOUSTIC EMISSION (AE) DURING THE ULTRAPRECISION MACHINING OF SINGLE CRYSTAL InSb

Helder A.T.Silva[(1)], Jaime G.Duduch, Arthur J.V.Porto
University of São Paulo (USP), Department of Mechanical Engineering,
Laboratory of Precision Engineering, São Carlos, BRAZIL.
(1)helderts@sc.usp.br

Abstract: The purpose of this work is to investigate the relationship between the material removal mechanism in the diamond turning of (100) single crystal indium antimonide (InSb) and the characteristics of acoustic emission (AE) spectral signal. The spectral characteristics of the raw AE signal and the surface finish were examined using Scanning Electron Microscopy (SEM) and correlated with the cutting mode. The results showed that it is possible to know the actual cutting mode during the machining of indium antimonide using AE.

Keywords: ultraprecision machining, diamond turning, brittle materials, acoustic emission.

1 Introduction

Single Point Diamond Turning (SPDT) is a machining process first developed for the production of optical components of ductile materials, such as aluminium and copper. This technology evolved to brittle materials in the optical and electronic industry to produce surfaces with form accuracy of the order of micrometers and roughness of the order of nanometers. (1, 2, 3). In order to achieve these levels of precision, there is a great demand on the machine tools to perform SPDT operations such as aerostatic bearings, high stiffness and micro/nano positioning systems along with a careful workpiece material selection which should be appropriate to a mirror like surface finish,

Silicon, germanium, indium antimonide, gallium arsenide and fine ceramics are among the brittle materials most used in industry. When submitted to stress, this kind of material presents cracks before significant plastic deformation takes place. This behaviour shows evidence of their brittle characteristic (4), which makes them difficult to machine through ductile material removal (cutting). Although this brittle characteristic renders the machining this sort of materials extremely difficult, if certain very restrict cutting conditions (depth of cut and feedrate) be respected, ductile removal can be obtained (1, 2). Several cutting models have been presented from results of interrupted face turning of brittle materials where the uncut shoulder was closely examined to classify the cutting mechanism. Basically, there are two types of material removal: ductile removal and brittle cracking. The region where brittle removal prevails is damaged and characterised by the presence of pits. The extension of this region is associated with chip thickness and geometry of cut. The region where the chip thickness is less than the critical dimension of cut for crack formation shows damage free. As a result of the development of the precision machining technology, the monitoring of machining processes is being advanced to cope with positioning demands increasingly higher. Among the various monitoring techniques, acoustic emission (EA) plays na important role and is being investigated and applied since its discovery in the 50's (5, 6). The AE RMS signal has been used in the monitoring of single crystal silicon diamond turning and the results make it clear the three distinct material removal

modes: brittle, brittle/ductile and purely ductile showing that this technique is sensitive to be used in the monitoring of single point diamond turning of brittle materials [7]. As the surface integrity deterioration increased (followed by increasing number of cracks), the AE signal level increased as well as its amplitude. However, during ductile cuts (and low removal rates with consequent low AE signal level) the analysis of the RMS signal has not been satisfactory since the signal could hardly be separated from the process noise even using frequency filters [7]. To make this and other important points clear, frequency spectral analysis will be used as an alternative technique to RMS analysis.

2 Experimental Details

A (100) indium antimonide sample was diamond faced on a Rank Pneumo ASG2500 machine. Coolant was continuously sprayed onto the workpiece surface during the machining. A –25 arc degree rake angle diamond tool with nose radius R=0.658mm was used in all tests. The feed rate was 2,4 and 8 μm/rev and the nominal depth of cut was 10 μm. These cutting conditions provided ductile and brittle regime of material removal, respectively. Spindle speed was kept constant at 1000 rpm. The AE signal was obtained using an AE piezoelectric sensor mounted on the toolholder and a microcomputer with a PCI-6111E 5MS/s National Instruments™ – DAQ board. The AE raw signal was acquired at a 10kHz sample rate. The spectral characteristics of the raw AE signal and the surface finish was examined using Scanning Electron Microscopy (SEM) and correlated with the cutting mode. Filters were not used in order that the raw signal could be obtained for a later frequency spectral analysis. LabView 5.1™ was used for data acquisition and processing of the signal.

3 Results and Discussion

The results showed that practically all cutting conditions yielded ductile material removal since the InSb "more ductile" than other brittle materials such as silicon, germanium and GaAs. The only exception was the most severe condition: f=8μm/rev, which exibited cracks both in the surface and in the uncut shoulder as shown in Figure 1. Figures 2 e 3 show SEM of surfaces machined with f=4μm/rev and 2μm/rev, respectively. The first shows a surface with a roughness worse than that with f=2μm/rev. However the extreme condition (f=8μm/rev) presents the worst surface integrity. The EA raw signal was analysed and displayed in charts which represent the signal spectrum, i.e., its Fourier transform (a), its time behaviour (b) and the signal power distribution as a function of time and frequency (c). The colour scales showed in (c) appear as a result of the larger amplitude of the signal, i.e., the highest peak (black) corresponding to 100% and the lowest (white) to 0%.

The conditions f = 2, 4 e 8μm/rev are represented in the graphs of Figures 4, 5 e 6 respectively. Analysing the time signals, one can observe that for the less severe conditions (2 e 4μm/rev, respectively), the mean signal is 0.12V e 0.18V, clearly distinct from the signal obtained for the most extreme condition (1.5V). Comparing these results with the SEM, one can conclude that the larger the number and concentration of cracks the higher the levels of EA signal. This tendency is also observed in the analysis of the frequency spectrum and spectrogram of the signal, with higher and better distributed frequencies for the most severe condition (responsible for crack propagation), different from the ones obtained for less severe conditions. One can conclude that there are characteristic frequencies for each removal mode: ductile, ductile/brittle or brittle and that these are distributed in a manner that high frequencies and high

level of signal are related with the presence of massive number of cracks, while lower frequencies and lower signal levels indicate ductile material removal.

4 Conclusions

The purpose of this work was to investigate the relationship between the material removal mechanism in the diamond turning of (100) single crystal indium antimonide (InSb) and the characteristics of acoustic emission (AE) spectral signal. The preliminary results presented showed AE has appropriate sensitivity to detect different material removal modes during machining. The time vs EA signal frequency analysis proved useful identifying the presence of cracks and, therefore, characterizing the integrity of the machined surface.

Acknowledgements

The authors would like to acknowledge that this work was supported by FAPESP (BRAZIL).

5 References

[1] Blackley, W.S & Scattergood, R.O.: "Ductile regime machining model for diamoond turning of brittle materials", Precision Enginnering, v.13, pp.95-103, 1991.

[2] Blake, P. N. & Scattergood, R.O.: "Ductile regime machining of germanium and silicon", Journal of American Ceramic Society, v.73, pp.949-957, 1990.

[3] Corbett, J., McKeown, P.A., Peggs, G.N. & Whatmore, R.: "Nanotechnology: international developments and emerging products", Annals of the CIRP, v.49, n.2, pp.523-545, 2000.

[4] Chao, C.L.: "Investigation of the machine glasses and other normally brittle materials in the ductile regime", PhD Thesis, Cranfield Institute of Technology, School of Industrial and Manufacturing Science, 1991.

[5] Dornfeld, D.A.: "In process recognition of cutting states", JSME International Journal, Series C, v.37, n.4, pp.638-650, 1994.

[6] Liu, J.J. & Dornefeld, D.A.: "Modeling and analysis of acoustic emission in diamond turning", Journal of Manufacturing Science and Engineering, v.118, p199-207, 1996.

[7] Silva, H.A.T., Duduch, J.G. & Jasinevicius, R.G.: "Study of the monitoring of ultraprecision machining of brittle materials using acoustic emission", 1st EUSPEN, v.1, pp.334-337, 1999.

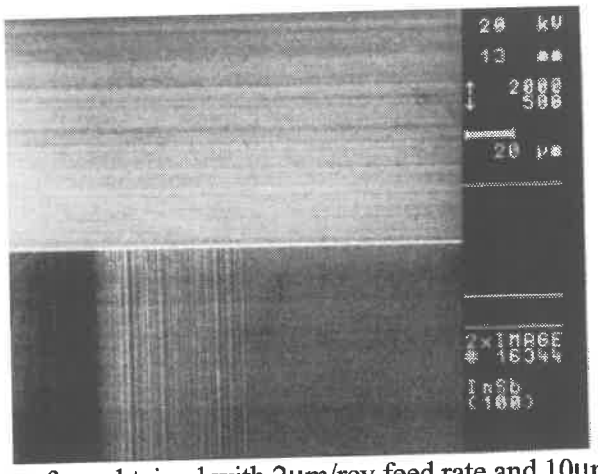

Figure 1: InSb surface obtained with 2µm/rev feed rate and 10µm depth of cut.

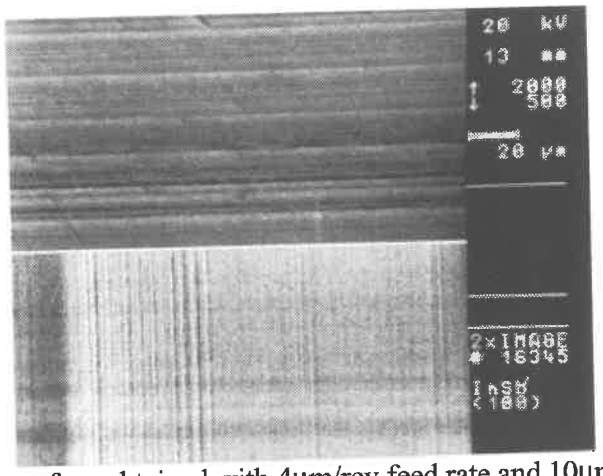

Figure 2: InSb surface obtained with 4µm/rev feed rate and 10µm depth of cut.

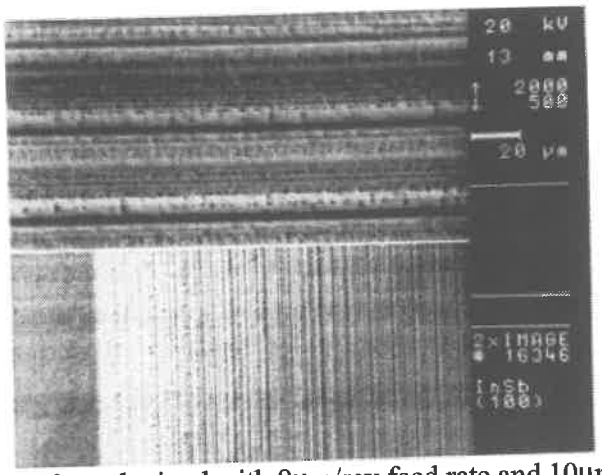

Figure 3: InSb surface obtained with 8µm/rev feed rate and 10µm depth of cut.

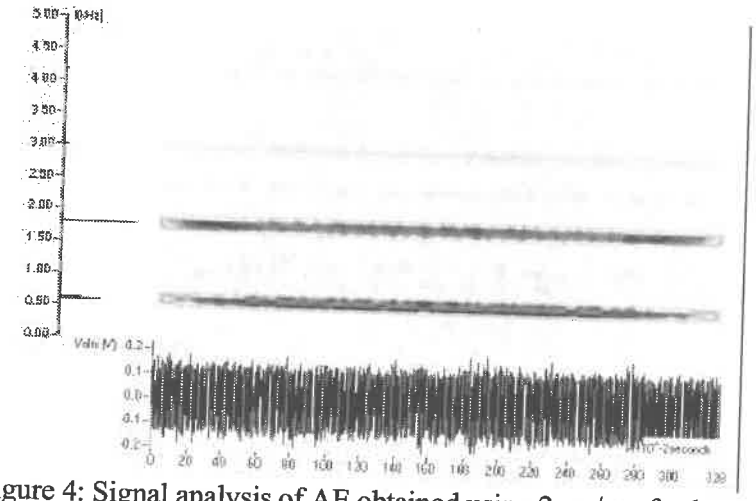

Figure 4: Signal analysis of AE obtained using 2μm/rev feed rate.

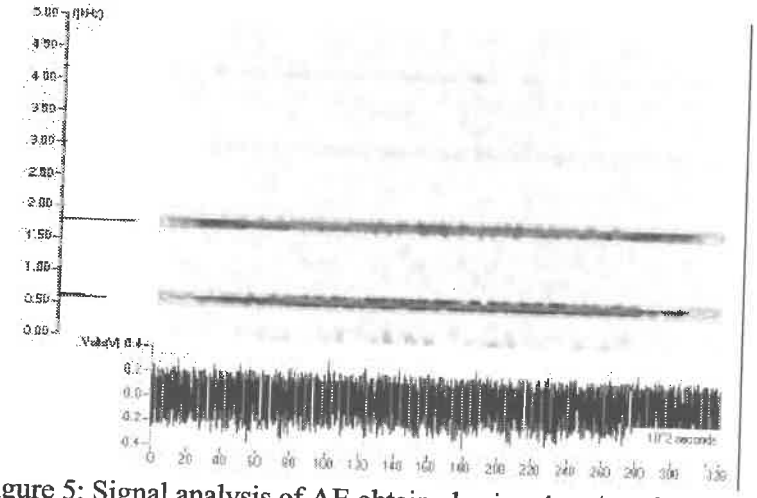

Figure 5: Signal analysis of AE obtained using 4μm/rev feed rate.

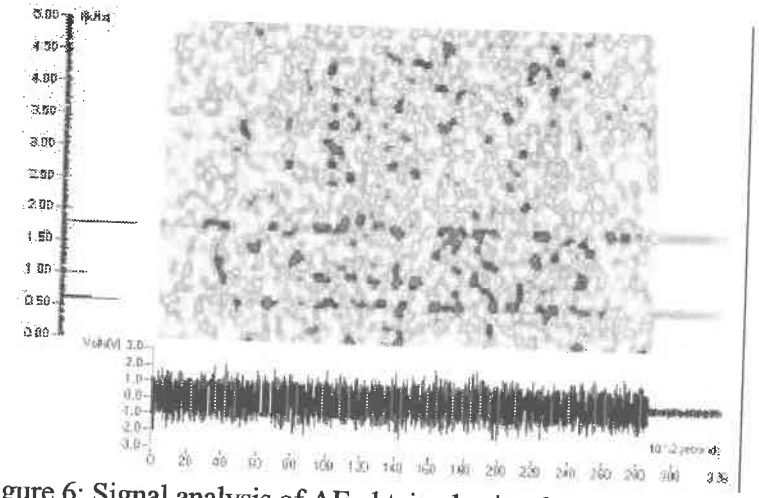

Figure 6: Signal analysis of AE obtained using 8μm/rev feed rate.

Observing Tool and Workpiece Interaction in Diamond Turning Using Graphical Analysis of Acoustic Emission and Force

C. M. Oliveira Valente[1], D. Echizenya[2], D. A. Dornfeld[2], and J. F. Gomes de Oliveira[1]
[1]University of Sao Paulo, Nucleus of Advanced Manufacturing, Sao Carlos, Brazil
[2]University of California, Laboratory for Manufacturing Automation, Berkeley, CA, USA

Abstract

A graphical mapping technique of the acoustic emission (AE) signal for a precision machining process has been developed for the *in-situ* characterization of the machining process physics. Machining at the precision scale involves chip formation at lengthscales representative of microstructural features of polycrystalline materials such as grain boundaries and grain orientation. The process-induced AE signal generated during precision machining can be used to characterize the interaction between tool and workpiece microstructure, and can be used as a way to characterize the workpiece microstructure and access the form error.

1. Introduction:

In precision machining, the uncut chip thickness typically ranges from several microns to several tenths of a micron. At such scales, surface finish and chip formation are much more intimately affected by the microstructure of the workpiece [1]. In particular, while cutting polycrystalline materials at the precision level, the material removal mechanism is highly influenced by individual grain size and orientation (see Figure 1). Therefore, unlike conventional metal cutting, the cutting mechanism in precision machining is significantly influenced by the crystallography and associated slip system within each randomly oriented grain.

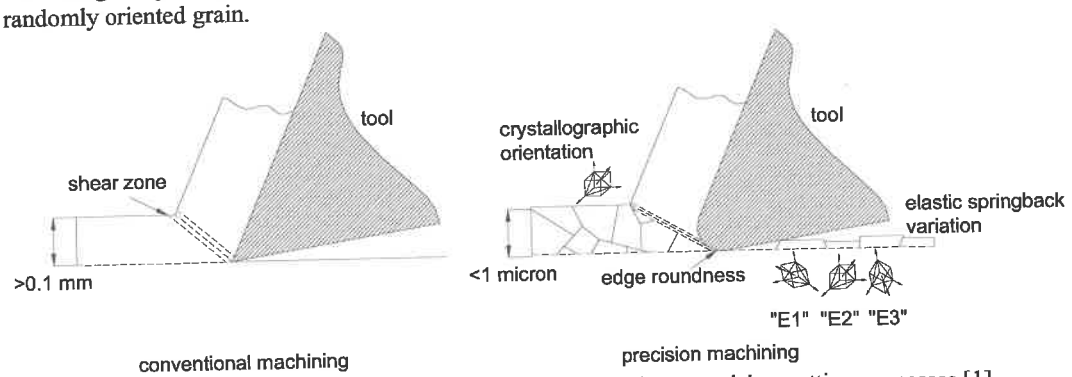

Figure 1: Relative scale comparison of conventional vs. precision cutting processes [1].

It has been demonstrated that the sensitivity of the cutting mechanism with respect to the grain orientation and the transition of the cutting tool across grain boundaries of OFHC copper can be measured to a certain extent using very sensitive load cells [2, 3]. The significance of the sensitivity of the cutting forces to the cutting mechanism becomes important not only to help understand the physics of the micro-cutting process, but also as a potential means of monitoring and controlling the machining process. However, when the depth of cut decreases further, the ability to monitor changes in the cutting forces at the grain boundaries approaches the resolution limit of current force transducer technology.

An alternative approach is to use acoustic emission (AE) to monitor and characterize the micro-cutting mechanism. As a form of process-induced high-frequency vibration, AE is generated by a number of different mechanisms, such as shear in the primary shear zone during machining and contact between the tool/workpiece in the secondary/tertiary shear zones. However, unlike force sensors, different levels of AE can be detected even at extremely low depths of cut [4]. This is true even when the chip formation process diminishes and the only remaining tool-material interaction involves rubbing and burnishing of the surface along different grain orientations. AE is particularly well-suited because of its ability to detect micro scale

deformation mechanisms within a relatively 'noisy' machining environment, thanks to it's improved signal-to-noise (S/N) ratio with the proper signal conditioning.

This paper proposes an innovative system where the interaction of the tool and workpiece during a precision cutting process can be represented in a 2D mapping of the process-induced AE and force signal. This graphical representation of the AE and force signal provides information about the cutting process parameters, such as cutting velocity and depth of cut, as well as the surface topography and microstructure features of the workpiece, such as grain boundaries and orientation. This system will serve as an in-situ means of monitoring and characterizing a precision cutting operation.

2. Experimental Setup:

The workpieces used for the experiment were 63.5 mm diameter (2.5") OFHC Cu flats that were cold worked at 60% and subsequently recrystallized at 830° C. The workpieces were recrystallized for different time durations (20-60 min.), resulting in a variation in recrystallized grain size from approximately 0.1 mm to 4 mm in average grain diameter. The primary machine tool was a highly-modified Rank Pneumo MSG-326 precision lathe donated from the Lawrence Livermore National Laboratory. This machine was equipped with an air bearing spindle and precision air-bearing lays. An HP laser interferometer was used to measure tool infeed position, and a Heidenhain linear encoder was used to measure crossfeed position and velocity.

The first experiment involved the creation of a series of nearly-parallel slow speed scratches on the surface of an OFHC Cu workpiece. A 0.274 mm nose radius single crystal diamond tool was chosen as tool of choice, since this represents an 'average' tool used for the fabrication of an aspheric optical quality surface. The load cell was a custom Kistler 9317A piezoelectric load cell, coupled with a Kistler 5429 distribution box and two Kistler 5010 charge amplifiers. Despite a high preload, the presence of the load cell reduced the stiffness of the tool structure, limiting its use to slow-speed machining and precluding its use from full-speed machining operations. A DECI SE900-MWB AE sensor was used due to its relatively high bandwidth compared to other sensors. The AE sensor was positioned directly on the tool shank and coupled with petroleum jelly to minimize signal attenuation. The workpieces were clamped onto the spindle of the lathe, and the spindle was alternately rotated and locked to allow for slow-speed scratches (see Figure 2). A scratch speed of 0.7 mm/sec was used, and the infeed (depth of cut/DOC) setting was set at a constant value of 10 microns throughout the experiment. After each scratch, the spindle was unlocked and rotated slightly (~1 degree) to produce a radial pattern of scratches (although the scratch pattern can be approximated as a raster scanning pattern over this small angle of rotation). The AE signal was filtered through a high-pass filter with a 50 kHz cutoff frequency to minimize any ambient acoustic noise from the system. The signal was subsequently amplified by 40 dB. The AE signal was then passed through a Root-Mean-Square (RMS) filter with a time constant of 1 millisecond. Likewise, the signal from the load cell was filtered though a low-pass filter at 10 Hz to cancel out the 60 Hz AC outlet noise, which was sufficient for a slow-speed scratch. Cutting force (force parallel to the scratch direction) and thrust force (force normal to the scratch direction) were obtained. Both signals were collected by a National Instruments PC-LPM-16/PnP 12-bit data acquisition board at a sampling rate of 10 kHz. The signal was then reduced and processed with MATLAB.

The second experiment involved a full-speed precision face turning operation. However, full-speed machining experiments with the Kistler load cell produced very poor results, due to the lack of stiffness in the tool holder/load cell assembly structure that resulted in a transverse vibrational mode and degraded the surface finish. For the full-speed experiments, the load cell was removed, and only the AE RMS signal was obtained with an RMS time constant of 0.2 milliseconds. A constant RPM of 1000 was used, corresponding to a maximum cutting velocity of about 6.6 m/sec on the outer circumference of the workpiece. A constant depth of cut of either 2 or 10 microns was used, and a diamond tool with nose radius of 0.274 mm was used with a feed range of 8-22 microns/rev. LABVIEW was used to collect and post-process the data. Otherwise, the signal conditioning parameters and experimental setup was similar to that used for the parallel scratch test.

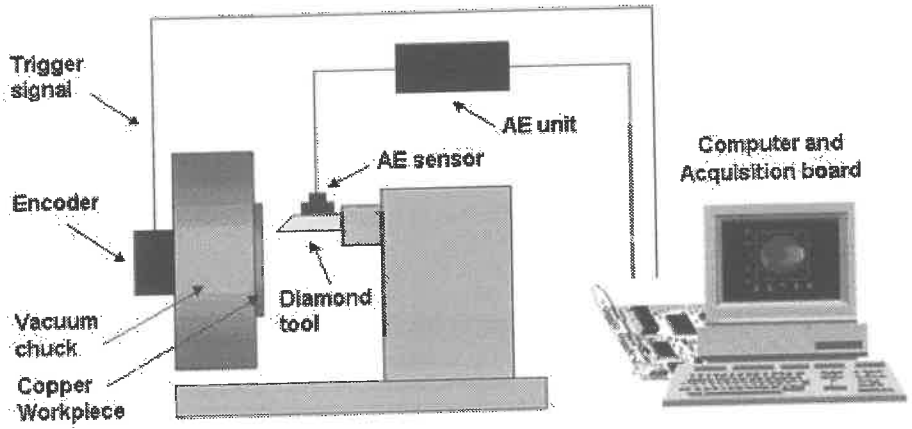

Figure 2: Experimental setup.

3. Results:

3.1. Parallel Scratch Experiment:

After collecting data from a series of scratches (typically on the order of 10 quasi-raster pattern scratches), the data was reduced, and a color intensity mapping function in MATLAB was used to plot the cutting force and AE signal as a function of position, with the color map representing the respective magnitude of the signal. Figure 3 shows a graphical representation of the cutting force and AE signal for a series of 15 scratches, along with a micrograph of the workpiece surface before scratching. Note that in the cutting force map, blue regions represent very low cutting force (on the order of 0.01 N), and red represents regions of high cutting force (on the order of 0.1 N). Likewise, red regions in the AE mapping correspond to AE RMS values of about 0.3 volts, while blue regions represent low (0.1 volt) AE RMS signal.

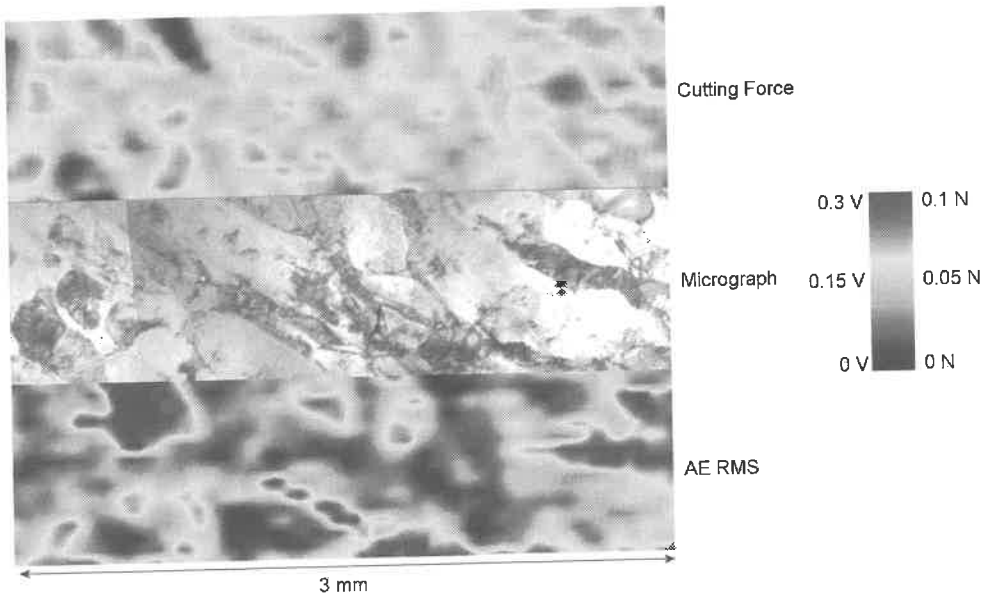

Figure 3: Force/AE response for 'quasi-raster' scratch pattern.

Both the cutting force and AE signal reproduce a crude representation of the grain structure of the material. The variation in force and AE signal is largely due to the fact that each grain has a particular crystallographic orientation, so as the tool passes from one grain to another, a new slip system in the grain is being activated, which changes the amount of applied stress (and cutting force) required to initiate deformation [5]. Likewise, the AE RMS signal has been found to be proportional to the specific energy (power divided by material removal rate) required to machine a material [6]. If the cutting speed and tool cross section are constant, then the AE RMS is simply proportional to the energy (and cutting force) required to initiate deformation. The activation of different slip systems as a function of grain orientation causes the energy of the AE signal to fluctuate accordingly.

The improved contrast in the force mapping seems to demonstrate that the force signal offers a more accurate representation of microstructure of the material. However, it is important to mention that the AE signal is extremely sensitive to any external or process-induced vibration. Phenomena not directly related to the cutting process, such as chip removal or non-process induced vibration (one source being imprecision in the slideways) could serve as noise sources and result in signal aliasing. Because of the low cutting speed, external noise sources (notably, the rubbing of the chip on the tool face during scratching) could be on the order of the cutting-induced AE signal, serving to alias the signal [7].

3.2. Contact Detection For Full-speed Machining:

For the second series of experiments, a face turning operation was conducted on a non-planar OFHC Cu workpiece without any pre-processing to demonstrate the contact detection capability of the mapping system. An initial touch-off operation was performed by visually aligning the tool with the workpiece, and an initial cutting pass was taken at 1000 RPM with a 1.4 mm nose radius diamond tool, initial depth of cut of 10 microns, and feed of 10 microns/rev. Figure 4 shows a polar map representation of the AE RMS signal, along with a Wyko Topo-3D interferometer image. Note that the AE RMS polar map matches the shape of the interferometer image, with dark yellow regions in the polar map representing contact between tool and workpiece, and black regions representing non-contact due to the initial non-flatness of the workpiece with respect to the plane of rotation of the spindle.

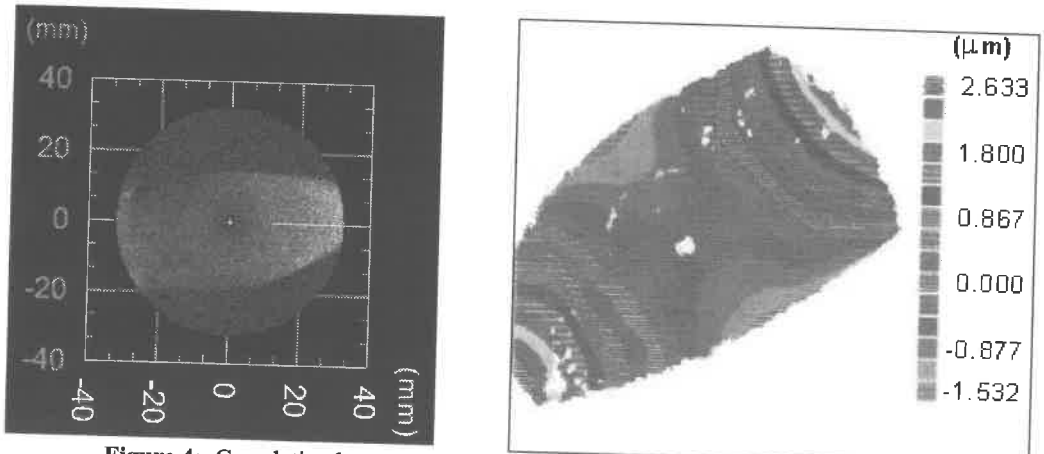

Figure 4: Correlation between AE polar map and laser interferometer image.

A series of four subsequent passes with DOC of 10 microns and cross-feed of 10 microns/rev were taken across the workpiece, and the resulting AE polar maps are shown in Figure 5. Note that the shape of the polar map evolves into a circle as the number of passes increases, corresponding to a greater portion of the workpiece being in contact with the diamond tool during machining. On the final pass, the polar map is a full circle, indicating that the entire surface of the workpiece has been machined. These plots demonstrate the capability of AE signal to be used as a contact detection tool.

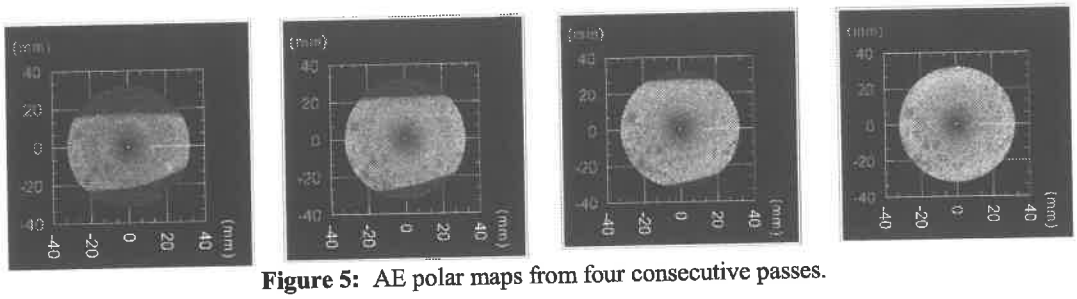

Figure 5: AE polar maps from four consecutive passes.

3.3. Microstructure Mapping During Full-speed Machining:

In the last series of experiments, the workpiece was machined to an optical quality surface finish of 58.2 nm R_a at 1000 RPM with a 0.274 mm nose radius diamond tool. No macro-scale surface defects could be observed with the naked eye. Figure 6 shows a polar intensity mapping of the AE RMS signal next to a micrograph of the actual OFHC Cu workpiece after etching with an ammonium hydroxide etch for 30 seconds to remove the process-induced strain hardened layer of material. Note that a rough correlation can be made between the large individual grains on the workpiece and the large dark regions on the AE polar map.

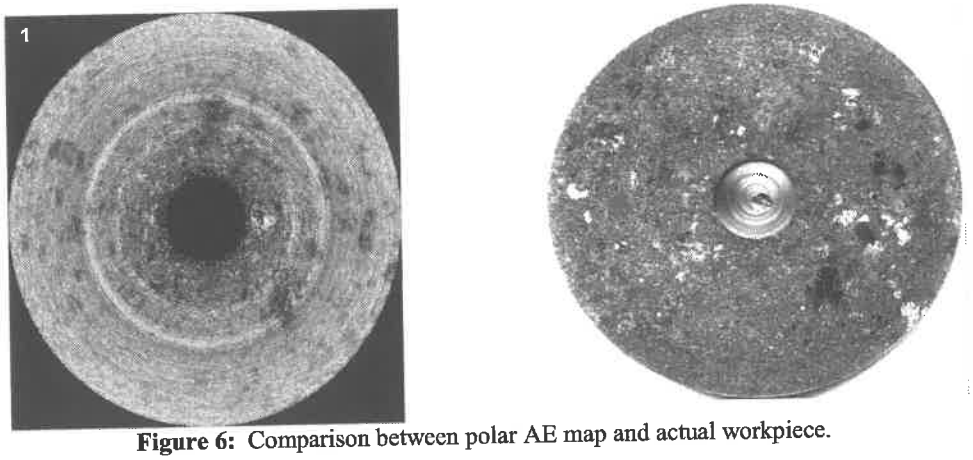

Figure 6: Comparison between polar AE map and actual workpiece.

A total of 16 subsequent passes with DOC of 2 microns were taken over the same workpiece, for a total depth of 32 microns of removed material. AE polar maps were collected every 5 passes (see Figure 7).

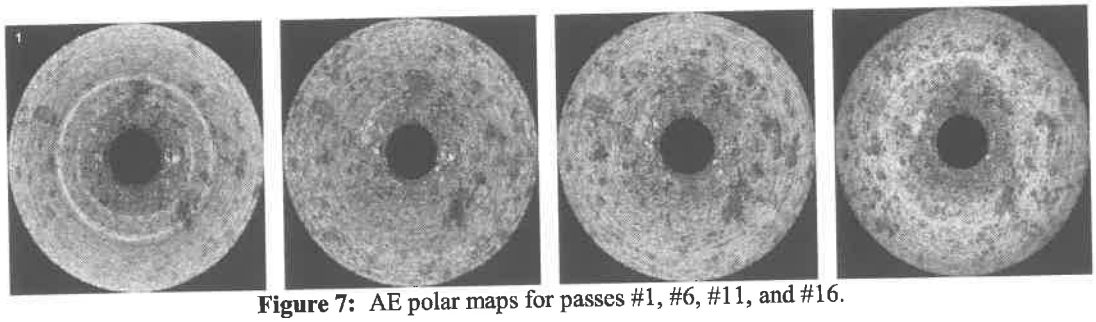

Figure 7: AE polar maps for passes #1, #6, #11, and #16.

As before, the AE polar map shows the presence of large recrystallized grains, demonstrating the capability of the polar map to detect microstructure variation in the workpiece. A variation in the mapping can be observed as the number of passes increases, corresponding to new grains being machined as previous layers of material are removed. Such a technique can be used, for instance, to verify whether a

workpiece has a coarse or fine grain structure. The polar maps can also indicate the position of large grains. Also, since it has been previously established that surface finish is a function of grain orientation in ultraprecision machining [5], the homogeneity of the polar map can also serve to represent overall homogeneity in the surface finish, although a more discrete relationship between surface finish and AE signal has yet to be found.

4. Conclusions/Future Work:

The AE mapping technique for precision machining has been performed with varying degrees of success. For the machining of OFHC copper, the force and AE RMS signal mappings represent the microstructure (grain orientation) of the workpiece, as well as large macro-scale defects like scratches. Ultimately, the AE mapping system can serve as a technique for characterizing the variation of the cutting process, which translates to a variation in the material properties or microstructure of the machined workpiece. The degree of heterogeneity in the graphical mapping can serve as a process metric for the quality of the machined part.

Some issues that need to be addressed in the future include…

1. Correlation between force and AE signal to the crystallographic orientation of individual grains.
2. Further cross calibration of the force and AE signal to other process metrics, such as surface finish. This includes additional metrology (profilometry, optical interferometry, etc…) to further characterize the surface.
3. Analytic modeling of the AE and force signal as a function of crystallography.
4. Investigation of the ability of the force and AE signal to detect other manufacturing defects in the workpiece.

5. References:

[1] Moriwaki, T., 1995, Experimental Analysis of Ultra-Precision Machining, International Japan Society of Precision Engineering, Vol. 29, No.4, pp.287-290.

[2] Furukawa, Y, Moronuki, N., 1988, Effect of Material Properties on Ultra-Precise Cutting Processes, CIRP Annals, 37/1:113-116.

[3] Brinksmeier, E., Schmütz, J., 1997, Generaltion and Texture of Surfaces In Ultraprecision Cutting of Copper, Machining Science and Technology, Vol.1, No.2, pp.185-193.

[4] Lee, Y, 2000, Monitoring and Planning for Open Architecture Manufacturing of Precision Machining Using Acoustic Emission, Ph.D. Thesis, University of California, Berkeley.

[5] Moriwaki, T. and Okuda, K., 1993, "Study of Ultraprecision Orthogonal Microdiamond Cutting of Single-Crystal Copper," *JSME, Series C.*, Vol. 36, No. 3, pp. 400-406.

[6] Lee, Y., Chang, A. K. and Dornfeld, D. A., "Ultraprecision Cutting and Acoustic Emission Monitoring of OFHC Copper," *Laboratory for Manufacturing Automation Technical Report, University of California Berkeley*, 1999.

[7] Ono, K., 1979, *Fundamentals of Acoustic Emission*, University of California, Los Angeles, pp. 167-207.

Microtools Shaped by Focused Ion Beam Milling and the Fabrication of Cylindrical Coils

M.J. Vasile, D.P. Adams#, and Y.N. Picard*

Sandia National Laboratories
P.O. Box 5800, MS 0959
Albuquerque, NM, 87185

Keywords: focused ion beam, microtool, diamond tool, microcoil, ultra-precision machining

* *Current address: Department of Materials Science and Engineering, University of Michigan, Ann Arbor, MI.*

Corresponding author, electronic mail address dpadams@sandia.gov (FAX): (505-844-2754)

Fabrication of microscale components with cylindrical symmetry is a significant challenge for prototyping and manufacturing. This is particularly difficult when using techniques that generate planar features, such as projection lithography. Extension of conventional machining to the microscale has the capability of producing structures with complex topology. Ultra-precision lathe machining is well-suited to work with cylindrical substrates or components, and many commercial instruments have nanometer-scale precision. However, one of the major difficulties with extending machining processes into the micron range is the reliable fabrication of cutting tools with the appropriate geometry and dimensions.

Focused ion beam (FIB) sputtering is currently being researched as a method for fabricating microscopic cutting tools with working dimensions in the tens of micron range. The major advantages to the FIB manufacture of microtools include: the variety of tool shapes, the control over tool geometry, the sub-micron dimensional resolution, and the observation of a tool during all stages of shaping. FIB sputtering creates tool shapes that cannot be fabricated easily by conventional techniques such as polishing and grinding.

This report is concerned with cutting tools for ultra-precision lathe turning of grooves on cylinders or other rotationally symmetric shapes. The immediate application of the lathe machining operations is to produce extremely small solenoids and the rotary element of a micro-screw pump. Small solenoids have proven to be very tedious to manufacture by winding techniques, particularly for wire diameters of 25 μm or less.

Microtool Fabrication by Focused Ion Beam Sputtering

Starting materials for microtool fabrication are commercially supplied, generally in the form of a tapered cylinder attached to a 3.175 mm diameter mandrel. The total length of the tool shank and mandrel is approximately 2.5 cm. High-speed steel and tungsten carbide tool blanks are available from National Jet, Co. as micro-punches. Tapered single crystal diamond tool blanks are obtained from Microstar, Inc. The final segment of diamond tool blanks is ~150 μm long with an approximate 40 μm square cross-section. A tool blank is mounted on an X-Y stage having sub-micron motion resolution, and full 360° rotational motion is available to the tool blank with 0.37° increments. The tool

materials selected for this study include M42 high-speed steel, C2 grade tungsten carbide, and single crystal diamond.

Diamond microtools

Figure 1 demonstrates the ability to tailor tool geometry by the FIB fabrication process. The tool shown in Fig. 1 is shaped from a single crystal diamond blank, but the ion milling patterns and sequences were chosen so that two rectangular cutting surfaces with 10 μm wide tips separated by 7.7 μm resulted. In general, any complex tool face geometry is possible. It is expected that shaping of similar diamond tools on this scale would be virtually impossible by conventional methods.

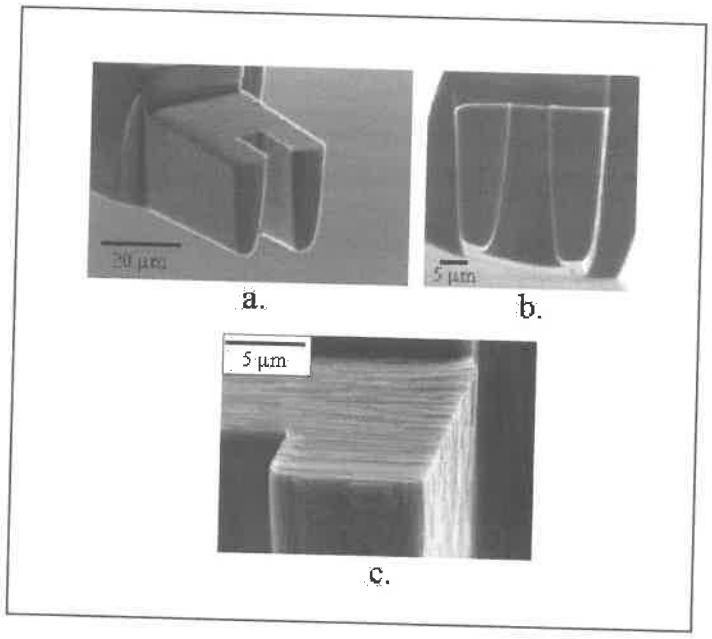

Figure 1: (a) Double tip, single crystal diamond tool. (b) End view of the tool shown in (a). (c) High magnification view of a single tip.

Specialized High Speed Steel Tools

Two high-speed steel tool sizes are shaped by FIB for different applications. The first application is the production of a cylinder with relatively wide rectangular cross-section grooves. The second application is the production of an ultra-fine triangular groove pair on a cylinder.

The rectangular cross-section grooves for the first application are large, having a 95 μm width, a 45 μm depth, and a 150 μm pitch. A set of tool blanks that are custom ground to dimensions slightly larger than the final tool size is obtained, and the cutting edges and the rake angles are finished by FIB.

Each custom-ground tool shaped by FIB cut one or more helical grooves in polyether etherketone (PEEK) cylinders. Multiple passes are made to achieve the final depth; a typical depth per pass is 2 μm or less.

Figure 2 shows portions of a groove cut in a PEEK cylinder. The groove consists of a long helix with a ring at both ends. Each ring is cut to the depth of the helix. The helical

portion of the groove begins at a distance of 2.55 mm from the lathe chuck. A portion of the helix is shown in Fig. 2(b).

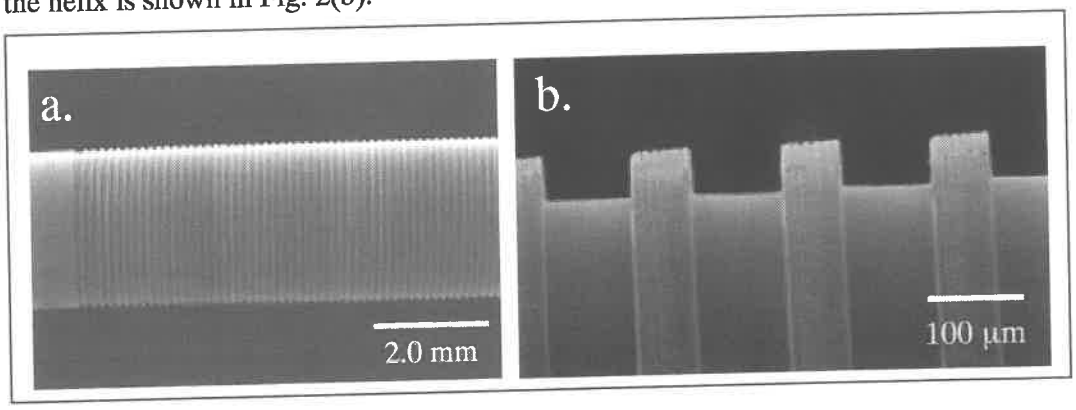

Figure 2: Groove machined in PEEK using focused ion beam-polished, custom ground lathe tool. (a) An image of the groove ending in a circumferential ring. (b) High magnification view of the smooth helical feature.

We find that for 3 mm diameter PEEK rods the groove dimensions are close to the intended values. Measurements of groove depth, width and pitch are made over arclengths of 225 mm, corresponding to a cylinder length of 3.8 mm. The width of the helical groove shown in Fig. 2 is 94.6 μm with a standard deviation of 0.63 μm. The groove depth is 44.6 μm with a standard deviation of 2.3 μm. The roughness of the machined feature bottom is determined by white light interferometry to be 0.22 μm (R_{rms}) and 0.14 μm (R_a).

The second application of high-speed steel tools includes machining a pair of closely spaced triangular grooves into the surface of a 3-mm diameter PEEK rod using a double tip tool.

This tests both the ability of FIB to make a two-tip tool having a nonrectilinear tool face shape and the ability of the lathe machine to position a microtool along the z-axis of the cylinder and to maintain rotational alignment. Figure 3 shows two views of the high-speed steel double tip tool, before the lathe operation. Each tip face is triangular and has an included angle of 62.5° as shown in Fig. 3 b. A back rake angle of 10° is also created for both tips. A relief angle of approximately 4° is established behind all cutting edges and behind the two end points of the tool.

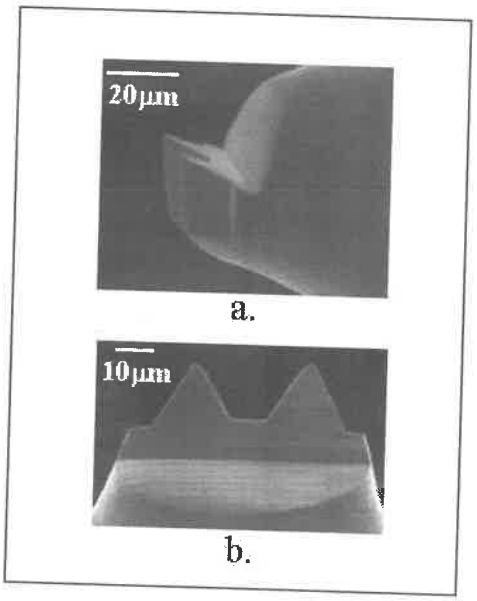

Figure 3: Two-tip microtool having triangular cutting faces. Tool is made of M42 high speed steel and is shaped by focused ion beam sputtering.

Figure 4 shows a portion of the triangular grooves cut into 3 mm diameter PEEK rod using the tool shown in Fig. 3. Qualitatively the tool shape appears to be replicated very well in the cross-section of the grooves. Both grooves in Fig. 4. have an angle of approximately 62.5°. The depths of the two grooves are also similar and close to the programmed depth of 15 μm. The pitch of the groove pair is 150 μm, and the total arc length of each groove is 18 cm.

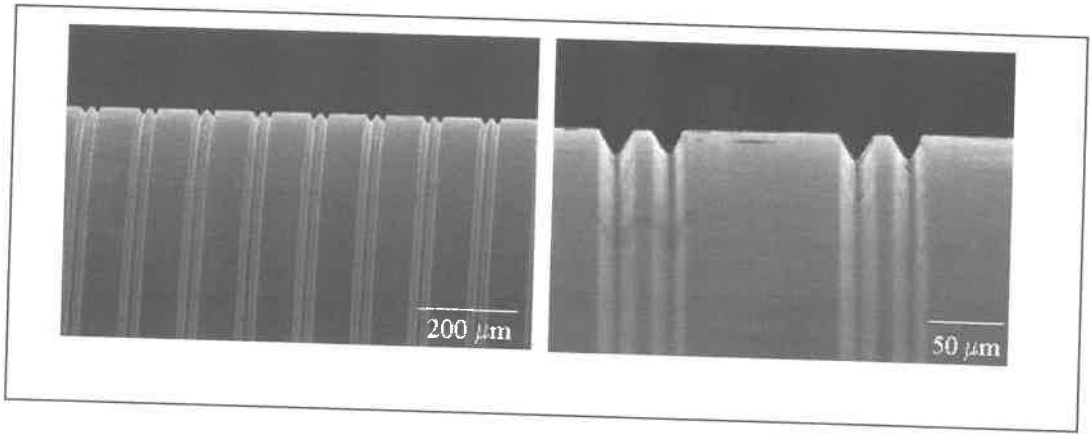

Figure 4: A portion of the PEEK workpiece machined using the focused ion beam shaped, two-tip tool shown in Fig. 3.

Fabrication of miniature solenoids

Two different processes for fabricating microcoil structures are developed. The first process involves coating a cylindrical-shaped polymer with a conducting layer. An FIB shaped tool is then employed in a precision lathe to cut the conductive layer in sequentially increasing depths until the insulating support is reached. The result is an electrically isolated helical winding in which the conductor cross-section is determined by the pitch of the micro-turning operation, the plating thickness, and the tool width. Figure 5 shows the helical cut in a copper coating on a 3.0 mm diameter PMMA rod. This helix has a pitch of 74 μm, leaving a conductor with a rectangular cross-section of 45 μm by 15 μm.

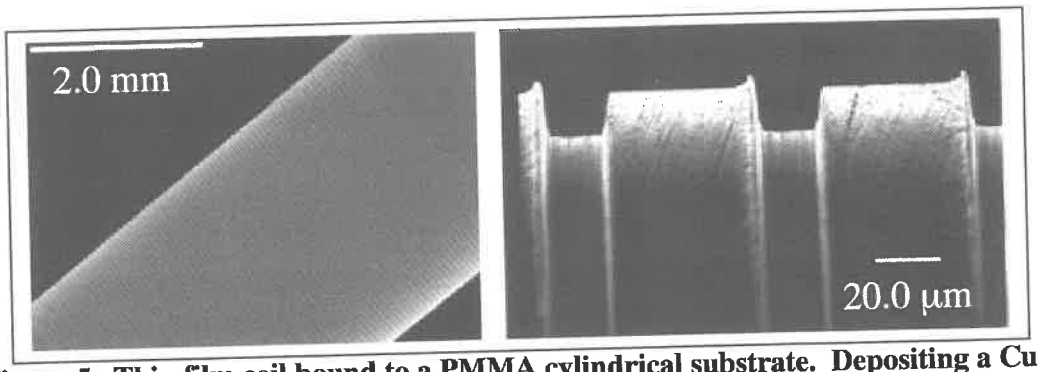

Figure 5. Thin film coil bound to a PMMA cylindrical substrate. Depositing a Cu film followed by ultra-precision lathe machining completes the component.

The second coil fabrication method is essentially an adaptation of the Damascene process. In our work, a 1.0 mm diameter Macor rod is the insulating substrate, and 20 μm wide grooves are machined into the surface using a FIB-made tool. Subsequently the sample is electroplated with copper to a thickness that exceeds the depth of the grooves in the Macor cylinder. The excess plated copper is then cut back until the insulating substrate is exposed, yielding electrically isolated windings.

Summary and future work

This work successfully extends conventional lathe machining techniques to the micron scale, using FIB made tools. We demonstrate methods that allow for control of feature cross-section, and the ability to tailor nonrectilinear feature shapes uniformly around the circumference of the workpiece. Coils with winding densities of 140 turns/cm have been achieved with conductor cross sections as small as 20 μm X 20 μm on a 1mm diameter cylinder.

SUBSTRATE CO-MOLDING OF MICRO AND MESO OPTICS

David D. Gill*, Thomas A. Dow, and Alex Sohn
Precision Engineering Center, North Carolina State University

INTRODUCTION

The objectives of this research were to develop a novel process of replicating thermally stable precision optics by injection molding the optical features directly onto glass substrates. The development of this technology will promote the use of optical communication in many settings including inside computers by creating inexpensive optics that can be co-molded directly onto printed circuit boards or silicon semi-conductors. Injection molded polymer optics offer high production volumes, but suffer from their high coefficient of thermal expansion and their hygroscopic nature. The investigation includes methods of promoting the adhesion of polymer to substrates and the performance of the co-molded optics in varying environments.

EXPERIMENTAL APPARATUS

To address the research goals, a series of experiments have been carried out on a laboratory-scale Nissei hydraulic injection molding machine at the Precision Engineering Center. The small size of the machine is necessary for the replication of meso optics with thickness below 350 micrometers and lens area less than1800 sq mm. The mold inserts are diamond turned and include spherical lenses, diffraction gratings, and Fresnel lenses. Features in the mold have step heights from 80nm to 170μm and include both smooth and sharp edges. The mold insert, optical features, and a replicated lens are shown in Figure 1.

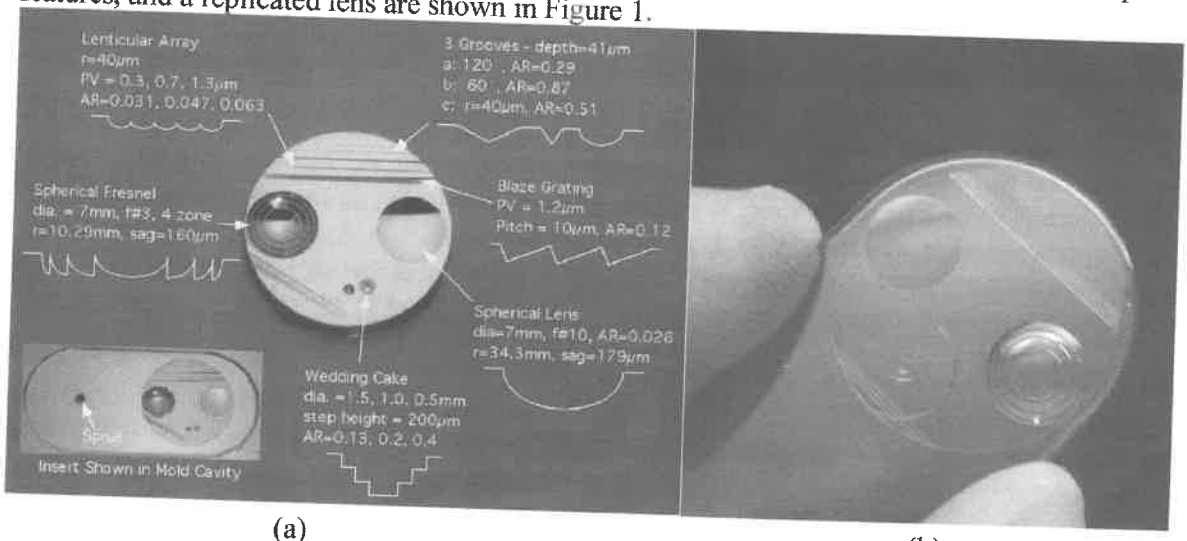

(a) (b)

Figure 1. Injection Mold Insert (a) and a Replicated Acrylic Lens (b) Showing Optical Features

* This author now at Sandia National Laboratories

The molding substrates included soda lime, borosilicate, and fused silica (quartz) microscope slides. The mold system was adapted to hold, accurately locate, and eject the substrates from the mold. Additionally, the mold system was designed so that lenses could be molded with or without the substrate. This design allowed the machine to be brought to equilibrium by molding all-polymer lenses before substrate co-molding began.

EXPERIMENTAL PROCEDURE

The first step in co-molding was to determine the molding process factors that had the greatest effect on the replication of meso and micro optics. A portion of this factors and effects test was reported at the ASPE 2001 Annual Meeting, but lens transmission tests had not been completed at that time. The factors and effects test included a reduced factorial, screening design of experiment that included 32 different sets of test conditions to determine the effects of 9 molding factors (process parameters). The tests required the molding of over 3000 lenses and the measurement of 100 of those lenses. The optical geometry of the replicated lenses was measured through interferometry, stylus profilometry, and atomic force microscopy.

Power transmission was chosen as the metric for comparison of lens transmission capabilities. This measurement is used in fiber optics to determine the ability of a lens to focus light into the end of a fiber optic. The power of an open light beam is measured and then compared to the power of light focused into the fiber. The result is reported as a percentage of the open beam power. Typical causes of power loss include optical astigmatisms that prevent the light from focusing at a single point, reflection off of lens surfaces, and absorption of light in the polymer material. For this research, a semi-conductor power meter was used in conjunction with 632.8nm light.

The second step in the co-molding research was to experiment with different substrates, cleaning methods, surface chemistry modifiers, and injection molding process parameters. The substrates used had a thickness of 1mm and the co-molded polymer optic was 150μm thick. The substrate materials were soda lime, borosilicate, and fused silica (quartz) glass. Cleaning methods included common solvents, glass cleaners, and the JTB1-1-1 method that is commonly used to clean silicon wafers. Immediately after cleaning, the substrates were either used for co-molding, or they were coated with a organofunctional silane solution to modify the inorganic surface of the substrate so that it would more easily bond with the organic polymer lens. Many molding factors were adjusted to promote adhesion including the injection pressure and temperature, mold temperature, screw rotation speed and cooling time in the mold.

RESULTS

The results of the factors and effects test revealed the factors having the greatest effect on the replication accuracy of the optical features. The factors with the greatest effect were found to be screw rotation speed and mold temperature. Other factors having statistically significant effects, though of a much smaller magnitude, were mold position, nozzle temperature, injection speed, hold time, and hold pressure. The magnitude of the effects due to the factors varied between the different optical features but the positive or negative influence was common to all features. For example, a higher mold temperature greatly increased the replication fidelity of the blaze diffraction grating. While the higher mold temperature did not affect the other features in nearly the magnitude of its effect on the diffraction grating, all of the other features had better or equal replication at the higher mold temperature tested. This agreement was not intuitive, as the features varied widely in size and shape. Table 1 shows the minimum error in each feature from the factors used in the design of experiment. It is expected that these errors could be even lower with further work refining the values of the factors, but from the 32 tested combinations of factors, the smallest error values are presented.

Table 1. Minimum Error Values for Geometric Measurements from the Screening Experiment

Feature	Measurement	Part #1 Error (nm)	Part #2 Error (nm)	Part #3 Error (nm)	Average Measured Error (nm)	Standard Deviation of Measurements (nm)
Spherical Lens	Astigmatism	773.9	572.7	488.5	611.7	146.6
	Coma	150.0	144.9	145.5	146.8	2.76
	Spherical Aberration	118.3	126.6	98.1	114.3	14.7
	PV Sphere Residual	836	651	585	690.7	130
	RMS Sphere Residual	160	119	103	127.3	29
Fresnel Lens	Astigmatism	252.5	237.3	358.2	282.7	65.8
	Coma	113.3	156.3	84.8	118.1	36.0
	Spherical Aberration	-689.8	-417.6	-1078.3	728.4	332.0
	PV Sphere Residual	460	392	493	448.3	52
	RMS Sphere Residual	75	62	90	75.7	14
Blaze Grating	Average Step Height Error	8.02%	6.96%	5.75%	6.9 %	1.10%
Wedding Cake	Average Step Height Error	0.93%	0.88%	0.83%	0.90%	0.08%

Not shown in the Table was the best power transmission which was 92% of the open aperture measurement. The power transmission was most effected by nozzle temperature and screw rotation speed.

The substrate co-molding experiments were performed to create adhesion between the polymer and the glass capable of withstanding the interfacial stresses due to the mismatch in coefficients in thermal expansion between the glass and the polymer. This mismatch is needed in the system so that the substrate can prevent the thin polymer optic from changing dimensions as thermal conditions change. Thermal stress analyses predicted that the polymer and substrate would be capable of withstanding the stresses induced during the cooling of the polymer after molding, but strength of the bond was still unknown. To test this bond, the lenses were molded and then monitored to determine the amount of time that the adhesion remained before the interfacial stresses became too great and separated the materials. This separation could be observed due to the interference patterns that appeared in the small gap between the polymer and substrate.

As determined by the length of time before delamination, the acrylic lenses were found to have better adhesion with soda lime glass than to fused silica or borosilicate glass. Though the soda lime glass has many more "impurities" than the other glasses, the coefficient of thermal expansion is somewhat higher, thus reducing the stress between the glass and the polymer.

Of the cleaning methods, JTB1-1-1 showed the best results for promoting adhesion. This method had the best results whether silane surface modifiers were used or not. An organofunctional silane was used to promote adhesion as well. Though this surface modifier did help, it did not work as well as expected. It is suggested that this poor performance may be due to possible impurities in the solution chemicals, inaccuracies in the measuring and mixing of the solution, and water absorption of the substrate surface prior to coating.

Most of the co-molded optics for this research delaminated to some extent within 30 minutes. The best result was achieved for a lens that was co-molded and then left in the mold to cool slowly overnight. This optic had good adhesion to the substrate and was able to withstand a load of 7.5psi as produced in a shear test. At that value, the 150μm thick polymer lens fractured.

This research found the injection molding process to be quite capable of producing quality meso and micro optics in common optical polymer. The research also showed the injection molding factors with the greatest effects on replication accuracy as measured by geometric form and light transmission capability. A series of experiments were performed to co-mold optics onto thermally stable substrates. These experiments identified materials that promoted adhesion, but no method was found that created permanent adhesion between the polymer and substrate.

ACKNOWLEDGEMENT

The authors wish to acknowledge the support of this research by the National Science Foundation (grant #9908223, Dr. K.P. Rajurkar, Program Director)

CLOSED LOOP CONTROL OF MILLING TOOL DEFLECTION

D. Hood, S. Clayton, G. Buckner, T. A. Dow, K. Garrard,
Precision Engineering Center, North Carolina State University

BACKGROUND

Injection molding is an important manufacturing process for optical and mechanical components. The hard steel dies used in injection molding play a direct role in the quality of molded parts. Traditionally, fabricating the dies involved rough milling followed by heat treatment, grinding and polishing. Recently, high-speed machining of heat-treated steel (hardness > 55 R_c) has become a viable approach for reducing fabrication times while retaining the necessary shape control. However, as feature sizes drop below 1 mm with dimensional tolerances on the order of 10 μm, tool deflection can create significant errors in the shape of mold surfaces.

A previous research effort at NC State developed open-loop correction techniques for tool deflection of small ball end mills [1]. This effort involved predicting tool forces and the resulting tool deflections for specified machining conditions and compensating for these deflections by modifying the tool path. A CAD model of the surface along with the planned tool path was used to determine the depth of cut, feed rate, and normal vector to the surface. This information was used to calculate the magnitude and direction of cutting forces that cause tool deflection. Compensation for tool deflection has proven very successful and errors can be reduced from 50 to less than 10 μm if the cutting conditions are known precisely. Unfortunately, this is not typically the case. For example, the tool or workpiece may have dimensions different than expected or be imprecisely positioned, resulting in cutting depths that are larger (or smaller) than expected. Open-loop compensation cannot correct for these types of errors.

This paper describes research to develop a real-time, force feedback control algorithm for milling operations that compensates for tool deflection. The workpiece is supported on a three-axis load cell and is machined using a small ball end tool driven by a high-speed (60,000 rpm) air bearing spindle. The output of the load cell provides feedback to control the depth of cut. As the tool deflects, the measured cutting forces drop in a predictable manner, and the controller changes the tool setpoint to correct for the error. Different depths of cut and loading angles change the magnitude and direction of the force and illustrate the accuracy and repeatability of this error correction scheme.

EXPERIMENTAL APPARATUS

The experiments described in this paper were conducted using a Nanoform 600 diamond turning machine with 3 orthogonal linear axes and a high-speed milling spindle. Figure 1 is a photograph of the machine. The spindle is a Westwind air bearing, air turbine unit with a maximum speed of 60,000 rpm. The cutting tools are two flute, ball end TiC milling cutters with a diameter of 0.8 mm and lengths from 0.8 to 7 mm. A three-axis load cell supports the workpiece, and is used to measure the tool forces that are fed back to correct for tool deflection. In this experiment, only the force perpendicular to the workpiece surface (the z-direction component) is corrected. The Delta Tau PMAC control system collects force data from the load cell in real time and computes the corrected slide command.

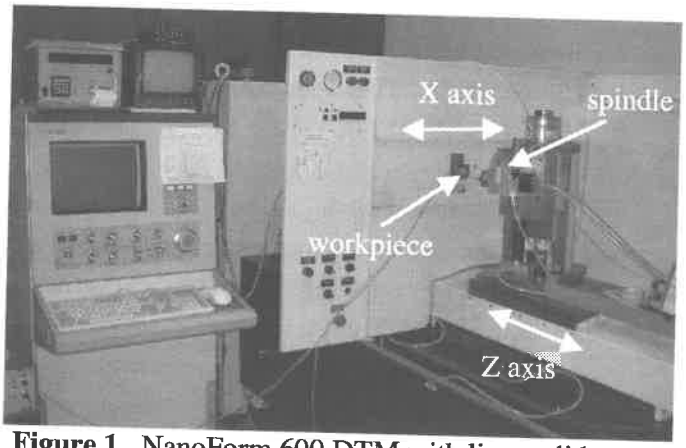

Figure 1. NanoForm 600 DTM with linear slideways and high-speed milling spindle.

TOOL FORCES

Predicted Forces The tool force model developed in [1] provides formulas for calculating the cutting and thrust forces developed during milling. Inputs to this model are the material properties (Rockwell hardness, Young's

modulus) and friction at the rake and flank faces of the tool. Tool geometry (ball end radius and number of flutes), spindle speed, upfeed and cross feed, depth of cut and tilt angle of tool are used to find the cross-sectional area of the chip and the area of contact between the flank face of the tool and the workpiece. The model can be written as:

$$F_c = \frac{HA_c}{3}\left(\frac{\cot\phi}{\sqrt{3}}+1\right)+\mu_f A_f\left(0.62H\sqrt{\frac{43H}{E}}\right) \quad (1)$$

$$F_t = \mu\left[\frac{HA_c}{3}\left(\frac{\cot\phi}{\sqrt{3}}+1\right)\right]+A_f\left(0.62H\sqrt{\frac{43H}{E}}\right) \quad (2)$$

where

A_c = cross sectional area of the chip
A_f = area of the tool flank face
ϕ = shear angle in the workpiece
μ = friction coefficient on the rake face
μ_f = friction coefficient on the flank face
H = Rockwell hardness of the workpiece
E = Young's modulus of the workpiece

These forces rotate with the flank face of the milling tool, but can be readily converted to orthogonal forces (in the x, y, and z machine directions) for comparison to measured forces.

Measured Forces Preliminary cutting experiments were conducted to validate the tool force models (1) and (2). Cutting forces were measured using a 3-axis piezoelectric load cell, pictured in Figure 2a. This load cell was mounted below the workpiece on the x-axis of the diamond turning machine, while the high-speed spindle was mounted on the z-axis slideway (Figures 1 and 2a). Experimental results for an S-7 steel workpiece machined at a spindle speed of 10,000 rpm, a feed rate of 20 μm/rev, and a cutting depth of 100 μm, are presented in Figure 2b. This figure compares the predicted forces with average force measurements for three consecutive revolutions of the tool. The z-component of force in Figure 2b is dominated by the tool thrust force - Equation (2) - because the tool is normal to the workpiece. The x and y force components are influenced more by the cutting force - Equation (1), that rotates in the plane of the workpiece and changes from an x-direction force to a y-direction force every quarter rotation of the tool.

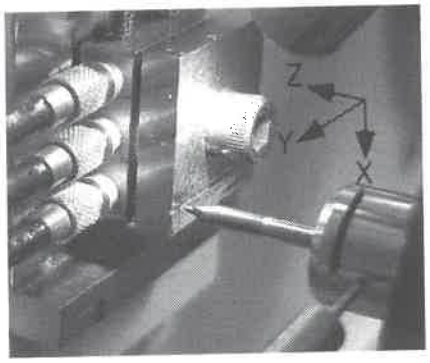

(a)

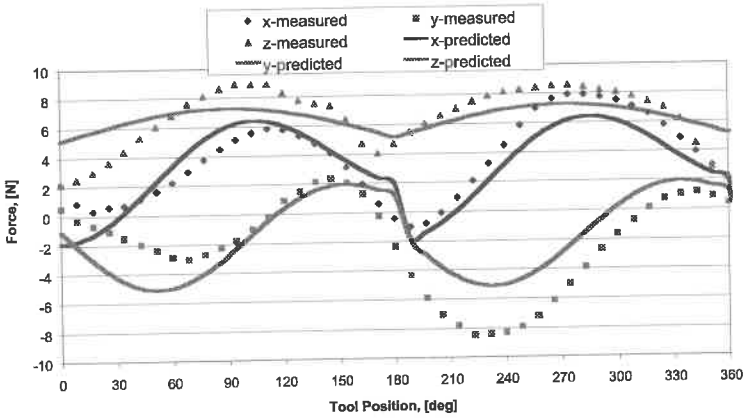

(b)

Figure 2. (a) Ball end milling tool and workpiece mounted on a 3-axis dynamometer
(b) Measured and modeled cutting forces for S7 steel workpiece: spindle speed = 10,000 rpm, feed rate = 20 μm/rev, depth of cut = 100 μm.

TOOL STIFFNESS AND DEFLECTION

The TiC milling tools have a 3 mm shank which tapers down to the ball diameter (0.8 mm). These tools come in two lengths, the longer tool having a 4 mm extended section equal to the diameter of the ball end. Since a ball mill is used to fabricate free form surfaces, the tool can be loaded in the axial direction, the radial direction, or both. The stiffness of the tool is significantly less in the radial direction (see Table 1), therefore regions of a machined surface where the tool is loaded in the radial direction will create dimensional errors.

Table 1. Experimental stiffness measurements for ball end milling tools

Tool Length (Stiffness direction)	Measured Stiffness, N/m
Short (Radial)	406,203
Short (Axial)	845,000
Long (Radial)	198,533
Long (Axial)	840,000

CONTROL SYSTEM DESIGN

With a validated cutting force model (Figure 2b) and tool stiffness measurements (Table 1), tool deflections during machining can be accurately predicted. Combining the model and stiffness measurements with real-time cutting force measurements enables the compensation of tool deflection errors. Compensation is done based on the average force per tool revolution in the direction of interest. Because the tool will be loaded in a variety of directions during a milling operation, the control algorithm must take into account both the magnitude and the direction of the forces.

A block diagram of the control algorithm is shown in Figure 3. The concept behind this algorithm is straightforward: calculate the expected z-axis force for a desired tool path, part position, and cutting conditions and compare it to measured z-axis force. If the measured force is equal to the predicted force, the z-axis setpoint is unchanged. If the measured force does not match the predicted force, the setpoint cutting depth is modified in accordance with the model. In this way, the system can correct for errors associated with tool deflection and workpiece positioning errors.

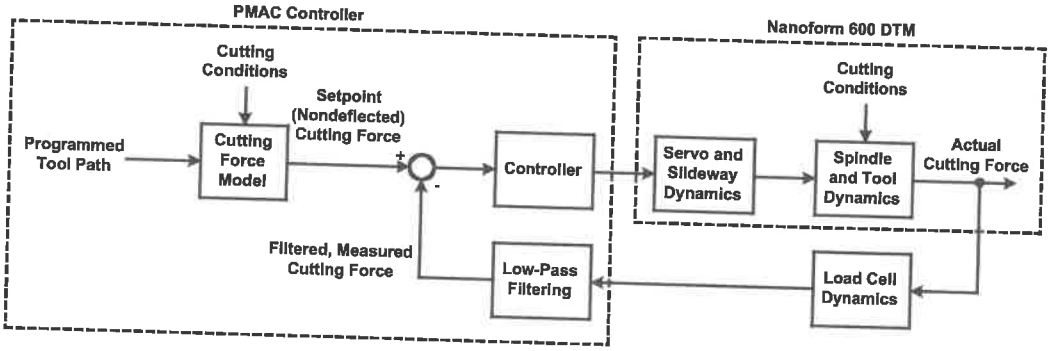

Figure 3. Block diagram of the tool deflection compensation algorithm

There are many practical considerations that make implementation of this algorithm difficult. First, the Nanoform 600 machine controller has safety limits on maximum axis velocity, acceleration, and following errors allowed during program execution. Using standard PMAC commands, it was determined that the machine could not move fast enough to compensate for tool deflection in the z-direction at the required x-direction feed rates (375 mm/min). To execute the correction scheme, a motion program was written that performs error measurement and PID closed loop control while the PMAC control loop operates in "open loop" mode. To facilitate this open loop controller/closed loop motion program, the proportional, integral, and derivative gains in the PMAC controller as well as the following error limits were set to zero. The axes were controlled through a motion program implementing PID control with output written directly to the DAC offset voltage register for each motor. Axes controller gains were tuned using Ziegler-Nichols techniques for the specific steps each axis would make during groove cuts. Additionally, low-pass filtering of the measured cutting force was necessary to achieve desirable performance. Finally, measuring "quasi-static" forces using a piezoelectric transducer is complicated by sensor drift and phase lag. This type of sensor would not be appropriate for extended cutting experiments.

CUTTING EXPERIMENTS

To evaluate the tool deflection compensation algorithm, a series of experiments was conducted on the Nanoform DTM. Full immersion slots with linearly varying depths of cut were machined in S-7 tool steel samples with and

without real-time deflection compensation. One preliminary set of experimental results is shown in Figure 4. This figure shows the measured and predicted cutting depths for a tool tilted at 25° to the surface normal. Grooves spanning 20 mm and 0-80 μm in depth were programmed, using a spindle speed of 10,000 rpm and a feed rate of 375 mm/min. The lower line represents the predicted uncompensated cutting depth, derived from the cutting force model, and the corresponding data points represent measurements made using a Form Talysurf at specific locations along the groove. The upper line represents the predicted compensated cutting depth, with actual measurements represented by data points. This data indicates that the cutting force model accurately predicts average tool deflections, as the experimental measurements are very close to the predicted curves. The data also shows that the deflection compensation algorithm significantly improves the accuracy of the machined groove, though the limited measurement spacing does not reveal higher-frequency variations.

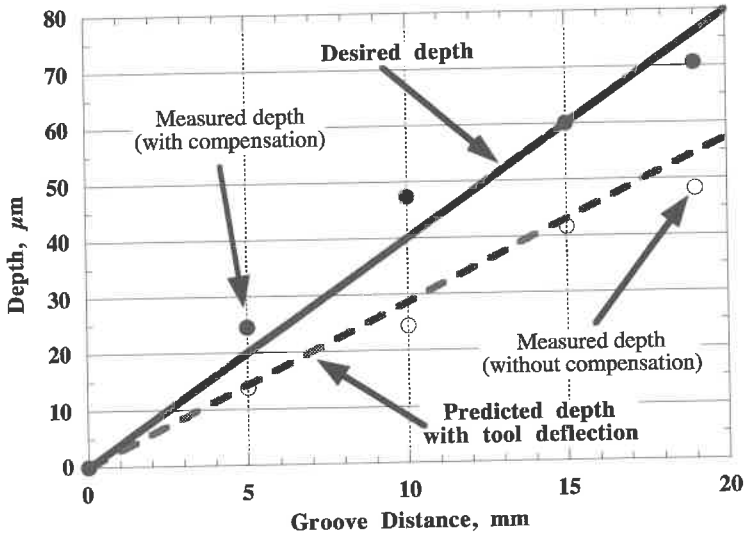

Figure 4. Measured and predicted cutting depths for a variable depth groove: with and without compensation (groove depth = 0-80 μm, groove distance = 20 mm, feed rate = 37.5 μm/rev, spindle speed = 10,000 rpm)

CONCLUSIONS

The forces generated during milling with a miniature tool are relatively small (less than 10N) because of the limited size and strength of the tool edge. However, tool deflections can be a significant source of surface errors because of the low stiffness of these ball end tools. The cutting force model accurately predicts these forces, and can be used to compensate errors arising from tool deflections and workpiece misalignment. The compensation algorithm presented here provides an avenue to reduce fabrication times and improve surface accuracies for hardened steel mold dies.

ACKNOWLEDGEMENT

This project is supported by the NSF under contract # DMI-0115175; J.Rajakar is the project monitor.

REFERENCES

1. T. Dow, E. Miller, A. Sohn and K. Garrard, Compensation of Tool Forces in Small Diameter End Mills, ASPE Proceedings, vol. 20, pp. 546-550 and to be published in Precision Engineering in 2003.

Modeling of residual stress on blasted surface using indenting method

Hiroshi Saito, Masami Masuda
Graduate School of Science and Technology, Niigata University
Ikarashi 2-no-cho, Niigata 950-2181, Japan

1. Introduction

The blast process applied on work surfaces is most effective in improving fatigue strength for moving components such as; crankshafts, gears, turbine blades etc., and contributes to the size reduction of products[1, 2]. However, the compressive residual stress in work surface layers caused by the blast process occasionally may produce undesired results, because most of the process conditions are, in the state of art, dependent on the skill of the workers. In minimum-cost processing, the process conditions in the blast process have not always been designed to optimize surface quality. For instance, over-peening may cause a decrease in fatigue strength and an increase in processing time to produce a desired maximum residual stress and/or a desired residual stress distribution.

Therefore, it is important that the maximum stress and the distribution in the residual stress can be estimated in order to design the optimal process conditions. Shot consisting of micro grains as blasting tools, however, come to complicate the blast process because of unknown factors in the statistical approach. Many researchers have discussed the generating mechanism of residual stress in blast process[3-7]. Procedures estimating residual stress distribution in the blast process are shown in Table 1. The indenting method seems to be useful for analyzing the residual stress, because covering the work surface with uniform dimples can simplify the effect of shot on the residual stress in practical blast processes.

In the following, the generating mechanism of residual stress in a blast process is analyzed experimentally using the indenting unit with a single crystal diamond indenter, where various errors can be compensated by optimizing the soft supporting mechanism. These results are compared with those in FEM analysis in order to discuss the compatibility of both processes.

Table 1
Estimation of residual stress distribution in blast process

Estimation method	FEM[4,5]	Estimation [6]	Quasi esti-mation [7]	Indenting
Parameter compatibility	×	△	△	○
Normalization to optimize process conditions	×	×	△	○
Simulation on production process	×	×	△	○
Estimation time	○	○	△	×

2. Experimental procedure and conditions

2.1 Blasted surface modeling with indenting method

A work surface is treated by colliding a large number of shot in the blast process. Here, the surfaces on which various shot collide repeatedly and the resulting overlapped dimples are modeled as normalized surfaces indented with a large number of uniform dimples at a regular pitch. Fig. 1 shows the compatibility of the control factors to produce similar surface quality in both processes.

2.2 Experimental equipment for indenting

It is very difficult to indent a uniform depth precisely on a conventional machine tool, because there are many position errors of the indenter relative to a work surface. In order to indent on work surfaces at several microns deep, an indenting unit has been newly developed with the use of a single crystal diamond indenter supported by parallel leaf springs with optimal damping. The experimental apparatus is shown schematically in Fig. 2.

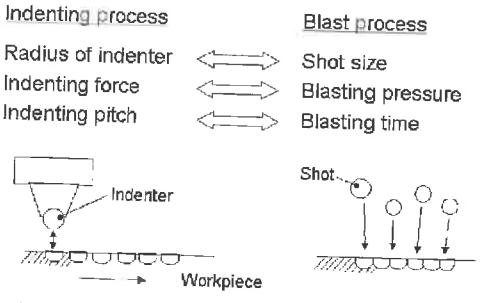

Fig.1. Compatibility of control factors in both processes

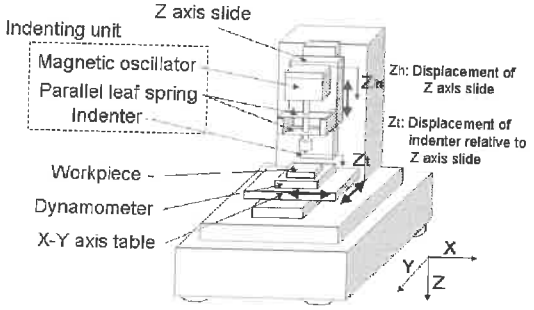

Fig.2. Experimental apparatus for indenting process

This indenting unit was installed on the quill of a tabletop NC milling machine. The indenting unit can compensate various sensitive errors caused between the indenter and a work surface, such as table motion error, thermal deformation of the workpiece relative to the indenter, chucking errors, and/or out-of-flatness of work surfaces. The displacement of the indenter (Zt) is relatively small, even if the displacement of the Z axis slide (Zh) is large (see Fig. 2). The contact of the indenter with the work surface was monitored by a piezo-type dynamometer(Kistler9257B). The indenting force ranged from 40mN to 3.3N in the experiments. The dimple depth of the indenting process is controlled by positioning the Z axis slide, according to the correlation among Zh, indenting force and the dimple depth.

2.3 Experimental procedure

Indenting experiments were carried out using the above-mentioned indenting unit. The contact starting point can be detected with an accuracy of ±1μm displacement (Zh; see Fig. 2) in the Z axis slide by the dynamometer. Work surfaces were formed with a large number of uniform dimples at a regular pitch from 2 to 100μm. Experimental conditions are shown in Table 2. The blast process was carried out on an air blast machine (Fuji Work Co. Ltd., "Newblaster"). Workpieces (W20mm×B20mm×T10mm), 0.5%C annealed steel, were lapped to less than 0.1μm Ra after grinding in advance of the experiments.

Table 2 Experimental conditions

Indenting process	
Indenting speed	2 cycles/s
Dimple pitch	10, 20, 40, 50, 100 μm
Indenter	R 20 μm, Single crystal diamond tip
Blast process	
Equipment	air type, air nozzle; φ 9 mm
Shot	size; φ 35-55 μm
	material; glass (HV≒900)
Blasting	time; 10 s
	pressure; 0.2 MPa
	distance; 100 mm
Workpiece	
Material	0.5%C steel (annealed)
Hardness	HV 240

The residual stress in work surface layers was measured using an X-ray method. The distribution of residual stress was obtained by repeated X-ray measurement on the work surface, each time removing 5μm deep using electrochemical polishing. The residual stress is defined as the average of the stresses in the X and Y directions for the homogeneous work surfaces treated.

3. Results and discussion

3.1 Indenting method

Fig.3 shows the relation between indenting force and dimple depth, when a spherical indenter of 20μm in radius was used. The dimple depth increases almost linearly with the increase of indenting force, although the correlation between them is in general considered linear to the square of the indenting force. Dimples of 2.0±0.2μm deep correspond to an indenting force of 0.64±0.064 N. Parallel leaf springs are inserted between an indenter and a tool holder. Fine control of the indenting force, with the compliance control mechanism, follows coarser positioning control of Zh. The indenting force forming a dimple should be similar to one loaded by individual blasting shot for the purpose of evaluating the blast process. The normal force in individual blasting shot is calculated to be approximately 0.64N, according to a report[8]. Here, the indenting force similar to the blast process, is taken to be 0.64N.

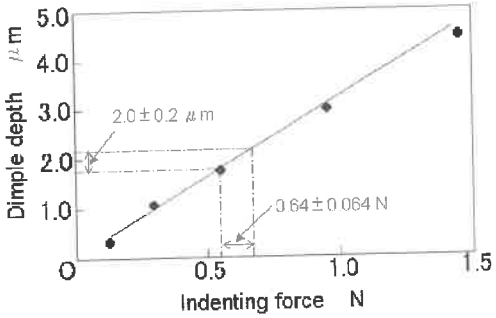

Fig. 3. Relation between indenting force and dimple depth

3.2 Coverage and residual stress

The blasted surfaces are produced by a large number of blast shot colliding with the work surface. The characteristics on a processed work surface would depend on the probability of colliding with the same area on the surface. The number of dimples on a work surface increases with increasing processing time. Ideally, a standard state called *"full coverage"*, or *"coverage 100%"* occurs when all the work surface is covered with dimple

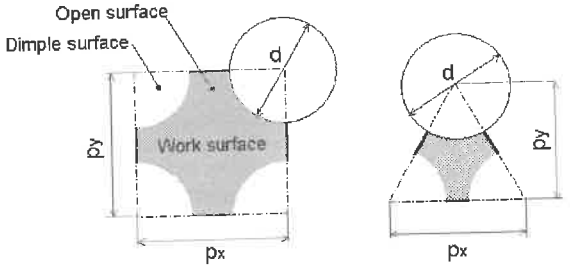

$$\text{Coverage} = \pi d^2 / 4 p_x \cdot p_y$$

px: dimple pitch of X axis
py: dimple pitch of Y axis
d: dimple diameter

Fig.4. Geometry of indenting with uniform pitch coverage

patterns, with neither any remaining open area of pre-finished surface nor any area of overlapped dimple patterns. In actual practise, the dimple pattern is circular in the indenting process. Fig. 4 shows geometry of indenting with uniform pitch coverge. p_x and p_y are described as p when $p_x = p_y$. The indenting experiments were done at coverages from 2% to 300% on various dimple pitches.

The influence of the coverage on the maximum residual stress is shown in Fig. 5. The experiments were carried out at an indenting speed of 2 cycles/s.

It is apparent that the compressive residual stress in work surface layers increases significantly with increasing the coverage, up to about 200%. The compressive residual stress ranges from 100MPa at a coverage of 2% to 470MPa at 100%. The plastic regions below a dimple increase in size with increasing the coverage. Thus, it was recognized that residual stress strongly correlated with the coverage.

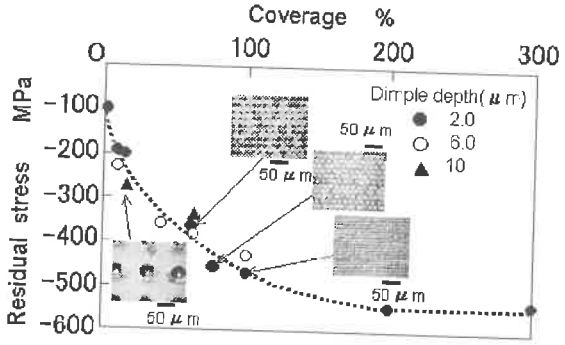

Fig. 5. Influence of coverage on maximum residual stress

3.3 Plastic regions

A half width in the X-ray diffraction shows a degree of the strain of polycrystals in a work surface layer. The influence of the coverage on a half width in the indenting process is shown Fig.6. It is clear that the half width in the blast process is similar to that in the indenting process at a coverage over 100%.

This means the strain of polycrystals in a work surface layer is comparable in both processes. Fig.7 shows Vickers hardness measured every 5 μm deep from the work surface. Each plot is the mean value of five Vickers hardness measurements. The hardened regions in the work surface layer increase with the increase of dimple depth in indenting, in accordance with the increasing plastic regions in a work surface layer. The hardened regions in both processes are approximately 60 μm. As a result, it seems that the effect of the collision speed on the depth of plastic regions would be negligibly small, because the processed depth might be shallow in indenting and blast processes.

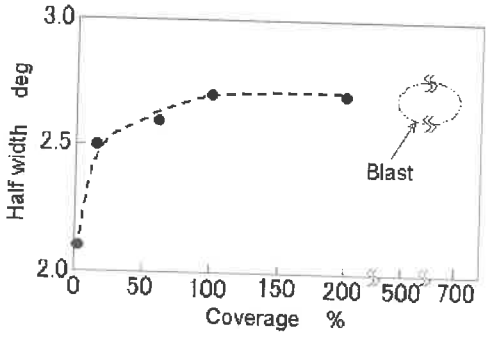

Fig.6. Influence of coverage on half width in indenting process

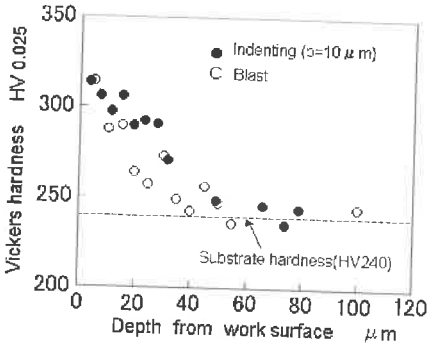

Fig. 7. Vickers hardness distributions of work surfaces treated using indenting and blast processes

3.4 Elastic-plastic analysis of plastic regions in indenting method

The finite element method is applied to analyze plastic regions generated in the indenting process. A rigid spherical indenter of 20μm in radius is shown as a two-dimensional plane strain model. The finite element mesh of the layered half-space. MARC v6.2 was used to solve the FEM. The material properties of the workpiece were as follows: Young's modulus; 206GPa, Poissons ratio; 0.3, yield stress; 300MPa, workpiece hardening slope; 2.06GPa, frictional coefficient; 0.2. Fig. 8 shows examples of plastic regions analyzed in the indenting process. It

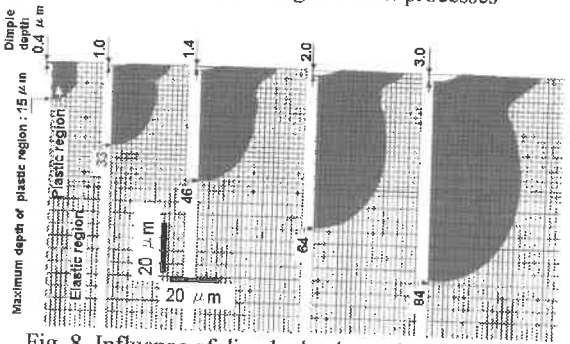

Fig. 8. Influence of dimple depth on plastic regions (FEM analysis)

is apparent that plastic regions increase with increasing indenting depth. The maximum depth of plastic regions at the center between two adjacent dimples with dimple depth 2.0 μm is 64μm. This result in the FEM analysis is similar to the maximum depth of hardened regions, 60μm deep, which seems to be in the plastic region. It indicates that it is possible to use FEM analysis to estimate the maximum depth of plastic regions.

3.5 Distributions of residual stress

Fig. 9 shows the distribution of residual stress below work surfaces created by blast and indenting processes. In the figure, the coverage is over 100% in the indenting process, and over 500% in the blast process. Almost the same stress distributions are obtained in the work surface layer to 50μm deep in both processes. The maximum compressive residual stress, about 450 MPa, exists in the vicinity of the work surface in each process. It was found that the distribution of residual stress in the indenting process simulated that in the blast process. As a result, it seems to be that the coverage in the blast process is excessive, even though the blasting conditions in normal production process were applied in the blasting experiments. It can be said that the coverage would be sufficient at around 200% in the blast process.

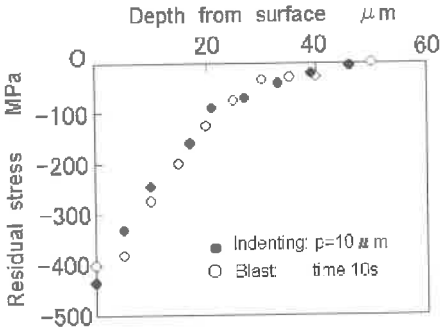

Fig.9. Residual stress distributions (coverage > 100%)

3.6 Work surface profiles

In the indenting process, the spherical shape of an R 20μm indenter is printed on a work surface regularly. On the other hand though, various shot collide and overlap on previous dimples, so that a work surface is irregular in the blast process. Undulations with 50-60μm in period are observed in both work surface profiles, in accordance with crystal sizes of work material. The P-V value of the work surface profile is about 2μm in each process. Therefore work surfaces in both processes would have similar characteristics.

4. Conclusions

The relationship between the indenting process and the blasting process has been discussed for residual stress and work surface profile. As a result, it is made clear that the surface characteristics treated in the blast process can be realized in the indenting process. The following conclusions were summarized:

(1) Plastic regions in the indenting process were estimated by a distribution of Vickers hardness and a half width in the X-ray diffraction pattern as well as the blast process. As a result, it is shown that the depth of a plastic region in the indenting process can simulate one in the blast process, and that the strain in polycrystals on a work surface layer can be comparable in both processes.

(2) The residual stress distribution in the indenting process can simulate one in the blast process.

(3) The compressive residual stress in the indenting process increases with the increase of the coverage up to almost 200%. This means the possibility of reducing blasting time drastically in present production lines.

References

[1]W.Welsch. Lubricating properties of shot peened gears. 52nd Annual Meeting in Kansas City, STLE, 1997, 1.

[2]P.G.Bailey, J.M.Whalen. Shot peen controls and aircraft engine requirements. International Conference on Surface Engineering , Toronto., 1990, 379.

[3]Tosha K, Iida K. Surface residual stresses produced by shot peening and grit blasting. J. JSAT., 1998, 42(2), 63. [in Japanese].

[4]Mori K, Osakada K, Shiomi M, Okada T. Three-dimensional finite element simulation of plastic deformation and residual stress in shot-peening (Deformation by single shot). J. JSME Trans. 1993, 59(566), 2420. [in Japanese].

[5]Mori K, Osakada K, Matsuoka N. Rigid-plastic finite element simulation of peening process with plastically deforming shot. J. JSME Trans. 1995,61(586),1337. [in Japanese].

[6]Y.F.Al-Obaid. A rudimentary analysis of improving fatigue life of metals by shot peening. J. Appl. Mech. ASME Trans., 1990, 57, 307.

[7]Watanabe Y, Hasegawa N, Matsumura Y. Simulation of residual stress distribution on shot peening. J. Soc. Mat. Sci.,Japan. 1995, 44(496), 110. [in Japanese].

[8]K. Ogawa, T. Asano. Theoretical prediction of residual stress produced by shot peening and experimental verification for carburized steel. Materials Science Research International, 2000, 6(1), 55.

An experimental investigation of heat pipes at low power inputs

Ajit Borundia and Hy D. Tran[1]
Department of Mechanical Engineering
University of New Mexico
Albuquerque, NM 87131

Abstract:
In most precision engineering applications, minimization of thermal distortions is done by the use of either active control using temperature controlled air or liquid showers, artificial heaters or ultra low expansion materials such as Invar, Zerodur. This paper explores the use of heat pipes at low heat loads (0.1 W – 5 W) in precision engineering applications where the requirement of stable and near uniform temperature is stringent. Experiments are performed on a commercial heat pipe and its performance characteristics such as effective thermal conductivity, transient response and temperature gradient at steady state are determined.

Introduction:
The process of miniaturization of existing technologies to the nano and micro level with applications in medical sciences, aerospace, communications, automobiles, electronics have put a tremendous demand for higher accuracy on the manufacturing processes and their concerning metrology. Of all the sources of inaccuracy in a precision machine tool, thermally induced distortions are the most prominent source of error and fortunately they are not random errors. These distortions are worsened by the increase in automation in precision machine tools and instruments since the gauging system is now thermally connected to the heat sources of the machine tool and also its dimensions are large compared to the manual gauging. It is a well-known fact that mitigating the thermal errors in machine tools results in increase in accuracy of the process by an order of magnitude and also improves the repeatability of the process. These effects can be reduced in 3 ways: (a) Compensation (b) Temperature controlled coolant shower (c) Passive cooling using heat pipes, heat sinks.

Compensation requires a thermal deformation model of the machine tool to determine the thermal displacements in real time and to account for these displacements in the process. Unfortunately most of the models that have been developed are either very complex and slow or very simple and inaccurate and do not represent the full range of the operating conditions. Also it is very difficult to compensate for the bending mode of deformation by using the position control system of machine tool.

Temperature controlled coolant shower method is widely used in machine tools since it is very simple to implement and has fast response. It has the added benefit of keeping the work area clean of chips, dust and other extraneous materials, which act as heat source or corrosion agent. Depending on the amount of heat removal and on the requirement of dry work area, the coolant can be air or fluid. Liquid shower has high heat capacity and therefore remove heat under near isothermal conditions thus minimizing thermal

[1] Address correspondence to tran@me.unm.edu. This work was supported by ARO DAAD.19.99.0196

distortions. On the other hand, air shower is better in reducing the effect of external heat sources on the machine tool. It has been found out that in the machine tools, the process of pumping the liquid coolant alone generates a significant amount of heat and acoustic vibration. Bryan et al [1] reports that for the production of mirror finishes a structural motion of less than 2 μ inches is required in the machine tool.

Passive cooling by heat pipes and heat sinks are effective at high operating temperatures and high heat flux. This paper explores the use of heat pipes as a means of passive cooling at low power inputs encountered in the lithography process and other precision engineering applications to maintain stable, very low temperature gradients across the surface. The effective thermal conductivity of heat pipes and the transient response of the heat pipe are determined for different heat inputs ranging from 0.1 W to 5 W at the operating temperatures of 0 C and 17 C respectively.

Experimental Apparatus:

A 4 mm diameter circular copper water heat pipe of length 125 mm from Noron Products with thermistors along its length is insulated as shown as in the Fig 1. A 5W flexible kapton heater (Watlow) is wrapped around the heat pipe at one end. The other end of the heat pipe is inserted into the condenser. A thermocouple is glued 17 mm from the end on the condenser section of the heat pipe. This entire set up is then placed in a vacuum chamber to further reduce the heat loss through convection and radiation to the surrounding environment. The lengths of the condenser and the evaporator sections are 57 mm and 43 mm respectively. The temperature of the condenser was allowed to vary + 0.5 deg C in the case of freezing water (0 deg C) and ± 0.5 deg C in the case of the tap water (17 deg C) to simulate the real life conditions.

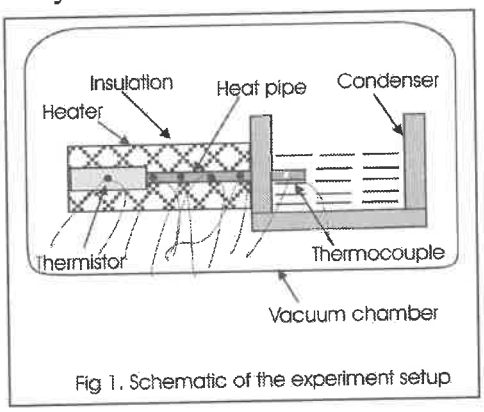

Fig 1. Schematic of the experiment setup

Results & Discussion:

The effective thermal conductivity, transient response, steady state temperature distribution of the heat pipe at 0 deg C and 17 deg C respectively are plotted in figures 2-7. The effective thermal conductivity of the heat pipe was found to be equal to that of copper at 0.4 W and 0.1 W of power input at 0 deg C and 17 deg C respectively. The heat pipe time constant was found to be ranging from 60 to 70 secs for both the cases thus indicating that the transient response was independent of the operating temperature of the heat pipe at low power inputs. The temperature gradient along the adiabatic section of the heat pipe at steady state was found to be varying linearly from –0.068 deg C /mm to –0.28 deg C/mm at 0 deg C and from –0.03 deg C/mm to –0.26 deg C/mm at 17 deg C between power inputs 0.1 W to 5 W respectively. This shows that the temperature gradient is not very sensitive to the operating temperature of the heat pipe.

The conductivity of OFHC copper is approximately 380 W/m-K. With heat flux levels as low as 1 W, the effective thermal conductivity of a heat pipe is several times that of a solid conductor.

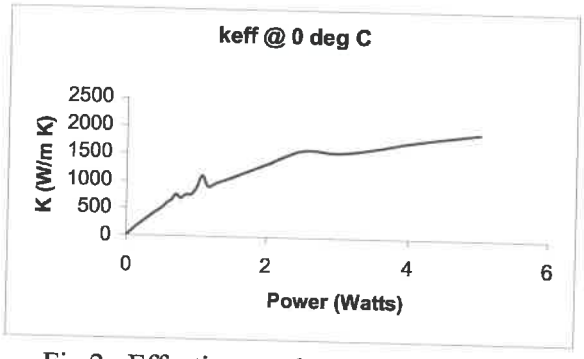

Fig 2. Effective conductivity at 0 deg C.

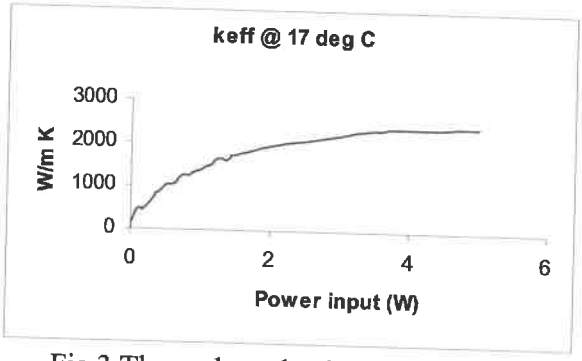

Fig 3 Thermal conductivity at 17 deg C

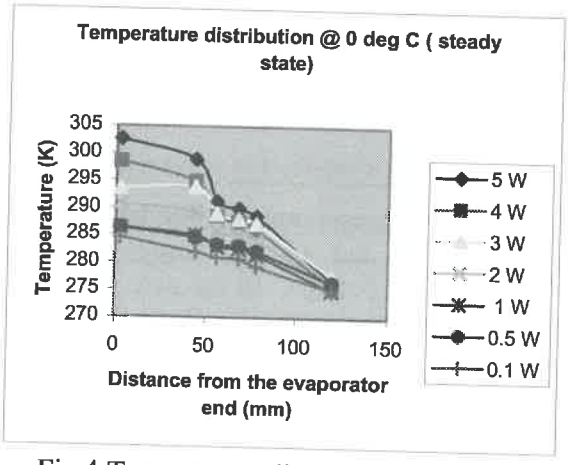

Fig 4 Temperature distribution at 0 deg C

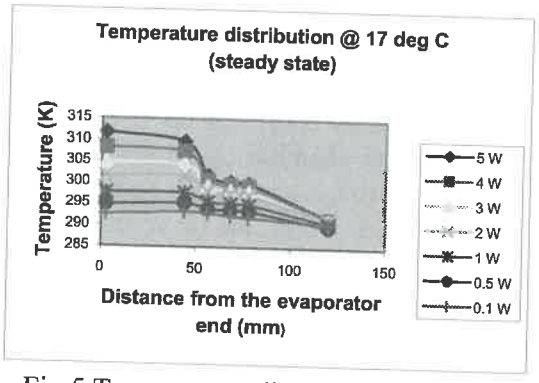

Fig 5 Temperature distribution at 17 deg C

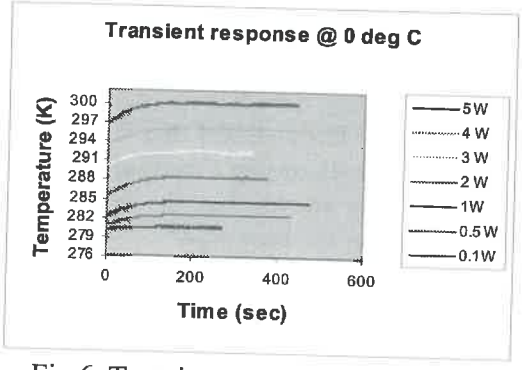

Fig 6 Transient response at 0 deg C

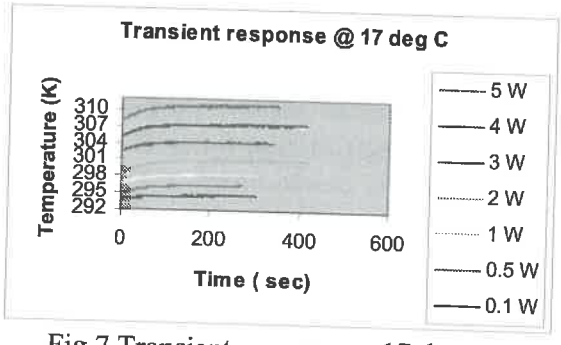

Fig 7 Transient response at 17 deg C

Conclusion:

The effective thermal conductivity, transient response and temperature gradient of the heat pipe at low power inputs were evaluated. From the results we conclude that heat pipes respond quite well in transporting randomly varying low heat loads which occur either due to friction between components in motion or due to concentrated heat input in case of the lithography process at stable temperature gradients. In the future, this would open up the possibility of manufacturing precision equipments by using a structure combining a structure with desirable mechanical properties with heat pipes and active thermal control to minimize thermally induced strain.

References:

1. Bryan J B et.al; A practical solution to the thermal stability problem in machine tools, SME Technical paper, No. MR72-1378 1972.
2. Cao Y, Gao M; Experiments and Analyses of Flat Miniature Heat pipes, Journal of Thermophysics and heat transfer vol 11 no.2 1997, pp 158-164.
3. El-Nasr A A, Haggar S M; Effective thermal conductivity of heat pipes, Heat and Mass transfer vol 32 1996, pp 97-101.
4. Fraser S, Attia M H, Osman M O M; Modeling, Identification and Control of Thermal Deformation of Machine Tool Structures, Part 5: Experimental Verification, Journal of Manufacturing Science and Engineering, vol 121, 1999, pp 517-523.
5. McClure R; Manufacturing Accuracy Through the Control of Thermal Effects, Thesis, LLNL, UCRL-50636 1969.

Surface Texture Peer to Peer Data Sharing System

Son H. Bui, Jay Raja*
Center for Precision Metrology
Mechanical Engineering and Engineering Science Department,
The University of North Carolina at Charlotte
Charlotte, NC 28224, USA

Abstract

This paper presents a surface texture peer to peer data sharing system, which applies Java and Internet technology to engineering metrology. The system provides the user with a mechanism to share and search surface texture data on computers in a network. The system includes a search engine, analysis tools, and a data file transfer mechanism. The most distinct feature of this system is that data files are not stored in a central server but computers that have the files are linked together to form a flexible network.

Keyword: Surface texture, Internet, data sharing

1. Introduction

In recent years, most large companies have moved away from in-house manufacturing to global manufacturing. They outsource machining of parts to vendors around the world. Global manufacturing gives large companies the advantage to reduce operating costs. However, one side effect of this global manufacturing is that it is challenging for large companies to monitor or control quality of machined parts made at vendor sites. Most of these vendors tend to be small and lack the metrology expertise needed to troubleshoot problems relating to quality. The large companies that design and build the products are still responsible for the quality and performance of the parts, and therefore must work with vendors to ensure process capability and reduce part variability. Since the manufacturing processes are geographically separated from the large companies, there is a need for a data sharing tool. This data sharing tool enables large companies to remotely access data located at vendor sites to analyze and troubleshoot processes.

This paper addresses this need by developing a surface texture peer to peer data sharing system. The system provides the user with a mechanism to share and search surface texture data files between computers on a network. It also provides the user analysis tools such as 2RC and Gaussian filter, power spectrum, autocorrelation, and calculation of surface parameters, etc. When the peer to peer data sharing system is installed on measuring instruments, it gives a large company the ability to troubleshoot when they deal with their vendors. The system allows the large company, which is geographically separated from their vendor, to connect directly to the measuring instrument at different vendor sites, search and download data files based on surface parameters, and compare surface profiles to check the quality and performance of the parts.

In the traditional Web model shown in figure 1a, users can use a web browser to download and view data files stored on remote Web servers. Peer to Peer data sharing model is different with the traditional Web model; each computer on the network can directly connect to each other. This is shown in figure 1b. Each computer on the network can be considered as a peer, which acts as both server and client. The information stored in the individual computers is linked together and spread among them. The advantage of this system is that not all information will be stored in a centralized server as shown in figure 1b. With a centralized system, shutting down the system can cause the whole network to go down. Therefore, a peer to peer data sharing system provides far greater flexibility and simplicity than a centralized server system.

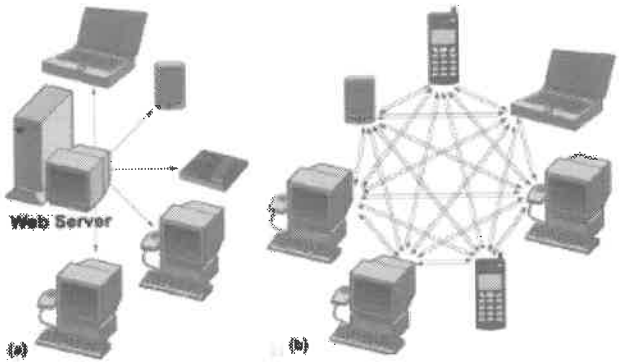

Figure 1. In (a) the traditional Web model, users can view files stored on remote Web servers. In (b) P2P mode, users connect their PCs directly with each other [1]

2. Software Design

The surface texture peer to peer data sharing system was designed using object oriented programming techniques. The use-cases diagram of the surface texture peer to peer data sharing system is shown in figure 2. The use-cases diagram defines how the external entities interact with the system and the requirements used to design the software. The surface texture peer to peer data sharing system allows the user to share data files with other peers on the network. The user can download or search data files based on surface parameters and instrument names from other peers. On the graphic user interface (GUI), the user can view a plot of primary profile and information of a data file. The user can also use analysis tools provided in the system to perform functions such as filter a profile using 2RC or Gaussian filter, calculate 10 surface parameters from ISO4287 [2], or perform autocorrelation and power spectrum analysis.

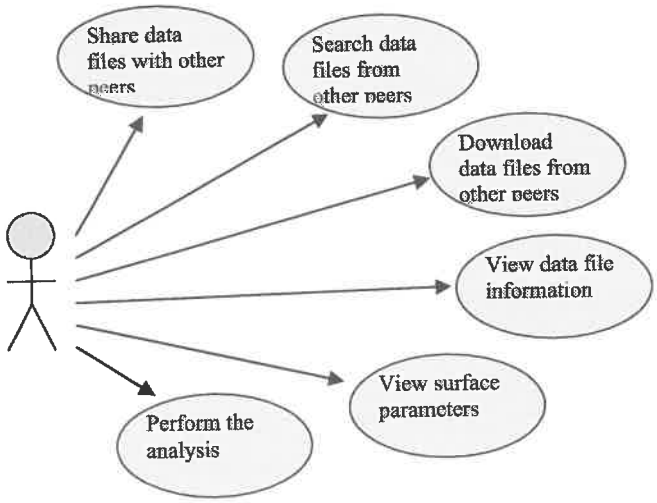
Share data files with other peers
Search data files from other peers
Download data files from other peers
View data file information
View surface parameters
Perform the analysis

Figure 2. Surface texture peer to peer data sharing system use-cases

3. Principle of peer to peer data sharing system

Peer to peer data sharing system works different from the traditional Web server model. Before your peer connects to other peers on a network, it must know the IP address of other peers on the network. Your peer will transmit a handshake message to the other peer to identify your peer to other peers. Then

your peer will send a PING request to the other peers to announce that it presents on the network. In this PING message, it contains TTL (Time to live) to identify how many times a message can be forwarded to the other peers. When the other peers receive the PING message, they will reply by sending a PONG message, which contains their IP addresses and file sharing information. To search a data file from other peers, your peer will send a QUERY message directly to every peer known to your peer. After receiving the QUERY message, each peer searches its local files for matches to your query. If it does not find anything, it does not reply. If there are one or more matches, a QUERY HITS message that contains IP address of sender and the data file name is routed to your peer. When you select one of search results for downloading, your peer will create a standard HTTP request and send this request to the peer, which returns a data file via HTTP.

Protocol defines the agreement between the communicating parties on how communication is to proceed [3]. The protocol of surface texture peer to peer data sharing system is designed based on the Gnutella Protocol V0.4 [4]. It consists of a set of descriptors used for communicating data a between servants and a set of rules governing the inter-servant exchange of descriptors. Gnutella protocol is used to exchange multimedia files between peers on the network.

4. System interfaces

The interface of the analysis tools of the surface texture peer to peer data sharing system is shown in figure 3. The interface shows all information of data files including their properties and surface parameters stored in a local disk. The user can load data to the analysis tools to perform the analysis. In addition the user can use an audio player to listen to the sound of data file before and after filtering.

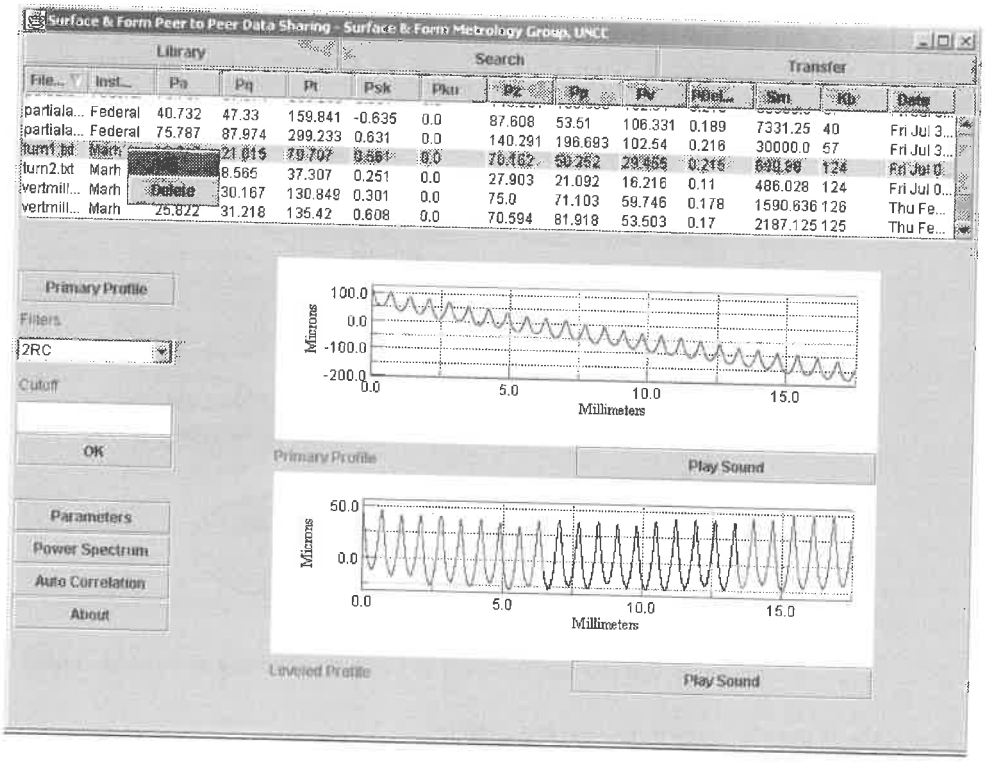

Figure 3. Search engine interface

The interface of a search engine of the system is shown in figure 4. The user can search data files from other peers on the network based on instrument names and surface parameters. On the result table, the user can view properties of data files; such as file name, file size, speed of connection, and surface parameters, etc. Every time the system starts running; it looks for new downloaded data files, determines properties of these data files, and stores their properties into a hash table. When the system receives a QUERY message from other peers on the network, it will search for matches from the hash table, and send search results to other peers. To download a data file, the user selects which data file will be downloaded and double clicks on that data file.

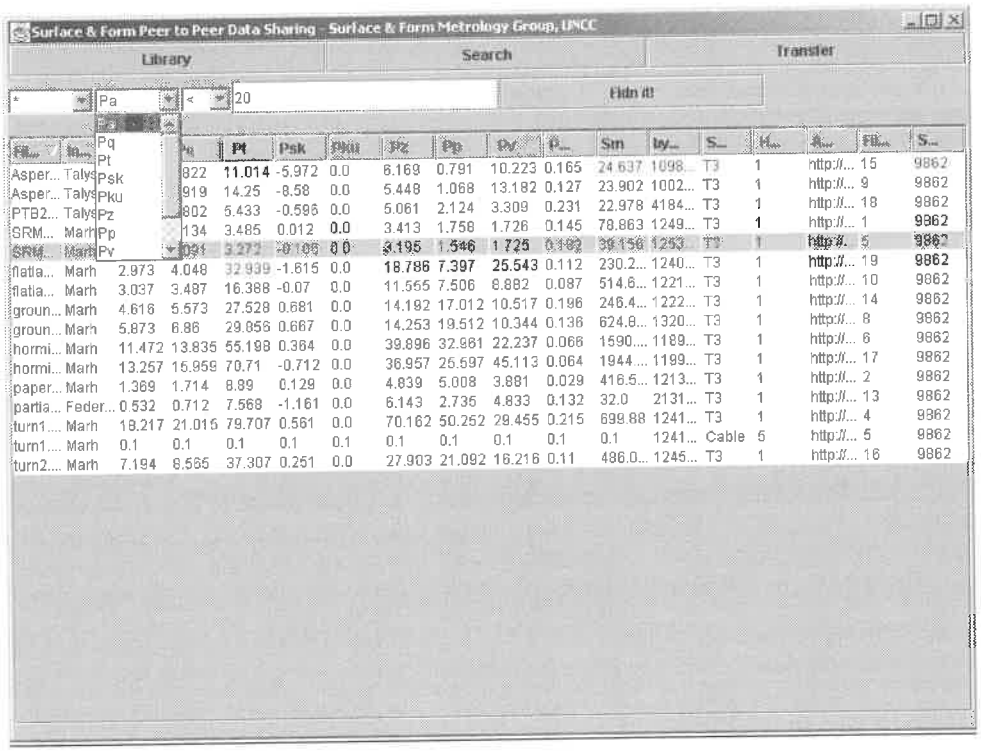

Figure 4. Data file library and analysis tools

5. Conclusion

The surface texture peer to peer data sharing system provides metrologists with a flexible way to search and share surface texture data files with others on the network without using a centralized server. It is hoped that metrologists will come forward and use this system for the work.

6. References

[1] Giovanni Flammia , "Peer to Peer is not for Everyone".
http://www.computer.org/intelligent/homepage/2001/03Flammia/Flammia1.htm (2001)
[2] ISO 4287:1997 Geometrical Product Specifications (GPS) – Surface texture: Profile method – Terms, definitions and surface texture parameters.
[3] Andrew S. Tanenbaum: Computer Networks. Prentice-hall, Inc. 1996
[4] Gnutella, "The Gnutella Protocol Specification v 0.4 Document Revision 1.1"
http://www.clip2.com/GnutellaProtocol04.pdf (3/28/01)

Fabrication of Grinding Wheel with Dispersed Hard Powder by Electrical Discharge Machining

Katsushi Furutani and Hirotaka Sunada[1]
Department of Advanced Science and Technology, Toyota Technological Institute
12-1, Hisakata 2-chome, Tempaku-ku, Nagoya 468-8511 Japan
Phone: +81-52-802-1111, Fax: +81-52-809-1796, e-mail: furutani@toyota-ti.ac.jp
[1] Teiho Plant, Toyota Motor Corp. at present

1. Introduction

Because industrial products have been becoming higher in performance and finer in size, machining with higher accuracy is required. Grinding process is one of the highly accurate machining methods and very effective for machining hard materials such as cemented carbide and hardening steel.

The abrasive layer of the grinding wheel generally composes 3 elements such as grains, a bond and pores. The abrasive grains on the working surface of a grinding wheel are easily shed and the thickness of an abrasive layer decreases during grinding the hard materials. The pores are loaded by debris during grinding soft materials. Consequently, the grinding wheel should be frequently dressed so that the life of the grinding wheel becomes shorter. Moreover, when the life of the grinding wheel is ended, the grinding wheel is disposed of even if its core is still usable. This is very wasted and makes the cost of the grinding process higher. Some fabrication methods of grinding wheels have been proposed to reduce the fabrication cost, or improve the gripping strength of grain and grinding performance [1][2].

In this paper, a fabrication method of an abrasive layer by electrical discharge machining (EDM) is proposed. The characteristics of the deposited layer are evaluated through a grinding process. This method is applicable to recycle a grinding wheel.

2. Fabrication method

A depositing method of a hard layer by electrical discharge machining (EDM) with a green compact electrode has been studied [3]. Fig. 1 shows an example of the WC-Co accretion with a thickness of 1 mm. The accretion is porous according to the electrical conditions. The green compact has composed only conductive materials. On the contrary, an abrasive, generally insulating material, is added into a mixture of WC and Co powders in the proposed method. In this case, the abrasive grain will be dispersed into the WC-Co accretion working as a bond as shown in Fig. 2. Consequently, the hard layer including the 3 elements can be fabricated by EDM.

A green compact electrode was made by compressing a mixture of WC: 63 wt%, Co: 27 wt% and an abrasive: 10 wt%, which was Al_2O_3, SiC or diamond. Then the abrasive layer was deposited under the conditions shown in Table 1. Fig. 3 shows some examples of the accretion including the abrasive grain observed by a scanning electron microscope (SEM) and energy dispersive X-ray spectroscopy (EDX). The layer in which each of the powders with a size of 20-100 μm dispersed could be deposited on a plate. Some other insulating grains used as the abrasive were also investigated. Fig. 4 shows the range of the grain size and thermal conductivity where the abrasive could be deposited. The grain size and the thermal conductivity mainly affect the deposit properties. Because the heat by discharge is not absorbed into the grains with low

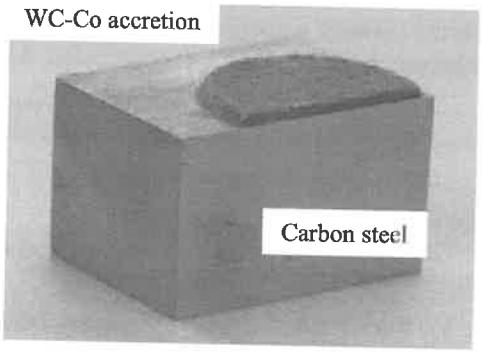

Fig. 1 WC-Co accretion by EDM

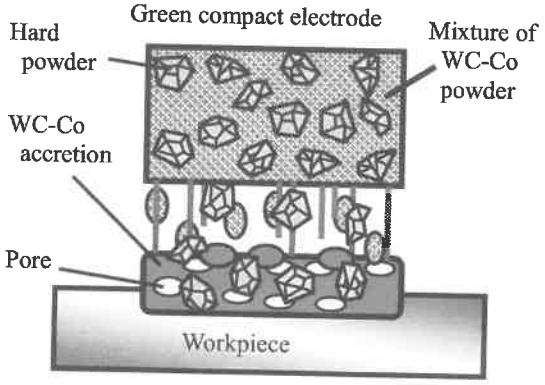

Fig. 2 Fabrication of abrasive layer by EDM

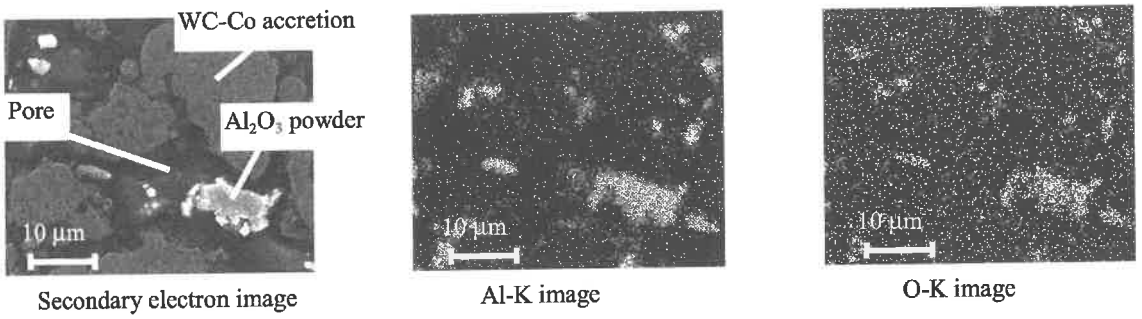

Secondary electron image | Al-K image | O-K image

(a) Al_2O_3 (average grain size: 35-50 μm)

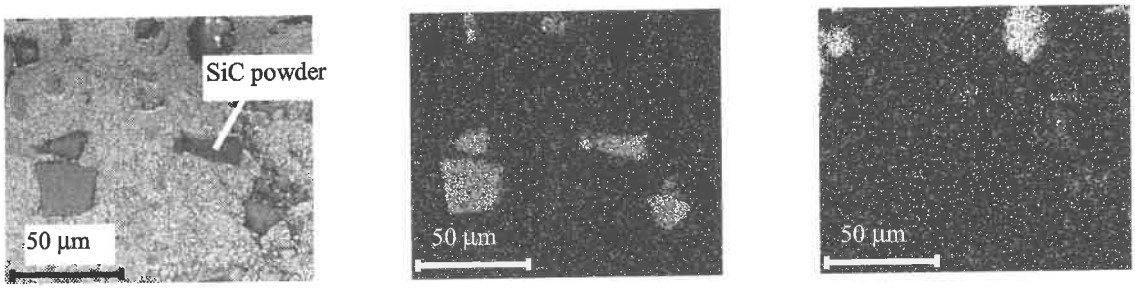

Secondary electron image | Si-K image | C-K image

(b) SiC (average grain size: 30-40 μm)

Fig. 3 Examples of accretion including abrasives

Table 1 Conditions for deposit EDM

Polarity of electrode	(-)
Discharge current	23 A
Discharge duration	8 μs
Pulse interval	1024 μs
Machining time	300 s
Load for green compact forming	540 MPa
Workpiece	Hot-rolled steel or JIS-SKD11/ ASTM-D2

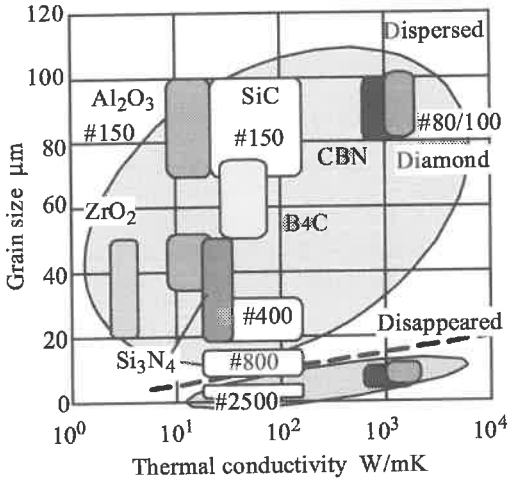

Fig. 4 deposit range of grain size and thermal conductivity

thermal conductivity such as Al_2O_3 and ZrO_2 but the WC-Co layer, the grain remains and the reaction of the WC-Co layer with the grain is promoted. On the other hand, the grains with high thermal conductivity such as diamond and CBN were easily disappeared because the whole grain immediately accumulates the heat so that they sublime.

Fig. 5 shows a setup to fabricate a mounted wheel. After a JIS-SKD11 (ASTM-D2) core with a diameter of 18 mm was rotated and translated like a rack-and-pinion during EDM, the mounted wheel shown in Fig. 6 could be fabricated. Its surface roughness was 22 μmR_z.

The grain volume percentage was evaluated with a partial section analyzed by EDX. The volume percentage for #150 or #400 SiC grain was 6% and 10%, respectively, when the volume ratios of the SiC grains in each electrode were 41% and 31%. These ratios are much smaller than that of conventional grinding wheels, 34-62% in nominal. The hardness of the WC-Co layer

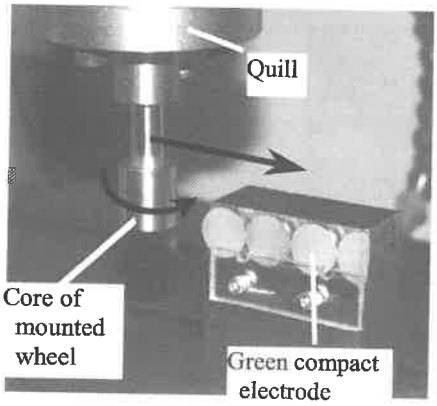

Fig. 5 Core of mounted wheel and green compact electrode

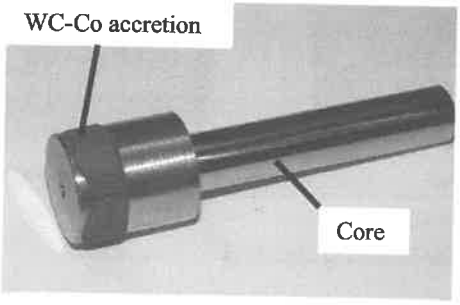

Fig. 6 Mounted wheel fabricated by EDM

Table 2 Grinding conditions for disks

Rotational speed	2200 min^{-1}
Peripheral speed	23.6 m/s
Grinding fluid	Soluble oil
Feed	330 mm/s
Depth of grinding	3 μm
Total depth	100 μm
Number of spark out	10

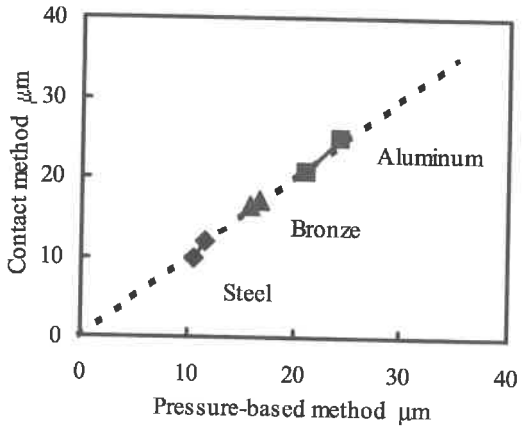

Fig. 7 Comparison of results by pressure-based and contact methods

without abrasive was 21 H_RB, harder than a vitrified bond wheel. And the hardness of the layer including SiC grain was -15 H_RB, corresponding to H grade.

3. Grinding performance

JIS-S50C (AISI-1049) carbon steel, aluminum and copper disks were ground with the #400 SiC abrasive layer fabricated on a JIS-SKD11 plate instead of fabricating a big grinding wheel. Table 2 shows grinding conditions. Both the pressure-based in-process measurement method [4] and the contact method were applied to measurement of a radius of the disks with a diameter of 205 mm. The peripheral speed and the depth of grinding a pass were set to 23.6 m/s and 3 μm, respectively. Fig. 7 shows the comparison of two methods. The dotted line shows the coincidence of the in-process measurement with the contact method. All the data exist on the dotted line. The difference between them are less than 0.6 μm. The grinding ratios against aluminum, copper and steel were 19.7, 11.3 and 6.9, respectively. With an increase of the volume percentage of the grains, the grinding ratio is increased. The volume percentage of the wheel used in the experiment was much smaller than conventional wheels. The percentage should be improved.

4. Recycling of wheel

The concept of the machining method by the feedback of shape data [5] was applied to recycle a used grinding wheel. Fig. 8 shows a recycling process. Deposit and removal machining are repeated in this method until the form error remains. The shape was measured with an electric comparator without dismounting the wheel from the quill.

The accretion without abrasive was fabricated to evaluate the strength of the bond. The maximum difference for a thickness of 350 μm was 14 μm by the shape feedback method.

Table 3 shows the grinding conditions. The roughness of the mounted wheels was 20-30 μmR_y after truing by EDM. Fig. 9 shows appearance of a ground area. The grinding ratios for wheels primarily deposited and recycled were 15.9 and 13.7, respectively. Though the new layer was deposited without any cleaning in the recycle process, the recycled wheel performed as well as the new wheel.

5. Conclusions

In this paper, the fabrication method of a grinding wheel is proposed. The conclusions can be drawn as

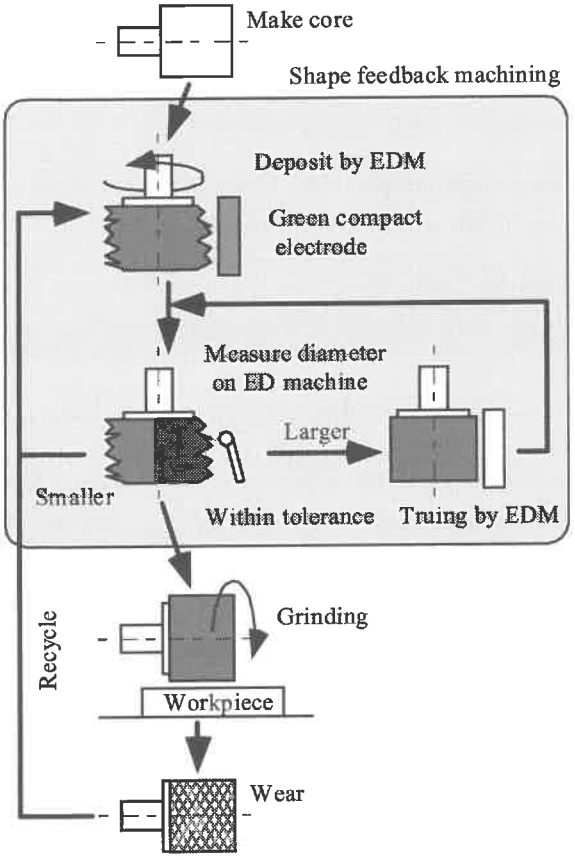

Fig. 8 Recycling process

follows.

(1) Many abrasives including super abrasives could be included in the WC-Co layer. The appropriate range of grain size and thermal conductivity exists.
(2) Though the volume ratio of the wheel fabricated by EDM was smaller than that of conventional wheel, the grade was the same. Steel could be ground with the wheel fabricated by EDM.
(3) The grinding wheel was recycled without a great decrease of the grinding ratio.

This method is an effective solution to solve the problems in grinding.

Acknowledgement

The authors wish to thank Prof. Kazuyoshi Kondo and Prof. Fumihiro Honda of Toyota Technological Institute (TTI) for their valuable advice and Mr. Masaru Ohta of TTI and the staff of Machinery Engineering Administration Division of Toyota Motor Corporation for their helpful cooperation. A part of this study is financially supported by Mitutoyo Association for Science and Technology and Grant-in-Aid for "Space Robotics Research Center" and for "Future Data Storage Materials Research Center" by the Ministry of Education, Culture, Sports, Science and Technology, Japan.

Table 3 Grinding conditions to evaluate recycled wheel

Rotational speed	24000 min^{-1}
Peripheral speed	23.4 m/s
Grinding fluid	Soluble oil
Feed	3.3 mm/s
Depth of grinding	5 μm
Total grinding depth	400 μm
Width of grinding	10 mm

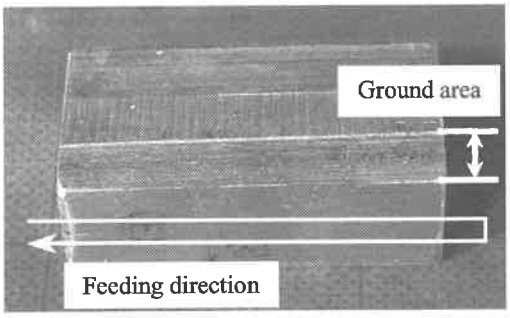

Fig. 9 Appearance of ground area

References

[1] Y. Hagiuda, T. Nakagawa, K. Karikomi: Manufacture of a Sintered Cast Iron Lapping Plate with Fixed Abrasives and Its Lapping Ability, Ann. CIRP, 30, 1, pp. 227-230 (1981).

[2] J. Ikeno, Y. Tani, H. Sato: Nanometer Grinding Using Ultrafine Abrasive Pellets, Manufacture of Pellets Applying Electrophoretic Deposition, Ann. CIRP, 39, 1, pp. 341-344 (1990).

[3] N. Mohri, N. Saito, Y. Tsunekawa: Metal Surface Modification by Electrical Discharge Machining with Composite Electrode, Ann. CIRP, 42, 1, pp. 219-222 (1993).

[4] K. Furutani, T. Katoh, N. Mohri: In-process Measurement of Wear of Grinding Wheel by Hydrodynamic Pressure, Proc. 14th Ann. Meet. Am. Soc. Precis. Eng., pp. 610-613 (1999).

[5] H. Takezawa, K. Furutani, N. Mohri: Precision Machining by Feedback of Shape Data (1st Report) -The Basic Concept and Examples of Corrective Machining-, Int. J. Jpn. Soc. Precis. Eng., 33, 3, pp. 209-214 (1999).

NANOPROBE CONCEPTS FOR FIELD EMISSION NANOMACHINING

Chris A. Trinkle*, R. Ryan Vallance*, and M. Pinar Mengüç†
Mechanical Engineering, University of Kentucky, Lexington, KY

Alaji Bah and Kazi Javed
Chemistry Department, Kentucky State University, Frankfort, KY

Apparao M. Rao
Department of Physics and Astronomy, Clemson University, Clemson, SC

Sungho Jin
Mechanical and Aerospace Engineering, University of California San Diego, San Diego, CA

Abstract

Multi-walled carbon nanotubes are excellent conductors and are considered ideal electron emitters since their high aspect ratios ensure concentrated electric fields. Their field emission characteristics and recent developments in growth of aligned nanotubes onto electrically conductive substrates make them promising for use in nano manufacturing. Combining resistive (Coulumb) heating, spot heating with a laser and abosorption of electrons emitted from the tips of nanotubes, nanoscale machined features may be produced on conductive substrates. Therefore, we are presently designing Nanoprobes that encorporate nanotubes for their tips to enable experimental tests. This paper presents several concepts for creating nanomachining probes utilizing established microfabrication methods—including discussion on the creation of probes onto which nanotubes can be attached, methods for attaching the nanotubes, and creating 1 and 2D patterns for parallel manufacturing and metrology processes.

Keywords: nanotube arrays, field emission, nanopatterning

Introduction

Carbon nanotubes (CNTs), first discovered in 1991 [1], are self-assembling hexagonal lattices of carbon atoms joined into long narrow tubes. Nanotubes are grown using several techniques including CVD or electric arc discharge in inert atmospheres [2]. Depending on the technique, nanotubes may be comprised of a single layer of graphene sheet (single walled nanotubes or SWNT) or multiple, concentric layers (multi-walled nanotubes, MWNT). Diameters for SWNTs are as small as 2 nm, while MWNTs are typically between a few nm and 100 nm in diameter. MWNTs are excellent conductors and are considered ideal electron emitters since their high aspect ratios ensure concentrated electric fields. Rao et al. [3] developed a CVD technique to grow MWNTs aligned perpendicular to a polished titanium nitride (TiN) substrate, which exhibited superb field emission properties. The field emission characteristics of these nanotubes encouraged us to investigate their potential application in nano manufacturing.

Fig 1 illustrates a potential nano-machining approach using energy transmitted during field emission from carbon nanotubes. We seek to remove clusters of atoms from workpiece surfaces using multiple energy sources. Bulk heating can be applied to the workpiece using resistive (Coulomb) heating or radiative heating. If necessary, further localization of the energy is achieved with a laser beam focused to a spot-size of a few microns. Finally, high resolution patterning capability might be obtained with the absorption of electrons emitted from the tips of nanotubes.

* *Precision Systems Laboratory, Mechanical Engineering, University of Kentucky, 210-A CRMS Building, Lexington, KY 40506. http://www.engr.uky.edu/psl.*
† *Radiative Transfer Laboratory, Mechanical Engineering, University of Kentucky, 514-D CRMS Building, Lexington, KY 40506.*

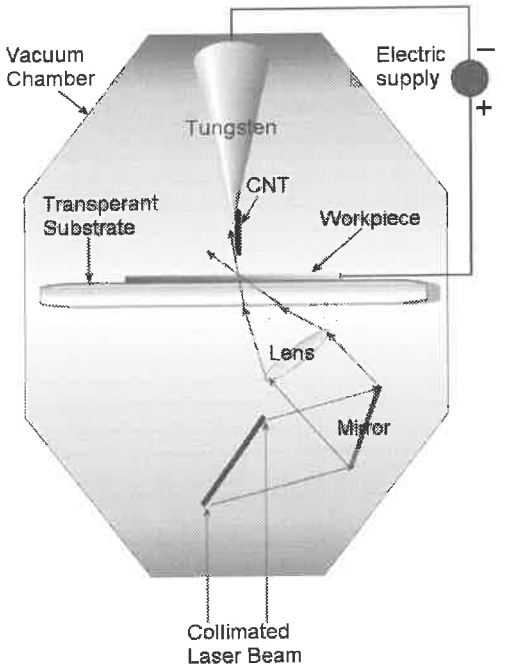

Fig 1: Setup for High-Resolution Nanomachining with Carbon Nanotubes

Recent simulations of the energy transferred during electron and laser absorption by a gold film deposited on quartz suggest the feasibility of this nanomachining approach [4]. Therefore, we are presently designing nanoprobes to enable experimental tests. As illustrated in Fig 2, we are interested in designing three categories of field-emission nanoprobes: 1) probes with only one NT for serial processing of the workpiece, 2) probes with 1D patterns of emitting NTs, and 3) probes with 2D patterns of emitting NTs. Probes in the first category are most appropriate for scientific investigation, but the second and third categories hold greater promise for manufacturing processes.

This paper presents several concepts for creating nanomachining probes utilizing established microfabrication methods. This includes discussion on the creation of probes onto which nanotubes can be attached, methods for attaching the nanotubes, and creating 1 and 2D patterns for parallel manufacturing and metrology processes.

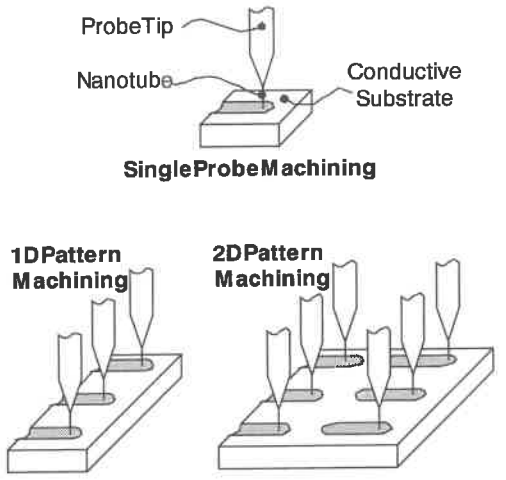

Fig 2: Field Emission Nanoprobes in serial, 1D pattern and 2D pattern configurations

Nanotube Synthesis

The synthesis process for nanotubes uses a chemical vapor deposition chamber to deposit the nanotubes on a suitable substrate, such as TiN, quartz, or nickel. Therefore, a suitable growing site can be created by selectively coating the probes with a thin layer of Ni at the tips using e-beam lithography. The location of the nanotubes is determined by the location of a nucleating catalyst particle—making the number of nanotubes grown on the probe a function of the nickel layer's surface area.

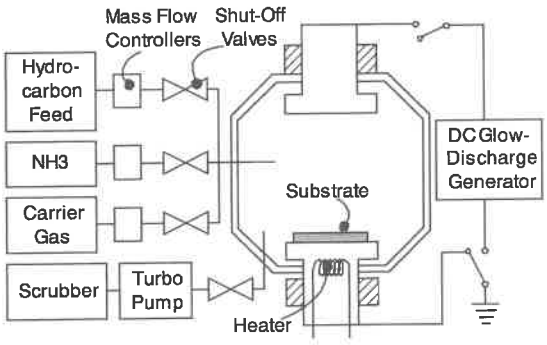

Fig 3: Plasma Enhanced CVD chamber for growth of carbon nanotubes

Growth of nanotubes directly onto an AFM tip has been demonstrated experimentally [5,6]. If repeatable on a larger scale, it would be the preferred method of obtaining nanotubes on the probe tips, as this would eliminate the need for additional equipment and attachment processes.

Another process would involve growing the nanotubes in a pattern directly onto a flat substrate—

eliminating the need for the probe tips entirely. This can be achieved by depositing the nickel catalyst in nano-sized dots using e-beam lithography, and then synthesizing the nanotubes in the PECVD chamber. Staggered heights for the nanotubes might be obtained by etching the substrate prior to the nickel deposition.

Joining Nanotubes to Probes

An alternate approach is necessary if growth of nanotubes directly onto probe tips is not a reliable solution. Nanotube tips can be attached after the growth process by transferring them from the growth substrate onto the tips. This process has been demonstrated using the electron beam from an SEM to weld the nanotube to an AFM tip [7]. Stephens, et al. produced similar results using an electrical arc discharge method in open air [8].

Probe Conceptual Designs

The ideal probe for integrating nanomachining and SPM requires at least two electrically isolated attachment sites for nanotubes. Making these sites close together is also preferable, as this makes it faster to obtain results on recently machined areas. It also facilitates alignment of the tip paths, increasing accuracy of the metrology information. We are also concerned with ease of fabrication; both for the probe tip manufacture and the subsequent attachment of the nanotubes.

Modified AFM Probe

One approach is to modify a commercially available SPM cantilevered probe. There have been documented results that demonstrate attaching nanotubes to cobalt coated AFM probes [8]. For our purposes, electroplating the tip with a thin layer of Ni would provide a conductive surface without drastically diminishing the sharpness of the tip—providing a catalytic base onto which nanotubes can be attached or grown.

The staggered tip necessary for integrated manufacture and metrology would be obtained using a lithographic etching process. Once the probe geometry shown in Fig 4 has been obtained, the two plateaus must be electrically isolated. By applying layers of conductive and dielectric materials via electron beam lithography to create the pattern shown in Fig 5, nanotubes on the two plateaus can be activated independently.

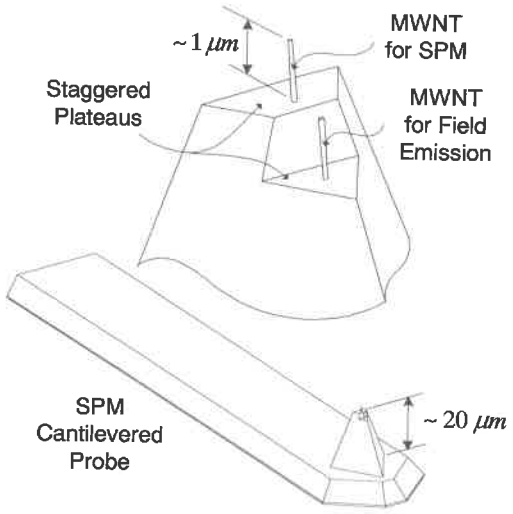

Fig 4: Proposed Staggered Plateau Probe with Two Nanotubes for Field Emission and Scanning Probe Microscopy

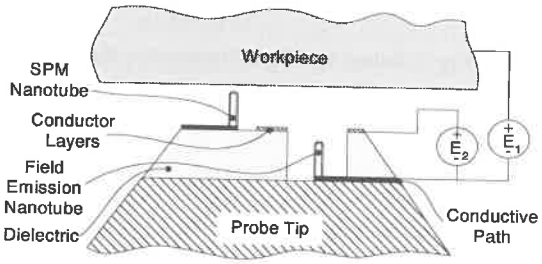

Fig 5: Staggered Probe Tips with Gated Nanotubes for Focusing Field Emitted Electron Beams

While this method has been proven for a single nanotube attachment, the staggered plateau and electrical isolation geometry provide a manufacturing challenge. Also, the commercial availability of the cantilevered probes provides limited control over many of the probe parameters.

Electrochemically Etched Tungsten Wire

Another method for preparing the tips utilizes electrochemical etching of tungsten wire. The etching process, shown schematically in Fig 6 has been well documented [9, 10] and can achieve a tip radius as small as 5 nm [11]. An optical microscope image of tungsten wire etched in this manner is shown in Fig 7.

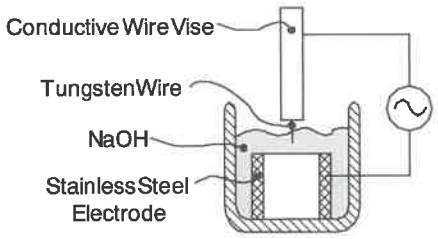

Fig 6: Electrochemical etching process for tungsten probe fabrication

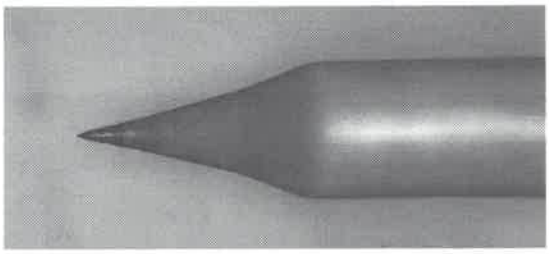

Fig 7: Electrochemically etched 300-μm diameter tungsten probe

In order to create multiple probe geometry, several of these sharpened wires would be mounted onto a silicon ferrule, illustrated in Fig 8. The ferrule can be created by taking advantage of [100]-oriented silicon's natural tendency to form v-groves with 54.74° inward angles when etched. The non-conductive nature of silicon would provide the necessary electrical isolation for using multiple tips.

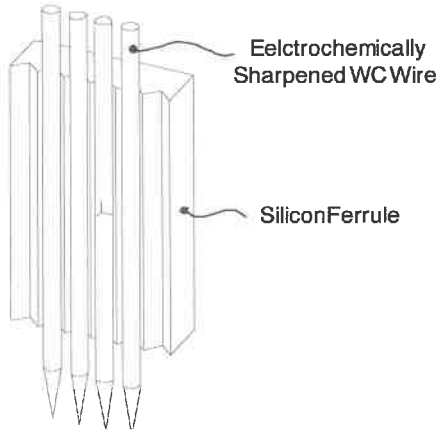

Fig 8: Multiple-tip probe comprised of etched WC wires in a silicon ferrule

This probe configuration is easy to manufacture and provides a convenient solution to the electrical isolation. Also, since the wires would be etched and assembled into the ferrules individually, it would offer a great deal of control over tip parameters—such as height, tip radius and slope. Also, as can be seen in Fig 8, it allows for more than two tips to be assembled into a single probe. This provides opportunities for two or more independent parallel processes in a single probe.

The wire and ferrule configuration has a few inherent drawbacks. First, it can only easily handle a linear pattern, not 2-D. Also, the distance between tips is severely limited by the diameter of the wire. It would be difficult to get closer than 20-30 um between wire tips, compared to 5-10 um that would be feasible with the cantilevered AFM probe.

Electrodeposited Patterned Tips

Another manufacturing process considered here is the use of x-ray lithography and electrodeposition to create a patterned probe. This process can produce patterns of nickel towers with diameters up to 500 μm in height as little as ~2 μm in diameter [12]. The towers can be electrochemically sharpened to produce a patterned probe, similar to that in Fig 9.

While this process does not inherently produce tips that are electrically isolated, it may be possible to achieve this by modifying the base structure. Our process would involve filling part of the gaps in the pattern with an electrically non-conductive material and then removing the nickel base, shown in Fig 9.

Towers of various heights can be created in the electroplating step, but it would be difficult to retain the exact height differences during the etching process. This procedure does have an advantage in its ability to easily produce 2-D patterned probe tips.

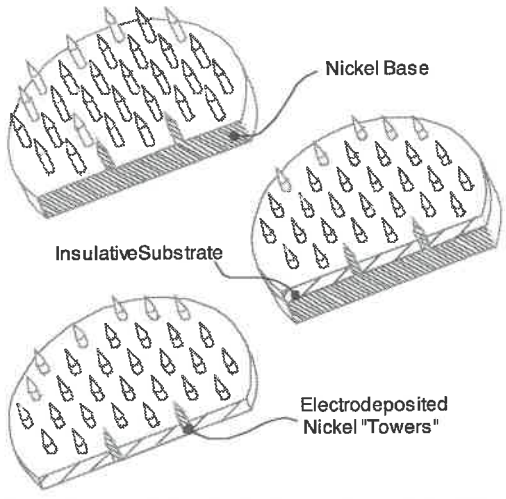

Fig 9: Patterned probe tips manufactured using x-ray lithography and electrodeposition

Conclusions

The field emission properties of carbon nanotubes may be useful in achieving nanoscale machining of conductive workpieces. This paper presents a variety of alternative approaches for fabricating probes for experimentally demonstrating such a process. The fabrication methods considered here incorporate conventional microfabrication methods. They provide varying degrees of difficulty with respect to fabrication, but all show promise for use in either experimental or bulk machining processes.

References

[1] S. Iijima. "Helical Microtubules of Graphitic Carbon." *Nature* 354 (1991) 56-58

[2] M.S. Dresselhaus, G. Dresselhaus, and P. C. Eklund. Science of Fullerenes and Carbon Nanotubes. Academic Press. San Diego, 1996. p. 778.

[3]Rao A. M., D. Jacques, R. C. Haddon, W. Zhu, C. Bower, and S. Jin. "In-Situ Grown Carbon Nanotube Array with Excellent Field Emission Characteristics". *Applied Physics Letters.* V. 76, No. 25 (2000) 3813-3815

[4] B. Wong, M. P. Menguc, R. Vallance, C. Trinkle. "Modeling of Energy Transfer in Field Emission of Carbon Nanotubes." Presented at 8th Joint AIAA/ASME Thermophysics and Heat Transfer Conference, St Louis, MO, June 21-24, 2002

[5] J. H. Hafner, C. L. Cheung, C. M. Lieber. "Growth of Nanotubes for Probe Microscopy Tips." *Nature* 398 (1999) 761-762

[6] L. Delzeit, C. V. Nguyen, R. M. Stevens, J. Han, M. Meyyappan. "Growth of Carbon Nanotubes by Thermal and Plasma Chemical Vapour Deposition Processes and Applications in Microscopy." *Nanotechnology* 13 (2002) 280-284

[7] H. Nishijima, S. Kamo, S. Akita, Y. Nakayama, K. Hohmura, S. Yoshimura, K. Takeyasu. "Carbon-Nanotube Tips for Scanning Probe Microscopy: Preparation by a Controlled Process and Observation of Deoxyribonucleic Acid." *Applied Physics Letters.* V. 74, No. 26 (1999) 4061-4063

[8] R. Stephens, N. Frederick, B. Smith, D. Morse, G. Stucky, P. Hansma. "Carbon Nanotubes as Probes for Atomic Force Microscopy." *Nanotechnology* 11 (2000) 1-5

[9] V. Weinstein, M. Slutzky, A. Arenshtam, E. Ben-Jacob. "A Method for Preparation of Pt-Ir Tips for the Scanning Tunneling Microscope." *Review of Scientific Instruments* V. 66, No. 4 (1995) 3075-3076

[10] M. Fotino. "Tip Sharpening by Normal and Reverse Electrochemical Etching." *Review of Scientific Instruments V.* 64, No. 1 (1993) 159-167

[11] Y. Nakamura, Y. Mera, K. Maeda. "A Reproducible Method to Fabricate Atomically Sharp Tips for Scanning Tunneling Microscopy." *Review of Scientific Instruments* V. 70, No. 8 (1999) 3373-3376

[12] A. Rogner, J. Eicher, D. Munchmeyer, R-P Peters, J. Mohr. "The LIGA Technique—What Are the New Opportunities." *Journal of Micromechanics and Microengineering.* 3 (1992) 133-140

MOLECULAR DYNAMICS SIMULATION FOR EDM DIE-SINKING EROSION PROCESS

Yongshun Zhao, Xingquan Zhang, Kazuo Yamazaki
IMS-Mechatronics Laboratory, University of California, Davis, California

1 INTRODUCTION

Our earlier paper [1] presented an overview of a linear motor equipped electrical discharge machining (EDM) process with a geometry based single spark model to describe the erosion process. Although experiments have verified the geometry simulation method, there is still not enough of a detail study of the linear motor equipped EDM characteristics. Based on these research achievements, this paper deals with a molecular dynamic simulation in order to predict and optimize the erosion process before actual machining and to provide machining strategies.

2 LITERATURE REVIEW

Molecular dynamic (MD) simulation was initiated in the late 1950's by Alder and Wainwright. It is a technique to compute the equilibrium and transport properties of a classical many-body systems [2-3]. In principle, the MD simulation method is very simple. It can be started by identifying the position and velocity of all atoms in a system, which is simulated. During the simulation, a response of the material of workpiece and tool will be evaluated by following the motion of each atom. Given the simplicity of the MD simulation, the number of users and applications today remains limited. The reason is that it requires too much computation and time to solve practical problems so that its application to machining field is only of recent origin [4]. For example, in the late 1980's, a group at Lawrence Livermore National Lab had conducted pioneering studies on MD simulation of nanometric cutting of copper with diamond tool [4-6]. And later, two Japanese Professor Inamura and Shimada explored and extended the MD simulation of nanometric cutting to many practical mechanical machining [7-10]. Shimada studied two-dimensional nanometric cutting of copper with a diamond tool. He investigated the effect of edge radius and minimum depth of cut on the chip formation process, subsurface deformation and specific cutting energy in two cutting directions of the workpiece. Inamura studied the MD simulation under quasi-static conditions to analyze the nanoscale cutting. Other successful researches such as Komanduri reported the effect of tool geometry, crystal orientation and direction in nanometric cutting of single crystal aluminum [11]. Rentsch applied MD simulation to abrasive process study. He investigated pile up phenomenon in abrasive machining [12]. Following these advancements, we know that all of these efforts are focused on the traditional mechanical metal cutting, no research has been found on the topic of the EDM.

3 METHODOLOGY FOR MD SIMULATION OF EDM

3.1 Erosion Process Analysis

Due to the fact that the machining condition settings and the erosion phenomena encountered in the EDM die-sinking are highly complicated, the erosion process is divided into three phases from the molecular point of view. These three principal phases (Ignition phase, Heating & removal phase and De-ionization phase), in turn, consist of sub-phases.

3.1.1 Ignition Phase

The ignition phase consists of two sub-phases: pre-ignition and breakdown of electric. The pre-ignition phase covers the starting stage of a discharge duration. In this sub-phase, a voltage is applied between an electrode (anode) and a workpiece (cathode). The discharge duration begins, meanwhile the electrode is seeking the workpiece until a minimum gap distance is reached. As shown in Figure 1(a), an electric field is created in this sub-phase. As shown in Figure 1(b), at the beginning of the breakdown sub-phase, electrons start to be ejected from top layers of the workpiece caused by an effort of the electric field and heating. With an increase of the amount of these ejected electrons, an expanding column has been established within the electric field, illustrated in Figure 1(c). Figure 1(d) shows the motion of electrons. These ejected electrons with strong forward momentum are accelerated by the electric field. Their moving direction is towards the electrode. During the process of electrons travelling in the discharge gap, two

kinds of collisions happen between electrons and atoms of the dielectric: elastic and in-elastic collision. The elastic collision, which will influence the direction of motion of these electrons only, will not be discussed in this paper. The in-elastic collision, which will contribute to the erosion, is targeting in this research. Figure 1(e) describes the in-elastic collision process between electrons and dielectric atoms in detail. As a result of the in-elastic collision, atoms of dielectric are decomposed into free electrons and positively charged ions with the exchange of energy. During the breakdown sub-phase, thousands of this kind of collisions and decompositions have been taken place according to the setting of machining conditions, such as discharge current, open circuit voltage, etc. Later, these positively charged ions are accelerated by electric field and moved towards the workpiece (Figure 1(f)). At the end of this sub-phase, the dielectric is reaching its point of breakdown, and a plasma-state has been prepared.

3.1.2 Heating and Removal

The workpiece/tool heating and material particle removal are two sub-phases in this phase. When these accelerated ions reach the cathode along the direction of the electric field, the heating sub-phase is started. The positively charged ions strike the surface of the workpiece and spark occurs. Due to the heating and thermal conduction, particles of workpiece begin to be torn out. That is the sub-phase of material removal (Figure 2(a) and 2(b)). As shown in Figure 2(c) and 2(d), lots of electrons travel in the gap, and arrive at the anode. The action of collisions between electrons and atoms at the surface of electrode causes wear of the electrode. Finally, with the reaching of the end of discharge duration time, both eroded crater on the surface of the workpiece and wear on the electrode are created.

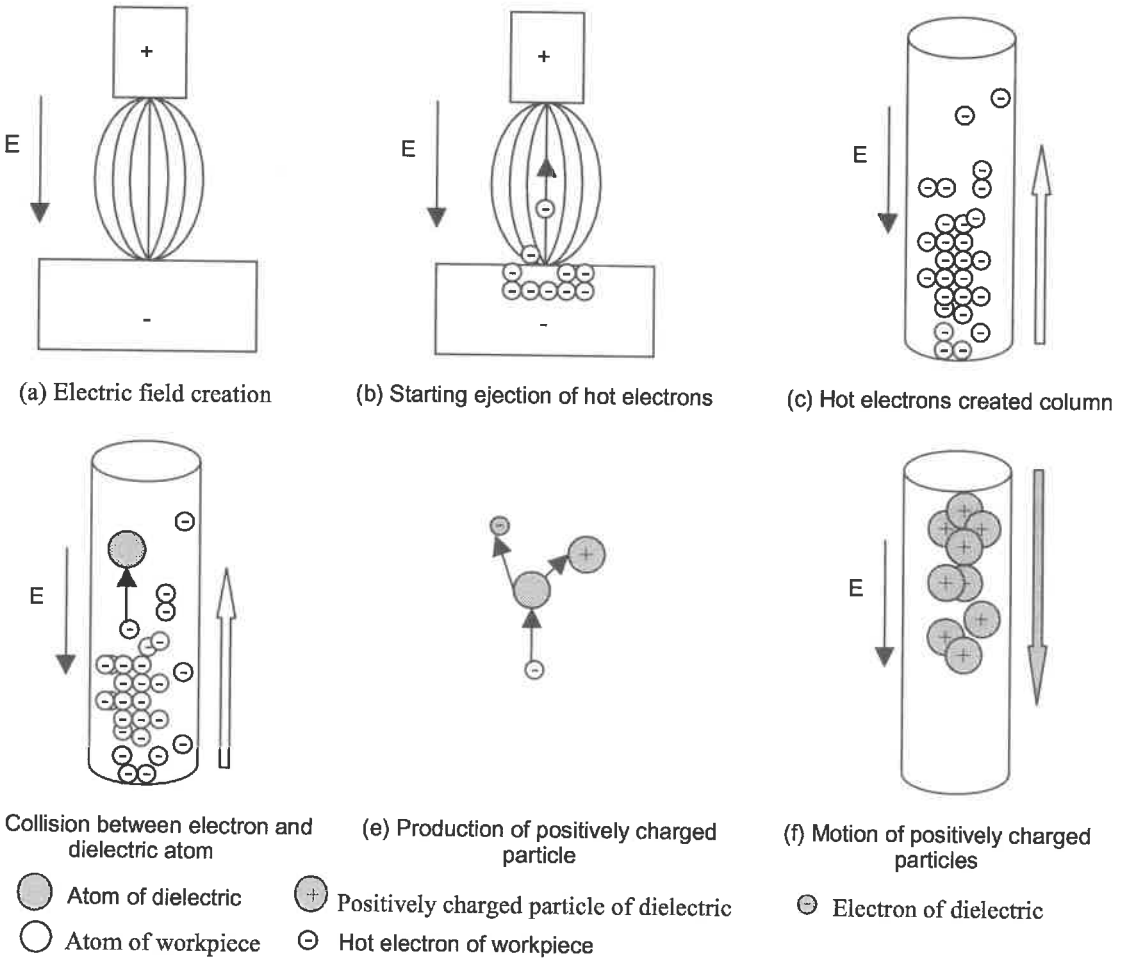

Figure 1: Ignition Phase

3.1.3 De-ionization Phase

The power is interrupted during pulse interval time. With the disappearance of the electric field, the motion of electrons and positively charged ions is slow down, the plasma channel collapses. The machining gap between workpiece and electrode is regenerated. The flowing electrons and ions will have a chance of re-combination. This is illustrated in Figure 2(e). The remaining particles within the discharge gap are taken away by the dielectric. The working conditions go to the pre-ignition sub-phase.

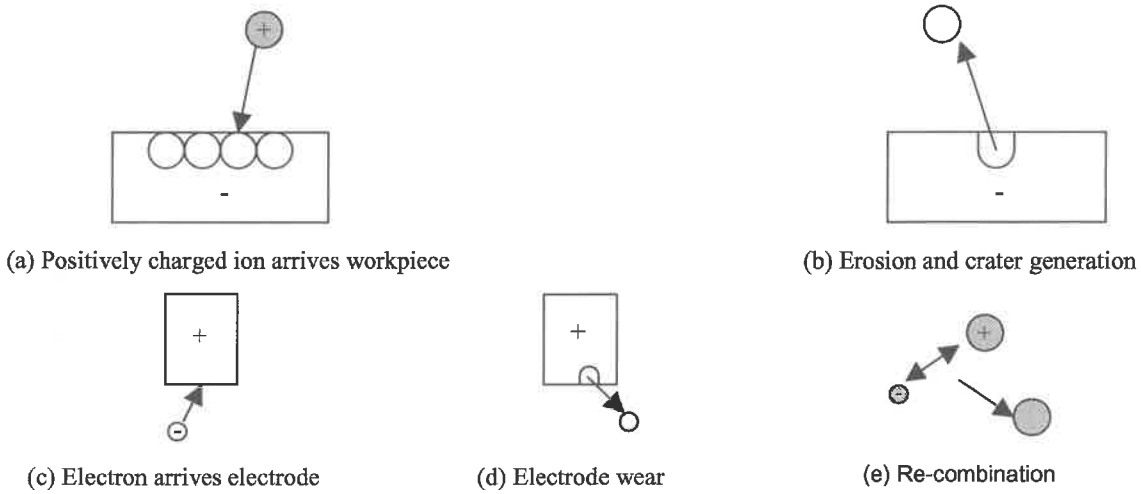
(a) Positively charged ion arrives workpiece
(b) Erosion and crater generation
(c) Electron arrives electrode
(d) Electrode wear
(e) Re-combination

Figure 2: Heating /Removal and De-ionization Phase

3.2 Simplified Cutting Model

In order to improve the calculation speed and reduce the simulation running time on virtual nano EDM simulation, a simplified erosion model is proposed as shown in figure 3. The workpiece, which is used for the purpose of virtual simulation, can be designed as thin as one layer of atom (0.25 nm), so that the 3D simulation can be simplified into 2D study (x-z plane), and only the Z direction motion of particles (electrons and ions) will be considered. Then, all of the vector mathematical equations will be simplified into one-dimensional calculation. Depth of the workpiece is 100 layers of atoms. The totally involved atoms in the workpiece side of simulation should be 10100. This is reasonable for the calculation and simulation running time using personal computer. Meanwhile, the effect of the electrode wear will not be considered.

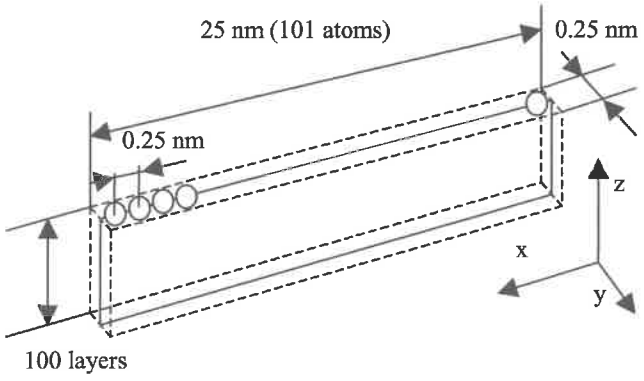

Figure 3: Simplified Cutting Model

4 SIMULATION RESULT AND DISCUSSION

In the following, the erosion process of the workpiece by single spark effect is presented. The single spark energy for this virtual erosion is designed for the removing of approximate five layers of atoms. Figures 4 (a) - (i) are the MD simulation plots of virtual linear motor equipped EDM erosion showing various stage at different number of the spark. The upper gray colored circles represent atoms of electrode, meanwhile atoms of the workpiece are described by black colored dots below. For example, figure 4 (a) is captured at the first spark, for the 10^{th} spark it is shown in figure 4 (c), etc. The animation was conducted using our developed simulation software, which is running on the PC workstation. In these figures, the position of the electrode is kept as a constant for the purpose of reference.

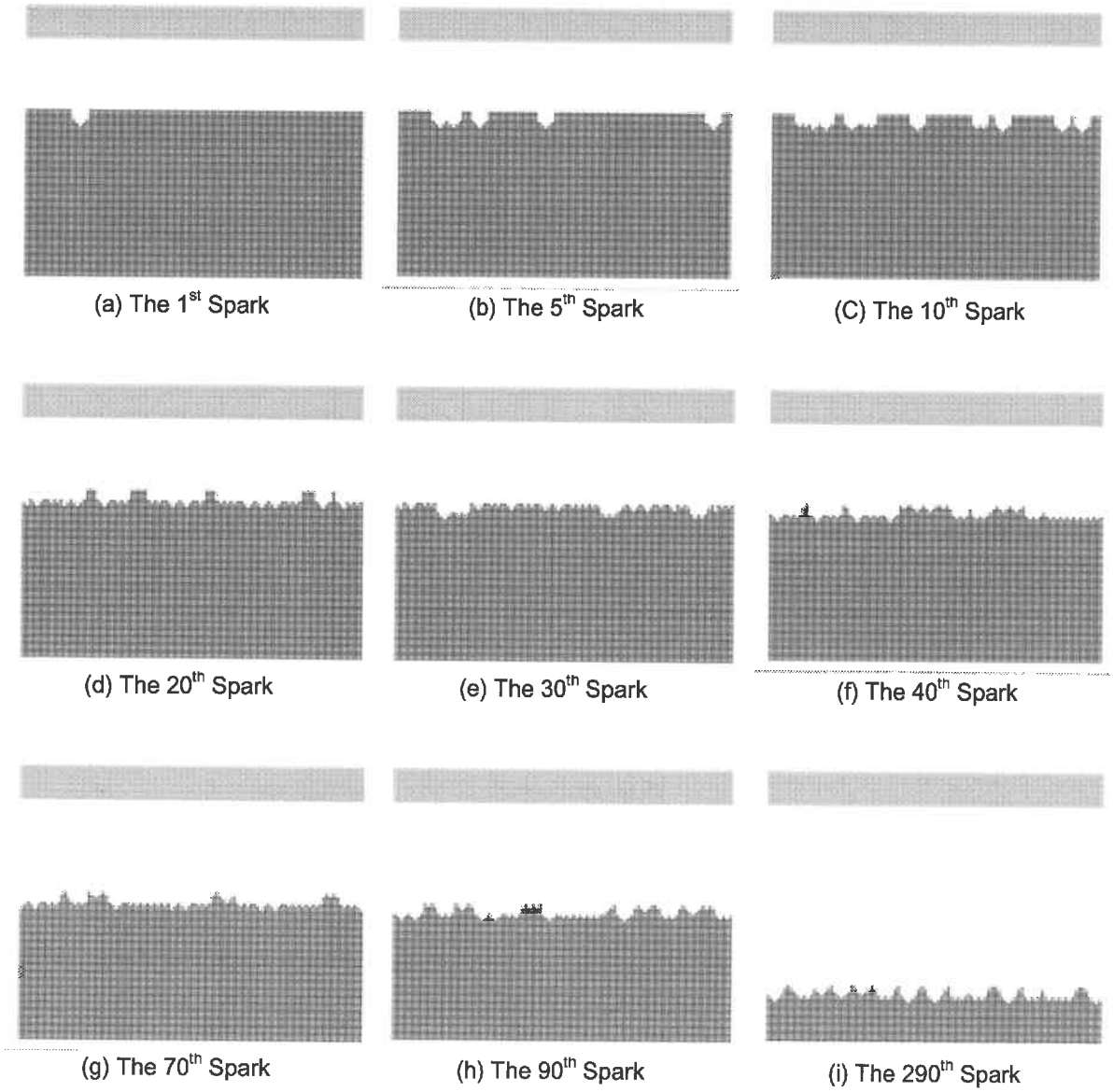
(a) The 1st Spark
(b) The 5th Spark
(C) The 10th Spark
(d) The 20th Spark
(e) The 30th Spark
(f) The 40th Spark
(g) The 70th Spark
(h) The 90th Spark
(i) The 290th Spark

Figure 4: Simulation Results

5 CONCULSIONS

This paper describes Molecular Dynamics analysis and simulation for linear motor equipped EDM. At current stage, the following conclusions are obtained:

- MD method has been introduced into EDM study;
- Linear motor equipped EDM erosion process has been analyzed from molecular point of view;
- A virtual nano simulation software for EDM has been developed;
- Based on the simplified cutting model, an initial simulation is achieved.

ACKNOWLEDGEMENT

The authors wish to express their sincere appreciation for the generous support of Sodick Co., Ltd. to make the research possible.

REFERENCE

1. Y.S. Zhao, K. Yamazaki, X.Q. Zhang, 2002, Geometrical Analysis and Simulation of Linear Motor Equipped EDM Die-Sinking Process by Single Spark Algorithm, 2002 Japan-USA Symposium on Flexible Automation, July 2002, Hiroshima, Japan.
2. B. Alder, T. Wainwright, 1959, Studies in Molecular Dynamics: I General Method, J. Chem. Phys. 31(2).
3. B. Alder, T. Wainwright, 1960, Studies in Molecular Dynamics: II Behavior of a Small Number of Elastic Sphere, J. Chem. Phys. 33(5).
4. J. Belak, 1994, Nanotribology: Modeling Atoms When Surfaces Collide, E&TR August.
5. I.F. Stowers, J. Belak, D.B. Boercker, 1993, Molecular Dynamics Simulation of Copper and Silicon Machining, International Conference on Machining of Advanced Materials, Gaithersburg, MD.
6. J. Belak, I.F. Stowers, 1992, Molecular Dynamics Modeling of the Mechanical Properties of Metal Surfaces at the Nanometer Scale, International Conference on Metallurgy Coatings and Thin Films, San Diego, CA.
7. T. Inamura, 1993, Mechanics and Engergy Dissipation in Nanoscale Cutting, Annals of the CIRP, Vol. 42/1.
8. S. Shimada, et al., 1992, Molecular Dynamics Analysis as Compared with Experimental Results of Micromachining, Annals of the CIRP, Vol. 41/1.
9. T. Inamura, et al., 1992, Atomic-Scale Cutting in a Computer Using Crystal Models of Copper and Diamond, Annals of the CIRP, Vol. 41/1.
10. S. Shimada, et al., 1994, Structure of Micromachined Surface Simulated by Molecular Dynamics Analysis, Annals of the CIRP, Vol. 43/1.
11. R. Komanduri, 2000, MD Simulation of Nanometric Cutting of Single Crystal Aluminum-Effect of Cystal Orientation and Direction of Cutting, Wear 242 (2000).
12. R. Rentsch, 1994, Molecular Dynamics Simulation for Abrasive Processes, Annals of the CIRP, Vol. 43/1.
13. R. Papoular, 1964, Electrical Phenomena in Gases.
14. D. Frenkel, B.Smit, 1996, Understanding Molecular Simulation – From Algorithms to Applications.
15. S.Wilson, G.H.F. Diercksen, 1997, Problem Solving in Computational Molecular Science – Molecular in Different Environments.
16. A.J. Walton, 1982, Three Phases of Matter.

CHARGING OF CAST IRON WITH ABRASIVE DURING LAPPING

Adam W. Barylski
Gdansk University of Technology, Gdansk, Poland

1. Introduction

The method of dosaging abrasive slurry or abrasive compound has an essential effect on the efficiency and quality of lapping [4-6]. Besides the unbound method of abrasive charging the lapping tool, where abrasive slurry is delivered as drops or the abrasive compound is laid on the lapping active face during the process, a new surface treatment with lapping tools force charged with abradents is developed. This technology has found, above all, a use for in very precise lapping. This surface treatment is characterized by a comparatively low efficiency and a small roughness of the lapped surface.

The charging process is usually done manually, with the use of a hardened disk or roller. First of all, after the cleaning of the active lapping face, the abrasive compound (e.g. diamond paste) is spread on it. Next the grains are pressed in manually with the use of a roller. This operation should be done a few times, in different directions, after which the active face should be additionally rolled with a steel disk or a sintered carbide disk. This action takes only over a dozen of seconds. The above allows to even-out the protrusions of the micrograins pressed into the lapping tool face. Directly before using the charged lapping tool it should be shower - washed and dried.

The manual charging can be applied to a single - disk lapper, for which the tool is rotated. The charging time is relatively long. The efficiency and the quality of the charging is not very high, due to the difficulties of the uniformly distribution of the abradent micrograins (Fig.1). An additional problem is that the compression of the charging elements is not constant, which causes differences in the micrograin penetration of the lapping tool face. From some time, research has been done about machine surface charging. Introducing a mechanical drive should eliminate the fundamental faults of the manual charging.

2. Technique and the kinematic of the fotced charging

The device presented on Figure 2 is composed of three arms (1-3) spaced every 120° and fixed to the lapping machines auxiliary table. The diameter of the lapping disk (5) which rotates is 900 mm. The arms (1-3) are spaced between the conditioning rings (4). A conical rubber roller (7) (Fig.3), provided for distributing the abrasive micrograins on the disk surface, is mounted on arm (1). Roller (7) is pressed to the lapping tool by a press bolt (9), and is lifted by springs (9). Strips (11) with conical charging rollers (6) in angle bearings are fixed to the other arms. Arm (11) with charging rollers (6) is lifted by springs (10), whereas the working load is exerted by a pneumatic servo-motor (16). To the arm (2) is fixed a movable strip (12) with a abradent storage bin (13). The abradent dosage, through the feeding pipe (14), is regulated by a regulating screw (15). After finishing the abrasive charging, the conical rollers (6) as well as the roller distributing the abradent (7), cannot be in contact with disk surface (5). Economical dosaging of the abradents has an essential meaning, especially in the case of super-hard abradents, which are expensive materials. The use of conical charging rollers eliminates the phenomenon of slipping between the roller and the disk, whereas the pneumatical pressing reduces the uniformity of the micrograin load. The proposed constructional solution gives a base for automation of such a type of lapping technology.

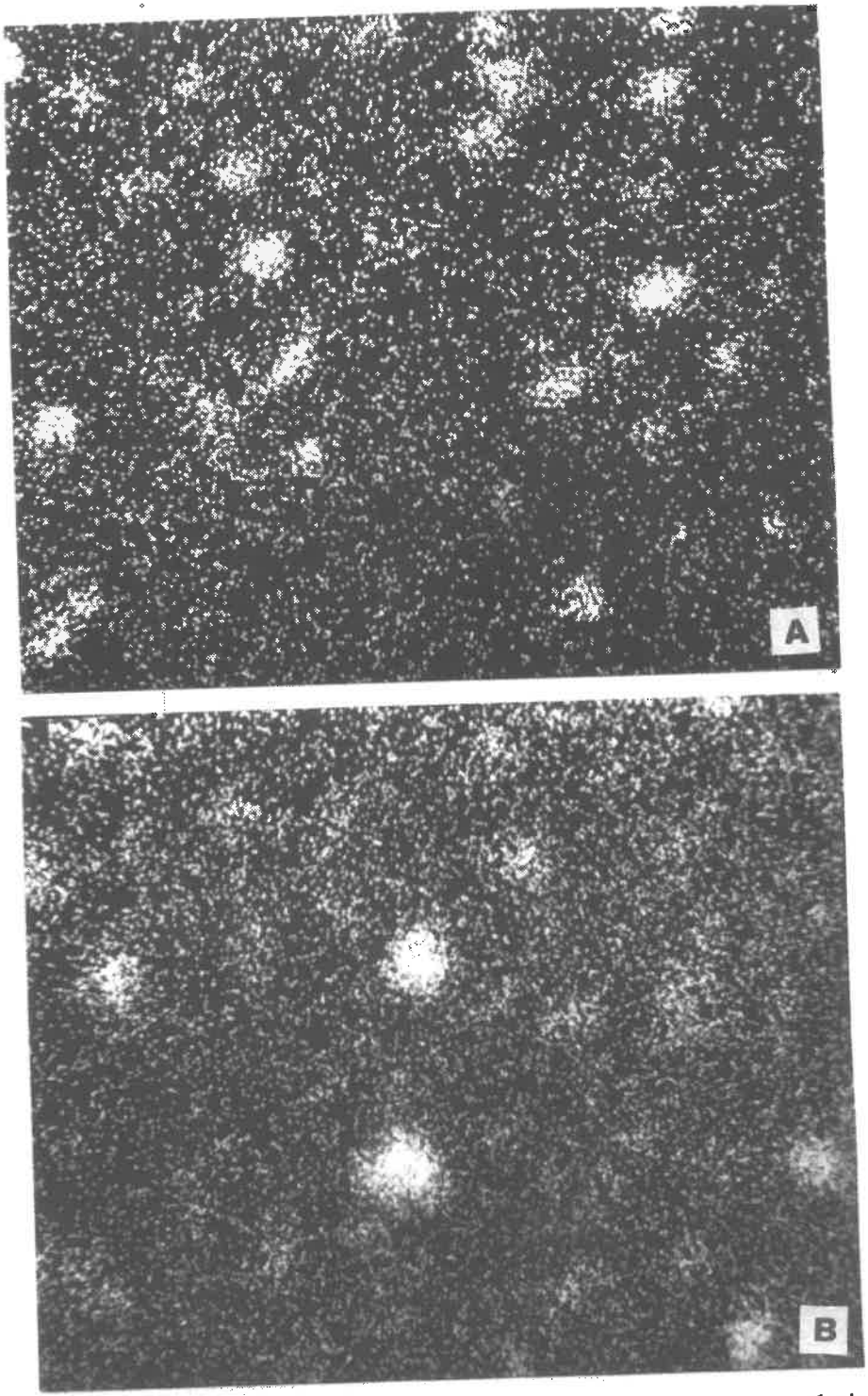

Fig.1. Microphotograph of Z_s50007 cast iron lapping tool: a) analysis I, b) analysis II; approximately 2000x (SiK_α , U=25kV)

2. Research of the forced charging

An evaluation of the charging quality was carried out on a lapping disk, which active area was equal to 84.82 cm^2. The research variable factors were the unit pressure p_z = 156.5 - 310.5 N/m, mean velocity v = 0.036 - 0.068 m/s and the charging time t_z = 60 - 240 s. The necessary amount of tests and the range of the tested factors change of value were determined during the preliminary tests. The disk surface was observed on a scanning electron microscope.

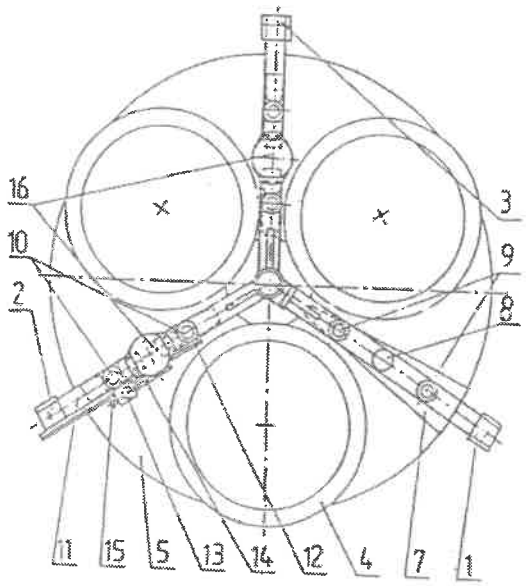

Fig.2. General top view of the productive version of the device for abrasive charging of the lapping tool surface

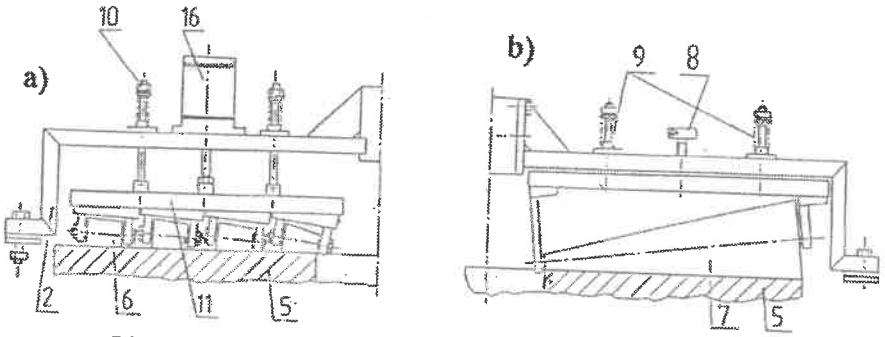

Fig.3. Conical roller assembly for lapping tool charging (a) and the position of the abrasive micrograin distributiong rubber roller (b)

The size of the micrograins embedded in the surface of the lapping tool decreased when the roller unit pressure and the charging time increase and so, for the charging of a Z_S50007 cast iron lapping tool with silicon carbide micrograins (99C) 320 was received z = 20 - 26 μm (p_z = 256.5 N/m, t_z = 180 s, v = 0.059 m/s), and by using 99C of a number 800 the following was observed z = 2 - 6 μm (p_z = 256.5 N/m, t_z = 300 s, v = 0.059 m/s).

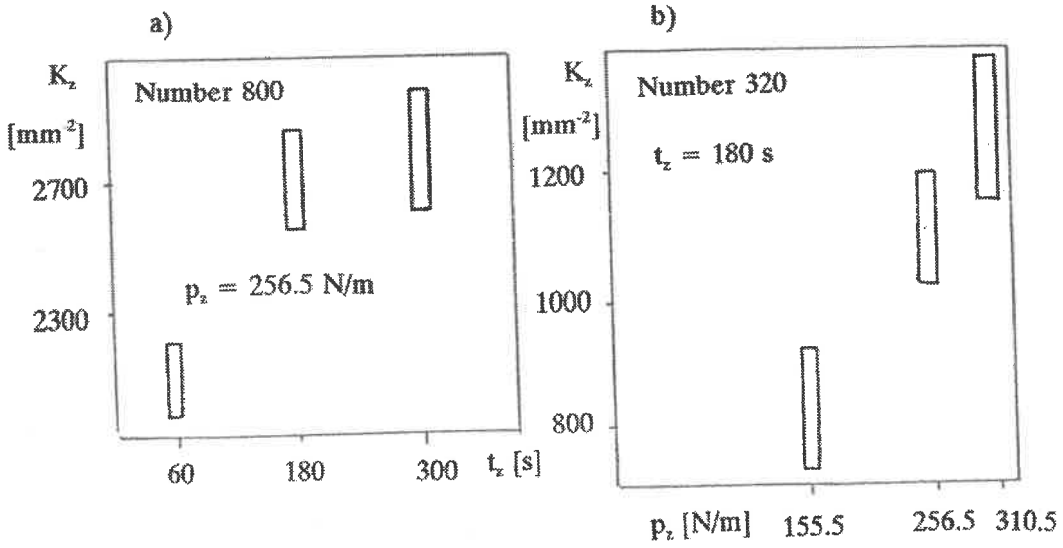

Fig.4. Concentration K_z of the micrograins which have penetrated into the Z_s50007 cast iron tool surface: a) the influence of the charging time t_z, b) the influence of charging force p_z

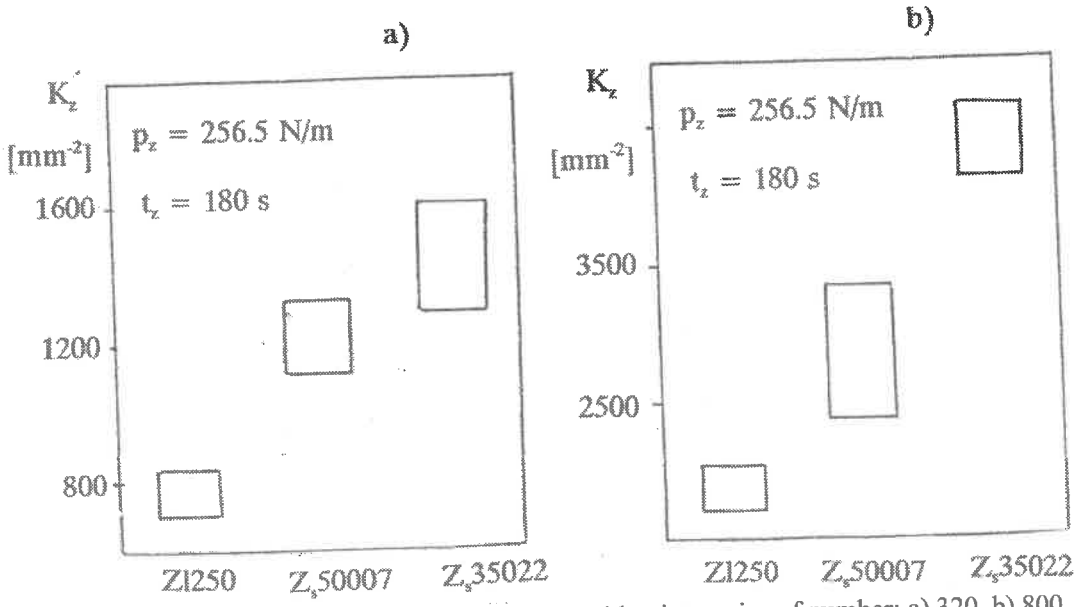

Fig.5. Intensity of cast iron lapping tool charging with micrograins of number: a) 320, b) 800

Figure 4 presents the influence of the pressure and the charging time on the amount of micrograins embedded in the surface of the Z_s50007 cast iron lapping tool, and on Figure 5 the influence of the micrograin number on the intensivity of the abrasive charging of grey cast iron. The highest intensity

was received for the Z_s35022 cast iron. The concentration of micrograins increased together with the increase of the charging time from t_z=180 to 300 s caused a minimum increase.

4. Conclusions

The carried out research shows [1-3] that in the case of large differences between the abradent grain size and the size of the cast iron graphite intrusions, there can be a simultaneous penetration of a few micrograins into the graphite. Other than charging the graphite there is also an intensive penetration into the cast iron metallic matrix, into the ferrite as well as the pearlite. A relatively high intensity of penetration of larger sized micrograins on the borders of graphite intrusions and in the ferrite halo were observed. An experiment was carried out to determine the empirical probability of the 800 micrograin (silicon carbide: expected value E(Z) = 6.81 μm, standard deviation D(Z) = 4.08 μm) penetration into the Z_s55003 cast iron graphite intrusions. The n_g X-ray patterns were analyzed, concerning the silicon lay-out, FeK_α and SiK_α, on the cast iron surface after t = 135 s (conditions for unbounded abradent charging: p = 0.19 MPa, v = 0.40 m/s). The experimental sample size n_g was specified on the basis of the preliminary test. According to research results, the empirical probability of the abradent penetration into the graphite amounts to P = 0.0814. Because the amount of graphite sections on one unit area amounts to $N_A = 98\ mm^{-2}$, therefore we can assume that on the area of 1 mm^2 there shall be 8 graphite intrusions penetrated by abrasive grains.

5. References

1. Barylski A.: Contamination of graphite with abrasive during lapping of cast iron. Stud. i Mater. Gorz. Osr. Bad. i Ekspertyz Nauk., 1985, Ref. T.IV, 1-2, 303-316 (Polish).
2. Barylski A.: Fundamentals of flat surface lapping with single-disk. Zesz. Nauk. P.Gdan., 1992, 491, 3-196 (Polish).
3. Barylski A.: Surface contamination of cast iron after lapping. Lubrication Engineering. 1996, 1, 63-67.
4. Barylski A.: Theoretical and experimental fundaments of flat surface lapping on disk lapping machine. Proceedings of the 7th Iternational Precision Engineering Seminar, Kobe, 1993, Suppl., 1-15.
5. Jascericyn P.I., Zajcev A.G., Barbotko A.I.: Tonkije dovodocnyje processy obrabotki detalej masin i proborov. Minsk, Nauka i Technika, 1976.
6. Ulegin V.G., Ogorodnikov A.P.: Fiziceskaja suscnost sarzirovanija. Almazy, 1973, 12, 10 –16.

Development of a Lapping Film Utilizing Agglomerative Fine Abrasives for Finishing of Optical Glass

Toshiyuki ENOMOTO [1] and Jun ZHANG [2]

[1] Institute of Industrial Science, The University of Tokyo, 4-6-1 Komaba, Meguro-ku, Tokyo, 153-8505 JAPAN
[2] Ricoh Company, Ltd., 1005 Shimo-Ogino, Atsugi-shi, Kanagawa, 243-0298 JAPAN
Tel&Fax: +81-3-5452-6602, E-mail: enomoto@iis.u-tokyo.ac.jp

Abstract

In the finishing process of optical glass, polishing with ceria, silica or zirconia slurry is conventionally adopted. The machining process, however, has problems involving inefficiency and a detrimental impact on the environment. Therefore, it is strongly recommended that the process be replaced with fixed-abrasive machining, but conventional fixed-abrasive tools have problems relating to low finishing efficiency or low finished-surface quality. In this study, a lapping film utilizing agglomerative superfine zirconia abrasives is introduced to overcome the above-mentioned problems. The finishing experiments revealed that the surface quality obtained was as good as that obtained by polishing with ceria slurry, while the finishing efficiency was much higher.

Key Words : Polishing, Fixed-abrasive machining, Lapping film, Optical glass, Agglomerative abrasive, Zirconia abrasive

1. Introduction

Loose-abrasive machining with ceria, silica or zirconia slurry is traditionally employed for finishing optical glass. However, the following major problems are associated with the process.

- low form accuracy of the workpiece due to deformation of the polishing pad
- low finishing efficiency
- high cost of slurry and polishing pad
- detrimental impact on the environment (i.e., dirty working environment and slurry disposal)

Therefore, it is strongly recommended that loose-abrasive machining be replaced with fixed-abrasive machining. However, conventional fixed-abrasive tools such as grinding stones and lapping films have problems involving low finishing efficiency or low finished-surface quality. In the case of a fixed-abrasive tool with large abrasives, the finishing efficiency is high, but the finished surface is rough. In contrast, the use of a tool with fine or superfine abrasives results in high surface quality but low finishing efficiency.

In this study, a lapping film utilizing agglomerative superfine abrasives [1] is introduced for finishing optical glass to overcome the above-mentioned problems, that is, to achieve both high finishing efficiency and high-quality surface finish. Furthermore, the composition of the lapping film and the finishing conditions are also discussed for the improvement of the finishing performance.

2. Problems associated with a lapping film utilizing conventional abrasives

2.1 Experimental procedure

Two types of lapping films with conventional abrasives were prepared, as shown in Table 1. Ceria, silica, iron oxide and zirconia powders are known to be abrasives suitable for polishing glass. In this experiment, zirconia was adopted because it is easy to obtain in various sizes.

Finishing experiments on optical glass (BK7) were carried out in a lapping machine of Lapmaster-type, with the lapping films pasted onto the lap plate. Table 2 lists the finishing conditions. The surface roughness

Table 1 Symbols for lapping films using conventional zirconia abrasive

Symbol	Mean diameter of abrasive
LZ	60 μm
SZ	0.5 μm
Abrasive content	30 area%
Binding resin	Polyurethane
Backing material	Polyethylene terephthalate (thickness: 75 μm)

Table 2 Finishing conditions

Workpiece	Φ 12 Optical glass (BK7) 3 pieces
Finishing pressure	46 kPa
Rotation of film	60 rpm
Rotation of workpiece	36 rpm
Finishing time	5 min
Finishing fluid	Pure water
Supply rate	0.9 mL/min

of the workpiece was adjusted to 2 μm Ry before finishing.

2.2 Experimental results and discussion

Figures 1 (a) – (c) show the workpiece surfaces and the surface profiles before and after finishing. A large amount of swarf was discharged when finishing with LZ, and as a result, many cracks were generated (Figure 1 (b), material removal rate: 7.5 μm/min). While in the case of using SZ, the roughness peaks were removed, but the pre-finished surface remained (Figure 1 (c), material removal rate: 10 nm/min).

From the above results, it could be deduced as following.

- The surface of a lapping film with 60 μm abrasives was so rough that the effective cutting edge density turned low, making the force on the cutting edge high. As a result, the finishing efficiency was high, while the finished surface was rough.
- The surface of a lapping film with fine abrasives was so smooth that the effective cutting edge density was high and then the force on the cutting edge was low. Thus, the surface roughness could only be improved limitedly because of extremely low efficiency.

To overcome the above-mentioned problems, that is, to achieve both high finishing efficiency and high-quality surface finish, we introduced agglomerated powders with superfine zirconia particles as the abrasives.

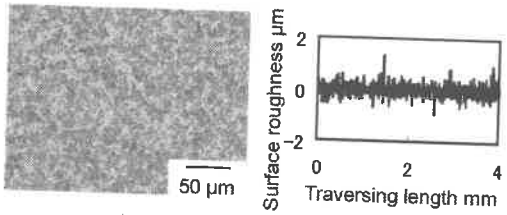

(a) Before finishing (2 μm Ry)

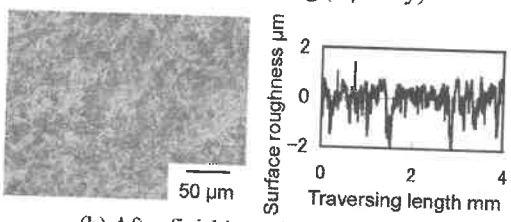

(b) After finishing with LZ (2.8 μm Ry)

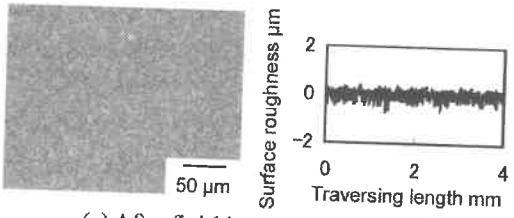

(c) After finishing with SZ (1.2 μm Ry)

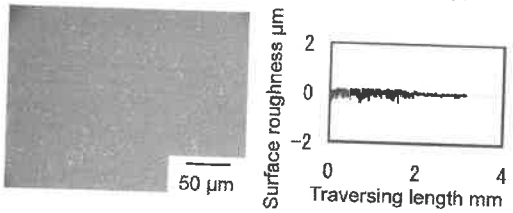

(d) After finishing with AZ-1 (0.7 μm Ry)

Figure 1 Surface of optical glass before and after finishing

3. Finishing performance of lapping film utilizing agglomerative superfine zirconia abrasive

The abrasive powder (mean diameter: 60 μm), in which zirconia superfine particles (mean diameter: 70 nm) were agglomerated, was used in the newly developed lapping film (symbol: AZ-1). The conceptual model of finishing with the lapping film is depicted in Figure 2. The finishing characteristics of the lapping film are considered to be as follows.

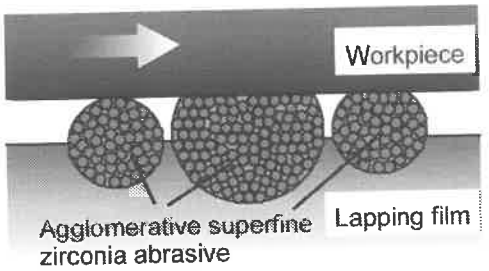

Figure 2 Conceptual model of finishing with the developed lapping film

- At the beginning of the process, the surface of the lapping film is rough. Therefore the effective cutting edge density is low, resulting in a high force acting on the edge. This improves the efficiency.
- In the final stage, the agglomerative abrasives are worn uniformly flat, thus the grain depth of cut becomes extremely small, and results in a fine surface finish.

A finishing experiment was carried out with the newly developed lapping film under the same conditions as those listed in Table 2. It was found that some improvement of the finishing performance was achieved (Figure 1 (d)). Although the finished surface roughness was finished to 0.7 μm Ry, the pre-finished surface still partly remained at this time (see Figure 1 (d)). Eventually, a mirror-finished surface (surface roughness: 35 nm Ry) was generated after an additional 15 minutes of continuous finishing.

To clarify the reason for the unexpectedly low efficiency (finishing efficiency: 0.13 μm/min), observation of the lapping film was carried out. As shown in Figure 3, although agglomerative abrasives were truncated in the way as expected according to the above-mentioned finishing model, the wear of abrasive was considerable. From this result, it could be considered that the low cutting point pressure, which stemmed from the low agglomerative strength among the primary superfine particles, caused the low finishing efficiency. Consequently, agglomerative strength optimization could be important in an effort to raise the finishing efficiency.

Three types of lapping films including AZ-1 were investigated, as shown in Table 3. Here, tensile

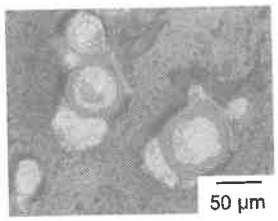

Figure 3 Top view of lapping film AZ-1 after 5 minutes of finishing

Table 3 Symbols for lapping films using agglomerative zirconia abrasive

Symbol	Tensile strength of abrasive
AZ-1	15 MPa
AZ-2	30 MPa
AZ-3	67 MPa

* Strength of abrasive of LZ : 326 MPa

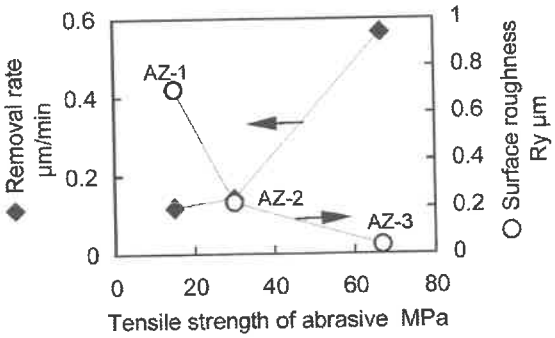

Figure 4 Relationships between material removal rate, finished surface roughness and tensile strength of abrasive

strength of the powder under compress-to-fracture testing was evaluated as a substitute for the agglomerative strength itself.

Figure 4 shows the effect of the tensile strength of the abrasives on finishing efficiency and finished surface roughness. The results indicate that the higher the agglomerative strength, the higher the finishing efficiency and the better the surface roughness. As shown in Figure 5, a scratch-free surface could be obtained by using lapping film AZ-3. In contrast, the finishing efficiency in the other lapping films was so low that the pre-finished surface could not be removed completely, and then resulted in rough surface. Furthermore, the abrasive wear of lapping film AZ-3

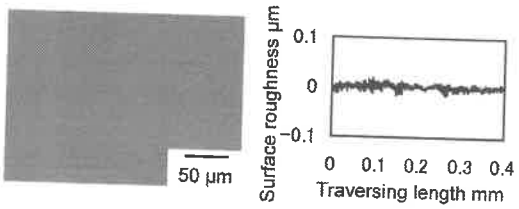

Figure 5 Surface of optical glass after finishing with AZ-3 (38 nm Ry)

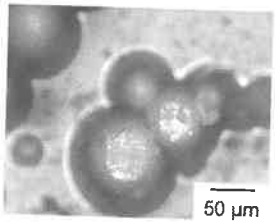

Figure 6 Top view of lapping film AZ-3 after 5 minutes of finishing

was also observed. From Figure 6, it was clearly shown that agglomerative abrasives were truncated in the same way, but the wear was small as compared with that of lapping film AZ-1.

Hence, it was suggested that the high wear resistance of agglomerative abrasives brings high cutting point pressure, which leads to high finishing efficiency.

Moreover, it was expected that the finishing efficiency could be improved with faster rotation of the plate, because the relative length of motion between abrasives and the workpiece in a certain amount of time would be lengthened. For comparison with the film lapping, polishing with ceria (mean diameter: 1.8 μm) slurry and a polishing pad (urethane foam containing ceria) was also carried out in the same manner as the conventional finishing method. The finishing conditions were basically the same as those listed in Table 2.

Figure 7 shows the effect of the rotation of the plate on finishing efficiency and finished surface roughness. In the case of film lapping, the finishing efficiency increased about twofold, namely 1.11 μm/min, due to the doubled rotation speed. In contrast, in the case of polishing, the finishing efficiency increased slightly. The reason for this is considered to be that the relative length of motion between abrasives and the workpiece would maintain almost the same due to the low holding strength of abrasives on the polishing pad. As for the finished surface quality, a scratch-free surface (surface roughness: about 35 nm Ry) was obtained, regardless of the finishing method or rotation speed.

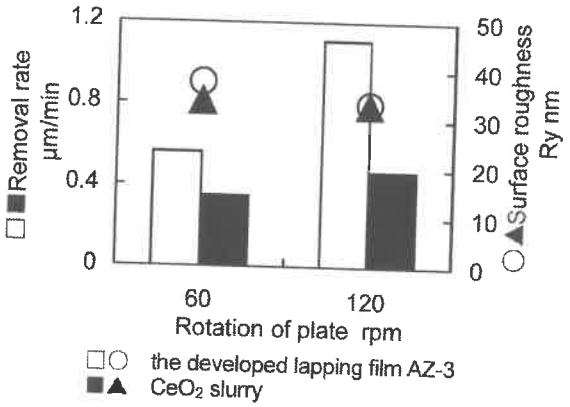

Figure 7 Relationships between material removal rate, finished surface roughness and rotation of plate

4. Conclusion

A lapping film utilizing agglomerative superfine zirconia particles as abrasive was developed for finishing optical glass BK7. It was clarified that the surface quality obtained was as good as that obtained by polishing and the finishing efficiency was much higher.

Acknowledgments

The authors thank Professor Y. Tani of the University of Tokyo for his kind suggestions and discussion.

Reference

[1] T. Enomoto, Y. Tani and K. Orii. Development of a lapping film utilizing agglomerative superfine silica abrasives for edge finishing of a silicon wafer. Proceedings of 10th International Conference on Precision Engineering 2001; 391-395.

Application of Fixed Abrasive Pad using Hydrophilic Polymer in STI CMP

[a]Hoyoun Kim, [a]Boumyoung Park, [a]Haedo Jeong, [b]David A. Dornfeld, [c]Sangick Lee
[a]Department of Precision Mechanical Engineering, Pusan National University, Pusan, Korea
[b]Mechanical Engineering Department, University of California at Berkeley, Berkeley, CA
[c]Memory Research Development Division, Hynix Semiconductor, Ichon, Korea

1. Introduction

DRAM has many cells consisting of one capacitance and one CMOS [1]. It is necessary for each cell to be isolated electrically for the independent work. The shallow trench isolation (STI) structure has been widely adopted on chip fabrications for the isolation of each cell [2,3]. It is made as filling a trench with dielectric materials. After deposition process for the filling of the trench, a residual film on the active region is removed by .the chemical mechanical polishing (CMP) [4]. The STI CMP, however, involves several issues such as trench dishing, oxide erosion and oxide rounding. For the reduction of dishing, even though the reverse etch mask technology has been introduced, it takes a disadvantage of increasing the step of process. Silicon nitride as the stop layer has been used to reduce dishing in CMP, because the silicon nitride has a high material selectivity against other materials. The dishing can be reduced as etching silicon nitride after the STI CMP. It takes an advantage from the viewpoint of the simplicity of process. In this paper, the fixed abrasive pad using hydrophilic polymers is introduced for the improvement of the pattern selectivity in STI CMP.

2. Deviation of pattern selectivity

Patterns with different density on the die have significantly an influence on the results of CMP. Fig. 1 shows the pattern profiles after CMP, and it indicates that the step height is a sensitive function of pattern densities.

Fig.2 shows the mechanism of over-polishing. This sensitivity of the pattern density causes the local region within a die to be over-polished. Consequently, it is one of reasons that expand regions for dishing to be generated. To reduce the effect of pattern density, the semiconductor design uses dummy patterns which are not concerned with the electrical operation. These dummy patterns, however, have a limit due to the

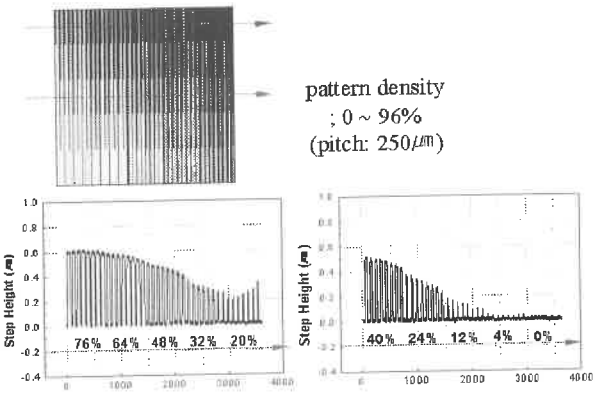

Fig. 1 Pattern profile as a function of pattern density

sacrificial capacitance. If the CMP results are independent on the pattern density, the over-polished regions will be able to be reduced, and defects such as dishing, erosion and rounding can be also reduced. In order to solve these issues, this paper introduces the effect of abrasives, pressure and relative velocity on the pattern selectivity.

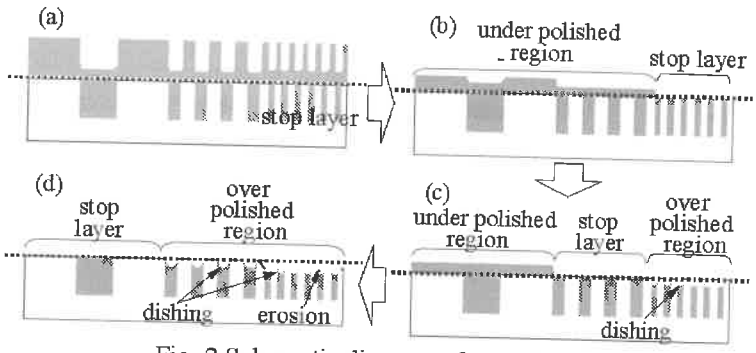

Fig. 2 Schematic diagram of over-polishing

The selectivity is generally classified as the material and pattern selectivity. The material selectivity is defined as the ratio of the removal rate of other materials to that of the specific material. For example, if the removal rate of TEOS is 3000Å/min and that of Si_3N_4 is 300Å/min, the material selectivity between two materials is 10:1.

The purpose of CMP is that the patterns on a wafer are removed to be flat, but the space between patterns is also removed during CMP. The pattern selectivity has been defined as the ratio of the removal rate at pattern to that at space between patterns. The pattern selectivity is 60:1 when the removal rate is 3000Å/min at the pattern and that is 50Å at the space. However, it is difficult to evaluate the pattern selectivity of entire die, because the die consists of regions having different densities. Therefore, this paper reports the deviation of pattern selectivity (DPS) for the evaluation on the pattern selectivity in the STI CMP. The DPS is defined as follows. The pattern selectivity is, first, defined as the ratio that it is the step height of the patterns at each density to that of the patterns at the highest density or the widest pitch within a die [eq 1]. The region with the highest density is used as the reference, because the removal rate is reduced as increasing of the density. That is to say, the DPS says how the results of the polished patterns within a die are deviated from the reference [eq. 2]. If the density is not influence on the CMP, the step height will be the same regardless of the pattern density, and the DPS shows zero. Consequently, as the DPS increases, the pattern density has a higher effect on the result of the CMP.

$$\text{P.S.} = \frac{\text{R.H. at each pattern density}}{\text{R.H. at the highest pattern density}} \qquad [1]$$

$$\text{DPS} = \frac{\Sigma\,(1-(\text{P.S.})_i)^2}{N} \qquad [2]$$

($(P.S)_i$.: pattern selectivity at each region, R.H.: relative height, N: number of regions)

3. Characteristics of pattern selectivity

It is necessary to consider the pattern selectivity to evaluate on the CMP parameters such as abrasives, pressure, relative velocity. To evaluate the effect of the pattern selectivity on abrasives, the concentration of cerium oxide abrasive is varied from 0.5 to 2.0 wt%, and the silicon oxide abrasive from 4 to 13 wt%. The pressure is fixed as 300 g/cm^2 and the relative velocity is 30/30 rpm. The polishing time is controlled to be the same total removal volume as each experimental condition makes difference on the removal rate.

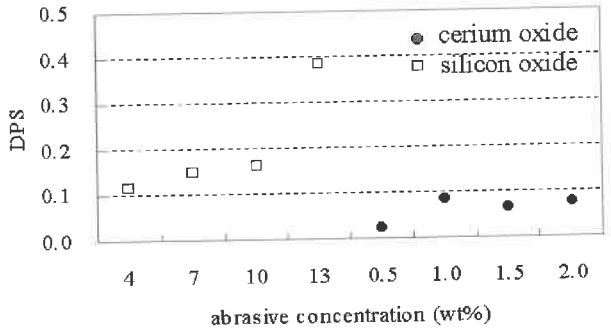

Fig. 3 Results of DPS as a function of abrasive concentration

Fig. 3 shows that the cerium abrasive has a better characteristic in terms of the pattern selectivity than the silicon oxide abrasive, and the DPS reduces as decreasing of the abrasive concentration. These results explain that more abrasives give worse influence on the pattern selectivity. This fact is also explained from the results as a function of the relative velocity (Fig.4). All experimental conditions including the concentration of abrasives are the same, and the relative velocity is only varied. As a result, the DPS increase as the relative velocity goes up. It is explained that the dynamic motion of abrasives gives a bad influence on the pattern selectivity. If the concentration of abrasives could be decreased without the reduction of the removal rate, over-polished regions within a die can be decreased.

The CMP process requires that the polishing pad should be conditioned to create sufficient surface roughness. The decay of the removal rate in the absence of conditioning is well known. The polishing pressure is changed to consider the relationship between the pattern selectivity and the contact area of the asperity on the pad. The contact area of the asperity on a pad will be expanded as the polishing pressure goes up. The polishing pad is conditioned with the electroplated diamond disk to be the same asperity. Fig. 5 shows the results of DPS as a function of the polishing pressure. The DPS is shown the highest when the pressure is 650 g/cm^2. Therefore, the asperity on a polishing pad has an effect on the pattern selectivity. It is expected to improve the characteristic of pattern sensitivity as reducing the abrasives in slurry and the asperity on a polishing pad.

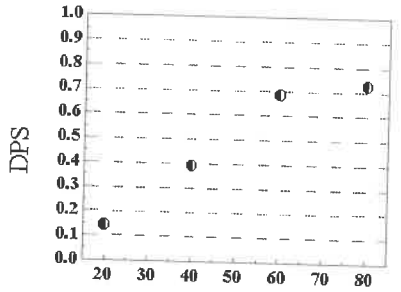

Fig. 4 Results of DPS as a function of relative velocity

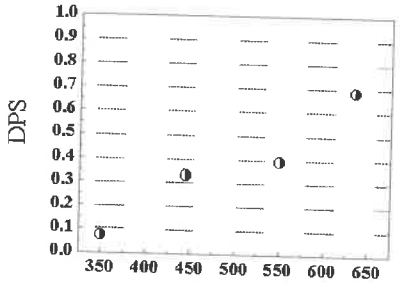

Fig. 5 Results of DPS as a function of polishing pressure

4. Fixed abrasive pad using hydrophilic polymer

The fixed abrasive pad using hydrophilic polymers is manufactured, and the cerium oxide abrasive is adopted because it has the high removal rate at the low concentration [8]. In the fixed abrasive pad, the special conditioning concept is needed to supply new abrasives to the wafer surface. It is very important to improve wafer-to-wafer non-uniformity between wafers. According to researches on the fixed abrasive pad, patterns on wafer play as diamond grits in regenerating new surface of pad. New abrasives can emerge from the surface of a fixed abrasive pad through this conditioning mechanism [5,6]. However, this conditioning using the patterns may have its limitations because the patterns are polished during CMP. This paper introduces the fixed abrasive pad using hydrophilic polymers with the swelling characteristic for the self-conditioning. The swelling mechanism is as follows. The hydrophilic polymers have hydrophilic radicals such as hydroxyl(-OH), carboxyl(-COOH), carbonyl group(-CO) etc [7]. When the hydrophilic polymers are in contact with an aquatic solution, the hydrophilic radicals along polymer chain attract water. Then, the polymer chain expands due to the permeation of water, and expanded polymers are easily removed by the friction force between a pad and a wafer (Fig. 6).

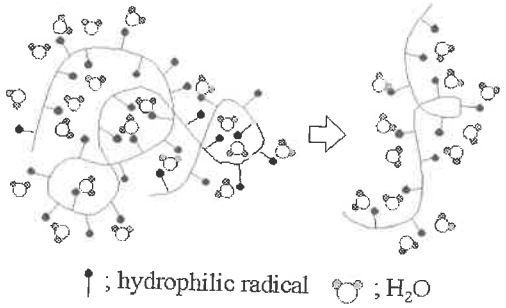

Fig. 6 Swelling mechanism of hydrophilic polymer

The manufactured fixed abrasive pad is performed on the visco-elastic behavior (Fig. 7). The

characteristic of the visco-elastic is very important for the repeatability between wafers. As a result, the visco-elastic curve of the fixed abrasive pad moves down about 1 um comparing with the polyurethane pad, about 4 um. It means that the visco-elastic characteristic is improved due to the harder polycarbonate film.

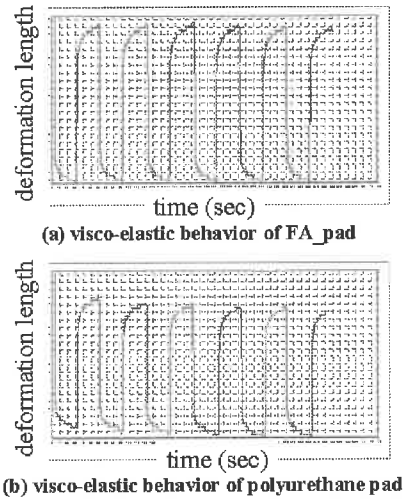

Fig. 7 Visco-elastic behavior of fixed abrasive pad comparing with polyurethane pad

5. Pattern selectivity of fixed abrasive pad

To evaluate on the fixed abrasive pad, the STI wafers designed by MIT are applied, which consists of patterns with different pitches and densities. The experiments are carried out on a rotary CMP machine, as given in Table 1.

Table 1. Experimental Condition

	FA_pad	Conventional CMP
Pressure	300 g/㎠	300 g/㎠
Relative velocity	60 / 60 rpm	60 / 60 rpm
Pad	FA_pad	IC1400™
Slurry	DI water	Fumed silica (13wt%, pH10.8)
Conditioning	Brush	diamond disk

Fig. 8 shows the results of the step height as a function of the density. The step heights of polished patterns are randomly distributed in the conventional CMP comparing with that of the fixed abrasive pad. The DPS in the conventional CMP is 0.185 larger three times than that in the fixed abrasive. Especially, in

the regions with the density of 30% and 50%, the step height in the conventional CMP is so different even though the regions have the same pattern density. These results are due to the effect of surrounding patterns, but not in the fixed abrasive pad.

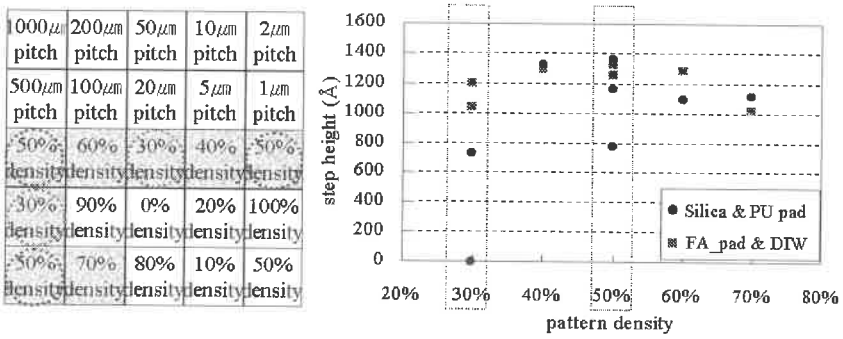

Fig.8 Results of step height as a function of pattern density in STI CMP

6. Conclusion

The pattern selectivity is sensitive to the density of patterns. For the effect of the pattern selectivity, experiments are performed changing the CMP parameters such as abrasives, pressure and relative velocity. It is known that the abrasives in slurry and the asperity on a polishing pad have a bad influence on the pattern sensitivity. To improve the pattern selectivity, the fixed abrasive pad using hydrophilic polymers is manufactured, and then is applied to the STI CMP. As a result, the DPS in the conventional CMP is 0.185, and 0.061 in the fixed abrasive. The patterns have little effect on the surrounding patterns in the fixed abrasive pad. The fixed abrasive pad apparently allows the pattern selectivity to improve for the reduction of dishing.

Reference

[1] S.R.Wilson et al,, Handbook of Multilevel Metallization for Integrated Circuits, Noyes Publications, New Jersey, 1993, p. 97.

[2] L.M.Cook, J. Non-Crystalline Solids, 120 (1990) 152.

[3] W.J.Patrick et.al., J. Electrochem. Soc., 138 (1991) 1778.

[4] K.Smekalin et al., J. Electrochem. Soc., 143 (1996) L281.

[5] V.Koinkar et al, Proc. 5th International CMP -MIC, Santa Clara, U.S.A., March, (2000) 58.

[6] A.Römer et al., Proc. 5th International CMP-MIC, Santa Clara, U.S.A., March, (2000) 265.

[7] L.H.Sperling, Introduction to Physical Polymer Science, John Wiley & Sons, INC., New-York, 1992.

[8] M.Baudin, M.Wojcik, K.Hermansson, Surface Science, 468 (2000) 51.

GENERATION OF QUALITY SURFACE IN EXTRUDE HONING

K. Narayanasamy, H.P.Raju
PEIL, Department of Mechanical Engineering
Indian Institute of Technology Madras, Chennai-600 036 India
E-mail: kns@iitm.ac.in

1.0 INTRODUCTION

Surface is a boundary that separates an object from another object or substance; it is either in contact with some other surface or will be open to atmosphere. Hence the surface quality assumes greater importance for proper functioning of any product with due importance to aesthetic aspect also. This necessitates production of required surface texture to perform a specific function. Now a days surfaces are being engineered to suit end application (1-2). Processes like traditional honing, lapping, grinding can be used to regular shapes. But for lapping, a flexible process, others being rigid in nature, are of little/no use to finish machining of irregular intricate shapes or contours like turbine blades. This has led to the development of a flexible abrasive process called Extrude honing (EH) process.

Extrude honing is relatively a new non traditional machining process used to finish, deburr, radius, polish, remove recast layer and to produce compressive residual surfacial stresses. This process removes material in small quantities by forcing abrasive laden viscoelastic polymeric material normally known as medium, which is the best candidate for finishing internal passages or holes which are inaccessible by any other processes (3-4).

Finishing of I.C.Engine manifolds, hydraulic components, and bio medical components are few areas of application. It is an alternative environmental friendly process for removal of protective aluminium nickel coating applied to certain turbine engine blades. Removal of sharp corners enhances the edge quality. It is a proven, reliable and accurate method that provides consistent results(5). Abrasive laden medium can be thought of as a flowing flexible grinding wheel. The irregular cutting edge geometry of abrasive grits and extremely small chips produced in this process makes it possible to concentrate the machining stress at very local points on the work. It is this ability which makes finishing of difficult to machine material possible. Large number of cutting edges with indefinite orientation and geometry makes the failure of any grits insignificant and does not affect the overall process performance(6). Medium being a proprietary item, is not easily available. In view of this, present study on extrude honing is concerned with an alternative medium for abrasive carrier, its performance and consequent surface texture production in extrude honing.

2.0 EXPERIMENTAL

Owing to their higher impact resistance and higher order fatigue life, SG Cast irons are very popular material in many applications. Considering the cost efficiency, SG Cast iron of grade 600 is selected as

work material. Apart from rheological properties better grit retention, bond uniformity, and higher abrasive exposure are few properties a material required to posses for satisfactory performance as a carrier medium. A select grade of silicone polymeric medium is thoroughly mixed with a volume fraction of 25% SiC abrasives of 36 grit size using a polymer mixing device. An experimental set-up was designed and developed to implement extrude honing process. Details of work material, carrier medium, process parameter used in the trials are presented in Table1.

Table1. Details of work material, carrier medium, process parameter

Work material		Carrier medium		Process parameter	
SG Cast Iron		Silicone polymer			
Carbon (%)	3.61	Appearance	Translucent	Temperature	Ambient
Tensile Strength (N/mm^2)	614	Density (kg/m^3)	$1.13X10^3$	Volume fraction	0.25
0.2% Proof Stress (N/mm^2)	372	Viscosity(Pa.s)	20250	Velocity (m/min)	0.4.0.6,1.0,1.2

3.0 RESULTS AND DISCUSSION

3.1 Surface roughness

Typical observed parametric influence of surface characteristics of extrude honed SG Cast Iron bored specimen is illustrated in Fig.1. It is seen that there is a visible / drastic reduction in R_t, R_a values during early phase of honing, followed by progressive reduction with number of passes.Removal of waviness/dominant asperities present over the bored surface during early phase of extrude honing results in appreciable reduction in R_t, R_a values.

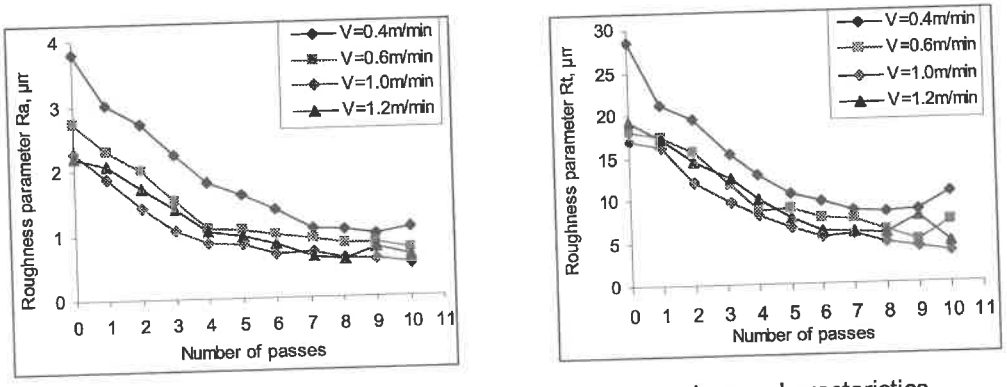

Fig.1. Typical observed parametrical influence of surface roughness characteristics

3.2 Bearing area characteristics

A surface texture can be better defined by referring to its bearing area fraction characteristics; a study on bearing area characteristics will bring about typical characteristics of a surface texture in terms of its core roughness, depth of profile allowing for crest flattening and valley fill up. It is observed from pass wise monitored individual profile (Fig.2) that, with progressive honing crest flattening gets saturated, there after improvement in core roughness, followed by change in valley depth.

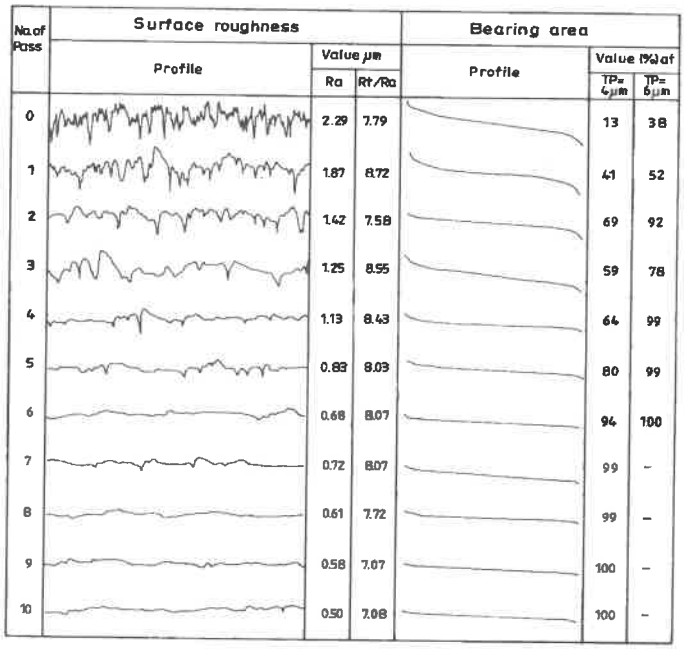

Fig.2. Typical observed profiles of surface roughness and bearing area fraction

3.3 Acoustic emission signal

On-line monitoring of acoustic emission signal using a broad band acoustic emission sensor presented mixed mode of emission during early phase indicating waviness correction/crest flattening. With subsequent passes a steady rise in rms value of the monitored acoustic emission signal as well as predominant peaks over lower frequency range 50-100 kHz were observed (Fig.3) indicative of progressive honing. In subsequent passes, a reduction in rms value as well as low power high frequency peaks were observed, indicative of glazing associated with localised spalling of material.

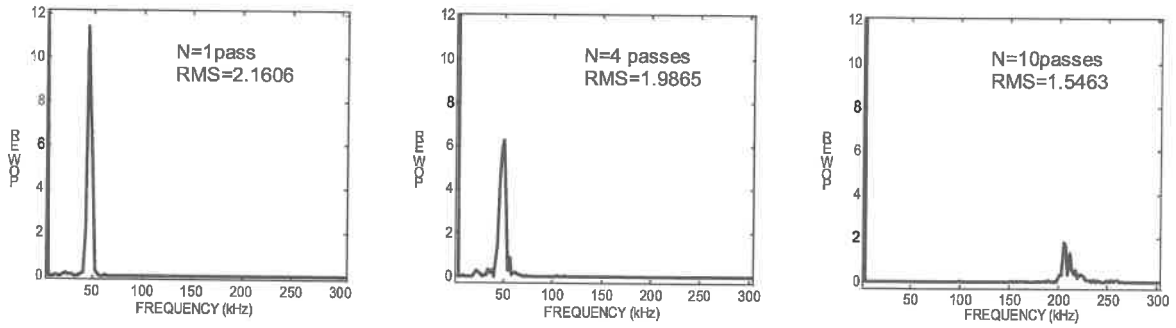

Fig.3 Typical power spectrum at different stages of stages of extrude honing

3.4 Residual stress induced

Measurement of residual stress on honed surface indicates tensile residual stress during early phase of honing, followed by compressive mode, with progressive honing and subsequent glazing (Fig.4). Impart of compressive residual stress on the surface results in enhanced fatigue life of the component.

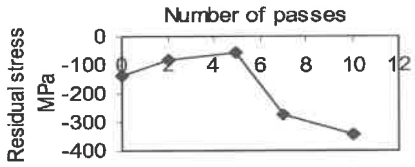

Fig. 4 Residual stress induced at the surface during extrude honing.

3.5 Scanning electron macrographs

For better understanding of the nature of texture produced by extrude honing, surfaces as bored and as honed were observed (Fig.5) through scanning electron microscope.

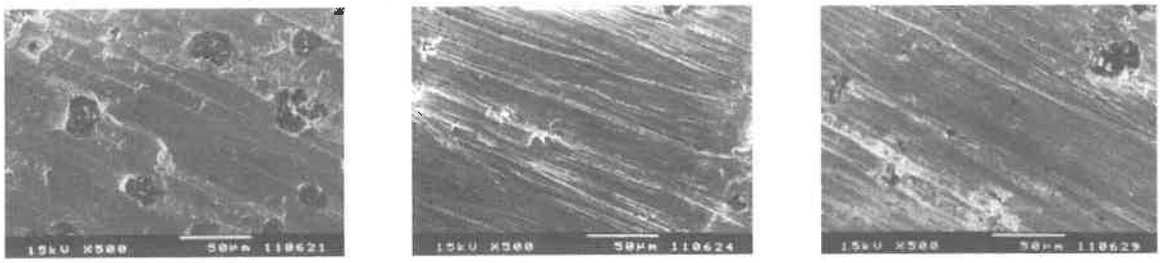

(a) as bored (b) after 5 passes (c) after 10 passes

Fig.5 Scanning electron macrographs of surface at different stages of extrude honing

After extrusion honing fairly uniform lay pattern with localised folding of asperity can be seen. Further, due to continuous honing, surface has experienced localised discrete glazed texture.

4.0 CONCLUSION

The major conclusions drawn based on the trials conducted are as follows.

1. A progressive improvement in surface roughness parameter and bearing area fraction is seen till eighth pass, beyond which the surface starts deteriorating.
2. Higher order residual compressive stresses induced on the surface with number of passes.
3. With the increased surface finish, characteristics of acoustic emission spectrum changes, this can be used for on line monitoring of the process.

5.0 REFERENCES

1. Chris J. Evans., James B. Bryan., "Structured", "Textured" or "Engineered" Surfaces Annals of the CIRP, Vol. 48/2/1999 541-556
2. A.R.Jones., J.B.Hull., "Ultrasonic flow polishing", Ultrasonics , 36 (1998) 97-101
3. L J.Rhoades., H. A.Clouser., "Abrasive Flow Machining", ASM Metals Handbook,16 (1989) 514-519
4. R.E. Williams, K.P.Rajurkar, "Stochastic Modeling and of Analysis of Abrasive Flow Machining", Trans.ASME. Journal of Engineering for Industry 144 (1992) 74-81
5. J. Matechen, John., "Advantages of abrasive flow machining", Abrasives, (1995) 20-21
6. I.Inasaki, H.K.Tonshoff, T.D.Howes, "Abrasive Machining in the Future", Annals of the CIRP, Vol. 42/2/1993 723-732

New development of combined electrochemical processes for mirror-like micro grooves

Jeong-Woo Park*, Eun-Sang Lee**, Young-Hun Moon***

* Graduate School of Mechanical Engineering Division, Pusan National University, Busan, Korea

** Mechanical Engineering Division, Inha University, Incheon, Korea

*** Mechanical Engineering Division, Pusan National University, Busan, Korea

Abstract

Pulse electrochemical machining process both with high current density and low current density may produce a non-lustrous surface on workpiece surface. The usual polishing process to remove a black layer from the surface has been hand polish the part. But the milli-to-micro meter scale structure formed by the electrochemical machining process may be destroyed while polishing process. The application of ultra short voltage pulses based on the analysis of electrical double layer charging process allows high resolution electrochemical machining and polishing. This technique was based on the specific polarization resistance from the comparison of ideal and experimental potential variation during short voltage pulses.

Key words: Pulse electrochemical machining/polishing, Electrical double layer, Specific polarization resistance

1. Introduction

Some investigators who have tried to achieve the highly smooth surface finish using electrochemical processes have reported that high current density produced lustrous surfaces while the opposite conditions produced a passive layer and had a tendency to produce a black surface. However, processing at a low current density may produce a non-lustrous surface but the improvement of dimensional accuracy of the surface is significant. It was found in previous study that the control of the machining depth with pulse electrical current is easier than continuous electrical current [1]. And it was also found that micro grooves within 20 micrometers in depth could be produced using electrochemical micro-machining (EMM) process with pulse current. The surface with pulse process was a bit more lustrous than with continuous current but the black passive layer still could be found at grooved surface. There are two ways to achieve highly smooth surface finish. One is brushing it with a brush, the other is electrochemical machining (ECM) with high current. The former method is the most common polishing practice, but not only may the surface obtained differ from operator to operator, but precision smooth surface on micro grooves are difficult to

obtain. The latter one recently has been used to produce a highly smooth surface after EDM process. However, the material removal rate in ECM with high current is relatively high. Hence the original shape of the micro grooves, which was formed by EMM process, may be destroyed.

In this study, an electrochemical polishing (ECP) process using pulse current is adopted as a possible alternative process when micro grooves, formed by EMM with pulse process, should be polished. This study will discuss the accurate control of physical and electrical conditions so as to achieve mirror-like micro grooves with lustrous and smooth surface without destroying the original shape of micro grooves.

2. Equivalent Electric Circuit Analysis in Electrochemical System

The concept of our method is based on a charging of electrical double layer (DL) where an electronic charge of electrode stands face to face with an ionic charge of solution. When an electrode is placed in an electrolyte solution, an equilibrium potential difference and the charging of DL usually become established between the electrode and solution. This potential difference arises from the transfer into solution of anodic metal ions and the simultaneous discharge of ions from the solution. Hence, these sequential charging and discharging of DL can be analyzed as a capacitor model when the short voltage pulses are applied. The electrical DL is composed of a compact DL (CDL), which covers from inner Helmholtz plane (IHP) to outer Helmholtz plane (OHP), and a diffuse DL (DDL), which covers the bulk electrolyte as shown in Fig. 1 [2].

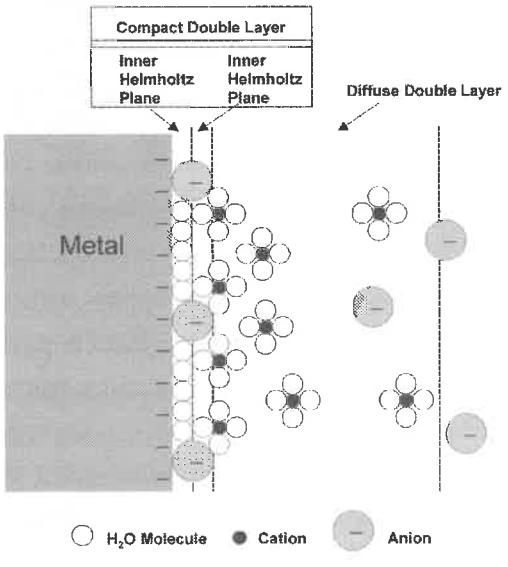

Fig. 1 The Electrical Double Layer

From the capacitor analysis, a time constant τ is defined as

$$\tau = RC = \rho d c_{DL} \qquad (1)$$

This time-constant of electrochemical system can be a criterion how fast the reaction occurs. The machining resolution d is proportional to the time constant τ,

because the specific resistance ρ, a factor defined by the electrolyte, and the electrical DL capacity c_{DL}, defined by the summation of c_{CDL} and c_{DDL}, are constant. Electrochemical system, where

electrodes are in close proximity, can be remodeled as a R-C equivalent electric system with capacitor behavior as shown in Fig. 2.

Two capacitors, c_{CDL} and c_{DDL}, are connected in series circuit in the Helmholtz DL. The net capacitance has the value of 10~20μF/cm^2, because the summation of different two capacitors with different capacitances approximates to the capacitor with small capacitance. The electrolyte resistance is classified into two independent resistances.

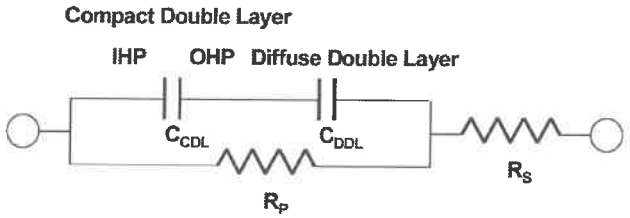

Fig. 2 Electrochemical Equivalent Circuit between Electrode and Electrolyte

One is polarization resistance (R_p) connected to net capacitor in a parallel circuit in Helmholtz DL. If the R_p and c_{DL} are connected in series circuit, direct current cannot pass through the electrochemical system [3]. Hence the electrochemical reaction with direct current is impossible. The other is electrolyte solution resistance (R_s) connected to the R_p - c_{DL} system in series circuit. But the resistance to analyze the time-constant (equation 1) is the polarization resistance. However, the resistance measured by a resistance tester shows not the electrolyte resistance but the combined impedance including capacitances. Hence, it is inadequate that regarding the value measured by the resistance tester as a polarization resistance that is used in analyzing the electrochemical system related to capacitor. To obtain approximate polarization resistance in electrochemical polishing of the micro grooves, the new method of comparison of ideal and experimental potential variations, indicating charging and discharging of electrical DL, is applied in this study.

3. Machining Resolution Analysis in Pulse Electrochemical Machining

The electrochemical reaction can occur with sufficient electrical charge in DL, when the pulse duration over time-constant is applied. This is understandable only for the static condition of electrolyte solution. As mentioned equation (1), τ is dependent on the ρ, d and c_{DL}. To specify this relation, Fig. 3 is plotted. In Fig. 3, the experimental machining resolution [(final width-tool width)/2-electrode distance], resulting after machining time of 1 min, is plotted for different pulse durations and 3.5M $NaNO_3$ with specific electrolyte resistance of 62.5Ω·cm and DL capacitance of 18μF/cm^2. Especially, the electrolyte solution is circulated with 1m/s velocity to flush the generated heat and gas away. Even though Rolf Schuster and Viola Kirchner showed the experimental results

are in agreement with the prediction in static $HClO_4$ and $CuSO_4$ solution [4], the experimental resolution has a tendency to be lower, according to the increment of the pulse duration, than the prediction in this study. When the pulse voltage is applied between the electrodes, the charging in the electrolyte and the starting of current flow occur through the movement of ion charge. Hence, the lower experimental resolution than prediction in this study is owing to the disturbance of the movement of ion charge by the forced electrolyte circulation.

Fig. 4 shows the anode surface micrograph resulting after EMM. In pulse width below 13μsec, the width of grooves is smaller than the pattern width of cathode tool about 100μm for lack of charging ions between the electrodes, the boundaries between treated and untreated metal are nevertheless distinct. In pulse width within 13μsec ~ 20μsec, the width of grooves is in agreement with the pattern width of cathode tool and the boundaries are distinct.

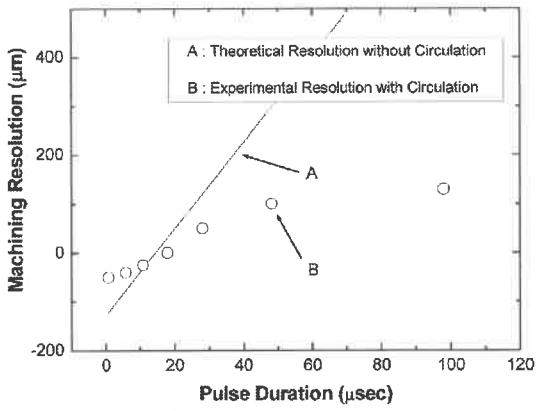

Fig. 3 Machining Resolution in Pulse ECM

In pulse width over 20μsec, the width of grooves is bigger than the pattern width of cathode tool about 100μm ~ 200μm for excessive charging ions, the boundaries between treated and untreated metal are vague compared to above conditions.

4. Pulse Electrochemical Polishing

Upon a single potential pulse voltage is applied the electrodes, the charging current is generated between electrolyte solution and electrode because of the abrupt potential difference. The charging current is equal to the capacity of DL by differential rate of voltage, $I = CdE/dt$, so the high differential rate of voltage brings about high current charging. If the charge of capacitor is zero at t = 0, the potential variation of charging and discharging of DL capacity is defined as

$$E = E_0(1 - e^{-\frac{t}{RC}}), \text{ for charging DL capacity} \quad (2)$$

$$E = E_0 e^{-\frac{t}{RC}}, \text{ for discharging DL capacity} \quad (3)$$

From above equations (2) and (3), the instantaneous potential variations of charging and discharging of DL capacity are plotted in Fig. 5 (a) according to various specific polarization resistances (ρ_p). In Fig. 5, A, B, C and D are simulations of potential variations of single pulse voltage (a) for ρ_p=74.0, 35.0, 14.8 and 3.7 Ω·cm respectively. The specific polarization resistance, ρ_p and net capacitance, c_{DL} are constant, when a certain electrolyte solution is chosen. The pulse width is plotted to 200μsec to compare with the experimental results.

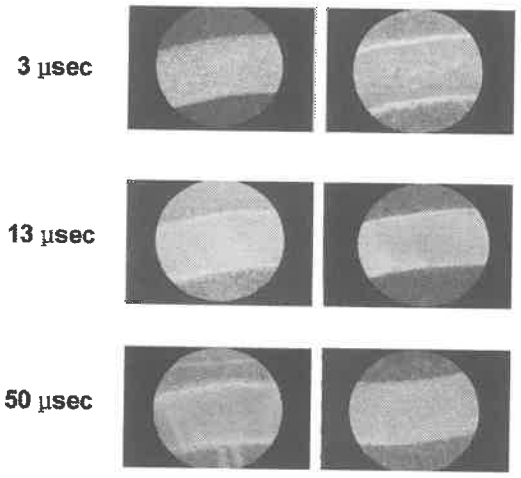

Fig. 4 Groove Patterns with Various Pulse Durations. Bright part shows electrochemically-machined groove and dark part shows untreated metal surface. In 3.5M $NaNO_3$ solution with 4.0V for 1 min.

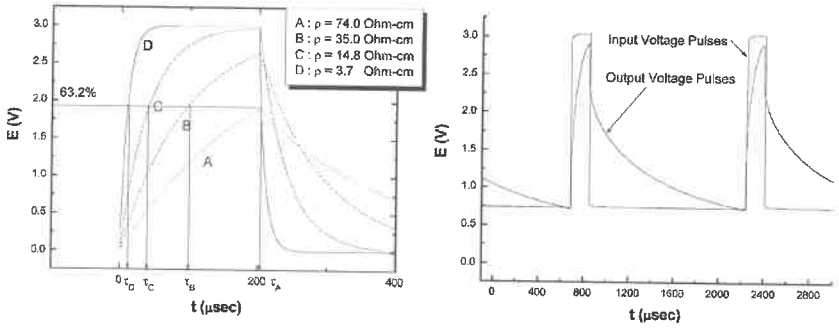

(a) (b)

Fig. 5 Potential Variation of Charging and Discharging of DL capacity. A, B, C and D are simulations of potential variations of single pulse voltage (a) for ρ_p=74.0, 35.0, 14.8 and 3.7 Ω·cm respectively. Experimental potential variation for 2.4M H_2SO_4 and 5.9M H_3PO_4 electrolyte, and 1cm^2 of electrode area (b).

For A, B, C and D in Fig. 5, the time-constants are defined 200, 94.5, 40 and 10μsec respectively. In case of A, if the voltage pulse of 200μsec-pulse width is applied, this pulse width is close to the time-constant. From experimental result, resulting after a polishing time of 10min, there is no polishing effect on metal surface even though the potential variation signal represents the charging and discharging of DL capacity. Hence, the experimental application of pulse width of the same as the time-constant is found to be inadequate. For more sufficient electrochemical reaction, series of pulse width over time-constant should be applied like B, C and D as shown in Fig. 5. Fig. 5 (b)

shows the experimental potential variation for 2.4M H_2SO_4 and 5.9M H_3PO_4 electrolyte, and $1cm^2$ of electrode area. The result is in agreement with the simulation, but does not represent the 'ideal' charging and discharging of DL capacity. From comparison Fig. 5 (a) with (b), ρ_p, representing the closest charging and discharging variation, can be obtained. A value of 14.8Ω·cm is the closest ρ_p for this electrolyte, so the time-constant is defined as 50μsec. Therefore the pulse width over 50μsec should be applied for more electrochemical reaction.

5. Conclusion

From the machining resolution analysis, the experimental resolution becomes lower than prediction owing to the disturbance of the movement of ion charge by the forced electrolyte circulation. To obtain approximate polarization resistance in electrochemical polishing of micro grooves, the new method of comparison of ideal and experimental potential variations, indicating charging and discharging of electrical DL, is applied in this study. The experimental potential variation for 2.4M H_2SO_4 and 5.9M H_3PO_4 electrolyte is in close agreement with the simulation with ρ_p of 14.8Ω·cm, so the time-constant is defined as 50μsec. Therefore the pulse width over 50μsec should be applied for more electrochemical reaction. From this result, some applications with pulse electrochemical process are shown in Fig. 6.

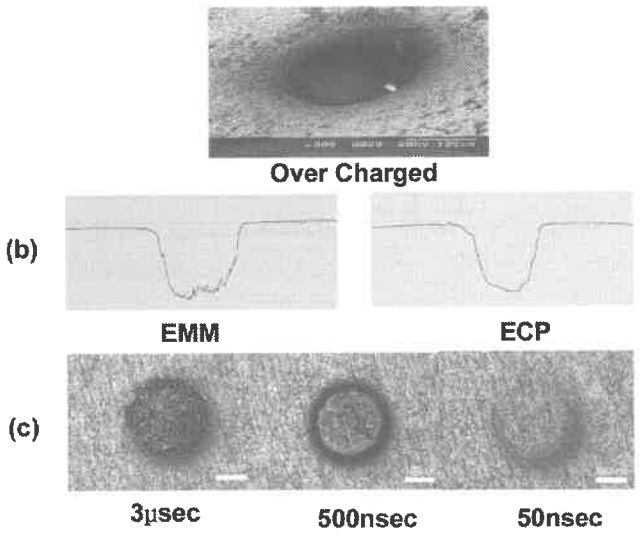

Fig. 6 Some Applications of Pulse Electrochemical Process. A Hole with over charged DL capacity (a), Comparison of EMM with rough groove surface and ECP with smooth groove surface (b), 250μm-diameter hole with various pulse width in DHF solution (c)

References

1. J.W. Park, E.S. Lee, Development of Electrochemical Micro Machining for Air-Lubricated Hydrodynamic Bearings, 12th annual symposium on ISPS, ASME, (2000)
2. J. A. McGeough, Principles of Electrochemical Machining, Chapman Hall, London (1974)
3. Giorgio Rizzoni, Principles and Applications of Electrical Engineering, 2nd ed., IRWIN (1996)
4. R. Schuster, V. Kirchner, Electrochemical Micromachining, Science, Vol. 289, pp98-101 (2000)

MATERIAL REMOVAL MECHANISMS IN ABRASIVE FLOW MACHINING

Szulczynski, Hubert; Uhlmann, Eckart
Institute for Machine Tools and Factory Management
Technical University Berlin

ABSTRACT

Abrasive flow machining (AFM) is a process for the production of excellent surface qualities of inner profiles that are difficult to access and outside edges, as well as for deburring and edge rounding. The grinding medium used in AFM consists of a polymer fluid, the so-called base, in which the abrasive grains are bound. The grinding medium is pressed along the contours at a defined pressure and temperature. Depending on the respective machining task, different specifications of media are used. The description of process-related metrial removal mechanisms requires the knowledge of material removal mechanisms in AFM. Based on findings in flow mechanism, analyses have been made on material removal mechanisms. The objective of the investigations at the Institute for Machine Tools and Factory Management - IWF in Berlin is to trace correlations capable of influencing the work result.

KEY WORDS: *Abrasive, Finishing,Polishing, Matreial Removal.*

1. INTRODUCTION.

Two American companies independently developed abrasive flow machining in the 60s [1, 2, 3]. Initially, the process was applied in aerospace to machine high-alloy components with inaccessible and complex inner shapes. Abrasive flow machining was initially applied for deburring and polishing operations which until then had to be carried out manually and hence were extremely time-consuming. Another drawback of manual machining was that even if altering the workpiece shape was possible it could not be done reproducibly.

A large field of application of abrasive flow machining is finishing in mold and die making. Typical components machined by abrasive flow machining include extrusion molding dies for aluminum profiles as well as crimping and stamping tools. AFM is used to remove the recast layer after EDM and laser machining. In most cases it is possible to use precisely rounded edge radiuses and polished surfaces to increase fatigue strength and life span [2, 4, 10]. The machining traces running in extrusion direction after AFM machining of extrusion molding matrices lead to an increase of the life span and also to a considerable reduction of the friction [3].

To date, only few models exist that describe the functional correlation between the process, the work result and the material removal mechanisms during abrasive flow machining. However, all of these models are based on analytic interpretations of empirical data for specific cases [3]. Therefore, universally valid parameters to describe the process are not available. The knowledge of these rules enables a purposeful process conception, process improvement and process control. Such a process improvement creates the framework for a purposeful and market-oriented technological advancement of the process.

The first step towards a target-oriented process optimization is to describe the existing knowledge of the fundamental mechanisms of abrasive flow machining and of the influence of the flow characteristics on the process. Moreover, the results of the rheologic measurements permit conclusions about the homogeneity of polymers, possible fluctuations of their composition and even about the molecular structure [12]. This makes it possible to set up the necessary criteria for the respective application and to use the rheologic properties for a quality assessment of abrasive flow machining media.

2. PROCESS TECHNOLOGY.

The grinding medium consists of the components base, abrasive and additives. The base which is also referred to as carrier binds the abrasive. Depending on the respective machining task, the abrasive is supplied with additives to

obtain particular flow properties of the grinding media. The carrier is produced in a variety of intrinsic viscosities. [1 - 9].

Prior to machining, the grinding medium is inserted into the lower cylinder. The workpiece is positioned in the specifically designed workpiece holder and clamped between the cylinder (figure 1a). Initially, the grinding medium is heated up to working temperature by the heater/cooler. After clamping, the grinding medium is pressed upwards into the workpiece holder along the machined workpiece shapes (figure 1b). After that, the process is repeated in the opposite direction (figure 1c). This machining cycle is repeated until the desired work result is obtained.

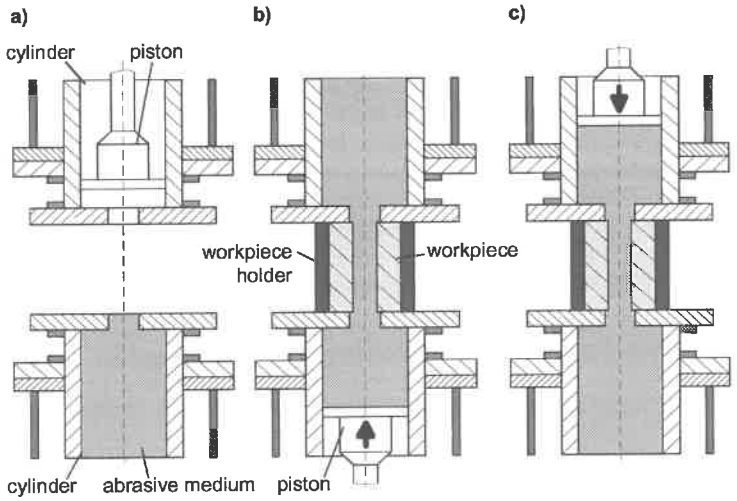

Figure 1. Process course during abrasive flow machining.

The two main tasks of the workpiece holder are to clamp the workpiece and to control the media flow. During the conception of the device, special attention has to be paid to the requirements of abrasive flow machining in order to minimize frictional loss. When parts with similar shapes or high batch numbers are produced it often occurs that exchangeable inserts are used. This way it is possible to buffer parts and to automatically charge the machine [1, 5].

The basic principle of AFM is that the abrasive and material removing effect of the grinding medium is in direct proportion to the speed of the abrasive. Following this principle, the conception of the workpiece holder determines the position of the highest speed of the grinding medium. The conception of the workpiece holder allows for an arrangement of the surfaces of the workpiece in such a way that there is no removal where machining is not supposed to take place. Often it is necessary to install sleeves, tubes or cores to obtain constant and high flow velocities [3, 7, 10].

The carrier consists of a silicone base polymer which is supplied with a gel consisting of a hydrocarbon oil and a metallic soap. Different intrinsic viscosities of the carrier are obtained by varying the volume percentages of the polymer and the gel [3]. The most frequently used abrasives are aluminum oxide, silicon carbide, boron carbide and cubic boron nitride (cBN) as well as diamond. In the case of conventional abrasives, grain sizes vary from 14 Mesh/inch to 1200 Mesh/inch, whereas it often occurs that two or three different sizes are mixed [3, 7, 8]. When the ultrahard cutting materials cBN and diamond are applied for particular machining tasks, grain sizes of 6 µm to 140 µm are used [7].

Normally, the composition of the grinding medium includes the base at 100 weight percent. Specifications concerning abrasive grains are given in weight percentage of the base [3]. 30 % to 80 % of abrasives with rougher grains and 10 % to 30 % of abrasives with finer grains are added to the base. PRZYKLENK [7] states the mixture of the polymer base and the grains in volume percentage, according to which it may contain 40 to 250 parts of the abrasive grains and 100 parts of the base material. In the cases of diamond and cBN, 100 parts of the base correspond to 100 to 250 parts of the abrasive grains.

The mixture ratio and the proportion of additives depends on the machining task, e.g. deburring or precise polishing. A high viscosity grinding medium works as a relatively elastic mass and enables extremely high material removal

rates during machining. Such a medium is mainly used to deburr of very strong burrs, for remove of recast layers after EDM machining and for the machining of large bore holes with a high diameter/length ratio. Thanks to good flow properties it is possible to machine grooves and orifices of a size of up to 0.1 mm if the viscosities are kept low [2]. In some cases it was even possible to machine bore holes of a size of 0.02 mm with AFM [4]. Grinding media with low viscosities are further used for the precise rounding of edges and for the machining of deep bore holes or bore holes with small diameter/length ratios [6].

3. SURFACE FORMATION

3.1 Structure and Realization of the Experiment

During the experimental investigation of abrasive flow machining, processes occurring at the contact zone can not be directly observed. However, the knowledge of the material removal mechanisms is crucial for the interpretation of the results obtained during machining. The method of sratch test with single diamond grits serves as an example for the machining with fixed grain. In these experiments, conclusions can be drawn from the elementary processes observed in favor of the real machining process. The observations made during the scratching with single diamond grit provide indications of the material removal mechanisms in the contact zone.

Therefore, an analogous process to abrasive flow machining was defined, in the course of which the singular engagement of individual abrasive grains on the surface of polished workpieces was generated maintaining the typical bonding of the grains in the fluid. Simple square workpieces were used as test workpieces which were polished on the side to be scratched. They were clamped into the machine by means of a workholding in a way that only the polished side was machined. Subsequently, the working pressure was set and the machining process was started with the medium preheated to working temperature. After activation, the machining process had to be interrupted as soon as the medium on the surface of the workpiece was actively involved in the process.

3.2 Surface Formation

Figure 2 depicts scratches of the abrasive grains at different stages of the scratching process. The scratch of the cutting edge in abrasive flow machining is characterized by a continuous scratch on the surface. Alongside cutting processes, elastic and elasto-plastic forming processes take place on the surface.

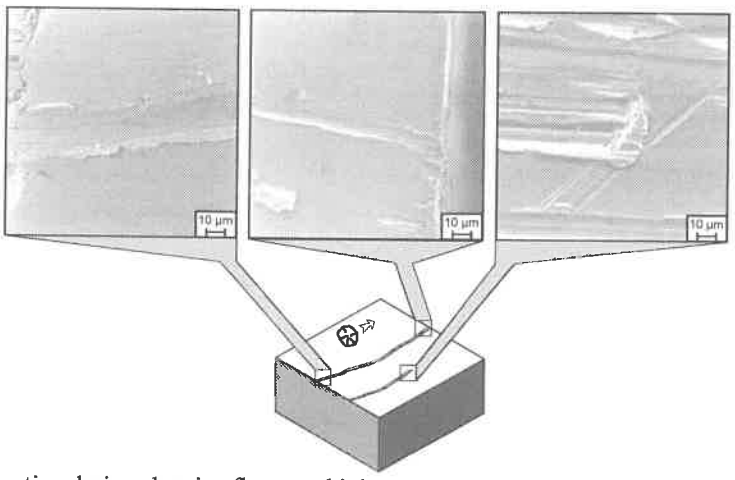

Figure 2: Surface formation during abrasive flow machining

Based on this observation it could be asserted, that due to the sum of the properties of the medium, the abrasive grains come into action on the material as quasi bound cutting edges. Literature often assumed that the sratch of the abrasive grains in abrasive flow machining corresponds to the mechanism involved in lapping. In the course of lapping, the grains are rolling between the surface of the workpiece and the shape-transferring counterpart. This

observation however was not made during scratching tests. In contrast, a continuous engagement of quasi bound cutting edges was observed almost during the entire process.

3.3 The Influence of the Grain Fraction

Figure 3 depicts electron microscopic images of the surfaces of the polished workpieces after simple scratching and multiple scratching with two polishing media of different grain fractions. In the course of simple scratching, depicted on the left side of the image, both abrasive medium specifications engender continuous traces on the surface of the workpieces.

In the case of a medium of a low grain fraction with the specification D100-20S(125)-NX(3), plastically deformed areas occur on one side of the simple scratch. On the opposite side, the scratch starts at one edge without plastic projection. In contrast, in the case of a medium of high grain fraction, the scratch was considerably wider. Due to the higher grain fraction of the medium with the specification D100-20S(200)-NX(3), it is assumed that the scratching forces in normal direction are much stronger than in the case of a medium specification of a lower grain fraction. With stronger normal forces, a broader chip can be cut off. Contrary to this, in the case of an abrasive medium of a lower grain fraction, the sratches are characterized by relatively smaller and sharper grain ranges.

Observations made during scratching of single grains can be transferred to the impact of several edges. On the right side of the image, the respective multiple scratches of each medium are depicted. In the upper image, alongside areas generated by larger grain sizes, there are scratches caused by single sharp edges. The lower image shows that during machining with this medium specification, much more edges are acting at the same time. The surface formed is more homogeneous and is marked by less single, clearly defined scratches.

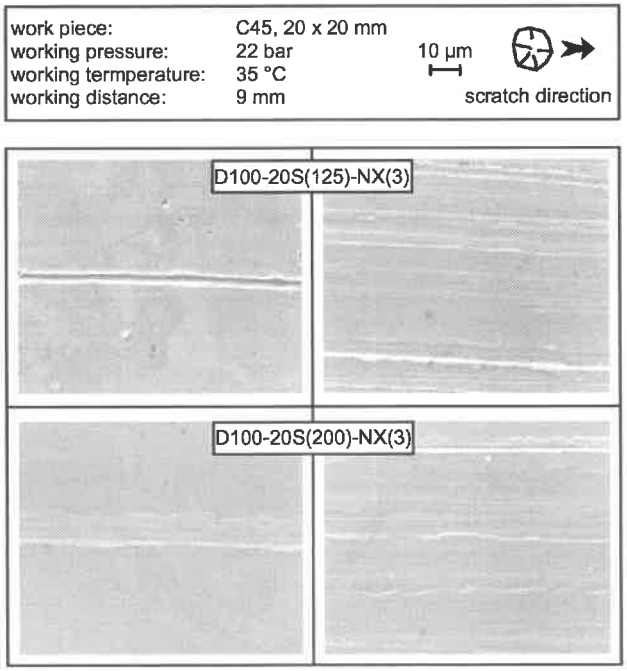

Figure 3: Influence of grain fraction on surface formation

3.4 The Influence of Additives

Figure 4 depicts the scratches generated by different additives of abrasive media. Surface formation during scratching with the abrasive medium with the specification D100-20S(200)-NX(3) at these settings was described in the last section. The images in the middle depict a surface machined with an additive for deburring. In single acting, the grains generate very thin scratches. During multiple scratching too, mainly thin scratches are generated on the

surface of the workpiece. Through the great number of thin scratches generated during machining, surface qualities are lower than after machining with a polishing media. Abrasive media for deburring are not suited for the formation of high surface qualities. Their aim is rather to maximize deburring during turning around a workpiece edge.

The adhesive media with the specification D100-20S(125)-400S(30), a mixture of coarse grain F20 and a fine-grained additive F400, is applied for machining processes in which a high material removal rate is to be achieved. Due to the relatively strong bonding of the adhesive grains caused by the fine-grained additive, a stronger normal force acts on the adhesive grains. It is assumed that the adhesive grains are thereby pushed much deeper into the surface than in the case of the same medium specification without fine-grained additive.

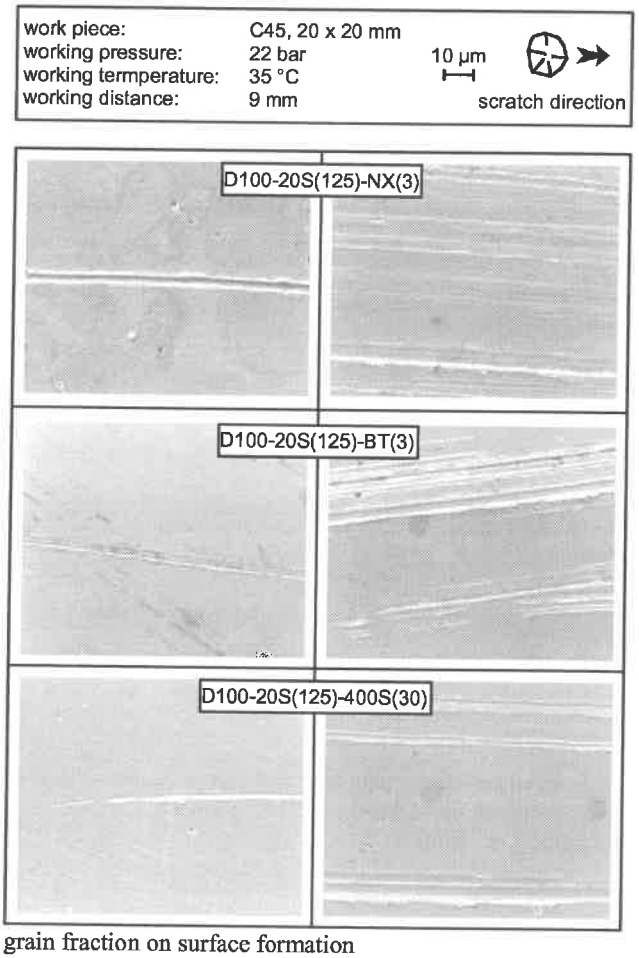

Figure 4: Influelnce of the grain fraction on surface formation

4. SUMMARY AND OUTLOOK

In the course of analogous tests, simple and multiple scratched surfaces were applied for the investigation of material removal mechanisms under varying influencing tool parameters such as grain fraction and additive.

On the basis of the scratches, it could be basically stated that during abrasive flow machining the surface is formed by quasi bound abrasive grains. In the case of surfaces formed by abrasive flow machining in several machining cycles, no surface traces referring to rolling grains were generated

During the application of polishing media, chip formation is very consistent. The surface is characterized by homogeneous traces and no clear single scratches can be observed. With a growing grain fraction, surface formation is becoming more and more even. In contrast, during scratching with deburring media, single and clearly visible

scratches were observed even after multiple scratching. The additive for deburring provokes chip formation in the area of laminar flow where there are no edges.

Based on the combination of the results of surface formation and the flow properties investigated before, a flow model of the process can be created and a qualified tool for process interpretation and for a better comprehension can be considered by means of numerical flow simulation. Furthermore, the correlation of the flow model, the numerical flow simulation and the surface formation will considerably contribute to the comprehension of the process.

5. REFERENCES.

1. BOTTKE, D.: " Strömungsschleifen als Alternative. Werkstatt und Betrieb 128 (1995) 4, S. 290.

2. N. N.: "Facelifting für Matrizen. Sekundärpolitur an gebrauchten Werkzeugen." Kunststoff-Journal (1995) 5, S. 54.

3. SPUR, G.; EICHHORN, H.; BOTTKE, D.: "Strömungsschleifen - Eine Verfahrensübersicht" Industrie Diamanten Rundschau, Band 31 (1997) No. 1, p. 84-88,90-94.

4. KUZMANOVIC, O. R.: "Flüssige Feile. Strömungsschleifen zur Feinbearbeitung von Bauteiloberflächen." Maschinenmarkt 100 (1994) 16.

5. KUZMANOVIC, O. R.: "Strömungsschleifen nach dem Dynaflow-Verfahren." Firmenschrift der Fa. Micro Technica GmbH, Kornwestheim, 1993.

6. N. N.: "Strömungsschleifen mit Diamant und CBN" Sonderdruck aus: IDR 26 (1992) 2.

7. PRZYKLENK, K.: "Druckfließläppen - Feinbearbeitung mit Schleifpasten." Jahrbuch Schleifen, Honen, Läppen und Polieren, 55. Ausgabe, Vulcan-Verlag Essen, 1988, S. 441-458.

8. RHOADES, L. J.: "Abrasive Flow and Ultrasonic Machining an Polishing", Technical Paper, American Society of Manufacturing Engineers, Dearborn, Michigan, USA, 1995, Paper-no. 95-190, p. 523-541.

9. PILZ, O.: "Entgraten, Abrunden und Polieren durch Preßläppen." Werkstatt und Betrieb 114 (1981) 10, S. 739-740.

10. BOTTKE, D.: "Applikationen des Verfahrens Preßläppen zum Entgraten und Polieren unter besonderer Berücksichtigung der Vorgänge an der Wirkstelle", Dissertation TU Dresden, 1992.

11. DE PLOEG, D. M.: "Kostensparendes Preßläppen von Strangpreßmatrizen", Aluminium 59 (1983) 3, S. 187-188.

12. SCHRAMM, G.: "Einführung in Rheologie und Rheometrie", Gebrüder Haake GmbH, Karlsruhe, 1995.

New Approach to Slicing and Lapping and Polishing in Precision Engineering

Takaya Watanabe

World Technology Instrument Co., Ltd.

533 Kamoshidacho, Aoba-Ku, Yokohama, Kanagawa 227-0033 Japan

Abstract

The analytical model of the optimum slicing of the Unidirectional Multi-Wire-Saw is inferred that grinding is advanced with the abrasive grain in the slurry layer in close relation to the run wire cohered triangular. On the other hand, the run wire repeats cycle of the acceleration, the moderation, and the stop movement in the Bidirectional Multi-Wire-Saw. It proposes a new optimization system that solves a basic operation defect of this Bidirectional Multi-Wire-Saw. The grinding efficiency is kept constant by radiating the mega sonic wave in the slurry supplied at the slicing, and supplying it while reproducing the abrasive grain. An excellent wafer without the saw-mark is obtained. The phenomenon of not generating etch pits and etch channels by doing etching more than the growth rate when quartz is synthesized is discovered, and the advantage that chemistry etching processing brings to the industrialization of the quartz plate is described.

1. Introduction

The Unidirectional Multi-Wire-Saw can supply the abrasive grain when grinding by speeding up the wire running speed to the cutting slice of the ingot with stability. It reported the pull cutting that was an ideal slicing processing to be possible.[1, 2] As for the ST-cut quartz wafer of thickness H=0.19mm examined here, the maximum size in the direction of X becomes D=77.6mm. Therefore, some aspect ratios are D/H=400. The direction of Z is 84mm or more, and it becomes D/H=440 or more. As for this, the slicing working accuracy more than 400mm in the diameter silicon (slicing thickness 1mm) to which development is being advanced as the next generation semiconductor large diameter silicon now is demanded. In this, the state-of-the-art slicing processing field is a technical domain of the unexplored. The establishment of this cut machining technology is from a viewpoint of the precision engineering to an indispensable research topic. On the other hand, the single crystal plate by the method of the abrasive machining based on a double-sided lapping and the mechanical polishing, especially the development of the thinned plate of quartz is advanced as for the wafer after the slicing. To our regret, it doesn't succeed in development though a fundamental research and practical use concerning chemistry etching of quartz are advanced in world each place. As follows, O.Cambon was describing the advantage that chemistry etching processing brings to the industrialization of the quartz plate. [3]

- The plate surface stresses produced by mechanical grinding and lapping are removed.
- This process is compatible with a collective and automatic treatment of blanks.
- Moreover, if the chemical etching does not damage the surface texture, it is possible to manufacture high frequency resonators starting from usual mechanically lapped plates.
- Finally, if this process is able to improve the surface texture of the ground plates, it is possible to suppress some lapping steps.

The author discovered the phenomenon of not generating etch pits and etch channels by doing etching more than the growth rate when quartz was synthesized. [4] The feature of this High-Speed Etching processing is shown as follows.

Ⅰ. #2000 finish wafer ～ → Polish wafer

Ⅱ. Polish wafer → Thin polish wafer

2. Unidirectional Multi-Wire-Saw

2.1 Factor to decide slicing accuracy

In the Unidirectional Multi-Wire-Saw, because the kerf-loss of the slicing is few, it is remarkable features that yield of the material is high. As for the wafer, TTV: Total Thickness Variation and the warp are greatly excellent compared with the wafer of other slicing methods. The wafer that processes the slicing is that there is neither uniform thickness nor a warp as for 400mm in the diameter silicon and the large diameter quartz. The Multi-Wire-Saw that is the grinding method by the free abrasive grain is used by the cut machining of these single crystals of the large diameter. In the large diameter silicon that processes the Multi-Wire-Saw, it is hoped that the Total Thickness Variation of the wafer after the slicing is zero. Especially, the warp of the wafer has a bad influence for the end-product performance. Therefore, the wafer should not have the warp.

2.2 Optimal cutting condition

The optimum machining condition of the ingot in the slicing in the Multi-Wire-Saw is examined. The slicing condition of the optimum that realizes the wafer of the uniform thickness is that the layer of the slurry cuts 3σ into the run wire in the state of the twining coagulation. Here, σ is a diameter of the abrasive grain. The damage at the slicing is a little, and the warp becomes small, too. In figure 2, the wire running speed is 2500m/minute width H1 of the groove of the entrance and width H2 of the groove at the exit become equal. This can realize the wafer of the uniform thickness. The oiliness liquid is used for the slurry. The abrasive grain uses GC#600. The grain diameter σ is 20μm. The diameter of the wire used is 160μm.

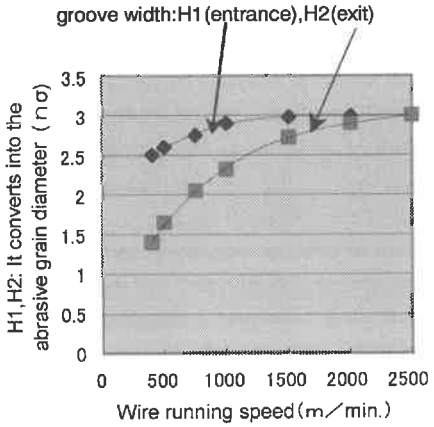

Figure 1 Influence of wire running speed given to width of slice groove

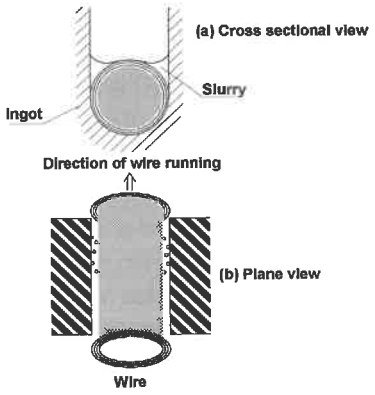

Figure 2 An optimum slicing model

The gap from which the abrasive grain is always supplied to 3σ between the ingot and the slicing groove is kept. Lifting speed of the stage is controlled. The slicing is begun by installing the dummy part of the groove of the diameter of wire plus 3σ on the ingot when the wire running speed cannot be sped up. The wafer of the uniform thickness can be realized by this method. The amount of the abrasive grain in close relation to the wire decreases to the width of the groove when the wire running speed is slow. Therefore, the width of the groove of the entrance broadens. The abrasive grain is not carried to the exit. The width of the groove narrows while going in the direction of the exit. The wafer after the slicing becomes a tapered boundary. On the other hand, when the wire running speed is fast, the abrasive grain in close relation to the run wire is almost constant in the groove. The difference decreases at the entrance and the exit of the width of the groove, and the abrasive grain

is carried to the exit. The groove with a good parallelism or more is formed. The flow of the slurry becomes early, and the shearing stress in the center part that hangs to the abrasive grain grows. The thickness of the wafer obtained after the slicing becomes uniform.

2.3 Theoretical consideration

The free abrasive grains in the slurry cohere like a triangular strain circle. This triangular strain circle is grinding the quartz ingot with the wire running. It is inferred that it is an analytical model of the optimum slicing condition.

Assumption: Lug in the cutting point is shaved off. It is harmony of lug in the cutting point and lug in the point on the other side of the cutting point.

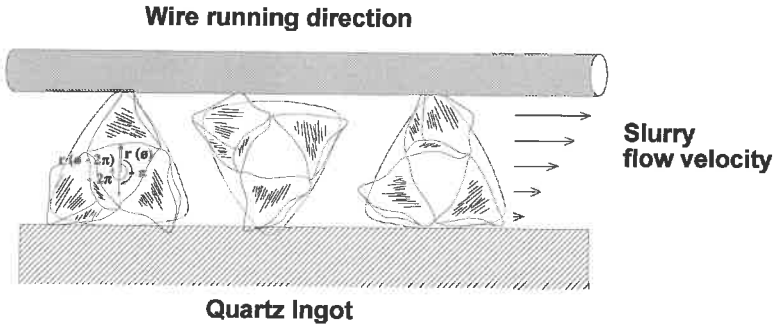

Figure 3 The Unidirectional Multi-Wire-Saw has been inferred from the grinding mechanism in a triangular distortion circle.

Figure 3 shows grinding mechanism in a triangular strain circle.
Only the change element is noteworthy. The incision is as follows.

$$t(\varphi) = r(\varphi - 2\pi) + r(\varphi - \pi)$$

New swell is shown as follows.

$$r(\varphi) = r(\varphi - 2\pi) - t(\varphi) = r(\varphi - 2\pi) - \{r(\varphi - 2\pi) + r(\varphi - \pi)\} = -r(\varphi - \pi)$$

Rotational angle φ is proportional at time t.

The Laplace transform is done for φ.

$$L\varphi = s\,,\ Lr(\varphi) = R(s) \quad R(s) = -R(s)e^{-\pi s} \qquad \therefore R(s)(1 + e^{-\pi s}) = 0$$

It puts with $s = jn$ and it returns to the frequency domain.

It becomes $R(jn)(1 + e^{-\pi jn}) = 0$. n is number per one revolution swell of the work piece.

As for $R(jn) = 0$, it is meaningless. $1 + e^{-\pi jn} = 0$ becomes a characteristic equation.

Odd numbers such as n=1, 3, and 5 are the obtained solutions. (Odd number strain circles)

The slicing mechanism of the Unidirectional Multi-Wire-Saw is grinding processing of the triangular strain circle.

3. Bidirectional Multi-Wire-Saw

Figure 4 is flow of the circulation of the slurry used by the actual experiment. It is a system that radiates the ultrasonic directly on the slurry storage tank where quartz that is the ingot for the slicing as shown in the figure is stored in the slurry. 1MHz megasonic wave was superimposed to the slurry flow supplied to the wire as a method of the slicing of achieving the improvement of the done wafer

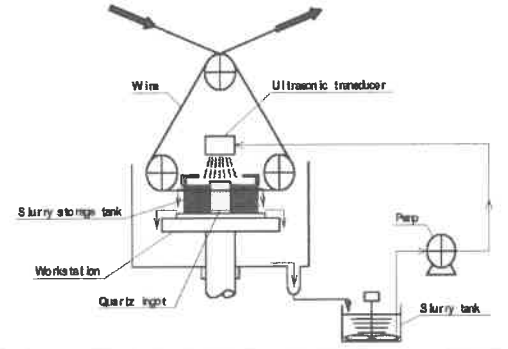

Figure 4. Diagram of the new slurry circulatory system

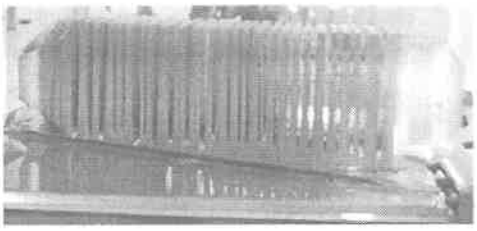

Photo1. After slicing of thequartz ingot

in the Bidirectional Multi-Wire-Saw and the reproduced fresh abrasive grain were always supplied. To realize the state that the slurry is always supplied in the slicing, the lumbered synthetic quartz crystal that is the ingot is stored in the slurry storage tank. The ingot and the slurry storage tank have been cut together. If the ingot is cut so that the direction of the run of the wire may do the slurry storage wall to the angle θ, the Leaked path is kept. The slurry is always round in the storage tank. Therefore, the liquid level of the slurry is always kept constant. The slicing of the lumbered Z-bar that uses the Multi-Wire-Saw, the mega sonic wave is radiated in the slurry supplied to the run wire and the ingot. The rubbish of cutting the abrasive grain and the re-attachment of the wire wear-out piece can be prevented by reproducing the slurry. The stable supply of the slurry can be realized in the slicing part of the ingot. Excellent quartz wafer ($77.6\times84.0\times0.19mm^3$) of the slicing shown in Photo1 is obtained.

4. Theoretical examination of high-speed Etching

It systematizes it from the theory and the experimental aspect for the High-Speed Etching that is the chemical etching method of quartz. Quartz is synthesized by the hydrothermal method, and a fundamental research is done for the growth rate and the quality. Developing the perfect crystal because quartz is synthesized based on the seed quartz with the lattice defects extremely in the difficulty. It is. Therefore, it is understood etch pits and etch channels are generated along with etching from the existence of the line defect in quartz in wet etching. Especially, the AT-cut quartz is being used voluminously as a quartz resonator in high frequency now by the excellent temperature characteristic. If the technology that suppresses etch pits and etch channels can be established in etching, it can be expected to become the method of processing the most ideal quartz. In current etching, etching has been done at a speed that is slower than the growth rate of quartz. It thought whether etch pits and etch channels were able to be suppressed by the process where the machining process named etching removed crystal lattice and catching, and making the etching speed earlier than the growth rate of quartz. Then, the etching speed accelerated with ten micrometers/minute by heating saturation NH_4HF_2 solution to 100℃ or more to achieve the etching speed that exceeded 0.5 micrometers at maximum etching speed/minute (NH_4HF_2 is heated to 75℃-85℃) to which the unswept quartz had been experimented up to now as pioneering experiment at 7.5 micrometers/minute of five micrometers/minute of 2.5 micrometers/minute of one

micrometer/minute. The trend shown in Figure 5 was obtained, and it became the result of the first forecast of the etching speed by about two micrometers/the minute. This High-Speed Etching technology can process the surface to the mirror condition while maintaining the basic characteristic of the quartz at the previous state of etching. It can be considered that isotropic etching because it is wet etching and the state of the finish of the surface becomes mirror finish. This High-Speed Etching

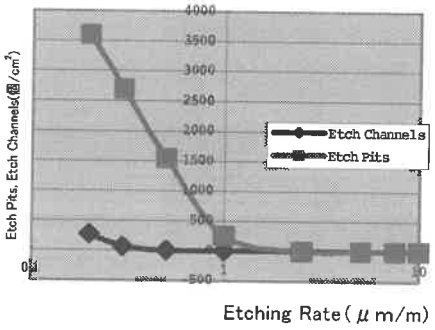

Figure 5. Relation among etching rate in quartz, etch pits, and etch channels

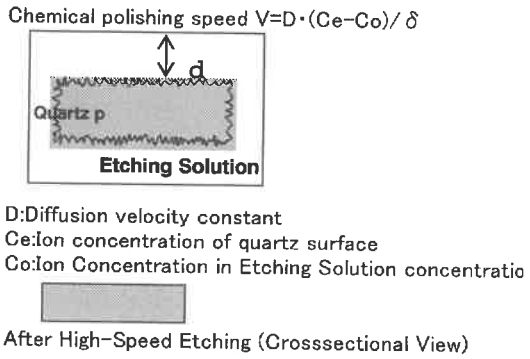

Figure 6. High-Speed Etching mechanism

technology can process the surface to the mirror condition while maintaining the basic characteristic of the quartz at the previous state of etching. It can be considered that isotropic etching because it is wet etching and the state of the finish of the surface becomes mirror finish. Figure 6 is a scheme that explains the mechanism of High-Speed Etching. The reaction is always continued as for the convex part, and polish is processed to flat as a result as for the quartz surface though the etching speed decreases from the stay of the etching liquid and the stay of the circulation of the solution in the concave portion at chemical polishing speed V. Chemical polishing speed V is shown by the next expression. **Chemical polishing speed V=D·(Ce-Co)/δ**

At chemical polishing speed V, the etching speed has decreased from the stay of the etching liquid and the stay of the circulation of the solution in the concave portion. The diffusion reaction is always continued as for the convex part, and polish is processed to flat as a result as for the quartz surface though it does. High-Speed Etching that is a chemical polishing method belongs to dipping type etching. On the other hand, the mechanochemical polishing of the wet process is a chemical action of the working fluid and what made a compound as for mechanical work by the abrasive grain. The chemical reaction of quartz with the working fluid in the mechanochemical polishing is thought to be an essentially similar to dipping type etching from the viewpoint of the thermal energy. The finish of the surface of grinding where excellent quartz of the parallelism after the slicing is obtained with High-Speed Etching that is dipping type etching becomes the same level as the mechanochemical polishing from this if there is no factor for etching to obstruct the chemical reaction such as contamination to the quartz surface.

5. Applications

If # 2000 finish quartz wafer of Φ5mm will be spread over cm^2 without the space, the number of wafers becomes 900. To become 7.5 micrometers at the etching speed/minute, saturation NH_4HF_2 solution is heated to 140°C. The amount of the quartz wafer turned on to the Teflon basket of Φ15 cm in this solution is changed, and the result of the experiment is shown. The thickness of the quartz crystal wafer at that time will become finish by 20μm (Resonant frequency is 83MHz) in four minutes at one processing time. This High-Speed Etching processing method can confirm the thickness of

quartz crystal is treatable stabilizing by about two micrometers by High-Speed Etching. Figure 7 shows AFM 3-D images of photographs. Figure 8 is sectional analysis at the center of a High-speed Etched quartz surface. In High-Speed Etching, slicing mechanical damage with the abrasive grain is not seen on the surface.

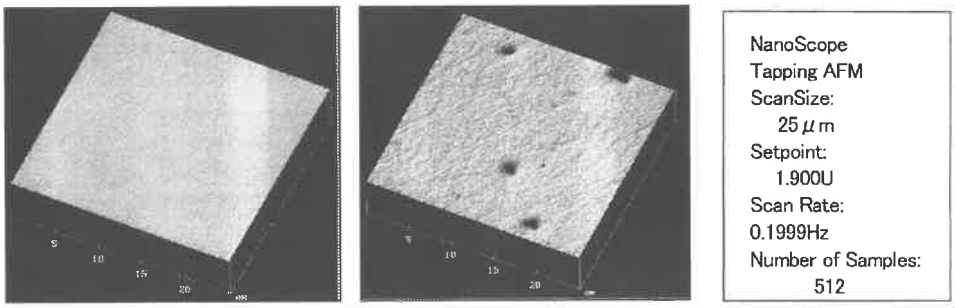

(1) High-speed Etching **(2) Mechanical Polishing**

Figure 7.AFM 3-D images of two kinds (X, Y=5μm/div, Z=1μm/div)

Figure 8. Section Analysis of High-Speed Etching

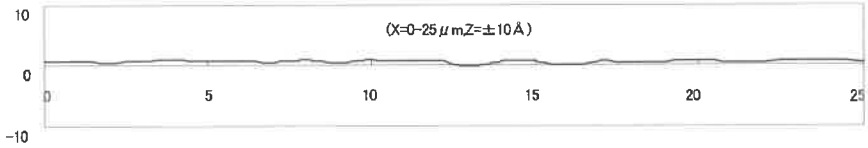

6. Conclusions

A new approach is tried for Slicing, Lapping, and Polishing of the ingot crystal. It becomes possible by taking this result in the field of the precision engineering to nanotechnology and the ultrasonic electronics that is the application to the new field.

It can explain the results as follows.

Ⅰ. The slicing condition of the optimum that realizes the wafer of the uniform thickness is that the layer of the slurry cuts 3σ into the run wire in the state of the twining coagulation.

Ⅱ. The slicing mechanism of the Unidirectional Multi-Wire-Saw is grinding processing of the triangular strain circle.

Ⅲ.The slicing of each slurry storage tank is effective to the highly precise working accuracy.

Ⅳ. The prospect of the slicing processing of the wafer by which the aspect ratio became 400 or more is obtained.

References

1. Takaya Watanabe and Masayasu Kojima "Research of quartz crystal slicing processing technology by Wire-Saw" Electronic telecommunication society technology research report, US2000-97, and EA2000-104(2001-01)

2. Takaya Watanabe "Optimization of quartz crystal slicing condition using supersonic vibration in Multi-Wire-Saw" Electronic telecommunication society technology research report and US2001-54(2001-09)

3. O.Cambon, M.Deleuze, J.P.Michel, J.P.Aubry, A.Goiffon and E.Philippot, "Controlled dissolution of quartz material.Part Ⅱ. Quartz chemical etching applied to blanks industrial manufacturing," Journal De Physique, Vol.4, pp.85-91, 1994

4. Takaya Watanabe "Mass production of quartz high-speed chemical etching applied to AT-cut wafers" 2001 IEEE international Frequency Control Symposium, pp.368-375, (2001-06)

High Removal Rate Ultra-Smoothness Polishing of NiP Plated Aluminum Magnetic Disk Substrate by Means of High Polishing Speed with High Polishing Pressure

Heiji YASUI*, Tomohiko FUKAMACHI*,
Shigehiko SAKAMOTO*and Susumu TAKAKURA*
*:Dept. of Mechanical Engineering & Materials Science,
Kumamoto University, Kumamoto 860, Japan

1. Introduction

The compact magnetic disk has been recently required to steadily reduce its price together with realizing a higher storage capacity. One of the methods for filling the requirement is to improve the ultra smoothness polishing technique of the magnetic disk substrate. Through our previous research [1], we have cleared the influence of polishing speed on the surface smoothness and removal rate in the polishing of non-electrolytic nickel phosphorus plated aluminum substrate over a wide range in excess of 5 times the usual polishing speed executed by the present conventional polishing machine. It has been found from the results that the high speed polishing is useful for simultaneously getting both high removal rate and ultra smoothness surface. Two types of abrasives - alumina abrasive of 0.5μm in nominal diameter and colloidal silica abrasive of 80nm in nominal diameter –were used in previous experiments. However, to realize a low price compact magnetic disk having the high storage capacity of 100Gb per disc substrate, hereafter, the better abrasives by which the substrate of ultra-smooth surface can be produced through lower costs will be strictly followed.

This is one piece of research in a series on the polishing of NiP plated aluminum magnetic disk substrate. The research aims to clear the influence of polishing speed and pressure on the surface smoothness and removal rate in the polishing of NiP substrate using a alumina abrasive of 50nm in nominal diameter.

2. Experiments

The schematic view of the polishing machine is shown in **Fig. 1**. The machine can obtain the polishing speed of 9m/s. This is 5 times in excess of the usual polishing speed executed by the present conventional polishing machine. The main experimental conditions are listed in **Table 1**. The NiP plated aluminum substrate used is a 3.5inch type of 95mm outer diameter and 0.8mm thickness. The experiments are executed at the polishing speed of 1.5m/s to 9.0m/s (1.5m/s is

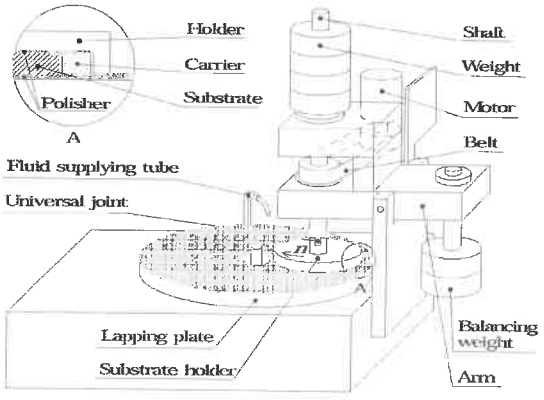

Fig.1 Shematic view of polishing machine

near the maximum polishing speed used in most of the substrate manufacturing factories). The substrate smoothness is evaluated from the standpoint of a slight undulation *H*wa(Ra) and surface roughness *H*ra(Ra), which are obtained by measuring 4mm and 240μm in lengths with WYKO, respectively. The slight undulation and the surface roughness before polishing are about 1.3nm(Ra) and 1nm(Ra). The data of slight undulation and surface roughness are obtained by averaging the values of two-dimensional profiles at five random positions on the WYKO three-dimensional images measured at four substrate surface locations.

Table 1 Experimental conditions

Workpiece	NiP Plated Aluminum Magnetic D
Polisher	Non-woven Urethanform :ANM (Hardness20°)
Polishing fluid	Abrasive:Al_2O_3 (φ50nm) Abrasive Content C_g:5.0wt% Supply flux S_g:6.0g/min
Polishing Condition	Pressure P:3.7-11.1kPa Speed V_a:1.5-9.0m/s

3. Results and discussion

Figure 2 shows the change in the removal depth *T*p with polishing time *t* for the polishing pressures *P* between 3.7kPa and 11.1kPa, under the polishing speed *V*a of 9m/s. In the figure, for the comparison, the result at the polishing conditions of *V*a=1.5m/s and *P*=3.7kPa is also expressed additionally. From the figure, the *T*p for all the cases is found to steadily increase linearly with the polishing time, though the data are scattered somewhat around straight line.

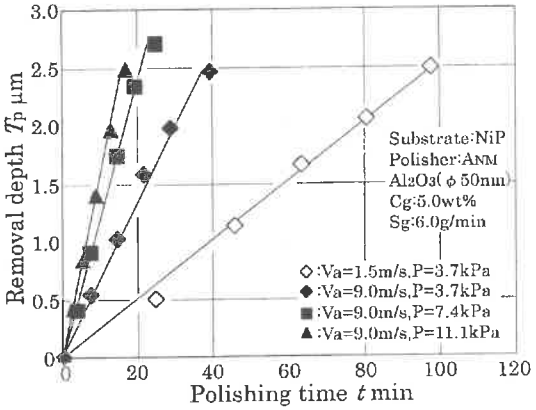

Fig.2 Change of the removal depth with polishing time

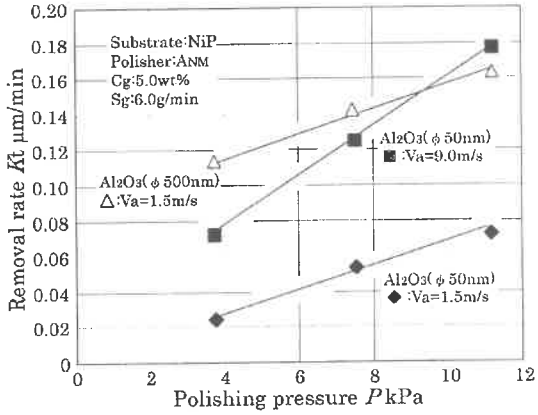

Fig.3 Relationship between the removal rate and the polishing speed

Figure 3 shows the relationship between the removal rate and the polishing pressure under the polishing speeds of *V*a=9.0m/s and 1.5m/s. In the figure, for the comparison, the result obtained using alumina abrasives of 0.5μm diameter at the polishing speed of *V*a=1.5m/s is also expressed additionally. From the figure, within the range between *P*=3.7kPa and 11.1kPa, the removal rate for both velocities of 1.5m/s and 9.0m/s is found to increase in approximate proportion to the polishing pressure. The removal rate for the velocity of *V*a=9.0m/s using alumina abrasives of 50nm is over two times as large as that of *V*a=1.5m/s. Compared with the same polishing pressure of P=11.1kPa, however, it is remarkable that the removal rate obtained using alumina abrasives of 50nm diameter at *V*a=9.0m/s is larger than that of alumina abrasives of 0.5μm

diameter at 1.5m/s.

The change of the slight undulation *H*wa and the surface roughness *H*ra with the polishing time for three kinds of polishing pressures under the polishing speed of *V*a=9.0m/s are shown in **Fig.4** and **Fig.5.** From the figures, the slight undulation and the surface roughness for all the cases decrease rapidly in the initial polishing time. After the initial polishing time, the decrease rate of *H*wa and *H*ra decrease gradually with polishing time. Finally the *H*wa and the *H*ra converge to a terminal slight undulation (*H*wa)t of about 0.47nm(Ra) and the terminal surface roughness (*H*ra)t of about 0.23nm(Ra), respectively. The time to attain the terminal surface roughness and slight undulation are shorter for higher polishing pressures.

The relationships between the slight undulation *H*wa, and the surface roughness *H*ra and the removal depth for three kinds of polishing pressures under the polishing speed of *V*a=9.0m/s are shown in **Fig. 6** and **Fig. 7**. It is obvious from the figure that the relationships are almost the same in quantitative aspects for all the cases. Therefore the relationships are considered to be influenced little by the polishing pressures. The minimum terminal removal depths required to attain the terminal slight undulation and the terminal surface roughness are about 1.5μm and 0.5μm, respectively. The minimum terminal removal depth depends on the surface smoothness before polishing. Accordingly the surface smoothness formed before polishing is one of the important points related to the productive efficiency in the polishing of disc substrate.

Figure 8 shows the Influence of the polishing pressure and the polishing speed on the terminal smoothness. In the figure, for the comparison, the result obtained using alumina abrasives of 0.5μm diameter at the polishing speed of *V*a=1.5m/s is also expressed additionally. From

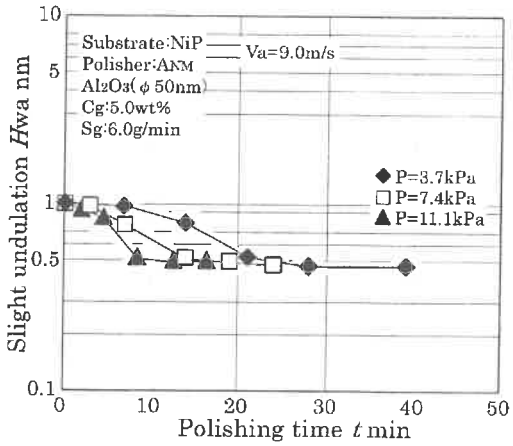

Fig.4 Change of the slight undulation with polishing time

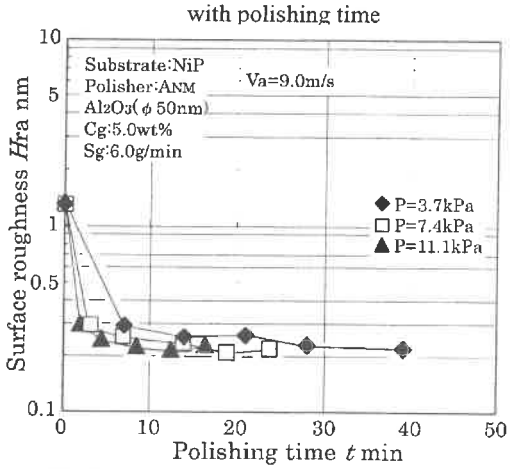

Fig.5 Change of the surface roughness with polishing time

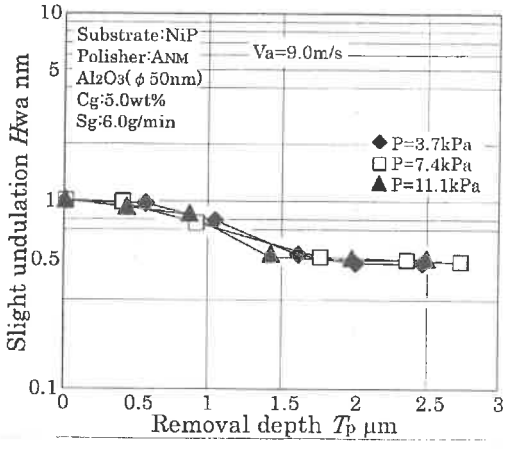

Fig.6 Relationship between slight undulation and removal depth

the figure, the (*H*ra)t is found to keep about 0.23nm(Ra) in the whole region of the polishing pressure between 3.7kPa and 11.1kPa for both polishing speeds of *V*a=1.5m/s and *V*a=9m/s. The (*H*wa)t also keeps almost the same value in the whole region of the polishing pressure between 3.7kPa and 11.1kPa.. The (*H*wa)t of about 0.47nm(Ra) at *V*a=9m/s, however, becomes larger than that of about 0.37nm(Ra) at *V*a=1.5m/s. It should be noted that the (*H*wa)t of about 0.47nm(Ra) at *V*a=9m/s using alumina abrasives of 50nm diameter is smaller than that of 0.57nm at 1.5m/s using alumina abrasives of 0.5μm diameter. As mentioned above, the removal rate obtained at *V*a=9m/s using alumina abrasives of 50nm is larger than that at *V*a=1.5m/s using alumina abrasives of 0.5μm diameter, which is used as rough polishing in substrate manufacturing factories. Accordingly it is referred that the high speed polishing is useful for simultaneously getting both high removal rate and ultra smoothness surface.

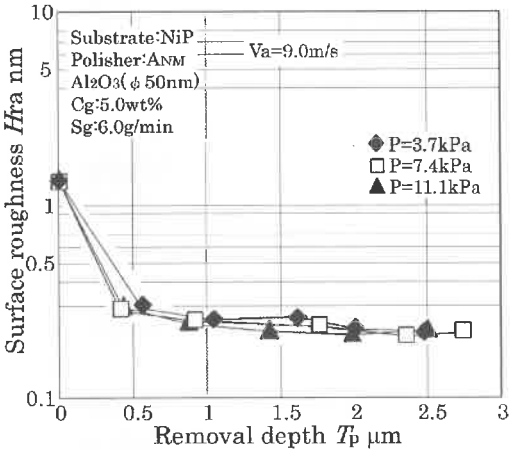

Fig.7 Relationship between surface roughness and removal depth

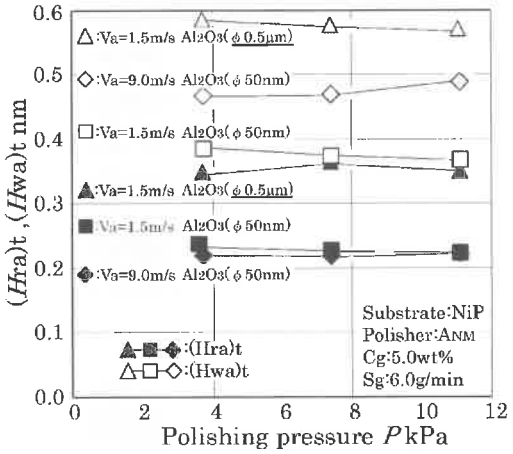

Fig.8 Influence of the terminal slight undulation and surface roughness on polishing speed

4. Summary

The main results obtained are as follows:

(1) The substrate removal rate becomes larger for higher polishing speed and pressure.

(2) The slight undulation and the surface roughness converge finally to a terminal value corresponding to a given polishing condition.

(4) The polishing pressure has little influence on the terminal slight undulation and the surface roughness.

(5) The terminal surface roughness is influenced little by polishing speed

(6). The terminal slight undulation of about 0.47nm(Ra) at *V*a=9m/s using alumina abrasives of 50nm diameter is becomes somewhat larger than that of about 0.37nm(Ra) at *V*a=1.5m/s.

(7) The surface smoothness and the removal rate at *V*a=9m/s using alumina abrasives of 50nm diameter is smoother and larger than those at 1.5m/s using alumina abrasives of 0.5μm diameter.

Reference

[1] H. Yasui *et al.*: High Removal Rate Ultra-Smoothness Polishing of NiP Plated Aluminum Magnetic Disk Substrate, Proc. ASPE 2001 Annual Meeting, Vol.25 (2001) pp. 545-548.

Authors Index

Abe, Takahiro 41
Adams, David Price 613
Ade, G. 57
Akamatsu, Koji 585
Aketagawa, Masato 373
Albertazzi Jr., Armando 238
Altintas, Yusuf 94
Anderson, Erik H. 83
Anderson, Gordon A. 285
Aoyama, Hisayuki 148, 271, 295
Araki, Takeshi 538
Araque, Carlos A. 279
Bah, Alaji 642
Baidyk, Tetyana 377
Baldwin, Jon M. 47
Bao, Paul 13
Barraja, Mathieu 478
Barylski, Adam W. 652
Bayly, Philip V. 132
Beck, U. 57
Borundia, Ajit 630
Brinksmeier, Ekkard 275, 542
Brown, Curtis W. 47
Buckner, Gregory D. 622
Bui, Son Hoang 634
Burns, Timothy J. 166
Busch, I. 57
Caballero-Ruiz, Alberto 228, 377
Carter II, James A. 182
Cattell, Joe 305
Chambers, V. John 73
Chang, Y. M. 32
Chao, Choung-Lii 32
Chen, Carl G. 83, 261
Chen, Jenq-Shyong 291
Chen, T. T. 32
Cheng, Kai 581
Cheung, Chi-Fai 546
Chikkamaranahalli, Sumanth B. 187
Choi, Hon-Zong 509
Choi, Jae Young 509
Chu, Ji-Young 411
Chung, Sung-Chong 204, 402
Clayton, Stuart 622
Combs, Dana 591
Cork, William 13
Culpepper, Martin L. 279, 285
Dambon, Olaf 105
Davies, Matthew A. 166
Davis, David W. 16
Deis, Michael 591
Dornfeld, David A. 602, 661
Dow, Thomas A. 115, 618, 622
Duduch, Jaime 602
Dunn, Thomas J. 89
Dutterer, Brian S. 132, 166
Echizenya , Dan 602
Eda, Hiroshi 534
Elmouelhi, Ahmed 305
Enomoto, Toshiyuki 657
Epshteyn, Yakov . . . . . *
Fan, Xiaorui 484
Ferra, Mark . . . . . *
Forest, Craig Richard 244, 261
Formica, Michael K. . . . . *
Frank, W. 57
Fuchiwaki, Ohmi 148
Fujimori, Akira 597
Fukamachi, Tomohiko 689
Furukawa, Masaru 328
Furutani, Katsushi 332, 638
Gao, Wei 328, 363, 538
Gao, Yongsheng 316, 320, 442, 446
Garimella, Viswanadham 13
Garrard, Kenneth P. 73, 622
Gatzen, Hans H. 551, 557, 562
Gee, Anthony E. 256, 338**
Ghimire, Shankar 27, 234
Gill, David D. 618
Gläbe, Ralf 275
Golini, Donald 120
Gomes de Oliveira, Joao F. 602
Goto, Akihiro 585
Grimme, Daniel 542
Günzel, Gerald 557
Gweon, Dae-Gab 162, 170, 199
Hanak, Thomas 152
Hanasaki, Shinsaku 505
Harada, Kazuaki 450
Harris, John O. 383
Hart, Anastasios John 193
Hasche, Klaus 57
Hashimoto, Hiroshi 567
Hausotte, Tino 299
Hayashi, Akira 295
Heilmann, Ralf K. 83, 261
Henke, Michael P. 47
Henke, Richard P. 47
Herrmann, K. 57
Hidaka, Shinta 460
Hii, King-Fu 391
Hlavac, Marcus 490

*Abstract unavailable at press time.

**Extended abstract not available at press time.

Hocken, Robert J. . . . 77
Hoffmeister, Hans-Werner . . . 490
Hong, Yong K. . . . 27, 234
Hood, David W. . . . 622
How, Peter . . . 305
Hsu, Wei-Yao . . . 291
Huang, Han . . . 495
Huang , Jin . . . 94
Hunsaker, Burke . . . 357, 478
Iijima, Daisuke . . . 295
Imai, Kenichiro . . . 567
Imai, Noboru . . . 396
Ishikawa, Ken-ichi . . . 501
Ito, Sumio . . . 295
Jäger, Gerd . . . 67, 299
Javed, Kazi . . . 642
Jeong, Eun-soo . . . 250
Jeong, Hae Do . . . 250, 509, 661
Jin, Sungho . . . 642
Jo, Nam-ju . . . 250
Jones, Gordon M. . . . 551
Joo, Chulmin . . . 83
Jung, Young-Dae . . . 250
Kamiya, Kazuhide . . . 460, 465
Kanada, Toru . . . 339
Kaneeda Ph.D., Toshiaki . . . 571
Karino, Takashi . . . 310
Karyazin, Alexey . . . 551, 562
Kawa, Hiroyuki . . . 339
Kawada, Masayoshi . . . 343
Kennedy, Michael D. . . . 166
Kiani, Sepehr . . . 182, 357, 478
Kim, Dongmin . . . 199
Kim, Eun-Kyoung . . . 176
Kim, Hoyoun . . . 661
Kim, Jun-Ho . . . 176
Kim, Kihyun . . . 162, 170, 199
Kim, Kyung-Don . . . 402
Kim, Min-Seok . . . 204
Kim, Nam Hun . . . 575
Kim, Seung-Woo . . . 411
Kimura, Keiichi . . . 37
Kitajima, Takayuki . . . 505
Kiyono, Satoshi . . . 328, 363, 538
Klocke, Fritz . . . 105
Kobayashi, Yoshikazu . . . 219
Kondo, Sumihisa . . . 597
Koning, Robert J. . . . 126
Konkola, Paul T. . . . 83
Korovin, Nikolay . . . *
Krishna Kumar, R. . . . 415
Kroll, Jeremy J. . . . 144
Krumrey, M. . . . 57
Kulawiec, Andrew W. . . . 89
Kussul, Ernst. . . . 228, 377
Lawrence, Tyson . . . 305
Lawton, Kevin M. . . . 353
Lee, Deug Woo . . . 575
Lee, Eun Sang . . . 575, 671
Lee, Hwa-Soo . . . 521, 525
Lee, Hyun Woo . . . 509
Lee, Moon-Goo . . . 162, 199
Lee, Sangick . . . 661
Lee, Seok Woo . . . 509
Lee, Simon . . . 89
Lee, Sung-Q . . . 176
Lee, Wing-Bun . . . 546
Lehman, John . . . 182, 357, 478
Leinvuo, Joni T. . . . 256
Levy, Miguel . . . 27, 234
Liddle, Alexander . . . 83
Lin, Hung-Yih . . . 32
Liu, Xiaojun . . . 316
Liu, Xiong-Wei . . . 581
Liu, Yih-Hung . . . 32
Lu, Xiaoming . . . 387
Luca, Liviu . . . 110
Lumpp Jr., James E. . . . 187
Ma, Kung-Jinn . . . 32
Mahaddalkar, Prasanna M. . . . 515
Manske, Eberhard . . . 299
Marinescu, Ioan D. . . . 110, 591
Marla, Sudhakar . . . 13
Masaki, Takeshi . . . 16
Masuda, Masami . . . 626
Matsushita, Hiroyuki . . . 521
Matushita, Satoshi . . . 571
McGuirk, Michael . . . 244
Menguc, Pinar . . . 642
Michaels, Robert . . . 89
Miller, Michele H. . . . 484, 515, 529
Mimura, Masato . . . 215
Mink, Ronald . . . 73
Mino, Masayuki . . . 460
Mishima, Nozomu . . . 210
Mito, Masami . . . 538
Mitsui, Kimiyuki . . . 343
Mitsuishi, Mamoru . . . 310
Miyoshi, Takashi . . . 37, 41, 367
Mohri, Naotake . . . 585
Moon, Kee S. . . . 27, 234
Moon, Young Hoon . . . 671
Moro, Toshio . . . 585
Morsbach, Caspar . . . 562
Müller, Uwe R. . . . 13
Muralikrishnan, Bala . . . 434
Nagata, Akiko . . . 465
Nakamura, Takashi . . . 332
Nakao, Masayuki . . . 20, 24
Nakao, Yohichi . . . 215

*Abstract unavailable at press time.

Namba Ph.D., Yoshiharu 450
Narayanasamy, K. 667
Neagu-Ventzel, Sorin 110
Negishi, Nobuhiko 115
Nguyen, Trong Hieu 332
Nishikawa, Masatoshi 367
Nitoh, Shinnosuke 219
Nokura, K. 501
Nomura, Takashi 460, 465
Norlund, Bruce K. 126
Novak, Erik L. 53
O, K. 446
Ogura, Ichiro 349
Ohguro, Noriyuki 332
Ohl, Raymond G. 73
Ohnishi, Naoyuki 450
Okazaki, Yuichi 349
Okuda, Seiichi 460, 465
Okuyama, Shigeki 505
Olszak, Artur G. 53
Ooi, Takeshi 20
Orji, Ndubuisi George 63
Park, Boumyoung 661
Park, Han-soo 250
Park, Jeong Woo 671
Park, Kang-Ho 176
Pati, Gour Shyam 83
Patno, Tim 13
Patterson, Steven R. 144, 324, 353, 474
Paul, Brian K. 138
Pavel, Radu 591
Petri, Patrick A. 285
Picard, Yoosuf 613
Porto, Arthur J. Vieira 602
Preuss, Werner R. 542
Procop, M. 57
Qin, P. 320
Rachakonda, Prem Kumar 357
Raja, Jayaraman 421, 434, 634
Raju, H.P. 63, 667
Ramesh, K. 495
Rao, Apparao M. 642
Rawasdeh, Osamah A 187
Ren, Dongmei 353
Rerkkumsup, Pongpun 373
Rhee, Hyug-Gyo 411
Rhorer, Richard L. 166
Robertson, Alec P. 223
Roblee, Jeffrey W. 126
Rodriguez, Marcos E. 279
Ruiz-Huerta, Leopoldo 228, 377
Ruoff, Wolfgang 152
Rzepniewski, Adam 223
Sadakata, Shin 373
Saito, Hiroshi 626
Saito, Nagao 585
Saito, Teruaki 438
Sakamaki, Yuki 20
Sakamoto, Shigehiko 597, 689
Salsbury, James G. 407
Sata, Toshio 585
Schädlich, S. 57
Schattenburg, Mark Lee 83, 244, 261
Schindler, A. 57
Schlueter, James . . . . . *
Schmit, Joanna 53
Schmitz, Tony L. 132
Schott, Walter 67, 299
Sebring, Robert . . . . . *
Shakarji, Craig M. 100
Shikauchi, Takeshi 521
Shim, Jong Youp 170
Shimizu, Hiroki 363
Shimizu, Jun 534
Shimizu, Shinji 396
Shinohara, Kazuhiro 534
Shirai, Kenji 219
Shiramatsu, Toshiya 343
Shreve, Shelby M. 182
Silva, Helder Augustus Treviso 602
Singaperumal, Makaram 415
Sinram, Keith 591
Slocum, Alexander H. 193, 223, 244, 305
Smith, Philip T. 454
Smith, Scott . . . . . *
Sohn, Alex 73, 115, 618
Somashekhar, S. Hiremath 415
Song, Ki-Bong 176
Soons, Johannes A. 132
Sousa, André Roberto 238
Spence, Allan D. 383
Spenko, Matthew J. 244, 261
Stein, Andrew J. 77
Storhoff, James 13
Stümpel, J. 57
Sudoh, Masasyu 538
Summerhays, Kim Dennis 47
Sun, Yanxia 244, 261
Sunada, Hirotaka 638
Suwabe, Hitoshi 501
Suzuki, Hirofumi 505
Szulczynski, Hubert 677
Takada, Koji 373
Takahashi, Satoru 32, 41, 367
Takakura, Susumu 689
Takaya, Yasuhiro 32, 41, 367
Take, Y. 501
Takubo, Hideharu 271
Tangpornprasert, Pairat 310
Tao, Zhengsu 442

*Abstract unavailable at press time.

Tashiro, Hatsuzo 460, 465
Thomsen-Schmidt, P. 57
Togawa, Kazuhito 438
Tran, Hy D. 267, 387, 630
Tricard, Marc 120
Trinkle, Christine Anne 642
Tronolone, Mark J. 89
Trumper, David L. 77
Tse, S. 320
Tsuchiya, Kensuke 20
Tushingham, Roger . . . . . *
Uhlmann, Eckart 677
Ulm, G. 57
Uneda, M. 501
Uppliappan, Babu 421
Valente, Carlos M. O. 607
Vallance, Robert R. . 182, 187, 357, 391, 454, 478, 642
Vasile, Michael J. 613
Veiga, Celso Luis 238
Velasco-Herrera, Graciela 377
Venkatachalam, Siva 421
Vorburger, Theodore V. 63
Wada, Toshihiko 16
Wakatomo, Toshihiro 505
Walcott, Bruce L. 187
Walter, Mark M. 126
Wang, Youjin 320, 470
Warisawa, Shin'ichi 310
Watanabe, Takahiro 339
Watanabe, Takaya 683
Watanabe, Tomonori 373
Wattanutchariya, Wassanai 138
Webb, Dave 581
Whatmore, R. W. 256
Wilhelm, Robert G. 429
Willemann, D. P. 238
Wilson, S. A. 256
Wolsing, Eric 391
Woronko, Andrew 94
Xie, Guangping 470
Xie, T. 446, 474
Yamada, Hisashi 585
Yamada, Takazo 521, 525
Yamaguchi, Y. 425
Yamanaka, Masashi 295
Yamazaki, Hiroshi 328
Yamazaki, Kazuo 425
Yanagi, Kazuhisa 438, 647
Yasui, Heiji 597, 689
Yin, Ling 495
Yoda, Makoto 24
Yokoyama, Sakari 525
Yoshida, Kunio 450
Yuen, K. 316
Yuen, Po Ki 13
Yui, Akinori 495, 505
Zeng, W. 446
Zhang, Jun 657
Zhang, Liang 474
Zhang, Ping 529
Zhang, Shuqing 324
Zhang, Xingquan 425, 647
Zhang, Yi 267
Zhao, Xiaoping 429
Zhao, Yongshun 647
Zhou, Libo 534
Zirn, Oliver 152

*Abstract unavailable at press time.